JOURNAL
OF THE
PHYSICAL SOCIETY
OF JAPAN

Volume 7
1952

Published by the
PHYSICAL SOCIETY OF JAPAN

JOURNAL OF THE PHYSICAL SOCIETY O JAPAN Vol. 7, No. 1, JAN.—FEB., 1952

Transition Energy and Volume Change at Three Transitions in Barium Titanate

By Gen SHIRANE and Akitsu TAKEDA*

Tokyo Institute of Technology, Oh-okayama, Tokyo

(Received April 26, 1951)

The specific heat and thermal expansion of high purity $BaTiO_3$ ceramics have been measured at temperatures from −120° to 150°C with the following results:

	transition energy	volume change
127°C	50 cal/mole	-0.062 A³
16°C	22 cal/mole	-0.014 A³
−73°C	8 cal/mole	$+0.006$ A³

These informations allow us to calculate the shifting rate of the transition temperature by hydrostatic pressure according to the Clapeyron-Clausius equation; the calculated values are in satisfactory agreement with the observations by Merz.

§1. Introduction.

Barium titanate has attracted much interest in recent years because of its peculiar ferroelectric properties. Though extensive progress[2] has been made in the study of the dielectric and structural properties of barium titanate, especially of the behavior at the three transitions in this crystal, yet exact knowledge of some important quantities are lacking, or at least insufficient, for a satisfactory explanation of these three transitions from a theoretical point of view.

With respect to the specific heat anomaly at the transition near 120°C several measurements[3)~6)] have been reported but they are not always in good agreement with each other. Though the specific heat anomaly at the transition near 0°C was also reported by Blattner, Känzig and Merz,[6] no results on the lowest transition near −80°C appear to have been published. To obtain a more detailed and reliable information concerning the specific heat anomalies at all three transitions, we have measured the specific heat of this substance at temperatures from −120°C to 150°C using high purity ceramics and single crystals as well.

X-ray study by Kay and Vousden[7] and by Rhodes[8] has clearly revealed the structure changes at the lower two transitions. But with respect to the volume change at the three transitions, which should have intimate relation to the change of spontaneous polarization at these points, no qualitative agreement has been obtained among these X-ray data, dilatometric ones[6) 9)] and theoretical values of Devonshire[10]. So we have also carried out a dilatometric measurement of our high purity ceramics in order to obtain exact values of the volume changes at respective three transitions.

§2. Specimen.

The ceramic specimens were prepared from high purity TiO_2 (99.2%) and $BaCO_3$ (99.6%) by a process of sintering at about 1400°C after preliminary calcination. By this refiring process we were able to obtain well sintered matures. Dielectric constant of this specimen shows three peaks at −73°C, 16°C and 127°C, corresponding respectively to the well known three transitions in this substance (Fig. 1). The very sharply defined maximum of permittivity at 127°C proves high purity of our ingredients.

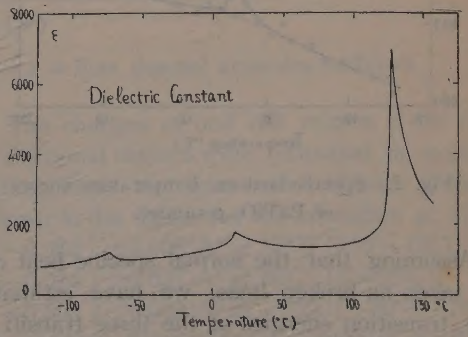

Fig. 1. Dielectric constant of $BaTiO_3$ ceramics at rising temperature (1 MC/sec).

---

* Now at Kobayashi Institute of Physical Research, Kokubunji, Tokyo.

§ 3. Specific Heat.

We have constructed an adiabatic calorimeter of Nagasaki-Takagi type,[11] which is an improvement of Sykes' one.[12] Our apparatus is, in principle, completely similar to the previous ones[6] [11], but a few points were modified to make it more suitable for low temperature measurement.

Powdered ceramics of about 25 g, contained in a thin glass vessel of 3.5 g, was heated by a rate of about 1°C/min. The heat capacity of empty calorimeter was determined by using silica sand as standard substance. Measurements were carried out in vacuum. Specific heat versus temperature curves for the ceramics are shown in Fig. 2.

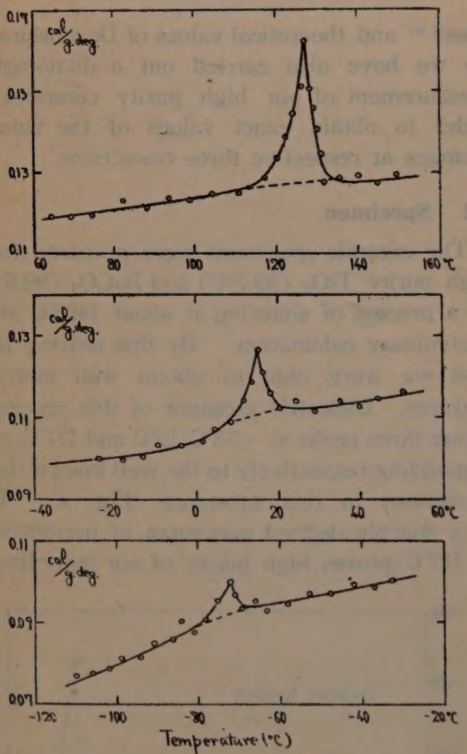

Fig. 2. Specific heat *vs.* temperature curves of $BaTiO_3$ ceramics.

Assuming that the normal specific heat can be taken as broken lines, we have estimated the transition energies at the three transitions as follows:

50 (±5) cal/mole at 127°C (115~135°C),
22 (±4) cal/mole at 16°C (8°~20°C),
8 (±2) cal/mole at −73°C (−79°~−69°C).

For comparison, we have measured the specific heat of single crystals which were obtained from ternary melts. A mass of small single crystals of about 25g was contained in the same glass vessel and measurements were carried out under completely the same condition as that used for ceramics. The results are shown in Fig. 3 from which the transition energies were estimated as follows:

52 cal/mole at 115°C,
20 cal/mole at 3°C,
6 cal/mole at −74°C.

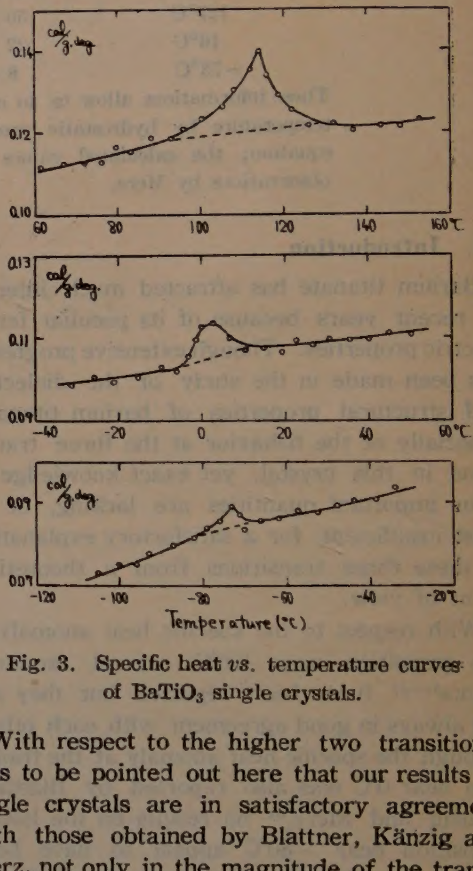

Fig. 3. Specific heat *vs.* temperature curves of $BaTiO_3$ single crystals.

With respect to the higher two transitions, it is to be pointed out here that our results on single crystals are in satisfactory agreement with those obtained by Blattner, Känzig and Merz, not only in the magnitude of the transition energies but also in the characteristic forms of the anomalous specific heat. It can be seen from Figs. 2 and 3 that the specific heat curves for a mass of single crystals are less sharp than those for ceramics. This may be presumably attributed to a little fluctuation in the transition temperature of each individual single crystal due to impurities which are inevitably included in the process of precipitation from the melt.

With respect to the Curie point at 120°C, two types of specific heat anomaly have been reported; the one[3] [4] is the abrupt change of the specific heat at the transition point and the other5) 6) is the peak of specific heat at this point. Our results, especially the curve for high purity ceramics, clearly show the rather sharp maximum of specific heat at the transition point suggesting the existence of latent heat.

Main part of the each transition energy at the three transitions may be a latent heat, but it is difficult to separate the latent heat from the total transition energy. Magnitude of the transition energies at the three transitions, at least in relative ratio, are in qualitative agreement with theoretical values given by Devonshire.

§ 4. Thermal Expansion.

Linear thermal expansion of the same ceramics has been measured at temperatures from −170° to 200°C. The dilatometric test sample has a cylindrical form, 3 cm in length and 4 mm in diameter. Differential dilatation of this specimen relative to a silica rod was magnified about 1000 times as large by means of an optical lever. Measuring limit of this apparatus is about $\Delta l/l=3\times10^{-6}$. Fig. 4 shows the heating curve of $l-l_0/l_0$ where l_0 denotes the length of the specimen at 0°C. Linear thermal expansion coefficient β is also plotted in the same figure. Cooling curve shows the same characteristics except a small temperature hysteresis at the transitions.

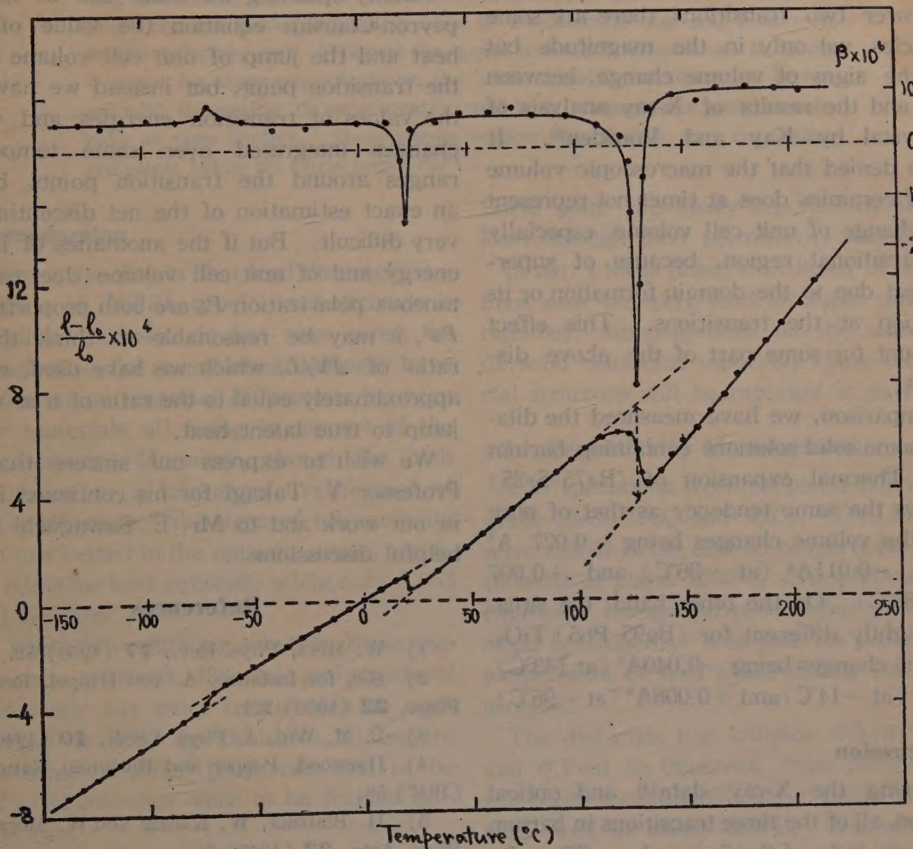

Fig. 4. Thermal expansion of BaTiO$_3$ ceramics; β is liner thermal expansion coefficient

The changes of unit cell volume at the three transitional regions were estimated by extrapolation from the linear part of each phase as shown in the figure for the transition at 127°C.

−0.062 (±0.008)A^3 at 127°C (110°∼135°C),
−0.014 (±0.003)A^3 at 16°C (15°∼25°C),
+0.006 (±0.002)A^3 at −73°C (−80°∼−70°C).

In addition, linear thermal expansion coefficient of this specimen was estimated for each phase as follows:

9.8×10^{-6}/°C above 127°C (Cubic phase),

6.5×10^{-6}/°C	127°~16°C	(Tetragonal phase),
4.6×10^{-6}/°C	16°~−73°C	(Orthorhombic phase),
5.2×10^{-6}/°C	below −73°C	(Trigonal phase).

With respect to the volume contraction at 120°C, our result shows qualitative agreement with the former dilatometric and X-ray measurements. But the observed contraction of our high purity ceramics is rather sharper and larger than the former ones. Concerning the volume changes at the lower two transitions there are some discrepancies, not only in the magnitude but also in the signs of volume change, between our data and the results of X-ray analysis of single crystal by Kay and Vousden⁷⁾. It cannot be denied that the macroscopic volume change of ceramics does at times not represent the true change of unit cell volume, especially at the transitional region, because of superfluous effect due to the domain formation or its reorientation at the transitions. This effect may account for some part of the above discrepancies.

For comparison, we have measured the dilatation of some solid solutions containing barium titanate. Thermal expansion of (Ba75-Sr25) TiO_3 shows the same tendency as that of pure $BaTiO_3$, the volume changes being −0.027 A^3 (at 34°C), −0.011A^3 (at −36°C) and +0.007 A^3 (at −86°C). On the other hand, the situation is slightly different for (Ba95-Pb5) TiO_3, the volume changes being −0.040A^3 (at 143°C), +0.007A^3 (at −14°C) and +0.006A^3 (at −96°C).

§ 5. Discussion.

Considering the X-ray data¹³⁾ and optical observation, all of the three transitions in barium titanate seem to be of the first order. Then the informations on transition energies and volume changes allow us to calculate the shifting rate of each transition point by hydrostatic pressure according to the Clapeyron-Clausius equation, i.e., $dTc/dP=Tc\cdot\varDelta V/L$ where Tc denotes transition temperature, L latent heat, $\varDelta V$ the volume change. With the observed values of L and $\varDelta V$, we get for the values of dTc/dP at the three transitions as shown in Table I. Concerning the higher two transitions, calculated values are in satisfactory agreement with direct observation by Merz¹⁾, which is also shown in Table I. Unfortunately, effect of the hydrostatic pressure on the lowest transition point has not been reported.

Table I.

L (cal/ mole)	ΔV (A^3)	dTc/dP (deg. cm^2/ dyne)	dTc/dP (by Merz)
127°C 50	−0.062	-6.7×10^{-9}	-5.7×10^{-9}
17°C 22	−0.014	-2.6×10^{-9}	-2.9×10^{-9}
−73°C 8	+0.006	$+2.0\times10^{-9}$	—

Strictly speaking we must use in the Clapeyron-Clausius equation the value of latent heat and the jump of unit cell volume just at the transition point, but instead we have used the values of transition energies and volume changes integrated over some temperature ranges around the transition points, because an exact estimation of the net discontinuity is very difficult. But if the anomalies of internal energy and of unit cell volume due to spontaneous polarization Ps are both proportional to Ps^2, it may be reasonable to think that the ratio of $\varDelta V/L$, which we have used, may be approximately equal to the ratio of true volume jump to true latent heat.

We wish to express our sincere thanks to Professor Y. Takagi for his continued interest in our work and to Mr. E. Sawaguchi for his helpful discussions.

References

1) W. Merz, Phys. Rev., **77** (1950) 52.
2) See, for instance, A. von Hippel, Rev. Mod. Phys., **22** (1950) 221.
3) B. M. Wul, J. Phys. USSR, **10** (1946) 95.
4) Harwood, Popper and Rushman, Nature, **160** (1947) 58.
5) H. Blattner, W. Känzig and W. Merz, Helv. Phys. Acta, **22** (1949) 35.
6) S. Sawada and G. Shirane, J. Phys. Soc. Japan, **4** (1949) 52.
7) H. F. Kay and P. Vousden, Phil. Mag. (7) **40** (1949) 1019.
8) R. Rhodes, Acta Cryst., **2** (1949) 417.
9) von Hippel, Breckenridge, Chesley and Tisza, Ind. Eng. Chem. **38** (1946) 1097.
10) A. F. Devonshire, Phil. Mag. (7) **40** (1949) 1040.
11) S. Nagasaki and Y. Takagi, J. App. Phys. Japan **17** (1948) 104.
12) C. Sykes, Proc. Roy. Soc., A **143** (1935) 422.
13) H. F. Kay, Acta Cryst., **1** (1948) 229.

JOURNAL OF THE PHYSICAL SOCIETY OF JAPAN Vol. 7, No. 1, JAN.—FEB., 1952

Phase Transitions in Solid Solutions of $PbZrO_3$ and $PbTiO_3$ (I) Small Concentrations of $PbTiO_3$

By Gen SHIRANE and Akitsu TAKEDA
Tokyo Institute of Technology, Oh-okayama, Tokyo

(Received March 23, 1951)

The dielectric, calorimetric and dilatometric measurements have been made on the solid solutions $Pb(Zr\text{-}Ti)O_3$ which contain small amounts of $PbTiO_3$ less than 10%. Besides the ordinary Curie point near 220°C, the existence of another transition, for example 140°C in $Pb(Zr95\text{-}Ti5)O_3$, was confirmed. It seems reasonable to interpret these two transitions as phase changes from paraelectric state to ferroelectric one and further to antiferroelectric one. Whereas the upper transition temperature is nearly constant for these concentrations, the lower transition temperature increases with decreasing Ti concentration and both temperatures seem to coincide at pure $PbZrO_3$. These results suggest that $PbZrO_3$ may be antiferroelectric below its Curie point 220°C.

§ 1. Introduction.

Whereas it is certain that lead titanate[1] is a ferroelectric of $BaTiO_3$ type[2], lead zirconate is not at all a ferroelectric but may surely be antiferroelectric, for recent investigations[3] have established many essential differences between the two materials all being in support of the above statement. Moreover, though the both are belonging to a tetragonal modification of perovskite structure,[4] the signs of tetragonality of them are indeed in the opposite sense, namely $c/a=0.988$ for lead zirconate while $c/a=1.063$ for lead titanate.

It is worth investigating whether these two characteristic contrasts, dielectric and structural ones, do imply any inner relationship to each other. And it may be desirable to inquire whether some peculiar properties are to be found if solid solutions were to be formed between the two.

Fortunately Waku and Hori[5] found in 1949 that these two materials really form solid solutions. But since they believed at that time the components are both ferroelectrics, they paid no special attention to the most interesting region, that is the very region wherein the tetragonality of the mixed crystal approaches unity. Now we have carried out detailed investigations on specific heat, thermal expansion and crystal structure as well as dielectric properties over the whole concentration range of this binary system, and we found in solid solutions containing small amounts of $PbTiO_3$ the existence of another transition besides the ordinary Curie point previously reported by Waku and Hori through their permittivity measurements.

In part I these phase transitions in solid solutions near the pure lead zirconate side shall be reported. Investigations on the whole range of solid solutions, especially those on the crystal structure will be reported in part II.

§ 2. Permittivity Measurement.

The specimens were prepared from reagent-grade PbO, ZrO_2 and TiO_2. The ingredients were mixed in the desired proportions and then sintered at about 1200°C after preliminary calcination. No special precaution, such as described by Roberts,[6] was paid for preventing the evaporation of lead oxide during the sintering process.

The dielectric test samples, 0.5 cm^2 in area and 0.1 cm in thickness, were coated on both sides with a conductive silver paint, which was then fired at about 600°C. The capacity of these specimens was measured by a resonance method at a frequency of 1MC/sec and a field strength of about 10V/cm.

Fig. 1 shows the dielectric constant versus rising temperature curves for $PbZrO_3$, $Pb(Zr95\text{-}Ti5)O_3$ and $Pb(Zr90\text{-}Ti10)O_3$. With increasing $PbTiO_3$ concentration, the Curie point of these solid solutions at first slightly decreases from 220°C of pure $PbZrO_3$[3)6)] and then increases towards 490°C for pure $PbTiO_3$[1)].

In $Pb(Zr97.5\text{-}Ti2.5)O_3$, another small peak was observed at 180°C besides the sharp maximum at the Curie point. This small peak corresponds to another transition as shown in the following sections. In Pb(Zr95–Ti5)O_3 a small peak of this type was observed at 140°C, and then the temperature of its occurrence thus turned out to decrease with increasing Ti concentration.

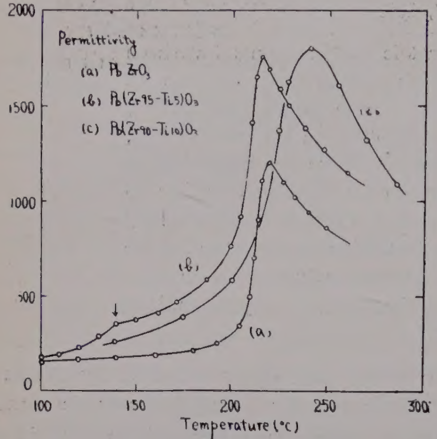

Fig. 1. Dielectric constant of $PbZrO_3$, Pb(Zr95–Ti5)O_3 and Pb(Zr90–Ti10)O_3.

§ 3. Hysteresis Loops.

Dielectric properties of these solid solutions were also studied from the temperature dependence of hysteresis loops using a method slightly modified from Sawyer and Tower's[7]. All specimens are of nearly the same dimensions, 1.0 cm² in area and 0.1 cm in thickness. Measurement was made in a liquid paraffin which was being stirred vigorously in order to obtain the uniformity of the temperature. A.C. field of 50 cycle/sec and $E_{max}=17KV/cm$ was mostly applied.

Hysteresis loops of Pb(Zr95–Ti5)O_3 clearly show the ferroelectric characteristic at temperatures from 140° to 215°C as shown in Fig. 2. Though these hysteresis loops do not show sufficient saturation at this field strength of 17KV/cm, yet we can roughly estimate the spontaneous polarization from these figures. Fig. 4 shows the maximum polarization P_m, the remanence polarization P_r and the spontaneous polarization P_s at rising temperature. The residual polarization above the Curie point may be accounted for by the conduction term at these relatively high temperatures. So we assume that the broken line shown in the figure can be interpreted as a superfluous effect due to increasing conductivities.

The spontaneous polarization of Pb(Zr95–Ti5)O_3 is shown in Fig. 5. As seen in the figure, a large temperature hysteresis was observed at the lower transition point of 140°C.

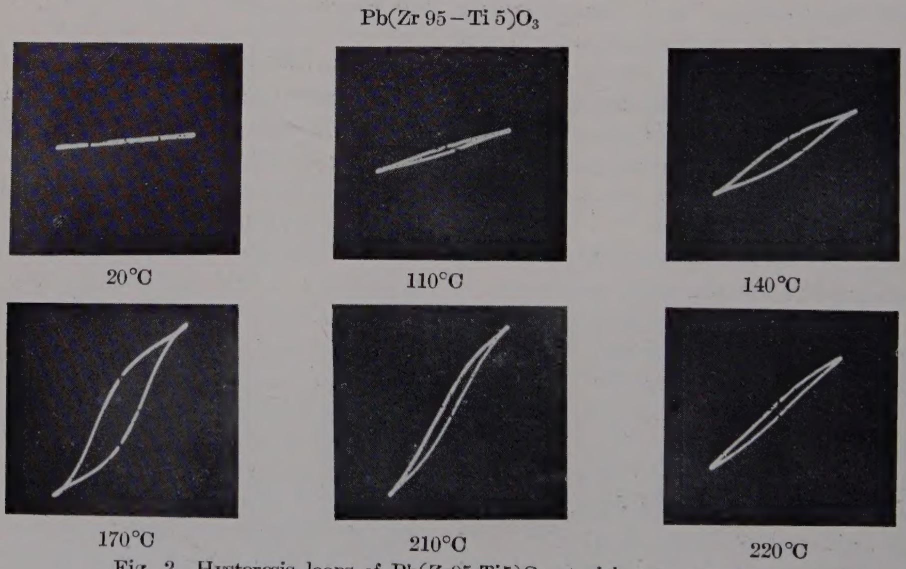

20°C 110°C 140°C

170°C 210°C 220°C

Fig. 2 Hysteresis loops of Pb(Zr95-Ti5)O_3 at rising temperature. $E_{max}=17$ KV/cm.

It must be noticed that a small peak at 140°C in the permittivity curve is just corresponding to the appearance of the spontaneous polarization at this point. This result is to be compared with the case of pure $PbZrO_3$[3], of which the hysteresis loops are almost always linear below the Curie point. The hysteresis loops of Pb(Zr90–Ti10)O_3 show the ferroelectric characteristic even at room temperature (Fig. 3). This fact suggests that the lower transition may

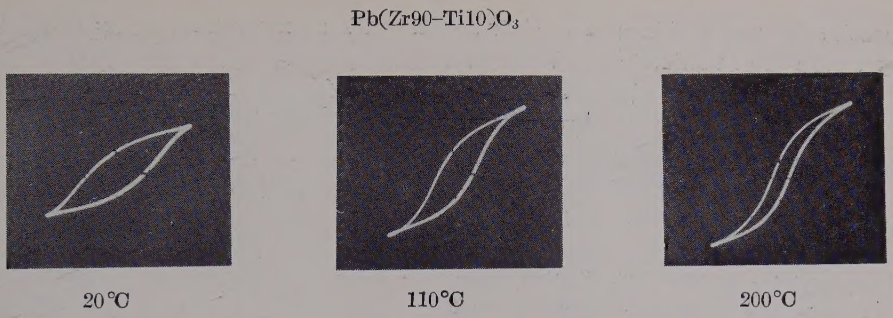

20°C 110°C 200°C

Fig 3 Hysteresis loops of Pb(Zr90-Ti10)O$_3$. E_{max}=20/KVcm.

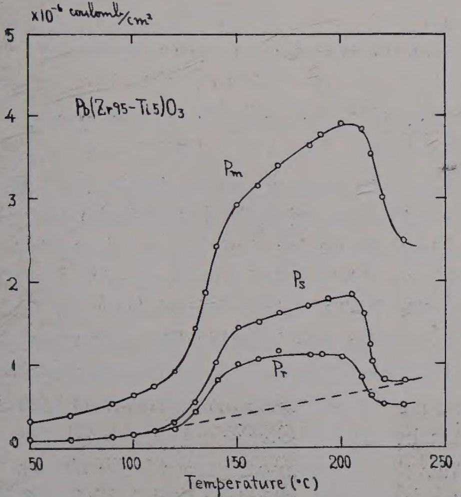

Fig. 4. Maximum polarization P_m, remanence polarization P_r and spontaneous polarization P_s of Pb(Zr95-Ti5)O$_3$ at rising temperature.

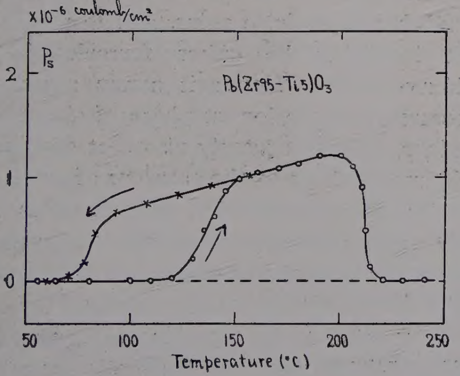

Fig. 5. Spontaneous polarization of Pb(Zr95-Ti5)O$_3$ at varying temperature, heating and cooling rate being about 1°C/min.

occur below the room temperature for this substance.

§ 4. Effect of D.C. Biasing Field on the Permittivity.

A study was made of the effect of a D.C. biasing field of 10KV/cm upon the dielectric constant of Pb(Zr95-Ti5)O$_3$ with the result shown in Fig. 6. Above the lower transition temperature of 140°C, remarkable decrease of permittivity was observed and at the same time the Curie point of 215°C was raised by about 5°C. These phenomena are quite similar to those found in BaTiO$_3$[8)9)], and, combined with the data of the spontaneous polarization, show therefore that the intermediate phase of this material between 140°C and 215°C is surely a ferroelectric one.

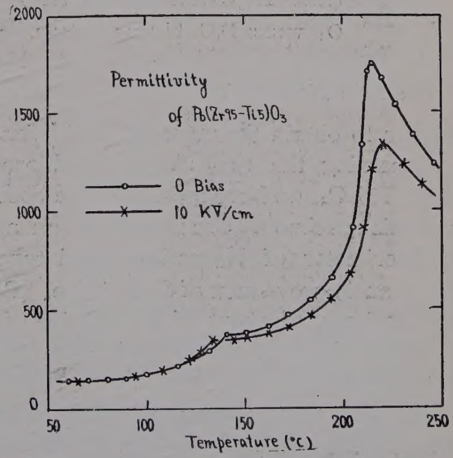

Fig. 6. Effect of D.C. biasing field of 10KV/cm upon the permittivity of Pb(Zr95-Ti5)O$_3$ at rising temperature.

On the other hand, below 140°C, the only effect of biasing field is to shift this transition point towards lower temperature by about 5°C.

These opposite signs of shiftings of the transition temperature are in intimate relation to the changes of spontaneous polarization at these points and will be discussed in the next section.

Fig. 7 shows the dielectric constant of $PbZrO_3$, $Pb(Zr95-Ti5)O_3$ and $Pb(Zr90-Ti10)O_3$ measured at room temperature (15°C) and at 1MC/sec versus the biasing voltage. Observed decrease of permittivity in $Pb(Zr90-Ti10)O_3$ is in accordance with the hysteresis loops of this substance shown in Fig. 3.

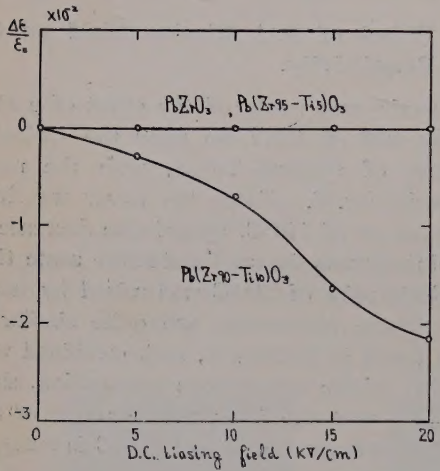

Fig. 7. Permittivity of $PbZrO_3$, $Pb(Zr95-Ti5)O_3$ and $Pb(Zr90-Ti10)O_3$ versus D.C. biasing voltage.

§ 5. Specific Heat.

In order to obtain the more detailed information concerning the two phase transitions in $Pb(Zr95-Ti5)O_3$, we have measured the specific heat of this specimen. Use is made of an adiabatic calorimeter of Nagasaki-Takagi type[10]), which is an improvement of Sykes' one. Powdered specimen of about 25 g, contained in a glass vessel of 2.5 g, was heated by a rate of about 2°C/min.

Specific heat versus rising temperature curve of this specimen is shown in Fig. 8. This curve shows a small hump at about 140 C besides a sharp maximum at 215°C, and the transition energies are estimated respectively at 80 cal/mole and 180 cal/mole.

If we assume tentatively these transitions are of the first order, the Clapeyron-Clausius equation should be available at these points, i.e. $-dTc/dE=Tc\cdot\Delta Ps/L$ were Tc denotes the transition temperature, L the latent heat, ΔPs the jump of spontaneous polarization. With the observed value of dTc/dE and the transition energies, we get for the change of spontaneous polarization $\Delta Ps=10$ microcoulomb/cm² at 140°C and $\Delta Ps=-15$ microcoulomb/cm² at 215°C. These results are in tolerable agreement with direct observation on the oscillograph and suggest that the spontaneous polarization surely be absent below 140°C.

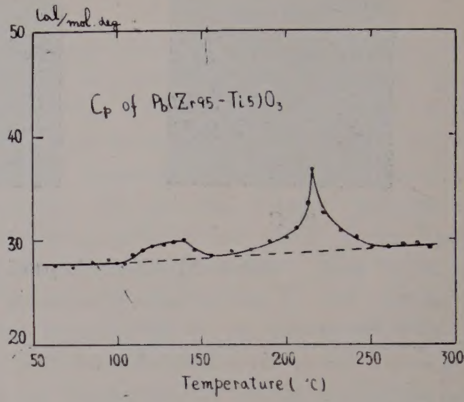

Fig. 8. Specific heat of $Pb(Zr95-Ti5)O_3$

Thus the above experiments have shown that in the lowest phase below 140°C, $Pb(Zr95-Ti5)O_3$ may not have spontaneous polarization at all, so, if it were truly so, this phase should necessarily be either paraelectric or antiferroelectric. Now as will be shown in the phase diagram (Fig. 13), this lowest phase has to be continuously connected to the phase of pure $PbZrO_3$ below its Curie point, and this, clearly, must inevitably be either ferroelectric or antiferroelectric. Hence it seems reasonable to assume that the lowest phase of above solid solutions, and consequently also that of $PbZrO_3$ itself, may belong to the category of antiferroelectrics, namely, in which each dipole is certainly subject to some restraint but its alignment never amounts to a net polarization as a whole.

Fig. 9. shows the specific heat curve of $Pb(Zr97.5-Ti2.5)O_3$, in which the lower transition was observed at 180°C in the permittivity measurement. As might have been expected, two peaks were really observed in this curve, and the transition energies are estimated at 130 cal/mole (at 180°C) and 160 cal/mole (at 220°C).

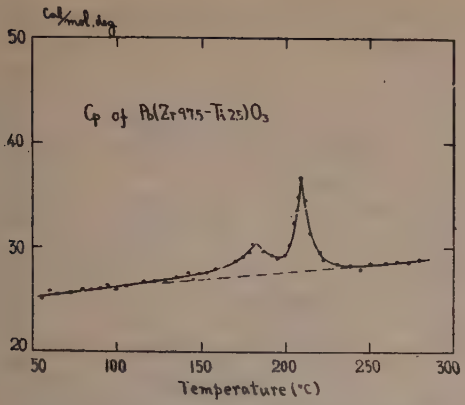

Fig. 9. Specific heat of Pb(97.5-Ti2.5)O$_3$

§ 6. Dielectric Residual Polarization.

Though above experiments, especially the observation on an oscillograph, have shown that the spontaneous polarization of Pb(Zr95-Ti5)O$_3$ really disappears below 140°C, leading us to the assumption of antiferroelectricity of the lowest phase, yet the similar phenomena would be observed if, alternatively, the coercive field were to increase suddenly at 140°C leaving the intrinsic polarization unchanged. To criticize the latter possibility more directly, we have carried out the following experiments.

It is well known that BaTiO$_3$ ceramics can be permanently polarized by an adequate input of high D.C. field[3]. So, for the measurement of the residual polarization of Pb(Zr95-Ti5)O$_3$, we have used the same specimen as that for the observation of hysteresis loops. At 160°C, which is in ferroelectric region, both electrodes of the specimen were at first connected to a biasing D.C. voltage of 10KV/cm for 5 minutes and then to a galvanometer circuit. After an initial discharging current had disappeared, we raised the temperature at a constant rate and found a sharp maximum of discharging current at the Curie point, as shown schematically in Fig. 10(a). This phenomenon is quite similar to that observed in barium titanate ceramics.[11]

After the same polarizing treatment at 160°C, now the temperature was lowered at the same rate as in heating. We observed, in this case too, a discharging current shown in Fig. 10(b) with a rather flat maximum at 80°C, which corresponds to the lower transition point on cooling(Fig. 5). What is to be noticed here is that the time integral of discharging current on heating is nearly the same order of magnitude as that on cooling. This seems to add another support to the statement that the spontaneous polarization in the lowest phase be surely absent. No discharging current was observed at any temperature if the same polarizing treatment was carried out at room temperature.

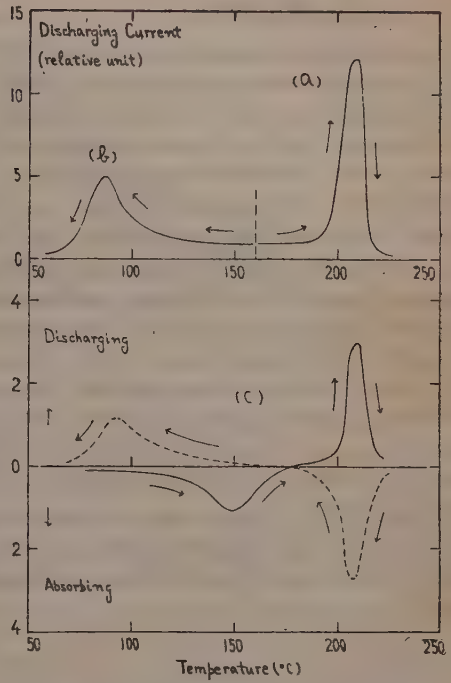

Fig. 10. Schematic diagram of discharging and absorbing currents of Pb(Zr95-Ti5)O$_3$ when the temperature is raised or cooled by a constant rate.
(a), (b) discharging current after polarizing treatment at 160°C. (C) absorbing and discharging current without polarizing treatment.

In the course of above experiments, we found the following interesting phenomenon. Once the specimen is highly polarized in ferroelectric region, it begins to show an absorbing and discharging currents as shown in Fig. 10 (c), even after it is heated until above the Curie point. The currents are however not large and become the less pronounced as the more frequently is the heat treatment repeated. This phenomenon presumably may be due to som small internal strain perhaps made up initially by a polarizing field and lasting afterward until above the Curie point. If it is cooled again, this stress will tend to polarize the specimen to the original direction. Though quantitative conclusion has not yet been obtained, it seems that the observed currents in figure (c) are approximately proportional to temperature derivative of the value of spontaneous polarization shown in Fig. 5.

§ 7. Thermal Expansion.

Linear thermal expansion of Pb(Zr95–Ti5)O_3 was measured at temperatures from −150°C to 300°C, and the anomalous volume changes of this specimen give a further support for the validity of the assumption proposed above.

Dilatometric test samples were cut out from ceramic disks and have cylindrical form of 3 cm in length and 0.5 cm in diameter. Differential dilatation of this specimen against silica tube was magnified about 1000 times as large by means of an optical lever. Fig. 11 shows $(l-l_0)/l_0$ as a function of temperature, where l_0 is the length of the specimen at 0°C. Heating and cooling rate is about 1°C/min. This figure shows large anomalous volume changes at about 140°C and 215°C. Large thermal hysteresis on cooling is to be compared with the corresponding hysteresis of spontaneous polarization (Fig. 5).

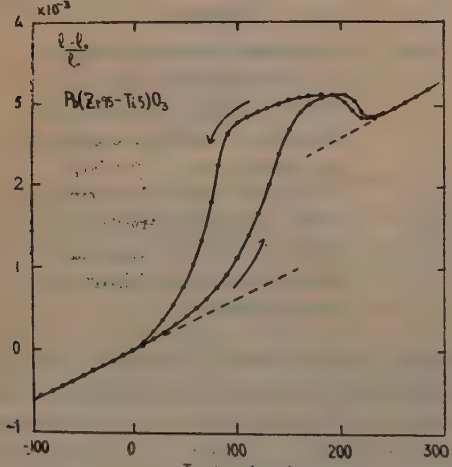

Fig. 11. Linear thermal expansion of Pb(Zr95–Ti5)O_3.

Comparison of this result with the volume changes observed in $PbZrO_3$[3)] and $BaTiO_3$[12)13)] clearly shows that the signs of volume changes at the two transitions are quite consistent with the assumed characteristics of the three phases of Pb(Zr–Ti)O_3. Namely, the volume contraction at 215°C is quite similar to that of barium titanate and so in good accordance with the well accepted behavior associated with a ferroelectric-paraelectric transition. On the other hand, the large volume expansion at the lower transition seems as if it were composed of two terms; one is due to the expansion characteristic of $PbZrO_3$ at its own transition point and the other is due to some anomalous expansion invariably associated with permanent polarization.

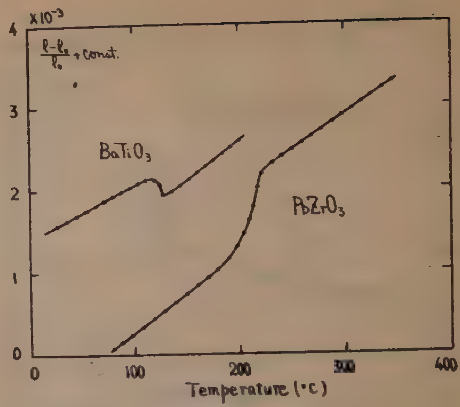

Fig. 12. Linear thermal expansion of $PbZrO_3$ and $BaTiO_3$.

§ 8. Phase Diagram and Discussion.

Investigations of Pb(Zr95–Ti5)O_3 have proved the existence of another transition at 140°C besides the ordinary Curie point. These transitions must be interpreted as phase changes from paraelectric state to ferroelectric one and further to antiferroelectric one. And the phase diagram of the $PbZrO_3$-$PbTiO_3$ system as shown in Fig. 13 has been obtained. As already shown in the case of hysteresis loops and thermal expansion, a large temperature hysteresis was observed at the lower transition. The lower phase boundary shown in the figure was determined from the measurements at rising temperature by a rate of about 1°C/min. What is to be emphasized here is that this phase diagram seems to support the assumption of antiferroelectricity of pure $PbZrO_3$ itself.

With increasing $PbTiO_3$ concentration, the lower transition becomes less sharp, perhaps on account of very slow rate of progress of transformation, so we cannot definitely determine the transition temperature if $PbTiO_3$ concentration becomes more than 7%. But the

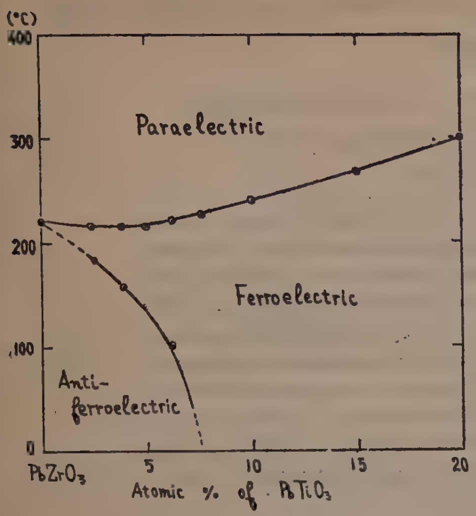

Fig. 13. Phase diagram of the $PbZrO_3$–$PbTiO_3$ system.

border line may perhaps be between 7–7.5 in Ti concentration at the room temperature, for a study of the dielectric properties of Pb(Zr92.5–Ti7.5)O_3 shows that it is already ferroelectric at room temperature. An X-ray study of the crystal structure of this system performed at room temperature also draws a line of demarcation of different phases at these compositions. Details of X-ray study will be discussed in part II.

For the study of these solid solutions, especially of importance is the purity of ZrO_2, which usually contains Si and Ti as impurities. Spectroscopic analysis of our ZrO_2* shows the existence of a few percents of Si as impurity. Effect of this impurity on the phase diagram was examined from a preliminary study of dielectric properties of $PbZrO_3$ and Pb(Zr95–Ti5)O_3 prepared from ZrO_2 of high purity which contained as impurities only small amounts of Ti(0.21%), Si(0.03%) and Fe(0.05%). The phase transitions observed in these specimens are completely of the same nature as described above except that all the transition temperatures are higher than those of ordinary ones by about 10°～15°C. So we think that if we had been allowed to avail ourselves of ZrO_2 of high purity all through this experiment, we would be to obtain all phase boundaries higher than those in Fig. 13 each by about 10°～15°C.

In conclusion, we wish to express our sincere thanks to Professor Y. Takagi for his kind guidance in the course of this research and to Mr. C. Kanzaki for taking troubles of chemical analysis of pure ingredient. We are also grateful to Mr. J. Hori for stimulating our interest in this problem and to Mr. E. Sawaguchi for his helpful discussions.

References

1) G. Shirane and S. Hoshino, J. Phys. Soc. Japan. **6** (1951) 265.
2) See, for instance, A von Hippel, Rev. Mod. Phys., **22** (1950) 221.
3) E. Sawaguchi, G. Shirane and Y. Takagi, J. Phys. Soc. Japan, **6** (1951) 333.
4) H.D. Megaw, Proc. Phys. Soc. London, **58** (1946) 133.
5) S. Waku and J. Hori, reported at the Committee for the Piezoelectric Material, Tokyo, May 1, 1950.
6) S. Roberts, J. Am. Ceram. Soc., **33** (1950) 63.
7) C. Sawyer and C. Tower, Phys. Rev., **35** (1930) 269.
8) S. Roberts, Phys. Rev., **71** (1947) 890.
9) L.E. Cross, A.T. Dennison, M.M. Nicolson and R. Whiddington, Nature, **163** (1949) 635.
10) S. Nagasaki and Y. Takagi, J. App. Phys. Japan, **17** (1948) 104.
11) E. Sawaguchi and T. Akioka, J. Phys. Soc. Japan, **4** (1949) 117.
12) S. Sawada and G. Shirane, J. Phys. Soc. Japan, **4** (1949) 52.
13) G. Shirane and A. Takeda, J. Phys. Soc. Japan, **6** (1951) 128.

---

* This ZrO_2 is not the same chemicals used for the previous investigation on $PbZrO_3$³⁾ by Sawaguchi, Takagi and one of the authors.

JOURNAL OF THE PHYSICAL SOCIETY OF JAPAN Vol. 7, No. 1, JAN.-FEB. 1952

Phase Transitions in Solid Solutions of $PbZrO_3$ and $PbTiO_3$ (II) X-ray Study

By Gen SHIRANE, Kazuo SUZUKI and Akitsu TAKEDA
Tokyo Institute of Technology, Oh-okayama, Tokyo

(Received March 23, 1951)

The phase diagram of the whole range of the $PbZrO_3$-$PbTiO_3$ system was determined by the dielectric and dilatometric measurements. According to the reason shown in part I, this phase diagram can be divided into three regions; paraelectric, ferroelectric and antiferroelectric phases. The crystal structure of this system was determined by the Debye photographs. In the antiferroelectric region solid solutions have a tetragonal modification of perovskite structure with $c/a<1$ and have some superstructure which seems to have intimate relation to the antiferroelectricity. In the ferroelectric region, except a region near antiferroelectric phase in which pseudo-cubic structure is observed, they have ordinary tetragonal structure of $c/a>1$ without any superstructure.

§ 1. Introduction.

In part I[1)] of this paper, an investigation was made on solid solutions of $PbZrO_3$ and $PbTiO_3$ ranging from pure $PbZrO_3$ to $Pb(Zr90-Ti10)O_3$. Now, a more thorough study has been made of the whole range of $Pb(Zr-Ti)O_3$ system by using dielectric, dilatometric and X-ray methods.

According to Megaw[2)], crystal structure of pure $PbZrO_3$ and $PbTiO_3$ belong to tetragonal modification of perovskite structure with the following lattice constants:

	a(A)	c/a
$PbZrO_3$	4.1503 (±0.001)	0.988 (±0.001)
$PbTiO_3$	3.8966 (±0.001)	1.0635 (±0.001)

It is a noticeable fact that the tetragonality of $PbZrO_3$ is less than unity in marked contrast with the case of lead titanate which has a tetragonality considerably larger than unity, so that it seems to be very interesting to study the variation of tetragonality of $Pb(Zr-Ti)O_3$ series as a function of concentration and its bearing upon the dielectric properties.

§ 2. Phase Diagram.

For the first place, we have determined the phase diagram of the whole range of this $Pb(Zr-Ti)O_3$ system by permittivity measurements. Fig. 1 shows permittivity versus rising temperature curves for a number of solid solutions. Dielectric constant of these specimens was measured at 1 MC/sec by a resonance method. Measurements were rather difficult for solid solutions containing $PbTiO_3$ more than 50% because of their high Curie temperature and of their increasing porosity. Above the Curie point, it was found that the Curie-Weiss law $\varepsilon=C/(T-T_p)$ holds sufficiently well for all specimens with the Curie constant $C=8\sim10\times10^4$°C. The phase diagram of this system thus determined is shown in Fig. 2.

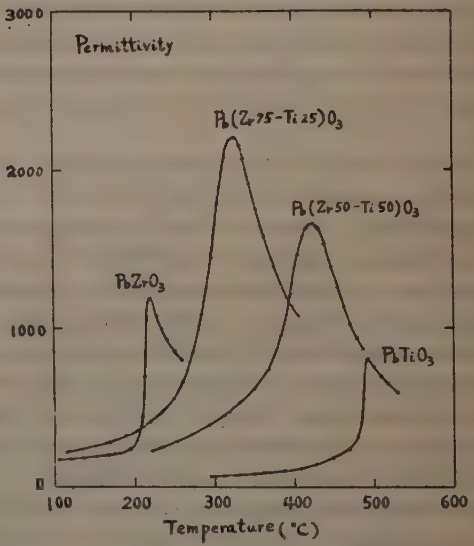

Fig. 1. Dielectric constant of $Pb(Zr-Ti)O_3$ compositions at rising temperature,

As for the reason why we have classified the left hand lowest corner of this phase diagram as an antiferroelectric region, the reader may refer to the part I, in which it was shown that all anomalies at this transition point can be well explained only if the above classification were accepted.

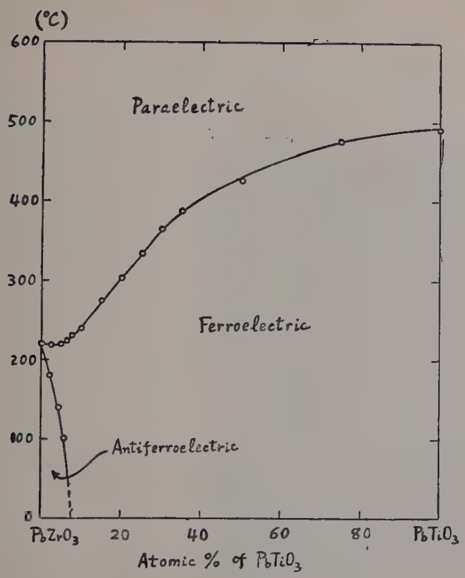

Fig. 2. Phase diagram of the PbZrO$_3$–PbTiO$_3$ system.

§ 3. Crystal Structure at Room Temperature.

A series of Debye photographs of powdered specimens were taken over whole range of Pb(Zr–Ti)O$_3$ compositions by using Cu Kα radiation. The camera radius was about 35 mm. All the photographs taken at room temperature were well explained by assuming tetragonal structures of perovskite type, except some weak lines found in solid solutions near the pure PbZrO$_3$ side. The lattice constants and the axial ratio c/a were calculated mainly from (*510*), (*143*) and (*134*) lines on photographs taken by back reflection method. The results are shown in Figs. 3 and 4. Figs. 5 shows a unit cell volume a^2c versus composition curve. All the numerical data are presented in Table I.

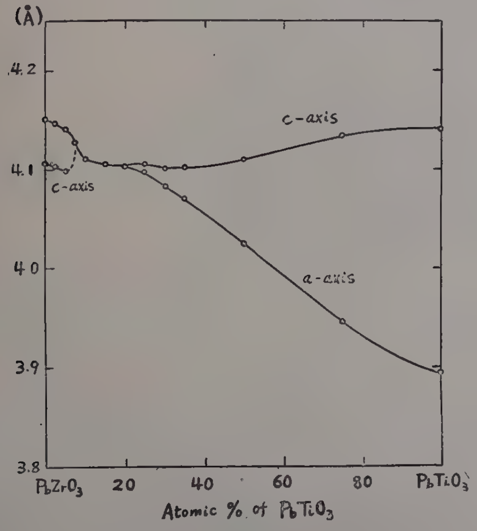

Fig. 3. Lattice spacing of PbZrO$_3$–PbTiO$_3$.

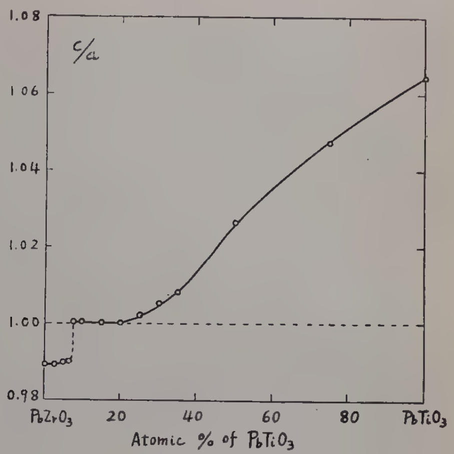

Fig. 4. Tetragonality c/a as a function of composition.

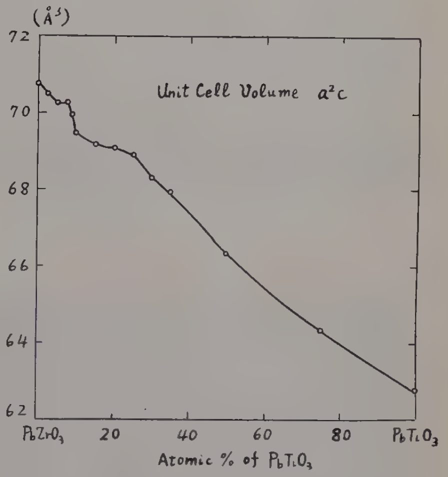

Fig. 5. Unit cell volume as a function of composition.

a) Pure PbZrO$_3$

Our results on pure PbZrO$_3$, a=4.151A and c/a=0.989, are in good agreement with the values due to Megaw. In the Debye photograph of this crystal, there are some extra lines besides the ordinary tetragonal lines. The existence of these extra lines was already reported by Hoffmann$^{3)}$ and by Megaw$^{4)}$. To illustrate them, a Debye photograph of pure PbZrO$_3$ and its roughly estimated intensity diagram are shown in Figs. 6 and 8. In the latter figure, too weak lines are omitted. The extra lines are indicated by open circles. For

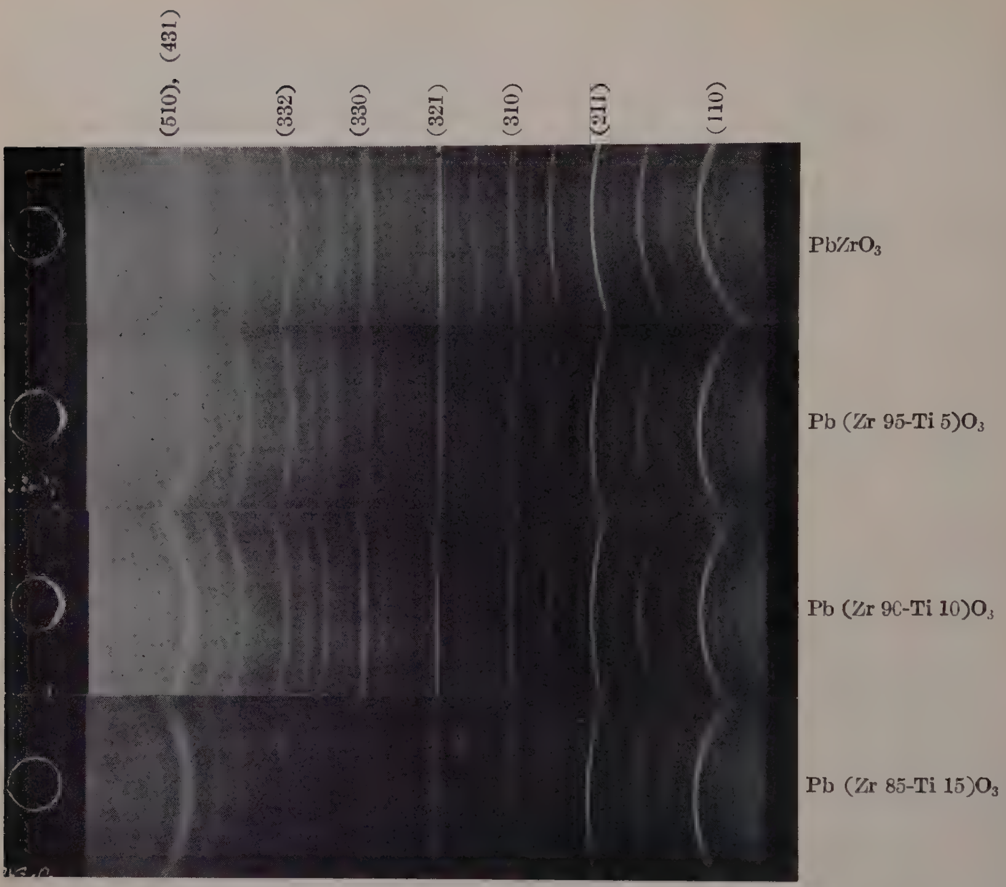

Fig. 6. Debye photographs of PbZrO$_3$-PbTiO$_3$ system (Cu Kα)

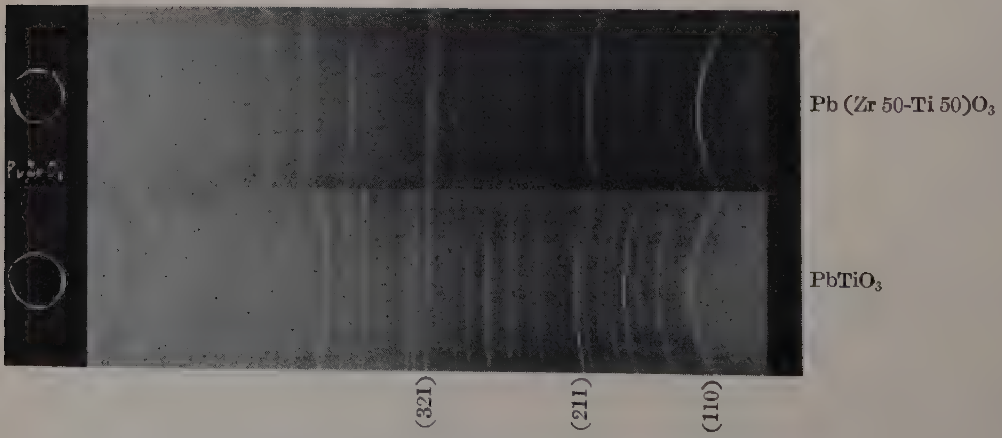

Fig. 7. Debye photograhps of Pb(Zr50-Ti50)O$_3$ and PbTiO$_3$ (Cu Kα).

comparison, intensities of Debye lines of perovskite structure with $a=4.150$ and $c/a=0.99$ are calculated by the following equation:

$$I \propto F^2 \cdot p \cdot \frac{1+\cos^2 2\theta}{\sin^2\theta \cdot \cos^2\theta} \cdot A$$

where F denotes the structure factor, p the number of multiplicity of the Debye line, θ the Bragg angle, A the absorption factor. The result is also shown in Fig. 8.

A comparison of observed lines with calculated ones revealed the fact that, besides the existence of the extra lines, observed intensities of

Table I. Lattice parameter of $Pb(Zr-Ti)O_3$

Atomic % of $PbTiO_3$	a(Å)	c(Å)	c/a	unit cell volume(Å3)
$PbZrO_3$	4.151	4.105	0.989	70.74
2.5	4.146	4.101	0.989	70.49
3.8	4.143	4.098	0.989	70.35
5	4.140	4.097	0.9895	70.23
6.3	4.139	4.098	0.990	70.21
7.5	4.126			70.23
8.8	4.120			69.92
10	4.111			69.49
15	4.105			69.15
20	4.102			69.03
25	4.097	4.105	1.002	68.90
30	4.081	4.100	1.005	68.28
35	4.070	4.101	1.008	67.94
50	4.014	4.119	1.026	66.37
75	3.946	4.133	1.047	64.36
$PbTiO_3$	3.894	4.140	1.063	62.77

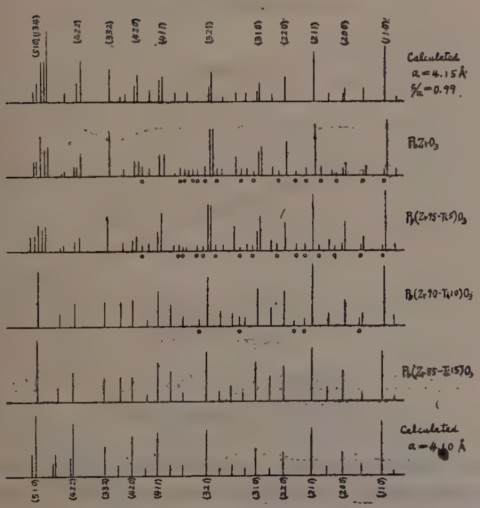

Fig. 8. Intensity diagrams of Debye photographs and the calculated line intensities of perovskite structure. Open circle indicates extra line.

some tetragonal lines, say (510) (143) and (321) etc., are not in good agreement with calculated values, though their spacings coincide completely. A study of $PbZrO_3$ single crystal, recently performed by E. Sawaguchi, H. Maniwa and S. Hoshino in our laboratory using the method of oscillation photographs (unpublished yet), suggests that this crystal has superstructure. The discrepancy in the line intensities, accordingly, may be accounted for by the existence of the superstructure lines superposed on the tetragonal lines.

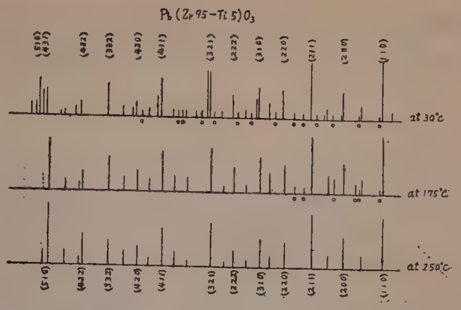

Fig. 9. Intensity diagrams of Debye photographs of Pb(Zr95-Ti5)O_3 as a function of temperature. Open circle indicates extra line.

b) Solid Solution.

With increasing $PbTiO_3$ concentration, the tetragonality remains at first almost constant ($c/a<1$) and then shows sudden increase to unity at a composition of 7.5% of $PbTiO_3$ (Fig. 4), which is just corresponding to the border line between antiferroelectric and ferroelectric regions at room temperature as shown in Fig. 2. The lattice parameter of solid solutions in a range from Pb(Zr92.5–Ti7.5)O_3 to Pb(Zr80–Ti20)O_3 was calculated on assuming their cubic structure, but the Debye lines of these substances are in fact diffuse (Fig. 6) suggesting that the crystal lattice of these substances might be not exactly cubic. This broadening may partly be due to the strain inhomogeneity. For the sake of brevity, we will hereafter simply denote this structure as *pseudo-cubic*.

The intensity diagram of Pb(Zr95–Ti5)O_3, Pb(Zr90–Ti10)O_3 and Pb(Zr85–Ti15)O_3 are shown in Fig. 8. For comparison, the calculated line intensities of cubic perovskite structure of $PbZrO_3$ with a=4.10A is also shown in the same figure. The higher the Ti concentration, the better becomes the agreement between the observed and calculated intensities. Enlarged figure of lattice spacings of solid solutions on the $PbZrO_3$ side is shown in Fig. 10.

Superstructure lines as found in pure $PbZrO_3$

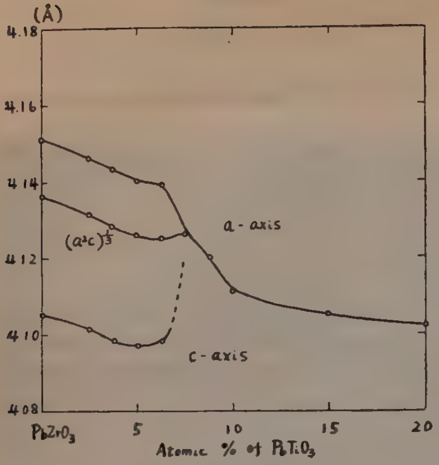

Fig. 10. Lattice parameters of solid solutions on the $\mathrm{PbZrO_3}$ side.

appear also in solid solutions as far as they have tetragonality $c/a<1$, though accompanied by only slight change of their intensities. They become gradually weak and then some of them suddenly disappear when tetragonality attains to unity, and at last in Pb(Zr85−Ti15)$\mathrm{O_3}$ all of them completely disappear (see Figs. 6 and 8). It seems reasonable to assume that this superstructure has intimate relation with the antiferroelectric properties. When the solid solutions contain $\mathrm{PbTiO_3}$ more than 20%, the tetragonality becomes $c/a>1$ thus similar to the case of barium titanate, and its axial ratio increases with Ti concentration, attaining to 1.063 for pure $\mathrm{PbTiO_3}$ (Fig. 7). The relation of the dielectric property and the crystal structure of this system is considered as follows:

Antiferroelectric	Ferroelectric
$c/a<1$ with superstructure	pseudo-cubic—$c/a>1$

As shown in Fig. 5, a unit cell volume of this system decreases with increasing $\mathrm{PbTiO_3}$ concentration, and this result is reasonable consequence of the difference of ionic radii between $\mathrm{Ti^{+4}}$ion (0.68A) and Zr^{+4}ion (0.80A). Small anomalies of volume change were found at the compositions containing 7.5% and 25% $\mathrm{PbTiO_3}$. These compositions coincide with the two ends of pseudo-cubic region. The anomaly at 7.5% $\mathrm{PbTiO_3}$ is clearly corresponding to the boundary of the antiferroelectric and ferroelectric regions and is of the nature similar to the anomalous large expansion observed at 140°C in the thermal expansion measurement for Pb(Zr95−Ti5)$\mathrm{O_3}$, as shown in part I and also in Fig. 11 of the present paper. We have at present, on the other hand, no satisfactory explanation for anomaly at composition of 25% of $\mathrm{PbTiO_3}$.

§ 4. Thermal Expansion.

Linear thermal expansion of ceramic specimens was measured on the several solid solutions. The specimen has a cylindrical form, 3cm in length and 0.5cm in diameter. Differential dilatation of the specimen to a silica rod was magnified by an optical lever by about 1000 times as large. Fig. 11 shows $l-l_0/l_0$ versus rising temperature for several Pb(Zr−Ti)$\mathrm{O_3}$ compositions, where l_0 is the length at room temperature.

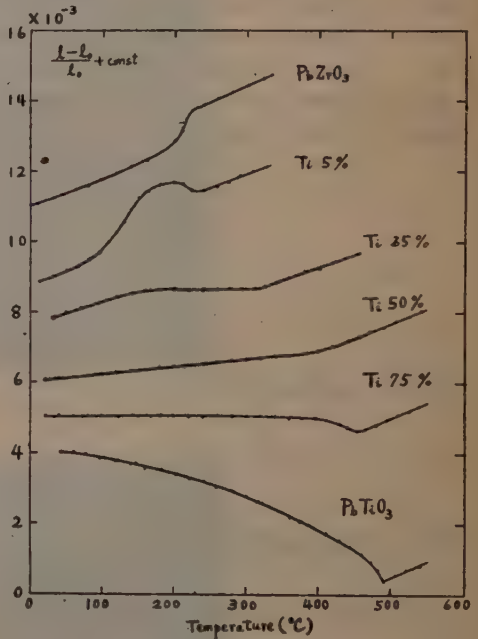

Fig. 11. Thermal expansion curves of Pb(Zr-Ti)$\mathrm{O_3}$ compositions.

As shown in part I, Pb(Zr95−Ti5)$\mathrm{O_3}$ shows an anomalous volume expansion at 140°C corresponding to the transition from antiferroelectric to ferroelectric region. At first we had expected that the ferroelectric region may increase with increasing $\mathrm{PbTiO_3}$ concentration accompanying more striking volume changes at the Curie point as well as at the lower transition point. But the true situation was found to be more complicated: though the lower transition temperature, which is 140°C in Pb(Zr95−Ti5)$\mathrm{O_3}$, is indeed lowered as the $\mathrm{PbTiO_3}$ concentration increases, yet the transition becomes less sharp and the volume change smaller. Similarly, though the Curie temperature, which is 215°C in Pb(Zr95–Ti5)O$_3$ increases with the concentration of PbTiO$_3$ as already shown by the permittivity measurements, yet no marked volume contraction at the Curie point can be detected with solid solutions of Pb(Zr75–Ti25)O$_3$ and Pb(Zr50–Ti50)O$_3$.

Though the thermal expansion coefficient in the ferroelectric region shows complicated behaviour with composition, the linear thermal expansion coefficient in the cubic region is nearly the same for all the compositions, that is, $6.5\sim8.5\times10^{-6}$/°C. We have estimated the unstrained volume at room temperature by extrapolation of the linear part of dilatation curve in the cubic region and compared it with the actual volume at room temperature. The volume strain $\Delta v/v$ thus estimated at room temperature is shown in Fig. 12. The volume change at the border line between antiferroelectric and ferroelectric states can clearly be seen in this figure.

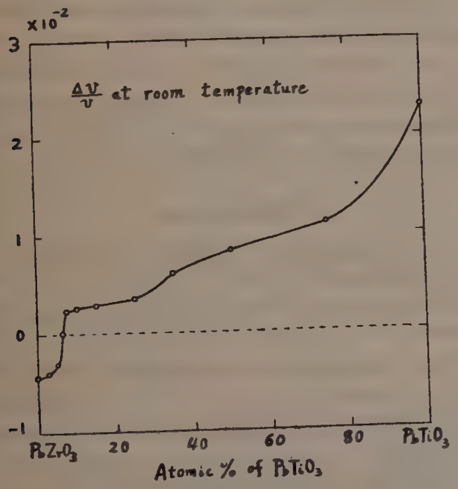

Fig. 12. Volume strain at room temperature estimated by extrapolation from the cubic region.

§ 5. X-ray Study near the Transition Points.

The two phase transitions in Pb(Zr95–Ti5)O$_3$ were studied in detail in part I. Now, a temperature dependence of lattice spacing of the same substance has been investigated at temperatures from 10° to 280°C. A series of Debye photographs were taken on powdered specimens by back reflection method, using Cu Kα radiation. A camera length was about 40mm. Lattice constants were calculated from (510), (143) and (134) lines and the results are shown in Fig. 13.

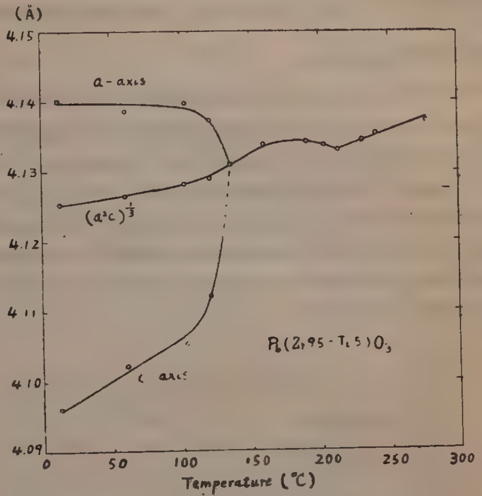

Fig. 13. Lattice spacing of Pb(Zr95–Ti5)O$_3$ as a function of temperature.

At rising temperature, the tetragonality becomes unity at the lower transition point of 140°C, but the Debye lines are very diffuse even at temperatures above this transition point. This broadening of lines may be of the same nature as that found for pseudo-cubic solid solutions ranging, at room temperature, from Pb(Zr92.5–Ti7.5)O$_3$ to Pb(Zr80–Ti20)O$_3$. Superstructure lines are found in the antiferroelectric region below 140°C and they become faint as the structure becomes pseudo-cubic.

If the temperature is raised further, the diffuseness of the powder reflection reduces, and the crystal structure of this substance has an exact cubic symmetry without any superstructure at temperatures above the Curie point. The behaviour of the Debye lines with temperature is shown schematically in Fig. 9. The temperature change of unit cell volume is just in accordance with that obtained by dilatometric measurement (Fig. 11). It must be noticed that a volume contraction occurs at the Curie point in similar way as in the case of pure barium titanate[4]), though the crystal structure in the ferroelectric region is not tetragonal but pseudo-cubic. Above results should be compared with the case of pure lead zirconate[5]).

Phase transition of Pb(Zr85–Ti15)O$_3$ was also roughly studied by the Debye photographs. In this substance, the powder reflections are very diffuse below the Curie point (pseudo-cubic) in marked contrast with the sharp lines above it. A volume contraction at the Curie point is also observed. No extra lines however found in this solid solution at any temperature.

§ 6. Discussions.

From the investigation already described, the crystal structure of the $PbZrO_3-PbTiO_3$ system can be divided into regions as shown in Fig. 14. Some of the superstructure lines appear even in the pseudo-cubic region near the border line to the antiferroelectric region, but they disappear gradually as the temperature is raised far above the line.

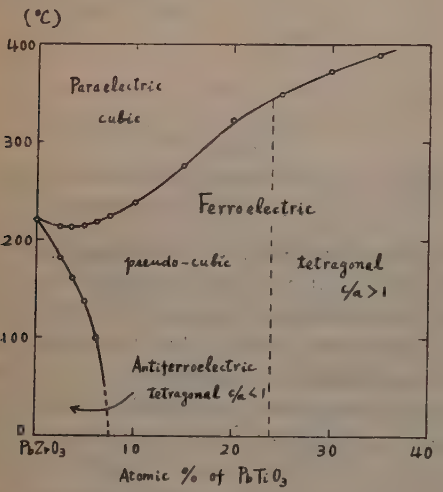

Fig. 14, Phase diagram and crystal structure of the $PbZrO_3$-$PbTiO_3$ system.

As shown in part I, solid solutions in pseudo-cubic region, for example $Pb(Zr90-Ti10)O_3$, show clearly ferroelectric characteristics and distinguish themselves from antiferroelectric ones. Of considerable interest may be a mechanism of ferroelectricity in this pseudo-cubic crystal, especially if it were compared with that of barium titanate type ferroelectrics with a net tetragonality, $c/a>1$. At present, we are unable to detect any essential difference between the properties of pseudo-cubic region and those of tetragonal region, except small anomaly of unit cell volume found at their border line (Fig. 5).

In connection with the above phenomenon, it should be emphasized that in the $Pb(Zr-Ti)O_3$ system, we are replacing B atoms in ABO_3 double oxide, in contrast with the cases of $(Ba-Sr)TiO_3$[6], $(Ba-Pb)TiO_3$[7] or $(Pb-Sr)TiO_3$[8] where A atoms are being replaced.

We have assumed the lowest phase in Figs. 2 and 14 to be in an antiferroelectric state. Of course, there may be alternative interpretation that the lowest phase is another ferroelectric state which has very large coercive field. We believe, however, our assumption of antiferroelectric state to be more reasonable and natural than the interpretation of another ferroelectric state. Of course, in order to decide the two alternatives, however, some crucial experiments, such as determination of the exact atomic positions by the X-ray analysis of $PbZrO_3$ single crystal, are necessary.

In conclusion, we wish to express our sincere thanks to Professors Y. Takagi and S. Miyake for their kind guidance and continued encouragement in the course of this research. We are also grateful to Mr. S. Hoshino and Mr. E. Sawaguchi for their helpful discussions. This research was helped by the research grant of the Ministry of Education.

References

1) G. Shirane and A. Takeda, J. Phys. Soc. Japan, **7** (1952) 5.

2) H. D. Megaw, Proc. Phys. London, **58** (1946) 133.

3) A. Hoffmann, Z. Phys. Chem. **B28** (1935) 65.

4) S. Sawada and G. Shirane, J. Phys. Soc. Japan, **4** (1949) 52.

5) R. Ueda and G. Shirane, J. Phys. Soc. Japan, **6** (1951) 209.

6) D. F. Rushman and M. A. Strivens, Trans. Faraday Soc., **42A** (1946) 231.

7) S. Nomura and S. Sawada, J. Phys. Soc. Japan, **6** (1951) 36 G. Shirane and K. Suzuki, ibid. **6** (1951) 274.

8) S. Nomura and S. Sawada, ibid. **5** (1950) 270.

JOURNAL OF THE PHYSICAL SOCIETY OF JAPAN, Vol. 7, No. 1, JAN.—FEB., 1952

On the Phase Transition in Cuprous Iodide

By Shizuo MIYAKE, Sadao HOSHINO and Toshio TAKENAKA
Tokyo Institute of Technology, Oh-okayama, Tokyo

(Read April, 1, 1951, Received June, 28, 1951)

The phase transition and the crystal structures of cuprous iodide (CuI) have been studied by the X-ray and calorimetric measurement. Two phase transitions at 369°C and 407°C were found and the corresponding energy and entropy changes were estimated from the specific heat-temperature curve. The crystal lattice of γ, β and α-phases were determined to be the cubic (ZnS type), hexagonal (ZnO type) and cubic, respectively, by the X-ray powder method. The intensity change with temperature was measured in detail by a new method by which the Debye temperature factor can be taken into account more exactly. From this measurement, it was found that the crystal structure of this substance begins to change anomalously already at about 200°C, and finally transforms into the high temperature form having an average structure. That is to say, there are some metastable positions around every copper position of the low temperature form and the probability of finding the Cu-atoms in these positions gradually increases with temperature and finally, in the α-phase region, the atoms are equally distributed over all the positions. It was concluded that these probable positions are $4(c)$: (1/4 1/4 1/4) and $16(e)$: $(xxx,\ x\bar{x}\bar{x},\ \bar{x}x\bar{x},\ \bar{x}\bar{x}x)$ of T_d^2 with the parameter $x \approx 0.34 \pm 0.01$. The entropy change expected from this proposed structure change is fairly in agreement with the value obtained by the calorimetric measurement.

§ 1. Introduction

It has been reported that there are three forms of the phase α, β and γ in cuprous iodide (CuI), the crystal lattice of the β and γ-phase being hexagonal and cubic respectively whereas that of the α-phase unknown yet, but there has been given little information concering the nature of their phase transitions. For instance, the transition temperatures reported by different investigators[1)2)3)] are not in agreement with one another. As this substance shows a large ionic conductivity at high temperatures[3)4)], it is suspected that the high temperature form might possess an average structure as found for AgI[5)], Ag_2HgI_4[6)7)] etc., though we have yet no decisive evidence for it.

The present study is to obtain more detailed informations about this substance, especially its behaviour concerning the phase transitions, by X-ray and calorimetric methods.

§ 2. Specific heat measurement

We measured, at first, the temperature change of the specific heat in order to determine the transition temperatures exactly and to know the energy and entropy changes at the phase transitions. The measurement was performed by use of an adiabatic calorimeter which is of a modified Sykes' type as reported by Nagasaki and Takagi[8)]. The sample was prepared by the following chemical process.

$$2CuSO_4 + 4KI \longrightarrow 2CuI_2 + 2K_2SO_4$$
$$2CuI_2 \longrightarrow 2CuI + I_2$$

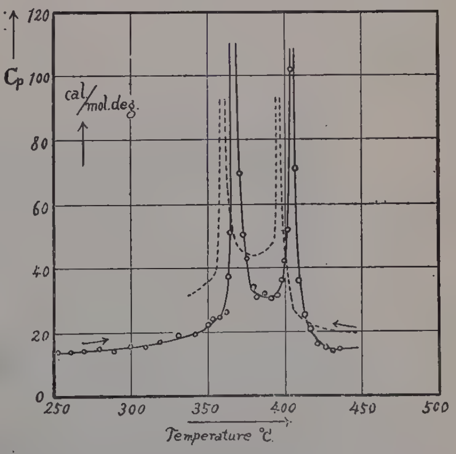

Fig. 1, Specific heat-temperature curve of CuI.

The specimen (14. 5g.) was sealed in a hard glass vessel (3g.). The heat input given to the specimen was about 0.004cal/gr.sec. The obtained specific heat—temperature curve is shown in Fig.1, wherein the dotted line corresponds to cooling curve and this one is indicated by an arbitrary scale. There are two main anomalies, the one at 369°C corresponding to the transition from the γ-phase to the β-phase and the other at 407°C to that from β to α. Besides, it was noticed that the curve begins to rise at temperatures pretty lower than the transition point 369°C, showing the fact that an anomalous change of the crystal structure already begins to occur at these temperatures.

From the curve we estimated transition energies ΔE and corresponding entropy changes ΔS as follows:

$\Delta E_1 = 1.70$Kcal/mol, $\Delta S_1 = 2.64$cal/mol.deg,
$\Delta E_2 = 0.77$Kcal/mol, $\Delta S_2 = 1.13$cal/mol.deg,

in which suffixes $_1$ and $_2$ refer to the phase changes from γ to β and from β to α respectively.

§ 3. Crystal lattices of three phases

The crystal structure of CuI for the three phases was studied by the Debye method with CuK$_\alpha$ and MoK$_\alpha$ radiations. A temperature range from 20° to 510°C was covered. The powder specimen was sealed in a thin hard glass capillary (diameter about 0.3mm) and was mounted in a small furnace placed in an X-ray camera with a radius of about 55.5mm. The temperature was measured by a copper constantan thermocouple calibrated beforehand.

The photograph at room temperature shows a face centered cubic pattern with the lattice constant $a=6.040_5$kX at 20°C (Fig.2,a), the relative intensities of the reflexion lines indicating that the structure of the γ-phase belongs to the zincblende type (the space group T_d^2) as was reported formerly.

Fig. 3 shows a temperature change of the lattice constant a calculated from (553) line in back reflexion photographs taken with CuK$_\alpha$ radiation.

The determination of the structure for the β-phase was not so easy as for the γ-phase, because the Debye lines always showed not smooth but fibrous characteristic, and also a rapid intensity decrease for the high order reflexions (Fig.2, c). Moreover, there was some disagreement among different photographs taken at the same temperature range. But from the positions of the diffraction lines and the extinction law of reflexion, it may be safe to say that the lattice is hexagonal with the lattice constants $a \approx 4.3_1$kX, $c \approx 7.7_0$kX and $c/a \approx 1.62_4$ at 370°C. The axial ratio and the qualitative comparison of the intensities of main spectra seems to show that the lattice in the β-phase may be of the wurtzite type.

Concerning the α-phase it was found that the feature of the Debye pattern is very similar to that for the γ-phase except for the effect of thermal expansion, suggesting that the lattice of α-phase is face centered cubic with the lattice

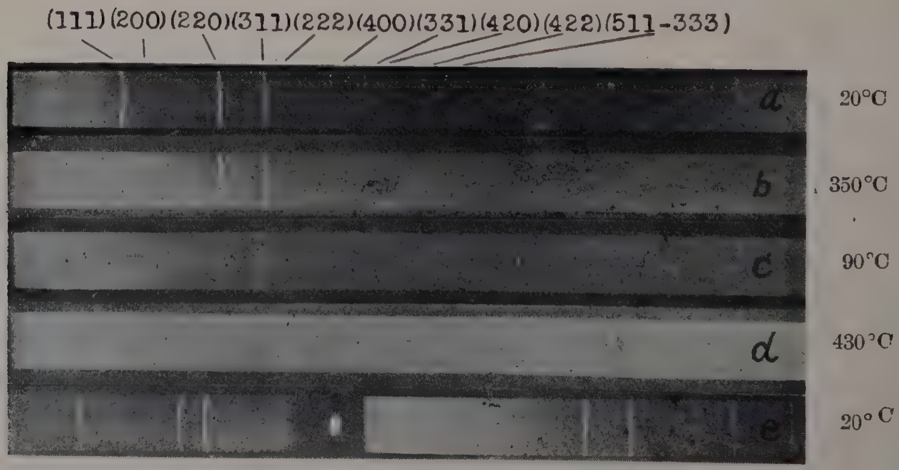

Fig. 2. The Debye photographs taken with CuK$_\alpha$ at various temperatures. The last one (e) shows an asymmetric diffraction pattern. The right hand side corresponds to reflexions from CuI at room temperature and the left hand side to those from copper wire used as the standard specimen.

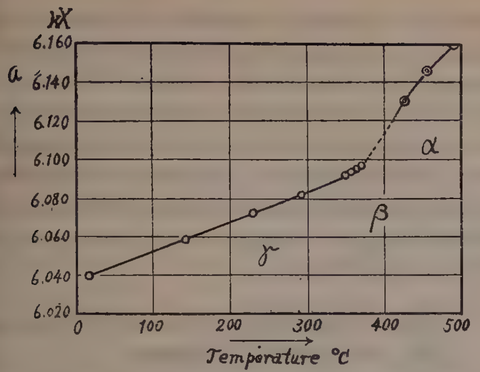

Fig. 3. Lattice constant as a function of temperature.

constant $a \approx 6.1_3$ kx at 430°C (Fig.2, d). In Fig. 3 the variation of a calculated from (311) reflexion is indicated. It was also noted that the relative intensities of spectra do not differ greatly from ones for the γ-phase, though the intensities of the higher order reflexions are considerably diminished as for the β-phase. These results seems to indicate that the crystal structure of the α-phase might be the same as that of the γ-phase, namely the zincblende type. But before drawing this conclusion a more accurate comparisons of the intensity distribution of Debye lines from these two phases may be necessary by taking into account the effect of the Debye temperature factor, and, especially, it seems to be advantageous to perform the intensity measurement for each line continuously over the whole temperature range. We carried out the measurement of this kind by using an intensity standard as described in the next section.

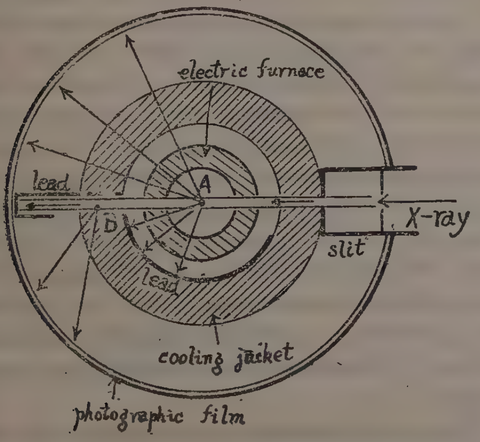

Fig. 4. The schematical diagram for the standard method.

§ 4. The relation between γ and α-phases

For the above purpose, we used a temperature camera as shown by Fig.4, wherein A is the sample to be examined and B is that for the intensity standard. With this camera an asymmetric Debye pattern is obtained on the film, namely, the reflexions from the sample (CuI) is exposed only on one half of it and the spectra from the standard specimen (a copper wire) only on another half (Fig.2, e). By this simple device we can observe the temperature dependency of intensities continuously by referring to some specific spectrum coming from the standard specimen. The result is shown for several important lines in Fig.5 where the ordinate show the reflexion intensity $I_{\rm obs}$ deduced by a formula

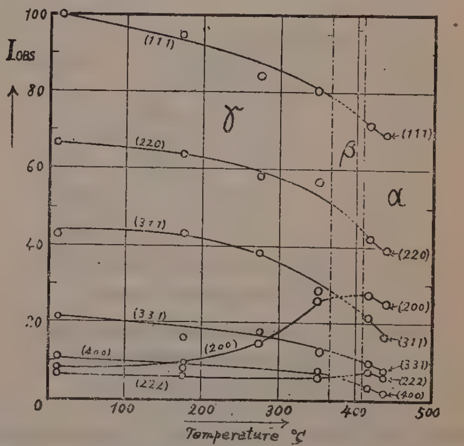

Fig. 5. The intensities of the several reflexions as functions of temperature.

$$I_{\rm obs} = I / p.A.(1+\cos^2 2\theta)/\sin^2\theta\cos\theta,$$

(I is the observed integrated intensity, p the multiplicity of lattice plane, A the absorption factor and θ the Bragg angle), given in a scale which makes the intensity of (111) at 20°C equal to 100.

From this figure we can draw some important conclusions. This figure and Table I indicate that the line intensities in the γ region at room temperature agree well to those expected from the zincblende structure. At higher temperatures they show a marked temperature effect in general. In it we can see a remarkable fact that every curve in the γ-phase range can be connected respectively to a corresponding curve in the α-phase range very smoothly by only extrapolating them to each other across the intermediate range separated by the β-phase. This fact seems to show that the α-phase can be regarded as a continuation of the γ-phase, the situation which is just similar to the relation between α and δ-phases of iron, whose continuation is interrupted by the intervention of the γ-phases. If we accept this interpretation, then the thermodynamical relation among α, β and γ-phases of CuI may be such a one that can be understood best by Fig. 6 showing the free energy-temperature curves schematically.

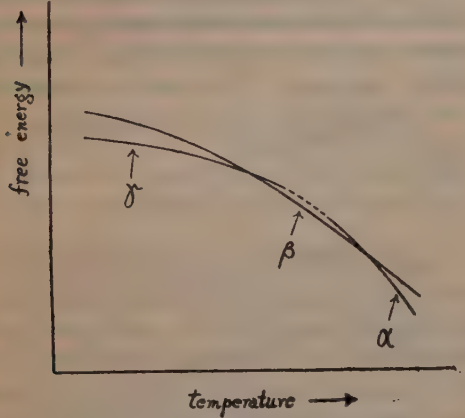

Fig. 6. The schematical free energy-temperature curves for the β and the $\gamma-\alpha$-phases.

The assumption that the γ and α-phases continue to each other does, however, not include the fact that the crystal structures of γ and α-phases are the same, since, as described in § 2, there is an anomalous entropy difference between them.

The intervention of the β-phase makes the circumstance somewhat complicated but there is no question regarding that $\Delta S = S_1 + \Delta S_2 \approx 3.8$cal/mol.deg should represent the entropy increase due to the structural difference between γ and α-phases. Besides, as shown in the next section, it was observed a peculiar intensity change of Debye lines with temperature rise from γ to α range (Fig.5), which can not be explained by taking into account the ordinary Debye factor.

We must therefore expect the existence of some structural difference between these two phases which should be responsible for both the entropy and X-ray intensity changes. This structural change is, moreover, supposed to begin already at about 200°C, a temperature pretty lower than the first transition point 369°C from γ to β-phase, since the anomalous heat evolution and also the variation of the X-ray intensity of Debye line commences there. It must also be noted the fact that, as Fig. 5 shows, the anomalous variation of the X-ray intensities does not take place in the temperature range of the α-phase except gradual decreases with temperature, as expected from the ordinary temperature effect.

§ 5. Intensity change of the Debye lines and the structure of α-phase.

Fig. 5 shows that there are two distinct types in the intensity changes of Debye lines according to their reflexion indices. The line intensities of (111), (220), (311), (400) etc. show decreases with temperature which are as expected, at least qualitatively, from the ordinary thermal effect, while, on the contrary, the intensities of (200), (222) and (420) show increases.

Concerning these tendencies we can notice the existence of the following relation: the square of the structure factors $|F_{hkl}|^2$ can be written for (111), (311), (331) etc. in a form $(f_I e^{-M_I})^2 + (f_{Cu} e^{-M_{Cu}})^2$, for (220), (400), (422) $(f_I e^{-M_I} + f_{Cu} e^{-M_{Cu}})^2$ and for (200), (222), (420) etc. $(f_I e^{-M_I} - f_{Cu} e^{-M_{Cu}})^2$, wherein f_I and f_{Cu} mean the atomic scattering factors and e^{-M_I} and $e^{-M_{Cu}}$ the Debye temperature factors for iodine and copper atoms respectively. The lines belonging to the former two categories show the intensity decrease with temperature, and the lines of the last category the intensity increase.

From this regularity it is easily known the fact that the temperature dependency of the intensity as actually observed can be understood qualitatively by assuming that the decrease of the Debye factor with temperature is especially larger for one of the two atoms. It may be reasonable to assume that it is Cu-atoms that suffer a larger temperature effect, since the ionic conductivity of this substance shown at higher temperatures is known to be due to Cu atoms[3][4]. This assumption being accepted the intensity increase of the line group (200), (222), (420) etc. can be explained at once, because the value of the structure factor $(f_I e^{-M_I} - f_{Cu} e^{-M_{Cu}})$ can increase in a certain temperature range when $e^{-M_{Cu}}$ decrease more drastically compared with e^{-M_I}.

The above consideration assuming only the animate temperature vibration of atoms, especially of Cu-atoms, however, is not sufficient to explain the anomalous entropy difference $\Delta S \approx 3.8$ cal/mol. deg between α and γ-phases as mentioned before. Moreover the Debye temperatures formally deduced from the observed intensity change are not constant. We can deduce the quantities proportional to $f_I e^{-M_I}$ and $f_{Cu} e^{-M_{Cu}}$ for every temperature by taking difference or sum of the line intensity having forms of the structure factor $(f_I e^{-M_I} + f_{Cu} e^{-M_{Cu}})$ and $(f_I e^{-M_I} - f_{Cu} e^{-M_{Cu}})$ respectively. The logarithms of the ratios of these quantities, $ln(fe^{-M_{T_1}}/fe^{-M_{T_2}})$, for the different temperatures T_1 and T_2 give the values of $(M_{T_2} - M_{T_1})_I$ and $(M_{T_2} - M_{T_1})_{Cu}$ for iodine and copper atoms respectively. In Fig. 7 values of $(M_{T_2} - M_{T_1}) \cdot (\lambda/\sin\theta)^2$, which is considered to be a function of Debye temperature, are indicated for the both atoms as the functions of temperature T_2 when T_1 is fixed at 293°K(20°c). We can see in this figure that the curve for iodine is, as it should be, linear in the whole tempereture range, but for copper the curve shows a systematic deviation from the linearity.

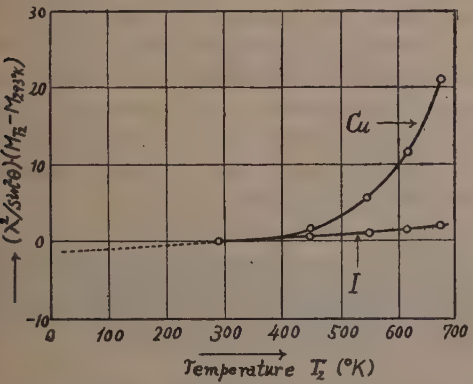

Fig. 7. $(M_{T_2} - M_{T_1}) \cdot (\lambda/\sin\theta)^2$, which is the mean value for the serveral reflexions, as a function of temperature T_2.

We are, therefore, obliged to search for more satisfactory structural model which is able to explain the temperature dependency of the line intensity and entropy change simultaneously. We will now propose a model of this kind as follows. The most stable positions of Cu-atoms may be in $4(c)$; (1/4 1/4 1/4), in accordance with the zincblende structure at room temperature, but there are new $N-1$ meta-stable positions around every $4(c)$ position and the probability of finding the Cu-atoms in the new positions gradually increases with temperature, and finally the atoms are equally distributed over all the positions at sufficiently high temperatures. Then we can expect the intensity variation which shows the temperature effect similar to that due to the temperature factor, and also an anomalous entropy change of about $R \ln N$, provided that these N positions are allowed to be occupied by only one atom at a time, where R is the gas constant. The most probable positions may be 16 (e); $(xxx, x\bar{x}\bar{x}, \bar{x}x\bar{x}, \bar{x}\bar{x}x)$ of T_d^2, deviating a distance δ from the $4(c)$ positions along [[111]] directions (Fig. 8).

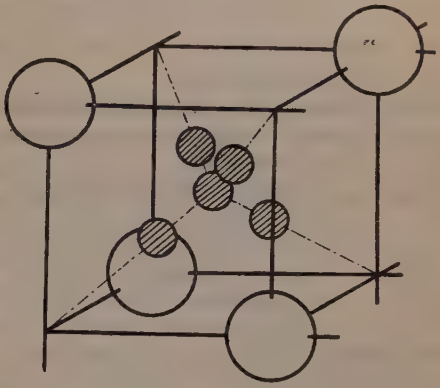

Fig. 8. Proposed structure of CuI at high temperatures, showing 1/8 of unit cell.
White circles: iodine atoms, Hatched circles: positions for copper atom.

We assume that the copper atoms are equally distributed over these five possible positions in a small cell corresponding to 1/8 of the unit cell, and use, for the sake of simplicity, a common intrinsic temeprature factor e^{-M_I} for iodine atoms for the both kinds of atoms, then it is found that the agreement of the line intensity for the α-phase is best when the parameter $x = 0.34 \pm 0.01$, or the deviation δ is about 0.9kX as seen in Table I, in which also the calculated intensities for some other probable structures are shown. According to the structure proposed here, the entropy change may be $R \ln 5 = 3.2$ cal/mol.deg, which is approximately in agreement with the observed value $\Delta S \approx 3.8$ cal/mol. deg.

More detailed investigations to confirm the proposed model, especially by using the single crystal, are now in progress*.

In conclusion the authors with to express their sinciere thanks to Professor Y. Takagi and Mr. M. Hirabayashi for the facilities of

Table 1
The observed and calculated intensities for the several reflexions.

hkl \ I	I_{obs} 20°C	I_{cal} ZnS type	I_{obs} 415°C	I_{cal} Ave.I	I_{cal} Ave.II	I_{cal} Ave.III
111	100	100	73	75	68	79
200	8	10	27	23	59	10
220	67	73	42	35	102	73
311	42	51	21	28	35	40
222	6	3	8	5	16	3
400	11	12	3	2	18	12
331	21	22	9	5	15	17
420	5	4	—	4	22	4

I_{obs}: observed intensity
I_{cal}: calculated intensity
Ave. I: The proposed average structure; 4Cu in 16(*e*)+4(*c*), the parameter $x=0.34$
Ave. II: A probable average structure; 4Cu in 8 prositions 4(*c*): (1/4 1/4 1/4)+4(*b*):(1/2 1/2 1/2)
Ave.III: A probable average structure; 4Cu in 8 positions 4(*c*): (1/4 1/4 1/4) +4(*d*); (3/4 3/4 3/4)
The notations of 4(*c*), 4(*b*) etc. are all for the space group T_d^2.

the specific heat measurement.

This work was supported by the grant for the promotion of science from the Ministry of Education.

References

1) Quercigh: Atti. d. Acad. Linc., **23**(1914), 446, 711, 825.

2) Hermann: Z. f. anorg. Chem., **71** (1911), 257.

3) T. Okada, M. Ohmi and Y. Uno: Proc. Phys. Soc. Japan, **3** (1948), 95.

4) C. Tubant, E. Rindorff and W. Jest: Z. f. anorg. Chem., **165** (1927), 195.

5) L. W. Strock: Z. phys. Chem., B **25**(1934), 441.

6) J. A. A. Ketelaar: Z. Krist., **87**(1934), 435.

7) 〃 : Z. phys. Chem., B**30** (1935) 53.

8) S. Nagasaki and Y. Takagi: J. App. Phys. Japan. **17** (1948), 104.

---

* We found by X-ray and calorimetric methods that the phase transition and the crystal structure of CuBr are also similar to those in CuI.

JOURNAL OF THE PHYSICAL SOCIETY OF JAPAN, Vol. 7, No. 1, JAN.—FEB., 1952

The Effect of Electric Field on the Domain Structures in Rochelle Salt

By Masakazu MARUTAKE
Kobayashi Institute of Physical Research, Kokubunji, Tokyo

(Received June 13, 1951)

The domain structures in the rochelle salt crystal were observed in polarized light under varied electric field. It was found that the motion of the domain boundaries shows hysteresis and relaxation phenomena, and sometimes Barkhausen effect. It was also found that the domain does not always penetrate the crystal and some domains are supposed to be wedge-shaped in the direction of thickness (along the *a*-axis).

§ 1. Introduction.

The rochelle salt crystal is the eldest of the ferroelectric materials and very abundant papers were reported on the dielectric, piezoelectric and other properties. These properties are, however, different under various conditions (*e.g.* temperature, humidity, growing condition of the crystal), and are so complicated that one is bewildered at first sight. (The results were summarized in order and exhaustively by S. Miyake¹⁾.) Above all, dielectric properties in the ferroelectric range were considered to be closely related with domain structures, and though X-ray studies²⁾³⁾ showed the existence of domains, the direct knowledge on their shapes and sizes were not obtained.

Last year, J. Furuichi and T. Mitsui⁴⁾ observed for the first time the domain structures in rochelle salt under a polarization microscope. (The domains in barium titanate, a younger ferroelectric, were found earlier⁵⁾.) They showed that the domains in rochelle salt have relatively simple structures and are mainly composed of slabs perpendicular to the *b*- or *c*-axis.

The author wanted to make clear the relation between these domain structures and dielectric properties, and observed the motion of the domain boundaries under d.c. electric field.

§ 2. Experimental.

All experiments were performed at room temperature (12°C~17°C). Samples of *a*-cut (1~5 mm. thick) were cut from large crystals that grew in water solution, polished on the surface with razor-edge, and placed between electrodes on the stage of polarization microscope (magnification: 75). Two copper plates, each having a circular hole (diameter: 4 mm.), were used as electrodes, and between the sample and electrodes the glycerin solution of sodium chloride was applied as conductor. The glycerin electrode is superior to the saturated water solution of rochelle salt because of smaller solubility, and at varied temperatures it spoils the surface of the sample more slowly. Its conductivity may be small, but it was sufficient in this experiment where only d.c. voltage was applied. The electrodes and the apparatus are schematically shown in Fig. 1.

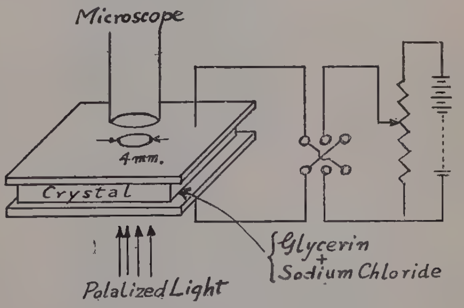

Fig. 1. The electrodes.

§ 3. Parallel Domains.

As above mentioned, most of domains in the rochelle salt crystal consist of thin paralled plates perpendicular to *b*-axis and sometimes to *c*-axis, and through a microscope parallel stripes along *c*-axis or along *b*-axis were observed. We shall call them, respectively, *c*-axis or *b*-axis domains.

When the electric field is applied, the response of the *b*-axis domains to changes in the field does not differ from that of *c*-axis domains, and therefore we measured the latter only as follows. The breadth of each domain (black or white stripe) being measured, the ratio of volume occupied by white domains to the whole (white plus black domains) is calculated on the assumption that all domains are parallel plates perpendicular to the *b*-axis (*cf*. Fig. 2). Fig. 3 and Fig. 4 show this ratio as a function of the electric field.

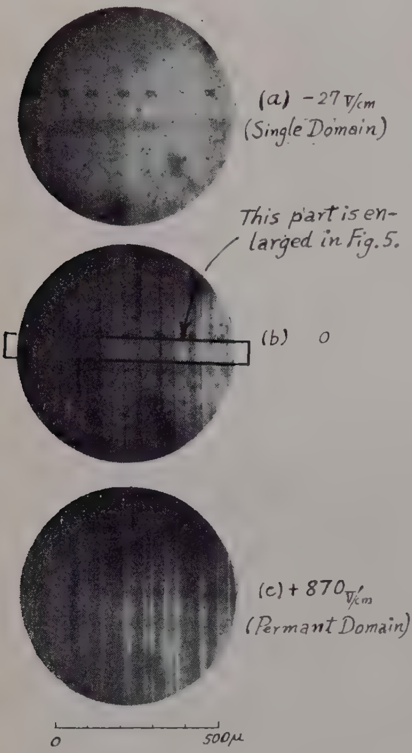

Fig. 2. Parallel permanent domains.

Fig. 3 is an example of normal type hysteresis curves. External d.c. field was changed step by step after having been applied for 3 minutes, the photographs were taken before the field was changed, and it took 36 minutes to draw one cycle. The curve is generally consistent with dielectric hysteresis curves measured by H. Takahasi and S. Hara[6], except that it is concave at the midway. It is seen that the curve is asymmetric with respect to the abscissa and to the coordinate, in agreement with the results previously reported as the origin of pyroelectricity.

Fig. 4 is a hysteresis curve of permanent domains, as shown in Fig. 2, which persist in one direction and cannot be reversed by applying an opposite field of about 1,000 V/cm. The experiment was performed in quite the same way as in Fig. 3, except that one cycle's time is 90 minutes. The permanent domains are not very uncommon, and there may be large internal strains perhaps produced while crystals grow. Fig. 4 is different from Fig. 3 in that (1) permanent domains exist, (2) coercive field is very weak, and (3) the curve is very concave at the midway and almost split in two parts at the zero field. The coercive field is not definite, but every domain boundary has its own coercive field as explained afterwards. The concave hysteresis curve at the midway, as shown in both Fig. 3 and Fig. 4, is due to the relaxation phenomenon that the polarization gradually comes to the stable value at the zero field, and this relaxation time is also different in each domain.

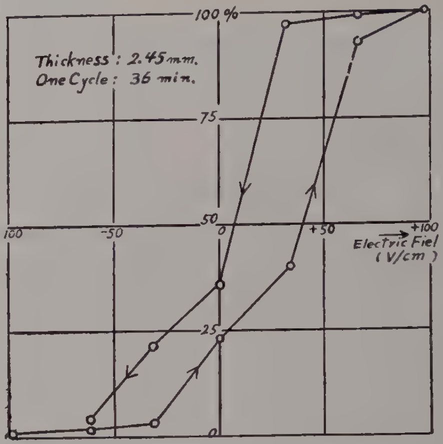

Fig. 3. Hysteresis curve (normal type).

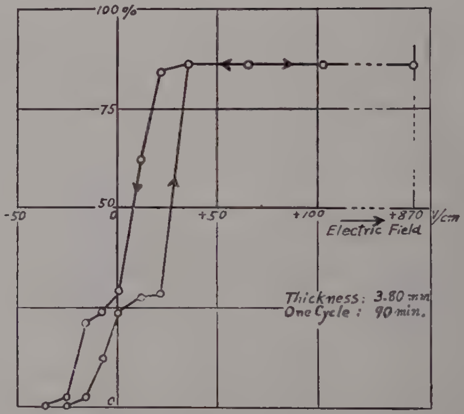

Fig. 4. Hysteresis curve (permanent domain).

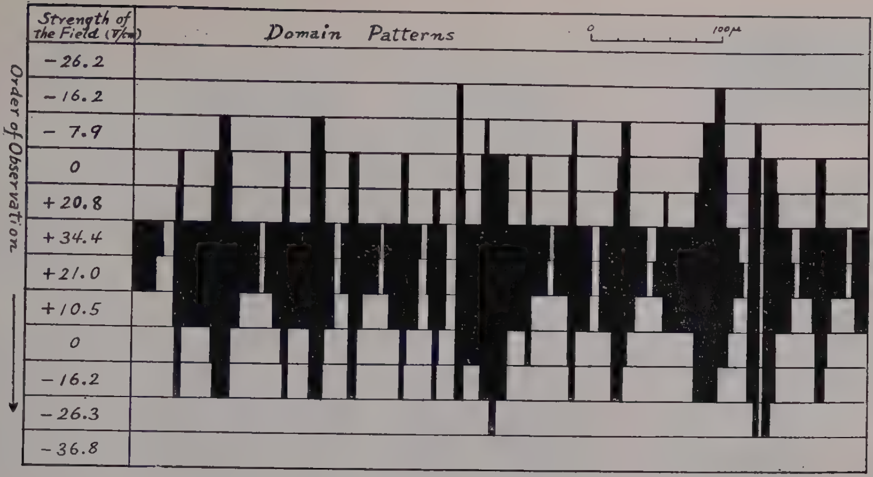

Fig. 5. The behavior of each domain.

Next, we will consider the behavior of each domain. In Fig. 5 there are shown domain stripes when the field is applied, each being a part of the photograph (*cf*. Fig. 2) corresponding to each point in Fig. 4. It is seen that (1) the domain's response is not uniform when the external field is changed, that is each domain boundary has its own hysteresis and relaxation time; (2) the response is not smooth, that is the boundary does not move till the field strength arrives at a certain value, then moves to a certain distance and is at rest again till the field is strong enough, and so on; (3) the reversal of the domain is caused by the birth of a new domain as well as by the motion of the boundary, that is when the field is strong enough, black domains appear in the midst of the white domains, or *vice versa*.

§ 4. Wedge-shaped Domains.

Wedge-shaped domains exist at the boundaries between c-axis domains and b-axis ones. They also appear at the boundaries of large domains. When the d.c. field is applied, the wedges move in and out (Fig. 6), the response shows hysteresis and relaxation phenomena in the similar way as in parallel domains, and wedge-shaped domains don't appear to move in weaker field than parallel ones as is the case in barium titanate5).

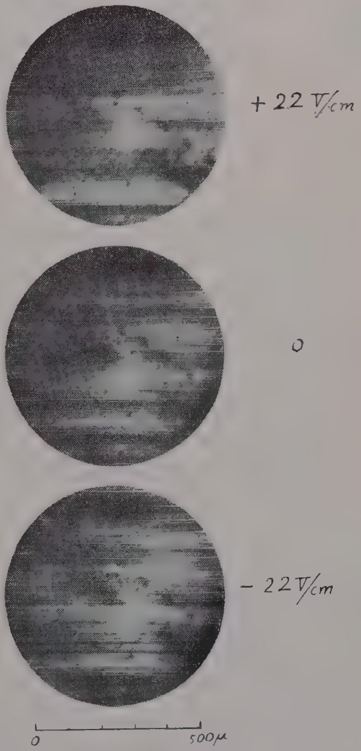

Fig. 6. Wedge-shaped damains.

Fig. 7 is an example of relaxation phenomena. The field of 74 V/cm is applied for one minute (a), and then both electrodes are short-circuited. The domain patterns undergo a gradual change ($b \rightarrow d$), and at last, about one minute later, arrive at the stable ones (e). In this process, it was observed, the wedge-shaped domains suddenly disappear and on behalf of them one b-axis domain appears (from b to c), where the change is very abrupt and may be considered as an example of large Barkhausen

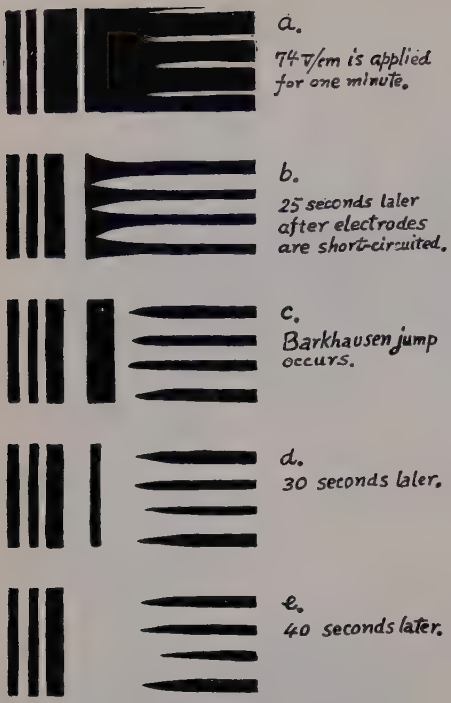
a.
74 V/cm is applied for one minute.
b.
25 seconds laler after electrodes are short-circuited.
c.
Barkhausen jump occurs.
d.
30 seconds laler.
e.
40 seconds later.

Fig. 7. Relaxation phenomena.

effects.

§ 5. Domain Structures along the *a*-Axis.

The domains generally penetrate the crystal along the *a*-axis, otherwise the space charge will appear at the boundary. Wedge-shaped domains, however, may penetrate in this direction, but as domains cannot be observed laterally it is impossible to determine definitely. Nevertheless, there is some evidence that the domains don't extend throughout the thickness of the crystal plate.

By focusing the microscope from the upper to the lower surface of the sample, it is sometimes observed that *c*-axis domains and *b*-axis ones exist in layers⁴⁾.

Fig. 8 shows another example. This sample has permanent domains, which persist in one direction of the applied field, and in the lower surface the direction is opposite to that in the upper surface. The sectional diagram in Fig. 8 shows domain structures schematically which are supposed to be the case in this sample.

§ 6. Conclusion and Discussion.

In this experiment, the response of the domain boundaries to changes in applied d.c. electric field was investigated, and was found to be consistent with the dielectric results previously reported. Each domain, however, has its own hysteresis and relaxation time and previous results on the hysteresis and relaxation phenomena were found to be the values averaged over the whole crystal.

It was found that some samples have permanent domains and, therefore, the values of spontaneous polarization obtained from dielectric hysteresis curves may be to some extent under-estimated.

The possibility was shown that wedge-shaped domains along the *a*-axis may exist, and if so, the birth of new domains when the field is applied may be due to the up and down motion of these wedge-shaped domains in the direction of the thickness.

Wedge-shaped domains (along *c*- or *b*-axis) behave in no particular way and the reversal of the domain orientation does not seem to contribute to the dielectric constant in the weak field.

The different response of each domain to a change in the field may be due to the internal stresses produced in the crystal while growing, and may have some relation with defects in the crystal which are to be observed in every crystal under a microscope⁷⁾, but it is beyond the scope of this experiment and is to be determined by further investigations.

In conclusion, the author wishes to express his sincere thanks to Dr. H. Kawai for his valuable suggestions and kind encouragement, and also to Mr. T. Mitsui for his helpful advices and discussions. This work was supported by the Scientific Research Expenditure of the Ministry of Education.

References

1) S. Miyake: "*Rochelle Salt*" (in Japanese), Koyama Shoten (1948).

2) S. Miyake: Proc. Phys.-Math. Soc. Jap. **23** (1941) 377, 810.

3) A. R. Ubbelohde and I. Woodward: Proc. Roy. Soc. **A185** (1946) 488.

4) J. Furuichi and T. Mitsui: Phys. Rev. **80** (1950) 93, Busseiron Kenkyu. **39** (1951) 96.

5) For instance, P.W. Forsbergh, Jr.: Phys. Rev. **76** (1949) 1187.

6) H. Takahasi and S. Hara: J. Phys. Soc. Jap. **4** (1949) 257, 261.

7) Y. Sakisaka: Unpublished.

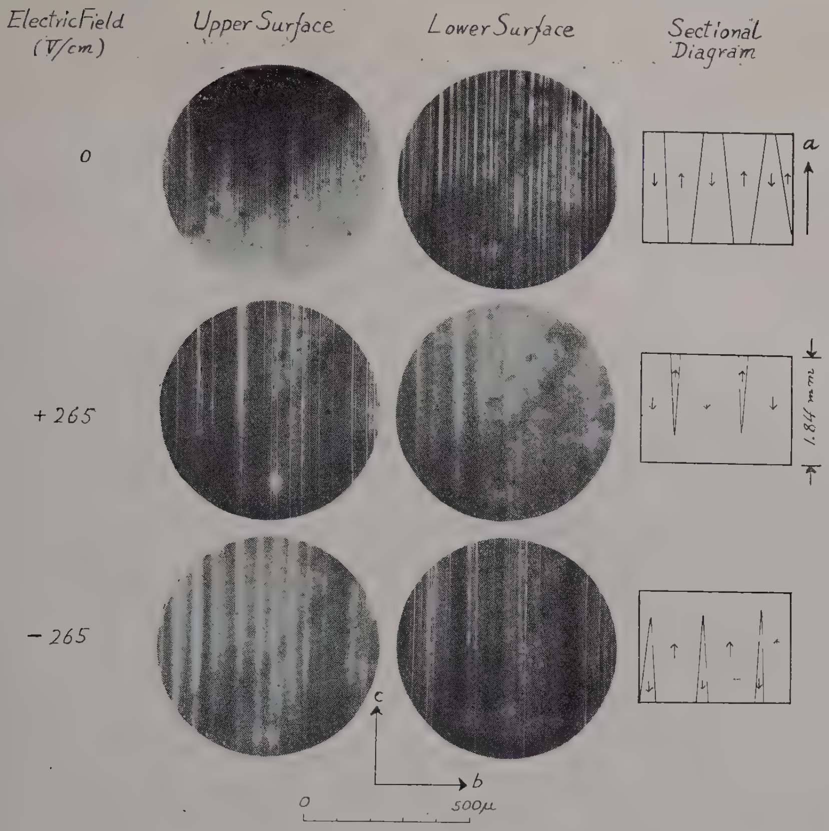

Fig. 8. The *a*-axis wedge-shaped domains.

JOURNAL OF THE PHYSICAL SOCIETY OF JAPAN Vol. 7, No. 1, JAN.—FEB., 1952

Intensity of X-ray Diffraction by an One-Dimensionally Disordered Crystal

(1) General derivation in cases of the "Reichweite" $S=0$ and 1

By Jiro KAKINOKI and Yukitomo KOMURA
(Institute of Polytechnics, Osaka City University)

(Received June 18, 1951)

The present paper shows the calculation of the intensity of X-rays diffracted by a one-dimensionally disordered crystal by the matrix method of Hendricks and Teller and has two purposes; the one is to make clear the relation between the above mentioned matrix method and the difference equation method used by Wilson and Jagodzinski, and the other is to rearrange the results obtained by Hendricks and Teller by introducing the general intensity equation from a rather simple and intuitive standpoint, assuming a finite number N of layers. The obtaind result for the former is $\overline{S_jS^*_{j+n}}=\mathrm{Spur}\,\boldsymbol{VFP}^n$. For the latter case, it is concluded that the matrix $\boldsymbol{\Phi}$ containing the phase shift $\exp(-i\varphi_s)$ is not a general matrix but a diagonal one, and the assumption of a finite number N of layers gives rise to a higher term in addition to the normal diffuse term and this higher term becomes the Laue function in special cases and can hardly be neglected at and near a special point and also when N is very small. In addition the physical meanings of some quantities which appeared in their paper are made clear. More general treatments for the general structure with any "Reichweite" and their relation to Wilson and Jagodzinski's results will be discussed in following papers.

§1. Introduction.

The intensity calculation for the X-rays diffracted by a one-dimensionally disordered crystal has been treated by many researchers. The matrix method[1] and the difference equation method[2][3][4][5], however, seem to be representative. In the present paper we treat the case of a finite number N of layers by the matrix method obtaining the usual diffuse term and a higher term which becomes the Laue function for the special values of parameters and considerably large when N is small. The intensity equations in several special cases for the "Reichweite" $S=0$ and 1 can be derived from the general equation. We also obtained the general relation between the matrix method and the difference equation one. We will use letters of the gothic type for matrices and those with arrows above them for vectors.

§2. General derivation.

Suppose that each mosaic crystallite in a single crystal has N layers consisted of R different kinds of layers each of which has L and M unit cells whose lengths are a and b along $\vec{a}$ and $\vec{b}$ directions, respectively. We assume that the interference between crystallites is incoherent. The layer form factor V_s of the layer s may be put as

$$V_s=\frac{\sin\pi L\alpha}{\sin\pi\alpha}\cdot\frac{\sin\pi M\beta}{\sin\pi\beta}\sum_j f_{sj}\exp 2\pi i(\alpha x_{sj}+\beta y_{sj}+\gamma z_{sj}),\quad s=1,2,\ldots\ldots,R\,,\qquad(1)$$

where f_{sj} is the atom form factor of the j-th atom at $(x_{sj}\vec{a}+y_{sj}\vec{b}+z_{sj}\vec{c})$ in the unit cell of the s-layer, α, β and γ are the coordinates of any point in the reciprocal lattice and they are connected with $\vec{s}_0$ and $\vec{s}$, which are unit vectors along the incident and diffracted beams respectively, by the equation

$$(1/\lambda)(\vec{s}-\vec{s}_0)=\alpha\vec{a}^*+\beta\vec{b}^*+\gamma\vec{c}^*\,,\qquad(2)$$

$\vec{a}^*$, $\vec{b}^*$ and $\vec{c}^*$ being the reciprocal vectors. When the thicknesses of R layers are different from each other it is convenient to take $c=1\,\text{Å}$ and $c^*=1\,\text{Å}^{-1}$ hence the phase shift φ_s along

$\vec{c}$ direction due to the s-layer of thickness of ζ_sÅ may be expressed as

$$\varphi_s=2\pi\gamma\zeta_s, \quad s=1,2,\ldots\ldots,R. \tag{3}$$

Put the probability of finding the s-layer at the q-th layer of any crystallite as f_s then immediately we get

$$\sum_{s=1}^{R} f_s=1. \tag{4}$$

Therefore the mean intensity contribution per crystallite $\overline{V^2}$ from all q-th layers to the total intensity may be expressed as

$$\overline{V^2}=\sum_{s=1}^{R} f_s V_s V_s^*. \tag{5}$$

Possible values of q's are 1, 2, ……, N and (5) is valid for each of them, then the mean intensity contribution per crystallite I_{self} from all layers to the total intensity is expressed as

$$I_{\text{self}}=N\overline{V^2}=N\sum_{s=1}^{R} f_s V_s V_s^*. \tag{6}$$

In order to obtain the mean intensity contribution per crystallite I_{cross} from the interferences between the different two layers, we put the probability of finding the t-layer at the $(q+1)$-th layers of the crystallites, the q-th layers of which are already known to be of kind s, as P_{st}. Then the probability $A_n^{(sht)}$ of finding the crystallites whose $(n+1)$ layers between the q-th and $p=(q+n)$-th layers including both ends are $V_s, V_{h_1}, V_{h_2}, \cdots, V_{h_{n-1}}, V_t$, respectively, is

$$A_n^{(sht)}=f_s P_{sh_1} P_{h_1h_2}\cdots P_{h_{n-2}h_{n-1}} P_{h_{n-1}t}.$$

The mean intensity $I_{sht}^{(qp)}$ from such two layers of the q-th and the p-th is then

$$I_{sht}^{(qp)}=A_n^{(sht)}[V_sV_t^*\exp\{-i(\varphi_s+\varphi_{h_1}+\cdots+\varphi_{h_{n-1}})\}+\text{conjugate}]. \tag{7}$$

Now if we introduce the following matrices

$$\left.\begin{aligned}
\boldsymbol{V}&=\begin{pmatrix} V_1^*V_1 & V_1^*V_2 & \cdots & V_1^*V_R \\ V_2^*V_1 & V_2^*V_2 & \cdots & V_2^*V_R \\ \vdots & \vdots & & \vdots \\ V_R^*V_1 & V_R^*V_2 & \cdots & V_R^*V_R \end{pmatrix}_R, \\
\boldsymbol{F}&=\begin{pmatrix} f_1 & & & \\ & f_2 & & \\ & & \ddots & \\ & & & f_R \end{pmatrix}_R, \\
\boldsymbol{P}&=\begin{pmatrix} P_{11} & P_{12} & \cdots & P_{1R} \\ P_{21} & P_{22} & \cdots & P_{2R} \\ \vdots & \vdots & & \vdots \\ P_{R1} & P_{R2} & \cdots & P_{RR} \end{pmatrix}_R,
\end{aligned}\right\} \tag{8}$$

$$\left.\begin{aligned}
\boldsymbol{\Phi}&=\begin{pmatrix} e^{-i\varphi_1} & & & \\ & e^{-i\varphi_2} & & \\ & & \ddots & \\ & & & e^{-i\varphi_R} \end{pmatrix}_R \\
\boldsymbol{Q}&=\boldsymbol{\Phi}\boldsymbol{P},
\end{aligned}\right| \quad (8)$$

where the suffix R outside of the bracket shows the order of the matrix, then (7) becomes

$$I_{sht}^{(qp)}=(\boldsymbol{V}\boldsymbol{F}\ {}_{ts}Q_{sh_1}Q_{h_1h_2}\cdots Q_{h_{n-2}h_{n-1}}Q_{h_{n-1}t} + \text{conjugate}. \tag{9}$$

Since this is the mean intensity due to such two layers each at the q-th and the p-th layers and of kind s and t respectively, and the $(n-1)$ layers between them are fixed, the mean intensity $I^{(qp)}$ due to any two layers at the q-th and the p-th layers can be obtained from (9) by the summations with respect to s, h_1, $h_2, \cdots, h_{n-1}$, and t from 1 to R as

$$I^{(qp)}=\sum_{s=1}^{R}\sum_{t=1}^{R}\sum_{h=1}^{R}\cdots\sum_{h_{n-1}=1}^{R} I_{sht}^{(qp)} = \text{Spur}\,\boldsymbol{V}\boldsymbol{F}\boldsymbol{Q}^n+\text{conj}. \tag{10}$$

(10) is valid for all the possible values of q's $1, 2, \cdots, (N-n)$ when n is fixed. Since n can take such values as $1, 2, \cdots, (N-1)$, then the mean intensity I_{cross} due to all cross terms is expressed as

$$I_{\text{cross}}=\sum_{n=1}^{N-1}(N-n)I^{(qp)} = \sum_{n=1}^{N-1}(N-n)\,\text{Spur}\,\boldsymbol{V}\boldsymbol{F}\boldsymbol{Q}^n+\text{conj}. \tag{11}$$

Then we obtain the mean intensity I per crystallite due to all crystallites

$$I=I_{\text{self}}+I_{\text{cross}}=N\,\text{Spur}\,\boldsymbol{V}\boldsymbol{F} + \sum_{n=1}^{N-1}(N-n)\,\text{Spur}\,\boldsymbol{V}\boldsymbol{F}\boldsymbol{Q}^n+\text{conj}. \tag{12}$$

Dividing (12) by N and putting $N\to\infty$ (12) becomes [29]*) obtained by Hendricks and Teller1). In order to sum up (12) with respect to n they used such a matrix $\boldsymbol{O}$ as diagonalizing $\boldsymbol{Q}$ as $\boldsymbol{O}\boldsymbol{Q}\boldsymbol{O}^{-1}=\boldsymbol{Q}^{(s)}$ where $\boldsymbol{Q}^{(s)}$ is a diagonal one. If $\boldsymbol{Q}^{(s)}$ has not any element of 1 (when an element is 1 its sum tends to infinite), then $\det(\boldsymbol{1}-\boldsymbol{Q})\neq 0$, hence there must be a matrix $(\boldsymbol{1}-\boldsymbol{Q})^{-1}$, the st-element of which is $M_{ts}/\det(\boldsymbol{1}-\boldsymbol{Q})$ where M_{ts} is the cofactor of the ts-element in $\det(\boldsymbol{1}-\boldsymbol{Q})$. Then (12) becomes

$$I=N\{\text{Spur}\,\boldsymbol{V}\boldsymbol{F}+\text{Spur}\,\boldsymbol{V}\boldsymbol{F}\boldsymbol{Q}(\boldsymbol{1}-\boldsymbol{Q})^{-1}+\text{conj.}\} + \text{Spur}\,\boldsymbol{V}\boldsymbol{F}(\boldsymbol{Q}^{N+1}-\boldsymbol{Q})(\boldsymbol{1}-\boldsymbol{Q})^{-2}+\text{conj.}, \tag{13}$$

in which the term with N is the diffuse term and the other the higher term.

---

*) The equations obtained by the other investigators are put in [ ].

§3. Notes on the matrices $\boldsymbol{P}$, $\boldsymbol{V}$ and $\boldsymbol{\Phi}$.

Since the s-layer at the q-th layer should be followed by any one of R kinds of layers at the p-th and also the t-layer at the p-th should follow any one of R kinds of layers at the q-th then we obtain following two relations as

$$\left.\begin{aligned} &\sum_{t=1}^{R}(\boldsymbol{P}^n)_{st}=1\,, && s=1,2,\cdots,R\,,\\ &\sum_{s=1}^{R}f_s(\boldsymbol{P}^n)_{st}=f_t\,, && t=1,2,\cdots,R\,,\end{aligned}\right\} \quad (14)$$

which are equivalent to the following two matrix relations

$$\boldsymbol{P}^n\boldsymbol{M}_0=\boldsymbol{M}_0 \text{ and } \boldsymbol{H}_0\boldsymbol{P}^n=\boldsymbol{H}_0\,,\ (\boldsymbol{H}_0=\boldsymbol{M}_0\boldsymbol{F}) \quad (15)$$

respectively, where $\boldsymbol{M}_0$ is a matrix, the elements of which are all 1. Therefore there are only $(R-1)^2$ independent elements of R^2 elements in $\boldsymbol{P}$ because of the relations of (4) and (14). The relation (15) will be used frequently in the following reports.

In their third and fourth sections Hendricks and Teller used such a matrix as $Q^{(H.T)}$ whose element is

$$Q_{st}^{(H.T)}=P_{st}\exp\left(-i\varphi^{(st)}\right)\,,$$

and $$\varphi^{(st)}=\varphi^{(s)}+\varphi^{(t)}\,, \quad (16)$$

which means physically that they take the origin of any layer at the middle of the layer, its thickness corresponding to $2\varphi^{(s)}$ for the s-kind layer. On the other hand, we took the origin at the bottom of the layer*), its thickness corresponding to φ_s, hence there must be the following relations between their $V^{(s)}$ and $\varphi^{(s)}$ and our V_s and φ_s:

$$\varphi_s=2\varphi^{(s)} \quad\text{and}\quad V_s=V^{(s)}\exp\left(i\varphi^{(s)}\right), \quad (17)$$

from which we can immediately show that

$$\text{Spur}\,\boldsymbol{V}\boldsymbol{F}=\text{Spur}\,\boldsymbol{V}^{(H.T)}\boldsymbol{F}$$

and $$\text{Spur}\,\boldsymbol{V}\boldsymbol{F}\boldsymbol{Q}^n=\text{Spur}\,\boldsymbol{V}^{(H.T)}\boldsymbol{F}\boldsymbol{Q}^{(H.T)n}\,.$$

§4. The "Reichweite" S.

As was done by Jagodzinski[3)], when the probability P_{st} of finding the layer of kind t after the preceding layer of kind s depends not only on the s-layer, but also on the kinds of all the preceding layers of number S including s, we define the "Reichweite" to be S**). The general intensity formula (12) was derived for $S=1$ but this is also valid for $S=0$ as shown in the following and also can be extended to the case of any values of S as will be seen from the next paper. $S=0$ means that the probability of finding the t-layer after V_s does not depend on the s-kind but only on the probability f_t of finding it at any layer, that is, $P_{st}=f_t$ is available for all s. Then if we put $\boldsymbol{P}$ for $S=0$ as $\boldsymbol{P}_0$ it becomes

$$\boldsymbol{P}_0=\boldsymbol{H}_0\,. \quad (18)$$

§5. Case $S=0$.

In this case as shown in the preceding section we can take $\boldsymbol{P}_0$ as $\boldsymbol{P}$ in (12) and easily show

$$\boldsymbol{P}_0^n=\boldsymbol{P}_0 \quad (19)$$

from (4). Using this relation and putting

$$G=\sum_{s=1}^{R}f_s\exp\left(-i\varphi_s\right)\,,\quad \overline{V}=\sum_{s=1}^{R}f_sV_s\,,$$

and $$\overline{V\varphi}=\sum_{s=1}^{R}f_sV_s\exp\left(-i\varphi_s\right)\,, \quad (20)$$

we can transform (12) into

$$I=N\overline{V^2}+\overline{V^*}\,\overline{V\varphi}\sum_{n=1}^{N-1}(N-n)G^{n-1}+\text{conj.} \quad (21)$$

$$=N\left(\overline{V^2}+\frac{\overline{V^*}\,\overline{V\varphi}}{1-G}+\frac{\overline{V}\,\overline{V^*\varphi^*}}{1-G^*}\right)$$

$$+\frac{\overline{V^*}\,\overline{V\varphi}(G^N-1)}{(1-G)^2}+\frac{\overline{V}\,\overline{V^*\varphi^*}(G^{*N}-1)}{(1-G^*)^2}\,. \quad (22)$$

The term with N in (22) is found to be the same as [20] by Hendricks and Teller by substituting the following relations into their C and $\overline{\varphi}$,

$$C^2=GG^*,\quad 2C\cos\overline{\varphi}=G+G^*\,,$$

and $$2iC\sin\overline{\varphi}=G^*-G\,. \quad (23)$$

which are derived from their implicit relations [16] and [17] by referring to (17) and (20).

When $\gamma=\Gamma$ at which the denominators in (22) become all 0 i.e. $G=G^*=1$,

$$\varphi_s=2\pi m_s \quad\text{and}\quad \Gamma\zeta_s=m_s\,,$$
$$s=1,2,\cdots,R\,.\ m_s\text{: any integer} \quad (24)$$

from (3) in which case (21) becomes

$$I(\Gamma)=N^2\overline{V_0}\,\overline{V_0^*}+N\left(\overline{V_0^2}-\overline{V_0}\,\overline{V_0^*}\right), \quad (25)$$

where the values of the necessary quantities at $\gamma=\Gamma$ are shown with suffix 0. The limiting value of the whole (22) at $\gamma=\Gamma$ is equal to (25), while that of the diffuse term only is finite and equal to

---

*) Generally speaking, we took the origin at the point higher by a constant height than the bottom.

**) Jagodzinski used the lettes s for this "Reichweite".

$$\lim_{\gamma\to\Gamma}\left(\overline{V^2}+\frac{\overline{V^*}\,\overline{V\varphi}}{1-G}+\frac{\overline{V}\,\overline{V^*\varphi^*}}{1-G^*}\right)=\overline{V_0^2}$$

$$+\frac{\overline{V_0}\,\overline{V_0^*}\,\overline{\zeta^2}-\overline{\zeta}\,\overline{(\overline{V_0}\,\overline{V_0^*\zeta}+\overline{V_0^*}\,\overline{V_0\zeta})}}{(\overline{\zeta})^2},\qquad(26)$$

where

$$\overline{\zeta}=\sum_{s=1}^{R}f_s\zeta_s\,,\ \overline{\zeta^2}=\sum_{s=1}^{R}f_s\zeta_s^2 \text{ and } \overline{V_0\zeta}=\sum_{s=1}^{R}f_sV_{s0}\zeta_s\,.$$

Case i) $\varphi_s=\varphi$. In this case (20) can be written as

$$G=\exp(-i\varphi)\quad\text{and}\quad\overline{V\varphi}=\overline{V}\exp(-i\varphi),$$

from which (22) becomes

$$I=\overline{V}\,\overline{V^*}\frac{\sin^2\pi N\gamma}{\sin^2\pi\gamma}+N(\overline{V^2}-\overline{V}\,\overline{V^*}).\qquad(27)$$

Our $\overline{V}$ is the same as U in [11] by Hendricks and Teller and their I_{uu}, I_{uw} and I_{ww} are calculated to be

$$NI_{uu}=\overline{V}\,\overline{V^*}\frac{\sin^2\pi N\gamma}{\sin^2\pi\gamma}\,,$$

$$NI_{uw}=0\quad\text{and}\quad NI_{ww}=N(\overline{V^2}-\overline{V}\,\overline{V^*})\,,$$

respectively, then (27) is equal to their $NI=N(I_{uu}+I_{uw}+I_{ww})$.

Similarly we obtain the following two equations for two or three-dimensionally disordered crystals respectively

$$I_2=\frac{\sin^2\pi L\alpha}{\sin^2\pi\alpha}\left\{\overline{S}\,\overline{S^*}\frac{\sin^2\pi M\beta}{\sin^2\pi\beta}\,\frac{\sin^2\pi N\gamma}{\sin^2\pi\gamma}\right.$$

$$\left.+MN(\overline{S^2}-\overline{S}\,\overline{S^*})\right\},\qquad(28)$$

$$I_3=\overline{S}\,\overline{S^*}\frac{\sin^2\pi L\alpha}{\sin^2\pi\alpha}\,\frac{\sin^2\pi M\beta}{\sin^2\pi\beta}\,\frac{\sin^2\pi N\gamma}{\sin^2\pi\gamma}$$

$$+LMN(\overline{S^2}-\overline{S}\,\overline{S^*}),\qquad(29)$$

where $\overline{S}$ is the mean structure factor and $\overline{S^2}$ the mean of the squares of the structure factors.

Case ii) $V_s=V$. Such a case is considered not to exist in a strict sense but is approximated by the case that the scattering powers of the additional layers are small compared with the fundamental layer as in Montmorionite in which the water layers intervene between the fundamental layers of Si, oxygen and metals. In this case (20) can be written as

$$\overline{V^2}=VV^*\,,\quad\overline{V}=V\,,\quad\overline{V\varphi}=VG\,,\qquad(30)$$

from which (21) and (22) are calculated as

$$I=VV^*\{N+\sum_{n=1}^{N-1}(N-n)G^n+\text{conj.}\}\qquad(31)$$

$$=VV^*\left\{N\frac{1-GG^*}{1-(G+G^*)+GG^*}\right.$$

$$\left.+\frac{G^{N+1}-G}{(1-G)^2}+\frac{G^{*N+1}-G^*}{(1-G^*)^2}\right\},\qquad(32)$$

respectively, the term with N in (32) is found to be the same as the last equation in §2 by Hendricks and Teller by referring to (23). In their §2, they did not use such $\varphi^{(st)}$ as in (16) but our φ_s and moreover in their example of $R=2$ and $f_1=f_2=1/2$ they stated that the diffuse term [6] became infinite at $\gamma=\Gamma$ as (24) but as seen from (26) and (30)

$$\lim_{\gamma\to\Gamma}\left\{VV^*\frac{1-GG^*}{1-(G+G^*)+GG^*}\right\}$$

$$=V_0V_0^*\frac{\overline{\zeta^2}-(\overline{\zeta})^2}{(\overline{\zeta})^2},$$

which does not become infinite but $V_0V_0^*\left(\frac{\zeta_1-\zeta_2}{\zeta_1+\zeta_2}\right)^2$ which is only a small value of $V_0V_0^*(3/23)^2$ for their example. The limiting value of the whole (32) including the higher term, however, becomes $N^2V_0V_0^*$ at $\gamma=\Gamma$ which corresponds to infinite.

§6. The relation between the matrix method and $\overline{S_jS^*_{j+n}}$ by Wilson2) and Jagodzinski3).

The general intensity equation obtained by Wilson2) may be expressed as

$$I=\sum_{n=-(N-1)}^{N-1}(N-|n|)\,\overline{S_jS^*_{j+n}}\exp(-in\varphi)\,^{*)}\qquad(33)$$

using our corresponding symbols for the one dimensional case. In (33) $\overline{S_jS^*_{j+n}}$ is the mean of the products of the layer form factors of the j-th and the $(j+n)$-th layers and expressed as

$$\overline{S_jS^*_{j+n}}=f_1V_1(V_1^*P_{11}+V_2^*P_{12}+\cdots$$
$$+V_R^*P_{1R})+f_2V_2(V_1^*P_{21}+V_2^*P_{22}+\cdots$$
$$+V_R^*P_{2R})+\cdots+f_RV_R(V_1^*P_{R1}$$
$$+V_2^*P_{R2}+\cdots+V_R^*P_{RR})$$

as seen from, for example, [11] by Wilson and the equation between [5] and [6] and [9] by Jagodzinski3). Using our notations this can be expressed as

$$\overline{S_jS^*_{j+n}}=\text{Spur}\,\boldsymbol{V}\boldsymbol{F}\boldsymbol{P}^n,$$

$$\overline{S_jS^*_{j-n}}=\text{Spur}\,(\boldsymbol{V}\boldsymbol{F}\boldsymbol{P}^n)^*$$

$$\overline{S_jS_j^*}=\text{Spur}\,\boldsymbol{V}\boldsymbol{F}.\qquad(34)$$

Putting $\boldsymbol{\Phi}=\exp(-i\varphi)\boldsymbol{1}$ and using (34), (12) can easily be transformed into (33). The validity of (34) can easily be verified also for the case of $S=0$ in which case

---

*) The − sign in exp. is added because he took the phase difference δ between atoms at $\vec{r}_j$ and $\vec{r}'_{j+n}$ as $\delta=(\vec{s}-\vec{s}_0)\cdot(\vec{r}_j-\vec{r}'_{j+n})$ and we took it as $\delta=(\vec{s}-\vec{s}_0)\cdot(\vec{r}'_{j+n}-\vec{r}_j)$.

$$\overline{S_jS^*_{j+n}}=\overline{S_jS^*_{j-n}}=\overline{V}\,\overline{V^*} \text{ and } \overline{S_jS_j^*}=\overline{V^2},$$

from which (33) becomes (27) which is the same as [2] by Jagodzinkski[3]. (34) is also valid for any values of S as will be seen in the following reports.

§7. Case $S=1$.

In this case the intensity formula is (12) itself but it may be frequently convenient to put

$$P_{st}=f_t(1+p_{st}) \quad \text{i.e.} \quad \boldsymbol{P}=\boldsymbol{P}_0+\boldsymbol{p}\boldsymbol{F}, \tag{35}$$

in which $(\boldsymbol{p})_{st}=p_{st}$. In this case (15) corresponds to

$$(\boldsymbol{p}\boldsymbol{F})^n\boldsymbol{P}_0=\boldsymbol{P}_0(\boldsymbol{p}\boldsymbol{F})^n=0. \tag{36}$$

From this and (19) we obtain

$$\boldsymbol{P}^n=\boldsymbol{P}_0+(\boldsymbol{p}\boldsymbol{F})^n. \tag{37}$$

Then (12) becomes

$$I=N\left(\overline{V^2}+\frac{\overline{V^*}\,\overline{V\varphi}}{1-G}+\frac{\overline{V}\,\overline{V^*\varphi^*}}{1-G^*}\right)$$
$$+\frac{\overline{V^*}\,\overline{V\varphi}(G^N-1)}{(1-G)^2}+\frac{\overline{V}\,\overline{V^*\varphi^*}(G^{*N}-1)}{(1-G^*)^2}$$
$$+\sum_{n=1}^{N-1}(N-n)\,\mathrm{Spur}\,\boldsymbol{V}\boldsymbol{F}\boldsymbol{q}^n+\text{conj.}, \tag{38}$$

where $\boldsymbol{q}=\boldsymbol{\Phi}\boldsymbol{p}\boldsymbol{F}$. Namely we can separate the intensity due to $S=1$ from that due to $S=0$.

When $\varphi_s=\varphi$ (38) becomes

$$I=\overline{V}\,\overline{V^*}\frac{\sin^2\pi N\gamma}{\sin^2\pi\gamma}+N(\overline{V^2}-\overline{V}\,\overline{V^*})$$
$$+\sum_{n=1}^{N-1}(N-n)e^{-in\varphi}\,\mathrm{Spur}\,\boldsymbol{V}\boldsymbol{F}(\boldsymbol{p}\boldsymbol{F})^n+\text{conj.} \tag{39}$$

§8. One dimensional alloy of $A_{f_1}B_{f_2}$.

When $R=2$, using only one parameter $a(-1\leq a\leq 1)$ because of (36) we may put

$$\boldsymbol{p}=\begin{pmatrix} a & -ab \\ -ab & ab^2 \end{pmatrix},$$

$$\boldsymbol{P}=\begin{pmatrix} f_1(1+a) & f_2(1-ab) \\ f_1(1-ab) & f_2(1+ab^2) \end{pmatrix}, \quad \text{where } b=f_1/f_2,$$

from which we can calculate $\boldsymbol{P}^n$ with (36) and (37) obtaining

$$(\boldsymbol{p}\boldsymbol{F})^n=\begin{pmatrix} f_1a^nb^{n-1} & -f_2a^nb^n \\ -f_1a^nb^n & f_2a^nb^{n+1} \end{pmatrix},$$

$$\boldsymbol{F}^n=\begin{pmatrix} f_1(1+a^nb^{n-1}) & f_2(1-a^nb^n) \\ f_1(1-a^nb^n) & f_2(1+a^nb^{n+1}) \end{pmatrix}.$$

Then (39) becomes

$$I=(f_1V_1+f_2V_2)(f_1V_1^*+f_2V_2^*)\frac{\sin^2\pi N\gamma}{\sin^2\pi\gamma}$$
$$+f_1f_2(V_1-V_2)(V_1^*-V_2^*)$$
$$\times\left(N\frac{1-a^2b^2}{D}+\frac{2abH}{D^2}\right), \tag{40}$$

where

$$\left.\begin{aligned} &D=1+a^2b^2-2ab\cos\varphi, \\ &H=2ab-(1+a^2b^2)\cos\varphi \\ &\quad+(ab)^N\{\cos(N+1)\varphi-2ab\cos N\varphi \\ &\quad+a^2b^2\cos(N-1)\varphi\}. \end{aligned}\right\} \tag{41}$$

When $ab=1$ and $\varphi=2m\pi$ i.e. $\gamma=m$ where m is any integer, the denominator D in (40) becomes 0, in which case $\boldsymbol{P}=\begin{pmatrix} 1 & 0 \\ 0 & 1 \end{pmatrix}$ and the limiting value of (40) becomes $N^2(f_1V_{1,0}V^*_{1,0}+f_2V_{2,0}V^*_{2,0})$ corresponding to the mixture of A and B metals with a ratio of f_1:f_2 *).

For the special values of $f_1=f_2=1/2$ i.e. $b=1$ (40) and (41) become

$$I=\frac{(V_1+V_2)(V_1^*+V_2^*)}{4}\frac{\sin^2\pi N\gamma}{\sin^2\pi\gamma}$$
$$+\frac{(V_1-V_2)(V_1^*-V_2^*)}{4}$$
$$\times\left(N\frac{1-a^2}{D_1}+\frac{2aH_1}{D_1^2}\right), \tag{42}$$

where

$$\left.\begin{aligned} &D_1=1+a^2-2a\cos\varphi, \\ &H_1=2a-(1+a^2)\cos\varphi \\ &\quad+a^N\{\cos(N+1)\varphi-2a\cos N\varphi \\ &\quad+a^2\cos(N-1)\varphi\}. \end{aligned}\right\} \tag{43}$$

respectively, in which the term $(1-a^2)/D_1$ is found to be equal to [23] by Hendricks and Teller by putting $a=4A$.

When $a=1$ ∴ $\boldsymbol{P}=\begin{pmatrix} 1 & 0 \\ 0 & 1 \end{pmatrix}$ (42) is equal to

$$I=\frac{V_1V_1^*+V_2V_2^*}{2}\frac{\sin^2\pi N\gamma}{\sin^2\pi\gamma},$$

which corresponds to the mixture of A and B metals with the same ratio*).

When $a=0$ ∴ $\boldsymbol{P}=\frac{1}{2}\begin{pmatrix} 1 & 1 \\ 1 & 1 \end{pmatrix}$ (42) is equal to

$$I=\frac{(V_1+V_2)(V_1^*+V_2^*)}{4}\frac{\sin^2\pi N\gamma}{\sin^2\pi\gamma}$$
$$+\frac{(V_1-V_2)(V_1^*-V_2^*)}{4}N, \tag{44}$$

which is the special case of (27) and corresponds to the complete disordered state of AB-alloy.

When $a=-1$ ∴ $\boldsymbol{P}=\begin{pmatrix} 0 & 1 \\ 1 & 0 \end{pmatrix}$ (42) is equal to

---

*) In such a case we assume that the thicknesses of both metals are the same as φ of that of the alloy.

$$I=\frac{(V_1+V_2)(V_1^*+V_2^*)}{4}\frac{\sin^2\pi N\gamma}{\sin^2\pi\gamma}+\frac{(V_1-V_2)(V_1^*-V_2^*)}{4}\frac{\sin^2\pi N(\gamma+\frac{1}{2})}{\sin^2\pi(\gamma+\frac{1}{2})},$$

which corresponds to the perfect ordered state of AB-alloy and the last term of which corresponds to the super lattice line.

Now in (42) crystallites having different ratios from 1:1 in their coherent region necessarily contribute to the total intensity, although small, as a result of such a way of derivation of the equation. On the other hand, the intensity due to only crystallites having a ratio of 1:1 in their coherent region when $a=0$, is calculated to be

$$I=\left\{\frac{(V_1+V_2)(V_1^*+V_2^*)}{4}-\frac{1}{N-1}\frac{(V_1-V_2)(V_1^*-V_2^*)}{4}\right\}\frac{\sin^2\pi N\gamma}{\sin^2\pi\gamma}+\frac{(V_1-V_2)(V_1^*-V_2^*)}{4}\left(N+\frac{N}{N-1}\right),$$

which becomes (44) if we assume that N is so large compared with 1 that the order of $1/N$ can be neglected. Hence (42) will hold generally.

§ 9. When N is very small.

When N is very small, for example $N=10$, the contribution of the higher term to the total intensity will become considerably large. Namely, for example, the curves of the last term in (42) for the cases of $N=10$ and $a=\pm 0.9$ and ± 0.8 are shown in Figs. 1 and 2, respectively, in which I_1, I_2 and I_3 are

$$I_1=N\frac{1-a^2}{D_1}=\frac{N(1-a^2)}{1+a^2-2a\cos\varphi},$$

$$I_2=\frac{2a\{2a-(1+a^2)\cos\varphi\}}{D_1^2},$$

$$I_3=\frac{2a(a)^N\{\cos(N+1)\varphi-2a\cos N\varphi+a^2\cos(N-1)\varphi\}}{D_1^2}$$

from (43) and I_1 is shown by a thin curve, (I_2+I_3) by a broken one, I_3 by a dotted one and the total $(I_1+I_2+I_3)$ by a thick curve. As seen from these curves, the contribution of the higher term (I_2+I_3) is so large that the curve I_1 is too high near $\gamma=0$ or 1/2. As seen from such an example, the higher term might have to be taken into consideration, for example, for the amorphous carbon.

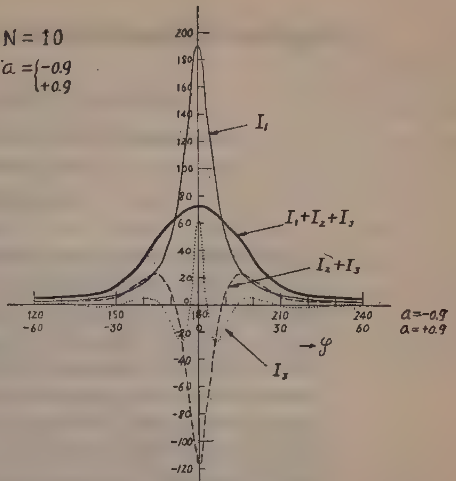

Fig. 1

Fig. 1.

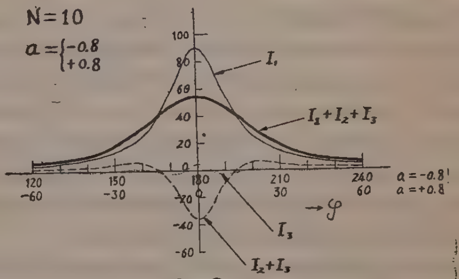

Fig. 2

Fig. 2.

In the second report the general treatment for the general structure with any S will be discussed showing a simple example. It will be shown there that the general intensity formula (12) will be also valid if the matrix elements will be properly taken. An application of this general treatment to the close packed structure with any S will be given in the third report and we shall obtain a general difference equation from which the difference equations [7] by Wilson²⁾ and [7] by Jagodzinski⁴⁾ will be derived for the special values of $S=2$ and 3, respectively.

References

1) S. Hendricks and E. Teller, J. Chem. Phys., **10** (1942) 147–167.

2) A. J. C. Wilson, Proc. Roy, Soc., A **180** (1942) 277–285.

3) H. Jagodzinski, Acta Cryst., **2** (1949) 201–207

4) H. Jagodzinski, Acta. Cryst., **2** (1949) 208–214.

5) H. Jagodzinski, Acta Cryst., **2** (1949) 298–304.

JOURNAL OF THE PHYSICAL SOCIETY OF JAPAN Vol. 7, No. 1, JAN—FEB., 1952

Electron Diffraction Study on the Ordered Alloy Au_3Cu

By Shiro OGAWA and Denjiro WATANABE

The Research Institute for Iron, Steel and Other Metals,
Tohoku University

(Received Augast 20, 1951)

Thin films of Au_3Cu were prepared by the evaporation method, and an imperfect, but sufficient order was formed in them after annealing at about 200°C for 100∼200 hrs. The films, whose transmissionp hotographs showed clear superlattice rings, were heated step by step up to 400°C or 500°C, and the collapsing manner of order was observed by gradual transition of diffuse superlattice rings to broad and faint bands, which persisted even at far higher temperatures than the transition point. our resalts coincided well with those of Germer and others in Cu_3Au, and these electron diffraction studies supported the results obtained by the specific heat measurements on the behaviour of Cu_3Au, Au_3Cu and CuAu at higher temperatures.

§ 1. Introduction.

The gold-copper system is one of the best known alloy-system and has been precisely examined by measurements of specific heat and electric conductivity and by X-ray diffraction. And two alloys, which belong to this system, namely Cu_3Au and CuAu, have the representative superlattices frequently referred to theoretical and experimental investigations.

Electron diffraction finds its own way in the research of the utmost surface crystalline state, which can not be attainable by other methods, and so we can utilize it for the study of metallic surfaces and films. In this case, the electron diffraction method may be applied together with the X-ray method, which is a big senior to the former in the field of the study for the structure of substances, to the various problems of metals, for example, order of alloys, aging, segregation and plastic deformation etc., each method playing its proper role. Germer and others[1)] have already shown by electron diffraction new results concerning the behaviour of ordered regions in Cu_3Au above the transition temperature, and Heidenreich and Shockley[2)] have revealed the structure of slip bands in metallic materials to be elucidated by electron diffraction together with electron microscope. Heidenreich[3)] has also developed by means of thin sections the applications of these methods to problems on the distortion of metallic crystals, cold-working and precipitation. The way for studying in these fields was thus showed to us.

There should be an ordered alloy Au_3Cu besides Cu_3Au and CuAu in the gold-copper system, but no conclusive evidence concerning it had been obtained when we started our work. According to Cowley's calculation[4)] the critical temperature of Au_3Cu is estimated at about 190°C, and so the difficulty of the formation of a considerable range of order can be ascribed to such a low critical temperature. But a small ordered region formed by low temperature annealing can be detected with comparative ease by electron diffraction owing to the short wavelength, which seemed to simplify the problem of Au_3Cu. Soon after we set to work, Hirabayashi[5)] reported the existence of the superlattice Au_3Cu, which was verified by the clear microphotometer trace of the X-ray photograph, the specific heat vs. temperature curves and the measurements of electric conductivity. In his work a specimen annealed at 200°C for 20 days showed λ-type peak of specific heat at 243°C, which is considerably higher than Cowley's estimation. In the present work the formation and the collapse of order in thin films of the alloy Au_3Cu were observed by electron diffraction.

§ 2. Experiments.

Gold and copper were successively evaporated in vacuum from fine wire (0.1 or 0.2 mm in diameter) suspended in a tungsten filament onto cleft surfaces of rocksalt or collodion films, their evaporated quantities being so controlled, that a film formed had an atomic composition of 75 Au and 25 Cu. All films* formed in such a way showed two kinds of face-centred cubic rings, namely those belonging to gold and copper, but after the films were homogenized in vacuum at 400°C for 30 min or 1 hr two kinds of rings converged on one kind of sharp ones, indicating the complete alloying of the films. Almost all of these films possessed such an orientation, that (111) is parallel to the film surface, which caused the anomalously larger intensity of (220) at the cost of (111) and (200).

The superlattice Au_3Cu must have perhaps the same lattice type as Cu_3Au, and hence the indices of the superlattice rings must be common, but the ratio of the intensities of the superlattice rings to that of the normal ones is greatly affected by the composition change. The integrated intensity of a diffraction ring, I, is porportional to $E^2pd^2_{hkl}$, where $E=|\Sigma S \exp(2\pi i\boldsymbol{r}\boldsymbol{h})|^2$, $S=2me^2/h^2\cdot(z-f)/d^2_{hkl}$, p a multilicity of a net plane, d_{hkl} is a spacing. Using the James-Brindley's approximation for the X-ray atomic scattering factor f, the values of I in each case of Cu_3Au and Au_3Cu are given in Table I. As seen from the table, the intensities of the superlattice rings of Au_3Cu are almost half those of Cu_3Au,and hence a sign of order is more difficult to distinguish in the former case than in the latter. The strong orientation in our specimens did not enable us to confirm the above computations for intensities, but facilitated the discrimination of the ordered region at its early stage of formation because of a larger intensity of (110) in spite of an anomalous faintness of (100).

Table I

	(100)	(110)	(111)	(200)	(210)	(211)	(220)
I for Cu_3Au	12.4	9.9	100	43.1	4.0	2.9	19.6
I for Au_3Cu	5.8	4.2	100	43.2	2.1	1.5	22.0

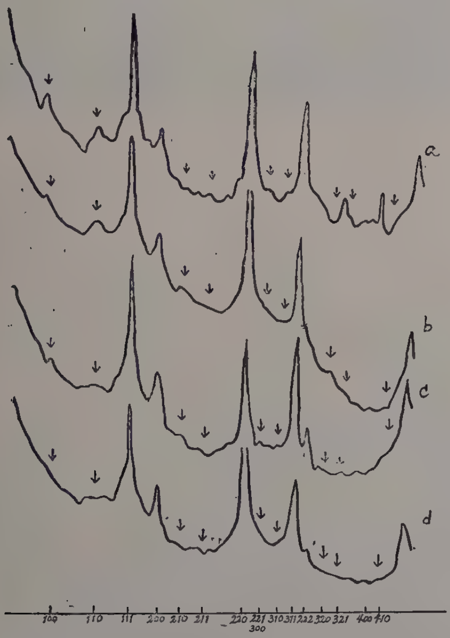

Fig. 1 Microphotometer curves of a series of diffraction patterns of films quenched at progressively higher temperatures.

a; 210°C, 50hrs., *b*; 210°C, 100hrs.
b; 230°C, 30hrs., *d*; 245°C, 15hrs.

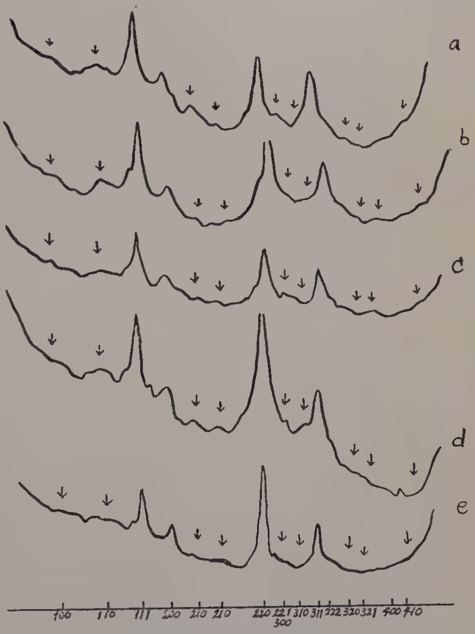

Fig. 2. Microphotometer curves of a series of diffraction patterns of films quenched at progressively higher temperatures.

a; 230°C, 30hrs., *b*; 245°C, 15hrs.
c; 260°C, 8hrs., *d*; 300°C, 2hrs.
e; 400°C, 1hrs.,

When one of the films, which had the composition of 75 Au and 25 Cu, was heated in vacuum at 210°C for 50 hrs., then faint diffuse maxima appeared at the positions of (100) and

---

* Several films, whose compositions were slightly different from each other, were prepared in order that the variation of the transition temperature of order-disorder due to different compositions was examined. But, owing to the inaccuracy in determining lattice parameters, this attempt did not succeed.

(110) rings as shown in the microphotometer trace in Fig. 1*a*. In the figures the arrows point to the positions, at which rings with mixed indices should appear. When this film was heated at the same temperature for 50 hrs. moreover, the diffuse maxima become slightly sharper as shown in Fig. 1*b* and Pl. I*a*, This means slack increases of ordered nuclei due to the prolonged heating. Among the films homogenized at 400°C and not heat-treated at lower temperature, only one showed a very faint, diffuse maximum at the (110) position.

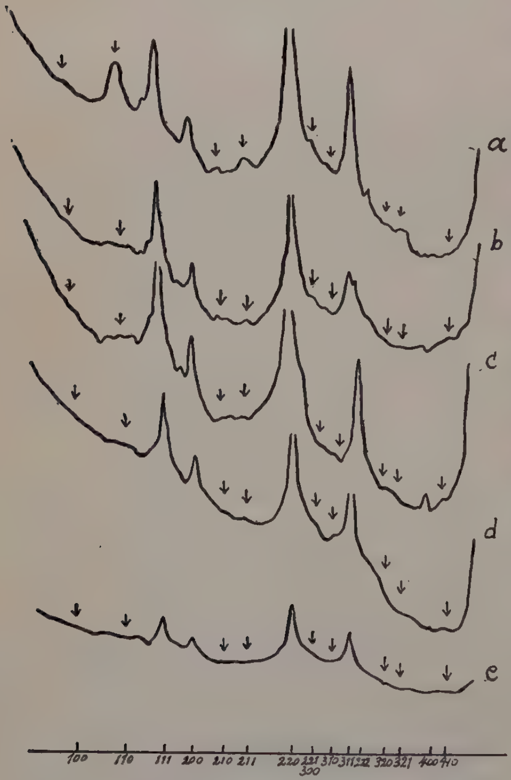

Fig. 3. Microphotometer curves of a series of diffraction patterns of films quenched at progressively higher temperatures.

a; 200°C, 210hrs., *b*; 250°C, 10hrs. *c*; 300°C, 3hrs., *d*; 400°C, 1hrs. *e*; 500°C, 30min.

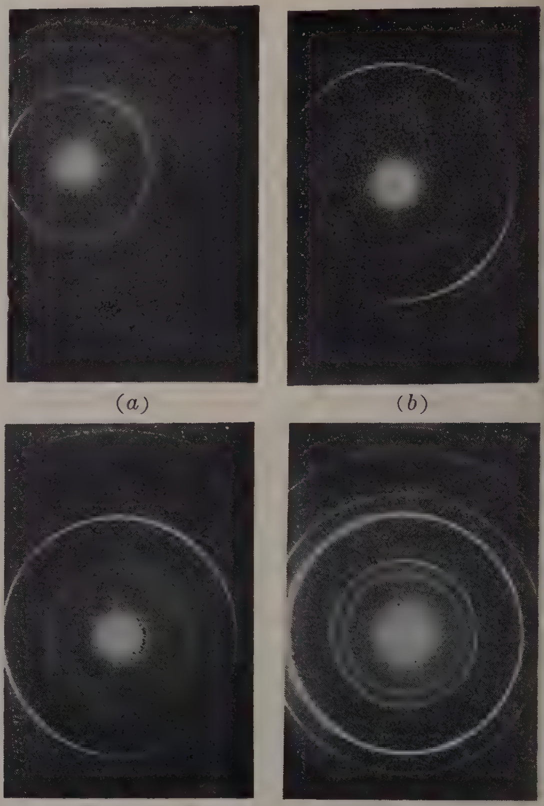
(*a*) (*b*)

(*c*) (*d*)

PL. I.

Photographs taken from Au$_3$Cu superlattice alloys. *a*: heated at 210°C for 100 hrs., two faint superlattice rings appear. *b*: heated at 230°C for 30 hrs. *c*: heated at 245°C for 15 hrs. after the treatment *b*. *d*: heated at 200°C for 210 hrs. This film shows a distinct superlattice structure, exhibiting (210) and (211) fairly. In each photograph a faint extra ring appears just inside (111).

The films, in which ordered regions were developed by 210°C annealing though not in a sufficiently large scale, were heated up to higher temperatures step by step, the collapsing manner of order being observed. At every observing temperature the film was heated sufficiently so long, that the equilibrium state was established in the specimen, which was rapidly cooled at the end of the heat-treatment. The quenching was performed by pouring water onto a silica tube, in which the specimen was enclosed. The ordered regions formed by the annealing at 210°C become smaller and smaller by heating up to 230°C and 245°C, the (110) superlattice ring becoming broader and fainter as shown in Fig. 1*c* and *d*. The diffraction photographs were taken for the heating durations of 30 hrs. and 50 hrs. at 230°C, and for 15 hrs. and 21 hrs. at 245°C. At each temperature both photographs corresponding to different durations showed no remarkable difference, and hence the equilibrium states seemed to be established in a satisfactory manner. Next, another film was heated at 230°C for 20 hrs. immediately after being homogenized at 400°C. Its photograph is seen in Pl. 1*b* and the photometer curve in Fig. 2*a*. In the latter the considerably broad (110) ring can be discerned together with the other superlattice rings (210) and (211). When this film was heated up to 245°C, 260°C, 300°C and 400°C for 15, 8, 2 hrs. and 1 hr. respectively, each superlattice ring become broader as shown in Fig. 2*b*, *c*, *d* and *e*, where it should be noted that the (110) trace exists as a broad and flat band even at 300°C and 400°C. Pl. I*c* shows the (110) band at 245°C. Lastly, a heat-treatment of the longest duration was imposed on another film at 200°C. Pl. I*d* corresponds to the heating of 210 hrs. In Fig. 3*a* the (110) ring is stronger than the normal (200) owing to the strong orientation of the specimen, and the other superlattice rings (210) and (211) are comparatively sharp. When this film was heated at 250°C for 10 hrs., 300°C for 3 hrs., 400°C for 1 hr. and 500°C for 30min., the superlattice rings turned gradually to the diffuse band with the temperature rise in the same manner as mentioned previously, and it can be seen from the photographs and also from the photometer curves of Fig. 3*d* and *e*, that the very broad band of (110) remains even at 400°C and 500°C.

It is well known that the grain size of crystals is given in the case of X-ray and electron diffraction by the following formula:

$$t=\frac{0.9\lambda}{B\cos\theta},$$

where t is the thickness of a crystallite, λ the wave-length, B the angular half breadth of diffraction lines and θ the Bragg angle. In electron diffraction the approximation $\cos\theta=1$ holds. Applying this method to the problem of order, the extent of the ordered region will be given from the half breadth of the superlattice ring. In our case this quantity, t, is estimated roughly from the (110) ring in each case, though there exists a considerable error. The values of t are given in Table II, where ΔR means the difference between the half breadth of diffraction rings and the breadth of the primary beam, 0.3 mm, and L the camera length. It is seen from this table that in the system 1 t seems to diminish abruptly at 245°C and in the system 3 the similar effect arises at 250°C, being accompanied by the slow decrease of t up to 500°C, while, in the system 2 there exists only the monotone decrease of t from 230°C to 400°C. But the detailed considerations on the above estimations may be somewhat insignificant owing to the considerable errors. It is, after all, concluded, that the destroyed ordered region has an extent of about 10 Å even at 500°C.

Table II $L=505$ mm $\lambda=0.064$ Å

	heating temp. (°C)	heating time (hrs.)	ΔR_{110} (mm)	$t=\frac{0.9L\lambda}{\Delta R}$ (Å)
1	210	50	1.2	32
	210	100	1.0	41
	230	30	1.3	29
	245	15	2.0	17
2	230	30	1.2	32
	245	15	1.3	29
	260	8	1.5	24
	300	2	1.8	19
	400	1	2.5	13
3	200	210	0.85	52
	250	10	1.8	19
	300	3	2.1	16
	400	1	2.3	14
	500	0.5	2.6	11

§ 3. Discussion.

We verified the existence of the Au_3Cu superlattice and described its behaviour by the electron diffraction study mentioned above, though this was performed in considerably oriented specimens. The results are almost analogous to that obtained by Germer and others in the Cu_3Au alloy, although the heat-treatments were carried out outside the diffraction comera in our case. The heat-treatment at 200°C for 210 hrs. was suffiicient to produce very distinct superlattice rings, thought not to complete the ordering of the specimen, and even the shorter duration of heating enabled us to observe the collapse of the ordered lattice by the successive heating up. It was perhaps due to the low transition temperature and the short heating duration, that Germer and others failed to observe the superlattice in this alloy. The transition temperature is not so low as that calculated by Cowley, but is in the vicinity of 240°C according to the specific heat measurements by Hirabayashi. In our electron diffraction study this temperature did not seem to have a special meaning concerning the size of the ordered region. The fact, that the film which was quenched at the far higher temperature than the above mentioned, namely at 500°C showed the broad superlattice band at the position of (110), coincides well with the results obtained by Germer and others, according to which the Cu_3Au film, whose transition temperature is 385°C, showed the broad (100) band even at 560°C. The size of the ordered region in Cu_3Au alloy was 38 Å at 247°C, 21 Å at 349°C and 11 Å at 560°C respectively. On the other hand, according to the same investigators, the ordered alloy of CuAu, which has the face-centred tetragonal lattice and has the transition at 425°C, gave no sign of diffuse bands at temperature above 400°C. These results obtained by electron difiraction confirm the specific heat measurements in Cu_3Au, Au_3Cu and CuAu as following: After Sykes and Johnes,6) in Cu_3Au the excess specific heat remained in the temperature range higher than that corresponding to the peak of λ type, and the same phenomenon was observed in Au_3Cu by Hirabayashi.5) In the ordered alloy CuAu, on the other hand, the circumstance is quite aifferent according to Hirabayashi and others7), that is, the specific heat-temperature curve above the transition temperature, at which the latet heat exist in this ordered ally, coincided with an extension of the ground line below the critical point. These experimental facts mean, that in the case of the face-centred cubic lattice, at least, the short range order, which does not exist in the 1 to 1 superlattice above the transition temperature, can be observed even at far higher temperature in the 3 to 1 superlattice, which is well supported directly by electron diffraction studies of Germer and others and of us.

References

1) L. H. Germer, F. E. Haworth and J. J. Lander, Phys. Rev., **61** (1942), 614.

2) R. D. Heidenreich and W. Shockley, J. App. Phys., **18** (1947), 1029.

3) R. D. Heidenreich, J. App. Phys., **20** (1949), 993.

4) J. M. Cowley, Phys. Rev., **77** (1950), 669.

5) M. Hirabayashi, Phys. Soc. Japan, **6** (1951), 129.

6) C. Sykes and F. W. Jones, Proc. Roy. Soc. A, **157** (1936), 213.

7) M. Hirabayashi, S. Nagasaki and H. Maniwa, Jap. Inst. Metals, **14** (1950), No. 3, 1.

JOURNAL OF THE PHYSICAL SOCIETY OF JAPAN, Vol. 7, No. 1, JAN.—FEB., 1952

On the Temperature Dependency of Magneto-resistance Effect of Iron Single Crystal

By Yasuo GONDO and Zenya FUNATOGAWA
Yokohama National University

(Received July 3, 1951)

Change of electric resistance of single crystal of iron rod induced by magnetization was measured by usual potentiometer and galvanometer deflection method at high temperature up to the Curie point. From these results $(\Delta R/R)_{111}$ and $(\Delta R/R)_{100}$ at several temperatures are calculated. $(\Delta R/R)_{100}$ remains constant from room temperature up to near 300°C and then decreases gradually to zero at the Curie point with increasing temperature. $(\Delta R/R)_{111}$ tends very smoothly to zero at the Curie point with increasing temperature. The large decrease of resistance near the Curie point is not anisotropic.

§ 1. Introduction.

Since Sir Wm. Thomson[1)] observed for the first time, in 1856, the change of electric resistance of nickel and iron by magnetization, this phenomenon has been investigated by many investigators. The magneto-resistance as well as galvano- and thermo-magnetic effects of non-ferromagnetic substances have contributed much to the success of the modern electronic theory of metal. A connection between ferromagnetics and conduction electrons may be one of the most important problems to be attacked in future theoretically. These effects should be examined with a single crystal because various ferromagnetic properties are of course anisotropic, but most of previous works have been carried out with polycrystals. The investigations with single crystals have been performed by this time by Webster[2)] and Shirakawa[3)] on iron, and by Kaya[4)] on nickel at room temperature. Shirakawa[3)] measured, moreover, the temperature variation of magneto-resistance effect of iron at low temperatures, but did not investigate a high temperature region. Temperature variations of anisotropy energy, magnetostriction, and magneto-thermoelectric power lately investigated by one[5)] of us, may be expected to have some formal connection with it. But we have not had such an examination of comparing the temperature variation of magneto-resistance effect with the other effects mentioned above over the range from room temperature to the Curie point. In order to obtain an exact information about the ferromagnetic anisotropy, therefore, a more detailed examination should be desired.

§ 2. Experimental method and samples.

A specimen was heated in a long uniform vaccum furnace winded non-inductively which was placed inside a magnetizing coil. Passing a suitable steady current of about 100 mA through a demagnetized specimen, the drop in potential was balanced by means of a galvanometer against a potentiometer. The change of resistance, when a magnetic field was applied, was calculated by a deflection of the galvanometer, its sensibility being 1.67×10^{-7}V. To elliminate various systematic errors, such as a potentiometer drop caused by a thermo-electric effect, or a certain change in the resistance of the specimen and the circuit due to some irregular variations in the temperature, a great care was taken about the connection by using heavy leads, and about obtaining a uniform temperature distribution as well as possible. Added to it, the final results were obtained by taking the mean of the values obtained with the current flowing in both directions.

The specimens used for this experiment were single crystal rods made from electrolytic Swedish iron by Edwards' recrystalization method. Their numerical data are given in Table I. We denote No. 10 by [100], No. 1 by [110] and No. 105 by [111] respectively.

§ 3. Experimental results.

The longitudinal effects at various temperatures up to the Curie points on descending hysteresis curves are shown in Figs. 1, 2 and 3. In these graphs the resistance-change $(\Delta R/$

R) is plotted as a function of the magnetic intensity. There is no remarkable difference between thermal and A.C. demagnetizing methods.

Table I.

Sample number	Diam. (mm.)	Length (mm.)	Direction cosines			Ir.
			β_1	β_2	β_3	
10	2.842	189.6	0.996	0.065	0.054	1535
1	1.930	140.0	0.794	0.571	0.167	1110
105	1.955	230.4	0.659	0.542	0.522	955

In the case of [100], as shown in Fig. 1, the change is so small that its measurement are very difficult. It decreases gradually with increasing temperature until it vanishes above 300°C. In both cases of [110] and [111], we can find out in Figs. 2 and 3 that the values of magnetic intensity, where the resistance-change appears, and also saturation values of $\Delta R/R$ decrease with increasing temperature. The saturation values of $\Delta R/R$ of our samples at several temperatures are shown in Fig. 4. Two of them gradually decrease, but the lowest curve remains constant up to about 300°C. The reason why this constancy occurs is not yet clear, though this may surely be caused by a magnetic origin.

In the region from 740°C to 780°C, which is near the Curie point, a large decrease of resistance is observed when a magnetic field is applied as already investigated by Potter[5] with polycrystals. As pointed out by Gerlach[7] and Mott[8], this decrease may be due to the increase of magnetization proportional to the magnetic field and hence we must distinguish it from the ordinary change at lower temperature. Accodingly, after the changes of resistance are measured as a function of the applied field at the several temperatures in the neighbourhood of the Curie point, the proper change can be distinguished from the measured value by the extrapolation to the field zero and can be represented by the smooth curves as shown in Fig. 4. The dotted curve in the figure represents the measured value at H=1200. The relation between this decrease and the direction of crystal axes is not recongnized.

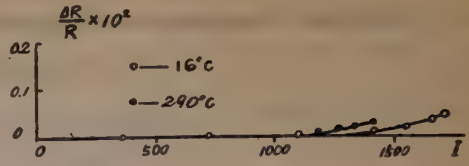

Fig. 1. Tetragonal crystal, No. 10.

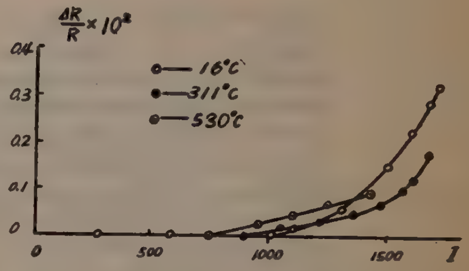

Fig. 2. Diagonal crystal, No. 1.

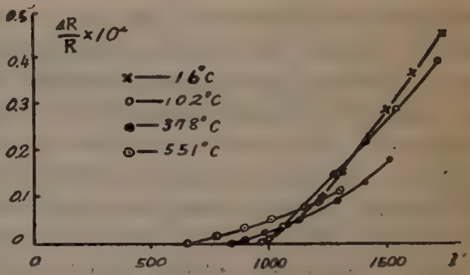

Fig. 3. Trigonal crystal, No. 105.

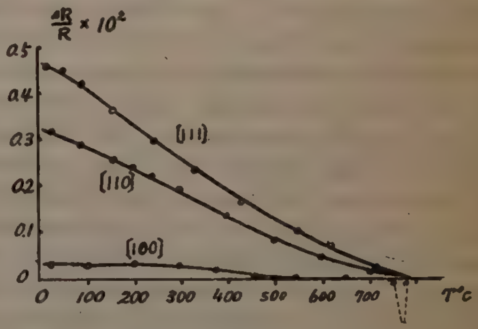

Fig. 4. Saturation values of $\Delta R/R$ at various temperatures. The values near the Curie point are obtained by the extrapolation to the applied magnetic field zero. The dotted curve represents the measured values at H=1200.

§ 4. Discussion.

When the change of resistance $\Delta R/R$ is plotted as a function of $(I/I_\infty)^2$, where I_∞ is a spontaneous magnetization at temperature T, and I is a magnetic intensity, the curves form a group of straiffht lines gathering to a fixed point as shown in each of Fig. 5. $(I/I_\infty)^2$ values of the fixed points obtained are 0.48 in [110] and 0.36 in [111], respectively. Thus we may assume that the distributions of the magnetic domains at these points, that is remanent points, are just the same as expected by Kaya's rule. So we can calculate anisotropy constants of magneto-resistance effect at any temperature by using our method.

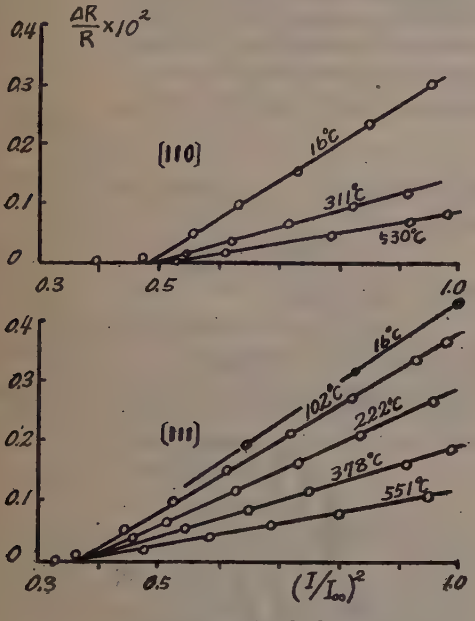

Fig. 5. Experimental relations between $\Delta R/R$ and $(I/I_\infty)^2$ at several temperatures.

With regard to the crystal symmetry, the change of electric resistance of the magnetically saturated crystal is given in the same way as well-known magnetostriction and so on as follows:—

$$\frac{\Delta R}{R}=\rho_0+\rho_1\sum\alpha_i^2\beta_i^2+\rho_2\sum_{i\neq j}\alpha_i\alpha_j\beta_i\beta_j$$

where α_i is direction cosines of magnetization with respect to principal axes, β_i the direction to measure resistance (in our case $\alpha_i=\beta_i$), and ρ_0, ρ_1 and ρ_2 are so-called anisotropy constants of magneto-resistance effect and must fill the following relations,

$$\rho_0=-\frac{1}{3}\rho_1,\quad \rho_1=\frac{3}{2}\left(\frac{\Delta R}{R}\right)_{100},\quad \rho_2=\frac{3}{2}\left(\frac{\Delta R}{R}\right)_{111}$$

where $(\Delta R/R)_{100}$ and $(\Delta R/R)_{111}$ are the saturation value in [100] and [111], respectively.

Calculatated ρ_1 and ρ_2 at various temperatures are shown in Fig. 6. The behaviour of ρ_2 is analogous to K_1 (anisotropic constant of magnetic energy) and λ_{111} (magnetostrictive constant), and very smoothly tends to zero with increasing temperature. On the other hand, any remarkable variation of ρ_1 is not seen from room temperature up to near 300°C. As ρ_1 is very small, it is too difficult to decide its value accurately enough, but the anomaly of ρ_1 is certainly existing. We have already observed an anomaly near 300°C in magneto-thermoelectric power, too. Although the reason of the anomaly is not clear as described above, we may suggest a necessity of considering it in connection with either anomalies of K_2 (magnetic anisotropy constant of energy) or the specific heat of iron near 300°C as pointed out by Awbery and Griffiths.[9)]

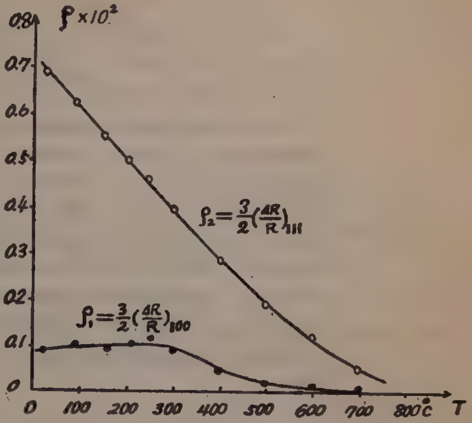

Fig. 6. Temperature dependency of anisotropy constants.

We should like to express our great appreciation and thanks to professor S. Kaya and the members of his laboratory.

References

1) W. Thomsom: Phil. Trans. London **146** (1856), 649.

2) N.L. Webster: Proc. Roy. Soc. A. **113** (1936), 196; **114** (1927), 611.

3) Y. Shirakawa: Sci. Rep. Tohoku Univ. **19** (1941), 132.

4) S. Kaya: Sci. Rep. Tohoku univ. **17** (1928), 1157.

5) Z. Funatogawa: J. Phys. Soc. Japan **5** (1950), 311; **6** (1951), 256.

6) H.H. Potter: Proc. Phys. Soc. **49** (1937), 671.

7) W. Gerlach & K. Schneiderhan; Ann. d. Phys. **6** (1930), 772.

8) N.F. Mott: Proc. Roy. Soc. A. **156** (1936), 368.

9) J. H. Awbery & E. Griffiths: Proc. Roy. Soc. A. **174** (1940), 1.

JOURNAL OF THE PHYSICAL SOCIETY OF JAPAN Vol. 7, No. 1, JAN.—FEB., 1952

Failure and Fracture of Metals as Nucleation Processes*

By Takeo YOKOBORI

Institute of Science and Technology,
University of Tokyo

(Received January 9, 1951)

The discontinuous phenomena in plasticity of metals, such as the yielding, the state of ultimate strength, and the brittle fracture, were regarded as a kind of Markoff process, and studied from the standpoint of nucleation theory. The fundamental features of these types of failures, namely, (1) the relation between strength and deformation velocity or stress velocity, (2) the temperature dependence of strength, (3) the size effect, (4) the transition temperature from ductile to brittle failure, (5) the fluctuation characteristics of strength were unifiedly interpreted. Theoretical criterions of failure and fracture of polycrystalline metals were also introduced.

§1. The Theory.

The term of failure stress used herein means the yielding stress and the ultimate stress at which the rate of slip is observed to increase rapidly or discontinuously with comparatively crude equipment. The fracture means the appearance of macro-crack. Yielding the state of ultimate strength, and fracture may be expected to correspond to the nucleation and the growth or propagation of dislocation or crack, respectively, in weak spots such as mosaic block or grain boundaries. In the usual failure or fracture, however, the nucleation process may be considered to be much slower than the growth or progagation one, and be a rate-determing process. Hence, the yielding, the state of ultimate strength, and the brittle fracture were taken as the nucleation process in this paper. As a fundamental case, a simple loading1) was considered for the stress state, that is,

$$S=vt \qquad (1)$$

where S is stress and v is stress velocity.

(a) The yielding. Formating of a dislocation line of racius r requires the work equal to an energy of the dislocation zone, which may be taken as proportional to r2) and expressed as Ar. On the other hand, a decrease of elastic energy accompanies the glide process. (Fig. 1) Since it is proportional to the dislocated area and to the depth of unstressed zone2), it may be expressed as BSr^3, where S is the shear stress in the slip plane, and B is a constant. The net work associated with the reversible formation of a dislocation line is, therefore,

$$W=Ar-BSr^3 \qquad (2)$$

W has a maximum

$$W_{\max}=2A^{3/2}/3\sqrt{3BS}=\beta/\sqrt{S}$$

with radius $r^*=\sqrt{A/3BS}$.

On the basis of the theory of nucleation3)6),

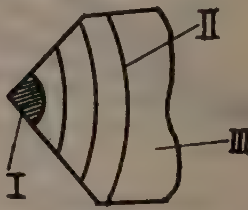

Fig. 1.

I —a nucleus of dislocation.
II —a full length of dislocation.
III—block.

the rate of formation of such dislocation in a specimen was derived as**

$$m=(ZkT/h)\exp\left[-(\Delta f^*-\alpha S+W_{\max})/kT\right]$$
$$=(ZkT/h)\exp\left[-(\Delta f^*-\alpha vt+\beta/\sqrt{vt})/kT\right] \qquad (3)$$

where Δf^* is the free energy of activation for the motion of a dislocation5)6), αS is the added energy term7) by shear stress, and Z is the constants proportional to the total number of weak spots available for dislocations.

The yielding will be assumed to correspond to the nucleation of one dislocation line. And the phenomenon of yielding will be regarded as a kind of Markoff proceis8)9). Hence, the probability distribution function $1-P$ is

---

* The previous paper on these problems is to be published in Japan Soc. Mech. Engrs. preprint (4th room) Apr. 3rd 1951, pp. 11~16, in which the author treated them as rate processes governed by the maximum shear stress, and paid no speculation as to the nature of the unit process.

$$dp/dt=-mp \qquad (4)$$

Hence, the probability density function q is

$$qdt=m\exp\left(-\int_0^t mdt\right)dt \qquad (5)$$

The yield stress may be said to correspond to the most probable value S_m which gives maximum value of q in Eq. (5). Differentiating Eq. (5) with t and putting to zero, we get

$$dm/dt=m^2 \qquad (6)$$

Substituting Eq. (3) in Eq. (6), the latter condition is written in the form

$$\begin{aligned}&(\alpha v/kT)(1+\beta/\alpha S_m^{3/2})\\&\quad=(ZkT/h)\exp[-(\varDelta f^*-\alpha S_m\\&\qquad+\beta/\sqrt{S_m})/kT] \qquad (7)\end{aligned}$$

(b) The state of ultimate strength. In the case of the ultimate stress which corresponds to maximum load initiating the necking***, the reversible formation of a circular crack of radius r is assumed instead of a dislocation line as nucleus. Hence, the net work associated with this formation is

$$W=2\pi r^2\rho-CF^2r^3 \qquad (1)'$$

in which F is the tensile stress in the direction normal to the plane of the crack, and C is a constant. The first term corresponds to the work by the interfacial tension ρ, and the second to the work to allow the reversible relaxatio of strain energy in the neighbourhood of the crack10). Hence, by the similar line of considerations used above, the similar type of equation as Eq. (7) is obtained as follows.

$$\begin{aligned}&(\alpha_1 v/kT)(1+4\beta_1/\alpha_1 F_m{}^5)\\&\quad=(Z_1kT/h)\exp\{-(\varDelta f_1{}^*\\&\qquad-[\alpha_1 S_m-\beta_1/F_m{}^4]_{\max})/kT\} \qquad (7)'\end{aligned}$$

where S_m is the shear stress on the plane of the crack, $\varDelta f_1{}^*$ is the free energy of activation for separating a pair of atoms, Z_1 and α_1 correspond to Z and α in Eq. (7) respectively and β_1 is a constant. A rate process in each chain reaction was assumed to be governed by S_m. Or in the term of S_m

$$\begin{aligned}&(\alpha_0 v/kT)(1+4\beta_0/\alpha_0 S_m{}^5)\\&\quad=(Z_1kT/h)\exp\{-(\varDelta f_1{}^*\\&\qquad-\alpha_0 S_m+\beta_0/S_m{}^4)/kT\} \qquad (7)_1'\end{aligned}$$

(c) The brittle fracture. The brittle fracture under the tensile stress will also be considered from the same line of considerations. In this case, the plane of the crack is normal to the applied tensile stress, and a rate process in each chain reaction was assumed to be governed by the tensile stress normal to the plane of the crack. Hence, the fracture stress F_m will be given by the relation

$$\begin{aligned}&(\alpha_2 v/kT)(1+4\beta_2/\alpha_2 F_m{}^5)\\&\quad=(Z_2kT/h)\exp\{-(\varDelta f_2{}^*\\&\qquad-\alpha_2 F_m+\beta_2/F_m{}^4)/kT\} \qquad (7)''\end{aligned}$$

where $\varDelta f_2{}^*$, Z_2, α_2 and β_2 correspond to $\varDelta f_1{}^*$, Z_1, α_1 and β_1 respectively in Eq. (7)′.

§2. The dependence of the strength on the stress velocity or deformation velocity and the temperature.

If $\beta/\alpha S_m^{3/2}<1$, the term invelving S_m explicitly in Eq. (7) are written in the form $\alpha S_m-\beta/\sqrt{S_m}-kT\beta/\alpha S_m^{3/2}$. This term can be found to be approximately equivalent to the form $\log(C_1S_m)^{1,n}$, where n and C_1 are suitably chosen constants. Hence, Eq. (7) will be reduced in the form

$$S_m\doteqdot(1/C_1)[C_0v\exp(\varDelta f^*/kT)]^{nkT} \qquad (8)$$

where $C_0=\alpha h/Zk^2T^2$.

The change of S_m with T involved in C_0, and also when $C_0v<1$, with T involved in the power coefficient nkT can be shown to be negligible compared with that of S_m with T involved in the term $\exp(\varDelta f^*/kT)$ in the case where temperature range is not so wide. In this case, Eq. (8) becomes the form

$$S_m=C^*[v\exp(\varDelta f^*/kT)]^\gamma \qquad (9)$$

in which C^* and γ are constants. When $4\beta_0/\alpha_0S_m{}^5<1$ or $4\beta_2/\alpha_2F_m{}^5<1$, the same type of equations as Eq. (8) and (9) are obtained as for the ultimate strength and brittle fracture stress from Eq. $(7)_1'$ and (7)″ respectively. It is reasonable to consider that deformation velocity is proportional to stress velocity unless the change of cross-sectional area of specimen is not so much. Under this condition, the equivalence of deformation velocity and temperature of the type Eq. (9) has first been

---

** Since Eq. (3) was obtained following Turnbull and Fishers' method6), details were not shown here In this case, however, $\left[\dfrac{d(\varDelta W_i)}{di}-\dfrac{2\alpha S}{i^*}\right]/2KT$ was assumed small compared with unity, and terms of higher orders with respect to S were neglected.

*** The necking may be assumed to be the phenomenon of the flow caused near the crack in order to smooth out the stress concentration.

found experimentally by Russian investigators, Wittmann and Stepanov[11], upon the brittle failure of steel, and later Zener[12] found the same formula as Eq. (9) experimentally upon plastic failure of steel. Recently, the same formula has also been observed in the resistance to plastic deformation by compression[13]. When $\alpha S_m \gg \beta/\sqrt{S_m}$ or $\alpha_0 S_m \gg 4\beta_0/S_m^4$, Eq. (7) or $(7)_1'$ reduces to

$$S_m \sim \log v + \text{constant} \qquad (10)$$

which is in good agreement with the experiments on yielding and tensile strength of mild steel and copper[14].

In general, in wide range of temperature and deformation velocity, Eq. (7) is expressed as

$$\log(S_m/S_0) = nkT \log(v/v_0) \qquad (11)$$

where S_0 refers to v_0. This formula is quite well in accordance with Davidenkov-Wittmann-Stepanov's general formula, which has recently demonstrated experimentally by Sokolov[15] upon many kindsof metals.

§3. The influence of size on the strength.

In the first approximation, when Z is regarded proportional to the speciment volume V, the following relation is obtained corresponding to Eq. (9)

$$S_m \sim V^{-\tau} \qquad (12)$$

or corresponding to Eq. (10)

$$S_m \sim \text{constant} - \log V \qquad (13)$$

The type of Eq. (12) is well in accordance with the experiments[16].

§4. The transition temperature from ductile to brittle failure.

If Eq. $(7)_1'$ is solved with respect to $\Delta f_1^* - \alpha_0 S_m/kT$, this term will be found to decrease with the decrease of temperature, when $(5/4)\alpha_0 S_m - \beta_0/S_m^4 > \Delta f_1^* + 2kT$. Hence, below a critical temperature, the mechanism of failure or fracture will be expected to change into the momentum transfer mechanism[7]. The author expects this temperature to be a critical or transition temperature from ductile to brittle failure. At critical point, within a limited range, the experimental quantative relation between velocity and temperature is expressed[17] as $\log v = C - Q/RT$, which can be derived from Eq. $(7)_1'$ under this condition.

§5. The fluctuations of strength.

As a first approximation for simplicity, the case where $d(\Delta W_i)/di \ll 2\alpha S/i^*$ was considered in this section.‖ This does not alter the essential characteristics in fluctuation phenomena in strength. In this case, the following frequency distribution curve is obtained corresponding to Eq. (5)

$$q\,dx = K \sinh x \exp[K(1 - \cosh x)]dx \qquad (14)$$

in which $K = (2k^2T^2Z)/h\alpha v \exp(-\Delta f^*/kT)$ and $x = \alpha vt/kT = \alpha S/kT$. It is shown with parameter K as in Fig. 2, It can be understood from Fig. 2 that the form of the frequency distribution curve is shifted from the possitively skewed type to the negative skewed one with a decrease of K. A decreaseof K corresponds to an increase of stress velocity v, and the activation energy Δf^*, a decrease of temperature, and Z (the specimen volume).

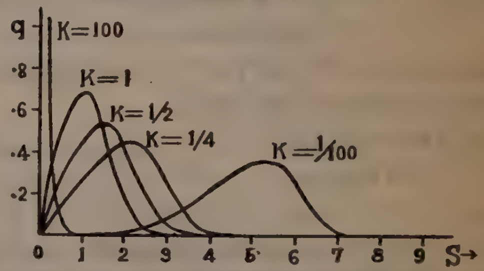

Fig. 2.

Fluctuation characteristics of strength.
(x should be read for S)

When $v=0$, i.e., when a constant load is applied at $t=0$, the frequency distribution of time required for fracture is given as in Fig. 3.

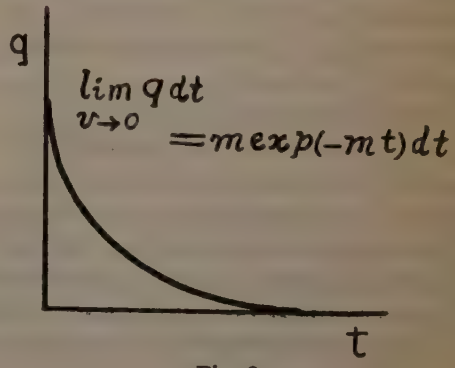

Fig. 3.

The frequency distribution of time required for fracture.

‖ This case is formally equivalent to that of simple rate process such as growth process of nucleus. See short note in this volume.

which has already been demonstrated by Prof. M. Hirata[8], and Prof. H. Kubota[18] with glass plates.

In the range of K near or equal to one, the good agreement is obtained with creep fracture of copper wire[19]. It has also been demonstrated[20] by experiments that the frequency distribution curve of fracture of glass continuously changes its form in the similar way as in Fig. 2 when v is increased. The case of $K \ll 1$ may be said to correspond to an appreciable value of v such as static test and impact test, and it can be seen that the curve are negatively skewed in this case as is so-called. It is also concluded from Eq. (14) that the smaller the specimen and the larger the stress velocity is, the wider the scatter is. The former fact is experimentally demonstrated by the experiments[16].

§6. Theoretical criterions of failure and fracture of polycrystalline metals.

(a) The yielding. From Eq. (7), the yielding is found to occur when shear stress attains a critical value.

(b) The state of ultimate strength. On the plane inclined by φ against some standard plane, $\alpha\tau-(\beta/\sigma^4)$ will have a maximum value M, where σ is the tensile stress normal to and τ is the shear stress in the plane of the crack, respectively. Thus the criterion is

$$(\alpha\tau-\beta/\sigma^4)_{\max}=\text{constant} \qquad (15)$$

It can be understood that this theory involves Mohr's theory in the modified form.

(c) The brittle fracture. The criterion for this case correspond to the maximum tensile stress theory as seen from Eq. (7)$''$.

The author wishes to express his deep thanks to Prof. M. Hirata for his active interest in this work and his useful suggestions. Thanks are also due to Dr. R. Hashiguchi for his enlightening discussions from the metallugical standpoint, Prof. K. Omori for some instructions upon the nucleation theory; Dr. J. Yamashita for his kindness of reading this paper, and Prof. Nakanishi for his kind discussions on the strength of materials.

References

1) A. A. Illyshin, Priklad, Mat. i. Mekh. **11** (1947) 293.

2) E. Orowan, Proc. Phys. Soc. London **52** (1940) 8.

3) J. Frenkel, J. Chem. Phys. **7** (1939) 538.

4) J. C. Fisher, J. H. Hollomon, and D. Turnbull, J. App. Phys. **19** (1948) 775.

5) J. C. Fisher, J. App. Phys. **19** (1948) 1062.

6) D. Turnbull, and J. C. Fisher, J. Chem. Phys. **17** (1949) 71.

7) S. Glasstone, K. J. Laidler and H. Eyring. The Theory of Rate Processes (1941)

8) M. Hirata, Bull. Math. Statis. (in Japanese) **3** (1949) 57.

9) T. Yokobori, Read at the 4th Regular Meeting of the Inst. of Sci. and Tech., Univ. of Tokyo, June 3–4, 1949,: J. Phys. Soc. Japan. **6** (1951) 78 and 81, in which ydy should be read for $\sqrt{ydy}$ in Eq. (7) at P. 85.

10) R. A. Sack, Proc. Phys. Soc. London, **58** (1946) 729.

11) F. F. Wittmann, and V. A. Stepanov, Zh. Tekh. Fiz. **9** (1939) 1070.

12) C. Zener, J. App. Phys. **15** (1944) 22.

13) F. F. Wittmann and N. A. Zlatin. Zh. tekh. Fiz. **19** (1949) 315.

14) H. Deutler, Phys. ZS. **33** (1932) 247.

15) L. D. Sokolov. Dokalady Akad. Nauk. **67** (1949) 459.

16) N. Davidenkov, E. Shevandin, and F. Wittmann, J. App. Mech. **14** (1947) 63.

17) C. W. MacGregor, N. Grossman, and P. R. Shepler, Weld. Res. Suppl. **12** (1947) 50.

18) H. Kubota, J. Appl Phys. Japan (in Japanese) **17** (1948) 286.

19) T. Yokobori, in this volume.

20) M. Hirata, and N. Terao, J. App. Phys. (in Japanese) **18** (1950) in press.

Note added. Unfortunately, the original papers of references (1), (11), (13) and (15) are not to be found in this country, and the author refered them from other papers and reports.

JOURNAL OF THE PHYSICAL SOCIETY OF JAPAN, Vol. 7, No. 1, JAN.—FEB., 1952

Creep Fracture of Copper as Nucleation Process*

By Takeo YOKOBORI

Institute of Science and Technology,
University of Tokyo

(Received January 9, 1951)

Creep fracture of copper wire was regarded as a kind of Markoff process, and studied from the standpoint of nucleation theory. The theory indicates the power relation between stress and time for fracture which is in good accord with experiments. The dependence of time for fracture on the stress, the temperature and the length of specimen was experimentally obtained. The fluctuation characteristics accompanying these phenomena were also studied. These experiments were interpreted from the theory.

§1. Theoretical considerations.

From the same standpoint as explained in the preceding paper1), the creep fracture was studied with copper wire. The author separated creep fracture into two stages, that is, necking and fracture. Hence, the rate of formation of circular cracks initiating the necking in a specimen is given by

$$m_1=(Z_1kT/h)\exp\left[-(\Delta f_1^*-\alpha_1 S+\beta_1/S^4)/kT\right] \quad (1)$$

where notations correspond to those in Eq. (3) in the preceding paper1). The fracture of a specimen following the necking is assumed to occur by the nucleation of a crack at weak spots where work hardening occured and the stress concentration increased after necking. Similiarly, the rate of formation of cracks causing fracture of a specimen is represented by

$$m_2=(Z_2kT/h)\exp\left[-(\Delta f_2^*-\alpha_2 S+\beta_2/S^4)/kT\right] \quad (2)$$

In ordinary creep test, S can be said to change little with time t, so that m_1, and m_2 may be regarded as nearly independent of time. Hence, the mean time $\bar{t}$ required for fracture from the instant of the application of load will be re lated in the following form

$$\bar{t}=1/m_1+1/m_2 \quad (3)$$

Since Δf_2^* map be expected to be larger than Δf_1^*, $1/m_1 \ll 1/m_2$ if $Z_1 \gg Z_2$. In such case, the second (fracture) process will be regarded as a rate-determing one. Hence, Eq. (3) reduces to

$$\bar{t}=1/m_2=(h/Z_2kT)\exp\left[\Delta f_2^*-\alpha_2 S+\beta_2/S^4)/kT\right] \quad (4)$$

or in the terms of ordinary logarithms, using the approximation1) $\alpha_2 S-\beta_2/S^4=\log(C_1S)^{1/n}$,

$$\log\bar{t}=\Delta f_2^*/kT+\log(1/T)-(1/nkT)\log(C_1S)+\log(h/Z_2k) \quad (5)$$

§2. Experimental Results.

The material used was commercial copper wire of 0.8 mm diameter. The time required till fracture was measured from the instant when each constant load was applied at various constant room temperatures. The steady creep strain rate was in a range extending from 2.5 $\times 10^{-3}$ to 2.2×10^{-5} per second. In these kinds of experiments, fluctuations of measured values are usually appreciable. Hence, the frequency distribution of the time required for fracture was determined using some hundred specimens in each series of test, and $\bar{t}$ was obtained from the curve .The curve of strain versus time for each constant load is showen as in Fig. 1. The

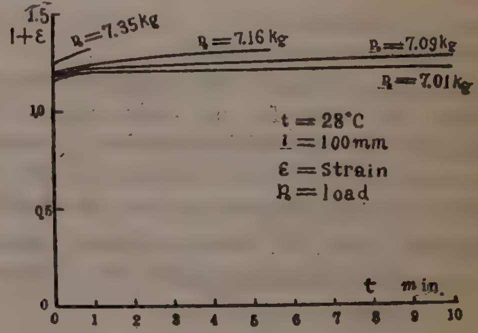

Fig. 1. Strain versus time curve.

---

* The previous paper on these problems is to be published in Japan Soc. Mech. Engrs. preprint (4th room) Apr. 3rd 1951 pp. 17~21, in which the author treated them as rate processes governed by the maximum shear stress, and paid no speculations as to the nature of the unit process.

increment of strain after the time t_0 when the transient creep vanished is very small compared with the strain ε_0 at the time t_0, and can be neglected. On the other hand, the increment of the strain after occurring of necking was not so conspicuous. Hence, it is reasonable to consider that S in Eq. (5) is given in the form[2)]

$$S=(1+\varepsilon_0)S_0 \qquad (6)$$

in which S_0 is load divided by cross-sectional area.

(1) The relation between stress and time for fracture

In Fig. 2, the logarithms of stress at three constant temperatures are plotted against the logarithms of the mean time $\bar{t}$ for fracture. If there is a heat of activation over the temperature range, these curves should become straight lines. This has been found to be the case. By Eq. (5), the slope of these lines gives $1/nkT$, and it can be seen from Fig. 2 that it is almost constant in the temperature range tested. Hence

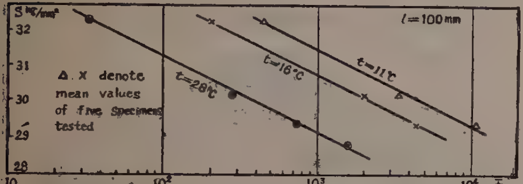

Fig. 2. $\log \bar{S} - \log t$ curve.

$$n \propto 1/T \qquad (7)$$

which is the similar relation as in static test[1)].

(2) Temperature dependence

The tests were carried out in a range of temperature extending from 10°C to 29°C under constant load. In Fig. 3, the temperature under two constant stress is plotted against the logarithm of $\bar{t}$, and these curves proved to be almost straight line. Since the change of $\bar{t}$ with T involved in the term $\log(1/T)$ is negligible compared with T in the term $\Delta f_2^*/kT$,

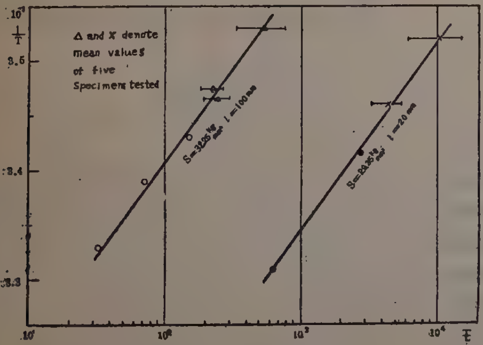

Fig. 3. $\dfrac{1}{T} - \log \bar{t}$ curve

$$\log \bar{t} = \Delta f_2^*/kT + \text{constant} \qquad (8)$$

which is well in accordance with experiments as shown in Fig. 3. From the tangents of these curves, Δf_2^* can be obtained. The free energy of activation per g atom, Q_2, thus determined becomes about 27,000 cal. per mol.

(3) Effect of the length of specimen.

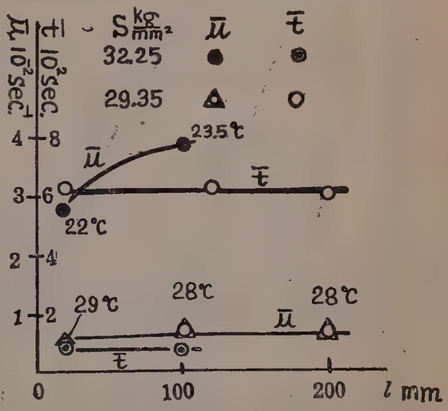

Fig. 4. The effect of the specimen length.

As can be seen from Fig. 4, the size effect on the time $\bar{t}$ was no marked in a range of specimen length extending from 20 to 200 mm. These results may be well understood from the fact that in this case the fracture process is a rate determing one, and that the volume where necking occurrs, therefore, Z_2 can be said to be almost iddependent of the total length l of the specimen.

(4) The fluctuation of the time required for fracture.

The frequency distribution of the time required for fracture had characteristic. The probability μ, of occurring of creep fracture per unit time are given by the negative derivative[2)] of the curve of $\log Z_0P$ versus t, in which Z_0 is the total number of specimens tested and P denotes the probability of occurring of fracture after the time t. The curve of $\log Z_0P$ versus t obtained were shown in Figs. 5, 6, 7, 8, and 9 corresponding to Figs. 2, 3 and 4 respec-

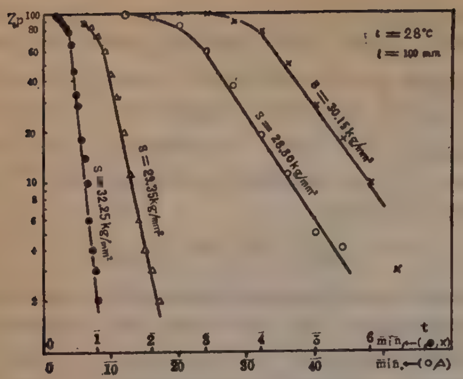

Fig. 5. log Z_0P-t curve (the effect of stress)

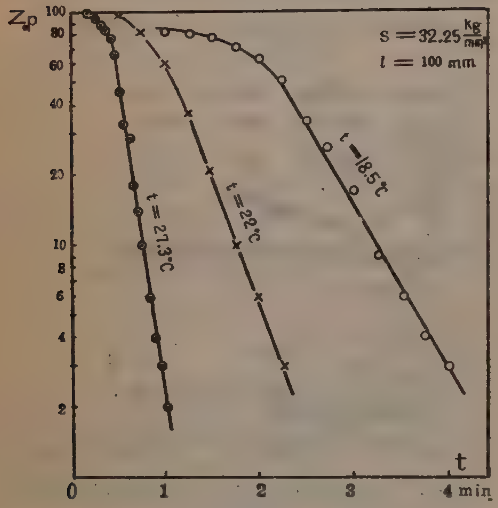

Fig. 6.
log Z_0P-t curve (The effect of temperature)

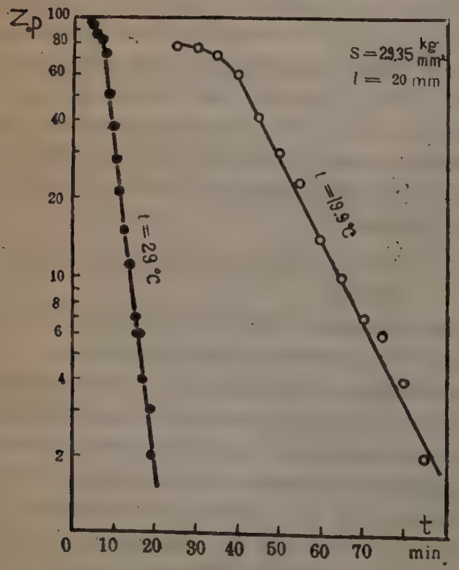

Fig. 7.
log Z_0P-t curve (The effect of temperature)

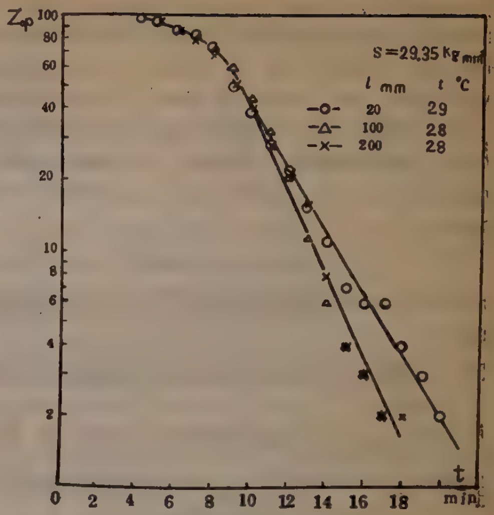

Fig. 8.
log Z_0P-t curve
(The effect of the specimen length)

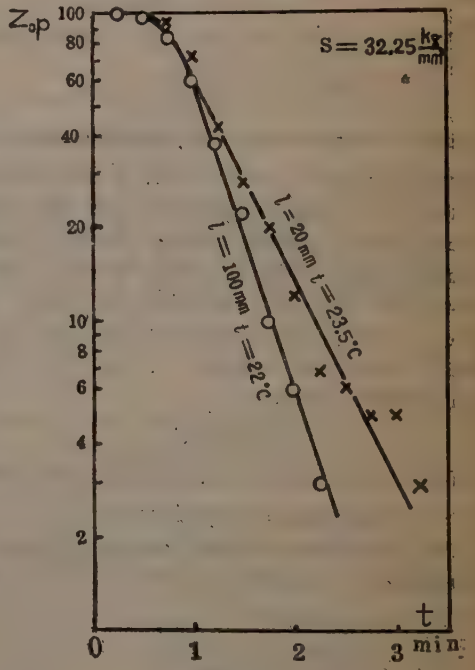

Fig. 9.
log Z_0P-t curve
(The effect of the specimen length)

tivelly. It can clearly be understood from these figures that the probability μ, of fracture begins to have some finite value at the lapse of some finite time t_* and increases with time. This increasing rate, however, is not so much that the average value $\overline{\mu}$ of the probability can be obtained when the slope is assumed as constant. The correlations between $\overline{\mu}$ obtained and

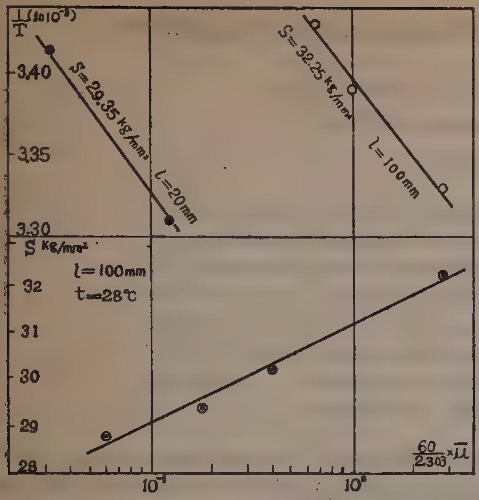

Fig. 10. The dependence of $\bar{\mu}$ on stress and temperature.

stress, temperature, and size respectively are shown in Figs. 10 and 4. Comparing these relations with those obtained in the paragraph (1), (2) and (3), $\bar{\mu}$ proved to be almost equal to $1/t$, therefore m_2. This means that the fluctuation of fracture values seems to be interpreted from the standpoint of nucleation process.

In concluding this report, it is hoped that more experiments will be carried out in more extensive range of stress and temperature, and in other metals for the development of this line of consideration.

The author is deeply indebted to Prof. M. Hirata for his valuable suggestions and encouragement during this research. Acknowledgment is also made to Dr. R. Hashiguchi for his enlightening discussions from the metallugical standpoint, Prof. K. Ōmori for some instructions upon the nucleation theory, Dr. J. Yamashita for his kindness of reading this paper, and Prof. F. Nakanishi for his kind disccusions on the strength of materials.

References

1) T. Yokobori, in this volume.

2) T. Yokobori, J. Phys. Soc. Japan., **6** (1951) 78, where S_0 is used in stead of S.

Note added: The creep fracture accompanied by necking as in these experiments seems to be better explained as the growth process of a crack nucleated than as the nucleation process treated in this paper. See short note in this volume (in press).

JOURNAL OF THE PHYSICAL SOCIETY OF JAPAN Vol. 7, No. 1, JAN.—FEB., 1952

Intensities of Forbidden Lines of Atoms in p^n-configuration

By Takahiko YAMANOUCHI and Hisashi HORIE
Physics Department, University of Tokyo

(Received June 11, 1951)

The intensities of the electric quadrupole and the magnetic dipole radiations of atoms and ions corresponding to the transitions between the states arising from the same electron configuration p^n are calculated. In constructing the eigenfunctions for each J-state, spin-orbit and spin-spin interactions between *different* electrons as well as the usual spin-orbit interactions of individual electrons are taken into account to make fit with the observed multiplet intervals. The results are expected to be improved by the inclusion of these previously neglected interactions.

§ 1. Introduction.

In connection with the astrophysical and upper-atomospheric problems, the calculation of the intensities of the spectral lines for the forbidden trnsisions of atoms and ions in p^n-configurations as a direct application of quantum mechanics has aroused the interest of some of the theoretical physicists and extensive studies have been carried out by Condon and others¹⁾. Among these lines of forbidden transitions, those of magnetic dipole origin come into play only through the breakdown of LS-coupling, which manifests in the separations of the multiplet components, each characterised by the inner quantum number J. The departure from LS-coupling is usually believed to be due to the spin-orbit interactions of individual electrons, from which the well-known Landé's rule for the multiplet intervals are obtained. The actual intervals for atoms in $2p^n$-configurations, however, do not strictly obey this rule. Araki²⁾ has shown by a great many examples of multiplet terms that the mutual spin-orbit and spin-spin interactions have considerable effects on the multiplet separations. We have therefore in this paper attempted to construct more precise eigenfunctions for each J state by inclusion these neglected interactions to obtain better values of the intensities of the forbidden lines. It is found that the multiplet splittings calculated in this way by the use of the analytic wave functions approximating the Hartree functions are in agreement with observed values, at least in so far as the interval ratios are concerned, and the disagreement of numerical values of term differences can be reasonably accounted for by the theoretical considerations. So we have determined the parameter values involving the radial eigenfunctions of atomic electron directly from the observed data, and the intensities of the lines are then calculated with these values, so to speak, semiempirically.

§ 2. Spin-orbit and Spin-spin Interactions.

As the interactions causing the departure from LS-coupling, the following three among the Breit's Hamiltonian³⁾ are considered, since the others will not affect the multiplet splittings:

$$\left.\begin{aligned}
\overset{(1)}{\Lambda}&=2\mu^2 Z\sum_i \frac{1}{r_i^3}(\boldsymbol{l}_i,\boldsymbol{s}_i)\,,\\
\overset{(2)}{\Lambda}&=-2\mu^2\sum_{i<j}\frac{1}{r_{ij}^3}\{(\boldsymbol{k}_{ij}+2\boldsymbol{k}_{ji},\boldsymbol{s}_i)\\
&\qquad+(\boldsymbol{k}_{ji}+2\boldsymbol{k}_{ii},\boldsymbol{s}_j)\}\,,\\
\overset{(3)}{\Lambda}&=-4\mu^2\sum_{i<j}\frac{1}{r_{ij}^3}\left\{\frac{3}{r_{ij}^3}(\boldsymbol{r}_{ij},\boldsymbol{s}_i)(\boldsymbol{r}_{ji},\boldsymbol{s}_j)\right.\\
&\qquad\left.-(\boldsymbol{s}_i,\boldsymbol{s}_j)\right\}
\end{aligned}\right\}\quad(1)$$

where

$$\boldsymbol{k}_{ij}=\frac{1}{i}[\boldsymbol{r}_{ij},\nabla_i]\,.$$

Same notations are employed as those of Araki²⁾. $\overset{(1)}{\Lambda}$ is the usual spin-orbit interaction which has been already taken into acount by other authors¹⁾. $\overset{(2)}{\Lambda}$ and $\overset{(3)}{\Lambda}$ are the spin-orbit and spin-spin interactions between different electrons respectively, the effects of which shall be investigated in this paper. The matrix elements of (1) in $SLJM$-scheme for p^n-configuration can be obtained by the similar method as in Araki's calculations for sl-configuration²⁾. The results are as follows:

$$\begin{array}{c|cc|c|cc|}
 & {}^1D_2 & {}^3P_2 & {}^3P_1 & {}^3P_0 & {}^1S_0 \\
\hline
{}^1D_2 & 0 & \sqrt{2}(\zeta+7\eta) & & & \\
{}^3P_2 & \sqrt{2}(\zeta+7\eta) & \zeta-32\eta & & 0 & \\
\hline
{}^3P_1 & & & -\zeta+40\eta & & \\
\hline
{}^3P_0 & & 0 & & -2\zeta+40\eta & -\sqrt{2}(2\zeta+5\eta) \\
{}^1S_0 & & & & -\sqrt{2}(2\zeta+5\eta) & \\
\hline
\end{array} \qquad (2;\ p^2)$$

$$\begin{array}{c|cc|c|cc|}
 & {}^1D_2 & {}^3P_2 & {}^3P_1 & {}^3P_0 & {}^1S_0 \\
\hline
{}^1D_2 & 0 & -\sqrt{2}(\zeta-22\eta) & & & \\
{}^3P_2 & -\sqrt{2}(\zeta-22\eta) & -\zeta-17\eta & & 0 & \\
\hline
{}^3P_1 & & & \zeta+25\eta & & \\
\hline
{}^3P_0 & & 0 & & 2\zeta+10\eta & \sqrt{2}(2\zeta-35\eta) \\
{}^1S_0 & & & & \sqrt{2}(2\zeta-35\eta) & \\
\hline
\end{array} \qquad (2;\ p^4)$$

$$\begin{array}{c|c|ccc|c|}
 & {}^2D_{\frac{5}{2}} & {}^2D_{\frac{3}{2}} & {}^4S_{\frac{3}{2}} & {}^2P_{\frac{3}{2}} & {}^2P_{\frac{1}{2}} \\
\hline
{}^2D_{\frac{5}{2}} & -37\eta & & & & 0 \\
\hline
{}^2D_{\frac{3}{2}} & & \frac{111}{2}\eta & -6\sqrt{5}\eta & \sqrt{5}(\zeta-\frac{15}{2}\eta) & \\
{}^4S_{\frac{3}{2}} & & -6\sqrt{5}\eta & 0 & 2(\zeta-\frac{15}{2}\eta) & \\
{}^2P_{\frac{3}{2}} & & \sqrt{5}(\zeta-\frac{15}{2}\eta) & 2(\zeta-\frac{15}{2}\eta) & -\frac{25}{2}\eta & \\
\hline
{}^2P_{\frac{1}{2}} & 0 & & & & 25\eta \\
\hline
\end{array} \qquad (2:\ p^3)$$

where

$$\left.\begin{aligned} \zeta &= (Z-\sigma)\mu^2\overline{r^{-3}}, \\ \eta &= \frac{1}{5}\zeta_{2p,\,2p}\,. \end{aligned}\right\} \qquad (3)$$

μ is Bohr magneton, Z the atomic number and σ is the screening constant defined by the following expression:

$$\left.\begin{aligned}
\sigma &= \sum_{n=1,2} 2(S_{ns,2p}+3\tilde{\zeta}_{ns,\,2p})/\mu^2\overline{r^{-3}}, \\
\overline{r^{-3}} &= \int_0^\infty \frac{1}{r^3}P_{2p}(r)^2dr, \\
\zeta_{2p,2p} &= -\mu^2\iint_0^\infty \frac{1}{r_2}\frac{\partial a_0}{\partial r_2}P_{2p}(r_1)^2 \cdot P_{2p}(r_2)^2dr_1dr_2, \\
\zeta_{ns,2p} &= -\mu^2\iint_0^\infty \frac{1}{r_2}\frac{\partial a_0}{\partial r_2}P_{ns}(r_1)^2 \cdot P_{2p}(r_2)^2dr_1dr_2, \\
\tilde{\zeta}_{ns,2p} &= -\mu^2\iint_0^\infty a_1P_{ns}(r_1)\frac{dR_{ns}(r_2)}{dr_2} \cdot P_{2p}(r_1)P_{2p}(r_2)dr_1dr_2,
\end{aligned}\right\} \qquad (4)$$

where

$$a_0=\begin{cases}\dfrac{1}{r_2} & (r_1\leqq r_2), \\[2mm] \dfrac{1}{r_1} & (r_1>r_2),\end{cases} \qquad a_1=\begin{cases}\dfrac{r_1}{r_2^{\,2}} & (r_1\leqq r_2), \\[2mm] \dfrac{r_2}{r_1^{\,2}} & (r_1>r_2),\end{cases}$$

and $R_{nl}(r)=P_{nl}(r)/r$ is the normalized radial wave function of the electron whose principal and azimuthal quantum numbers are n and l, respectively.

In the expression of ζ, $Z\mu^2\overline{r^{-3}}$ arises from the spin-orbit interaction of each single p-electron and $\sigma\mu^2\overline{r^{-3}}$ appears as the screening effect due to the spin-orbit interactions between p-electrons and core-electrons. η arises from both the spin-orbit and spin-spin interactions between p-electrons. It is noticed that in $(2;\ p^4)$ the coefficients of ζ have the different signs from corresponding ones of $(2;\ p^4)$, while this is not the case for the coefficients of η.

§ 3. Multiplet Intervals.

The multiplet intervals and deviations from Russel-Saunders coupling can be obtained by calculating the matrix elements of spin-orbit and spin-spin interactions. In our case, since the multiplet intervals are much smaller than intermultiplet separactions, the second order perturbation method will give the results in sufficient accuracy. Thus the multiplet intervals are found, if the perturbed level be denoted by ${}^{2s+1}L_J'$, as follows:

$$\left.\begin{aligned} {}^3P_2'-{}^3P_1 &= 2\zeta-72\eta-\frac{2(\zeta+7\eta)^2}{{}^1D_2-{}^3P_2}, \\ {}^3P_1-{}^3P_0' &= \zeta \qquad\quad +\frac{2(2\zeta+5\eta)^2}{{}^1S_0-{}^3P_0}, \end{aligned}\right\}(5;p^2)$$

$$\left.\begin{aligned} {}^3P_2'-{}^3P_1 &= -2\zeta-42\eta-\frac{2(\zeta-22\eta^2)}{{}^1D_2-{}^3P_2}, \\ {}^3P_1'-{}^3P_0 &= -\ \zeta+15\eta+\frac{2(2\zeta-35\eta)^2}{{}^1S_0-{}^3P_0}, \end{aligned}\right\}(5;p^4)$$

$$\left.\begin{aligned} {}^2D_{\frac{5}{2}}-{}^2D'_{\frac{3}{2}} &= -\frac{185}{2}\eta \\ &\quad -\frac{180\eta^2}{{}^2D_{\frac{3}{2}}-{}^4S_{\frac{3}{2}}}+\frac{5(\zeta-\frac{15}{2}\eta)^2}{{}^2P_{\frac{3}{2}}-{}^2D_{\frac{3}{2}}}, \\ {}^2P'_{\frac{3}{2}}-{}^2P'_{\frac{1}{2}} &= -\frac{75}{2}\eta \\ &\quad +\frac{4(\zeta-\frac{15}{2}\eta)^2}{{}^2P_{\frac{3}{2}}-{}^4S_{\frac{3}{2}}}+\frac{5(\zeta-\frac{15}{2}\eta)^2}{{}^2P_{\frac{3}{2}}-{}^2D_{\frac{3}{2}}}, \end{aligned}\right\}(5;p^3)$$

The numerical values of multiplet intervals are calculated using Obi's analytical expressions of radial wave functions of oxygen, nitrogen and carbon in various stages of ionization[4] which approximate the wave functions of Hartree's self-consistent field. The results are shown in Table I. Then, the multiplet intervals are calculated by (5), in which the observed term values[5] are used for the energy denominators, as in Table II. For p^2- and p^4-configurations, the calculated multipet intervals using Hartree's self-consistent wave functions are much smaller than the observed ones, but the calculated ratios of intervals show good agreements with observed values. Such a situation is observed in the similar calculations by several authors[6] using wave functions of self-consistent fields. In this respect, we notice that the theoretical intervals will be in better agreement with experimental ones if we use the wave function of Hartree-Fock's self-consistent field with ex-

Table I.

	p^2			p^4	p^3	
	CI	NII	OIII	OI	NI	OII
$\overline{r^{-3}}$	1.268	3.003	6.080	4.013	2.251	4.552
σ	3.090	3.122	3.140	3.074	3.090	3.124
η (cm^{-1})	0.061	0.167	0.332	0.189	0.078	0.214
ζ (cm^{-1})	10.9	33.8	86.6	57.6	25.6	64.6

Table II.

		p^2			p^4
		CI	NII	OIII	OI
${}^3P_2-{}^3P_1$	cal.	17.0	54.0	147.1	−123.3
	obs.	27.1	82.2	193.4	−158.5
${}^3P^2-{}^3P_0$	cal.	10.8	33.4	87.3	− 54.0
	obs.	16.4	49.1	113.4	− 68.0
$\dfrac{{}^3P_2-{}^3P_1}{{}^3P_1-{}^3P_0}$	cal.	1.58	1.62	1.69	2.28
	obs.	1.65	1.67	1.71	2.33

		p^3	
		NI	OII
${}^2D_{5/2}-{}^2D_{3/2}$	cal.	−6.9	−18.3
	obs.	−8.0	−21.0
${}^2P_{3/2}-{}^2P_{1/2}$	cal.	−2.5	− 6.1
	obs.	——	− 1.5

(in cm^{-1} units)

change. In fact, the wave functtons of $2p$-electrons approach toward atomic nucleus by the exchange effect so that $\overline{r^{-3}}$, which gives the main term of multiplet intervals, becomes larger than that without exchange. (For example, we obtain $\overline{r^{-3}}$ as 4.98 and 4.85 atomic unit for ^3P and ^1S of OI, respectively, by numerical integrations using the wave functions of Hartree, Hartree and Swirls[7].) The results for p^3-configuration are poor, since ζ vanishes in diagonal elements and non-diagonal terms give rather large contributions. It might be necessary to take into account configuration interaction with other configurations such as $(1s)^2(2s)^2(2p)^2 3p$.

The calculated multiplet intervals using Hartree wave function are much smaller than the observed values as mentioned above. Therefore, in this stage of our knowledge, it seems more reasonable to use for the later calculation the parameters determined so as to give the observed multiplet intervals. The parameters determined in this way are given in Table III. For OII, the values are still unreliable, but we shall not discuss this difficulty any more.

Table III.

	p^2			p^4	p^3
	CI	NII	OIII	OI	OII
ζ	14.72	49.4	113.6	73.5	202
η	0.026	0.201	0.456	0.250	0.372

(in cm^{-1} units)

§ 4. Perturbed Eigenfunctions.

The eigenfunctions of perturbed states by the spin-orbit and spin-spin interactions can easily be derived. Those eigenfunctions are represented by $\Psi(^{2S+1}L'_J)$ since the deviations from $\Psi(^{2S+1}L_J)$ in Russel-Saunders coupling are very small. Then

$$\left.\begin{aligned}\Psi(^1D_2')&=\Psi(^1D_2)+\beta_2\Psi(^3P_2)\,,\\ \Psi(^3P^{2\prime})&=-\beta_2\Psi(^1D_2)+\Psi(^3P_2),\\ \Psi(^3P_0')&=\Psi(^3P_0)+\beta_0\Psi(^1S_0)\,,\\ \Psi(^1S_0')&=-\beta_0\Psi(^3P_0)+\Psi(^1S_0)\,,\end{aligned}\right\}\begin{aligned}&(6;\\ &p^2,p^4)\end{aligned}$$

$$\left.\begin{aligned}\Psi(^2D'_{3/2})&=\Psi(^2D_{3/2})\\ &\quad-\alpha\Psi(^4S_{3/2})-\beta\Psi(^2P_{3/2})\,,\\ \Psi(^4S'_{3/2})&=\alpha\Psi(^2D_{3/2})\\ &\quad+\Psi(^4S_{3/2})-\gamma\Psi(^2P_{3/2})\,,\\ \Psi(^2P'_{3/2})&=\beta\Psi(^2D_{3/2})\\ &\quad+\gamma\Psi(^4S_{3/2})+\Psi(^2P_{3/2})\,,\end{aligned}\right\}(6;p^3)$$

where

$$\left.\begin{aligned}\beta_2&=\frac{\sqrt{2}(\zeta+7\eta)}{^1D_2-{}^3P_2},\\ \beta_0&=\frac{\sqrt{2}(2\zeta+5\eta)}{^1S_0-{}^3P_0}.\end{aligned}\right\}(7;p^2)$$

$$\left.\begin{aligned}\beta_2&=-\frac{\sqrt{2}(\zeta-22\eta)}{^1D_2-{}^3P_2},\\ \beta_0&=-\frac{\sqrt{2}(2\zeta-35\eta)}{^1S_0-{}^3P_0},\end{aligned}\right\}(7;p^4)$$

$$\left.\begin{aligned}\alpha&=\frac{6\sqrt{5}\,\eta}{^2D_{3/2}-{}^4S_{3/2}},\\ \beta&=\frac{\sqrt{5}(\zeta-\frac{15}{2}\eta)}{^2P_{3/2}-{}^2D_{3/2}},\\ \gamma&=\frac{2(\zeta-\frac{15}{2}\eta)}{^2P_{3/2}-{}^4S_{3/2}}.\end{aligned}\right\}(7;p^3)$$

Table IV.

	p^2			p^4
	CI	NII	OIII	OI
β_2	0.00234	0.00466	0.00790	−0.00597
β_0	0.00216	0.00424	0.00733	−0.00576

	p^3
	OII
α	0.000157
β	0.0244
γ	0.00737

Inserting the values of Table III, we obtain these coefficients as in Table IV.

§ 5. Strengths of Forbidden Lines.

Since the methods for obtaining strengths of magnetic dipole and electric quadrupole radiation in intermediate coupling are fully explained in the papers of reference (1), we will not reproduced them here. The spontaneous transition probability due to magnetic dipole radiation is given by

$$\mathrm{A}(A,B)=\frac{\sigma^3\mathrm{S}(A,B)}{2J_A+1}\times 3.53\times 10^4\,\mathrm{sec}^{-1}\,,\tag{8}$$

where σ is the wave number of the line due to transition $A \rightarrow B$ in Rydberg unit, and line-strengths $\mathbf{S}(A, B)$ are in the unit of μ^2 as follows:

	$^1D_2'$	$^3P_2'$	$^3P_1$	$^3P_0'$	$^1S_0'$
$^1D_2'$	30	$\frac{15}{2}\beta_2^2$	$\frac{5}{2}\beta_2^2$	0	0
$^3P_2'$	$\frac{15}{2}\beta_2^2$	$\frac{135}{2}$	$\frac{5}{2}$	0	0
$^3P_1$	$\frac{5}{2}\beta_2^2$	$\frac{5}{2}$	$\frac{27}{2}$	2	$2\beta_0^2$
$^3P_0'$	0	0	2	0	0
$^1S_0'$	0	0	$2\beta_0^2$	0	0

(9; p^2, p^4)

	$^2D_{5/2}$	$^2D'_{3/2}$	$^4S'_{3/2}$	$^2P'_{3/2}$	$^2P'_{1/2}$
$^2D_{5/2}$	$\frac{378}{5}$	$\frac{12}{5}$	$\frac{12}{5}\alpha^2$	$\frac{12}{5}\beta^2$	0
$^2D'_{3/2}$	$\frac{12}{5}$	$\frac{48}{5}$	$\frac{4}{15}(9\alpha-10\beta\gamma)^2$	$\frac{4}{15}(4\beta+15\alpha\gamma)^2$	$\frac{4}{3}\beta^2$
$^4S'_{3/2}$	$\frac{12}{5}\alpha^2$	$\frac{4}{15}(9\alpha-10\beta\gamma)^2$	60	$\frac{4}{15}(5\gamma+6\alpha\beta)^2$	$\frac{4}{3}\gamma^2$
$^2P'_{3/2}$	$\frac{12}{5}\beta^2$	$\frac{4}{15}(4\beta+15\alpha\gamma)^2$	$\frac{4}{15}(5\gamma+6\alpha\beta)^2$	$\frac{80}{3}$	$\frac{4}{3}$
$^2P_{1/2}$	0	$\frac{4}{3}\beta^2$	$\frac{4}{3}\gamma^2$	$\frac{4}{3}$	$\frac{2}{3}$

(9; p^3)

The spontaneous transition probability due to electric quadrupole radiation is given by

$$\mathbf{A}(A, B) = \frac{\sigma^5 \mathbf{S}(A, B)}{2J_A+1} \times 2.773 \times 10^3 \text{ sec}^{-1}; \tag{10}$$

where line strengths $\mathbf{S}(A, B)$ are as follows:

	$^1D_2'$	$^3P_2'$	$^3P_1$	$^3P_0'$	$^1S_0'$
$^1D_2'$	28	$7\beta_2^2$	$9\beta_2^2$	$(2\beta_2-4\beta_0)^2$	16
$^3P_2'$	$7\beta_2^2$	7	9	4	$(4\beta_2-2\beta_0)^2$
$^3P_1$	$9\beta_2^2$	9	3	0	0
$^3P_0'$	$(2\beta_2-4\beta_0)^2$	4	0	0	0
$^1S_0'$	16	$(4\beta_2-2\beta_0)^2$	0	0	0

$\times \frac{1}{15}\mathbf{s}_2^2$ (11; p^2, p^4)

	$^2D_{5/2}$	$^2D'_{3/2}$	$^4S'_{3/2}$	$^2P'_{3/2}$	$^2P_{1/2}$
$^2D_{5/2}$	0	$7\beta^2$	$7\gamma^2$	7	2
$^2D'_{3/2}$	$7\beta^2$	$12\beta^2$	$3(\gamma+\alpha\beta)^2$	3	3
$^4S'_{3/2}$	$7\gamma^2$	$3(\gamma+\alpha\beta)^2$	$12\alpha^2\gamma^2$	$3(\alpha-\beta\gamma)^2$	$3\alpha^2$
$^2P'_{3/2}$	7	3	$3(\alpha-\beta\gamma)^2$	$12\beta^2$	$3\beta^2$
$^2P_{1/2}$	2	3	$3\alpha^2$	$3\beta^2$	0

$\times \frac{8}{25}\mathbf{s}_2^2$ (11; p^3)

$$\mathbf{s}_2 = \int_0^\infty r^2 P_{2p}(r)^2 dr. \tag{12}$$

The numerical values of s_2 are as follows:

	CI	NII	OIII	OI	OII
$\mathbf{s}_2$	4.81	2.49	1.24	2.44	1.75

The values for CI and NII we obtained by Obi's analytic wave functions and others are values derived by numerical integration using wave functions of Hartree and Black8). Then, line strengths $\mathbf{S}(A, B)$ for magnetic dipole and electric quadrupole radiation are determined by (9) and (11), respectively. The intensities of the forbidden lines thus obtained are shown in Table V.

Table V (a).

		CI	NII	OIII	OI	
$\mathbf{A}(^1S_0, {}^3P_2)$	e	3.22×10^{-5}	3.15×10^{-4}	7.42×10^{-4}	4.65×10^{-4}	
$\mathbf{A}(^1S_0, {}^3P_1)$	m	2.53×10^{-3}	3.34×10^{-2}	2.29×10^{-1}	6.74×10^{-2}	
$\mathbf{A}(^1S_0, {}^1D_2)$	e	8.49×10^{-1}	1.822	1.805	2.04	
$\mathbf{A}(^1D_2, {}^3P_0)$	e	9.28×10^{-3}	7.08×10^{-7}	2.23×10^{-6}	1.59×10^{-6}	
$\mathbf{A}(^1D_2, {}^3P_1)$	m	7.72×10^{-5}	1.03×10^{-3}	6.74×10^{-3}	1.85×10^{-3}	
$\mathbf{A}(^1D_2, {}^3P_1)$	e	2.89×10^{-7}	2.32×10^{-6}	6.68×10^{-6}	4.26×10^{-6}	
$\mathbf{A}(^1D_2, {}^3P_2)$	m	2.30×10^{-4}	3.03×10^{-3}	1.96×10^{-2}	5.69×10^{-3}	
$\mathbf{A}(^1D_2, {}^3P_2)$	e	2.22×10^{-7}	1.76×10^{-6}	4.94×10^{-6}	3.46×10^{-6}	
$\mathbf{A}(^3P_2, {}^3P_0)$*	e	3.35×10^{-14}	2.32×17^{-12}	3.89×10^{-11}	1.65×10^{-10}	
$\mathbf{A}(^3P_2, {}^3P_1)$**	m	2.67×10^{-7}	7.41×10^{-6}	9.65×10^{-5}	8.85×10^{-5}	
$\mathbf{A}(^3P_2, {}^3P_1)$**	e	7.08×10^{-15}	4.87×10^{-13}	8.70×10^{-12}	6.22×10^{-11}	
$\mathbf{A}(^3P_1, {}^3P_0)$***	m	7.84×10^{-8}	2.11×10^{-6}	2.59×10^{-5}	1.68×10^{-5}	sec^{-1} units.

* For OI, this must be replaced by $\mathbf{A}(^3P_0, {}^3P_2)$.
** For OI, these must be replaced by $\mathbf{A}(^3P_1, {}^3P_2)$.
*** For OI, this must be replaced by $\mathbf{A}(^3P_0, {}^3P_1)$.
e: electric quadrupole radiation.
m: magnetic dipole radiation.

Table V (b).

	OII	
	m	e
$\mathbf{A}(^2P_{1/2}, {}^4S_{3/2})$	6.41×10^{-2}	1.09×10^{-6}
$\mathbf{A}(^2P_{1/2}, {}^2D_{5/2})$	——	1.36×10^{-1}
$\mathbf{A}(^2P_{1/2}, {}^2D_{3/2})$	2.70×10^{-2}	2.02×10^{-1}
$\mathbf{A}(^2P_{1/2}, {}^2P_{3/2})$	6.01×10^{-11}	1.93×10^{-24}
$\mathbf{A}(^2P_{3/2}, {}^4S_{3/2})$	1.60×10^{-1}	1.31×10^{-8}
$\mathbf{A}(^2P_{3/2}, {}^2D_{5/2})$	2.44×10^{-2}	2.37×10^{-1}
$\mathbf{A}(^2P_{3/2}, {}^2D_{3/2})$	4.32×10^{-2}	1.01×10^{-1}
$\mathbf{A}(^2D_{3/2}, {}^4S_{3/2})$	5.34×10^{-6}	1.61×10^{-4}
$\mathbf{A}(^2D_{3/2}, {}^2D_{5/2})$	1.49×10^{-7}	1.23×10^{-18}
$\mathbf{A}(^2D_{5/2}, {}^4S_{3/2})$	5.00×10^{-6}	2.49×10^{-4}

sec^{-1} units

m: magnetic dipole radiation
e: electric quadrupole radiation

§ 6. Discussions.

The intensities of the magnetic dipole lines are determined only by the parameter values of ζ and η, so that the accuracy of the obtained results depends on the correctness of their determination. In our case, only two data (term differences) are available for their determination, so that we are not certain how far they are to be relied upon. But similar calculations of Araki make us convince that they are fairly correct, and we can at least expect improvement compared to former calculations. As for the electric quadrupole lines, another parameter s_2, depending quadratically on the wave function of $2p$-electron, is introduced. The Hartree function, which is not very good for evaluation of $\overline{r^{-3}}$ as is mentioned before, might be so for $\overline{r^2}$ too, so that the results for electric quadrupole lines can be inferior to those of magnetic dipole lines. Yet, the calculated values may be sufficiently accurate to make comparison with obserbed data, considering the their roughness under the present condition.

This work was supported by the Grant in Aid for Fundamental Scientific Research.

Referecces

1) E. U. Condon, Astrophys. J. **79** (1934) 217.
A. F. Stevenson, Proc. Roy. Soc. **A 137** (1932) 298.
M. Mashiko, Subutsu Kaishi **17** (1943) 121 (in Japanese).

2) G. Araki, Proc. Phys.-Math. Soc. Japan **19** (1937) 128; Prog. Theor. Phys. **3** (1948), 152, 262.

3) G. Breit, Phys. Rev. **34** (1929) 553.

4) S. Obi, unpublished.

5) "*Atomic Energy Levels*", National Bureau of Standards, Circular No. 467 (1949).

6) S. Tutihasi, J. Phys. Soc. Japan **3** (1948) 137.
W. Watari, Prog. Theor. Phys. **4** (1949) 42; ibid (1949) 314.
S. Tutihasi, Prog. Theor. Phys. **4** (1949) 317.

7) D. R. Hartree, W. Hartree and B. Swirles, Phil. Trans. **A 239** (1939) 229.

9) D. R. Hartree and M. M. Black, Proc. Roy. Soc. **A 139** (1933) 311.

JOURNAL OF THE PHYSICAL SOCIETY OF JAPAN Vol. 7, No. 1 JAN.—FEB., 1952

Line Strengths for Transitions $d^n \rightarrow d^{n-1}p$ and $d^n \rightarrow d^{n-1}f$, and Probabilities of Photo-Ionization and Recombination $d^n \rightleftarrows d^{n-1}$

By Hisashi HORIE
Department of Physics, University of Tokyo

(Received July 17, 1951)

General formulas for the line strengths of transition as well as the probabilities of photo-ionization and recombination are obtained. They are expressed in simple forms by Racah's coefficients of fractional parentages. Auxiliary tables useful for their computation for the case $l=2$ are given.

§ 1. Introduction.

The multiplet strengths between two atomic configurations can be found by the principle of spectroscopic stability if the jumping electron is not equivalent to other electrons in either configuration1). Yamanouchi2) calculated them for the case that the electron is equivalent to other electrons in one of the configurations by group-theoretical method, but the multiply-occuring terms cannot be separated in a convenient manner. By adopting the method of Racah3), we can not only simplify the calculations, but also avoid the above-mentioned difficulty by making use of the seniority numbers for d^n-configurations, since each state belonging to these configurations is completely specified by these numbers. (For f^n-configurations, for which the seniority numbers are insufficient to specify the individual states, Racah has introduced new numbers to distinguish them4).) Probabilities of photo-ionization and recombination can easily be obtained by suitable summation of the formulas for the line strengths.

§ 2. Line Strengths.

The line strengths S is defined as the sum of squared matrix components of the electric moment between all the sub-levels of the initial and the final states:

$$\mathrm{S}(\gamma SL \rightarrow \gamma' SL') = \sum_{M_S, M_L, M_L'} |(\gamma SLM_SM_L|P|\gamma' SL'M_SM_L')|^2 \quad (1)$$

with

$$P = \sum_i p_i, \quad p_i = -er_i,$$

in usual notations. In the case of Russel-Saunders coupling, the selection rules are given by $\Delta S=0$, $\Delta L=0$, ± 1 as is well known. The summation with respect to M_S, M_L and M_L' can easily be carried out by RII(29) and (20a), and the results are given as

$$\mathrm{S}(\gamma SL \rightarrow \gamma' SL') = (2S+1)(\gamma SL \| P \| \gamma' SL')^2. \quad (2)$$

This equation corresponds to TAS $2^9(6)$, as is seen from RII(30), and holds for any transition due to electric dipole radiation.

Now, if we restrict the configurations of initial atomic state to l^n, then the final configurations are forced to be $l^{n-1}l'$, where $l'=l\pm 1$, since parity must be changed. We designate the final state as $l^{n-1}(\alpha_1S_1L_1)l'SL'$, where $l^{n-1}(\alpha_1S_1L_1)$ represents the parent term. Then, the quantity we have to find is $(l^n\alpha SL \| P \| l^{n-1}(\alpha_1S_1L_1)l'SL')$. By making use of the coefficients of fractional parentages (c.f.p.) which Racah introduced in RIII, we have by RIII(27),

$$\begin{aligned}(l^n\alpha SL \| P \| l^{n-1}(\alpha_1S_1L_1)l'SL') &= \sqrt{n}(l^n\alpha SL\{|l^{n-1}(\alpha_1S_1L_1)lSL)\cdot \\ &\quad \cdot (L_1l_nL \| p_n \| L_1l_n'L),\end{aligned} \quad (3)$$

in which $(l^n\alpha SL\{|l^{n-1}(\alpha_1S_1L_1)lSL)$ is the the c.f.p. $(L_1l_nL \| p_n \| L_1l_n'L')$ is obtained by RII (44b) and (30):

$$\begin{aligned}(L_1l_nL \| p_n \| L_1l_n'L') &= (-1)^{L_1+1-l-L'}(l \| p \| l')\cdot \\ &\quad \cdot [(2L+1)(2L'+1)]^{\frac{1}{2}} W(lLl'L';L_11),\end{aligned}$$

where

$$\left\{\begin{aligned}&(l \| p \| l-1) \\ &\quad = \sqrt{l(2l-1)(2l+1)}\,\mathbf{s}(nl, n'l-1), \\ &(l \| p \| l+1) \\ &= \sqrt{(l+1)(2l+1)(2l+3)}\,\mathbf{s}(nl, n'l+1),\end{aligned}\right. \quad (4)$$

with

$$\begin{aligned}\mathbf{s}(nl, n'l-1) &= \mathbf{s}(n'l-1, nl) \\ &= \frac{-e}{\sqrt{4l^2-1}}\int_0^\infty rR(n,l)R(n',l-1)r^2dr. \quad (4')\end{aligned}$$

$R(n, l)$ is the radial wave function of electron whose principal and azimuthal quantum numbers are n and l, respectively. Thus, the line strengths for the transition $l^n\alpha SL \to l^{n-1}(\alpha_1 S_1 L_1)l'SL'$ are found as follows:

$$\begin{aligned}&\mathbf{S}(l^n\alpha SL \to l^{n-1}(\alpha_1 S_1 L_1)l'SL')\\ &\quad = n(2S+1)(2L+1)(2L'+1)(l\|p\|l')^2\cdot\\ &\qquad \cdot(l^n\alpha SL\{|l^{n-1}(\alpha_1 S_1 L_1(lSL)^2\cdot\\ &\qquad\quad \cdot W(lLl'L';L_1 1)^2, \qquad (5)\end{aligned}$$

where $(l\|p\|l')$ is given by (4).

§ 3. Probabilities of Photo-Ionization and Recombination.

The formulas of probabilities of photo-ionization and recombination has already been given by Yamanouchi[5)], but, for the sake of completeness, we shall reproduce the formulas here.

The probability that an atom in γSL-state is ionized in unit time by the radiation of density $U(\nu)$, with the production of an ion in $\gamma_1 S_1 L_1$-state, is given by

$$W_{\gamma SL}^{\gamma_1 S_1 L_1} = \frac{4\pi^2}{2L+1}\int_{\nu_0}^{\infty} J_{\gamma SL}^{\gamma_1 S_1 L_1} U(\nu)d\nu, \quad (6)$$

where $\nu_0 = E_{\gamma_1 S_1 L_1} - E_{\gamma SL}$, and $J_{\gamma SL}^{\gamma_1 S_1 L_1}$ will be given in the following. The corresponding cross section, that an atom in γSL-state is ionized into $\gamma_1 S_1 L_1$-state by a light quantum of frequency ν, is

$$Q = \frac{4\pi^2\nu}{(2L+1)c} J_{\gamma SL}^{\gamma_1 S_1 L_1} \quad (7)$$

The probability of photo-recombination, the inverse process, is given, if the space density of free electron with energy between $\varepsilon = k^2/2$ and $\varepsilon + d\varepsilon$ is $N(\varepsilon)d\varepsilon$, by*)

$$\begin{aligned}W^{*}{}_{\gamma SL}^{\gamma_1 S_1 L_1} &= \frac{4\pi^4(2S+1)}{(2S_1+1)(2L_1+1)}\\ &\int_0^{\infty}\frac{1}{k}N(\varepsilon)J_{\gamma SL}^{\gamma_1 S_1 L_1}\left\{U(\nu)+\frac{\nu^3}{\pi^2 c^3}\right\}d\varepsilon, \quad (8)\end{aligned}$$

where $\nu = (E_{\gamma_1 S_1 L_1} - E_{\gamma SL}) + \varepsilon$. The corresponding cross section, that an electron with velocity k is captured by an ion in $\gamma_1 S_1 L_1$-state, with the emission of a light quantum of frequency ν and production of an atom in γSL-state, is given by

$$\begin{aligned}Q^{*} &= \frac{4\pi^4(2S+1)}{(2S_1+1)(2L_1+1)} J_{\gamma SL}^{\gamma_1 S_1 L_1}\cdot\\ &\qquad\cdot\left\{U(\nu)+\frac{\nu^3}{\pi^2 c^3}\right\}. \quad (6)\end{aligned}$$

In these formulas, $J_{\gamma SL}^{\gamma_1 S_1 L_1}$ are defined as follows:

$$\begin{aligned}J_{\gamma SL}^{\gamma_1 S_1 L_1} &= \frac{1}{3(2S+1)}\sum_{l',L'}\sum_{M_S,M_L,M_L'}\cdot\\ &\cdot|(\gamma SLM_SM_L|\boldsymbol{P}|\gamma_1 S_1 L_1, l'SL'M_SM_L')| \quad (10)\end{aligned}$$

or by (1), in terms of line strength $\mathbf{S}$,

$$\begin{aligned}J_{\gamma SL}^{\gamma_1 S_1 L_1} &= \frac{1}{3(2S+1)}\sum_{l',L'}\mathbf{S}(\gamma SL\\ &\qquad \to \gamma_1 S_1 L_1, l'SL'). \quad (11)\end{aligned}$$

Again, if we restrict ourselves to the atomic configurations l^n, the line strengths given by (5) have to be summed up with respect to l' and L', where l' is $l\pm1$. On the other hand, the summation over L' in (11) can be carried out after introducing (5) and by making use of RII(40a) and (42). Thus,

$$\begin{aligned}J_{\alpha SL}^{\alpha_1 S_1 L_1} &= \frac{1}{3}n(2L+1)(l^n\alpha SL\{|l^{n-1}(\alpha_1 S_1 L_1)\\ &\qquad lSL)^2\cdot\sum_{l'}(l\|p\|l')^2/(2l+1). \quad (12)\end{aligned}$$

Taking account of (4), this may be written as

$$\begin{aligned}J_{\alpha SL}^{\alpha_1 S_1 L_1} &= \frac{1}{3}n(2L+1)(l^n\alpha SL\{|l^{n-1}(\alpha_1 S_1 L_1)\\ &\quad lSL)^2\{l(2l-1)I_{l-1}{}^2 + (l+1)(2l+3)I_{l+1}{}^2\}, \\ &\qquad\qquad (13)\end{aligned}$$

where $I_{l\pm1}$ have the same expressions as $\mathbf{S}(l, l\pm1)$, with the difference of meaning that n' of $R(n', l\pm1)$ in (4′) signifies the continuous state.

The probabilities of photo-ionization and recombination of atoms and ions in the right-hand side of the periodic table $l^{4l+3-n} \rightleftarrows l^{4l+2-n}$ are intimately connected with those of $l^n \rightleftarrows l^{n-1}$ as follows. By RIII(19):

$$\begin{aligned}&(l^{4l+3-n}\alpha_1 S_1 L_1\{|l^{4l+2n}(\alpha SL)lS_1L_1)\\ &\quad = (-1)^{S+S_1+L+L_1-l-\frac{1}{2}}\cdot\\ &\qquad \cdot\left[\frac{n(2S+1)(2L+1)}{(4l+3-n)(2S_1+1)(2L_1+1)}\right]^{\frac{1}{2}}\cdot\\ &\qquad\qquad \cdot(l^n\alpha SL\{|l^{n-1}(\alpha_1 S_1 L_1)lSL)\end{aligned}$$

$(2S_1+1)J_{\alpha_1 S_1 L_1}^{\alpha SL}$ for

$$l^{4l+3-n}(\alpha_1 S_1 L_1) \rightleftarrows l^{4l+2-n}(\alpha SL)$$

equals to $(2S+1)J_{\alpha SL}^{\alpha_1 S_1 L_1}$ for

$$l^n(\alpha SL) \rightleftarrows l^{n-1}(\alpha_1 S_1 L_1),$$

though the numerical values of I_{l-1} and I_{l+1} must be appropriately evaluated corresponding to $l^{4l+3-n} \rightleftarrows l^{4l+2-n}$.

As a supplement, we shall derive here the sum rule for the line strengths for the transitions $l^n \rightleftarrows l^{n-1}l'$. By the summation over L', we obtain, on account of the unitarity of c.f.p. (RIII(13)),

---

*) In these formulas, the radial function of free electron is normalized with respect to energy.

$$\sum_{\alpha_1,S_1,L_1,L'} S(l^n\alpha SL \rightleftarrows l^{n-1}(\alpha_1 S_1 L_1)l'SL') = n(2S+1)(2L+1)(l\|p\|l')^2/(2l+1) . \quad (14)$$

Similarly, the sum of $J_{\alpha SL}^{\alpha_1 S_1 L_1}$ over α_1, S_1 and L_1 is given by

$$\sum_{\alpha_1,S_1,L_1} J_{\alpha SL}^{\alpha_1 S_1 L_1} = \frac{1}{3} n(2L+1)\{l(2l-1)I_{l-1}{}^2 + (l+1)(2l+3)I_{l+1}{}^2\} . \quad (15)$$

They are useful as the checks for the calculations of line strength and $J_{\alpha SL}^{\alpha_1 S_1 L_1}$, respectively.

The author wishes to express his sincere thanks to Professor T. Yamanouchi for his kind guidance.

References

1) E. U. Condon and G. H. Shortley, "*Theory of Atomic Spectra*", Cambridge University Press, London (1935). Referred to as TAS.

2) T. Yamanouchi, Proc. Phys. Math. Soc. Japan **23** (1941) 1059 and 1963.

3) G. Racah, Phys. Rev. **62** (1942) 438; **63** (1943), 297, referred to as RII and RIII, respectively.

4) G. Racah, Phys. Rev. **76** (1949) 1352.

5) T. Yamanouchi, Proc. Phys. Math. Soc. Japan **22** (1940) 33.

Apendix.

Tables of $\sqrt{(2L+1)(2L'+1)}\cdot W(2Ll'L';L_1 1)$ for $l'=1$ and 3.

$\sqrt{(2L+1)(2L'+1)}\cdot W(2L1L';L_1 1)$

L	L_1	$L'=P$
S	D	$\sqrt{1/5}$

L	L_1	$L'=S$	P	D
P	P	$-\sqrt{1/3}$	$-\sqrt{1/4}$	$\sqrt{1/60}$
	D	0	$\sqrt{9/20}$	$-\sqrt{3/20}$
	F	0	0	$\sqrt{3/5}$

L	L_1	$L'=P$	D	F
D	S	1	0	0
	P	$-\sqrt{3/4}$	$\sqrt{1/4}$	0
	D	$\sqrt{7/20}$	$-\sqrt{7/12}$	$\sqrt{1/15}$
	F	0	$\sqrt{2/3}$	$-\sqrt{1/3}$
	G	0	0	1

L	L_1	$L'=D$	F	G
F	P	$\sqrt{7/5}$	0	0
	D	$-\sqrt{14/15}$	$\sqrt{7/15}$	0
	F	$\sqrt{2/5}$	$-\sqrt{7/8}$	$\sqrt{1/8}$
	G	0	$\sqrt{7/8}$	$-\sqrt{21/40}$
	H	0	0	$\sqrt{7/5}$

L	L_1	$L'=F$	G	H
G	D	$\sqrt{9/5}$	0	0
	F	$-\sqrt{9/8}$	$\sqrt{27/40}$	0
	G	$\sqrt{11/24}$	$-\sqrt{231/200}$	$\sqrt{14/75}$
	H	0	$\sqrt{27/25}$	$-\sqrt{18/25}$
	I	0	0	$\sqrt{9/5}$

$\sqrt{(2L+1)(2L'+1)}\cdot W(2L3L';L_1 1)$

L	L_1	$L'=P$
S	D	$\sqrt{1/5}$

L	L_1	$L'=S$	P	D
P	P	0	0	$\sqrt{3/5}$
	D	0	$-\sqrt{1/5}$	$-\sqrt{2/5}$
	F	$\sqrt{1/7}$	$\sqrt{2/7}$	$\sqrt{66/35}$

L	L_1	$L'=P$	D	F
D	S	0	0	1
	P	0	$-\sqrt{1/9}$	$-\sqrt{8/9}$
	D	$\sqrt{1/35}$	$\sqrt{2/7}$	$\sqrt{24/35}$
	F	$-\sqrt{1/7}$	$-\sqrt{3/7}$	$-\sqrt{3/7}$
	G	$\sqrt{3/7}$	$\sqrt{25/63}$	$\sqrt{11/63}$

L	L_1	$L'=D$	F	G
F	P	$\sqrt{1/315}$	$\sqrt{1/9}$	$\sqrt{9/7}$
	D	$-\sqrt{1/35}$	$-\sqrt{3/10}$	$-\sqrt{15/14}$
	F	$\sqrt{4/35}$	$\sqrt{1/2}$	$\sqrt{11/14}$
	G	$-\sqrt{20/63}$	$-\sqrt{11/18}$	$-\sqrt{33/70}$
	H	$\sqrt{5/7}$	$\sqrt{1/2}$	$\sqrt{13/70}$

L	L_1	$L'=F$	G	H
G	D	$\sqrt{1/70}$	$\sqrt{3/14}$	$\sqrt{11/7}$
	F	$-\sqrt{1/14}$	$-\sqrt{33/70}$	$-\sqrt{44/35}$
	G	$\sqrt{3/14}$	$\sqrt{243/350}$	$\sqrt{156/175}$
	H	$-\sqrt{1/2}$	$-\sqrt{39/50}$	$-\sqrt{13/25}$
	I	1	$\sqrt{3/5}$	$\sqrt{1/5}$

L	L_1	$L'=G$	H	I
H	F	$\sqrt{11/5}$	0	0
	G	$-\sqrt{33/25}$	$\sqrt{22/25}$	0
	H	$\sqrt{13/25}$	$-\sqrt{143/100}$	$\sqrt{1/4}$
	I	0	$\sqrt{77/60}$	$-\sqrt{11/12}$
	(K)	0	0	$\sqrt{11/5}$

L	L_1	$L'=H$	I	(K)
I	G	$\sqrt{13/5}$	0	0
	H	$-\sqrt{91/60}$	$\sqrt{13/12}$	0
	I	$\sqrt{7/12}$	$-\sqrt{143/84}$	$\sqrt{11/35}$
	(K)	0	$\sqrt{52/35}$	$-\sqrt{39/35}$
	(L)	0	0	$\sqrt{13/5}$

L	L_1	$L'=G$	H	I
H	F	$\sqrt{1/35}$	$\sqrt{11/35}$	$\sqrt{13/7}$
	G	$-\sqrt{3/25}$	$-\sqrt{143/225}$	$-\sqrt{13/9}$
	H	$\sqrt{8/25}$	$\sqrt{22/25}$	1
	I	$-\sqrt{24/35}$	$-\sqrt{33/35}$	$-\sqrt{4/7}$
	(K)	$\sqrt{9/7}$	$\sqrt{44/63}$	$\sqrt{68/315}$

L	L_1	$L'=H$	I	(K)
I	G	$\sqrt{2/45}$	$\sqrt{26/63}$	$\sqrt{15/7}$
	H	$-\sqrt{6/35}$	$-\sqrt{39/49}$	$-\sqrt{90/49}$
	I	$\sqrt{3/7}$	$\sqrt{52/49}$	$\sqrt{272/245}$
	(K)	$-\sqrt{55/63}$	$-\sqrt{2431/2205}$	$-\sqrt{153/245}$
	(L)	$\sqrt{11/7}$	$\sqrt{39/49}$	$\sqrt{57/245}$

JOURNAL OF THE PHYSICAL SOCIETY OF JAPAN Vol. 7, No. 1, JAN.—FEB., 1952.

The Electronic Energies of the CH_2 Radical

By Kazuo NIIRA and Kiyoshi OOHATA
Tokyo Institute of Technology

(Received May 26, 1951)

The CH_2 radical is considered to have the bond angle of 140 degrees and the dissociation energy of 205 kcal. It may be possible to explain these values of the CH_2 radical by the calculation of its electronic energies, assuming both the s^2p^2 and sp^3 electronic configurations of the carbon atom, and using the atomic orbital approximation. The result of our calculation shows that the ground state of CH_2 has the dissociation energy 9.25 eV (204 kcal.) and the equilibrium bond angle 140 degrees, the symmetry state of which being $^3B_1$ having its nodal plane in the moleclar plane. If we compare the result of our calculation with the estimation given by Mulliken using the method of molecular orbital, it may be observed that there is a good correspondence between those two methods of approximation except a few numbers of term reversal.

§1. Introduction.

The spectrum about 4050 A, which was observed in comets and the electrodless discharge through methane, was identified by Herzberg¹⁾ with the rotational spectrum of the CH_2 radical, and was suggested to give the bond angle of this radical of 140 degrees. Recently, Rosen²⁾ and Douglas³⁾ took a spectrum of discharge through deuterium, using carbon electrode, which was the same as that found by Herzberg in comets, and they did not observe any difference between CH_2 and CD_2. There seems, therefore, to be a little doubt about Herzberg's identification. Further work is in progress under Herzberg's direction to obtain the spectrum of CH_2 in both emission and absorption, but we, to date, do not know anything about the results.

The dissociation energy of CH_2, by Laidler and Casey⁴⁾, is deduced from thermochemical data, as the heat of formation from the atom

C(^3P) and 2H(^2S), to be >205 kcal., assuming a heat of sublimation of graphite of 170 kcal., (or>160 kcal., assuming a heat of sublimation of graphite of 120 kcal.).

If we use the method of atomic orbital assuming the carbon atom in the s^2p^2 configuration and use the numerical values for energy integrals semiempirically estimated, further if we neglect the interaction between two hydrogen atoms, then the result of calculation gives 90 degrees as for the bond angle of CH_2[5]. Voge[6] made a calculation based upon s^2p^2 configuration of carbon atom, assuming 90 degrees of the bond angle and obtain the Values 8.03 eV for the dissociation energy.

In this paper we compute the bond angle and the dissociation energy of CH_2 using the atomic orbital approximation both the s^2p^2 and sp^3 configurations of the carbon atom taking into account.

§ 2. The Basic Wave Functions for the CH₂ Radical.

If we take the s^2p^2 and sp^3 electronic configurations for the carbon atom into account, there are 13 possible kinds of electronic orbital wave functions for the whole radical, which are given by products of atomic orbitals:

$$\begin{aligned}
\Phi_1&=(k)\,(k)\,(s)\,(s)\,(p_x)\,(p_x)\,(h)\,(h'),\\
\Phi_2&=(k)\,(k)\,(s)\,(s)\,(p_y)\,(p_y)\,(h)\,(h'),\\
\Phi_3&=(k)\,(k)\,(s)\,(s)\,(p_z)\,(p_z)\,(h)\,(h'),\qquad (1)\\
\Phi_4&=(k)\,(k)\,(s)\,(s)\,(p_x)\,(p_y)\,(h)\,(h'),\\
\Phi_5&=(k)\,(k)\,(s)\,(s)\,(p_x)\,(p_z)\,(h)\,(h'),\\
\Phi_6&=(k)\,(k)\,(s)\,(s)\,(p_y)\,(p_z)\,(h)\,(h')
\end{aligned}$$

in the s^2p^2 configuration of the carbon atom, and

$$\begin{aligned}
\Psi_1&=(k)\,(k)\,(s)\,(p_x)\,(p_x)\,(p_y)\,(h)\,(h'),\\
\Psi_2&=(k)\,(k)\,(s)\,(p_x)\,(p_y)\,(p_y)\,(h)\,(h'),\\
\Psi_3&=(k)\,(k)\,(s)\,(p_x)\,(p_x)\,(p_z)\,(h)\,(h'),\\
\Psi_4&=(k)\,(k)\,(s)\,(p_y)\,(p_y)\,(p_z)\,(h)\,(h'),\qquad (1')\\
\Psi_5&=(k)\,(k)\,(s)\,(p_x)\,(p_z)\,(p_z)\,(h)\,(h'),\\
\Psi_6&=(k)\,(k)\,(s)\,(p_y)\,(p_z)\,(p_z)\,(h)\,(h),\\
\Psi_7&=(k)\,(k)\,(s)\,(p_x)\,(p_y)\,(p_z)\,(h)\,(h')
\end{aligned}$$

in the sp^3 configuration of the carbon atom, where k, s, p_x, p_y and p_z are the 1s, 2s, 2px, 2py and 2pz atomic orbitals of the carbon atom, and h and h' are the 1s orbitals of the hydrogen atoms, respectively. We assume the spatial configuration of CH_2 as an isosceles triangle, and take x and y axes in the molecular plane, and θ as the angle between the one of the two CH bond axes and x or y axis (see Fig. 1). Then the angle HCH is $\pi/2+2\theta$.

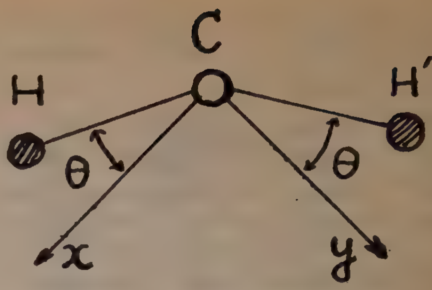

Fig. 1. Axes and notation for CH_2.

Since the spatial symmetry of CH_2 belongs to the symmetry group C_{2v}, and electronic terms with different multiplicity or symmetry do not interact, the basic wave functions for this radical, which are constructed from (1) and (1′) as to fit the Pauli principle, can be classified by the irreducible representations of C_{2v} (A_1, A_2, B_1 and B_2), in both singlets and triplets. Thus it is shown that there are eight basic wave functions belonging to the type of $^1A_1$ and six, seven and five for the types of $^1A_2$, $^1B_1$ and $^1B_2$, respectively, and also eight, ten, eleven and ten basic wave functions for the types of $^3A_1$, $^3A_2$, $^3B_1$ and $^3B_2$, respectively. (For the designations of irreducible representations we follow after Sponer-Teller and Mulliken[7]).

§ 3. The Secular Equations.

Using these antisymmetrized basic wave functions, which are linearly independent with each other, we obtain a secular equation for each symmetry type. We use as the total Hamiltonian of our system

$$\mathbf{H}=-\frac{1}{2}\sum_{i=1}^{8}\Delta_i+Z/R_{ch'}+Z/R_{ch}+\frac{1}{R_{hh'}}-\sum_{i=1}^{8}\frac{Z}{r_{ci}}-\sum_{i=1}^{8}\frac{1}{r_{hi}}-\sum_{i=1}^{8}\frac{1}{r_{h'i}}+\sum_{\substack{i,j=1\\(i\neq j)}}^{8}\frac{1}{r_{ij}},\qquad (2)$$

where R_{ch} and $R_{ch'}$ are the nuclear distances between the carbon atom and each hydrogen atom. r_{hi} and $r_{h'i}$ are the distances between each hydrogen atom and the i-th electron, and r_{ij} is the distance between i-th and j-th electrons. Z is the atomic number of the carbon ($Z=6$).

Then we can set up, for instance, the secular equation of eleven dimensions of the $^3B_1$, assuming all atomic orbitals to be orthogonal to each other:

$$\det |H_{ij}-W\delta_{ij}|=0,$$
$$i,j=1,2,\ldots\ldots,\ 11,$$
$$\delta_{ij}=\begin{cases}1 & \text{for } i=j,\\ 0 & \text{for } i\neq j,\end{cases} \qquad (3)$$

where the typical terms of H_{ij} 's are

$$H_{11}=W_C({}^3P)+2W_H({}^2S)+2W_1+4Q_s-2J_s+Q_\sigma+3Q_\pi+Q_{HH}-J_{HH}+(Q_\sigma-Q_\pi)\sin 2\theta,$$

$$H_{77}=W_C({}^3D^0)+2W_H({}^2S)+2W_1+\frac{3}{2}J_{sp}-\frac{3}{2}F_2+2Q_s+\frac{1}{2}J_s+2Q_\sigma+4Q_\pi-2J_\sigma-\frac{3}{2}J_\pi+Q_{HH}+J_{HH},$$

$$H_{12}=\sqrt{\frac{1}{2}}(J_\pi-J_\sigma)(1+\sin 2\theta),$$

$$H_{17}=-\sqrt{\frac{5}{3}}\,(C_{s\sigma}-N_{s\sigma})\sin\left(\frac{\pi}{4}-\theta\right),$$

$$H_{78}=-\sqrt{\frac{5}{12}}\,(J_{sp}+3F_2-J_s-J_\pi).$$

$W^C({}^3P)$ and $W_C({}^3D^0)$, which are the electronic energies of the carbon atom in the normal and the excited states, respectively, are given as[5]

$$W_C({}^3P)=W_0+F_0-5F_2,$$
$$W_C({}^3D^0)=W_0+3F_0-6F_2-2J_{sp}, \qquad (4)$$

where W_0 is the sum of energies concerning the K shell electrons and the Coulomb energies between $2s$ orbitals and between $2s$ and $2p$ orbitals in the carbon atom, and further W_1 is the interaction energy between K shell of the carbon atom and the $1s$ orbital of each hydrogen atom. And other energy integrals are defined as follows:

$$Q_\alpha=\iint\alpha(1)h(2)\left(\frac{1}{r_{12}}+\frac{1}{R_{ch}}-\frac{1}{r_{h1}}-\frac{1}{r_{c2}}\right)\alpha(1)h(2)d\tau_1d\tau_2,$$

$$J_\alpha=\iint h(1)\alpha(2)\left(\frac{1}{r_{12}}+\frac{1}{R_{ch}}-\frac{1}{r_{h1}}-\frac{1}{r_{c2}}\right)\alpha(1)h(2)d\tau_1d\tau_2, \qquad (5)$$

$$C_{\alpha\beta}=\iint\alpha(1)h(2)\left(\frac{1}{r_{12}}+\frac{1}{R_{ch}}-\frac{1}{r_{h1}}-\frac{1}{r_{c2}}\right)\beta(1)h(2)d\tau_1d\tau_2,$$

$$N_{\alpha\beta}=\iint h(1)\alpha(2)\left(\frac{1}{r_{12}}+\frac{1}{R_{ch}}-\frac{1}{r_{h1}}-\frac{1}{r_{c2}}\right)\beta(1)h(2)d\tau_1d\tau_2,$$

where α or β takes s, σ and π.

§ 4. The Dependence of the Electoronic Energies on the Bond Angle.

The energy difference between the states ${}^3D^0$ and ${}^3P$ of the carbon atom is deduced from the spectroscopic data(8):

$$W_C({}^3D^0)-W_C({}^3P)=7.90\,\text{eV}, \qquad (6)$$

and we take W_1 as a parameter, such as to be consistent with the spectroscopic data of the CH radical. Because of the reason explained in the next section, we choose $W_1=0.50$ eV. All other energy integrals are deduced from the table by Kotani and Amemiya(9), assuming the following well-known Zener type functions for the $2s$ and $2p$ wave functions of the carbon atom(10):

$$s=\sqrt{\frac{\delta^5}{3\pi}}e^{-\delta r}r,$$
$$p_x=\sqrt{\frac{\delta^5}{\pi}}e^{-\delta r}x, \qquad \text{etc.,} \qquad (7)$$

where the value of δ is chosen as 1.59 (in the atomic unit) for the carbon atom. The internuclear distance between the carbon atom and the hydrogen atom is not known experimentally for the CH_2 radical, so we assume tentatively 1.12 A (the equilibrium distance of CH radical) for its value. The values of energy integrals are as follows:

$$\begin{array}{llll} Q_s=-0.60\ \text{eV}, & J_s=-2.75\ \text{eV}, & \\ Q_\sigma=-1.89\quad , & J_\sigma=-1.67\quad , & (8)\\ Q_\pi=\ \ 0.04\quad , & J_\pi=\ \ 0.66\quad , & \\ C_{s\sigma}=-1.57\quad , & N_{s\sigma}=-2.55\quad . & \end{array}$$

All other energy intgrals vanish. Further we take the interaction energy between two hydrogen atoms from the Morse curve of the H_2 molecule as in the usual manner.

Using these values, we can compute the electronic energies W from the secular equation (3) and so on at each angle θ, and obtain the electronic energy of each level, varying the angle θ from 0 to $\pi/4$, as plotted in Fig. 2. The secular equations of higher degrees have been reduced to the lower ones after inserting appropriate values for W and proper values for W which make the determinant vanish have been found numerically. The result of calculation gives the numerical value 9.25 eV as for the dissociation energy of the ground state, its symmetry being given by ${}^3B_1$ and 140 degrees as for the bond angle. The first excited state (${}^1B_1$) is 1.5 eV above the ground state.

§ 5. The Electronic Energies of the CH Radical.

We can compute the electronic energies of CH in the same way as in CH_2. In this case, the electronic levels are classified by the irreducible representations (i.e. Σ^+, Σ^-, Π, Δ,

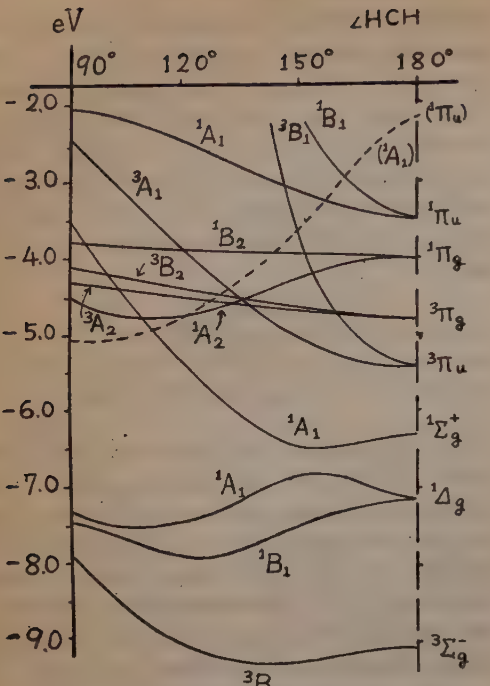

Fig. 2. Electronic energies of CH_2

The nuclear distance between the carbon atom and each of two hydrogen atoms is assumed to be 1.12 A (the equilibrium distance of the CH radical). The orgin of the energy is chosen to be $C(^3P)+2H(^2S)$. All of the states in the above figure are stable for the dissociation into CH and H. Dotted curve is the lowest state arising from the s^2p^2 electronic configuration (without sp^3) of the carbon atom.

etc.) of the spatial group $C_{\infty v}$, to which CH belongs. Each level has equal shift due to varying the parameter W_1, so we choose its probable value to fit the experimental data The result of our calculation is shown in Table 1, compared with the experimental values. As seen from Table 1, there is a good correspondence between the result of our calculation and the experimental values. The lowest state of CH in our calculation is $^4\Sigma^-$, which is not observed, but the result is the same in the molecular orbital approximation[11].

Table 1. Electronic energies of CH.

	calc. (eV)	exp. (eV)
$^2\Sigma^+$	0.31	0.33
$^2\Sigma^-$	−0.18	−0.42
$^2\Delta$	−1.14	−0.74
$^2\Pi$	−2.95	−3.60
$^4\Sigma^-$	−3.00	—

We take $C(^3P)+H(^2S)$ as the origin of energy.

§ 6. Discussions.

The dissociation energy of CH_2 calculated to be 9.25 eV (204 kcal.), agrees with the one deduced from thermochemical data by Laidler and Casey[4]. From the point of view of the molecular orbital approximation, the ground states of polyatomic molecules are in general total symmetric and singlet. According to Mulliken[12] the ground state of CH_2 may be $^1A_1$ from the analogy between CH_2 and CF_2. Comparison of the result by Mulliken with ours is as follows:

$$\left.\begin{array}{lllllllll}
 & & \text{(Mulliken)} & & & & & \text{(Our result)} & \\
1a_1)^2 & 2a_1)^2 & 1b_2)^2 & 3a_1)^2 & & {}^1A_1\ (0) & & \nearrow & {}^3B_1\ (0),\quad {}^1B_1\ (1.5), \\
 & [25] & [16] & [12] & & & & & \\
 & 2a_1)^2 & 1b_2)^2 & 3a_1) & 1b_1)^2 & {}^3B_1\ (1), & {}^1B_1\ (3) & \searrow & {}^1A_1\ (2), \\
 & & & & [11] & & & & \\
 & 2a_1)^2 & 1b_2)^2 & & 1b_1)^2 & {}^1A_1\ (4) & & \rightarrow & {}^1A_1\ (3),\quad {}^3A_1\ (4), \\
 & 2a_1)^2 & 1b_2) & 3a_1)^2 & 1b_1) & {}^3A_2\ (5), & {}^1A_2\ (7) & \rightarrow & {}^3A_2\ (4.5),\ {}^1A_2\ (4.7), \\
 & 2a_1)^2 & 1b_2) & 3a_1) & 1b_1)^2 & {}^3B_2\ (6), & {}^1B_2\ (8) & \rightarrow & {}^3B_2\ (4.5),\ {}^1B_2\ (5.5), \\
 & \cdots\cdots & \cdots\cdots & \cdots\cdots & \cdots\cdots & \cdots\cdots & \cdots\cdots & & \\
 & 2a_1) & 1b_2)^2 & 3a_1)^2 & 1b_1) & {}^3B_1\ (15), & {}^1B_1\ (17) & \nearrow & {}^1A_1\ (6.5), \\
 & 2a_1) & 1b_2)^2 & 3a_1) & 1b_1)^2 & {}^3A_1\ (16), & {}^1A_1\ (18) & \searrow & {}^3B_1\ (6.5),\ {}^1B_1,
\end{array}\right\}\quad (9)$$

where the figures in square brackets are the ionization energies (in eV) of the molecular orbitals, and those in parentheses are the exciation energies (in eV) of the electronic states of the radical.

From (9), we see that the ground state of CH_2 is different between molecular and atomic orbital approximations and some electronic levels are reversed, but a good correspondence may be observed between them. But the contradiction between the molecular orbital approximation and the atomic one is not so fundamentally serious if we regard that the energy differences involved are small. Laidler and Casey[4] also point out that the ground state is possibly a singlet state and the first excited state is a triplet, which is 19 kcal. (~0.9 eV) above that, while recently, Mulliken [12)] remarks that the observed emission and absorption spectrum of the CF_2 radical is understood much more reasonably if the electronic levels involved are triplet rather than singlet, with the ground state of the type which we conclude for CH_2. It would be necessary to have more spectroscopic data to decide whether the ground state of CH_2 is singlet or triplet.

Further it is interesting that the bond angle of CH_2 is 140 degrees by our calculation, which contradicts with the suggestion by Laidler and Casey[13)], according to whom CH_2 in triplet state might have a linear configuration.

But our result may not be considered so conclusive because of the approximate nature of our calculations, neglecting the ionic states of the radical and the overlap integrals between the atomic orbitals. It may be desirable to calculate more accurately the electronic states of CH_2.

The authors wish to express their sincere thanks to Professor R. S. Mulliken, who called their attention to the calculation of the triplet states of CH_2, for his valuable discussions and kind suggestions, and to Doctor E. J. Casey for his valuable discussions and kind communication. The authors also thanks cordially to Professor T. Inui of the University of Tokyo for his incessant encouragement. Thanks are also due to Professor G. Araki of the University of Kyoto for his kind advice.

This work is indebted to the Ministry of Education for its research grant.

References

1) G. Herzberg, Rev. Mod. Phys. **14** (1942) 195; Astrophys. J. **96** (1942) 314.
R. Herman, Comptes Rendus **22** (1946) 280.
2) B. Rosen according to the private communication from E. J. Casey.
3) Douglas, unpublished.
4) K. J. Laidler and E. J. Casey, J. Chem. Phys. **17** (1949) 1087.
5) M. Kotani, *Quantum Chemistry* (Kyoritsu Sha, Tokyo, 1939) Section 12 (in Japanese).
6) H. H. Voge, J. Chem. Phys. **4** (1936) 581; **16** (1948) 984.
7) R. S. Mulliken, Phys. Rev. **43** (1933) 279.
H. Sponer and E. Teller, Rev. Mod. Phys. **13** (1941) 75.
8) B. Edler, Zeits. f. Physik **84** (1933) 746.
9) M. Kotani and A. Amemiya, Proc. Phys.-Math. Soc. Japan **22** Extra No. 1 (1940).
10) C. Zener, Phys. Rev. **36** (1930) 51.
11) R. S. Mulliken, Rev. Mod. Phys. **4** (1932) 1
12) R. S. Mullken, Private communication.
13) K. J. Laidler and E. J. Casey, J. Chem. Phys. **17** (1949) 213.

JOURNAL OF THE PHYSICAL SOCIETY OF JAPAN Vol. 7, No. 1, JAN.—FEB., 1952

The Aging Phenomenon in Inert Gas Discharge Tubes

by Michika MIYANISHI and Kunihiko WATADANI

Department of Applied Physics, Faculty of Technology, Hiroshima University

(Received June 13, 1951)

The white light emitted from a neon discharge tube at its initial discharge, changes to red gradually with the time of discharge. This aging phenomenon was studied by a spectroscopic method. The white light mainly was that of Ångström bands of CO molecules. The recombination of carbon atoms and oxygen atoms produced by the dissociation of CO molecules in the tube was arrested by the neon gas. The carbon thus freed, therefore, was fixed on the wall of the tube gradually. This was the main cause giving the phenomenon. The similar phenomenon was also observed in the case of helium discharge tubes.

In the excitation of spectra of impurities in inert gas discharge tubes scharacteristic phenomena are observed. MacLennan and Shrum[1] have found that the auroral green line λ 5577 is excited in discharge tubes of inert gases when a very small quantity of oxygen is contained in it. Higher members of Balmer series have been observed by Takamine and Suga[2] in the light emitted from a discharge tube of neon gas containing trace of hydrogen. It is noticed by makers of neon sign tubes that the white light emitted from them at initial discharge becomes red gradually with time of discharge. This is called the "aging of neon sign tubes". In our discussion of the excitation of auroral green line λ 5577 in inert gas discharge tubes, it was required to study also the mechanism of this aging effect of inert gases. In the present paper the result of our experiment on the aging phenomenon will be given.

An ordinary neon sign tube whose length of about 20cm long was used. After the discharge tube was cleaned with heating and with bombardment, pure neon gas was introduced into it, the pressure of the gas being about 3 mm, Hg. The tube thus prepared was excited with a neon transformer of 0.35 kw. At the beginning of the discharge, the colour of light emitted from the tube was not red but bluish white. This was due to the light emitted from carbon mono-oxide coming from the gass wall and the electrodes of the tube under the influence of discharge. The colour, however, became red gradually with time of discharge and after about one hour it exhibited the characteristic red colour of neon.

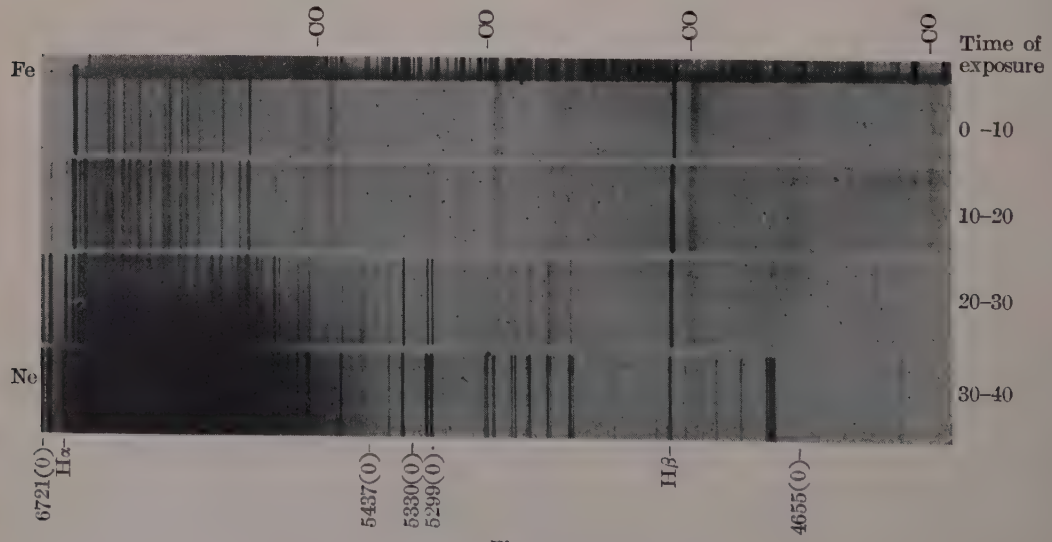

Fig. 1

The spectrograms of spectra of light emitted from the tube, during the intervals of discharge 0–10, 10–20, 20–30, 30–40 minutes were taken side by side on Oriental hyper-sensitive panchromatic plates. The spectrographs used were a Hilger constant deviation prism spectrograph and a quartz spectrograph of small size. One of the photograph thus taken is shown in Fig. 1. As is seen in the figure in the light emitted during the time of discharge 0–10 minutes, Ångström bands of CO λλ5610, 5198, 4835, 4511 appeared strongly, while neon lines lying in the spectral regions of wave-length longer than λ5800 remarkably.

All strong neon lines given during the first ten minutes belong to the electron transition $2p_{1,2,\dots,10} \longrightarrow 1s_{2,3,4}$, the term notations being taken from those given by Paschen. In the next exposure during 10–20 minutes Ångström bands of CO still appeared strongly. In the third exposure 20–30 minutes the bands became very weak and in addition to the neon lines mentioned above those corresponded to the electronic transitions $3s'_1-2p_2$, $4d_{2,3,4,5}-2p_{6,7,8,9,10}$, $4d'_1-2p_{8,9}$, $4s'''_1-2p_{6,7,8}$, $5d_{2,3,4,5}-2p_{3,6,8,9}$, $5d'-2p_6$, $5d''_1-2p_{5,7,8,9}$, $4s''''_1-2p_{6,7}$, $5s_1''''-$

Table I

λ	M	Series	Intensity 0–1	10–20	20–30	30–40
6929	Ne	$1s_2-2p_6$	0	0	2	4
6721	O		0	2	5	7
6678	Ne	$1s_2-2p_4$	1	5	6	8
6599	Ne	$1s_2-2p_2$	1	4	7	9
6563	H_α		10	9	7	3
6533	Ne	$1s_3-2p_7$	1	3	7	9
6507	Ne	$1s_4-2p_8$	5	7	9	10
6456	O	$3p^5P_3-5s^5S$	1	2	3	4
6402	Ne	$1s_5-2p_9$	7	8	9	10
6383	Ne	$1s_4-2p_7$	4	6	8	9
6334	Ne	$1s_5-2p_8$	5	7	9	10
6305	Ne	$1s_5-2p_6$	3	5	7	9
6266	Ne	$1s_3-2p_5$	5	7	9	10
6217	Ne	$1s_5-2p_7$	3	5	7	8
6182	Ne	$3s_5-2p_9$	1	2	3	5
6164	Ne	$1s_3-2p_2$	5	7	8	9
6143	Ne	$1s_5-2p_6$	6	8	9	10
6096	Ne	$1s_4-5p_4$	6	8	9	10
6074	Ne	$1s_4-2p_3$	6	8	9	10
6030	Ne	$1s_4-2p_2$	4	5	7	8
6001	Ne	$2p_6-4d_5$	0	1	2	3
5988	Ne	$2p_6-4d_3$	0	1	2	3
5976	Ne	$1s_5-2p_5$	4	6	7	8
5962	Ne	$2p_2-3s_1'$	0	1	2	4
5959	O	$3p^3P-5d^3D$	1	2	3	4
5945	Ne	$1s_5-2p_4$	5	6	7	8
5914	Ne	$2p_7-4d_2$	0	1	3	4
5902	Ne	$2p_4-4s_1'''$	0	2	4	6
5882	Ne	$1s_5-2p_2$	5	7	9	0
5852	Ne	$1s_2-2p_1$	7	9	10	10
5820	Ne	$2p_8-4d_4$	1	3	4	5
5811	Ne	$2p_8-4d_2$	0	2	4	5
5804	Ne	$2p_8-4d_1'$	0	1	3	4
5764	Ne	$2p_9-4d_4, 4d_4'$	0	3	5	8
5748	Ne	$2p_9-4d_1'$	0	2	4	6
5719	Ne	$2p_6-4s_1'''$	0	0	2	4
5690	Ne	$3s_5-2p_{10}$	?	2	3	4
5657	Ne	$2p_7-4s_1''''$	0	2	4	5
5610	CO	(0, 3)	6	5	2	0
5563	Ne	$2p_8-4s_1'''$	0	1	2	4
5534	Ne	$4s_5-2p_4$	1	?	?	1
5512	O	$3p^3P-6d\,D$	1	?	?	1
5449	Ne	$3s_3-2p_{10}$	0	0	1	1
5437	O	$3p^5P_3-6s^5S$	1	2	2	3
5401	Ne	$1s_4-5p_1$	2	4	5	6
5375	Ne	$2p_3-5d_2$	0	0	1	1

λ	M	Series	Intensity 0–10	10–20	20–30	30–40
5341	Ne	$2p_{10}-4d_5$	0	2	4	6
5331	O	$3p^5P_3-5d^5D$	1	3	4	6
5305	Ne	$4s_4-2p_7$	0	0	1	1
5299	O		0	0	1	2
5234	Ne	$4s_5-2p_8$	0	0	0	1
5222	Ne	$4s_4-2p_8$	0	0	1	2
5209	Ne	$2p_6-5d_3$	0	0	1	2
5204	Ne	$2p_6-5d'_1$	0	0	1	3
5198	CO	(0, 2)	9	8	2	0
5193	Ne	$2p_2-5s_1''''$	0	0	1	2
5189	Ne	$4s_5-5p_9$	0	0	1	3
5152	Ne	$2p_7-5d_1''$	0	0	1	2
5145	Ne	$2p_4-5s_1''''$	0	1	2	3
5121	Ne	$2p_5-3s_1'$	0	0	1	2
5177	Ne	$2p_{10}-4s_1''''$	1	2	3	4
5080	Ne	$2p_8-5d_4$	0	1	3	4
5074	Ne	$2p_8-5d_1''$	0	1	2	2
5038	Ne	$2p_9-5d_4$	0	1	2	4
5031	Ne	$2p_9-5d_1''$	0	1	1	2
5005	Ne	$2p_6-5s_1''''$	0	0	0	1
4974	Ne	$2p_5-6d_1''$	0	0	0	1
4957	Ne	$2p_7-5s_1''''$	0	1	1	2
4931	Ne	$5s_3-2p_2$	1	1	0	0
4928	Ne	$5s_2-2p_2$	1	1	0	0
4885	Ne	$2p_8-5s_1'''$	0	1	1	2
4861	H_β		10	9	6	4
4837	Ne	$4s_5-2p_{10}$	0	0	2	3
4835	CO	(0, 1)	10	8	2	0
4818	Ne	$2p_7-6d_1''$	?	?	?	1
4810	Ne	$2p_4-6s_1'''$	1	1	1	2
4789	Ne	$5s_5-2p_9$	1	1	1	3
4753	Ne	$2p_8-6d_4$	0	1	1	3
4750	Ne	$2p_8-6d_1''$	0	1	1	?
4715	Ne	$2p_9-6d_4, d_4'$	0	1	2	3
4709	Ne	$2p_{10}-5d_5$	0	1	2	4
4704	Ne	$2p_{10}-5d_3$	0	1	1	3
4680	Ne	$2p_6-7d_4$	?	?	1	1
4663	Ne	$2p_5-8d_1''$	0	0	1	1
4655	O		0	0	0	1
4651	O		0	0	0	1
4582	Ne	$2p_3-6s_1'''$	0	0	1	1
4511	CO	(0, 0)	4	3	2	1
4368	O		0	0	1	2
4340	H_γ		4	3	1	0

$2p_{2,4,6,7,10}$, $6d_4-2p_{3,9}$, $6d''_1-2p_{7,8}$, $6s'''_1-2p_4$, $7d_4-2p_6$, $8d''_1-2p_5$ etc. were intensified. In the last exposure the CO bands disappeared and all neon lines mentioned above became strong.

Besides the bands and the lines, hydrogen lines H_α, H_β and H_γ and oxygen ones $\lambda\lambda$ 6721, 6456, 5959, 5512, 5437, 5331, 5299, 4655, 4651, 4368 etc. were also detected. The intensities of bands and lines, estimated roughly for the photographs obtained at each exposure, are indicated in Table I. From this table it will be seen that the intensity of hydrogen lines H_α, H_β and H_γ becomes weak with the time of discharge, but on the contrary that of oxygen lines strong.

In this experiment the remarkable feature is that, as long as the CO bands appeared strongly, only the neon lines belonging to the electron transition $2p_{1,2,\ldots,10} \rightarrow 1s_{2,3,4}$ were excited and the other lines of neon began to appear when the intensity of CO bands became weak. For this phenomenon we considered as follows. The energy levels of CO and Ne are shown in Fig. 2. The data of the former were taken from Jevons'book[3)] and those of the latter from the book edited by Paschen-Götze[4)]. As is shown in the figure the exciting energies of CO are less than those of Ne. Consequently when large quantity of CO is contained in the discharge tube, the energy in it will be absorbed mainly by CO. As the Ångström bands $B^1\Sigma-A^1\Pi$ appeared most strongly, the existence of the $A^1\Pi$ state will be considered. The potential energy difference between the term $A^1\Pi$ and the term $a^3\Pi$ is 2.0 V., and those between the terms $2p_{1,2,\ldots,10}$ and the terms $1s_{2,3,4}$ take the values lying from 1.6 V. to 2.4V. The mean value of the latter is 2.0 V. $1s_{2,3,4}$ are the meta-stable states of Ne. It seemed, therefore, that the energy of CO was absorbed by Ne and the lines of series $1s_{2,3,4}-2p_{1,2,\ldots,10}$ were emitted. When number of CO molecules decreased the kinetic energy of ions would increase and the energy played a rôle of excitation of higher members of series lines of Ne.

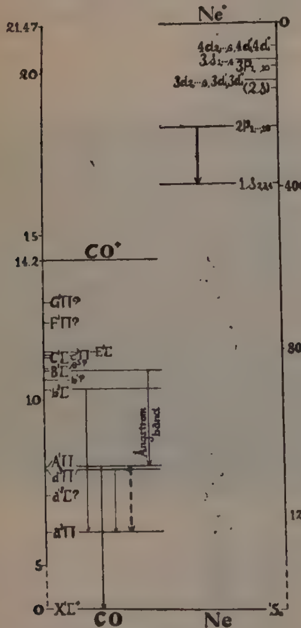

Fig. 2

The next problem was that why the number of CO molecules was decreased with the time of discharge. At the beginning of the discharge CO molecules would be set free from electrodes and glass walls. In the course of the discharge they will be dissociated by the collision with running ions. The recombination of the dissociation products thus produced will be prevented by neon gas for they are mixing with the gas. The carbon atoms, therefore, may be set on the glass walls and oxygen atoms will be separated completely from carbon. Although some oxygen atoms thus produced will combine with hydrogen atoms contained in the discharge tube greater parts of them will be remained in the form of atoms. Under this view, the intensity change of oxygen lines and hydrogen ones observed in this experiment will be explained.

The similar aging action was observed for the discharge tube of helium. Consequently from the present experiment it may be considered that the impurity gases in the inert gas discharge tubes are well separated into atoms and keep their state during comparatively long time. In the excitation of the auroral green line and that of higher members as Balmer lines using inert gas discharge tubes, the oxygen or hydrogen molecules contained in the gas would be separated by the aging action, but it is doubtful that excited inert gas atoms play a rôle of the excitation directly. This remains as a next problem.

This study was aided by the research grant given from the Ministry of Education.

References

1) McLennan & Shrum: Proc. Roy. Soc. **108**, (1925) 501.

2) Takamine & Suga: Sc. Pap. I. P. C. R. **14** (1930) 117.

3) W. Jevons: Report on Band-Spectra of Diatomic Molecules (1932) 268.

4) Paschen-Götze: Seriengesetze der Linienspektren (1922).

JOURNAL OF THE PHYSICAL SOCIETY OF JAPAN Vol. 7, No. 1, JAN.—FBE., 1952

The Effect of Hydrogen Gas on the Exciation of Auroral Green Line λ5577 in Discharge Tubes

by Michika MIYANISHI and Kunihiko WATADANI
Department of Applied Physics, Faculty of Technology,
Hiroshima University

(Received June 13, 1951)

It has been communicated by us that, the auroral green line λ5577 observed in the night sky would be excited by the recombination energy of hydrogen atoms in the upper atmoshere higher than 300 km. In the present experiment the green line was newly excited in a small capillary discharge tube containing a small quantity of oxygen gas, and in a case of a helium discharge tube or neon discharge tube which was used to excite the green line hitherto, it was especially intensified when hydrogen gas was added.

The result of the experiment, therefore, seems to give one of supports to the mechanism of excitation of the green line mentioned above.

In our previous paper1) it was communicated that the emission of auroral green line in the night sky is due to the recombination energy of hydrogen atoms. The height of the emission layer of the line in the upper atmosphere have been estimated from the increase of its intensity with zenith distance and from the effect of sun rise by Rhijn(2), Uchiumi(3) and Furuhata respectively. According to their estimations the values of the height, 340, 400, 650, 700 km. have been obtained. It may be considered that in such a high emission layer, the density of the atmoshere is very small. The layer will consists of hydrogen containing oxygen, nitrogen and helium as very rare impurities. These gases will be dissociated into atoms by the ction of sun light, and they will be so rare that the greater parts of them will remain in the night, without forming molecules. A cyclic reaction shown below, therefor, was considered in our paper mentioned above.

$$H+H+O(^3P) \longrightarrow H^2+O(^1S_0)+0.38\ V.$$
$$O(^1S_0) \longrightarrow O(^1D_2)+h\nu(\lambda 5577)$$
$$O(^1D_2) \longrightarrow O(^3P) \longrightarrow h\nu(\lambda 6364,\ \lambda 6300)$$
$$H+H+O(^3P) \longrightarrow H_2+O(^1S_0)+0.38\ V.$$

Thus a process of the emmission similar to that of phosphorescence in the case of solid or liquid bodies was considered. In the present experiment, therefore, the influence of hydrogen gas on the excitation of the auroral green line in discharge tubes was studied. Using a large discharge tubes containing helium and oxygen respectively, the pressuer of the former being 2—4 mm, Hg, and that of the letter 1—2 mm, Hg, McLennan and Shrum(5) observed the green line. The spectrograms shown in their paper show that the green line was excited strongly with lines of hydrogen H_α and H_β, while the line became very feeble when the lines H_α and H_β disappeared on account of the tube was cooled with liquid air. The appearance of the line in their experiment, therefore, seems to have a relation with hydrogen gas.

In the present experiment we used a small discharge tube consisting of a capillary tube whose length was 20 cm, and inner diameter 1 mm. The electrode were constructed with nickel plates. Using a transformer of 1.5 KW., 60000 volts, we discharged the tubes intermittently during 6 houres to take one photograph of a spectrum. The time of exposure, therefore, was about one hour and the photographs of spectra were taken on Fuji panchromatic plates with a Hilger spectrograph having a constant deviation prism.

1) The spectrum of the light emitted from the discharge tube containing a mixture H_2 (15 mm, Hg)+O_2(2 mm, Hg): The hydrogen and oxygen gases used were obtained by the electrolysis of water, and they were well dried. The partial pressures of the mixture were measured with a mercury manometer. The mixture was introduced into the discharge tube and the spectrum of the light emitted from it was photographed by the method mentioned above. The spectrum thus obtained is shown in Fig. 1, (a) and Table I. It has been considered that the auroral green line is excited when discharge tubes of inert gases containing a small quantity of oxygen. While in the pre-

Table I.

λ	$He+O_2$	$He+O_2+H_2$	McLennan	Hicks	M	Series
	I_1	I_2	I_3	I_4		
6678	–	–	4	6	He	$^1P—^1D$
6563	1	5	–	–	Hα	
6454-5-6	–	–	9	9	O	$3p^5P_{3,2,1} - 5s^5S$
6156-7-8	9	10	10	10	O	$3p^5P - 4d^5D$
6046	5	5	5	7	O	$3p^3P - 6s^3S$
5959	5	5	4	6	O	$3p^3P - 5d^3D$
5890-96	10	10	–	–	Na	$3s^2\,S - 3p^2P_{3/2,1/2}$
5875	9	9	7	10	He	$2p^3P_{0,1,2} - 3d^3D$
5577	1	4	3	–	O	$^1S_0 - {}^1D_2$
5555	2	3	2	6	O	$3p^3P - 7s^3S$
5512	1	1	1	5	O	$3p^3P - 6d^3D$
5461	1	1	–	–	Hg	$6p^3P_2 - 7s^3S$
5435-6-7	5	8	7	8	O	$3p^5P_{3,2,1} - 6s^5S$
5410	1	1	–	–	O	
5329-30-1	7	6	8	10	O	$3p^5P_{3,2,1} - 5d^5D$
5198	–	3	–	–	CO	$A^1\Pi - d^1\Sigma$
5140	2	2	–	–	Hg	
5019-20	2	2	2	5	O	$3p^5P_{3,2,1} - 7s^5S$
5015	3	3	2	6	He	$2s\,^1S - 3p^1P$
4967-8-9	2	3	4	6	O	$3p^5P_{3,2,1} - 6d^5D$
4816	6	10	–	–	Hβ	

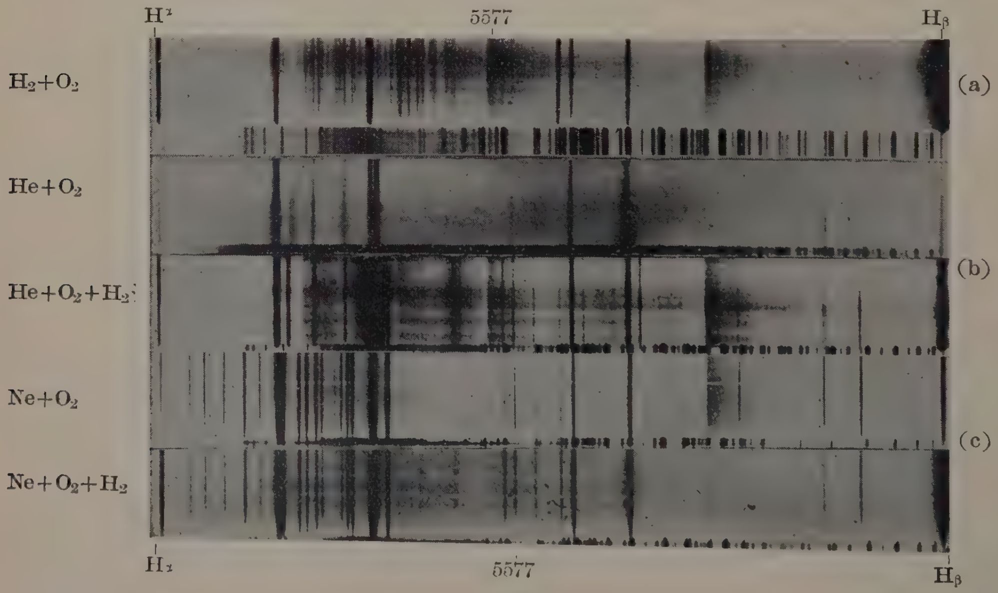

Fig. 1.

sent experiment the line was also obtained cleary, using a hydrogen discharge tube containing a small quantity of oxygen as shown in the Figure 1, (a).

2) The spectra of lights emitted from discharge tubes of the mixtures He(15 mm, Hg) $+O_2$(2 mm, Hg) and He(15 mm, Hg)$+O_2$(2 mm Hg)$+H_2$(5 mm, Hg): The spectra obtained in this case are shown in Fig. 1, (b) and Table I. As are shown in the Figure and the Table, although no hydrogen gas was added, hydrogen lines appeared. This will be due to the hydrogen gas contained in helium used, and the green line appeared weakly. Next when hydrogen gas was added, the green line was intensified remarkably as well as hydrogen lines.

3) The spectra of lights emitted from discharge tubes of the mixtures Ne(15 mm, Hg) $+O_2$(4 mm, Hg) and Ne(15 mm, Hg)$+O_2$(4mm, Hg)$+H_2$(2 mm, Hg): In this case the green line was also intensified similarly in the case of 2 when hydrogen gas was added to the mixture

of neon and oxygen. The result are shown in Fig. 1, (c) and Table II.

Discussion of the Result.

As already mentioned the auroral green line λ 5577 is considered to be excited in the discharge tube of inert gas when a small quantity of oxygen is contained in it. In the present experiment, however, it was excited in the hydrogen discharge tube when a small quantily of oxygen was added. Inert gases used in the present experiment contained hydrogen gas as an impurity. In the discharge tubes of the mixtures of these gases and a small quantity of oxygen, the auroral green line was excited weakly, while when hydrogen gas was added the line was enhanced remarkably as well as the lines of hydrogen.

In a former experiment⁽⁶⁾ of the aging phenomenon in discharge tubes of inert gases following result was obtained. At the biginning of discharge for the discharge tubes, the light of carbon mono-oxide was emitted strongly as compared with those of the gases, while the colour of the light emitted from the tubes changed gradually and became that of pure gas own after about one hour discharge. The spectroscopic study of the light showed that carbon mono-oxide molecules coming out from electrodes and glass walls dissociated gradually into carbon atoms and oxygen ones. The former adhered to the walls of the tubes and the latter were contained in the inert gases. This was due to the obstraction for the recombination of the dissociation products owing to the existence of the inert gases.

Table II

λ	$Ne+O_2$	$Ne+O_2+H_2$	M	Series
	I	I		
6563	2	7	Hα	
6457	2	2	O	$3p^6P_3 - 5s^5S$
6402	3	3	Ne	$1s_5 - 2p_9$
6383	1	1	Ne	$1s_4 - 2p_7$
6334	3	3	Ne	$1s_5 - 2p_8$
6305	1	1	Ne	$1s_4 - 2p_6$
6266	5	5	Ne	$1s_3 - 2p_5$
6217	3	3	Ne	$1s_5 - 2p_7$
6156-7-8	10	10	O	$3p^5P_{3,2,1} - 4d^5D$
6143	6	6	Ne	$1s_5 - 2p_6$
6096	6	6	Ne	$1s_4 - 2p_4$
6074	6	6	Ne	$1s_4 - 2p_3$
6046	6	6	O	$3p^3P - 6s^3S$
6030	3	3	Ne	$1s_4 - 2p_2$
5988	1	1	Ne	$2p_6 - 4d_3$
5975	3	3	Ne	$1s_5 - 2p_5$
5959	5	5	O	$3p^3P - 5d^3D$
5945	6	6	Ne	$1s_5 - 2p_4$
5890–96	10	10	Na	$3s^2S - 3p^2P_{3/2,1/2}$
5882	2	2	Ne	$1s_5 - 2p_2$
5852	8	8	Ne	$1s_2 - 2p_1$
5683–88	1	1	Na	$^2P - {}^2D$
5610	2	2	CO	$A^1\Pi - b^1\Sigma$
5577	3	5	O	$^1S_0 - {}^1D_2$
5555	3	2	O	$3p^3P - 7s^3S$
5512	2	2	O	$3p^3P - 6d^3D$
5461	3	3	Hg	$6p^3P_2 - 7s^3S$
5435-6-7	8	8	O	$3p^5P_{3,2,1} - 6s^5S$
5299	1	1	O	
5198	3	3	CO	$A^1\Pi - b^1\Sigma$
5140	2	1	Hg	
5019–20	3	2	O	$2s^1S - 3p^1P$
4967-8-9	4	4	O	$3p^5P_{3,2,1} - 6d^5D$
4861	7	10	H_β	

From these results the mechanism of the appearance of the auroral gaeen line λ 5577 in the discharge tubes mentioned above is considered by dividing into three steps. At first, when a small quantity of oxygen molecules is contained in the inert gas discharge tube, they dissociate into their atoms and greater parts of them keep their atomic state without forming molecules, they being arrested by the gas similarly to the phenomenon of aging. Next when hydrogen gas is added to the discharge tube, hydrogen molecules will also dissociate into atoms and the most of them will keep their atomic state. Thus the atomic state of oxygen and hydaogen is formed in the inert gas. It was, therefore, considerd that the state similar to that of the upper atmospher to emit the auroral green line was given. The former is formed in an inert gas discharge tube, while the latter in the very rare upper atomsphere by the action of sun light. Finally when the oxygen atoms and hydrogen atoms thus given in the tubes draw near to each other the reactions mentioned at the beginning of this paper with equations will parhaps take place. Consequently it may be considered that, in the present experiment the result to support our mechanism of the emission of the green line in the upper atmosphere was obtained.

This study was aided by the research grant given from the Ministry of Education.

References

1) M. Miyanishi: Jour. Phys. Soc. Japan, **5** (1950) 1.

2) P. J. Van Rhijin: Pub. Astr. Lab. Groningen, No. 31 (1921).

3) Uchiumi: Kakioka Chijiki Kansoku-sho Yoho, **5**, No. 1 (1934).

4) M. Fnruhata: Collection of paper of Denriso-Kenkyu Tokubetsu Iinkai in Japan, No. 1.

5) McLennan & Shrum: Proc. Roy. Soc. **108** (1925) 501.

6) M. Miyanishi & K. Watadani: Jour. Phys. Soc. Japan **7** (1952) 72.

JOURNAL OF THE PHYSICAL SOCIETY OF JAPAN Vol. 7, No. 1, JAN.—FEB., 1952

Optical Constants of *ZnS* Films

By Goro KUWABARA and Kozo ISIGURO
Department of Physics, University of Tokyo

(Received July 23, 1951)

The optical constants of the evaporated *ZnS* film were determined by the photometric and interferometric methods for the wave-length between 400 mμ and 1000 mμ. The results obtained by both methods agree within the experimental error, and the density of the film calculated by Lorenz-Lorenz formula is ca. 0.98 of that of the bulk *ZnS*.

The refractive index of a thin film plays an important role in producing the anti-reflection film and the interference filters of reflection or transmission type. The optical constants of the evaporated film can not be assumed the same as those of the bulk, and various methods of measurement have been proposed by many authors.

We determined the optical constants of *ZnS* film in the wave-length between 400 mμ and 1000 mμ by measuring the transmittance, the reflectance and the phase shift of the transmitted light.

The general formulas for the reflectance and transmittance of the thin film on a transparent material have been given by Brattain and Briggs¹⁾. Especially, in the case of a non-absorbing film on the glass in air, the maximum values of the reflectance for normal incidence are given by the following formulas;

$$R_{\max}=\left(\frac{n^2-n_0}{n^2+n_0}\right)^2 \quad \text{for} \quad nd=\frac{\lambda}{4}(2m+1)$$

$$R_{\min}=\left(\frac{n_0-1}{n_0+1}\right)^2 \quad \text{for} \quad nd=\frac{\lambda}{4}\cdot 2m$$

where n and n_0 are the refractive indices of the film and the glass respectively; $(m+1)$ is the order of interference; d is the thickness of the film and λ is the wave-length. Accordingly, if the order of interference is known, then the refractive index of the film for that wave-length and the thickness can be determined from the maximum reflectance. The thickness thus being determined, the optical constants for any wave-length can be calculated with the general formulas.

The phase shift Δ_m for the wave-length, which gives the extremum of reflectance, produced by transmitting through a thin film is expressed as follows;

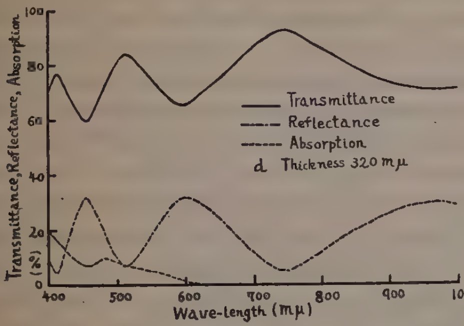

Fig. 1. Transmittance, reflectance and absorption of a ZnS film.

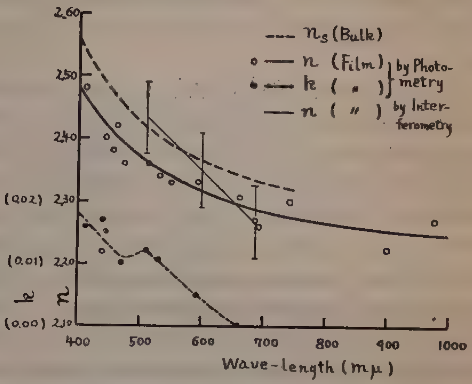

Fig. 2. Optical constants of ZnS films.

Table 1.

Specimen Number	Extremum of Refl.	Wavelength (mμ)	Transmittance (%)	Reflectanc (%)	n	k	n (interferometry)
					(Photometry)		
1	Min.	412	77.3 (77.5)	4.9 (6.0)	2.48	0.016	
2	Max.	440	60.9 (62.0)	27.5 (34.0)	2.22	0.017	
3	Max.	443	58.9 (59.6)	33.8 (32.5)	2.40	0.015	
1	Max.	454	60.4 (60.7)	32.8 (32.2)	2.38		
4	Max.	460	67.0 (67.2)	34.2 (34.0)	2.42		
2	Min.	472	86.0 (86.0)	6.3 (5.6)	2.36	0.010	
1	Min.	512	84.5 (83.5)	7.0 (5.6)	2.36	0.012	2.43
3	Min.	534	91.8 (91.7)	5.4 (4.3)	2.34	0.011	2.38
2	Max.	550	65.1 (65.0)	30.3 (29.7)	2.30		2.28
1	Max.	594	66.0 (66.0)	31.0 (29.4)	2.33	0.005	2.47
4	Min.	660	94.1 (95.8)	4.4 (4.3)	2.31	0.000	2.22
2	Min.	680	93.4 (95.8)	4.9 (4.2)	2.26	0.000	2.22
3	Max.	685	68.9 (70.0)	29.6 (30.0)	2.27	0.000	2.35
1	Min.	740	93.3 (95.0)	5.2 (5.0)	2.30	0.000	
2	Max.	900	69.8 (70.6)	28.5 (29.4)	2.23	0.000	
1	Min.	980	71.5 (70.6)	30.0 (29.4)	2.27	0.000	

Specimen	1	2	3	4
Thickness (mμ)	320	300	228	142

Transmittance and reflectance in the bracket are calculated by the general formulas with the optical constants shown as a solid line in Fig. 2.

$$\Delta_m=\frac{\pi}{2}m-2\pi\cdot\frac{d}{\lambda}=\frac{m\pi}{2}\left(1-\frac{1}{n}\right),$$

$$nd=\frac{\lambda}{4}\cdot m$$

Accordingly, we can also obtain the refractive index independently by measuring the phase shift Δ_m.

We evaporated ZnS on the glasses (Borosilicate-Crown) from the heated tungsten coil, which were placed at various distances (10∼20 cm) from the source and obtained the films of various thickness. The vacuum was ca. 10^{-4}mm Hg. The films were evaporated thicker than usual in order to obtain many maxima and minima of interference. The transmittance T_R and reflectance R_R of the coated glass relative to the uncoated glass were measured by the photoelectric photometer combined with a double monochromator. The photocell used was Ag-Cs vacuum type and photo-current was amplified as usual with an electrometer tube. The true transmittance T and reflectance R of the film were calculated with the following formulas;

$$R=\frac{R_R\left(\frac{2}{1+r}\right)-\left(\frac{T_R}{1+r}\right)^2}{1-\left(\frac{T_R r}{1+r}\right)^2}\,r$$

$$T=T_R\frac{1-R\cdot r}{1+r}$$

where r is the reflection coefficient of a glass surface. The phase shift was measured by the double slit interferometer, which has been reported by one of the authors²⁾.

The typical curves of the reflectance, the transmittance and the absorption of a film are illustrated in Fig. 1.

According to this figure, the absorption above 600 mμ can be neglected, so in this region, we can easily determine n for the wave-length which gives the extremum of reflectance and the thickness d directly by the formulas. ZnS films, however, show perceptible absorption below 600 mμ, therefore, in this region, we should use the general formulas above cited with the thickness determined above 600 mμ, putting the refractive index as $(n-ik)$. The results obtained are shown in Table 1 and Fig. 2. The refractive index determined by the interferometry shows fairly large fluctuation than that by the photometry, but they agree with each other within the experimental error. Recently, Rood³⁾ has also measured the refractive index of ZnS films by the photometry and obtained lower values than ours. This discrepancy might be due to the differences in the thickness of the films, materials used, and the conditions of evaporation.

Assuming Lorenz- Lorenz formula between the refractive index and density, we can calculate the porosity p of the film defined by the following formula;

$$p=\frac{\rho}{\rho_S}=\frac{n^2-1}{n^2+2}\cdot\frac{n_S{}^2+2}{n_S{}^2-1}$$

where ρ_S and n_S are the density and the refractive index of the bulk ZnS; ρ and n are those of the evaporated film. The mean value of p for these films was 0.98, which shows that the density of the film was quite near to that of the bulk ZnS.

In conclusion authors wish to express their thanks to the financial aid of the Expenditure of Scientific Research of the Ministry of Education.

References

1) W. H. Brattin and H. B. Briggs. Phys. Rev. **75** (1949) 1705.
2) K. Isiguro. Jour. Phys. Soc. Jap. **5** (1950) 187.
3) J. L. Rood. J.O.S.A. **41** (1951) 201.

JOURNAL OF THE PHYSICAL SOCIETY OF JAPAN Vol. 7, No. 1, JAN.—FEB., 1952

On the Lamellar Reflectivity and Phase Shift for Multiple Reflections*

By Shigenori NAWATA

The Research Institute for Scientific Mesurements,
University of Tōhoku

(Received June 9, 1951)

An expression for calculating the lamellar reflectivity of a single layer on a surface of metal is given by extending Nathanson and Bartberger's equation. Then, interpreting this expression as reflectivity for a surface of hypothetical medium with an "effective refractive index", we calculated the reflectivity and the phase shift due to the reflection of two or more thin films on a surface of metal and the results were compared with the experiments of A. F. Turner and G. Hass. It was ascertained that the results of calculation show a good coincidence with the experimental data, except in case of very thin aluminium film, in which the optical constants different from those of bulk aluminium must be used. This method of calculation is useful for producing the interference filter, and reflection increasing or reducing by multilayer films, etc. Finally, from the result of the calculation, a method of obtaining a reflection-type interference filter using ZnS was induced.

§ 1. Lamellar Reflectivity for Multiple Layers.

The reflectivity of a layer on a metal surface, obtained by the method of Nathanson and Bartberger,[1] as an extension of reflectivity for a layer on glass surface given by them, is as follows:

$$R=\frac{(A^2+B^2)-2\alpha\{(Aa+Bb)\cos\theta-(Ab-Ba)\sin\theta\}+\alpha^2(a^2+b^2)}{(C^2+D^2)-2\alpha\{(Cc+Dd)\cos\theta-(Cd-Dc)\sin\theta\}+\alpha^2(c^2+d^2)}, \tag{1}$$

where

$$\left.\begin{aligned}
A&=(n_2-n_1)(n_2+n_3)-(n_2k_2-n_1k_1)(n_2k_2+n_3k_3)\,,\\
B&=(n_2-n_1)(n_2k_2+n_3k_3)+(n_2+n_3)(n_2k_2-n_1k_1)\,,\\
a&=(n_2+n_1)(n_2-n_3)-(n_2k_2+n_1k_1)(n_2k_2-n_3k_3)\,,\\
b&=(n_2+n_1)(n_2k_2-n_3k_3)+(n_2-n_3)(n_2k_2+n_1k_1)\,,\\
C&=(n_2+n_1)(n_2+n_3)-(n_2k_2+n_1k_1)(n_2k_2+n_3k_3)\,,\\
D&=(n_2+n_1)(n_2k_2+n_3k_3)+(n_2+n_3)(n_2k_2+n_1k_1)\,,\\
c&=(n_2-n_1)(n_2-n_3)-(n_2k_2-n_1k_1)(n_2k_2-n_3k_3)\,,\\
d&=(n_2-n_1)(n_2k_2-n_3k_3)+(n_2-n_3)(n_2k_2-n_1k_1)\,,\\
\alpha&=\exp(-k_2\theta)\,,
\end{aligned}\right\} \tag{2}$$

and

$$\theta=4\pi n_2x/\lambda_0 \tag{3}$$

in which n_1, n_2, n_3, and k_1, k_2, k_3, are refractive indices and absorption coefficients for air, layer and medium, respectively, as shown in Fig. 1.

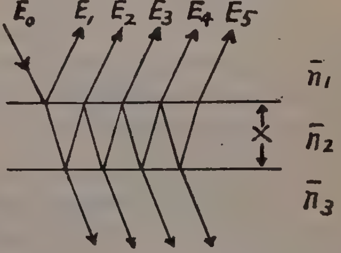

Fig. 1. Multiple reflections within a film.

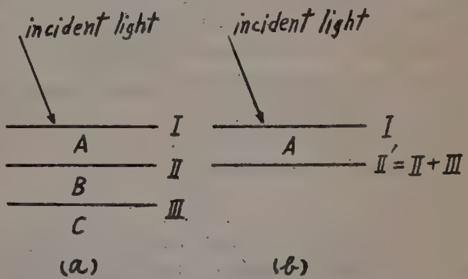

Fig. 2. Reduction of reflection from two layers to reflection from one equivalent layer.

---

* Read at the meeting of Physical Society of Japan, April 2, 1951.

To obtain the lamellar reflectivity of two and more thin films, we used the method of "hypothetical surface" of Vasicek[2]. Consider two thin films, B and A coated successively on a basic medium C, whose boundaries are indicated as I, II and III, as shown in Fig. 2 (a). Now, we consider firstly the reflection from boundaries II and III, assuming that the boundary II contacts with air directly, and we substitute this reflection for that by hypothetical boundary II′ (see Fig. 2 (b)). Then, Fresnel reflection coefficient of this hypothetical surface is $(1-\overline{n})/(1+\overline{n})=(1-n+ink)/(1+n-ink)$ using an "effective refractive index" $\overline{n}$. Then considering n and k as n_3, k_3 of (2), respectively, the resultant lamellar reflectivity for layers A and B on C can be calculated by (1). To know n and k, we put $(1-\overline{n})/(1+\overline{n})=P-iQ$, then

$$\left.\begin{aligned} n_3&=\frac{1-(P^2+Q^2)}{(P^2+Q^2)+2P+1}\,,\\ k_3&=\frac{2Q}{(P^2+Q^2)-1}\,, \end{aligned}\right\}\quad (4)$$

where

$$P=-\frac{LJ+KM}{J^2+K^2}\,,\quad Q=-\frac{JM-KL}{J^2+K^2}\,,\quad (5)$$

in which

$$\left.\begin{aligned} J&=C-c\alpha\cos\theta+d\alpha\sin\theta\,,\\ K&=D-c\alpha\sin\theta-d\alpha\cos\theta\,,\\ L&=A-a\alpha\cos\theta+b\alpha\sin\theta\,,\\ M&=B-a\alpha\sin\theta-b\alpha\cos\theta\,. \end{aligned}\right\}\quad (6)$$

Here, n_1, n_2 and k_1, k_2, are the values of upper medium of A and A-layer, respectively. (see Fig. 2 (b))

Resultant reflectivity of lamella with more than two layers on a basic medium can also be calculated in the same way as shown above, reducing the number of boundaries successively from the lowest layer[3].

§ 2. Numerical examples.

Case I.

As an example to obtain the reflectivity of a layer on a basic material, the reflectivities of the opaque aluminium surface covered with various dielectric layers were calculated and are shown for curve 1, 2, 3, in Fig. 3. The complex refractive index of bulk aluminium, *i.e.*, $1.36(1-4.45\,i)$ for $\lambda_0=5890$ Å was used as $\overline{n_3}$.

Case II.

As an example to obtain the reflectivity of two layers on a basic material, the reflectivity of the mirror: [Al (opaque)+Al_2O_3 (fixed thickness)+Al], were calculated and are plotted in Fig. 4. The thicknesses corresponding to $\theta=0.7\pi$, 0.85π of Al_2O_3 are 580Å, 725Å, respectively, using $n=1.73$ as the refractive index of Al_2O_3. The resultant reflectivities decrease markedly between 0 and 0.05π of θ. Also, the reflectivity of the mirror [Al (opaque) +$MgF_2(\lambda_0/4)$+ZnS] is indicated as curve 4 in Fig. 3. As the reflectivity of opaque aluminium mirror is 87.1%*, the reflectivity of mirror with ZnS-layer of $\theta=\pi$, has larger reflectivity than that of the aluminium mirror alone. Such an improved reflector has been made by A. F. Turner[5].

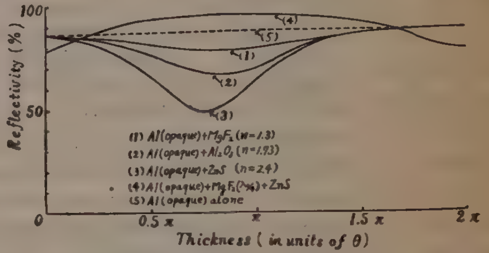

Fig. 3. Reflectivity of an aluminium surface covered with a dielectric layer and of mirror [Al (opaque)+$MgF_3(\lambda_0/4)$ +ZnS], as a function of the thickness of final layer.

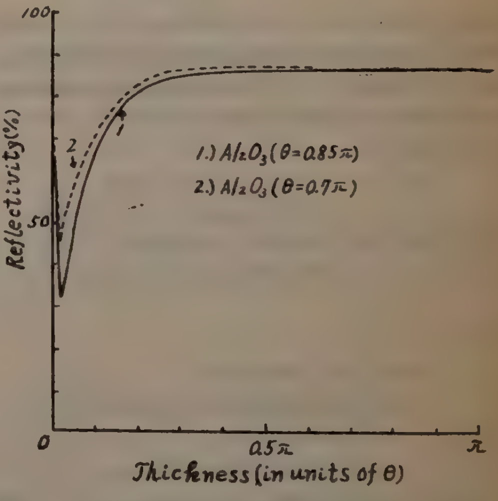

Fig. 4. Reflectivity of mirror which consists of [Al (opaque)+Al_2O_3($\theta=0.7\pi, 0.85\pi$) +Al], as a function of the thickness of final film.

---

* This value is the reflectivity for opaque aluminium film on glass. This was calculated by the equation (I) using the optical constants of bulk lauminium ($n=1.36$, $k=4.45$) and this value corresponds to the metallic reflectivity of aluminium.

§ 3. Comparison with the experimental data of G. Hass.6)

G. Hass made the reflection-type interference filter with Al_2O_3 dielectric layer. This filter [Al (opaque) + Al_2O_3 (580Å thick)+ Al (transparent appr. 50Å thick)] reduces the visible reflectivity to less than 2%. The Al_2O_3-layer was prepared by anodic oxidation in 3% ammonium tartrate, whose thickness is a functions of the applied voltage and time. As there was no description as to the incident angle of observation in his paper, we have compared the result of calculation of normal incidence with his data. The errors introduced by such an assumption would not exceed one precent so far the angle of observation of Hass were within 15° from the normal of surface7). The thickness (580Å) of Al_2O_3 at which reflectivity is approximately minimum, corresponds to about $\theta=0.7\pi$ (see Fig. 3). So, G. Hass might have formed Al_2O_3—layer so as to make the reflectivity minimum.

The curves 1, 2 in Fig. 4 indicate the minimum reflectivity at about $\theta \doteqdot 0.019\pi$ and this value corresponds to about 20Å of aluminium, using $n=1.36$ for $\lambda_0=5890$Å. In all cases, these values are nearly equal to the thickness (appr. 50Å) of G. Hass. But as to the residual reflectivity, there is remarkable discrepancy between the results of our calculation and Hass's value. His resultant reflectivity was about 2% in visible region whereas the result of present author's calculation was about 32% in the case of curve 1 and about 47% in case of curve 2. This discrepancy may be the result of use of inappropriate optical constants, which must be different from those of bulk aluminium.

The reflectivity of the metal surface for normal incidence is given by the well-known expression8),

$$r=\frac{n^2(1+k^2)-2n+1}{n^2(1+k^2)+2n+1}. \qquad (7)$$

We have searched for the various combinations n and k which given $r=0.871$* using this equation. For these various combinations of n and k, the resultant reflectivity were calculated and are shown in Fig. 5 taking the thickness of aluminium film as abscissa. The reflectivity descends to about 2% as Hass's value in the case of the combination ($n=8.0$, $k=1.16$). For these values of n and k coinciding with experimental data, n is larger and k is smaller than the value for bulk aluminium ($n=1.36$, $k=4.45$) respectively. Similar difference was also observed in very thin silber film9).

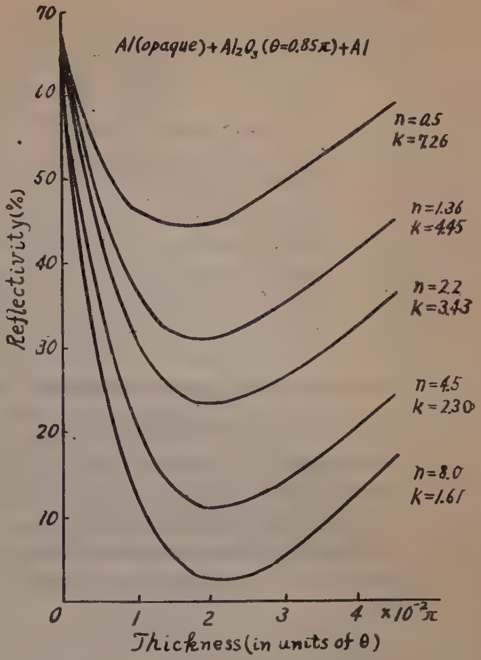

Fig. 5. Reflectivity of interference filter which consists of [Al (opaque)+Al_2O_3 ($\theta=0.85\pi$)+Al], as a function of the thickness of final aluminium with various optical constants.

§ 4. Reflection-type interference filter with ZnS dielectric layer.

Fig. 6 shows the result of calculation of the reflectivity of filter [Al (opaque)+ZnS($\theta=0.75\pi$)+Al)], in which the optical constants of final aluminium film are taken as $n=8.0$ and $k=1.61$.

This filter shows that the same reflection-type interference filter that G. Hass made, can also be made only by means of the method of evaporation. This is a very favourable fact as we are able to coat ZnS to the desired thickness using I. C. I. chromaticity graph of the color of ZnS layer10).

The spectral reflectivity of a reflection filter [Al (opaque)+ZnS($\theta=0.75\pi$:460Å)+Al (appr. 20Å thick)] in visible region is shown in Fig. 7, comparing with that of glass. The reflectivity of this filter is larger than that of glass for the wave length from 4360Å to 5800Å but does not exceed 4%, while it be-

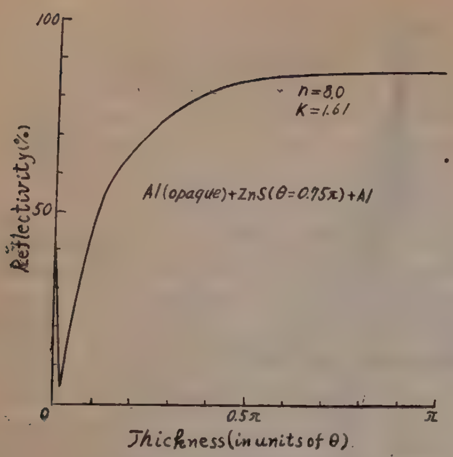

Fig. 6. Reflectivity of reflection-type interference filter which consists of [Al (opaque)+ZnS($\theta=0.75\pi$)+Al], as a function of the thickness of final aluminium ($n=8.0$, $k=1.61$) (calculation).

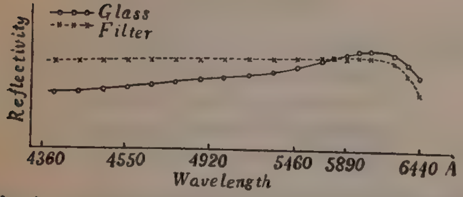

Fig. 7. Reflectivity of reflection-type interference filter which consists of [Al (opaque)+ZnS($\theta=0.75\pi$)+Al (appr. 20Å)], as a function of wavelength from 4360Å to 6440Å.

comes smaller than that of glass in the region beyond 5800Å.

§ 5. Phase shift on reflection.

The phase shift due to reflection by multiple layers can be calculated using the equation (5) as $\tan^{-1}(Q/P)=\tan^{-1}[(JM-KL)/(LJ+KM)]$.

The dotted line in Fig. 8 shows the phase shift of the reflected light from an opaque aluminium surface covered with ZnS, whose curve of reflectivity is given in Fig. 3, taking the thickness of ZnS as abscissa. It is seen that the rate of increase of phase shift is greatest at the position of minimum reflection.

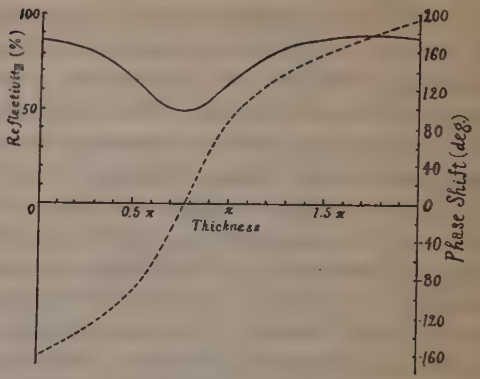

Fig. 8. Reflectivity and phase shift of the reflected light from an opaque aluminium surface covered with ZnS, as a function of the thickness of ZnS.

In conclusions the writer expresses his hearty thanks to Miss K. Yoshida for her earnest help during the numerical calculations and to Mr. K. Takashima for his assistance during the experiments.

References

1) J. B. Nathanson & C. L. Bartberger, J. O. S. A. **29** (1939) 417.
2) A. Vasicek, J. O. S. A. **37** (1947) 623.
3) W. L. Wilcock, J. O. S. A. **39** (1949) 889.
5) Landolt-Börnstein, *Physikalisch-chemische* Tabel. 5, Auf. II, 906.
5) A. F. Turner, J. O. S. A. **36** (1946) 711.
6) G. Hass, J. O. S. A. **39** (1949) 532.
7) L. Rood, J. O. S. A. **39** (1949) 854.
8) P. Drude, *Theory of Optics*, London (1913) 364.
9) K. Ishiguro & G. Kuwahara, Phys. Soc. Japan, **6** (1951) 71.
10) H. Kubota, J. O. S. A. **40** (1950) 146.

On the Effects of Errors of Micoid Disc in Polanret Microscope

By Hiiro NAKAMURA and Hiroshi KUBOTA

Institute of Industrial Science, Tokyo University, Chiba-City

(Received August 29, 1951)

According to the theory of polanret microscope, it is expected that we can vary the phase difference and the intensity ratio of the diffracted and the direct rays of the polanret microscope to any desired values, independently of each other. But, this is permissible only when there is no errors of manufacture in the micoid disc of the microscope. If we take the errors of this disc into account, above assumption is no longer true. In this paper, we studied the effects of errors introduced in the micoid disc upon the function of the polanret microscope. It was found that the effect of error in $\lambda/4$-plate (deviation of retardation from $\lambda/4$) upon the intensity ratio becomes maximum when the phase difference is $\pi/2$. This is the worst effect, as the polanret microscope is used at $\pi/2$ most frequently. All other effects become zero or minimum when the phase difference is $\pi/2$. Graphs showing the results of calculations are given to determine the limits of the tolerable errors in the micoid disc.

In an ordinary phase microscope, a disc called "phase plate" is placed on the focal plane of the objective lens to give phase difference and absorption to either the direct ray or rays diffracted by the object. But, in this case the amounts of phase difference and absorption are not variable, as they are determined by the dimensions of the phase plate.

In the polanret microscope⁽¹⁾, however, phase difference and absorption are made variable by using polarized light. For this purpose, in the polanret microscope, a polarizer is set in front of the condenser lens while an analyser is set behind the eye-piece, and a micoid disc, a small disc consisting of a quarter wave length plate (we shall denote it $\lambda/4$-plate hereafter) and a zonal polarizer is placed in place of the phase plate of the ordinary phase microscope.

According to the theory, it is understood that the amount of absorption (that is, the intensity ratio of direct and diffracted rays) is made variable by the rotation of the analyser without affecting the amount of the phase difference and the phase difference is also varied by rotating the polarizer without changing the intensity ratio. But this is true only when the micoid disc is made perfectly, and in practice, as it is nearly impossible to manufacture a micoid disc having exactly the given dimensions, the polanret microscope does not work as is expected from the theory. In this paper, we shall study the effects of errors introduced in the micoid disc upon the function of the polanret microscope, with the purpose of giving the limits of the tolerable errors of the micoid disc.

§ 1. **Ideal case.** (When the micoid disc without error is used.)

The essential parts of the polanret microscope is shown in Fig. 1. In the figure, P is the polarizer placed in front of the condenser lens C, whose plane of polarization is OP, the angle between OP and X is ρ. X and Y are the principal axes of the $\lambda/4$-plate. Q is the zonal polarizer, whose plane of polarization of the conjugate area (the area conjugate to the opening of the annular stop S) is OG, and the plane of polarization of the complementary area is OD. The angle between OD and OG is equal to $\pi/2$. The $\lambda/4$-plate and the zonal polarizer are so cemented together that X becomes a bisector of ∠GOD. This cemented complex is called a micoid disc. A is an analyser whose plane of polarization OA makes an angle θ with X.

The amplitudes of X- and Y-components of light after passing through $\lambda/4$ plate, when the light coming out from the polarizer is taken as $e^{i\omega t}$, are as follows:

$$A_X = \cos\rho\, e^{i\omega t}, \qquad A_Y = \sin\rho\, e^{i(\omega t+\pi/2)}. \qquad \cdots\cdots(1)$$

Thus after passing through zonal polarizer, the amplitudes of diffracted and direct rays become,

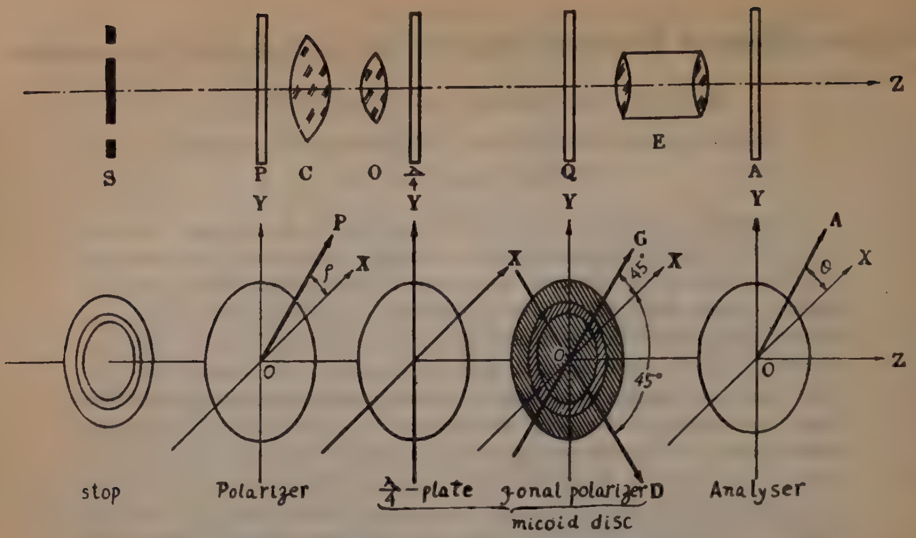

Fig. 1(a). Optical system of polanret microscope.

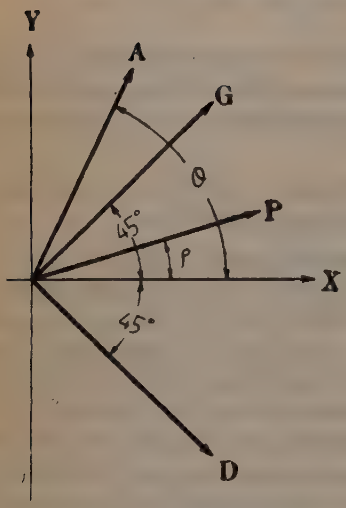

Fig. 1(b). Angular relation between planes of polarization.

$$\left.\begin{aligned} A_G &= A_X\cos(\pi/4)+A_Y\sin(\pi/4) \\ &= \frac{1}{\sqrt{2}}e^{i(\omega t+\rho)} \\ A_D &= A_X\sin(\pi/4)-A_Y\cos(\pi/4) \\ &= \frac{1}{\sqrt{2}}e^{i(\omega t-\rho)} \end{aligned}\right\}\cdots(2)$$

so the phase difference δ between these two rays becomes 2ρ, while their amplitude ratio is still eqal to 1.

Lastly, amplitude of light coming out from the analyser becomes,

$$A_A=\frac{1}{2}(\cos\theta+\sin\theta)\,e^{i(\omega t+\rho)}+\frac{1}{2}(\cos\theta-\sin\theta)\,e^{i(\omega t-\rho)}.$$

The first term of this equation is the amplitude of the direct ray and the second term is that of the diffracted ray, so that their amplitude ratio is

$$g=(\cos\theta+\sin\theta)/(\cos\theta-\sin\theta).$$

As is clear from this equation, g involves θ only, while δ depends on ρ only, so the rotation of polarizer or analyser is expected to change δ or ρ respectively, each independent of the other.

§ 2. When the errors of micoid disc are taken into account.

In practice, however, errors of manufacture introduced in micoid disc are unavoidable. We shall consider the effects of errors in the following.

There are following two sorts of errors of manufacture in micoid disc,

(a) that the retardation of $\lambda/4$-plate is not exactly-$\lambda/4$.

Retardation of $\lambda/4$ is $\pi/2$ in phase angle for correct plate, so we can put the retardation of $\lambda/4$-plate χ as, using small quantity ε,

$$\chi=\pi/2+\varepsilon. \qquad \cdots\cdots(3)$$

(b) that the angles between the planes of polarization are not made exactly.

If we put the deviation of $\angle GOD$ from $\pi/2$ as 2α and the angle between the bisector of $\angle GOD$ and X-axis as β (see Fig. 2), then we can put,

$$\left.\begin{aligned} \angle GOX &= \psi=\pi/4+(\alpha+\beta), \\ \angle DOX &= \psi'=\pi/4+(\alpha-\beta). \end{aligned}\right\}\cdots(3)'$$

If we take these errors into account, Eq. (1) becomes,

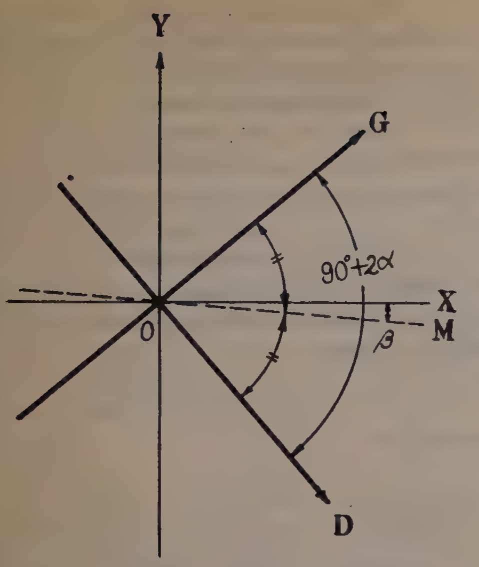

Fig. 2. Errors introduced in micoid disc.

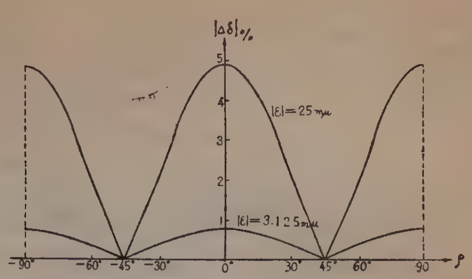

Fig. 3. Effect of ε upon δ.

$$A_X=\cos\rho\, e^{i\omega t},\qquad A_Y=\sin\rho\, e^{i(\omega t+\chi)}.$$

Hence after passing through the zonal polarizer, we have

$$\left.\begin{array}{l} A_G=\cos\rho\cos\psi\, e^{i\omega t}+\sin\rho\sin\psi\, e^{i(\omega t+\chi)}, \\ A_D=\cos\rho\cos\psi'\, e^{i\omega t}-\sin\rho\sin\psi'\, e^{i(\omega t+\chi)} \end{array}\right\}$$

Putting *Eqs.* (3) & (3)′ into these equations and writing them in the form,

$$A_G=Ae^{i(\omega t+B)},\qquad A_D=A'e^{i(\omega t+B')},$$

we get,

$$\left.\begin{array}{l} B=tg^{-1}\dfrac{\sin\rho\,[\cos(\alpha+\beta)+\sin(\alpha+\beta)\cos\varepsilon]}{\cos\rho[\cos(\alpha+\beta)-\sin(\alpha+\beta)]-\sin\rho\,[\cos(\alpha+\beta)+\sin(\alpha+\beta)\sin\varepsilon]}, \\ B'=tg^{-1}\dfrac{\sin\rho\,[\cos(\alpha-\beta)+\sin(\alpha-\beta)\cos\varepsilon]}{\cos\rho[\cos(\alpha-\beta)-\sin(\alpha-\beta)]+\sin\rho\,[\cos(\alpha+\beta)+\sin(\alpha+\beta)\sin\varepsilon]}, \end{array}\right\}\quad\cdots\cdot(4)$$

$$\left.\begin{array}{l} A=\dfrac{1}{\sqrt{2}}[1-\cos 2\rho\cdot\sin 2(\alpha+\beta)-\sin 2\rho\cos 2(\alpha+\beta)\sin\varepsilon]^{1/2}, \\ A'=\dfrac{1}{\sqrt{2}}[1-\cos 2\rho\cdot\sin 2(\alpha-\beta)+\sin 2\rho\cdot\cos 2(\alpha-\beta)\sin\varepsilon]^{1/2}. \end{array}\right\}\quad\cdots\cdot(4)'$$

The phase difference between the diffracted and the direct rays $B-B'=\delta$ becomes

$$\delta=tg^{-1}\frac{\sin 2\rho\cos\varepsilon\cos 2\alpha}{\cos 2\rho\cos 2\beta-\sin 2\rho\sin 2\beta\sin\varepsilon-\sin 2\alpha}\quad\cdots\cdot(5)$$

That is, δ is no longer 2ρ. The amplitude ratio of these two rays $g=A/A'$ is also no longer equal to 1. And moreover, as g becomes a function of ρ and θ, rotation of the polarizer changes not only δ but also g, that is, phase difference can no longer be varied without affecting the amount of the intensity ratio.

Now, we shall consider the effects of α, β and ε separately for each case.

§ 3. When $\varepsilon\neq 0$, $\alpha=\beta=0$ (when $\lambda/4$-plate is not made perfectly correct).

(a) Effect upon the phase difference. If we put $\alpha=\beta=0$ in *Eq.* (5), then

$$\delta=\tan^{-1}(\tan 2\rho\cos\varepsilon).$$

So the deviation from the value of $\varepsilon=0$ (that is $\delta=2\rho$) is,

$$\Delta\delta=[\tan^{-1}(\tan 2\rho\cos\varepsilon)/2\rho-1],$$

Values of $\Delta\delta$ caluculated from the above equation is shown in Fig. 3. In this case, maxima of $\Delta\delta$ occur when $\rho=0$ and $\pm\pi/2$, whereas $\Delta\delta=0$ when $\rho=\pm\pi/4$. This is a very favorable fact for practice, as the cases of $\rho=\pm\pi/4$ (that is the cases of $\delta=\pm\pi/2$) are used most frequently in practice. So we can say, ε almost does not affect the value of δ in practice so long as ε is not very large.

If $\varepsilon=0.0125\pi$ (about 3 mμ), $\Delta\delta$ is less than about 1%.

(b) Effect upon the amplitude ratio. Putting $\alpha=\beta=0$ in Eq. (4) and squaring them, we get as the intensities of the direct and the diffracted rays before entering analyser,

$$\left.\begin{array}{l} I_G/2=1-\sin\varepsilon\sin 2\rho, \\ I_D/2=1+\sin\varepsilon\sin 2\rho, \end{array}\right\}$$

so the deviation of the intensity ratio from the values when $\varepsilon=0$, that is, from 1, is,

$$\Delta g^2=1-I_G/I_D=2\sin\varepsilon\sin 2\rho/(1+\sin\varepsilon\sin 2\rho).$$

We calculated Δg^2 for the cases of following ε values, the results of which are shown in Fig. 4.

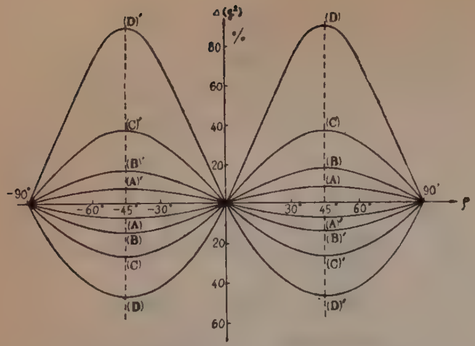

Fig. 4. Effect of ε upon g².
(A) ε=0.0125
(A′) ε=−0.0125 etc.

	(A)	(B)	(C)	(D)
ε radian	0.0125	0.025	0.05	0.10
ε mμ*	3.125	6.25	12.5	25.0

* (λ=500 mμ)

As is clear from this figure, Δg^2 becomes maximum when $\rho=\pm\pi/4$ and it becomes zero when $\rho=0$ and $\pm\pi/2$. This is, contrary to the former case, very unfavorable fact for the practical purpose. If we assume $\varepsilon=0.0125\pi$ as before, Δg^2 becomes about 10%.

§4. When $\varepsilon=0$, $\alpha, \beta \neq 0$ (When angles between X-axis and the planes of polarization are not correct.).

(a) Effect upon the phase difference.

If we put $\varepsilon=0$ in Eq. (4), then,

$$\delta=\tan^{-1}\frac{\sin 2\rho\cdot\cos 2\alpha}{\cos 2\rho\cos 2\beta-\sin 2\alpha}\ .$$

In this case, difference between δ and 2ρ is minimum when $\rho=\pm\pi/4$. This is also a favorable fact for practice. For the cases of $2|\alpha|=|\beta|=30'$, 2.5° and 5°, we calculated the values of $\Delta\delta=\dfrac{\delta}{2\rho}-1$ and plotted them in fig. 5, taking ρ as abscissa. As is clear from this figure, $\Delta\delta$ is smaller than 5% when $2|\alpha|(=|\beta|)<2.5°$.

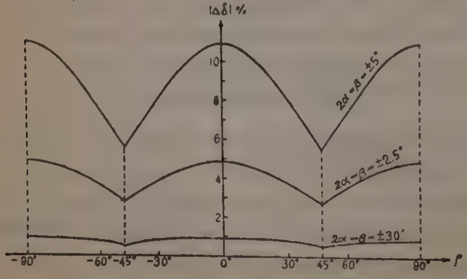

Fig. 5. Effect of α, β upon δ.

(b) Effect upon the amplitude ratio.

The intensities of the direct and the diffracted rays before entering analyser is, putting $\varepsilon=0$ in Eq. (4) and squaring them,

$$\left.\begin{array}{l} I_G/2=1-\cos 2\rho\sin 2(\alpha+\beta)\,, \\ I_D/2=1-\cos 2\rho\sin 2(\alpha-\beta)\,. \end{array}\right\}$$

So, deviation of the intensity ratio from 1 is,

$$\Delta g^2=1-\frac{1-\cos 2\rho\sin 2(\alpha+\beta)}{1-\cos 2\rho\sin 2(\alpha-\beta)}\ .$$

As is clear from this equation, $\Delta g^2=0$ when $\rho=\pm\pi/4$. This is also a favorable fact for practice as before.

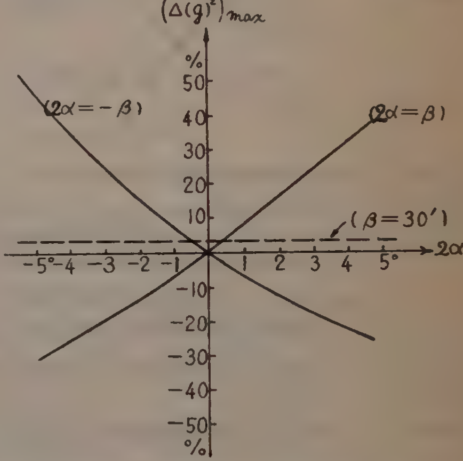

Fig. 6. Effect of α, β upon g².

As it is too complicated to discuss the general case thoroughly, we assumed $2|\alpha|=|\beta|$ and calculated Δg^2 from the above equation and plotted it in Fig. 6 with full lines taking 2α as abscissa. As shown in this figure, Δg^2 increases as $2\alpha(=\beta)$ increases. But if we assume $2\beta<30'$, then as shown dotted line in the figure, Δg^2 does not exceeds 4% until 2α becomes 5°. Especially, when $\beta=0$, as is clear from the above equtations, $\Delta g^2\equiv 0$ regardless the value of α. So, to reduce the effects of errors as much as possible, it is necessary to make the bisector of $\angle GOD$ as near to X-axis as possible. But, if $\alpha\neq 0$, it is impossible to make the intensity of light from the conjugate area zero, that is, no perfect dark field illumination ($g^2=0$) is obtainable, though the intensity of the residual light is very small so long as α is not very large.

§5. Summary.

In this paper, we have studied the effects of errors of manufacture introduced in micoid disc upon the function of polanret microscope. Conclusions are as follows.

(1) Although it is shown in the theory of polanret microscope,(1) that the amplitude ratio or the phase difference of the diffracted and the direct rays can be changed independently by the rotation of the analyser or polarizer respectively, this is true only when there is no errors in micoid disc. When the errors of manufacture exist, then, change of phase difference by the rotation of polarizer is followed by the change of amplitude ratio. But the change of amplitude ratio by the rotation of analyser does not affects the phase difference even when micoid disc is not manufactured correctly.

(2) If the angle between the planes of polarization of conjugate and complementary areas of zonal polarizer is not exactly $\pi/2$, we can not make the amplitude ratio zero by any way, that is, no perfect dark field illumination is obtainable. But, as the intensity of residual light is very small, we can assume the field to be sufficiently dark in practice.

(3) Among the effects of errors of micoid disc, the one which is maximum when $\delta=\pm\pi/2$, accordingly the worst one for practice, is the effects of deviation of retardation of $\lambda/4$-plate upon the intensity ratio g^2. All other effects of the errors become zero or minimum when $\delta=\pm\pi/2$.

(4) To make the effects of errors upon δ and g^2 not exceed 5%, it is necessary to keep the angle between planes of polarization of two areas of the zonal polarizer within $90°\pm 2.5°$, and its bisector must lay within $30'$ to X-axis.

(5) For the purpose of using a polanret microscope merely as a variable phase microscope (not for the purpose of knowing δ or g^2 from the values of ρ or θ), it is not necessary to take these errors into account, except α. If $\alpha\neq 0$, we can not make the field perfectly dark.

(6) In this paper, restriction as being done in the theory of usual phase microscope is made neither on the form nor the dimensions of the object to be observed, that is, the object is not necessary a sort of phase grating etc. This is a great merit of this treatment.

---

(1) H. Osterberg. Jour. Opt. Soc. Am., **37** (1947) 726.

JOURNAL OF THE PHYSICAL SOCIETY OF JAPAN Vol. 7, No. 1, JAN.—FEB., 1952

A Light Effect of a Diamond Alpha Ray Counter

By Shoji KOJIMA and Soji KONO

Tokyo University of Education

(Received June 23, 1951)

A diamond, cut in the form of plate, was coated in the parallel faces with evapolated aliminium. When the crystal was bombarded by alpha rays *on the side*, the counting rate was decreased by light. The wave length responsible for the effect was about 5000 Å. This light, applied more than one hour, did not increase the rate. In this point the effect differed from that of Willardson and Danielson. In the case of the bombardment *through an electrode serface* an opposite effect appeared. The rate was increased by the irradiation of the visible light to an equilibrium value, which depended on the wave length. But the light including ultraviolet, which makes a remarkable photoionization, decreased the rate after the maximum point.

The increasing effect is understood by the release of the space charge as the experiment of Chynoweth. The decreasing effect seems to be attributed to the recombination of the carrier with the trapped one by the aide of the light, for the effect is observed only when the charge carrier drift in the plasma layer where both electrons and holes are trapped.

§ 1. Introduction.

When certain insulating crystals are bomberded with an ionized particle, some of the electrons in filled bands of the crystal may be raised to the conduction band and produce a pulse under an applied electric field. Such crystals are used as a counter of ionized particles. Wooldrige, Ahearn and Burton[1] reported diamond crystals to be applicable for a counter in 1947. At the study on counting properties they found that the counting efficiency decreased after several thousands counts. This phenomenon was interpreted by the space charge effect resulting from the captured electrons in the traps of the crystal. The reason was that the space charge acts to cancel the applied field. Hofstadter[2] suggested a method to release the trapped electron and Chynoweth[3] experimentaly showed to eliminate the space charge through the irradiation of light from a Nernst lamp. Recently Willardson ard Danielson[4] found a new effect that a good counting diamond showed a decrease of counting efficiency by the irradiation of violet light and a little increase after ther emoval of the light. A bad diamond, however, showed an increase by the light.

We have studied the counting properties of a diamond for alpha rays in the arrangement shown in Figs. 1 (a) and 1 (b). The diamond used was cut in the form of plate about 1 mm in thickness and 4×3 mm^2 in area. The two major faces was coated with an evaporated aluminium. One of the electrode was connected directly to the grid of the first valve of the amplifier. In the case of Fig. 1 (a) alpha-rays incident upon the crystal through the electrode, which we shall call the surface incidence, whereas in the case of Fig. 1 (b) the rays incident upon the side of the crystal, which we

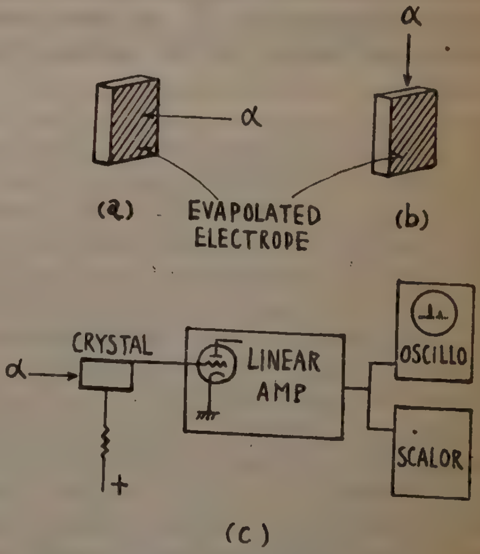

Fig. 1. Crystal arrangement and block diagram of the apparatus.

shall call the side incidence. We have found that the space change effect is different in the two cases. In this paper these effects are described and some interpretations are given.

§ 2. Counting properties of diamond.

The block diagram of the counting device is shown in Fig. 1 (c). The amplifier was resistance-capacitance-coupled three stage linear amplifier having a flat charactor for the frequency between 100 and 10,000 c/s with a voltage gain of about 100 db. The output pulses were counted by a discriminator scaler and simultaneously observed by an oscilloscope. When the diamond was connected, the input capacity of the amplifier was about 12 pf. As an alpha-ray source, about 1 e.s.u. of polonium deposited electrochemically upon a nickel disc of about 3 mm diameter, was used.

At first, experiments were performed with the side incidence. The measured result on the variation of pulse height with the strength of the applied electric field is reproduced in Fig. 2. It shows that the pulse height reaches to a saturation at the field of about 2500 V/cm.

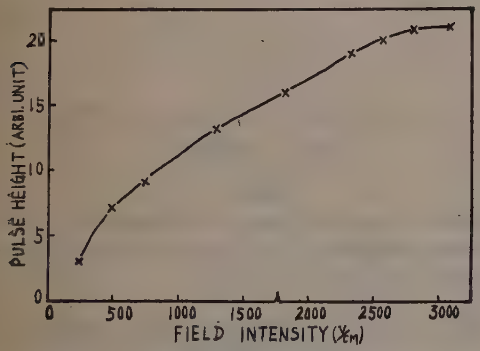

Fig. 2. Change of pulse height with the field intensity of the diamond counter.

In the following experiments we have counted always at this field, where the counting rate was nearly constant and the decrease by the space charge effect was negligible. The size of the pulses obtained was the same order of magnitude as that of air ionization chamber. From the maximum pulse height the charge of the pulse was deduced to about 9.7×10^{-14} coulomb, which corresponds to about 7×10^{5} electron pairs per alpha particle. Assuming the energy of polonium alpha rays to be 5.4 Mev, the meani onization energy is obtained as about 8 ev. The distribution of pulse heights was measured varying the discriminator bias of the scaler with a constant gain of the amplifier. The result is shown in Fig. 3, where (a) is the curve measured under daylight and (b) is that in night. In our case the phenomenon of the decrease of counting rate by the light had been found from these experiment.

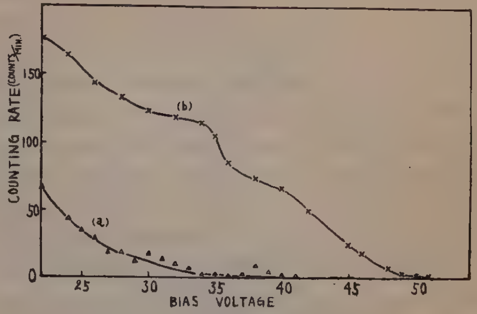

Fig. 3.
Curve of counting rate *vs* pulse height.
(a): Counting rate under a daylight.
(b): Counting rate in night.

§ 3. The light effect to decrease the counting efficiency.

On the diamond kept in the dark the change of counting rate was studied illuminating with a 500 watt electric lamp. The rate changed with the time from the beginning of illumination as shown by the curve (a) in Fig. 4. It shows a remarkable decrease by the light. What light was responsible for the effect was studied using monochromatic lights which were separated with a prism. As a measure of the effect the decrease of counting rate after 15 min. illumination was measured. The obtained re-

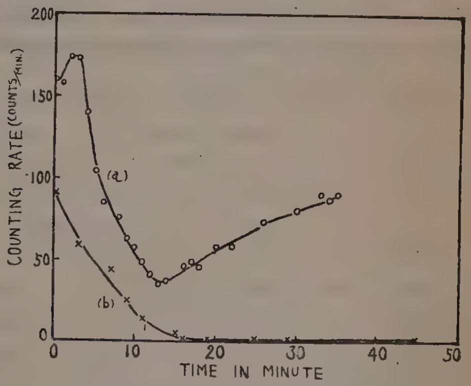

Fig. 4. Effect of light on counting rate.
(a): white light.
(b): green light.

sults is reproduced in Fig. 5. It shows that the wave length of the most effective light is about 5000 Å. When the counter was illuminated by this monochromatic light, the change of the counting rate showed a monotonous decrease with time as indicated by the curve (b) in Fig 4. Contrary to the effect mentioned by Willardson and Danielson we could not observe increasing counting rate by the illumination more than 1 hour. After the removal of the light the counting rate in any cases increases veyr slowly and approaches to an equilibulium value.

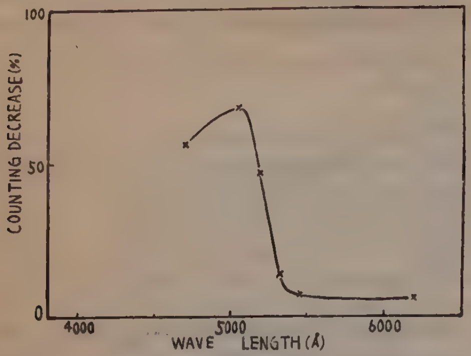

Fig. 5. Spectral analysis of the light effect to decrease the counting rate.

§ 4. The light effect to increase the counting rate.

In the case of above mentioned experiment, alpha-rays were irradiated whole the side of the diamond. When alpha-rays were limited to strike a portion of the side by the aide of a slit, the decrease of counting rate by the space charge effect became pronounced. In this case counting rate increased by light on the contrary. An example of the results is shown in Fig. 6. More pronouncing effect of this type was expected in the arrangement in Fig. 1 (a). The result is seen by the solid curve in Fig. 7.

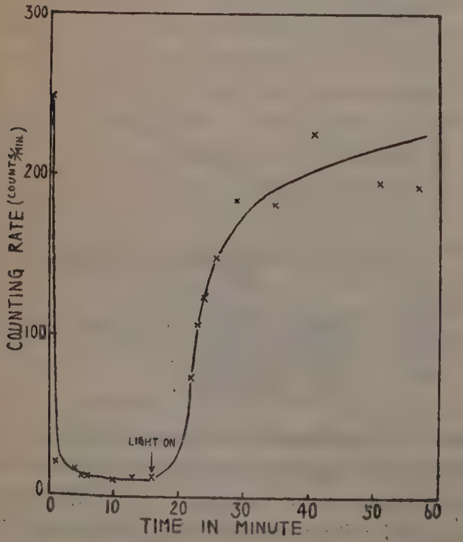

Fig. 6. Effect of light to increase the counting rate (the side incidence).

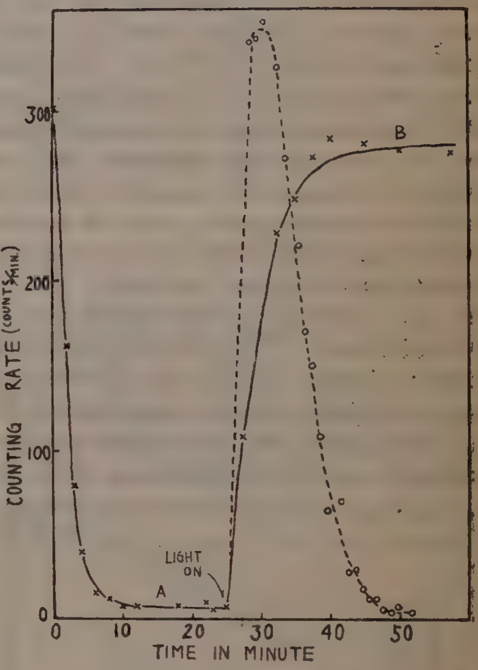

Fig. 7.
Effect of light to increase the counting rate (the surface incidence) Full curve by green light; dotted curve by white light.

This is a simillar effect found by Cynoweth.

Further study about this light effect was carried out by monochromatic lights. Taking the wave length of lights as parameter the observed counting rate *vs* time are plotted in Fig. 8. The counting rate was increased by the light to an equilibrium value, which depended on wave length of light but not on its intensity. The equilibrium value is the larger for the shorter wave length, until saturation takes place at the wave length of about 4700 Å.

The effect to increase counting rate is probably due to the release of trapped electrons by light quanta. In fact, at the point A on the curve shown in Fig. 7 the space charge field of the order of 1850 V/cm was observed by the method mentioned by Ahearn[5], while at B there was no such field. The equilibrium

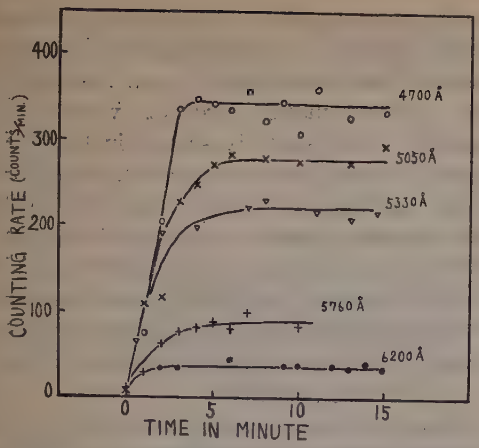

Fig. 8. Energy dependence of the increasing light effect.

values in Fig. 8 relate to the number of traps released by the corresponding monochromatic light. Hence, if we assume the light quantum of energy $h\nu$ can release the trap within the depth of the energy, we get the density distribution of traps for the depth. This is shown in Fig. 9.

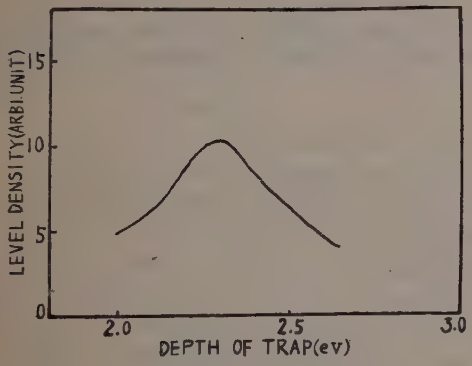

Fig. 9. Level density of electron traps

In some cases, however, as shown by the dotted curve of Fig. 7, the countingr ate decreases again through the maximum point. Cynoweth's result also shows a small maximum of counting rate if examined carefully. Any explanation about this phenomenon has not yet given.

To determine whether this decrease was due to the space charge effect or not, a measurement was performed by the Ahearn's method and it was found that there was no appreciable space charge. As mentioned above the light in visible region makes only to increase the counting rate, the light to decrease the rate must be ultraviolet.

§ 5. Discussion about the light effect.

It is important to interprete the phenomena that the effect of light is different in two arrangement, i.e. the surface incidence and the side incidence. The incident alpha-rays penetrate in the diamond about 10^{-3} cm and produce ionization. Within the layer, extending to this depth from the front face, both electrons and positive holes are to be found, which is so called plasma layer5). In the case of the surface incidence the electrons freed by ionization leave the plasma layer and drift in the non-ionized region of the crystal. Some of these electrons are trapped in the crystal and set up space charge. In the case of side insidence both the electrons and the positive holes produced by the ionization drift always in the plasma layer. Though some of them may be trapped in the crystal, the positive charge of the holes and the negative charge of the electrons cancel out each other. This is the reason why the space charge effect is not pronouncing in this case. Since the decreasing light effect appears in the side incidence only, this effect relates to that the path of the charge carriers is limitted in the plasma layer. The decreasing light effect shown by the dotted line in Fig. 7 must be considered on this standpoint. In this case the plasma layer would be produced by photoioni-zation. The experiments on photo-conductivity, which will be described in § 6, verify it. For the light of short wave length produce a rather large conduction current. Then the plasma layer seems to extend whole the crystal. There for the decreasing light effect appears only in the case where the path of carrier remains in the plasma layer.

In general the counting rate depend on the electric field in the crystal and on the mean free path of the carriers. In the case where the space charge is negligible the electric field does not change. Hence the decrease of the counting rate comes from the decrease of the mean free path. This occurs when the probability of recombinations increases. Since the light effect mentioned above is observed when the carriers drift only in the plasma layer, the carriers may easily recombine with the trapped carrier of opposite sign by the light. The process of the recombination perhaps may be as follows: the carriers at first are raised in the excited state by the light and then recombine with traps. Althouph this consideration is only a trial, it is certain that the above mentioned light effect occurs when charge carrier drift through the plasma layer where a number of electrons and holes are trapped.

§ 6. Photoconduction of diamond.

Since the photo-current of the diamond is very small, we adopted a method of a.c. amplification⁽⁶⁾. The light was modulated about 200 cycles per sec.. The alternating photo currtent was amplified with the same amplifi as the counting, and detected by a valve voltmeter. The photo-current was measured for the monochromatic light of various wavelengths. The result is shown in Fig. 10. It shows that the photo-current increases abruptly by the light of shorter than about 4500 Å. The absolute value of the photo-current at 4000 Å was the order of 8.5×10^{-12} A in the counter diamond. Some other diamonds showered the photo-current of the order of 10^{-10} A. These large photo-conducting diamond did not show counting properties.

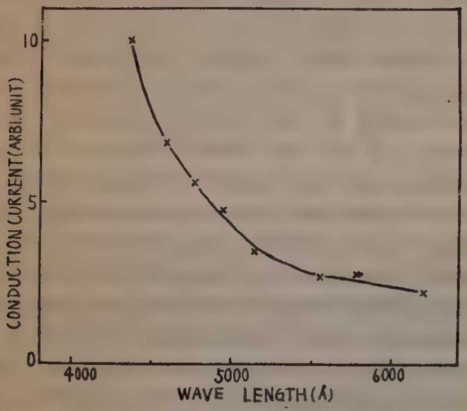

Fig. 10. Spectral photoconductivity curve of the diamond.

This study was partly supported by the Scientific Reserch Expenditure of the Ministry of Education.

References

1) D. E. Wooldridge, A. J. Ahearn and J. A. Burton, Phys. Rev. **71** (1947) 913.
2) R. Hofstadter, Nucleonics **4** (1949) 14.
3) A. G. Chynoweth, Phys. Rev. **76** (1949) 310.
4) R. K. Willardson and G. C. Danielson, Phys. Rev. **77** (1950) 300.
5) R. R. Newton, Phys. Rev. **75** (1949) 234.
6) S. Kono, *Hikari no Kagaku*(Rep. Opt. Res. Inst. Tokyo University of Education) (1951) 98.

JOURNAL OF THE PHYSICAL SOCIETY OF JAPAN Vol. 7, No. 1 JAN.—FEB., 1952

Counting Losses of Long Beaded Counters for X-Ray Measurements

By Itaru NONAKA

Department of Physics, Faculty of Science,
Kyusyu University, Fukuoka

(Read November 4. 1950, Received July 11, 1951)

It has been verified experimentally that a Geiger-Müller counter having several glass beads on its central wire is very useful in X-ray measurement because of its law counting losses (Reference (1)).

The counting losses of such beaded counters were calculated theoretically in several cases. The losses are reduced to about $1/n$ of non-beaded counters in the cases of short wave lengths, n being the number of sections, and this factor increases with the wave length of X-rays. The effects of the finite ranges of secondary electrons in the counter gas is negligibly small, and the effect of the finite spreading probability of counter discharges beyond the beads is to increase slightly the reducing factor.

§1. Introduction.

Recently Geiger-Müller couters are frequently used in X-ray studies of crystal structures. The most efficient method is to use a long counter letting the X-rays to pass through in the axial direction. In such a counter, however, the counting losses due to the dead time of the counter become consiberable when slightly intense X-rays are measured.

To reduce the above counting losses to a considerable extent, we tried previously⁽¹⁾ to use a long beaded counter having several glass beads on its entral wire. In such a beaded counter the discharge along the central wire can not spread beyond the beads⁽²⁾ and is constricted within the section between two adjacent beads. Therefore, a secondarye lectron ejected even within the dead time after the preceding one has produced a discharge can be counted so long as it is ejected in any section other than that of the proceding electron.

The results of the experiment show that the counting losses of a beaded counter are really far smaller than that of a non-beaded one.

Now, we intend to calculate the couting losses of beaded counter to know to what extent the losses are reduced compared with non-beaded ones.* If we denote by N_0 the average number of secondary electrons ejected per sec. in the counter, then the number of electrons N_1 counted per sec. by a non-beaded counter will be⁽³⁾.

$$N_1=\frac{N_0}{1+N_0\tau} \qquad (1)$$

Or, the counting losses ΔN_1 is given as follows,

$$\Delta N_1=N_0-N_1=N_0\left(1-\frac{1}{1+N_0\tau}\right)\sim N_0{}^2\tau \quad (2)$$

We obtain $N_0{}^2\tau$ as an approximate value of ΔN_1 neglecting the terms higher than $(N_0\tau)^2$ in the expansion of $1/(1+N_0\tau)$.

§2. The Case Where the Ranges of Secondary Electrons Can be Neglected.

At first we make two assumptions; (i) the discharge of the counter never spread beyond the beads, (ii) the ranges of secondary electrons in the counter gas are sufficiently short compared with the length l of one section of the beaded counter.

In such a simple case, each sections may be considered as independent counters and a rigorous treatment can be made⁽⁴⁾. But we treat the problem in a slightly different way which make possible to calculate the more complicated cases described in the following sections.

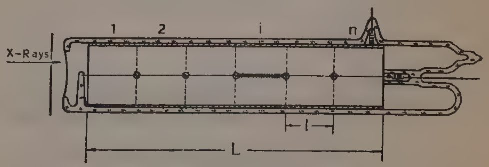

Fig. 1. Beaded counter

---

[*] We consider the counting losses of the counter itself not including the amplifier circuit and the recording system. Our intention lies in the discussion of the effect of beads on the counting losses.

Now, we put the probability of an ejected secondary electron lies in the i-th sections to be $p(i)$, then

$$p(i)=\frac{e^{-\mu l(i-1)}(1-e^{-\mu l})}{1-e^{-\mu L}} \qquad (3)$$

where μ is the absorption coefficient of the X-rays in the counter gas.

The electrons which may be missed in the beaded counter are those which have the immediately preceding electrons within τ sec. before. The number of these electrons is $N_0\{1-\exp(-N_0\tau)\}\approx N_0^2\tau$. Among these $N_0^2\tau$ electrons, those which are ejected in the i-th section are $N_0^2\tau p(i)$, and those which are missed in that section are the electrons of which preceding ones are also ejected in the same i-th section,* namely $N_0^2\tau p(i)^2$. Then the total number of missed electrons will be

$$\varDelta N_n=\sum_{i=1}^{n} N_0^2\tau p(i)^2. \qquad (4)$$

As the counting losses of a non-beaded counter are $N_0^2\tau$ in an approximation of Eq.(1), we obtain as the ratio of counting losses of a beaded counter to a non-beaded one,

$$\frac{\varDelta N_n}{\varDelta N_1}=\sum_{i=1}^{n} p(i)^2=\left(\frac{1-e^{-\mu l}}{1-e^{-\mu L}}\right)^2\left(\frac{1-e^{-2\mu L}}{1-e^{-2\mu l}}\right). \qquad (5)$$

Some examples of the values of $\varDelta N_n/\varDelta N_1$ are shown in Table I and Fig. 2 for a counter which is 20 cm in total length L and filled with 150 mm Hg of argon and 15 mm Hg of C_2H_5OH. In a limiting case when the absorption coefficient is very small and $\exp(-\mu L)$ can be expanded as-$(-\mu L)$, the values of $\varDelta N_1/\varDelta N_n$ become independent of the wave length of X-rays and

$$\frac{\varDelta N_n}{\varDelta N^1}=\frac{1}{n} \qquad (6)$$

Table I.

$\varDelta N_n/\varDelta N_1$ for a counter; $L=20$ cm, 150 mm Hg argon +15 mm Hg C_2H_5OH.

λ	n	2	3	4	5	7
0.71 Å	$\varepsilon=0$	0.50	0.33	0.25	0.20	0.14
	$\varepsilon=0.1$	0.55	0.38	0.29	0.23	0.17
1.54 Å	$\varepsilon=0$	0.53	0.36	0.26	0.21	0.15
	$\varepsilon=0.1$	0.52	0.40	0.30	0.24	0.18
2.50 Å	$\varepsilon=0$	0.74	0.55	0.44	0.35	0.26
	$\varepsilon=0.1$	0.77	0.59	0.47	0.39	0.29
3.57 Å	$\varepsilon=0$	1.00	1.00	0.80	0.71	0.56
	$\varepsilon=0.1$	1.00	1.00	0.83	0.74	0.60

For and counter above mentioned this condition realises when the wave length is shoter than 0.71 Å.

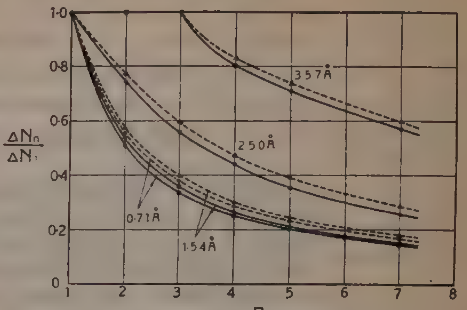

Fig. 2. Counting losses of beaded counters; $L=20$ cm, 150 mm Hg of argon and 15 mm Hg of C_2H_5OH. Solid curves; Spreading over probability $\varepsilon=0$ (Eq. (5)) Broken curves; $\varepsilon=0.1$ (Eq. (17)).

§ 3. The Casd Where the Ranges of Secondary Electrons are Taken into Account.

We consider the case where the assumption (ii) in the preceding section does not hold. In this case some of the secondary electrons ejected in the i-th section will excite descharges not only in the i-th section but also in the $(i-1)$- or $(i+1)$-th section, because the electrons ejected in the boundary part of the section can penetrate in to the neighbouring section.

Now, we consider a effective lengh δ of the ranges of secondary electrons in the counter, which means the average of the compnents of the ranges in the direction of the incident X-ray beam.

$$\delta=\langle R\cos\theta\rangle_{Av}=\frac{\int_0^{\frac{\pi}{2}} R\cos(\theta)n(\theta)d\Omega}{\int_0^{\frac{\pi}{2}} n(\theta)d\Omega} \qquad (7)$$

where R is the effective range of the photoelectron in the counter gas, $n(\theta)$ is the angular distribution function of the photo-electrons, and θ is the angle of ejection.

---

* This consideration is approximate, because the electrons which are really missed are those which have the preceding discharges (not electrons) in the same i-th section, and some of the preceding electrons do not excite any discharge within τ sec. before. The rigorous treatment will give a following result instead of Eq. (5),

$$\frac{\varDelta N_n}{\varDelta N_1}=\sum_{i=1}^{n} p(i)^2\frac{1+N_0\tau}{1+N_0\tau\, p(i)}.$$

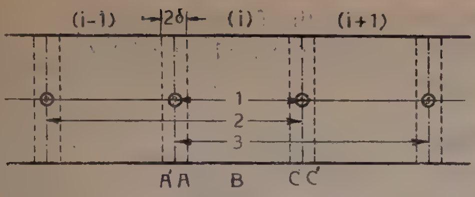

Fig. 3. Three types of counter discharge when finite ranges of secondary electrons are considered.

When the incident X-rays are not polarized,

$$n(\theta)d\Omega \sim \sin^2\theta d\Omega$$

and we obtain for δ as follows,

$$\delta = \frac{3}{8}R \qquad (8)$$

Examples of the values of δ for the counter mentiond in the preceding section are listed in Table II, where the ratio of the true range R_0 to the effective range R was taked to be 2.

In considering the behaviour of electrons in the boundary parts of each sections we assume all the electrons are ejected with a fixed range δ parallel or antiparallel to the incident beam. There will be three types of discharge by the electrons ejected in the i-th section as shown in Fig. 3 by (1), (2) and (3). What type of discharge will be excited is determined by the position and direction of that electron.

Table II

Values of δ for acounter filled with 150 mm Hg of argon and 15 mm Hg of C_2H_5OH.

	Wave length of X-rays			
	3.57Å	2.50Å	1.54Å	0.71Å
δ (cm)	0.018	0.037	0.099	0.46
μ (cm^{-1})	0.431	0.169	0.0416	0.46×10^{-2}
$\mu\delta\times10^2$	0.793	0.625	0.412	0.213

The probabilities $p_1(i)$, $p_2(i)$ and $p_3(i)$ that the ejected electron has the position and direction to excite one of these three types of discharge (1), (2) and (3) respectively are as follows,

$$\left.\begin{aligned} p_1(i) &= \frac{1}{2}\{A\}+\{B\}+\frac{1}{2}\{C\} \\ &= \frac{e^{-\mu l(i-1)}}{1-e^{-\mu L'}}\left\{\frac{1}{2}(1-e^{-\mu\delta}) + e^{-\mu\delta}(1-e^{-\mu(l-2\delta)}) + \frac{1}{2}e^{-\mu(l-\delta)}(1-e^{-\mu\delta})\right\} \\ p_2(i) &= \frac{1}{2}\{A\} = \frac{e^{-\mu l(i-1)}}{1-e^{-\mu L'}}\left\{\frac{1}{2}(1-e^{-\mu\delta})\right\} \\ p_3(i) &= \frac{1}{2}\{C\} = \frac{e^{-\mu l(i-1)}}{1-e^{-\mu L'}}\left\{\frac{1}{2}e^{-\mu(l-\delta)}(1-e^{-\mu\delta})\right\} \end{aligned}\right\}, \qquad (9)$$

where L' means the effective total length of the counter including the both end regions of δ, and there exists the following relation,

$$1-e^{-\mu L'} = \frac{1}{2}e^{\mu\delta}(1-e^{-\mu\delta}) + (1-e^{-\mu L}) + \frac{1}{2}e^{-\mu L}(1-e^{-\mu\delta}) \qquad (10)$$

An electron ejected in the i-th section can really excite a discharge or not is determined by the direction and position of the immediately preceding electron within τ sec. before. The probabilities $q_1(i)$, $q_2(i)$ and $q_3(i)$ that an ejected electron has such direction and position for the three types of discharge (1), (2) and (3) respectively are given as follows,

$$\left.\begin{aligned} q_1(i) &= \frac{1}{2}\{A'\}+\{A+B+C\}+\frac{1}{2}\{C'\} \\ &= \frac{e^{-\mu l(i-1)}}{1-e^{-\mu L'}}\left\{e^{\mu\delta}\frac{1}{2}(1-e^{-\mu\delta}) + (1-e^{-\mu l}) + e^{-\mu l}\frac{1}{2}(1-e^{-\mu\delta})\right\} \\ q_2(i) &= \frac{1}{2}\{A'\}+\frac{1}{2}\{A\} = \frac{e^{-\mu l(i-1)}}{1-e^{-\mu L'}} \left\{e^{\mu\delta}\frac{1}{2}(1-e^{-\mu\delta}) + \frac{1}{2}(1-e^{-\mu\delta})\right\} \\ q_3(i) &= \frac{1}{2}\{C\}+\frac{1}{2}\{C'\} = \frac{e^{-\mu l(i-1)}}{1-e^{-\mu L'}} \left\{e^{-\mu(l-\delta)}\frac{1}{2}(1-e^{-\mu\delta}) + e^{-\mu l}\frac{1}{2}(1-e^{-\mu\delta})\right\} \end{aligned}\right\}. \qquad (11)$$

Among the $N_0{}^2\tau$ electrons which have possibilities of being missed, those which are really missed in the beaded counter are

$$\Delta N_n = \sum_{i=1}^{n}\Delta N_n{}^{(i)} = \sum_{i=1}^{n} N_0{}^2\tau\left\{p_1(i)q_1(i)+p_2(i)q_2(i) + p_3(i)q_3(i)\right\}. \qquad (12)$$

In the above summation, however, we must take into account the fact that when $i=1$ or n p's and q's can not be given by the general froms of (9) and (11) respectively, because the first and the last section have their neighbours only in one side, and also the fact that the δ regions before the first section and after the last section have some contributions and must be added in the summation.

Putting (9), (10) and (11) into (12) and neglecting the terms higher than $\mu^2\delta^2$ in the expansion of $\exp(-\mu\delta)$, we obtain the following result for the counting losses,

$$\frac{\Delta N_n}{\Delta N_1}=\left(\frac{1-e^{-\mu l}}{1-e^{-\mu L}}\right)^2\left(\frac{1-e^{-2\mu L}}{1-e^{-2\mu l}}\right)\left\{1+A(\delta)\right\}, \tag{13}$$

where

$$A(\delta)=\mu\delta\left\{\frac{1+e^{-2\mu L}e^{\mu l}}{1-e^{-\mu l}}\left(\frac{1-e^{-2\mu l}}{1-e^{-2\mu L}}\right)-\frac{1+e^{-\mu L}}{1-e^{-\mu L}}\right\}$$
$$+\frac{1}{4}\mu^2\delta^2\frac{1+e^{-\mu l}}{(1-e^{-\mu l})^2}\left(1+\mu\delta+e^{-2\mu L}e^{\mu l}\right)$$
$$\left(\frac{1-e^{-2\mu l}}{1-e^{-2\mu L}}\right). \tag{14}$$

The values of $A(\delta)$ for the counter previously mentioned have been calculated for $\lambda=0.71\sim3.57$ Å and $n\leqq7$, but they are all smaller than 0.4×10^{-2} and can be neglected in the accuracy of our approximation. Thus we may conclude the effect of the finite ranges of secondary electrons upon the counting losses is not serious in general and Eq.(5) holds whenever the discharges donot spread beyond the beads.

§ 4. The Case Where the Discharges Can Spread Beyond the Beads.

In general, counter discharges have some probability of spreading beyond the beads. We describe this probability by ε and assume ε^2 can be neglected relative to one. This means that there is no discharge longer than $2l$.

According to the result in the preceding section we can neglect the ranges of electrons without losing sufficient accuracy. In this case the probability $p(i)$ of an electron lies in the i-th section is also given by (3). Among the $N_0{}^2\tau p(i)$ electrons which are ejected in the i-th section and have their immediately preceding electrons whithin τ sec. before, those which are missed are the electrons whose preceding ones have induced discharges in the i-th section. The probability $q(i)$ that an electron has the direction and position to excite a discharge in the i-th section according to Fig. 4 is given by

$$q(i)=\{B\}\varepsilon+\{A\}+\{C\}\varepsilon$$
$$=\frac{e^{-\mu l(i-1)}}{1-e^{-\mu L}}\Big\{e^{\mu l}(1-e^{-\mu l})\varepsilon+(1-e^{-\mu l})$$
$$+e^{-\mu l}(1-e^{-\mu l})\varepsilon\Big\}. \tag{15}$$

Then the total counting losses are given by

$$\Delta N_n=\sum_{i=1}^{n}\Delta N_n^{(i)}=\sum_{i=1}^{n}N_0{}^2\tau p(i)q(i). \tag{16}$$

Considering the fact that the first and the last section have their neighbours only in one side, we botain the following result,

$$\frac{\Delta N_n}{\Delta N_1}=\left(\frac{1-e^{-\mu l}}{1-e^{-\mu L}}\right)^2\left(\frac{1-e^{-2\mu L}}{1-e^{-2\mu l}}\right)\left(1+\varepsilon B\right), \tag{17}$$

whene

$$B=\frac{2e^{\mu l}(^{-2\mu l}-e^{-2\mu L})}{1-e^{-2\mu L}} \tag{18}$$

Examples of the values of $\Delta N_n/\Delta N_1$ for the counter described previously are shown in Table I and Fig. 2, taking the spreading over probability ε is equal to 10 per cent. The effect of ε is not so serious but it increases with the number of section n.

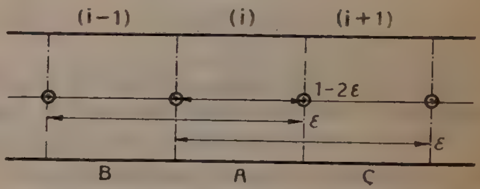

Fig. 4. The case where the discharge has a probability ε of spreading beyond the bead. (ε^2 is neglected)

§ 5. Discussion.

In our previous experiment⁽¹⁾ the counting losses of a non-beaded counter of the same dimmension and gases as in Table I amounted to 14 per cent at $N_1=60{,}000$/min. ($N_0\sim70{,}000$/min.) and the losses of a beaded counter of five sections were negligibly small in the measurement of X-rays of 1.54 Å.

Form the results of the above calculations the losses of the beaded counter should be about 3 per cent, and this agree with the experimental results in the limit of the accuracy of the experiment,

To set some beads on the central wire of a counter is a very simple technique, so it is desirable to use beaded counters always in the X-ray measurement. The effect of the beads in reducing the counting losses is known to be very remarkable from the above calculations and the experiment.

This work is indebted to the Ministry of Education for the Scientific Research Expenditure.

References

1) I. Nonaka and Z. Shimazu: J. Phys. Soc. Japan 5(1950) 283.
2) H. G. Stever: Phys.Rev. **59**(1941) 765.
3) A. E. Ruark and F. E. Brammer: Phys. Rev. **52** (1937) 322.
4) G. Shinoda and T. Tomura: Lecture in the Annual Meeting of Phys. Soc. Japan at Osaka, Nov. 6, 1950.

JOURNAL OF THE PHYSICAL SOCIETY OF JAPAN Vol. 7, No. 1, JAN.—FEB., 1952

On the Intensities of γ-Rays of RaC

By Seizaburo KAGEYAMA

Physical Institute, Tokyo University of literature and Science

(Received July 12, 1951)

The intensities of γ-rays of RaC were investigated with a semi-circular focusing magnetic spectrometer and coincidence technique of G-M counters.

The efficiencies of thick radiator for γ-rays of various energies were calculated according to the experimental straggling curves obtained by White and Millington and also taking the scattering losses into concideration. And the intensities of γ-rays were determined from the maximum heights of momentum distribution curve of Compton recoil electrons projected from a thick target of aluminium. From these values and the relative intensities of conversion electrons reported in our former paper, the internal conversion coefficients were calculated and compared with the results of former authors, and with theoretical values.

Both the intensities of γ-rays of RaC and the internal conversion coefficients obtained are in accord with the results of Ellis and Aston.

§ 1. Introduction.

To determine the nuclear level scheme, the knowledges on the energies, multiple order and intensities of the γ-rays emitted are necessary as well as the energies and intensities of the components of β- and α-particles.

Serveral authors(1, 2) performed the investigation of natural β-ray spectrum of RaC and determined the energies of γ-rays and the relative intensities of the internal conversion electrons. We[3] have also examined the relative intensities of the internal conversion electrons and ascertained that the results of English authors were more reliable than those obtained by Ukrainian authors.

The multiple order of low energy γ-rays emitted by light elements is easily determined by observing the ratio α_K/α_L of internal conversion coefficients. For high energy γ-rays emitted by heavy elements, as is studied in the present paper, however, this ratio is not so sensitive to the multiple order of the rays. So the latter is usually determined by obserbing both the intensities of the conversion electrons and those of corresponding γ-rays and calculating the absolute values of conversion coefficients theirfrom.

Ellis and Aston[1] measured the intensities of the γ-rays of RaC by observing the number of K photoelectrons at the peak of the line, using a thick target of heavy element. On the other hand, Latyshev-Kompaneetz-Borisov-Gusak[4] and Itoh-Watase[5] measured these intensities by observing the secondary recoil electrons from a thin target of light element respectively. Alichanov and Latyshev[6] also estimated them from the internally converted positive electrons.

But their results on the intensities of RaC γ-rays, as well as their conclusions on the multiple order of the rays, are not in accord with each other in several points. And so we have re-examined the recoil electron spectrum of RaC γ-rays from a thick Al target and studied these points in question carefully.

§ 2. Correction Factor for observed Intensities.

Ukrainian authors[4] succeeded in separating each group of recoil electrons by using a thin target, so that they could estimate the intensities of γ-rays from the area under the distribution curves. As we aimed to determine the relative intensities of intense γ-rays only, we used a thick targed and sacrificed the resolution of each group of recoil electrons so as to obtain a reasonable counts in a moderate time. So, we were obliged to derive the intensities of γ-rays from the relative heights of corresponding electron groups.

The height of the peak of an electron group observed is a complicated function of the efficiency of radiator and the transmission factor of the slit system. The latter factor was treated by several authors[7]. Lawson and Tyler's method of the treatment has been adopted in our case. But the former factor is a complicated ascending function of γ-ray energies. If one has an appropriate artificial radioactive bodies whose energies and intensities of γ-rays are known, it is desirable to determine the relation between the heights at the peak and the true intensities for different γ-ray energies from the experimental data. The relation obtained experimentally will surely more reliable than that calculated. Unfortunately we had no such γ-emitter at hand and had to derive this relation theoretically. We have done the computation following Richardson and Kurie[8].

The distribution in energy of the Compton recoil electrons ejected from an infinitely thin radiator is given by the formula of Klein and Nishina. To extend the treatment to a radiator of finite thickness, we proceed in the following manner.

(1). Calculation of the momentum distribution curve of the homogeneous electrons projected in a certain direction from a thin layer dx at the depth x from the surface of target.

(2). Integration of the momentum distribution curves obtained in (1) throughout the thickness of target.

(3). Integration of the momentum distribution curves obtained in (2) with respect to the angle θ between the initial direction of electron and of γ-rays.

(1). To calculate the momentum distribution curve of the electrons projected to a certain direction at the depth x, we must determine the shape of the momentum distribution curve and the total probability of an electron of energy E remaining within a cone of effective solid angle after traversing a distance x.

In the rough calculation performed here, we may neglect the slight change in the effective path length due to the obliquity of the direction of γ-rays and also may assume uniform angular distribution of elertrons as they emerge from the surface. Then, the shape of the momentum distribution at the surface of target would correspond to the well-known straggling curves for homogeneous β-particles. Recently, Landau and Blunck-Leisegang[9] have re-calculated the form of the straggling curves. But their results as well as Williams[10] definitely deviate from the experimental straggling curves obtained by White and Millington and Birkhoff[11]. Therefore, we have used the experimental straggling curves on the assumption that x be small compared with the total range of electrons.

In the region of multiple scattering, the probability $Q(W_0, x)$ of an electron of total energy $W_0=E+mc^2$ remaining within a cone of angle ψ after travelling a distance x cm is obtained from the multiple scattering theory developed by Bothe and Fowler-Lauritsen-Lauritsen[12] in the form

$$Q(W_0, x)=1-\exp\left[-\psi^2 W_0(W_0-4.8x)/21.6x\right],$$

where W_0 is the initial total energy of electrons in MeV.

The above expression will hold until the most probable scattering angle becomes so large that diffusion will set in. The contribution of the electrons ejected from so deep layer, as the above expression does not hold, may be completely neglected in our case. Because they have no influence on the height at the peak of momentum distribution curve.

The experimental straggling curve multiplied by $Q(W_0, x)$ gives the relative contribution of the recoil electrons projected in a certain direction to the total curve.

(2). The momentum distribution of the recoil electrons projected in a certain direction from all parts of the radiator can be obtained by integrating the curves obtained in (1) throughout the thickness of target. This has been done by graphical means, assuming that the contributing depth is given by the fundamental straggling curve obtained by White and Millington.

(3). To obtain a resultant momentum distribution curve observed, we must not neglect the influences of those electrons whose original directions make angles greater than ψ_{max}, which are defined by the defining slit, with the forward direction of γ-rays. Some of them will be scattered into the effective angular zone without large energy loss, and so contribute to the height of the momentum distribution curve. We have calculated these contribution considering the change in the effective path length and neglecting the variation of ejection probability with angle. The resultant momentum distribution curve has been obtained by the same method described in (2) by taking the variation of contributing angular range into consideration. The electrons involved under this distribution curve obtained, unless they suffer any scattering in vacuum chamber and mica window of the counter, will be all effectively counted.

The procedure described above has been carried through for x=5, 10, 20, 40, and 60 mg/cm² and $\theta=0°$, 3°, 6°, and 9° for several γ-ray energies ranging from 606 KeV to 2,4 MeV.

The momentum distribution curve observed can be obtained by integrating the momentum distribution curve given above, taking the transmission factor into consideration. These processes have been carried out again graphically for several γ-ray energies. The momentum distribution curve thus calculated was found almost similar to each other, and is shown in Fig. 4. The correction factors to be applied to the observed intensity are plotted against the energy of γ-rays in Fig. 1.

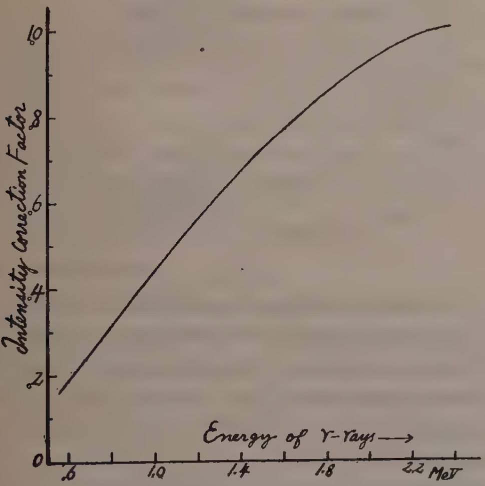

Fig. 1. The ratio of the true intensity against the peak intensity observed.

We have further considered the influences of radiation losses and large collision losses to the correction factors. We have estimated both the retardation of the peak and the reduction of the height of momentum distribution curve due to the radiation loss. They were however found to be completely negligible even for γ-rays of the heighest energy concerned. The effect of large collision losses were treated by Richardson[13] in the range 0.24 MeV. to 2.6 MeV. According to his results, this effect is almost independent of energy and may also ben eglected in our treatment.

§ 3. Experimental Arrangement and Procedures.

We have used the same magnetic spectrometer and experimental procedures as described in the previous paper[3]. Rn sealed in a small glass tube of about 10 mm long and 1–2 mm in diameter was used as a source of γ-rays of RaC. This tube was placed about 7 cm apart from the target in a rectangular canal of 3×10 mm². Al plate of 1 cm in thickness was used as the target. As we have only deal with the γ-rays whose energies are higher than 0.6 MeV, almost all of the secondary electrons observed were Compton recoil electron. The arrangement of baffles, made of Al plate 5 mm thick, was much the same as before, except that the width of the slits were chosen a little broader. The defining slit of the central baffle was 1 cm high and 1.5 cm broad.

The usual G-M counter having a slit of 1×10 mm² was used in coincidence as a detector. The thickness of the mica window of counter was about 0.6 mg/cm².

The strength of magnetic field was determined only relatively as in the previous experiment.

Observation records were usually taken at an interval of about 20 in Hρ and 5–6×10³ particles were counted at each point except in the region of the highest γ-ray energy.

§ 4. Experimental Results.

The experimental results are shown in Fig,. 2 and tabulated in Table 1. In Fig. 2 the ordinate gives the number of electrons observed per constant Hρ interval $\Delta N/\Delta(H\rho)$ and the abscissa the value of Hρ in gauss-cm. Several groups of electrons, each corresponding to a definite γ-ray line, can be clearly recognized. From the momenta of upper edges of these electron groups, which are shown with arrows in Fig. 2, we have calculated the energies of corresponding γ-rays. The energies of γ-rays thus determined were in accord, within the experimental error, with those we confirmed in the previous experiment on internal conversion lines. They are given near the arrows of the figure in KeV.

In Table 1, the energies of corresponding γ-rays in KeV are shown in the first column. The maximum height of momentum distribution curves of each electron group are given in the second. The relative intensities calculated by the maximum heights and the correction factors derived in § 2 are given in the third, by taking the intensity of 606 KeV γ-rays as 9.

For the convenience of comparison, the results obtained by English authors and Itoh-Watase have been re-calculated in the same manner, and are given in the fourth and fifth respectively. The agreement of the relative intensity of 2200 KeV γ-rays, which was adopted as the standard by Ukrainian authors' between English authors' and Itoh-Watase's results is not good. For the convenience of comparison with Ukrainian authors' results, the relative intensities of Itoh-Watase are again re-calculated by taking the intensity 2200 KeV γ-rays as unity and are given in the same column. Ukrainian authors' results deduced from the recoil electron and internally converted positive electron spectra are given in the sixth and seventh respectively.

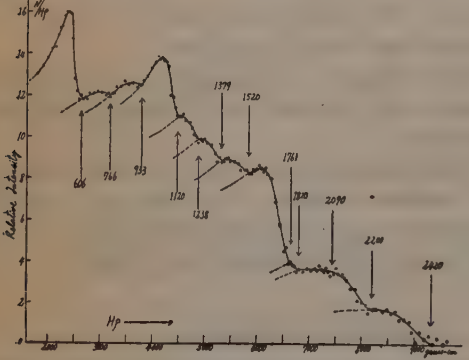

Fig. 2. Recoil electron spectrum of γ-rays.

Now, we can calculate the relative internal conversion coefficients α_K, from the relative intensities of internal conversion lines obtained in the previous experiment and the present results. We have further estimated the absolute values in the following way. The strongest 606 KeV γ-rays is surely a dipole radiation and the absolute conversion coefficient for this line has been caluculated by Hulme et al[14] half-empirically. Accepting their values, therefore, we can calculate the absolute conversion coefficients for the other lines. Conversion coefficients thus estimated are plotted in Fig. 3 together with the results obtained by English authors and Itoh-Watase. In the figure, curve

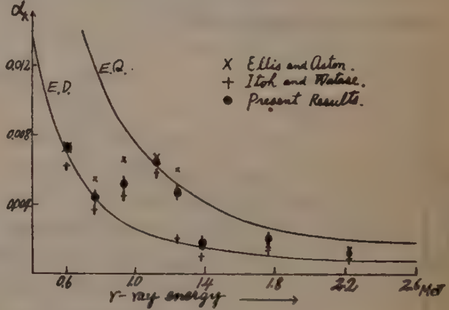

Fig. 3.

Internal conversion coefficients of RaC γ-rays for K shell. E.D. and E.Q. denote the electric dipole and electric quadrupole radiations respectively.

Table 1. The relative intensities of RaC γ-rays

Energy of γ-rays in KeV	Present Writer		Ellis and Aston	Itoh and Watase	Ukrainian authors	
Secondary electron observed	Recoil electron		Photo-electron	Recoil electron	Recoil electron	Positive electron
	Observed heights	Relative intensities				
606	52	9	9	9 (5.5)	—	—
766	11	1.3±0.2	0.9	—	—	—
933	12	1.1±0.2	0.92	1.1 (0.67)	—	—
1120	33	2.6±0.3	2.8	2.9 (1.7)	1.76	—
1238	16	1.0±0.2	0.86	2.3 (1.4)	0.41	0.2
1379	15	0.9±0.2	0.87	2.5 (1.5)	1.32	1.19
1520	13	0.7±0.2	—	0.95 (0.58)	0.56	0.52
1761	65	3.2±0.4	3.5	4.4 (2.67)	2.51	2.45
1820	4.5	0.22±0.06	—	—	0.32	0.3
2200	23.5	1.00±0.2	1.00	1.6 (1.00)	1.00	1.00
2420	14	0.5±0.1	—	—	0.32	0.36

Table 2. The multiple order of RaC γ-rays

Energy of γ-rays in Kev	Present Writer	Ellis and Aston	Itoh and Watase	Ukrainian authors
606	D.	D.	D.	—
766	D.	D.	—	—
933	D.–Q.*	Q.–D.*	D.	—
1120	Q.	Q.	Q.	Q.
1238	Q.	Q.	D.	Q.
1379	D.	D.	D.	Q.
1520	—	—	—	Q.
1761	Q.–D.*	D.–Q.*	D.	Q.
1820	—	—	—	Q.
2200	D.	Q.–C.*	D.	Q.

* shows that the observed points are nearer to the former than to the latter. D.: electric dipole radiation. Q.: electric quadrupole radiation.

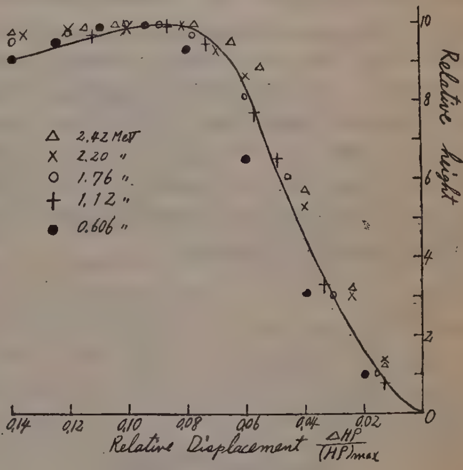

Fig. 4.

Relative form of the intensity distribution of recoil electrons. The full curve shows the calculated result.

E.D. and E.Q. show the internal conversion coefficients calculated for electric dipole and electric quadrupole radiations respectively.

The multiple order of γ-rays are easily determined from the figure, except in few cases, and tabulated in Table 2.

§ 5. Discussions.

In our arrangement, the width of the target was a little larger than the optimum value requested by the defining slit. Consequently, the spectrum obtained was not so sharp as expected. There was, however, no serious umbiguity in the estimation of the height of each component of momentum distribution curve except in few case, as will be seen in Fig. 2.

As discussed in § 3, the change of relative shape of intensity distribution curves with γ-ray energies is expected to be very little. This fact has been confirmed experimentally, as will be seen in Fig. 4, in which the relative intensity calculated is plotted against relative displacement $\Delta(H\rho)/(H\rho)_{\max}$ together with the observed points.

Let us next consider the observed results in some details. The intensities of 766 and 933 KeV γ-rays obtained are in accord with the results English authors and those of Itoh-Watase. The internal conversion coefficient of 766 KeV γ-rays just corresponds with the calculated for dipole radiation, but that of 933 KeV does not correspond with neither value of dipole nor that of quadrupole radiation.

The intensities of 1120, 1238, 1379 and 1761 KeV γ-rays obtained and their internal conversion coefficienst were in accord with the results obtained by English authors. According to Itoh-Watase, the intensity of 1238 KeV γ-rays is almost comparable with that of 1120 KeV γ-rays and its internal conversion coefficient lies on the curve of electric dipole radiation. The accurate estimation of the height is very worrisome in this region. However, there is no doubt that this line is not so intense as 1120 KeV line as is seen in Fig. 2. It may be mentioned that the results obtained by Nakagawa and his co-workers[15)] by means of absorption of Compton electrons also support our findings. On the contrary, the results obtained by Ukrainian authors' seems to be too weak.

As mentioned in the previous paper, we missed to find out the internal conversion line of 1520 KeV γ-rays. But in the present experiment we have clearly recognized the existence of the γ-rays, and the intensity observed was in accord with the results of Latyshev et al and also that of Itoh-Watase within the experimental error.

The weak 1820 and 2090 KeV γ-rays whose existence were recognized in the spectra of Ukrainian authors were hardly observed in our previous experiment on β-rays. In order to determine the intensities of 1761 and 2200 KeV γ-rays precisely, and also to ascertain the form of intensity distribution curve against $\Delta(H\rho)/(H\rho)_{\max}$, we have carefully repeated the measurement of this part. Fig. 5 shows one of the results without re-calculation for equal $H\rho$ interval. The 1820 KeV line can clearly be seen in the figure. The form of the spectrum around $H\rho=7000$–8000 seems also to implicate the existence of 2090 line, though not quite evident. The estimation of the intensity of 1820 KeV line is not easy and the intensity given in the table is somewhat doubtful.

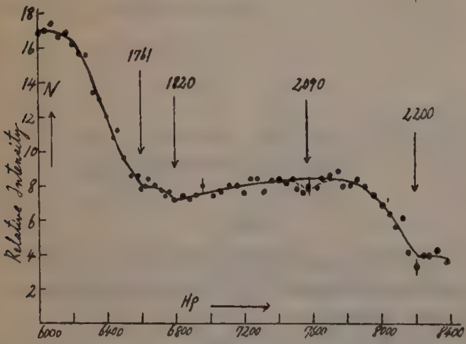

Fig. 5.

Recoil electron spectrum between 1761 and 2200 KeV lines, without re-calculation for equal interval of $H\rho$.

In higher energy region than the recoil electron of 2200 KeV line, we were unable to obtain enough counts to determine whether the spectrum was a combined one of many γ-ray lines or not. The error in the estimation of the intensity of 2420 KeV line, therefore, may again be very large.

In conclusion, the author expresses his sincere gratitudes to Prof. Y. Fujioka for his encouragement and to Prof. M. Miwa for helpful suggestions and valuable discussions. The author wishes to express his thanks to the Japanese Foundation for Cancer Research for the supply of radon through Dr. K. Tsukamoto and Mr. Y. Onai with helpful interests, and also to Ministry of Education for finantial aids.

References

1) C. D. Ellis and G. H. Aston, Proc. Roy. Soc. **A129** (1930) 180.

2) A. A. Constantinov and G. D. Latyshev, J. Phys. U.S.S.R. **5** (1941) 251.

3) M. Miwa and S. Kageyama, J. Phys. Soc. Jap. **5** (1950) 416.

4) Latyshev, Kompaneetz, Borisov and Gusak, J. Phys. U.S.S.R. **3** (1940) 251.

5) J. Itoh and Y. Watase, Prco. Phys. Math. Soc. Jap. **20** (1938) 142.

6) A. I. Alichanow and G. D. Latyshev, C. R. Acad. Sci. U.S.S.R. **20** (1938) 429.

7) B. Shull and D. M. Dennison: Phys. Rev. **71** (1947) 681, **72** (1947) 256. E. Perisico and C. Geofferion: Rev. Sci. Inst. **21** (1950) 945. G. E. Owen, ibid. **20** (1949) 916. J. L. Lawson and A. W. Tayler: Rev. Sci. Inst. **11** (1940) 6.

8) J. Richardson and F. N. D. Kurie: Phys. Rev. **50** (1936) 999.

9) L. Landau: J. Phys. U.S.S.R. **8** (1944) 201. O. Blunck and S. Leisegang: ZS. Phys. **128** (1950) 420.

10) E. J. Williams: Proc. Roy. Soc. **A125** (1929) 420.

11) P. White and G. Millington: Proc. Roy. Soc. **A120** (1928) 701. R. D. Birkhoff: Phys. Rev. **82** (1951) 448.

12) W. Bothe, *Handbuch der Physik*, XX, 11/2 (1933). W. A. Fowler, C. C. Lauritsen and T. Lauritsen: Phys. **20** (1948) 236. M. Sonoda: Rev. Mod. J. Phys. Soc. Jap. **5** (1950) 403.

13) H. O. W. Richardson: Proc. Phys. Soc. **63** (1950) 234.

14) Hulme, Mott, Oppenheimer and Tayler: Proc. Roy. Soc. **A115** (1936) 315.

15) S. Nakagawa, I. Sumoto and M. Arai: Proc. Imp. Acad. Tokyo XIX (1944) 373.

JOURNAL OF THE PHYSICAL SOCIETY OF JAPAN, Vol. 7, No. 1, JAN.—FEB., 1952.

On the Binding Energies of Light Nuclei

By Jyumpei SANADA and Yasukazu YOSHIZAWA
Department of Physics, Faculty of Science,
Osaka University

(Received July 26, 1951)

The binding energies of the last neutron and proton, and of the last neutron-proton pair in nuclei, whose mass number $A \leqq 36$, are investigated by utilizing mass values. Those of the last neutron-proton pair in nuclei having $A \sim 61$ are also investigated. The curves of the binding energy *vs.* nucleon number show the large binding energies and the breaks at 6 and 14 neutrons or protons and 28 protons like those occuring at the positions of shell closing in atoms.

§1. Introduction.

Many nuclear properties such as spins, magnetic moments, electric quadrupole moments, isomerisms, neutron capture cross sections and binding energies have been studied from the viewpoint of the shell structure, since M. G. Mayer[1] first pointed out the paticural stability of nuclei containing 20, 50, 82 and 126 neutrons or protons. And it has been generally recognized that nuclear shells close at 2, 8, 20, 50, 82 and 126 neutrons or protons, while there are some evidences[2-5] which support that nuclei with 10, 14, 16 and 28 neutrons or protons are particularly stable.

From the analogy of the atomic shell structure considerable variations of the binding energies are expected at the nuclei which form closed shells. The binding energies of the nuclei containing 8 and 20 neutrons or protons were discussed by W. H. Barkas[6] and recently K. Way[7], using energy values of alpha- and beta-paricles from radioactive elements, showed that the binding energies of the last nucleon undergoes a change by 2 Mev at 126 neutrons and about 2.5 Mev at 82 protons. J. A. Harvey[8], measuring Q-values of (d,p) reactions, found that the deviations of about 2 Mev of mass energy from the Bohr-Wheeler's semi-empirical mass formula occur at 50 and 126 neutrons. On the other hand, analysing the mass values in the neighbouring region of calcium, W. Low and C. H. Townes[9] pointed out that the closing of the major shell at 20 nucleons appears quesionable, and that the large isotope spread of calcium is probably due to the exceptional stability of Ca^{40} and a shell at 28 neutrons.

In the present work, we compute the binding energies of light nucley by utilizing the recent mass data and try to find evidence for the single particle model, while for the lightest nuclei other effects, *e.g.* the effects of alpha-clustering[10], may be rather predominant.

§2. Binding Energies of the Last Nucleons.

Lately mass values are decided by methods of mass spectrograph and microwave resonance absorption, and by measuring energies in nuclear reactions and beta-decays. Since the relative accuracy of mass values is important in the present work, we must calculate the binding energies according to mass values which have small systematic error. On this account we used Mattauch and Flammersfeld's table[11] and mainly mass values of nuclei having neutron excess $T=N-Z=0$, 1 and -1, which are the most accurate part in the mass data of light nuclei, where N and Z are the numbers of neutrons and protons respectively.

The binding energies calculated were corrected for the effects of Coulomb interactions which were estimated from the differences of the binding energies of mirror nuclei. The binding energies of the last proton in nuclei which have $T=0$, even N and even Z are shown as Curve 1 in Fig. 1. The binding energies of the last neutron in these nuclei showed the same properties as those of Curve 1 except for the small differences which will be discussed in the following. Curve 2 in Fig. 1 shows the binding energies of the lastp roton in nuclei which have $T=-1$, odd N and even Z. Those of the last neutron in nuclei which have $T=1$, even N and odd Z are almost similar. Since the decay schemes and energies of beta-rays for light nuclei which have $T=2$

are fairly precise, the accuracy of the mass values of these nuclei is expected to be nearly equal to that of the mass values of nuclei which have $T=0$. Curve 3 in Fig. 1 shows the binding energies of the last neutron in these nuclei. In addition, the binding energies of the last neutron-proton pair in nuclei which have $T=0$, even N and even Z are shown in Fig. 2.

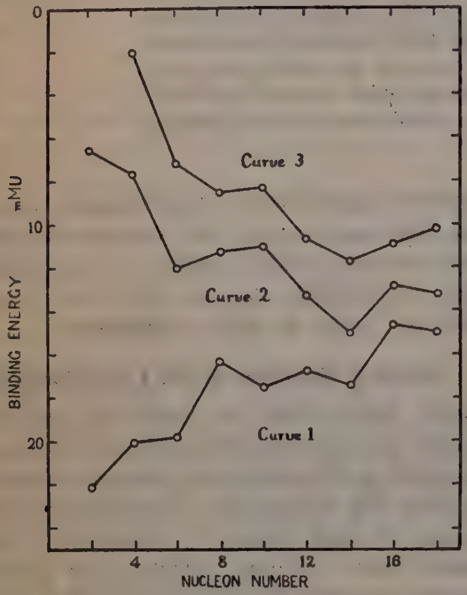

Fig. 1. The binding energy of the last neutron or proton *vs.* the number of neutrons or protons.

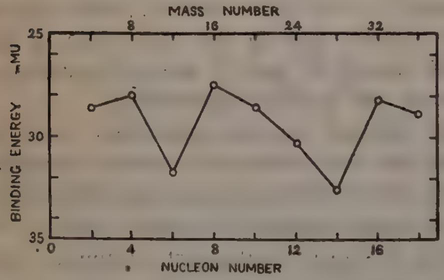

Fig. 2. The binding energy of the last neutron-proton pair vs. mass number for nuclei having $T=0$, even N and even Z.

Curve 1 and Curve 2 in Fig. 3 show the binding energies of the last neutron-proton pair for nuclei which have $T=1$ and 5 respectively. The number of neutrons is not equal to that of protons and both even-odd and odd-even nuclei are plotted. The binding energies in Cuve 2 was calculated from the mass values of nuclei in the neighbouring region of $_{28}Ni^{61}$ determined by H. E. Duckworth.[12]

Errors of the mass values used were less than 0.1m MU for nuclei of mass number $A\leqq19$ and 0.3 mMU for nuclei of $A\leqq36$ with only an exception of the mass of $_{9}F^{20}$ which had an error of 0.5 mMU. The effects of Coulomb interactions were estimated from the binding energies of mirror nuclei and the deviations of the formula $0.630Z(Z-1)A^{-\frac{1}{3}}$ from the experimental values were less than 0.2 mMU exceptfor nuclei of $A=11$, 21, 23 and 29. The deviation at $A=23$ was about 1.5 mMU and those at $A=11$, 21 and 29 were less than 1 mMU. Each of mass values of nuclei in the neighbouring region of $_{28}Ni^{61}$ had an error less than 0.41 mMU.

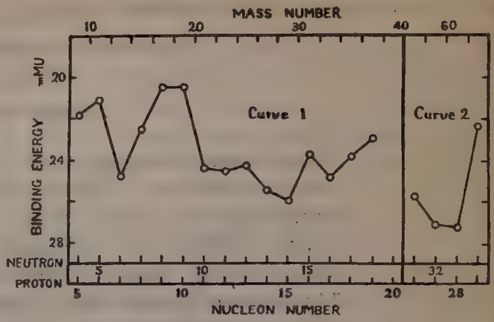

Fig. 3. The binding energy of the last neutron-proton pair *vs.* number of neutrons or protons.

The data of mass values are now being revised and extended and, hence, the results of the present analysis are temporal. The mass values of nuclei of $A<19$ which are described in the table proposed thereafter, however, do not differ from those of Mattauch and Flammersfeld's table. For the region between $A\sim20$ and $A\sim35$ we can calculate the binding energies of the last nucleon using the recent data of the reaction energy[13]; though the curves of the binding energy *vs.* nucleon number deviate in some points from the curves shown above, the tendency is not changed.

§ 3. Discussion.

Binding Energies. Nuclear masses and hence the binding energies of heavier nuclei are expressed by Bohr-Wheeler's formula, which was used as the standard in the above described papers[7-9]. However, we have no suitable formula for the binding energies of light nuclei. So we assumed that the binding energies of light nuclei are composed of the terms which are non-oscillatory functions of mass number and neutron excess, the term depending on the odd-even character of neutrons and protonss the Culomb interaction term of $0.630Z(Z-1)\cdot A^{-\frac{1}{3}}$, and the term concerned with nuclear structure. If one compares the binding energies of the last nucleon in nuclei which have the same neutron excess and the same odd-even charactor after correcting for the effects of Coulomb interactions, the curves of the binding energy *sv.* the number of nucleons may become monotonous apart from the effects of nuclear structure. Hence, the larger binding energies or breaks in such curves may be attributed to the effects of nuclear structure.

For all curves in Fig. 1 and 2 the large binbing energies are found at 6 and 14 neutrons or protons and especially the tendency of the curves near 14 neutrons or protons shows the breaks like those occuring at the positions of shell closing in atoms. In Fig. 2, if the situations of neutrons in nucleus are the same as those of protons apart from Coulomb interactions, the binding energy of the last neutron-proton pair may be more sensitive to the shell structure. It is noteworthy that the values at 8 neutrons or protons are not so large.

In Fig. 3, though the curves are not so sensitive as the case of Fig. 2, the large binding energies at $A=27$ or 29 in curve 1 ($T=1$) are probably due to the gap of energy level which follows 14 neutrons or protons respectively and a break at $A=61$ in Curve 2 ($T=5$) probably indicates the gap of energy level which follow 28 protons. For the neighbouring nuclei of calcium we calculated the binding energies using W. Low and C. H. Townes' data[9] of masses and found also no evidence of a gap of energy level at 20 neutrons or protons.

Electric Quadrupole Moment.[14] W. Gordy[15] and C. H. Townes *et al.*[16] found that the electric quadrupole moments of nuclei having about 50 and 82 protons change from positive to negative with increasing the number of protons. It was shown lately that this change occurs also at 40 neutrons.[17] We can draw a curve from positive to negative at 14 and 28 protons in the same manner as described above, which may support the shell closing at 14 and 28 protons, though this is not conclusive because of the scarcity of data in these regions. The fact that the electric quadrupole moment of ${}_7N^{14}$ and ${}_8O^{17}$ are positive and negative respectively seems to support the shell closing at 8 nucleons. But the positive electric quadrupole moment of ${}_3Li^7$ would contradict with the shell closing at 2 protons from the viewpoint of the empirical rule which is found in the electric quadrupole moments of heavier nuclei.

Delayed Neutron Emitter. The particular stabilities[1, 20] of ${}_8O^{16}$, ${}_{36}Kr^{86}$ and ${}_{53}Xe^{136}$ having 8, 60 and 82 neutrons respectively are expected from the fact that ${}_8O^{17}$, ${}_{36}Kr^{87}$ and ${}_{54}Xe^{137}$ are the emitters of delayed neutron. That ${}_2He^5$ decays to ${}_2He^4$ with emission of a neutron indicates particular stability of ${}_2He^4$.

§ 4. Conclusion.

The present analysis of the binding energies of light nuclei shows the large binding energies of the 6th and 14th neutrons or protons, and 28th proton. About the 14th and 28th nucleons we have found no serious dispute introduced from other evidences. But the situations for the very light nuclei are considerably complicated as discussed in the last section. The results point out that there exist the gaps of energy level which follows the 6th, 14th and 28th neutrons or protons, provided that the gap following the 6th neutron or proton is not so conclusive. It is interesting to note that in the spin-orbit coupling model[21] the numbers 6, 14 and 28 appear after completion of the $j=l+\frac{1}{2}$ orbits which have the largest l values in each of the total quantum numbers n like the numbers 50, 82 and 126. Namely, 6, 14 and 28 are led by the level splittings between $1p_{3/2}$ and $1p_{1/2}$. $1d_{5/2}$ and $1d_{3/2}$ $1f_{7/2}$ and $1f_{5/2}$, in the same way as 50, 82 and 126 by the level splittings, between $1g_{9/2}$ and $1g_{7/2}$, $1h_{11/2}$ and $1h_{9/3}$, $1i_{13/2}$ and $1i_{11/2}$ respectively.

§ 5. Acknowledgment.

The authors wish to express their thanks to Dr. K. Ogata to whom theauthors were indebted for mass data and to Professor J. Itoh for the discussions about the electric quadrupole moments.

References

1) M. G. Mayer: Phys. Rev. **74** (1948) 235.
2) J. S. Smart: Phys. Rev. **76** (1949) 439.
3) Seidlitz, Bleuler and Tendam, Phys. Rev. **76** (1949) 861.
4) A. E. Kempton: Nature, **165** (1950) 801.

5) Haxel, Jensen and Suess: Zeits. f. Phys. **128** (1950) 295.
6) W. H. Barkas: Phys. Rev. **55** (1939) 691.
7) K. Way: Phys. Rev. **75** (1949) 1448.
8) J. A. Harvey: Phys. Rev. **81** (1951) 353.
9) W. Low and C. H. Townes: Phys. Rev. **79** (1950) 198
10) L. R, Hafstad and E. Teller: Phys. Rev. **54** (1938) 681.
11) J. Mattauch and A. Flammersfeld, "*Isotopic Report*", Publisher of Zeits. f. Naturforch, 1949.
12) H. E. Duckworth and R. S. Preston: Phys Rev. **79** (1950) 402, and private communication to Dr. K. Ogata.
13) D. E. Alburger and E. M. Hafner: Rev Mod. Phys. **22** (2950) 373.
14) The authors wish to thank sincerely Professors C. H. Townes and W. Gordy for kindly communications and discussions.
15) W. Gordy: Phys. Rev. **76** (1949) 139.
16) Townes, Foley and Low: Phys. Rev. **76** (1949) 1415.
17) J. M. Mays and C. H. Townes: Phys. Rev. **81** (1951) 940.
18) J. E. Mack: Rev. Mod. Phys. **22** (1950) 64.
19) C. H. Townes: private communication.
20) S. Podger: Phys. Rev. **76** (1949) 1271.
21) M. G. Mayer: Phys. Rev. **76** (1951) 940.

JOURNAL OF THE PHYSICAL SOCIETY OF JAPAN Vol. 7, No. 1, JAN.—FEB., 1952.

Proton Magnetic Resonance Absorption in Hydrogen Perchlorate Monohydrate and the Structure of the Oxonium Ion I.

By Yoshinobu KAKIUCHI,* Hisao SHONO,* Hachiro KOMATSU*
and Kunihiko KIGOSHI**

* *Institute of Science and Technology, University of Tokyo,*
Meguro-ku, Tokyo
** *Gakushuin University, Mejiro, Toshima-ku, Tokyo*

(Received July 21, 1951)

The shape of proton magnetic resonance absorption line in hydrogen perchlorate monohydrate was observed. The line was found to be simple and narrow at the room temperature, and to show the complicated structure corresponding to "three proton system" at the temperature below 150°K. These results were interpreted as follows: the crystal is composed of the *oxonium ion* OH_3^+ and the perchlorate ion ClO_4^-, the orientation of the oxonium ion being well fixed at lower temperatures. At high temperatures, above the transition point at 150°K, however, the oxonium ion begins to *rotate* around the centre of mass, resulting the narrowing of the absorption line. H–H distance in the oxonium ion was estimated to be 1.6∼1.7 Å, in good accord with the expected value from our knowledge about the structure of the water molecule.

§ 1. Introduction

The formation of the *oxonium ion* OH_3^+ in water was often assumed in explaining the abnormal mobility of protons through water1). The first and the most concrete experimental evidence for its exsistence would be the fact that the structure of the crystal of the hydrogen perchlorate $HClO_4 \cdot H_2O$ as revealed from X-ray studies is isomorphous to that of ammonium perchlorate NH_4ClO_4. Since the structure of the latter crystal is known to have an ionic character which may be represented by $NH_4^+ClO_4^-$, Volmer2) has concluded that the former crystal has the similar structure $OH_3^+ClO_4^-$. The above discussion, however, is still an indirect one, because the X-ray diffraction method is in itself, insufficient for determining the positions of hydrogen atoms.

The recent developements of the method of nuclear magnetic resonance enabled us to determine the relative distance of protons in crystals, for instance protons in various organic molecules as well as the water of crystallization in certain crystals[3]. The shape of the absorption line for the powdered crystal is known to resemble to the humps of the camel for two proton systems[4] and to a shouldered peak for three proton systems[5] (Fig. 1). Therefore, if we observe the proton resonance absorption by $HClO_4 \cdot H_2O$ crystals, it may be possible to get some information wether the water remains as the usual water of crystallization or exsists in the form of OH_3^+ in the crystal. The results of the experiment conducted along these lines, together with discussions about the structure of the oxonium ion are described in the following[6].

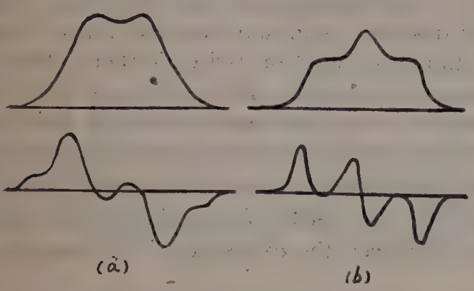

Fig. 1.
Absorption curves and their derivative for two proton systems (a) and three proton systems (b).

§ 2. The experimental procedure.

The sample sealed in a small glass tube, about 8∼10 mm in diameter and 10∼15 mm in length was placed between two pole pieces properly shimmed, 6 cm in diameter and 3 cm distant with each other. A magnetic field of about 3500 gauss was produced by a current of 5 amperes, applying a 30 volts D. C. voltage from batteries equipped for the present purpose exclusively. The inhomogeneity of the field was less than 1 gauss per centimeter. The #26 enameled wire was wound directly around the glass tube containing the sample, and served as inductance in the Colpitts' circuit. The frequency of the radiofrequency field was varied through the resonance frequency, by changing the capacity, the magnetic field being kept constant. Change of the level of the oscillation due to the change of the impedance of the coil resulting from the resonance absorption was detected by the *autodyne method*[7]. (Fig. 2)

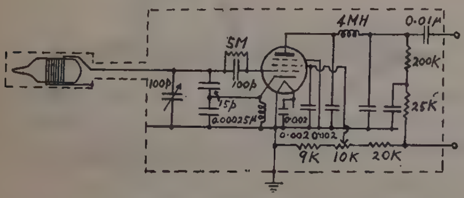

Fig. 2.
Circuit diagram for the autodyne detector.

The field of the magnet was modulated by an alternating current whose frequency being 230 cycles per second. The output signal was amplified through the narrow band amplifier, and then detected by a phase sensitive detector[8]. The final record was taken by a galvanometer of long period. The modulation amplitude was made so small, that the derivative of the absorption curve, not the curve itself was recorded. (Fig. 3)

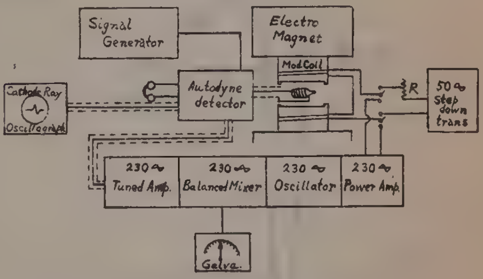

Fig. 3,
Block diagram of the measuring system.

In order to be kept at the necessary low temperature, the sample was inserted into a cavity made in a copper block, which was directly in contact with liquid air. Because the eddy current produced in the block due to the modulated magnetic field induced signals which cannot be filtered through the narrow band amplifier tuned with the modulation frequency, the device to minimize the eddy current was of primary importance. Seven vertical and one lateral cuts were made in the block as shown in Fig. 4 for this purpose.

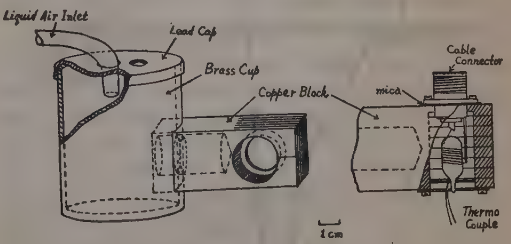

Fig. 4.
Cooling Assembly.

§ 3. Preparation of the sample.

The sample was prepared from 60 percent

aqueous solution. Because the monohydrate cannot be obtained by mere recrystallization from the above solution, as is obvious from the knowledge of its solubility[9)], 100 percent hydrogen perchlorate was first prepared. 36 grams of 62.2 percent aqueous solution of hydrogen perchlorate was added *with* 120 gram of fuming sulfuric acid containing 8 percents of SO_3, and then distilled under the reduced pressure less than 2 mmHg. To the flask was attached a receiver, which was cooled with liquid air. After distilling for about an hour at the temperature of 75~95°C using a waterbath 7~8 cc of anhydrous acid was obtained, which, was distilled again and then left for 10 hours. Destilling it once or twice further, about 10 grams of colorless, oily anhydrous acid was obtained, which showed no further coloration after being left for a long time. Neither sulfuric acid ions nor chlorine ions were recognized, and the result of acid titration by baryta water showed the existence of 100 percent of

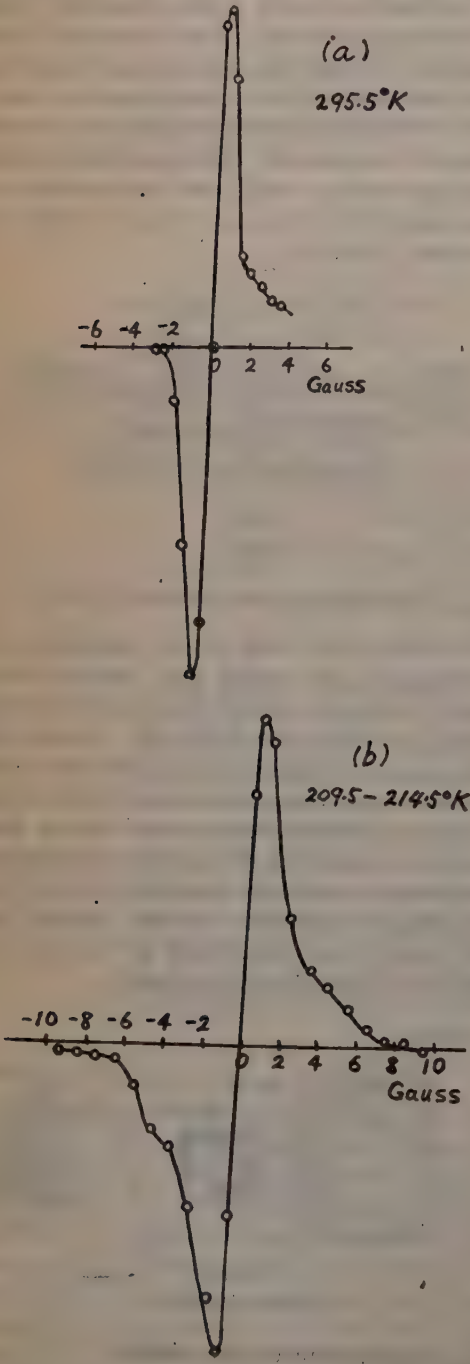

Fig. 5-a-b.

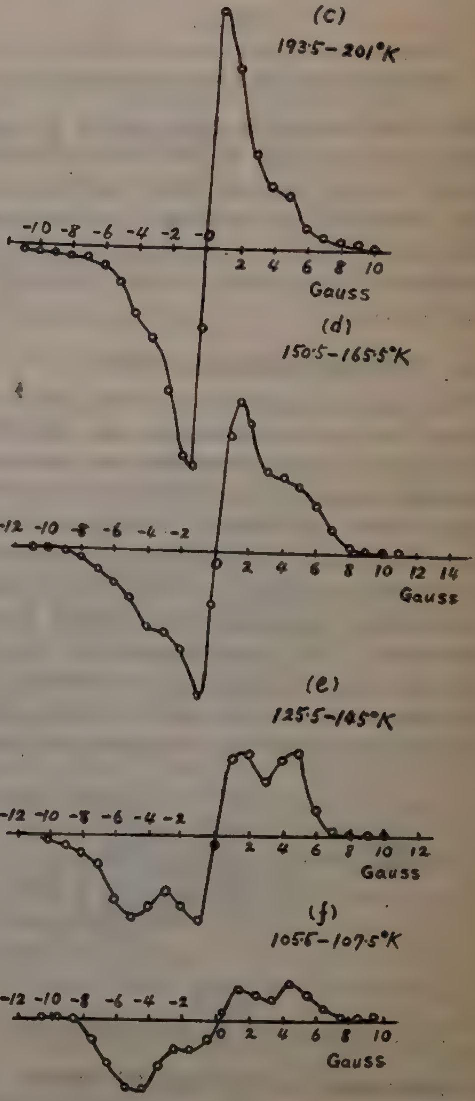

Fig. 5-c-f.

$HClO_4$. The anhydrous acid was put into a small glass container with an ampoule at the bottom, and then weighed. The necessary amount of 62.2 percent aqueous solution was added to anhydrous acid so as to just form monohydrate crystals and evacuated and then sealed. The mixture was warmed above 50°C and the monohydrate was transferred into the ampoule. The monohydrate was analysed after the measurement by acid titration with baryta water and was found to contain 85.6 weight percent of anhydrous acid (theoretical value of the percentage for $HClO_4 \cdot H_2O$ is 84.8). The result of the quantitative analysis for ClO_4^- ions as natron salt[10] showed the percentage of the anhydrous acid to be 85.7 in perfect accord with the result of acid titration. Therefore neither detectable impurities nor decomposition products were considered to be present.

§ 4. The result of the experiment.

The result of the measurement at the room temperature is shown in Fig. 5*a*, the curve corresponding to the derivative of the absorption line. The shape of the absorption line is of simple bell shape as is easily seen from the curve. The similar measurements were repeated on the samples corresponding to perchlorate percentages of 89.8, 85.6, 83.2 and 80.7 but the change in the breadth of the absorption line due to difference in water content as was suspected was hardly observed. Therefore, it may safely be concluded that the shape and the width of the absorption line is *little affected* by the small amount of excess or deficiency of the water of crystallization. As the temperature was lowered, the line was gradually broadened and its structure became more complicated as shown in Fig. 5*b*~5*f*. The phenomena of relaxation were apparent at low temperatures, and the shape of the curve became asymmetric when the curve was swept with comparatively large velocity, because of the effect of *saturation*. It was necessary, therefore, to change the frequency of the radiofrequency field very slowly. In Fig. 7 is shown an example of the careful measurements at the low temperature. The curve *a* is the derivative of the absorption line, and the curve *b* is the absorption curve obtained by integrating the curve *a* graphically which seems to corresponds to the absorption curve due to *three proton system*.

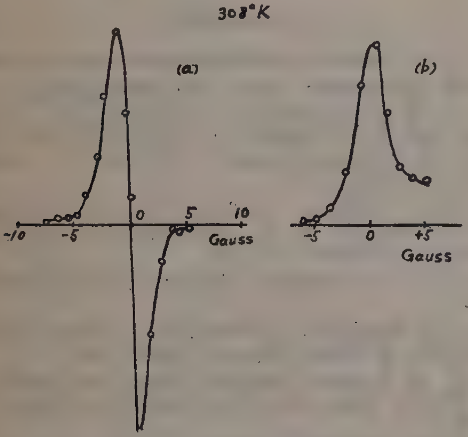

Fig. 6.
Absorption at the room temperature.

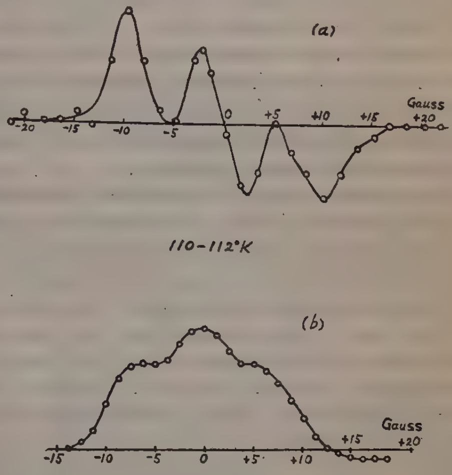

Fig. 7.
Absorption at the lower temperature.

§ 5. Discussions.

As was described in the previous section, the shape of the absorption line is of simple bell shape and its half width is of the order of 3 gauss at the room temperature. The curve changes rapidly into three proton type at about 150°K. Its half width becomes also larger, and it reaches to 18 gauss at 110°K. *There is, therefore, ample justice to believe the exsistence of the oxonium ion at least at lower temperatures*. But how we may explain the bell shaped absorption line at the room temperature?

According to the former investigations on the proton magnetic resonance absorption in NH_4Cl and NH_4NO_3 crystals, the shape of the absorption curve has a complicated structure and its width is also large at lower temperatures where NH_4 ions are fixed[11]. At high temperatures, where NH_4 ions are believed to rotate around their centres of mass, however, the curve becomes bell shaped and its width is 2~3 gauss. Besides these, there are many evidences that the width of the line becomes narrower as the result of the molecular rotation[12]. Therefore, in our case also, the oxonium ion is considered to be fixed, at lower temperatures, and begin to *rotate* above 150°K.

Now let us consider about the structure of the oxonium ion. Neglecting the effect of the protons contained in other oxonium ions, the separations of the energy levels of the three proton system belonging to one and the same oxonium ion and hence the scale of the separation curve also is inversely proportional to the third power of the distance r between protons. Therefore the probable value of r may be obtained by adjusting its magnitude properly so as the calculated absorption line is best fitted to the observation. The result of the estimation gives the value of 1.70 Å, in good accord with our expectation, assuming the pyramidal structure of the ion and O-H distance 0.98 Å and the bond angle H-O-H 110° as in the case of the water molecule.

The second moment[13)] obtained graphically from the curve *b* in Fig. 7 amounts 33.4 gauss^2. The total second moment must be equal to the sum of the moment $\Delta H^2_{H\text{-}H}$ due to the interaction between protons belonging to the same ion, $\Delta H^2_{H\text{-}H'}$ due to the proton H of one ion and the proton H′ of another, finally $\Delta H^2_{H\text{-}Cl}$ due to protons of oxonium ions and chlorine nuclei of perchlorate ions. At the present stage where the structure analysis of the crystal is still incomplete, we are unable to attempt any further detailed discussions.

If we assume, however, the ionic radius of the OH_3^+ ion to be 1.44 Å and that of ClO^-_4 ion to be 2.23 Å further oxonium and perchlorate ions are arranged alternately as ions in rock salt crystal, as is really the case in high temperature modification of NH_4ClO_4[14)], the closest possible distance between proton and Cl nucleus would be roughly 2.79 A. Therefore, the contribution of proton chlorine interaction to the second moment is less than 0.01 gauss^2, which is negligibly small compared with the total second moment. The amount of $\Delta H^2_{H\text{-}H'}$ is estimated to be 3.6 gauss^2 by assuming all the distances between pairs of protons each belonging to different oxonium ions, to be equal to the smallest possible value 3.40 Å, the true value of the second moment $\Delta H^2_{H\text{-}H'}$ being probably less than this value, and would not exceed 3.7 gauss^2 even when the effect of the next nearest neighboring ions are taken into account. Therefore, the value of $\Delta H^2_{H\text{-}H}$ is roughly equal to and perhaps larger than 33.4 gauss^2−3.7 gauss^2 =29.7 gauss^2, and the magnitude of the distance between protons in an oxonium ion is calculated from the above data to be 1.7 Å. Theoretical absorption curve obtained, based upon these numerical data agrees well with the observation. (Fig. 8). Further detailed discussions would be hardly possible unless further information on the crystal structure is available and the accuracy of the measurement is more raised. X-ray diffraction experiment at lower temperatures is now under planning.

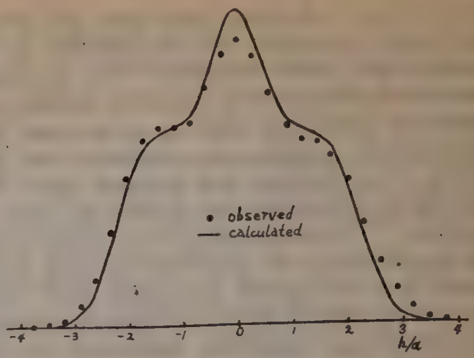

Fig. 8.
Observed absorption and theoretical curve, assuming proton distances 1.70 Å and second moment due to neighboring oxonium ion 3.7 gauss^2. h=shift of the line in Gauss, $\alpha=3\mu/2r^3$.

In conclusion, the authors wish to express their sincere thanks to Prof. H. Kumagai for his putting his magnet at their disposal, and their thanks are also due to Profs. T. Muto and S. Inoue for their many valuable discussions and encouragements.

References

1) E. Hückel: Z. f. Electrochem. **34** (1918) 536.

2) M. Volmer: Lieb. Ann. **440** (1924) 200.

3) H. S. Gutowsky, G. B. Kistiakowsky, G. E. Pake and E. M. Purcell: J. Chem. Phys. **17** (1949) 972. H. S. Gutowsky and G. E. Pake: J. Chem. Phys. **16** (1949) 1164.

4) G. E. Pake: J. Chem. Phys. **16** (1948) 327. H. S. Gutowsky, G. B. Kistiakowsky, G. E. Pake and E. M. Purcell: loc. cit.

5) E. R. Andrew: J. Chem. Phys. **18** (1950) 159.

6) Y. Kakiuchi, H. Shono, H. Komatsu and K. Kigoshi: J. Chem. Phys. **19** (1951) 159.

7) A. Roberts: Rev. Sci. Instr. **18** (1951) 845. H. Shono: Rep. Inst. Sci. Tech. Univ. Tokyo, in press.

8) H. A. Thomas, R. L. Driscoll and J. A. Hipple: Rep. Nat. Bureau Stand. **44** (1950) 569.

9) van Wyk: Z. Anorg. Chem. **48** (1906) 1.

10) O. Loebich: Z. Analyt. Chem. **68** (1926) 97.

11) H. S. Gutowsky and G. E. Pake: loc. cit.

12) E. R. Andrew: J. Chem. Phys. **18** (1950) 607.

13) J. H. Van Vleck: Phys. Rev. **74** (1948) 1168.

14) C. Finback and O. Hassel: Z. f. Phys. Chem. **32** (1936) 130. K. Herrman and W. Ilge: Z. f. Krist. **75** (1930) 41.

Short Notes

J. PHYS. SOC. JAPAN **7** (1952) 107

Electrical Resistivity of SiC

By Wataru SASAKI.
Electrotechnical Labolatory, Tanashi-machi, Kitatama-gun, Tokyo

(Received October 29, 1951)

The electrical resistivity of a number of SiC samples has been measured over the temperature range from liquid oxygen to 100°C. Samples measured were about $0.5\times0.3\times0.1\ \mathrm{cm}^3$ in size and cut out of single crystals possessing a hexagonal face plane.

Some of the experimental results are shown in Fig. 1. The ordinate is the resistivity in logarithmic scale and the abscissa is the inverse absolute temperature. The curves A and B are the results for black samples and C is for a green sample. Every curve consists of two straight lines expressed by

$$\rho=\rho_0\exp(\varepsilon/kT). \qquad (1)$$

ε is estimated at about 0.027 ev in the lower temperature range and 0.13 ev in the higher temperature range for all these three cases. If the motion of charge carriers in non-polar semiconductors is scattered only by the lattice vibrations, their mobility varies as $T^{-3/2}$, or

$$\mu=\mu_0T^{-3/2}. \qquad (2)$$

Charge carrier density n is expressed as

$$n=\frac{g(2\pi m^*kT)^{3/2}}{h^3}\exp(-\zeta/kT), \qquad (3)$$

where ζ is the energy difference of Fermi level and the bottom of conduction band or the top of filled band. Using (2) and (3) ρ is expressed as

$$\rho=\frac{1}{e\mu n}=\frac{h^3}{e\mu_0g(2\pi m^*k)^{3/2}}\exp(\zeta/kT). \qquad (4)$$

Comparing (1) and (4),

$$\varepsilon=\zeta. \qquad (5)$$

The temperature variation of ε, or ζ by (5), suggests the existence of two impurity energy levels at 0.054 ev and 0.26 ev from the band edge.

It was also intended to measure Hall coefficient, but the Hall voltage was too small to be detected by the *galvanometer-and-potentiometer* method. The fluctuations of the galvanometer in the Hall voltage circuit give the upper limit of Hall voltage. The upper limit of Hall mobility estimated from the upper limit of Hall voltage is about 10 cm²/V·sec at 110°K, and for such a small value of mobility the validity of the equation (2) is rather doubtful. Moreover other sources of scattering, which make the matter more complicated, must be involved.

Metallic point contacts on samples A and C show rectification, while those on sample B do not. The easy current direction infer that the charge carriers are holes in A and electrons in C.

The author wishes to represent his sincere thanks to Mr. M. Hatoyama for his suggestion of this work and to Mr. M. Shibuya and Mr. M. Kikuchi for their valuable discussions and to Miss M. Kuno for her assistance in experiments.

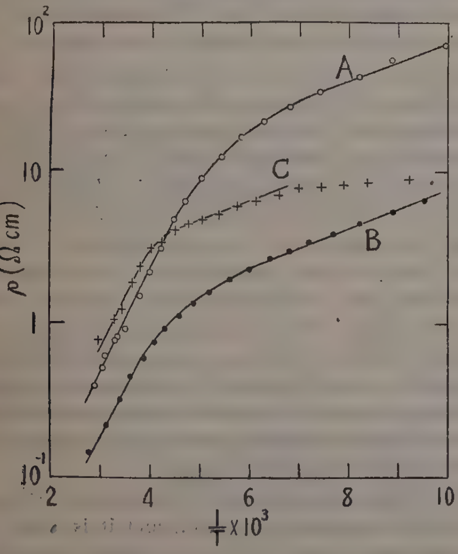

Fig. 1. Temperature dependence of electrical resistivity of three SiC samples.

J. PHYS. SOC. JAPAN **7** (1952) 107–109

On the Bleaching of Color Centers (M-Center) in KCl Crystal with Polarized Light

By Masayasu UETA
Department of Physics, University of Kyoto, Kyoto

(Received November 5, 1951)

With the purpose to determine the structure of complex color centers in alkali halide crystals many experiments and theoretical considerations have been worked. Among them, Seitz's model[1)] for Molnar's M-band consisting of one pair of vacancies and a F-center might be only generally accepted one. However, even for M-band any direct experiment which definitely prove the model has not yet been found. Experiments reported here were carried out to verify the C_{2v} symmetry of M-center.

M-centers were grown from additively colored F-centers by irradiation of crystal with the light lying in its absorption band. The crystal containing M-centers was placed behind the exit slit of the monochromator in such a way as [011] of crystal makes the angle of 45° to the slit. Nicol polarizer, before the entrance slit, was set as can be rotated in the plane perpendicular to the light path, and measurements of absorption curves of M-band were performed with two sorts of polarized lights of which electric vectors have the directions parallel to [011] and [0$\bar{1}$1] (Fig. 1). Absorption curves, after the crystal was irradiated with the [011] polarized M-light were shown in Fig. 1; subscripts R and L in the figure indicate the measurement with the [011] and [0$\bar{1}$1] polarized light. Curve I is the absorption spectrum of M-centers grown up initially from F-centers, and curves II–VII are those of after bleaching with the [011] polarized M-light for 10, 25, 40, 75, 150, 195 minutes respectively. After 195 minutes' bleaching when the crystal is irradiated in turn by the [0$\bar{1}$1] polarized light perpendicular to the [011], VII$_L$ curve is found to be reduced to the VII$_R$. As shown in figure, absorption coefficients measured with two polarized lights are considerably different. This shows that M-centers are distributing along both directions which can be bleached or not by the [011] polarized light. From the relation between absorption coefficients at the wavelength of M-band maximum and bleaching time shown in Fig. 2, it is indicated that the M-centers which can be bleached by the [011] light are almost destroyed after irradiation for 195 minutes.

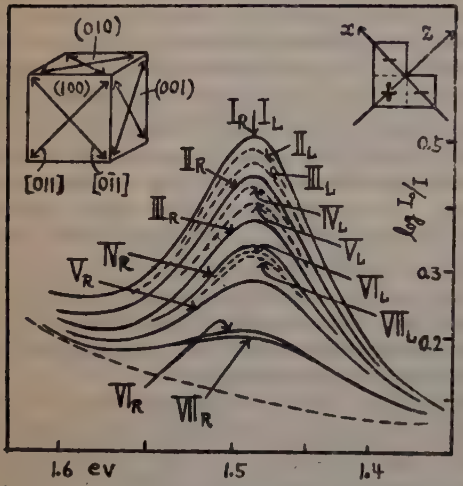

Fig. 1. Absorption curves of M-centers after bleaching with polarized light of which electric vector is parallel to [011] of crystal (at 20°C).

The decrease of absorption coefficient from the initial value: 0.31 (difference of log I$_0$/I in Fig. 2), gives the total coefficients of M-centers which can be bleached by the light, and the coefficient due to the M-centers which is not bleached by the [011] light: 0.13, is about 1/2.4 of the total one.

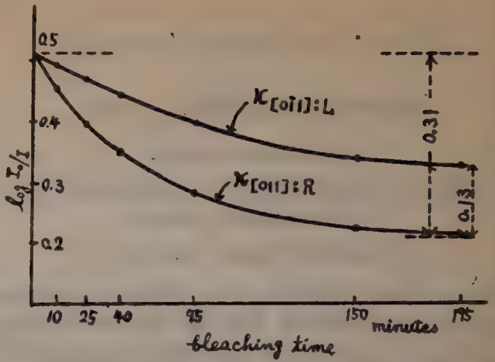

Fig. 2. Relation between absorption coefficients at wavelength of M-band maximum and bleaching times.

After bleaching for 195 minutes by the [011] light, the crystal was warmed up to the 60°C for 20 minutes, then absorption coefficient with [011] light increases, and reversely, that measured with [0$\bar{1}$1] light decreases. This fact indicates that M-centers which remained unbleached and were taking a particular direction rotate to the other directions by acquiring heat energy. More detailed experiments on this fact are going to be carried out.

Our experiments are well explained by assuming the C_{2v} or D_{2h} symmetry to the model of M-center. For the simplicity, we assume the C_{2v} after Seitz, then the two-fold axis Z of M-center are initially distributing uniformly along the six directions joining two negative ions. By the irradiation of light polarized parallel to [011], if the excited state is B_1, (ground state is probably A_1) M-center in (100) plane and have Z axis along [0$\bar{1}$1] are bleached and not the centers along [011]. M-centers in (010) and (001) planes are also bleached, but bleaching rate will be 1/4 of that of (100) plane centers. After irradiation for t minutes, the density will be $n_0 \exp -\beta t$ for centers in (100) plane, and $n_0 \exp -\beta t/4$ for centers in (010) and (001) plane. (n_0 is initial density, and β is bleaching constant). Therefore, absorption coefficients for the [011] and [0$\bar{1}$1] polarized light are respectively: $\kappa_{[011]:R}=\alpha n_0(\exp-\beta t+\exp-\beta t/4)$, $\kappa_{[0\bar{1}1]:L}=\alpha n_0(1+\exp-\beta t/4)$; αn_0 is absorption coefficient due to the M-centers initially existed in (100) plane. Therefore, when $t=0$, $\kappa_{[011]}=\kappa_{[0\bar{1}1]}=2\alpha n_0$, and $t\rightarrow\infty$, $\kappa_{[0\bar{1}1]}-\kappa_{[011]}=\alpha n_0=1/2$ initial coefficient of total M-centers. It is because of the disturbance of states of polarized lights due to the refraction in the monochromator that the experimental value 1/2.4 is somewhat smaller.

The same conclusions hold to the excited state A_1 or the D_{2h} symmetry of model, and it is clear that excited state is not B_2 of C_{2v}. On the other hand Inui[2] and his collaborators calculated the energy difference between A_1 and B_1 taking the model of C_{2v} and showed it coincides approximately to that of experimental M-band maximum. From this and above mentioned experiments on the symmetry of M-center, the model given by Seitz is considered fairly probable.

The experiment such as this will be another method to classify the nature of color centers, in addition to measurements of magnetic susceptibility3), paramagnetic resonance4), or temperature dependency, and it is desirable to extend to the other centers, particularly K5), K′6)-centers which were discovered in our laboratory. In conclusion, the author wishes to express his cordial thanks to professor Y. Uchida for the encouragement through the present work.

References

1) F. Seitz, Rev. Mod. Phys. **18** (1946) 384.
2) T. Inui, Y. Uemura and Y. Toyosawa, Busseiron Kenkyu **35** (1951) 1.
3) A. B. Scott and L. P. Bupp, Phys. Rev. **79** (1950) 346.
4) E. E. Schneider and T. S. England Physica **17** (1951) 221.
5) Y. Uchida, M. Ueta and Y. Nakai, J. Phys. Soc. Japan **6** (1951) 107.
6) M. Ueta, Memoirs College Science, Univ. Kyoto, Ser. A, **26** (1950) 69.

J. Phys. Soc. Japan **7** (1952) 109–110

Absorption of Color-centers in the Region between F-band and M-band

By Yôichi Uchida and Hisao Yagi
Institute of Physics, University of Kyoto

(Received November 6, 1951)

In the region between the *F*-band and the *M*-band of alkalihalides, Molnar1) first found so called R_1 and R_2 bands and reported some properties of these bands. Then Seitz2) proporsed F_2 or $F_2{}^+$ model for these absorbing centers, especially on the ground of stableness and non-existing photoconduction. The experiment of Obery3), on the other hand, proved photoconductivity and that of Pringsheim4) the unstableness of these centers by irradiation. Petroff5) also studying this region on additive-colored crystals, found another band. Thus, the general feature of the absorption in this region is not yet distinct.

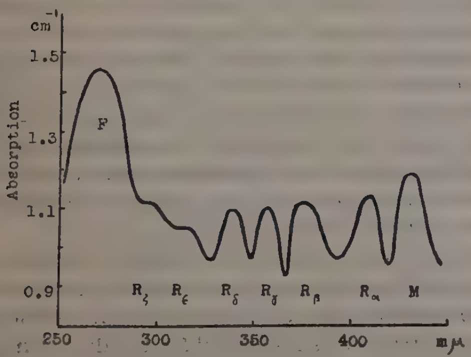

Fig. 1. Absorption bands of LiF. (*K*-colored)

Re-examinations were undertaken in this laboratory and it might be interesting to note some results. Synthetic crystals of NaCl, KCl, KBr and LiF* colored either by X-ray irradiation or electron put-in were used. Almost same results were obtained in these two methods of coloring but in general the absorption bands appeared more easily in X-ray colored crystals. A large apertured glass-prism spectrophotometer with 1.5 meter focal length objective and a quartz-prism spectrophotometer of medium size were used in visible and ultra violet regions respectively. A Beckman D. U. Spectrophotometer was also used.

In our experiments, six bands called provisionally R^{α}, R_β, R_γ, R_δ, R_ε and R_ζ were obtained in every crystal as shown in the figure 1 for LiF. A brief summary of the band maxima is given in the accompanying table, in which our measured wave-lengths of *K* and *K*′6) bands are also contained.

Among these *R* bands, a peculiar wave-number relation will be seen as follows:

$$\frac{\nu_\alpha-\nu_\beta}{\nu_\gamma-\nu_\delta}=\frac{\nu_\beta-\nu_\varepsilon}{\nu_\delta-\nu_\zeta}\quad\text{approximately.}$$

This means that, each six bands may be classified into group *A* including R_α, R_β and R_ε, and group

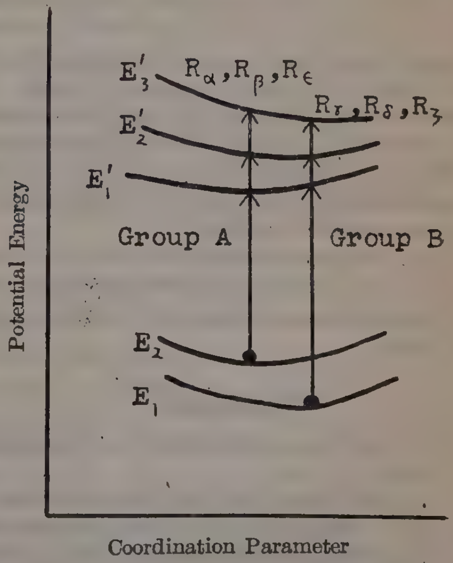

Fig. 2. Electronic Levels of *R*-bands.

---

* Experiments were carried out on crystals of our own growing7) as well as those kindly sent at our disposal from Professor P. Pringsheim to whom the writers are indebted.

Table. Spectral Location of the Absorption Bands

Absorption Peaks	Crystals							
	NaCl		KCl		KBr		LiF	
	mμ	eV	mμ	eV	mμ	eV	mμ	eV
N	830	1.49	980		1100		530	2.33
M	725 (700)	1.70	835 (800)	1.48	899 (875)	1.37	468 (427)	2.63
R_α	660	1.87	782	1.56	847	1.46	408	3.02
R_β	620	1.99	738	1.67	795	1.55	377	3.27
R_γ	596	2.07	700	1.76	780	1.58	355	3.47
R_δ	572	2.16	671	1.84	741	1.66	338	3.65
R_ε	552	2.23	635	1.94	704	1.75	315	3.91
R_ζ	526	2.34	608	2.03	669	1.84	297	4.15
F	465	2.65	560	2.20	631	1.95	270	4.57
K	292	4.21	307	4.02	320	3.85		
K'	258	4.78	267	4.62	290	4.25		

These results were obtained at room temperature.

Wave-lengths in parentheses of M-bands were obtained when measured on the crystals colored by the method of electron put-in.

B including R_γ, R_δ and R_ζ. The fact that group A enhances at higher temperature while group B at lower temperature, may be another evidence of this classification. Moreover, when the crystal irradiated by a light in any one of R bands, it was found while M, F, K and K' absorptions increase suddenly for a while, then decrease, approaching to final equilibrium values, all remaining R bands decrease monotonously side by side with the illuminated R band. This suggests strongly that all six R-bands are attributable to a single kind of center. Perhaps, each group A or B is due to transitions between each of two lower electronic levels and common three higher electronic levels as shown in the figure 2.

All the above-mentioned characters of R bands pave the way to establish the structure of the center. In this connection a full note will be written in the near future.

References

1) J. P. Molnar: (Unpublished). See Reference (2).
2) F. Seitz: Rev. Mod. Phys. **18** (1946) 384.
3) J. J. Oberly and E. Burstein: Report from Am. Phys. Soc. Washington. April 28 (1950). (Unpublished).
4) R. Casler, P. Pringsheim and P. Yuster: Jour. Chem. Phys. **18** (1950) 1564.
5) S. Petroff: ZS. für Phys. **127** (1950) 443.
6) Y. Uchida, M. Ueta and Y. Nakai: Jour. Phys. Soc. Jap. **6** (1951) 107.
7) Y. Uchida and H. Yagi: Jap. Jour. App. Phys. **16** (1947) 65.

J. PHYS. SOC. JAPAN **7** (1952) 110–111

Lattice Constant of $PbZrO_3$

Etsuro SAWAGUCHI

Tokyo Institute of Technology, Oh-okayama, Tokyo

(Received November 8, 1951)

Antiferroelectricity of $PbZrO_3$ has recently been confirmed[1)2)3)]. Concerning the lattice parameter *vs.* temperature relation of this material, Ueda and Shirane[4)] have already performed a fairly detailed investigation and have concluded that its lattice symmetry changes from tetragonal to cubic at the Curie point of about 220°C. But since the precise cell dimension near the Curie point has not yet been determined, and since the knowledge of these data has become very important for understanding the antiferroelectricity of this material more thoroughly, we have undertaken an X-ray study of the temperature change of lattice parameters.

Samples were prepared by firing the mixtures of pure $PbCO_3$ and ZrO_2 at about 1200°C. A platinum wire covered with a thin coat of fine powder of $PbZrO_3$ was used as a standard for the determination of lattice parameters. The Debye-Scherrer photographs were taken by the back reflexion method using Cu-Kα radiation and 50.3 mm camera. To begin with, for simplicity, we have regarded the basic perovskite lattice of this material as being tetragonal, though it has been proved that the true crystal symmetry below the Curie point is slightly orthorhombic[3] and the cell must be doubled in order to give the true lattice period. To above approximation, the lattice constant and the axial ratio were calculated from (510) and (105) lines. The results are shown in Figs. 1 and 2. The lattice parameters at 20°C are:

$$a=4.152\text{A} \quad c=4.101\text{A} \quad \text{and} \quad c/a=0.9877.$$

(If the true orthorhombic unit cell is adopted, the true a and b axes must be chosen to bisect the angles between the above two axes, and the cell must be doubled for taking account of the superstructure, that is:

$$a=4.152\text{A}\times\sqrt{2}=5.872\text{A}$$
$$b=4.152\text{A}\times2\sqrt{2}=11.744\text{A}$$
$$c=4.101\text{A}\times2=8.202\text{A}.)$$

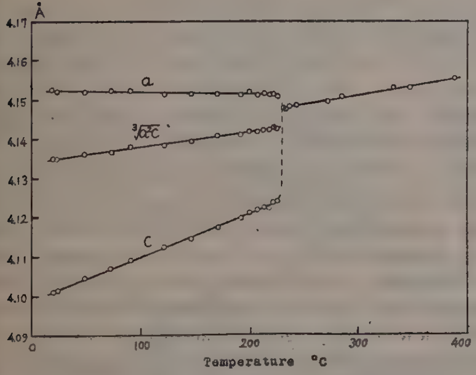

Fig. 1. Lattice constant *vs.* temperature curve. Below Curie point the basic perovskite lattice is assumed, for convenience, as tetragonal.

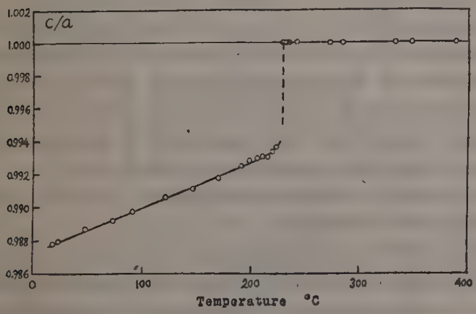

Fig. 2. Tetragonality c/a *vs.* temperature curve.

As the temperature is raised, the axial ratio increases almost linearly until at last the structure changes abruptly from tetragonal lattice with $c/a=0.9935$ to cubic one just at the Curie point of 230°C, where the superstructure lines, main characteristic of antiferroelectricity, disappear. It may be sure that this transition is of the first order. The thermal expansion coefficients of the lattice are,

in the tetragonal region,

$$\beta_a \fallingdotseq -0.05\times10^{-5}, \qquad \beta_c \fallingdotseq 2.8\times10^{-5},$$

and, in the cubic region, $\beta_a \doteqdot 1.10\times10^{-5}$.

The parameter a does not change appreciably below the Curie point. Cell dimension as a function of T°C is given as follows:

$$T<230^\circ\text{C} \quad V=70.65\times(1+2.7\times10^{-5}T)\ \text{A}^3$$
$$T>230^\circ\text{C} \quad V=71.38\times(1+3.3\times10^{-5}(T-230))\ \text{A}^3$$

Hence, anomalous volume change at the transition is found to be $\Delta V/V=4.1\times10^{-3}$ i.e. 0.29A^3 per unit cell.

The author is indebted to Professor Y. Takagi and Mr. G. Shirane, for their valuable advice. He also wishes to acknowledge the helpful assistances of Mr. T. Kittaka. This study was helped by the research grant from the Ministry of Education.

References

1) E. Sawaguchi, G. Shirane and Y. Takagi: J. Phys. Soc. Japan **6** (1951) 333.
2) G. Shirane, E. Sawaguchi and Y. Takagi: Phys. Rev. **84** (1951) 476.
3) E. Sawaguchi, H. Maniwa and S. Hoshino: Phys. Rev. **83** (1951) 1078.
4) R. Ueda and G. Shirane: J. Phys. Soc. Japan, **6** (1951) 209.

J. PHYS. SOC. JAPAN **7** (1952) 111–112

On the Range-Energy Relation and Ionization-Energy Relation for Alpha-Particles in Air

By Kiichi KIMURA, Ryutaro ISHIWARI, Kazunori YUASA, Sukeaki YAMASHITA, Kozo MIYAKE, and Sadao KIMURA

Institute for Chemical Research, Kyoto University

(Read April 3, 1951; Received October 29, 1951)

The range-energy curve for alpha-particles in air established by Holloway and Livingston[1] was revised by Bethe[2] and Jesse et al.[3] so as to fit in with the data obtained from several nuclear reactions[4] in low energy region. This revision was based on the Jesse's experiments[3][5] on the ionization-energy relation which indicated that the ionization in argon is exactly proportional to the alpha-energy, while the ionization in air shows marked and essential deviation from the proportionality.

It should be noted, however, that similar deviations will be expected if the saturation of the pulse height is not fully attained for columnar recombination. For, in such cases, the degree of recombination will increase according as the particle loses energy and the ion density increases along the path of the particle.

In the present study, we have measured the specific ionization curve for Po alpha-particles in air with almost the same arrangement as Holloway and Livingston's experiment, and examined the effect of columnar recombination by varying the field strength. An ionization chamber of 1 mm in depth was used. The front window of the chamber was covered with aluminium foil of 0.41 mg/cm^2 in thickness. All distance measurements were corrected to 15°C, 760 mm, and the change of the stopping power of the aluminium foil with alpha-energy was also taken into account.

In order to examine straightforwardly the effect of columnar recombination, we have measured the ratio of the specific ionizations at two definite points, the peak of the specific ionization curve (residual range 4 mm) and the point 18 mm apart from the peak (residual range 22 mm), by applying the chamber voltages 50 V/mm, 135 V/mm and 1,140 V/mm in turn. The results are shown in Table I.

Table I.

Run	Applied Voltage 50 V/mm	 135 V/mm	 1,140 V/mm
1	1.87_6	1.98_5	2.00_1
2	1.93_1	1.98_2	2.01_3
3	1.89_4	1.99_6	2.06_5
4	1.85_7	1.95_9	2.03_3
5	1.91_7	1.97_3	
Mean	1.89_4 ±0.014	1.97_9 ±0.006	2.02_8 ±0.013

The observed ratio has shown a definite increase from 1,89 to 2.03 with the rise of the applied voltage. The rate of the increase of the ratio is in agreement with the Jaffé's theory[6] of columnar recombination. On the other hand, the corresponding ratio taken from the Holloway and Livingston curve[7] is only 1.86. This fact indicates definitely that the Holloway and Livingston curve is influenced considerably by the effect of columnar recombination.

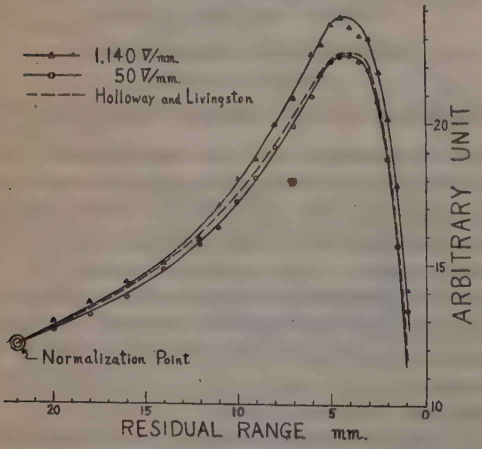

Fig. 1. Specific ionization curves observed with 50 V/mm and 1,140 V/mm and the H. and L. curve.

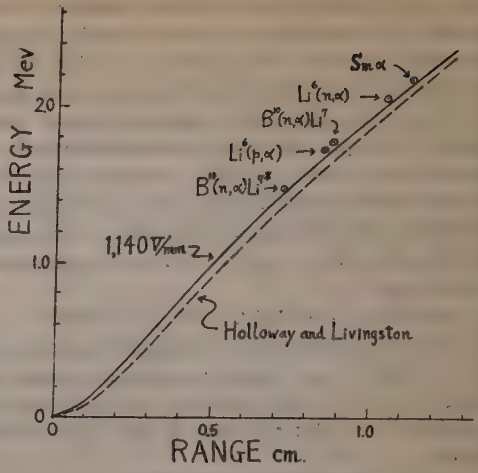

Fig. 2. Integrated curve of the curve observed with 1,140 V/mm. Curves are normalized at Po-point.

We have also measured the whole specific ionization curve (residual range (~22 mm) with the applied voltage 50 V/mm and 1,140 V/mm. The curve obtained with 50 V/mm nearly agrees with the Holloway and Livingston curve, while the curve obtained with 1,140 V/mm shows larger ionization in the low energy region according to the results given in Table I (Fig. 1). Integrating the latter curve, we have obtained a range-energy curve which nearly agrees with the fixed points determined from nuclear reactions (Fig. 2).

We can conclude from the present results that the origin of the error contained in the Holloway and Livingston curve is to be attributed almost entirely to columnar recombination rather than the essential deviation of the ionization-energy relation in air, and consequently the proportionality of the ionization-energy relation for alpha-particles in air should be much better than announced by Jesse et al.

The details of the experiment will be soon published in this Journal.

We wish to express our sincere thanks to Prof. H. Yamaguchi of Osaka University who kindly offered the Rn-tubes for the preparation of the Po-sources.

References

1) M. G. Holloway and M. S. Livingston, Phys. Rev. **54** (1938) 18.
2) H. A. Bethe, Rev. Mod. Phys. **22** (1950) 213.
3) W. P. Jesse and J. Sadauskis, Phys. Rev. **78** (1950) 1.

4) These are summarised in Ref. 3).
5) W. P. Jesse, H. Forstat and J. Sadauskis, Phys. Rev. **77** (1950) 782.
6) G. Jaffé, Ann. Physik **42** (1913) 303.
7) Fig. 9. in Holloway and Livingston's paper.

J. Phys. Soc. Japan **7** (1952) 113

A Simple Method Obtaining a Large Single Crystal of Sodium Nitrate

By Tasaburô YAMAGUTI
Physical Department, University of Chiba

(Received November 15, 1951)

In some preliminary experiments on the growth of sodium nitrate crystals from the melt, it was known that, if we follow a method analogous to Ramsperger-Melvin's[1], chances of the growth to only one single crystal are small, and moreover orientations of the optical axis are not definite with respect to the crucible. We adopted a new method, more simple compared with Stockberger's[2], by which the crystal growth in one single crystal is certain and the orientation is also definite, and moreover removal of the crystal from the crucible is quite easy. In the following we will describe briefly about the apparatus used and the experimental procedures.

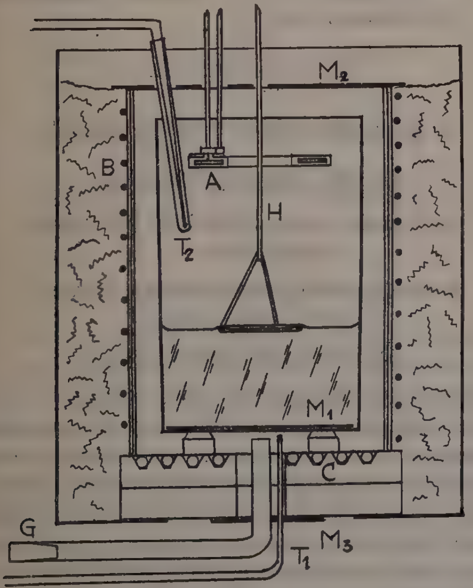

Fig. 1.

The figure shows a section of the furnace at the time when the growth of the crystal is finished. The furnace contains three heaters A, B and C. A, being a ring formed heater made of nichrome wire and protected by "Almite" plate from vapours of $NaNO_3$, is used to prevent solidification starting from the upper surface of the melt. A nichrome wire of B is wound on a stainless steel cylinder of 16 cm inside diameter, covered by an asbestos cloth. Through a canal, in the centre of the heater C, a glass tube G with a plug adjustable for air supply and a thermocouple T_1 are inserted towards the bottom of the brass crucible, which is 0.8 mm in thickness, 20 cm in height and 12.5 cm in inside diameter.

Sodium nitrate of about 1.2 kg, purified by recrystallization from the solution in distilled water, were put on a clean cleaved surface of a mica sheet M_1 placed in the bottom of the crucible. When the materials had melted and had reached the temperature of about 350°C, a holder H made of a stainless steel wire was lowered until its lower end forming a loop dipped beneath the surface of the melt. Then, by both gradual decrease of the current of C to zero and gradual opening of the plug, temperature difference between T_1 and T_2 reaches to 50°C, meanwhile temperature T_2 being kept to about 315°C. By such control of temperature, crystallization starts from the centre of the mica sheet, gradually increasing both its area and its height, and finally, from 10 to 20 hours later, reaches the upper surface, embedding the loop of the holder in the surface. When the crystallization had finished, the electric circuit of A was opened to lower the temperature of the surface, and after one hour elapsed, the crystal and the crucible were lifted a few centimeters by drawing the embedded holder upwards. By subsequent rapid heating of the crucible with heaters B and C, boundaries of the crystal melt and the crucible drops down. To avoid further meltings of the crystal, the temperature of the furnace lowered rapidly to about 270°C by opening the circuit C and by a sudden decrease of considerable amount in B current, and furthermore this current was decreased by means of some automatic device to zero so that the temperature gradually lowered to the room temperature in a time interval of three days.

A single crystal thus made has a weight slightly exceeding 1 kg and its optical axis is perpendicular to the cleaved surface of mica. The crystals are used practically to make polarization prisms of Feussner's type and sizes of the crystal being expected to be increased by the use of larger crucibles.

In the end, author's thanks are due to the Educational Department for financial support and also to Dr. I. Makino of the Hitachi Works for his kind assistance.

References

1) H. C. Ramsperger and E. H. Melvin: J.O.S A. **15** (1927) 359.
2) D. C. Stockbarger: J.O.S.A. **2** (1937) 416.

J. PHYS. SOC. JAPAN 7 (1952) 114

On the Theory of Multi-terminal Network Synthesis and the Theory of Equivalent Networks

By KIYASU Zen'iti and Nobuichi IKENO

Electrical Communication Laboratory

(Received November 17, 1951)

One of the authors (Kiyasu) has proved that any two-terminal network is synthesised as an input impedance of a reactance 4-terminal network terminated with one resistance[1]. About the same time, this theorem was proved independently by W. Cauer, H. Piloty, S. Darlington and G. Cocci[2]. At that time Kiyasu expected that any $2n$-terminal network will be realized in the form of input $2n$-terminal network of a reactance $4n$-terminal network terminated with n resistances. The proof of this expectation has been accomplished by Y. Oono. Kiyasu has paid attention to the fact that, in the case of two-terminal networks, this theorem has intimate relations to the insertion loss theory of reactance 4-terminal networks, and has believed that if we develop the insertion loss theory of reactance multi-terminal networks, Oono's theorem will be proved by another method. Upon this standpoint, he proceeded the research, and has solved the chief part of this problem. Recently we were noticed by Dr. Oono that Belevitch was investigating the same problem. Our results are almost equal to what Belevitch has published without proofs. Although the detailed report is intended to be published some day, we want to present the outline.

(1) In the case when the impedance matrix Z or the admittance matrix Y exists, the matrix $S(\lambda)$ defined by

$$S(\lambda)=\{E+Z(\lambda)\}^{-1}\{Z(\lambda)-E\}=\{E+Y(\lambda)\}^{-1}\{E-Y(\lambda)\}$$

is called efficiency or scattering matrix of a $2n$-terminal network. This can also be defined and exists for a multi-terminal network having neither Z nor Y. The necessary and sufficient conditions for S-matrix being realizable as a physical multi-terminal network are that the elements are analytic and rational functions in the right half plane and on its boundary, S is symmetric and Hermitian form of $E-S\bar{S}$ is non-negative on the imaginary axis.

(2) S is realized as a reactance $2(n+\rho)$-terminal network terminated with ρ resistances, when the rank of $E-S\bar{S}$ is ρ, the order S is n, and the above conditions are satisfied. Accordingly, if $S\bar{S}=E$, S represents a reactance $2n$-terminal network.

(3) To prove this theorem, we begin with the consideration of the case $\rho=n$. Now, we substitute S_{11} for S, then there exist other matrices S_{12}, S_{21} and S_{22}, so that the matrix S newly defined by

$$S=\begin{bmatrix} S_{11} & S_{12} \\ S_{21} & S_{22} \end{bmatrix}$$

satisfies the conditions described in (1) and $S\bar{S}=E$. This is shown as follows: First, we deform $E-S_{11}\bar{S}_{11}$ as

$$E-S_{11}\bar{S}_{11}=2(E+Z)^{-1}(Z+\bar{Z})(E+\bar{Z})^{-1}$$

and factorize the elements of D properly, namely $D=F\bar{F}$. Now put

$$\tilde{S}_{12}=2(E+Z)^{-1}AF,\quad \tilde{S}_{21}=\tilde{S}'_{12},$$
$$\tilde{S}_{22}=-\tilde{S}'_{12}\bar{S}_{11}\tilde{S}'^{-1}_{12},$$

then $$\tilde{S}=\begin{bmatrix} S_{11} & \tilde{S}_{12} \\ \tilde{S}_{21} & \tilde{S}_{22} \end{bmatrix}$$

will be proved to be symmetric and its elements are rational functions and also $\tilde{S}\bar{\tilde{S}}=E$. Next we can prove the existence of innumerable n order unitary matrices Σ which satisfy the following relation. Namely matrix S defined by

$$S=N'\tilde{S}N \quad (N=E+\Sigma)$$

is the desired one.

In the case of $\rho<n$, it will be effective to use the method of limitation as Oono has adopted.

(4) As to equivalent circuits, we can state similar arguments as Belevitch's letter, but there is a question whether it is possible or not that all equivalent n order efficiency matrices are transformed one another by unitary transformation corresponding to connections of physical networks.

References

1) Kiyasu-Z. and others: Denkitûsin Gakkai-Zassi, 1940, 541.

2) W. Cauer, Theorie der linearen Wechselstromschaltungen, 1941.

J. PHYS. SOC. JAPAN 7 (1952) 114–115

On the Dipping Counter

By Tadashi OSHIDA, Hirohide MIWA and Toshio KATO

Kobe Kogyo Corporation, Okubo Factory, Akashi, Hyogo, Japan

(Received November 29, 1951)

Radioactive Isotopes have been imported from U.S.A. and tracer technique has made a remarkable progress in these several years. The necessity of the dipping type Geiger Mueller counter increased rapidly which enables the experimenters to perform their tracer work more easily by its large effective solid angle and easy preparation of the active samples as liquid form.

The construction method of a thin window is of great problem. A conventional mica window counter can not be used as a dipping type, because the special glass of mica to glass seal can not stand the attack of strong chemicals. Several papers were published on that construction. For example, the one of G.

Hevesy's[1] is typical (See Fig. 1 (a)), where thin glass cylinder is employed as a radiation penetrating window and near the end of the window its thickness increases gradually as going apart from the window to the other parts. So, whatever method may be employed, it will be very difficult to get the desired thickness, diameter and length of the window from the melting glass or other halfdone states. This demands the highest practice for the most skilled worker and the shrinkage of this production process would become very poor. But we have tried successfully to find a new method of construction which meets our demand better. We shall illustrate our method in the followings.

The detail is shown in Fig. 1 (b). Judging from the present glass work technique it is rather easy to get the uniform glass cylinder, 20–30 mg/cm^2 thick, 10 mm diameter and 50–100 mm long, but much care must be taken of the handling of that fragile glass tube. The desired length of the tube can be cut by fusing away the part that touches the hot nichrome wire, which must be stretched straight and moved very slowly perpendicular to the axis of the tube while cutting.

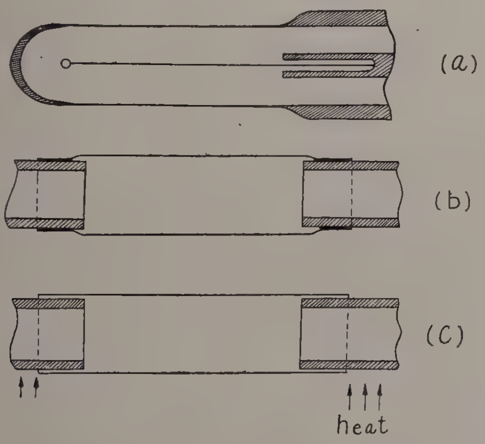

Fig. 1. Construction of a thin window.

After its thickness is examined, the previously prepared thick tube to be joined is inserted into the above mentioned thin tube as shown in Fig. 1 (c). And a small part of thick tube just outside of the end of the thin one is heated locally and uniformly by rotating them near the burner flame or the electric heater. Meanwhile the part near the end of the thick tube, that is, a little inner part of the thin one from its end must be kept carefully from heating. So, only the end of the thin tube becomes melted and shrinks narrower and narrower by surface tension until it touches the thick one. Then both tubes must be melted together for a short time enough to ensure the hermetic seal. After seal is completed the temperature should be decreased slowly and the whole process of annealing must be done without overheating and deformation of the thin tube. After same process is carried out for the other end, the perfect thin window part is obtained. Hereafter the conventional technique of glass work can be used, but further attention must be paid to avoid the damage of the fragile thin window.

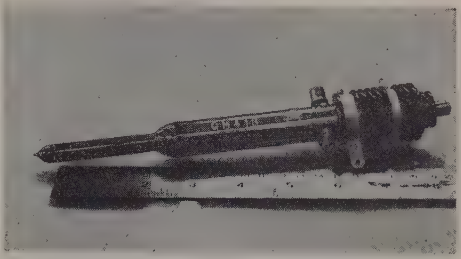

Fig. 2. The dipping counter constructed by us.

An example composed of this type of a window is photographed in Fig. 2 and this type is modeled as GM-134, where the copper cathode is chemically plated on the inner surface of the glass. A vacuum evaporated cathode proved to fail to connect with the conductive layer on the thick tube owing to the shadow formed by the thick tube ends (See Fig. 1 (b)). Special consideration is necessary to ensure the good insulation between cathode and anode for the dipping use. Particular design of the base and the guardring method as seen in Fig. 2, are very effective for this purpose. The anode is 0.05 mm ϕ tungsten wire and starting voltage is nearly 1000 V. Plateau length is about 150 Volts, back ground count is about 30 per minute and window thickness is 26 mg/cm^2, the absorption of which proved to follow the equation of R. D. Evance for most of β emitters.

Reference

1) G. Hevesy, Radioactive Indicators, P. 71, Interscience Publishers.

J. PHYS. SOC. JAPAN **7** (1952) 115–117

The Magnetoeffect in Germanium Point Contacts

By Masao TOMURA and Yukiaki ABIKO
Institute of Polytechnics of Osaka City University

(Received, November 30, 1951)

When an n-type germanium point contact is placed in magnetic fields in such positions that the direction of the current is perpendicular to the fields; the currents of the forward direction increase or decrease corresponding to the directions of the magnetic field around the axis of the electric field as shown in Fig. 1. The ratios of the increment or decrement of the flow to the original flow $\Delta I/I$ are linear with the magnetic field H approximately. (See Fig. 2). The magnitude of $\Delta I/I$ decreases abruptly when the forward bias voltage becomes smaller than about 0.5 volts as shown in Fig. 3.

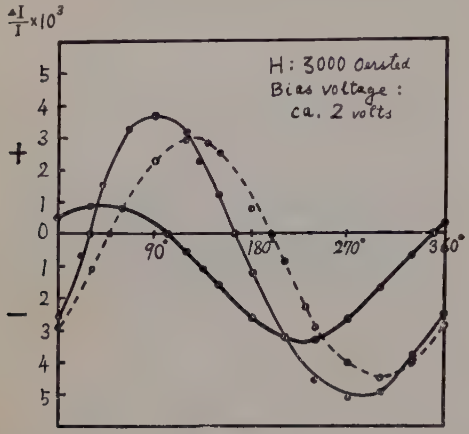

Fig. 1.

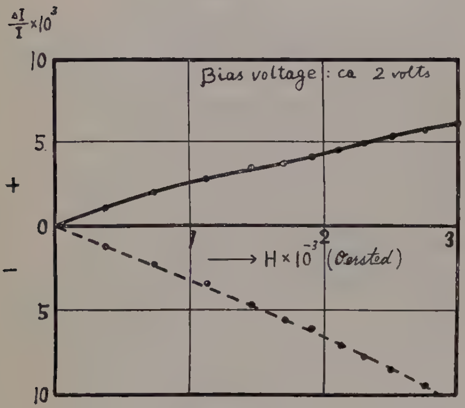

Fig. 2.

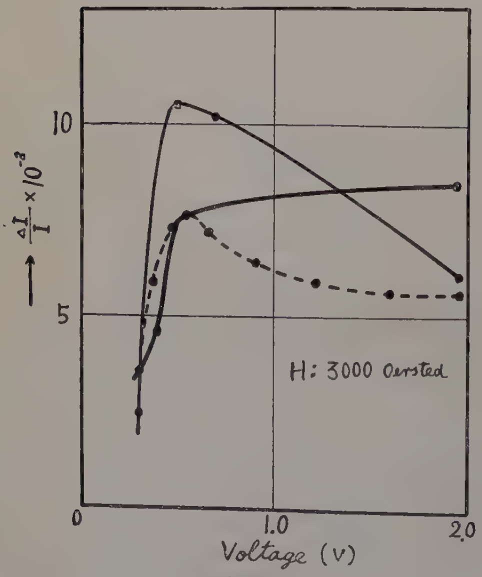

Fig. 3.

These effects are not the so-called magnetoresistance effect[1], for the latter has such characteristics that $\Delta I/I$ is proportional to the square of H in the region of the present measurements and is always negative[1]. Furthermore, the maximum value of $\Delta I/I$ of our effect is larger than the magnetoresistance effect by about ten times.

It has been known that holes of germanium injected from the metal whisker disappear when they collide with defects on the surface of germanium[2]. This process of surface trapping of injected holes may well explain the above new effect of the germanium point contact in the magnetic field. The path of injected holes is bent in the transverse magnetic field by the Hall angle θ which is given by the next equation.

$$\theta = 10^{-8}(3\pi/8)\mu H \quad \text{radian.}$$

Here μ is the mobility of holes (cm²/volt·sec) and H in oersted. If the path of holes is bent onto the surface defects, the current diminishes due to the surface trapping; and if the primary flow bends away from the surface defects, it increases on the contrary.

On the other hand, the dependence of $\Delta I/I$ on the bias voltage and the absence of the effect in the backward direction mean that the above process takes place in the barrier layer, because the change of the electric field in the bulk germanium does not alter the Hall angle for a given magnetic field. The change of bias voltage smaller than 0.5 volts, that is about the contact potential of the germanium detector, induces the change of the internal field in the barrier layer, as the thickness of the barrier layer is so thin that the internal field in that layer reaches about $10^4 \sim 10^5$ volt/cm at the bias voltages smaller than the contact potential. The injected holes accelerated by such high fields gain larger energies than the thermal energy, and their mobility becomes smaller than the normal one at a lower field[3]. Thus the bending of the path of holes decreases and the magnetoeffect becomes smaller at lower bias voltages. In the backward direction the internal field in the barrier layer is much larger and the effect will be much smaller. Thus we can conclude that the surface defects which act as trapping defects may exist in the neighbourhood of the barrier layer. An alternative explanation of the absence of the effect in the backward direction may be obtained from the fact that holes are not emitted from the base metal electrode[4].

The surface of the detector is perhaps very rough in the dimension of the thickness of the barrier layer as shown in Fig. 4. A part of the injected holes from the whisker will collide with or avoid the depressed part of the surface in the neighbourhood of the barrier layer, if the direction of the magnetic field is appropriate.

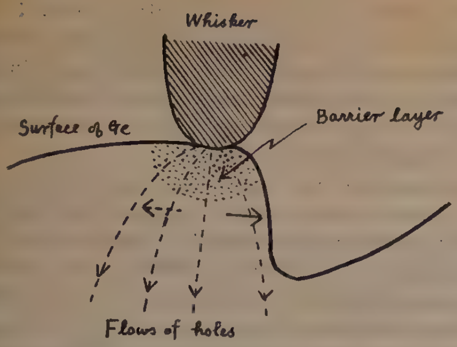

Fig. 4. Proposed structure of the surface of the germanium detector. If the flow of holes bends to right (solid arrow), the current diminishes; and if to left (dotted arrow), it increases.

In the present case, θ is in the order of 10^{-2} radian. The quantity of holes which bend onto or away from the surface defects will be proportional to H approximately for such a small value of θ.

The chance that the whisker sets itself near one depressed part of the surface of germanium may be great, resulting one maximum and minimum of $\Delta I/I$ through the total angle of 360° around the axis of the current flow.

References

1) I. Estermann and A. Foner: Phys. Rev. **79** (1950) 365.
2) G. R. Hayrres and W. Shockley: Phy. Rev. **81** (1941) 835.
3) F. Seitz: Phys. Rev. **76** (1949) 1376.
4) W. Shockley, G. L. Pearson and J. R. Haynes: Bell Syst. Tech. J. **28** (1949) 344.

J. PHYS. SOC. JAPAN **7** (1952) 117–118

Dispersion of Ultrasonic Waves in Ethylene

By Otohiko NOMOTO, Takuro IKEDA and Tadashi KISHIMOTO

Kobayasi Institute of Physical Research, Kokubunji, Tokyo

(Read November 2, 1950; Received December 4, 1951)

The molecular dispersion of ultrasonic velocity in ethylene has been investigated by Richards and Reid1)2) already. Their measurements, however, are performed at 94 kc/sec and 476 kc/sec and lack the upper part of the dispersion curve. Moreover, molecular vibration data were not available at that time, so that the value of the vibrational specific heat was not to be calculated theoretically. We performed the dispersion measurement on ethylene in order to supplement the result of Richards and Reid concerning these points.

Ethylene was generated by dehydration of absolute alcohol, previously deprived of water by sodium, by phosphoric acid at 195°∼205°C and deprived of the impurities, CO_2, O_2, and water vapour in streaming slowly through two ice-cooled traps, three washing bottles containing solutions of potassium hydroxide, pyrogallol, and concentrated sulphric acid, three calcium chloride tubes, two phosphorus pentoxide tubes and two dry-ice traps. The volumetric analysis indicated 0.7∼0.85% impurity (nitrogen). Mass-spectrum analysis performed by Dr. Toyozo Kambara revealed other hydrocarbons of higher molecular weight, but this content was reduced to a trace by maintaining the temperature of the generating apparatus in the above-mentioned range. The overall impurity content was presumably about 1%.

The measurements were performed at two frequencies 0.4760 Mc/sec and 1.42261 Mc/sec, which were determined by hetrodyne method with reference to two standard quartz oscillators of 470.00 kc/sec and 1430.00 kc/sec respectively, and at various pressures ranging between 60 mm and 760 mm Hg employing an ultrasonic interferometer with Pierce-type circuit.

Dispersion curves velocity *vs.* log (frequency/pressure) were obtained for the two frequencies employed assuming the Van der Waals' equation of state for ethylene and employing the dispersion formula for a Van der Waals' gas obtained by one of the authors3)

$$\begin{aligned} V^2{}_{\text{real}} = \frac{RT}{M}\Bigg[&\left\{1-\frac{2p}{RT}\left(\frac{a}{RT}-b\right)\right\} \\ &+\left(1+\frac{2p}{RT}b\right)\frac{R}{C_0} \\ &+\left(1+\frac{2p}{RT}b\right)\frac{RC_s}{C_0C_\infty}\frac{(\omega/p)^2\tau_0^2}{1+(\omega/p)^2\tau_0^2} \\ &+\frac{1}{4}\left\{3-\frac{2p}{RT}\left(\frac{a}{RT}\frac{C_0}{C_0+R}-3b\right)\right\} \\ &\times\frac{R^2C_s^2}{(C_0+R)C_0C_\infty^2}\frac{(\omega/p)^2\tau_0^2}{1+(\omega/p)^2\tau_0^2}\Bigg] \end{aligned} \tag{1}$$

where V means the velocity of sound at pressure p and circular frequency $\omega(=2\pi f)$, M the molecular weight, and C_0 the molar specific heat at constant volume at sufficiently low frequency, C_∞ the molar specific heat at constant volume at sufficiently high frequency, C_s the molar vibrational specific heat, and τ_0 the relaxation time of vibrational energy at atmospheric pressure, which is related with the 'period of adjustment of the vibrational energy' β_0 by the formula

$$\tau_0=\beta_0 C_\infty/C_0 \tag{2}$$

(τ_0 means the relaxation time to follow the change of thermal equilibrium at constant volume, i.e., after ending of an instantaneous volume change, while the commonly used quantity β_0 means the relaxation time to follow the change of thermal equilibrium in an sinusoidal volume change, i.e., accompanying a sinusoidal change of the equilibrium state in a sound wave (cf. Nomoto[4]).

Dispersion curve for the hypothetical 'ideal gas' ethylene was computed by the formula given by one of the authors[5)3)]

$$V_{\text{ideal}}^2=\frac{RT}{M}\left[1+\frac{R}{C_0}+\frac{RC_s}{C_0C_\infty}\frac{(\omega/p)^2\tau_0^2}{1+(\omega/p)^2\tau_0^2}\right.$$
$$\left.+\frac{3}{4}\frac{R^2C_s^2}{(C_0+R)C_0C_\infty^2}\frac{(\omega/p)^2\tau_0^2}{\{1+(\omega/p)^2\tau_0^2\}^2}\right] \quad (3)$$

Squares of the experimental velocity data were multiplied by the correction factor

$$k=V^2{}_{\text{ideal}}/V^2{}_{\text{real}} \quad (4)$$

to make comparison with the 'ideal gas' dispersion curve. Eq. (3) gives a common dispersion curve as function of (f/p) for all the frequencies employed.

These calculations were performed by employing the values of the specific heats $C_\infty=3R=5.96$ cal/mole, $C_0=C_\infty+C_s=8.41$ cal/mole, $C_s=1.235R=2.45$ cal/mole, and the relaxation time of the vibrational energy

$$\tau_0=1.52\times10^{-7}\,\text{sec} \quad (5)$$

(at 27° and atmospheric pressure).

The vibrational specific heat was computed by the Planck-Einstein's formula employing the molecular vibrational data of Arnett and Crawford[6]. In computing the velocity for the real gas we employed the same values of the Van der Waals' constants as employed by Richards and Reid: $a=4.47\times10^6$ cm^6 atm./mole$=4.53\times10^{12}$ cm^4 dyne/mole, and $b=57.14$. The value of τ_0 was determined so as to fit the experimental data sufficiently closely. We obtain from this the value of the 'period of adjustment of vibrational energy' for ethylene

$$\beta_0=2.15\times10^{-7}\,\text{sec}$$

(at 27°C and atmospheric pressure), (6)

which compares with the value obtained by Richards and Reid $\beta_0=2.38\times10^{-7}$ sec (at 30°C) fairly well.

The accompanying figure represents the dispersion curve for the 'ideal gas' ethylene. Rough estimate of the absorption coefficient was also performed and indicated the existence of an absorption peak (for the absorption coefficient per wave-length) nearly in the middle of the dispersion region, although quantitative absorption measurements are not to be performed by Pierce-interferometer method.

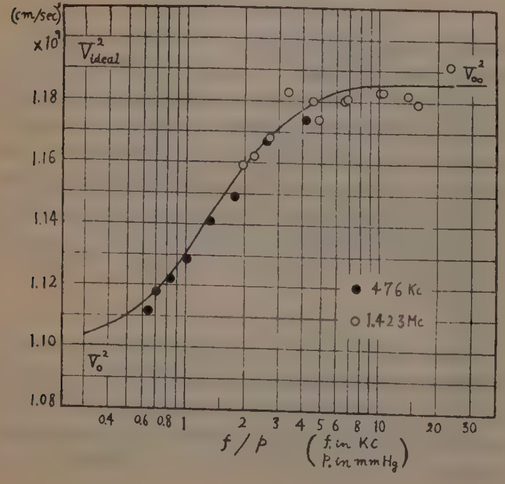

In conclusion, we express our hearty thanks to Prof. Kenzi Tamaru of the Yokohama University for kindly instructing the method of generation of the ethylene gas, to Dr. Toyozo Kambara of the Central Research Institute, Hitachi Seisakujo Co., for obtaining and interpreting the mass-spectra of the sample gases, to Prof. Seiichi Okui of the Pharmaceutical Institute, Medical Faculty, Tokyo University, for purification and preparation of the chemicals, and to Prof. San'ichiro Mizushima of Tokyo University for indicating us the molecular vibrational data of ethylene and giving kind advices. Financial Aid for this research was supplied by the Ministry of Education in a Grant in Aid of Research. Detailed account of this research will be published in Bulletin of the Kobayasi Institute of Physical Research.

References

1) W. T. Richards and J. A. Reid, J. Chem. Phys. **2** (1934) 206.
2) W. T. Richards, J. Chem. Phys. **4** (1936) 561.
3) O. Nomoto, Bull. Kobayasi Inst. Phys. Res. **1** (1951) 162.
4) O. Nomoto, Proc. Phys.-Math. Soc. Japan **22** (1940) 77.
5) O. Nomoto, Kagaku (Science, in Japanese) **18** (1948) 473.
6) R. L. Arnett and B. L. Crawford, J. Chem. Phys. **18** (1950) 118.

J. PHYS. SOC. JAPAN **7** (1952) 118-119

Micro Analysis of Solutions by Arc of Alternating Currents

By Tasaburô YAMAGUTI and Minoru NISHINO

Department of Physics, University of Chiba and University of Ibaraki

(Received November 15, 1951)

The purpose of the present work is to detect minimal quantities of the elements contained in a solution by the spectrum analysis of an arc discharge passing through the solution filling the gap between electrodes, which are connected with a source of alternating voltage of 100 volts.

A satisfactory stable arc was passed between the electrodes by a method of superposition of high frequency oscillations as is already described in a preveous paper[1], The electric circuit is given in the

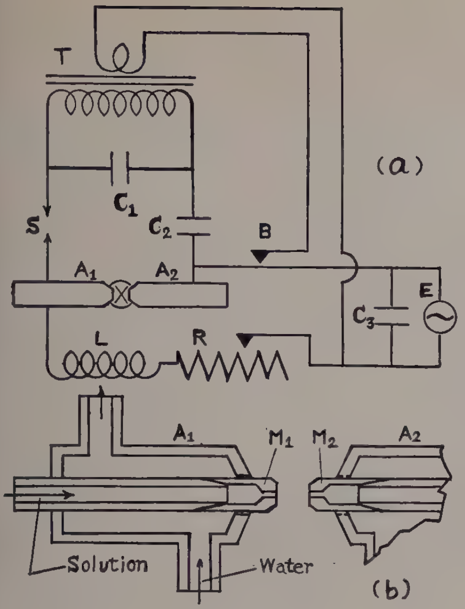

Fig. 1.

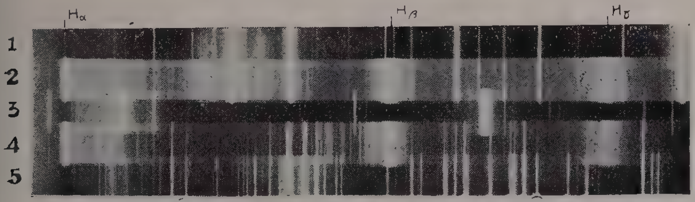

Fig. 2. Spectrograms of arcs, formed between silver electrodes (1), silver electrodes covered by LiCl solution (2), carbon containing LiCl powder (3), copper covered by LiCl solution (4), and copper electrodes (5).

Fig. 1a. The Fig. 1b shows a section of the electrodes. Tops M_1, M_2 made of copper or silver of the electrodes can be renewed, if necessary, by removing them from the bodies of the electrodes. Each of the tops has a canal along the central axis, through which the solution spouts out and covers the tops. By the cooling effect of the solution spouting out and of running water, the tops keep low temperatures and do not change their shapes even when the arc of 8 amperes is passing between them. A source of constant luminosity of the arc light thus obtained was used for the spectrum analysis by means of both the constant deviation spectrograph and the quartz spectrograph. The exposure time for minimal detection is two minutes and volumes of the solution flowing out in this time interval are 30 cc.

Substances examined are dilute solution of $LiNO_3$, LiCl, $CdCl_2$ and KCl. The spectrum of a solution of $LiNO_3$ obtained with the use of copper electrodes shows both the spark and the arc lines of copper, lithium, nitrogen, oxygen and hydrogen. Balmer lines H_α, H_β and H_γ have strong intensities and remarkable breadths. Origins of the broadening are not yet investigated quantitatively. They may be attributed, however, to the pressure effect and Stark effect on the illuminating atoms by fields of neighbouring atoms. The Fig. 2 is the spectrogram of a solution of LiCl, concentration of which being 1 mgr. per 100 cc.

Amount easily detectable by the present method for lithium, cadmium and potassium are given in the table with those obtained by Beckman flame spectrophotometer²⁾ and the inorganic analysis with organic reagents³⁾. A rather large value for potassium in the present method is due to the fact that Oriental Hyper Sensitive Panchromatic Plates used in the experiment are not sensitive for potassium lines of 6939 and 6911 A. The present method for spectrum analysis of solutions will be useful to medical science, chemical industry and others.

Table. Amount Easily Detectable in ppm.

Elements	The present method	Beckman flame photometer	Chemical method
Li	0.01	0.05	6.6
Cd	0.00006	500	0.002
K	500	0.05	0.8

References

1) T. Yamaguti and M. Nishino: J. Phys. Soc. Jap. **6** (1951) 127.
2. H. H. Willard, L. L. Merritt and J. A. Dean: Instrumental Method of Analysis, 1948.
3) The "Union internationale de Chemie": Tables of Reagents for Inorganic Analysis, 1937.

J. Phys. Soc. Japan 7 (1952) 119–121

On some Hypothetical Gases

By Nobuo Inoue
Faculty of Engineering, Doshisha University, Kyoto

(Received November 26, 1951)

In the mechanics of non-viscous compressible fluids, two kinds of hypothetical gases have been introduced, one of which has transformed the fundamental equation into such simple forms as to be accessible to analytical treatments, without violating the essential properties of the equation, and the other

no.	pressure-density relations	velocity-stress correspondences	yield conditions	types
"plane stress" problem of the mass of sand				
1	$p/\rho^\gamma=\mathrm{const}$ $\gamma=\sin\phi$	$q/q_0=(\sigma_0/\sigma)^{\frac{1-\sin\phi}{2\sin\phi}}$, $\theta=\alpha_1$	$k=\|\sigma\|\sin\phi$	supersonic; $M=2^{\frac{1}{2}}(1-\gamma)^{-\frac{1}{2}}$
2	$\gamma=-\sin\phi$	$q/q_0=(\sigma/\sigma_0)^{\frac{1+\sin\phi}{2\sin\phi}}$, $\theta=\alpha_2$		
"plane strain" problem of the perfectly plastic material				
3	$p/\log\rho=\mathrm{const}$	$q/q_0=\exp[(\sigma_0-\sigma)/(2\mathrm{K})]$, $\theta=\alpha_1$	$k=K$	supersonic; $M=2^{\frac{1}{2}}$
4		$q/q_0=\exp[(\sigma-\sigma_0)/(2\mathrm{K})]$, $\theta=\alpha_2$		
"plane stress" problem of the perfectly plastic material				
5	$p/\log\rho=\mathrm{const}$	$q/q_0=\exp[(\sigma_0-\sigma)/(2\mathrm{K})]$, $\theta=\alpha_1$	$k=K$, $\|\sigma\|\leqq K$	supersonic; $M=2^{\frac{1}{2}}$
6		$q/q_0=\exp[(\sigma-\sigma_0)/(2\mathrm{K})]$, $\theta=\alpha_2$		
7	$p\rho=\mathrm{const}$	$q/q_0=(2\mathrm{K}-\sigma)/(2\mathrm{K}-\sigma_0)$, $\theta=\alpha_1$	$\sigma_1=2\mathrm{K}$, $2\mathrm{K}\geqq\sigma>\mathrm{K}$	sonic; $M=1$
8		$q/q_0=(2\mathrm{K}+\sigma)/(2\mathrm{K}+\sigma_0)$, $\theta=\alpha_2$	$\sigma_2=-2\mathrm{K}$, $-2\mathrm{K}\leqq\sigma\leqq-\mathrm{K}$	
9	$p/\sin\left(\frac{1}{\sqrt{3}}\log\rho\right)=\mathrm{const}$	$\frac{q}{q_0}=\left[\frac{4\mathrm{K}^2-\sigma^2}{4\mathrm{K}^2-\sigma_0^2}\right]^{\frac{1}{4}}\exp\left[\frac{\sqrt{3}}{2}\left(\sin^{-1}\frac{\sigma_0}{2\mathrm{K}}-\sin^{-1}\frac{\sigma}{2\mathrm{K}}\right)\right]$, $\theta=\alpha_1$	$2\mathrm{K}\geqq\sigma>-\sqrt{3}\mathrm{K}$ $\sigma_1^2-\sigma_1\sigma_2+\sigma_2^2=4\mathrm{K}^2$,	supersonic where $\|\sigma\|<\sqrt{3}\mathrm{K}$, sonic where $\|\sigma\|=\sqrt{3}\mathrm{K}$, and subsonic where $2\mathrm{K}\geqq\|\sigma\|>\sqrt{3}\mathrm{K}$
10		$\frac{q}{q_0}=\left[\frac{4\mathrm{K}^2-\sigma^2}{4\mathrm{K}^2-\sigma_0^2}\right]^{\frac{1}{4}}\exp\left[\frac{\sqrt{3}}{2}\left(\sin^{-1}\frac{\sigma}{2\mathrm{K}}-\sin^{-1}\frac{\sigma_0}{2\mathrm{K}}\right)\right]$, $\theta=\alpha_2$	$-2\mathrm{K}\leqq\sigma<\sqrt{3}\mathrm{K}$	
11	$p(\rho+1)^2(\rho-1)^{-1}$ $\times\left(\rho+\frac{1}{3}\right)^{-1}=\mathrm{const}$	$\frac{q}{q_0}=\frac{(1+\sqrt{2})\mathrm{K}-\sigma}{(1+\sqrt{2})\mathrm{K}-\sigma_0}$, $\theta=\alpha_1$	$(1+\sqrt{2})\mathrm{K}\geqq\sigma>-(1+\sqrt{2})\mathrm{K}$ $2k=\frac{\mathrm{K}}{1+\sqrt{2}}\left[(1+\sqrt{2})^2-\left(\frac{\sigma}{\mathrm{K}}\right)^2\right]$,	supersonic where $\|\sigma\|<(1+\sqrt{2})\mathrm{K}$, and sonic where $\|\sigma\|=(1+\sqrt{2})\mathrm{K}$
12		$\frac{q}{q_0}=\frac{(1+\sqrt{2})\mathrm{K}+\sigma}{(1+\sqrt{2})\mathrm{K}+\sigma_0}$, $\theta=\alpha_2$	$-(1+\sqrt{2})\mathrm{K}\leqq\sigma<(1+\sqrt{2})\mathrm{K}$	

has yielded a mechanical analogy of the gas flow to a water flow. As a typical example of the former we can point out a gas, the specific-hearts-ratio γ of which is -1, and a gas with $\gamma=2$ represents the latter. However, there are another kind of hypothetical gases, which deform the fundamental characteristics of the real gas wholly in some points, and transform the gasdynamics into other kinds of mechanics.

Hypothetical gases, which we introduce here, differ from the real gas in the following two points: first the local sound velocity of our gas at rest is null in each case, and second, γ is not equal to 1.405, the value for the real gas. If p, ρ, q, θ denote the pressure, density, magnitude of the velocity vector, and the angle between the x-axis and the velocity vector respectively in our hypothetical gases, and σ_1, σ_2 denote the magnitudes of the algebraically greater and smaller principal stresses, α_1, α_2 the angle between the x-axis and the directions of the greater and smaller principal stresses respectively in a perfectly plastic material or in a mass of sand, and $\sigma=(\sigma_1+\sigma_2)/2$, $k=(\sigma_1-\sigma_2)/2$, it will be seen after some calculations that a two-dimensional steady irrotational flow of our hypothetical gases represents a statically determinate state of stress in the plastic masses, as is shown diagrammatically in the above indicated table, where ϕ is the angle of internal friction of the sand, 2K is the yield stress of the perfectly plastic material in tension, and the suffix 0 means that the values with it are to be taken at an arbitrary but fixed point. In the case of the mass of sand, weight of the sand is neglected, considering external loads to be sufficiently large. For example, a two-dimensional irrotational flow of a hypothetical gas, the pressure-density relation of which is given by $p/\rho^{\sin\phi}=\mathrm{const.}$, becomes a state of stress in the mass of sand, the yield condition of which is given by $\sigma_1-\sigma_2$

$=2|\sigma|\sin\phi$, when the gas velocity is translated into the plastic stress by a relation $q/q_0=(\sigma_0/\sigma)^{\frac{1-\sin\phi}{2\sin\phi}}$, $\theta=\alpha_1$. The gas flow is everywhere supersonic, having the same local Mach number $2^{\frac{1}{2}}(1-\gamma)^{-\frac{1}{2}}$ throughout it. The others are to be understood in the same way.

The analogies (1)~(12) can be applied also to a body of revolution, if the x-axis is taken to be the axis of symmetry, and the xy-plane to be the meridian plane, assuming that a plastic principal stress, directed perpendicularly to the meridian plane, is equal to the greater or smaller of the two principal stresses, lying in the meridian plane, according as the analogies (1),(3),(5),(7),(9),(11) or (2),(4),(6), (8),(10),(12) are employed.

By making use of the above mentioned analogies, the useful methods of the gasdynamics, such as the hodograph method of Chaplygin, have been able to be introduced into the theory of plasticity[1)2)] and the soil mechanics, and their general solutions have been obtained, as will be seen in our forthcoming papers.

References

1) N. Inoue: J. Phys. Soc. Japan **6** (1951) 460.
2) N. Inoue: Doshisha Engineering Review **2** (1951) 1 (in Japanese).

J. PHYS. SOC. JAPAN **7** (1952) 121–122

The Pulse Size Distribution of the Pre-breakdown Noise

By Hazimu KAWAMURA and Masami ONUKI

Department of Science and Industry,
Osaka City University, Osaka

(Received October 31, 1951)

Previously we have measured the mean size of the electron avalanches at the pre-breakdown region[1)]. The present report is concerned with the measurement of the distribution of these avalanche sizes.

The pulse voltage appearing at resistance R, which was inserted in a high voltage circuit in series with the specimen, was amplified by a seven stage feed back linear amplifier whose gain was 80 db up to 3.5 mc. The amplified pulses which are greater than some desired value were picked up by a discriminator and counted by a counting rate meter. The apparatus was checked with shot noise, and it was confirmed that the distribution of the noise pulse sizes is given by a normal distribution $p=1/\tau\exp(-V^2/2\langle V^2\rangle)$, and that $\langle V^2\rangle$ in the above equation coinsides with the calculated value within the limit of 16% error. If a charge en flow through resistance R in a sufficiently short time as compared with the response time of the amplifier, the amplified pulse voltage is given by

$$V=2enR\int_0^\infty G(\nu)/[1+(2\pi\nu Rc)^2]d\nu,$$

where $G(\nu)$ is the gain of the amplifier. Thus we can calculate the 'effective' avalanche size n from V.

The specimens were muscovites (Indian micas) about $1.5\sim3.0\times10^{-4}$ cm in thickness. The processing of the specimen was the same as the previous report. Applying high voltages near the breakdown limit, the integrated distribution $\nu(n)$ of the avalanche size was measured, and plotted in log-log scale as in Fig. 1. The distributions seem to be of two parts. The size of the distribution for the larger n differs for the different specimen as shown in the figures, and also this part predominates during the change of the applied voltage and decreases when it is set constant. Therefore, this part may be ascribed to the noise of Schoenfeld type[2)] due to the sudden discharge of the local space charge trapped between the specimen and the electrode or in some defect in the interior of the specimen. Replotting the same points in semi-log scale we obtain the almost straight lines for small n as in Fig. 2.

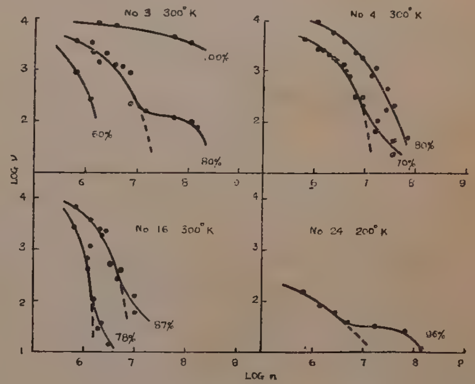

Fig. 1.

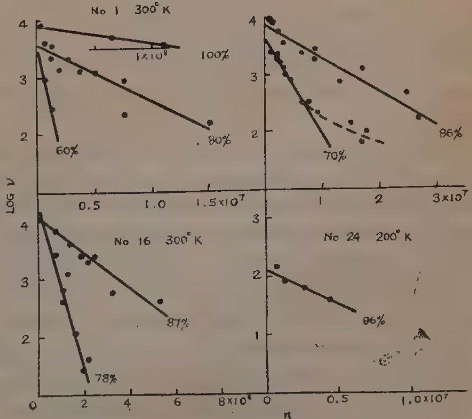

Fig. 2

If an electron produces one secondary electron in the path length λ on the average, the probability that one electron is multiplied to n electrons after the path L is given by[3]

$$P(L)=\exp(-L/\lambda)[1-\exp(-L/\lambda)]^{n-1}.$$

As the average of n is given by $\exp(L/\lambda)$, the above equation is reduced to $P(L)=1/\langle n\rangle(1-1/\langle n\rangle)^{n-1}$. This equation is further reduced to

$$P=1/\langle n\rangle\exp(-n/\langle n\rangle),$$

by the assumption $n\gg 1$. If the number of the starting electrons is $\nu_0$1/sec, the integrated distribution of the avalanche size is given by

$$\nu(n)=\nu_0\int_n^\infty Pdn=\nu_0\exp(-n/\langle n\rangle).$$

ν_0 and $\langle n\rangle$ can be determined graphically from the curves of Fig. 2. The measurements were done for various specimens under various field strengths at 300°K and 200°K (dry ice). Analysing these data by the above method, we obtain Fig. 3. ν_0, $\langle n\rangle$ and the dc current i_0 at the breakdown field strength obtained by the extraporation were given in the following table.

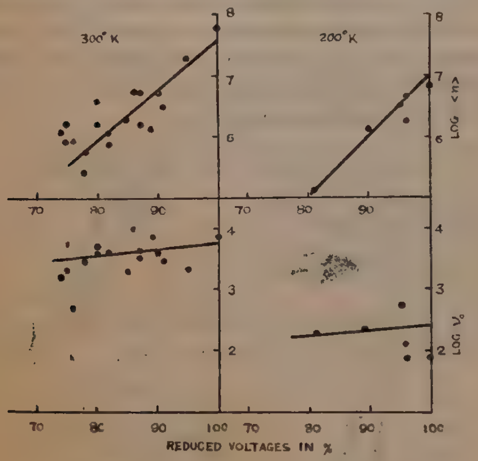

Fig. 3.

	$\langle n\rangle$	ν_0	$i_0(A)$	$e\nu_0\langle n\rangle(A)$
300°K	3×10^7	6×10^3	5.7×10^{-5}	2.8×10^{-8}
200°K	1×10^7	3×10^2	3.0×10^{-6}	4.6×10^{-10}

ν_0 does not change remarkablly with the field strength and its temperature variation is almost equal to the temperature variation of i_0, which seems to be the indication that the starting electrons of the avalanches are the conduction electrons in the dielectrics. But the current $e\nu_0\langle n\rangle$ due to the avalanches is only 10^{-3}~10^{-4} times i_0. Therefore, it could be assumed that the occurence of avalanches is limited to an extreme locality. The average size of avalanches at breakdown field is in the order of 10^7 which is far smaller than 10^9 obtained in the previous study[1]. This may be due to the fact that the Schoenfeld noise was not eliminated in the last study.

References

1) H. Kawamura, M. Onuki: J. Phys. Soc. Jap. **6** (1951) 283.
2) H. Schoenfeld: Ann. d. Phys. **19** (1934) 733.
3) W. H. Furry: Phys. Rev. **52** (1937) 569.

J. PHYS. SOC. JAPAN **7** (1952) 122–123

Failure and Fracture of Metals as Rate Processes

By Takeo YOKOBORI

Institute of Science and Technology, University of Tokyo

(Received December 13, 1951)

The yielding may be said to correspond to the nucleation, the growth and the movement of dislocations. In this note, a dislocation movement in the case of failure such as yielding and the beginning state of necking, and the growth of a crack nucleus in the fracture were considered as rate-determing respectively. As to the failure, the chance m that a dislocation is activated per unit time is[1]

$$m=(2ZkT/h)\exp(-\Delta H/kT)\exp(\Delta\phi/k)\sinh(\alpha S/kT), \tag{1}$$

the notations being the same as the preceding report[2][7]. In the case when $S=vt$, the following two approaches may be possible.

(i) If the phenomena were regarded as a Markoff process[2], the probability function is,

$$qdx=K\sinh x\exp[K(1-\cosh x)]dx \tag{2}$$

where $x=\alpha vt/kT=\alpha S/kT$. When $\alpha S_m/kT\gg 1$, the strength may be expected to correspond to the most probable value S_m in Eq. (2). Hence,

$$S_m=(kT/\alpha)([\log v+\Delta H/kT+2\log(1/T) \\ -\log Z-\Delta\phi/k+\log(\alpha h/k^2)] \tag{3}$$

(ii) In another approch, m is considered to correspond to $-dz/dt$. Hence, from Eq. (1)

$$-\int_z^{z-1}dz/z=(2kT/h)\exp(-\Delta H/kT)\exp(\Delta\phi/k) \\ \times\int_0^t\sinh(\alpha vt/kT)dt \tag{4}$$

When $\alpha S_m/kT\gg 1$, the same equation as (3) is obtained.

In the case of brittle fracture, the tensile stress F may be used in stead of shearing stress S used above. From Eq. (3), we can obtain

$$S_m\propto\exp[v\exp(\Delta H/kT)] \tag{5}$$

in stead of $S_m\propto[v\exp(\Delta f/kT]^T$ obtained as nucleation processes[2]. Experimental data obtained by many investigators[3][4][5] were plotted in Fig. 1, S_m/T in ordinates, $1/T$ in abscissa. Since Eq. (3) assumes the form $S_m/T\propto(\Delta H/\alpha T+\text{const.})$, the theory seems to be in good agreement with experiments on harder metals. The derivative of each curve with respect to $1/T$ gives $\Delta H/\alpha$. If S_m versus $\log v$ curve is deter-

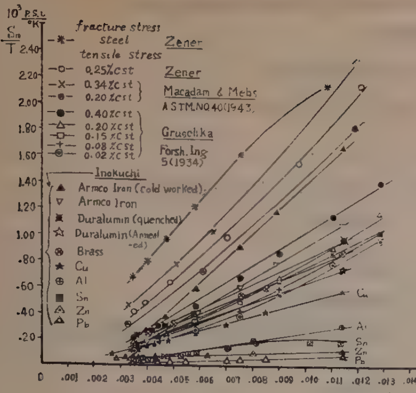

Fig. 1.

mined experimentally, α can be obtained from the tangent of the curve according to Eq. (3). ΔH can also be obtained from $\Delta H/\alpha$ using this value of α. In some of curves in Fig. 1, the inclination increases slightly with respect to $1/T$, and it leads to the indication that α increases with temperature similarly as in creep strain rate⁶⁾ and creep fracture⁷⁾.

The fluctuation characteristics of strength²⁾ can also be understand from this standpoint.

The creep fracture after necking occurred seems to be better explained as the growth process of a crack nucleus than as the nucleation process⁷⁾. In this case,

$$\bar{t}=1/m_2=(h/2Z_2kT)\sinh[(\Delta f_2^*-\alpha_2F)/kT] \quad (6)$$

This gives $F-\log\bar{t}$ relation which is also in good agreement with the experiments⁷⁾. In conclusion the author expresses his cordial thanks to Prof. M. Hirata for his continuous encouragement and guidance.

References

1) W. Kauzmann: Trans. Am. Inst. Min. Met. Eng. **143** (1941) 57.

2) T. Yokobori: J. Phys. Soc. Japan **7** (1952) 44.

3) C. Zener: Rev. Mod. Phys. **17** (1945) 20.

4) C. Zener: J. App. Phys. **15** (1944) 22.

5) T. Inokuchi: Kinzoku-no-Kenkyu (in Japanese) **14** (1927) 447.

6) S. Dushman etal: J. App. Phys. **15** (1944) 108.

7) T. Yokobori: J. Phys. Soc. Japan **7** (1952) 48.

ERRATA

A Method for Determining the Concentration Dependence of Diffusion Coefficient

By Hiroshi FUJITA and Akira KISHIMOTO

J. Phys. Soc. Japan Vol. 6 (1951) 408–409

P. 408 left column			
line 26	...Fisheries University of...	should be read	...Fisheries, University of...
line 34	assciates	〃	associate
right column			
line 7	A	〃	*A*
line 13	contracted	〃	contacted
line 14	Here, $K(C_f)$ is to be...	〃	Here, $K(C_f)$ is a certain function of C_f to be...
line 15	D(c)	〃	$D(C)$
line 25	$\surd D(\bar{0})C_f$	〃	$\sqrt{D(0)}\cdot C_f$
line 27	$\int_0^{C_f} D(c)dc$	〃	$\int_0^{C_f} D(C)dC$
line 32	$D(c)$	〃	$D(C)$
line 35	$D(c)$	〃	$D(C)$
line 37	...in the above.	〃	...in the above. From Eq. (2.2) we have
line 38	$K(c_f)$	〃	$K(C_f)$
line 40	$D(0)$	〃	$D(0)$
line 42	$D(10)$	〃	$D(0)$
	lim	〃	$\lim_{C_f \to 0}$
line 43	$D(c)$	〃	$D(C)$
	polynomical	〃	polynomial
line 43–44	...representatational representai representation...	〃	...representation...
line 45	$D(c)=D(0)(1+k_1C+k_2C^2+\ldots)$	〃	$D(C)=D(0)(1+k_1C+k_2C_2+\ldots)$
P. 409 left column			
line 1	tfimined	〃	mined
	ting	〃	fitting
line 7	from	〃	form
	$D(c)$	〃	$D(C)$
line 9	$D(c)=D(0)\exp(\lambda c)$	〃	$D(C)=D(0)\exp(\lambda C)$
line 21	$=1.50\ \ 10^{-9}$	〃	$=1.50\times10^{-9}$
line 31	*E* (Table 5th column)	〃	*K*
line 36	fith	〃	fifth
line 39	polynomical	〃	polynomial
line 40	$D(c)$	〃	$D(C)$
line 43	Boyer, R.E.,	〃	Boyer, R.F.,
line 44	Earaday	〃	Faraday

Mechanical Barkhausen Effect

By Tohru KAMEI

J. Phys. Soc. Japan Vol. 6 (1951) 260

The title "Mechanical Barkhausen Effect" should read "Mechanical Barkhausen Effect in Single Crystals of Iron".

On High Frequency Power Loss of Dielectrics.

By Ken'iti HIGASHI and Yasumoto OZAWA

J. Phys. Soc. Japan 6 (1951) 280

Author name "Yasumoto OZAWA" should be read "Yasutomo OZAWA"

Shoji NISHIKAWA

(1883—1952)

Obituary Notice of Professor Shoji NISHIKAWA

At the age of 67, Professor Shoji Nishikawa, Emeritus professor of the University of Tokyo and Member of the Academy of Japan, suddenly died of an apoplectic stroke on January 5, 1952. By his death, Japan has lost one of the most distinguished pioneers in modern experimental physics, particularly in the field of X-rays and electron diffraction. His introduction of the notion of space group into X-ray analyses of crystals as early as in 1915 successfully paved the road into this subject, which has been very little explored at that time. His study of the structure of the Spinel Group crystals rightly acquired the fame of being called a classic. Much of the fruitful results in this field which followed it owe a great deal, directly or indirectly, to Prof. Nishikawa's inherent ingenuity, well manifested in his study. The famous experiments which were made in collaboration with Dr. S. Kikuchi in 1928, on the diffraction of electron waves by crystals are again another example of his great contribution to physical sciences. Prof. Nishikawa's name will long be remembered together with uniquely beautiful photographs of the diffractions which are universally known by their reproductions in a number of books and monographs.

Prof. Nishikawa was born in 1883 at Hachioji near Tokyo, as the third son of Mr. Jihei Nishikawa, a textile dealer. He entered the Department of Experimental Physics, College of Science, Tokyo Imperial University in 1907. Graduating from the University in 1910, he took the post graduate course under the subject of the theory of electron, a subject ambitious enough at that time. In 1916, he got the title of Rigakuhakushi (Dr. of Science).

The discovery by Laue of the diffraction of X-rays by crystal atoms in 1912, greatly impressed our young and fresh post graduate student, who, in 1913, published a study of X-ray diffractions by fibrous, laminar and granular substances and showed a promising possibility of studying the structures of these substances by this method.

In the study of the structure of the crystals belonging to the Spinel Group which appeared soon later, he first introduced the notion of the space group and pursued the study with admirable elegance and completeness. The Imperial Academy of Japan, awarded him a Prize for this work.

In the same year, he was appointed an associate research member of the Institute of Physical and Chemical Research, Tokyo, and was sent abroad by the Institute.

After a few year sojourn in abroad, he came back to Japan in 1920 and in the next year, he was appointed a research member of the Institute of Physical and Chemical Research. In the same year he was appointed an assistant professor of the Imperial University of Tokyo, his Alma Mater.

Many able assistants and students gathered around Prof. Nishikawa. The subjects of study covered by the Nishikawa Laboratory were diverse yet penetrating. To cite a few, besides the analyses of structures of various kinds of crystals, we may mention the extinction of X-rays in crystals, the effect of piezo-electric oscillation, stress distribution, temperature and of grade of surface polish, etc. on X-ray diffractions.

In 1925, Prof. Nishikawa succeeded in determining the structures of α- and β-quartz, of which, however, the results were not published, because, by a display of coincidence a paper of Sir William Bragg on the same subject happened to reach him just after he had finished his own work.

One of the original studies of Prof. Nishikawa which has to be mentioned is the experimental evidence he gave of detecting a certain hemihedry in the crystal of zincblende by using an X-ray having the wave-length near its absorption edge. It became clear that Friedel's law which states the impossiblity of this attempt is sometimes violated. In the meantime, Prof. Nishikawa did never neglect the applications of X-rays to the researches of medical and metallurgical problems.

In 1924, he was appointed a professor of the Imperial University of Tokyo, which position he kept until his retirement in 1945. In 1925, he was elected a member of the National Research Council.

As soon as the experiments of Davisson and Germer, and Thomson of the diffractions of electron waves by crystal atoms were published, Prof. Nishikawa fully recognised the significance of these experiments and he started his own, being collaborated by Dr. S. Kikuchi. The photographs which were obtained by them by making electron beams incident on thin sheets of mica and other crystals are universally known by the names of P, N, L patterns. A team of many able young scientists in the Nishikawa Laboratory attacked a number of problems by electron diffractions, namely, the refraction of electron waves, inner potential and surface conditions of crystals, etc. That Japan keeps a prominent position in this particular branch of physics is mainly due to the original and pioneering studies which came out from the Nishikawa Laboratory.

In 1934, Prof. Nishikawa visited Europe and U.S.A. During this 6 month journey, he heard of the expriments of Fermi on neutrons. As soon as he got home, he started to tackle the kindred problems and soon published the important results on the energy distribution of neutrons emitted from various elements.

In 1937, he was elected a member of the Imperial Academy of Japan.

In recognition of his outstanding contributions to physics, a Bunkakunsho (Order of Cultural Merits) was conferred on him in 1951, and on the same occasion, his native city made him its first honorary citizen.

He was not strong physically. His health badly went down during the awkward period of the war time.

He was survived by his wife, three sons and one daughter.

(Chuji Tsuboi)

JOURNAL OF THE PHYSICAL SOCIETY OF JAPAN Vol. 7, No. 2, MAR.—APR., 1952

Polarization of Electrons by Scattering, I

By Norio RYU
Department of Physics, Faculty of Science, Kyusyu University

(Read April 2, 1951; Received July 11, 1951)

The double scattering experiment has been repeated to find out the evidence by polarization expected by theories. The scatterers used were gold foils of about 5×10^{-6} cm in thickness and the energy of the electrons ranged from 60 to 130 kev. The experiments were carried out on the scattering through angles of 105° and 120° at the first and the second foil. At 120 kev the values of $-200\,\delta^2$ are 14.7 ± 1.7 and 16.9 ± 2.0, respectively, which are smaller than the half of the theoretical values predicted by Mohr at 121 kev. The results at 120° are somewhat larger than those at 105°, but the mean errors in counting are too large to be compared precisely. The azimuthal dependency of the polarization effect agrees with the theory qualitatively.

§ 1. Introduction

Mott[1)] has investigated, theoretically, the effect of the spin on the scattering of electrons and showed that if electrons were made to undergo double large angle deflections by atoms of large atomic number, its intensity would have azimuthal asymmetry at the second scattering which is large enough to be observed. It has long been recognized as a source of direct information about the spin nature of electrons. Before Mott has published his theory a number of experiments were made to find the evidence of polarization by the methods suggested by analogy with the phenomena of light or X-rays. In these early experiments, any conclusive results had not been obtained, Dymond[2)], Thomson[3)], and Richter[4)] investigated experimentally the effect of polarization following faithfully the Mott's conditions: (1) the velocity of the electrons is comparable with that of light, (2) the angles of scattering at both nuclei are large, and (3) the atomic number of scattering nuclei are large. Unfortunately, their results did not agree with the theory. In order to reconcile this discrepancy between the theory and the experiments, many authors investigated theoretically; for example, the effect of crystal lattiece of the scatterer by Weisskopf and others[5)] and the depolarization by multiple scattering and exchange scattering by Rose and Bethe[6)], but none was successful in explaining the discrepancy. Massey and Mohr[7)] have recalculated the effect of polarization considering the screening effect by electrons in place of pure Coulomb field which is used in Mott's theory[1)], and obtained values somewhat larger than Mott's one. In spite of these efforts the gulf between the theory and the experiments had remained.

Though it is comparatively easy to fulfil the Mott's conditions, the theory requires a hard restriction that single scattering should be insured at both foils. Goertzel and Cox[8)], and the present author[9)] have pointed out that if the electron beam incident obliquely to the foil there is a number of electrons which suffer two deflections of rather large angles in the same foil, and it plays an important part in polarization experiments. If the electron beam is incident on the foil at 45° and scattered to the incident side, as the case of Dymond, Thomson, and Richter, we are afraid that the effects of polarization may be masked by these plural scattering, Hereafter, we call this side "reflecting-side" and the other side "transmitting-side" in which the plural scatterings are far less than in the former. In order to avoid the plural scattering, Shull, Chase and Myers[10)], and Shinohara and Ryu[11)] have used the transmitting side and observed experimentally the asymmetry caused by polarization.

The intensity of electrons twice scattered is inversely proportional to the forth power of accelerating voltages. If we derive the asymmetry from the intensity in each directions measured at different times, the errors are some eight times the errors in voltage measurements, and it may be larger than the asymmetry expected by the theory. To avoid the disturbance mentioned above it was used the symmetric method, i.e. simultaneous measurements in two directions in which the evidence is remarkable. This will give little error so long as the evidence by polarization does not vary rapidly with the accelerating voltage.

Mohr[13] has calculated the effects of polarization at other angles than 90° and showed fairly larger ones than the other theories. We investigated experimentally, therefore, at angles of 105° and 120° and compared with the theoretical values.

§ 2. Experimental Apparatus

Incident electrons were emitted from a thoriated tungsten filament of 0.2 mm diameter in a Wehnelt cylinder which was maintained at lower potential than the filament from ten to thirty volts. The high tension was generated by a equipment of Cockroft type and was divided by four high resistances of about 250 $M\Omega$. The electrons were accelerated by these divided voltages and we get a sharp and strong beam because the accelerator plays as a lens stet on the electron beam. The voltages were measured with a microammeter and a high resistance of about 4000 $M\Omega$ which was made of a mixture of 1 per cent picric acid, about 90 per cent benzene and about 10 per cent alcohol. The solution was contained in a glass tube and the out side of the lower parts of the tube was coated with aluminium which was connected electrically to the ground to avoid the disturbance by the leakage current at glass surface. The temperature coefficient of the high resistance was measured by a static voltmeter calibrated previously at 20 kv. The current in the accelerator was so small that the voltages were proportional to the primary voltages at the main transformer. Variations of the generated voltages were kept less than one per cent.

The scattering chambers are shown in Fig. 1. Through the diaphragm S_1 of 2.5 mm in diameter, the electron beam enter the scattering chamber and become narrow because of the lens type in the accelerator. After passing through two defining diaphragms S_2 of 1.5 mm diameter, the electrons fall on the first scatterer which works as a polarizer. Gold foils of thickness about 5×10^{-6} cm were used as the first and the second scatterer. The polarizer was mounted on an aluminium plate having an elliptic hole whose longer and shorter axes are 6 and 3 mm, respectively, and are large enough to be free from the edge scattering. The foil orientated at 30° with the incident beam and was placed in the transmitting position, as shown in Fig. 1. The foil was somewhat movable with diaphragms S_2 to get the best condition at each measurements. The part of polarizing chamber containing the polarizer foil was made of 6″ brass tube and extended 40 cm from the foil in the direction of the incident beam.

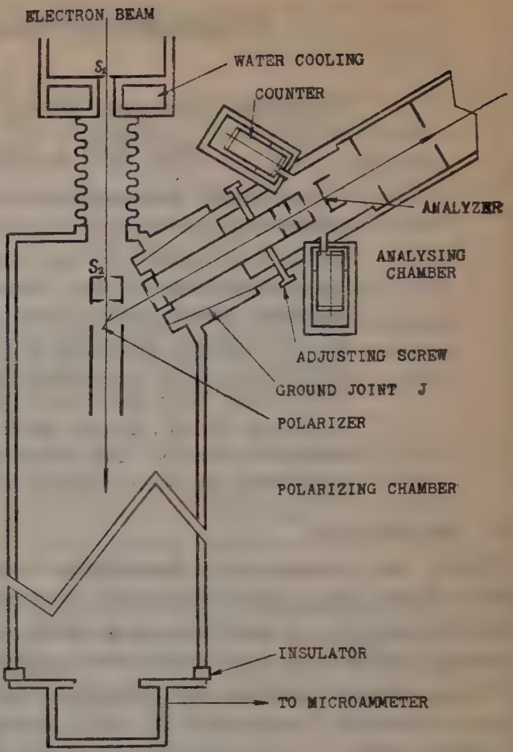

Fig. 1. Schematic diagram of scattering chambers.

Electrons which have been scattered at the first foil through angles of 120° or 105° pass through five limitting diaphragms 1 mm diameter and fall on the second scatterer which will be called hereafter the analyzer. The analyzer was mounted on a hole of 3 mm diameter and placed perpendicular to the path of the incident electrons. Electrons which have been scattered again at the analyser through angles of 105° or 120° pass through the window of aluminium and thence into the Geiger Müller counters which are mounted in the directions antiparallel and parallel to the primary beam, as shown in Fig. 1. The analyzing chamber was extended 15 cm from the foil and have two baffles of aluminium.

To reduce the stray electrons as small as possible, each chambers were made of long tube and all diaphragms, baffles and cylinders in which electrons passed were made of aluminium. Since we can by no means exclude a large number of stray electrons in analyzing chamber, the windows of the counters were aluminium foils of about 1.8×10^{-3} cm in thickness to stop these electrons which had lost some energy and secondary electrons originated in analyzing chamber. The measurement below 110 kev were completely free from stray electrons while if we use foils of 9×10^{-4} cm in thickness the counted stray electrons at 100 kev amount to 10 per cent of the electrons twice scattered.

Besides the stray electrons, X-rays originated at any part where knocked by electrons of high speed play an important part of the background. Thick lead plates and cylinders were inserted, not shown in Figure, between all possible sources of X-rays and counters. Counts by X-rays began at 120 kv and increased rapidly with accelerating voltages and it is the same with the stray electrons.

It was designed that the whole of the analysing chamber containing the analyser and counters could be rotated by the ground joint *J* so as to measure the evidence by the symmetric method as mentioned in the following section. Since irregular results were obtained when the direction of electrons defined by the diaphragms in analyzing chamber differed from the axis of rotation, the cylinder containing the diaphragms was adjusted by four screws as shown in Fig. 1.

The Geiger Müller counters of copper cylinder of 1.2 cm in diameter, were filled with argon (about 15 cm Hg pressure) and alcohol vapour (about 1.5 cm Hg pressure) were operated at the voltages of one hundred volts higher than threshold and the natural counts were about 8 per minuite. The scaling circuit published by Wolfe and Steele[14)] were used. To reduce the disturbance by the discharge at high tension the vacuum tubes of the first stage in amplifiers were close to the counter and shielded strictly.

§ 3. Experimental Procedure

To avoid the large errors caused by the fluctuation of high voltages it was designed that the analysing chamber was symmetric to the axis of rotation. The intensities in two directions which differ 180° in azimuthal angle were measured simultaneously. The Fig. 2 shows the case of $\phi=0$ and scattering angles are 120°. If a/b is the ratio of efficiencies of two counters including the geometrical asymmetry, the ratio x of the number of counts of one counter to that of another at one disposition is

$$x=\frac{a(1-\delta^2\cos\phi)}{b(1+\delta^2\cos\phi)}\,, \qquad (1)$$

since the intensity of electrons twice scattered should be proportional to $1-\delta^2\cos\phi$, according to the theory of Mott, where ϕ is the azimuthal angle, zero in the direction of antiparallel to primary beam. and $(-\delta^2)$ is the evidence by polarization which have been calculated by theorists. Since δ is the pure imaginary, the direction of $\phi=0$ is that of maximum intensity. After five or ten minuites counting, we rotate the whole of analyzing chamber containing the analyzer and counters through angles of 180°. Then the ratio of numbers counted at each counters becomes

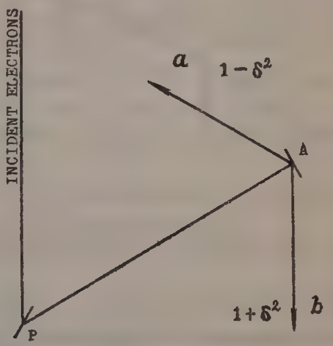

Fig. 2. Directions and intensities of the scattered electrons.

$$y=\frac{a(1+\delta^2\cos\phi)}{b(1-\delta^2\cos\phi)}\,. \qquad (2)$$

From the values of x and y, the evidence by polarization can be obtained as follows:

$$-2\delta^2\cos\phi \doteqdot \frac{x-y}{x+y}+\frac{1}{4}\left(\frac{x-y}{x+y}\right)^2. \qquad (3)$$

The second term in Eq. (3) is negligible in the case of small asymmetry. It is expected by theory and experiments as shown in later section that the evidence by polarization does not vary so rapidly with the accelerating voltages. Consequently the fluctuation in high tension cannot become a source of considerable errors. Since the Eq. (3) is independent of a/b, i.e. the asymmetry in the analyzing chamber, the errors caused by faulty geometry is very small so long as the electron path in analyzing chamber does not differ from the axis of rotation.

§ 4. Results and Discussion

Table I and Figs. 3 and 4 show the values of $-200\,\delta^2$, obtained for the electrons of the energy 60–130 kev, at the angles of 105° and 120°, respectively. The experimental values are shown by $\overset{\top}{\underset{\bot}{\odot}}$ in the figures. The errors shown in the figures are derived from the mean errors in counting. Although the theoretical values obtained by Mohr at 121 kev are 0.3 and 0.4 for $-2\,\delta^2$ at 105° and 120°, respectively, the experimental ones are less than the half of theoretical ones. Unfortunately, there is no theoretical values between 121 and 33 kev at which the effects are 0.09 and 0.14 at angles of 105° and 120°, respectively. The experimental values of polarization effect become large with increasing accelerating voltages and the values at 120° are somewhat larger than those of 105° except the values at 130 kev, this tendency agrees with the theory.

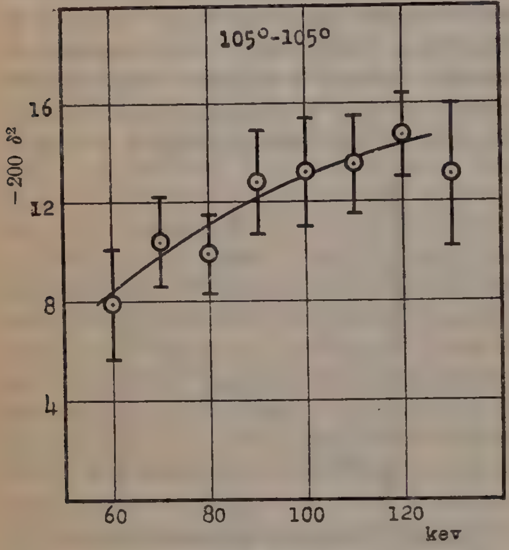

Fig. 3. Values of $-200\,\delta^2$ at double scattering through angles of 105° as a function of energy of electrons.

Table I. Values of $-200\,\delta^2$

Energy of electrons (kev)	105°–105°	120°–120°
60	7.9±2.2	9.1±2.2
70	10.4±1.8	11.1±1.8
80	9.9±1.6	11.8±2.0
90	12.8±2.1	14.4±1.7
100	13.2±2.2	15.0±1.6
110	13.5±2.0	14.5±1.9
120	14.7±1.7	16.9±2.0
130	13.1±2.9	11.6±2.3

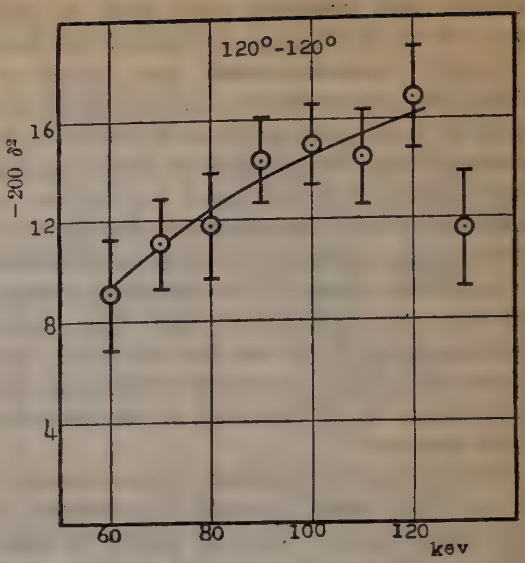

Fig. 4. Values of $-200\,\delta^2$ at double scattering through angles of 120° as a function of energy of electrons.

The azimuthal dependency of $-200\,\delta^2$ at 80 kev is shown in Fig. 5 and the curve shows the cosine curve fitted at zero azimuth with the experimental value. The experimental results show the correctness of the relation that the intensities of electrons twice scattered are proportional to the $1+(-\delta^2)\cos\phi$.

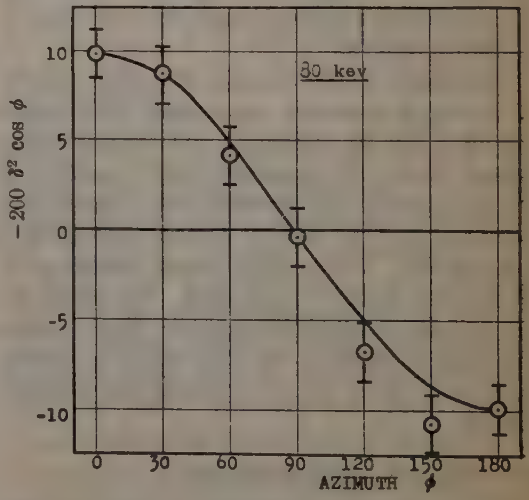

Fig. 5. Values of $-200\,\delta^2\cos\phi$ at 80 kev as a function of azimuthal angles. The scattering angles at both foils are 105°. It is shown the cosine curve, fitted with the experimental values at zero azimuth.

The values at voltages higher than 110 kev are obtained after eliminating backgrounds which was measured without analyzer. The ratio of the number of the background to the number of electrons counted increase rapidly at higher voltages and it amount to 4, 12 and 18 per cent at 110, 120 and 130 kev, respectively, in the experiment of 120°. The backgrounds are composed of stray electrons and X-rays, the former has no asymmetry while the later have some asymmetry. Since the corrections of background are larger than the mean error, results at 130 kev are somewhat uncertain.

As mentioned earlier the plural scattering in scatterers plays an important role in polarization experiments. It seems that the plural scattering at polaryzer may be negligible in these working voltages. It must be noticed that the analyzer was placed in the position of reflecting side. The less the angles θ between the plane and the direction of detector, the more effect of plural scattering will be occured, and it is inversely proportional to the third power of the $\sin\theta$. If the plural scattering is prominent the experimental results will show the effects of polarization at 90° at analyzer. At lower voltages and at 105°, it seems likely that the considerable plural scattering would occur. The detailed analysis on the plural scattering at normal incidence is now in progress.

The results here obtained agree qualitatively with those of Shull, Chase and Myers10), Trounson and Simpson11), and Shinohara and Ryu12), while those are contrary to those of Dymond2), Thomson3), and Richter4). This will be understood if one takes account the plural scattering. The detailed discussion on the sources of errors will be made in the following paper.

The present author wishes to express his sincere thanks to Prof. I. Nonaka and Prof. K. Shinohara for their kind guidance. His hearty thanks are also due to Prof. T. Muto for his kind interest and suggestions. This work has been supported by the Scientific Research Expenditure of the Department of Education.

References

1) N. F. Mott: Proc. Roy. Soc. **A 124** (1929) 425; *ibid.* **A 135** (1932) 429.
2) E. G. Dymond: Proc. Roy. Soc. **A 136** (1932) 638; *ibid.* **A 145** (1934) 657.
3) G. P. Thomson: Phil. Mag. **17** (1934) 1058.
4) H. Richter: Ann. der Physik **28** (1937) 533.
5) V. Weisskopf: Zeits. f. Physik **93** (1935) 561; E. David: *ibid.* **105** (1937) 747.
6) M. E. Rose and H. A. Bethe: Phys. Rev. **55** (1939) 277.
7) H. S. W. Massey and C. B. O. Mohr: Proc. Roy. Soc. **A 177** (1941) 341.
8) G. Goertzel and R. T. Cox: Phys. Rev. **63** (1943) 37.
9) N. Ryu: J. Phys. Soc. Japan **5** (1950) 423.
10) C. G. Shull, C. T. Chase and F. E. Myers: Phys. Rev. **63** (1943) 29.
11) E. Trounson and J. A. Simpson: Phys. Rev. **63** (1943) 55.
12) K. Shinohara and N. Ryu: Phys. Rev. **75** (1949) 1762; J. Phys. Soc. Japan **5** (1950) 119.
13) C. B. O. Mohr: Proc. Roy. Soc. **A 182** (1943) 189.
14) A. E. Wolfe and F. G. Steele: Electronics **22** (1949) 75.

JOURNAL OF THE PHYSICAL SOCIETY OF JAPAN, Vol. 7, No. 2, MAR.—APR., 1952

Polarization of Electrons by Scattering, II

By Norio RYU

Department of Physics, Faculty of Science,
Kyusyu University

(Read April 2, 1951, Received July 11, 1951)

The polarization of electrons were investigated experimentally by double scattering where the scattering angles at the polarizer and the analyzer are different. The results obtained ($-200\,\delta_1\delta_2$) are 14.1±1.8, 17.0±3.0, 15.7±2.1 and 20.4±2.8 at 120 kev at angles of 105°−120°, 105°−135°, 120°−105° and 120°−135°, and are smaller than a half of Mohr's theory. The large differences between the evidences at angles of 90°, 105°, 120° and 135°, shown in Mohr's paper, could not be obtained. The plural scattering, which is the combination of rather large angle deflections at same foil, plays an important role in this experiments, but it is difficult only by this cause to explain the discrepancy between the experiments and the theory. But the evidences by polarization increase with scattering angles, and this tendency agrees with Mohr's theory.

§ 1. Introduction

In a previous paper[1] (Part I) experiments by double scattering were described to detect the evidence by polarization of electrons which had suffered twice scatterings through rather large angles by gold atoms. The scattering angles were same at both scatterers which we call the polarizer and the analyzer, respectively. Some large asymmetries by the polarization of electrons were obtained at the scattering angles of 105° and 120°. Results obtained are, however, far smaller than the theoretical values published by Mohr[2].

It is interesting to carry out experiments using a combination of different angles of scattering at the polarizer and the analyzer, especially when plural scatterings are expected to occur. According to the theory[3][4], the intensity of electrons which will enter the detector after they suffer twice scatterings is given by

$$I=\Phi_1\Phi_2(1-\delta_1\delta_2\cos\phi)\,, \qquad (1)$$

where Φ_1 and Φ_2 are the symmetric part of cross sections at the polarizer and the analyzer, respectively, $\delta_1\delta_2$ is evidence by polarization, and ϕ is the azimuthal angle around the direction of electrons incident to the analyzer and is zero when the direction of the detector is antiparallel to the initial electron beam. δ is pure imaginary and it is usual to describe δ as $-\delta^2$ in other papers and values of $-2\delta^2$ are calculated by many authors[2][3][5][6].

According to Eq. (1), similar results must be obtained in experiments when the conbination of scattering angles at each scatterers is same. If the signs of δ in each scattering are different, it is possible to observe an opposit asymmetry to the experiments whose scattering angles are same at each foils. According to Mohr* δ's at 33 kev and 121 kev have a same sign at angles here used.

§ 2. Experimental Apparatus and Results

The same apparatus as in Part I[1] was used. The polarizing chamber and the analyzing chamber were able to detect the scattering through angles of 105°, 120° and 135°. The similar procedure as described in Part I was made except that the scattering angles at the first and the second scatterer were different.

Results obtained are shown in Table I and Figs. 1, 2, 3 and 4. According to Eq. (1) the theoretical values which are obtained by using the different angles are given by the geometrical mean of evidences by polarization at each scattering angles. When the scattering angles at the polarizer and the analyzer are 105° and 120°, respectively, we call this, hereafter, the experiment of 105°−120°. The results in experiments of 105°−120° and 120°−105° are same within the limits of errors, but slightly larger the latter and this may be attributed to some effect of the plural scattering at the analyzer. The detail of the plural scattering will be discussed in the following section. The values obtained at 120 kev are far smaller than the theoretical values calculated by

---

* The present author is indebted to Prof. Mohr for his kind information.

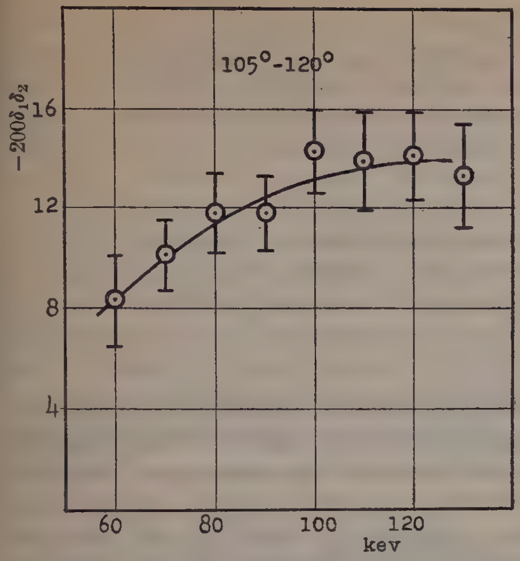

Fig. 1. Values of $-200\delta_1\delta_2$ in the experiment of 105°−120° as a function of the energy of electrons.

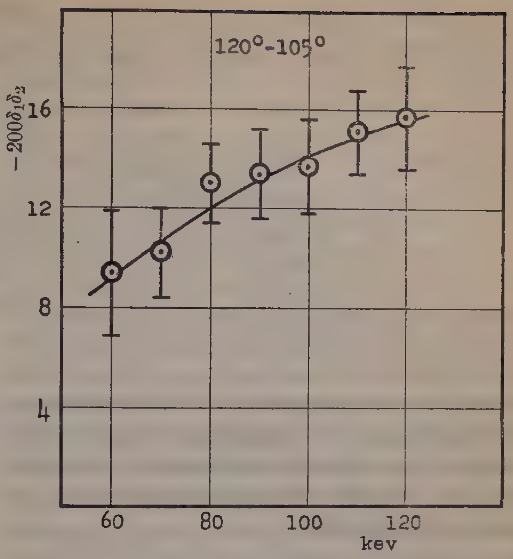

Fig. 2. Values of $-200\delta_1\delta_2$ in the experiment of 120°−105° as a function of the energy of electrons.

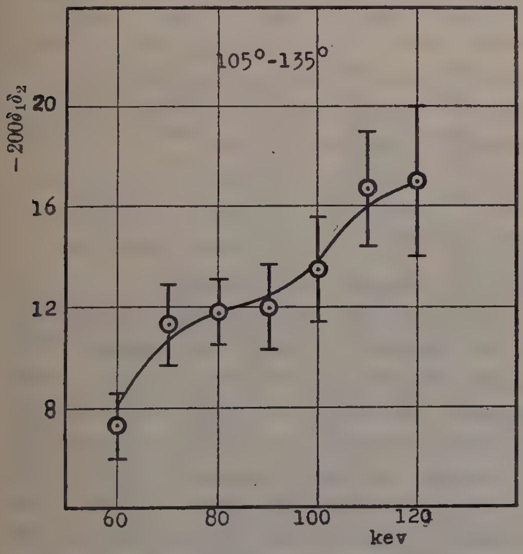

Fig. 3. Values of $-200\delta_1\delta_2$ in the experiment of 105°−135° as a function of the energy of electrons.

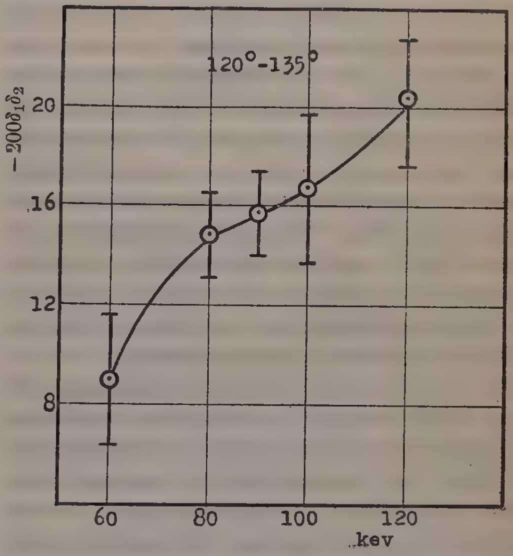

Fig. 4. Values of $-200\delta_1\delta_2$ in the experiment of 120°−135° as a function of the energy of electrons.

Mohr[2]. Indeed, a great number of electrons perform plural scatterings at the analyzer as is shown in the following section, but they will show the evidence by polarization at angle of 90° because a great number of such electrons suffer the scattering through angle of 98° in the direction of the detector. Even if one takes account of these masking effects extremely, experimental results are still small compared with the theory. According to the theory of Mohr, $(-2\delta^2)$'s at 121 kev are 0.14, 0.3, 0.4 and 0.5 at 90°, 105°, 120° and 135°, respectively. If there are large amounts of differences between 90° and other angles, as expected by the theory, the effect of the plural scatteriug ought to be seen distinctly in the present experiments. Unfortunately, we could not obtain such large differences between the evidences at these angles. It is remarkable that when the same scattering angles are used

Table I. Valuse of $-200\delta_1\delta_2$

kev	105°-105°	105°-120°	105°-135°	120°-105°	120°-120°	120°-135°
60	7.9±2.2	8.3±1.8	7.3±1.3	9.4±2.5	9.1±2.2	9.0±2.6
70	10.4+1.8	10.1±1.4	11.3±1.6	10.2±1.8	11.1±1.8	—
80	9.9±1.6	11.8±1.6	11.8±1.3	13.0±1.6	11.8±2.0	14.8±1.7
90	12.8±2.1	11.8±1.5	12.0±1.7	13.4±1.8	14.4±1.7	15.7±1.7
100	13.2±2.2	14.3±1.7	13.5±2.1	13.7±1.9	15.0±1.6	16.7±3.0
110	13.5±2.0	13.9±2.0	16.7±2.3	15.1±1.7	14.5±1.9	—
120	14.7±1.7	14.1±1.8	17.0±3.0	15.7±2.1	16.9±2.0	20.4±2.8
130	13.1±2.9	13.3±1.9	—	—	11.6±2.3	—

at the analyzer the results of 120° scattering at the polarizer are larger than those of 105°. It is concluded that the evidence by polarization increases with the scattering angle in the range of angles used.

§ 3. Plural Scattering

Goertzel and Cox[7] have pointed out that with electrons obliquely incident on the foil the serious deviation from Wentzel's criterion for single scattering may be caused by the plural scattering, i.e. the combination of two or more deflections of large angles in the same foil. In some experimental conditions, it is usual to count the electrons which are suffered single scattering together with those electrons suffered plural scattering. Since the evidence by polarization is derived from small differences between the intensities of scattered electrons, the plural scattering play an important part on the experiment of double scattering.

Goertzel and Cox[7], and the present author[4] have calculated roughly these plural scattering and showed that if one use the transmitting side to detect the electrons stet it becomes very small compared with the reflecting side. In our experiments, the thickness of the foils were about 5×10^{-6} cm so the scattering at the polarizer is free from the plural scattering except its low energy region.

Unfortunately, we must use the reflecting side at the analyzer to get a large amount of polarization asymmetry and to use the symmetric process. The plural scattering, in this case, is much more serious. The number of electrons which are suffered plural scatterings is calculated roughly at these normal incidences using a similar method described in the previous paper[4]. The ratio r of the number of plurally scattered electrons to that singly scattered are tablated in Table II. As shown in the previous paper the calculated number of these electrons is small to explain the experimental results of "reflection-transmission effect". It is, therefore, adequate to think that the electrons suffered plural scatterings are more numerous than that expected from Table II.

Table II. The ratios of plurally scattered electrons to singly scattered electrons. (Gold foil of 5×10^{-6} cm in thickness)

β	kev	105°	120°	130°
0.3	25	—	2.6	1.2
0.4	47	4.8	0.9	0.4
0.5	79	2.1	0.4	0.2
0.6	127	1.0	0.2	0.1
0.7	204	0.5	0.1	—
0.8	340	0.2	—	—

In the case where the scattering angle is 105° at the analyzer, it may be supposed that plurally scattered electrons are amazingly more numerous than singly scattered electrons. If one take account of the fact that the intensity of scattered electrons decreases rapidly with increase of the scattering angle, a large part of plurally scattered electrons which enter the counter is those scattered in the foil in the direction of the detector. These electrons, therefore, will show the evidence by polarization for 90°. It seems that the results in the experiment of 105°-105° shows the intermediate values between the polarization asymmetry of 105°-90° and 105°-105°, and a similar conclusion will be obtained in the experiment of 120°-105°.

Although there is a number of plural scatterings at the scattering angle of 120° at the analyzer, it is hard to think a severe depolarization would occur at the energy of 120 kev.

Then the fact that experimental values are about a half of the theoretical ones at 121 kev, shows a essential discrepancy between the present experiment and the theory. A similar conclusion will be obtained for the scattering at 135°.

Though experiments were carried out with a intention of investigating the plural scattering, it is impossible, unfortunately, to make a clear discussion about it because of two reasons, the first that the errors are comparatively large, and the second that the differences between the experimental results at various angles are small, while the theory2) shows large amounts of differences.

§ 4. Sources of Error

It is obvious that with the experiments of double scattering, stray effects may play an important role owing to the smallness of the asymmetry to be expected from polarization of electrons; these effects must be examined precisely.

1. Stray Electrons

In the analyzing chamber, it must be taken into account that a large number of stray electrons—the electrons suffered scatterings many times and enter the analyzing chamber by complicated processes—may exist. There are, moreover, many secondary electrons produced by bombardment of the limiting diaphragms, but by far a great number of secondrry electrons have a small energy. In order to reduce these stray electrons and secondary electrons, the diaphragms and the walls of the chambers where electron beam passed were made of aluminium. And a large part of these electrons have already lost some energy and will fail to penetrate the aluminium window of the counter. The masking effect by this cause becomes larger rapidly with increase of accelerating voltages. When aluminium foils of 9×10^{-4} cm in thickness were used as the counter windows, the counts by stray electrons become somewhat large at 100 kev in the experiment of 120°—120°, of the order of 10 per cent of the total counting rate, and disappear when more thick foils of 1.8×10^{-3} cm in thickness were used. Since a aluminium foil of 1.8×10^{-3} cm in thickness was used as the window of the counter in the measurements of the intensities, most of stray electrons could not likely to enter the counter at lower energy than 120 kev, but only a small part of the background at 130 kev may be ascribed to the stray electrons.

2. X-rays

It was found that X-rays were produced at any points bombarded by fast electrons, especially the material in the neighbourhood of S_1 and S_2 became strong sources of X-rays. To reduce the counts by X-rays lead pieces were inserted in- and outside of the analyzing chamber, not shown in the Fig. 1 in Part I. More than 3 cm of lead were inserted between S_1 and counters. The counters were further shielded from the X-rays by surrounding them with lead of about 5 mm in thickness. In order to prevent X-rays originated in the analyzing chamber, a lead cylinder of 5 mm in thickness with narrow holes through which electrons could pass to the detector was inserted in the analyzing chamber. The outer part of the polarizing chamber was shielded by lead plate in the side of the counters. By this method of inserting lead pieces as possible, it was impossible to reduce completely the counts by X-rays at the higher region of the voltages and they have some asymmetry contrary to the case of stray electrons.

In order to obtain the counts due to X-rays and stray electrons the counts were taken with the analyzer foil removed. It is assumed that the X-rays and the stray electrons which enter the detector after scattered by the analyzing foil were negligibly small. Results in Table I were corrected by these backgrounds. The corrections were serious in the experiments for large scattering angles and high energy region since the counts by doubly scattered electrons become remarkably small. In the experiments of scattering angle of 135° at the analyzer the correction is necessary at higher than 100 kev, and in other cases higher than 110 kev.

3. Multiple Scattering

The multiple scattering resulting from a number of scatterings of small angles in the foils has been examined by Rose and Bethe3), and by the present author4). It exerts no appreciable effect in the present experiments in which the thickness of foils were about 5×10^{-6} cm. The plural scattering is more serious and makes it impossible to detect the evidence by polarization where the effect of multiple scattering would appear.

4. Faulty Geometry

Although in the analyzing chamber it is impossible to ensure the exact symmetry of all the defining diaphragms and the foil around the path of the beam, the errors caused by these asymmetry are very much reduced by using the symmetric method, i.e, the simultaneous measurement of intensities in two directions different by an angle of 180° and rotation of the analyzing chamber together with counters by ground joint J in Fig. 1. in Part I. However, if the scattered beam defined by diaphragms in the analyzing chamber lies somewhat off the true axis of rotation, it becomes impossible to expect the exact results. So the diaphragms are adjusted by four screws shown in Fig. 1 in Part I. In order that the main beam, defined by the diaphragms S_2, strike the polarizer at a point on the axis of rotation of the analyzer, the polarizing foil is made somewhat movable together with the diaphragms S_2 and larger diameter of diaphragms are used at S_2 than those of the diaphragms in analyzing chamber. It is important, therefare, to know if the scatterers and the defining diaphragms are placed at the correct positions. Fig. 5 shows the apparent polarization asymmetry at various heights of the polarizer foil. The solid line shows $-200\delta_1\delta_2$ as a function of heights of the analyzer at 90 kev in the experiment of 120°−135°. Within the limits of ±0.4 mm the variation of intensity is very small while the values at the heights of 0.55 mm and of −0.5 mm decreased to less than a half of that at normal position. The dotted line shows the results at 80 kev in the experiment of 120°−120°. The part giving a constant results shows the allowable range of position of the foil and it is easy to set up the polarizer within the limits of ±0.4 mm.

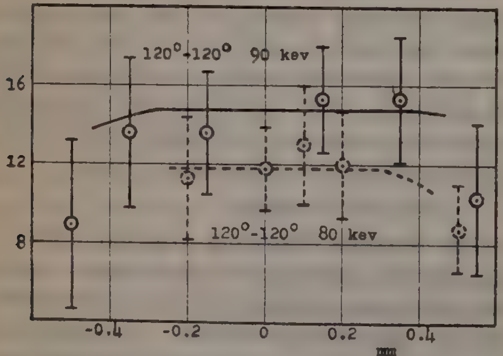

Fig. 5. Height of the polarizer and values of the measured asymmetry.

Consequently, it is concluded that the faulty geometry produces no appreciable errors.

5. Other Sources

Unsteadiness of the accelerating voltage E which is controled within 1 per cent exerts little effects in the experiments so far the symmetric method is used, while it is important in the case of Dymond[9] and Thomson[10] since the intensity of twice scattered electrons is proportional to E^{-4}. The error caused by it is negligibly small compared with the mean errors of counting because the theoretical and the experimental results show only a slow increase with the increase of accelerating voltages.

The fluctuations in the intensity of the original beam gives no effect on the results obtained by the symmetric method.

§ 5. Discussion

The results shown in Part I and II indicate positive polarization effects. It is interesting to compare the results with the theoretical values at 121 kev calculated by Mohr. Even though the plural scattering is far more than single scattering at analyzer, results in experiments of 105°−105° and 120°−105° are less than the theoretical ones. It is reasonable to consider a little depolarization would occur in scattering angles of 120° and 135° at the analyzer. Results obtained in these experiments are about a half of the theoretical ones, and it is impossible to expect such depolarization by the plural scattering. According to the theory, $-2\delta^2$ for 90°, 105°, 120° and 135° are 0.14, 0.3, 0.4 and 0.5, respectively, while the experiments did not show such large variation. Since this discrepancy could not be explained by taking account of the plural scattering only, it seems to us likely that the evidence by polarization would not vary so rapidly as shown by Mohr or some depolarization effects would occur. Unfortunately, we could not get any precise knowledge about the plural scattering by these experiments because of comparatively large errors and small differences of polarization asymmetries between these angles here used. Then, it is meaningless to make a further detailed numerical discussion of the experimental values.

A number of earlier experiments carried out before Mott's theory were either negative or were rendered questionable by later experimental and theoretical developements on this problem. Results of Dymond[9], Thomson[10], and Richter[11] are contrary to our results but this contradiction may disappear if one takes account the plural scattering and the unsteadiness of accelerating voltages. It would appear from figures given in their papers that all of the electrons studied by them were scattered in the direction of reflecting side. The present author[4] has already discussed the plural scattering in the type of their experiments. Results of Shull et. al., Trounson and Simpson[13], and Shinohara and Ryu[14] agree with ours qualitatively and it is exciting that all of the experiments which have obtained positive results take the method which cut down the effect of plural scattering by using transmitting side in scattering. According to Mohr's theory[2] the evidence by polarization at 75° are so small that it seems the results of Shinohara and Ryu in the experiment of 90° $-78°$ have good agreement with theory. Their results, however, are enlarged by the plural scattering to some extent since the evidence at angles of 90° is far larger than that of 75°. Kikuchi's results[15] agree completely with Mott's theory[3] using the thick target ($\sim 10^{-3}$ cm) of gold as the polarizer and also using reflecting side. His experiment has already been pointed out by Rose[16] that a large depolarization by multiple scattering would occur. If one takes account, moreover, the plural scattering, his experimental asymmetry have to be rendered to other causes.

The present author wish to express his sincere thanks to Prof. I. Nonaka and Prof. K. Shinohara for their kind guidance. His hearty thanks are also due to Prof. T. Muto for his kind interest and suggestions. This work has been supported by the Scientific Research Expenditure of the Department of Education.

References

1) N. Ryu: J. Phys. Soc. Japan **7** (1952) 125.
2) C. B. O. Mohr: Proc. Roy. Soc. **A 182** (1943) 189.
3) N. F. Mott: Proc. Roy. Soc. **A 135** (1932) 429.
4) N. Ryu: J. Phys. Soc. Japan **5** (1950) 423.
5) H. S. W. Massey and C. B. O. Mohr: Proc. Roy. Soc. **A 177** (1941) 341.
6) J. H. Bartlett and R. E. Watson: Phys. Rev. **56** (1939) 612.
7) G. Goertzel and R. T. Cox: Phys. Rev. **63** (1943) 37.
8) M. E. Rose and H. A. Bethe: Phys. Rev. **55** (1939) 277.
9) E. G. Dymond: Proc. Roy Soc. **A 135** (1932) 638; *ibid.* **A 145** (1934) 657.
10) G. P. Thomson: Phil. Mag. **17** (1934) 1058.
11) H. Richter: Ann der Physik **28** (1937) 533.
12) C. G. Shull, C. T. Chase and F. E. Myers: Phys. Rev., **63** (1943) 29.
13) E. Trounson and J. A. Simpson: Phys. Rev. **63** (1943) 55.
14) K. Shinohara and N. Ryu: Phys. Rev. **75** (1949) 1762; J. Phys. Soc. Japan **5** (1950) 119.
15) K. Kikuchi: Proc. Phys.-Math. Soc. Japan **22** (1940) 805.
16) M. E. Rose: Phys. Rev. **57** (1940) 280.

JOURNAL OF THE PHYSICAL SOCIETY OF JAPAN Vol. 7, No. 2, MAR.—APR., 1952

Backward Scattering of D-D Neutrons

By Shotaro YAMABE and Jyumpei SANADA

Department of Physics, Faculty of Science, Osaka University

(Received July, 27, 1951)

Backward scattering cross sections of 3.1 Mev neutrons scattered by C, O, Fe, Cu and Pb were obtained at angles between 130° and 160° in the laboratory system, assuming that the scattering were entirely elastic. Detector used was a methane filled ionization chamber connected to electrometer. For C and Pb, differential cross sections are rising at large scattering angle, but there are no deviation from flat distribution for other elements. In the case of C it seems to be reasonable to assume that the scattering is entirely elastic, and together with our previous results about the forward distribution whole angular distribution in the centre of mass system can be represented as following

$$\sigma(\theta)=(6.8+6.0\cos\theta+23\cos^2\theta)\times10^{-26}\ \mathrm{cm}^2.$$

But in the case of Pb this backward rising cannot be ascribed to the elastic scattering only because there may be some contribution from the inelastically scattered neutrons for which our detector has a different efficiency.

§ 1. Introduction

S. Kikuchi, H. Aoki and T. Wakatsuki[1] studied the angular distribution of d-d neutrons scattered by the atoms. Their results show that the angular distribution curves can be analysed roughly in two parts, the one corresponding to the spherically symmetric part and the other corresponding to the rising part in the small angle region. This predominance of the small angle scattering was considered to be the characteristic feature of the elastic scattering, and was explained by S. Kikuchi and T. Wakatsuki[2] introducing "Nuclear form factor" analogous to X-ray scattering and by G. Placzeck and H. A. Bethe[3] considering the diffraction scattering of neutron waves. E. Amaldi *et al.*[4], using 14 Mev neutrons, found the second maximum in the forward scattering and this result seems to support the theory of Placzeck and Bethe. Recent results[5] concerning the forward distribution using 90 Mev neutrons also indicate that the diffraction model is a coinsiderably good approximation.

As to the backward scattering of d-d neutrons, J. H. Manley *et al.*[6] reported the results using a directional detector. But to decide whether the values of differential cross sections of large angle scattering are constant or not at the energy of d-d neutrons, it seems desirable to obtain more experimental results as the results hitherto obtained have relatively large experimental errors or poor angle definitions. We therefore, measured the differential scattering cross sections of C, O, Fe, Cu, and Pb at large scattering angles.

§ 2. Experimental arrangement and procedure

Experimental arrangement and procedure were very similar to those of our previous works[7]. The neutron source used was from the d-d reactions by a Cockcroft-Walton set, and the neutron energy was 3.1 Mev in the forward direction.

The arrangement of the target, ring scatterer, and detector is shown in Fig. 1. C_1 and C_2 were the methane filled ionization chambers connected to electrometers, and were used as the detecter and the monitor respectively. S was the ring scatterer.

We measured the ratio $\Delta I/I_0$, where I_0 was the ionization current in C_1 produced by neutrons coming directly from the target (Geometry B) and ΔI was the increase of the ionization current in C_1 when the ring scatterer was placed in position (Geometry A). B, an absorber of paraffin cone, was inserted to reduce the background ionization when we measured ΔI.

If we assume that the scattering are entirely elastic, the relation between the differential scattering cross section $\sigma(\theta)$ and the measured ratio $\Delta I/I_0$ is as follows

$$\Delta I/I_0=G\cdot N\cdot\sigma(\theta)\,.$$

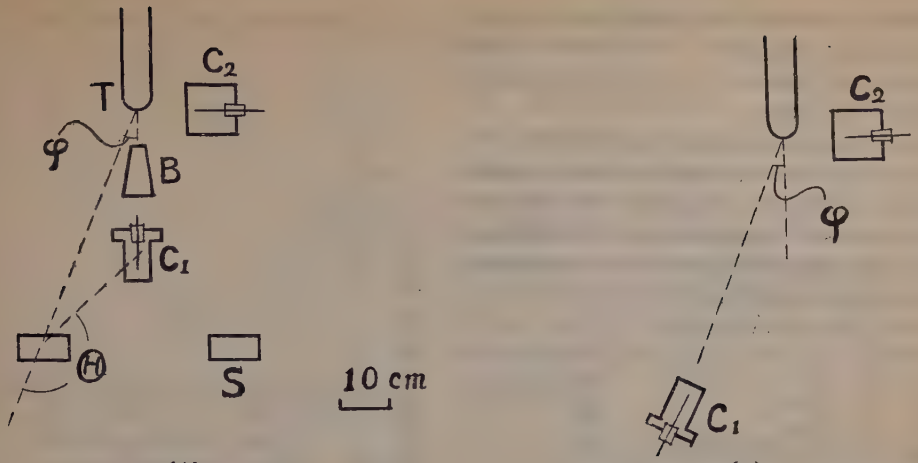

(A)　　(B)

Fig. 1. The arrangement of the target, ring scatterer and detector.

G: geometrical factor including the correction factor of absorption in the scatterer, and was calculated by numerical integrations. In this factor we neglected the effect of the double scattering of neutrons in the scatterer as we had done in our previous work. The correction, due to the circumstances that the efficiency of the detector for neutrons was different according to an angle of impinging neutrons with respect to the axis of the detector, could be obtained experimentally and was also included in this factor. The correction due to the energy loss of the neutrons in the process of the elastic scattering was allowed assuming that the ionization current in the detector was proportional to the value of $\sigma_t(E)\cdot E$, where E is the energy of neutrons and $\sigma_t(E)$ is the total scattering cross section of neutrons by proton at that energy.

N: Total number of atoms contained in the scatterer.

The scattering angle was changed by both the size of the ring scatterers and the distance between the target and the scatterer.

§ 3. Results

The results are tabulated in Table I. In the last column the differential cross sections in

Table I. Experimental results

Sample	Sample size in cm. inner dia.	outer dia.	thickness	Mean scattering angle in degree	$\Delta I/I_0$ in %	$\sigma(\theta)$ in 10^{-25}cm^2
Pb	28	48	4.0	161	2.83±0.12	4.49±0.35
Pb	20	40	4.0	152	5.06±0.19	2.97±0.21
Pb	28	48	4.0	131	6.55±0.20	2.12±0.13
Cu	28	48	5.0	156	2.06±0.14	1.18±0.12
Cu	20	40	4.0	152	4.51±0.29	1.04±0.11
Cu	28	48	5.0	130	8.17±0.19	1.27±0.07
Fe	28	48	5.0	156	2.43±0.13	1.48±0.13
Fe	20	40	5.5	148	5.27±0.15	1.43±0.09
Fe	28	48	5.0	129	8.65±0.14	1.43±0.07
H_2O	28	48	4.35	156	0.54±0.12	0.58±0.15
H_2O	20	40	4.2	152	1.03±0.17	0.55±0.11
H_2O	28	48	4.86	130	2.98±0.18	0.82±0.08
C	28	48	6.0	160	3.29±0.15	1.87±0.15
C	20	40	6.0	150	7.44±0.23	1.60±0.11
C	20	40	3.5	152	4.16±0.20	1.56±0.12
C	28	48	6.0	128	9.98±0.20	1.21±0.06
$C_{25}H_{52}$	20	40	4.6	151	3.36±0.16	1.60±0.14

the laboratory system are shown assuming that the scattering are elastic and errors in this column are the standard error plus errors from the geometrical factor.

The differential scattering cross section *vs.* scattering angle in the centre of mass system are plotted in Fig. 2. Together with the results1)7)8) obtained about forward distribution, whole angular distribution in the centre of mass system are shown in Fig. 3.

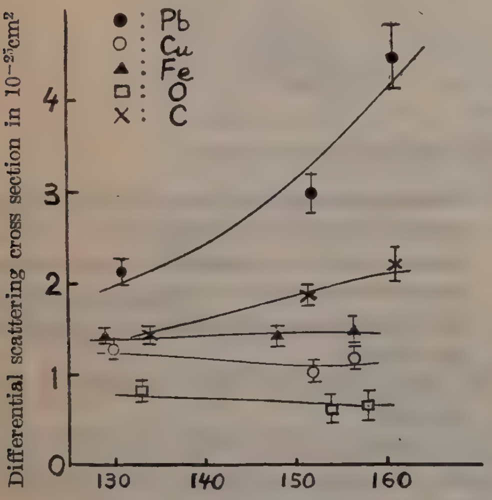

Scattering angle in deg.

Fig. 2. Backward scattering cross sections in the centre of mass system.

For oxygen, water was used as the scatterer and the ionization due to the scattering by protons in water was neglected because the scattering angle between neutrons and protons can not exceed 90 degrees in the laboratory system. To check the geometrical factor in this case we adopted paraffin as the scatterer for carbon in which carbon is almost the same situation as oxygen in water, and obtained the result coincided with that of graphite within the experimental error.

In the case of carbon, we used both thin and thick scatterers of graphite to check some systematic error especialy in the geometrical factor and found that the agreement was very satisfactory.

§ 4. Discussion

a) Carbon and Oxgen.

The neutron energy used was about 3.1 Mev, and both for C^{12} and O^{16} no excited state up to 3.1 Mev above their ground states9) was found. Thus we may interpret that the scattering are entirely elastic. The circumstances of the large angle scattering seem to be very different between carbon and oxygen. This backward rising of carbon cannot be explained by the diffraction scattering. However this is not so surprising because the approximation of the diffraction scattering is only correct when λ (neutron wave length divided by 2π) is far smaller than the nuclear radius R, and this condition is not fulfilled in this energy and atomic number regions.

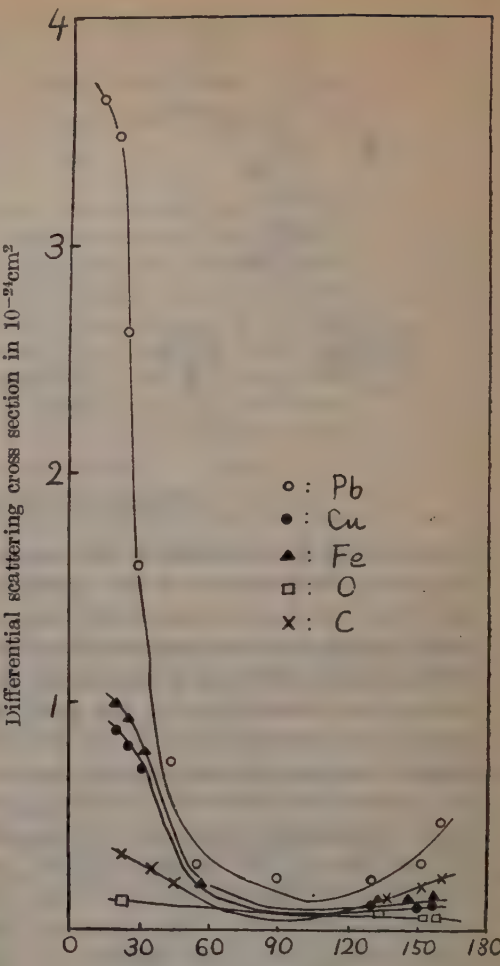

Scattering angle in deg.

Fig. 3. Whole angular distribution in the centre of mass system.

In the case of carbon, whole angular distribution curve can be represented as following

$$\sigma(\theta)=(6.8+6.0\cos\theta+23\cos^2\theta)\times10^{-26}\ \mathrm{cm}^2 .$$

This representation is normalized to the total scattering cross section for carbon, 1.83 barns,7) and is shown in Fig. 4. θ is the angle in the centre of mass system.

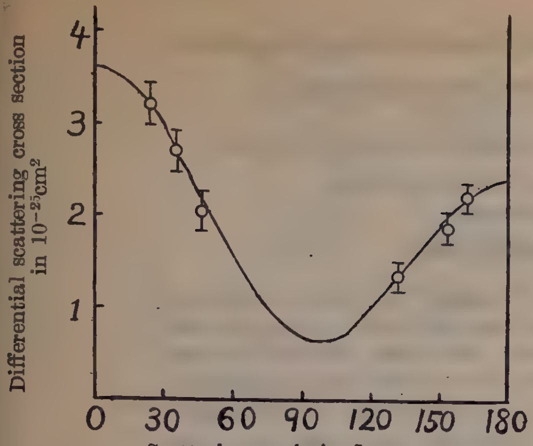

Fig. 4. Angular distributon of carbon. Solid curve is an angular distribution calculated from $\sigma(\theta)=(6.8+6.0\cos\theta+23\cos^2\theta)\times10^{-26}\text{cm}^2$.

b) Fe, Cu and Pb

As to the data of Fe, Cu and Pb there may be some contributions from the inelastically scattered neutrons, and the interpretation is complicated and can not be unique because our detector has a different sensitivity to low energy neutrons. It may be safely concluded that in the case of Pb at least either elastically or inelastically scattered neutrons have a maximum in backward direction.

Elastical backward scattering cross sections obtained by J. H. Manley *et al*[6)], can not be compared with ours because their detector had sharp sensitivity for high energy neutrons and their mean scattering angle were different from ours.

Further investigation about the backward scattering is now undergoing using the detector such as the nuclear plate which can select the energy of neutrons.

§ 5. Acknowledgement

We wish to express our thanks to prof. S. Kikuchi for his encouragement, to Dr. S. Sengoku for the preparation of graphite, to Messrs. T. Wakatsuki, Y. Oda and K. Sugimoto for discussions. Our thanks are also due to Mr. O. Takayanagi for his technical assistances.

This work was supported by the grant for the promotion of science from the Ministry of Education.

References

1) S. Kikuchi, H. Aoki and T. Wakatuki, Proc. Phys. Math. Soc. Japan **21**, (1939) 410. T. Wakatuki and S. Kikuchi, *ibid.* **21**, (1939) 656.

2) S. Kikuchi and T. Wakatuki, Proc. Phys. Math. Soc. Japan **22**, (1940) 142.

3) G. Placzeck and H. A. Bethe, Phys. Rev. **57**, (1940) 382.

4) E. Amaldi, D. Bocciarelli, B. N. Cacciapuoti, and G. C. Trabachi, Phys. Soc. Camb. Conf. (1947) 97.

6) A. Bratenahl, S. Fernbach, R. H. Hildebrand, C. E. Leith, and B. J. Moyer, Phys. Rev. **77** (1950) 597.

6) J. H. Manley, H. M. Agnew, H. H. Barschall, W. C. Bright, C. H. Coon, E. R. Graves, T. Jorgensen and B. Waldman Phys. Rev. **70** (1946) 602.

7) Y. Oda, J. Sanada and S. Yamabe, Jour. Phys. Soc. Japan **6** (1951) 153.

8) Y. Oda, J. Sanada and S. Yamabe, to be published.

9) W. F. Hornyak, T. Lauritsen, P. Monison and W. A. Fowler, Rev. Mod. Phy. **22** (1951) 291.

JOURNAL OF THE PHYSICAL SOCIETY OF JAPAN Vol. 7, No. 2, MAR.—APR., 1952

Energy Dependence of the Capture Cross Sections of Ag, Cu and Al for Fast Neutrons

By Shotaro YAMABE, Masao NOZAWA and Jumpei SANADA

Department of Physics, Faculty of Science,
Osaka University

(Received August 11, 1951)

Relative cross sections of Ag^{107}, Cu^{63} and Al^{27} for radiative capture of neutrons were determined at energies from 2.3 Mev to 3.1 Mev by the method of observing the induced activity. For Ag^{107} and Cu^{63}, capture cross sections decreased almost as $1/E$, where E is the energy of neutrons. For Al^{27}, deviation from monotonous decrease was found. This seemed to be caused by the resonance effects, which had been observed in the measurements of the total cross section for Al. Cross section of (n, p) reaction for Al^{27} was estimated at 3 Mev and was found to be about the same order of magnitude as that of (n, γ) reaction.

§ 1. Introduction

D. J. Hughes *et al.*[1] measured the neutron capture cross sections for 32 isotopes at an effective energy of 1 Mev., and normalizing the capture cross sections for fast neutrons obtained up to that date to those for Au^{197} which had been carefully investigated by Los Alamos group, they found, with only one definite exception for In^{115}, that the neutron capture cross sections for medium and heavy isotopes decreased almost smoothly as $1/E$ at energies above a few hundred Kev. They discussed these features connecting with the theory of H. Feshbach *et al.*[2] in which many resonance levels were treated as average.

On the other hand, R. L. Henkell and H. H. Barshall[3] measured the energy dependence of the neutron capture cross sections for Al, F, V and Cu with high resolution of energy and found many resonances between 0.1 and 0.7 Mev which seemed to be caused by individual levels as were found in the measurement of the total cross sections for neutrons.

At the energy of d-d neutrons, 2~3 Mev, the absolute and the relative capture cross sections for some elements have been obtained by many authors[4)5)6)7)], and Y. Oda[6] also investigated the energy dependence for Ag.

We measured relative cross sections of Ag^{107}, Cu^{63} and Al^{27} for radiative capture of neutrons between 2.3 and 3.1 Mev. In this energy region and with about the same resolution of energy of neutrons as our present work, the energy dependences of the total cross sections and the γ-ray excitation cross sections for many elements were measured by H. Aoki[8] and I. Nonaka[9] respectively and their results showed that these cross sections varied not always monotonously with respect to the energy of neutrons.

§ 2. Experimental arrangement and procedure

Neutrons used were from d-d reaction and were produced in heavy ice target by unanalysed beam of 300 μA and 300 Kev deuterium ions accelerated by a Cockcroft-Walton set. Samples, hollow cylinder of 4.5 cm long and 2.0 cm inner diameter divided into two pieces along its axis, were covered by the shielding boxes for slow neutrons and were placed at 7.5 cm apart from the target as are shown in Fig. 1. The shielding boxes were composed of 0.90 g/cm² B_2O_3 and 0.45 g/cm² Cd and were ensured experimentally to be sufficient for the purpose. The energy of neutrons was changed by varing the mean angle θ between the primary deuteron beams and ejecting neutrons, and the resolution of energy was about 200 Kev at $\theta=0°$ and 150 Kev at $\theta=90°$.

The samples used and the angles at which measurements were performed are tabulated in Table 1.

After about half-life irradiation we covered the detector with the samples which was a cylindrical Geiger-Müller counter of aluminium with wall thickness of about 0.15 mm, and the counting were continued during the half-life. The time interval between the end of irradia-

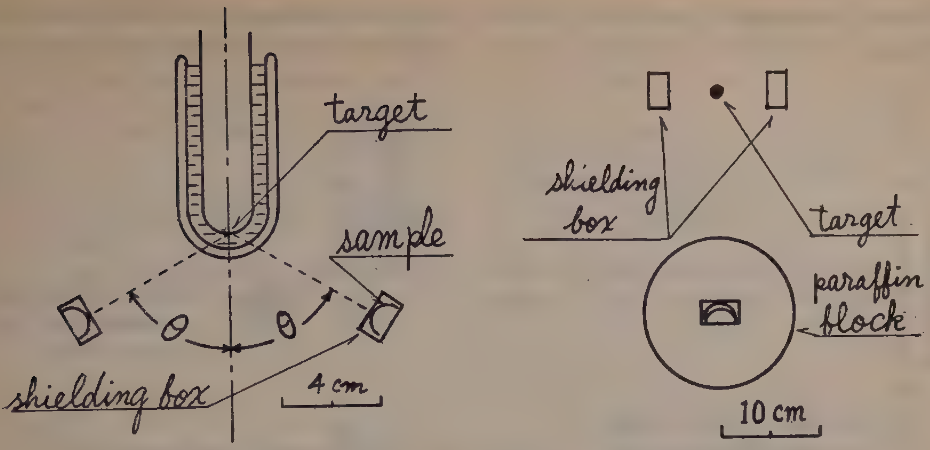

Vertical view Horizontal view

Fig. 1. Experimental arrangement.

Table I.

(The angles where measurements were performed are indicated by open circles.)

Capturing nucleus	Half-life of activity	Measured angles θ in degree									
		0	20	30	40	60	80	90	100	110	120
Al^{27}	2.3 min.	○	○	○	○	○	○	○	○	○	
Cu^{63}	5 min.	○	○		○	○	○		○		○
Ag^{107}	2.5 min.	○			○	○	○		○		○

tion and the beginning of counting was about 40 seconds. The detector was surrounded by lead of 10 cm thickness to reduce the background counts.

To monitor the yield of neutrons another sample of the same material as detecting samples was inserted during the irradiation in the centre of a paraffin block which was placed about 20 cm apart from the target, and the activities which were several ten times stronger than those of the detecting samples were counted by a Geiger-Müller counter of thin window. The counting ratio of detector to monitor thus obtained was not influenced by any fluctuation of neutron intensity.

To obtain the relative cross sections from the counting ratio above described, the knowledge about the relative angular yield of our neutron source was necessary and it was measured by methane filled ionization chambers connected to electrometers. In this procedure we assumed that the ionization current in the chamber was proportional to the value of $\sigma(E)\cdot E$, where E was the energy of neutrons and $\sigma(E)$ was the total cross section of neutrons for protons. Taking the effective energy of deuteron as 200 Kev, the relative angular yield of our source obtained in the centre of mass system were as follows

$$I(\varphi)=1+1.0\cos^2\varphi\,,$$

where φ was the angle between the incident deuterons and the ejected neutrons in the centre of mass system.

The effects of neutrons which came into the samples not directly from the target were very small and were neglected. The effect of the shielding box for the fast neutrons was also neglected because there were some compensation between the effects of scattering in and scattering out.

§ 3. Results and discussion

1) Ag and Cu

In the case of Ag^{107}, to reduce the effect from Ag^{109}, producing the 24 sec. activity of Ag^{110}, we waited 2 minutes after irradiation and then began to count. The data thus obtained might be affected by Ag^{109} about 1%.

For Ag^{107} and Cu^{63} relative cross sections are shown in Fig. 2 and 3. The relative cross sections seem to decrease roughly as $1/E$ as D. J. Hughes *et al.*[1] have reported.

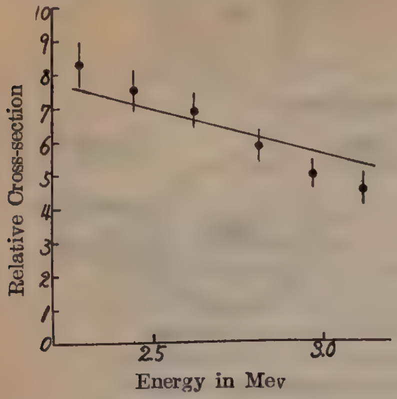

Fig. 2. Relative cross sections for Ag^{107}. Solid line represents $1/E$ slope.

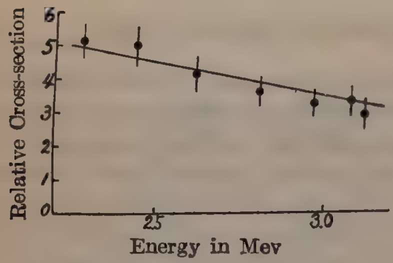

Fig. 3. Relative cross sections for Cu^{63}. Solid line represents $1/E$ slope.

The data obtained by Y. Oda[6] shows that the capture cross section for Ag decrease less rapidly than $1/E$, but this cannot be compared directly with ours because his data must be so interpreted that the main contribution come from Ag^{109}. From these fact it may be said that the capture cross section for Ag^{109} decreases less rapidly than $1/E$. And this does not contradict with the results of D. J. Hughes *et al.*[1].

2) Al

For Al at neutron energy near 3 Mev we adopted the arrangement shown in Fig. 4. to reduce the different contributions of neutrons which scattered into the sample from the other shielding box, and the data were jointed at $\theta = 60°$ above with the usual arrangement (Fig. 1). In Fig. 5. relative cross sections for Al^{27} are shown. The deviation from monotonous decrease in this case seems to be caused by the resonance effects, which have been observed in the measurements of the total cross section for Al.

The calculated threshold of (n, p) reaction for Al^{27}, producing the 10 minutes activity of Mg^{27}, is about 2.1 Mev and the cross section of this process was obtained as 0.03 b. by H. T. Gittings *et al.*[13] at the energy above 3 Mev, and our data might be affected by this reaction. A rough estimation was made by measuring the rates of decay and it was found that the contribution in our data from (n, p) reaction was about a few percent at 3 Mev and probably smaller below this energy. But this contribution was not subtracted in our data because our knowledge about the energy dependence of this reaction was not enough.

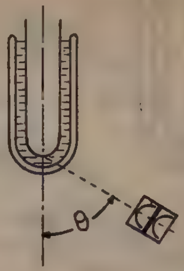

Fig. 4. Experimental arrangement for Al near 3 Mev.

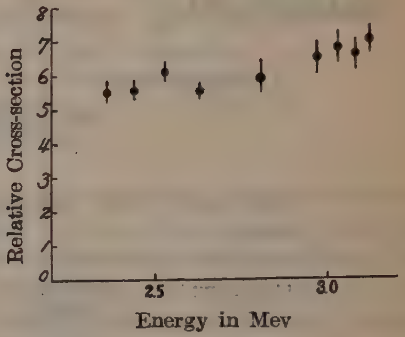

Fig. 5. Relative cross sections for Al^{27}.

The estimated cross section of (n, p) reaction at 3 Mev was about the same order of magnitude as that of (n, γ) reaction.

§ 4. Acknowledgment

We wish to express our thanks to Prof. S. Kikuchi for his encouragement, to Messrs. T. Wakatsuki, Y. Oda and K. Sugimoto for discussions. Our thanks are also due to Mr. O. Takayanagi for his technical assistances.

This work was supported by the grant for the promotion of science from the Ministry of Education.

References

1) D. J. Hughes, W. D. B. Spatz and N. Goldstein: Phys. Rev. **75** (1949) 1781.

2) H. Feshbach, D. C. Peaslee and V. F. Weisskopf: Phys. Rev. **71** (1947) 145.

3) R. L. Henkell and H. H. Barshall: Phys. Rev. **80** (1950) 145.

4) E. T. Booth and C. Hurst: Proc. Roy. Soc. **161** (1937) 149.

5) H. Reddemann: Nature **142** (1937) 124.

6) Y. Oda, Scientific Paper from the Osaka Univ. No. 8 (1949).

7) M. G. Meschenyakov: Comp. Red. U. R. S. S. **48** (1945) 555.

8) H. Aoki: Proc. Phys.-Math. Soc. Japan **21** (1939) 232.

9) I. Nonaka: Proc. Phys. Soc. Japan **22** (1941) 925.

10) M. R. Macphail: Phys. Rev. **57** (1940) 669.

11) Allen, Burcham, and Wilkinson: Proc. Roy. Soc. **192** (1947) 114.

12. Bernard L. Cohen: Phys. Rev. **81** (1951) 184.

13) H. T. Gittings, H. H. Barshall, and G. G. Everhart: Phys. Rev. **75** (1949) 1610.

Journal of the Physical Society of Japan Vol. 7, No. 2, Mar.—Apr., 1952

On States not in Thermal Equilibrium, II

(Miscellaneous Notes and Correction of the Previous Paper[1])

By Naruo TAKETA and Toyoki KOGA

Faculty of Engineering, Nagoya University

(Received July 7, 1950)

In the previous paper of Koga of the same title as the present, the results are more or less different from those of Enskog and Chapman. At first sight, it seemed that the treatment of Enskog and Chapman might not be correct for lacking of interpretation of the physical meanings. But later we arrived at the conclusion: Enskog-Chapman's solution is correct formally, and further we can show that the variables adopted by them are of the same physical meanings as those in Koga's treatment. Although we cannot yet mention any mistake positively in Koga's results, yet some lacks necessary of verifications are found on Koga's side.

§1. Enskog (1917) and Chapman (1916)[2] succeeded in obtaining the exact mathematical solution of transport phenomena by solving Boltzmann's equation. Nevertheless, general considerations lead us to the conclusion that in Enskog-Chapman's method the physical meaning is not clear because of their abstract mathematical treatment in obtaining the expression of distribution function.

In 1945, one of us carried out the treatment of this problem,[1] by generalizing the method of Meyer,[3] giving physical interpretation carefully and introducing some other physical conceptions. As a first approximation, we found a result somewhat different* from that of Chapman and Enskog. Considering the defects of interpretation of the physical meanings (experimental meanings) in Enskog-Chapman's treatment, it seemed, at first sight, that their treatment might not be correct. But later, studying carefully the problem we arrived at the conclusions:

i) Taking the deviation from thermal equilibrium small, Boltzmann's Eq. is correctly applicable to the present case.

ii) In spite of obscurity of the physical meaning of the variables adopted, Enskog-Chapman's solution is correct formally (or mathematically) as a first approximate solution of Boltzmann's Eq.

iii) We can show that the variables adopted by Enskog and Chapman are of the same physical meanings as those in Koga's treatment.

iv) Although we cannot yet mention any mistake positively in Koga's results, there are in fact found some missings necessary of verifications.

---

* Cf. Eq. (4.1), 4) in the previous paper[1]. The terms $\sigma_p\frac{\partial p}{\partial x}$, etc. seems superfluous.

§2. When the states deviate slightly from thermal equilibrium, Boltzmann's Eq. of continuity is considered to have a physical meaning. Then the mathematical from of the problem leads us to the consideration that we can conveniently adopt the distribution function of the same form as in thermal equilibrium as a first approximation and apply the notations *called* temperature, density, mass-velocity, as variables characterizing the states. Still, we cannot give physical meanings to these variables in non-uniform state, for instance, we have not appropriate means to distinguish thermal energy from mass-motion energy. Enskog and Chapman introduced these variables formally without taking into account their physical meanings and call them temperature T, density n and mass-velocity u, v, w as usual. The definitions adopted by them are as follows[4]:

$$\begin{aligned}&\int f_{(0)}dc = n\left(=\int f dc\right),\\ &\int f_{(0)}c_x dc = nu\left(=\int f c_x dc\right),\\ &\int f_{(0)}\,c_y dc = nv\left(=\int f c_y dc\right),\\ &\int f_{(0)}c_z dc = nw\left(=\int f c_z dc\right), \qquad\qquad (1)\\ &\int \frac{1}{2}mC^2 f_{(0)}dc = \frac{1}{2}nkT\left(=\int\frac{1}{2}mC^2 f dc\right),\\ &C(C_x,C_y,C_z) = c(c_x,c_y,c_z) - V(u,v,w),\end{aligned}$$

where $f_{(0)}$ and f denote the distribution functions in thermal equilibrium and in non-equilibrium state respectively, C the so-called peculiar velocity, c molecular velocity and V mass-velocity. On the other hand, Koga defined the variables in connection with macroscopic physical meanings as follows:

$$\begin{aligned}&(m)/m = \tilde{n},\\ &(M)_x/m = [m]_x/m = \tilde{n}\tilde{u},\\ &(M)_y/m = [m]_y/m = \tilde{n}\tilde{v},\\ &(M)_z/m = [m]_z/m = \tilde{n}\tilde{w},\\ &(E') = \frac{1}{2}\tilde{n}k\tilde{T}, \qquad\qquad (2)\end{aligned}$$

where the notations are the same as explained in the previous paper.[5] The terms in the parentheses in (1) coincide with the left hand terms of (2) in physical meanings. hence T, n, u, v, and w in (1) are equal to $\tilde{T}$, $\tilde{n}$, $\tilde{u}$, $\tilde{v}$, and $\tilde{w}$ in (2) respectively. Here, in both cases, these variables should be regarded as mere parameters. If we assume that the state comes to thermal equilibrium conserving the same mass, momentum and energy in unit volume as those in non-equilibrium, the parameters T, n, u, v, and w express respectively temperature, density and mass-velocity in usual meaning. In usual hydrodynamics where the state is not in equilibrium, we treat T, n, u, v, and w as quantities having directly experimental meanings. This treatment is not correct and these variables should be regarded as mere parameters. The relations between these parameters and the quantities to be measured experimentally were fully discussed by Koga.[5] The result leads us to a conclusion that only on a wall we can give to these parameters directly experimental meanings.

§3. Now Koga expresses the 17 quantities[5][7] in terms of the parameters $\tilde{T}$, $\tilde{n}$, $\tilde{u}$, $\tilde{v}$, $\tilde{w}$ without attempting to solve directly Boltzmann's equation. This process corresponds to that of expressing f in terms of c_x, c_y, c_z, T, n, u, v, w in Enskog-Chapman's treatment. He introduces the quantities $\overline{T}$, $\bar{n}$, $\bar{u}$, $\bar{v}$, $\bar{w}$, which are defined as follows: As a first approximation, he cuts out a small domain of field where the state is assumed to be locally in equillibrium, and introduces notations $\overline{T}$ for tamperature, $\bar{n}$ for density, $\bar{u}$, $\bar{v}$, $\bar{w}$ for mass-velocity in each domain. Further each domain or cell may be assumed to be so small that we can differenciate all quantities all over the field as if they are continuous. He assumes that the deviations of actual states from this artificially constructed states, in which each small domain is in equilibrium, are of small quantities of the first order. The probability of encounters between molecules in thermal equilibrium being known, we can calculate, for this artificially constructed state, the 17 quantities by integrating over all the past time and the space. *This result itself is correct so long as we treat the artificially constructed state.* Now so far as we have only five quantities $(\overline{m})$, $(\overline{M})_i$, $(\overline{E'})$, $(\overline{E''})$, $[\overline{M}]_{ii}$, these quantities are able to be equal to those of actual state as there are five parameters to be defined. But there are further 12 quantities (namely $[M]_{ij}$, $[\overline{E'}]_i$, ⋯⋯etc.) left to be identified with those of the actual state, while there is no other parameter to be defined anew. Koga said that these 12 quantities also have the values of actual state automatically, if we neglect small quantities of the second order. Evidently, it is true that $[M]_{xy}-m\hat{n}\tilde{u}\tilde{v},\cdots$etc., are constructed of terms of small values, so functional forms of these quantities are left unaffected by alternation of parameters $\bar{T}$, $\bar{n}$, $\bar{u}$, $\bar{v}$, $\bar{w}$. But this does not justify that his statement is necessarily correct. Although we cannot yet mention evidently and directly the reason of saying that Koga is not correct, his solution is different from that of Enskog and Chapman when their solution are considered to be accurate formally. Perhaps the origin of the discrepancy may be found in the mode of encounter. This seems to be the essential difficulty inherent in handling the problems in such a way as adopted by Meyer.[3] Without these considerations, we shall meet paradoxical results. The strange paradoxidal inconsistency mentioned in Jeans' text-book of gases[6] also may be an example. As described previously, Enskog-Chapman and Koga adopt incidentally the same parameters. But in general the selection of parameters might be quite arbitrary to construct the theory, if one can suitablly connect them with experimental results.

References

1) T. Koga: J. Phys. Soc. Japan **4** (1949) 34.

2) S. Chapman and T. G. cowling; *The Mathematical Theory of non-uniform Gasses* (Cambridge University press), 1939.

3) J. H. Jeans: *The Dynamical Theory of Gases*, 4th edition, 1929, p. 291.

4) S. Chapman and T. G. Cowling: loc. cit., chap. 7.

5) T. Koga, loc. cit.

6) J. H. Jeans, loc. cit. p. 295.

7) N. Taketa, J. Phys. Soc. Japan **4** (1949) 359.

JOURNAL OF THE PHYSICAL SOCIETY OF JAPAN, Vol. 7, No. 2, MAR.—APR., 1952

Statistical Theory of Rotational Phase Transition, I

By Takehiko OGUCHI and Yutaka TAKAGI

Tokyo Institute of Technology, Oh-okayama, Tokyo

(Received May 10, 1951)

The rotational phase transition is discussed along the line of Kikuchi's method for order-disorder transformation in binary alloys. The potential energy for a pair of neighbouring molecules are $-J/2\cos(i,j)$, where (i,j) is the angle between neighbouring molecular axes and J is the constant. The transition point $J/2kT_c$, that is a branching point of the integral equation, is 1.150 in the case of two-dimensional square lattice. This value is the lowest compared with those obtained by other theories. The discontinuity of the specific heat at the transition point is calculated, though some assumption has to be made to avoid the complexity of the calculation. The transition point does not vary even when an anisotropic potential is introduced.

§ 1. Introduction

In many molecular crystals, we often see anomalous specific heats of λ-type at relatively low temperatures. They are attributed to the transition from the ordered state of the orientations of the axes of molecules at low temperatures to the disordered state due to the thermal agitation, and the phenomena are called the rotational phase transitions. The behavior of the rotational phase transitions is qualitatively similar to the order-disorder transition in binary alloys. So the studies about the former can be performed also with respect to the latter. In fact, the study of Kirkwood[1] corresponds to the Bragg-Williams approximation in binary alloys and the studies of Chang[2], Kubo-Hashimura[3] and Nakamura[4] correspond to the Bethe approximation and the study of Yoshida[5] corresponds to the moment method of Kirkwood in binary alloys. In order to proceed with the theory still further, two ways are considered. One is an improvement of the potential form between the molecules so as to express more closely the situations in a real crystal, along which studies are performed by Nagamiya⁶⁾ and Kubo-Hashimura⁷⁾, and the other is an improvement of the process of statistical treatment. This paper belongs to the latter.

In binary alloys better approximations than the Bethe's one are made by Kramers-Wannier⁸⁾ by means of the variational method and recently by Kikuchi⁹⁾ by means of the combinatorial method. It is shown by Kikuchi that these two results agree completely.

In this paper, using the Kikuchi's method, the improvement of the statistical treatment of rotational phase transition is shown in the case of two-dimensional square lattice.

§ 2. Outline of the theoretical treatment

The molecules are arranged on square lattice sites. The number of total lattice sites is N. The sites are divided into four classes: 1st, 2nd, 3rd and 4th as shown in Fig. 1. The orientation of the axis of molecule on 1st site is denoted by (θ_i, φ_i) in polar coordinate. We abbreviate it by (i). In the same way, those of 2nd, 3rd and 4th sites are denoted by (j), (k) and (l) respectively. The bond connecting 1st and 2nd sites is named as I type as shown in Fig. 1. In the same way, connecting bonds between 2nd and 3rd sites, 3rd and 4th sites, and 4th and 1st sites are named as II, III and IV types respectively. Let the number of molecules on 1st sites whose molecular axes are (i), be denoted by $n_1(i)$. $n_2(j)$, $n_3(k)$ and $n_4(l)$ are defined in the same way respectively. (see Fig. 2.) Let the number of conncting bonds of type I whose end molecules which are on 1st and 2nd sites, are (i) orientation and (j) orientation respectively, be denoted by $f_{\mathrm{I}}(i,j)$. $f_{\mathrm{II}}(j,k)$, $f_{\mathrm{III}}(k,l)$ and $f_{\mathrm{IV}}(l,i)$ are respectively defined in the same way as shown in Fig. 2. Lastly, we define $s(i,j,k,l)$ as the number of squares composed of 1st, 2nd, 3rd and 4th sites whose molecular orientations are (i), (j), (k) and (l) respectively. Using the method of Kikuchi for approximating the number of ways of constructing a crystal, the configurational entropy Φ can be approximated as

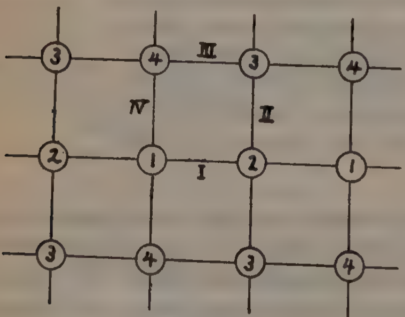

Fig. 1.

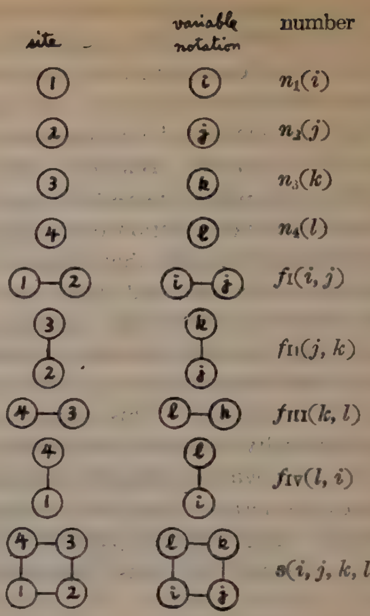

Fig. 2.

$$
\begin{aligned}
\frac{\Phi}{k}=&\sum_{i,j} f_{\mathrm{I}}(i,j)\ln f_{\mathrm{I}}(i,j)+\sum_{j,k} f_{\mathrm{II}}(j,k)\ln f_{\mathrm{II}}(j,k)\\
&+\sum_{k,l} f_{\mathrm{III}}(k,l)\ln f_{\mathrm{III}}(k,l)\\
&+\sum_{l,i} f_{\mathrm{IV}}(l,i)\ln f_{\mathrm{IV}}(l,i)\\
&-\sum_{i,j,k,l} s(i,j,k,l)\ln s(i,j,k,l)\\
&-\sum_{i} n_1(i)\ln n_1(i)-\sum_{j} n_2(j)\ln n_2(j)\\
&-\sum_{k} n_3(k)\ln n_3(k)-\sum_{l} n_4(l)\ln n_4(l) \qquad (2\cdot1)
\end{aligned}
$$

k on left hand side is Boltzmann constant. Don't confuse it with the angle variable on 3rd site. Since the orientational variables are considered as continuous, above summations can be substituted by integrals, as follows,

$$
\begin{aligned}
\frac{\Phi}{k}=&\iint f_{\mathrm{I}}(i,j)\ln f_{\mathrm{I}}(i,j)+\text{similar terms}\\
&-\iiiint s(i,j,k,l)\ln s(i,j,k,l)\,didjdkdl
\end{aligned}
$$

$$-\int n_1(i)\ln n_1(i)di-\text{similar terms} \quad (2\cdot2)$$

where integral $\int\cdots di$ denotes $\int_0^{2\pi}\int_0^{\pi}\cdots\sin\theta_i d\theta_i d\varphi_i$. As easily seen, following relations must be kept among n's, f's and s's:

$$f_{\mathrm{I}}(i,j)=\frac{1}{2}\iint s(i,j,k,l)dkdl\,, \qquad f_{\mathrm{II}}(j,k)=\frac{1}{2}\iint s(i,j,k,l)didl$$

$$f_{\mathrm{III}}(k,l)=\frac{1}{2}\iint s(i,j,k,l)didj\,, \qquad f_{\mathrm{IV}}(l,i)=\frac{1}{2}\iint s(i,j,k,l)djdk$$

$$n_1(i)=\frac{1}{2}\int f_{\mathrm{I}}(i,j)dj=\frac{1}{2}\int f_{\mathrm{IV}}(l,i)dl=\frac{1}{4}\iiint s(i,j,k,l)djdkdl$$

$$n_2(j)=\frac{1}{2}\int f_{\mathrm{I}}(i,j)di=\frac{1}{2}\int f_{\mathrm{II}}(j,k)dk=\frac{1}{4}\iiint s(i,j,k,l)didkdl$$

$$n_3(k)=\frac{1}{2}\int f_{\mathrm{II}}(j,k)dj=\frac{1}{2}\int f_{\mathrm{III}}(k,l)dl=\frac{1}{4}\iiint s(i,j,k,l)didjdl$$

$$n_4(l)=\frac{1}{2}\int f_{\mathrm{III}}(k,l)dk=\frac{1}{2}\int f_{\mathrm{IV}}(l,i)di=\frac{1}{4}\iiint s(i,j,k,l)didjdk \qquad (2\cdot3)$$

Using these relations, the entropy is

$$\frac{\Phi}{k}=\left[\frac{1}{2}\iiiint s\{\ln\iint sdidj\}didjdkdl+\frac{1}{2}\ln\frac{1}{2}\cdot\iiiint sdidjdkdl\right]+\text{cyclic change of }(i,j)$$
$$-\iiiint s\ln sdidjdkdl-\left[\frac{1}{4}\iiiint s\{\ln\iiint sdjdkdl\}didjdkdl+\frac{1}{4}\ln\frac{1}{4}\iiiint sdidjdkdl\right]$$
$$-\text{cyclic change of }(j,k,l) \qquad (2\cdot4)$$

In order to simylify the calculation, we take the two important assumptions about the potential energy between molecules. One is that the forces on each molecules depend on the orientations of its immediate neighbours, and the other is that the potential energy between nearest neighbours depends only on the angles between two molecular axes, as in the following form,

$$V_{\mathrm{I}}(i,j)=-\frac{J}{2}\cos(i,j)$$
$$=-\frac{J}{2}\{\cos\theta_i\cos\theta_j$$
$$+\sin\theta_i\sin\theta_j\cos(\varphi_i-\varphi_j)\} \quad (J>0) \qquad (2\cdot5)$$

This potential energy form is called "Kirkwood potential".

According to the above two simplifications, the total energy of the system is

$$E=\sum_{i,j}V_{\mathrm{I}}(i,j)f_{\mathrm{I}}(i,j)+\sum_{j,k}V_{\mathrm{II}}(j,k)f_{\mathrm{II}}(j,k)$$
$$+\sum_{k,l}V_{\mathrm{III}}(k,l)f_{\mathrm{III}}(k,l)+\sum_{l,i}V_{\mathrm{IV}}(l,i)f_{\mathrm{IV}}(l,i)$$
$$=-\frac{J}{4}\iiiint\{\cos(i,j)+\cos(j,k)+\cos(k,l)$$
$$+\cos(l,i)\}sdidjdkdl \qquad (2\cdot6)$$

Thus, from (2·4) and (2·6), the free energy F of the system is

$$\frac{F}{kT}=\iiiint\Big[-\frac{1}{2}K\{\cos(i,j)+\cos(j,k)$$
$$+\cos(k,l)+\cos(l,i)\}$$
$$-\left\{\frac{1}{2}\ln\iint sdidj+\frac{1}{2}\ln\frac{1}{2}\right\}$$
$$-\text{cyclic change of }(i,j)$$
$$+\ln s$$
$$+\left\{\frac{1}{4}\ln\iiint sdidjdk+\frac{1}{4}\ln\frac{1}{4}\right\}$$
$$+\text{cyclic change of }(i,j,k)\Big]sdidjdkdl \qquad (2\cdot7)$$

where

$$K=J/2kT \qquad (2\cdot8)$$

In order to minimize the free energy under supplementary condition,

$$\iiiint sdidjdkdl=N \qquad (2\cdot9)$$

the usual method of undetermined multipliers gives immediately the first order variational equation;

$$-\frac{1}{2}K\{\cos(i,j)+\text{cyclic change of }(i,j)\}$$
$$-\frac{1}{2}\ln\iint sdidj-\text{cyclic change of }(i,j)$$
$$+\ln s$$
$$+\frac{1}{4}\ln\iiint sdidjdk+\text{cyclic change of }(i,j,k)$$
$$+\text{const.}=0 \qquad (2\cdot10)$$

Using (2·3), we substitute above integrations by f's term, and after several rearrangement, (2·10) becomes

$$\lambda s(i,j,k,l)$$
$$=\frac{[f_{\text{I}}(i,j)\cdot f_{\text{II}}(j,k)f_{\text{III}}(k,l)f_{\text{IV}}(l,i)]^{\frac{1}{2}}}{[n_1(i)\cdot n_2(j)\cdot n_3(k)\cdot n_4(l)]^{\frac{1}{4}}}$$
$$\times\exp\Big[\frac{K}{2}\{\cos(i,j)+\cos(j,k)+\cos(k,l)$$
$$+\cos(l,i)\}\Big] \tag{2·11}$$

Integrating both sides of (2·11) with (k) and (l), doing several rearrangement, we get,

$$2\lambda[f_{\text{I}}(i,j)]^{\frac{1}{2}}[n_1(i)\cdot n_2(j)]^{\frac{1}{4}}$$
$$\times\exp\Big[-\frac{K}{2}\cos(i,j)\Big]$$
$$=\iint\frac{[f_{\text{II}}(j,k)f_{\text{III}}(k,l)f_{\text{IV}}(l,i)]^{\frac{1}{2}}}{[n_3(k)n_4(l)]^{\frac{1}{4}}}$$
$$\times\exp\Big[\frac{K}{2}\{\cos(j,k)+\cos(k,l)$$
$$+\cos(l,i)\}\Big]dkdl \tag{2·12}$$

If we remove the classification of the sites and the connecting bond types and regard all types as equivalent, we get,

$$f_{\text{I}}(i,j)=\frac{1}{4}f(i,j)\quad f_{\text{II}}(j,k)=\frac{1}{4}f(j,k)$$
$$f_{\text{III}}(k,l)=\frac{1}{4}f(k,l)\quad f_{\text{IV}}(l,i)=\frac{1}{4}f(l,i) \tag{2·13}$$

where $f(i,j)$ is the number of any connecting bonds between molecules whose orientations are (i) and (j) respectively. Including all constants into λ, we obtain,

$$\lambda[f(i,j)]^{\frac{1}{2}}\Big[\int f(i,j)dj\cdot\int f(j,k)dk\Big]^{\frac{1}{4}}$$
$$\times\exp\Big[-\frac{K}{2}\cos(i,j)\Big]$$
$$=\iint\frac{[f(j,k)\cdot f(k,l)\cdot f(l,i)]^{\frac{1}{2}}}{\Big[\int f(k,l)dl\cdot\int f(l,i)di\Big]^{\frac{1}{4}}}$$
$$\times\exp\Big[\frac{K}{2}\{\cos(j,k)+\cos(k,l)$$
$$+\cos(l,i)\}\Big]dkdl \tag{2·14}$$

This is the fundamental integral equation.

§ 3. Solutions of the integral equation

Since the integral equation (2·14) is the function of two variables (i) and (j), it is difficult to be analytically treated. So we integrate both sides of (2·14) with (j) as follows,

$$\lambda\int\Big[f(i,j)\Big]^{\frac{1}{2}}\Big[\int f(i,j)dj\cdot\int f(j,k)dk\Big]^{\frac{1}{4}}$$
$$\times\exp\Big[-\frac{K}{2}\cos(i,j)\Big]dj$$
$$=\iiint\frac{[f(j,k)\cdot f(k,l)\cdot f(l,i)]^{\frac{1}{2}}}{\Big[\int f(k,l)\,dl\cdot\int f(l,i)\,di\Big]^{\frac{1}{4}}}$$
$$\times\exp\Big[\frac{K}{2}\{\cos(j,k)+\cos(k,l)$$
$$+\cos(l,i)\}\Big]djdkdl \tag{3·1}$$

Eq. (3·1) includes the singularity of Eq. (2·14), so henceforth we will treat Eq. (3·1) which is the function of only one variable (i).

We expand $\exp[K\cos(i,j)]$ into two axes spherical harmonics as follows,

$$\exp[K\cos(i,j)]=\sum_{l=0}^{\infty}(2l+1)\sqrt{\frac{\pi}{2K}}I_{l+\frac{1}{2}}(K)$$
$$\times\sum_{m=-l}^{l}P_l^{|m|}(\cos\theta_i)P_l^{|m|}(\cos\theta_j)e^{im(\varphi_i-\varphi_j)} \tag{3·2}$$

where $P_l^{|m|}(\cos\theta_i)$ is the associated Legendre function and $I_{l+\frac{1}{2}}(K)$ is connected to Bessel function $J_{l+\frac{1}{2}}(K)$ as follows,

$$I_{l+\frac{1}{2}}(K)=e^{il\pi/2}J_{l+\frac{1}{2}}(K)\quad l=0,1,2,\cdots \tag{3·3}$$

As may be seen,

$$f(i,j)=\frac{1}{\mu}\frac{1}{4\pi}\exp[K\cos(i,j)] \tag{3·4}$$

is the solution of (3·1), and the characteristic value corresponding to it is

$$\lambda_0=4\pi\Big\{\sqrt{\frac{\pi}{2K}}I_{\frac{1}{2}}(K)\Big\}^2\equiv4\pi\{H(K)\}^2 \tag{3·5}$$

and μ is the normalization factor. Considering from the physical meaning, the solution (3·4) is the form of the Boltzmann distribution and the energy of it depends only on the angle between the orientations of nearest neighbour molecules, and is independent of the orientations of all other molecules. So there is no long range order.

When the temperature is lower, the solution which corresponds to the ordered state should exist. In order to obtain such solution, we expand $f(i,j)$ as following;

$$f(i,j)=\exp[K\cos(i,j)]$$
$$\times\sum A_{l,l'}^{m,m'}P_l^{|m|}(\cos\theta_i)$$
$$\cdot P_{l'}^{|m'|}(\cos\theta_j)e^{im\varphi_i}e^{im'\varphi_j} \tag{3·6}$$

As (3·6) should be symmetric about polar axis, m' must be equal to $-m$. In the same way, from the considerations on the symmetries, we obtain,

$$A_{l,l'}^{m,-m}=A_{l',l}^{m,-m}\equiv A_{l,l'}^{m} \tag{3·7}$$

Thus

$$f(i,j)=\exp[K\cos(i,j)]$$
$$\times\sum_{l=0}^{\infty}\sum_{l'=0}^{\infty}\sum_{m=0}^{\text{minimum of } l \text{ or } l'} A^m_{l,l'}P_l^{|m|}(\cos\theta_i)$$
$$\times P_{l'}^{|m|}(\cos\theta_j)\cos m(\varphi_i-\varphi_j) \qquad (3\cdot 8)$$

When all the coefficients except $A^0_{0,0}$ vanish, (3·8) equals to (3·4) which is the solution of disordered state. The solution of disordered state exists in all temperature ranges. The solution corresponding to the ordered state is that in which $A^0_{1,0}$ etc. do not vanish. It is expected that as the temperature becomes sufficiently lower, a point will appear on and below of which $A^0_{1,0}$ accordingly $A^0_{2,0}$ etc. will take the real value different from zero. Such a point corresponds to the branching point of the integral equation (3·1). Of course, the integral equation (3·1) has many branching points, and one of them is the point at which $A^0_{1,0}$ does not vanish. (A point at which $A^0_{1,0}$ vanishes but $A^0_{2,0}$ etc. do not vanish is another branching point). We regard this point as transition point. We shall show in the next section that if we regard $A^0_{0,0}$ as zeroth order, $A^0_{1,0}$ is of first order, $A^0_{2,0}$ is of second order, that is, $A^0_{2,0}$ is of the order of $(A^0_{1,0})^2$. So in order to determine the transition temperature it is enough to calculate up to the order of $A^0_{1,0}$. We put

$$f(i,j)=\frac{1}{\mu}\frac{1}{4\pi}\exp[K\cos(i,j)]$$
$$\times[1+A^0_{1,0}\{P_1(\cos\theta_i)+P_1(\cos\theta_j)\}\cdots] \qquad (3\cdot 9)$$

We substitute (3·9) into both sides of (3·1). The formulae used in the calculations are tabulated in Appendix. Thus the left hand side of (3·1) is

$$\lambda\sqrt{4\pi}\{H(K)\}^{\frac{1}{2}}\left[1+A^0_{1,0}\left\{\frac{3}{4}+\frac{1}{4}\frac{H'(K)}{H(K)}\right\}\right.$$
$$\left.\times P_1(\cos\theta_i)\cdots\right], \qquad (3\cdot 10)$$

and right hand side of (3·1) is

$$(4\pi)^{\frac{3}{2}}\{H(K)\}^{\frac{5}{2}}\left[1+A^0_{1,0}\left\{\frac{1}{2}+\frac{3}{4}\frac{H'(K)}{H(K)}\right.\right.$$
$$\left.\left.+\frac{1}{2}\left(\frac{H'(K)}{H(K)}\right)^2+\frac{1}{4}\left(\frac{H'(K)}{H(K)}\right)^3\right\}P_1(\cos\theta_i)\cdots\right] \qquad (3\cdot 11)$$

From (3·10) and (3·11), we pick up the first order terms and obtain,

$$A^0_{1,0}\left[\left\{\frac{H'(K)}{H(K)}\right\}^3+2\left\{\frac{H'(K)}{H(K)}\right\}^2\right.$$
$$\left.+2\left\{\frac{H'(K)}{H(K)}\right\}-1\right]=0 \qquad (3\cdot 12)$$

If $A^0_{1,0}$ does not vanish, the coefficient of it must vanish. As easily seen, the function $H'(K)/H(K)$ equal to Langevin function $L(K)$, and from (3·12) we obtain

$$\{L(K_c)\}^3+2\{L(K_c)\}^2+2L(K_c)-1=0 \quad (3\cdot 13)$$

This is the formula which gives the branching point i.e. the transition temperature. Explanations will be given in detail in next section. From (3·13), we obtain the transition temperature as follows,

$$K_c=1.150 \qquad (3\cdot 14)$$

As seen from Table I, the transition temperature becomes lower with the progress of statistical treatment, and this situation is similar to the transition temperature of order-disorder in binary alloys.

Table I

	K_c
Kirkwood	0.75
Chang	1.074
Authors	1.150

§ 4. The specific heat

We shall be content in the following to find only the specific heat discontinuity at the transition temperature. To obtain it, the terms up to the order of $(A^0_{1,0})^3$ must be calculated. The calculations are so troublesome that in this paper we introduce an assumption to avoid the complexity of the calculation. Tedious calculations without any assumption are now being performed. The assumption is that, in stead of (3·8) which is rigorous as $f(i,j)$, we adopt next form,

$$f(i,j)=\frac{1}{\mu}\frac{1}{4\pi}\exp[K\cos(i,j)]$$
$$\times[1+c_1P_1(\cos\theta_i)+c_2P_2(\cos\theta_i)\cdots]$$
$$\times[1+c_1P_1(\cos\theta_j)+c_2P_2(\cos\theta_j)\cdots] \qquad (4\cdot 1)$$

This formula is analogous to that of Bethe approximation. We now substitute (4·1) in both sides of (3·1). From left hand side of (3·1), we get,

$$A_0+A_1P_1(\cos\theta_i)+A_2P_2(\cos\theta_i)\cdots \quad (4\cdot 2)$$

where

$$A_0=\lambda(4\pi)^{\frac{1}{2}}H^{\frac{1}{2}}(1+a_{0,2}c_1{}^2\cdots)$$
$$A_1=\lambda(4\pi)^{\frac{1}{2}}H^{\frac{1}{2}}(a_{1,1}c_1+a_{1,3}c_1{}^3+a'_{1,3}c_1c_2\cdots)$$
$$A_2=\lambda(4\pi)^{\frac{1}{2}}H^{\frac{1}{2}}(a_{2,2}c_2+a'_{2,2}c_1{}^2\cdots) \quad (4\cdot 3)$$

From right hand side of (3·1), after performing some tedious integrations, we get

$$B_0+B_1P_1(\cos\theta_i)+B_2P_2(\cos\theta_i)\cdots \quad (4\cdot 4)$$

where

$$B_0=(4\pi)^{\frac{3}{2}}H^{\frac{5}{2}}(1+b_{0,2}c_1^2\cdots)$$
$$B_1=(4\pi)^{\frac{3}{2}}H^{\frac{5}{2}}(b_{1,1}c_1+b_{1,3}c_1^3+b'_{1,3}c_1c_2\cdots)$$
$$B_2=(4\pi)^{\frac{3}{2}}H^{\frac{5}{2}}(b_{2,2}c_2+b'_{2,2}c_1^2\cdots)\,, \qquad (4\cdot5)$$

where all the a's and b's are complicated functions of K. In order to identify (4·2) with (4·4), it is necessary and sufficient that $A_0=B_0$, $A_1=B_1$, $A_2=B_2$, $\cdots$. The set of equations admits a solution $c_1=c_2=\cdots=0$, because equations $A_j=B_j(j\geq1)$ have no constant terms. It may admit, however, a non-zero solution. When the c_i's are all small and very nearly equal to zero, we see from the relation $A_2=B_2$ that c_2 is of the order of c_1^2, and quite generally, from the equations not written here, that the coefficients $c_j(j\geq3)$ are of still higher order. Henceforth, from the equation $A_2=B_2$, we obtain

$$c_2=\alpha(K)c_1^2\,, \qquad (4\cdot6)$$

where $\alpha(K)$ is complicated known function of K. The explicit form is not written here. We substitute c_2 into the equation $A_0=B_0$, and we get.

$$\lambda=\lambda_0+\beta(K)c_1^2\,, \qquad (4\cdot7)$$

where $\beta(K)$ is also complicated known function of K and λ_0 is the characteristic value of the integral equation in the case when all c_i's vanish. We substitute (4·6) and (4·7) into the equation $A_1=B_1$ and we obtain

$$c_1^3=\frac{[\{L(K)\}^3+2\{L(K)\}^2+2\{L(K)\}-1]}{\gamma(K)}c_1\,, \qquad (4\cdot8)$$

where $\gamma(K)$ is also complicated known function of K and has positive value.

When the temperature is high enough, the function $L(K)$ takes small positive value, so the coefficint of c_1 in (4·8) is of negative sign, and accordingly c_1 has no real root except zero. As the temperature increases, however, the value of $L(K)$ increases gradually and the coefficient of c_1 in (4·8) changes sign, consequently c_1 has non-zero real root. It is just the transition temperature at which the coefficient of c_1 in (4·8) changes the sign, and it agrees completely with (3·13) already obtained.

The specific heat C is the temperature derivative of the energy which is given in (2·6). Thus the specific heat at just below the transition temperature is

$$C(K_c+0)=2RK_c^2\left[\left\{\frac{H''}{H}-\left(\frac{H'}{H}\right)^2\right\}\right.$$
$$\left.+\frac{1}{3}\frac{dc_1^2}{dK}\left\{\frac{H''}{H}-\left(\frac{H'}{H}\right)^2\right\}\right]_c, \qquad (4\cdot9)$$

and the specific heat at the temperature just above it is

$$C(K_c-0)=2RK_c^2\left\{\frac{H''}{H}-\left(\frac{H'}{H}\right)^2\right\}_c, \qquad (4\cdot10)$$

where suffix c denotes the value at the trantition temperature, and R is the gas constant. The first term in (4·9) contributes to the specific heat both above and below the transition temperature. The second term contributes to the specific heat below the transition temperature only and it is responsible for the discontinuity of the specific heat. The value of discontinuity is

$$\varDelta C=2RK_c^2\frac{1}{3}\left(\frac{dC_1^2}{dK}\right)_c\left\{\frac{H''}{H}-\left(\frac{H'}{H}\right)^2\right\}_c. \qquad (4\cdot11)$$

From (4·8), we can calculate $(dC_1^2/dK)_c$. Thus we obtain the numerical value of $\varDelta C$ as $3.0\,R$. We give for a reference, the values of $\varDelta C$ in various approximations.

Table II

	$\varDelta C$
Kirkwood	2.5 R
Chang	3.05 R
Authors	3.0 R

§ 5. The modified Kirkwood potential

Kirkwood potential is the most simplified form, but it is not appropriate for dipole-dipole potential, because Kirkwood potentials in the cases in which two dipoles are arranged sideways and are arranged lengthways, are of same form so long as the angles between two dipolar orientations are same. But it is not right for dipole-dipole potential. So, as the first approximation for dipole-dipole potential, we take the following forms which we call the modified Kirkwood potential,

$$V_{\rm I}(i,j)=\frac{J}{2}\cos(i,j)\,,$$
$$V_{\rm II}(j,k)=-\frac{J}{2}\cos(j,k)\,,$$
$$V_{\rm III}(k,l)=\frac{J}{2}\cos(k,l)\,,$$
$$V_{\rm IV}(l,i)=-\frac{J}{2}\cos(l,i)\,, \qquad (5\cdot1)$$

Suffices I~IV denote the type of connecting bonds as in § 2. In this case, the relations between f's and n's are following;

$$n_1(i)=\frac{1}{2}\int f_{\rm I}(i,j)dj=\frac{1}{2}\int f_{\rm IV}(l,i)dl\,,$$

$$n_2(j)=\frac{1}{2}\int f_{\mathrm{I}}(i,j)di=\frac{1}{2}\int f_{\mathrm{II}}(j,k)dk\,,$$

$$n_3(k)=\frac{1}{2}\int f_{\mathrm{II}}(j,k)dj=\frac{1}{2}\int f_{\mathrm{III}}(k,l)dl\,,$$

$$n_4(l)=\frac{1}{2}\int f_{\mathrm{III}}(k,l)dk=\frac{1}{2}\int f_{\mathrm{IV}}(l,i)di\,,$$

$$n_1(i)=n_4(l)=n_2(\pi-j)=n_3(\pi-k)$$

$$f_{\mathrm{I}}(i,j)=f_{\mathrm{III}}(l,k)$$

$$f_{\mathrm{IV}}(l,i)=f_{\mathrm{II}}(\pi-j,\ \pi-k) \qquad (5\cdot2)$$

where $(\pi-j)$ means $(\theta_j-\pi,\ \varphi_j-\pi)$. The fundamental integral equation is given in the same way, as follows,

$$\lambda\int\Big[f_{\mathrm{I}}(i,j)\Big]^{\frac{1}{2}}\Big[\int f_{\mathrm{IV}}(l,i)dl\cdot\int f_{\mathrm{II}}(j,k)\,dk\Big]^{\frac{1}{4}}$$
$$\times\exp\Big[\frac{K}{2}\cos(i,j)\Big]dj$$
$$=\iiint\frac{[f_{\mathrm{II}}(j,k)f_{\mathrm{III}}(k,l)f_{\mathrm{IV}}(l,i)]^{\frac{1}{2}}}{\Big[\int f_{\mathrm{II}}(j,k)dj\cdot\int f_{\mathrm{IV}}(l,i)\,di\Big]^{\frac{1}{4}}}$$
$$\times\exp\Big[\frac{K}{2}\{\cos(j,k)-\cos(k,l)$$
$$+\cos(l,i)\}\Big]djdkdl \qquad (5\cdot3)$$

We find the solution of the integral equation (5·3) which satisfies the condition (5·2), as following,

$$f_{\mathrm{I}}(i,j)=\frac{1}{\mu}\frac{1}{4\pi}\exp[-K\cos(i,j)]$$
$$\times[1+c_1\{P_1(\cos\theta_i)-P_1(\cos\theta_j)\}\cdots]$$
$$f_{\mathrm{II}}(j,k)=\frac{1}{\mu}\frac{1}{4\pi}\exp[+K\cos(j,k)]$$
$$\times[1-c_1\{P_1(\cos\theta_j)+P_1(\cos\theta_k)\}\cdots]$$
$$f_{\mathrm{III}}(k,l)=\frac{1}{\mu}\frac{1}{4\pi}\exp[-K\cos(k,l)]$$
$$\times[1-c_1\{P_1(\cos\theta_k)-P_1(\cos\theta_l)\}\cdots]$$
$$f_{\mathrm{IV}}(l,i)=\frac{1}{\mu}\frac{1}{4\pi}\exp[K\cos(l,i)]$$
$$\times[1+c_1\{P_1(\cos\theta_l)+P_1(\cos\theta_i)\}\cdots]$$
$$(5\cdot4)$$

Using (5·4), the branching point of the integral equation (5·3) is determined in the similar way as before. The formula which gives the transition temperature perfectly agrees with (3·13). It is interesting that the transition temperature does not change even in above anisotropy. The calculation of other lattice type and other potential forms will be studied henceforth.

The authors wish to express their sincere thanks to Professor R. Kubo and R. Kikuchi for giving valuable discussions and suggestions. The expence of this research has been defrayed from the Scientific Expenditure of Department of Education.

Appendix

If we define the function

$$H(K)=\sqrt{\frac{\pi}{2K}}I_{\frac{1}{2}}(K)$$

and use the recurrence formula $I_{n+1}(K)=K^n d(K^{-n}I_n(K)/dK$, the following formulae are easily obtained;

$$I_{\frac{1}{2}}(K)=\sqrt{\frac{2K}{\pi}}H(K)$$
$$I_{\frac{3}{2}}(K)=\sqrt{\frac{2K}{\pi}}H'(K)$$
$$I_{\frac{5}{2}}(K)=\sqrt{\frac{2K}{\pi}}\frac{1}{2}\{3H''(K)-H(K)\}$$
$$I_{\frac{7}{2}}(K)=\sqrt{\frac{2K}{\pi}}\frac{1}{2}\{5H'''(K)-3H'(K)\}$$
$$(A\cdot1)$$

Expanding $\exp[K\cos(i,j)]$ into two axes spherical harmonics and using (A·1), the following formulae are obtained;

$$\frac{1}{4\pi}\int\exp[K\cos(i,j)]dj=H(K)$$
$$\frac{1}{4\pi}\int\exp[K\cos(i,j)]P_1(\cos\theta_j)dj$$
$$=H'(K)P_1(\cos\theta_i)$$
$$\frac{1}{4\pi}\int\exp[K\cos(i,j)]P_2(\cos\theta_j)dj$$
$$=\frac{1}{2}\{3H''(K)-H(K)\}P_2(\cos\theta_i)$$
$$\frac{1}{4\pi}\int\exp[K\cos(i,j)]P_1(\cos\theta_j)\cdot P_2(\cos\theta_j)dj$$
$$=\frac{2}{5}H'(K)P_1(\cos\theta_i)+\frac{3}{10}\{5H'''(K)$$
$$-3H'(K)\}P_3(\cos\theta_i)$$
$$\frac{1}{4\pi}\int\exp[K\cos(i,j)]\{P_1(\cos\theta_j)\}^2dj$$
$$=\frac{1}{3}H(K)+\frac{1}{3}\{H''(K)-H(K)\}P_2(\cos\theta_i)$$
$$\frac{1}{4\pi}\int\exp[K\cos(i,j)]\{P_1(\cos\theta_j)\}^3dj$$
$$=\frac{3}{5}H'(K)P_1(\cos\theta_i)+\frac{1}{5}\{5H'''(K)$$
$$-3H'(K)\}P_3(\cos\theta_i) \qquad (A\cdot2)$$

References

1) J. G. Kirkwood: J. Chem. Phys. **8** (1940) 205.
2) T. S. Chang: Proc. Camb. Phil. Soc. **33** (1937) 524.
3) R. Kubo and T. Hashimura: Lecture in the Meeting of the Phys. Soc. Japan 1949.
4) T. Nakamura: Busseiron Kenkyu **29** (1950)

44 (in Japanese).
5) K. Yoshida: Busseiron Kenkyu **20** (1949) 80, (in Japanese).
6) T. Nagamiya: "*Many Problems in Modern Physics*" Iwanami, (1948) p. 113 (in Japanese).
7) R. Kubo and T. Hashimura: Lecture in the Meeting of the Phys. Soc. Japan 1950.
8) H. A. Kramers and G. H. Wannier: Phys. Rev. **60** (1941) 263.
9) R. Kikuchi: Busseiron Kenkyu **24** (1950) 52, (in Japanese), and Phys. Rev. **79** (1950) 718.

JOURNAL OF THE PHYSICAL SOCIETY OF JAPAN Vol. 7, No. 2, MAR.—APR., 1952

Absorption of Carbon Mono-oxide by the Barium Getter
Part I. Experiments at Low Temperatures

By Tetsuya ARIZUMI and Seiichi KOTANI
Kobe Kogyo Corporation, Kobe

(Received December 27, 1950)

The absorption properties of flashed barium getters below 0°C were studied in c.f and c.v- methods. The getter absorbed a comparatively large amount of carbon mono-oxide even at −185° C, not so much differing from that at 0° C, indicating that the absorption is not a simple physical adsorption. The pressure changes in the c.v. method are represented by

$$\frac{dp}{dt}=-\alpha p(a-bp) \qquad \text{and} \qquad \frac{dp}{dt}=-\beta p$$

respectively for lower and higher temperature ranges. Raising the temperature of the getter mirror stepwisely, from −180° C, the absorbed gas was desorbed at first, but it began to be absorbed again by the getter. For comparison, the absorption properties of Cu−CO system was also studied.

Introduction

Only a few papers[1)−4)] have been published on the gettering process, but none of them did not touch the mechanism of gas absorption. The authors[5)] and Imaeda[6)8)] have studied the absorption of barium getter for oxygen, nitrogen, hydrogen and carbon dioxide. In Part 1 of the present paper the absorption of carbon mono-oxide by the barium getter will be prerented. To our surprise, the absorption ability at −180° C does not differ from that at room temperature. Such curious phenomena cannot be understood by the simple adsorption or diffusion in any way, but shall be confirmed to be due to the existence of many lattice defects in the getter film as shall be discused in Parts 2 and 3.

Experimental Procedure

1. Control of Temperature

Special cares were taken for the control of temperature as almost all experiments had to be carried out at a precisely controlled low temperature. Fig. 1 is the schematic diagram of experimental arrangement for the temperature control. In the figure, a is a finely adjustable air bulb. Compressed air from a was dried at first through two U-tubes, b-1 and b-2, containing calcium chloride and diphosphorus peroxide respectively, and then cooled through two coiled glass tubes, f-1 and f-2, immersed in mixture of dry ice and ether, and liquid air respectively. Sufficiently cooled air was introduced into the bottom of a thin walled glass vessel g, put in a Dewar vessel e-3. 1 is a glass capillary and M is a mercury manometer used as the flow meter. d is a double-walled glass tube whose inside was silver-plated and evacuated. This connection tube could not be removed to send the sufficiently cooled air into g.

P, G and S are a Pirani gauge, a capillary

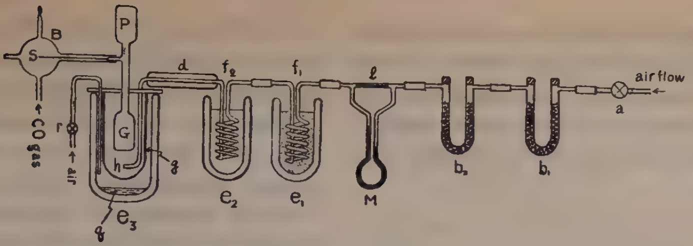

Fig. 1. Experimental arrangement for temperature control.

tube and a getter chamber of a experimental tube, described in the foregoing papers.5)6) The end of the capillary S is put in a glass vessel B full of carbon mono-oxide.

When a proper amount of liquid air (*q*) was poured into the Dewar vessel e-3, the temperature in g was kept nearly at −180° C. Then, when the compressed air began to flow through the air bulb a, the temperature in g became to be mainly controlled by the introduced air. Thus the temperature in g could be controlled arbitrarily if the amount of air is finely adjusted by watching the flow meter M. If the temperature in g to be controlled is beyond −70° C, the mixture of dry ice and ether was poured into e-2 instead of liquid air and also liquid air in e-3 had to decrease moderately. The glass tube r is an auxiliary means to promote the evaporation of liquid air in e-3 by sending compressed air. These procedures made acurate temperature control in g from −180° C to O° within±0.5° C possible.

As the gas manometer is ideal for the measurement of temperature, but it takes long time for the measurement, a copper-constantan thermocouple of dia. 0.5 mm was used. The length of the thermometer wire was prolonged by bending zigzagly, for preventing the thermal conduction.

2. Generation of Carbon Mono-oxide

The apparatus for the generation and purification of carbon mono-oxide is shown in Fig. 2. Carbon mono-oxide, generated by the titration of concentrated sulphuric acid in formic acid, was at first lead to the carbon dioxide absorber, F, containing caustic potash and then lead to the oxygen absorber, D, containing alkali solution of thiosulphate. The purified carbon mono-oxide was then dried through the concentrated sulphuric acid, calcium chloride and liquid air, and sent into the glass vessel B of about 100 ccs. It was safe to connect J to the compressed air line for preventing the reactants from swirling. Carbon mono-oxide was combused continuously at the outlet I. In the glass vessel B the capillary S of the experimental tube was inserted.

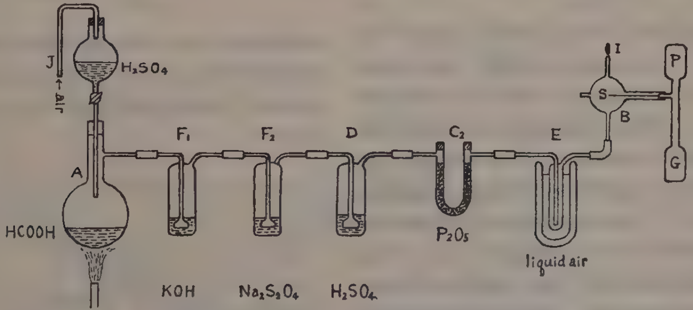

Fig. 2. The apparatus for generation and purification of carbon moto-oxide.

3. Measurements of Pressure

The measurements of pressure and the calibration of the capillary followed to the procedure described in the foregoing papers.5)6) The getter to be tested was flashed at room temperature.

Experimental Results

1. Pressure Change in the Constant Flow Method

Although the end of the capillary S was broken to introduce carbon mono-oxide with a definite speed into the getter chamber G put in the low temperature vessel g, the pressure was kept almost unvaried for rather a long time, indicating that almost all amount of introduced gas is absorbed by the getter mirror. A typical example is given by the curve No. 4-5 in Fig. 3. The curve No. 2-6 is the pressure curve obtained at room temperature. Comparing both curves it is seen that the inclination of the curve No. 4-5 is smaller than that of the curve No. 2-6. This curious result was always experienced in many other examples.

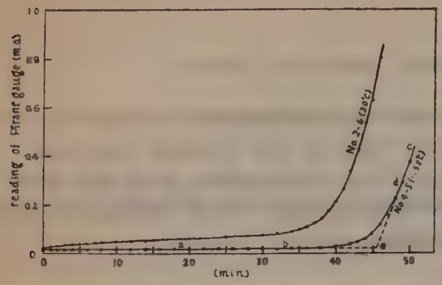

Fig. 3. The pressure changes in the c. f. method.

As the measure of the period in which the pressure is kept almost unvaried, the amount Q will be introduced, which is defined as the amount of introduced gas in the time interval oe, (e is the cross point of extrapolations of ab and cd as shown in Fig. 3). Q depends largely upon the flashing conditions of getter, but, as summerized in Table 1, Q-values at low temperatures are almost equal to those at room temperature, suggesting that the absorption at low temperatures can not simply be attributed to the physical adsorption.

Table I. Values of Q at low temperatures and at room temperature

room temperature			low temperature		
tube No.	temp. (°C)	Q (mol)	tube No.	temp. (°C)	Q (mol)
1-2	14	0.76×10^{-6}	4-5	-158	5.85×10^{-6}
1-6	13	1.68×10^{-6}	4-6	-157	4.80×10^{-6}
1-10	13	1.92×10^{-6}	4-8	-153	12.0×10^{-6}
1-11	14	1.28×10^{-6}	4-10	-155	20.8×10^{-6}
2-1	30	5.6×10^{-6}	4-15	-165	2.6×10^{-6}
2-3	30	5.2×10^{-6}	4-21	-162	11.5×10^{-6}
2-6	30	3.4×10^{-6}	4-23	-167	3.3×10^{-6}

2. Pressure Changes in the Constant Volume Method

When the capillary was sealed until the pressure began to increase rapidly, the pressure did not almost change. Such an example is seen in Fig. 5. If the capillary was sealed after the sufficient increase of pressure, the pressure, in general, began to decrease gradually as ab in Fig. 4. The approximate empirical expression, obtained for nitrogen⁶⁾ at room temperature, does not hold for carbon monooxide at low temperatures. Thus, if the quantities

$$\alpha=-\frac{1}{p}\frac{dp}{dt} \qquad (1)$$

at each moment are plotted against p, α is found to be a linear function of p as illustrated in Fig. 5. Thus the pressure change in the c. v. method can be represented by the empirical formula.

$$\frac{dp}{dt}=-\alpha p(a-bp) \qquad (2)$$

indicating that the physical absorption becomes predominant after a large amount of gas has already been absorbed, as will be discussed in Part 3.

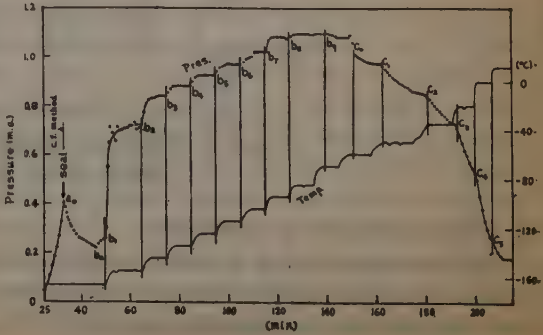

Fig. 4. The pressure change in the c.v. method.

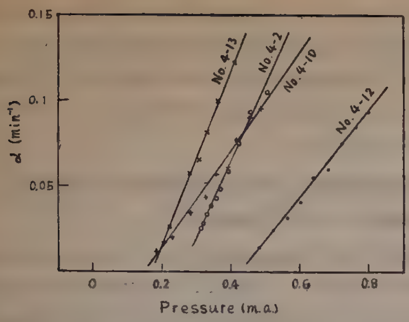

Fig. 5. Relations between α and pressures.

3. Influence of Temperature

Sealing the capillary at any point, the pressure began to decrease, but taking out the getter chamber from the low temperature vessel g suddenly, the getter releases one part of absorbed gas in a moment and then absorbed the released gas rapidly, as shown by marks 1, 2, 3, 4, and 5 in Fig. 6. The amount of released gas increased with the total amount of absorbed gas, but it was much smaller than the total absorbed gas. In the case 5, the momentary pressure change was found to be followed by a slow pressure decrease.

When the temperature of the getter chamber was increased stepwisely, by about 10°C, the pressure increased stepwisely as indicated by b-0, b-1, b-2 and so on in Fig. 4. Fig. 7 is another example. As, below -150°C, the pressure was very sensitive to the temperature, the measured pressures dispersed slightly, but reached at last to an almost constant value b-2. Similarly, corresponding to each temperature, the definite equilbrium pressures were found. The equilibrium pressure increased at higher temperature, but beyond about -80°C no more increase was observed, and moreover beyond -65°C it began to decrease. These temperatures, however, differs from one getter to another.

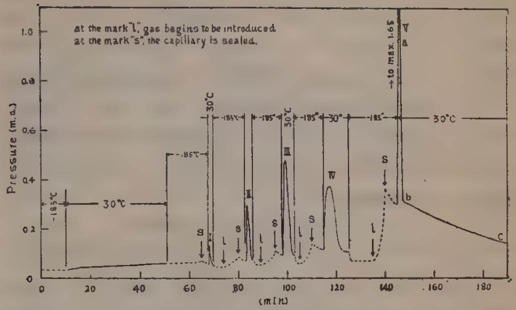

Fig. 6. The pressure change obtained when the getter chamber is taken out from the vessel g: the dotted line shows the experiments at low temperature and the full line the experiments at room temperature.

Sometimes slightly different pressure changes were obtained as illustrated in Fig. 7. In the curve No. 4-6 no increase in the equilibrium pressure was observed, while in the curve No. 4-9, even at -180° C, the gradual pressure decrease was experienced.

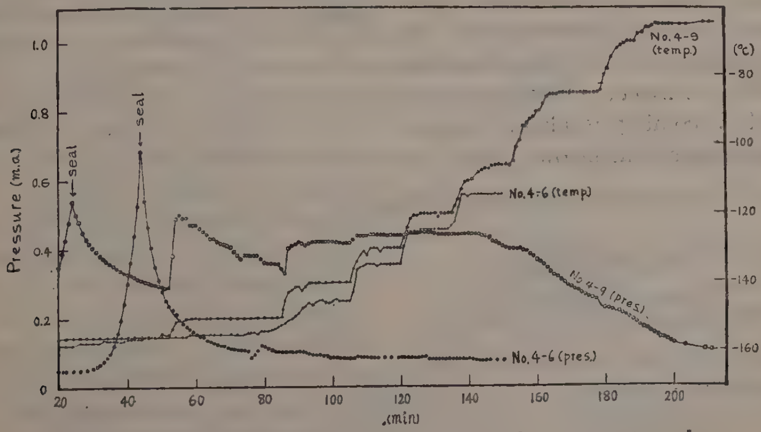

Fig, 7. The pressure change obserbed when the temperature is raised stepwisely.

If carbon mono-oxide is adsorbed physically, the adsorption and desorption of the gas is the reversible process. Experiments in Fig. 8 were carried out to confirm this prediction. Stopping the gas flow to the getter chamber at -165°C, the pressure decreased as the curve ab. Then, rising temperature to -150°C, the pressure increased to bd, but lowering temperature again to −164.5°C, the pressure lowered down almost reversibly to e. Strictly, however, the pressure e is slightly smaller than the estimated value c extrapolated from the curve ab. In the second cycle between −162°C and -130°C, the pressure change was almost reversible, but the pressure did not increase so much as d. These results indicate that at −130°C some amount of gas is absorbed irreversibly, while at −150°C almost all part of gas is absorbed reversibly.

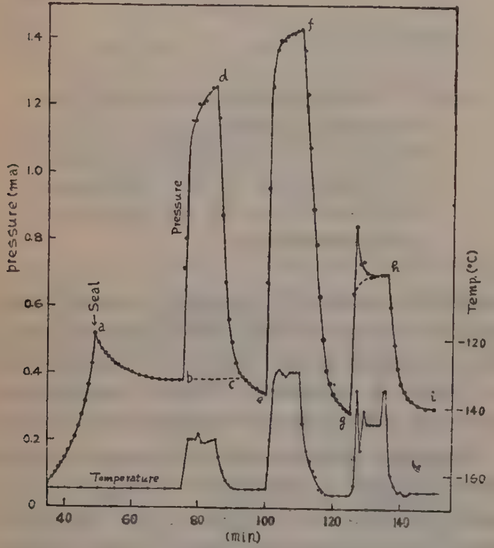

Fig. 8. The adsorption and desorption of carbon mono-oxide at low temperatures.

The logrithmic values of equilibrium pressures are plotted in Fig. 9, showing that the curves are composed of two lines breaking sharply at −150°C. Beyond −150°C the slopes are not parallel, becoming gradually smaller at higher temperatures, but below −150°C the slopes seem to be parallel each other with its activation energy being 2.34 Kcal/g. mol. This energy corresponds to the sum of the adsorption and the desorption energies as will be discussed in Part 2.

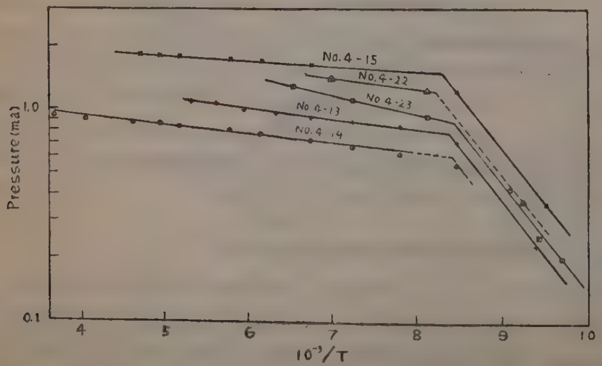

Fig. 9. The dependencies of the equilibriumpressure on temperature.

4. Absorption at Temperature Range between −100°C and 0 C

Rising the temperature of the getter mirror gradually from −185°C, the pressure increased at first, but beyond about −80°C it began to decrease as c-1, c-2,····in Fig. 4. The temperature beyond which the pressure begins to decrease differs from each other, ranging from −120°C to −10°C. This temperature has no special dependency upon other several quantities and seems to depend on the flashing conditions of the getter mirror.

Differing from the pressure change below −150°C, the pressure decrease at these higher temperatures can be represented by

$$\frac{dp}{dt}=-\alpha p \tag{3}$$

approximately, as presented in Fig. 10. The coefficient α becomes larger at higer temperature and plotting the logarithmic values of α against $1/T$, the inclinations are found to be almost parallel with each other (Fig. 11). Thus α is expressed by the formula.

$$\alpha=\alpha_0 \exp\left(-\frac{Q}{RT}\right) \tag{4}$$

in which Q is evaluted to be 6.53 Kcal/g. mol. This energy is considered to be the activation energy for the activated adsorption.

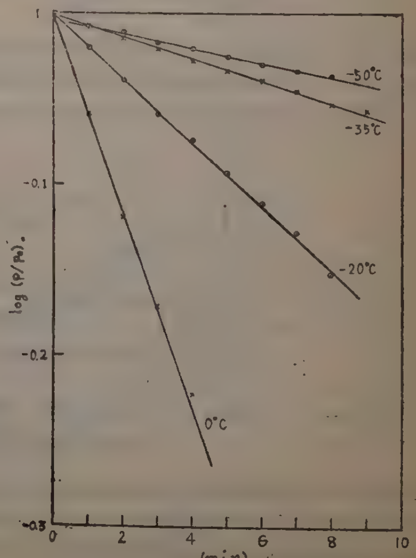

Fig. 10. The time change of pressure.

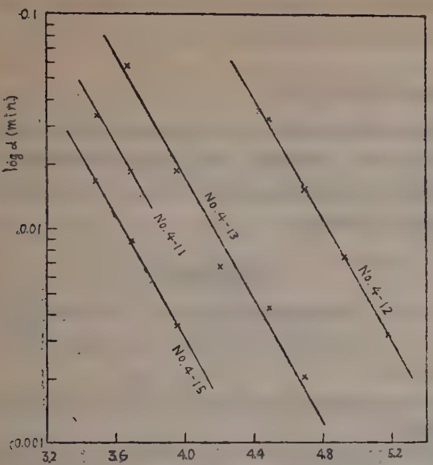

Fig. 11. The logarithmic plots of α against $1/T$.

5. Heat treatment of the getter mirror

If the getter mirror was heated at about —300°C for several ten minutes before the experiments, the absorption ability decreased remarkably, similarly as in the case of nitrogen at room temperature.[6] For example the length of oe in Fig. 3 became much shorter. In extreme case it became only several minutes. These results seem to suggest that the absorption of nitrogen at room temperature and of carbon mono-oxide at low temperatures are due to almost similar mechanism.

6. Repetation of Experiments

After the first experiments of similar procedure as described in Sections 3 and 4, the getter chamber was immersed in the low temperature vessel g again and then the gas began to be introduced through the capillary. Even in the second experiment the pressure remained unvaried for a while, indicating the slight recovering of absorption ability. Comparing with the first experiments, however, (1) *M* was much shorter than in the case of first experiment. (2) The pressure change in the c.v. method become very slower. (3) The maximum value of the equilibrium pressure was larger. (4) The temperature beyond which the pressure begins to decrease became higher.

7. Absorption of Carbon Mono-oxide by the Evaporated Copper Film

The absorption properties of the evaporated film of copper at low temperatures were studied for the comparism. Differing from barium, the pressure began to increase almost linearly as soon as the gas began to be introduced and no unvaried pressure part was observed. Fig. 12 is an example. Comparing the pressure change in the blank test, the copper film apparently has the absorption ability. Sealing the capillary at c, the pressure did not decrease. Rising the temperature to the room temperature, almost all amount of absorped gas was released to increase the pressure (de in Fig. 12), but lowering the temperature to −165°C again, the pressure reduced almost to the initial value. In the second cycle of experiment the pressure change was found to be quite reversible. These experiments indicate that even at −180° C carbon mono-oxide is not adsorbed physically by the evaporated film of barium.

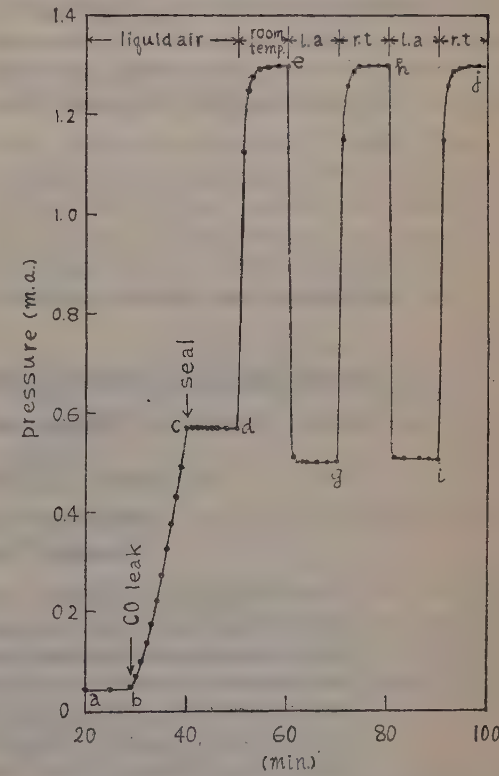

Fig. 12. The absorption of carbon mono-oxide by the evaporated film of copper.

Summary

Several important results are summerized as followed:

(1) The absorption ability of the evaporated film of barium at temperatures below −150°C is almost equal to that at room temperature.

(2) Rising the temperature of the getter chamber in the c.v. method, the pressure increases gradually at first, but begins to decrease at higher temperature. The pressure change below −150° C is expressed by the empirical formula (2), while beyond about −100° C, it is replaced by the expression (3). The coefficient α in (3) depends on temperature as followed:

$$\alpha=\alpha_0\exp\left(-\frac{Q}{RT}\right)$$

in which the activation energy Q is 6.43 Kcal/g. mol.

(3) The curves of the equilibrium pressures versus $1/T$ are composed of two lines breaking sharply at about −150° C. The activation energy determined from the straight lines below −150° C is 2.43 Kcal/g. mol.

(4) Differing from the barium getter, the absorption of carbon mono-oxide by the evaporated film of copper is a perfect reversible process. In parts 2 and 3 of this paper these experimental results described herein shall be theoretically discussed.

Acknowledgement

The authors wish to express their appreciations to Mr. Imaeda for his co-operation and valuable discussion and Mrs. Yasui for her analytical works.

References

1) A. L. Reimann: Phil. Mag. **18** (1934) 1117.
2) L. Ehrke & M. C, Slack: J. App. Phys. **11** (1940) 129.
3) N. Kameyama: Musen Shiryo, Dec. (1940) in Japanese.
4) O. Harazima: J. Elec. Comm., **27** (1943) 548 in Japanese.
5) T. Arizumi & S. Kotani: J. Phys. Soc. Japan, **5** (1950) 70.
6) T. Arizumi & K. Imaeda: ebenda **5** (1950) 169.
7) K. Imaeda: unpublished.
8) K. Imaeda: unpublished.

JOURNAL OF THE PHYSICAL SOCIETY OF JAPAN Vol. 7, No. 2, MAR.—APR., 1952.

Absorption of Carbon Mono-oxide by the Barium Getter
Part II. Theory of Physical Adsorption

By Tetsuya ARIZUMI and Seiichi KOTANI
Kobe Kogyo Corporation, Kobe

(Received December 27, 1950)

The simple theory of physical adsorption was found to hold only for the getter having already absorbed a sufficient amount of carbon mono-oxide. The large absorption ability of a fresh getter is due to the existence of large number of lattice imperfections in it. The activation energy of physical adsorption, desorption and activated adsorption for Ba−CO system were found 1.0, 1.4 and 6.5 Kcal/gmol respectively. The new theory assuming the existence of lattice imperfections was developed.

1. Introduction

In part I of the present paper, the sorption properties of carbon mono-oxide by the evaporated film of barium at the temperature range from −185° C to room temperature were studied in details. The results seem to suggest that even at −185° C, carbon mono-oxide is mainly absorbed by some other process than the physical adsorption. In parts 2 and 3 the theoretical analysis of the obtained results will be described. Any kind of gas has been known to be adsorbed physically on the surface of ordinary metals at −185° C[1]. Thus in this part the general theory of physical adsorption will be applied to the experimental results and it will be found that the theory is applied successfully to some phenomena, but it fails to explain many others.

2. Theory of Physical Adsorption

Let us assume that gas molecules are adsorbed only physically on the surface of getter. If the amount of gas per unit time introduced through the capillary be s mol, the initial number of adsorption sites be N_0, the occupied area per one adsorption site be L^2, and the energy for physical adsorption be Q_1, the pressure change in the constant flow (c.f.) method will be given by the following expression.2)

$$\frac{dp}{dt}=\frac{RT}{V}s-\frac{L^2p}{\sqrt{2\pi MRT}}\left\{N_0-\left(sNt-\frac{NV}{RT}p\right)\right\}\exp\left(\frac{Q_1-q\theta w}{RT}\right) \qquad (1)$$

in which V is the total volume of the experimental tube, θ the fraction of the total surface that is covered with adsorbed molecules, w the repulsive interaction energy, and R, T, N and q are gas constant, absolute temperature, Loschmidt number and the proportional constant respectively. For the deduction of (1), the interaction of adjacent adsorbed molecules is assumed to be fairly strong and thus the apparent activation energy of adsorption decreases as the covering fraction becomes larger.

As in the c.v. method s is put to zero, we obtain the following relation,

$$\frac{dp}{dt}=-\frac{L^2p}{\sqrt{2\pi MKT}}\left\{N'_0-\frac{NV}{RT}(p_0-p)\right\}\cdot\exp\left(\frac{Q_1-q\theta w}{KT}\right) \qquad (2)$$

in which N'_0 and p_0 are the number of remaining adsorption sites and the initial pressure, just at sealing the capillary.

As the pressure remains almost unvaried in the initial stage of the c.f. method, the term $(NV/RT)\,p$ may well be neglected in comparison with the term sNt, giving the expression,

$$\beta\equiv\frac{RT}{V}s-\frac{1}{p}\frac{dp}{dt}=(A_0-B_0t)\exp\left(\frac{Q_1-q\theta w}{RT}\right) \qquad (3)$$

or

$$\log\beta=\log(A_0-B_0t)+\frac{Q_1-q\theta w}{RT} \qquad (4)$$

In the c.f. method the covering fraction θ is considered to increase almost in linear proportion with time and thus (4) may well be written approximately in the form,

$$\log\beta\fallingdotseq a_0-b_0t \qquad (5)$$

If the interaction of adsorbed molecules is neglected, (3) becomes

$$\beta=A_1-B_1t \qquad (6)$$

where A_1 and B_1 are gived by

$$A_1=\frac{L^2N_0}{\sqrt{2\pi MRT}}\exp\left(\frac{Q_1}{RT}\right) \qquad (7)$$

and

$$B_1=\frac{L_2sN}{\sqrt{2\pi MRT}}\exp\left(\frac{Q_1}{RT}\right) \qquad (8)$$

respectively, expressing that β is the linear function of time whose slope depends only on the amount of flow s. Eliminating the exponential term from (7) and (8), N_0 is estimated by the relation,

$$N_0=\frac{A_1}{B_1}RN \qquad (9)$$

Similarly the following relations are deduced from (2) in the c.v. method if the interaction can be neglected.

$$\alpha=-\frac{1}{p}\frac{dp}{dt}=A_2-B_2p \qquad (10)$$

$$A_2=\frac{L^2}{\sqrt{2\pi MRT}}\left(N'_0-\frac{NV}{RT}p_0\right)\exp\left(\frac{Q_1}{RT}\right) \qquad (11)$$

$$B_2=\frac{NV}{RT}\,\frac{L^2}{\sqrt{2\pi MRT}}\exp\left(\frac{Q_1}{RT}\right) \qquad (12)$$

α is the linear function of p whose inclination is constant, independently of the surface area of the getter mirror, its flashing condition and the amount of adsorbed molecules just at sealing the capillary. The combination of (11) and (12) leads to the following equation.

$$N'_0=\frac{NV}{RT}\left(\frac{A_2}{B_2}+p_0\right) \qquad (13)$$

making the calculation of the total number of un-adsorbed sites just at sealing the capillary possible.

3. Adsorption to the Evaporated Film of Copper

Preceding to the analysis of the absorption experiments of the Ba–CO system, the theory described in the preceding section will be discussed on the evaporated film of copper. From the experimental result in Fig. *I*-12,* β is found to be represented by

$$\log\beta=a-bt \qquad (14)$$

approximately, in qualitative agreement with (5), but finally the curve becomes to deviate from the relation (14), probably because the pressure increase is rather large compared to the total amount of introduced gas.

This result seems to suggest that in the Cu–CO system the interaction of adsorbed molecules

---

* Fig. I-12 means Fig. 12 in Part I of this paper.

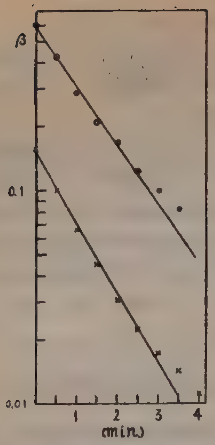

Fig. 1. The change of β for the Cu–CO system.

is fairly strong.

Differentiating (3) with time and tending dp/dt to zero, the value of B for the fresh copper film will be evaluated, as θ becomes zero at $t \to 0$. The obtained value of B is 4.17×10^{-4} (sec^{-2}), while the theoretical value $L^2sN / \sqrt{2\pi MRT}$ is 2.76×10^{-6}, with the activation energy being 950 cal/g. mol. This value is of reasonable order for the activation energy of physical adsorption.

Even stopping the gas flow, the pressure does not decrease in the case of Cu–CO system and almost all adsorbed gas molecules were released when the getter chamber was taken out from the low temperature vessel and reversely the getter absorbed again the released gas when the getter chamber was immersed into liquid air. These results prove that carbon mono-oxide is adsorbed only physically on the copper film and also the above theory is applicable to the phenomena of pure physical adsorption.

4. The Pressure in the C. F. Method for the Ba–CO system

The pressure change in the Ba–CO system differs largely from that of the Cu–CO system. Although in the Cu–CO system the pressure begins to increase as soon as the gas begins to be introduced, there exists in the Ba–CO system a long period during which the pressure and thus β remain unvaried even though the gas is continuously introduced, as shown in Figs. I-3 and II-2. If gas molecules are adsorbed only physically, β is expected theoretically to be the function of time given by (5) or (6), in disagreement with the experimental results, suggesting that in the initial stage of the c.f. method the process is not always the physical adsorption. However, the initial stage in the c.f. method during which the pressure remains unvaried will be discussed in Part III and in this section the discussion will be restricted only to the region of rapid pressure change, for example, the region bed in Fig. I-3.

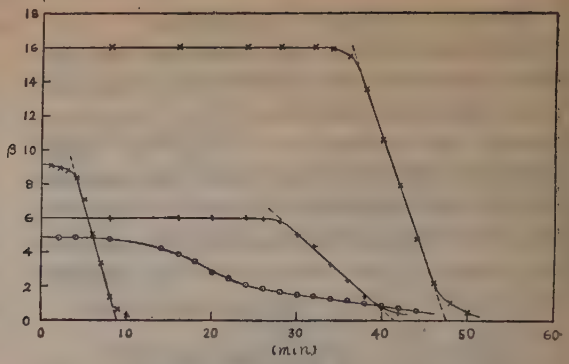

Fig. 2. The change of β for the Ba–CO system. almost unvaried.

As the pressure becomes to increase like bed, β begins to decrease as shown in Fig. II-2 and Table I in which t represents the time during which the extrapolated value of β becomes to zero, and B the slope of the curve. Except several cases β seems to be almost linear with time and in spite of large difference in t, B is $4.35 \pm 0.35 \times 10^{-4}$ in four cases of eleven examples and in eight cases it has the same order. These results support that the theory of the physical adsorption is applied almost correctly to the pressure change at these states.

Table I. B and t in the Ba–CO system.

size of capillaries	tube No.	t (min.)	B	theoretical
1.3×10 (mol.)	4-5	47.4	4.0×10^{-4}	5.13×10^{-6} (118 K)
	4-6	41.4	1.25×10^{-4}	
	4-7	—	—	non-linear
	4-8	64.9	1.67×10^{-4}	
	4-9	—	—	non-linear
	4-10	160.	4.45×10^{-4}	
	4-11	9.5	4.53×10^{-4}	
	4-12	—	—	composed of two curves
	4-13	3.43	4.67×10^{-4}	
	4-14	5.92	2.5×10^{-4}	
	4-15	15.4	1.44×10^{-4}	
3.3×10^{-7} (mol.)	4-21	23.3	1.24×10^{-4}	1.3×10^{-6} (118 K)
	4-22	very short	?	
	4-23	very short	?	

Perhaps, after the getter absorbed as much amount of gas as the pressure begins to increase rather rapidly, gas molecules become to be adsorbed almost physically.

All curves have slight tails as shown by bc in Fig. II–2, indicating that there exists the slight interaction between adsorbed molecules when the covering fraction becomes large.

5. The Pressure Change in the C.V. Method

The pressure change in the c.v. method is represented by the empirical expression,

$$\frac{dp}{dt}=\alpha p(A-Bp) \qquad (15)$$

in good agreement with the theoretical formula (10). Values of B_2 and N_0, calculated from the experimental slopes, are shown in the table II.

Table II. The pressure change in the c.v. method.

tube Nos.	temperature	N'_0	B_2 (exp.)	B_2 (theory)
4–1	—	—	°3.8×10^{-5}	6.0×10^{-5} (150° C)
4–2	—	—	1.2×10^{-4}	
4–3	—	—	1.6×10^{-4}	
4–5	−157° C	3.1×10^{17}	1.3×10^{-4}	
4–6	−156	4.2×10^{17}	8.5×10^{-5}	
4–8	−150	8.0×10^{17}	°2.2×10^{-6}	
4–9	−155	—	1.5×10^{-4}	
4–9	−150	5.7×10^{17}	°5.7×10^{-5}	
4–10	−152	3.8×10^{17}	8.3×10^{-5}	
4–12	−144	8.9×10^{17}	1.03×10^{-4}	
4–13	−166.5	3.8×10^{17}	1.4×10^{-4}	
4–14	−165	3.7×10^{17}	1.73×10^{-4}	

B_2 seems constant within experimental errors independently on the properties of the getter mirror and its amount, except only three examples marked by small circles and moreover they agree satisfactorily with the numerical value $(NV/RT)\times(L^2/\sqrt{2\pi MRT})$, suggesting that the theory of the physical adsorption holds for the present process of the c.v. method. The number of remaining adsorption sites just at sealing the capillary corresponds to the surface area of 80 to 120 cm² of the getter mirror, slightly larger than the apparent surface area. Assuming that all molecules are adsorbed physically the evaluated area seems too large for the un-adsorbed sites, because the getter has already absorbed a large amount of gas. These results support the suggestion that the absorption of carbon mono-oxide is not a simple process of the physical adsorption at the initial stage of the gettering process. Comparing theoretical values $(L^2sN/\sqrt{2\pi MRT})$ and $(NV/RT)\times(L^2/\sqrt{2\pi MRT})$ with experimental values B_1 and B_2 in Tables I and II respectively, the activation energy for adsorption can be estimated as presented in Table III.

Table III. The activation energy for the adsorption.

tube Nos.	temperature	Q_1 (c.f. method)	Q_1 (c.v. method)
4–5	−157° C	×1,000cal/g.mol.	154 cal/g. mol.
4–6	−156	725	61
4–10	−152	×1,064	70
4–12	−144	—	156
4–13	−166.5	× 951	126
4–14	−165	833	181
mean		1,005	

The activation energy calculated from the c.v. method are found to be always smaller than those from the c.f. method, suggesting that in the Ba—CO system the interaction of adsorbed molecules becomes unable to be neglected when the covering fraction become larger. In three cross-marked examples of six ones in Table III, the slopes of β versus t curves are parallel to each other as expected from the theory of physical adsorption. Thus the mean activation energy for the physical adsorption of these three examples is evaluated to be about 1.0 Kcal/g. mol. The estimated value is of reasonanable order compared with the activation energy for the physical adsorption of other metal-gas system.

6. The Pressure Decrease at Higher Temperature Range

Differing from the pressure change at low temperatures below −150° C, the pressure decrease at higher temperatures than −100° C is represented by the empirical formula,

$$\frac{dp}{dt}=-\alpha p \qquad (16)$$

and the process is irreversible. α in (16) is a function of temperature, given by the expression,

$$\alpha=\alpha_0\exp\left(-\frac{Q_3}{RT}\right) \qquad (17)$$

and Q_3 is estimated 6.53 Kcal/g. mol.

In the system Ba—N_2[3)] the relation (16) was observed to hold even at room temperature, as reprinted in Fig. II–3. The activation energy estimated from the low temperature parts of two curves a and c is 11.0 Kcal/g. mol.* The activation energy becomes much larger at such high temperatures that the getter mirror was remarkably decolourized. These results suggest that the obtained activation energy is perhaps the energy for the activated adsorption and at higher temperatures the activated adsorption changes gradually to the diffusion-determined state with the larger activation energy.

---

* In the previour paper the activation energy was written to be 0.24 e.v. by the authors' error and this energy was considered to be the diffusion energy.

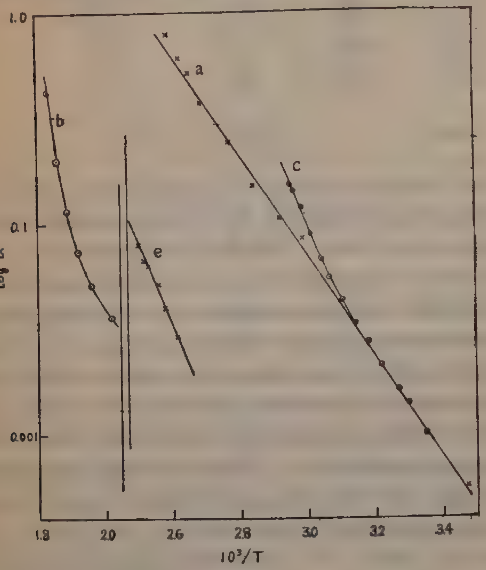

Fig. 3. The change of α for the Ba$-N_2$ System.

The activation energy for the Ba$-O_2$ system[4] at the corresponding temperature range is 5.8 Kcal/g. mol., of about the same order as that for the Ba$-$CO system. Comparison with the energy for the activated adsorption for other metal-gas systems are shown in Table IV, in which the activation energy for the Ba$-$CO system is found to be smaller than those for other metal-gas systems. The above analysis shows that carbon mono-oxide is, in general, adsorbed in the activated state in the temperature range from about -100°C to room temperature.

Table IV. The activation energy for the activated adsorption of several kinds of metal-gas system.

System	temperature range (°C)	Activation energy for activated adsorption
Ba$-$CO	$-120-20$	6.530 cal/g. mol.
Ba$-O_2$	$-120-0$	5.800
Ba$-N_2$	$-40-200$	11.000
Cu$-H_2$	$-$	9.000$-$14.000
Cu$-$CO	0	9.000$-$30.000
Ni$-H_2$	$-$	10.000$-$30.000
Pd$-$CO	$0-184$	7.000$-$15.000

7. Desorption Energy

Rising the temperature stepwisely from -180° C, the getter released gas already absorbed, but its amount is much smaller than the total amount of absorbed gas, as shown in Fig. 1-4. The equilibrium pressure has a sharp discontinuity at about -150° C and below this temperature the pressure changes almost reversibly, while beyond this temperature it becomes to change irreversibly as presented in Fig. 1-8. In many other tubes the similar phenomena were observed, but there existed several exceptional cases as seen in Fig. 1-7.

If carbon mono-oxide is adsorbed only physically, the phenomena must be reversible as experienced in the Cu-CO system, suggesting that the theory of physical adsorption is applicable only in the temperature range between -180° C and -150° C in which the pressure change is reversible and that only in this range the desorption energy is able to be determined. Eyring has shown that the rate of desorption is given by the following expression,

$$\frac{dv}{dt}=\frac{RT}{Nh}L^2(n_0-N_0)\exp\left(-\frac{Q^2}{RT}\right) \qquad (18)$$

where n_0 is the total number of adsorption sites, N_0 number of un-adsorbed sites and Q_2 the activation energy for desorption. In the equilibrium state the rate of adsorption must be equal to the rate of desorption and thus the following relation is deduced.

$$\frac{PL^2}{\sqrt{2\pi MRT}}N_0\exp\left(\frac{Q_1}{RT}\right)=k\frac{RT}{Nh}$$
$$L^2(n_0-N_0)\exp\left(-\frac{Q_2}{RT}\right) \qquad (19)$$

This formula is no other than the Langmuir's isotherm. As the total number of gas molecules in the experimental vessel is equal to the sum of number of adsorbed molecules and the number of molecules in gas state, the following relation is obtained.

$$n_0-N_0+\frac{NpV}{RT}=\mathfrak{N} \qquad (20)$$

From (19) and (20), we obtain

$$p\left(\mathfrak{N}-n_0-\frac{NpV}{RT}\right)=k\frac{RT}{Nh}\sqrt{2\pi MRT}$$
$$\left(\mathfrak{N}-\frac{NpV}{RT}\right)\exp\left(-\frac{Q_1+Q_2}{RT}\right) \qquad (21)$$

So long as p is still small, the p term in the blacket can be neglected and we obtain a approximate expression,

$$p \doteqdot c \exp\left(-\frac{Q_1+Q_2}{RT}\right) \qquad (22)$$

Thus Q_1+Q_2 can be estimated from plots in Fig, 1-9. As Q_1+Q_2 is estimated 2.43 Kcal/g. mol. and Q_1 is 1.0 Kcal/g. mol., Q_2 becomes 1.43 Kcal/g. mol. Comparing the desorption energy for several kinds of metal-gas system, this value seems to be reasonable.

References

1) C. J. Smithells: Gases and Metals (1937).

2) S. Glasstone, K. J. Laidler and H. Eyring: *The Theory of Rate Processes* (1941), McGraw-Hill Book Co.

3) T. Arizumi and K. Imaeda: J. Phys. Soc. Japan, **5** (1950) 169.

4) T. Arizumi and S. Kotani: to be published in near future.

JOURNAL OF THE PHYSICAL SOCIETY OF JAPAN Vol. 7, No. 2, MAR.—APR., 1952

Absorption of Carbon Mono-oxide by the Barium Getter
Part III. Lattice Imperfections

By Tstsuya ARIZUMI and Seiichi KOTANI

Kobe Kogyo Corporation, Kobe

(Received December 27, 1950)

This paper is a continuation of the preceding Parts. The analysis in Part II showed that only a small portion of whole gettering process of barium was explained by the simple adsorption theory. However, the phenomena shall be thoroughly clarified assuming that the getter mirror contains a large number of lattice imperfections, whose evidences shall be found in many experimental results. And the new theory will be presented which agrees qualitatively with the obtained results.

8. Several Phenomena Unable to be Explained by the Theory of Physical Adsorption

In Part II we have seen that several phenomena were explained by the simple theory of physical adsorption, but there remained many other experimental results, as described in the followings, which could not be explained by this theory.

(1) The amount of gas desorbed by the getter is always much smaller than the amount of gas absorbed by the getter. In general the former is about 10^{-3} times smaller than the latter.

(2) In the c.f. method the pressure remains almost unvaried for a rather long time. Assuming all gas molecules are adsorbed only physically, the surface area is, in most cases, estimated to be about 10^3 times larger than the apparent area. Even the number of unadsorbed sites just at sealing the capillary is evaluated to be 10^{17}, several times larger than the apparent area.

Even though the getter mirror is of fine granular structure, these results seem to be unreasonable.

(3) The time interval in which the pressure remains almost unvaried in the c.f. method does not almost differ at low temperature from at room temperature. Assuming that all molecules are adsorbed at room temperature in the activated state on the surface, the getter does not adsorb such large amount of gas as obtained in our experiments.

(4) The time interval of constant pressure becomes very shorter both at low and room temperatures, when the getter mirror is heated at about 300°C for several ten minutes preceding to the experiments. In most cases the heat treatment makes the time interval of constant pressure several tenth times shorter than the untreated getter.

(5) In the c.v. method it has been sometimes observed that the pressure does not almost increase even when the temperature of getter

is raised gradually, giving a disproof to the simple theory of physical adsorption.

(6) In most cases the equlibrium pressure in the c.v. method has a sharp discontinuity at nearly −150°C, suggesting the overlapping of at least two different phenomena.

(7) Once raising the temperature of the getter, having already absorbed a large amount of gas, to about 0°C, the getter recovers slightly its absorption ability at liquid air temperature. The result leads to the reasoning that gas molecules adsorbed on the surface diffuse into the interior at room temperature.

(8) Even at room temperature the resistance of the getter mirror does not almost change, as will be seen in Part IV of this paper, even though the getter absorbes a large amount of gas.

One of these experimental results cannot be explained satisfactorily by the theory of physical adsorption.

9. Lattice Imperfections

L. Ehrke and M. C. Slack[2] found that the thin film of some kinds of metal, condensed by evaporation, absorbes a large amount of gas and that the diffuse getter evaporated in the argon atmosphere absorbes much larger amount of gas than the getter evaporated in a low pressure. Our recent results[3] also confirms their results: The getter mirror flashed in nitrogen atmosphere of 10^{-1} to 1.0 mmHg absorbes from several times to several ten times larger amount of gas than the getter flashed at 10^{-4} mmHg. These results may be explained by the increase of the surface area of the getter mirror, but the special properties of the mirror must necessary be taken into consideration.

The resistance of the getter mirror[4] is from several hundred to several thousands times larger than that of bulk metal and even at room temperature it decreases gradually and continuously. Moreover, when the getter mirror is heated at high temperature, its resistance decreases suddenly. These results suggest that the properties of the getter mirror differ from that of the bulk metal and that it contains a large number of lattice imperfections, lattice defects, vacancies or surface pits.

The gradual change of the resistance indicates that these imperfections change gradually to the normal lattice arrangement. Fig. 4-a is a schematic diagramm of lattice imperfections existing along the grain boundaries and Fig. 4-b represents vacancies in the interior and pits on the surface.

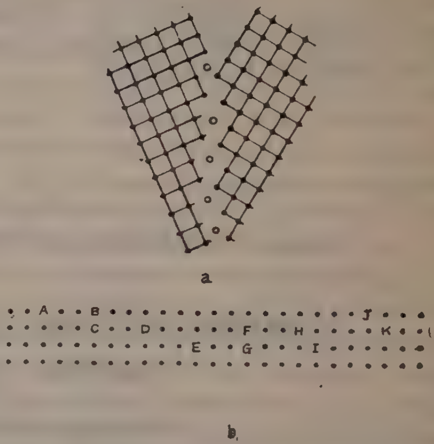

Fig. 4. Lattice imperfections, vacancies and surface pits.

The surface pit, such as A, B or C in Fig. 4-a, absorbes more stably a gas molecule than other surface atom. If lattice imperfections, vacancies or lattice defects situate nearly at the surface, they disturb the periodic potential distribution and perhaps lower down the potential hill at the midst of two atoms. The adsorption of electro-negative gas may act to lower the potential hill furthermore. Thus, molecules adsorbed on the surface may roll into these imperfections rather easily, resulting in the recovering of the adsorption ability of the surface. If these imperfections exist adjacently each other as shown by FG, HI and JK in Fig. 4-b and in the boundaries in Fig. 4-a, a molecule captured in the lattice imperfection penetrate into the interior passing through these imperfections. For the desorption of physically adsorbed molecules the comparatively small energy is required and thus the process is reversible, while the desorption energy of molecules captured in the lattice imperfections is naturally large, making the process irreversible.

This hypothesis interpretes almost all phenomena of gettering process below room temperature. Assuming that most part of gas molecules are captured in the lattice imperfections, (1), (2), (3) and (5) in Section 8 shall be understood without any objection. As the heat treatment acts to destroy these imperfections, the shortening of the time interval of constant pressure is easily explained. The capture of gas molecules in imperfections perhaps does not affect seriously the resistance of the mirror, in qualitative agreement with the result (8). Raising the temperature, molecules adsorbed on the surface become to diffuse into the interior through the series of lattice imperfections, forming new adsorption ability (7). The result (6) will be interpreted as followed: after the getter absorbes a large amount of gas, gas molecules are mainly adsorbed physically, but beyond −150°C some part of gas molecules are captured in lattice imperfections.

It was shown in Part II that the theory of physical adsorption holds for several phenomena and especially for phenomena experienced after the getter absorbes a large amount of gas. Probably gas molecules are mainly captured in lattice imperfections at the initial stage of gettering process, but after most of these imperfections are occupied, gas molecules become to be adsorbed only physically on the getter surface.

10. Absorption Theory Assuming Lattice Imperfections

In this paragraph the absorption theory will be deduced assuming the existence of numerous lattice imperfections. At first gas molecules are adsorbed on the surface of the getter mirror, giving the similar equations as (1) or (2). If the total number of adsorbed molecules is n, (1) or (2) can be written in the following form:

$$\frac{dp}{dt}=\frac{RT}{V}s-k_A p(N_0-n) \qquad (23)$$

where k_A is given by

$$k_A\equiv\frac{L^2}{\sqrt{2\pi MRT}}\exp\left(\frac{Q_1}{RT}\right)$$

The increase of adsorbed molecules is proportional to the difference between the number of newly adsorbed molecules on the surface and the number of molecules rolling into lattice imperfections from the surface. The latter amount is considered to be proportional to the density of surface-adsorbed molecules and thus the time change of adsorbed molecules is represented by

$$\frac{dn}{dt}=-k_s n+k_A\frac{NV}{RT}p(N_0-n) \qquad (24)$$

where k_s is the proportional constant, which is a function of the number of remaining lattice imperfections and temperature, and thus strictly it is a function of time. In the present calculation, however, k_s is considered to be a constant; limiting the time interval to a sufficiently short range, k_s may well be assumed constant. Eliminating n from (23) and (24), we obtain the following fundamental equation.

$$p\frac{d^2p}{dt^2}=\left(k_s p+k_A\frac{NV}{RT}p^2-\frac{dp}{dt}\right)\times\left(\frac{RT}{V}s-\frac{dp}{dt}\right)-k_A k_s N_0 p^2 \qquad (25)$$

Using β defined by (3), the formula (25) is very simplified:

$$\frac{d\beta}{dt}=-\beta\left(k_s+k_A\frac{NV}{RT}p\right)+k_A k_s N_0 \qquad (26)$$

If p is a constant, (26) can be easily integrated as followed;

$$\beta=a+(\beta_0-a)\exp(-k_s a t) \qquad (27)$$

where

$$a=\frac{k_A N_0}{1+\dfrac{k_A}{k_s}\dfrac{NV}{RT}p} \qquad (28)$$

Equations (26) and (27) are applicable to almost all phenomena of the gettering process observed below room temperature.

In the case of c.v. method, s must be put zero and then we obtain

$$p\frac{d^2p}{dt^2}-\left(\frac{dp}{dt}\right)^2=-\frac{dp}{dt}\left(k_s p+k_A\cdot\frac{NV}{RT}p^2\right)-k_A k_s N_0 p^2 \qquad (29)$$

This equation is easily integrated as followed:

$$\frac{1}{p}\left(\frac{dp}{dt}\right)=-\left\{k_s\log\frac{p}{p_0}+k_A\frac{NV}{RT}(p-p_0)\right\}-k_A k_s N_0 t+\left[\frac{1}{p}\frac{dp}{dt}\right]_{t=0} \qquad (30)$$

By comparing with (23), we obtain

$$\left[\frac{1}{p}\frac{dp}{dt}\right]_{t=0}=k_A N_0 \qquad (31)$$

Thus (30) is written in the form,

$$\frac{dp}{dt}=k_A p\left\{\frac{NV}{RT}(p_0-p)\right\}-k_s p\left(k_A N_0 t+\log\frac{p}{p_0}\right) \qquad (32)$$

The first term is the contribution of the physical adsorption and the second is the contribution of diffusion of surface molecules into the interior through lattice imperfections. As in the c.v. method k_s is supposed to be sufficiently small, gas molecules may well be considered to be adsorbed physically, showing that the theory developed in Part II is valid for the phenomena in the c.v. method.

11. Approximate Solution

It is difficult to solve strictly (25), but in the initial stage of c.f. method $(dp/dt)^2$ and d^2p/dt^2 are neglected, because the pressure change is always very small. Thus the approximate expression

$$\frac{dp}{dt}=\frac{(RT/V)sk_sp+k_Ak_SN_0p^2-Nk_Asp^2}{(RT/V)s+k_sp+(NT/RT)k_Ap^2} \tag{33}$$

is obtainad. Neglecting small quantity terms, (33) becomes

$$\frac{dp}{dt}\doteqdot\frac{V}{RTs}p\left(\frac{RTs}{V}k_s-k_AsNp)\right) \tag{34}$$

Solving and rearranging, the pressure is represented by a function of time as followed:

$$p=\frac{\exp(kst)}{1-(V/RT)p_0k_A\{1-\exp(kst)\}} \tag{35}$$

Expanding the exponential term in series, the first order approximation is given by

$$\frac{p}{p_0}=\frac{1+k_st}{1+(V/RT)k_ANp_0t} \tag{36}$$

in which p_0 is the residual pressure at the beginning of the experiment. The formula (36) means that no pressure change is observed if the following condition is satisfied.

$$k_s\leq\frac{k_ANVp_0}{RT} \tag{37}$$

As mentioned in the preceding section, k_s is, strictly speaking, a function of time and it becomes smaller as the getter absorbes the gas. In such extreme case (33) is written by

$$\frac{dp}{dt}=\frac{V}{RT}Nk_Ap^2 \tag{38}$$

showing that p is a parabolic function of t, in agreement with the experimental results. As k_s is also a function of temperature, the following condition becomes to be satisfied at sufficiently high temperature.

$$k_s\geqq\frac{k_ANVp_0}{RT} \tag{39}$$

In such cases the pressure increases linearly with time as will be experienced at room temperature.

12. Conclusion

In Parts II and III the theoretical analysis was carried out on the experimental results described in Part I of this paper. In Part II the theory of physical adsorption was found to be correctly applied to several phenomena, such as the later part of c.f. method and the pressure change at sufficiently low temperature in the c.v. method. Above −100°C carbon monoxide becomes to be adsorbed mainly in the activated state. Through the comparism of the theoretical value with experimental one, the activation energy for the physical adsorption was evaluated to be about 1.0 Kcal/g. mol. and from the analysis of the equilibrium pressure below −150°C, the activation energy for desorption was estimated to be 1.43 Kcal/g. mol. Furthermore, from the temperature dependencies of α, the activation energy for the activated adsorption was determined to be 6.53 Kcal/g. mol.

However, whole phenomena obtained in the Ba-CO system could not be explained by the theory of physical adsorption. Thus the new conception of lattice imperfections was introduced in Part III and the mathematical treatment was developed. The new theory was satisfactory for the qualitative understanding of whole experimental results obtained in the Ba-CO system. For the getter, absorbed already a large amount of carbon mono-oxide, this theory was found to be approximated by the theory of physical adsorption. The extremely strong ability of gas absorption of the flashed getter mirror is probably due to the existence of numberous number of the lattice imperfections. This shows that the barium getter must be flashed in order to include as possible as large number of imperfections; in other words, the getter must be flashed explosively at rather high pressure and the wall onto which the evaporated getter is condensed must be kept at as possible as low temperature. The detailed results on the flashing conditions shall be pubished in future.

References

1) T. Arizumi and S. Kotani: to be published in this journal.

2) L. Ehrke and M. C. Slack: J. App. Phys. **11** (1940) 129.

3) T. Arizumi and S. Kotani: unpublished.

4) T. Arizumi and S. Kotani: unpublished.

JOURNAL OF THE PHYSICAL SOCIETY OF JAPAN Vol. 7, No. 2, MAR.—APR., 1952

The Non-Uniform Natures of the Selenium Rectifier

By Masao TOMURA and Yukiaki ABIKO

The Institute of Polytechnics of Osaca City University

(Received, January 30, 1951)

Non-uniform natures of selenium rectifiers are studied by comparing the rectification characteristics of several small rectifier elements which are cut out of a conventional mother element of normal size. Non-uniformities of various kinds of characteristics, such as spreading resistance, contact potential, experimental value of e/kT and maximum back voltage etc, are observed with each element. They depend especially on the dimensions of the elements.

The distribution of contact potential is found to be different from that of local thin patches in the barrier layer. The contact potential distributes itself continuously at least within the area compared with the dimensions of our elements, namely 0.1 mm². But the local thin patches exist here and the mean distance between them is estimated as the order of several times of 1 mm.

Elements which have no local thin patches where currents due to tunnel effect flow show very high back voltrges such as above 100 volts.

§ 1. Introduction

Two kinds of non-uniform natures of the selenium rectifier were pointed out in the previous reports.[1],[2] The one was related to distribution of the contact potential between the metal and selenium semi-conductor, resulting in low values of e/kT appearing in the current *versus* voltage equation of the forward direction; and the other type of non-uniform structure came from the existence of small local patches through which current flowed owing to tunnel effect.

The problem of the non-uniform natures is very important in manufacturing the rectifier, so it is desirable to have more knowledge about these natures.

Analysis of observed data is so cumbersome and difficult for going into these problems, that a direct method to find each rectification characteristics at various points of a selenium rectifier was taken up. This procedure can be carried on by cutting out small rectifier elements from a larger rectifier of normal size. Observations of their rectification characteristics will give the first step leading to the survey of the non-uniform natures of the selenium rectifier.

§ 2. Measurements and Characteristics of the Rectifier Elements

The selenium rectifier used in these experiments was prepared in just the same way as reported before[1] with an effective area of ca. 10 cm². Several small rectifier elements with effective areas of 0.1 mm²∼20 mm² were cut out of the mother element at random positions. Since a conventional rectifier was utilized as our material, these small samples were obtained by stripping them off from the base metal electrode.

The current *versus* voltage characteristics of these elements including that of the original element were measured in the forward and reverse directions by the normal method. These results are shown in Fig. 1 and 2, which are reduced for the area of 1 cm². All measurements were carried on at room temperatures after sufficient electric formation at the maximum reverse voltage in the measurements.

From the linear part of the curve in the forward direction we can obtain the spreading resistance R_s. The intercept of extrapolation of the above linear line with the valtage axis gives the contact potential V_0.

The results are very interesting, showing just the non-uniform natures of the elements in both directions of current flow. Different characteristics given afterwards are found in the forward direction for each specimen and variations of the maximum back voltage are observed in a distinct manner at the same time. Here the maximum back voltage is meant roughly as the voltage at which the hard flow increases rapidly. The back voltage of

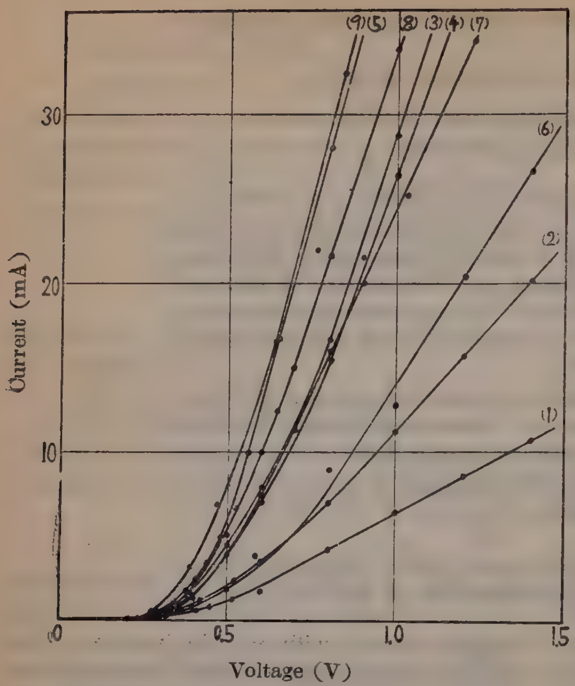

Fig. 1. Current *versus* voltage curves of the elements in the forward direction.

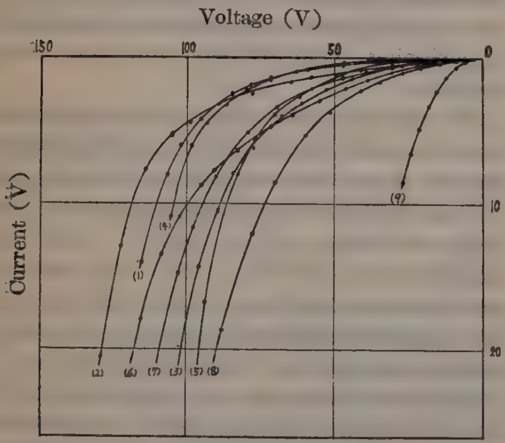

Fig. 2. Current *versus* voltage curves of the elements in the backward direction.

120 volts for the sample No. 2 is the largest one reported before. We could not apply higher voltages than 30 volts for the mother element, because the metal electrode begins to melt owing to elevation of temperature at that voltage. On the other hand, such effects did not appear in the case of the elements of high back voltage even at 120 volts.

As reported before,[3] creep phenomena were observed in the measurments of hard flows, whereby detailed analysis of backward characteristics was impossible to be carried out.

§ 3. Analysis of the Forward Characteristics

The easy flow i of the rectifier is shown as

$$i = A\{\exp[e(V_a - iR_s)/kT] - 1\}. \quad (1)$$

Here V_a is the applied valtage across the rectifier, R_s the spreading resistance and A a nearly constant quantity. By plotting log $(i+A)$ versus $V_a - iR_s$, and determing A and R_s* by trial to produce a straight line of intercept A with the current axis, we can obtain the experimental values of (e/kT) exp. in Eq. (1) from the slope of the line. (See Fig. 3.)

Some curves in Fig. 3 show slight humps at the lower voltage region. This is because the internal field of the barrier layer is still large even in the forward direction and the current by the tunnel effect superposes on the current by the thermoionic effect. These humps disappear at high temperature on account of the predominance of the thermoionic current, whereby it is assured that the humps are not caused by the irregular distribution of the contact potential.

In cases of the larger samples, the humps mentioned above are seen to appear, from which we know the existence of the tunnel effect as before.[1] But for the smaller samples which show high back voltages, we can detect no humps. Humps such as these are caused by the existence of local thin patches through which the tunnel current flow, so the existence of patches depends on the area of the element.

The experimental values e/kT are much smaller than the theoretical values. Ratios of $(e/kT)_{\text{exp.}}$ to $(e/kT)_{\text{theoret.}}$ are listed in Table 1 as α. $(e/kT)_{\text{exp.}}$ in the table is not accurate for the elements of larger size owing to the appearing of the humps mentioned above. The fact that α is less than unity, as Jearian pointed out,[4] means the distribution of contact potential V_0. The values of α in our case are all smaller than unity, resulting in that the contact potential are distributed continuously at least within the area compared with the dimensions of our elements, namely 0.1 mm². Of course the contact potential has not only distribution, but the distribution of contact potential itself differs in each sample as known from Table 1. In other words, there are two kinds of non-uniformity of contact potential.

---

* Rs mentioned here is larger in most cases than that obtained by the method in § 2.

Table 1. Several characteristics of rectification of the elements. They are reduced for the area of 1 cm².

Element No.	V_0 (volt)	Rs (ohm)	e/kT (volt^{-1})	α	back voltage(volt)	area (mm²)	temp. (°C)
1	0.42	95.0	19.2	0.47	90	0.10	13.0
2	0.50	42.8	20.2	0.50	110	0.17	11.5
3	0.53	16.7	13.8	0.34	80	0.21	13.0
4	0.43	18.2	23.5	0.58	95	0.27	12.0
5	0.43	12.8	24.6	0.61	80	0.60	15.0
6	0.56	33.0	20.6	0.51	100	1.56	12.3
7	0.44	25.0	25.1	0.62	90	7.50	14.0
8	0.45	16.7	20.2	0.51	70	20.0	14.0
9	0.41	12.7	26.8	0.66	15	992	12.5

As for the values of V_o and R_s, they differ for each element respectively, but we cannot go into detailed analysis of these values. The higher the back voltage of the element, about which we will discuss in the next section, the value of R_s is likely to be the larger. This relation may be attributed to the non-uniform existence of impurity centres such as iodine mixed into selenium. Locally concentrated impurity centres may decrease the spreading resistance as well as make thin the barrier layer at that place, or make the patches which reduce the value of back voltage.

§ 4. Non-uniform Natures of the Backward Direction

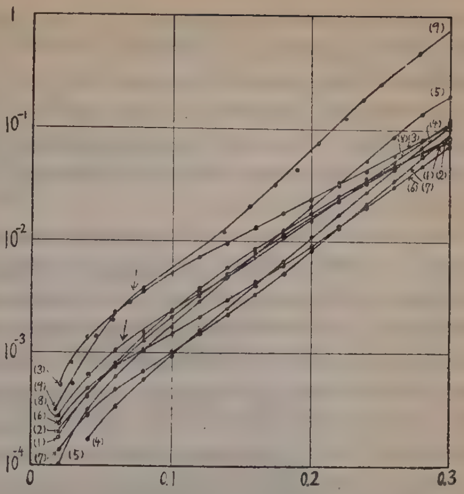

Fig. 3. Forward characteristics in a semi-log scale. Arrows show the humps by the tunnel effect.

Fig. 2 shows how different the backward natures are for several elements used. Remarkably high back voltages as high as about 120 volts are found for the cases of the smaller samples. As the back voltage is limited by its lowest value in the case of a sample which has non-uniform natures, in other words, by the local patch where the barrier layer is thin, the element which has no thin local patches will show a high back voltage. From the fact that the smaller the area of the element, the higher is the back voltage, it is clear that the patches do not distribute continuously as does the contact potential. The patches exist here and there as expected in the preceding report[1)] and the possibility of containing the patches in the element of unit area decreases with the diminution of the area of the sample. The dimensions of the areas of samples listed in Table 1 suggest the order of mean distance between the patches. Fig. 4 shows that the back voltage tends to a finite value with the diminution of the area of the element, meaning that the elements whose areas correspond to the above finite back voltage have no probability of containing the patches. Thus the mean distance between the patches will be estimated as the order of several times of 1 mm. This estimation is consistent with the results shown in Fig. 6 in the report(1).

For the elements of sufficiently large area comparing with the distance between the patches, their back voltage will become constant again, for they must contain the same number of patches per unit area on the average. But Fig. 4 does not show this tendency. It may be

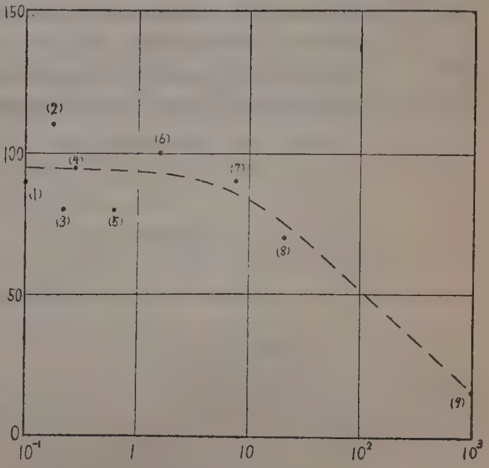

Fig. 4. The relation between the back voltages and the areas of the elements.

attributed to the rare exsistence of large patches* and the chances of containing these large patches in the elements increase with the size of the element, resulting in low values of the back voltage. Thus the constancy of the back voltage at large areas cannot be observed till the area of $10^3\,mm^2$ yet.

The size of patches in Fig. 6 in the previous report (1) differs with each other. Thus we must notice the non-uniform size of the patches themselves. At the same time the thickness of the patch, that is, the thicknass of the barrier layer at the patch, also shows non-uniformity. The latter fact is known from the following experiment. In the process of electric formation, the stepwise elevation of formation voltage results in the stepwise decrease of hard flows. This is because the thinner patches are damaged by tne lower voltages and the thicker ones are damaged only by the higher voltages.

§ 5. Conclusion

In the present paper, non-uniform natures of the selenium rectifier are studied by comparing the rectification characteristics of several small rectifier elements which are cut out of a mother elements of normal size. Non-uniformities of various kinds of characteristics, such as R_s, V_0, distribution of V_0 and back voltage etc., are observed with each element and discussed.

The distribution of contact potential is found to be different from that of local thin patches. The former is continuous compared with the size of elements used here and the latter is discontinuous, or the patches rather exist here and there.

Relations between the values of R_s and the area of the elements are pointed out, but the number of the specimen is too small to analyze other relations between V_0, α, R_s and the area of elements.

Considering these non-uniform natures of the selenium rectifier, it is natural to find difficulty in manufacturing rectifiers of uniform characteristics. And these natures must not be forgotten in discussing the data of the rectifier.

It is most important to find origins of the non-uniform natures, especially of the existence of local thin patches. Studies on materials of selenium semi-conductor and metal electrode as well as impurities added to them may give the key to this problem.

The temperature variation of the above characteristics will present more clear knowledge on tne non-uniformities of the rectifier, and impedance measurements at audio-frequency will supply the necessary data at the same time.

It is disirable to deal with more rectifier elements than this survey to make accurate discussions; or rather to extend the method used in this report, that is, cutting out small samples at random positions of the mother element to the method of obtaining the rectification contour which is carried on by cutting out small samples almost continuosly.

The authors thank Dr. H. Kawamura for his encouragement in this work.

References

1) M. Tomura: J. Phys. Soc. Jap. **5** (1950) 222.
2) M. Tomura: J. Phys. Soc. Jap. **5** (1950) 349.
3) M. Tomura: J. Phys. Soc. Jap. in press, Read at the meeting of the Phys. Soc. Jap. April, 1950 (Tokyo).
4) e. g. H. C. Torrey and C. A. Whitmer: *"Crystal Rectifier,"* 88, Mc Graw-Hill Press (1948).

---

* The existence of these large patches have been ovserved in Fig. 6 in the report (1).

JOURNAL OF THE PHYSICAL SOCIETY OF JAPAN Vol. 7, No. 2, MAR.—APR., 1952

Electrical Dispersion of Selenium Rectifier at High Frequency

By Jiro YAMAGUCHI, Takeshi MIYAUCHI
and Hideo MORI

Faculty of Engineering, Osaka University

(Read Apr. 3, 1951, Received May 28, 1951)

Measuring capacitance and conductance of the seleninm rectifier by means of the reactance variation method, the electrical dispersion was found at about 1 Mc. per sec.

This problem is approximately interpreted with the relaxation theory, which Lawson treated for the metal rectifier.

Applying our results of measurement to the equations derived by Lawson, the value of $\varDelta E$ is nearly 0.05 eV and B_0 (ionization probability B is expressed as $B_0 \exp - \varDelta E/kT$) may be estimated at about 3×10^7 sec^{-1}.

§ 1. Introduction

The selenium rectifier is expected to have the electrical dispersion phenomena. Lawson$^{1)}$ assumed that, when electrons are transferred from the impurity centers into the conduction band of a semiconductor there is a relaxation effect, and he discussed this phenomena theoretically for the metal rectifier, and derived the characteristic equation of its capacity and conductance. Ono$^{2)}$ also treated this problem and reported experimental results on selenium rectifiers, In his report he shows that the frequency of the dispersion is about 1.5 Mc for the usual selenium rectifier.

In this report, the frequency characteristics of the selenium rectifier are more precisely investigated and moreover the temperature characteristics are discussed.

§ 2. General principle and method of calculation

By Lawson the relations between capacitance (C) or conductance (G) and frequency are expressed by following equations (1)—(5) assuming that; when the bias voltage is applied to the metal rectifier which has the physical barrier, the width of barrier changes with the variation of bias voltage (dV), and the transfer of a bound electron in the variant part (df) of barrier from an impurity center into the conduction band of an N-type semiconductor has a relaxation time, but the time for inverse process, i. e. electron is captured by an ionized center, is short compared with that of the former.

$$G/\omega = C_0 \frac{N-n_0}{N} F_1(x) \tag{1}$$

$$C = C_0\left[1-\frac{N-n_0}{N} F_2(x)\right] \tag{2}$$

$$F_1(x) = \frac{x}{2(1+x^2)}\left[1+\frac{1}{2\pi}\left(1-e^{-\frac{2\pi}{x}}\right)\frac{2x^3}{1+x^2}\right] \tag{3}$$

$$E_2(x) = \frac{x^2}{2(1+x^2)}\left[1+\frac{1}{2\pi}\left(1-e^{-\frac{2\pi}{x}}\right)\frac{x(x^2-1)}{1+x^2}\right] \tag{4}$$

$$C_0 = eN\frac{df}{dV} \tag{5}$$

$$x \equiv \frac{\omega}{B}$$

where ω is the angular velocity of a. c. voltage impressed on the rectifier, B the probability per unit time for ionization of an impurity atom, and e the electronic charge. N and n_0 are respectively the number of impurity centers and that of free electrons in unit volume of the semiconductor at equilibrium state.

Now let the capture cross section of an empty donor level be σ and the depth of impurity level below the conduction band be $\varDelta E$. Then B is written as

$$B = \frac{2\pi m(kT)^2}{h^3}\sigma\sqrt{6\pi}e^{-\frac{\Delta E}{kT}}$$

and taking $\sigma=10^{-15}\,\mathrm{cm}^2$

$$B = 1.5\times10^{11}e^{-\frac{\Delta E}{kT}}\mathrm{sec}^{-}.$$

However$^{1)3)}$ Seitz has estimated 10^{10} sec^{-1} as an upper limit for B_0, the coefficient of $e^{-\Delta E/kT}$, with aid of quantum mechanics and also it has been reported that B_0 may take smaller values under some conditions of semiconductor materials.

The above-mentioned theory was for N-type semiconductors, but also for p-type semiconductor, the quite same way is treated.

Equation (1) is maximum at $x = 1.47$. If it is assumed that this point is equivalent to the frequency at which the experimental value of G/ω is maximum, the value of B is obtained from $\omega/B = 2\pi f/B = 1.47$. Since it is difficult to obtain the value of C_0 (that is the value of C when $\omega = 0$), C_0 is assumed to be the asymptotic value of C at the range of frequencies lower than the dispersion frequency. n_0 is calculated as follows. In equilibrium

$$\frac{n_0^2}{N-n_0} = \left(\frac{2\pi mkT}{h^2}\right)^{3/2} e^{-\frac{\Delta E}{kT}}$$

and by assuming $N \gg n_0$,

$$n_0 = \sqrt{N}\left(\frac{2\pi mkT}{h^2}\right)^{3/4} e^{-\frac{\Delta E}{2kT}}$$

For the calculation of the conductance (G) and capacitance (C) in equations (1) & (2), we neglected the effect of the 2nd harmonic and higher harmonic currents, that occur at applying sine wave voltage to the metal rectifier. By calculating the magnitude of the higher harmonics, these are found not to be negligibly small compared with the fundamental. But it is impossible to exclude the effect of higher harmonics in the results obtained by measurements.

§ 3. Method of measurement

Specimens used are selenium-rectifiers in Japanese market, the electrode of which is Wood's metal, and its diameter is 1.5 mm. The conductance and capacitance are measured by the reactance variation method(as shown in Fig. 1). The frequency characteristic are taken for the range of frequencies from 50 kc to 10 Mc at room temperature (10°C), and the temperature-characteristics for the rangs from −60° to 45°C at the frequencies 380, 1,000 and 2,600 kc.

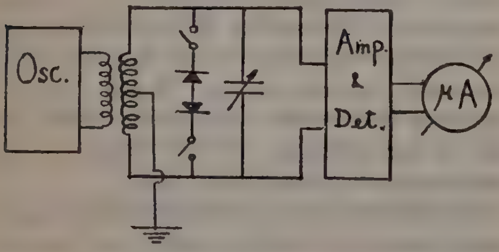

Fig. 1.

§ 4. Results obtained

In Fig. 2 are shown the frequency-characteristics of the capacitance and conductance of a selenium-rectifier. They show dispersion at about 1 Mc. Therefore the value of B at room temperature is calculated to be 4.2×10^6 sec^{-1} by the above-mentioned method and moreover C_0 is estimated to be 1000 $\mu\mu$ F from Fig. 2.

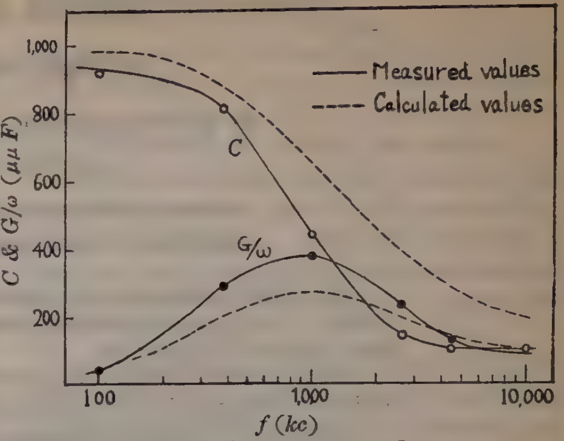

Fig. 2. The relation between conductance or capacitance and frequency

In Figs. 3, 4 and 5 are shown the temperature-characteristics that are measured respectively at 380, 1,000 and 2,600 kc. The full lines in these figures are experimental, while the broken lines show the results calculated by equations (1) and (2), assuming $\Delta E = 0.05$ eV4) and $N = 10^{18}$ cm^{-8}, and using B and C_0 obtained by the frequency-characteristics.

From Figs. 2, 3, 4, and 5, the experimental

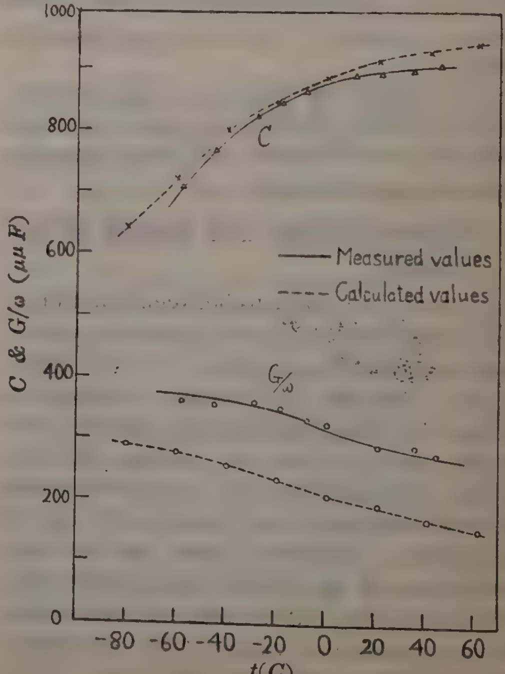

Fig. 3. Conductance and capacitance versus temperature at 380 kc.

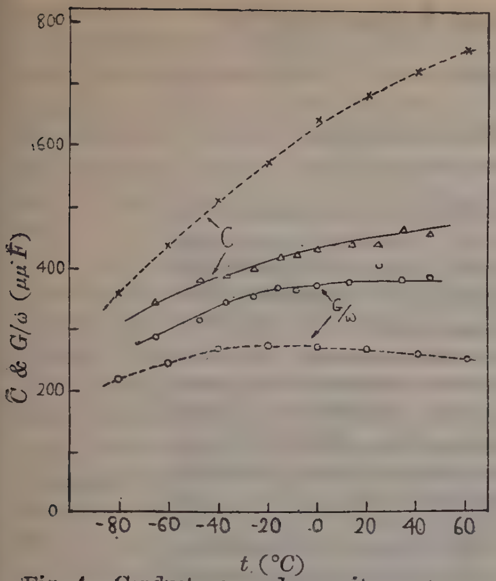

Fig. 4. Conductance and capacitance versus temperature at 1,000 kc.

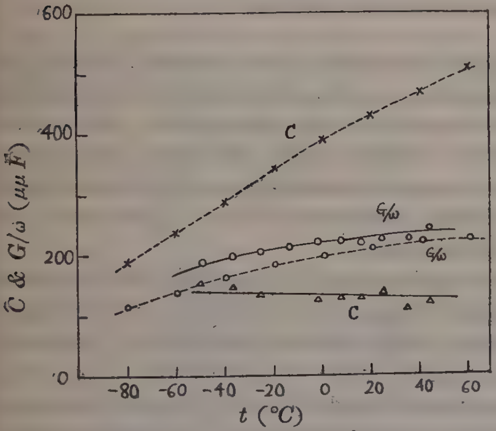

Fig. 5. Conductance and capacitance versus temperature at 2,600 kc.

data are said to be approximately consistent with the calculated results except the value of C at higher frequencies. By this reason it is, perhaps, permitted that the value of $\varDelta E$ amounts to 0.05 eV, and so B_0 may be estimated to be 3×10^7 sec^{-1}. A better agreement between experimental and calculated results would be obtained if the following causes could be avoided; (i) the uncertainty of the value C_o, (ii) the effect of d.c. resistance of the barrier and (iii) the influence of higher harmonics. However the discrepancy of C, especially that of the temperature-characteristics at 2,600 kc, (as showd in Fig. 5), must be paid more attention and this problem requires further consideration and discussion.

§ 5. Summary

The electrical dispersion of the selenium-rectifier occurs at about 1 Mc at room temperature and is explained to be due to the relaxation effect of an electron (hole) that is transferred from an impurity center to the conduction band (filled band). The value of B (at 10°C) may be estimated at 4.2×10^6 sec^{-1} by Lawson's equation.

The temperature-characteristics G/ω obtained from the experiments coincide well with the results calculated by assuming that $\varDelta E=0.05\ eV$ and $N=10^{18}\ \mathrm{cm}^{-3}$. B_o may be about 3×10^7 sec^{-1}.

The authors wish to express their gratitude to the Shin-Dengen Co. and the Fuji-Denro Co. that gave them specimens used in this work and to Mr. K. Kobatake for his kind help.

This research was done under the Grant in Aid for Fundamental Scientific Research, Minister of Education.

References

1) H. C. Torry & C. A. Whitmer: Crystal Rectifiers Part 1, Chap-4.

2) M. Ono: Memmo. of Faculty of Eng. Nagoya Univ. Vol. 1 No, 2 1949.

3) F. Seitz: Transition probability for excitation from bound level. Columbia Univ. Sept. 11, 1943,

N. F. Mott & R. W. Gurney: Electronic process of ionic crystals, Chap. 4.

R. Kubo: J. Phy. Soc. Japan **3** (1948) 254 **4** (1949) 322 and **4** (1949) 326.

4) Ueda, Tokiba & Ikeda: Bussiron-Kenkyu **34**-go (1951) 37.

JOURNAL OF THE PHYSICAL SOCIETY OF JAPAN Vol. 7, No. 2, MAR.—APR., 1952

Magnetic After Effect of Cold Rolled Iron (I)

By Yuzo TOMONO

Department of Physics, Tokyo Uuiversity

(Received August 24, 1951)

In part I, the magnetic after effect of cold rolled iron is studied both by semi-static and dynamic measurements. It is verified that the static after effect in a weak field and the so called Jordan's constant are not observable in contradiction to Schulze's measurements. But the after effect is observable in the range of irreversible magnetisation. The after effect of iron, annealed after being cold rolled, is also investigated. The after effect in the range of initial permeability becomes observable in a recrystallised state, in agreement with Schulze's results. In addition it is found that the part of loss angles, observed at low frequencies, attributable to the macroscopic eddy currents is larger than the theoretical value. It suggests the existence of a relaxation due to another origin which has not been taken into account in the analysis of loss angles. Hence, in part II, the measurements of apparent permeability at higher frequencies are carried out for the cold rolled iron. The time of relaxation in the range of initial permeability is estimated to be of the order of $10^{-6} \sim 10^{-7}$ sec. It satisfactorily explains the difference between loss angles observed and calculated.

§ 1. Introduction

In 1924, H. Jordan1) analysed the loss angles* of iron core, observed in alternating magnetic field, and found the so-called Jordan's constant over a wide range of audio-frequencies. This is obtained from the observed loss angles by subtracting the parts due to hysteresis and eddy currents. Schulze2) applied the same method to the analysis of loss angles for an annealed iron, and found an after effect, in a weak field, which was strongly dependent on temperature. This temperature dependence agrees with that of static after effect in a weak field observed by Richter3) in the same iron. After effect of this kind is also found in silicon steel and low carbon steel. But many ferromagnetic materials except these show the magnetic after effect only in the irreversible magnetisation, but not in a weak field, although small Jordan's constants, which are little dependent on temperature, are often observed.

The only one correspondence between the results obtained with static and dynamic methods, except that in iron and alloys near iron, was obtained by Preisach4) for the alloy of 40% Ni, 60% Fe. But his work has several doubtful points. He estimated the magnitude of static after effect in the range of initial permeability, where his dynamic measurements were performed, by extrapolating the coefficients of after effect observed in the magnetic field larger than 0.1 oe. to the initial range. But, as his alloy has a fairly high permeability, the magnetisation process where the static after effect was observed contains irreversible displacement of domain boundaries, and so differs from that of initial range.

For cold worked iron, small Jordan's constant was also observed by Schulze5). But the magnitude is much smaller than that of annealed iron, and so might be considered to be within the errors of decade bridge. Therefore we must examine to what extent these Jordan's constants are reliable and have physical meanings.

§ 2. Magnetic After Effect of Annealed Iron

Before everything the relation between the static after effect and the loss angles observed in audio-frequency measurements must be examined. The measurements of Richter and Schulze coincide in temperature dependence, but not in the magnitude of after effect, probably because Richter's static measuments were performed outside the initial range. The writer has tried to do both measurements in the range of initial permeability.

---

* Strictly speaking "loss angle" in this paper must be replaced by "loss factor," that is tan δ, where δ is the loss angle or the phase difference between magnetic field and flux density. But these are confused as δ is a small quantity. These are proportional to energy dissipated per cycle.

The specimen is a spirally wound ribbon of Armco iron, annealed at 800°C after cold rolling. The ribbon is 0.1 mm in thickness and 2 cm in width. Total diameter and cross-sectional area are 4.5 cm^2 and 0.53 cm^2 respectively. Every layer of spiral is insulated with mica.

(A) Static Measurements

It is verified that initial magnetisation curve is linear up to 0.015 oe. At first a constant magnetic field of 0.015 oe. is applied for 5 minutes. Then the field is cut off and after a certain time interval, the search coil (1500 turns) is connected with ballistic galvanometer, the quarter period of which is about 60 secs. This time interval is controlled with pendulum. Fig. 1 shows the observed relaxation of induction vs. the lapse of time after the field change. As the relaxation due to eddy currents in this specimen finished within 10^{-4} sec., these relaxations are attributable to the magnetic after effect. The magnitudes of after effect which are obtained by extrapolating these curves to $t=0$ are about 30% of total changes. Every curve is expressed by an exponential function, exp $(-t/\tau)$, where τ is the time of relaxation. In the previous researches, the after effect was analysed on the assumption of continuous distribution of the times of relaxation[6]. But the breadth of this distribution can be assumed to be small, as our curve can be approximated by the exponential function with a single time of relaxation. τ, estimated in this way, becomes smaller at higher temperatures, Log τ vs. $1/T(°K)$ is shown in the lower part of Fig. 3.

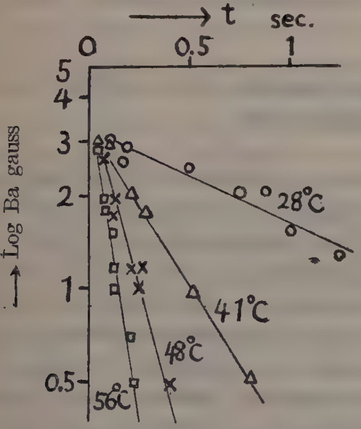

Fig. 1. The magnetic after effect in the range of initial permeability for iron annealed at 800°C. Total changes in induction are 11.6, 13.4, 12.7 and 12.1 gauss, at 28°C 41°C, 48°C and 56°C, respectively.

(B) Low Frequency Measurements

The loss angle is given by $\delta R/\omega L$, where δR is the increment of resistance of search coil due to energy dissipation in the specimen and L is self-inductance of search coil. For the measurements of effective resistance and self-inductance, the impedance bridge shown in Fig. 7 is used, including Wagner's earthing device to compensate the stray current due to asymmetric earth capacity.

In order to subtract the loss angle due to hysteresis loss angles are observed in the alternating fields of amplitudes in the range between 0.002 oe. and 0.020 oe., and the value at vanishing amplitude is estimated.

The loss angle due to eddy currents is given by

$$\pi\mu_0 d^2\omega/3c^2\rho \qquad (1)$$

where ρ, μ_0 and d are resistivity, initial permeability and thickness of specimen, respectively. But there is another method to estimate the loss angle attributable to eddy currents, as following. As, at room temperature, the time of relaxation of after effect is the order of second and the frequencies in the measurements are more than 100 cps, the observed loss angles must be independent of after effect and so must be linear vs. frequencies. This is found to be the case. Thus the coefficient of ω in the loss angles due to eddy currents can be estimated from the inclination of the observed loss angles vs. frequencies at room temperature. But at higher temperatures the time of relaxation of after effect becomes smaller and loss angles are no more linear vs. frequencies. This makes the direct determination difficult. Hence the coefficient at higher temperature is estimated by correcting that of room temperature in the way that μ_0/ρ is substituted by the value of higher temperature. However, the coefficients determined in this way are found larger than the theoretical values obtained from Eq. (1). This discrepancy will be disscussed later.

The part of loss angle, obtained from total loss angle by subtracting the parts due to hysteresis and eddy currents is the part attributable to the magnetic after effect. This part ξ_a is shown in Fig. 2 vs. temperatures. This is quite similar to Schulze's results. ξ_a of a given frequency shows a maximum at higher temperature as the frequency is higher. This

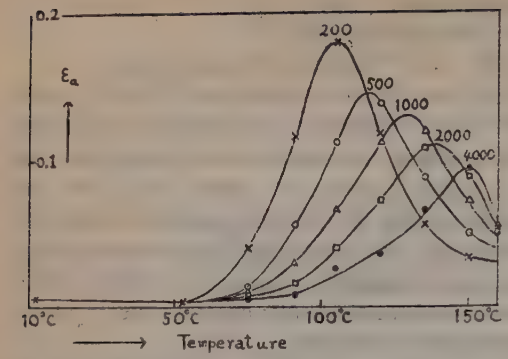

Fig. 2. The loss angle due to magnetic after effect vs. temperature, for Armco iron annealed at 800°C. The parameter for each curve indicate frequency.

means that τ becomes smaller at higher temperature.

Now these results must be analysed with a single time of relaxation. The total change in induction δB, due to the change in magnetic field δH, is expressed by assigning a fraction of after effect γ as

$$\delta B = \mu_0 \delta H(1+\gamma) = \mu_0 \delta H + B_a(t)_{t=\infty} \quad (2)$$

where $\mu_0 \delta H$ is the instantaneous increment and $B_a(t)$ is the part of after effect. $B_a(t)$ is determined by the equation,

$$dB_a(t)/dt = -(1/\tau)[B_a(t) - \gamma\mu_0\delta H] \quad (3)$$

In static measurements δH can be seen as constant, hence

$$B_a(t) = \gamma\mu_0\delta H\,[1-\exp(-t/\tau)] \quad (4)$$

In audio-frequency measurements, $\delta H = H_0 \cos \omega t$, hence

$$B_a(t) = \frac{\gamma\mu_0 H_0(\cos \omega t + \omega\tau \sin \omega t)}{1+(\omega\tau)^2} \quad (5)$$

Hence the loss angle ξ_a due to magnetic after effect is

$\gamma\omega\tau/[1+(\omega\tau)^2+\gamma]$, therefore

$$(\xi_a)_{max} = \gamma/2\sqrt{1+\gamma}, \text{ when } \tau=\sqrt{1+\gamma}/\omega \quad (6)$$

τ and γ can be determined from Eq. (6). As for τ, the plotted points in the upper part of Fig. 3, which are estimated from the audio-frequency measurements, are just on the same lines as those obtained from the static measurements. τ is expressed by the equation; $\tau = \tau_\infty \exp(U/kT)$, where U is 0.99 ev.

γ is about 0.4 in static experiments, but in dynamic experiments it is 0.36 at 100°C and decreases at higher temperatures.

In static measurements γ becomes smaller as δB increases, and in dynamic measurements γ decreases as the superposed static field increases.

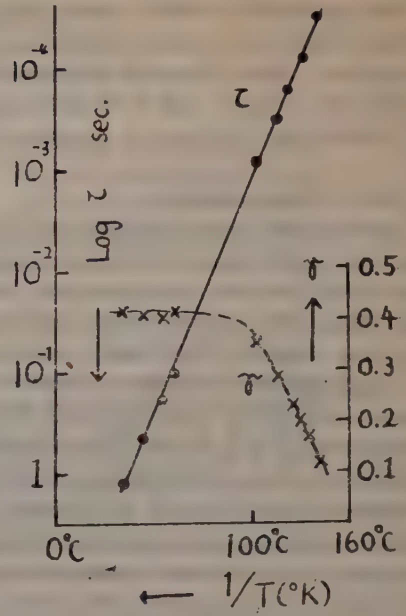

Fig. 3. Log τ and γ vs. 1/T(°K) for Armco iron annealed at 800°C.

§ 3. The Magnetic After Effect of Cold Rolled Iron

Specimens are prepared by five times repeated intermediate annealing and cold rolling, and the final thicknesses are 0.1 mm. Then these are tempered at 400°C, 500°C and 600°C. Thus four kinds of specimens are prepared, including the non-annealed specimen. For these, measurements of magnetic torque curves, and the microscopic observation of grain size are carried out. Then it is concluded that recystallisation bigins to take place at 600°C. Before recystallisation, grains have irregular forms elongated to the direction of roll. The dimensions of their longer and shorter boundaries are about $3\cdot10^{-3}$ cm and $1.5\cdot10^{-3}$ cm respectively. After recrystallisation, grains are in the form of normal polygon about $5\cdot10^{-6}$cm² in area.

The ribbons of these specimens are spirally wound. The total cross-sectional area is about 0.5 cm² in every specimen. As the thickness of these ribbons is 0.1 mm and every layer is insulaled each other with mica, the relaxation due to eddy currents is safely neglected in static measurements.

At first the magnetic after effec is investigated in specimens before recrystallisation.

Now a rough survey in a wide range of magnetic field is performed. In this case the turn number of search coil is about 1800. Electromotive force induced in the search coil by the induction change of specimen is magnified by a direct current amplifier which is connected to the electro-magnetic oscillograph. The natural frequency of its vibrator is about 4 kc. The observations of magnetic relaxation are performed, changing the magnetisation from residual point to the state in coercive force along the descending branch of the hysteresis curve, and from demagnetised state to a certain magnetisation along the initial magnetisation curve. The direct current amplifier is not necessary when the total change in induction is large.

But the results observed without amplifier contain an exponential relaxation, as shown in Fig. 5, the time of relaxation of which is given by $L/(R_c+R_s)$, where L and R_c are the inductance and the resistance of search coil and R_s is the series resistance connecting the search coil and the vibrator. Moreover if the stray capacity in the search coil is large, strictly speaking, $4CR_s(R_c+R_s)/L > 1$, a damped oscillation takes place. But this is not the case, because $C \cong 500\mu\mu f$, $R = 95\Omega$, $0 \leq R_s \leq 5k\Omega$ and $0.2 < L < 1.5h$. A schema of this circuit is shown in Fig. 4. The similar relaxation takes place in the magnetising circuit, but it exerts no effect on the obserevation, because the self-inductance of the magnetising coil is much smaller. This is verified experimentally.

By increasing R_s this apparent relaxation can be reduced within 10^{-3} sec., as shown in Fig. 6, that is comparable with the natural period of the vibrator. Thus the magnetic after effect can be observed.

Along the descending branch of the hysterisis curve, a small after effect is observed as shown in Fig. 5. But along the initial magnetisation curve, no after effect is observed after the time elapses more than 10^{-3} sec.

These results are found in the specimens, cold rolled and tempered at 400°C.

Furthermore the writer has tried to investigate the same problem by the more accurate method described in sec. 2. The turn number of search coil is 9500, and 1 mm in the deflection of galvanometer corresponds to 0.025 gauss in the intensity of magnetisation. In addition it must be noted that before the search coil is connected to galvanometer, a damped oscillation takes place in the search coil, induced by the abrupt change in magnetisation. In order to quench this oscillation, the search coil is shunted with the resistance of critical damping.

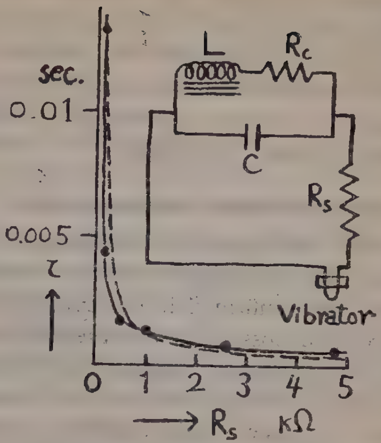

Fig. 4. Schematic of the search coil circuit, and the reduction of the time of relaxation due to circuit elements with increasing R_s. Broken lines is the calculated curve.

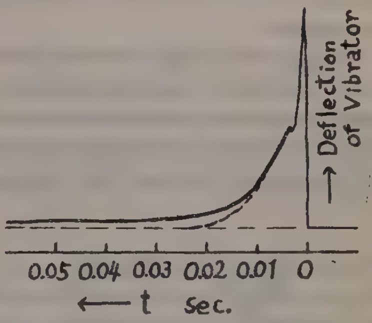

Fig. 5. Oscillogram obtained for a cold rolled iron as the field is change from zero (residual point) to coercive force. Broken line is the relaxation due to L.

In these measurements the same results are obtained as befored. In the irreversible magnetisation, a small after effect is observed, which is expressed by $c_1+c_2 \log t$, where c_1 and c_2 are constants. The fraction of after effect in specimens, cold rolled and tempered at 500°C, are 0.3% and 1.5% at $t=0.01$ sec., respectively. But no after effect is observed, near the range of initial permeability, and even in the initial magnetisation process, where total change in induction is about 1000 gauss.

§ 4. Low Frequency Measurements

Now that the existence of the magnetic after effect in the cold rolled iron in a weak field has not been confirmed in our experiment, the small constant loss angle observed by Schulze seems to be due to another sort of energy dissipation, or the errors in the impedance bridge. To answer this question, a precise measurements should be done, in the same specimens before recrystallisation as in the preceeding section.

In case of measurements of loss angle $\delta R/\omega L$, we can obtain a comparatively reliable L-value, but δR is usually much smaller than R itself which is not so reliable as L, and so δR is often in the range of errors. For accurate measurements, emphasis should be laid in the following points.

(a) The arm-ratio must be one to one, that is $R_A = R_B$ in Fig. 6, and both resistance must be equally constructed with the same wire. Otherwise the unbalance of stray capacity and residual inductance furnishes the erroneous results.

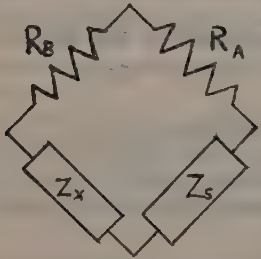

Fig. 6. Schematic diagram of impedance bridge.

(b) The turn number of search coil must not be too small. The L-value is proportional to square of turn number n^2, and also δR is proportional to n^2. But static resistance R_0 is proportional to n. Hence the accuracy of δR, namely $\delta R/R_0$, is proportional to n. But n must not be too large, because the resonance frequency due to L and stray capacity in the coil of specimen should be much higher than the frequency of measurement.

(c) Wagner's earthing device is recommended, to compensate the troublesome effect of asymmetric earth capacity.

(d) The amplitude of applied alternating field must be as small as possible in order to eliminate completely the part due to hysteresis because loss angles are not necessarily linear vs. amplitudes.

Among the measurements performed by the writer, two examples will be shown. In these the amplitudes of applied alternating fieled are in the range between 0.002 oe. and 0.015 oe.

Case 1. Specimen is a cold rolled iron. L is about 15 mh. The bridge used is of Butter-worth's type shown in Fig. 7, where $R_A=1000\Omega$, $R_P = 100\Omega$, R_B and U are variable, and $C_s = 0{,}219\mu f$. As this bridge is balanced,

$$R_X = R_B R_P / R_A$$

$$L_X = C_S(R_P - r)[(R_A + R_B)U + (R_A + r)R_B]/R_A \qquad (7)$$

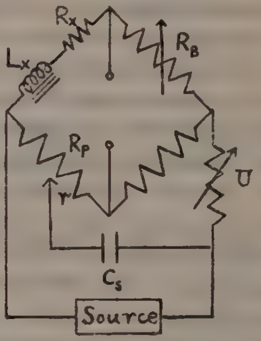

Fig. 7. Butter-worth's bridge.

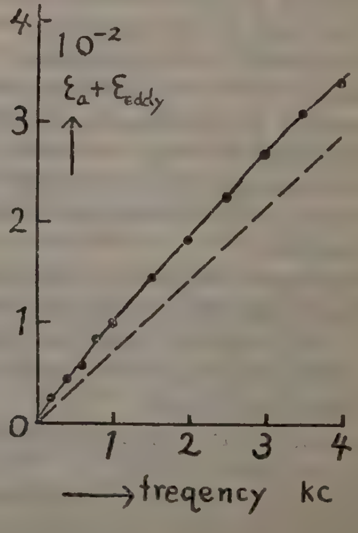

Fig. 8. Loss angle vs. frequency for a cold rolled iron (hysteresis part is subtracted). The broken line is the calculated eddy current part.

The results obtained from the observed loss angles by subtracting the part due to hysteresis are shown in Fig. 8. The loss angles start linearly from zero point and curve down at higher frequencies. This curving down seems to be due to the error stated in (a). In this case R_B is about twice as large as R_A. And as the residual inductance and stray capacity in R_B are larger than those in R_A, the apparent resistance of R_B increases at higher frequencies more repidly than that of R_A, and so the observed ratio R_B/R_A in Eq. (7) becomes smaller at higher frequencies than the intrinsic value. Hence δR decreases more rapidly. Regardless of such error, the observed loss angles are larger than those calculated from Eq. (1), which is shown as a broken line in Fig. 8.

Case 2. Specimen is tempered (at 500°C) after cold rolling. The bridge used is shown in Fig. 9, where $R_A = R_B = 1000\Omega$. The results obtained shown in Fig. 10. Curves a and b are obtained for L=4.02mh. and 30.4mh., respectively. Curve a does not pass through zero point, but b does so nearly. In curve a L is so small that δR is in the range of error. In curve b the effect of stray capacity can be seen at higher frequencies but still it does not affect the fact that curve b nearly intersects zero point.

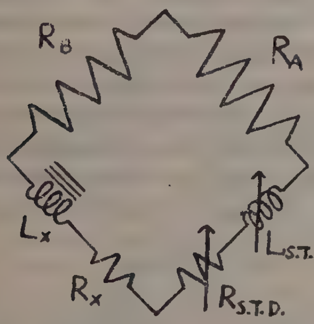

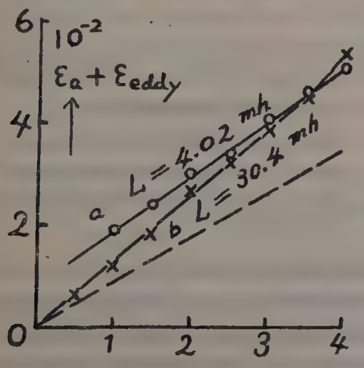

Fig. 10. The loss angle (hysteresis part subtracted) vs. frequency for a iron after cold rolling tempered (at 500°C). The broken line shows the part due to eddy currents calculated from Eq. (1).

Through these measurements, it is concluded that the small loss angle (about $3 \cdot 10^{-3}$) observed by Schulze which is constant over a wide range of low frequencies is not so reliable as to afford a certain physical meanings. This conclusion is consistent with that of sec. 3.

The magnetic after effect in a weak field appears first when the cold rolled iron is annealed at 600°C, where the recrystallisation takes place. This fact was found by Schulze. Fig. 11 shows ξ_a vs. temperature, in which ξ_a is obtainted by subtracting the part due to eddy currents calculated from Eq. (1). Loss angles have a steeper inclination against frequencies than that calculated from Eq. (1), as seen from the plots at room temperature. This discrepancy is common in Figs. 8, 10, and 11. This will be discussed in the following paper.

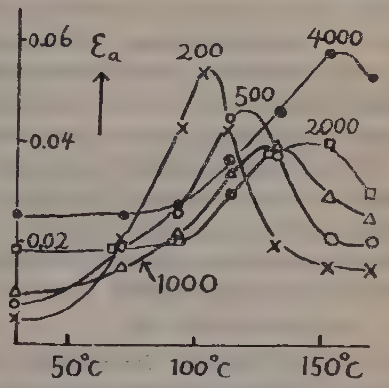

Fig. 11. The loss angle attributable to magnetic after effect vs. temperature for a recrystallised iron annealed at 600°C. The perameter for every curve is frequency.

References

1) H. Jordan: E. N. T. **1** (1924) 7.

2) H. Schulze: Wiss. Veroeff. Siemens-Werk. **17** (1938) 39.

3) G. Richter: Ann. Phys. Lpz. **29** (1937) 605, **32** (1938) 685.

4) F. Preisach: Z. Phys. **94** (1935) 277.

5) H. Schulze: Wiss. Veroeff. Siemens-Werk. **17** (1938) 59.

6) Becker & Doering: "Ferromagnetismus" p. 247.

JOURNAL OF THE PHYSICAL SOCIETY OF JAPAN Vol. 7, No. 2, MAR.—APR., 1952

Magnetic After Effect of Cold Rolled Iron (II)

By Yuzo TOMONO

Department of Physics, Tokyo University

(Received August 24, 1951)

§1. Introduction

As pointed out in the preceding paper, the parts of observed loss angles attributable to eddy currents are liniar against frequencies but larger than the theoretical values. This means that other frictional force in addition to the macroscopic eddy currents contributes to the relaxation of domain boundary. The possible origin of this frictional force is the so called microscopic eddy currents, or the time lag in the inversion process of electron spin induced by the lattice vibration studied by Katayama[1)] and Huzimura[2)], or the classical damping force of domain boundary introduced by Kittel[3)]. The equation of motion for a domain boundary in the range of initial permeability is given by

$$F\dot{x}+Kx=H \qquad (1)$$

where $F\dot{x}$ is the frictional force stated above and Kx is the restoring force due to the increase in potential energy of the wall for the displacement x. When an alternating field $H_0 \cos \omega t$ is applied,

$$x=[H_0/(K^2+\omega^2F^2)](K\cos\omega t+\omega F\sin\omega t) \quad (2)$$

and loss angle is $(F/K)\omega$.*

When a static field is changed from zero to H in the range of initial permeability,

$$x=(H/K)\ [1\text{-}\exp\ (\text{-}Kt/F)] \quad (3),$$

as $x=0$ at $t=0$, therefore the time of relaxation is F/K.

These formulas are valid for a single domain boundary, but does not change their character for the average over specimen.

As seen from Eq. (2), initial permeability is reduced by one half as $\omega=K/F$. And so if F/K is known from the measurements at higher frequencies, it gives the order of magnitude for the time of relaxation in the range of initial permeability. It must also explain the discrepancies in the low frequency measurements in the preceeding paper.

§2. Experimental Procedure and Results

Specimens for the measurements in higher frequencies are the same cold rolled iron as in the preceding paper. The self-inductance of the coil wound on the specimen is observed with the bridge shown in Fig. 9 of the preceding paper up to 8 kc, with resonance bridge from 10 kc up to 50 kc and by the resonance method at higher frequencies. The amplitude of applied alternating field is 0.010 oe. In order to obtain the intrin-sic value of L, the stray capacity in the coil of specimen is precisely determind,as following. The self-inductance of an air core coil which has the same form and turn number, and is made of the same wire and insulator, as in specimen, is observed at different frequencies by resonance method. The values of resonance capacity observed in this way are plotted vs. $1/f^2$, where f is frequency, and the intersecting point of this curve with the axis of capacity at $1/f^2=0$ gives the stray capacity. The results obtained are shown in Fig. 1. Curves a and b are respectively for the cold rolled iron and tempered (at 500°C) iron. The broken lines are the calculated curves for the reduction of permeability due to macroscopic eddy currents. Up to 10 kc, μ is almost constant that is in proof of the conclusion in the preceding paper

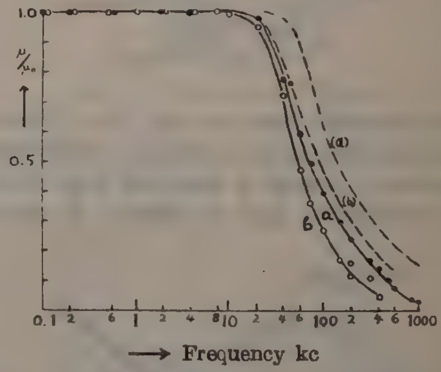

Fig. 1. μ/μ_0 vs. f. Curve a; cold rolled iron. $\mu_0=93.5$. Curve b; iron tempered at 500° C. $\mu_0=152$. Broken lines show the simple skin effect.

---

* This is approximately additive to the loss angle due to macroscopic eddy currents at low frequencies.

that there is no observable after effect in the range of audio-frequencies, but at higher frequencies every curve goes downwards more rapidly than the skin effect curves. The angular frequencies, where the values of apparent permeability are reduced by one half against skin effect curves, are $2.8\cdot10^6$ cps. and $1.3\cdot10^6$ cps. respectively for curves a and b. Hence the times of relaxation for the displacement of domain boundary in the range of initial permeability are about $3.6\cdot10^{-7}$ sec. and $7.7\cdot10^{-7}$ sec., when the macroscopic eddy currents are not taken into account. Therefore loss angles due to this relaxation are $3.6\cdot10^{-7}\omega$ and $7.7\cdot10^{-7}\omega$ respectively, which are in good agreement in their order with the differences between solid and broken lines in Figs. 8 and 10.

§3. Discussions

The measurements in part (I) and (II) have made clear the difference between two sorts of the magnetic after effects.

One is observable in the range of irreversible magnetisation and is less dependent on temperature than the other. This is observed not only in a cold rolled iron as stated before, but also in a recrystallised iron, accompanied with the after effect of the other type.** One possible mechanism of this after effect, suggested by Preisace[4)] and studied by Néel[5)], is based on the idea that thermal fluctuation gives rise to a jerky movement of domain wall in a magnetic field, weaker than the critical field which is necessary to ride past an obstacle. But the concept of thermal activation can be also applied to the discontinuous rotation of spontaneous magnetisation in the small island precipitated in a less ferromagnetic matrix. The after effects of these kinds have been observed in Alnico V[6)7)8)], Cr-permalloy[9)] and Ni_3Mn[10)]. In addition it must be noted that Huzimura[11)] observed the retarded Barkhausen jumps in Cr-permalloy.

The other is observable in a weak field and is much more dependent on temperature. The origin of this after effect is believed to be the microdiffusion of impurity atoms. The effect of impurities such as carbon and nitrogen on magnetic and elastic after effects, in the annealed iron, has been studied by Snoek[12)], Polder[13)] and Dijkstra[14)]. The magnetic after effect of this type has not yet been observed in other substances except iron and alloys near iron. This fact seems to be explained by the larger diffusion coefficients of carbon and nitrogen in iron than in any other ferromagnetic substances.

In the analysis of low frequency measurements, the loss angle due to magnetic after effect is obtained from the estimated value at vanishing alternating field, in order to subtract the part due to hysteresis. Therefore if a substance shows the after effect only in the irreversible magnetisation, the Jordan's constant can not be observed. Néel's theory on the magnetic after effect in the range of Rayleigh is valid in the magnetic field more than about 0.02 oe for iron.

Another problem in which the writer is interested is about the origin of frictional force $F\dot{x}$ in Eq. (1). In order to decide which of the microscopic eddy currents or the other mechanisms stated above play the more important part in this frictional force, the exact calculation of microscopic eddy currents must be done. The writer, however, has not succeeded in it. The similar decrease of μ at high frequencies more than those due to skin effect has been observed by Snoek[15)] and others in several ferromagnetic metals, alloys and semi-conductors. On the origin of this decrease, Snoek assumed that the time lag in the inversion process of electron spin played the most important part because this effect was observed also in semi-conductors in which the eddy currents were negligibly small. But his theory on the relation between high frequency after effect and Jordan's constant does not agree with the conclusion in this paper. And it seems to be true that in ferromagnetic metals the microscopic eddy currents play the most important part.

In conclusion the writer wishes to make an acknowledgement to Prof. S. Kaya in Tokyo University for his valuable suggestions. The writer is also indebted to The Educational Ministry for the financial aid.

References

1) T. Katayama: J. Phys. Soc. Jap. **4**(1948) 202.
2) T. Huzimura: Ibid. **5** (1650) 56.
3) C. Kittlet: Phys. Rev. **80** (1950) 918.

** Read by the writer at the annual meeting of Physical Society of Japan in October 1949.

4) F. Preisach: Z. Phys. **94** (1635) 227
5) M. L. Meel: J. Phys. Rad. **11** (1950) 49
6) R. Street and J. C. Wooley: Proc. Phys. Soc. B **63** (1950) 509
7) J. C. Barbier: C. R. Acad. Sci. **230** (1950) 1040
8) M. L. Llibutry: Ibid. **230** (1950) 1042
9) S. Maeda: J. Phys. Soc. Jap. **5** (1950) 358
10) T. Taoka: Read at the annual meeting of Physical Society Of Japan in November 1950.
11) T. Huzimura: J. Phys. Soc. Jap. **5** (1950) 293
12) J. L. Snoek: Physica **5** (1938) 663; **6** (1932) 161, 591, 794; **8** (1941) 711, 734, 745; **9** (1942) 862; New Development in Ferromagnetic Materials. Amsterdam, 1947 p. 42.
13) D. Polder: Philips Res. Rep. 1 (1945) 5.
14) L. J. Dijkstra: Ibid. 2 (1947) 357.
15) J. L. Snoek: N. D. F. M. p. 56.

JOURNAL OF THE PHYSICAL SOCIETY OF JAPAN Vol. 7, No. 2 MAR.—APR., 1952

A Note on the Theory of the High Polymer Solution

By Hiroshi ICHIMURA
Tokyo Institute of Technology

(Recieved July 30, 1951)

The free energy of mixing of the dilute high polymer solution is calculated by a new approximational method which may clarify how the interaction between the solvent and the solute molecules should be taken into account. It is based on the idea somewhat analogous to the cage model theory of the liquid state and may be considered to unite the quasi-lattice model theory and the gas-like model theory. But it does not use the idea of the potential of the average force as in Zimm's theory. The osmotic pressure formula is derived and it is shown that the second osmotic coefficient depends explicitly on the solvent-segment interaction through a complicated function even in the simplest case where the solute molecule may be expressed with the rigid sphere with the well type attraction potential.

§1. Introduction

In recent years, remarkable advances have been made on the theory of the high polymer solution and the main characteristic features of high polymer solutions have been clarified from the molecular standpoint. But in most of these theories[1-3], the interaction between the solvent molecules and the solute molecules has been negrected or taken into account in very unsatisfactory ways.

In the present note, a new approximate method of the treatment is given which may shows how this interaction should be taken into account. We treat the osmotic pressure of the solution and show the so-called second osmotic coefficient (i. e. the coefficient of the square term in the expansion formula in powers of the volume fraction of the solute) are more essentially affected by the interaction of the single solute molecule with the solvent molecules than in the theroy of Zimm[3]. In his theory, the effect of the solvent enters only in the potential of the average force between the solute molecules.

The auther's former treatment[4] based on the lattice model may be interpreted as an approximation to the general formulation proposed here.

§2. Free Energy of the System

We consider a system of N_1 solvent molecules which are simple and rigid, and p solute molecules which are deformable and made of n segments in a container of volume V and at $T°$ K. Here the segment means the appropriate unit of the solute molecule. The free energy F of this system can be calculated by the statistical mechanics by the relation

$$e^{-\beta F}=K_1^{N_1}K_p^{P}\frac{Z\,(N_1,\,P)}{N_1!\,P!} \tag{1}$$

$$Z\,(N_1,\,P)=\int\cdots\cdots$$

$$\int\exp\left(-\beta U(W,R)\right)\,dW_1\ldots\ldots dW_{N_1}$$

$$dR_1\ldots\ldots dR_p$$

were $\beta={}^1/kT$; K_1 and K_p are the momentum parts of the phase integral concerning the solvent and solute respectively; $Z\ (N_1,\ P)$ is the configurational parts and $U\ (W,\ \mathrm{R})$ represents the potential energy of the system which is the function of all the coordinates of the particles in this system; $W_1\ldots\ldots W_{N1}$, represent the coordinates of the solvent molecules and $\mathrm{R}_1\ldots\ldots\mathrm{R}_p$ represent the groups of the coordinates of the segments of each polymer (solute) molecule.

For our liquid-like aggregate, the integration in Z can only be performed with some approximate and model-like reasonings. The quasi-lattice model which has been used in many theories may be regarded as one of the approximational methods.

§3. Approximate Evaluation of $Z\,(N_1,\,P)$

For simplicity, we assume the interactions between the particles (solvent-solvent, solvent-segment and segment-segment) are the two-body forces and are determind only by the distance between them. Of course the chemical bonds between the segments in a polymer molecule are excluded. So $U\ (W,\ \mathrm{R})$ may be set in the form

$$U\ (W,\ \mathrm{R})=\tfrac{1}{2}\sum_{i\neq j}\sum u(i,\ j)+\sum_i\sum_\lambda\sum_a u(i,\ \lambda_a)$$
$$+\tfrac{1}{2}\sum_\lambda\sum\sum_{a\neq b}u(\lambda_a,\ \lambda_b)+\tfrac{1}{2}\sum_{\lambda\neq\mu}\sum\sum_a\sum_b u(\lambda_a,\ \lambda_b) \tag{2}$$

where i, j indicate the solvent molecules and λ, μ the polymer molecules, and λ_a means the ath segement of the λth polymer. $u\ (x,\ y)$ represents the potential energy between the x and y particles. We assume further that these interactions are all short range types.

To carry out the integration with the coordinate W_i, we proceed as follows. We set u_i for all the terms in (2) which contain the coordinate W_i,

$$u_i=\tfrac{1}{2}\sum_{j\neq i}^{N1}u(i,\ j)+\sum_\lambda\sum_a u(i,\ \lambda_a) \tag{3}$$

and assume that this takes a certain constant value $-\varepsilon_i$ which is independent on W_i and all other W_j in so far as the ith molecule is surrounded by the other solvent molecules, and takes another constant value $-\varepsilon_{12}$ when it comes in the influence range of a segment. These assumptions may correspond to the uniform and rather compact arrangement of the particles in V for which we assume the value $N_1\delta_1+pn\delta_s$ (δ_1 is the volume of the solvent molecule and δ_s is that of the segment) and to the assumption that we can change the position of one solvent molecule with so small modifications of the positions of its near neighbours as they can be assumed to be fixed. With these considerations, we get as the result of the integration with W_i, the following factor

$$(V-pn\delta_s-\sum_\lambda\omega_\lambda+\tfrac{1}{2}\sum_{\lambda\neq\mu}\sum\omega_{\lambda\mu})\exp(\beta\varepsilon_1)$$
$$+(\sum_\lambda\omega_\lambda-\tfrac{1}{2}\sum_{\lambda\neq\mu}\sum\omega_{\lambda\mu})\exp(\beta\varepsilon_{12}) \tag{4}$$

where ω_λ means the volume of the effective influence range of the λth polymer which can be occupied by solvents or segments of the other polymers. Naturally this is the function of the form of this molecule and can be considered as the function of the coordinates of this polymer. And $\omega_{\lambda\mu}$ means the part of ω_λ which is occupied by the segment of the μth polymer. The factor (4) does not depend on i, so the result of the integration with all the solvent coordinates may be put in the form

$$\{(V-pn\delta_s-\sum_\lambda\omega_\lambda+\tfrac{1}{2}\sum_{\lambda\neq\mu}\sum\omega_{\lambda\mu})\exp(\beta\varepsilon_1)$$
$$+(\sum_\lambda\omega_\lambda-\tfrac{1}{2}\sum_{\lambda\neq\mu}\sum\omega_{\lambda\mu})\exp(\beta\varepsilon_{12})\}^{N1} \tag{5}$$

or, after rearranging the terms we get

$$(N_1\ \delta_1)^{N1}\exp(\beta N_1\varepsilon_1)(1+x)^{N1} \tag{6}$$
$$x=(\sum_\lambda\omega_\lambda-\tfrac{1}{2}\sum_{\lambda\neq\mu}\sum\omega_{\lambda\mu})J/N_1\delta_1$$
$$J=(\exp(\beta(\varepsilon_{12}-\varepsilon_1))-1)$$

In the case of the dilute solution, we can assume that $x\ll 1$ and N_1 is very large, so the approximation $(1+x)^{N1}=\exp(N_1x)$ may be used. Hence we obtain

$$Z(N_1,\,p)=(N_1\delta_1)^{N1}\exp(\beta N_1\varepsilon_1)\int\ldots\ldots\int\exp(N_1x)$$
$$\times\exp\Bigl[-\frac{\beta}{2}\Bigl(\sum_\lambda\sum\sum_{a\neq b}u(\lambda_a,\ \lambda_b) \tag{7}$$
$$+\sum_{\lambda\neq\mu}\sum\sum_a\sum_b u(\lambda_a,\ \mu_b)\Bigr)\Bigr]d\mathrm{R}_1\ldots\ldots d\mathrm{R}_p$$

Rearranging the integrand as

$$\exp\Bigl[\sum_\lambda(J\omega_\lambda/\delta_1-\beta\sum\sum_{a<b}u(\lambda_a,\ \lambda_b)\Bigr]$$
$$\times\exp\Bigl[-\sum\sum_{\lambda>\mu}(J\omega_{\lambda\mu}/\delta_1+\beta\sum_a\sum_b u(\lambda_a,\ \mu_b))\Bigr]$$

we apply Ursel's method of expansion for the product of the second factor. We put

$$1-f(\lambda,\ \mu)=\exp\Bigl[-(J\omega_{\lambda\mu}/\delta,+\beta\sum_a\sum_b u(\lambda_a,\ \mu_b))\Bigr] \tag{8}$$

and get

$$Z\ (N_1,\ p)=(N_1\delta_1)^{N1}\exp(\beta N_1\varepsilon_1)\int\ldots\ldots\int$$
$$\times\exp\Bigl[\sum_\lambda(J\omega_\lambda/\delta_1-\beta\sum\sum_{a>b}u(\lambda_a,\ \lambda_b))\Bigr]$$

$$\times\Big(1-\sum_{p\geq\lambda>\mu\geq 1}\sum f(\lambda,\ \mu)+\ldots\ldots\Big)\ dR\ldots\ldots dR_p \tag{9}$$

Further terms in the expansion may be negrected here.

If we put

$$\int \exp\Big(J\omega_\lambda/\delta_1-\beta\sum_{a>b}\sum u(\lambda_a,\ \lambda_b)\Big)dR\lambda=V\cdot C \tag{10}$$

$$\int \exp\Big[\Big(J\omega_\lambda/\delta_1-\beta\sum_{a>b}\sum u(\lambda_a,\lambda_b)\Big)+\Big(J\omega_\mu/\delta_1 -\beta\sum_{a>b}\sum u(\mu_a,\mu_b)\Big)\Big]f(\lambda,\mu)dR_\lambda\,dR_\mu=VB \tag{11}$$

it results finally

$$Z(N_1,\ p)=(N_1\delta_1)^{N_1}\exp(\beta N_1\varepsilon_1)V^pC^p \times\left(1-\frac{p(p-1)}{2}\ \frac{B}{VC^2}\ \ldots\ldots\right) \tag{12}$$

So we obtain the free energy of this system as

$$F(N_1,\ p)=-kT\Big\{N_1\log K_1+p\log K_p +N_1\log N_1\delta_1+\beta N_1\varepsilon_1-N_1\log N_1-p\log p +p\log V+p\log C+\log\left(1-\frac{p^2}{2}\ \frac{B}{VC^2}\right)\Big\} \tag{13}$$

§ 4. Osmotic Pressure Formula

From our $F(N_1,\ p)$ in (13), we can derive the free energy of mixing and furthermore the partial molar free energy of mixing for the solvent $\Delta\bar{F}_1$ by the usual procedure. So the osmotic pressure Π in our case becomes

$$\Pi=-\frac{\Delta F}{\bar{V}_1}=\frac{RT}{\bar{V}_1}\left[\frac{p}{V}+\frac{p^2}{2}\ \frac{B\delta_1}{V^2C^2}\right]$$

$$\text{or}\quad =\frac{RT}{\bar{V}_1}\left[v_2/n\sigma+\frac{1}{2}v_2{}^2B/(n\sigma)^2\delta_1C^2\right] \tag{14}$$

where

$$v_2=pn\delta_s/N_1\delta_1+pn\delta_3,\qquad \sigma=\delta_s/\delta_1$$

As may be seen from the equations (10) and (11), the coefficient of the $v_2{}^2$ term in (14) contains the interaction between the single polymer molecule and the solvent molecules explicity through the function ω_λ. Although our derivation of (4) or (5) contains very rough approximation, it can be said that the function such as ω_λ appear explicitly in the second osmotic coefficient formula when the solute molecules can easily be deformed. In our treatment the potential of the average force does not appear. so we can see the difference between our's and Zimm's. But in the case of the zero heat of mixing ($\varepsilon_{12}=\varepsilon_1$), J becomes zero and our results have the same from as the results in Zimm's treatment.

Examples

1). For the long chain polymers, the evaluation of C and B will be very complicated. We do not intend the detailed calculation here and only mention that the author's former treatment[4] may be regarded as the approximate evaluation of the integrals.

2). For the rigid sphere molecule, ω_λ's do not appear and C becomes equal to 1. We can evaluate the integral B approximately as follows. Let a be the redius of the molecule and r_0 the outer radius of the potential well of this molecule. We set

$$\begin{aligned} u(\lambda,\ \mu)=u(r_{\lambda\mu})&=0 && r_{\lambda\mu}>r_0+a\\ &=-U_0 && 2a<r_{\lambda\mu}\leq r_0+a\\ &=+\infty && r_{\lambda\mu}\leq 2a \end{aligned} \tag{15}$$

In this case, $\omega_{\lambda\mu}$ can be given as the intersection of the sphere of radius r_0+a and of radius $2a$, but the exact evaluation of the integral of $exp\,(-J\omega_{\lambda\mu}/\delta_1)$ is very tedious, so we replace $\omega_{\lambda\mu}$ by a suitable average value ω for the moment.

Considering the definition of $f(\lambda,\ \mu)$, we get approximately

$$B=\frac{4\pi}{3}(2a)^3+\left\{\frac{4n}{3}(r_0+a)^3-\frac{4\pi}{3}(2a)^3\right\}\Big(1 -\exp(-J\omega/\delta_1+U_0/kT)\Big) \tag{16}$$

We can see that even in this simple case the effect of the solvent-segment interaction enters in the second osmotic coefficient through J.

The partial molar heat of mixing can easily be delived in this case as

$$\Delta\overline{H}_1=\frac{2\pi N_0}{3\sigma^2\delta_1}(r_0+a)^3-(2a)^3)\exp(-J\omega/\delta_1 \; U_0/kT)\times\{\omega\exp[\ \xi_{12}-\xi_1)/kT]\cdot(\xi_{12}-\xi_1) -U_0\} \tag{17}$$

where N_0 is the Avogadro number.

§ 5. Conclusion

By our rather simple formulation, it has been shown that even in the simplest cases the theoretical evaluation of the second osmotic coefficient is not so simple when we consider the heat of mixing. When we introduce suitable models for the deformable solute moleculs the integrals may be evaluated.

Finally the auther expresses his sincere thanks of Prof. A. Harashima for the valuable discussion on this problem.

Refrences

1) P. J. Flory: J. Chem. Phys. **10** (1942) 51. **13** (1645) 425, **18** (1950) 1086.
2) M. L. Huggins: J, Phys. Chem. **46**(1942)151
3) B. H. Zimm: J. Chem. Phys. **14** (1946) 164.
4) H. Ichimura: J, Phys. Soc. Jap. **3**(1948),308.

JOURNAL OF THE PHYSICAL SOCIETY OF JAPAN Vol. 7, No. 2 MAR.—APR., 1952

Microwave Circuit Theory

By Tokio SAKURAI

Electrical Communication Laboratory, Ministry of Telecommunications

(Received October 12, 1949)

The electric current $\dot{I}$ and the volage $\dot{V}$ on the imagined surface S are defined by $\dot{I}\boldsymbol{F}=\boldsymbol{H}^t$, $\dot{P}=\dot{V}\tilde{I}$ or $\dot{I}\boldsymbol{F}=\boldsymbol{E}$, $\tilde{P}=\dot{V}\tilde{I}$, where $\boldsymbol{H}^t$, $\boldsymbol{E}^t$ are tangential magnetic and electric field components on S, and $\boldsymbol{F}$ is a vector function depending only on the distribution of $\boldsymbol{H}^t$ and $\boldsymbol{E}^t$ on S and $\hat{I}$ is a scalar complex constant depending only on the total strength of $\boldsymbol{H}^t$ or $\boldsymbol{E}^t$, $\dot{P}$ is the apperent power flowing through S, and$\sim$expresses the conjugate value of the quontity. It is proved that $\partial\dot{Z}/\partial\lambda$ is positive and $\|\partial Z_{kh}/\partial\lambda\|$ ispo sitive definite form in reactive case, where $\lambda=j\omega$, $\dot{Z}$ and $\dot{Z}_{kh}$ are impedance and impedance matrix element respectively, and $Q=(1/r)\sqrt{L/C}$ in resonant case, werer r, L, C are resistance, inductance, and capacity.

§ 1. Two Terminal Impedances

The fundamental properties of impedance $\dot{Z}$ of two terminal networks are

(i) $\partial\dot{Z}/\partial\lambda>0$, $(\lambda=j\omega)$ when the circuit is purely reactive.

(ii) $r/(\omega\partial X/\partial\lambda)=1/2Q$ and $Q=(1/r)\sqrt{L/C}$ for the caes X is the imaginary part of $\dot{Z}$ and L, C, r are inductance, capacity, and resistance.

We shall now discuss what shall we do to maintain these properties even in microwave region. By combining two Maxwell's field equations

$$\nabla\times\boldsymbol{E}+j\omega\mu\boldsymbol{H}=0,\ \nabla\times\boldsymbol{H}-j\omega\varepsilon\boldsymbol{E}=\sigma\boldsymbol{E} \quad (1.1)$$

$$-\nabla\boldsymbol{S}=-\frac{1}{2}\nabla\cdot(\boldsymbol{E}\times\boldsymbol{H})$$

$$=\frac{\sigma}{2}E\tilde{E}+\frac{j\omega}{2}(\mu\boldsymbol{H}\cdot\tilde{\boldsymbol{H}}-\varepsilon\boldsymbol{E}\cdot\tilde{\boldsymbol{E}}), \quad (1.2)$$

where $\boldsymbol{S}$ is the complex Poynting vector and $\sim$ expresses the conjugate value. ε, μ may be functions of place in electromagnetic field but are assumed not depending on ω. In reactive case $\sigma=0$ and (1.2) becomes with the aid of (1.1)

$$-2\nabla\cdot\boldsymbol{S}=j\omega\mu\boldsymbol{H}\cdot\tilde{\boldsymbol{H}}+(1/j\omega\varepsilon)(\nabla\times\boldsymbol{H})(\nabla\times\tilde{\boldsymbol{H}}), \quad (1.3)$$

from which we have

$$-2\frac{\partial}{\partial\omega}\nabla\boldsymbol{S}=j\mu\boldsymbol{H}\cdot\tilde{\boldsymbol{H}}+\frac{j}{\varepsilon\omega^2}(\nabla\times\boldsymbol{H})\cdot(\nabla\times\tilde{\boldsymbol{H}})+j\omega\mu\frac{\partial}{\partial\omega}(\boldsymbol{H}\cdot\tilde{\boldsymbol{H}})+\frac{1}{j\omega\varepsilon}\frac{\partial}{\partial\omega}\{(\nabla\times\boldsymbol{H})\cdot(\nabla\times\tilde{\boldsymbol{H}})\}. \quad (1.4)$$

Since

$$\frac{1}{j\omega\varepsilon}\frac{\partial}{\partial\omega}\{(\nabla\times\boldsymbol{H})\cdot(\nabla\times\tilde{\boldsymbol{H}})\}=\nabla\cdot\left\{\frac{\partial\boldsymbol{H}}{\partial\omega}\times\left(\frac{1}{j\omega\varepsilon}\nabla\times\tilde{\boldsymbol{H}}\right)\right\}+\frac{\partial\boldsymbol{H}}{\partial\omega}\nabla\times\left(\frac{1}{j\omega\varepsilon}\nabla\times\tilde{\boldsymbol{H}}\right)$$
$$+\nabla\cdot\left\{\frac{\partial\tilde{\boldsymbol{H}}}{\partial\omega}\times\left(\frac{1}{j\omega\varepsilon}\nabla\times\boldsymbol{H}\right)\right\}+\frac{\partial\tilde{\boldsymbol{H}}}{\partial\omega}\nabla\times\left(\frac{1}{j\omega\varepsilon}\nabla\times\boldsymbol{H}\right)$$
$$=\frac{1}{j\omega\varepsilon}\left\{\nabla\cdot\left[\frac{\partial\boldsymbol{H}}{\partial\omega}\times(\nabla\times\tilde{\boldsymbol{H}})\right]+\nabla\cdot\left[\frac{\partial\tilde{\boldsymbol{H}}}{\partial\omega}\times(\nabla\boldsymbol{H})\right]\right\}-j\omega\mu\frac{\partial}{\partial\omega}(\boldsymbol{H}\cdot\tilde{\boldsymbol{H}}), \quad (1.5)$$

$$-\frac{\partial(\nabla\cdot\mathbf{S})}{\partial\lambda}=\frac{\varepsilon}{2}\mathbf{E}\cdot\tilde{\mathbf{E}}+\frac{\mu}{2}\mathbf{H}\cdot\tilde{\mathbf{H}}-\frac{1}{2}\left\{\nabla\left(\frac{\partial\mathbf{H}}{\partial\lambda}\times\tilde{\mathbf{E}}\right)-\nabla\cdot\left(\frac{\partial\tilde{\mathbf{H}}}{\partial\lambda}\times\mathbf{E}\right)\right\}, \tag{1.6}$$

where $\lambda=j\omega$

If we integrate (1.6) over the volume V of the domain of the field in consideration and apply Gauss' divergence theorem, we have

$$-\int_{S_1}\boldsymbol{n}\cdot\frac{\partial\mathbf{S}}{\partial\lambda}dS=\int_V\left(\frac{\varepsilon}{2}\mathbf{E}\cdot\tilde{\mathbf{E}}+\frac{\mu}{2}\mathbf{H}\cdot\tilde{\mathbf{H}}\right)dV$$
$$+\frac{1}{2}\int_{S_1}\left\{(\boldsymbol{n}\times\tilde{\mathbf{E}})\cdot\frac{\partial\mathbf{H}}{\partial\lambda}-(\boldsymbol{n}\times\mathbf{E})\cdot\frac{\partial\tilde{\mathbf{H}}}{\partial\lambda}\right\}dS. \tag{1.8}$$

If we write (1.2) in the form

$$-\nabla\cdot\tilde{\mathbf{S}}=j\omega\varepsilon\mathbf{E}\cdot\tilde{\mathbf{E}}+\frac{1}{j\omega\mu}(\nabla\times\mathbf{E})\cdot(\nabla\times\tilde{\mathbf{E}}) \tag{1.9}$$

with the aid of the first relation of (1.1), and proceed exactly in the same mannar as that we have obtained (1.8) from (1.3), we get

$$-\int_{S_1}\boldsymbol{n}\cdot\frac{\partial\tilde{\mathbf{S}}}{\partial\lambda}dS=\int_V\left(\frac{\varepsilon}{2}\mathbf{E}\cdot\tilde{\mathbf{E}}+\frac{\mu}{2}\mathbf{H}\cdot\tilde{\mathbf{H}}\right)dV$$
$$+\frac{1}{2}\int_{S_1}\left\{\left(\boldsymbol{n}\times\frac{\partial\tilde{\mathbf{E}}}{\partial\lambda}\right)\cdot\tilde{\mathbf{H}}-\left(\boldsymbol{n}\times\frac{\partial\tilde{\mathbf{E}}}{\partial\lambda}\right)\cdot\mathbf{H}\right\}dS, \tag{1.10}$$

where S_1 expresses the part of the total surface S of V not coinciding with the perfect conductor surface. Since the tangential component $\mathbf{H}^t$ of magnetic field has relation with energy flow through S_1, we define the electric current $\dot{I}$ of two terminals imagined on S_1 by

$$\dot{I}\mathbf{F}=\mathbf{H}^t,\quad (\text{on } S_1) \tag{1.11}$$

where $\mathbf{F}$ is a vector function of position on S_1 relating to the distribution of $\mathbf{H}^t$ but does not depend on frequency and total strength of $\mathbf{H}^t$, and $\dot{I}$ is a scalar constant relating to the total strength of $\mathbf{H}^t$ and having the dimension of electric current. The impedance $\dot{Z}$ of two terminals on S_1 is defined by

$$\dot{P}=-\int_{S_1}\boldsymbol{n}\cdot\mathbf{S}dS=\dot{Z}|\dot{I}|^2, \tag{1.12}$$

where $\dot{P}$ is apperent power flowing through S_1 into the domain. If we substitute (1.12) in (1.8) hold $\dot{I}$ independent of λ, then by (1.11) $\mathbf{H}^t$ becomes independent of λ and the last surface integral of (1.8) vanishes, and we get

$$\frac{\partial\dot{Z}}{\partial\lambda}|\dot{I}|^2=\int_V\left(\frac{\varepsilon}{2}\mathbf{E}\cdot\tilde{\mathbf{E}}+\frac{\mu}{2}\mathbf{H}\cdot\tilde{\mathbf{H}}\right)dV. \tag{1.13}$$

If we define the electric current $\dot{I}$ of two terminals imagined on S_1 with the aid of tangential component vector $\mathbf{E}^t$ of the electric field on S_1 by

$$\dot{I}\mathbf{F}=\sqrt{\varepsilon/\mu}\,\mathbf{E}^t,\quad (\text{on } S_1) \tag{1.14}$$

and define the impedance $\dot{Z}$ on S_1 by

$$\tilde{P}=-\int_{S_1}\boldsymbol{n}\cdot\dot{\mathbf{S}}dS=\dot{Z}|\dot{I}|^2, \tag{1.15}$$

and if we substitute (1.15) in (1.10) holding $\dot{I}$ independent of λ, we get (1.13) again. Since the right-hand side integral of (1.13) is positive, $\partial\dot{Z}/\partial\lambda$ is positive, and thus (i) is hold even in microwave region.

Electric and magnetic energies stored in the volume V are

$$U=\int_V\frac{\varepsilon}{4}\mathbf{E}\cdot\tilde{\mathbf{E}}dV,\quad T=\int_V\frac{\mu}{4}\mathbf{H}\cdot\tilde{\mathbf{H}}dV \tag{1.16}$$

respectively. The total energy wasted in V is

$$W=\int_V\frac{\sigma}{2}\mathbf{E}\cdot\tilde{\mathbf{E}}dV. \tag{1.17}$$

Now Q of the domain is defined by

$$Q=\omega(T+U)/W. \tag{1.18}$$

The equivalent resistance r of the domain is

$$r=W/|\dot{I}|^2. \tag{1.19}$$

The imaginary part X of $\dot{Z}$ is of the same form as $\dot{Z}$ in reactive case. Hence by (1.13) and (1.16)

$$\partial X/\partial\lambda=2(T+u)/|\dot{I}|^2. \tag{1.20}$$

If we combine (1.18), (1.19), (1.20), we get the relation

$$r/(\omega\partial X/\partial\lambda)=1/2Q. \tag{1.21}$$

Let us now define equivalent inductance L and equivalent capacity C by

$$T=\frac{1}{2}L|\dot{I}|^2,\quad U=\frac{1}{2C}\frac{|\dot{I}|^2}{\omega^2}. \tag{1.22}$$

If we substitute (1.19) and (1.22) in (1.18) and remember that $T=U$ in resonant case, we get

$$Q=\omega L/r=1/(\omega Cr)=(1/r)\sqrt{L/C}. \tag{1.23}$$

Hence all properties in (ii) are satisfied. If we put

$$U=\frac{1}{2}L|\dot{I}|^2,\quad T=\frac{1}{2C}\frac{|\dot{I}|^2}{\omega^2}, \tag{1.24}$$

we also get (1.23). The relation (1.22) is convenient when we use $\dot{I}$ defined by (1.11), but (1.24) is convenient when $\dot{I}$ is defined by (1.14)

§ 2. Inpedance Matrix

Let us denote by

$$S_1,\ S_2, \ldots\ldots S_n;\ S_1',\ S_2', \ldots\ldots S_n' \qquad (2.1)$$

the portions of the total surface S of the volume V, and S_0 is the remaining portion of S, which coincides with perfect conductor surface. Then the electromagnetic field $\boldsymbol{E}_m$, $\boldsymbol{H}_m$ whose source is the current $\dot{I}_m$ defined by (1.11) on S_m satisfies following conditions

$$\left.\begin{aligned} &\boldsymbol{n}\times\tilde{\boldsymbol{H}}_m=\boldsymbol{n}\times\boldsymbol{H}_m{}^t,\ (\text{on } S_m)\\ &\boldsymbol{n}\times\boldsymbol{H}_m=0,\ (\text{on } S_k, \text{ where } k=1,\ 2,\ldots\ldots,\\ &\qquad n \text{ but } k\neq m)\\ &\boldsymbol{n}\times\boldsymbol{E}_m=0,\ (\text{on } S_k', \text{ where } k'=1',\ 2',\ldots\ldots,\\ &\qquad n') \end{aligned}\right\} \qquad (2.2)$$

The electromagnetic field $\boldsymbol{E}_m'$, $\tilde{\boldsymbol{H}}_m'$ whose source is the current $\dot{I}_m'$ defind by (1.14) on S_m' satisfies followiug conditions:

$$\begin{aligned} &\boldsymbol{n}\times\boldsymbol{E}_m'=\boldsymbol{n}\times\boldsymbol{E}^t{}_m',\quad (\text{on } S_m')\\ &\boldsymbol{n}\times\boldsymbol{E}_m'=0,\ (\text{on } S_k' \text{ where } k'=1',\ 2',\ \ldots\ldots,\\ &\qquad n' \text{ but } k'\neq m') \qquad (2.3)\\ &\boldsymbol{n}\times\boldsymbol{H}_m'=0,\ (\text{on } S_k \text{ where } k=1,2,\ \ldots\ldots,\ n) \end{aligned}$$

In addition $\boldsymbol{n}\times\boldsymbol{E}_r=0$, (on S_0) (2.4)

for $r=1,\ 2,\ldots\ldots,\ 1',\ 2',\ \ldots\ldots,\ n'$. We now use the notation

$$\sum_r=\sum_{k=1}^{n}+\sum_{k'=1'}^{n'} \qquad (2.5)$$

The apperent power flowing through S_m and S_m' into the domain are

$$\left.\begin{aligned} \dot{P}_m&=-\frac{1}{2}\int_{S_m}\Big(\sum_r\boldsymbol{E}_r\times\tilde{\boldsymbol{H}}_m{}^t\Big)\cdot\boldsymbol{n}dS\\ \dot{P}_m'&=-\frac{1}{2}\int_{S_m}\Big(\boldsymbol{E}^t{}_m'\times\sum_r\tilde{\boldsymbol{H}}_r\Big)\cdot\boldsymbol{n}dS \end{aligned}\right\} \qquad (2.6)$$

respectively by (2.2) and (2.3). We can put

$$\left.\begin{aligned} &\boldsymbol{E}_r{}^t=\sqrt{\frac{\mu}{\varepsilon}}\sum_{m=1}^{n}\boldsymbol{T}_{rm}\cdot\boldsymbol{H}^t{}_m+\sum_{m'=1'}^{n'}\boldsymbol{T}_{rm}'\cdot\boldsymbol{E}^t{}_m,\\ &\boldsymbol{H}_r{}^t=\sum_{m=1}^{n}\boldsymbol{T}^*_{rm}\cdot\boldsymbol{H}_m{}^t+\sqrt{\frac{\varepsilon}{\mu}}\sum_{m'=1'}^{n'}\boldsymbol{T}^*_{rm}{}'\boldsymbol{E}^t{}_m',\\ &\qquad (r=1,\ 2,\ldots,\ n,\ 1',\ 2',\ldots,\ n') \end{aligned}\right\} \qquad (2.7)$$

where $\boldsymbol{T}_m$, $\boldsymbol{T}_{rm}'$, $\boldsymbol{T}^*_{rm}$, $\boldsymbol{T}^*_{rm}{}'$ are tensors of some determined form. If we substitute (2.7) in (2.6) and make use of (1.11), (1.14), we have

$$\begin{aligned} -2\left\{\sum_{m=1}^{n}\dot{P}_m+\sum_{m'=1'}^{n'}\dot{P}_n'\right\}=&\sqrt{\frac{\mu}{\varepsilon}}\sum_{m=1}^{n}\Bigg[\sum_{k=1}^{n}\sum_r\dot{I}_k\tilde{I}_m\int_{S_m}\{(\boldsymbol{T}_{rk}\boldsymbol{F}_k)\times\tilde{\boldsymbol{F}}_m\}\cdot\boldsymbol{n}dS\\ &+\sum_{k'=1'}^{n'}\sum_r\dot{I}_k'\tilde{I}_m\int_{S_m}\{(\boldsymbol{T}_{rk}'\cdot\boldsymbol{F}_k')\times\tilde{\boldsymbol{F}}_m\}\cdot\boldsymbol{n}dS\Bigg]\\ &+\sqrt{\frac{\mu}{\varepsilon}}\sum_{m'=1}^{n'}\Bigg[\sum_{k=1}^{n}\sum_r\tilde{I}_k\dot{I}_m'\int_{S_m}\{(\tilde{\boldsymbol{T}}^*_{rk}\cdot\tilde{\boldsymbol{F}}_k)\times\boldsymbol{F}_m'\}\cdot\boldsymbol{n}dS\\ &+\sum_{k'=1'}^{n'}\sum_r\tilde{I}_k'\dot{I}_m'\int_{S_m'}\{(\tilde{\boldsymbol{T}}^*_{rk'}\cdot\tilde{\boldsymbol{F}}_k')\boldsymbol{F}_m'\}\cdot\boldsymbol{n}dS\Bigg] \end{aligned} \qquad (2.8)$$

On the other hand by network theory

$$\left.\begin{aligned} \dot{V}_m&=\sum_{k=1}^{n}\dot{Z}_{mk}\dot{I}_k+\sum_{k'=1'}^{n}\dot{Z}_{mk}'\dot{I}_k',\\ \dot{V}_m'&=\sum_{k=1}^{n}\dot{Z}_{m'k}\dot{I}+\sum_{k'=1'}^{n'}\dot{Z}_{m'k'}\dot{I}_{k'}. \end{aligned}\right\} \qquad (2.9)$$

By (1.12) and (1,15)

$$\dot{P}_m=\tilde{V}_m\dot{I}_m,\qquad \dot{P}_m'=\tilde{V}_m'\dot{I}_m'. \qquad (2.10)$$

If we substitute (2.9) in (2.0), substitute again the result thus obtained in (2.8), and compare term on both sides, we have

$$\left.\begin{aligned} \dot{Z}_{mk}&=-\frac{1}{2}\sqrt{\frac{\mu}{\varepsilon}}\sum_r\int_{S_m}\{(\boldsymbol{T}_{rk}\cdot\boldsymbol{F}_k)\times\tilde{\boldsymbol{F}}_m\}\cdot\boldsymbol{n}dS\\ \dot{Z}_{mk}'&=-\frac{1}{2}\sqrt{\frac{\mu}{\varepsilon}}\sum_r\int_{S_m}\{(\boldsymbol{T}_{rk}'\cdot\boldsymbol{F}_k')\times\tilde{\boldsymbol{F}}_m\}\cdot\boldsymbol{n}dS\\ \dot{Z}_{m'k}&=-\frac{1}{2}\sqrt{\frac{\mu}{\varepsilon}}\sum_r\int_{S_{m'}}\{(\boldsymbol{T}^*_{rk}\cdot\boldsymbol{F}_k)\times\tilde{\boldsymbol{F}}_{m'}\}\cdot\boldsymbol{n}dS\\ \dot{Z}_{m'k'}&=-\frac{1}{2}\sqrt{\frac{\mu}{\varepsilon}}\sum_r\int_{S_{m'}}\{(\boldsymbol{T}^*_{rk'}\cdot\boldsymbol{F}_{k'})\times\tilde{\boldsymbol{F}}_m\}\cdot\boldsymbol{n}dS \end{aligned}\right\} \qquad (2.11)$$

The existence of the relation

$$Z_{r,q}=Z_{q,r} \qquad (r,q=1,\ 2,\ \dots,\ n,\ 1',\ 2'\ \dots,\ n') \tag{2.12}$$

has already proved in my previous paper[3].

Now we shall try to get properties of impedance matrix corresponding (i) in the foregoing section assuming that $\sigma=0$. Proceeding in the same manner as we have obtained (1.8), and if we notice that the integration over S all vanishes except over S_m by (2.2), (2.3) and (2.4), we get

$$\begin{aligned}-\frac{1}{2}\int_{S_m} n\cdot\frac{\partial}{\partial\lambda}(\boldsymbol{E}_k\times\tilde{\boldsymbol{H}}_m)dS &= \int_V\left(\frac{\varepsilon}{2}\boldsymbol{E}_k\cdot\tilde{\boldsymbol{E}}_m+\frac{\mu}{2}\boldsymbol{H}_k\cdot\tilde{\boldsymbol{H}}_m\right)dV\\ &+\frac{1}{2}\int_{S_m}\left\{(n\times\tilde{\boldsymbol{E}}_m)\cdot\frac{\partial\boldsymbol{H}_k}{\partial\lambda}-(n\times\boldsymbol{E}_k)\cdot\frac{\partial\tilde{\boldsymbol{H}}_m}{\partial\lambda}\right\}dS\end{aligned} \tag{2.13}$$

We have again

$$\begin{aligned}-\frac{1}{2}\int_{S} n\cdot\frac{\partial}{\partial\lambda}(\boldsymbol{E}_{k'}\times\tilde{\boldsymbol{H}}_m)dS &= \int_V\left(\frac{\varepsilon}{2}\boldsymbol{E}_{k'}\cdot\tilde{\boldsymbol{E}}_m+\frac{\mu}{2}\boldsymbol{H}_{k'}\cdot\tilde{\boldsymbol{H}}_m\right)dV\\ &+\frac{1}{2}\int_{S}\left\{(n\times\tilde{\boldsymbol{E}}_m)\cdot\frac{\partial\boldsymbol{H}_k'}{\partial\lambda}-(n\times\boldsymbol{E}_{k'})\cdot\frac{\partial\tilde{\boldsymbol{H}}_m}{\partial\lambda}\right\}dS.\end{aligned} \tag{2.14}$$

The integration over S of (2.14) all vanishes except over S_m and S_k' by (2.2), (2.3) and (2.4). If we use the relation

$$\begin{aligned}-\frac{1}{2}\int_{S_{k'}}(n\times\boldsymbol{E}_{k'})\cdot\frac{\partial\tilde{\boldsymbol{H}}_m}{\partial\lambda}\,dS &= -\frac{1}{2}\int_{S_{k'}} n\cdot\frac{\partial}{\partial\lambda}(\boldsymbol{E}_{k'}\times\tilde{\boldsymbol{H}}_m)dS\\ &+\frac{1}{2}\int_{S_{k'}}\left(n\times\frac{\partial\boldsymbol{E}_k'}{\partial\lambda}\right)\cdot\tilde{\boldsymbol{H}}_m dS\end{aligned} \tag{2.15}$$

on S_k and remember the vanishment of $\partial\boldsymbol{H}^t{}_{k'}/\partial\lambda$ on S_m and $\boldsymbol{E}^t{}_m$ on $S_{k'}$ by (2.2) and (2.3), (2.14) becomes

$$\begin{aligned}-\int_{S_m} n\cdot\frac{\partial}{\partial\lambda}(\boldsymbol{E}_{k'}\times\tilde{\boldsymbol{H}}_m)dS &= \int_V\left(\frac{\varepsilon}{2}\boldsymbol{E}_{k'}\cdot\tilde{\boldsymbol{E}}_m+\frac{\mu}{2}\boldsymbol{H}_{k'}\cdot\tilde{\boldsymbol{H}}_m\right)dV\\ &-\frac{1}{2}\int_{S_m}(n\times\boldsymbol{E}_{k'})\cdot\frac{\partial\boldsymbol{H}_m}{\partial\lambda}dS+\frac{1}{2}\int_{S_{k'}}\left(n\times\frac{\partial\boldsymbol{E}_{k'}}{\partial\lambda}\right)\cdot\tilde{\boldsymbol{H}}_m dS\end{aligned} \tag{2.16}$$

We also get similar results as (2.13) and (2.16) for

$$-\frac{1}{2}\int_{S_{k'}} n\cdot\frac{\partial}{\partial\lambda}(\tilde{\boldsymbol{E}}_{k'}\times\boldsymbol{H}_{m'})dS, \qquad -\frac{1}{2}\int_{S_{k'}} n\cdot\frac{\partial}{\partial\lambda}(\tilde{\boldsymbol{E}}_{k'}\times\boldsymbol{H}_m)dS \tag{2.17}$$

respectively. If we substitute (2.9) in (2.10), we get

$$\sum_{m=1}^{n}\dot{P}_m+\sum_{m'=1'}^{n'}\tilde{P}_{m'}=\sum_r\sum_q\dot{Z}_{rq}\dot{I}_q\tilde{I}_r. \tag{2.18}$$

If we differentiate both sides of (2.18) by λ holding $\dot{I}_q$, $\tilde{I}_r$ unchanged and substitute (2.13), (2.16) and similar results for (2.17) in the places of $\partial\dot{P}_m/\partial\lambda$, $\partial\tilde{P}_m/\partial\lambda$ and remember that the last surface integrals of (2.13), (2.16) and similar integrals for (2.17) all vanish by (1.11), (1.14) when $\dot{I}_m$, $\dot{I}_{k'}$ are hold independent of λ we get

$$\begin{aligned}\sum_r\sum_q\frac{\partial\dot{Z}_{rq}}{\partial\lambda}\dot{I}_q\tilde{I}_r &= \int_V\left(\frac{\varepsilon}{2}\boldsymbol{E}\cdot\tilde{\boldsymbol{E}}\right.\\ &\left.+\frac{\mu}{2}\boldsymbol{H}\cdot\tilde{\boldsymbol{H}}\right)dV,\end{aligned} \tag{2.19}$$

where

$$\boldsymbol{E}=\sum_r\boldsymbol{E}_r, \qquad \boldsymbol{H}=\sum_r\boldsymbol{H}_r. \tag{2.20}$$

(2.19) shows that the quadratic form on the left-hand side of (2.19) is positive definite form. Consequently arbitrary minors of the matrix

$$\|\partial Z_{rq}/\partial\lambda\|, \qquad (r,\ q=1,\ 2,\ \dots,\ n,\ 1',\ 2',\ \dots,\ n',) \tag{2.21}$$

along its principal axis are all non-negative.

§ 3. Individual Applications

If the terminal current $\dot{I}$ is properly defined, F, Z, $\dot{V}$ can be all evalûated by (1,11),(1.14), (1.12), (1.15) and (2.9). Henee we shall investigate what quantity is to be chosen as $\dot{I}$ in individual practical cases.

(a) *Wave Guide.* Terminals are considered on orthogonal cross section of wave guide (including the cross section of the wall). $\dot{I}$ is convenient to define as the total current (both displacement and conducting current) flowing outward inward through the cross section. With regard to practical examples and applications are my previous papers[1)2)3)].

(b) *Circular Symmetrical Cavity Resonator and Conductor.* $\dot{I}$ is convenient to define as the loop value of the total conducting current passing through the cross section of the wall by the plane perpendicular to the symmetrical axis.

(c) *Non-Circular Symmetrical Cavity Resonator and Conductor.* $\dot{I}$ is convenient to define as the quotient of the total conducting current on any selected portion of the conductor surface surrounded by a nodal line of the current distribution by the length of this nodal line.

The terminal surface in (b) and (c) is a line the surface of the conductor, and with regard to applications of (b) and (c) see my other paper[4)].

(d) *Slit Antenna.* $\dot{I}$ is convenient to define as $\sqrt{\varepsilon/\mu}$ multiples of the loop value of magnetic current flowing along the slit. Practical applications are mentioned in my previous papers[5)6)7)8)].

(e) *Small Hole.* $\dot{I}$ is convenient to define as $\sqrt{\varepsilon/\mu}$ multiples of the quotient of the total magnetic current on the hole surface by the contour length of the hole. This application is in my previous paper[9)].

The terminal surface in (d) and (e) is the cross section of slit or hole surface.

It is easy to that all $\dot{I}$'s above defined has the same dimension as the electric current of common networks and that $\dot{I}$ defined in (a), (b), (c) is of the type (1.11) while $\dot{I}$ defined n (d), (e) is of the type (1.14).

References

1) T. Sakurai: Circuit Theoretical Studies on Wave Guide, Collected Papers of the Institute of Electrical Engineers of Japan **5** (1944) 291.

2) T. Sakurai: Theory of *H*-wave Antenna in Wave Guide, Collected Papers of the Institute of Electrical Engineers of Japan **5** (1944) 449.

3) T. Sakurai: Circuit Theoretical Studies on the Singular Places of Wave Guide. The Journal of the Institute of Electrical Engineers of Japan **66** (1946) 127.

4) T. Sakurai: Theory of Resonant Circuit System, The Journal of the Institute of Electrical Communication Engineers of Japan **33** (1950) 487.

5) T. Sakurai: Fundamental Theory of Slit Antenna, The Journal of the Institute of Electrical Engineers of Japan **67** (1947) 153.

6) T. Sakurai: Radiation Impedance of System of Magnetic Current Antenna and Slit Antenna, The Journal of the Institute of Electrical Engineers of Japan **67** (1947) 183.

7) T. Sakurai: Theory of Slit Antenna on the Plate settled in Wave Guide, The Journal of the Institute of Electrical Engineers of Japan **67** (1947) 229.

8) T. Sakurai: Researches on Slit Antenna, Researches of the Electrotechnical Laboratory of Ministry of Communications in Japan, No. 493 (March 1948)

9) T. Sakurai: Circuit Theoretical Studies on Cavity Resonator, The Materials for the Fundamental Researches of Electrical Communication Laboratory of Ministry of Telecommunications in Japan, No. 2, p. 1 (August 1949)

JOURNAL OF THE PHYSICAL SOCIETY OF JAPAN Vol. 7, No. 2 MAR.—APR., 1952

On the Transient Phenomena in the Wave Guide

By Mikio NAMIKI and Kazuo HORIUCHI

Department of Applied Physics, Faculty of Science and Engineering
Waseda University, Tokyo

(Received February 23, 1951)

In this paper, we investigate of deformation of waves travelling in a nonloss wave guide owing to the dependence of the phase velocity on the frequency. The general formula was applied to the case in which a sinusoidally cscillating source is impressed at the time $t=0$. In this illustrative example, the wave front and the signal front travel in the wave guide with the velocities $(1/\sqrt{\mu\varepsilon})$ and $(1/\sqrt{\mu\varepsilon}\ s_p)$, respectively. ($s_p=\rho/\sqrt{\rho^2-1}$, $\rho=$ ratio of the excitation to the cut-off frequency.) The initial oscillations before the signal front have considerably small amplitudes, while the amplitudes of the signal waves are order of magnitude of the steady wave. After arrival of the signal the transient disturbances decrease for increasing time and the steady wave only remains there. The oscillations with a finite time interval are also considered.

§ 1. Introduction

Since the phase velocities of electromagnetic waves in the wave guide depend on the frequency, it is concluded that the shape of travelling wave undergoes some deformations notwithstanding no energy loss. Such deformations due to the frequency dependence of phase velocity are characteristic of the dispersive media and the essential behaviors was investigated by Sommerfeld and Brillouin[1]. In this paper we shall study in detail the features of these phenomena in the wave guide.

The electromagnetic fields in the wave guide are described by the wave function $\psi(r, t)$ satisfying the appropriate boundary condition and obeying the wave equation

$$\nabla^2\psi-\mu\varepsilon\frac{\partial^2\psi}{\partial t^2}=g(r, t) \qquad (1)$$

where $(1/\sqrt{\mu\varepsilon})$ is the propagation velocity of electromagnetic waves and $g(r, t)$ is the function representing the source density. Let z-axis of the coordinate system be the axis of the wave guide and let $u_{mn}(x, y)$ be the normalized eigenfunctions of the wave guide satisfying the same boundary condition as the wave function, then the required wave function is represented by the expression

$$\psi(r, t)=\sum_{mn}u_{mn}(x, y)\int dv'\bar{u}_{mn}(x', y')$$

$$\int d\omega\frac{g(r, \omega)}{2i\gamma_{mn}}\exp\left[i\gamma_{mn}|z-z'|-i\omega t\right] \qquad (2)$$

where $g(r, \omega)$ is the Fourier component of the function $g(r, t)$ and $\gamma_{mn}=\sqrt{\mu\varepsilon}\sqrt{\omega^2-\omega_{mn}^2}$, ω_{mn} being the cut-off frequency for the (m, n)-th wave. For the usual case in which the sources are standing waves, $g(r, t)=G(r)f(t)$. Accordingly the integral with respect to ω in eq. (2) is replaced with the following function $S(|z-z'|, t)$

$$S(\zeta, t)=\frac{1}{2i}\int\frac{f(\omega)}{\gamma_{mn}}\exp\left[i\gamma_{mn}\zeta-i\omega t\right]d\omega, \qquad (3)$$

where $f(\omega)$ is the Fourier component of $f(t)$. Thus, for our purpose, it is necessary to investigate the behaviors of the transient function $S\ \zeta, t)$.

Moreover, if the extension along z-axis of the source is considerably small in comparison with the wave length in the wave guide and the distance from the source to the observation point, we can conclude that the time dependence of the waves is directly determined by the function S.

§ 2. Transient Functions

Hereafter we shall consider the case when the source is impressed on the wave guide at the time $t=0$, that it, $f(t)=0$ for $t<0$. In this case, our mathematical manipulation of the problem involves the function $f(\omega)$ which is a rational function with several (or no) poles and the contour of integration which goes over somewhat above the all singularities from $+\infty$ to $-\infty$. For instance, if we take the function $f(t)=F_0\exp(-i\omega_0 t)$ for $t>0$, $f(\omega)=(F_0/2\pi i)(1/\omega-\omega_0)$. This example will be taken up as an illustrative case (we denote it with (A)). Thus, the above integral (3) vanishes for the time $t<\zeta\sqrt{\mu\varepsilon}$ because of the exponential factor in the integrand, whereas after $t_0=\zeta\sqrt{\mu\varepsilon}$ the integral has non-vanishing value. This is the well-known fact that the wave front moves with the velocity $(1/\sqrt{\mu\varepsilon})$. For $t>t_0$, the function $S(\zeta,t)$ is given by the integral (3) on the contour of integration which is a closed curve including the all poles of $f(\omega)$ and the two branch points of γ_{mn}. Now, if we use the quantities $\varphi=\cos^{-1}(\omega/\omega_{mn})$ as the variable of integration and $s=(t/t_0)$ as the time variable, the function S becomes

$$S(\zeta,t)=\frac{1}{2\sqrt{\mu\varepsilon}}\int_C f(\omega_{mn}\cos\varphi)\exp[-i\omega_{mn}t_0\sqrt{s^2-1}\cos(\varphi-i\alpha)]d\varphi \qquad (4)$$

where $s>1$ and $\tanh\alpha=(1/s)$. The contour C is the curve running from $-\pi$ to $+\pi$ above the all poles of $f(\omega)$. The contour of the example (A) is shown in Fig. 1 for the interesting case $\omega_0>\omega_{mn}$, where the position of the pole is given by $\varphi=i\beta$ and $\cosh\beta=(\omega_0/\omega_{mn})$.

Since it is interesting to observe the transient phenomena at large distance from the source, we shall consider only the case $\omega_{mn}t_0\gg 1$. This condition means that the observation is performed at sufficiently large distance from the source in comparision with the cut-off wave length of the (m, n)-th wave. According to this condition, the inequality $\omega_{mn}t_0\sqrt{s^2-1}\gg 1$ holds for all time after a few cycles of initial oscillations. Hence, the saddle points of the integrand of eq. (4) are $\varphi=i\alpha+n\pi(n=0,\pm1,\cdots)$ with good approximation. Only exceptional case occurs when the saddle points approach closely to the poles, which we shall consider later. The contribution Q to the integral of the saddle points is

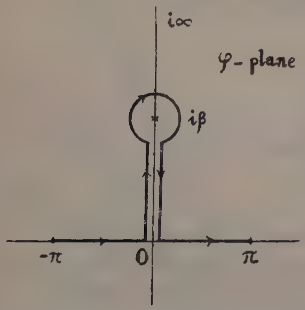

Fig. 1. The contour of integration on the φ-plane for the example (A).

$$\left.\begin{aligned}Q\simeq A_+&\exp\left[i\omega_{mn}t_0\sqrt{s^2-1}-i\frac{\pi}{4}\right]\\&+A_-\exp\left[-i\omega_{mn}t_0\sqrt{s^2-1}+i\frac{\pi}{4}\right]\\A\pm&=\sqrt{\left(\frac{\pi}{2\mu\varepsilon}\right)\Big/(\omega_{mn}t_0\sqrt{s^2-1})}\\&\cdot f\left(\mp\frac{\omega_{mn}s}{\sqrt{s^2-1}}\right)\end{aligned}\right\}\qquad(5)$$

The amplitudes for the example (A) becomes

$$\begin{aligned}A\pm=\mp&\frac{1}{\sqrt{2\pi\mu\varepsilon}}\cdot\frac{F_0}{2i\sqrt{\omega_{mn}t_0}}\\&\cdot\frac{\sqrt[4]{s^2-1}}{\omega_{mn}s\pm\omega_0\sqrt{s^2-1}}\end{aligned}\qquad(6)$$

Since α moves from infinity to zero for increasing s, the contour passing the saddle point $i\alpha$ jumps over the pole of $f(\omega)$ at a time $s=s_p$, where the denominator of the amplitude A_- vanishes. For the example (A),

$$s_p=\frac{(\omega_0/\omega_{mn})}{\sqrt{(\omega_0/\omega_{mn}{}^2-1}}\qquad(7)$$

Hence, $S=Q$

during the time $1<s<s_p$ and

$$S=2\pi i\sum B+Q$$

for $s>s_p$, where B's is the residue of $f(\omega)$ at the pole and the summation is over the passed poles. For the example (A), this term represents the wave function in steady state

$$(F_0/2i\gamma_{mn}(\omega_0))\exp[i\gamma_{mn}(\omega_0)\zeta-i\omega_0 t]\qquad(8)$$

The expressions (5) or (6) of the amplitude A_- break down for the time $s\sim s_p$. We obtain by rough estimation

$$|A_-|=\frac{1}{2\sqrt{2\pi\mu\varepsilon}}\cdot\frac{|F_0|}{\sqrt{\omega_0{}^2-\omega_{mn}{}^2}}\cdot\Big/\left\{1+\left[1-((\omega_0/\omega_{mn})^2-1)\sqrt{\frac{\omega_{mn}t_0}{2}\sqrt{s_p{}^2-1}\cdot|s-s_p|}\right]^2\right\}^{\frac{1}{2}}$$

for the example (A). Hence, it is concluded that the amplitude rapidly changes by the factor $(1/\sqrt{\omega_{mn}t_0})$ at the time $s=s_p$. That is, the essential part of the waves arrives at the observation point after the $t_1=s_p t_0$. From this point of view $(1/\sqrt{\mu\varepsilon}\,s_p)$ may be considered as the signal volocity* and it is evident that the singnal velocity is smaller than the propagation velocity because of $s_p > 1$. We have plotted in Fig. 1 the ratio of the signal to propagation velocity against (ω_0/ω_{mn}) for the example (A). It is to be noticed that the signal velocity rapidly decrease as the frequency approaches to the cut-off frequeucy. In Fig. 3 we give the curve of the reaching time $t_1 = s_p t_0$ of the signal front vs. the distance ζ from the source to the observation point. After the last s_p, the transient disturbance Q decrease for increasing s and vanish in the limiting case $s \to \infty$. In the example (A), the steady wave only remains there for that time. As an illustration of these situations, we show graphically in Fig. 4 the amplitudes of the wave at the place $2\pi\omega_{mn}t_0 = 100$, where $(\omega_0/\omega_{mn}) = 1.2$ and the trasient function is normalized to make the amplitude in the steady state unity. We have plotted A_- only because $A_- \gg A_+$.

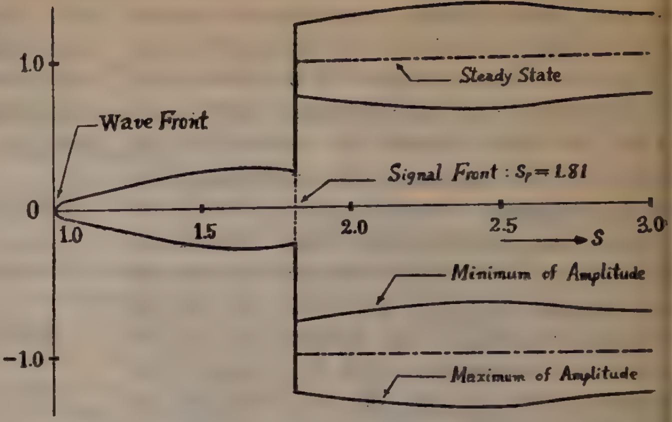

Fig. 4. The standing-up curve of the amplitude and the damping curve of the transient disturbance at the place $2\pi\omega^{mn}t_0 = 100$ for the case $(\omega_0/\omega_{mn}) = 1\cdot 2$. The reaching time is $s_p = 1.81$.

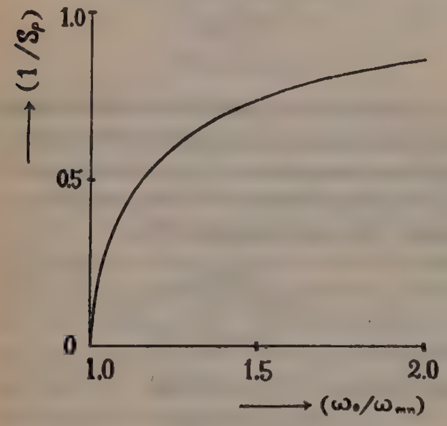

Fig. 2. The ratio of the signal to propagation velocity vs. (ω_0/ω_{mn}).

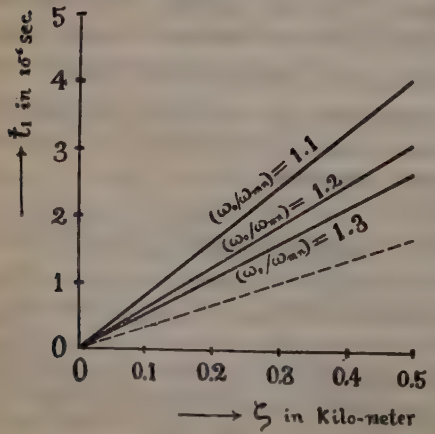

Fig. 3. The reaching time of the signal front vs. the distance from source to observation point. The dotted line is the reaching time of the wave front.

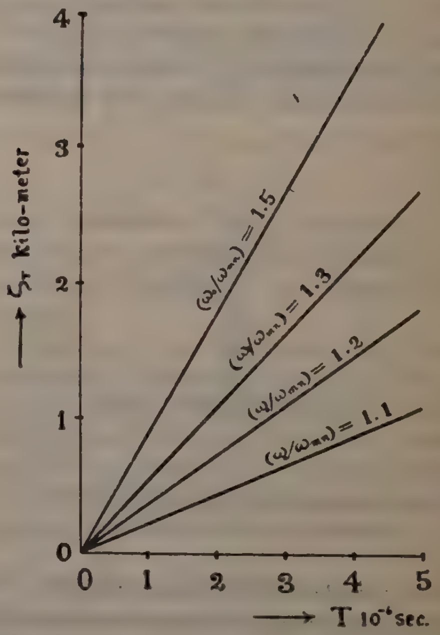

Fig. 5. The critical distance for keeping the shape in the oscillation with a finite time interval T.

---

* It is easily shown that the signal velocity is the very group velocity as expected.

§ 3. Concluding Remarks

From the previons consideration, it is concluded that the transient disturbances must be taken into account for the observations at large distance from the sources and the phenomena with a finite time interval. For example, let us consider the case when a sinusoidal oscillation with the frequency ω_0 is impressed on the wave guide during $0<t<T$, that is,

$$f(\omega)=(F_0/2\pi i)[(1-\exp iT(\omega-\omega_0))/(\omega-\omega_0)]$$

Before the time t_0, any waves can not arrive at there. During the time $t_0<t<t_0+T$, the transient function is written just by the function of the example (A), because the term including T in $f(\omega)$ gives no contribution to the integral. Since the function $f(\omega)$ has no pole, the wave function is given by the function Q only after t_0+T. Thus, if $1+\frac{T}{t_0}<s_p$, that is, $\zeta>\zeta_T=\frac{1}{\sqrt{\mu\varepsilon}}\frac{T}{s_p-1}$, the shape of the wave would entirely break down. We have plotted in Fig. 5 this critical distance ζ_T against the time interval T. Moreover, the transient phenomena in the wave guide with imperfect conducting wall are more complicated than the present case. Although, at any rate, we can neglect the deformations of travelling wave in small apparatus, the long-distance transmission with hte wave guide may be affected by such transient phenomena.

Finally the authors wish to express their sincere gratitude to Professor S. Koizumi for his advises. This report is one part of the researches performed with support of the financial assistance of the Department of Education.

Reference

1) Sommerfeld: Ann. d. Phys. **44** (1914) 177. Brillouin: *ibid.*, 203.

Journal of the Physical Society of Japan Vol. 7. No. 2, Mar.—Apr. 1952

On the Abnormal Rotation of OH Radicals*

By Kazuo NIIRA

Tokyo Institute of Technology, Oh-okayama, Tokyo

(Received July 19, 1951)

The abnormal rotational intensity distribution of the OH band spectrum $^2\Sigma^+-{}^2\Pi$ emitted through discharge in water vapour has been interpreted to be due to simultaneous dissociation of H_2O and excitation of OH. A quantum-mechanical calculation of electronic energies of H_2O molecules by semiempirical AO approximation shows that in two electronically excited states of H_2O, both of them being characterised by symmetry type of $^1A_1$ and $^3B_2$, respectively, a hydrogen atom of H_2O takes a path of particular direction in the dissociation process to excite OH^* radical ($^2\Sigma^+$) into a rotational state. Such an elementary process for dissociation can be understood by an interaction between different symmetry types resulting from deformation of the configuration of H_2O molecule from an isosceles into a scalene triangle at the decomposition. Greater energy released in the $^3B_2$ than in the $^1A_1$ is responsible for the abnormal rotation ($J\sim20$) of OH^* from the $^3B_2$, and the $^1A_1$ gives OH^* of $J\sim5$. Another treatment by MO method is reviewed.

§1. Introduction

A spectroscopic study of the radiation emitted through discharge in gas can give much information about the distribution of rotational states of the molecules in the electronically excited states. When the distribution is expressed by a Boltzmann type we may define a rotational temperature T_r by

$$\frac{I}{i} \propto \mathrm{epx}\left(-E_{rot}/kT_r\right) \qquad (1)$$

$$= \exp\left(-\hbar^2 J(J+1)/2AkT_r\right)$$

where I means the intensity of the line with a rotational quantum number J, i the intensity factor, A the moment of inertia. We have an abnormal rotational intensity distribution in the case of an extraordinary value of T_r. Among various causes for it this paper deals with abnormal rotation which is due to an anomalous dissociation process of an electronically excited molecule, for the case of H_2O molecule. This abnormality is observed also in discharges of C_2H_2, C_2H_4, CH_4 etc..

The rotational intensity distribution of the OH band of the ${}^2\Sigma^+-{}^2\Pi$ transition through the ring discharge in water vapour at 0.08mm Hg and 600°K is shown in Fig. 1[1].

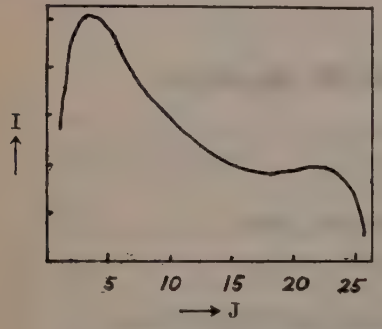

Fig. 1. (0,0) band of OH ${}^2\Sigma^+-{}^2\Pi$; Q branch.

The OH radicals produced by dissociation of H_2O molecule can be considered as a mixture of two groups, one of them in the rotational states of around $J=5$ ($T_r=1500$°K) and the other of around $J=20$ ($T_r'=8000$°K). In the glow discharge of water vapour the similar result has been observed[2] and the value of T_r of the former group which depends on the conditions of the discharge extends from 800°K to 3500°K, while a striking feature, that the latter group possesses a steep maximum, is common to various conditions of discharge[3]. This phenomenon of abnormal rotation of OH radical has been studied by many workers[4] and is interpreted that the OH bands are produced by simultaneous dissociation of H_2O and excitation of OH as follows:

$$H_2O + electron \rightarrow H_2O^* \rightarrow OH^* + H,$$
$$OH^*({}^2\Sigma^+) \rightarrow OH({}^2\Pi) + h\nu. \qquad (2)$$

The experimental evidences for (2) are:

(a) The intensity I is linear to electron current.

(b) The absorption spectrum of OH after transition into the ground state (${}^2\Pi$) never exhibits the anomaly.

(c) A trace of water vapour in a helium gas does not exhibit the abnormal rotation of the OH radical, which has dissipated its excess rotational energy by collisions with helium atoms before its transition into the ground state.

Since a momentum transfer from an impinging electron is unimportant, a clue to interpret the abnormal rotation of OH^* is to explore the characteristic feature of the dissociation process $H_2O \rightarrow OH^*$. If in this process a hydrogen atom (indicated by H′ in Fig. 2) flies apart into a (tangential) direction of impact parameter p, the OH gets by reaction an angular momentum L such as[5]

$$\frac{L^2}{2M}\left(\frac{1}{p^2}+\frac{1}{a^2}\right) = \Delta E,\ L^2 = \hbar^2 J(J+1) \qquad (3)$$

where ΔE means the dissociation energy of $H_2O^* \rightarrow OH^* + H$, M the mass of the hydrogen atom and a the nuclear distance in OH^*. (We assume classical motion for the H atom throughout in this paper). As the electronic energies are equal to these of D_2O, it supports our interpretation that the abnormal rotation is observed also in D_2O[6]. Taking the values of p and a to 1 A and 0.96 A, respectively, (the latter is an equilibrium distance in OH radical) we have ΔE of 2.08 eV for $J=20$ and 0.12 eV for $J=5$.

§2. Treatment by AO approximation

We shall calculate electronic energy of H_2O molecules in the excited states by AO approximation, assuming electronic configurations of O: $(1s)^2(2s)^2(2p)^4$, H: $(1s)$ and H′: $(1s)$, tentatively. We assume an isosceles triangle for the configuration of the H_2O molecules, the electronic energies of them being function of the angle HOH′ $(=\pi/2+2\theta)$. The electronic levels are classified by irreducibler epresentations of the space group C_{2v}, i. e. A_1, A_2, B_1 and B_2. From the electronic configurations above mentioned we obtain the following functions for H_2O:

---

* Translated from the papers originally in Japanese, appearing in the Busseiron Kenkyu **11** (1948) 1; **31** (1950) 16.

$$\left.\begin{aligned}
\Psi^{xy} &= (k,\ k,\ s,\ s,\ \sigma_x,\ \sigma_x,\ \sigma_y,\ \sigma_y,\ h,\ h'),\\
\Psi^{yz} &= (k,\ k,\ s,\ s,\ \sigma_y,\ \sigma_y,\ \sigma_z,\ \sigma_z,\ h,\ h'),\\
\Psi^{xz} &= (k,\ k,\ s,\ s,\ \sigma_x,\ \sigma_x,\ \sigma_z,\ \sigma_z,\ h,\ h'),\\
\Psi^{x} &= (k,\ k,\ s,\ s,\ \sigma_x,\ \sigma_x,\ \sigma_y,\ \sigma_z,\ h,\ h'),\\
\Psi^{y} &= (k,\ k,\ s,\ s,\ \sigma_y,\ \sigma_y,\ \sigma_x,\ \sigma_z,\ h,\ h'),\\
\Psi^{z} &= (k,\ k,\ s,\ s,\ \sigma_z,\ \sigma_z,\ \sigma_x,\ \sigma_y,\ h,\ h'),
\end{aligned}\right\} \tag{4}$$

where k means the $1s$ orbital of O atom; s the $2s$; σ_x, σ_y and σ_z are three independent $2p$ orbitals of O atom, z axis being perpendicular to the plane of the molecule and x or y axis making an equal angel θ with OH or OH′, respectively, and further h (h') is the $1s$ orbital of H (H′) atom. The functions is (4) must be antisymmetrized. From their transformation properties under the operations of the group C_{2v}, we find that the A. S. functions constructed from the left column correspond to the irreducible representations of the right column in the following table:

$$\left.\begin{array}{rll}
\Psi^{xy} & : {}^1A_1 & ;\ {}^3B_2,\\
\frac{1}{\sqrt{2}}(\Psi^{yz}+\Psi^{xz}) & : {}^1A_1 & ;\ {}^3B_2,\\
\frac{1}{\sqrt{2}}(\Psi^{yz}-\Psi^{xz}) & : {}^1B_2 & ;\ {}^3A_1,\\
\Psi^{z} & : {}^1A_1, {}^1A_1 & ;\ {}^3A_1, {}^3B_2, {}^3B_2; {}^5A_1,\\
\frac{1}{\sqrt{2}}(\Psi^{x}+\Psi^{y}) & : {}^1A_2, {}^1B_1 & ;\ {}^3A_2, {}^3A_2, {}^3B_1; {}^5A_2,\\
\frac{1}{\sqrt{2}}(\Psi^{x}-\Psi^{y}) & : {}^1A_2, {}^1B_1 & ;\ {}^3A_2, {}^3B_1, {}^3B_1; {}^5B_1,
\end{array}\right\} \tag{5}$$

where the designations for the representations of C_{2v} are followed to Mulliken and Sponer-Teller7)*. If we neglect overlap integrals between each orbitals and take the values of various integrals between orbitals from the semiempirical ones8) which are compatible with the observed spectrum of OH radical, we can compute the electronic energies of the molecule for each electronic state. The secular equations for ${}^1A_1$ and ${}^3B_2$, for instance, are as follows:

${}^1A_1$:

$$\begin{vmatrix}
H_{11}-W & 3\sqrt{2}F_2 & 0 & 0\\
3\sqrt{2}F_2 & H_{22}-W & 0 & H_{24}\\
0 & 0 & H_{33}-W & H_{34}\\
0 & H_{24} & H_{34} & H_{44}-W
\end{vmatrix}=0, \tag{6 A}$$

$$\left.\begin{aligned}
H_{11} &= W_0+9F_2+4Q_\sigma+4Q\pi+Q_h'-2J\sigma-2J\pi\\
&\qquad +J_h',\\
H_{22} &= W_0+12F_2+2Q\sigma+6Q\pi+Q_h'-\\
&\qquad -J\sigma-J\pi-J_h',\\
H_{33} &= W_0+2Q\sigma+6Q\pi+Q_h'+J\sigma-J\pi-J_h',\\
H_{44} &= W_0+6F_2+2Q\sigma+6Q\pi+Q_h'\\
&\qquad -J\sigma-3J\pi+J_h',\\
H_{24} &= (J\pi-J\sigma)\sin 2\theta+2(Q\sigma-Q\pi)\sin 2\theta,\\
H_{34} &= \sqrt{3}\,(J\pi-J\sigma)\cos 2\theta;
\end{aligned}\right\} \tag{6 B}$$

${}^3B_2$:

$$\begin{vmatrix}
H_{11}-W & 3\sqrt{2}F_2 & 0 & 0\\
3\sqrt{2}F_2 & H_{22}-W & 0 & H_{24}\\
0 & 0 & H_{33}-W & H_{34}\\
0 & H_{24} & H_{34} & H_{44}-W
\end{vmatrix}=0, \tag{7 A}$$

$$\left.\begin{aligned}
H_{11} &= W_0+9F_2+4Q\sigma+4Q\pi+Q_h'\\
&\qquad -2J\sigma-2J\pi-J_h',\\
H_{22} &= W_0+12F_2+4Q\sigma+4Q\pi+Q_h'\\
&\qquad -J\sigma-3J\pi-J_h',\\
H_{33} &= W_0+2Q\sigma+6Q\pi+Q_h'-J\sigma-3J\pi-J_h',\\
H_{44} &= W_0+6F_2+2Q\sigma+6Q\pi+Q_h'\\
&\qquad -J\sigma-3J\pi-J_h',\\
H_{24} &= 2(Q\pi-Q\sigma)\mathrm{sih}2\theta+(J\sigma-J\pi)\sin 2\theta,\\
H_{34} &= (J\pi-J\sigma)\cos 2\theta,
\end{aligned}\right\} \tag{7 B}$$

where

$$W_0=W(\mathrm{O}:\ {}^3P)+2W(\mathrm{H}:\ 1s)+2W_1.$$

The notations W (O: ${}^3P$) and W (H: $1s$) in (6) and (7) are the energies of the ground states of the oxygen atom and the hydrogen atom, respectively and W_1 is a sum of the interaction energies of $(1s)^2$ and $(2s)^2$ of the oxygen atom with $1s$ electron of the hydrogen atom.

$$\left.\begin{aligned}
Q_j &= \iint \varphi_j(1)\varphi_h(2)H_1\varphi_j(1)\varphi_h(2)d\tau_1 d\tau_2,\\
J_j &= \iint \varphi_j(1)\varphi_h(2)H_1\varphi_h(1)\varphi_j(2)d\tau_1 d\tau_2,\\
&\qquad\qquad (j=\sigma,\ \pi,\ h'),\\
H_1 &= e^2\left(\frac{1}{r_{12}}+\frac{1}{R}-\frac{1}{r_{H1}}-\frac{1}{r_{02}}\right),
\end{aligned}\right\} \tag{8}$$

---

* In the reference (15) the designation of specie. B_1 and B_2 are opposite to those in the present texts

R: the internuclear distance between O and H atoms.

F_2 is a Slater-Condon term for atomic integral, and is assumed to be 0.30 eV, the value adjusted to the observed spectrum of the O atom[9]:

$$W(\mathrm{O}{:}\ {}^1D)-W(\mathrm{O}{:}\ 3_p)=6F_2=1.96\ \mathrm{eV}.$$
$$W(\mathrm{O}{:}\ {}^1S)-W(\mathrm{O}{:}\ 3_p)=15F_2=4.18\ \mathrm{eV}.$$

According to Stehn and King[8] we assume that

$$Q\sigma=Q\pi,$$
$$J\sigma=-2.13\ \mathrm{eV}$$
$$J\pi=0.92\ \mathrm{eV}$$

And further we put

$$W_1+4Q\pi=-1.69\ \mathrm{eV},$$

which is adjusted to obtain agreement with the observed value of the dissociation enery of the H_2O molecule (10 eV). (The equilibrim distances between O and H atoms amount to 0.96A for the OH radical and 0.955 A for the H_2O molecule being nearly equal). The electronic energies are computed for various angles of HOH′ with the fixed nuclear distance between O and H or H′ atoms. Neglecting the HH′ interaction ($Q_h'=J_h'=0$) we obtain the values in Table 1.

Table 1. Electronic energies of H_2O (in eV).

	∠HOH′=$\pi/2$	∠HOH′=π (linear)
$^1A_1$	−10.00	−6.43 ($^1\Pi_u$)
	−1.00	−4.49 ($^1\Sigma_g{}^+$)
	1.38	0.84 ($^1\Delta_g$)
	2.34	2.77 ($^1\Sigma_g{}^+$)
$^1B_1$	−3.93	−6.43 ($^1\Pi_u$)
	1.39	0.84 ($^1\Delta_g$)
$^1A_2$	−3.93	−2.21 ($^1\Pi_g$)
	1.39	2.72 ($^1\Sigma_n^-$)
$^1B_2$	−2.21	−2.21 ($^1\Pi_g$)
$^3A_1$	−5.22	−8.29 ($^3\Pi_u$)
	−2.21	0.86 ($^3\Pi_u$)
$^3B_1$	−5.81	−8.29 ($^3\Pi_u$)
	−0.38	−0.95 ($^3\Sigma_g^-$)
	0.86	0.86 ($^3\Pi_u$)
$^3A_2$	−5.81	−4.01 ($^3\Pi_u$)
	−0.38	0.85 ($^3\Delta_u$)
	0.86	0.88 ($^3\Sigma_u^-$)
$^3B_2$	−6.20	−4.59 ($^3\Sigma_u{}^+$)
	−1.00	−4.01 ($^3\Pi_g$)
	0.07	0.85 ($^3\Delta_u$)
	2.34	2.87 ($^3\Sigma_u{}^+$)
$^5A_1$	−2.80	−2.80 ($^5\Pi_u$)
$^5B_1$	−2.80	−2.80 ($^5\Pi_u$)
$^5A_2$	−2.80	−2.80 ($^5\Sigma_n^-$)

The origin of energy is $W(\mathrm{O}{:}\ 3_p)+2W(\mathrm{H}{:}\ 1s)$

The ground state of the H_2O molecule is found to be $^1A_1$, the angle HOH′ being just a right angle. If we choose the value of −1.84 eV for $W_1+4Q\pi$ which gives the observed energy of the OH radical the dissociation energy of H_2O becomes to 10.15 eV. Van Vleck and Cross[10] gave a similar result by an electron pair bond approximation. When we include the HH′ interaction by semiempirical manner after Eyring[11], it is found that the equilibrium bond angle becomes rather smaller than $\pi/2$, contrary to that anticipated by the electron pair model (the reason for this is that in our scheme, Q_h' gives a more dominant contribution than J_h', and the distance between both H atoms being 1.34 A at the angle HOH′=$\pi/2$, is larger than that of 0.74 A in the H_2 molecule), so that we must take into accout an ionic repulsion between both H atoms, to interpret the correct value of 105 degrees of the bond angle. We assume that the HH′ interaction cancels the ionic repulsion in the configuration of the angle HOH′ which is not so small. The calculated energy values for $^1A_1$, $^1B_2$, $^3A_1$ and $^3B_2$ which are responsible for the abnormal rotation are plotted in Fig. 2 as function of the angle HOH′ (or θ).

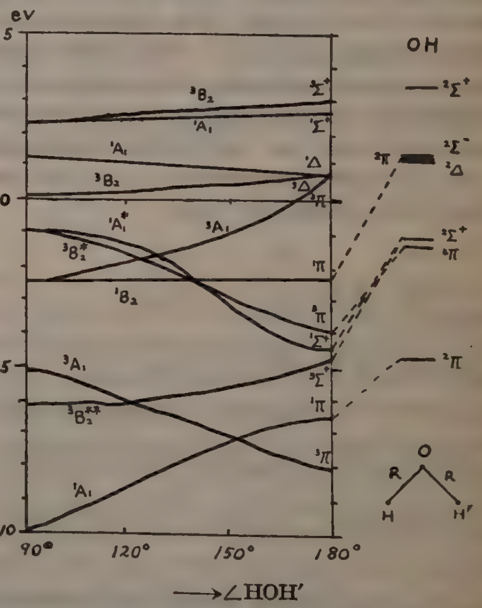

Fig. 2. Electronic energies of $^1A_1$, $^1B_2$, $^3A_1$ and $^3B_2$ of H_2O (R=0.96 A).
The origin of energy is $W(\mathrm{O}{:}\ 3_p)+2W(\mathrm{H}{:}\ 1s)$.

§ 3. Elementary Processes for the Dissociation of H_2O in the Excited Electronic States

The excited electronic states of $^1A_1$ and $^3B_2$, both of excitation energy of 9 eV (denoted by

$^1A_1^*$ and $^3B_2^*$, respectively in Fig. 2) are unstable to the dissociation into OH* ($^2\Sigma^+$) and H′ (1s), and may be participating the abnormal rotation of the OH* radical. Inclusion of the HH′ interaction makes $^3B_2^*$ rather higher than $^1A_1^*$ (by an amount $-2J_h'$). The ground state of the H_2O molecule is well approximated by electron pair bonds between $2p\sigma_x$ ($2p\sigma_y$) of the O atom and 1s electron of the H (H′) atom, and both of $^1A_1^*$ and $^3B_2^*$ arise from a transition of the $2p\sigma_x$ (or $2p\sigma_y$) orbit into a $2p\sigma_y$ (or $2p\sigma_x$) orbit. The $^1A_1^*$ can be excited by direct collisions of electrons, while $^3B_2^*$ solely by exchange or rearrangement collisions of them.

As the potential surface of the $^1A_1^*$ intersects at the angle HOH′=134 degrees with the $^1B_2$, the dissociation into OH ($^2\Sigma^+$) and H′ (1s) does actually occur in the nuclear configurations of the angle HOH′ which is greater than 134 degrees. The reason for it is as follows. Under the assumption that the dissociation takes place in the planar configuration of HOH′, the process for it causes the HOH′ triangle to deform from an isosceles into a scalene one. Then an interaction between $^1A_1^*$ and $^1B_2$ arises to separate the intersection into upper and lower parts (see Fig. 3). Due to this effect the $^1A_1^*$ is in the angle HOH′, smaller than 134 degrees, dissociated into OH ($^2\Pi$) and H′ (1s) and is stable for this process. The dissociation into OH* ($^3\Sigma^+$) and H′ (1s) should take place in the region of the angle HOH′, greater than the above value, and therefore the H′ atom flies apart into the (tangential) direction with impact parameter not vanished. An analogous consideration can be made in the $^3B_2^*$ state as may be seen from Fig. 2. In the configuration with the angle HOH′ above the intersection with $^3A_1$ which is situated just below $^3B_2^*$ the dissociation into a radial direction in $^3B_2^*$ cannot occur. $^3B_2^*$, in which H_2O is dissociated into OH ($^4\Pi$) and H′ (1s) adiabatically, intersects with $^3B_2^{**}$ at the OH′ distance, larger than the equilibrium value (see Fig. 2) and makes a radiationless transition into $^3B_2^{**}$ to give OH* ($^2\Sigma^+$) and H′ (1s). In this case the transition is forbidden in the linear configuration of HOH′ owing to the different symmetry property between them (Σ and Π), so that the probability of the dissociation into OH* ($^2\Sigma^+$) and H′ (1s) would be very small at the angle HOH′ near to 180 degrees to result in the sharp distribution of J around 20. Inclusive of HH′ interaction $^3B_2^*$ state has a greater dissociation energy than $^1A_1^*$, as mentioned above, and gives a greater J. From these considerations we can conclude that the excitations into $^1A_1^*$ and $^3B_2^*$ give the OH* radicals of $J=5$ and $J=20$, respectively. The excitation energy of 9 eV (exclusive of HH′ interaction) is consistent with the observed value of 10 ±2 eV by Hayakawa[12].

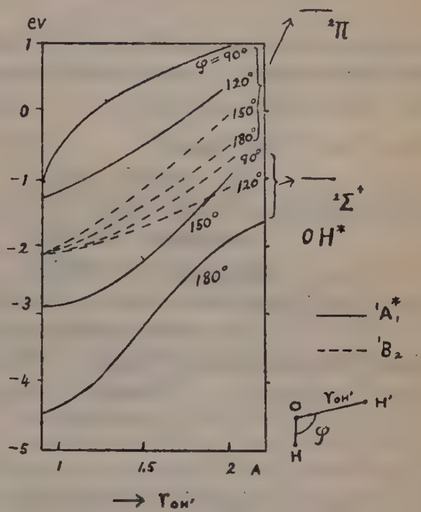

Fig. 3. Potential surfaces for $^1A_1^*$ and $^1B_2$.

The values of J_σ and J_π for arbitrary r_{OH}'s are obtained by the extrapolation according to the semiempirical method of Eyring[11].

Our treatment is based upon a crude semiempirical approximation[*] but we can interpret the potential valley into a tangential direction by an interaction between different types (A_1 and B_2 in our case) which arises by a deformation from the equilibrium configuration. A lowering of the energy surface into a direction of the greater angle ef HOH′ may not necessarily lead us to conclude that the dissociation process prevails only in such direction.

§ 4. Consideration by MO approximation

According to Mulliken[13], the relatively lower electronic states of the H_2O molecule are given by molecular orbitals such as

---

[*] Some of our results may be modified by the recent work of Prof. Gaydon (to be published in the Proc. Roy. Soc.) on the predissociation of OH radicals.

$$\left.\begin{array}{l} 2sa_1, \\ [yb_2]=a(2py)+b\dfrac{\alpha-\beta}{N}, \\ [xa_1]=c(2px)+d\dfrac{\alpha+\beta}{N}, \\ 2zb_1=2pz, \\ 3sa_1, \\ \quad \alpha\equiv \mathrm{H}(1s), \quad \beta \mathrm{H}'\equiv(1s), \end{array}\right\} \quad (9)$$

where the z axis is perpendicular to the plane of the molecule and x axis bisects the angle HOH′. They are:

$$\left.\begin{array}{ll} (2sa_1)^2[yb_2]^2[xa_1]^2\ 2zb_1)^2 & {}^1A_1 \\ \qquad \text{(the ground state),} & \\ (2sa_1)^2[yb_2]^2[xa_1]^2(2zb_1)(3sa_1) & {}^{3,1}B_1 \\ \qquad \text{(responsible for the} & \\ \qquad \text{absorption of } \lambda\ 1608\text{),} & \\ (2sa_1)^2[yb_2]^2[xa_1](2zb_1)^2(2sa_1) & {}^{3,1}A^1 \\ \qquad \text{(we denote as } {}^{3,1}A_1\text{),} & \\ (2sa_1)^2[yb_2][xa_1]^2(2zb_1)^2(3sa_1) & {}^{3,1}B_2, \\ (2sa_1)^2[yb_2][xa_1]^2 \qquad (3sa_1)^2 & {}^1A_1, \\ \cdots\cdots\cdots\cdots\cdots\cdots & \end{array}\right\} \quad (10)$$

As in a linear configuration of the H_2O

$$3sa_1\to\sigma \text{ (denoted by } \sigma^*\text{)},$$
$$[yb_2]\to\sigma, \qquad [xa_1],\ 2zb_1\to\pi,$$

then it is found that

$$\left.\begin{array}{l} {}^1A_1\to\sigma^2\pi^4:\ {}^1\Sigma_g{}^+, \\ {}^{3,1}B_1,\ {}^{3,1}A_1\to\sigma^2\pi^3\sigma^*:\ {}^{3,1}\Pi_u, \\ {}^{3,1}B_2\to\sigma\pi^4\sigma^*:\ {}^{3,1}\Sigma^+{}_u. \end{array}\right\} \quad (11)$$

From (11) we observe that the excitation into ${}^{3,1}B_2$ by a transition of $[yb_2]$ into $3sa_1$ is responsible to the abnormal rotation. Horie et al.[3] inferred that in ${}^1B_2$ a hydrogen atom makes a dissociation into a radial direction and never excites the abnormal rotation of the OH radical, while in ${}^3B_2$ the dissociation into a tangential direction causes the abnormal rotation of $J=20$. Their qualitative discussion is as follows. The ground state H_2O is assumed to be approximated by electron pair bonds. When a $2p$ electron makes a transition into a $3s$ orbit, sp hybridization brings in ${}^1B_2$ a linear configuation of the H_2O and owing to the weak $2p$-$3s$ bond strength the dissociation immediately follows. It would be in a radial direction due to the larger bond length of sp-H(1s) than pure p-H(1s). On the other hand, in ${}^3B_2$ the resultant repulsion between a H(1s) and a 3s electron of the O atom (their spins are parallel with each other) and between 1s electrons of both H atoms rejects a H atom into a tangential direction to excite abnormal rotatian ($J=20$) of OH* radical. It would be possible to compute the electronic energies of the above mentioned states of H_2O molecules by the method given by G. Mayer and Sklar[14] for the benzene.

As we have seen in the previous section, in the AO approximation we interpret the abnormal rotation of OH* radicals as due to the transition of $2p\sigma_x\to 2p\sigma_y$, while in the MO theory we consider it as due to $[yb_2]\to 3s$ transition. For both transitions we can calculate excitation cross sections by impacts of fast electrons under the assumption that the ground state of the H_2O molecule is well approximated by electron pair bonds. Neglecting exchange collisions we calculate them by Bron approximation as

$2p\sigma_x\to 2p\sigma_y$[15]:

$$Q_p=\frac{48}{35\pi a_0{}^2}\ \frac{\lambda^{12}}{k^2}\left\{\frac{1}{[\lambda^2+B_0{}^2]^7}-\frac{1}{[\lambda^2+A_0{}^2]^7}\right\}, \tag{12}$$

$2p\sigma_x\to 3s$:

$$Q_s=\frac{0.631}{\pi a_0{}^2}\ \frac{\lambda^5\delta^7}{\mu^{14}}\ \frac{1}{k^2}\left[\log\frac{A_0}{B_0}-\log\frac{A}{B}-\sum c_n\mu^{2n}-\frac{16}{25}c_8\mu^{16}-\frac{64}{25}c_9\mu^{18}\right]\times\left\{\begin{array}{l}\frac{1}{2}\ (\mathrm{P})\\ \frac{1}{6}\ (\mathrm{A}),\end{array}\right. \tag{13}$$

where radial were functions for $2p$ and $3s$ electrons are assumed to be

$$R_{2p\sigma}=\frac{1}{\sqrt{N}}r\exp\left(-\frac{\lambda}{2}r\right)$$
$$R_{3s}=\frac{1}{\sqrt{N'}}r^2\exp\left(-\frac{\delta}{3}r\right), \qquad \mu=\frac{\lambda}{2}+\frac{\delta}{3},$$

and

$$k^2=8\pi^2mE/h^2, \quad k'^2=8\pi^2m(E-E_e)/h^2,$$
$$A_0=(k+k')^2, \qquad A=(k+k')^2+\mu^2,$$
$$B_0=(k-k')^2, \qquad B=(k-k')^2+\mu^2,$$
$$c_n=\frac{1}{n}\left(\frac{1}{B^n}-\frac{1}{A^n}\right), \qquad (n=1,\ 2,\ldots\ldots 9),$$

E: energy of the impinging electron,
E_e: excitation potential (10 eV by experiment[12]),
a_0: Bohr radius of hydrogen atom.

And further $P(A)$ means a state in which orientation of spins of 1s electron of both H atoms is parallel (antiparallel). According to Slater[16] we take the values of $2.275/a_0$ and $0.583/a_0$ for $\lambda/2$ and $\delta/3$, respectively, and compute Q_p and Q_s as shown in Fig. 4, where they are suitably adjusted with experiment[16] at 100 eV. As seen from the figure, Q_s is the same order of magnitude as Q_p but shows more good agreement with

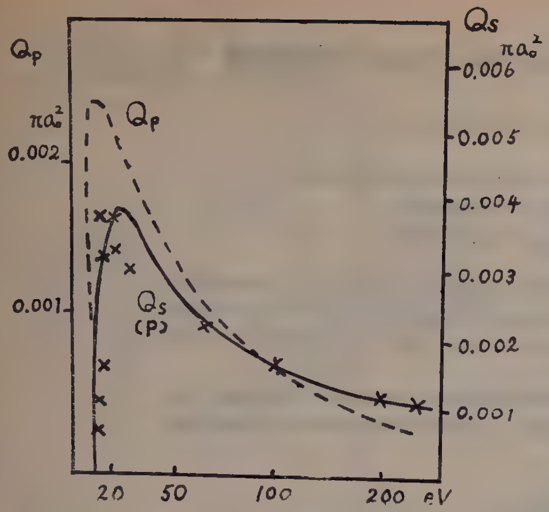

Fig. 4. Excitation cross section of H_2O by electron impact.

Crosses are observed value for the relative intensity of OH $^2\Sigma^+-^2\Pi$, 0−0 band[17].

the experiment in the asymptotic behavior at large electron energy.

§ 5. Concluding Remark

In the both interpretation by AO and MO methods we have concluded that a singlet excited state gives OH radicals of $J=5$ and a triplet gives abnormal rotation of OH radicals of $J=20$. Therefore, it is anticipated that if we operate under the condition of impinging electrons of specified energies the intensity of abnormally rotational lines ($J\sim20$) should be diminished at large energies of electrons, and it would be never observed by collision of protons. The experiments for the former effect were performed by Ninomiya[6] and Horie et al.[3], independently; Ninomiya obesrved no indication for it, while Horie et al. supported our interpretation. It might be possible that in Ninomiya's experiment excitation of OH radicals after transitions into the ground state also took place. The experiment for the canal ray impact made at the Horie laboratory shows disappearance of the anomalous peak of $J=20$[18].

The author wishes to express his cordial gratitude to Associate Professor T. Horie of the Osaka University, under whose kind guidance this work was commenced, for his useful discussions and incessant encoragement. And the author expresses his sincere thanks to Professors M. Kotani and T. Inui and Dr. M. Ninomiya of the Tokyo University for their kind discussions and useful suggestions on this matter and their encouragement in the course of study. Thanks are also due to Dr. K. E. Shuler of the Johns Hopkins University for his adequate advice and kind communication and to Professor G. Araki of the Kyoto University for his helpful remark.

This wark is indebted to the Ministry of Education for its research grant.

References

1) T. Horie: J. Phys. Soc. Japan. **1** (1946) 6.

2) E. R. Lyman: Phys. Rev. **53** (1938) 379; **56** (1939) 466.

3) T. Horie, T. Nagura and Y. Honda: Busseiron Kenkyu **23** (1950) 18 (in Japanese); J. Phys. Soc. Japan, in press.

4) K. F. Bonhoeffer and T. G. Pearson: ZS. f. phys. Chemie **14** (1931) 1.
O. Oldenberg: Phys. Rev. **46** (1934) 210.
H. Wakesima: Proc. Phys.-Math. Soc. Japan **24** (1942) 267; J. Phys. Soc. Japan **2** (1947) 12.

5) O. Oldenberg: l. c.

6) M. Ninomiya: J. Phys. Soc. Japan **4** (1949) 275.

7) R. S. Mulliken: Phys. Rev. **43** (1933) 279.
H. Sponer and E. Teller: Rev. Mod. Phys. **13** (1941) 75.

8) J. R. Stehn: J. Chem. Phys. **5** (1937) 186.
G. W. King: ibid. **6** (1938) 378.

9) E. U. Condon and G. H. Shortley: *The Theory of Atomic Spectra* (Cambridge Univ. Press, 1935) p. 300.

10) J. H. Van Vleck and P. C. Cross: J. Chem. Phys. **1** (1933) 357. A similar calculation for CH_2 has been made by M. Kotani: *Quantum Chemistry* (Kyoritsu Sha, Tokyo, 1939) Section 12 (in Japanese).

11) H. Eyring, S. Glasstone and K. J. Laidler: *The Theory of Rate Process* (Mc Graw Hill, New York, 1941) p. 82.

12) G. Hayakawa: Private communication.

13) R. S. Mulliken: J. Chem. Phys. **3** (1935) 506, 586.

14) M. G. Mayer and A. L. Sklar: ibid. **6** (1938) 645.

15) K. Niira: J. Phys. Soc. Japan **4** (1949) 230.

16) J. C. Slater: Phys. Rev. **38** (1930) 57.

17) G. Hayakawa: Proc. Phys.-Math. Soc. Japan **26** (1944) 78.

18) T. Horie and M. Outsuka: J. Phys. Soc. Japan, in press.

JOURNAL OF THE PHYSICAL SOCIETY OF JAPAN Vol. 7. No. 2. MAR.—APR. 1952

On the Shock Wave in the Elastic Medium

By Ken-ichi KUSUKAWA

Physical Institute, Faculty of Science, Tokyo
Metropolitan University

(Received March 5, 1951)

As the result of the four conservation laws i. e. those of the conservation of mass, momentum, energy and the area of the section of the tube of flow, we have obtained following conclusions for the shock wave induced in the elastic medium.

1. When the wedge moved with the supersonic speed z, the angle between the shock wave and the direction of undisturbed velocity denoted by α is

$$\alpha=\mathrm{Sin}^{-1}(\mathrm{M}^{-1})+\theta$$

where $$\theta=\frac{(3\lambda+2\mu)}{(\lambda+2\mu)}\,\frac{\mathrm{M}^4a^2\beta\delta^2}{4C_0(\mathrm{M}^2-1)^{2/3}}\quad\text{and}\quad \mathrm{M}=z/a.$$

a, β, c_0, λ and μ, and δ denote the speed of sound, the coefficient of the linear expansion, the specific heat, Lamé's constants of the elastic medium, and the half vertex angle of the wedge resp..

2. The plane shock wave is reflected by the plane rigid wall. α and α' denoting the angles included between the incident or reflected waves and the wall, we have

$$x'=\frac{\eta x(1+\eta^2x^2)-x(1-\eta^2)\{1+\eta^2x^2(\eta^2-1)\}^{1/2}}{(1+\eta^2x^2)\{1+\eta^2x^2(\eta^2-1)\}^{1/2}+\eta x^2(1-\eta^2)},$$

where $x=\tan\alpha$ $x'=\tan\alpha'$, and $(1-\eta^2)$ represents the strength of shock.

§1. The Growth and the Existence of the Shock Wave

It is well known that the reason of the growth of the shock wave in the compressible fluid by the finite compression lies in the non-linear character of the equation of motion. Precisely saying, the stable shock wave grows because the propagating velocity of infinitesimal disturbances (or velocity of sound), denoted by $\sqrt{\gamma p/\rho}$, increases by an adiabatic compression.

In the elastic medium, on the other hand the stable shock wave will not grow by compressing the medium, because the propagating velocity of the sound, denoted by $\sqrt{\lambda+2\mu/\rho}$, rather decreases by an adiabatic compression.

The shock wave, however, exists stably, when the disturbances are given continuously by supersonic velocities, on which I discussed in my papers (1) and (2).

§2. Interaction of the Shock Wave and the Rigid Wall in the First Approximation

We shall consider the interaction of the rigid wall and the shock wave, which is grown up by such a thin wedge with super-sonic velocities as one discussed in the paper (1). Indeed we must consider this effect, when the wedge moves throgh the elastic medium surrounded by the plane rigid wall.

We have obtained the following results from the discussion of the paper (1). When the vertex angle of the wedge is very small, and strains are sufficiently small, and then we neglect the quantity of heat grown up by the compression in comparison with the variation of the elastic energy, the angle α included between the plane shock wave and the direction of the flow in front of it, can be represented by

$$\alpha=\mathrm{Sin}^{-1}(1/\mathrm{M})=\mathrm{Sin}^{-1}(a/z)\qquad(2,1)$$

where a, z and M are the speed of sound, the speed of flow, and Mach's number in front of the shock wave resp.. (cf. Fig. 1).

Now, we shall discuss the reflection of the shock wave by the plane rigid wall. It is convenient to take the coordinates fixed with respect to the shock wave. We shall presume the flow pattern shown in Fig. 2, where I and R denote the incident and the reflected plane shock wave resp., α and α' denote the angles

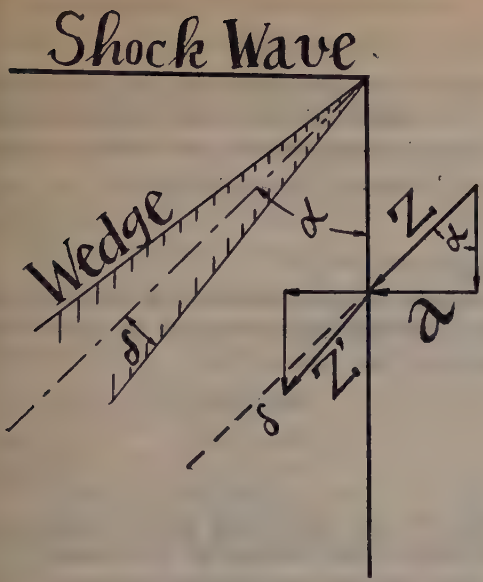

Fig. 1

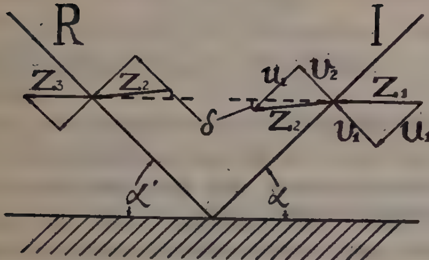

Rigid Wall
Fig. 2

included between them and the rigid wall resp., δ denotes the angle of deflection of the flow, and suffixes, 1, 2, and 3 represent the physical quantities of the flow in front of, or behind the incident wave and behind the reflected wave resp.. The x-and y-axes are both in the plane of incidence, and while x-axis is in the plane of shock wave, the y-axis is orthogonal to it. The z-axis is orthogonal to the plane of incidence. u, v and w denoting the components of the velocity, ρ, ε, γ, and a denote the density, the normal strains, the shearing strains, and the speed of sound resp., and λ and μ denote the Lamé's constants.

We have the following formulae from the conservation of momentum:

$$\rho_1 v_1(v_2-v_1)=(\lambda+2\mu)(\varepsilon_{y_2}-\varepsilon_{y_1}), \qquad (2,\ 2)$$

$$\rho_1 v_1(u_2-u_1)=0. \qquad (2,\ 3)$$

From (2, 1) reducing $a_1=v_1$, and considering $a_1=\sqrt{\lambda+2\mu/\rho_1}$, we obtain

$$\tan(\alpha-\delta)=\tan\alpha(1+\varepsilon_{y_2}-\varepsilon_{y_1}). \qquad (2,\ 4)$$

Considering the reflected shock wave, we have

$$\begin{aligned} z_2\sin(\alpha'+\delta)&=v_2\sin(\alpha'+\delta)/\sin(\alpha-\delta)\\ &=\sin(\alpha'+\delta)\cdot a_1(1+\varepsilon_{y_2}-\varepsilon_{y_1})/\sin(\alpha-\delta)\\ &=a_2 \end{aligned} \qquad (2,\ 5)$$

As we have the following relation from the conservation of mass

$$\rho_1 v_1=\rho_2 v_2, \qquad (2,\ 6)$$

we obtain

$$\rho_2=\rho_1/(1+\varepsilon_{y_2}-\varepsilon_{y_1}),$$

or $$a_2=a_1\sqrt{1+\varepsilon_{y_2}-\varepsilon_{y_1}}. \qquad (2,\ 7)$$

From (2, 5) and (2, 7), we have

$$\sin(\alpha'+\delta)=\sin(\alpha-\delta)/(1+\varepsilon_{y_2}-\varepsilon_{y_1})^{1/2}. \qquad (2,\ 8)$$

Considering the formulae (2, 4) and (2, 8), we obtain the following solution

$$x'=\frac{\eta x(1+\eta^2x^2)-x(1-\eta^2)\{1+\eta^2x^2(\eta^2-1)\}^{1/2}}{(1+\eta^2x^2)\{1+\eta^2x^2(\eta^2-1)\}^{1/2}+\eta x^2(1-\eta^2)}, \qquad (2,\ 9)$$

where $\eta=(1+\varepsilon_{y_2}-\varepsilon_{y_1})^{1/2}$, $x=\tan\alpha$ and $x'=\tan\alpha'$.

Some solutions of (2, 9) with respect to given values of $\varepsilon_{y_2}-\varepsilon_{y_1}$, are tabulated in Table 1.

Table 1

$\varepsilon_{y_2}-\varepsilon_{y_1}=-0.0020$			$\varepsilon_{y_2}-\varepsilon_{y_1}=-0.0905$		
α	α'	δ	α	α'	δ
5°	4°59′ 8″	0°0′35″	5°	4°19′15″	0°27′ 1″
10°	9°58′16″	0°1′10″	10°	8°40′ 9″	0°53′19″
26°	10°56′52″	0°2′11″	20°	17°33′27″	1°40′59″
30°	29°56′ 4″	0°2′56″	30°	26°52′52″	2°17′42″
40°	39°56′ 6″	0°3′22″	40°	36°51′22″	2°38′58″
50°	49°57′23″	0°3′21″	50°	47°43′25″	2°41′35″
00°	60° 0′ 4″	0°2′48″	60°	59°52′36″	2°24′24″
70°	70° 4′48″	0°2′12″	70°	74°58′24″	1°48′36″
80°	80°17′20″	0°1′10″	73°59′50″	88°30′ 5″	1°29′55″
85°	85°39′24″	0°0′35″			
87°30′12″	89°59′42″	0°0′18″			
$\varepsilon_{y_2}-\varepsilon_{y_1}=-0.1786$			$\varepsilon_{y_2}-\varepsilon_{y_1}=-0.2887$		
α	α'	δ	α	α'	δ
5°	3°38′47″	0°53′23″	5°	2°47′ 5″	1°26′20″
10°	7°20′26″	1°45′33″	10°	5°38′ 3″	2°51′ 4″
20°	15° 4′ 7″	3°21′20″	20°	11°48′10″	5°29′ 6″
30°	23°35′ 8″	4°37′44″	30°	19° 5′54″	7°40′23″
40°	33°20′29″	5°25′31″	40°	28°15′10″	9°10′ 8″
50°	44°54′31″	5°36′41″	50°	40°20′51″	9°42′41″
60°	59° 8′ 7″	5° 6′13″	60°	57°56′53″	9° 3′55″
65°	69° 3′56″	4°35′ 4″	65°37′12″	81°52′40″	8° 7′20″
69°2′35″	85°57′27″	4° 2′33″			

α and α' are the angle of incidence and reflection resp., and δ is the angle of deflection of the flow.

As the formula (2, 9) has the real solution only within the following condition:

$$\alpha\leqq\alpha_c=\tan^{-1}\{\eta^{-1}(1-\eta^2)^{-1/2}\}, \qquad (2,\ 10)$$

there can not exist the interaction shown in Fig. 2, for α which is larger than α_e. The relations of $\varepsilon_{y_2}-\varepsilon_{y_1}$ and α_e are shown in Table 2.

Table 2.

$-(\varepsilon_{y_2}-y_1)$	α_e	$-(\varepsilon_{y_2}-\varepsilon_{y_1})$	α_c
0.0020	87°30′12″	0.1786	69° 2′35″
0.0076	85° 2′21″	0.2132	67°43′33″
0.0171	82°37′37″	0.2500	66°35′14″
0.0302	80°17′47″	0.2887	65°37′12″
0.0468	78° 4′ 8″	0.3289	64 50′ 9″
0.0670	75°57′50″	0.3705	64°13′ 9″
0.0905	73°59′50″	0.4132	63°47′ 4″
0.1170	72°10′57″	0.4564	63°31′19″
0.1464	70°31′36″	0.5000	63°26′ 6″

$\varepsilon_{y_2}-\varepsilon_{y_1}$ is the difference of the strains, and α_e is the extreme angle of incidence.

It is remarkable that α' may become negative for

$$\eta<\eta_e=(\sqrt{5}-1)/2=0.61803. \quad (2, 11)$$

The solution of (2, 9) which is correct only for very small strains, has no physical meaning in this range.

Naturally the coefficients of friction of the wedge's and the rigid wall's surfaces must take some suitable values for the purpose of existence of these flow patterns. (cf. (1))

§ 3. Rigorous Theory of Shock Wave

We shall discuss the plane shock wave rigorously in this paragraph, though in papers (1) and (2) the higher order terms of the strains and the quantity of heat grown up by compression are neglected.

β and T denote the coefficient of linear expansion and the absolute temperature resp., and the coordinates and other notations are same with those with respect to incident shock wave in § 2.

From the conservation of mass, we have

$$\rho_1 v_1=\rho_2 v_2=m, \quad (3, 1)$$

when the irrotational motion is assumed, from the conservation of momentum, we have

$$m(v_2-v_1)=(\lambda+2\mu)(\varepsilon_{y_2}-\varepsilon_{y_1})+\lambda(\varepsilon_{x_2}-\varepsilon_{x_1})$$
$$+\lambda(\varepsilon_{z_2}-\varepsilon_{z_1}) \quad (3, 2)$$

$$u_1=u_2 \quad (3, 3)$$

$$w_1=w_2, \quad (3, 4)$$

$$\gamma_{zy_2}=\gamma_{zy_1}, \quad (3, 5)$$

$$\gamma_{xy_2}=\gamma_{xy_1}. \quad (3, 6)$$

And from the conservation of energy we have,

$$\{m(v_2^2-v_1^2)/2\}+v_2U_2-v_1U_1=(\lambda+2\mu)$$
$$\times(\varepsilon_{y_2}v_2-\varepsilon_{y_1}v_1)+\lambda(\varepsilon_{x_2}v_2-\varepsilon_{x_1}v_1)$$
$$+\lambda(\varepsilon_{z_2}v_2-\varepsilon_{z_1}v_1) \quad (3, 7)$$

where U is the internal energy per unit volume.

The relation of the density and the specific volume is represented by the following form:

$$\rho_2(1+3\beta t+\varepsilon_{x_2}+\varepsilon_{y_2}+\varepsilon_{z_2})=\rho_1(1+\varepsilon_{x_1}+\varepsilon_{y_1}+\varepsilon_{z_1}), \quad (3, 8)$$

where $t=T_2-T_1$.

Finally we have the following relations from the continuity of the shape and the area of the section of the tube of flow:

$$\beta t+\varepsilon_{x_2}=\varepsilon_{x_1} \quad (3, 9)$$

$$\beta t+\varepsilon_{z_2}=\varepsilon_{z_1}, \quad (3, 10)$$

$$\gamma_{xz_2}=\gamma_{xz_1}. \quad (3, 11)$$

Thus we can solve these eleven equations, if the form of the function of U is known.

Now, the first law of thermodynamics in this case is

$$d'Q=dU+dA,$$

where

$$-dA=\sigma_x d(\varepsilon_x+\beta t)+\sigma_y d(\varepsilon_y+\beta t)$$
$$+\sigma_z d(\varepsilon_z+\beta t)+\tau_{yz}d\gamma_{zx}+\tau_{zx}d\gamma_{zx}+\tau_{xy}d\gamma_{xy} \quad (3, 12)$$

In this formula, Q and A denote the quantity of heat given by the surrounding system to the considered system, and the work done by the considered elasitic system to the surrounding system resp., σ and τ denote normal and shearing stresses resp., and t is equal to $T-T_1$.

The internal energy being the function of ε, γ, and t, dU is represented in the following perfect differntial form.

$$dU=(\partial U/\partial t)dt+\sum(\partial U/\partial\varepsilon)d\varepsilon$$
$$+\sum(\partial U/\partial\gamma)d\gamma \quad (3, 13)$$

When all stresses vanish, (3, 12) becomes

$$d'Q=(\partial U/\partial t)dt,$$

therefore

$$d'Q/dt=\partial U/\partial t=c_0\rho_0, \quad (3, 14)$$

where c_0 and ρ_0 are the specific heat and the density in the case where ε, γ, σ, τ and t vanish.

From (3, 14) we have

$$U=c_0\rho_0 t+F(\varepsilon, \gamma). \quad (3, 15)$$

Considering (3, 15), (3, 12) becomes the following form when the process is isothermal or $dt=0$.

$$d'Q=\sum(\partial F/\partial\varepsilon-\sigma)d\varepsilon+\sum(\partial F/\partial\gamma-\tau)d\gamma, \quad (3, 16)$$

If the considered system is perfect elastic, and has no internal friction, $d'Q$ vanishes for arbitrary $d\varepsilon$ and $d\gamma$. Therefore we have

$$\partial F/\partial\varepsilon=\sigma,\quad \partial F/\partial\gamma=\tau. \qquad (3,\ 17)$$

From (3, 16) and (3, 17), the internal energy may be represented in the following form

$$U=c_0\rho_0 t+\lambda\{(\varepsilon_x+\varepsilon_y+\varepsilon_z)^2/2+\mu\{\varepsilon_x{}^2+\varepsilon_y{}^2+\varepsilon_z{}^2 +(\gamma^2{}_{yz}+\gamma^2{}_{zx}+\gamma^2{}_{xy})/2\}. \qquad (3,\ 18)$$

Substituting (3, 18) into (3, 12), we have

$$d'Q=\{c_0\rho_0-\beta(3\lambda+2\mu)(\varepsilon_x+\varepsilon_y+\varepsilon_z)_{t=0}\}dt$$

Putting $c_0\rho_0-\beta(3\lambda+2\mu)(\varepsilon_x+\varepsilon_y+\varepsilon_z)_{t=0}=c_\varepsilon\rho_0$, we obtain the variation of the entropy in the following form

$$dS=\frac{d'Q}{T}=\frac{c_\varepsilon\rho_0}{T_1+t}dt. \qquad (3,\ 19)$$

Integrating (3, 19), we have

$$S_t-S_1=c_\varepsilon\rho_0\log\{(T_1+t)/T_1\} \qquad (3,\ 20)$$

where we know experimentally for c_ε to be positive.

In the case where ε_{x_1}, ε_{y_1}, ε_{z_1}, γ_{yz_1}, γ_{zx_1}, and γ_{xy1} all vanish, we have the following equation from the above described formulae;

$$F(x)=Ax^2-(A+B+C)x+B=0, \qquad (3,\ 21)$$

where $A=(3\lambda+2\mu)^{-2}[(\lambda/2)\{(3\lambda+6\mu)s^2-4\mu\}^2 +2\mu(\lambda+2\mu)^2(1-s^2)^2+\mu\{(\lambda+2\mu)s^2 +2\lambda\}^2]$,

$B=\rho_1 a_1{}^2 s^2/2$,

$C=\{(\lambda+2\mu)/(3\lambda+2\mu)\}(c_0\rho_1/\beta)(s^2-1)$,

and $x=v_2/v_1$ and $s=v_1/a_1$.

And the variation of the entropy becomes

$$S_t-S_0=c_0\rho_0\log\{(T_1+t)/T_1\}, \qquad (3,\ 22)$$

where $t=\left(\dfrac{\lambda+2\mu}{3\lambda+2\mu}\right)(v_2-v_1)\{1-(v_1/a_1)^2\}/\beta v_1$.

As v_1 is larger than a_1 because the shock wave grows only in the super-sonic flow, and S_t-S_0 has to be positive because the considered process is adiabatic, v_2 must be smaller than v_1.

Indeed, we have the following results from the equation (3, 21)

$$F(+\infty)\to+\infty,\ F(1)=\left(\frac{\lambda+2\mu}{3\lambda+2\mu}\right)c_0\rho_1(1-s^2)/\beta<0,$$

and $F(0)=\rho_1 v_1{}^2/2>0$.

Therefore (3, 21) having the real roots x_1 $(0<x_1<1)$, and $x_2(1<x_2<+\infty)$ only x_1 is the solution with physical meaning.

§4. Solution about the Thin Wedge in the Second Approximation.

α and δ denoting the angle included between the shock wave and the direction of undisturbed velocity, and the half vertex angle of the wedge resp., other notations are equal to those of §3.

From the geometrical condition we have

$$\tan(\alpha-\delta)/\tan\alpha=v_2/v_1=x.$$

Considering the case of small δ, we shall put the following form

$$x=1-\xi=1-\delta/\sin\alpha\cos\alpha, \qquad (4,\ 1)$$

and $$s=v_1/a_1=1+\eta, \qquad (4,\ 2)$$

where ξ and η are infinitesimal quantities.

Substituting (4, 1) and (4, 2) into (3, 21), we obtain

$$\xi=\{(\lambda+2\mu)/(3\lambda+2\mu)\}^{1/2}(2/a_1)(c_0/\beta)^{1/2}\eta^{1/2}, \qquad (4,\ 3)$$

where $\eta=s-1=M\sin\alpha-1$, and $M=z_1/a_1$.

From (4, 3), we can calculate the angle α, in the following form:

$$\alpha=\sin^{-1}(M^{-1})+\theta, \qquad (4,\ 4)$$

where $$\theta=\left(\frac{3\lambda+2\mu}{\lambda+2\mu}\right)\frac{M^4 a_1{}^2\beta\delta^2}{4c_0(M^2-1)^{3/2}}$$

This result is more rigorous than that of paper (1), where α is reduced to be $\sin^{-1}(M^{-1})$.

Finally, I thank heartily Prof. I. Imai for his useful suggestions.

References

1) K. Kusukawa: Journ. Phys. Soc. Jap. **6**(1951) 163—165.

2) K. Kusukawa: Journ. Phys. Soc. Jap. **6**(1951) 166—167.

JOURNAL OF THE PHYSICAL SOCIETY OF JAPAN Vol. 7, No. 2. MAR.—APR., 1952

On the Propagation of Elastic Waves in an Isotropic Homogeneous Sphere

By Yûkichi NOMURA and Kôshun TAKAKU

Department of Applied Science, Faculty of Engineering
Tôhoku University
Department of Arts and Science, Fukushima University

(Received June 18, 1951)

In this paper the elastic waves propagating in a large homogeneous spherical medium are calculated. The results are convenient for a further discussion owing to their very clear and simple form, in which the laws of geometrical optics are contained. Various modes of reflection are considered and the intensity of reflected waves relative to the primary is calculated numerically.

§ 1. Introduction

The theory of propagation of elastic waves in the isotropic homogeneous sphere is very important, as it is related with that of the seismic waves. One of the present authors has already given an extensive discussion[1] about it. The primary waves from a source and various reflected once at the spherical surface are superposed together, so that the resultant waves become much complicated. He discussed about the resultant waves, and calculated approximately when the source and the observer were both on the spherical surface, and found that not only the surface wave (Rayleigh wave) but also P-wave (irrotational wave) and S-wave (distortional wave) propagate along the surface with their own velocities.

In the actual observation of the seismic wave, however, the main object of discussion is not the resultant wave, but the primary wave from the source and once or twice reflected one. Therefore it is more essential to discuss each component wave separately in stead of the resultant wave.

We shall discuss here how the spherical wave from a source is reflected many times at a free spherical surface. For simplicity the source is assumed to oscillate with no diminution. Then the amplitude of the resultant wave would become infinite if there were no viscosity in the medium. But the diminution due to the viscosity will become remarkable only after many reflections, so the viscosity may be neglected, as far as only the primary wave and once or twice reflected ones are concerned.

§ 2. The Equations of Motion

Using the polar coordinates r, θ, φ and denoting the components of displacement by $\bar{u}$, $\bar{v}$, $\bar{w}$ respectively, the general equations of motion of an elastic body are as follows;

$$\left.\begin{aligned}
\rho\frac{\partial^2\bar{u}}{\partial t^2}&=(\lambda+2\mu)\frac{\partial\bar{\varDelta}}{\partial r}-2\mu\frac{1}{r\sin\theta}\frac{\partial(\bar{\omega}_\varphi\sin\theta)}{\partial\theta},\\
\rho\frac{\partial^2\bar{v}}{\partial t^2}&=(\lambda+2\mu)\frac{1}{r}\frac{\partial\bar{\varDelta}}{\partial\theta}+2\mu\frac{1}{r}\frac{\partial(r\,\bar{\omega}_\varphi)}{\partial r},\\
\rho\frac{\partial^2\bar{w}}{\partial t^2}&=-2\mu\left\{\frac{1}{r}\frac{\partial(r\,\bar{\omega}_\theta)}{\partial r}-\frac{1}{r}\frac{\partial\bar{\omega}_r}{\partial\theta}\right\},
\end{aligned}\right\}\tag{1}$$

where ρ is constant density, λ, μ are Lame's constants and

$$\left.\begin{aligned}
\bar{\varDelta}&=\frac{1}{r^2\sin\theta}\left\{\frac{\partial(\bar{u}r^2\sin\theta)}{\partial r}+\frac{\partial(\bar{v}r\sin\theta)}{\partial\theta}\right\},\\
2\bar{\omega}_r&=\frac{1}{r^2\sin\theta}\frac{\partial(\bar{w}\,r\sin\theta)}{\partial\theta},\\
2\bar{\omega}_\theta&=-\frac{1}{r\sin\theta}\frac{\partial(\bar{w}\,r\sin\theta)}{\partial r},\\
2\bar{\omega}_\phi&=\frac{1}{r}\left\{\frac{\partial(r\,\bar{v})}{\partial r}-\frac{\partial\bar{u}}{\partial\theta}\right\}.
\end{aligned}\right\}\tag{2}$$

If $\bar{u}$, $\bar{v}$, $\bar{w}$ are eliminated from (1), (2), we get

$$\left.\begin{aligned}
\rho\frac{\partial^2\bar{\varDelta}}{\partial t^2}&=\lambda+2\mu\left\{\frac{\partial^2\bar{\varDelta}}{\partial r^2}+\frac{1}{r}\frac{\partial\bar{\varDelta}}{\partial r}\right.\\
&\qquad\left.+\frac{1}{r^2\sin\theta}\frac{\partial}{\partial\theta}\left(\sin\theta\frac{\partial\bar{\varDelta}}{\partial\theta}\right)\right\},\\
\rho\frac{\partial^2\bar{\omega}_r}{\partial t^2}&=\mu\left\{\frac{\partial^2\bar{\omega}_r}{\partial r^2}+\frac{4}{r}\frac{\partial\bar{\omega}_r}{\partial r}+\frac{2}{r^2}\bar{\omega}_r\right.\\
&\qquad\left.+\frac{1}{r^2\sin\theta}\frac{\partial}{\partial\theta}\left(\sin\theta\frac{\partial\bar{\omega}_r}{\partial\theta}\right)\right\},
\end{aligned}\right.$$

$$\left.\begin{aligned}
&\rho\frac{\partial^2\overline{\omega}_\theta}{\partial t^2}=\mu\left\{\frac{1}{r}\,\frac{\partial^2(r\,\overline{\omega}_\theta)}{\partial r^2}-\frac{1}{r}\,\frac{\partial^2\overline{\omega}_r}{\partial r\partial\theta}\right\},\\
&\rho\frac{\partial^2\overline{\omega}_\varphi}{\partial t^2}=\mu\left\{\frac{\partial^2\overline{\omega}_\varphi}{\partial r^2}+\frac{2}{r}\,\frac{\partial\overline{\omega}_\varphi}{\partial r}\right.\\
&\qquad\left.+\frac{1}{r}\,\frac{\partial}{\partial\theta}\left[\frac{1}{\sin\theta}\,\frac{\partial}{\partial\theta}(\sin\theta\,\overline{\omega}_\varphi)\right]\right\}.
\end{aligned}\right\}\qquad(3)$$

When the motion is simple harmonic;

$$\overline{\Delta}=\Delta e^{-i\sigma t},\ \overline{\omega}_r=\omega_r e^{-i\sigma t},\ \overline{\omega}_\theta=\omega_\theta\,e^{-i\sigma t},$$
$$\overline{\omega}_\varphi=\omega_\varphi\,e^{-i\sigma t},$$

where Δ, ω_r, ω_θ, ω_φ without bar are independent of time t, and are functions of r, θ, φ only. For simplicity these functions are assumed to depend on r, θ only, then equations (3) become,

$$\left.\begin{aligned}
&\frac{\partial^2\Delta}{\partial r^2}+\frac{2}{r}\,\frac{\partial\Delta}{\partial r}+\frac{1}{r^2\sin\theta}\,\frac{\partial}{\partial\theta}\left(\sin\theta\frac{\partial\Delta}{\partial\theta}\right)\\
&\qquad+h^2\Delta=0,\\
&\frac{\partial^2\omega_r}{\partial r^2}+\frac{4}{r}\,\frac{\partial\omega_r}{\partial r}+\frac{2}{r^2}\omega_r\\
&\qquad+\frac{1}{r^2\sin\theta}\frac{\partial}{\partial\theta}\left(\sin\theta\frac{\partial\omega_r}{\partial\theta}\right)+k^2\omega_r=0,\\
&\frac{\partial^2\omega_\theta}{\partial r^2}+\frac{2}{r}\,\frac{\partial\omega_\theta}{\partial r}-\frac{1}{r}\,\frac{\partial^2\omega_\theta}{\partial r\partial\theta}+k^2\omega_\theta=0,\\
&\frac{\partial^2\omega_\varphi}{\partial r^2}+\frac{2}{r}\,\frac{\partial\omega_\varphi}{\partial r}+\frac{1}{r^2}\,\frac{\partial}{\partial\theta}\left(\frac{1}{\sin\theta}\,\frac{\partial(\omega_\varphi\sin\theta)}{\partial\theta}\right)\\
&\qquad+k^2\omega_\varphi=0,
\end{aligned}\right\}$$
$$(4)$$

where

$$h=\sqrt{\frac{\rho}{\lambda+2\mu}}\,\sigma,\qquad k=\sqrt{\frac{\rho}{\mu}}\,\sigma.\qquad(5)$$

Further putting $\omega_r=\omega_\theta=0$, the first and fourth equations of (4) are satisfied by

$$\zeta_n^{(i)}(hr)\,P_n(\cos\theta),\ \zeta_n^{(i)}(kr)\frac{d\,P_n(\cos\theta)}{d\theta},$$
$$(i=1,\ 2)$$

respectively, where $\zeta_n^{(i)}(x)=\sqrt{\dfrac{\pi}{2x}}H_{n+\frac{1}{2}}^{(i)}(x)$ and the terms with $\zeta_n^{(1)}(hr)$ or $\zeta_n^{(1)}(kr)$ mean diverging spherical wave from the center of the sphere, while $\zeta_n^{(2)}(hr)$, $\zeta_n^{(2)}(kr)$ correspond to converging spherical waves.

§ 3. Coefficients of Reflection

When the diverging P-wave

$$\Delta^{(d)}=\zeta_n^{(1)}(hr)\,P_n(\cos\theta)\qquad(6)$$

is reflected at the spherical surface $r=a$, there arise converging P- and S-waves;

$$\Delta_p^{(c)}=F_n\frac{\zeta_n^{(1)}(ha)}{\zeta_n^{(2)}(ha)}\zeta_n^{(2)}(hr)\,P_n(\cos\theta),\qquad(7)$$

$$2\omega_p^{(c)}=\frac{G_n}{\zeta_n^{(2)}(ha)\,\zeta_n^{(2)}(ka)}\zeta_n^{(2)}(kr)\frac{dP_n(\cos\theta)}{d\theta}$$

where F_n and G_n are constant coefficients of reflection. Displacements of the waves (6) and (7) have components

$$\left.\begin{aligned}
&u_p^{(d)}=-\frac{1}{h}\zeta_n^{(1)\prime}(hr)P_n(\cos\theta),\\
&v_p^{(d)}=-\frac{1}{h^2r}\zeta_n^{(1)}(hr)\frac{dP_n(\cos\theta)}{d\theta},\\
&w_p^{(d)}=0,
\end{aligned}\right\}\qquad(8)$$

and

$$\left.\begin{aligned}
&u_p^{(c)}=-\left\{\frac{1}{h}F_n\frac{\zeta_n^{(1)}(ha)}{\zeta_n^{(2)}(ha)}\zeta_n^{(2)\prime}(hr)\right.\\
&\qquad\left.+\frac{n(n+1)}{k^2r}\,\frac{G_n}{\zeta_n^{(2)}(ha)\zeta_n^{(2)}(ka)}\zeta_n^{(2)}(kr)\right\}\\
&\qquad\qquad\cdot P_n(\cos\theta),\\
&v_p^{(c)}=-\left\{\frac{F_n}{h^2r}\,\frac{\zeta_n^{(1)}(ha)}{\zeta_n^{(2)}(ha)}\zeta_n^{(2)}(hr)\right.\\
&\qquad\left.+\frac{1}{k^2r}\cdot\frac{G_n}{\zeta_n^{(2)}(ha)\zeta_n^{(2)}(ka)}\,\frac{d}{dr}[r\zeta_n^{(2)}(kr)]\right\}\\
&\qquad\qquad\cdot\frac{dP_n(\cos\theta)}{d\theta},\\
&\omega_p^{(c)}=0,
\end{aligned}\right\}$$
$$(2)$$

respectively. Putting $u_p=u_p^{(d)}+u_p^{(c)}$, $v_p=v_p^{(d)}+v_p^{(c)}$, $\Delta=\Delta_p^{(d)}+\Delta_p^{(c)}$, and substituting them into the boundary conditions of the free spherical surface;

$$\left.\begin{aligned}
&\lambda\Delta+2\mu\frac{\partial u}{\partial r}=0,\\
&\frac{\partial v}{\partial r}-\frac{v}{r}+\frac{1}{r}\,\frac{\partial u}{\partial\theta}=0,
\end{aligned}\right\}\qquad(10)$$

we get

$$F_n=A_n/B_n,\qquad(11)$$
$$G_n=(ik^2/k^2a\ \{k^2a^2-2(n+1)(n-2)\}/B_n,$$
$$(12)$$

where

$$\begin{aligned}
A_n=&\,n(n+1)\{f_n^{(2)}(ha)-1\}\{f_n^{(1)}(ha)-1\}\\
&-\{2f_n^{(1)}(ha)+k^2a^2/2-n(n+1)\}\\
&\qquad\{f_n^{(2)}(ka)+k^2a^2/2-n(n+1)+1\},\\
B_n=&-n(n+1)\{f_n^{(2)}(ha)-1\}\{f_n^{(2)}(ka)-1\}\\
&+\{2f_n^{(2)}(ha)+k^2a^2/2-n(n+1)\}\\
&\qquad\{f_n^{(2)}(ka)+k^2a^2/2-n(n+1)+1\},
\end{aligned}$$

with $f_n^{(i)}(x)=x\zeta_n^{(i)\prime}(x)/\zeta_n^{(i)}(x)$.

Similarly, when the diverging S-wave

$$\omega^{(d)}=\frac{1}{2}\zeta_n^{(1)}(kr)\frac{dP_n(\cos\theta)}{d\theta}\qquad(13)$$

is reflected at the surface $r=a$, converging P- and S-waves:

$$\left.\begin{aligned}\Delta_s^{(\sigma)}&=\frac{M_n\zeta_n^{(2)}(hr)}{\zeta_n^{(2)}(ha)\zeta_n^{(2)}(ka)}P_n(\cos\theta),\\ \omega_s^{(\sigma)}&=\frac{N_n}{2}\frac{\zeta_n^{(1)}(ka)}{\zeta_n^{(2)}(ka)}\zeta_n^{(2)}(kr)\frac{dP^u(\cos\theta)}{d\theta}\end{aligned}\right\}\tag{14}$$

are produced where M_n and N_n are the coefficients of reflection, and are given by

$$M_n=ih^2n(n+1)/(k^3a)\{k^2a^2-2(n-1)(n+2)\}/B_n,\tag{15}$$

$$N_n=C_n/B_n,\tag{16}$$

where

$$\begin{aligned}C_n=&-n(n+1)\{f_n^{(1)}(ka)-1\}\{f_n^{(2)}(ha)-1\}\\&+\{2f_n^{(2)}(ha)+k^2a^2/2-n(n+1)\}\\&\cdot\{f_n^{(1)}(ka)+k^2a^2/2-n(n+1)+1\}.\end{aligned}$$

§ 4. Expressions of Reflected Waves

Denoting the primary P-wave from a point source Q $(b,\ 0,\ 0)$ by

$$\bar{\Delta}=-\ h^2R^{-1}\ e^{i(hR-\sigma t)}=\Delta e^{-i\sigma t},\tag{17}$$

where R is the distance between the source and an observing point P $(r,\ \theta,\ 0)$, the function Δ can be expanded into the well-known form,

$$\left.\begin{aligned}\Delta&=-\frac{ih^3}{2}\sum_{n=0}^{\infty}(2n+1)\{\zeta_n^{(1)}(hb)+\zeta_n^{(2)}(hb)\}\zeta_n^{(1)}(hr)\cdot P_n(\cos\theta)\quad r>b,\\&=-\frac{ih^3}{2}\sum_{n=0}^{\infty}(2n+1)\zeta_n^{(1)}(hb)\{\zeta_n^{(1)}(hr)+\zeta_n^{(2)}(hr)\}P_n(\cos\theta)\quad r<b.\end{aligned}\right\}\tag{18}$$

This function splits into two parts

$$\left.\begin{aligned}\Delta_0&=-\frac{ih^3}{2}\sum_0^{\infty}(2n+1)\zeta_n^{(2)}(hb)\zeta_n^{(1)}(hr)\cdot P_n(\cos\theta)\qquad r>b,\\&=-\frac{ih^3}{2}\sum_0^{\infty}(2n+1)\zeta_n^{(1)}(hb)\zeta_n^{(2)}(hr)\cdot P_n(\cos\theta)\qquad r<b.\end{aligned}\right\}\tag{19}$$

$$\Delta_0'=-\frac{ih^3}{2}\sum_0^{\infty}(2n+1)\zeta_n^{(1)}(hb)\zeta_n^{(1)}(hr)\cdot P_n(\cos\theta).\tag{20}$$

When each diverging spherical wave, which constitutes the primary ones Δ_0 and Δ_0', is reflected at the surface $r=a$, then converging P- and S-waves are produced. These are reflected at an infinitesimal rigid sphere assumed to be at the center of the elastic sphere, giving rise to the diverging P- and S-waves which again are reflected at the surface $r=a$, and so on. Applying in each case the results obtained in the previous article, we get: When the primary P-wave Δ_0 makes

$$\left.\begin{aligned}&p\text{ times P}\rightarrow\text{P reflections,}\\&q\text{ times P}\rightarrow\text{S reflections,}\\&r\text{ times S}\rightarrow\text{P reflections,}\\&s\text{ times S}\rightarrow\text{S reflections,}\end{aligned}\right\}\tag{21}$$

where $p+q+r+s=\kappa$, at the surface $r=a$, and the final reflected P- and S-ones $\Delta_{p\kappa}$, $\omega_{p\kappa}$ are given by

$$\begin{aligned}\left.\begin{aligned}\Delta_{p\kappa}\\2\omega_{p\kappa}\end{aligned}\right\}=&-\frac{ih^3}{2}\sum_{n=0}^{\infty}(2n+1)\zeta_n^{(2)}(hb)\\&\cdot\left\{F_n\frac{\zeta_n^{(1)}(ha)}{\zeta_n^{(2)}(ha)}\right\}^p\left\{\frac{G_n}{\zeta_n^{(2)}(ha\,\zeta_n^{(2)}(ka)}\right\}^q\\&\cdot\left\{\frac{M_n}{\zeta_n^{(2)}(ha)\zeta_n^{(2)}(ka)}\right\}^r\left\{N_n\frac{\zeta_n^{(1)}(ka)}{\zeta_n^{(2)}(ka)}\right\}^s\\&\cdot\left\{\begin{aligned}&\zeta_n^{(2)}(hr)P_n(\cos\theta)\\&\zeta_n^{(2)}(kr)dP_n(\cos\theta)/d\theta'\end{aligned}\right.\end{aligned}\tag{22}$$

where the suffix $p\kappa$ means that the primary waves are dilatational, and are reflected κ-times. On the other hand, if the primary is Δ_0', we get similar results as (22), with $\zeta_n^{(2)}(hb)$ replaced by $\zeta_n^{(1)}(hb)$.

If the primary is S-wave

$$\begin{aligned}\bar{\omega}=&-\frac{k^2}{2}\frac{\partial}{\partial\theta}\frac{exp\{ikR-i\sigma t\}}{R}\\&=\omega\,exp\{-i\sigma t\},\end{aligned}\tag{23}$$

then as above

$$\left.\begin{aligned}\omega&=-\frac{ik^3}{4}\sum_0^{\infty}(2n+1)\{\zeta_n^{(1)}(kb)+\zeta_n^{(2)}(kb)\}\cdot\zeta_n^{(1)}(kr)\frac{dP_n(\cos\theta)}{d\theta},\quad r>b\\&=-\frac{ik^3}{4}\sum_0^{\infty}(2n+1)\zeta_n^{(1)}(kb)\{\zeta_n^{(1)}(kr)+\zeta_n^{(2)}(kr)\}\frac{dP_n(\cos\theta)}{d\theta},\quad r<b\end{aligned}\right\}\tag{24}$$

which splits into

$$\left.\begin{aligned}\omega_0&=-\frac{ik^3}{4}\sum_0^{\infty}(2n+1)\zeta_n^{(2)}(kb)\zeta_n^{(1)}(kr)\cdot\frac{dP_n(\cos\theta)}{d\theta}\quad r>b\\&=-\frac{ik^3}{4}\sum_0^{\infty}(2n+1)\zeta_n^{(1)}(kb)\zeta_n^{(2)}(kr)\cdot\frac{dP_n(\cos\theta)}{d\theta}\quad r<b,\end{aligned}\right\}\tag{25}$$

and

$$\omega_0'=-\frac{ik^3}{4}\sum_0^{\infty}(2n+1)\zeta_n^{(1)}(kb)\zeta_n^{(1)}(kr)\cdot\frac{dP_n(\cos\theta)}{d\theta}\tag{26}$$

When the wave ω_0 makes reflections as given by (21), the final reflected waves are

$$
\left.\begin{matrix}\varDelta_{s\varkappa}\\ 2\omega_{s\varkappa}\end{matrix}\right\}=-\frac{ik^3}{2}\sum_0^\infty(2n+1)\zeta_n^{(2)}(kb)
\left\{F_n\frac{\zeta_n^{(1)}(ha)}{\zeta_n^{(2)}(ha)}\right\}^p\left\{\frac{G_n}{\zeta_n^{(2)}(ha)\zeta_n^{(2)}(ka)}\right\}^q
\left\{\frac{M_n}{\zeta_n^{(2)}(ha)\zeta_n^{(2)}(ka)}\right\}^r\left\{N_n\frac{\zeta_n^{(1)}(ka)}{\zeta_n^{(2)}(ka)}\right\}^s
\left\{\begin{matrix}\zeta_n^{(2)}(hr)P_n(\cos\theta)\\ \zeta_n^{(2)}(kr)dP_n(\cos\theta/d\theta\end{matrix}\right. \tag{27}
$$

If the primary is ω_0', it suffices to change $\zeta_n^{(2)}(kb)$ in (27) into $\zeta_n^{(1)}(kb)$.

§ 5. Geometrical Ray Waves

The waves (22) can be transformed into a clear and simple form by the method of Van der Pol and H. Bremmer[2)], which was applied to the calculation of the electromagnetic waves. Remembering

$$\zeta_n^{(1)}(z)=(-1)^n\zeta_n^{(2)}(-z),$$
$$\zeta_n^{(2)}(z)=(-1)^n\zeta_n^{(1)}(-z),$$
$$P_{n-\frac{1}{2}}(-z)=(-1)^nP_{n-\frac{1}{2}}(z),$$

the function (22) will be transformed into an integral form

$$
\varDelta_{p\varkappa}=-\frac{h^3}{2}\int_L ndn\left\{\frac{\zeta^{(2)}_{n-1/2}(-ha)}{\zeta^{(2)}_{n-1/2}(ha)}F_{n-1/2}\right\}^p\left\{\frac{G_{n-1/2}}{\zeta^{(1)}_{n-1/2}(-ha)\zeta^{(2)}_{n-1/2}(ha)}\right\}^q\left\{\frac{M_{n-1/2}}{\zeta^{(1)}_{n-1/2}(-ka)\zeta^{(2)}_{n-1/2}(ha)}\right\}^r
\cdot\left\{\frac{\zeta^{(2)}_{n-1/2}(-ka)}{\zeta^{(2)}_{n-1/2}(ka)}N_{n-1/2}\right\}^s\zeta^{(1)}_{n-1/2}(-hb)\zeta^{(2)}_{n-1/2}(hr)\frac{P_{n-1/2}\{\cos(\theta-\kappa\pi)\}}{\cos n\pi}, \tag{28}
$$

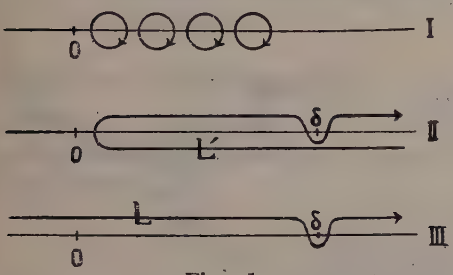

Fig. 1.

where the path of integration is the sum of circles round the poles of the function $(\cos n\pi)^{-1}$ as is shown in Fig. 1. I. This path is transformed into the loop L′ in Fig. 1. II, which does not encircle the pole of the functions $F_{n-1/2}$, $G_{n-1/2}$, $M_{n-1/2}$, $N_{n-1/2}$ which lies on or near the positive real axes. Owing to

$$\zeta^{\overset{(1)}{(2)}}_{-n-1/2}=e^{\pm in\pi}\zeta^{\overset{(1)}{(2)}}_{n-1/2},\quad P_{-n-1/2}=P_{n-1/2},$$

the integrand of (28) is evidently even function of n, so the loop L′ of Fig. 1. II can be transformed into L in Fig. 1. III. Multiply both the denominator and the numerator of the integrand in (28) by

$$\{\zeta^{(1)}_{n-1/2}(ha)\}^p\{\zeta^{(2)}_{n-1/2}(-ha)\,\zeta^{(1)}_{n-1/2}(ka)\}^q\{\,\zeta^{(2)}_{n-1/2}(-ka)\,\zeta^{(1)}_{n-1/2}(ha)\}^r\{\zeta^{(1)}_{n-1/2}(ka)\}^s$$

and the exponential character of the denominator disappears. Now we put

$$
\left.\begin{aligned}
\zeta^{(1)}_{n-1/2}(z)&=\frac{1}{\sqrt{2\pi z}}\int_{i\infty-\pi/2}^{-i\infty+\pi/2}exp\left\{iz\cos\tau+in\left(\pm\tau-\frac{\pi}{2}\right)\right\}d\tau,\\
\zeta^{(2)}_{n-1/2}(z)&=\frac{1}{\sqrt{2\pi z}}\int_{i\infty+\pi/2}^{-i\infty-\pi/2}exp\left\{-iz\cos\tau-in\left(\pm\tau-\frac{\pi}{2}\right)\right\}d\tau,
\end{aligned}\right\} \tag{29}
$$

$$P_{n-1/2}\{\cos(\theta-\kappa\pi)\}=\frac{1}{2\pi}\int_{-\pi}^{\pi}\frac{exp\{n\log[\cos(\theta-\kappa\pi)+i\sin(\theta-\kappa\pi)\cos\phi]\}}{[\cos(\theta-\kappa\pi)+i\sin(\theta-\kappa\pi)\cos\phi]^{1/2}}d\phi, \tag{30}$$

$$(\cos n\pi)^{-1}=2\sum_{m=0}^\infty(-1)^m exp\{(2m+1)n\pi i\} \tag{31}$$

into (28). The term with m means the wave which travels m-time round the surface of the sphere and reaches P. If we take account of the viscosity, we can neglect all terms except for $m=0$, and (28) becomes

$$
\varDelta_{p\varkappa}=\frac{h^3(-1)^\varkappa}{(2\pi)^{\varkappa+2}h\sqrt{br}\,i(hai)^p(\sqrt{hk}\,i)^{q+r}(kai)^s}\int_{-\infty}^{\infty}dnA(n)
\cdot\int_{-\pi}^{\pi}\frac{d\phi}{[\cos(\theta-\kappa\pi)+i\sin(\theta-\kappa\pi)\cos\phi)^{1/2}}\int d\tau_1\ldots\ldots d\tau_{2\kappa+2}e^{f(\tau)}, \tag{32}
$$

where we put

$$
f(\tau)=-ihb\cos\tau_1+iha\sum_{\nu=2}^{\varkappa_1+1}\cos\tau_\nu+ika\sum_{\varkappa_1+2}^{\varkappa_1+\varkappa_2+1}\cos\tau_\nu-ihr\cos\tau_{2\varkappa+2}
+in\left\{-\tau_1+\sum_{\nu=2}^{2\varkappa+1}\tau_\nu-\tau_{2\varkappa+2}+\pi\right\}+n\log\{\cos(\theta-\kappa\pi)+i\sin(\theta-\kappa\pi)\cos\phi\}, \tag{33}
$$

$$(\kappa_1=2p+q+r;\ \kappa_2=q+r+2s),$$

$$A(n)=n\left\{\frac{F_{n-1/2}}{\zeta^{(1)}_{n-1/2}(ha)\,\zeta^{(2)}_{n-1/2}(ha)}\right\}^p\left\{\frac{G_{n-1/2}}{\zeta^{(1)}_{n-1/2}(-ha)\zeta^{(2)}_{n-1/2}(-ha)\zeta^{(1)}_{n-1/2}(ka)\zeta^{(2)}_{n-1/2}(ka)}\right\}^q$$
$$\cdot\left\{\frac{M_{n-1/2}}{\zeta^{(1)}_{n-1/2}(-ka)\zeta^{(2)}_{n-1/2}(-ka)\zeta^{(1)}_{n-1/2}(ha)\zeta^{(2)}_{n-1/2}(ha)}\right\}^r\left\{\frac{N_{n-1/2}}{\zeta^{(1)}_{n-1/1}(ka)\zeta^{(2)}_{n-1/2}(ka)}\right\}^s \tag{34}$$

We shall calculate the function (32) by the method of saddle point. When the path of integration L meets the pole of $A\ (n)$ whilst deforming into the steepest descent curve through the saddle point, this integral is determined as the sum of two terms. One is the value near the saddle point, and the other is the residue of the pole. The former is geometrical ray waves and the later a surface one.

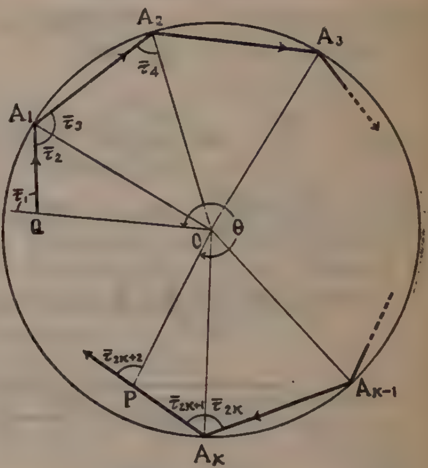

Fig. 2.

The saddle point of $f(\tau)$ on the $2\kappa+4$ dimensional $(\tau_1,\ldots\ldots,\ \tau_{2\kappa+2},\ n,\ \phi)$ complex plane is determined by

$$\frac{\partial f}{\partial\tau_1}=\ldots\ldots=\frac{\partial f}{\partial\tau_{2\kappa+2}}=\frac{\partial f}{\partial n}=\frac{\partial f}{\partial\phi}=0. \tag{35}$$

Denote the solutions of these equations by $\bar\tau_1,\ldots\ldots,\ \bar\tau_{2\kappa+2},\ \bar n,\ \bar\phi,$

$$\left.\begin{aligned}&\bar\phi=0,\\&\bar n=hb\sin\bar\tau_1=ha\sin\bar\tau_2=\ldots\ldots=ha\ \sin\bar\tau_{\kappa_1+1}=ka\\&\qquad\cdot\sin\bar\tau_{\kappa_1+2}=\ldots\ldots=ka\sin\bar\tau_{2\kappa+1}=hr\sin\bar\tau_{2\kappa+2},\\&\theta=\bar\tau_1-\bar\tau_2+\sum_{\nu=3}^{2\kappa}\left(\frac{\pi}{2}-\bar\tau_\nu\right)+(\bar\tau_{2\kappa+2}-\bar\tau_{2\kappa+1}).\end{aligned}\right\} \tag{36}$$

These values can be interpreted as shown in Fig. 2. After some calculation, (32) becomes (37)

$$\varDelta_{p\kappa}=\frac{h^3(-1)^\kappa A(\bar n)(\sqrt{2\pi}\,i\,)^{2\kappa+4}exp\left\{-i\dfrac{(\theta-\kappa\pi)}{2}+f(\bar\tau)\right\}}{(2\pi)^{\kappa+2}h\sqrt{br}\,i(hai)^p(\sqrt{hk}\,ai)^{q+\nu}(kai)^s\sqrt{det\,f}}, \tag{37}$$

where

$$\left.\begin{aligned}&det\,f=i^{2\kappa+3}(-1)^{2\kappa}h^{\kappa_1+2}k^{\kappa_2}a^{2\kappa}br\cos\bar\tau_1\ldots\ldots\cos\bar\tau_{2\kappa+2}\bar n\sin(\theta-\kappa\pi)\\&\qquad\cdot exp\{-i(\theta-\kappa\pi)\}\cdot\partial\theta/\partial n,\\&\frac{\partial\theta}{\partial n}=\frac{1}{hb\cos\bar\tau_1}-\sum_{\nu=2}^{\kappa_1+1}\frac{1}{ha\cos\bar\tau_\nu}-\sum_{\kappa_1+2}^{\kappa_1+\kappa_2+1}\frac{1}{ka\cos\bar\tau_\nu}+\frac{1}{hr\cos\bar\tau_{2\kappa+2}},\end{aligned}\right\} \tag{38}$$

and

$$f(\bar\tau)=i\{h\overline{QA_1}+h\overline{A_1A_2}+k\overline{A_2A_3}+\ldots\ldots+k\overline{A_{\kappa-1}A_\kappa}+h\overline{A_\kappa P}\}. \tag{39}$$

In (39) we assume for example the waves on A_1A_2, A_2A_3,……, $A_{\kappa-1}A_\kappa$ are P-, S-……, S-wave respectively.

By the same method as above it can be shown that equations (19), (20) are the approximate form of (17). If we transform (19) into an integral form, put (29), (30), (31) into it, and take the term $m=0$ only, we get

$$\varDelta_0=-\frac{h^3}{(2\pi)^2h\sqrt{br}}\int_{-\infty}^{\infty}ndn\int_{-\pi}^{\pi}\frac{d\phi}{[\cos(\theta-\pi)+i\sin(\theta-\pi)\cos\phi]^{\frac{1}{2}}}\iint d\tau_1d\tau_2exp\,f(t),$$

where

$$f(\tau)=i(-hb\cos\tau_1+hr\cos\tau_2)+in(\tau_2-\tau_1+\pi)+n\log\{\cos(\theta-\pi)+i\sin(\theta-\pi)\cos\phi\}.$$

The saddle point of $f(\tau)$ is given by

$$\bar\phi=0,\ \bar n=hb\sin\bar\tau_1=hr\sin\bar\tau_2,\ \theta=\bar\tau_1-\bar\tau_2.$$

The meaning of these values can be given as shown in Fig. 3, and we can easily get

$$\varDelta_0=-\frac{h^3n(\sqrt{2\pi}\,i)^4}{(2\pi)^2h\sqrt{br}\sqrt{det\,f}}\,e^{f(\bar\tau)+i(\pi-\theta)/2},$$

where

$$f(\bar\tau)=i(-hb\cos\bar\tau_1+hr\cos\bar\tau_2)=i\overline{QP}=iR,$$

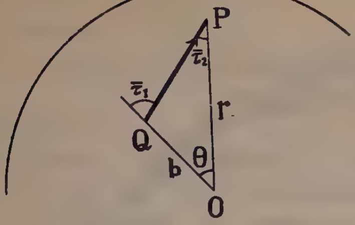

Fig. 3.

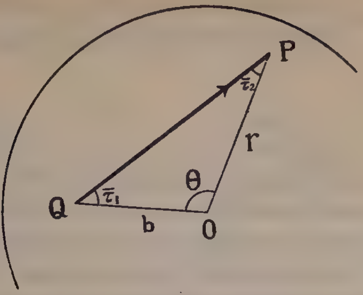

Fig. 4.

$$\det f = hn \sin\theta \, exp\{-i(\theta-\pi)\}R,$$

and therefore

$$\Delta_0 = -\frac{h^2}{R} e^{ihR}.$$

By the same method the values $\bar{\tau}_1$, $\bar{\tau}_2$ at the saddle point for (20) are interpreted as shown in Fig. 4. As the result of calculation, we get

$$\Delta_0' = -h^2 R^{-1} e^{ihR}.$$

§ 6. PP-, PS-, SP-, SS-Waves

When the primary P-wave Δ_0 is reflected at the surface $r=a$ into PP- and PS-ones, PP wave is obtained by putting $p=1$, $q,r,s=0$, $\kappa=1$, $\kappa_1=2$, $\kappa_2=0$ into the equations (37), (38), (39) as follows:

$$\Delta_p = \frac{h^3}{(2\pi)^2 h\sqrt{bri}} \frac{(-1)(\sqrt{2\pi}\ i)^6}{2\pi hai\sqrt{\det f}} A(\bar{n}) e^{-i\,(\theta-\pi)/2+f(\bar{\tau})}\ , \tag{40}$$

where

$$\det f = ih^3 a^2 br\bar{n} \sin\theta\, e^{-i(\theta-\pi)} \cos^2\bar{\tau}_2 [\overline{QA_1} r \cos\bar{\tau}_4 + \overline{A_1P_1}\, b \cos\bar{\tau}_1], \tag{41}$$

$$f(\bar{\tau}) = i(-hb\cos\bar{\tau}_1 + ha\cos\bar{\tau}_2 + ha\cos\bar{\tau}_3 - hr\cos\bar{\tau}_4) = ih(\overline{QA_1} + \overline{A_1P}), \tag{42}$$

and

$$A(\bar{n}) = \bar{n} F_{\bar{n}-1/2} / [\zeta^{(1)}_{\bar{n}-1/2}(ha)\, \zeta^{(1)}_{\bar{n}-1/2}(ha)].$$

Since

$$\zeta^{(1)}_{\bar{n}-1/2}(ha)\, \zeta^{(2)}_{\bar{n}-1/2}(ha) \sim (ha\sqrt{h^2a^2-\bar{n}^2}^{\,-1}, \quad \bar{n} = ha\sin\bar{\tau}_2, \tag{43}$$

we get

$$A(\bar{n}) = (ha)^3 \cos\bar{\tau}_2 \sin\bar{\tau}_2\, F_{\bar{n}-1/2}. \tag{44}$$

Putting (41), (42), (43), (44) into (40), the final form is

$$\Delta_p = -\frac{h^2 a\cos\bar{\tau}_2 \sin\bar{\tau}_2\, F_{\bar{n}-1/2} exp\{ih(\overline{QA_1} + \overline{A_1P})\}}{[br\sin\bar{\tau}_2 \cos\bar{\tau}_2 \sin\theta(\overline{QA}, r\cos\bar{\tau}_4 + A_1P\, b\cos\bar{\tau}_1)]^{\frac{1}{2}}} \tag{45}$$

When the observing point P is near the first reflecting point A_1, we may put $\bar{\tau}_4 = \bar{\tau}_2$, $r=a$, $\overline{QA_1}\sin\bar{\tau}_2 = b\sin\theta$, and (45) becomes

$$\Delta_p = -h^2 F_{\bar{n}-1/2} (\overline{QA_1})^{-1} e^{ih\overline{QA}_1} = F_{\bar{n}-1/2}\Delta_0. \tag{46}$$

Remembering the radius a is very large, and putting

$$z\cdot\zeta_n^{(1)(2)\prime}(z)/\zeta_n^{(1)(2)}(z) \sim \pm i\sqrt{z^2-n^2} \tag{47}$$

we get

$$F_{\bar{n}-1/2} = \frac{\sin 2\bar{\tau}_2 \sin 2\bar{\tau}_3 - k^2/h^2 \cos^2 2\bar{\tau}_3}{\sin 2\bar{\tau}_2\, \mathrm{siu}\, 2\bar{\tau}_3 + k^2/h^2 \cos^2 2\bar{\tau}_3}, \tag{48}$$

which is the same result as in the case of plane boundary, where $\bar{\tau}_2$ is the incident angle of the primary P-wave and $\bar{\tau}_3$ is the reflective angle of S-wave. On the other hand when the point P lies near the second reflecting point A_2, then

$$\varDelta_p=-\frac{h^2a\cos\bar\tau_2\sin\bar\tau_2 F_{\bar n-1/2}\,exp\{ih(\overline{QA_1}+\overline{A_1A_2})\}}{[ba\sin\bar\tau_2\cos\bar\tau_2\sin\theta(\overline{A_1A_2}\,b\cos\bar\tau_1-\overline{QA_1}\,a\cos\bar\tau_2)]^{\frac{1}{2}}}. \tag{49}$$

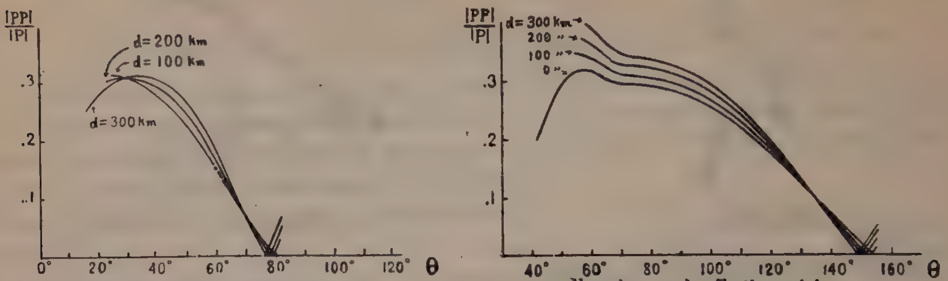

Near the first reflecting point. Near the second reflecting point.

Fig. 5.

Numerical calculation of |PP|/|P| near A_1 and A_2 gives the result shown in Fig. 5. In the similar way we get as PS-wave

$$2\omega_p=\frac{h^3}{(2\pi)^2 i\sqrt{kkbr}}\,\frac{-1}{2\pi ai\sqrt{hk}}\,\frac{(i\sqrt{2\pi})^6}{\sqrt{det\,f}}\,i\bar nA(\bar n)e^{-i\frac{(\theta-\pi)}{2}+f(\bar\tau)}, \tag{50}$$

where

$$f(\bar\tau)=i\{-hb\cos\bar\tau_1+ha\cos\bar\tau_2+ka\cos\bar\tau_3-kr\cos\bar\tau_4\}=i(h\overline{QA_1}+k\overline{A_1P}), \tag{51}$$

$$det\,f=h^2ka^2\sin\bar\tau_2\sin\theta\,exp\{-(\theta-\pi)\}\cdot(\overline{QA_1}kr\cos\bar\tau_3\cos\bar\tau_4+\overline{A_1P}\,hb\cos\bar\tau_1\cos\bar\tau_2), \tag{52}$$

$$\bar nA(\bar n)=-h^4k^2a^6\sin^2\bar\tau_2\cos\bar\tau_2\cos\bar\tau_3\,G_{\bar n-1/2}. \tag{53}$$

Putting (51), (52), (53) into (50), we get

$$\omega_p=\frac{ia^4h^5k\sin^2\bar\tau_2\cos\bar\tau_2\cos\bar\tau_3\,G_{\bar n-1/2}\,exp\{i(h\overline{QA_1}+k\,\overline{A_1P})\}}{2[kbr\sin\bar\tau_2\sin\theta(\overline{QA_1}kr\cos\bar\tau_3\cos\bar\tau_4+\overline{A_1P}\,hb\cos\bar\tau_1\cos\bar\tau_2\ ]^{\frac{1}{2}}}. \tag{54}$$

When the point P is near A_1,

$$\omega_p=\frac{ia^3h^5\sin\bar\tau_2\cos\bar\tau_2}{2\overline{QA_1}}G_{\bar n-1/2}\,exp\{ih\overline{QA_1}\}=-\frac{ia^3h^3\sin2\bar\tau_2}{4}G_{\bar n-1/2}\varDelta_0 \tag{55}$$

Since the radius a is very large, we get from (12)

$$G_{\bar n-1/2}=\frac{4ik^2}{h^5a^3}\,\frac{\cos2\bar\tau_3}{\sin2\bar\tau_2\sin2\bar\tau_3+(k^2/h^2)\cos^2 2\bar\tau_3}, \tag{56}$$

therefore

$$\omega_p=\frac{k^2}{h^2}\cdot\frac{\sin2\bar\tau_2\cos2\bar\tau_3}{\sin2\bar\tau_2\sin2\bar\tau_3+(k^2/h^2)\cos^2 2\bar\tau_3}\varDelta_0, \tag{57}$$

which is the same result as in the case of plane boundary.

Let the primary be S-wave

$$\omega_0=-\frac{k^2}{2}\,\frac{\partial}{\partial\theta}\,\frac{exp(ikR)}{R}\sim-\frac{ik^3}{2}\,\frac{exp(ikR)}{R}r\sin\tau\quad(\tau=\widehat{Rr}) \tag{58}$$

and denote the reflected P-, S-waves by $\varDelta_s$, ω_s respectively; then the following results can be obtained easily;

$$\varDelta_s=\frac{k^4ha^3\sin\bar\tau_2\cos\bar\tau_2\cos\bar\tau_3\,M_{\bar n-1/2}\,exp(ik\overline{QA_1}+ih\overline{A_1P})}{[hbr\sin\bar\tau_2\sin\theta(\overline{QA_1}\,hr\cos\bar\tau_3\cos\bar\tau_4+\overline{A_1P}\,kb\cos\bar\tau_1\cos\bar\tau_2)]^{\frac{1}{2}}}, \tag{59}$$

$$\omega_s=\frac{ik^3a^2\cos\bar\tau_2\sin^2\bar\tau_2\,N_{\bar n-1/2}\,exp\{ik(\overline{QA_1}+\overline{A_1P})\}}{2[br\sin\bar\tau_2\sin\theta(\overline{QA_1}\,r\cos\bar\tau_4+\overline{A_1P}\,b\cos\bar\tau_1)]^{\frac{1}{2}}}, \tag{60}$$

Approximate values of $M_{\bar n-1/2}$, $N_{\bar n-1/2}$, when a is very large, are

$$\left.\begin{aligned}M_{\bar n-1/2}&=\frac{4i(ka)^{-1}\sin^2\bar\tau_2\cos2\bar\tau_2}{\sin2\bar\tau_2\sin2\bar\tau_3+(k^2/h^2)\cos^2 2\bar\tau_2},\\ N_{\bar n-1/2}&=\frac{\sin2\bar\tau_2\sin2\bar\tau_3-(k^2/h^2)\cos^2 2\bar\tau_2}{\sin2\bar\tau_2\sin2\bar\tau_3+(k^2/h^2)\cos^2 2\bar\tau_2},\end{aligned}\right\} \tag{61}$$

where $\bar{\tau}_2$ is the incident angle of the primary S-wave and $\bar{\tau}_3$ is reflective angle of P-wave. When the point P is near A₁,

$$\left.\begin{aligned} \Delta_s &= ika \cot \bar{\tau}^2 M_{\bar{n}}\, \omega_0 \\ \omega_s &= N_{\bar{n}}\, \omega_0 \end{aligned}\right\} \qquad (62)$$

and these equations give the meaning of $M_{\bar{n}}$ and $N_{\bar{n}}$.

§ 7. Summary

We have treated the reflections of elastic waves at the free surface of a homogeneous sphere. The coefficients of reflections were obtained and these were found to be the same as those of plane boundary in the limiting case $r \to \infty$. By means of these coefficients we have calculated the reflectee waves by the method of saddle point and obtained the reflected geometrical ray waves and surface waves. The latter were already discussed in the previous paper.[1] The former which have a very clear and simple form are convenient to discuss the intensity of them numerically.

In the next paper we shall discuss the reflection and refration of them in the case where the medium is not homogeneous. The results of the calculation are interesting as they seem to be applicable immediately to the actual seismic waves.

References

1) Y. Nomura: Sc. Rep. Tohoku Imp. Univ. (1) **27** (1939) 211.

2) B. Van der Pol and H. Bremmer: Phil. Mag. **24** (1937) 579.

Journal of the Physical Society of Japan Vol. 7, No. 2 Mar.—Apr., 1952

On the Recurrent Figure of a Jet

By Yoshimasa WADA

Yamanashi University

(Read April 2, 1951, Recieved August 9, 1951)

Introducing a small viscosity, a fundamental equation is obtained which gives the relation between the wave-length of standing surface waves of an infinitely long cylindrical flow and its common velocity. From the graph of the first approximation we see that there is always a minimum velocity for the appearance of the waves of any assigned mode for any radius of the jet and that this minimum velocity is inversely proportional to the radius. The graph informs us also that with increasing velocity, waves of successively higher mode are superposed and the surface becomes gradually ruffled. When the velocity is greater than the minimum value, the equation gives two wave-lengths. The longer and shorter ones belong respectively to the waves occurring below and above the disturbance; this is investigated to the second approximation.

§1. Introduction

When a liquid jet issues with moderate velocity from an orifice, we observe usually a recurrent figure on the jet. If the orifice is perfectly circular, we cannot observe such a figure, as was discussed by the author[1] in a previous paper, but whatever the shape of the orifice may be, if the velocity of the liquid is less than certain magnitude, the section of the jet retains the circular form. With a little greater velocity we observe chain-like figure as was reported by Lord Rayleigh[2], and the figure increases its complexity with increasing velocity. The hydrodynamical consideration of this recurrent figure has already been made by Lord

Rayleigh[3)] including dimensional investigation, but we can get some further informations using the method reported by the author[1)].

§ 2. Minimum Velocity for a given Mode

Let the fluid have a common velocity W vertically downwards, and we take cylindrical coordinates z, r, θ where the positive direction of z coincides with that of W. Then let us suppose that the standing surface wave of the infinitely long circular cylinder of the fluid, whose mean radius is a, is given by

$$r=a+\sum_{n}\alpha_n e^{in\theta}e^{ikz}, \tag{1}$$

where each of these Fourier components may be considered to be independent of the others. We assume that the disturbance at $z=0$ is given by the form

$$z=\sum_{n}\alpha_n e^{in\theta}. \tag{2}$$

The velocity potential is written as

$$\phi=-\frac{W\alpha_n}{J_n'(ika)}J_n(ikr)e^{in\theta}e^{ikz}-Wz. \tag{3}$$

Substituting (1) and (3) in the pressure equation

$$p/\rho=\nu(\phi+Wz)-q^2/2, \tag{4}$$

where ν is the viscosity coefficient which may be considered to be small, we get the fundamental equation between W and k,

$$kW^2-\frac{T}{\rho a^2}(k^2a^2+n^2-1)\left\{\frac{n}{ka}+\frac{I_{n+1}(ka)}{I_n(ka)}\right\}=i\nu W, \tag{5}$$

where T denotes the surface tension.

As ν is a small quantity, we obtain the equation for the first approximation of k by neglect of ν, as follows,

$$kW^2=\frac{T}{\rho a^2}(k^2a^2+n^2-1)\left\{\frac{n}{ka}+\frac{I_{n+1}(ka)}{I_n(ka)}\right\}. \tag{6}$$

Dividing the both sides of (6) by k, we get

$$W^2=\frac{T}{\rho a^2 k}(k^2a^2+n^2-1)\left\{\frac{n}{ka}+\frac{I_{n+1}(ka)}{I_n(ka)}\right\}. \tag{7}$$

Right side of this equation has a form of $(T/\rho a)\times${a function of (ka)}, and we can rewrite (7) as

$$W^2=\frac{T}{\rho a}\chi_n(ka). \tag{8}$$

In Fig. 1 is represented this relation between k and W^2 with n, the mode (in this paper we discuss the case of $n\geq 2$), and a, the radius of the jet, as parameters. From the form of (8) the curves for a given value of n are similar and similarly situated to each other and their ordinates and abscissae are inversely proportional to a. This is characteristic of these curves.

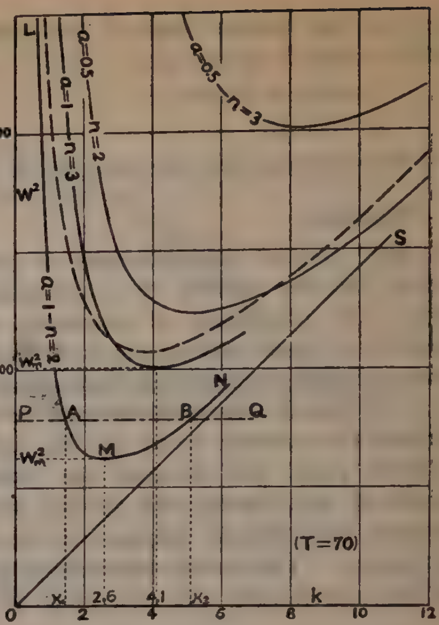

Fig. 1. Square velocity *versus* k. Broken line represents Kelvin's formula and *os* the Tk/ρ (in c. g. s. units)

Drawing a straight line representing W^2 $=const.$ (for example line PQ in Fig. 1), we obtain the point of intersection (A and B) of this line and one of the curves (LMN, when $n=2$ and $a=1$), then the abscissae of these points are the required values of k corresponding to the given value of W for n and a belonging to that curve.

Each of these curves has another branch symmetric to the ordinate-axis, but since the values of k given by this branch are the negatives of the above-obtained values, in the following discussion of the wave-lengths, we use only the curve in the first quadrant.

In this region the curves resemble very well the curve given by the formula

$$U^2=\frac{T}{\rho}k+\frac{g}{k}, \tag{9}$$

which was given by Lord Kelvin[4)] for the waves on the plane surface. Because our curves have also the minimum points, there is the minimum velocity W_m for the formation of waves for any assigned mode and for any a. According to the characteristic of the curves, W_m ought to be inversely proportional to a when n is given, and k_m, which gives the critical wave-length corresponding to W_m, is also inversely proportional to a. By numerical calculation for the case of $a=1$, we get the following formulae;

for $n=2$: $W_m=4.33\ T/\rho a$, $k_m=2.6/a$,

for $n=3$: $W_m=7.05\ T/\rho a$, $k_m=4.1/a$,

……………………………………………

Thus for a jet which has a definite radius a, the minimum velocity of appearance of the waves of lower mode is less than that of higher mode; by gradually increasing the flowing velocity of a jet, the recurrent figure becomes to include the waves of successively higher modes, and complexity of the figure gradually increases. And with equal velocities and same shape of orifice, the larger the orifice, the more ruffled the surface, so that a smooth circular jet is readily obtainable with a thin tube. These are phenomena of daily experience.

§ 3. Waves Above and Below the Disturbance

When the velocity of the jet is greater than the above-mentioned minimum value, we have always two points of intersection, so that two real wave-lengths correspond to a certain velocity. By application of the method reported previously by the author[1], we can see that the waves of the shorter wave-length occur above and those of the longer one below the disturbance, as was investigated by Lord Rayleigh[5] in the case of plane surface.

For that purpose, in order to obtain the second approximation of k, we come back to the equation (5), and for simplicity we write it as follows,

$$F(k)=i\nu W, \tag{11}$$

where

$$F(k)=kW^2-\frac{T}{\rho a^2}(k^2a^2+n^2-1)\left\{\frac{n}{ka}+\frac{I_{n+1}(ka)}{I_n(ka)}\right\} \tag{12}$$

As the first approximation, we take $F(k)=0$, which gives two roots κ_1 and κ_2, $(\kappa_1<\kappa_2)$. Then we have

$$F'(k)\Delta k=i\nu W,$$

or

$$\Delta k=i\nu W/F'(k). \tag{13}$$

Therefore the second approximation of k is $\kappa_1+i\nu W/F'(\kappa_1)$ or $\kappa_2+i\nu W/F'(\kappa_2)$. Substituting this expression into the exponential function including k in (1), we obtain a factor

$$\exp\{-\nu Wz/F'(\kappa_1)\} \text{ or } \exp\{-\nu Wz/F'(\kappa_2)\} \tag{14}$$

In Fig. 2 the curve $L'M'N'$ represents the second term of the right-hand side of (12) and the straight line OQ' the kW^2, (we take $n=2$, $a=1$ in this Fig.), and they correspond respectively to the curve LMN and the line PQ in Fig. 1. Their points of intersection A' and B' correspond respectively to A and B. Because $F'(k)$ is the difference of the gradients of the line OQ' and the curve $L'M'N'$ we can easily see that $F'(\kappa_1)>0$ at A' and $F'(\kappa_2)<0$ at B'. In order that the term (14) might not diverge for very large values of $|z|$, we prefer κ_1 for $z>0$ and κ_2 for $z<0$. So that the lefthand part LM from the minimum point corresponds to the waves bellow the disturbance and the right-hand part MN to those above it.

In Fig. 2 other branches of the curve are perfectly symmetric with respect to the origin, $F'(-\kappa_1)$ and $F'(-\kappa_2)$ are equal to $F'(\kappa_1)$ and $F'(\kappa_2)$ respectively, so that the result is quite same for this region.

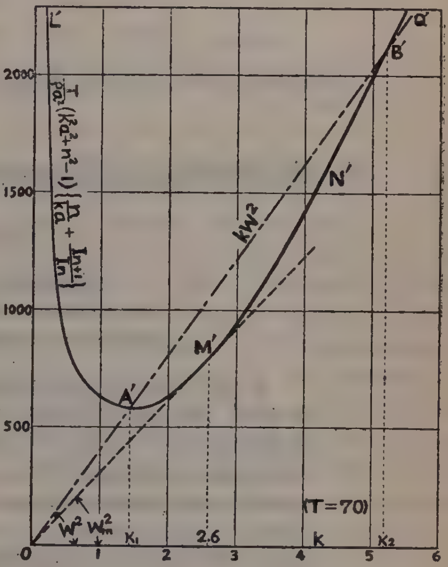

Fig. 2. Diagram for second approximation (in c. g. s. units)

§ 4. Discussions

In his measurement of surface tension, Rayleigh[2] used the formula which states that for a jet issuing from an elliptical orifice the wave-length varies proportionally to the velocity of flow when $ka<1$. As $ak_m=2.6$ at the minimum point of the curve, the velocity at the place where $ka=1$ is considerably greater than W_m; moreover under far greater velocity there enters the vibration of higher modes and the surface of the jet is covered with complex wave-patterns. So that Rayleigh's approximation holds under a little but not too great velocity.

He said also in his dimensional consideration[3] that for a given liquid and shape of orifice there is complete dynamical similarity if the pressure be taken inversely proportional to the linear dimension. This means that in (8) if T and n be given and if W be taken inversely proportional to a, then $\chi_n(ka)$ and hence, ka ought to be constant, so that the wave-length is proportional to the radius of the jet.

Although we cannot usually observe the recurrent figure above the disturbance, i. e. practically in the tube, the phenomena above the disturbance and disappearance of waves at the velocity of W_m for $n=2$ can be clearly observed by using the electrical attraction as the disturbance. For the experiment we make the jet flow between two electrodes which consist of thin metal plates placed horizontally with their edges oposite each other. One of them is charged in positive and another in negative high potential and the jet is earthened. Then the cross-section of jet is deformed nearly elliptically when it flows down.

In conclusion the auther expresses his gratitude to Professors K. Honda and I. Imai of Tokyo University and Professor T. Yasaki of Yamanashi University for their advice and discussion.

References

1) Y. Wada: Journ. Phys. Soc. Jap. **5** (1950) 439.
2) Lord Rayleigh: Proc. Roy. Soc. **47** (1890) 231.
3) Lord Rayleigh: Proc. Roy. Soc. **29** (1879) 71.
4) Lord Kelvin: Phil. Mag. **13** (1871) 375.
5) Lord Rayleigh: Proc. London Math. Soc. **15** (1883) 69.

JOURNAL OF THE PHYSICAL SOCIETY OF JAPAN Vol. 7, No. 2 MAR.—APR., 1952

Sonde Method of Measuring the Ultrasonic Field Intensity

By Sakae MORITA

Matsuda Research Laboratory,
Tokyo Shibaura Electric Co., Ltd. Kawasaki

(Read April 2, 1951, Received June 22, 1951)

A new sonde method of measuring the field intensity of ultrasonics was devised. The sonde is made of a small ball (about 2 mm in diameter) of sound-absorbing material, in which a thermistor of much smaller dimension is included in its centre. From experimental results and theoretical considerations, two noteworthy facts are derived. They are "surface heat generation" (on the surface of any solid material heat is generated in ultra sonic field) and the cooling effect of ultrasonic wave.

§ 1. Introduction and Experimental Technique

The temperature of a piece of sound-absorbing material would rise in ultrasonic field by absorbing the sound energy. If we can measure the temperature change, we will be able to determine the field intensity of the ultrasonics.

For this purpose special sonde as shown in Fig. 1 (a) or (b) was used in our experiments. ((b) is mechnically stronger than (a)). It is made of a small ball (about 2mm in diameter) of sound-absorbing material, in which a thermistor of much smaller dimension (0.3～0.5mm in dia.) suspended by fine platinum wires is included in its centre. The thermistor is, as well-known, a semiconductor which has a large negative tempera-

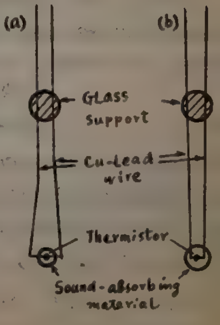

Fig. 1. Sondes

ture coefficient of electric resistivity. To determine the temperature change of the thermistor, its resistance was measured by means of a Wheatstone bridge, employing a.c. voltage of 1000 c./sec. The terminal voltage on the thermistor was kept constant at about 0.5 volt. The balance of the bridge was observed on the screen of a Braun tube, amplifying the bridge output about 65 db.

Several of the sound-absorbing materials were tested, including pitch, paraffin wax, some vinyl resins, bakelite varnish, glass and others. The material must be stable within the range of the temperature measured, since softening of the material gives erroneous results because of the change of sensitivity of the sonde to sound.

The experiments utilizing such sondes were carried, up to present mainly to measure the sound field of 450 kc ultrasonics, whose wave length being about 3 mm in transformer oil.

§ 2. Experimental Results

In Fig. 2 an example of measurements is shown. The absolute intensity of the sound is determined by N-tube method proposed by Dr. J. Saneyosi1). The sensitivity of the sonde is extremely high, showing an temperature rise of about 20°C for the sound intensity of 1W/cm², and the temperature of the sonde increases to 100°C or more in the field of higher intensity. But in the sound field of the intensity more than 3~4 W/cm², the measurement becomes usually unstable.

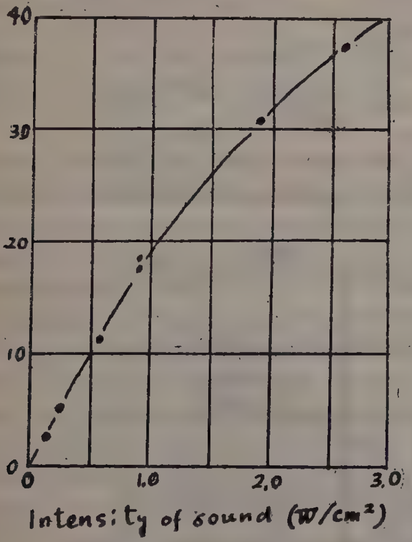

Fig. 2. Sensitivity

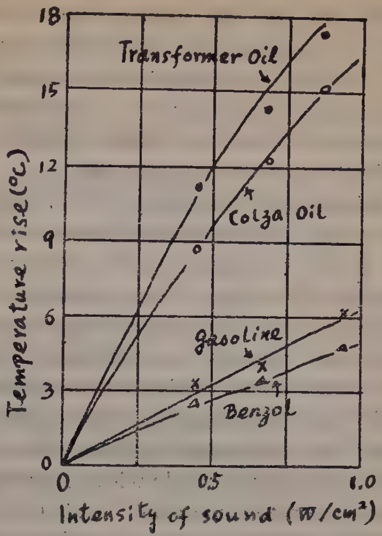

Fig. 3. Effect of changing mediums

It seems that changing of the absorbing materials does not change so much the sensitivity, and a glass ball has also the sensitivity of the same order as other materials.

By changing the dimensions of the sonde i.e. changing the amount of absorbing material using the same thermistor, their sensitivities were tested. With the sonde smaller than 1 mm in diameter, the sensitivity is low, but if a larger one is used (perhaps when the diameter is larger than about half the wave length), the sensitivity does not change in noticeable amount. The time constant change linearly with the dimensions of the sonde. (The time constant of the sonde is in the order of 1~3 seconds.)

By changing the medium surrounding the sonde, the sensitivity changes as shown in Fig. 3. In this experiment the medium surrounding the sonde are transformer oil, gasoline, benzene

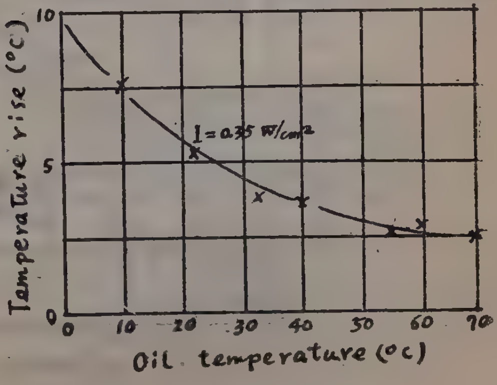

Fig. 4. Effect of temperature

and colza oil. In less viscous liquid such as gasoline or beezene, the sensitivity seems to drop. In this experiment the quarts plate radiating the ultrasonic wave, is in transformer oil and the sonde is in a smaller celluloid vessel containing the medium under test.

By changing the temperature of the surrounding the sonde, the sensitivity changes as shown in Fig. 4. It is noticed that the higher is the temperature, the lower is the sensitivity.

When the sonde is preliminarily heated by direct current through the thermistor, the sensitivity lowers down and in some cases the sensitivity becomes negative, that is, the cooling effect of ultrasonics appears. In Fig. 5, (a) is obtained by a sonde with gryptal vanish as sound-absorbing material, and (b) by a thermistor without any sound-absorbing material. The currents noted in the figure are the preheating d. c. current, and the degrees in the brackets are initial temperature rise of the sonde caused by the current without applying any ultrasonics.

For the sonde without sound-absorbing material, that is, the sonde consisting only of a thermistor, (even when it has a large dimension), the sensitivity is low (about 1/3~1/30 of that of the sonde with sound-absorbing material). Moreover the sensitivity of such sondes varies very much for each thermistor. In this case the sensitivity is much improved if we coat the sonde with a very thin layer of sound-absorbing material.

§ 3. General Theoretical Concicerations

Assuming the thermistor and the sonde to be spherical (radius a_0 and a_1), and the heat generation by ultrasonics to be uniform in the absorbing material, the heat equation becomes at steady state

$$\frac{\alpha I}{J}\frac{4\pi}{3}\left(r^3-a_0^3\right)=-4\pi r^2 k\frac{d\theta}{dr}, \qquad (1)$$

where I is the intensity of the sound in Watt /cm², α the absorption coefficient of the material (including the transmitivity at the surface of the sonde), $J=4.18$ (mechanical equivalent of heat), r the radius of an arbitrary spherical shell in the absorbing material, k the coefficient of heat conduction and θ the temperature rise from that of the medium surrounding the sonde.

As the boundary condition at the surface we can put

$$\frac{\alpha I}{J}\frac{4\pi}{3}(a_1^3-a_0^3)=4\pi a_1^2\lambda\theta_1, \qquad (2)$$

where λ is the coefficient of heat transfer of the surface to oil, θ_1 the temperature rise of the surface of the sonde. If we denote with θ_0 the temperature of the thermistor, it becomes

$$\theta_0=\frac{\alpha I}{3J}\left\{\frac{1}{\lambda}\left(a_1-\frac{a_0^3}{a_1^2}\right)+\frac{1}{k}\left(\frac{a_1^2}{2}+\frac{a_0^3}{a_1}-\frac{3}{2}a_0^2\right)\right\} \qquad (3)$$

$$=\theta_1+\frac{\alpha I}{3Jk}\left(\frac{a_1^2}{2}+\frac{a_0^3}{a_1}-\frac{3}{2}a_0^2\right) \qquad (3')$$

For the sonde used ($a_0=0.03$ cm and $a_1=0.085$ cm), applying the presumed values to α

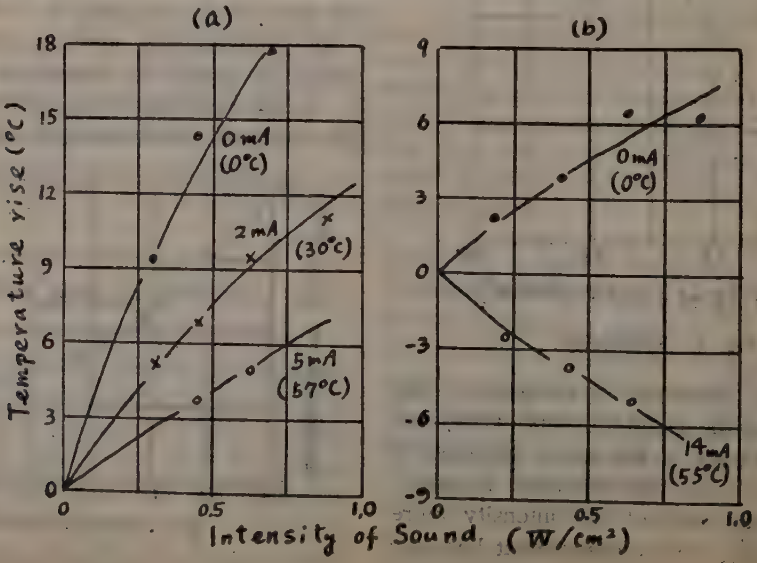

Fig. 5. Effect of pre-heating

and k ($\alpha=0.2\sim0.5$, $k=0.5\sim1.0\times10^{-3}$), we obtain for $I=1$ W/cm², $0.02^\circ<\theta_0-\theta_1<0.2^\circ$. Experimentally we know that θ_0 is about 20°C, so we can conclude that the temperature of the sonde is almost uniform in the sonde, that is, θ_1 equals to θ_0.

Now assuming the temperature of the sonde to be uniform also in transient state, the heat equation for transient state becomes

$$W\frac{d\theta}{dt}=\frac{\alpha I}{J}V-\lambda S\theta, \tag{4}$$

where W is the heat capacity of the sonde, V the volume of the absorbing material, S the surface area of the sonde, t the time. Integrating (4)

$$\theta=\frac{\alpha IV}{J\lambda S}\left(1-e^{-\frac{\lambda S}{W}t}\right)=\theta_0\left(1-e^{-\frac{t}{T}}\right), \tag{5}$$

$$\theta_0=\frac{\alpha IV}{J\lambda S}, \tag{6}$$

$$T=\frac{W}{\lambda S}, \tag{7}$$

where θ_0 is the temperature rise of the sonde at steady state ($t=\infty$), and T is the time constant. (5) is the formula for building-up state, and for decaying state we obtain

$$\theta=\frac{\alpha IV}{J\lambda S}e^{-\frac{\lambda S}{W}t}=\theta_0 e^{-\frac{t}{T}} \tag{8}$$

Applying the above numerical values to a_0 and a_1, and also presumed values to W,

$$\theta_0\fallingdotseq 0.0068\frac{\alpha I}{\lambda}, \tag{6'}$$

$$T\fallingdotseq 0.015/\lambda. \tag{7'}$$

Experimentally $T=1\sim3$ sec., so $\lambda=0.005\sim0.015$ and so $\theta_0<0.7$°C for $I=1$ W/cm². This value is very small compared with the experimental value $\theta_0=20$°C. If we start the calculation without assuming α, α must be $20\sim30$ in order to have $\theta_0=20$°C. This value is too large.

Thus we can not explain the experimental sensitivity of the sonde by assuming the body absorption as mentioned above. We must now see if there is some other cause of heat generation. We would like to introduce a concept "surface heat generation." This would be due to the heat generation by particle motion in viscous thin layer surrounding the sonde.

§ 4. Surface Heat Generation

Assuming that the heat generation is equally distributed all over the surface of the sonde, and putting the coefficient of the surface heat generation β, we obtain

$$W\frac{d\theta}{dt}=\frac{\beta IS}{J}-\lambda S\theta. \tag{9}$$

For building-up state

$$\theta=\frac{\beta I}{J\lambda}(1-e^{-\frac{\lambda S}{W}t})=\theta_0(1-e^{-\frac{t}{T}}), \tag{10}$$

and for decaying state

$$\theta=\frac{\beta I}{J\lambda}e^{-\frac{\lambda S}{W}t}=\theta_0 e^{-\frac{t}{T}}, \tag{11}$$

where

$$\theta_0=\frac{\beta I}{J\lambda}=0.24\frac{\beta I}{\lambda} \tag{12}$$

T being the same as in (7). Putting the experimental values $T=1\sim3$ sec., β is $0.4\sim1.2$. In the equation (6), θ_0 depends linearly on the dimension of the sonde, but in (12) θ_0 is independent of it. We have experimentally confirmed that the sensitivity of the sonde does not depend on its dimension. Hence it may be concluded that (12) explains the experimental results better than (6).

The facts that the absorbing material does not affect the sensitivity and that the medium surrounding the sonde affect the sensitivity strikingly, are also explained by the surface heat generation. Especially the sensitivity of a glass ball or the thermistor itself can not be explained by the theory of body heat generation.

§ 5. Cooling Effect of the Ultrasonics

Now we can calculate λ by introducing the experimental values of time constants into the formula (7). The building-up curves and decaying curves are obtained at various conditions as shown in Fig. 6. From decaying curves for various temperature, we obtain

$$\lambda=a+b\theta, \tag{13}$$

and from building-up curves for various intensity of ultrasonics, using their starting inclinations

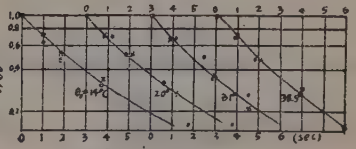

(a) Decaying curve

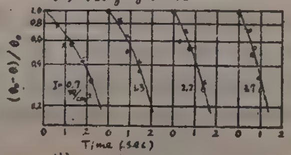

(b) Building-up curve

Fig. 6. Time characteristics.

$$\lambda=a+cI, \tag{14}$$

where a, b and c are constants. Combining (13) and (14)

$$\lambda=a+b\theta+cI. \tag{15}$$

For examples, for a gryptal sonde ($a_1=0.085$) in transformer oil,

$$\lambda=(4.5+0.055\,\theta+2.6\,I)\times10^{-3}, \tag{15'}$$

and for the same sonde in gasoline

$$\lambda=(6.4+0.077\,\theta+6.0\,I)\times10^{-3}. \tag{15''}$$

Both numerical values are for 10~15°C of the medium temperature.

The cI of λ means the cooling effect of ultrasonics. In gasoline c is greater than in transformer oil. This result seems to indicate that in more viscous medium the cooling effect is smaller.

§ 6. Empirical Formula for Sensitivity

Apllying λ of (15) (putting θ_0 as θ) into (12), we obtain

$$\theta_0=\frac{0.24\,\beta I}{a+b\theta_0+cI}. \tag{16}$$

Comparing (16) and the experimental relation between I and θ_0 which can be derived from Fig. 2, we can determine β. The result obtained is written

$$\beta=d'+e'\theta, \tag{17}$$

where d' and e' are constants. Thus the empirical formula relating θ_0 and I is given as follows (in β also putting θ_0 as θ)

$$\theta_0=\frac{(d+e\theta_0)I}{a+b\theta_0+cI}. \tag{18}$$

For the gryptal sonde in transformer oil (oil temperature being 10°~15°C)

$$\beta=0.44+0.009\,\theta, \tag{17'}$$

and

$$\theta_0=\frac{(106+2.16\,\theta_0)I}{4.5+0.055\,\theta_0+2.6I} \tag{18'}$$

or

$$I=\frac{(\theta_0+81.8)\theta_0}{1920-8.0\,\theta_0} \tag{18''}$$

This is the empirical formula for Fig. 2 or the linearity of the sensitivity of our sonde method under conditions mentioned. If the intensity of the sound is low, the relation between θ_0 and I becomes linear as

$$\theta_0\fallingdotseq23.5\times I. \tag{18'''}$$

§ 7. β and Viscocity

Changing the oil temperature, we can determine λ in relation to the oil temperature θ. We obtain

$$\lambda=(4.2+0.022\,\theta)\times10^{-3}, \tag{19}$$

using above sonde in transformer oil. Using this λ and the relation between θ_0 and oil temperature shown in Fig. 4, the relation between β and oil temperature is determined. The result is shown in Fig. 7 as the curve. The viscocity of the oil was measured at the same time. The times of flowing of the oil in 50cc. pipette between two constant levels are shown by circular points in Fig. 7. It seems that β varies with viscocity in similar manner. This is another verification of our theory of surface heat generation.

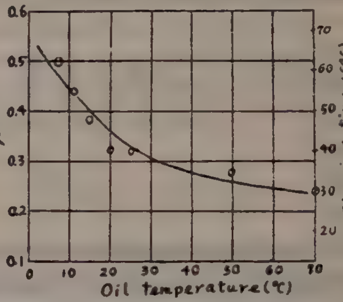

Fig. 7. Temperature effect on β and viscocity.

By this conclusion, the fact that the sensitivity is low in less viscous medium as gasoline or benzol, is also explained. The fact that λ is larger in less viscous medium as obtaine din paragraph 5, also contribute to lower the sensitivity. (In colza oil the viscocity seems too high to follow this same principle.)

§ 8. Experiments on Pre-heating

The experimental results on the pre-heating by d.c. can be explained as follows. When the heating by electric current exists with the heating by ultrasonics at the same time, the relation between θ_0, i (d.c. current) and I (intensity of the sound) is obtained as follows

$$\theta_0=\frac{Ri^2}{4\pi J}\left\{\frac{1}{k}\left(\frac{1}{a_0}-\frac{1}{a_1}\right)+\frac{1}{a_1{}^2\lambda}\right\}+\frac{\beta I}{J\lambda}, \tag{20}$$

where R is the resistance of the thermistor corresponding θ_0. The first term is due to the current heating and the second due to the acoustic heating. If we know k and its temperature coeficient, knowing λ from (13) and β from (17), we can calculate θ_0 corresponding to any i and I.

If we do not know k, we must calculate it. For this purpose we can use this experiment also. Without sound, the temperature rise θ_0 is determined by the first term of (20). Since we know λ from (13), we can calculate k by varying i. (Putting the θ of (13) as the assumed surface temperature of the sonde).

The cause of the low sensitivity under the ultrasonic wave is mainly due to the cooling effect of the wave affecting on the first term of (20). The order of numerical value of the sensitivity was confirmed by such a calculation.

When the sensitivity is low as in the case of a thermistor without any sound-absorbing material, the cooling effect predominates and the sensitivity becomes negative as shown in Fig. 5 (b).

§ 9. An Example of Applications

In Fig. 8 as an example of the applications of this method, the experimental result on the field distribution of sound in front of a vibrating quartz is shown. This experiment was performed by a quartz radiating the sound horizontally in a shallow vessel. (The dimension of the vessel is $40 \times 30 \times 7\,\text{cm}^3$). As shown in the figure, the field neibouring the vibrator is very complicated. Changing the manner of holding the quartz, the distribution changes strikingly. To obtain this figure the field intencities at about 500 points in the vessel were measured. (The time needed for the measurement was only half a day.)

Conclusions

A new sonde method of measuring the field intensity of ultrasonics was devised by the author and utilized in the experiments. From experimental results two noteworthy facts are derived. They are "surface heat generation" (heat is generated on the surface of any solid material in ultrasonic field) and the cooling effect of ultrasonic wave. With both of these facts most of the experimental results are explained. Since the sonde is very small in dimension and has high sensitivity, this method is very suitable to measure the field distribution of rather weak sound (below about 3 W/cm^2). In this region it is very stable and reliable.

Reference

(1) J. Saneyosi & K. Harada, "A Simple Measuring Method of Intense Ultrasonics in Liquid." Oyobutsuri (Applied Physics), **18** (1949) 217. (in Japanese).

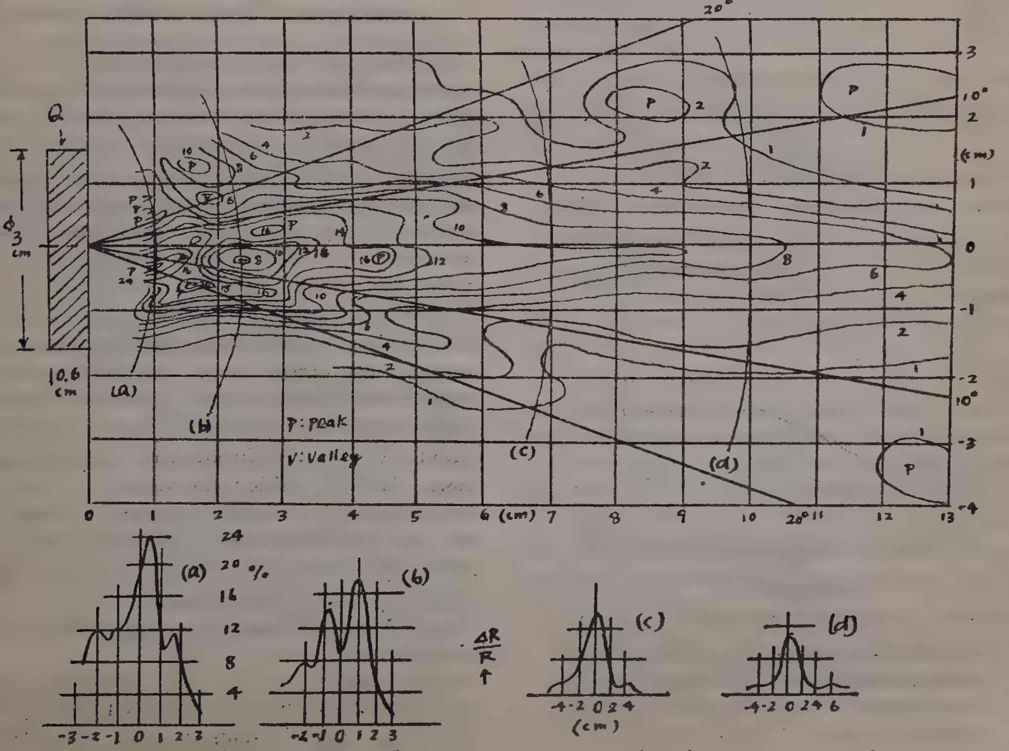

Fig. 8. The field distribution of sound in front of a vibrating quartz (450 kc)

Short Notes

J. PHYS. SOC. JAPAN **7** (1952) 220-221

Electron Multiplication in Hard Flows of Selenium Rectifiers

By Masao TOMURA and Yukiaki ABIKO

Institute of Polytechnics of Osaka City University

(Read, April 3, 1951; Received, May 15, 1951)

The abnormal temperature dependencies of hard flows of a selenium rectifier were reported by one of the authors,[1] where in increase of hard flows with decrease of temperature at high voltages in the blocking direction of the rectifier was observed. As the barrier layer of the rectifier is so thin that the internal field in this layer reaches ca. 10^6 volt/cm by application of the inverse voltage. Thus electron multiplication[3] owing to very high field may occur, altering characteristics of the hard flow.

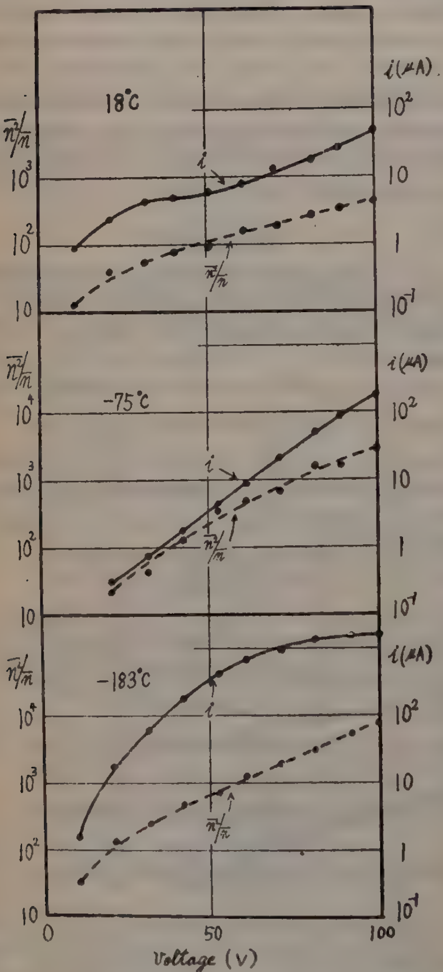

Fig. 1. Dependence of hard flows and $\overline{n^2}/\bar{n}$ on applied voltages at various temperatures. $\overline{n^2}/\bar{n}$ is a kind of average value of the number n of unit charge in a single avalanche group. i is the hard flow.

In the present work we hove adopted the method of F. E. Haworth and R. M. Bozorth[3] to detect the existence of noises owing to electron avalanche. Temperature and voltage dependences of hard flows as well as the noises are shown in Fig. 1. The rectifier tested was just the same as reported before[1] whose area was ca. 1mm^3. This sample is one which showed a very high maximum reverse voltage[4]. By this feature the conspicuous abnormal characteristics were observed in this cases. (See Fig. 2)

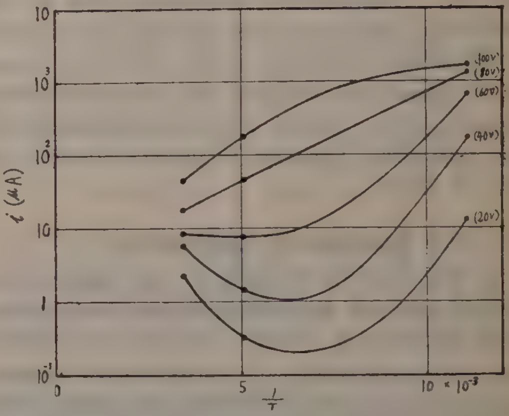

Fig. 2. Relation between hard flows and temperature at various applied voltages.

Dependence of electron avalanche noises on temperature and voltage are explained semi-quantitatively by electron multiplication theory of F. Seitz[2]. With the decrease of temperature, the average path of electron for producing secondary electron by impact ionization decreases, increasing the size of avalanche and then enlarging the hard flows. The slow elevation of $\bar{n}^2/\bar{n}$ with applied voltages leads us to suppose that impact ionization of impurities occur as in the case of glass[3], or it may rather be supposed that the slow elevation is attributed to the non-uniformity of the barrier layer. But the fact that the current *versus* voltage curve is steeper than $\bar{n}^2/\bar{n}$ *versus* voltage curve, shows a rather narrow distribution of avalanche size in contrast with the case of glass. Thus by taking the ratios of i to $\bar{n}^2/\bar{n}$, we can obtain the incident numbers of charge carriers into the barrier layer. At lower voltages these numbers are attributed to Schottky emission and at higher voltages to field emission.

No such avalanche noises are detected in the forward direction.

These results tell us that in the analysis of the back ward characteristics of the rectifier we must notice the electron multiplication especially at higher voltages.

Nextly, we can explain the fact which was observed in the previous work (1) that the differential resistance at a high voltage in the blocking direction was smaller than the spreading resistance especially at low temperature. Increase of charge carriers owing to electron multiplication makes the apparent resistance of the bulk semiconductor smaller than that which is obtained from the forward characteristics in which the charge carrier consists of single charge.

The details of this work will follow in this journal.

References

1) M. Tomura: J. Phys. Soc. Japan **5**(1950) 349.
2) F. Seitz: Phys. Rev. **76** (1949) 1376.
3) F. E. Haworth and R. M. Bozorth: Physics **5** (1934) 15.
4) M. Tomura and Y. Abiko: J. Phys. Soc. Japan in press.

J. PHYS. SOC. JAPAN **7** (1952) 221–222

The Interpretation of Nijboer Theory for BaO from the View-point of Co-existence of Various Impurity Levels

By Shin-ichiro NARITA
Kobe Kogyo Corp. Kobe

(Received July 13, 1951)

It is widely known that Nijboer's theory is well applied to oxide coated cathode[1]. However, recent discovery of p-type conduction by Wright[2] in the cathode and several experiments[3] on the stand-point of existence of numerous kinds of levels in the oxide which were done being stimulated from the discovery of various kinds of centres in alkali halide, have made it necessary to reexamine the position and the limitation of the application of Nijboer's theory to oxide coated cathode.

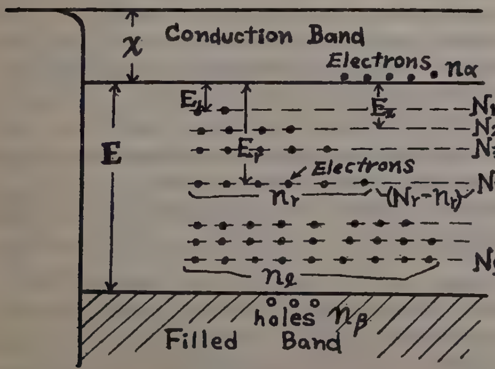

Fig. 1. Energy level diagram for oxide-coated cathode

We may assume l kinds of levels in the forbidden band of the oxide, on which we may place number in order of height of energy as shown in Fig. 1.

For the purpose of this discussion following symbols are used. E_r and E: the depths of the rth levels and the filled band from the bottom of the conduction band respectively.

N_r: the number of the rth levels.

n_r: the number of electron in the rth levels.

n_α and n_β: the number of electron in conduction band and that of positive hole in filled band respectively.

m_{e*} and m_{h*}: the effective mass of the electron and the positive hole respectively.

$\sum_d$: summation only to donar type level.(which have a electron at the neutral state.)

and the other notations having their usual meanings.

Then we may express the electron states in the oxide crystals, according to statistical mechanics, as follows.

$$\frac{n_\alpha(N_r-n_r)}{n_r}=2(2\pi m_{e*}kT/h^3)^{3/2}\exp(-E_r/kT) \qquad (1)^r$$

$$n_\alpha n_\beta=4[(2\pi kT)^3(m_{e*}m_{h*})^{3/2}/h^6]\exp(-E/kT) \qquad (2)$$

and

$$\sum_d N_r-\Sigma n_r=n_\alpha-n_\beta \qquad (3)$$

Eq. $(1)^r$ represents the rth of l equations and can be neglected in the evaluation of free electrons, n_α, when n_r is very small comparing to the number of the other levels or E_r is too large to contribute electrons to the conduction band at the measuring temperature, and also be disregarded in the calculation of positive holes, n_β, when (N_r-n_r) is very small or $(E-E_r)$ is so large.

When the oxide-coated cathode is in equillibrium with the outer oxygen pressure, the number of the rth levels, N_r, may be given by.

$$N_r=\alpha_r p^{S_r/2}\exp(-Q_r/kT) \qquad (4)$$

Where α_r is a constant determined from statistical mechanics, p is the outer oxygen pressure, S_r means that a rth level is produced by removing S_r barium atoms or S_r oxygen atoms from the lattice point, and Q_r represents the heat of the formation of a rth level.

As a simple example of this theory, both donar level of F-centre type and acceptor level of V-centre type are assumed to coexist in oxide coated cathode and the energy difference between the conduction band and the filled band is supposed to be so high that the coexistence of free electrons and free positive holes in a crystal is impossible. In this case, the equations upper described are abbreviated to the following four equations.

If $N_n > N_p$,

$$\frac{n_\alpha(N_p+n_\alpha)}{N_n-N_p-n_\alpha}=2\left(\frac{2\pi m_{e*}kT}{h^3}\right)^{3/2}\exp(-E_n/kT) \qquad (5)$$

If $N_p > N_n$,

$$\frac{n_\beta(N_n+n_\beta)}{N_p-N_n-n_\beta}=2\left(\frac{2\pi m_{h*}kT}{h^3}\right)^{3/2}\exp(-E_p/kT) \quad (6)$$

and

$$N_n=\alpha_n p^{-1/2}\exp(-Q_n/kT) \quad (7)$$

$$N_p=\alpha_p p^{1/2}\exp(\ \ Q_p/kT) \quad (8)$$

Where N_n and N_p is the number of donars and acceptors respectively, E_n, is the energy difference between donars and the conduction band and E_p is that between acceptors and the filled band.

When N_p is constant which is considered to realize in some experiments, by Eq. (5) is meant Nijboer's theory and N_p may be equivalent to froze-in-hole in the theory.

For the purpose of the numerical calculation of Eqs (5) and (6), following values are used and the results shown in Fig. 2 are obtained

$$E_n=E_p=1.0\,eV, \qquad Q_n=Q_p=0.4\,eV,$$

and $N_n=6.919\times10^{16}$, $N_p=1.445\times10^{12}$ at the oxygen pressure of $10^{-6}\,mmHg$.

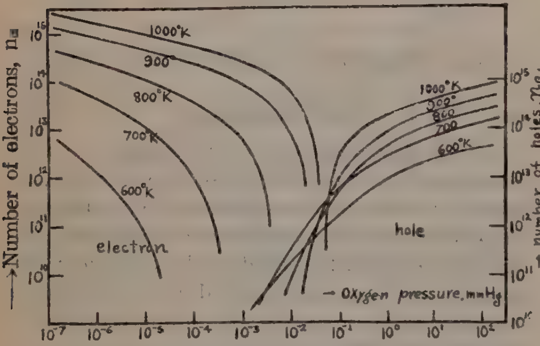

Fig. 2. The numerical calculation of the concentration of conduction electrons and holes

From the theory, we may understand the p-n transition accompanied with the change of temperature reported by Wright[3] and p-type conduction at high oxygen pressure observed by Ishikawa and his colaborators[4]

References

1) H. Kawamura: Su-butsu Gakkaishi in Japanese **17** (1943) 159.
T. Arizumi and S. Narita: J. Phys. Soc. Jap. **3** (1948) 356.
T. Arizumiand S. Narita: J. Phys. Soc. Jap. **6** (1951) 15.
2) D. A. Wright: Nature **164** (1949) 714
3) T. Hibi: Phys. Rev. **83** (1951) 566
H. B. DeVore and J. W. Dewdney: Phys. Rev. **83** (1951) 805
4) Y. Ishikawa, T. Sato, O. Okumura & T. Sasaki: oral presentation to the meeting of Phys. Soc. Japan.

J. PHYS. SOC. JAPAN **7** (1952) 222-223

Color Centers of Quartz and Fused Quartz

By Ryosuke YOKOTA

Matsuda Research Laboratory, Tokyo Shibaura Electric Co., Kawasaki, Kanagawa-ken

(Received November 28, 1951)

Quartz with the size-edge parallel to the principal axis (10×20×1 mm) is discolored dark brown by exposing to X-rays (100 KV, 3mA, tungsten target) during 56 hours. Its absorption is measured by the Beckman spectrophotometer in the range from 200 to 1200 mμ as shown in Fig. 1 (A). The new band* having its peak at 2.68 ev has been disclosed, its shape being of rather broad bell-type.

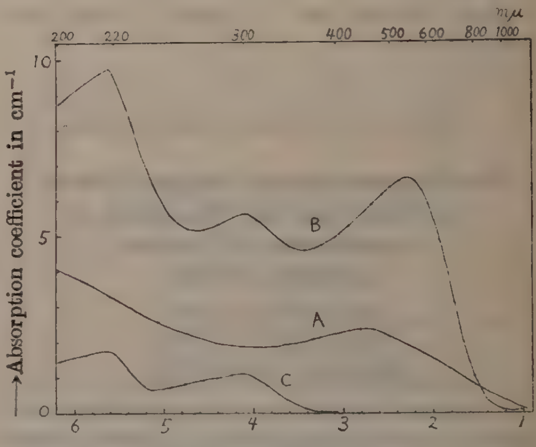

photon energy in e v

Fig. 1. (A): The absorption bands in quartz after the exposure to X-rays.
(B) and (C): The absorption bands in the fused quartz prepared in the reducing and oxidizing conditions respectively.

Fused quartz, prepared in a strongly reducing condition, has been exposed to X-rays in the same condition. The violet discoloration is produced and its absorption curve is shown in Fig. 1 (B). The three bands with peaks at 2.3, 4.1 and 5.6 ev respectively have been observed, the shapes being rather sharper than those in quartz crystal.

When the fused quartz, prepared in a mildly oxidizing condition, is exposed to X-rays in the same condition, no discoloration, is produced in the visible region, but the absorption curve shown in Fig. 1 (C) has indicated the existence of two bands with peaks at 4.1 and 5.6 ev respectively.

---

* Since 1925, quartz has been found to be discolored by the exposure to X-rays, but its absorption had not been measured. G. Forman (J.O.S.A. **41** (1951) 377), who has measured its absorption only in the visible region failed to find the absorption band found by the author.

The facts that the distinct absorption bands are produced in fused quartz may indicate, together with the results of the X-ray analysis¹⁾ and the thermal conductivity measurement,²⁾ that the fused quartz has in fairly extent the local order having the cristobalite-like structure, in view of the absorption band being affected mainly by the situation of the neighborhood of the color center.

The curious fact that each band in fused quartz is rather sharper than that in quartz may be partly explained by the fact that in fused quartz the degree of the covalent character of Si-O-Si bond is smaller than in quartz, according to the consideration of the molecular refraction.³⁾

It seems to be considered generally, for example, by Fröhlich,⁴⁾ Simpson⁵⁾ and Turner and Lewis,⁶⁾ that in the glass there are large numbers of defects in the lattice which act as the trapping centers of electrons or positive holes.

On the other hand, from the measurement of the density and lattice constant of quartz, Addink⁷⁾ has concluded that quartz is a fairly perfect crystal probably next to diamond.

The saturation of coloration takes place approximately after the exposure to X-rays during 56 hours in both quartz and fused quartz.

The absorption curves in Fig. 1 show that the concentration of color centers in fused quartz prepared in the reducing condition is only two or three times that of quartz, while the concentration in fused quartz prepared in a mildly oxidizing condition is about one fourth that of quartz. This seems to be apparently inconsistent with the model of the glass adopted by Fröhlich *et al*, which, however, may partly be removed by the following tentative consideration.

According to the measurement of O. Gayling v. Altheim,⁸⁾ the activation energy for diffusion of vacancy, which is obtained from the temperature dependence of the electrical conductivity, is 1.53 ev in fused quartz and 1.06 ev in quartz along the direction perpendicular to the principal axis. Therefore the number of vacancies can hardly increase during the exposure to X-rays in the case of fused quartz, but can increase in the case of quartz. To verity the above reasoning, the measurement of density before and after exposure to X-rays is being planned.

A further detailed study of the above curious facts in color centers in both quartz and fused quartz may lead to one of the keys to solve the problem 'what is a glass' in view of the difference of glass and crystal being the most important problem in physics of glass.

References

1) B. E. Warren: J. Appl. Phys. **13** (1942)602; R. Yokota: J. Phys. Soc. Japan **5** (1950) 354
2) C. Kittel: Phys. Rev. **75** (1949) 972
3) R. Yokota: J. Phys. Soc. Japan **6** (1951) 489
4) H. Fröhlich: Proc. Roy. Soc. **A 188** (1947) 521
5) J. H. Simpson: Proc. Phys. Soc. **A 63** (1950) 86
6) C.H.M. Turner and W.E.Lewis: Nature **159** (1947) 334
7) N.W.H. Addink; Recueil des Trav. Chim. d. Pays-Bas **70** (1951) 202
8) O. Gayling von Altheim: Ann. d. Phys. **35** (1939) 417

J. PHYS. SOC. JAPAN **7** (1952) 223–225

Construction of a Far Infra-Red Spectrometer with Echelette Grating

By Hiroshi YOSHINAGA and Yahiko YAMADA
Department of Applied Physics, Faculty of Engineering, Osaka University

(Received December 18, 1951)

In order to analyze the far infra-red radiation, we have ruled echelette gratings and constructed a far infra-red spectrometer with the grating.

As the material for echelette gratings, we used the copper plates which were polished into good surface on the soft pitch disk with chromium oxide as the abrasive. The surface had the precision of 5 fringes tested by Newton's ring method.

The ruling of echelette grating was performed by a modified comparator of which the principal screw was of 1 mm pitch and attached worm and worm gear of 1/40 gear ratio. The ruling cutter was the edge of the diamond polished artificially into pyramid. To rule good grooves it was desired that the edge of the cutter was fixed towards the direction of ruling and the slow slope came in touch with next new groove which would be ruled.

To reduce the error of grating constant the direct reading method was used in the ruling by a micrometer microscope. With this method the error of grating constant was reduced to 0.2μ at 25μ gratings.

It is important to examine the controlled groove forms which contribute to concentrate the energy into the first order spectrum of one side. Fig. 1 shows the groove form by means of celluloid printing method, and Fig. 2 shows the microscopic photography of the echelette grating surface focused upon the top of the groove, which are of 64× and 400× respectively.

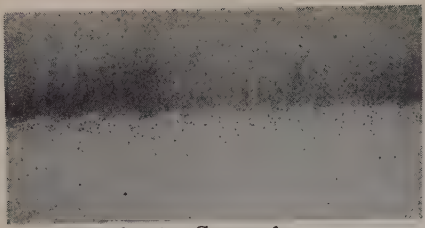

Fig. 1. Groove form.

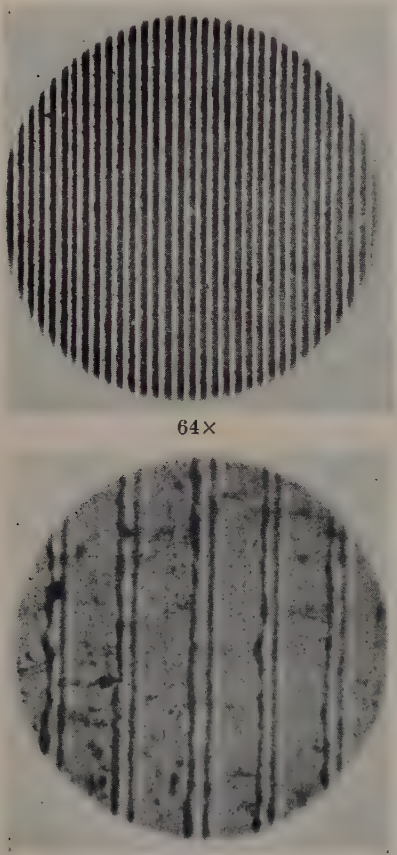

64×

200×

Fig. 2. Microscopic photography of the grating surface.

In order to examine the practical energy distribution on each order spectrum, we used the residual ray 8–9μ from crystalline quartz plates as the monochromatic source as this ray was too short in wave-length for 25μ gratings but very strong. Integrating the curves of distributed energy by a planimeter, we get the results in table I. for a 25μ grating.

Table I. Energy distribution on each order (%)

Order	4	3	2	1	0	−1	−2	−3	−4
Cal.	0.03	2.48	0.68	79.66	0.04	7.84	2.85	3.16	3.08
Obs.	0.1	6.0	14.7	60.7	10.8	2.9	3.2	1.6	0

The calculated values from the Stamm's equation[1] are listed for comparizon with ours.

Fig. 3 shows the schematic diagram of the spectrometer. It is the type of the Michigan Spectrometer[2] and is consisted of the grating (14×16cm), the collimating mirror (paraboloidal, 34cm in dia., 161cm in f and $\Delta f/4f<1/10000$ for each zone, and used lower half-part), and two bilateral slits (2 cm in length). The grating table may be swung into desired position by means of the worm gear at minimum adjustment of 0.0110μ at the wave-length of 25μ. The source is the globar and the detector is a thermopile of 2 tellurium-constantan junctions, connected through a galvanometer.

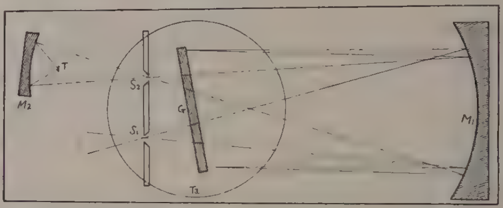

Fig. 3. Schematic diagram of the far infrared spectrometer.
S_1: entrance slit;
M_1: paraboloidal collimating mirror:
G: echelette grating; S_2: exit slit;
M_2: spherical mirror; T: thermopile;
Ta: grating table.

The residual rays from crystalline quartz plate: 8–9μ, 20.7μ; fluorite plate: 23μ, 32.8μ; MgO plate: 15–19μ; calcite plate: 29.4μ; were used for the test of the spectrometer, and the absorption of a few chemical compounds, CCl_4(3) and CS_2(4), were measured, in the cell which was 3cm long and fitted with 0.5mm KBr plate windows, contained CCl_4 and CS_2 vapor saturated at room temperature (24°C), and at the slit width of 0.9mm. Some results of these measurements are shown in Figs. 4 and 5.

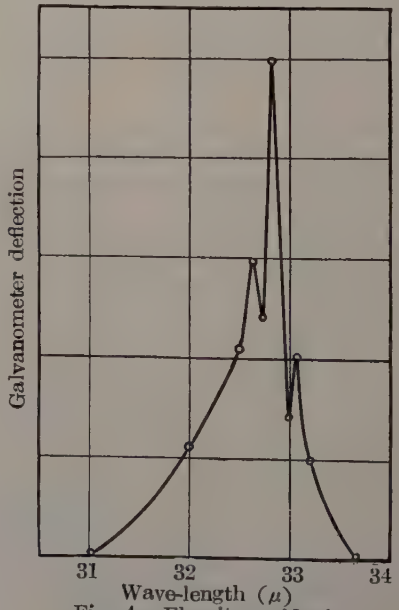

Fig. 4. Fluorite residual ray.

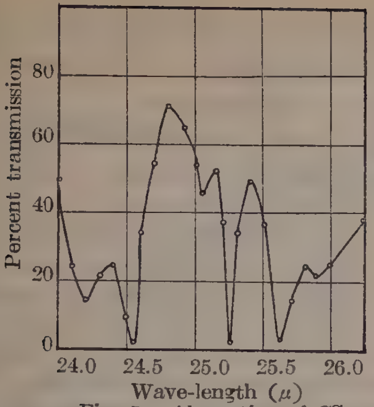

Fig. 5. Absorption of CS_2.

The theoretical resolution of this type spectrometer is dependent upon the following three factors. The slit width 1mm of this spectrometer (equal width for both slits) contains the interval of 0.213 cm^{-1} at 400 cm^{-1}, by the error of the collimating mirror 1/10000 the wave-number error is 0.20 cm^{-1} at 400 cm^{-1}, and the flatness of the grating causes the error of 0.005 cm^{-1} at 400 cm^{-1}. These three factors amount about 0.5 cm^{-1} at 400 cm^{-1}, but from the above results of the measurements the practical resolving power is 0.8 cm^{-1} (0.05μ) at about 400 cm^{-1} (25μ). This spectrometer is useful till 35μ or more, and will be used for the investigation of the structure of molecules and crystals.

References

1) R.F. Stamm and J.J. Whalen: J.O.S.A. **34** (1944) 1.
2) H.M. Randall: R.S.I. **3** (1932) 196.
H.M. Randall and F.A. Firestone: R.S.I. **9** (1938) 404.
H.M. Randall: Rev. Mod. Phys. **10**(1938) 72
3) H.H. Marvin: Phys. Rev. **33** (1929) 952.
4) D.M. Dennison and N. Wright: Phys. Rev. **38** (1931) 2077.
P.P. Barchewitz and M. Parodi: J. de Phys. **10** (1939) 143.

J. PHYS. SOC. JAPAN **7** (1952) 225-226

Electron Avalanche and Dielectric Breakdown in Solids II

By Chiyoe YAMANAKA and Tokuo SUITA
Faculty of Engineering, Osaka University

(Received December 20, 1951)

We have reported the mean size of electron avalanches in alkali-halide crystals under a high electric field which was measured in the same way as Haworth and Bozorth1)2). Now we report some interesting results7) about the distribution of avalanches which we could get by the electronic counter and the pulse amplifier.

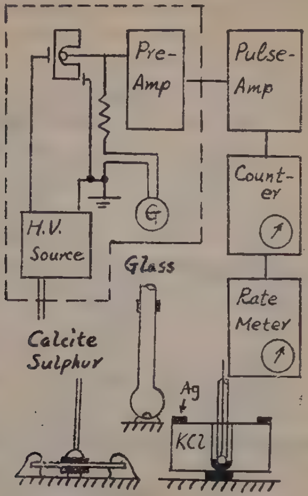

Fig. 1. Experimental Arrangement and Specimens.

Our measuring apparatus and specimens are shown in Fig. 1. The pulse amplifier had the properties of rise time 0.1μ sec., and maximum gain 10^6. The specimens of KCl crystal were bored at the center provided guard rings and quartz tubes. The calcite and sulphur specimens were coated with paraffin. Their electrodes were made by silver sputtering. The distance between the electrodes was less than 0.5mm. But the glass specimens were in the form of bubbles blown from small tubes with mercury electrodes. Their thickness was less than 0.05mm.. The specimens of KCl had been treated by applying a weak field at 300°C., producing dendrites, by which the boundary seemed to keep good contact.

The probabilty3)4) that one initial electron from the cathode has grown to an avalanche of n electrons at a distance x from the cathode can be written, if $n \gg 1$,

$$P(n,x) \doteqdot 1/\bar{n} \cdot \exp(-n/\bar{n}).$$

The expectation value of n is, $\bar{n} = \exp(x/\Lambda)$, where Λ is the distance that the electron travels before recieving sufficient energy to produce a secondary electron. If we write the number of initial electrons from cathode, ν_0 and the number of initial electrons which are liberated from the unit length of bulk solid, ν_i, the frequency of avalanches, k, is,

$$k \doteqdot (\nu_0/n + \nu_i \Lambda/n)\exp(-n/\bar{n}).$$

and also we get the measured mean current i,

$$i = 2\nu_{eff} \int_0^d n(x)/d \cdot dx \doteqdot 2\nu_{eff} \varepsilon \Lambda/d \cdot \exp(d/\Lambda),$$

where ε: electronic charge, d: distance between electrodes, ν_{eff}: effective number of initial electrons. From this equation we can estimate Λ. (See Table I), The average frequency of avalanche that has more than n electrons is,

$K = \nu_{eff} \cdot \exp(-n/\bar{n})$.

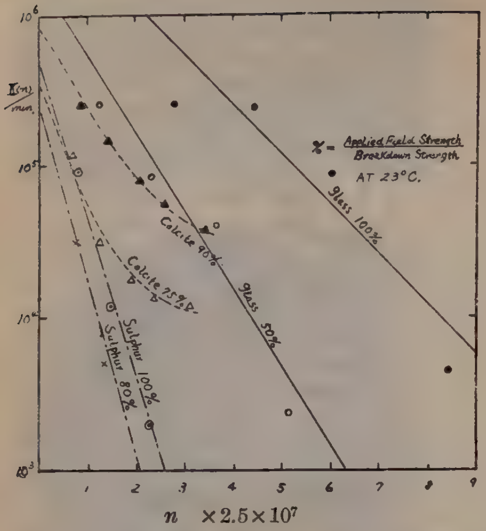

Fig. 2. Probability Distribution in Glass, calcite and sulphur.

In Fig. 2 and Fig. 3 we show K and n of calcite, glass, sulphur and KCl. The behaviour of avalanche distributions in KCl is very interesting. At the higher temperatures than 170°C. at which the dendrites began to appear, the avalanches were rather small in magnitude and many in number; on the other hand, at the temperature lower than this threshold, very large avalanches began to appear and their numbers tended to decrease. The avalanches in glasses were large in magnitude and many in number. In sulphur, the avalanches were not measured until the field strength reached more than 80 percent of the breakdown strength.

These results seem to show that at the lower temperatures the fewer but more energized electrons are dominant to cause the breakdown; and at the higher temperatures the more numerous, but less energized electrons chiefly contribute to the determination of breakdown. This interpretation seems to coincide with the experimental results of the breakdown path direction.⁵⁾ Comparing the results of KCl with sulphur, initial electrons of KCl are larger in frequency than sulphur. The effect of this difference has been observed in the experiment on breakdown time-lag.⁶⁾ In all cases the number of initial electrons varies with applied field and temperature. Under these high electric fields Furry's distribution approximately holds.

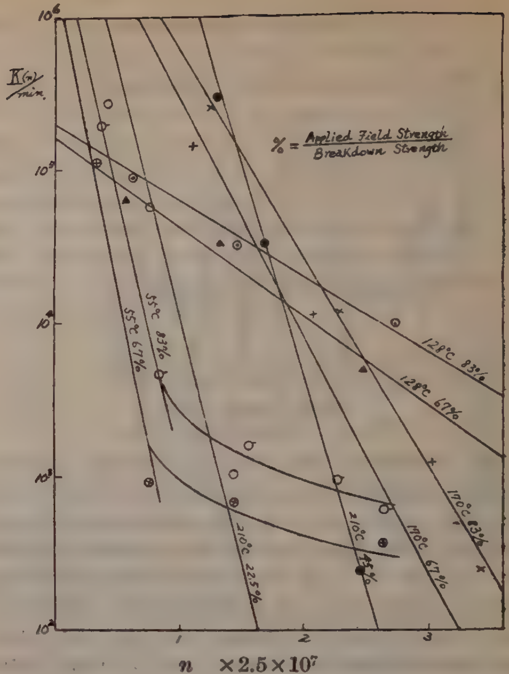

Fig. 3. Probability distribution in KCl.

Table I

specimen	KCl								Calcite		Glass		Sulphur	
temperature C.	210°		170°		128°		55°		23°		23°		23°	
$\frac{\text{applied field}}{\text{breakdown field}}$ %	45	22.5	83	67	83	67	83	67	90	62.5	100	50	100	80
Λ 10^{-3} cm.	2.5	2.9	1.6	2.0	1.5	1.7	2.6	2.9	2.8	2.9	0.23	0.28	2.6	2.8

Reference

1) C. Yamanaka, T. Suita; J. P. S. Japan **6** (1951) 194.

2) H. Kawamura, M. Onuki; Ibid, 283

3) W. H. Furry; Phys. Rev., **52** (1937) 569.

4) K. A. Wijsman; Phys. Rev., **75** (1949) 833

5) T. Suita; Read before the annual Kansai meeting of I.E.E. Japan **I**, 1–17. (1951)

6) Y. Inuishi; Ibid. **I**, 1–18.

7) Y. Inuishi, C. Yamanaka and T. Suita; Tech. Rep. of Osaka University. **2** (1952) 70.

J. PHYS. SOC. JAPAN **7** (1952) 227

The Light Scattering by Non-Spherical Particles in Solutions, II, Analytical Formulation

By Nobuhiko SAITÔ and Yuichi IKEDA

Kobayasi Institute of Physical Research, Kokubunzi, Tokyo

(Received December 27, 1951)

We have published an article[1)]* about the light scattering by non-spherical particles, where we have been imposed to lend ourselves to numerical calculations in the final stages. Dr. Gerald Oster kindly informed us that the angular distribution of the light scattered by spheroidal particles treated in § 3 of the previous paper (I) has been obtained by Roess and Shull[2)] in series expansion using hypergeometric function. Suggested by their work, we have obtained an analytical representation for the angular distribution of the scattered light by cylindrical particles treated in § 4 of (I).

From Eqs. (7–I) and (24–I) we have

$$\frac{J}{J_0}=2\int_0^{\pi}\frac{\sin^2(\alpha\cos\theta)}{\alpha^2\cos^2\theta}\,\frac{[J_1(\beta\sin\theta)]^2}{\beta^2\sin^2\theta}\sin\theta\,d\theta. \quad (1)^{**}$$

Expanding each factor of the integrand in series α and β[3)] we obtain

$$\frac{J}{J_0}=2\int_0^{\pi}\sum_{n=0}^{\infty}\sum_{m=0}^{\infty}\frac{(-)^{m+n}\Gamma(2m+3)\alpha^{2n}\beta^{2m}\sin^{2m+1}\theta\cos^{2n}\theta}{2^{2(m-n)+1}m!(2n+2)!(m+2)!\{(m+1)!\}^2}d\theta. \quad (2)$$

By virtue of the relation

$$\int_0^{\pi}\sin^{2m+1}\theta\cos^{2n}\theta\,d\theta=\frac{\Gamma(n+1/2)m!}{\Gamma(n+m+3/2)}, \quad (3)$$

we finally obtain

$$\frac{J}{J_0}=\sum_{m=0}^{\infty}\sum_{n=0}^{\infty}\frac{(-)^{m+n}\Gamma(2m+3)\Gamma(n+1/2)\alpha^{2n}\beta^{2m}}{(2n+2)!\Gamma(m+3)\{\Gamma(m+2)\}^2\Gamma(n+m+3/2)}\cdot\frac{1}{2^{2(m-n)}}$$

$$=\sum_{k=0}^{\infty}\frac{(-)^k(2\alpha)^{2k}}{\Gamma(k+3/2)}\sum_{m=0}^{k}\frac{\Gamma(2m+3)\Gamma(k-m+1/2)}{\Gamma(m+3)\{\Gamma(m+2)\}^2\Gamma(2k-2m+3)}\frac{1}{(4f)^{2n}}, \quad (4)$$

or

$$\frac{J}{J_0}=\sum_{k=0}^{\infty}\frac{(-)^k(2\beta)^{2k}}{\Gamma(k+3/2)}\sum_{m=0}^{k}\frac{\Gamma(2m+3)\Gamma(k-m+1/2)}{\Gamma(m+3)\{\Gamma(m+2)\}^2\Gamma(2k-2m+3)}\frac{f^{2(k-m)}}{4^{2m}}, \quad (5)$$

where $f=a/b$,

In the limiting case of $f\to 0$, *i. e.*, for circular disk, Eq. (5) leads to

$$\frac{J}{J_0}=\frac{2}{\beta^2}\left\{1-\frac{1}{\beta}J_1(2\beta)\right\}. \quad (6)$$

The authors wish to express their sincere thanks to Dr. Gerald Oster for his valuable informations and criticisms.

Notes and References

* In this Short Note this paper[1)] is cited as (I) and the equations therein as, for example, (24–I). The notations are same as in (I).

** J/J_0 is the ratio of the intensity of the scattered light in an arbitrary direction to that in the direction of the incident light. J_1 in Eqs. (1) and (6) is the Bessel function of the 1st order. They should not be confused.

1) N. Saitô, Y. Ikeda: J. Phys. Soc. Japan **6** (1951) 305.

2) L. C. Roess, C. G. Shull: J. Appl. Phys. **18** (1947) 308.

3) G. N. Watson: *Theory of Bessel Functions*, Cambridge, 1922, p. 147.

J. PHPY. SOC. JAPAN. **7** (1952) 227–228

Electronic Mobilities in Diamond at High Electrostatic Fields

Masao TOMURA and Takeo KIKUCHI

Institute of Polytechnics of Osaka City University.

(Received, November 7, 1951)

In the absence of an external electrostatic field, the conduction electrons of an insulator or semiconductor will possess the Maxwell-Boltzmann distribution. As the field intensity grows, however, the distribution may be altered because an electron possessing thermal energies may gain energy from the field more rapidly than it loses it to the lattice vibrations. F. Seitz[1)] has calculated the increase with energy of the collision of a free electron in a non-polar crystal. According to the well-known condition that the rate of gain of energy of a conduction electron is counter-balanced by the rate of transfer of energy to the lattice vibrations, the following relation is derived

$$E^2=(4/9\pi)(mC^2k^3/Mn_0e\hbar\mu) \quad (1)$$

in which the notations are the same as those in Seitz's paper and the coupling of electrons with the optical modes of vibrations has been neglected. Since the equation[1)] gives us a definite electron energy at which the energy balance is established under the influence of the electrostatic field E, we can estimate the critical field strength Ec at which the Maxwell-Boltzmann distribution begins to be appreciably distorted.

Since no exact knowledge of the distribution function of conduction electrons has been known, at present above the critical field Ec, we shall tentatively assume the validity of Eq. (1) in order to derive the field dependencies of the current density at high electrostatic fields. The Eq. (1) is easily shown to lead to the result that the current density is proportional to the square root of the applied field and the apparent mobility decreases with the increase of the field strength. In the present paper the current density and the apparent mobility at high electrostatic field below the breakdown strength has been described to behave in accordance with the above result.

Diamond is a non-polar monatomic single crystal and its Debye temperature is so high as 1800°K that the interaction of electrons with the acoustital lattice-vibrations is dominant below 1000°K, on account of which the neglection of the optical coupling in Eq. (1) has been justified.

As, in the room temperature region, diamond shows no correct volume conductivity owing to the space charge effect, the dependencies of the current densities on the field were measured in the temperature region of about 1000°K where the space charge effect may nearly be neglected. The results are shown in Fig. 1. The sample *B* shows that the apparent mobility begins to decrease above 5 kV/cm. At the lower fields the small amount of space charge effects seems still to remain. Above Ec the relation between the current and the field does not follow the above mentioned one, which states of affairs may be due to the residual space charge or some other causes. On the other hand, the current-field curve is linear till 30 kV/cm in the sample *A*. Above 30 kV/cm the surface leakage became dominant because of the small size of the sample and the observation could not be carried through.

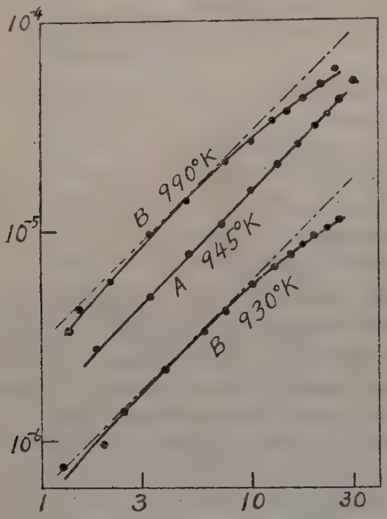

Fig. 1. abscissa; Field in kv/cm.
ordinate; Current density in amp./cm²

The directional effect of the fields with respect to the crystal axises were not yet observed in both samples.

According to the observation of E. A. Pearlstein and R. B. Sutton[2)], the mobilities of diamond are found to be 6.3×10^3 cm²/volt·sec at 1.5kV/cm, 3.5×10^3 cm²/volt·sec at 6 kV/cm and 8.7×10^2 cm²/volt·sec at 25kV/cm respectively in the room temperature region. By the use of the high temperature value of the mobility extrapolated from 6.3×10^3 cm²/volt sec at the room temperature according to the $T^{-3/2}$ law and the value of *C* estimated from the mobility observation, we are able to obtain, by the above equation (1), $Ec=6.5$ kV/cm at 1000°K, which value is found to agree well with the observed value in Fig. 1. Although C. C. Klick and and R. J. Maurer[3)] observed the electron mobility in diamond through the Hall constant measurement, their values are too small compared with those of Pearlstein and Sutton. Further, according to W. Shockley[4)], the Hall mobility is shown to be smaller than the drift mobility and the microscopic mobility, on account of which the experimental data of the Hall mobility are not taken into account in our discussion,

References

1) F. Seitz; Phys. Rev. **73** (1918) 549. **76** (1949) 1376

2) E. A. Pearlstein and R. B. Sutton; Phys. Rev. **79** (1950) 907

3) C. C. Klick and R. J. Maurer; Phys. Rev. **81** (1951) 124

4) e. g. J. R. Haynes and W. Shockly; Phys. Rev **82** (1951) 935

J. Phys. Soc. Japan **7** (1952) 228–230

Microwave Generation on Opening Electrical Contacts

By Taiji Arakawa
Toyokawa Branch of Nagoya University

(Received December 22, 1951)

When electrical contacts are opened, microwaves are generated, which are deeply connected with the discharge phenomena between the contacts. Experiments reported here were undertaken to observe these relations.

The circuit used was made of the contacts S, storage battery E, rheostat R, inductance *L* and condenser C (Fig. 1.) The opening of contacts was carried out by a electromagnet M. The average speed of seperat-

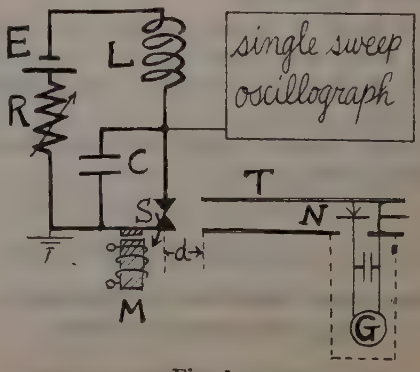

Fig. 1.

ing contacts during the time interval of 2×10^{-3} sec. after the metallic break was about 2 cm/sec. In order to detect microwaves genearted on opening the contacts S, a rectangular waveguide T (which was placed at a distance d from the contacts so that the H_{01} waves with the cut-off wave-length $\lambda_c=10$cm might be excited), a crystal rectifier N and a ballistic galvanometer G (current sensitivity: 1.36×10^{-10}A/mm, period 24 sec.) were equipped as seen in Fig. 1. The maximum deflection of G by microwaves generated impulsively was measured on each opening of contacts. The detecting circuit was sufficiently shielded and the length of T was long enough (40 cm) so that the deflection of G might be due to microwaves only. It was ascertained experimentally that, by short circuiting by a metal plate over the opening of T, the deflection of G reduced to zero. The life times of the arc, spark and glow discharge were measured by observing the transient waveforms of potential across the contacts on a single sweep cathoderay oscillograph.

The deflection of G and the life time of each discharge stage were measured at each value of the initial current I $(=E/R)$ which varied from 0.1A to 5.0 A in appropriate intervals under the conditions: $E=6$V, $L=0.1$ H, $C=0$, $\lambda_c=10$ cm. The contact metals examined were tungsten, platinum, copper, silver, aluminium, gold, nickel and zinc. Their surfaces were polished at the beginning of each series of measurements. An example of results in the case of silver is shown in Fig. 2. From this figure, we can see that with the increase in the initial current I, the deflection of G passes through the maximum and then becomes too small to be detected at large values of I, and that the life time of spark stage shows a similar behavior with the deflection of G, while those of arc and glow stages do not. These features were observed in cases of all other contact metals mentioned above. It must be added that one of the dashed curves in Fig. 2 represents the transient region of spark stage which could not be easily distinguished from the arc stage, and the other represents the glow stage which was unstable in the case above. Consequently, it is concluded that the generation of microwaves on opening contacts is mainly due to the spark discharge and their intensity is maximum at a certain value of the initial current. This spark stage is known to consist of a number of single spark discharges succeeding intermittently[1)], and therefore, the increase of the deflection of G with that of the initial current at a smaller value can be presumably ascribed to that of the number of single spark discharges. The curves of deflection of *G versus* initial current for the various contact metals obtained under same conditions are hown in Fig. 3. The initial current *Im*, which gives the maximum deflection of G, and the minimum arcing current at minimal length arc characteristics are collected together in Table I. We can see that the sequence of magnitude of the former is in agreement with that of the latter provided that the experimental conditions are the same. This result is reasonable, if we consider that the spark, and accordingly the generation of microwaves is largely suppressed by the appearance of the arc as seen in Fig. 2. The value of *Im* will vary with the experimental conditions. It was observed that this value reduced with the increase of L (0.01∼2 H) or the decrease of C (0∼0.005 μF) and was almost the same in both cases of $\lambda_c=10$ cm and 3 cm. Moreover we can see in Fig. 3 and Table I that the intensity of generated microwaves is large in the case of the

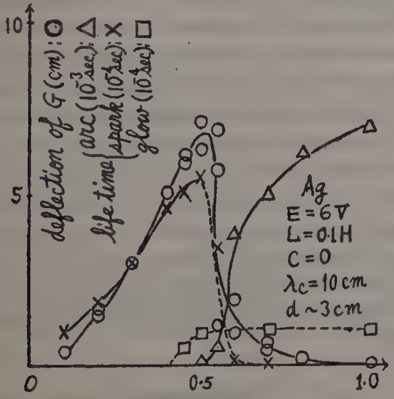

initial current (A)
Fig. 2.

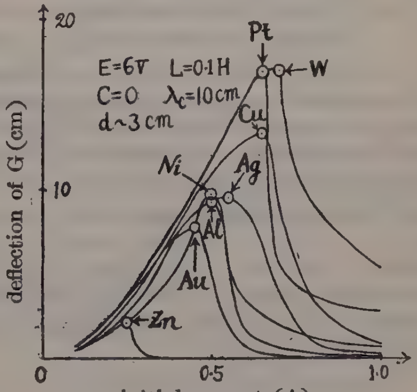

initial current (A)
Fig. 3.

Table I (in A)

	Im	minimum arcing current	
		Holm[2)]	Fink[3)]
W	0.70	1.0	1.27
Pt	0.65	0.9	1.0
Cu	0.65	0.43	——
Ag	0.55	0.4	0.9
Al	0.50	——	——
Ni	0.50	0.5 (in N_2)	0.2
Au	0.45	0.32 (in N_2)	0.42
Zn	0.25	(0.1)	0.36

contact metal having a large minimum arcing current at minimal length arc characteristics.

The writer wishes to express his gratitude to Prof. H. Kumagai, Institute of Science and Technology, University of Tokyo, and to assistant Prof. Y. Mizuno Mizuho Branch of Nagoya University, for their kind encouragements.

Referencies

1) A. M. Curtis: Bell Sys. Tech. Jour. **19** (1940) 40

2) R. Holm: Wiss. Veröff aus dem Siemens-Werken 1939

3) H. P. Fink: Wiss Veröff. aus dem Siemens-Werken **17** (1938) 251

J. PHYS. SOC. JAPAN 7 (1952) 230

On the Relation between Fermions and Bosons

By Morikazu TODA

Institute of Physics,
Tokyo Bunrika University

(Received February 1, 1952)

The method of sound developed by Einstein[1], Bloch[2], Tomonaga[3] and others aims to approximate a system by an aggregate of harmonic oscillators. If we restrict ourselves to the problem of a Fermion-system and its corresponding Boson-system, the fundamentals of the relation between them will be as follows:

Consider a system of non-interacting particles in a harmonics field. In terms of the Hermite polynomials the normalized wave function for a particle may be written in suitable units as

$$u_n(x)=(2^n n!\sqrt{\pi})^{-1/2}e^{-x^2/2}H_n(x)$$

its eigenvalue being $n+\frac{1}{2}$. We construct antisymmetric wave functions, or determinants

$$\phi_\lambda=\frac{1}{\sqrt{N!}}\sum_p(-)^p u_{\lambda_1}(1)\,u_{\lambda_2}(2)\cdots\cdots u_{\lambda_N}(N)$$

and symmetric wave functions, or permanents

$$\phi_\mu=\frac{1}{\sqrt{N!}}\sum_p u_{\mu_1}(1)\,u_{\mu_2}(2)\cdots\cdots u_{\mu_N}(N)$$

in which we place the λ's and μ's as

$$0\leq\lambda_1<\lambda_2<\cdots\cdots<\lambda_N,\quad 0\leq\mu_1\leq\mu_2\leq\cdots\cdots\leq\mu_N,$$

and the summations are to be taken over the permutations of the particles $1, 2, \cdots\cdots, N$.

If we put, for instance,

$$\mu_n=\lambda_n-n+1$$

then the equivalence between the Formi-oscillators and the Bose-oscillators is established, because there is one-to-one correspondence between ψ's and ϕ's, and the eigenvalues of these systems differ only by a constant. They are

$$E_\lambda=\lambda_1+\lambda_2+\cdots\cdots+\lambda_N+N/2,$$
$$E_\mu=\mu_1+\mu_2+\cdots\cdots+\mu_N+N/2$$

the lowest state of E_λ being $E_0=N^2/2$. It may be said that the excitation quanta of the Fermi-oscillators obey the Bose statistics. It must be noticed that the numbers of Fermions and Bosons are equal in this case.

The degree of the degeneracy of E_λ and E_μ being equal, the well-known generating functions must be written as follows

$$\prod_{n=0}^{\infty}(1+zx^n)=\sum_{N=0}^{\infty}z^N x^{N(N-1)/2}\chi_N(x),$$
$$\prod_{n=0}^{\infty}(1-zx^n)^{-1}=\sum_{n=0}^{\infty}z^N\chi_N(x)$$

Indeed these expansions can be readily verified with the partition function of N Bose-oscillators

$$\chi_N=1/(1-x)(1-x^2)\cdots\cdots(1-x^N);$$

thus the partition function for Fermi-oscillators approaches, with increasing N, to that of Bose-oscillators, i. e. to $\prod_0^\infty(1-x^n)^{-1}$. This is an extension of a tneorem of the θ-functions:

$$\sum_{n=0}^{\infty}q^{n(n+1)/2}=\prod_1^{\infty}(1-q^n)\prod_1^{\infty}(1+q^n)^2$$

Now, turning to the field theory, we construct the quantized wave functions which are

$$\Psi=\sum a_n u_n(x),\qquad \Phi=\sum b_n u_n(x)$$

where a_n and b_n, the annihilation operators, together with their conjugates a_n^+ and b_n^+, the creation operators, fulfil the commutation relations

$$[a_n,\ a_m^+]_+=[b_n,\ b_m^+]_-=\delta_{n,m}.$$

The correspondence between the Fermion and Boson-fields may be summerized as follows: The wave equations

$$\frac{1}{2}\left(-\frac{d^2}{dx^3}+x^2\right)\begin{pmatrix}\Psi\\ \Phi\end{pmatrix}=i\frac{\partial}{\partial t}\begin{pmatrix}\Psi\\ \Phi\end{pmatrix}$$

with the commutation relations

$$[\Psi(x),\Psi^+(x')]_+=[\Phi(x),\Phi^+(x')]_-=\delta(x-x')$$

can be unified. Ψ and Φ are counterparts of each other.

If the levels for a Fermion are not equidistant the above mentioned equivalence will be no longer rigorous. However, the weak excitation of Fermions can be approximated by Bosons. In this case we have only to replace the neighbourhood of the Fermi surface by equidistant levels appropriately chosen. This can be considered as the basis of the method of sound.

A difference between the present wethod and Tomonaga's must be mentioned. The above treatment handles with the wave function itself, whereas Tomonaga's the density operator. The merit of the latter is seen in dealing with the interaction term. A detailed account and applications will be published elsewhere.

References

1) A. Einstein: Ann. d. Phys. **33** (1910) 1275.

2) F. Bloch: Helv. Phys. Acta **7** (1934) 385.

3) S. Tomonaga: Prog. Theor. Phys. **5** (1950) 544.

JOURNAL OF THE PHYSICAL SOCIETY OF JAPAN Vol. 7, No. 3, MAY—JUN. 1952

Statistical Thermodynamics of the Superconducting State

Hiroshi ICHIMURA

Department of Physics, Tokyo Institute of Technology

(Received August 23, 1951)

An attempt has been made to interpret the superconducting state of the conduction electrons in the metal by the statistical mechanical treatment, introducting the second order effect of the lattice vibration on the electrons which has first been used by Fröhlich for this problem as the source of the attractive force in the momentum space. Using some reasonable simplifications, we can show the existence of a special equilibrium state which is stable below a certain temperature. If we consider this special state as the superconducting state, we can calculate the jump of the specific heat ΔC and the threshold magnetic field curve which represent well the experimental results: $\Delta C=\gamma T_c$ (γ is the electronic specific heat coefficient and T_c is the transition temperature), $H=2\pi^3Nk^2(T_c-T)/3\mu_0$ (μ_0 is the Fermi energy, N is the number of the electrons in 1 cm^3 and k is the Boltzman's constant).

§1. Introduction

Recently many quantum mechanical theories concerning the super-conducting state of the metallic electrons have been put forward. Heisenberg$^{1)}$ sought the origin of the superconductivity in the Coulomb interaction between electrons. On the other hand, Fröhlich$^{2)}$ and Bardeen$^{3)}$ took up the second order effect of the lattice vibration on the electrons as the source of the attractive force between electrons in k-space. Although both theories are far from satisfactory, Fröhlich's theory shows the hope to explain the isotopic mass dependency of the transition temperature and tells that there is some relation between the room temperature resistivity of the metal and the interaction energy which is thought to be acting in the superconducting state. But most of theories treat the system at 0° K and the quantitative statements concerning the transition can not be expected.

Here we give a theory at finite temperatures, adopting Fröhlich's interaction as its basis. With some assumptions, it can be regarded as the quantum mechanical refinement of the author's previous statistical mechanical theory.$^{4)}$ We can derive some relations between the experimental quantities such as the transition temperature, the jump of the specific heat at the transition, and the threshold magnetic field. In our opinion, however, it will go too far to say some metal should become superconducting or not in the present stage of our knowledges.

§2. General Formulations

a) We consider a metallic body of volume V, in which there are $N=\nu N_A$ conduction electrons. The total Hamiltonian H of this electron system can be written as

$$H=He+H'+H_I$$

$$H_e=-\frac{\hbar^2}{2m}\sum_i^N \Delta_i+\sum_i^N\sum_n^{NA} V(\boldsymbol{w}_i-\boldsymbol{R}_n)$$

$$H'=\epsilon^2\sum_{j>k}^N\sum^N\frac{1}{r_{jk}},\qquad r_{ik}=|\boldsymbol{w}_j-\boldsymbol{w}_k|$$

$$H_I=\sum_i^N\sum_n^{NA}(\boldsymbol{u}_i\cdot\mathrm{grad}\ V(\boldsymbol{w}_i-\boldsymbol{R}_n))\qquad(1)^{**}$$

$$\boldsymbol{u}_i=\frac{1}{\sqrt{N_A}}\sum_q\sum_\sigma e_{q\sigma}(a_{q\sigma}\exp(i\boldsymbol{q}\cdot\boldsymbol{w}_i)+a^*_{q\sigma}(-i\boldsymbol{q}\cdot\boldsymbol{w}_i))$$

where H_e is the Hamiltonian of the electrons in the periodic potential of the lattice ions, H' is the interaction between electrons and H_I is the interaction between electrons and lattice vibrations. We treat H' and H_I as the perturbation, using the one-electron picture for the conduction electrons and the normal mode

---

** We used the notations in the reference (5): $\boldsymbol{u}_i$ means the displacement of the electron in the lattice, q is the wave number vector of the normal mode, $a_{q\sigma}$ is its amplitude, and $e_{q\sigma}$ indicates the direction of the polarization.

decomposition for the lattice vibration.

The total unperturbed electronic wave function may be written in the from

$$\Phi_0=\frac{1}{\sqrt{V^N N!}}\,\mathrm{det.}\,|\,\Psi_{kj}(w_k)S_k\,| \qquad (2.2)$$

as usual, where Ψ_{kj} satisfy the equations

$$\left(-\frac{\hbar^2}{2m}\Delta+\sum V(w-R_n)\right)\Psi_{kj}(\mathrm{w})=\varepsilon^{(0)}\Psi_{kj}(w) \qquad (2.3)$$

and s_k are the spin functions. By the Bloch's theorem, we get

$$\Psi_{kj}(w)=\frac{1}{\sqrt{V}}\exp\,(i\boldsymbol{k}\cdot w)u_k(w) \qquad (2.4)$$

$$\varepsilon^{(0)}=\varepsilon^{(0)}(\boldsymbol{k}_j)$$

where $\mathbf{k}_j$ means the wave number vector.

It will not be a easy matter to obtain these u_{kj} functions for the real metals, but particular properties of each metal are supposed to be contained in these periodic functions.

In the lowest state at 0° K, the $\mathbf{k}_j$ values in Φ_0 fill up the so-called Fermi sphere.

Following the usual perturbation procedure, we can calculate the first order energy $E_0^{(1)}$ for H^I and the second order energy E_0^2 for H_I (the first order energy for this term vanishes).

For $E_0^{(1)}$ we get

$$E_0^{(1)}=\sum\sum\,(C(\boldsymbol{k},\boldsymbol{k}')-A(\boldsymbol{k},\boldsymbol{k}'))$$

$$C(\boldsymbol{k},\boldsymbol{k}')=\frac{e^2}{V^2}\int\frac{1}{\gamma_{12}}u^*_{k'}(w_1)u_{k'}(w_1)u_k{}^*(w_2)\,u_k(w_2)dw_1dw_2$$

$$A(\boldsymbol{k},\boldsymbol{k}')=\frac{e}{V_2}\int\frac{1}{\gamma_{12}}\exp\,\{\boldsymbol{k}'-\boldsymbol{k})(w_1-w_2)\}\times u^*_k{}'(w_1)u_{k'}(w_2)u^*_k(w_2)u_k(w_1)dw_1dw_2 \qquad (2.5)$$

where the spin degenerady is taken into account and the summations are carried out in accordance with the Pauli principle.

For $E_0^{(2)}$, we must consider the excited wave function Φ_1 in which one electron has its $\boldsymbol{k}$ value above the Fermi maximum. We obtain the matrix element $(\Phi_0|H_I|\Phi_1)$, between Φ_0 and Φ_1 (more precisely $\Phi_1(\boldsymbol{k}',\boldsymbol{k}_j)$, which means $\boldsymbol{k}_j$ state in the Fermi sphere is vacant and $\boldsymbol{k}'$ state in the outside region is occupied) as,

$$(\Phi|H_I|\Phi_1|^2=\frac{\hbar}{2M\omega_q N_A}\,\frac{4}{9}C^2q^2(N_q,\text{ or }N_q+1)$$

$$C=\frac{\hbar^2}{2m}\int_0(\mathrm{grad}\ u_k)^2dw,\quad q=|q|=|\boldsymbol{k}'-\boldsymbol{k}_j| \qquad (2.6)^*$$

where N_q is the number of the lattice quantum with the wave number q, ω_q is its circular frequency, and M is the mass of the atom. So we obtain

$$E_0^{(2)}=2\frac{4\hbar C^2}{9N_AM}\sum_{k'}{}'\sum_{kj}{}'\frac{q^2}{\omega_l}\left[\frac{N_q}{\hbar^2(\boldsymbol{k}_j^2-\boldsymbol{k}'^2)/2m+\hbar\omega_q}+\frac{N_q+1}{\hbar^2(\boldsymbol{k}_j^2-\boldsymbol{k}'^2)2m-\hbar\omega_q}\right]\times f(\boldsymbol{k}_j)(1-f(\boldsymbol{k}')) \qquad (2.7)$$

where we can sum freely without the fear of the violation of the Pauli principle, since we have introduced the functions $f(\boldsymbol{k})$ which takes the value 0 or 1 according as the $\boldsymbol{k}$-state is empty or is occupied, and the dash on the summation symbol means that the values for which the denominators of the summand become zero are to be omitted. The first factor 2 is the consequence of the spin degeneracy.

Rearranging the terms, it becomes

$$E_0^{(2)}=2B\sum_{k'}{}'\sum_{kj}{}'\,F(\boldsymbol{k}',\boldsymbol{k}_j)f(\boldsymbol{k}_j)$$

$$-2(2\hbar B\sum_{k'}{}'\sum_{kj}{}'\,G(\boldsymbol{k}'.\,\boldsymbol{k}_j)f(\boldsymbol{k}_j)f(\boldsymbol{k}')$$

$$F(\boldsymbol{k}',\boldsymbol{k}_j)=\frac{q^2}{\omega_q}\left(\frac{N_q}{\hbar^2(\boldsymbol{k}_j^2-\boldsymbol{k}'^2)/2\mathrm{m}}+\frac{N_q+1}{\hbar^2(\boldsymbol{k}_j^2-\boldsymbol{k}'^2)/2\mathrm{m}-\hbar\omega_q}\right) \qquad (2.8)$$

$$G(\boldsymbol{k}',\boldsymbol{k}_j)=q^2\left\{\left(\frac{\hbar^2}{2m}(\boldsymbol{k}_j^2-\boldsymbol{k}'^2)\right)^2-(\hbar\omega_q)^2\right\}^{-1}$$

$$B=4\hbar C^2/9N_AM$$

Then the energy of our electron-system may be written as

$$E=N\varepsilon_0+\sum\varepsilon^{(0)}{}_j+E_0^{(1)}+E_0^{(2)} \qquad (2.9)$$

where ε_0 is determined by the choise of the energy zero.

b) The above consideration for the energy is valid only for the system at the absolute zero of the temperature. In general, we must consider the statistical ensemble of the systems. If we set the probability for the occupation of the one-electron energy state of a system in this ensemble as $\sigma(\boldsymbol{k}_j)$, the average energy of our system is given as follows.

$$<E>=2\sum_j\varepsilon_j{}^{(0)}\sigma(\boldsymbol{k}_j)\Delta_j+2\varepsilon^{(0)}\sum\sigma(\boldsymbol{k}_j)\Delta_j$$

$$+\sum_j\sum_k(\mathrm{C}(\boldsymbol{k}_j,\boldsymbol{k}_k)-A(\boldsymbol{k}_j,\boldsymbol{k}_k)\sigma(\boldsymbol{k}_j)\sigma(\boldsymbol{k}_k)\Delta_j\Delta_k$$

$$+2B\sum_j{}'\sum_k{}'\,F(\boldsymbol{k}_k,\boldsymbol{k}_j)\sigma(\boldsymbol{k})\Delta_j \qquad (2.10)$$

$$-2(2\hbar B)\sum_j{}'\sum_k{}'\,G(\boldsymbol{k}_k,\boldsymbol{k}_j)\sigma(\boldsymbol{k}_j)\sigma(\boldsymbol{k}_k)\Delta_j\Delta_k$$

where Δ_j denotes the leveldensity. Of course, the condition

$$N=2\sum_j\sigma(\boldsymbol{k}_j)\Delta_j \qquad (2.11)$$

must be satisfied.

---

* See the reference (5), page 513.

The entropy S of our Fermi-Dirac system for this distribution is given by

$$S=2k\sum_j\{(\sigma(\boldsymbol{k}_j)-1)\log(1-\sigma(\boldsymbol{k}_j))\}$$
$$-\sigma(\boldsymbol{k}_j)\log\sigma(\boldsymbol{k}_j)\}\Delta_j \qquad (2.11)$$

So the equilibrium distribution $\sigma(\boldsymbol{k})$ can be determined by maximizing this entropy under the conditions $<E>=$const. and $N=$const. That is, the variations $\delta\sigma(\boldsymbol{k})$ must satisfy the condition

$$\delta(S-k\beta<E>-kaN)=0 \qquad (13)$$

where $k\beta$ and ka are the usual indeterminate multipliers, and

$$\delta S=2\sum_j\delta\sigma(\boldsymbol{k}_j)\Delta_j\{\log(1-\sigma(\boldsymbol{k}_j)-\log(\boldsymbol{k}_j)\}$$

$$\delta N=2\sum_j\delta\sigma(\boldsymbol{k}_j)\Delta_j$$

$$\delta<E>=2\sum_j\delta\sigma(\boldsymbol{k}_i)\Delta_j(\varepsilon^{(0)}+\varepsilon_0)$$
$$+\sum_j\sum_k((C-A)'\sigma(\boldsymbol{k}_k)\delta\sigma(\boldsymbol{k}_j)+\sigma(\boldsymbol{k}_j)\delta\sigma$$
$$(\boldsymbol{k}_k))\Delta_f\Delta_k+2B\sum_j{}'\sum_n{}'\delta\sigma(\boldsymbol{k}_f)\Delta_jF(\boldsymbol{k}_k,\boldsymbol{k}_j)$$
$$-2(2\hbar B)\sum_j\sum_k(\sigma(\boldsymbol{k}_k)\delta\sigma(\boldsymbol{k}_j)$$
$$+\sigma(\boldsymbol{k}_j)\delta\sigma(\boldsymbol{k}_k,\boldsymbol{k}_j)$$

After suitable arrangements, we put the coefficient of each $\delta\sigma(\boldsymbol{k})$ equal to zero and get

$$\log(1-\sigma(\boldsymbol{k}_j))/\sigma(\boldsymbol{k}_j)$$
$$-a+\beta[\varepsilon_0+\varepsilon^{(0)}+U_j+V_j+W_j]=0$$
$$U_j=\sum_k\{C(\boldsymbol{k}_j,\boldsymbol{k}_k)-A(\boldsymbol{k}_j,\boldsymbol{k}_k)\}\sigma(\boldsymbol{k}_k)\Delta_k$$
$$V_j=B\sum_k{}'F(\boldsymbol{k}_k,\boldsymbol{k}_j) \qquad (2\,14)^*$$
$$W_j=-2(2\hbar B)\sum{}'G(\boldsymbol{k}_k,\boldsymbol{k}_j)\sigma(\boldsymbol{k}_k)\Delta_k$$

or,

$$\sigma(\mathbf{k}_j)=\frac{1}{1+\exp[a+\beta(\varepsilon_0+\varepsilon^{(0)}{}_j+U_j+V_j+W_j)]} \qquad (2.15)$$

Putting $\beta=1/kT$ as usual, equations (11) and (15) may be regarded as the system of equation from which we can determine $\sigma(\boldsymbol{k})$ and a. We write $a=-\zeta/kT$, where ζ is the Gibbs free energy per one electron of the system. From ζ, we can derive all the thermodynamical behavior of this system.

§3. Superconducting State

We now present an approximate treatment which may show the existence of a special equilibrium state which is stable below a certain critical temperature. The procedures are similar to that of the reference 4.

If the interaction energies U_j, V_j and W_j had no special characters and could be smoothed out, the solution of (2.15) will be of the form

$$\sigma^f(\boldsymbol{k}_j)=\frac{1}{1+\exp[(\varepsilon^{(0)}{}_j-\zeta_f)/kT]} \qquad (3.1)$$

and ζ_f may be determined from the condition (2.11), approximately as

$$\zeta_f=\mu_0-\frac{\pi^2}{12}\frac{(kT)^2}{\mu_0} \qquad (3.2)$$

where μ_0** is the maximum energy at 0°K.

In the present case, W_j shows a peculier features as was remarked by Fröhlich. It is positive when $(\boldsymbol{k}_j^2-\boldsymbol{k}_k^2)^2$ is small, but it is negative when this quantity is large. We consider that the ordinary Fermi distribution in $\boldsymbol{k}$-space suffers a modification on account of the presence of this term and it will be limitted in the narrow region near the surface of the Fermi sphere owing to the nature of this interaction.

For the modified distribution we put σ^s and ζ_s instead of the above σ^f and ζ_f. Since we have smoothed out the interaction energies and adjusted the energy zero suitably in obtaining the formula (1) from (2.15), an additional term ΔW_j* appears as follows.

$$\sigma^s(\boldsymbol{k}_j)=\frac{1}{1+\exp[(\varepsilon^{(0)}{}_j+\Delta W_j-\zeta_s)/kT} \qquad (3.3)$$

$$\Delta W_j=-2(2\hbar B)\sum_k{}'G(\boldsymbol{k}_k,\boldsymbol{k}_j)(\sigma^s(\boldsymbol{k}_k)$$
$$-\sigma^f(\boldsymbol{k}_k))\Delta_k \qquad (3.4)$$

Expanding the exponential in (3), we get

$$\sigma^s(\boldsymbol{k}_j)-\sigma_0{}^s(\boldsymbol{k}_j)=\frac{2(2\hbar B)}{kT}$$
$$\times\frac{\exp[(\varepsilon^{(0)}{}_j-\zeta_s)/kT]}{\{1+\exp[(\varepsilon^{(0)}{}_j-\zeta_s)/kT]\}^2}$$
$$\times\sum_k{}'G(\boldsymbol{k}_k,\boldsymbol{k}_j)\ \sigma^s(\boldsymbol{k}_k)-\sigma^f(\boldsymbol{k}_k))\Delta_k \qquad (3.5)^{***}$$

From this we obtain a integral equation for the determination of $\sigma^s(\boldsymbol{k})$, which, however is very difficult to solve. Hence, we shall take another way for the present.

As in Fröhlich's paper, we can say that the energy ΔW_j tends to expel the electrons from the inside of the Fermi surface to the outer region, that is, $\sigma^s(\boldsymbol{k}_k)-\sigma^f(\boldsymbol{k}_k)$ will be negative in the region where the denominator is negative and positive when that is positive. For the sufficiently low $\boldsymbol{k}_j$ state ΔW_j is very small, since for $\boldsymbol{k}_k$ near $\boldsymbol{k}_j$, $\sigma^s(\boldsymbol{k}_k)-\sigma^f(\boldsymbol{k}_k)$

---

* In the following we can write $\sigma(k)$ instead of $\bar{\sigma}(k)$ without the fear of the confusion.

** See the equ. (3 12)

*** See the equ. (3.6)

will be nearly zero and for distant $\boldsymbol{k}_k$ the denominator will become very large. Hence we can assume

$$\sigma_0^s(\boldsymbol{k}_j)=\frac{1}{1+\exp[\varepsilon_j^{(0)}-\zeta_s)/kT]} \tag{3.6}$$

for these states up to some k^+ state.

Near the Fermi surface, ΔW_j becomes appreciable and we write in this region as

$$\sigma^s(\boldsymbol{k}_\lambda)=\frac{1}{1+\exp[(\varepsilon_\lambda^{(0)}-\Delta W_\lambda-\zeta_s)/kT]} \tag{3.7}$$

Then the equ. (2.11) becomes

$$N=2\sum_{|\boldsymbol{k}_j|<k+}\sigma_0^s(\boldsymbol{k}_j)\Delta_j+2\sum_{|\boldsymbol{k}_\lambda|>k+}\sigma^s(\boldsymbol{k}_\lambda)\Delta_\lambda \tag{3.8}$$

$$N-n=2\sum_1^\infty\sigma_0^s(\boldsymbol{k}_j)\Delta_j$$

$$n=2\sum_{|\boldsymbol{k}_\lambda|>k+}(\sigma^s(\boldsymbol{k}_\lambda)-\sigma_0^s(\boldsymbol{k}_\lambda))\Delta_\lambda \tag{3.9}$$

If we use the ordinary formura

$$\Delta_j=2\pi V(2m/\hbar^2)^{3/2}\sqrt{\varepsilon}\,d\varepsilon \tag{3.10}$$

and the assumption

$$\varepsilon_j^{(0)}=\frac{\hbar^2}{2m}k_j^2 \qquad k_j=|\boldsymbol{k}_j| \tag{3.11}$$

we get from (9)

$$N-n=\frac{3}{2}N(kT/\mu_0)^{3/2}\int_0^\infty\frac{x^2dx}{1+\exp[x-\zeta_s/kT]} \tag{3.12}$$

$$x=\varepsilon/kT,\quad \mu_0=(3N/\pi V)^{2/3}h^2/8\text{m}=\hbar^2k_0^2/2m$$

where k_0 is the wave number which corresponds to μ_0. We can assume $n\ll N$ and $\zeta_s\gg kT$, so we can use the Sommerfeld expansion for ζ_s. It becomes

$$\zeta_s=\mu_0-\frac{\pi^2}{12}\frac{(kT)^2}{\mu_0}-\xi,\qquad \xi=\frac{2}{3}\frac{n}{N}\mu \tag{3.13}$$

From the equations (9), (6) and (13), we get

$$n=\sum_{|k\lambda|>k}\left\{\frac{1}{1+\exp\left[\left(\frac{\hbar^2}{2m}k_\lambda^2-(\zeta_f-\xi)+\Delta W_\lambda\right)/kT\right]}-\frac{1}{1+\exp\left[\left(\frac{\hbar^2}{2m}k_\lambda-(\zeta_f-\xi)\right)/kT\right.}\right\}\Delta_\lambda \tag{3.14}$$

and

$$\Delta W_\lambda=-2(2\hbar B)\sum_{|k_k|<k\pm}{}'G(\boldsymbol{k}_k,\boldsymbol{k}_\lambda)(\sigma^s(\boldsymbol{k}_k)-\sigma^f(\boldsymbol{k}_k))\Delta_k-2(\hbar B)\sum_{|k_\mu|>k+}{}'G(\boldsymbol{k}_\mu,\boldsymbol{k}_\lambda)(\sigma^s(\boldsymbol{k}_\mu))\Delta_\mu \tag{3.15}$$

Further we make following rather rough assumptions: (i) we can replace all ΔW_λ with its value at $|\boldsymbol{k}_\lambda|=k_0$; (ii) the first term in (15) may be neglected; (iii) the second term may be replaced by

$$-4(2\hbar B)\sum G(\boldsymbol{k}_\mu,\boldsymbol{k}_\lambda)(\sigma^s(\boldsymbol{k}_\mu)-\sigma_0^s(\boldsymbol{k}_\mu))\Delta\mu \tag{3.16}$$

considering $\sigma^s(\boldsymbol{k}_\mu)-\sigma^f(\boldsymbol{k}_\mu)$ to be negative in region where $G(\boldsymbol{k}_\mu,\boldsymbol{k}_0)$ is negative and to be positive outside that region as in Frohlich's reasoning, and $\sigma^s(\boldsymbol{k}_\mu)-\sigma_0^s(\boldsymbol{k}_\mu)$ may be assumed to be nearly zero and to be positive in these regions respectively.

We introduce the new variables

$$x=k_\mu-k^0,\qquad q^2=4k_0^2\sin\theta/2$$
$$u=2\sigma_0\sin\theta/2,\ \sigma_0=ms/\hbar,\ \omega_q=sq \tag{3.17}$$

where θ is the angle between $\boldsymbol{k}_\mu$ and $\boldsymbol{k}_\lambda$, and s is the velocity of the lattice wave (sound), assuming the dispersion to be zero. So we obtain

$$\Delta W_\lambda=-4(2\hbar B)\frac{4m^2V}{h^2(2\pi)^3}\int_{k^+}^\infty\varphi(k')\frac{\sin^2(\theta/2)}{x^2-4\sigma_0^2\sin^2\theta/2}k'^2dk'd\omega$$

by putting

$$\Delta_\mu=\frac{V}{(2\pi)^3}k'^2dk'd\omega,\quad \varphi(k)=\sigma^s(\boldsymbol{k})-\sigma_0^s(\boldsymbol{k})$$

in which $d\omega$ means the solid angle in k-space, the polar axis being taken in the direction of $\boldsymbol{k}_\lambda$. Further it becomes

$$\Delta W_\lambda=-4(2\hbar B)\frac{m^2\pi Vk_0^2}{\hbar^2(2\pi)^3\sigma_0^4}\int_{k^+-\kappa_0}^\infty\varphi(x)dx\int_0^{2\sigma}\frac{2u^3}{x^2-u^2}du$$

where σ means the limit in θ and may be written as $\sigma=\sigma_0q_0/2k_0^2$, in which q_0 is the q value of the maximum frequency normal mode of the lattice vibration in Debye theory*, and the assumption $k'^2dk'=k_0^2dk'$ is used. The last integral in the above has the singular character if $x^2<(2\sigma)^2$, but on account of our special assumption on $\varphi(x)$, it will be sufficient to evaluate it for the case $x^2>2(\sigma)^2$.

$$4\sigma^2\int_0^1\frac{2u'^3}{(x/2\sigma)^2-u'^2}du'=4\sigma^2\left(\frac{1}{2}\left(\frac{2\sigma}{x}\right)^2+\frac{1}{3}\left(\frac{2\sigma}{x}\right)^4+\dots\right)$$

assuming the width of the range in which $\varphi(x)$ is appreciably positive to be the order of several multiple of σ, we replace this integral by a constant value $\eta(4\sigma^2)$, where η is the numerical factor of the order of 1/10;

Considering (3.9), we finally obtain

$$\Delta W_\lambda=-\eta\phi\frac{n}{N};\quad \phi=\frac{16\nu^{1/3}}{2^{2/3}9}\frac{C^2}{Ms^2} \tag{3.18}$$

---

* $q_0^3=3(2\pi)^2N_A/2$

$$\Delta W_\lambda = -\tau\xi \qquad \tau = 3\eta\psi/2\mu_0$$

Then the equ. (3.14) may be regarded as the equation for determining ξ and can be written in the form

$$\xi = \mu_0\left(\frac{kT}{\mu_0}\right)^{3/2}\delta\left\{\int_c^\infty \frac{x^{\frac{1}{2}}dx}{1+\exp[x-(\zeta_f+(\tau+1)\xi)/kT]} \right. \tag{3.19}$$

$$\left. -\int_c^\infty \frac{x^{\frac{1}{2}}dx}{1+\exp[x-(\zeta_f-\xi)/kT]}\right\},$$

$$c = \frac{\hbar^2}{2m}k^{+2}/kT$$

where $\delta=(m'/m)^{3/2}$ is introduced in order to take into account that the effective mass m' of the electrons which is in the special state be different from that which is used in μ_0. In the integral in (12), the difference of the effective masses in various parts of the k-space are included in μ_0 as the averaged effective mass. The divergence of the effective mass in (19) from the averaged one is important for our theory, as will be seen later.

For ε^+, we assume $\varepsilon^+=\mu_0+a$, $a>0$.

It is easily seen that (19) has always the solution $\xi=0$ and the non-zero (>0) solution appears at some temperature. We consider this non-zero ξ state which is more stable than the ordinary state below the critical temperature as the superconducting state of our electron system, and call it *s*-state. The ordinary state with ζ_f will be called *f*-state.

b) Using the expansion at $\xi=0$, we get approximately

$$\frac{\xi}{kT} = \left(\frac{kT}{\mu_0}\right)^{\frac{1}{2}}\delta\tau\left(\frac{\xi}{kT}\right)\int_c^\infty \frac{\exp(x-\zeta_f/kT)}{\{1+\exp(x-\zeta_f/kT)\}^2}x^{\frac{1}{2}}dx$$

$$+\left(\frac{kT}{\mu_0}\right)^{\frac{1}{2}}\delta\frac{\tau(\tau-2)}{2}\left(\frac{\xi}{kT}\right)^2\int_c^\infty \frac{(\exp(x-\zeta_f/kT)-1)\exp(x-\zeta_f/kT)}{\{1+\exp(x-\zeta_f/kT)\}^2}x^{\frac{1}{2}}dx \tag{3.20}$$

From this quadratic equatioion, we can determine the values of ξ, $\partial\xi/\partial^2\xi/\partial T^2$ in the neighbourhood of $\xi=0$. The condition for the phase change is that the equation has the double root at $\xi=0$. Thus

$$1-\delta\tau\left(\frac{kT}{\mu_0}\right)^{\frac{1}{2}}\int_c^\infty \frac{\exp(x-\zeta_f/kT}{\{1+\exp(x-\zeta_f/kT)\}^2}x^{\frac{1}{2}}dx \tag{3.21}$$

In our case, the condition for the second order phase change must also be fulfilled and it can be written as

$$\left(\frac{\partial\xi}{\partial T}\right)_{\xi=0}=0 \tag{3.22}$$

From these two equations, we obtain

$$a/kT_c+\pi^2kT_c/12\mu_0=\delta\tau-2 \tag{3.23}$$

$$a=\pi^2(kT_c)^2/12\mu_0 \tag{3.24}$$

respectively, or combining

$$\frac{\pi^2}{6}\,\frac{kT_c}{\mu_0}=\delta\tau-2 \tag{3.25}$$

If we know the values of δ and τ theoretically, we can determine T_c from (25), but on account of our insufficient knowledges on these quantities, it will be impossible at the present.

But it is to be remarked here that $\delta\tau$ should be very close to 2 to give observed T_c and δ should be smaller than unity as will be seen later.

c) When we want to investigate the behavior of our system near 0°K, it becomes necessary to assume some modified formula instead of (10) to obtain reasonable results. We assume arbitrarily

$$\Delta = 2\pi V\left(\frac{2m}{\hbar^2}\right)^{\frac{t}{2}+1}\varepsilon^{t/2}\,d\varepsilon \tag{3.26}$$

in our special region in k-space near the Fermi surface. Using this, we can proceed as in b) and get

$$B\xi = \left(\frac{1}{\mu_0}\right)^{t/2}\delta_*\left\{\int_{\varepsilon^+}^\infty \frac{\varepsilon^{\frac{t}{2}}d\varepsilon}{1+\exp[(\varepsilon-(\zeta_f+(\tau-1)\xi))/kT]}\right.$$

$$\left.-\int_{\varepsilon^+}^\infty \frac{\varepsilon^{t/2}d\varepsilon}{1+\exp[(\varepsilon-(\zeta_f-\xi))/T]}\right\}$$

$$B=\left(\frac{\pi V}{3N}\right)^{(t-1)/3}2^{t-1}.$$

where δ_* is the value of δ in this case. When the temperature becomes sufficiently low, the second term in the bracket can be negrected, anticipating $\xi=\xi^*>0$ at 0°K.

So from

$$\frac{\mu_0{}^{t/2}}{\delta_*}B\xi^* = \int_{\varepsilon^+}^{\mu_0+(\tau-)\xi^*}\varepsilon^{t/2}\,d\varepsilon$$

we get

$$\varepsilon^+=\mu_0+a, \quad a=\left((\tau-1)-\frac{B}{\delta^*}\right)\xi^* \tag{3.27}$$

Putting

$$\xi=\xi^*+\Delta\xi, \; \mu_1=\mu_0-\frac{\pi^2}{12}\,\frac{(kT)^2}{\mu_0}+(\xi^*+\Delta\xi)(\tau-1),$$

$$\varepsilon_1=\mu_1-\varepsilon^+=\frac{B}{\delta^*}\,\xi^*-\frac{\pi^2}{12}\,\frac{(kT)^2}{\mu_0}+\Delta\xi\,\tau-1),$$

we get

$$\frac{\mu_0{}^{t/2}}{\delta_*}\,B(\xi^*+\Delta\xi)=\int_0^\infty\frac{(\varepsilon^++\varepsilon')^{t/2}\delta\varepsilon'}{1+\exp(\varepsilon'-\varepsilon_1)/kT}$$

where we have changed the variable from ε to $\varepsilon'=\varepsilon-\varepsilon^+$. Considering that ε_1 is certainly positive at sufficiently low temperatures, we can use the usual expansion method for the integral and obtain

$$\frac{\mu_0{}^{t/2}}{\delta_*}B(\xi^*+\Delta\xi)=\Big\{\frac{2}{t+2}(\mu_1{}^{(t+2)/2}-\varepsilon^{+(t+2)/2})$$
$$+\frac{\pi^2}{6}(kT)^2\,\frac{t}{2}\,\mu_1{}^{(t-2)/2}\Big\}$$

Expanding μ_1 and ε^+, we get

$$\Delta\xi=-\frac{(t-1)\delta_*}{\delta_*(\tau-1)-B}\,\frac{\mu^2}{12}\,\frac{(kT)^2}{\mu_0}$$

Hence

$$\xi=\xi_*-\frac{(t-1)\delta_*}{\delta_*(\tau-1)-B}\,\frac{\pi^2}{12}\,\frac{(kT)^2}{\mu_0}\qquad(3.28)$$

$$\left(\frac{\partial\xi}{\partial T}\right)_{T=0}=0\qquad(3.29)$$

$$\left(\frac{\partial^2\xi}{\partial T^2}\right)_{T=0}=-\frac{(t-1)\delta_*}{\delta_*(\tau-1)-B}\,\frac{\pi^2k^2}{6\mu_0}\qquad(3.30)$$

§4. The Thermodyramical Quantities and The Critical Magnetic Field

a) In the previous section, we have obtained the Gibbs free energy for our s-state, so we can calculate the specific heart discontinuity ΔC at the transition.

$$\Delta C=(C_s-C_f)_{Tc}=V_AN\Big(T_c\left(\frac{\partial^2\zeta_f}{\partial T^2}\right)_{Tc}$$
$$-T_c\left(\frac{\partial^2\zeta_s}{\partial T^2}\right)_{Tc}\Big)$$
$$=V_ANT_c\left(\frac{\partial^2\xi}{\partial T^2}\right)_{Tc}=2\gamma T_c=2\gamma T_c/(\tau-2)\qquad(4.1)$$

where

$$\gamma=V_AN\frac{\pi^2}{6}\,\frac{k^2}{\mu_0},\quad C_f=\gamma T,\quad V_AN=\nu N_0\qquad(4.2)$$

and N_0 is the Avogadro number. Further, we get

$$\left(\frac{\partial C_s}{\partial T}\right)T_c=\gamma T_c+2\gamma T_c/(\tau-2)\qquad(4.3)$$

b) When the magnetic field is applied, the superconducting sample shows the so-called Meissner effect. For the magnetic behavior of our system, we proceed semi-phenomenologically as follows. We assume that microscopically the energy of the electron is not perturbed by the magnetic field owing to its cancellation in the substance, but macroscopically the superconducting body behaves as if its substance has the susceptibility $-1/4\pi$. In the consequence, the Gibbs free energy per unit volnme of the superconducting body has the additional term $H^2/8\pi$, where H is the intensity of the uniform applied field.

Hence, it will be sufficient for the determination of the shift of T_c due to H to put $\zeta_f+H^2/8\pi$ instead of ζ_f in (3.20). So the condition (3.23) becomes

$$a/kT-H^2/8\pi kT+\pi^2kT/12\mu_0=\pi^2kT_c/6\mu_0$$

and we get

$$H=\left(\frac{\pi^2k^2}{12\mu_0}\times8\pi N\right)^{\frac{1}{2}}(T_c-T)\qquad(4.5)$$

$$-\left(\frac{\partial H}{\partial T}\right)=\left(\frac{\pi^2k^2}{12\mu_0}\times8\pi N\right)^{1/2}\qquad(4.6)$$

Of couse the condition (3.22) is destroyed, but we can calculate the latent heat of the transition by

$$Q=T(S_f-S_s)=V_ANT\left(\frac{\partial\zeta_s}{\partial T}-\frac{\partial\zeta_f}{\partial T}\right)\qquad(4.7)$$
$$=-V_ANT(\partial\xi/\partial T)_{\xi=0}$$

We obtain

$$Q=2\gamma T(T_c-T)/(\tau-2)\qquad(4.8)$$

It is to be remembered that these relations are valid only for the temperatures which are close to the zero-field transition temperature.

§4. Comparison with the Experiments and Discussions

We have shown that one can deduce a special equilibrium state for the system of the conduction electrons which is stable below a certain temperature on the basis of the Frohlich's interaction. We do not enter here into the probrem of the validity of the perturbation procedure.

In the course of the derivation, we have omitted Coulomb and exchange interactions ($\sim1eV$) which will be very much greater than Fröhlich's interaction ($\sim10^{-5}eV$) if they remained without cancellation. So very slight variations with k of these interaction terms are required for the justification of the omittion, considering our special assumption of the form of $\sigma^s-\sigma^f$ in this region. It will go too far, therefore, to say whether some metal should become superconducting or not without settling the above mentioned energy problem.

But some of the relations between the experimental facts in the superconducting metals may be derived by our theory.

a) From the thermodynamical theory of Gorter and Casimir, the relations

$$\Delta C = V_A T_C (\partial H/\partial T)^2_{T_C}/4\pi\,,$$
$$Q = -V_A T (\partial H/\partial T)/4\pi \qquad (4.9)$$

are deduced and agree very well with the experiments. So if we know the relation between the threshold magnetic field and the transition temperature, we can determine ΔC and Q by the above formulas. It is found that these quantities calculated from (4.6) by (5.1) are consitent with our purely theoreticall results (4.1) and (4.9), if the relation

$$\tau - 2 = 2 \qquad (5.2)$$

is satisfied.

On the other hand, τ can be estimated from the formula for the electrical conductivity σ_e at room temperature T_r, except η.

$$\sigma_e = \frac{8\nu^{2/3}}{\pi^2}\,\frac{e^2}{k\hbar}\,\mu_0{}^2\frac{Ms^2}{C^2}\left(\frac{3N_A}{4\pi}\right)^{1/3}\Big/T_r \qquad (5.3)$$

From (3.18) and (5.3), we get

$$\frac{\eta\psi}{\mu_0} = n\frac{32}{3\pi}\,\frac{e^2\hbar}{m}\,\frac{\nu^{5/3}N_A}{kT_r\sigma_e} \qquad (5.4)$$

The calculated values are shown in Table I.

Table I.

Metal	N_A 10^{22}/c.c	$1/\sigma_e$ 3) 10^{-16} esu	ψ/μ_0	η
Al	5.96	0.03	5.05	0.53
V	6.75	0.20	35.32	0.075
Zn	6.58	0.065	12.08	0.22
Sn	3.72	0.13	13.63	0.19
Ta	5.53	0.17	26.51	0.10
Hg	4.49	0.30	38.06	0.07
Pb	3.31	0.24	22.44	0.12

In calculating ψ, we put $\nu=1$ for all metals.[2]

It is to be noticed here that the relation (3.25) is very critical, in other words, a slight change in τ will change T_c drastically. The approximate constancy of τ can be regarded as to favour this situation. Probably, these facts are due to the approximation of using one ξ instead of many $\sigma(\boldsymbol{k})$.

Using (5.2), we get

$$\Delta C = \gamma T_c \qquad (5.5)$$

This is satisfied well by Al, Zn, Sn, and Ta. For Hg, Pb the observed ΔC is near $2\gamma T_c$. Without touching τ, we can say that there should be the following relation between $\partial H/\partial T$ and γ by the equ. (4.6).

$$V_A\left(\frac{\partial H}{\partial T}\right)^2\Big/4\pi\gamma = 1 \qquad (5.6)$$

This is approximately fullfilled as in Table II.

Table II.

Metal	T_c °K	[6] γ_c 10^{-4} cal/mol. deg.	ΔC_{obs} 10^{-4} cal/mal.deg.	$V_A(\partial H/\partial T)^2_{H=0}/4\pi\gamma$
Al	1.15	2.98	4.07[7]	1.36
V	4.3		116.27[8]	
Zn	0.95	1.29	1.58[7]	1.22
Sn	3.71	11.86–14.65	19.30[8]	1.50–1.31
Ta	4.4	62.08	93.05[8]	1.49
Hg	4.15	15.56–18.68	38.04[8]	2.45–2.04
Pb	7.22	51.12	96.6[8]	1.84

We have calculated ΔC_{obs} from the observed $(\partial H/\partial T)_{H=0}$.

Considering roughness of our approximations, these may be rather good agreements. It is interesting that those metals which have their threshold field curves closely linear in the neighbourhood of the no-field transition temperature instead of parabolic ones, satisfy the relations (5.5) and (5.6) good.

b) Near 0°K, the thermodynamical theory also requirs

$$(\Delta S)_{T=0} = 0 \qquad (5.7)$$
$$-\left(\frac{\partial}{\partial T}(\Delta S)\right)_{T=0} = \gamma \qquad (5.8)$$
$$V_A\frac{H_0{}^2}{8\pi} = (\Delta U)_0 \qquad (5.9)$$

where $(\Delta U)_0$ means the difference of the internal energy per mol at 0°K, and H_0 is the threshold strength at 0°K.

On the other hand, from (3.28) and (3.29) we get

$$(\Delta S)_0 = N(\partial\xi/\partial T)_0 \qquad (5.10)$$
$$(\partial\Delta S/\partial T) = N(\partial^2\xi/\partial T^2) \qquad (5.11)$$
$$(\Delta U_0) = N(\Delta(\zeta - T\partial\zeta/\partial T)) = N_0\xi^* \qquad (5.12)$$

It is seen the condition (5.6) is satisfied by our theory. From (5.11) and (5.12) and the definition of γ

$$\frac{(t-1)\delta^*}{\delta_*(\tau-1)-B} = 1 \qquad (5.13)$$

must be satisfied.

From (5.9) and (5.12) and (3.27), we get

$$\frac{V_A H_0^2}{8\pi} = \frac{\nu N A \delta_*}{\{\delta_*(\tau-1)-B\}} \frac{\pi^2 k^2 T_c^2}{12\mu_0} \quad (5.14)$$

Using the experimental values for H_0 and γ, we can determine t and δ_* from these conditions.

c) Unfortunately, due to the ambiguities in η and the lack of knowledge on $\partial V_A/\partial M$, we can not estimate the isotopic mass dependency of T_c.

In conclusion the auther expresses his hearty thanks to Prof. T. Sakai for the introduction into this research and the kind guidance.

References

1) W. Heisenberg: Zeit. fur Naturforsh. 2a(1947) 185; 3a (1948) 65.
2) H. Frohlich: Phys. Rev. **79** 1950) 845.
3) J. Bardeen: Phys. Rev. **80** (1950) 567.
4) H. Ichimura: Journ. Phys. Soc. Japan **4** (1947) 265.
5) A. Sommerfeld & H. Bethe Handbuch d. Phys 24/II (1933).
6) J. G. Daunt; Phys. Rev. **80** (1950) 911.
7) J. G. Daunt & C. V. Heer: Phys. Rev. **76** (1949) 1324.
8) D. Shoenberg: *Superconductivity* (1938) Cambridge.

JOURNAL OF THE PHYSICAL SOCIETY OF JAPAN Vol. 7, No. 3, MAY—JUN., 1952

On the Discontinuous Elongation of Aluminium Crystals, IV

Tomoyosi KAWADA

The Government Mechanical Laborators, 132 Sumiyoshi-cho, Suginami-ku,
Tokyo, Japan

(Received August 27, 1951)

In the previous paper the discontinuous elongations of magnitude of a few micron were observed for coarse grain polycrystal specimens of commercial aluminium. In this paper the behaviour of slip lines near the grain boundary was observed and it was found that when the slip lines continued across the grain boundary the discontinuous elogation was not observed, while the jumps occured when the slip lines terminated at the grain boundaries. From these results the cause of the discontinuous elongation was discussed.

§1. Introduction

In the previous paper[1)] we reported that the discontinuous elongation of the magnitude of a few micron were observed when coarse grain polycrystal specimen of commercial aluminium was elongated by a specially designed extensometer at the temperature range between 100° and 350°C. In this paper we observe the behaviour of slip lines near the grain boundary and discuss the cause of discontinuous elongation.

Many workers have observed the behaviour of slip lines near grain boundary. For example, D. Hanson and M. A. Wheeler[2)], W. Boas and M. E. Hargreaves[3)], and W. A. Wood and W. A. Rachinger[4)] observed the slip lines near grain boundaries with aluminium specimen. While N. F. Nye[5)] observed them with silver chloride. Recently E. Fujita, T. Suzuki and T. Hibi[6)] photographed the slip lines near grain boundary and H. Czyzewski[7)] photographed branching of slip lines at twin boundary with electronmicroscope.

We observed the behaviour of slip lines in connection with the discontinuous elongation and found that the discontinuous jump did not occur when the slip lines continued across the grain boundaries, while jumps occurred when slip lines terminated at the grain boundary. From these results we discussed the cause of the discontinuous elongation.

§2. Behaviour of Slip Lines Near Grain Boundary

As mentioned in the previous paper, we used aluminium specimens consisting of 2, 3 and 4 crystals polished their surfaces electrolytically and elongated them with the Polanyi type testing machine. As reported by W. Boas aud M. E. Hargreaves the elongation given to the specimen is not uniform but widely different from grain to grain when a coarse grain polycrystal specimen was elongated, moreover it is not uniform even over one grain. In the following we will pick up typical photomicrographs and give explanations about them.

1. 99.99% aluminium. As the behaviours were similar from room temperature to 350 C, we will show, as an sxample, the case of room temperature. Fig. 1 shows the case in which neighbouring crystals have almost similar orientation.

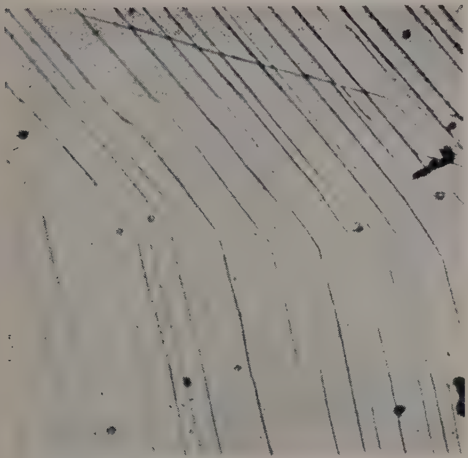

Fig. 1. Tensile temperature 20°C
Elongation 6%

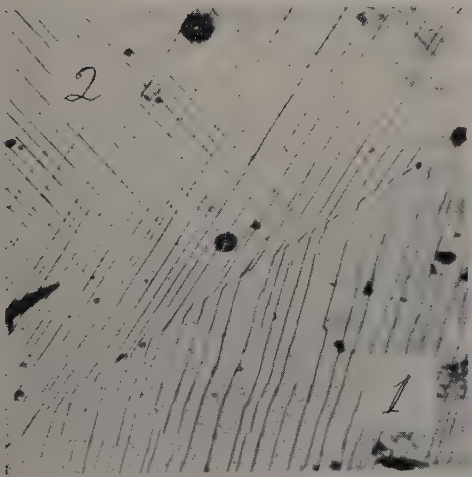

Fig. 2. Tensile temperature 20°C
Elongation 6%

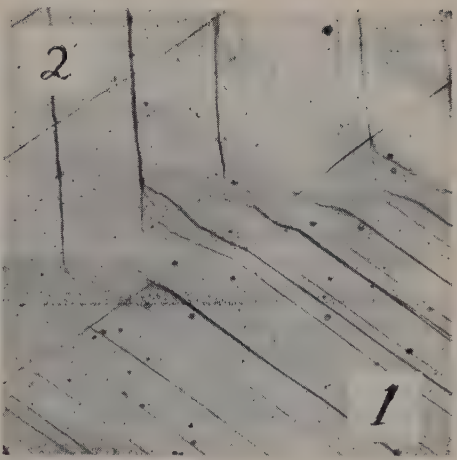

Fig. 3. Tensile temperature 20°C
Elongation 6%

The lines continue across the grain boundary, turning their direction of slip at the boundary. The grain boundary does not appear nearly as clear as line on the surface. The slip lines of the second and the third system appear faintly near the grain boundary. Moreouer the continuations of slip lines at the grain boundary were observed on both surfaces of the specimen. Fig. 2 is the case in which appears single slip in grain 1 while double slip in grain 2 and the slip lines in grain 1 continue to the second system of slip lines in grain 2. In this case, too, the grain boundary does not appear clearly as lines. The most general cases is that in which the primary system of slip lines in the grain 1 continues to the secondary system in the grain 2 and the primary system in the grain 2 continues to the secondary system of grain 1. Fig. 3 is a special case in which the slip lines run straightly in the grain 1, but after they have crossed over the grain boundary, they run in a zigzag way and are connected to the slip lines of the grain 2. When we observed all over the specimen, the slip lines did not necessarily continue across the grain boundary and at some places they terminated at the grain boundary. But the above results are thought to be a distinctive characteristics when we elongate the coarse grain polycrystal specimen of 99.99% aluminium.

2.1. Commercial aluminium elongated at room temperature. In this case the behaviour of the slip lines near grain boundary was almost similar to the 99.99% aluminium.

2.2. Commercial aluminium elongated between 100°C to 350°C. In this case the behaviour of slip lines near grain boundary was different from the above case. In Fig. 4 we can observe the first, second and third systems of slip lines in each of the neighbouring grains but none of them continues to each other at the grain boundary. Moreover the grain boundary appeares clearly. Fig. 5 is the case in which the orientation of the neighbouring grains are almost similar. In this case, too, the slip lines do not continue at the grain boundary. Fig. 6 is the case in which the grain boundary is very meandering and the grain 1 caves in the grain 2 very deeply and we observed, besides slip lines, some undulating smoky patterns on the surface. Fig. 7 is the case which we often observed at the earlier stage of elongation and in this figure the slip lines in grain 1 come to the grain boundary and then they turn their direction and run along the grain boundary.

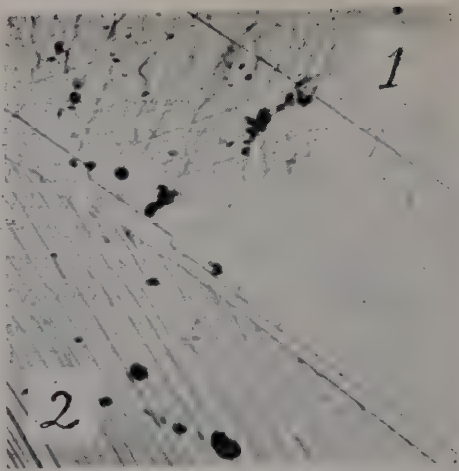

Fig. 6. Tensile temperature 100°C
Elongation 10%

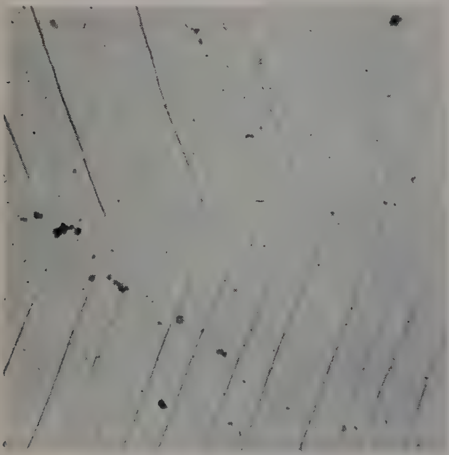

Fig. 4. Tensile temperature 200°C
Elongation 2%

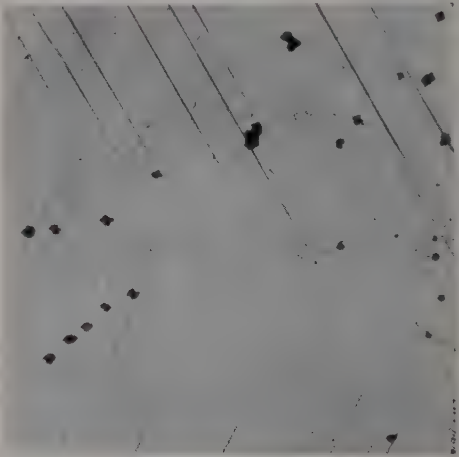

Fig. 7. Tensile temperature 100°C
Elongation 2%

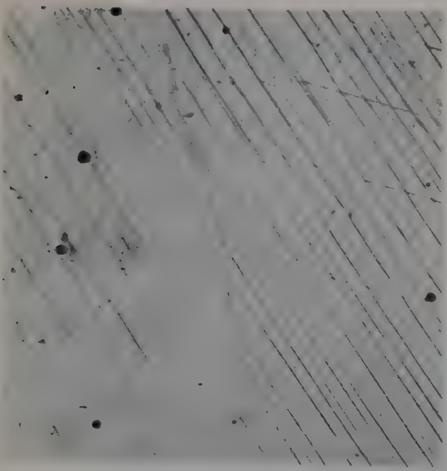

Fig. 5. Tensile temperature 200°C
Elongation 4%

Thus in general the slip lines do not continue to those of the neighbouring crystal and the grain boundary appears clearly.

2.3. Commercial aluminium elongated higher than 350°C. As indicated by W. A. Wood and W. A. Rachinger, appearances of slip lines abruptly above 350°C. Figs 8 and 9 are the typical ones and in these cases the specimens are mainly elongated near the

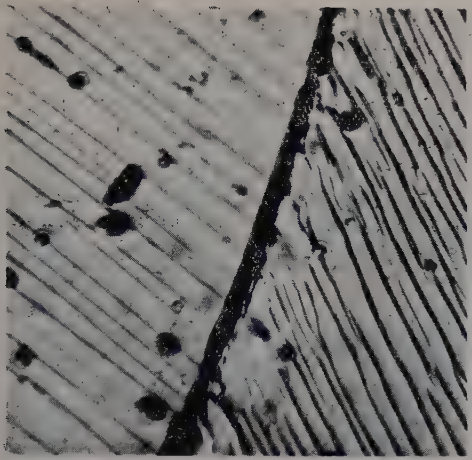

Fig. 8. Tensile Temperature 350°C
Elongation 2%

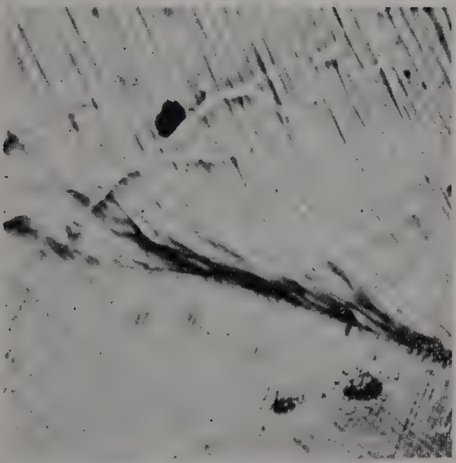

Fig. 9. Tensile Temperature 350°C
Elongation 2%

grain boundaries. Thus in Fig. 8 and 9 the rate of local elongation near the grain boundary is greater than the overall elongation of specimen and the slip lines appear mainly near the grain boundary. The grain boundary is observed to be very wide and this may partly due to the thickening of the grain boundary and partly due to the step formed between the neighbouring crystals. The slip lines are irregular and curued near the grain boundary as if one grain slipped relatively to the other along the grain boundary.

§ 3. Discussion

F. C. Frank and W. T. Read[8] have clarified generation of slip line, while many workers[9] have discussed about the model of grain boundary. Taking into consideration of these theories we will discuss the above photomicrographs and the cause of discontinus elongation. In the first place we will discuss about the behaviour of slip lines in the 99.99% aluminium specimen. It may be supposed that when the orientations of the neighbouring crystals are similar a dislocation reached to the grain boundary in one of them can casily go across the grain boundary and the resultant slip lines become continuous over the grain boundary.

The fact that slip lines continue across the grain boundary on both surfaces of the flat specimen leads us to the following supposition: When dislocations reached to the grain boundary they may at first go across the grain boundary at the surface of the specimen. Then it necessarily follows that at the interior of the specimen dislocations are formed from segments of edge and screw dislocations as indicated by Cottrell[10] and in such form they will go across the grain boundary. This supposition may be supported by Fig. 3; in this photomicrograph the slip lines of zigzag forms seems as if they are formed by joining together sements of edge and screw dislocations, and this phenomenon may be explained that the behaviour of dislocations at the grain boundary in the interior of the specimen comes out to the surface of specimen runs shallowly under the surface of the specimen.

Besides the first system of slip lines, there appear the second and the third system to cancel the internal stress near the grain boundary as much as possible. Thus there is little discontinuity in elongation near the grain boundary and the grain boundary does not appear as a line in the photomicrograph.

The above discussion may also be applied to the case in which the direction of slip planes of the neigbouring crystal are similar. In case of slip as shown in Fig. 2, the internal stress will arise near the grain boundary if each crystal deforms only by the primary slip system. To cancel this internal stress the crystal should deform by the second slip system of the in the direction similar to the primary slip system of the neighbouring crystal. Thus the slip lines of the grain 1 penetrate over the grain boundary continusly.

Next we will discuss the case of commercial aluminium. As indicated by many workers decomposition for the lattice vibration.

The total unperturbed electronic wave function may be written in the from

$$\Phi_0=\frac{1}{\sqrt{V^N N!}}\,\text{det.}\,|\Psi_{kj}(w_k)S_k| \tag{2.2}$$

as usual, where Ψ_{kJ} satisfy the equations

$$\left(-\frac{\hbar^2}{2m}\Delta+\sum V(w-R_n)\right)\Psi_{kj}(\mathrm{w})=\varepsilon^{(0)}\Psi_{kj}(w) \tag{2.3}$$

and s_k are the spin functions. By the Bloch's theorem, we get

$$\Psi_{kj}(w)=\frac{1}{\sqrt{V}}\exp(i\boldsymbol{k}\cdot w)u_k(w) \tag{2.4}$$

$$\varepsilon^{(0)}=\varepsilon^{(0)}(\boldsymbol{k}_j)$$

where $\mathbf{k}_j$ means the wave number vector.

It will not be a easy matter to obtain these u_{kj} functions for the real metals, but particular properties of each metal are supposed to be contained in these periodic functions.

In the lowest state at 0° K, the $\mathbf{k}_j$ values in Φ_0 fill up the so-called Fermi sphere.

Following the usual perturbation procedure, we can calculate the first order energy $E_0^{(1)}$ for H^I and the second order energy E_0^2 for H_I (the first order energy for this term vanishes).

For $E_0^{(1)}$ we get

$$E_0^{(1)}=\sum\sum(C(\boldsymbol{k},\boldsymbol{k}')-A(\boldsymbol{k},\boldsymbol{k}'))$$

$$C(\boldsymbol{k},\boldsymbol{k}')=\frac{e^2}{V^2}\int\frac{1}{r_{12}}u^*_{k'}(w_1)u_{k'}(w_1)u_k^*(w_2)u_k(w_2)dw_1dw_2$$

$$A(\boldsymbol{k},\boldsymbol{k}')=\frac{e}{V_2}\int\frac{1}{r_{12}}\exp\{\boldsymbol{k}'-\boldsymbol{k})(w_1-w_2)\}\times u^*_{k}{}'(w_1)u_{k'}(w_2)u^*_k(w_2)u_k(w_1)dw_1dw_2 \tag{2.5}$$

where the spin degenerady is taken into account and the summations are carried out in accordance with the Pauli principle.

For $E_0^{(2)}$, we must consider the excited wave function Φ_1 in which one electron has its $\boldsymbol{k}$ value above the Fermi maximum. We obtain the matrix element $(\Phi_0|H_I|\Phi_1)$, between Φ_0 and Φ_1 (more precisely $\Phi_1(\boldsymbol{k}',\boldsymbol{k}_j)$, which means $\boldsymbol{k}_j$ state in the Fermi sphere is vacant and $\boldsymbol{k}'$ state in the outside region is occupied) as,

$$(\Phi|H_I|\Phi_1|^2=\frac{\hbar}{2M\omega_q N_A}\,\frac{4}{9}C^2q^2(N_q,\text{ or }N_q+1)$$

$$C=\frac{\hbar^2}{2m}\int_c(\text{grad }u_k)^2dw,\quad q=|q|=|\boldsymbol{k}'-\boldsymbol{k}_j| \tag{2.6)*}$$

where N_q is the number of the lattice quantum with the wave number q, ω_q is its circular frequency, and M is the mass of the atom. So we obtain

$$E_0^{(2)}=2\frac{4\hbar C^2}{9N_AM}\sum_{k'}{}'\sum_{kj}{}'\frac{q^2}{\omega_q}\left[\frac{N_q}{\hbar^2(\boldsymbol{k}_j^2-\boldsymbol{k}'^2)/2m+\hbar\omega_q}+\frac{N_q+1}{\hbar^2(\boldsymbol{k}_j^2-\boldsymbol{k}'^2)2m-\hbar\omega_q}\right]\times f(\boldsymbol{k}_j)(1-f(\boldsymbol{k}')) \tag{2.7}$$

where we can sum freely without the fear of the violation of the Pauli principle, since we have introduced the functions $f(\boldsymbol{k})$ which takes the value 0 or 1 according as the $\boldsymbol{k}$-state is empty or is occupied, and the dash on the summation symbol means that the values for which the denominators of the summand become zero are to be omitted. The first factor 2 is the consequence of the spin degeneracy.

Rearranging the terms, it becomes

$$E_0^{(2)}=2B\sum_{k'}{}'\sum_{kj}{}'F(\boldsymbol{k}',\boldsymbol{k}_j)f(\boldsymbol{k}_j)$$

$$-2(2\hbar B\sum_{k'}{}'\sum_{kj}{}'G(\boldsymbol{k}'.\,\boldsymbol{k}_j)f(\boldsymbol{k}_j)f(\boldsymbol{k}')$$

$$F(\boldsymbol{k}',\boldsymbol{k}_j)=\frac{q^2}{\omega_q}\left(\frac{N_q}{\hbar^2(\boldsymbol{k}_j^2-\boldsymbol{k}'^2)/2\mathrm{m}}+\frac{N_q+1}{\hbar^2(\boldsymbol{k}_j^2-\boldsymbol{k}'^2)/2\mathrm{m}-\hbar\omega_q}\right) \tag{2.8}$$

$$G(\boldsymbol{k}',\boldsymbol{k}_j)=q^2\left\{\left(\frac{\hbar^2}{2m}(\boldsymbol{k}_j^2-\boldsymbol{k}'^2)\right)^2-(\hbar\omega_q)^2\right\}^{-1}$$

$$B=4\hbar C^2/9N_AM$$

Then the energy of our electron-system may be written as

$$E=N\varepsilon_0+\sum\varepsilon^{(0)}{}_j+E_0^{(1)}+E_0^{(2)} \tag{2.9}$$

where ε_0 is determined by the choise of the energy zero.

b) The above consideration for the energy is valid only for the system at the absolute zero of the temperature. In general, we must consider the statistical ensemble of the systems. If we set the probability for the occupation of the one-electron energy state of a system in this ensemble as $\sigma(\boldsymbol{k}_j)$, the average energy of our system is given as follows.

$$\begin{aligned}<E>&=2\sum_j\varepsilon_j^{(0)}\sigma(\boldsymbol{k}_j)\Delta_j+2\varepsilon^{(0)}\sum\sigma(\boldsymbol{k}_j)\Delta_j\\&+\sum_j\sum_k(\mathrm{C}(\boldsymbol{k}_j,\boldsymbol{k}_k)-A(\boldsymbol{k}_j,\boldsymbol{k}_k)\sigma(\boldsymbol{k}_j)\sigma(\boldsymbol{k}_k)\Delta_j\Delta_k\\&+2B\sum_j{}'\sum_k{}'F(\boldsymbol{k}_k,\boldsymbol{k}_j)\sigma(\boldsymbol{k})\Delta_j\\&-2(2\hbar B)\sum_j{}'\sum_k{}'G(\boldsymbol{k}_k,\boldsymbol{k}_j)\sigma(\boldsymbol{k}_j)\sigma(\boldsymbol{k}_k)\Delta_j\Delta_k\end{aligned} \tag{2.10}$$

where Δ_j denotes the leveldensity. Of course, the condition

$$N=2\sum_j\sigma(\boldsymbol{k}_j)\Delta_j \tag{2.11}$$

must be satisfied.

---

* See the reference (5), page 513.

The entropy S of our Fermi-Dirac system for this distribution is given by

$$S=2k\sum_j\{(\sigma(\boldsymbol{k}_j)-1)\log(1-\sigma(\boldsymbol{k}_j))\}$$
$$-\sigma(\boldsymbol{k}_j)\log\sigma(\boldsymbol{k}_j)\}\Delta_j \qquad (2.11)$$

So the equilibrium distribution $\sigma(\boldsymbol{k})$ can be determined by maximizing this entropy under the conditions $<E>=$const. and $N=$const. That is, the variations $\delta\sigma(\boldsymbol{k})$ must satisfy the condition

$$\delta(S-k\beta<E>-kaN)=0 \qquad (13)$$

where $k\beta$ and ka are the usual indeterminate multipliers, and

$$\delta S=2\sum_j\delta\sigma(\boldsymbol{k}_j)\Delta_j\{\log(1-\sigma(\boldsymbol{k}_j)-\log(\boldsymbol{k}_j)\}$$

$$\delta N=2\sum_j\delta\sigma(\boldsymbol{k}_j)\Delta_j$$

$$\delta<E>=2\sum_j\delta\sigma(\boldsymbol{k}_i)\Delta_j(\varepsilon^{(0)}+\varepsilon_0)$$
$$+\sum_j\sum_k((C-A)'\sigma(\boldsymbol{k}_k)\delta\sigma(\boldsymbol{k}_j)+\sigma(\boldsymbol{k}_j)\delta\sigma$$
$$(\boldsymbol{k}_k))\Delta_j\Delta_k+2B\sum_j{}'\sum_n{}'\delta\sigma(\boldsymbol{k}_j)\Delta_jF(\boldsymbol{k}_k,\boldsymbol{k}_j)$$
$$-2(2\hbar B)\sum_j\sum_k(\sigma(\boldsymbol{k}_k)\delta\sigma(\boldsymbol{k}_j)$$
$$+\sigma(\boldsymbol{k}_j)\delta\sigma(\boldsymbol{k}_k,\boldsymbol{k}_j)$$

After suitable arrangements, we put the coefficient of each $\delta\sigma(\boldsymbol{k})$ equal to zero and get

$$\log(1-\sigma(\boldsymbol{k}_j))/\sigma(\boldsymbol{k}_j)$$
$$-a+\beta[\varepsilon_0+\varepsilon^{(0)}+U_j+V_j+W_j]=0$$
$$U_j=\sum_k\{C(\boldsymbol{k}_j,\boldsymbol{k}_k)-A(\boldsymbol{k}_j,\boldsymbol{k}_k)\}\sigma(\boldsymbol{k}_k)\Delta_k$$
$$V_j=B\sum_k{}'F(\boldsymbol{k}_k,\boldsymbol{k}_j) \qquad (2\,14)^*$$
$$W_j=-2(2\hbar B)\sum{}'G(\boldsymbol{k}_k,\boldsymbol{k}_j)\sigma(\boldsymbol{k}_k)\Delta_k$$

or,

$$\sigma(\mathbf{k}_j)=\frac{1}{1+\exp[a+\beta(\varepsilon_0+\varepsilon^{(0)}{}_j+U_j+V_j+W_j)]} \qquad (2.15)$$

Putting $\beta=1/kT$ as usual, equations (11) and (15) may be regarded as the system of equation from which we can determine $\sigma(\boldsymbol{k})$ and a. We write $a=-\zeta/kT$, where ζ is the Gibbs free energy per one electron of the system. From ζ, we can derive all the thermodynamical behavior of this system.

§3. Superconducting State

We now present an approximate treatment which may show the existence of a special equilibrium state which is stable below a certain critical temperature. The procedures are similar to that of the reference 4.

If the interaction energies U_j, V_j and W_j had no special characters and could be smoothed out, the solution of (2.15) will be of the form

$$\sigma^f(\boldsymbol{k}_j)=\frac{1}{1+\exp[(\varepsilon^{(0)}{}_j-\zeta_f)/kT]} \qquad (3.1)$$

and ζ_f may be determined from the condition (2.11), approximately as

$$\zeta_f=\mu_0-\frac{\pi^2}{12}\frac{(kT)^2}{\mu_0} \qquad (3.2)$$

where μ_0** is the maximum energy at 0°K.

In the present case, W_j shows a peculier features as was remarked by Fröhlich. It is positive when $(\boldsymbol{k}_j{}^2-\boldsymbol{k}_k{}^2)^2$ is small, but it is negative when this quantity is large. We consider that the ordinary Fermi distribution in $\boldsymbol{k}$-space suffers a modification on account of the presence of this term and it will be limitted in the narrow region near the surface of the Fermi sphere owing to the nature of this interaction.

For the modified distribution we put σ^s and ζ_s instead of the above σ^f and ζ_f. Since we have smoothed out the interaction energies and adjusted the energy zero suitably in obtaining the formula (1) from (2.15), an additional term ΔW_j* appears as follows.

$$\sigma^s(\boldsymbol{k}_j)=\frac{1}{1+\exp[(\varepsilon^{(0)}{}_j+\Delta W_j-\zeta_s)/kT} \qquad (3.3)$$

$$\Delta W_j=-2(2\hbar B)\sum_k{}'G(\boldsymbol{k}_k,\boldsymbol{k}_j)(\sigma^s(\boldsymbol{k}_k)$$
$$-\sigma^f(\boldsymbol{k}_k))\Delta_k \qquad (3.4)$$

Expanding the exponential in (3), we get

$$\sigma^s(\boldsymbol{k}_j)-\sigma_0{}^s(\boldsymbol{k}_j)=\frac{2(2\hbar B)}{kT}$$
$$\times\frac{\exp[(\varepsilon^{(0)}{}_j-\zeta_s)/kT]}{\{1+\exp[(\varepsilon^{(0)}{}_j-\zeta_s)/kT]\}^2}$$
$$\times\sum_k{}'G(\boldsymbol{k}_k,\boldsymbol{k}_j)\,\sigma^s(\boldsymbol{k}_k)-\sigma^f(\boldsymbol{k}_k))\Delta_k \qquad (3.5)^{***}$$

From this we obtain a integral equation for the determination of $\sigma^s(\boldsymbol{k})$, which, however is very difficult to solve. Hence, we shall take another way for the present.

As in Fröhlich's paper, we can say that the energy ΔW_j tends to expel the electrons from the inside of the Fermi surface to the outer region, that is, $\sigma^s(\boldsymbol{k}_k)-\sigma^f(\boldsymbol{k}_k)$ will be negative in the region where the denominator is negative and positive when that is positive. For the sufficiently low $\boldsymbol{k}_j$ state ΔW_j is very small, since for $\boldsymbol{k}_k$ near $\boldsymbol{k}_j$, $\sigma^s(\boldsymbol{k}_k)-\sigma^f(\boldsymbol{k}_k)$

---

* In the following we can write $\sigma(\boldsymbol{k})$ instead of $\bar{\sigma}(\boldsymbol{k})$ without the fear of the confusion.

** See the equ. (3 12)

*** See the equ. (3.6)

will be nearly zero and for distant $\boldsymbol{k}_k$ the denominator will become very large. Hence we can assume

$$\sigma_0^s(\boldsymbol{k}_j)=\frac{1}{1+\exp[\varepsilon_j^{(0)}-\zeta_s)/kT]} \qquad (3.6)$$

for these states up to some k^+ state.

Near the Fermi surface, ΔW_j becomes appreciable and we write in this region as

$$\sigma^s(\boldsymbol{k}_\lambda)=\frac{1}{1+\exp[(\varepsilon_\lambda^{(0)}-\Delta W_\lambda-\zeta_s)/kT]} \qquad (3.7)$$

Then the equ. (2.11) becomes

$$N=2\sum_{|k_j|<k+}\sigma_0^s(\boldsymbol{k}_j)\Delta_j+2\sum_{|k_\lambda|>k+}\sigma^s(\boldsymbol{k}_\lambda)\Delta_\lambda \qquad (3.8)$$

$$N-n=2\sum_{1}^{\infty}\sigma_0^s(\boldsymbol{k}_j)\Delta_j$$

$$n=2\sum_{|k_\lambda|>k+}(\sigma^s(\boldsymbol{k}_\lambda)-\sigma_0^s(\boldsymbol{k}_\lambda))\Delta_\lambda \qquad (3.9)$$

If we use the ordinary formura

$$\Delta_j=2\pi V(2m/\hbar^2)^{3/2}\sqrt{\varepsilon}\,d\varepsilon \qquad (3.10)$$

and the assumption

$$\varepsilon_j^{(0)}=\frac{\hbar^2}{2m}k_j^2 \qquad k_j=|\boldsymbol{k}_j| \qquad (3.11)$$

we get from (9)

$$N-n=\frac{3}{2}N(kT/\mu_0)^{3/2}\int_0^\infty\frac{x^2dx}{1+\exp[x-\zeta_s/kT]} \qquad (3.12)$$

$$x=\varepsilon/kT, \quad \mu_0=(3N/\pi V)^{2/3}h^2/8\mathrm{m}=\hbar^2k_0^2/2m$$

where k_0 is the wave number which corresponds to μ_0. We can assume $n\ll N$ and $\zeta_s\gg kT$, so we can use the Sommerfeld expansion for ζ_s. It becomes

$$\zeta_s=\mu_0-\frac{\pi^2}{12}\frac{(kT)^2}{\mu_0}-\xi, \quad \xi=\frac{2}{3}\frac{n}{N}\mu \qquad (3.13)$$

From the equations (9), (6) and (13), we get

$$n=\sum_{|k_\lambda|>k}\left\{\frac{1}{1+\exp\left[\left(\frac{\hbar^2}{2m}k_\lambda^2-(\zeta_f-\xi)+\Delta W_\lambda\right)/kT\right]}-\frac{1}{1+\exp\left[\left(\frac{\hbar^2}{2m}k_\lambda-(\zeta_f-\xi)\right)/kT\right.}\right\}\Delta_\lambda$$

and (3.14)

$$\Delta W_\lambda=-2(2\hbar B)\sum_{|k_k|<k\pm}{}' G(\boldsymbol{k}_k,\boldsymbol{k}_\lambda)(\sigma^s(\boldsymbol{k}_k)-\sigma^f(\boldsymbol{k}_k))\Delta_k$$
$$-2(\hbar B)\sum_{|k_\mu|>k+}{}' G(\boldsymbol{k}_\mu,\boldsymbol{k}_\lambda)(\sigma^s(\boldsymbol{k}_\mu))\Delta_\mu \qquad (3.15)$$

Further we make following rather rough assumptions: (i) we can replace all ΔW_λ with its value at $|\boldsymbol{k}_\lambda|=k_0$; (ii) the first term in (15) may be neglected; (iii) the second term may be replaced by

$$-4(2\hbar B)\sum G(\boldsymbol{k}_\mu,\boldsymbol{k}_\lambda)(\sigma^s(\boldsymbol{k}_\mu)-\sigma_0^s(\boldsymbol{k}_\mu))\Delta\mu \qquad (3.16)$$

considering $\sigma^s(\boldsymbol{k}_\mu)-\sigma^f(\boldsymbol{k}_\mu)$ to be negative in region where $G(\boldsymbol{k}_\mu,\boldsymbol{k}_0)$ is negative and to be positive outside that region as in Frohlich's reasoning, and $\sigma^s(\boldsymbol{k}_\mu)-\sigma_0^s(\boldsymbol{k}_\mu)$ may be assumed to be nearly zero and to be positive in these regions respectively.

We introduce the new variables

$$x=k_\mu-k^0, \qquad q^2=4k_0^2\sin\theta/2$$
$$u=2\sigma_0\sin\theta/2\,,\ \sigma_0=m\,s/\hbar,\ \omega_q=sq \qquad (3.17)$$

where θ is the angle between $\boldsymbol{k}_\mu$ and $\boldsymbol{k}_\lambda$; and s is the velocity of the lattice wave (sound), assuming the dispersion to be zero. So we obtain

$$\Delta W_\lambda=-4(2\hbar B)\frac{4m^2V}{h^2(2\pi)^3}\int_{k^+}^{\infty}\varphi(k')\frac{\sin^2(\theta/2)}{x^2-4\sigma_0^2\sin^2\theta/2}k'^2dk'd\omega$$

by putting

$$\Delta_\mu=\frac{V}{(2\pi)^3}k'^2dk'd\omega\,,\quad \varphi(k)=\sigma^s(k)-\sigma_0^s(k)$$

in which $d\omega$ means the solid angle in k-space, the polar axis being taken in the direction of $\boldsymbol{k}_\lambda$. Further it becomes

$$\Delta W_\lambda=-4(2\hbar B)\frac{m^2\pi Vk_0^2}{\hbar^2(2\pi)^3\sigma_0^4}\int_{k^+-\kappa_0}^{\infty}\varphi(x)dx\int_0^{2\sigma}\frac{2u^3}{x^2-u^2}du$$

where σ means the limit in θ and may be written as $\sigma=\sigma_0q_0/2k_0^2$, in which q_0 is the q value of the maximum frequency normal mode of the lattice vibration in Debye theory*, and the assumption $k'^2dk'=k_0^2dk'$ is used. The last integral in the above has the singular character if $x^2<(2\sigma)^2$, but on account of our special assumption on $\varphi(x)$, it will be sufficient to evaluate it for the case $x^2>2(\sigma)^2$.

$$4\sigma^2\int_0^1\frac{2u'^3}{(x/2\sigma)^2-u'^2}du'=4\sigma^2\left(\frac{1}{2}\left(\frac{2\sigma}{x}\right)^2+\frac{1}{3}\left(\frac{2\sigma}{x}\right)^4+\dots\right)$$

assuming the width of the range in which $\varphi(x)$ is appreciably positive to be the order of several multiple of σ, we replace this integral by a constant value $\eta(4\sigma^2)$, where η is the numerical factor of the order of 1/10;

Considering (3.9), we finally obtain

$$\Delta W_\lambda=-\eta\psi\frac{n}{N}\,,\quad \psi=\frac{16\nu^{1/3}}{2^{2/3}9}\frac{C^2}{Ms^2} \qquad (3.18)$$

---

* $q_0^3=3(2\pi)^2N_A/2$

$$\varDelta W_\lambda = -\tau\xi \qquad \tau = 3\eta\psi/2\mu_0$$

Then the equ. (3.14) may be regarded as the equation for determining ξ and can be written in the form

$$\xi = \mu_0\left(\frac{kT}{\mu_0}\right)^{3/2}\delta\left\{\int_c^\infty \frac{x^{\frac{1}{2}}dx}{1+\exp[x-(\zeta_f+(\tau+1)\xi)/kT]} \right. \tag{3.19}$$

$$\left. -\int_c^\infty \frac{x^{\frac{1}{2}}dx}{1+\exp[x-(\zeta_f-\xi)/kT]}\right\},$$

$$c = \frac{\hbar^2}{2m}k^{+2}/kT$$

where $\delta = (m'/m)^{3/2}$ is introduced in order to take into account that the effective mass m' of the electrons which is in the special state be different from that which is used in μ_0. In the integral in (12), the difference of the effective masses in various parts of the k-space are included in μ_0 as the averaged effective mass. The divergence of the effective mass in (19) from the averaged one is important for our theory, as will be seen later.

For ε^+, we assume $\varepsilon^+ = \mu_0 + a$, $a > 0$.

It is easily seen that (19) has always the solution $\xi = 0$ and the non-zero (>0) solution appears at some temperature. We consider this non-zero ξ state which is more stable than the ordinary state below the critical temperature as the superconducting state of our electron system, and call it *s*-state. The ordinary state with ζ_f will be called *f*-state.

b) Using the expansion at $\xi = 0$, we get approximately

$$\frac{\xi}{kT} = \left(\frac{kT}{\mu_0}\right)^{\frac{1}{2}}\delta\tau\left(\frac{\xi}{kT}\right) \int_c^\infty \frac{\exp(x-\zeta_f/kT)}{\{1+\exp(x-\zeta_f/kT)\}^2}x^{\frac{1}{2}}dx$$

$$+\left(\frac{kT}{\mu_0}\right)^{\frac{1}{2}}\delta\frac{\tau(\tau-2)}{2}\left(\frac{\xi}{kT}\right)^2 \int_c^\infty \frac{(\exp(x-\zeta_f/kT)-1)\exp(x-\zeta_f/kT)}{\{1+\exp(x-\zeta_f/kT)\}^2}x^{\frac{1}{2}}dx \tag{3.20}$$

From this quadratic equatioion, we can determine the values of ξ, $\partial\xi/\partial^2\xi/\partial T^2$ in the neighbourhood of $\xi = 0$. The condition for the phase change is that the equation has the double root at $\xi = 0$. Thus

$$1 - \delta\tau\left(\frac{kT}{\mu_0}\right)^{\frac{1}{2}}\int_c^\infty \frac{\exp(x-\zeta_f/kT}{\{1+\exp(x-\zeta_f/kT)\}^2}x^{\frac{1}{2}}dx \tag{3.21}$$

In our case, the condition for the second order phase change must also be fulfilled and it can be written as

$$\left(\frac{\partial\xi}{\partial T}\right)_{\xi=0} = 0 \tag{3.22}$$

From these two equations, we obtain

$$a/kT_c + \pi^2 kT_c/12\mu_0 = \delta\tau - 2 \tag{3.23}$$

$$a = \pi^2(kT_c)^2/12\mu_0 \tag{3.24}$$

respectively, or combining

$$\frac{\pi^2}{6}\frac{kT_c}{\mu_0} = \delta\tau - 2 \tag{3.25}$$

If we know the values of δ and τ theoretically, we can determine T_c from (25), but on account of our insufficient knowledges on these quantities, it will be impossible at the present.

But it is to be remarked here that $\delta\tau$ should be very close to 2 to give observed T_c and δ should be smaller than unity as will be seen later.

c) When we want to investigate the behavior of our system near 0°K, it becomes necessary to assume some modified formula instead of (10) to obtain reasonable results. We assume arbitrarily

$$\varDelta = 2\pi V\left(\frac{2m}{\hbar^2}\right)^{\frac{t}{2}+1}\varepsilon^{t/2}\,d\varepsilon \tag{3.26}$$

in our special region in k-space near the Fermi surface. Using this, we can proceed as in b) and get

$$B\xi = \left(\frac{1}{\mu_0}\right)^{t/2}\delta_*\left\{\int_{\varepsilon^+}^\infty \frac{\varepsilon^{\frac{t}{2}}d\varepsilon}{1+\exp[(\varepsilon-(\zeta_f+(\tau-1)\xi))/kT]}\right.$$

$$\left. -\int_{\varepsilon^+}^\infty \frac{\varepsilon^{t/2}d\varepsilon}{1+\exp[(\varepsilon-(\zeta_f-\xi))/T]}\right\}$$

$$B = \left(\frac{\pi V}{3N}\right)^{(t-1)/3} 2^{t-1}$$

where δ_* is the value of δ in this case. When the temperature becomes sufficiently low, the second term in the bracket can be negrected, anticipating $\xi = \xi^* > 0$ at 0°K.

So from

$$\frac{\mu_0^{t/2}}{\delta_*}B\xi^* = \int_{\varepsilon^+}^{\mu_0+(\tau-)\xi^*} \varepsilon^{t/2}\,d\varepsilon$$

we get

$$\varepsilon^+ = \mu_0 + a, \quad a = \left((\tau-1) - \frac{B}{\delta^*}\right)\xi^* \tag{3.27}$$

Putting

$$\xi = \xi^* + \varDelta\xi, \quad \mu_1 = \mu_0 - \frac{\pi^2}{12}\frac{(kT)^2}{\mu_0} + (\xi^* + \varDelta\xi)(\tau-1),$$

$$\varepsilon_1=\mu_1-\varepsilon^+=\frac{B}{\delta^*}\,\xi^*-\frac{\pi^2}{12}\,\frac{(kT)^2}{\mu_0}+\Delta\xi\,\tau-1),$$

we get

$$\frac{\mu_0{}^{t/2}}{\delta_*}\,B(\xi^*+\Delta\xi)=\int_0^\infty\frac{(\varepsilon^++\varepsilon')^{t/2}\delta\varepsilon'}{1+\exp(\varepsilon'-\varepsilon_1)/kT}$$

where we have changed the variable from ε to $\varepsilon'=\varepsilon-\varepsilon^+$. Considering that ε_1 is certainly positive at sufficiently low temperatures, we can use the usual expansion method for the integral and obtain

$$\frac{\mu_0{}^{t/2}}{\delta_*}B(\xi^*+\Delta\xi)=\left\{\frac{2}{t+2}(\mu_1{}^{(t+2)/2}-\varepsilon^{+(t+2)/2})\right.$$

$$\left.+\frac{\pi^2}{6}(kT)^2\,\frac{t}{2}\,\mu_1{}^{(t-2)/2}\right\}$$

Expanding μ_1 and ε^+, we get

$$\Delta\xi=-\frac{(t-1)\delta_*}{\delta_*(\tau-1)-B}\,\frac{\mu^2}{12}\,\frac{(kT)^2}{\mu_0}$$

Hence

$$\xi=\xi_*-\frac{(t-1)\delta_*}{\delta_*(\tau-1)-B}\,\frac{\pi^2}{12}\,\frac{(kT)^2}{\mu_0}\qquad(3.28)$$

$$\left(\frac{\partial\xi}{\partial T}\right)_{T=0}=0\qquad(3.29)$$

$$\left(\frac{\partial^2\xi}{\partial T^2}\right)_{T=0}=-\frac{(t-1)\delta_*}{\delta_*(\tau-1)-B}\,\frac{\pi^2k^2}{6\mu_0}\qquad(3.30)$$

§4. The Thermodyramical Quantities and The Critical Magnetic Field

a) In the previous section, we have obtained the Gibbs free energy for our s-state, so we can calculate the specific heart discontinuity ΔC at the transition.

$$\Delta C=(C_s-C_f)_{Tc}=V_AN\left(T_c\left(\frac{\partial^2\zeta_f}{\partial T^2}\right)_{Tc}\right.$$

$$\left.-T_c\left(\frac{\partial^2\zeta_s}{\partial T^2}\right)_{Tc}\right)$$

$$=V_ANT_c\left(\frac{\partial^2\xi}{\partial T^2}\right)_{Tc}=2\gamma T_c=2\gamma T_c/(\tau-2)\qquad(4.1)$$

where

$$\gamma=V_AN\frac{\pi^2}{6}\,\frac{k^2}{\mu_0},\quad C_f=\gamma T,\quad V_AN=\nu N_0\qquad(4.2)$$

and N_0 is the Avogadro number. Further, we get

$$\left(\frac{\partial C_s}{\partial T}\right)T_c=\gamma T_c+2\gamma T_c/(\tau-2)\qquad(4.3)$$

b) When the magnetic field is applied, the superconducting sample shows the so-called Meissner effect. For the magnetic behavior of our system, we proceed semi-phenomenologically as follows. We assume that microscopically the energy of the electron is not perturbed by the magnetic field owing to its cancellation in the substance, but macroscopically the superconducting body behaves as if its substance has the susceptibility $-1/4\pi$. In the consequence, the Gibbs free energy per unit volnme of the superconducting body has the additional term $H^2/8\pi$, where H is the intensity of the uniform applied field.

Hence, it will be sufficient for the determination of the shift of T_c due to H to put $\zeta_f+H^2/8\pi$ instead of ζ_f in (3.20). So the condition (3.23) becomes

$$a/kT-H^2/8\pi kT+\pi^2kT/12\mu_0=\pi^2kT_c/6\mu_0$$

and we get

$$H=\left(\frac{\pi^2k^2}{12\mu_0}\times8\pi N\right)^{\frac{1}{2}}(T_c-T)\qquad(4.5)$$

$$-\left(\frac{\partial H}{\partial T}\right)=\left(\frac{\pi^2k^2}{12\mu_0}\times8\pi N\right)^{1/2}\qquad(4.6)$$

Of couse the condition (3.22) is destroyed, but we can calculate the latent heat of the transition by

$$Q=T(S_f-S_s)=V_ANT\left(\frac{\partial\zeta_s}{\partial T}-\frac{\partial\zeta_f}{\partial T}\right)\qquad(4.7)$$

$$=-V_ANT(\partial\xi/\partial T)_{\xi=0}$$

We obtain

$$Q=2\gamma T(T_c-T)/(\tau-2)\qquad(4.8)$$

It is to be remembered that these relations are valid only for the temperatures which are close to the zero-field transition temperature.

§4. Comparison with the Experiments and Discussions

We have shown that one can deduce a special equilibrium state for the system of the conduction electrons which is stable below a certain temperature on the basis of the Frohlich's interaction. We do not enter here into the probrem of the validity of the perturbation procedure.

In the course of the derivation, we have omitted Coulomb and exchange interactions ($\sim1eV$) which will be very much greater than Fröhlich's interaction ($\sim10^{-5}eV$) if they remained without cancellation. So very slight variations with k of these interaction terms are required for the justification of the omission, considering our special assumption of the form of $\sigma^s-\sigma^f$ in this region. It will go too far, therefore, to say whether some metal should become superconducting or not without settling the above mentioned energy problem.

But some of the relations between the experimental facts in the superconducting metals may be derived by our theory.

a) From the thermodynamical theory of Gorter and Casimir, the relations

$$\Delta C = V_A T_c (\partial H/\partial T)^2_{T_c}/4\pi\,,$$
$$Q = -V_A T (\partial H/\partial T)/4\pi \qquad (4.9)$$

are deduced and agree very well with the experiments. So if we know the relation between the threshold magnetic field and the transition temperature, we can determine ΔC and Q by the above formulas. It is found that these quantities calculated from (4.6) by (5.1) are consitent with our purely theoreticall results (4.1) and (4.9), if the relation

$$\tau - 2 = 2 \qquad (5.2)$$

is satisfied.

On the other hand, τ can be estimated from the formula for the electrical conductivity σ_e at room temperature T_r, except η.

$$\sigma_e = \frac{8\nu^{2/3}}{\pi^2}\,\frac{e^2}{k\hbar}\,{\mu_0}^2\frac{Ms^2}{C^2}\left(\frac{3N_A}{4\pi}\right)^{1/3}\Big/T_r \qquad (5.3)$$

From (3.18) and (5.3), we get

$$\frac{\eta\psi}{\mu_0} = n\frac{32}{3\pi}\,\frac{e^2\hbar}{m}\,\frac{\nu^{5/3}N_A}{kT_r\sigma_e} \qquad (5.4)$$

The calculated values are shown in Table I.

Table I.

Metal	N_A 10^{22}/c.c	$1/\sigma_e$[3] 10^{-16} esu	ψ/μ_0	η
Al	5.96	0.03	5.05	0.53
V	6.75	0.20	35.32	0.075
Zn	6.58	0.065	12.08	0.22
Sn	3.72	0.13	13.63	0.19
Ta	5.53	0.17	26.51	0.10
Hg	4.49	0.30	38.06	0.07
Pb	3.31	0.24	22.44	0.12

In calculating ψ, we put $\nu=1$ for all metals.[2]

It is to be noticed here that the relation (3.25) is very critical, in other words, a slight change in τ will change T_c drastically. The approximate constancy of τ can be regarded as to favour this situation. Probably, these facts are due to the approximation of using one ξ instead of many $\sigma(\boldsymbol{k})$.

Using (5.2), we get

$$\Delta C = \gamma T_c \qquad (5.5)$$

This is satisfied well by Al, Zn, Sn, and Ta. For Hg, Pb the observed ΔC is near $2\gamma T_c$. Without touching τ, we can say that there should be the following relation between $\partial H/\partial T$ and γ by the equ. (4.6).

$$V_A\left(\frac{\partial H}{\partial T}\right)^2\Big/4\pi\gamma = 1 \qquad (5.6)$$

This is approximately fullfilled as in Table II.

Table II.

Metal	T_c °K	γ_c[6] 10^{-4} cal/mol. deg.	ΔC_{obs} 10^{-4} cal/mal.deg.	$V_A(\partial H/\partial T)^2_{H=0}/4\pi\gamma$
Al	1.15	2.98	4.07[7]	1.36
V	4.3		116.27[8]	
Zn	0.95	1.29	1.58[7]	1.22
Sn	3.71	11.86–14.65	19.30[8]	1.50–1.31
Ta	4.4	62.08	93.05[8]	1.49
Hg	4.15	15.56–18.68	38.04[8]	2.45–2.04
Pb	7.22	51.12	96.6[8]	1.84

We have calculated ΔC_{obs} from the observed $(\partial H/\partial T)_{H=0}$.

Considering roughness of our approximations, these may be rather good agreements. It is interesting that those metals which have their threshold field curves closely linear in the neighbourhood of the no-field transition temperature instead of parabolic ones, satisfy the relations (5.5) and (5.6) good.

b) Near 0°K, the thermodynamical theory also requirs

$$(\Delta S)_{T=0} = 0 \qquad (5.7)$$
$$-\left(\frac{\partial}{\partial T}(\Delta S)\right)_{T=0} = \gamma \qquad (5.8)$$
$$V_A\frac{{H_0}^2}{8\pi} = (\Delta U)_0 \qquad (5.9)$$

where $(\Delta U)_0$ means the difference of the internal energy per mol at 0°K, and H_0 is the threshold strength at 0°K.

On the other hand, from (3.28) and (3.29) we get

$$(\Delta S)_0 = N(\partial\xi/\partial T)_0 \qquad (5.10)$$
$$(\partial\Delta S/\partial T) = N(\partial^2\xi/\partial T^2) \qquad (5.11)$$
$$(\Delta U_0) = N(\Delta(\zeta - T\partial\zeta/\partial T)) = N_0\xi^* \qquad (5.12)$$

It is seen the condition (5.6) is satisfied by our theory. From (5.11) and (5.12) and the definition of γ

$$\frac{(t-1)\delta^*}{\delta_*(\tau-1)-B} = 1 \qquad (5.13)$$

must be satisfied.

From (5.9) and (5.12) and (3.27), we get

$$\frac{V_A H_0^2}{8\pi} = \frac{\nu N A \delta_*}{\{\delta_*(\tau-1)-B\}} \frac{\pi^2 k^2 T_0^2}{12\mu_0} \quad (5.14)$$

Using the experimental values for H_0 and γ, we can determine t and δ_* from these conditions.

c) Unfortunately, due to the ambiguities in η and the lack of knowledge on $\partial V_A/\partial M$, we can not estimate the isotopic mass dependency of T_0.

In conclusion the auther expresses his hearty thanks to Prof. T. Sakai for the introduction into this research and the kind guidance.

References

1) W. Heisenberg: Zeit. fur Naturforsh. 2a(1947) 185; 3a (1948) 65.
2) H. Frohlich: Phys. Rev. **79** 1950) 845.
3) J. Bardeen: Phys. Rev. **80** (1950) 567.
4) H. Ichimura: Journ. Phys. Soc. Japan **4** (1947) 265.
5) A. Sommerfeld & H. Bethe Handbuch d. Phys. 24/II (1933).
6) J. G. Daunt; Phys. Rev. **80** (1950) 911.
7) J. G. Daunt & C. V. Heer: Phys. Rev. **76** (1949) 1324.
8) D. Shoenberg: *Superconductivity* (1938) Cambridge.

JOURNAL OF THE PHYSICAL SOCIETY OF JAPAN Vol. 7, No. 3, MAY—JUN., 1952

On the Discontinuous Elongation of Aluminium Crystals, IV

Tomoyosi KAWADA

The Government Mechanical Laborators, 132 Sumiyoshi-cho, Suginami-ku,
Tokyo, Japan

(Received August 27, 1951)

In the previous paper the discontinuous elongations of magnitude of a few micron were observed for coarse grain polycrystal specimens of commercial aluminium. In this paper the behaviour of slip lines near the grain boundary was observed and it was found that when the slip lines continued across the grain boundary the discontinuous elogation was not observed, while the jumps occured when the slip lines terminated at the grain boundaries. From these results the cause of the discontinuous elongation was discussed.

§1. Introduction

In the previous paper[1)] we reported that the discontinuous elongation of the magnitude of a few micron were observed when coarse grain polycrystal specimen of commercial aluminium was elongated by a specially designed extensometer at the temperature range between 100° and 350°C. In this paper we observe the behaviour of slip lines near the grain boundary and discuss the cause of discontinuous elongation.

Many workers have observed the behaviour of slip lines near grain boundary. For example, D. Hanson and M. A. Wheeler[2)], W. Boas and M. E. Hargreaves[3)], and W. A. Wood and W. A. Rachinger[4)] observed the slip lines near grain boundaries with aluminium specimen. While N. F. Nye[5)] observed them with silver chloride. Recently E. Fujita, T. Suzuki and T. Hibi[6)] photographed the slip lines near grain boundary and H. Czyzewski[7)] photographed branching of slip lines at twin boundary with electronmicroscope.

We observed the behaviour of slip lines in connection with the discontinuous elongation and found that the discontinuous jump did not occur when the slip lines continued across the grain boundaries, while jumps occurred when slip lines terminated at the grain boundary. From these results we discussed the cause of the discontinuous elongation.

§2. Behaviour of Slip Lines Near Grain Boundary

As mentioned in the previous paper, we used aluminium specimens consisting of 2, 3 and 4 crystals polished their surfaces electrolytically and elongated them with the Polanyi type testing machine. As reported by W. Boas aud M. E. Hargreaves the elongation given to the specimen is not uniform but widely different from grain to grain when a coarse grain polycrystal specimen was elongated, moreover it is not uniform even over one grain. In the following we will pick up typical photomicrographs and give explanations about them.

1. 99.99% aluminium. As the behaviours were similar from room temperature to 350 C, we will show, as an sxample, the case of room temperature. Fig. 1 shows the case in which neighbouring crystals have almost similar orientation.

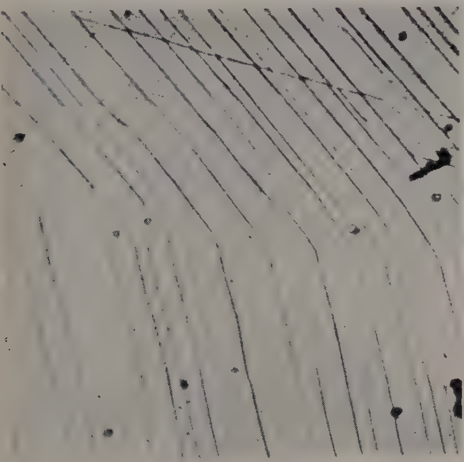

Fig. 1. Tensile temperature 20°C
Elongation 6%

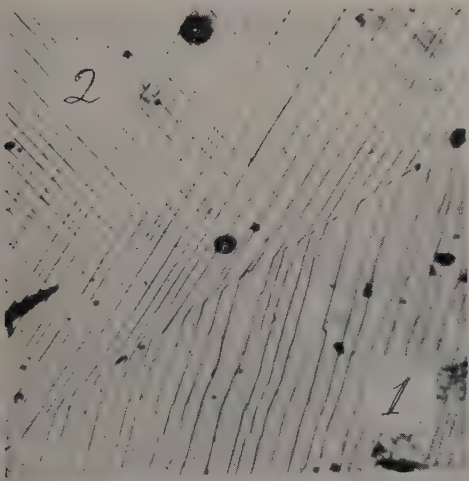

Fig. 2. Tensile temperature 20°C
Elongation 6%

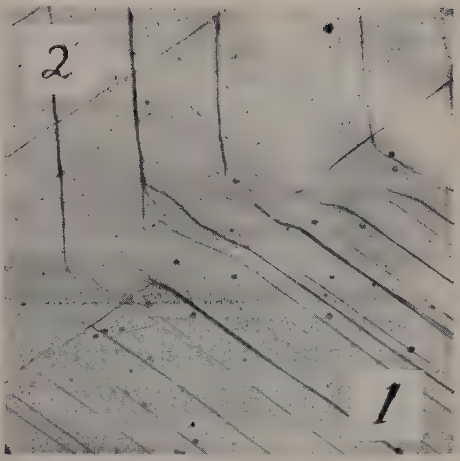

Fig. 3. Tensile temperature 20°C
Elongation 6%

The lines continue across the grain boundary, turning their direction of slip at the boundary. The grain boundary does not appear nearly as clear as line on the surface. The slip lines of the second and the third system appear faintly near the grain boundary. Moreouer the continuations of slip lines at the grain boundary were observed on both surfaces of the specimen. Fig. 2 is the case in which appears single slip in grain 1 while double slip in grain 2 and the slip lines in grain 1 continue to the second system of slip lines in grain 2. In this case, too, the grain boundary does not appear clearly as lines. The most general cases is that in which the primary system of slip lines in the grain 1 continues to the secondary system in the grain 2 and the primary system in the grain 2 continues to the secondary system of grain 1. Fig. 3 is a special case in which the slip lines run straightly in the grain 1, but after they have crossed over the grain boundary, they run in a zigzag way and are connected to the slip lines of the grain 2. When we observed all over the specimen, the slip lines did not necessarily continue across the grain boundary and at some places they terminated at the grain boundary. But the above results are thought to be a distinctive characteristics when we elongate the coarse grain polycrystal specimen of 99.99% aluminium.

2.1. Commercial aluminium elongated at room temperature. In this case the behaviour of the slip lines near grain boundary was almost similar to the 99.99% aluminium.

2.2. Commercial aluminium elongated between 100°C to 350°C. In this case the behaviour of slip lines near grain boundary was different from the above case. In Fig. 4 we can observe the first, second and third systems of slip lines in each of the neighbouring grains but none of them continues to each other at the grain boundary. Moreover the grain boundary appeares clearly. Fig. 5 is the case in which the orientation of the neighbouring grains are almost similar. In this case, too, the slip lines do not continue at the grain boundary. Fig. 6 is the case in which the grain boundary is very meandering and the grain 1 caves in the grain 2 very deeply and we observed, besides slip lines, some undulating smoky patterns on the surface. Fig. 7 is the case which we often observed at the earlier stage of elongation and in this figure the slip lines in grain 1 come to the grain boundary and then they turn their direction and run along the grain boundary.

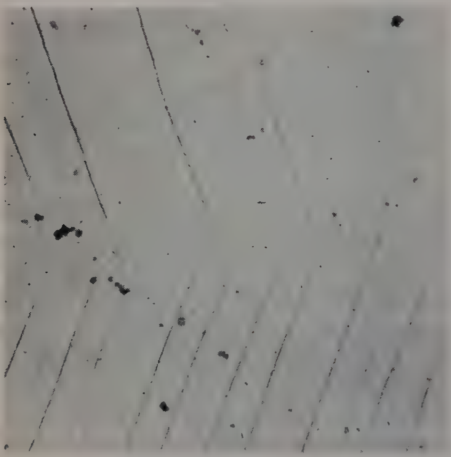

Fig. 4. Tensile temperature 200°C
Elongation 2%

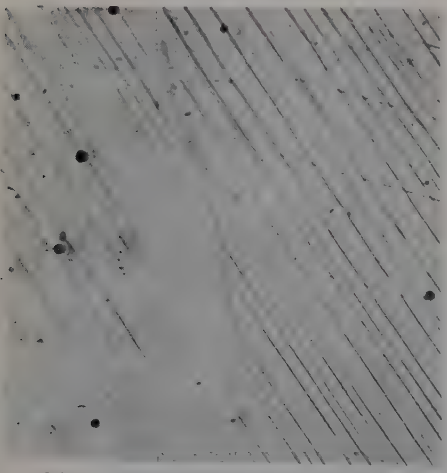

Fig. 5. Tensile temperature 200°C
Elongation 4%

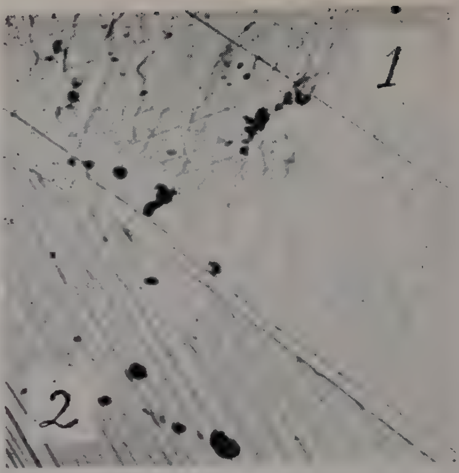

Fig. 6. Tensile temperature 100°C
Elongation 10%

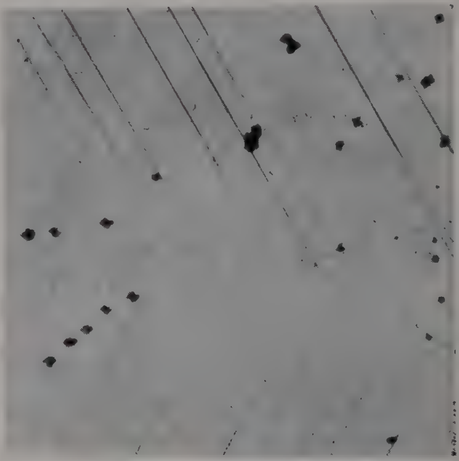

Fig. 7. Tensile temperature 100°C
Elongation 2%

Thus in general the slip lines do not continue to those of the neighbouring crystal and the grain boundary appears clearly.

2.3. Commercial aluminium elongated higher than 350°C. As indicated by W. A. Wood and W. A. Rachinger, appearances of slip lines abruptly above 350°C. Figs 8 and 9 are the typical ones and in these cases the specimens are mainly elongated near the

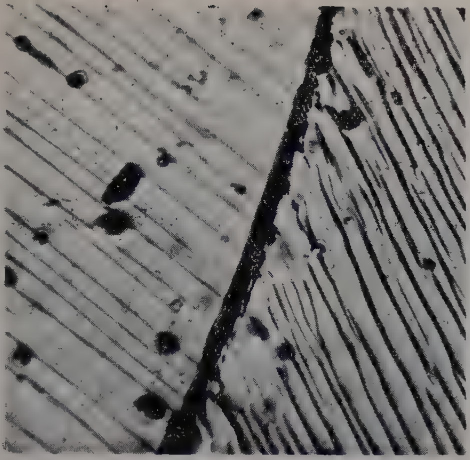

Fig. 8. Tensile Temperature 350°C
Elongation 2%

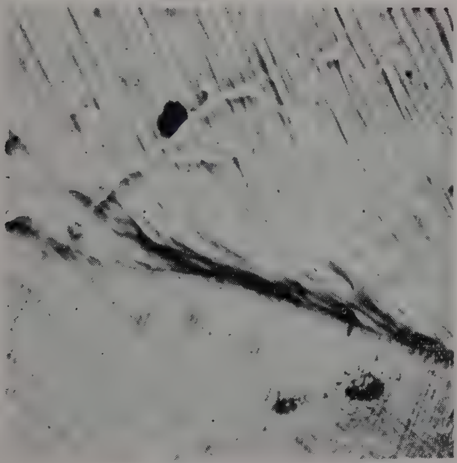

Fig. 9. Tensile Temperature 350°C
Elongation 2%

grain boundaries. Thus in Fig. 8 and 9 the rate of local elongation near the grain boundary is greater than the overall elongation of specimen and the slip lines appear mainly near the grain boundary. The grain boundary is observed to be very wide and this may partly due to the thickening of the grain boundary and partly due to the step formed between the neighbouring crystals. The slip lines are irregular and curued near the grain boundary as if one grain slipped relatively to the other along the grain boundary,

§ 3. Discussion

F. C. Frank and W. T. Read[8)] have clarified generation of slip line, while many workers[9)] have discussed about the model of grain boundary. Taking into consideration of these theories we will discuss the above photomicrographs and the cause of discontinus elongation. In the first place we will discuss about the behaviour of slip lines in the 99.99% aluminium specimen. It may be supposed that when the orientations of the neighbouring crystals are similar a dislocation reached to the grain boundary in one of them can easily go across the grain boundary and the resultant slip lines become continuous over the grain boundary.

The fact that slip lines continue across the grain boundary on both surfaces of the flat specimen leads us to the following supposition: When dislocations reached to the grain boundary they may at first go across the grain boundary at the surface of the specimen. Then it necessarily follows that at the interior of the specimen dislocations are formed from segments of edge and screw dislocations as indicated by Cottrell[10)] and in such form they will go across the grain boundary. This supposition may be supported by Fig. 3; in this photomicrograph the slip lines of zigzag forms seems as if they are formed by joining together sements of edge and screw dislocations, and this phenomenon may be explained that the behaviour of dislocations at the grain boundary in the interior of the specimen comes out to the surface of specimen runs shallowly under the surface of the specimen.

Besides the first system of slip lines, there appear the second and the third system to cancel the internal stress near the grain boundary as much as possible. Thus there is little discontinuity in elongation near the grain boundary and the grain boundary does not appear as a line in the photomicrograph.

The above discussion may also be applied to the case in which the direction of slip planes of the neigbouring crystal are similar. In case of slip as shown in Fig. 2, the internal stress will arise near the grain boundary if each crystal deforms only by the primary slip system. To cancel this internal stress the crystal should deform by the second slip system of the in the direction similar to the primary slip system of the neighbouring crystal. Thus the slip lines of the grain 1 penetrate over the grain boundary continusly.

Next we will discuss the case of commercial aluminium. As indicated by many workers the impurity atoms may be rich in the grain boundary and in general it is difficult to discuss about the model of grain boundary in such a case. According to the theory of A. H. Cottrell[11] an atmosphere of solute atoms is formed around a dislocation and anchors it. It may be plausible that when a dislocation reaches to the grain boundary containing impurity atoms it is hard for the dislocation to go across it at once. But since we observed that the slip lines were continuous across the grain boundary when the specimen was elongated to the room temperature, it is likely that if many dislocations concentrated at one point, they will go across the grain boundary.

But when the temperature rises, the diffusion of dislocations will take place, i.e., when a dislocation reaches to the grain boundary it will be stopped there and at once diffuses along the grain boundary. These diffused dislocations will concentrated gradually along the grain boundary and thus a large internal stress will be created near the grain boundary. The degree of the concentration of the accumulated dislocations will depened upon the form of the grain boundary, and with increasing tensile stress they will overflow from the grain boundary producing slip lines of the second or the third system in the neighbouring crystal.

Macroscopically speaking, if each grain deforms without slipping across the grain boundary, the internal stress may be created and the degree of concentration of the internal stress will depend upon the form of the grain boundary, and as described by T. S. Kê[11] a concentration of stress will be built up at the grain corner, and upon proper conditions the local stress concentration may be large enough to initiate slip at the grain corners. Now A. W. McReynolds[13] found that in a stair-step stress-strain curve of aluminium containing small quantity of copper, the discontinuous jumps are due to the propagation of waves of plastic deformation along all or part of the specimen length. In our experiment it may be quite the same. When a slip is initiated at one place of the grain boundary and the internal stress there is released, this stress release, i.e., the initiation of slip will necessarily infect to the neighbouring part along the grain boundary. In this way the stored stress along the grain boundary will be released and elongation of the specimen will occur in a short time interval and this effect is observed as a discontinuous jump. In this case the slip lines of the second system are created from the grain corners, thus they do not necessarily continue to the slip lines of the primary system of the neighbouring crystal.

As mentioned before, when the temperature rises above 450°C it seems that the neighbouring crystals slip on each other along the grain boundary. Thus no internal stress can be accumulated at the grain boundary and no discontinuous jump occur.

§4. Conclusion

As mentioned in the previous paper we attributed the cause of discontinuous elongation to the existence of grain boundary because no jump was observed when a single crystal specimen was elongated. In this paper we found the relation between the behaviour of slip lines at the grain boundary and the occurrence of discontinuous jump, and from these results we discussed the mechanism of discontinuous jump.

In conclusion the author wishes to express his hearty thanks to Prof. S. Kaya of University of Tokyo for his kind interest in this work.

References

1) T. Kawada: J. Phys. Soc. Jap. **5** (1940) 60, 64.

2) D. Hanson and M. A. Wheeler: J. Inst. Met. **45** (1931) 229.

3) W. Boas and M. E. Hargreaves: Proc. Roy. Soc. **193** (1948) 89.

4) W. A. Wood and W. A. Rachinger: J. Inst. Met. **67** (1949) 237.

5) N. F. Nye: Proc. Roy. Soc. **198** (19s9) 47.

6) E. Fujita, T. Suzuki and T. Hibi: read April, 1951.

7) H. Czyzewski: J. App. Phys. **22** (1951) 846.

8) F. C. Fronk and W. T. Read: Phys. Rev. **79** 722.

9) e.g. W. T. Read and W. Schockley: Phys. Rev. **78** (1950) 275.

10) A. H. Cottrell: Progress in Metal Physics (1949) 80.

11) A. H. Cottrell: Rep. Conf. on Strength of Solid (1948) 30.

12) T. S. Kê: J. Appl. Phys. **21** (1950) 414.

13) A. W. MoReynolds: Trans. A. I. M. E. **185** (1949) 32.

JOURNAL OF THE PHYSICAL SOCIETY OF JAPAN Vol. 7, No. 3, MAY—JUN., 1952

On the Mathematical Analysis of the Problem of the Heat Conduction with the Variable Transfer Coefficient

Tunezo SATOH

Faculty of Engineering, University of Tokyo

(Received August 27, 1951)

The integro-differential equation for the temperature $v(x, t)$ of an infinite cylinder, which is kept at const. temperature initially, and loses heat by the radiation from its surface with variable transfer coefficient $h(t)$ is set up as follows:

$$V(x,t)=H(t)\sqrt{x}-\frac{\partial}{\partial t}\int_0^1 G^*(x, s)V(s,t)ds, \quad V(x,t)=\sqrt{x}\,v(z, t).$$

The surface temperature $H(t)$ is determined by the relations

$$\frac{1}{2}\int_0^t H(t)dt-\int_t^\infty P(t)dt-\int_0^t P(t-s)H(s)ds+\frac{1}{32}$$
$$=\frac{1}{2}t-\int_0^t (t-s)H(s)h(s)ds\,,$$

where $P(t)=2\sum \exp(-\lambda^2{}_n t)/\lambda^2{}_n$, from which further relations between $H(t)$ and $h(t)$

$$P(t)-\int_0^t P'(t-s)H(s)ds=\frac{1}{2}-\int_0^t H(s)h(s)ds\,,$$
$$H(t)h(t)=\int_0^t H'(t-s)P'(s)ds$$

are obtained. It is shown that in the special case where h=const. known result can be obtained from these relations. The Fourier transforms of $H(t)h(t)$, $H(t)$ and $V(x,t)$ denoted by $K^*(\zeta)$, $H^*(\zeta)$ and $V^*(x,\zeta)$ respectively, are found to satisfy

$$V^*(x,\zeta)=\frac{\sqrt{x}J_0(kx)}{J_0(k)}H^*(\zeta)+\frac{\sqrt{x}}{\sqrt{2\pi}}\,\frac{J_0(kx)-J_0(k)}{k^2J_0(k)}\,,$$
$$K^*(\zeta)=\left(i\zeta H^*(\zeta)+\frac{1}{\sqrt{2\pi}}\right)J_1(k)/kJ_0(k)\,,\quad i\zeta=k^2\,.$$

In this paper, we shall treat the problem that an infinite circular cylinder kept at constant initial temperature loses heat by the radiation from the surface, on which the transfer coeffient is in general variable.

Let θ be the temperature at time t and at distance r from the axis of cylinder. Then our problem is stated mathematically as follows:

$$\frac{\partial\theta}{\partial t}=K\left(\frac{\partial^2\theta}{\partial r^2}+\frac{1}{r}\,\frac{\partial\theta}{\partial r}\right),\ 0<r<a,\ t>0\,,$$
$$\theta=\text{finite at } r=0;$$
$$\theta=\theta_0 \text{ (const.) at } t=0;$$
$$\frac{\partial\theta}{\partial r}+h\theta=0 \quad\text{at } r=a\,.$$

By suitable transformations of variables, however, the above statements will be simplified as follows:

$$\frac{\partial v}{\partial t}=\frac{\partial^2 v}{\partial^2 x}+\frac{1}{x}\,\frac{\partial v}{\partial x}\,,0<x<1,\ t>0\ldots\ldots(1)$$
$$v=\text{finite at } x=0;\ldots\ldots(2)$$
$$v=1 \quad\text{at}\quad t=0;\ldots\ldots(3)$$
$$\frac{\partial v}{\partial x}+hv=0 \quad\text{at}\quad x=1.\ \ldots\ldots(4)$$

Let $L[y]=(xy')'$. After the usual definition, the Green's function belonging to the differential equation $L[y]=0$ and satisfying the boundary conditions (2) and (4), is given by

$$G_t(x,\xi)=1/h(t)+G(x,\xi)\,,\ \ldots\ldots(5)$$

where

$$G(x,\xi)=-\log\xi\ (x\leqq\xi);\ =-\log x\ (x\geqq\xi)$$

It is well known that $G(x,\xi)$ is the Green's function, belonging to the differential equation $L[y]=0$ and satisfying the boundary conditions:

$$y(0)=\text{finite},\quad y(1)=0\,.$$

Hence if we put

$$G^*(x,\ \xi)=\sqrt{x\xi}\,G(x,\ \xi)\,,$$

and denote the eigenvalue by λ_n^2 and its corresponding eigenfunction by $\Phi_n(x)$, then

$$J_0(\lambda_n)=0\,,\quad \Phi_n(x)=\sqrt{2x}\,J_0(\lambda_n x)/J'_0(\lambda_n),$$

where $J_0(x)$ is the Bessel's function of zero order, and eigenfunctions constitute orthogonal and normalysed system.

Next, let $\Gamma(x,\ \xi\,;\ \lambda)$ be the Green's function, belonging to $L[y]+\lambda^2xy=0$ and satisfying the same boundary conditions as $G(x,\ \xi)$, and let

$$\Gamma^*(x,\ \xi\,;\ \lambda)=\sqrt{x\xi}\,\Gamma(x,\ \xi\,;\ \lambda)\,.$$

Then, as is well known, $-\Gamma^*$ is (nothing else than) the reciprocal kernel of G^*, and the following relations hold:

$$G^*(x,\ \xi)=\sum_{n=1}^{\infty}\frac{\Phi_n(x)\Phi_n(\xi)}{\lambda^2_n}.$$

$$\Gamma^*(x,\ \xi;\ \lambda)=\sum_{n=1}^{\infty}\frac{\Phi_n(x)\Phi_n(\xi)}{\lambda^2_n-\lambda^2}$$

and

$$\int_0^1\Gamma^*(x,\ x;\ \lambda)dx=-J'_0(\lambda)/2\lambda J_0(\lambda),$$

where two series is the first and second expressions are absolutely and uniformly convergent with respect to $(x,\ \xi)$.

We now proceed to solve our problem. The required function $v(x,\ t)$ is expressed in term of G_t as follows:

$$v(x,\ t)=-\int_0^1 G_t(x,\ \xi)\xi\frac{\partial v(\xi,t)}{\partial t}d\xi\,.$$

If we put

$$-H(t)h(t)=\int_0^1\xi\frac{\partial v}{\partial t}d\xi,\ \ldots\ldots\ldots\ldots(6)$$

the above equation will be also written in the form:

$$v(x,\ t)=H(t)-\int_0^1 G(x,\ \xi)\xi\frac{\partial v}{\partial t}\,d\xi.\ \ldots(7)$$

Furthermore, if we put

$$V(x,\ t)=\sqrt{x}\,v(x,\ t),$$

the equations (6) and (7) will be

$$-H(t)h(t)=\int_0^1\sqrt{\xi}\,\frac{\partial V}{\partial t}d\xi.\ \ldots\ldots\ldots\ldots(6')$$

and

$$V(x,\ t)=H(t)\sqrt{x}-\frac{\partial}{\partial t}\int_0^1 G^*(x,\ \xi)V(\xi,\ t)d\xi$$
$$\ldots\ldots\ldots\ldots\ldots\ldots(7')$$

If we put $x=1$ in $(7')$, we have $V(1,\ t)=H(t)$. so that $H(t)$ is the temperature on the surface of the cylinder.

Integrating $(6')$ with respect to t and using the initial condition (3), we have

$$\int_0^1\sqrt{\xi}\,V(\xi,\ t)d\xi=\frac{1}{2}-\int_0^t H(s)h(s)ds$$
$$\ldots\ldots\ldots\ldots\ldots\ldots\ldots\ldots(8)$$

By applying Hilbert-Schmid's expansion theorem to the integral term in the right side of $(7')$, it is expressed as

$$V(x,t)=H(t)\sqrt{x}-\sum_{n=1}^{\infty}\frac{\Phi_n(x)}{\lambda^2_n}\psi'_n(t)\ \ldots(9)$$

where $\psi_n(t)$ is defined by the equation

$$\psi_n(t)=\int_0^1 V(\xi,\ t)\cdot\Phi_n(\xi)d\xi\ \ldots\ldots\ldots\ldots\ (10)$$

Substitute (9) into (10). Then it follows

$$\psi_n'(t)+\lambda_n^2\psi_n(t)=c_n\lambda_n^2H(t)\,,$$

from which $\psi_n(t)$ is so determined as

$$\psi_n(t)=c_n\exp(-\lambda_n^2t)+c_n\lambda_n^2\int_0^t H(\tau)\exp$$
$$[-\lambda^{2n}(t-\tau)]\ \ldots\ldots\ldots\ldots(11)$$

In this case the constant c_n is equal to

$$\psi_n(0)=\int_0^1\sqrt{x}\,\Phi_n(x)dx\,,$$

namely,

$$\int_0^1\sqrt{x}\sqrt{2x}\,J_0(\lambda_nx)dx/J_0'(\lambda_n)=\sqrt{2}/\lambda_n\,.$$

Thus we have relation:

$$c_n=\psi_n(0)=\sqrt{2}/\lambda_n\ \ldots\ldots\ldots\ldots\ldots\ldots\ldots(2)$$

Now, regarding the series in the right side of (9) to be uniformly convergent and replacing it in (8), we have

$$\frac{1}{2}H(t)-\sum_{0}^{\infty}\frac{c_n}{\lambda^2_n}\psi_n'(t)=\frac{1}{2}-\int_0^t H(s)h(s)ds$$
$$(13)$$

For the present case it will be noted that if we assume

$$\int_0^1 V^2(\xi,\ t)d\xi\,,\quad \int_0^1\left(\frac{\partial V}{\partial t}\right)^2d\xi$$

to be bounded in t, then by Schwarz's inequality, $\psi_n(t)$ and $\psi_n'(t)$ will be bounded in t and n. On the other hand, it is evident that

$$\int_0^1 G^*(x,\ x)dx=\sum_1^{\infty}\frac{1}{\lambda^2_n}=-\int_0^1 x\log x\,dx=\frac{1}{2}$$
$$\ldots\ldots\ldots\ldots\ldots\ldots(14)$$

Hence from (12) we have

$$\sum_1^{\infty}c^2_n=\frac{1}{2}\,.\ \ldots\ldots\ldots\ldots\ldots\ldots\ldots\ldots(14')$$

Thus it may be concluded that the series in the left side of (13) is absolutely and uniformly convergent.

Therefore, if we integrate (13), we get, by (12),

$$\frac{1}{2}\int_0^t H(s)ds-\sum_1^\infty\frac{c_n}{\lambda^2_n}\psi_n(t)+\sum_1^\infty\frac{c^2_n}{\lambda^2}$$
$$=\frac{1}{2}-\int_0^t(t-s)H(s)h(s)ds\,,$$

while, by using the second repeated kernel $G^*_2(x, y)$, we obtain

$$\int_0^1 G^*_2(x,x)dx=\sum_1^\infty\frac{1}{\lambda^4_n}=\frac{1}{2}\sum_1^\infty\frac{c^2_n}{\lambda^2_n}\,.$$

On the other hand simple calculation shows that

$$\int_0^1 dx\int_0^1[G^*(x, y)]^2dy=1/64\,.$$

Hence we have

$$\sum_1^\infty c^2_n/\lambda^2_n=1/32\,.$$

Putting this result and the relation (11) into the above obtained equation, we have

$$\frac{1}{2}\int_0^t H(t)ds-\int_t^\infty P(s)ds-\int_0^t P(t-s)H(s)ds$$
$$+\frac{1}{32}=\frac{1}{2}t-\int_0^t(t-s)H(s)h(s)ds,\ \ldots(15)$$

where

$$P(t)=\sum_1^\infty c^2_n\exp(-\lambda^2_n t)=2\sum_1^\infty\exp(-\lambda^2_n/\lambda_n t)^2$$
$$\ldots\ldots\ldots\ldots\ldots\ldots\ldots(16)$$

This equation shows the relation between the surface temperature: $H(t)$ and transfer coefficient: $h(t)$.

Let $t=0$ in (16). Then by (14′), $P(0)=1/2$. Using this result, and differentiating (15) with respect to t, we have

$$P(t)-\int_0^t P'(t-s)H(s)ds=\frac{1}{2}-\int_0^t H(s)h(s)ds.$$
$$\ldots\ldots\ldots\ldots\ldots\ldots(17)$$

Again, differentiating (17), we get

$$H(t)h(t)=\int_0^t H'(t-s)P'(s)ds\,,\ \ldots(18)$$

since $H(0)=1$. Each of (17) and (18) also shows the relation between the surface temperature and the transfer coefficient.

Remark. (I) It will be noticed that for sufficiently large n, λ_n/n tends to a fixed number.

(II) For any fixed t,

$$\lim_{n\to\infty}\lambda^2_n\int_0^t H(s)\exp[-\lambda^2_n(t-s)]ds=H(t);$$

hence from (11), $\psi_n(t)=O\left(\frac{1}{\lambda_n}\right)$.

(III) Differentiating (11), we have

$$\psi_n'(t)=\sqrt{2}\,\lambda_n\Big\{-e^{-\lambda_n^2t}+H(t)$$
$$-\lambda_n^2\int_0^t H(s)e^{-\lambda_n^2(t-s)}ds\Big\}\,.$$

In order that $\psi_n'(t)$ may be bounded in n, it should be

$$-e^{-\lambda_n^2t}+H(t)-\lambda_n^2\int_0^t H(s)e^{-\lambda_n^2(t-s)}ds$$
$$=O\left(\frac{1}{\lambda_n}\right).$$

Especially for $t=0$,

$$-1+H(0)=O\left(\frac{1}{\lambda_n}\right).$$

Consequently we must have $H(0)=1$.

(IV) For $t>0$, we can prove that if $H(t)$ is bounded, and satisfies the Lipschitz's condition, then

$$H(t)-\lambda_n^2\int H(s)\exp[-\lambda_n^2(t-s)]ds=O\left(\frac{1}{\lambda_n^2}\right).$$

For, in general, consider the integral

$$\lambda\int_0^x H(t)e^{-\lambda(x-t)}dt=\int_0^{\lambda x}H\left(x-\frac{\xi}{\lambda}\right)e^{-\xi}d\xi\,;$$

and let

$$\varphi(\lambda)=\int_0^{\lambda x}\left\{H\left(x-\frac{\xi}{\lambda}\right)-H(x)\right\}e^{-\xi}d\xi\,.$$

Then

$$|\varphi(\lambda)|\leqq\int_0^{\sqrt{\lambda}x}\left|H\left(x-\frac{\xi}{\lambda}\right)-H(x)\right|e^{-\xi}d\xi$$
$$+2G.\int_{\sqrt{\lambda}x}^{\lambda x}e^{-\xi}d\xi\,.$$

where $|H|<G$. The first integral in the last result is

$$=\int_0^{x/\sqrt{\lambda}}|H(x-t)-H(x)|\,\lambda e^{-\lambda t}dt\,;$$

for sufficiently large λ,

$$\leqq K\int_0^{x/\sqrt{\lambda}}\lambda te^{-\lambda t}dt=\frac{K}{\lambda}\int^{x\sqrt{\lambda}}ue^{-u}du\leqq Ke^{-1}x/\lambda\,;$$

while, the second integral is

$$2G.e^{-\sqrt{\lambda}x}\cdot(1-e^{-(\lambda-\sqrt{x})\lambda})\leqq 2Ge^{-\sqrt{\lambda}x}$$

Example. Let $h=$const. We shall show then that, the well known result can be obtained from (18).

For this purpose, let H^* and P^* be each Fourier transform of H and P respectively. Then

$$\int_0^\infty H'(t)e^{it\alpha}dt=-1-aiH^*(a),$$

and $$\int_0^\infty P'(t)e^{it\alpha}dt=-\frac{1}{2}-iaP^*(a).$$

From the convolution theorem on Fourier transforms for (18), it follows:

$$\left(a^2P^*(a)-\frac{ia}{2}+h\right)H^*(a)=\frac{1}{2}+iaP^*(a).$$

Now if we evaluate the value of $P^*(a)$ by using (16) and (14),

$$P^*(a)=\frac{2}{ia}\sum\frac{1}{\lambda_n^2-ia}-\frac{1}{2a}$$

or $$iaP^*(a)+\frac{1}{2}=2\sum\frac{1}{\lambda_n^2-ia}\ ;$$ accordingly

$$a^2P^*(a)-\frac{ia}{2}+h=h-2ia\sum\frac{1}{\lambda_n^2-ia}.$$

Hence we have formally

$$\int_{-\infty}^\infty H^*(a)e^{-iat}da=\int_{-\infty}^\infty\frac{2\sum(\lambda_n^2-ia)^{-1}}{h-2ia\sum(\lambda_n^2-ia)^{-1}}$$
$$\times e^{-iat}da=\int_{-i\infty}^{i\infty}(ia=u)e^{-ut}du/i\ \ldots\ldots\ldots(\mathrm{i})$$

On the other hand,

$$\int_0^1\Gamma^*(x,x;\lambda^2)dx=\sum\frac{1}{\lambda_n^2-\lambda^2}$$

and moreover the left side is $-J'_0(\lambda)/2\lambda J_0(\lambda)$. Consider the following contour integral in λ-plane:

$$2i\int_L\frac{J'_0(\lambda)e^{-\lambda^2t}}{hJ_0(\lambda)+\lambda J'_0(\lambda)}d\lambda\ \ \ldots\ldots\ldots\ldots\ldots\ldots(\mathrm{ii})$$

where L is the contour surrounding the sector shown in the figure. Now, all the zeros of $hJ_0(\lambda)+\lambda J'_0(\lambda)$ are situated on the real axis, symmetrically with respect to the origin, and are all simple. Hence if we denote these positive zeros by $k_1, k_2,\ldots\ldots,k_n,\ldots\ldots$, the residue at $\lambda=k_n$ will be given by

$$\frac{J_0(k_n)J_1(k_n)e^{-k^2{}_nt}}{k_n\{J^2{}_0(k_n)+J^2{}_1(k_n)\}},$$

using the relation $\frac{d}{d\lambda}\{hJ_0(\lambda)-\lambda J_1(\lambda)\}=hJ'_0(\lambda)-\lambda J_0(\lambda)$. Furthermore, the contour integral along the arc of the sector vanishes as soon as its radius tends to infinity. Finally the above stated contour integral (ii) becomes to equal to the values of integral (i). Thus we have proved:

$$H(t)=\frac{1}{2\pi}\int_{-\infty}^\infty H^*(a)e^{-iat}da$$
$$=2\sum\frac{J_0(k_n)J_1(k_n)\exp(-k_n^2t)}{k_n\{J_0^2(k_n)+J_1^2(k_n)\}}.$$

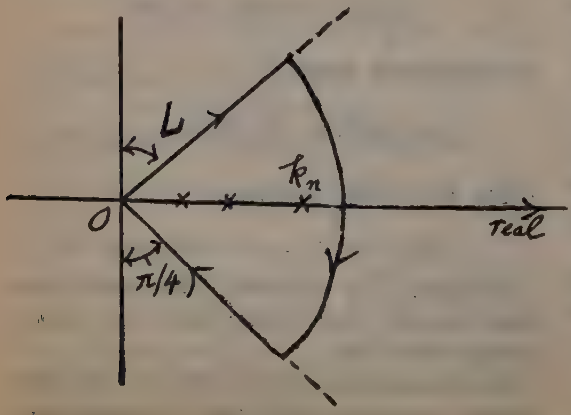

Fig. 1.

Now by the above example, it is suggested that in solving the integro-differential equation (7′), the Fourier transforms are very useful means.

In general, we assume $V(x,t)=O(e^{ct})$, $c<0$, and $h(t)\ \varepsilon L_1(0,\infty)$. Then the function of ζ, defined by

$$V^*(x,\zeta)=\frac{1}{\sqrt{2\pi}}\int_0^\infty V(x,t)e^{i\zeta t}dt,\quad \zeta=\xi+i\eta,$$

will be analytic for $\eta>c$.

Regarding $V(x,0)=\sqrt{x}$,

$$\frac{1}{\sqrt{2\pi}}\int_0^\infty\frac{\partial V}{\partial t}e^{i\zeta t}dt=-\left(\frac{\sqrt{x}}{\sqrt{2\pi}}+i\zeta V^*(x,\zeta)\right).$$

Hence from (6′) and (7′), it follows:

$$K^*(\zeta)=\int_0^1\left\{\frac{x}{\sqrt{2\pi}}+i\zeta\sqrt{x}\,V^*(x,\zeta)\right\}dx\ldots(19)$$

and

$$V^*(x,\zeta)=\sqrt{x}\,H^*(\zeta)+\frac{1}{\sqrt{2\pi}}\int_0^1G^*(x,s)\sqrt{s}\,ds$$
$$+i\zeta\int_0^1G^*(x,s)V^*(s,\zeta)ds,\ldots\ldots(20)$$

where

$$K^*(\zeta)=\frac{1}{\sqrt{2\pi}}\int_0^\infty H(t)h(t)e^{i\zeta t}dt,$$

and $$H^*(\zeta)=\frac{1}{\sqrt{2\pi}}\int_0^\infty H(t)e^{i\zeta t}dt;$$

accordingly both $K^*(\zeta)$ and $H^*(\zeta)$ are analytic for $\eta>c$, and besides $H^*(\zeta)\pm V^*(1,\zeta)$.

Since $i\zeta$ is non eigenvalue of G^*, by using the reciprocal kernel and applying the reciprocal relation between G^* and Γ^*, the equation (20) can be written as follows:

$$V^*(x,\zeta)=\sqrt{x}\,H^*(\zeta)+\left\{\frac{1}{\sqrt{2\pi}}+i\zeta H^*(\zeta)\right\}$$
$$\times\int_0^1\Gamma^*(x,s;i\zeta)\sqrt{s}\,ds.\ \ \ldots\ldots(20')$$

Putting this result in (19) we obtain the relation

$$K^*(\zeta)=\left(\frac{1}{\sqrt{2\pi}}+i\zeta H^*(\zeta)\right)$$

$$\times\left(\frac{1}{2}+i\zeta\iint_0^1 \Gamma^*(x,s;i\zeta)\sqrt{xs}\cdot dxds\right) \quad \text{...(19')}$$

Now if we evaluate the values of integrals in (20′) and (19′) by utilizing identities among cylindrical functions, consequently

$$\int_0^1 \Gamma^*(x,s;i\zeta)\sqrt{s}\,ds$$
$$=\sqrt{x}\{J_0(kx)-J_0(k)\}/k^2J_0(k).$$

$$\iint_0^1 \Gamma^*(x,s;i\zeta)\sqrt{xs}\cdot dxds$$
$$=\{2J_1(k)-kJ_0(k)\}/2k^3J_0(k).$$

where $i\zeta=k^2$. Therefore (20′) and (19′) become

$$V^*(x,\zeta)=\frac{\sqrt{x}J_0(kx)}{J_0(k)}H^*(\zeta)$$
$$+\frac{\sqrt{x}}{\sqrt{2\pi}}\frac{J_0(kx)-J_0(k)}{k^2J_0(k)} \quad \text{......(21)}$$

$$K^*(\zeta)=\left(i\zeta H^*(\zeta)+\frac{1}{\sqrt{2\pi}}\right)J_1(k)/kJ_0(k) \quad \text{.. (22)}$$

In the particular case stated before: $h=$ const., $K^*(\zeta)=hH^*(\zeta)$. Hence from (22) we get

$$H^*(\zeta)=\frac{1}{\sqrt{2\pi}}\frac{J_1(k)}{k\{hJ_0(k)-kJ_1(k)\}}.$$

Thus it is easily shown that the transform of $H^*(\zeta)$ is given by the sum of residues of

$$\frac{J_1(k)e^{-k^2t}}{hJ_0(k)-kJ_1(k)}.$$

In conclusion, the author expresses his thanks to Prof. Toshizo Matsumoto and Prof. Takahiko Yamanouchi for their advice and encouragements. He is also indebted to the Ministry of Education for financial aids.

JOURNAL OF THE HYSICAL SOCIETY OF JAPAN Vol. 7, No. 3, MAY—JUN., 1952

On the Excitation of Gamma-rays by Fast Neutrons

Tetsuo WAKATSUKI and Kenzo SUGIMOTO

Department of Physics, Faculty of Science, Osaka University

(Received September 5, 1951)

Fluorescent gamma-rays from 32 elements excited by Li-D neutrons were observed by aluminium wall Geiger-Müller counter. Effective mean neutron energy was estimated to be about 10 Mev. Observed gamma-ray intensities, after correcting for experimental conditions and divided by the number of atoms in the specimens, increase almost linearly with atomic weight A up to $A\cong 120$ and then become almost constant or slightly decrease at heavier elements. Gamma-ray intensity of uranium is strong but would be ascribed to fission.

These results were discussed utilizing statistical theory and it is suggested that the apparent level spacings beyond $A\cong 120$ do not decrease with A, or even become greater, possibly due to the partial excitation of nucleus.

Mean energies of gamma-rays for several elements were estimated by the absorption in lead plates and were found to lie between 0.6 and 3 Mev.

§1. Introduction

Although considerable experimental data have been accumulated on the level structures of light nuclei, there has been little informations on the level structures of heavier elements except for some of the lowest states.

Theoretically, statistical treatment is possible for heavier elements and nuclear level densities are expected to increase with mass numbers A and excitation energy. According to Weisskopf1) the level density is expressed as $\omega(E)=C\exp[2(E/D)^{1/2}]$ where C and D are constants to be determined from experimental data and E is the excitation energy.

For heavier elements ($A>50$) and above a few Mev excitation energy, level spacings are usually very small and the analysis of the particle emission spectra from nuclear reactions permits the comparison of the experimental data with theoretical predictions.

Recently, Gugelot2) studied the neutron spectra from (p, n) reactions for six elements with 16 Mev protons. Stelson and Goodman3) studied the energy distribution of neutrons resultiong from inelastic scattering of 14 Mev neutrons by Pb, Fe and Al.

Those authors found the energy spectra to be represented by the curve of the form const·E. exp$(-E/T)$ as predicted by the Weisskopf's statistical theory, T being the nuclear temperature.

To obtain informations about the level spacings in various nuclei, it is desirable to carry out such experiments for many elements at various excitation energy.

Another data for the survey of level spacings in various nuclei are obtained from the inelastic scattering cross section measurements for fast neutrons.4)

Inelastic scattering may be studied also by observing the gamma-rays resulting from the excitation of nucleus.

When nucleus is excited by fast neutrons, the product nucleus usually emits the excitation energy as one or more gamma-rays. From the energies and intensities of these gamma-rays, it should be possible to derive information concerning the level structure of the target (product) nucleus and the relative cross sections for the excitation of the various levels.

Lea5) measured the gamma-ray intensities using Po (α)−Be neutrons (of mean energy about 5 Mev) on 12 elements. Kikuchi et al.6), and later Aoki7) investigated 41 elements using monochromatic neutrons of 2.5 Mev and obtained the results which seem to be different in some respects with that of Lea. The feature of his result is that gamma-ray intensities do no increase for heavier elements above $A\sim 100$, and even fall for the heaviest elements investigated.

Although many assumptions must be added to deduce the variation of level spacings from these gamma-ray intensities, yet it seems interesting that gamma-ray intensities observed by Aoki are small at closed shell nuclei as was pointed out by Yamabe and Sanada.8)

From the circumstances that only few levels can be excited by 2.5 Mev neutrons in most elements, Aoki's results may be influenced by the position of the lowest levels.

To investigate the variation of level spacings in various nuclei, it is necessary to use so energetic neutrons that many levels can be excited in most elements.

We have measured the gamma-ray intensities of 32 elements excited by Li−D neutrons which have enough energy to excite many levels. The energy spectrum of Li−D neutrons is heterogeneous and extends up to 14 Mev with mean energy of about 7 Mev11). Heterogeneity of energy spectrum may be expected to have further effects to average the resonance effect as was observed by Nonaka9) and thus to smooth out the influence of indivisual levels.

§2. Experimental Arrangements

Experimental arrangements are similar to

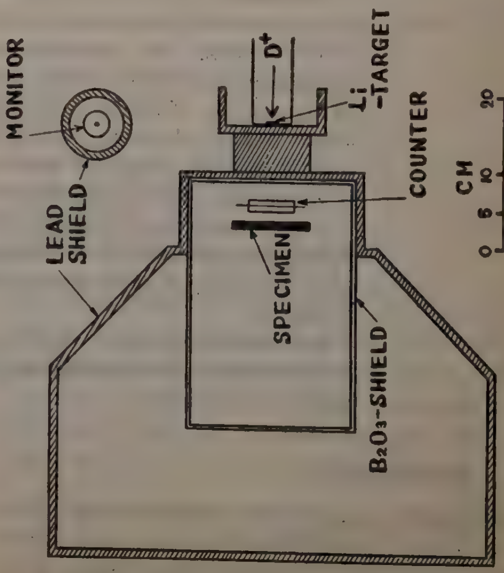

Fig. 1 Experimental arrangement

those used by Aoki and are shown in Fig. 1. Fast neutrons were produced by bombarding thick lithium metal by 0.9 Mev deuterons accelerated by Osaka static generater.

A Geiger-Müller counter made of aluminium placed at 11 cm from the target and connected to amplifier and scale of 128 recorder was used as the detector of gamma-rays. To shield the counter from the effects of gamma-rays produced in Li-D reaction and X-rays, 7 cm lead was interposed between the neutron source and counter.

By the preliminary experiment it was shown that considerable amount of gamma-rays is produced in lead traversed by fast neutrons. To reduce the effect of background gamma-rays due to lead, the backward part of lead shield box, which was used to protect the counter from X-rays, was made as large as possible. The counter and specimens under examination were also schielded from slow neutrons by B_2O_3 plates as are shown in Fig. 1.

From the increase of counts in the counter when specimens were placed behind the counter, relative intensity of gamma-rays per atom were computed.

The size of the specimens were usually 7.5×10 cm² and the thicknesses were between 0.5 and 2cm.

The geometrical corrections for the different thicknesses for the different substances were determined by observing the increase of counts due to 5mm thick iron sheet placed at various distances from the counter. As this correction factor is relatively large, this was further tested using gamma-rays from ThO_2 inclosed in the vessel of 7.5×10×0.5 cm³ placed at various distances from the counter. When the variation of neutron intensity at each point was corrected, correction factor obtained in this way agreed within experimental errors with that obtained by the above manner.

As the monitor for the neutron intensity, a high pressure ionization chamber filled with hydrogen at 15 atm. pressures connected to electrometer was used. In later work, this was replaced by another Geiger-Müller counter connected to scale of 100 recorder and placed at 22 cm from the target. This counter was surrounded by thick lead and the gamma-ray intensity excited in lead was used to measure the neutron intensity.

§3. The Gamma-Ray Yield Determination

When the target was bombarded by unresolved ion beam of about 2 microamperes, the counter discharges at the rate of about 10000 per minute. When the substance under examination was placed behind the counter, several up to ten per cent increase due to excited gamma-rays was observed in most cases as shown in Fig. 2. The large background counts are mostly due to gamma-rays excited in substances in the vicinity of the counter and is proportional to the intensity of neutrons. Therefore we have always measured the per cent increase over the background due to substances placed near the counter. After correcting for the geometrical conditions, this per cent increase was divided by the number of atoms contained in the specimens. This quantity is taken as the ordinate of Fig. 3 and is listed in Table 1.

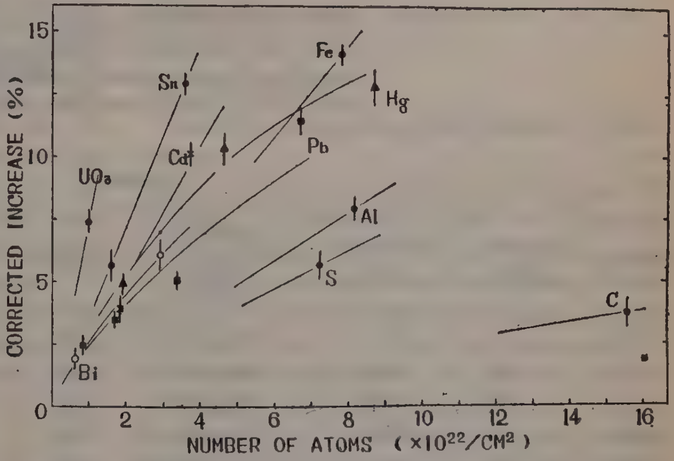

Fig. 2. Counting rate increase in per cent vs. number of atoms per cm² of specimens.

As the specimens were enough thin for neutrons, the decrease of neutron intensity in the specimens could be neglected. Therefore the gamma-ray intensity measured by the counter can be expressed as follows,

$$I \propto n\sigma_\gamma \varepsilon \mu^{-1}[1-\exp(-\mu d)], \quad (1)^*$$

where n denotes the number of atoms per unit volume, σ_γ the cross section for gamma-ray excitation, μ the absorption coefficient for

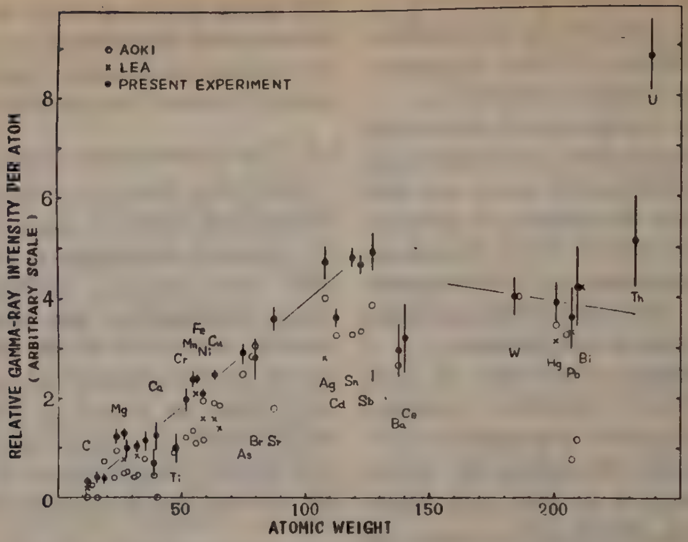

Fig. 3. Relative gamma-ray intensities observed by aluminium wall counter vs. atomic weight. Ordinate is arbitrary for the present experiment, figures in 10^{-24} cm^2 for Aoki's and Lea's data.

Table 1.

Element	Atomic number	Substance used	Relative gamma-ray intensity per atom	Element	Atomic number	Substance used	Relative gamma-ray intensity per atom
C	6	C	0.32±0.05	As	33	As	2.90±0.20
O	8	H_2O	0.41±0.12	Br	35	KBr	2.83±0.39
F	9	CaF_2	0.40±0.08	Sr	38	SrO	3.58±0.22
Mg	12	Mg	1.24±0.12	Ag	47	Ag	4.71±0.32
Al	13	Al	1.31±0.08	Cd	48	Cd	3.62±0.17
Si	14	Si	1.01±0.17	Sn	50	Sn	4.81±0.17
S	16	S	1.05±0.11	Sb	51	Sb	4.64±0.17
Cl	17	CCl_4	1.16±0.21	I	53	I	4.92±0.36
K	19	K	0.68±0.26	Ba	56	$BaCO_3$	2.96±0.54
Ca	20	Ca	1.27±0.28	Ce	58	CeF_3	3.19±0.67
Ti	22	TiO_2	1.02±0.31	W	74	W	4.01±0.35
Cr	24	Cr_2O_3	1.97±0.24	Hg	80	Hg	3.9±0.4
Mn	25	Mn	2.40±0.14	Pb	82	Pb	3.6±0.6
Fe	26	Fe	2.40±0.07	Bi	83	Bi	4.2±0.8
Ni	28	Ni	2.09±0.07	Th	90	ThO_2	5.13±0.89
Cu	29	Cu	2.47±0.08	U	92	UO_3	8.78±0.68

the emitted gamma-rays in cm^{-1} and d the thickness of the substance in cm. ε is the excitation energy which will be discussed in §5. For sufficiently small value of μd, this equation becomes

$$I \propto n\sigma_\gamma \varepsilon d\ , \qquad (2)$$

from which the product of the cross section for gamma-ray excitation and excitation energy can be evaluated. This relation can be checked experimentally by varying the thicknesses of specimens and observing the linear increase of gamma-ray intensities.

It was shown in this way that relation (2) holds up to 1 cm thicknesses of iron, cadmium and tin. For heavier elements, the absorption of gamma-rays in the specimen becomes more important and the relation (2) holds only at thin samples as is shown in Fig. 2.

The errors indicated are calculated from the statistical fluctuation of counts only. Relatively large errors of uranium and thorium are due to strong gamma-rays emitted from the specimens. Activation of counter walls due to (n,p) or (n,α) processes were noted in the experiment and corrected for.

§4. The Gamma-ray Energy Estimation

As highly excited nuclei usually emit more than one gamma-ray to return to their ground states, observed gamma-rays are heterogeneous in energy. The determination of the energy spectrum in this case being very difficult, we have tried to measure the absorption of gamma-rays in 1 cm lead plate to obtain a rough estimate of the energy. The same specimens as are used in yield determination were displaced 1 cm further from the counter. The per cent increase due to the specimen was compared with and without lead plate bet ween the specimen and the counter. After correcting for the effect of lead plate on counts, this ratio gives the absorption of gamma-rays in lead plate.

The results are shown in Fig. 4.

For comparison, absorption of gamma-rays from ^{60}Co (about 1.2 Mev) were measured under the same geometrical conditions. As is clear from Fig. 4, gamma-ray energies are different for various nuclei. Gamma-rays from iron and copper are about 1 Mev and those from antimony and tin are about 0.7 Mev. Gamma-rays from silver and cadmium are more hard but could not be determined in these rough experiment.

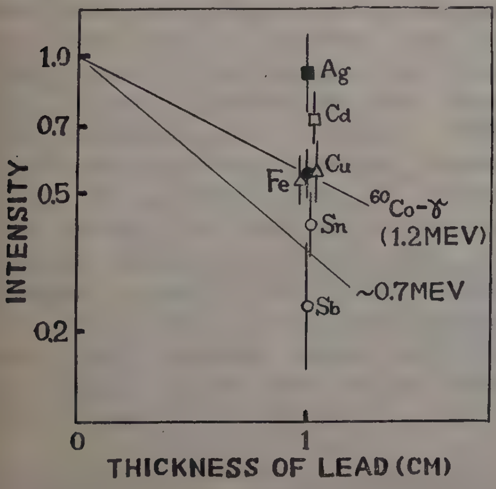

Fig. 4. Absorption of fluorescent gamma-rays in lead. For comparison, absorption of ^{60}Co gamma-rays is shown.

Energies of gamma-rays from mercury, lead and bismuth may be calculated from Fig. 2 by self absorption of gamma-rays using Eq. (1). In this way, the energies of gamma-rays from mercury and bismuth were estimated to be about 1.5 Mev. The mean energy of lead gamma rays was about 1 Mev but there is indication of the existence of soft (0.5 Mev) and hard (3 Mev) components. This will not, however, seriously affect the value in Table 1.

§5. Discussions

General consideration and effective neutron energy:

When fast neutrons have enough energy to excite a number of nuclear levels, because of the rapid decrease of level spacing with excitation energy, there are more levels available for the excitation of higher energy states. On the other hand, the partial width for neutron emission of the excited states is greater for the low lying levels, because of its dependence on the energy of the emitted neutron, resulting in a greater probability, per level, for the emission of faster neutron. The net effect of these two conflicting tendencies is that the energy loss of scattered neutrons, hence the excitation energy ε of the target nuclei, will be peaked at some energy intermediate between zero and the incident energy.

Excited energy ε is then emitted as one or more gamma-rays. Because of more levels available at higher energy states, there is greater probability to fall to higher energy states. On the other hand, transition to low energy states is more probable as the energy difference between two levels is greater. If the transition takes place again to the lower

---

* The former authors omitted the factor ε in Eq, (1) to obtain the gamma-ray yield per atom. This is justified only when ε can be assumed constant for various nuclei.

excited state, gamma-ray is emitted further.

As the result, the number of quanta emitted per collision will usually be more than one and the emitted gamma-ray spectrum have a complicated nature possibly having a broad maximum.

Now, our gamma-ray detector consists of aluminium wall counter and its sensitivity increases linearly with gamma-ray energies up to 25Mev.(10) Therefore, decrease of counter efficiency with gamma-ray energies is just compensated by the numerousness of gamma-ray quanta and the counter efficiency can be deemed in a first approximation to be proportional to the excitation energy of the target nucleus ε irrespective of the energy spectrum of gamma-rays.

The per-cent increase of gamma-ray counts over background due to specimen divided by the number of atoms is proportional, therefore, to the product of the cross section for gamma-ray excitation and excitation energy as is shown in Eq. (1)

According to Weisskopf's statistical theory,(1) the energy of scattered neutrons can be expressed by a Maxwell type energy distribution which can be calculated from the average level spacing of the lower levels D and incident neutron energy E_0. The average energy is

$$\bar{E}=2T\cong 2(DE_0)^{1/2}. \qquad (3)$$

From (3) the mean excitation energy becomes

$$\varepsilon=E_0-E\cong E_0-2(DE_0)^{1/2}.$$

The value of σ_γ can be replaced by the inelastic cross section σ_i, and this in turn by $\pi R^2\xi$, where R is the nuclear radius and ξ the sticking probability. For higher neutron energy ξ is usually taken as 1. Thus the yield of gamma-rays per atom oberved is proportional to

$$I/nd\propto\sigma_i\xi\{E_0-2(DE_0)\}^{1/2}, \qquad (4)$$

where $\sigma_i=\pi R^2\xi\propto A^{2/3}\xi$.

As the value of E_o, we must insert effective mean energy of fast neutrons and this can be calculated approximately using (4) assuming the value of D and taking $\sigma_i=$ constant for variation of E_o. As the primary neutron spectrum emitted from the source, the result of Richards(11) was utilised. Calculated value was $\bar{E}_o=9.0$ Mev with $D=0.1$ Mev and $\bar{E}_0=10.0$ Mev with $D=0.2$ Mev.

We may, therefore, take as $E_o=10$ Mev in this experiment.*

Discussions on the present experiment:

As is evident from Fig. 3, observed gamma-ray intensity per atom increases almost linearly with A up to $A\cong 120$ and then becomes constant or even decreases at larger atomic weights.

This general trend is quite similar to both the results of Aoki and Lea except for the difference of a few elements and can be cosidered as a characteristic feature which needs explanation.

The value for U is very large but this may perhaps be attributed to fission. The value for Th is also slightly larger than that of Bi but this contains also the contributions from fission. When the part due to fission is subtracted it is expected to be lowered. The difference of the values of U and Th seems reasonable considering the fission cross sections of both elements.

From Eq. (4), if σ_i varies as $A^{2/3}$ and D is assumed proportional to roughly $1/A$, then the curve should increase somewhat steeper than $A^{2/3}$ as A increases.

This will explain the behavior of the curve up to $A\cong 120$ but is in contradiction for the heavier elements.

We must next examine the factor influencing the observed behavior of the curve in Fig. 3 beyond $A\cong 120$. First, we shall examine the factor σ_i.

Amaldi et al.(4) measured the inelastic scattering cross sections of Al, Fe, Hg and Pb for 14 Mev neutrons. Though they have concluded that σ_i is nearly equal to half the total cross sections, it seems from their figures that σ_i for Hg and Pb are slightly smaller than are expected from $A^{2/3}$ law. Soltan(4) measured, with several thres hold detectors, the inelastic cross sections of Li-D neutrons for many elements. His results show that σ_i increases more slowly than $A^{2/3}$, suggesting $\xi<1$ for heavier elements. Collie, Griffiths(4) and Grahame, Seaborg(4) measured the inelastic scattering cross sections with similar methods. Both these authors results show that σ_i increases less rapidly at $A>100$ than in the region $A<100$.

---

* The values of σ_i are usually constant or slowly decreasing in the energy region in consideration. If we asume $\sigma_i\propto 1/E_0$then E_0becomes 8 Mev and no serious alternation is necessary in the following discussions.

Allen and Hurst[4] also measured σ_t for 3.1 Mev neutrons with the results that σ_t, increasing up to $A=120$, becomes almost constant at higher atomic weights.

From these experimental evidences, the values of σ_t for 10 Mev neutrons are supposed to increase with A beyond 120, though not so rapidly as $A^{2/3}$. This increase must be compensated by the second factor of Eq. (4), which will lead to wider level spacing of target nucleus at heavier elements as is evident from Eq. (4).

Considering the circumstances that the experiments for the measurement of σ_t all utilized threshold detectors and thus the values obtained are lower limits, we shall assume the increase of σ_t over $A=120$ to be proportional to $A^{2/3}$ and estimate the values of D necessary to compensate this increase. By the assumption of $A^{2/3}$ increase, σ_t at $A=200$ would be about 40% greater than at 120.

Assuming $D=0.1$ Mev at $A=100$, the value of D at $A=200$ must become 0.3, 0.5 and 0.7 Mev to make the second factor of Eq. (4) to 18, 31 and 41% smaller respectively.

D is the effective average level spacing and as large a value of 0.7 Mev for $A=200$ seems extraordinary, but this is a parameter in the exponential expression of level density and has a meaning only statistically. It needs not to be equal to the real spacing of the lowest energy levels.

That D becomes very large than expected from statistical theory will mean that the nucleus is partially excited, that is, not excited as a whole and behaves like a light nucleus in this case.

If σ_t is smaller than is assumed in the preceding discussions, it would mean that the level spacing of compound nucleus is large at heavy nucleus, thus indicating also the partial excitation of compound nucleus.

It is interesting, here, to note that capture cross sections of 1 Mev neutrons, increasing very rapidly with A up to $A\cong100$, become almost constant at heavier elements.[14]

The fact that level spacing becomes greater than predicted by statisticl treatment at high excitation[12] or at large A are becoming recognized from various experiments. These will be explaind by the finite thermal conductivity of nucleus which suggests the limits of the idea of the compound nucleus.

Gugelot[2] has also concluded from the study of (p, n) reactions that nuclear temperature $T=(DE_{\circ})^{1/2}$ decreases with A up to $A\cong100$ and then becomes constant up to $A=200$. Stelson and Goodman[8] also found that nuclear temperature T of Pb is 0.7 Mev at $E=14$ Mev and is greater than the value of 0.6 Mev at Fe, but they ascribed this effect to nuclear closed shell in Pb.

Feld[13] interpreted the data on the inelastic scattering of D-D neutrons (less than 3 Mev).

He found that the inelastic scattering of W can be interpreted by statistical theory but scattering of Fe and Pb can not be analysed statistically. This was the result of wide level spacing at Fe and Pb and 3 Mev energy was not sufficient to excite enough many levels.

If the level spacing is narrow, the mean gamma-ray energy emitted from such element will be soft and vice versa. It seems reasonable, therefore, that Sn and Sb gamma-rays are soft and Hg and Bi gamma-rays are hard, and the gamma-rays from Fe and Cu are intermediate. But this deduction is not conclusive as the gamma-rays from Ag and Cd are hard and seems contrary to the above discussion.

The effect of shell structure:

As is seen from Fig. 3, anomalously smaller values at magic number nuclei are only seen at Ba and Ce (for which isotopes of neutron number 82 are 72 and 89 per cent respectively).

That the gamma-ray intensity observed by Aoki with 2.5 Mev neutrons were small at almost all magic number nuclei would perhaps be attributed to the circumstances that the lowest few levels are higher or have wide level spacing than the neighbouring nuclei rather than to the wide level spacing up to considerable higher energies.

The very small intensity at Pb observed by Aoki will be explained by the fact that ^{208}Pb (52 per cent abundance) has the first excited state at 2.6 Mev and can not be excited by 2.5 Mev neutrons.

The values of Lea, though in rough agreement with ours in general tendencies, can not be directly compared, as his detecter was a thick wall (2.5 cm of iron) ionization chamber and absorption of gamma-rays by the wall is considerable for some elements which emit soft gamma-rays.

The small variation of the gamma-ray intensities with A will not be discussed as the experimental errors are relatively large and necessary data are lacking in the present stage.

§6. Acknowledgment

We wish to express our gratitude to Prof. S. Kikuchi for his interest in the work, to Professors T. Asada and J. Itoh for the loan of some of the specimens. Thank are also due to Messrs. Y. Oda, J. Sanada and S. Yamabe for discussions and to Mr. O. Takayanagi for technical assistances.

This work was supported by the grant for the promotion of science from the Ministry of Education.

References

1) V. F. Weisskopf: Phys. Rev. **52** (1937) 295; V. F. Weisskopf and D. H. Ewing: Phys. Rev. **57** (1940) 427.

2) P. C. Gugelot: Phys. Rev. **81** (1951) 51.

3) P. H. Stelson and C. Goodman: Phys. Rev. **82** (1951) 69.

4) C. H. Collie and J. H. Griffiths: Proc. Roy. Soc. **155** (1936) 434; D. C. Grahame and G. T. Seaborg: Phys. Rev. **53** (1938) 795; A. Soltan: Nature **142** (1938) 252; E. Amaldi, D. Bocciarelli, B.N. Cacciapuoti, and G. C. Trabacchi: Phys. Soc. Cambridge Conference, p. 97, (1947); W. D. Allen and C. Hurst: Proc. Phys. Soc. **52** (1940) 501.

5) D. E. Lea: Proc. Roy. Soc. **150** (1935) 637.

6) S. Kikuchi, H. Aoki and K. Husimi: Proc. Phys. Math. Soc. Japan, **18** (1936) 115.

7) H. Aoki: ibid. **19** (1937) 369.

8) S. Yumabe and J. Sanada: Prog. Theor. Phys. **5** (1950) 1.

9) I. Nonaka: Proc. Phys. Math. Soc. Japan **23** (1941) 925; **26** (1944) 66.

10) W. A. Fowler; C. C. Lauritsen and T. Lauritsen: Rev. Mod. Phys. **20** (1948) 264.

11) H. T. Richards: Phys. Rev. **59** (1941) 796.

12) For instance: W. Stetter and W. Bothe, ZS. f. Naturforsch. **6** (1951) 61.

13) B. T. Feld: Phys. Rev **75** (1949) 1115.

14 D. J. Hughes, W. D. B. Spatz, and N. Goldstein: Phys. Rev. **75** (1949) 1781.

JOURNAL OF THE PHYSICAL SOCIETY OF JAPAN Vol. 7, No. 3, MAY—JUN., 1952

The End Effects in Geiger Mueller Counters

Ryumyo ITO

Institute for Optical Research, Tokyo University of Education

(Received September 10, 1951)

The end effects—namely the diminution of the effective length and the change of counting probability at the end—in Geiger Mueller counters which have considerably thicker rods at both ends of the central wire than the wire itself are experimentally investigated under various conditions of the filling, and some theoretical interpretations for them are tried. The agreement of the experimentally observed results with the theoretically expected ones is fairly good, and we may conclude that the diminution of the effective length depends not only upon the bend of the lines of electric field but also upon the centrifugal force which affects on the primary electrons traversing along the curved line, and that the change of counting probability at the end of the thin wire is caused by the diffusion of the primary electrons in the axial direction.

§1. Introduction

Cylindrical counters—proportional counters and Geiger Mueller counters—with considerably thicker rods at both ends of the central wire than the wire itself are often used. In such counters, the region in which the counting probability or gas multiplication is not sufficient extends over about one radius of the cylinder, and the effective length is shorter than the wire length.[1,2] Roughly, the diminution of effective length may be easily understood from the aspect of the electrostatic field in the counter,[3] but the amount of the diminution depends not only on the electric field in the counter, but also on the conditions of the filling. The author has measured experimentally the diminution of the effective length and the steepness of the change of the counting probability at the end of a Geiger Mueller counter under various conditions of the filling, and has shown some theoretical interpretations for the behaviour such end effects.

§2. Experimental Procedure and Results

Counting rate *versus* position of the birthpoint of primary electron relations were measured by means of a Geiger Mueller photoelectron counter whose cathode is illuminated by ultraviolet light (λ 2537 Å) under various conditions of the filling. From these relations, the effective length and the steepness of counting probability change defined by the half-width of the differential curve of count-birthpoint curve near the end of the wire were calculated.

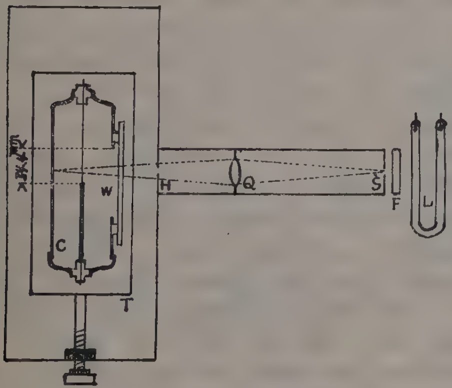

Fig. 1. Apparatus.
C, Geiger Mueller photoelectron counter; W, Quartz window; H, Pin hole; Quartz lens; S, Slit; F, Fused silica filter; L, Low pressure mercury lamp; T, Sliding table.

The apparatus is shown in Fig. 1. The cylindrical cathode is 35 mm in inner radius and 100 mm long, and has a slot 5 mm in width, 50 mm long and parallel to the axis to admit ultraviolet light. The central wire is a 3 mil tungsten wire and one side from its centre is covered by a glass pipe 0.11 mm in diameter and made conductible by metaphosphoric acid. The slot is sealed by a quartz window and the counter ends are sealed by glass insulators. The counter is set on a table movable parallel to the counter axis, and the counter position can be read precisely. The image of a slit illuminated by ultraviolet light from a low pressure mercury lamp is focused on the inner surface of the cylinder by a quartz lens. The dominant light is λ 2537 Å, and another resonant light λ 1850 Å is filtered out by a fused silica plate. The image of the slit and the light beam are precisely adjusted to make them perpendicular to the counter axis. The fillings are hydrogen, argon or argon-alcohol mixture. A high resistance (about 1×10^8 ohm) is used to quench the counter discharge, and a very small titanie condenser (2μF) is used to couple the wire system to an amplifier to diminish the time constant of the circuit as much as possible.

The pulses are fed by a scale of eight scaling circuit and then registered.

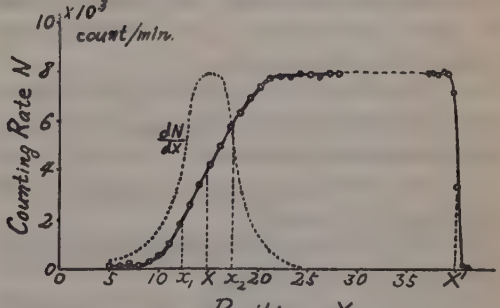

Fig. 2. Counting rate *versus* position curve.

An example of counting rate *versus* position curve is shown in Fig. 2. The left-hand side change of counting rate of this curve is due to the change of thickness at the end of the thin wire, and the right-hand side one is caused by shading of the light beam at the end of the entrance slot. The distance from this end of the slot to the end of the thin wire is 34.4 mm in the direction of the counter axis. The distance between the two points which show respectively the half values of the maximum changes of the counting rate in both sides may be considered as the effective length, and the difference from 34.4 mm is the diminution of the effective length by end effect per one end. The

Table 1.

Fillings	Pressure	Threshold voltage	Working voltage	Half width of counting probability change		Effective length
	mmHg	volt	volt	obs. mm	cal. mm	mm
Hydrogen	10	475	490	2.2	1.8	27.3
	20	570	590	2.1	1.4	27.1
	40	675	690	2.0	1.1	26.7
	60	760	780	1.9	1.0	26.8
	80	840	860	1.9	0.9	26.5
Argon	40	435	500	2.9	3.2	28.9
	60	480	540	2.9	3.0	28.6
	80	540	590	3.1	2.9	28.4
	100	580	630	2.9	2.9	28.2
Argon and Alcohol	{90 {10	690	730	1.5		26.5
			750	1.4		26.7
			770	1.3		27.5
			790	1.3		28.1
			810	1.3		29.0
			830	1.2		29.4
			850	1.2		29.4

steepness of the counting rate change defined by the half width of the differential curve (dotted curve) is shown by the half of the distance between the two points showing respectively the one quarter and three quarters of the counting rate change.

The results are listed in Table 1. One may draw qualitatively the following conclusions from the results.

(1) The effective length is longer in argon filled counters than in hydrogen or argon-alcohol mixture filled ones.

(2) The effective length decreases with increasing gas pressure.

(3) The effective length increases with increasing counter voltage.

(4) The half width of the differential curves is larger in argon filled counters than in hydrogen or argon-alcohol mixture filled ones.

(5) The half width decreases with increasing gas pressure.

(6) The half width in argon-alcohol mixture filled counters decreases with increasing counter voltage.

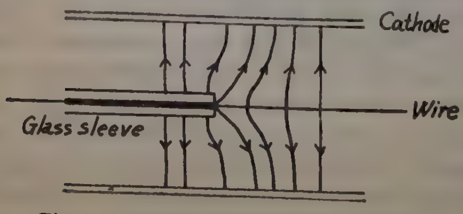

Fig. 3. Field lines in a counter with a sleeve on the wire.

§ 3. Theoretical Interpretation

The electric field in a counter with thicker rod at an end of the central wire is complicated as shown in Fig. 3, but the line of field starting from the end of the thin wire makes a comparatively simple curve convexed to the wire. Photoelectrons emitted from the cathode near the end of the wire are accelarated along those curved lines. Of cource, the electrons make numerous collisions with gas molecules and diffuse away from the line of field. We assume here that the collisions are spherically symmetric. If the motion of electrons just after a collision separated into two componants, then the motion paralle to the line of field must show the mean direction of drifting, and the perpendicular motion must introduce the diffusion from the mean direction. However, the electrons having their velocities along the line of field are pushed out from the line during a free motion, since the line of field is curved. Assuming here that all velocities just after collisions are the same, and the velocity gain during a free motion is far smaller than the initial velocity, the shift δr from the line of field during two successive collisions is given by the following eqation:

$$\delta r = v^2 \delta t/2r$$

where v is the mean velocity in the dierction of field ust after a collision (equals to a half of mean velocity), r the radius of curvature of the line of field, δt the duration between two succssive collisions. If we assume that the line of field is circular over the distance between the electrodes, the shift from the initial line of field after many collisions is

$$\Delta r=\sum\delta r=\lambda tv/4r \propto \lambda tE^{\frac{1}{2}}/r, \qquad (1)$$

where $\lambda=2v\delta t$ is the mean free path of electrons, and E the mean kinetic energy. As will be seen, Δr represents the longation of the effective length from that found only with the electrostatic field. The experimental results listed in Table 1 can be explained from Eq. 1 as follows: At the higher counter voltages and the lower pressures E becomes larger, so Δr or the effective length becomes longer. In argon filled counters E is larger and the effective lengths is longer than in hydrogen filled ones. λ and E decrease with pressure and therefore the effective length decreases.

Now we consider the diffusion of electrons. In this case, we assume that the central wire is uniform and the field lines are perpendicular to the axis, and that the collisions are sorted into two kinds—namely, elastic collisions and inelastic ones. We assume also that in elastic collisions an electron maintains its kinetic energy, and gains energy more and more as it approaches the anode, but when its kinetic energy exceeds a critical value it makes an inelastic collision and loses a definite energy (eV_{ex}) and therefore possesses a definite energy (eV_r) after the inelastic collision. We assume further that an electron repeats numerous inelastic collisions during the travel from the cathode to the anode. The mean displacement of electrons along the line of field and perpendicular to it between two successive collisions are shown respectively as follows.

$$\bar{x}=-(X/2)(e/m)(\lambda/v)^2, \qquad (2)$$
$$|\bar{y}|=\lambda/2,$$

where X is the field strength, e/m the ratio of charge to mass of election, λ the mean free path and v the mean velocity of electrons. At a position r from the axis an electron possesses the kinetic energy.

$$mv^2/2=eV_r+eV_0\ ln(r_i/r)/\ ln(r_c/r_w), \qquad (3)$$

where r_i is the position of the electron when it makes the latest inelastic collision, r_c and r_w the radii of the cathode and the anode respectively and V_0 the counter voltage. Therefore,

$$x=\lambda^2V_0/4r\{V_r\ln(r_c/r_w)+V_0\ln(r_i/r)\}. \qquad (4)$$

If Δr is the mean displacement in the direction of the field during two successive inelastic collisions, the average number of elastic collisions in Δr is

$$N_{el}=\int_{\Delta r}\frac{dx}{\bar{x}} \qquad (5)$$

The displacement perpendicular to the field line while an electron makes N_{el} elastic collisions is solved in the same manner as a random walk problem and the probability that the displacement equals y is given as follows:

$$P(y)=(2\pi^{-\frac{1}{2}}(Nel\,\bar{y})^{-\frac{1}{2}}\exp(-\bar{y}^2/2\bar{y}^2Nel), \qquad (6)$$

and the half width of this distribution is

$$B_{el}=\sqrt{2}\,c\,N_{el}^{\frac{1}{2}}\bar{y},$$

where c is a constant equal to 0.477. During the travel from the cathode to the anode numerous inelastic collisions are repeated, and the square of the half width becomes

$$B^2=2c^2\int_{r_c}^{r_w}\bar{y}^2N_{el}(\Delta r)^{-1}\,dr. \qquad (7)$$

Substituting the Eq. (4) and Eq. (5) into Eq. (7), we obtain

$$B^2=c^2(r_c^2-r_w^2)(V_r+V_{ex}/2)\ln(r_c/r_w)/V_0.$$

If we put $e(V_r+V_{ex}/2)$, representing the mean kinetic energy of electrons, equal to E, then

$$B=cr_c\{\ln(r_c/r_w)\}^{\frac{1}{2}}(E/eV_0)^{\frac{1}{2}}, \qquad (8)$$

The mean kinetic energy of electrons is uniquely determined by the ratio of field intensity to pressure (X/p). The mean value of X/p calculated by taking path length as the weight is

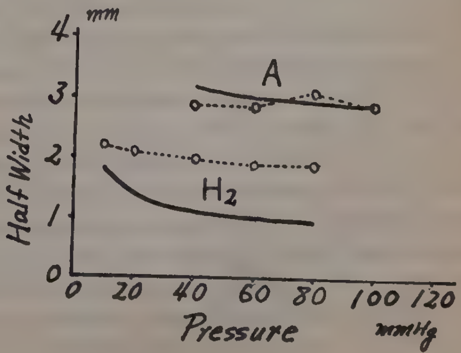

Fig. 4. Half width as a function of pressure.
Solid curve: Theoretical.
Dotted curve: Experimental.

$$(\overline{X/p}) \approx V_0/p r_c .$$

E can be estimated from the corresponding X/p. We quoted the Townsend's data[4] for it, and the calculated half width B is shown in Table 1 and Fig. 4. As shown in Fig. 4 the calculated half width of diffusion in argon filled counters agrees with the half width of the differential curves of counting rate *versus* position couves, but that in hydrogen filled ones does not in absolute values. Since our assumptions are somewhat rough, however, the disagreement is rather probable, and the agreement in argon filled counters seems accidental. Notwithstanding the disagreement in the absolute values, the qualitative behaviour of diffusion bears out the observed results as follows: The larger half width in argon filled counters than that in hydrogen filled ones depends on the higher effective excitation energy or the higher mean kinetic energy. The decrease with gas pressure in hydrogen counters is also caused by diminution of the kinetic energy. The comparatively small pressure dependence of the half width in argon filled counters is due to the constancy of the mean energy against the variation of X/p. The dependence of the half width on the counter voltage can be easily understood from Eq. (8).

§ 4. Conclusion

The effective length and the steepness of the change of counting probability near the end of the wire of a Geiger Mueller counter whose central wire has a considerably thicker rod than the wire itself have been measured under various conditions of the filling, and a theory that seems to give qualitative explanation for the experimental results has been shown.

The author wishes to express his thanks to Professor Y. Fujioka for his kind suggestions and deep interest in the present work. Also he is much indebted to Professor T. Miyajima who gave helpful advices in the theoretical treatment.

References

1) Curran, Angus and Cockroft: Phil. Mag. **40** (1949) 36.
2) Greisen and Nereson: Phys. Rev. **62** (1942) 316.
3) Blachman: Rev. Sci. Inst. **20** (1949) 477.
4) Townsend: Phil. Mag. **44** (1922) 1033.

JOURNAL OF THE PHYSICAL SOCIETY OF JAPAN Vol. 7, No. 3, MAY—JUN., 1952

On the Electronic States of the Doubly-charged Negative Ions of Oxygen in Oxide Crystals

Jiro YAMASHITA and Masao KOJIMA
Institute of Science and Technology, University of Tokyo

(Received September, 19, 1951)

The Oxygen atoms are supposed to become the doubly-charged negative ions within oxide crystals. There is, however, no experimental evidence of the existence of such ions in gas phase, which fact suggests us that they are probably very unstable in the free state. We, therefore, may reasonably suppose that they are stable only within oxide crystals due to the effects of the surrounding ions. In order to elucidate the above situation quantitatively, we have here attempted to work the electronic states of the oxygen ions within the oxide crystals by the variational method, which we adopted already for the calculation of the cohesive energy of LiF. Thus, we have confirmed, for MgO, that the doubly-charged negative ion of oxygen may be actually stable in such crystals. Furthermore, we have calculated also the electronic affinity of the ions and diamagnetic susceptibility of MgO crystals, which results seem to show rather good agreements with the experimental observations as far as our computational accuracy does concern.

§1. Introduction

Although there are vast experimental observations regarding the various kinds of physical properties of the oxide crystals, the detailed investigation of such oxide crystals from the viewpoint of the modern theory of solid seems to remain untouched so far in spite of the fact that we have already rather fruitful phenomenological theories of the mentioned crystals. At the present stage of the theory of oxide crystals, the stable existence of the doubly-charged negative oxygen ions within such crystals may be considered to be a useful presupposition in order to clarify the many physical properties of the crystals in spite of the wellknown fact that the doubly-charged negative oxygen ions have not been observed in gaseous phase[1]. In view of the above situation we have attempted to confirm, from the quantum theory of solids, the stable existence of the doubly-charged negative oxygen ions within the crystals by taking into account the effects of the surrounding ions. For such purpose we can not use Hartree's wave function for free ions as a first approximation to the crystalline wave function, as we usually do in the case of alkali halide crystals, but we must take into account the characteristic situation of the oxygen ion imbedded in the crystal under the influence of other ions. Generally we have two methods of approximation to work theoretically the electronic state of oxygen ion, the one of which is the cellular method of Wigner-Seitz[2], and the other the method of Heitler and London with variational wave functicn. In the latter we assume some reasonable functional form with variable parameters for electronic state of oxygen ion within the crystal and these parameters are determined so as to minimize the total energy of the whole crystal. Here we shall adopt, for convenience, the latter method, which has been used successfully in determining the electronic state of F^- ion in LiF crystal[3]. Since the wave function of F^- ion in the free state has been found not to be widely different from that in the crystalline state in accordance with the experimental observations of the free F^- ion, our variational method has been shown to become one of the refining procedures for such crystal. For the oxide crystals, however, the variational method will play a decisive role in our problem under consideration as seen in the following computation.

§2. Wave Function

In the following, we shall proceed to work out the electronic state of oxygen ion in MgO crystals, supplying the above mentioned variational procedure. For Mg^{++} ions we shall use the Hartree-Fock's wave functions[4] for free Mg^{++} ions. Furthermore, we also shall use approximately the Hartree-Fock's wave functions of O^- free ion[5] for those corresponding to $(1s)$ and $(2s)$ electrons in the inner shell of O^{--} ion. For $(2p)$ electron in the outer shell of O^{--} ion we use the following way.

We shall assume that all the six outermost electrons of O^{--} ion have the same character as that of $(2p)$ electrons of F^- ion, which leads to the following variational function.

$$P_2(r)=Ar^2[\exp(-\alpha r)+B\exp(-\beta r)], \qquad (1)$$

where α, β and B are variational parameters. The charge distributions of $2p$ electrons in the oxygen ion within the crystal may be considered to deviate, to a more or less amount, from the assumed spherical distribution due to the mutual interactions of the surrounding ions. For the construction of a more accurate variational function for $2p$ electrons, therefore, we should take into account the above situation through the appropriate form of the wave functions. We however have neglected, for simplicity, the mentioned deformation of $2p$ wave function, since our present computations are of rather preliminary nature.

From the one electron functions mentioned above we are able to construct the wave function of ψ of the whole crystal, in accordance with Pauli principle, in the conventional way.

§3. Total Energy

In this case the computation of energy is performed by a quite similar way as the case of F^- ion. In the case of F^- ion, however, we can minimize its energy even in free state by choosing the suitable values for parameters. In the case of O^{--} ion, on the contrary, we can not find, in free state, the value of parameters to minimize the energy. As Table I shows, for certain value of α, the energy has no minimum for the variation of the parameter β. When the O^{--} ion is imbedded in oxide crystal, we should take into account, besides the atomic energy of free state, Madelung energy and exchange energy and electrostatic overlapping energy between the nearest six Mg^{++} ions. For simplicity, we shall neglect the interaction between the O^{--} ion and its next-nearest twelve O^{--} ions, which neglection may perhaps result in the rather large spreading of the charge distribution of O^{--} ion. In order to get the ionization energy of O^{--} ion, we have to calculate the difference between the atomic energies of the two configuration (2^6p) of O^{--} and $(2p)^5$ of O^-. The energy of $(2p)^5$ of O^- ion is calculated by a similar variational procedure. The results of our calculation is as follows (we use atomic unit):

Table I

α	β	B	$E(O^{--})$	$Etot$
2.3	1.0	0.10	−6.008	−7.578
2.5	1.0	0.10	−6.075	−7.630
2.8	1.0	0.10	−6.171	−7.688
2.8	1.1	0.15	−6.167	−7.742
2.9	1.0	0.10	−6.211	−7.718
2.9	1.1	0.15	−6.193	−7.761
2.95	0.95	0.05	−6.238	−7.703
2.95	1.09	0.10	−6.222	−7.725
2.95	1.05	0.12	−6.211	−7.748
2.95	1.10	0.15	−6.189	−7.754
2.95	1.20	0.20	−6.108	−7.718
3.0	0.95	0.10	−6.221	−7.666
3.0	1.0	0.10	−6.221	−7.718
3.2	1.0	0.10	−6.176	−7.655
4.0	1.0	0.10	−5.587	−7.017

$(2p)$-wave function of O^{--} ion:

$$P=6.872r^2[\exp(-2.9r)+0.15\exp(-1.1r)], \qquad (2)$$

atomic energy of O^{--} ion:

$$E(O^{--})=-6.193+[\text{energy of }(1s)^2(2s)^2]$$

ionic distance $=2.10\times10^{-8}$ cm (at real crystal),

Madelung energy $=-1.765$,

exchange energy $=0.224$,

correction of electrostatic energy $=-0.027$,

total energy:

$$E=-7.761+[\text{energy of }(1s)^2(2s)^2].$$

(2p)-wave function of O^- ion (determined by variational method):

$$P=8.77r^2[\exp(-2.9r)+0.10\exp(-1.1r)], \qquad (3)$$

atomic energy of O^- ion:

$$E(O^-)=-6.630+[\text{energy of }(1s)^2(2s)^2].$$

Then the ionization energy of O^{--} ion in MgO is

$$E(O^{--})-E(O^-)=11.8.\ \text{ev}.$$

Clearly O^{--} ion is seen not to be stable in free state, but stable in MgO crystal.

§4. Comparison with Experiments

(1) Ionization energy (electron affinity)

The ionization energy of O^{--} ion has been found 11.8 ev.. As the free ion is not stable, so its ionization energy can not be observed directly. By using the Born cycle, however, Mayer has evaluated approximately the total electron affinity of O^{--} ion, which values have been tabulated in Table II⁷⁾. On the other hand, the affinity of a neutral oxygen for one electron has been found experimentally to be of 2.2±0.2 ev by Lozier⁸⁾ and of 3.07 ev by Vier-Mayer⁹⁾ respectively. With the use of these data we may derive approximately the ionization energy of O^{--} ion as tabulated in Table II. The Agreement between our result and the empirical ones seems to be rather good, taking into account both the approximate character of our computatians and the degree of accuracy involved in Mayer's methods. Moreover, the empirical values of the ionization energy has been found, in the table, to be at variance with each other from material to material. We may interprete this fact as follows: as $2p$-electronic state of O^{--} ion is determined only in the crystalline state, so the different electronic states of oxygen ions involved may be realized according to the different characteristics of the oxide crystals, which leads to the different ionization energy.

Table II

	Affinity of O^{--} ion (Kcal/Mol)	Ionization Energy (ev)	
		Mayer-Lozier	Mayer-Mayer
MgO	−190	10.2	11.0
CaO	−165	9.2	10.0
SrO	−144	8.3	9.1
BaO	−147	8.4	9.2

(2) Diamagnetic susceptibility

By the use of the wave function of O^{--} ion obtained above, we have calculated the diamagnetic susceptibility of MgO crystal. The results are as follows.

The calculated values:

$$\chi(Mg^{++}) = -3.7\times10^{-6},$$

$$\chi(O^{--}) = -21.0\times10^{-6}.$$

If we assume the additibity-rule. we have

$$\chi(MgO) = -24.7\times10^{-6}.$$

The observed value¹⁰⁾ is -18.8×10^{-6}, so the calculated value is about 30% too large. The discrepancy between the computation and the observation may be perhaps be improved to some extent by taking the $O^{--}-O^{--}$ interaction into account. As the above discrepancy is not very large in comparison with that in Cl^- (21%) and, further, the accurate measurements of the diamagnestic susceptibilities of the crystal are hardly possible, we are permitted to take for the electronic state of O^{--} ion in MgO crystal to have nearly spherical symmetry. By the use of the wave function (3) obtained above, the diamagnetic susceptibility of O^- ion is found to be -15.1×10^{-6} while, for the ordinary Hartree-Fock function, -14.4×10^{-6}, which results suggest us the approximate correctness of our O^- wave function computed above.

The authrs wish to express their sincere thanks to Prof. T. Muto for his continued interest and advice during the course of this work.

References

1) H. S. W. Massey: *Negative Ions* (1938). p. 20.
2) F. Seitz: *Modern Theory of Solids* (1940).
3) J. Yamashita: J. Phys. Soc. Jap. **7** (1952) No. 3.
4) Yost: Phys. Rev. **58** (1940) 557.
5) D. R. Hartree, W. Hartree and Swirles: Phil. Trans **238** (1939) 229.
6) K. Landshoff: Zeits. f. Physik **102** (1930) 771.
7) F. Seitz: loc. cit. p. 89.
8) W. W. Lozier: Phys. Rev. **46** (1934) 268.
9) Vier and Mayer: J. Chem. Phys. **12** (1944) 28.
10) K. Kido: Sci. Rep. Tohoku Univ. **21** (1932) 149; 288; 869.

JOURNAL OF THE PHYSICAL SOCIETY OF JAPAN Vol. 7, No. 3, MAY—JUN., 1952

Statistical Theory of Hindered Rotation in Molecular Crystals

Tutô NAKAMURA

Physics Department, Faculty of Science, Kyusyu University

(Received October 8, 1951)

We propose a theory of hindered rotation in molecular crystals, whose basis is on the Kirkwood model. Some values characteristic of the phase trasition due to the molecular hindering are calculated. We obtained for the Curie point, H_0, 1.075, 0.615 and 0.434 for the square, simple cubic and body-centred lattices respectively, where we assumed $J/2\cos\gamma$, for the interaction between two neighbouring molecules, whose relative orientation is specified by γ, and we put $H=J/2kT$. The leap values of the specific heat, $\Delta C_v/R$, are obtained as 2.280, 2.466 and 2.514 for the square lattice etc. In contrast with the theory of binary alloys, $\Delta C_v/R$ is not improved with compare to Bragg-Williams' value 2,500. It is different from Chang's result, according to which $\Delta C_v/R$ is larger than Bragg-Williams' value considerably. However Chang's point of view is criticized.

§1. Introduction

L. Pauling[1] attributed the phenomena, which accompany the thermal and dielectric anomalies in some molecular crystals, to the phase transition from the state of vibrational motion of molecules to that of free rotation. Hereafter, though Frenkel[2] considered its phenomena are due to the phase transition from the vibrational state to the same, these theories are somewhat qualitative. A theory proposed by Fowler[3] may be interested in considering these phenomena from the point of view of Bragg-Williams' theory of the order-disorder problem, but his definition of the degree of order was vague. This ambiguity was, however, eliminated by Kirkwood[4], thus the statistical theory of hindered rotation was completed at the stage of Bragg-Williams' approximation.

Some attempts were tried to improve Kirkwood's theory, in the mechanical model on the one side[5] and in the statistical approximation on the other[6],[7],[8]. We have an interest in the latter problem now. Prior to Kirkwood, Chang[6] calculated the values characteristic of the phase transition, that is the location of the Curie point and the leap value of the specific heat, at the stage of Bethe's approximation. But, according to our point of view, Chang's calculation seems to be wrong in the application of Bethe's aprroximation. Hence it would be desirable to report the results of the correct application of Bethe's approximation.

§2. Derivation of the Fundamental Equation

Let us consider the identical diatomic molecules to be localized at the lattice points, which are divided into two sites, the *a* and the *b* sites, where a molecule on the *a* site is surronnded by *z* molecules on the *b* sites and vice versa. The probability that the *i*-th molecule on the *a* site are found in the configurational element $d\omega_i$ at ω_i is denoted by

$$(1/4\pi)g_a(\omega_i)d\omega_i\,, \quad \ldots\ldots\ldots\ldots\ldots\ldots\ldots\ldots \quad (1)$$

where ω_i being the orientation angle of the *i*-th molecule, written in (θ_i, ϕ_i) in the polar coordinate. The distribution function $g_b(\omega)$ is also defined in the same manner. In the same way,

$$(1/4\pi)^2\, g_{ab}(\omega_i, \omega_j)\, d\omega_i\, d\omega_j \quad \ldots\ldots\ldots\ldots \quad (2)$$

denotes the probability that the two neighbouring molecules, the *i*-th and the *j*-th molecules, are found in the configurational element $d\omega_i\, d\omega_j$ at ω_i and ω_j. These distribution functions are subject to the following normalization conditions to give the total probability equal to unity:

$$(1/4\pi)\int g_s(\omega_i)d\omega_i=1\,;\ s=a \text{ or } b, \ \ldots\ldots \quad (3)$$

$$(1/4\pi)^2\iint g_{ab}(\omega_i, \omega_j)\, d\omega_i\, d\omega_j=1. \quad (4)$$

Introducing the average potential per interaction bond of the *i*-th molecule on the *a* site, $u_a(\omega_i)$, and assuming the Boltzmann distribution, we have

$$g_a(\omega_i)=(1/\Lambda')\exp[-\beta z\, u_a(\omega_i)];\ \beta=1/kT, \quad (5)$$

$$u_a(\omega_i)=(1/4\pi)\int u(\omega_i,\omega_{i'})g_{ab}(\omega_i,\omega_{i'})d\omega_i', \quad (6)$$

where $u(\omega_i,\omega_{i'})$ is the potential energy between two neighbouring molecules, and Λ' is the constant value dependent only on the temperature, which is determined by the normalization condition of $g_a(\omega_i)$. The similar expression for $g_b(\omega)$ may be omitted. We further obtain the expression for $g_{ab}(\omega_i,\omega_j)$:

$$g_{ab}(\omega_i,\omega_j)=(1/\Lambda'')\exp[-\beta u(\omega_i,\omega_j) -\beta(z-1)\{u_a(\omega_i)+u_b(\omega_j)\}] \quad (7)$$

in the same way, where the Λ'' is determined by the same procedure as in (5).

Substituting the expression:

$$\exp[-\beta\, u_a(\omega)]=[\Lambda' g_a(\omega)]^{1/z} \quad (8)$$

derived from (5) and the similar expression for $g_b(\omega)$ into (7), we have

$$\lambda g_{ab}(\omega_i,\omega_j)=[g_a(\omega_i)g_b(\omega_j)]^{(z-1)/z} \times\exp[-\beta u(\omega_i,\omega_j)], \quad (9)$$

$$\lambda=\Lambda''/(\Lambda'_a\Lambda'_b)^{(z-1)/z}. \quad (10)$$

By integrating (9) with respect to ω_j, we get the fundamental equation of our treatment:

$$\int K(\omega,\omega')[g_b(\omega')]^{(z-1)/z}d\omega'=\lambda[g_a(\omega)]^{1/z}, \quad (11)$$

$$K(\omega,\omega')=(1/4\pi)\exp[-\beta u(\omega,\omega')]. \quad (12)$$

It is interesting to notice that the λ gives the partition function per interaction bond, accordingly $-\beta^{-1}\ln\lambda$ gives the free energy per interaction bond.[9]

Following Kirkwood[4], we assume the expression

$$u(\omega,\omega')=J/2\cdot\cos\gamma, \quad (13)$$

$$\cos\gamma=\cos\theta\cos\theta'+\sin\theta\sin\theta'\cos(\varphi-\varphi'),$$

for the potential function and so the antiparallel configuration is the the ordered state if $J>0$. When J is negative, the parallel configuration is realized as the ordered state. Since the result of the calculation gives the same in these two cases, we take the case: $J>0$, which is more interesting in the physical situation than the other.

§3. The Solution in the One Dimensional Case

In one dimensional case (11) reduces to the linear homogeneous equations

$$\int K(\omega,\omega')\psi^j(\omega')d\omega'=\lambda\psi^i(\omega)$$

$$\psi^i(\omega)=[g_i(\omega)/4\pi]^{1/2} \quad (14)$$

$$i\neq j=a \text{ or } b$$

subject to

$$\int[\psi^i(\omega)]^2 d\omega=1, \quad (15)$$

that is the eigen-value problem.

We have now the bi-linear expansion formula for the kernel

$$K(\omega,\omega')=(1/4\pi)\exp[-H\cos\gamma];$$

$$H=\beta J/2, \quad (16)$$

which is written

$$\exp[-H\cos\gamma]=\sqrt{\frac{\pi}{2H}}\sum_{l=0}^{\infty}(-)^l(2l+1)I_{l+1/2}(H)P_l(\cos\gamma), \quad (17)$$

$$P_l(\cos\gamma)=P_l(\cos\theta)P_l(\cos\theta')+2\sum_{m=1}^{l}\frac{(l-m)!}{(l+m)!}P_l^m(\cos\theta)\,P_l^m(\cos\theta')\cos m(\varphi-\varphi'),$$

$I_{l+1/2}(\rho)$ being the Bessel function of imaginary argument.

Regarding this expansion formula, the eigen-values and eigen-functions of the eigen-value problem (14) are given by

$$(-)^l\lambda_l(H)=(-)^l\sqrt{\frac{\pi}{2H}}\,I_{l+1/2}(H), \quad (18)$$

$$\psi_{lmi}{}^a(\omega)=\psi_{lmi}{}^b(\omega)=\sqrt{\frac{2l+1}{2\pi}\frac{(l-m)!}{(l+m)!}}\,P_l{}^m(\cos\theta)\begin{matrix}\cos m\varphi, & i=s\\ \sin m\varphi, & i=a\end{matrix},\ m\neq 0, \quad (19)$$

$$=\sqrt{\frac{2l+1}{4\pi}}\,P_l(\cos\theta),\ m=0,$$

respectively. The integral kernel is then written in terms of ψ_{lmi}'s as follows:

$$K(\omega,\omega')=\sum_{l=0}^{\infty}\sum_{m=0}^{l}\sum_{i=a,s}(-)^l\lambda_l\psi_{lmi}{}^a(\omega)\psi_{lmi}{}^b(\omega'). \quad (20)$$

In the complete parallel with the case of the Ising model, the partition fuuction, Z, of the ring composed of N molecules is given by

$$Z=\underbrace{\int\int\cdots\int}_{N}\prod_{i=1}^{N}\exp[-H\cos\gamma_{i,\,i+1}]\,d\omega_1\ldots d\omega_N=(4\pi)^N\sum_{l=1}^{\infty}(2l+1)\lambda_l{}^N. \tag{21}$$

The λ_0 gives the largest eigen-value, whose eigen-function is the constant equal to unity, corresponding to the disordered state. From the situation that the largest eigen-value suppresses the others for a large N, the one dimensional crystal is in the disordered state at any temperature. And then we have

$$Z=(4\pi)^N\lambda_0{}^N=(4\pi)^N(\sinh H/H)^N. \tag{22}$$

The average energy, E, and specific heat, C_v, are written

$$E/RT=-H\cdot L(H),\quad C_v/R=H^2L'(H). \tag{23}$$

respectively, where $L(\rho)$ is the Langevin function:

$$L(\rho)=\coth\rho-1/\rho. \tag{24}$$

§4. The Solution of the Non-linear Integral Equation

In our model, the ordered state is the anti-parallel configuration in the absence of the external field, and hence in the coodinate system, in which the polar axis is taken as parallel to this anti-parallel direction, $g_a(\omega)$ may be expanded as

$$g_a(\omega)=1+\sum_{l=1}^{\infty}c_l\psi_l(\omega), \tag{25}$$

where we regarded the normalization condition of $g_a(\omega)$ and put

$$\psi_l(\omega)\equiv\psi_{l0}(\omega)=P_l(\cos\theta),$$

for simplicity. By the transformation: $\theta\to\theta+\pi$, $g_a(\omega)$ is transformed into $g_b(\omega)$, thus we have

$$g_a(\omega)=1+\sum(-)^lc_l\psi_l(\omega). \tag{26}$$

Then we have

$$[g_a(\omega)]^{1/z}=\sum_{l=0}^{\infty}A_l\psi_l(\omega), \tag{27}$$

$$A_0=1-\frac{1}{6}\frac{z-1}{z^2}c_1^2-\frac{1}{10}\frac{z-1}{z^2}c_2^2+\frac{1}{15}\frac{(2z-1)(z-1)}{z^3}c_1^2c_2 -\frac{1}{120}\frac{(3z-1)(2z-1)(z-1)}{z^4}c_1{}^4+\ldots, \tag{27a}$$

$$A_1=\frac{1}{z}c_1-\frac{2}{5}\frac{z-1}{z^2}c_1c_2+\frac{1}{10}\frac{(2z-1)(z-1)}{z^3}c_1{}^3+\ldots, \tag{27b}$$

$$A_2=\frac{1}{z}c_2-\frac{1}{2}\frac{z-1}{z^2}\left(\frac{2}{3}c_1^2+\frac{2}{7}c_2{}^2+\frac{6}{5}c_1^2c_2+\frac{6}{7}c_1c_3\right) +\frac{11}{42}\frac{(2z-1)(z-1)}{z^3}c_1^2c_2-\frac{1}{42}\frac{(3z-1)(2z-1)(z-1)}{z^4}c_1^4+\ldots. \tag{27c}$$

In (27) we substitute $(z-1)/z$ for $1/z$, and reverse the sign of the terms: c_l, $l=$odd, and then $[g_b(\omega)]^{(z-1)/z}$ may be obtained as follows:

$$[g_b(\omega)]^{(z-1)/z}=\sum_{l=0}^{\infty}B_l\psi_l(\omega), \tag{28}$$

$$B_0=1-\frac{1}{6}\frac{z-1}{z^2}c_1^2-\frac{1}{10}\frac{z-1}{z^2}c_2{}^2+\frac{1}{15}\frac{(z+1)(z-1)}{z^3}c_1^2c_2-\frac{1}{120}\frac{(2z+1)(z+1)(z-1)}{z^4}c_1^4+\ldots, \tag{28a}$$

$$B_1=-\frac{(z-1)}{z}\left\{c_1-\frac{2}{5}\frac{1}{z}c_1c_2+\frac{1}{10}\frac{z+1}{z^2}c_1^3+\ldots\right\}, \tag{28b}$$

$$B_2=\frac{(z-1)}{z}\Big\{c_2-\frac{1}{2}\frac{1}{z}\Big(\frac{2}{3}c_1^2+\frac{2}{7}c_2^2+\frac{6}{5}c_1^2c_2+\frac{6}{7}c_1c_3\Big)+\frac{11}{42}\frac{z+1}{z^2}c_1^2c_2-\frac{1}{42}\frac{(2z+1)(z+1)}{z^3}c_1^4+\dots\Big\}. \tag{28c}$$

Equation (11) is now written

$$\sum_{l=0}^{\infty}B_l\lambda_l\psi_l(\omega)=\lambda\sum_{l=0}^{\infty}A_l\psi_l(\omega), \tag{29}$$

which we may write as

$$\lambda_lB_l=\lambda A_l,\quad l=0,1,2\,\dots, \tag{30}$$

in view of the linear independency of $\{\psi_l(\omega)\}$.

Using the relations (30) for $l\geq 2$, we have the expression for $\{c_l\}$, $l\geq 2$ in terms of c_1, which may be substituted in (30) for $l=1$ to obtain the transcendental equation concerning the c_1. As a solution this equation has $c_1=0$, which induces $c_l=0$, $l\geq 2$, accordingly $c_1=0$ corresponds to the disordered state, but it has $c_1\neq 0$ as real solutions which corresponds to the ordered state. The λ's determined by this solutions cross λ_0, which gives λ for $c_1=0$, at a certain value of H, as H increases. Of these λ's, the λ which crosses λ_0 firstly is important. As H decreases the real roots $c_1\neq 0$ approach the origin from the left and right sides and move onto the imaginary axis above the Curie point. Hence at the Curie point (30) for $l=1$ has $c_1=0$ as threehold roots. In the other words, the Curie point, H_c, is determined by

$$\Big[\frac{\partial}{\partial c_1}(\lambda_1B_1-\lambda A_1)\Big]_{c_1=0,\ H=H_c}=0. \tag{31}$$

If we neglect the higher order tems, assuming that $c_l=O(c_1{}^l)$, from (30) for $l=2$, C_2 is given by

$$c_2=\frac{1}{3}\frac{z-1}{z}\frac{\lambda-\lambda_2}{\lambda-(z-1)\lambda_2}c_1^2. \tag{32}$$

Substituting (32) in (30) for $l=1$, as the non-zero solution we have

$$c_1^2\cong 30\Big(\frac{z}{z-2}\Big)^2\frac{(z-1)\lambda_1-\lambda}{3\Big(\frac{2z-1}{z-1}\lambda-\frac{z+1}{z-1}\lambda_1\Big)-4\frac{(\lambda-\lambda_1)(\lambda-\lambda_2)}{\lambda-(z-1)\lambda_2}}. \tag{33}$$

And further from (30) for $l=0$ we have

$$\lambda=\lambda_0-\frac{1}{30}\frac{(z-1)(z-2)}{z^3}(2c_2-c_1^2)c_1^2\lambda_0+O(c_1^6), \tag{34}$$

from which we obtain an expression for λ below the Curie point by use of (32) and (33).

§5. Calculation of the Physical Quantities

As is shown in §4 the approximate solution is valid in the cases of small c_l's, which correspond to the cases in the neighbourhood of the Curie point.

Let us find the location of the Curie point. If we neglect the terms of $O(c_1{}^4)$, the λ in (34) may be replaced by the λ_0. In this approximation, substituting (32) in (27*b*) and (28*b*), we write (31) as

$$\lambda_0(H_c)=(z-1)\lambda_1(H_c), \tag{35}$$

which means

$$\sqrt{\frac{\pi}{2H_c}}I_{1/2}(H_c)=(z-1)\sqrt{\frac{\pi}{2H_c}}I_{3/2}(H_c). \tag{36}$$

By use of the relations:

$$\begin{aligned}\sqrt{\frac{\pi}{2H_c}}I_{1/2}(\rho)&=\sinh\rho/\rho,\\ \sqrt{\frac{\pi}{2H_c}}I_{3/2}(\rho)&=1/\rho\cdot(\cosh\rho-\sinh\rho/\rho),\end{aligned} \tag{37}$$

(36) becomes

$$L(H_c)=1/(z-1), \tag{38}$$

which has already been derived by Chang[8] and Kubo-Hasimura[8].

To inquire into the anomaly of the physical quantities at the Curie point, let us introduce two parameters, s and σ, which correspond to the degree of long range order and that of short range order, defined by

$$|<\cos\theta>_{AV}|=s, \tag{39}$$

$$|<\cos\gamma>_{AV}|=\sigma, \tag{40}$$

respectively.

Let us find an expression for σ in terms of s. Using (9) and (40), we have

$$\sigma=-(4\pi)^{-2}\iint\cos\gamma\, g_{ab}(\omega,\omega')\,d\omega\, d\omega'$$

$$\cong\frac{\lambda_1}{\lambda_0}+\left(\frac{z-1}{z}\right)^2\left\{1-\frac{3}{z-1}\frac{\lambda_1}{\lambda_0}+2\frac{\lambda_2}{\lambda_0}\right\}\frac{c_1{}^2}{9} \tag{41}$$

on the one hand, and s is written

$$s=\left|(4\pi)^{-1}\int\cos\theta_\kappa\, g_\kappa(\omega)\,d\omega\right|=c_1/3;\ \kappa=a \text{ or b} \tag{42}$$

on the other. Hence

$$\sigma\cong\frac{\lambda_1}{\lambda_0}+\left(\frac{z-1}{z}\right)^2\left\{1-\frac{3}{z-1}\frac{\lambda_1}{\lambda_0}+2\frac{\lambda_2}{\lambda_0}\right\}s^2. \tag{43}$$

The first term of the right-hand side represents the short range effect, remaing above the Curie temperature.

The function $s=s(H)$ consists of two different parts of the analytical function, which are contact with each other and discontinuous from the first derivative at the Curie point. This discontinuity, which gives the degree of cooperation, is calculated from (33) as

$$\left[\frac{ds^2}{dH}\right]_{H_c+}\cong\frac{10}{3}\cdot\frac{z^2}{z-1}\cdot\left.\frac{(\lambda_1/\lambda_0)'}{3\left(\frac{2z-1}{z-1}-\frac{z+1}{z-1}\frac{\lambda_1}{\lambda_0}\right)-4\frac{(1-\lambda_1/\lambda_0)(1-\lambda_2/\lambda_0)}{1-(z-1)\lambda_2/\lambda_0}}\right|_{H_c}, \tag{44}$$

where

$$(\lambda_1/\lambda_0)'_{H_c}=L'(H_c)=1/H_c{}^2-(1/\sinh H_c)^2, \tag{45}$$

$$(\lambda_2/\lambda_0)_{H_c}=1-3/H_c\cdot L(H_c).$$

The average energy, E, and the specific heat, C_v, due to the molecular hindering are expressed as follows:

$$E=-\frac{1}{2}Nz\frac{J}{2}\sigma, \tag{46}$$

$$C_v=-\frac{1}{2}Nz\frac{J}{2}\frac{d\sigma}{dT}. \tag{47}$$

Substituting (43) in (47), we have

$$(C_v/R)_{H_c+}\cong\frac{z}{2}H_c^2L'(H_c)+\frac{z}{2}\left(\frac{z-1}{z}\right)^2\left(1-\frac{9}{5}\frac{1}{(z-1)^2}\right)H_c^2\left[\frac{ds^2}{dH}\right]_{H_c+}, \tag{48}$$

$$(C_v/R)_{H_c-}=\frac{z}{2}H_c^2L'(H_c), \tag{49}$$

hence

$$\Delta C_v/R\cong\frac{z}{2}\left(\frac{z-1}{z}\right)^2\left(1-\frac{9}{5}\frac{1}{(z-1)^2}\right)H_c^2\left[\frac{ds^2}{dH}\right]_{H_c+}. \tag{50}$$

Table I

z	H_c	$\Delta C_v/R$
4	1.075	2.280
6	0.615	2.466
8	0.434	2.514

The equation (49) is in accordance with (23) except the factor $z/2$. It is easy to see that all quantities inclusive of the partition function are identical with that of one dimensional lattice above the Curie point at the stage of Bethe's approximation.

§6. Comparison with Other Theories

The numerical values of H_c and $\Delta C_v/R$ estimated from (38) and (50) respectively are tabulated in Table 1. While the values of the H_c's only reproduce Chang's results[6], the $\Delta C_v/R$'s do not agree with, but are lower than Chang's values. However Chang's formulation is criticized below and the present values seem to be correct at the stage of Bethe's approximation. We conclude that concerning the $\Delta C_v/R$'s Bethe's approximation does not improve Bragg-Williams' one, since the results from the former are almost equal to that from the latter, in which $\Delta C_v/R=5/2$.

As was described above, Chang formulated the theory concerning the same problem and obtained the higher values of the $\Delta C_v/R$'s than ours. According to our point of view Chang's theory does not correspond to Bethe's approximation. Chang considered that the local partition function of $z+1$ molecules may be given by

$$\underbrace{\int\int\cdots\int}_{z+1} \exp\left(H\sum_{i=1}^{z}\cos\gamma_i\right)\prod_{i=1}^{z}g(\omega_i)\prod_{i=1}^{z}\frac{d\omega_i}{4\pi}\cdot\frac{d\omega_0}{4\pi}, \tag{51}$$

where the centre molecule is denoted by 0, the neigbouring one by i and γ_i is the angle between the centre and neigbouring molecules.

But the local partition function of $z+1$ molecules should involve z interaction bonds, which branch off from the centre molecule, and $z(z-1)$ interaction bonds, which branch off from the molecules neighbouring with the centre to the outside environment, and hence it should involve z^2 interaction bonds, while as may be seen from (5), (51) involves z^2+z interaction bonds, which are in excess. The correct form of the local partition function should then be written

$$\int\int\cdots\int \exp\left(H\sum_{i=1}^{z}\cos\gamma_i\right)\prod_{i=1}^{z}[g(\omega_i)]^{(z-1)/z}\prod_{i=1}^{z}\frac{d\omega_i}{4\pi}\;\frac{d\omega_0}{4\pi}\,. \tag{52}$$

The somewhat tedious calculations after Chang based on (52) show the agreement with ours. In comparison with the calculations along this manner our formulation seems to be more simple.

As in the theory of binary alloys, the approximate methods should be checked by the results from the moment expansion method. We have now the results by K. Yosida[7], who calculated the same problem by this method to the second moment. Comparing our results with his, we have

$$H_c=\begin{cases}\dfrac{3}{z}\left(1+\dfrac{1}{z}+\dfrac{2}{z^2}+\cdots\right), & \text{the moment method}\\[2ex] \dfrac{3}{z}\left(1+\dfrac{1}{z}+\dfrac{8}{5}\dfrac{1}{z^2}+\cdots\right), & \text{the present method}\end{cases} \tag{53}$$

$$\frac{\Delta C_v}{R}=\begin{cases}\dfrac{5}{2}\left(1+\dfrac{1}{5}\dfrac{1}{z}+\dfrac{54}{25}\dfrac{1}{z^2}+\cdots\right), & \text{the moment method}\\[2ex] \dfrac{5}{2}\left(1+\dfrac{1}{5}\dfrac{1}{z}-\dfrac{26}{25}\dfrac{1}{z^2}+\cdots\right), & \text{the present method.}\end{cases} \tag{54}$$

According to the theory of binary alloys[12], Bethe's approximation is correct to the third moment. It is the future problem to inquire into this situation.

References

1) L. Pauling: Phys. Rev. **36** (1930) 430.
2) J Frenkel: Acta Physicochimica, **3** (1935) 23.
3) R. H. Fowler: Proc. Roy. Soc., **149** (1935) 1.
4) J. G. Kirkwood: J. Chem. Phys. **8** (1940) 205.
5) T. Nagamiya: *The Problems in Modern Physics* (in Japanese) P. 113.
6) T. S. Chang: Proc. Camb. Phil. Soc. **33** (1937) 524.
7) K. Yosida: Bussiron Kenkyu (in Japanese) **20** (1949) 80.
8) R. Kubo and T. Hasimura: Read at the meeting of Phys. Soc. Japan at Kyoto, autumn, 1949.
9) T. Nakamura: Prog. Theor. Phys., **7** (1952) 241.
10) G. N. Watson: *The Theory of Bessel Function,* 1922, P. 369.
11) Concerning the same problem for the plane rotator, E. W. Montroll, Annal. of Math. Stat. **18** (1947) 18.
12) H. A. Bethe and J. G. Kirkwood: J. Chem. Phys. **7** (1939) 578.

JOURNAL OF THE PHYSICAL SOCIETY OF JAPAN Vol. 7, No. 3, MAY—JUN., 1952

Theory of Diffuse Scattering of X-rays by Local Lattice Distortions

Takeo MATSUBARA

Department of Physics, Osaka University

(Received October 23, 1951)

A general formula for the diffuse scattering of X-rays is derived for the crystal which has a local lattice distortion due to any kind of lattice defect. The intensity is expressible in terms of the Fourier transform of the potential energy parameters, similar to that introduced by Begbie and Born in their theory of diffuse scattering by lattice vibrations, and that of external forces causing the distortion. It is shown that our diffuse scattering may be observed in some crystal in which the density of the lattice defect exceeds a certain value.

Introduction

In the present paper we give a general intensity formula for the diffuse scattering of X-rays by a crystal which has local lattice distortions due to any kind of lattice defect, for instance, the existence of impurity atoms. H. Ekstein[1] has given a theory on the same problem treating the latticed istortions on the basis of the elasticity theory of continuum. The theory we are presenting here may be regarded as an atomistic counterpart of his theory, but it is more general, and will provide a more convenient method of calculation when applied to practical problems.

§1. General Theory

Let us consider a crystal lattice containing s atoms in its unit cell. In the unstrained state, the positions of the atoms shall be indicated by a set of radius vectors:

$$\boldsymbol{r}^l_k=\boldsymbol{r}^l+\boldsymbol{r}_k=l_1\mathbf{a}_1+l_2\mathbf{a}_2+l_3\mathbf{a}_3+\boldsymbol{r}_k, \quad (1)$$

where $\mathbf{a}_1$, $\mathbf{a}_2$ and $\mathbf{a}_3$ are three elementary vectors, l_i $(i=1,2,3)$ are integers and $k=1,2,\ldots\ldots,s$. We assume that there exists a lattice defect of a certain kind, by which each atom is displaced from its equilibrium position given by (1) to another through a displacement vector $\boldsymbol{u}^l_k$. Then the intensity for the scattered X-rays from this distorted lattice will be given by*

$$I=I_e\,|\sum_{lk} f_k(\boldsymbol{b})\exp[2\pi i(\boldsymbol{b}\cdot\boldsymbol{r}^l_k+\boldsymbol{u}^l_k)]\,|^2. \quad (2)$$

The symbols appearing in this formula have the following meaning:

I_e : the Thomson factor,

$\boldsymbol{b}=\boldsymbol{k}-\boldsymbol{k}_0$,

$\boldsymbol{k}_0$: the wave vector of the incident beam,

$\boldsymbol{k}$: the wave vector of the scattered beam,

$f_k(\boldsymbol{b})$: the atom form factor of the k-th kind of atom.

Neglecting the squares and the higher powers of $2\pi(\mathbf{b}.\,\boldsymbol{u}^l_k)$, I is expressible as a sum of two terms, i.e. the term representing the intensity for the Laue scattering, I_{Laue}, and that for the diffuse scattering, $J_{strain}(\boldsymbol{b})$:

$$I=I_{Laue}+J_{strain}(\boldsymbol{b})\,; \quad (3)$$

where

$$I_{Laue}=I_e\,|\sum_{lk} f_k(\boldsymbol{b})\exp[2\pi i(\boldsymbol{b}\cdot\boldsymbol{r}^l_k)]\,|^2$$

$$=\frac{I_e}{4\pi^2\boldsymbol{b}^2}\left\{\sum_{k\alpha}\sum_{k'\beta}W_\alpha(k)W_\beta{}^*(k')\right\}$$

$$\prod_{i=1}^{3}\frac{\sin^2 N_i\pi(\boldsymbol{b}\cdot\mathbf{a}_i)}{\sin^3\pi\,(\boldsymbol{b}\cdot\mathbf{a}_i)}\,, \quad (4)$$

$$J_{strain}(\boldsymbol{b})=I_e\,|\,2\pi i\sum_{lk} f_k(\boldsymbol{b})(\boldsymbol{b}\cdot\boldsymbol{u}^l_k)$$

$$\exp[2\pi i(\boldsymbol{b}\cdot\boldsymbol{r}^l_k)]\,|^2$$

$$=I_e\,|\sum_{k\alpha} S_\alpha(k)W_\alpha(k)\,|^2. \quad (5)$$

In these expressions $S_\alpha(k)$ and $W_\alpha(k)$ $(a=1,2,3,)$ denote the rectangular components of $2s$ vectors $S(k)$, $W(k)$, $k=1,2,\ldots\ldots,s$, defined by

$$S(k)=\sum_l \boldsymbol{u}^l_k\exp[2\pi i(\boldsymbol{b}\cdot\boldsymbol{r}^l\,], \quad (6)$$

$$W(k)=2\pi\boldsymbol{b}f_k(\boldsymbol{b})\exp[2\pi i(\boldsymbol{b}\cdot\boldsymbol{r}_k)]. \quad (7)$$

$N=N_1N_2N_3$ is the total numbers of unit cells in the crystal.

---

* For the sake of brevity, we omit here certain terms which are to be added to or subtracted from (2) and which depend on the particular nature of the distortion center. They must be dealt with separately for each case. See the example given in § 2, which all the terms will be taken into account.

We shall now denote the rectangular components of u^l_k by $u_\alpha(^l_k)$. Their values are to be determined from the condition that the deformation energy of the lattice, W, expressed as a function of the displacements, should be minimum with respect to their small variations. Assuming small displacements, W may be written in the form

$$W=\frac{1}{2}\sum_{\substack{lk\\\alpha}}\sum_{\substack{l'k'\\\beta}}\Phi_{\alpha\beta}\binom{l-l'}{kk'}u_\alpha\binom{l}{k}u_\beta\binom{l'}{k'}$$

$$+\sum_{\substack{lk\\\alpha}}\Psi_\alpha\binom{l}{k}u_\alpha\binom{l}{k}, \qquad (8)$$

where $\Phi_{\alpha\beta}\binom{l-l'}{kk'}$ are constants representing the quasi-elastic forces between the two points r^l_k and $r^{l'}_{k'}$, and $-\Psi_\alpha\binom{l}{k}$ is the α-component of the external force acting on the atom located at the position r^l_k. The postulate of the minimum energy

$$\frac{\partial W}{\partial u_\alpha\binom{l}{k}}=0 \qquad (9)$$

leads to the following equation:

$$\sum_{\substack{l'k'\\\beta}}\Phi_{\alpha\beta}\binom{l-l'}{kk'}u_\beta\binom{l'}{k'}+\Psi_\alpha\binom{l}{k}=0. \qquad (10)$$

Multiplying (10) by $\exp[2\pi i(\boldsymbol{b}\cdot\boldsymbol{r}^l)]$ and summing up over all l, one gets the following Fourier transform of the equation (10):

$$\sum_{k'\beta}\Phi_{\alpha\beta}\binom{\boldsymbol{b}}{kk'}S_\beta(k')-E_\alpha\binom{\boldsymbol{b}}{k}=0, \qquad (11)$$

where $S_\alpha(k)$ is defined by (6), and $\Phi_{\alpha\beta}\binom{\boldsymbol{b}}{kk'}$ and $E_\alpha\binom{\boldsymbol{b}}{k}$ are the Fourier transform of $\Phi_{\alpha\beta}\binom{l}{kk'}$ and $-\Psi_\alpha\binom{l}{k}$, respectively, defined by the relations

$$\Phi_{\alpha\beta}\binom{\boldsymbol{b}}{kk'}=\sum_l\Phi_{\alpha\beta}\binom{l}{kk'}\exp[2\pi i(\boldsymbol{b}\cdot\boldsymbol{r}^l)], \qquad (12)$$

$$E_\alpha\binom{\boldsymbol{b}}{k}=-\sum_l\Psi_\alpha\binom{l}{k}\exp[2\pi i(\boldsymbol{b}\cdot\boldsymbol{r}^l)]. \qquad (13)$$

If we consider $\Phi_{\alpha\beta}\binom{\boldsymbol{b}}{kk'}$ as the elements of a matrix $\Phi(\boldsymbol{b})$, with pairs of indices (α, k) and (β, k') representing the row and the column indices, respectively, and denote by $\Phi^{-1}_{\alpha\beta}\binom{\boldsymbol{b}}{kk'}$ the elements of its reciprocal matrix $\Phi^{-1}(\boldsymbol{b})$, then we have the solution of the equation (11) in the form

$$S_\alpha(k)=\sum_{k'\beta}\Phi^{-1}_{\alpha\beta}\binom{\boldsymbol{b}}{kk'}E_\beta\binom{\boldsymbol{b}}{k'}. \qquad (14)$$

Putting (14) into (5) and assuming that there are n lattice defects of the same type in the crystal, we have for the intensity of the diffuse scattering the final formula

$$J_{strain}(\boldsymbol{b})=I_e n\left|\sum_{k\alpha}\sum_{k'\beta}\Phi^{-1}_{\alpha\beta}\binom{\boldsymbol{b}}{kk'}E_\beta\binom{\boldsymbol{b}}{k'}W_\alpha(k)\right|^2. \qquad (15)$$

§2. A Simple Example

To illustrate our method, we shall give an example of the diffuse scattering by a monoatomic simple cubic lattice which has one vacant lattice point situated at the origin.

Using the same notations as in §1, but dropping the indices k, k', since only one kind of atom is here concerned with, the intensity of the scattered X-rays is given by

$$I=I_e\left|\sum_l{}' f(\boldsymbol{b})\exp[2\pi i(\boldsymbol{b}\cdot\boldsymbol{r}^l+\boldsymbol{u}^l)]\right|^2, \qquad (16)$$

in which the accent in $\sum'$ means that $l=0$ should be omitted. In the approximation of neglecting the squares and the higher powers of $2\pi(\mathbf{b}\cdot\boldsymbol{u}^l)$, I can be written as

$$I=I_e|f(\boldsymbol{b})|^2|G_0(\boldsymbol{b})+G_1(\boldsymbol{b})|^2, \qquad (17)$$

$$G_0(\boldsymbol{b})=\sum_l\exp[2\pi i(\boldsymbol{b}\cdot\boldsymbol{r}^l)]=\prod_{i=1}^{3}\frac{\sin N_i\pi(\boldsymbol{b}\cdot\mathbf{a}_i)}{\sin\pi(\boldsymbol{b}\cdot\mathbf{a}_i)}, \qquad (18)$$

$$G_1(\boldsymbol{b})=2\pi i\sum_l{}'(\boldsymbol{b}\cdot\boldsymbol{u}^l)\exp[2\pi i(\boldsymbol{b}\cdot\boldsymbol{r}^l)]-1. \qquad (19)$$

Since $G_0(\boldsymbol{b})$ is a functions which has a large value only for such $\boldsymbol{b}$ that coincides with any one of reciprocal lattice vectors,

$$\boldsymbol{b}=h_1\frac{\mathbf{a}_2\times\mathbf{a}_3}{[\mathbf{a}_1\mathbf{a}_2\mathbf{a}_3]}+h_2\frac{\mathbf{a}_3\times\mathbf{a}_1}{[\mathbf{a}_1\mathbf{a}_2\mathbf{a}_3]}+h_3\frac{\mathbf{a}_1\times\mathbf{a}_2}{[\mathbf{a}_1\mathbf{a}_2\mathbf{a}_3]}$$

(h_i being integer),

the terms containing $G_0(\boldsymbol{b})$ in (7) correspond to the Laue scattering, and the intensity of the diffuse scattering, $J_{strain}(\boldsymbol{b})$, results from the remaining term in (17):

$$J_{strain}(\boldsymbol{b})=I_e|f(\boldsymbol{b})|^2|G_1(\boldsymbol{b})|^2. \qquad (20)$$

According to the general theory developed in §1, $G_1(\boldsymbol{b})$ can be transformed as

$$G_1(\boldsymbol{b})=2\pi i[\boldsymbol{b}\cdot\Phi^{-1}(\boldsymbol{b})\cdot\boldsymbol{E}(\boldsymbol{b})]-1, \qquad (21)$$

where the elements of the matrix $\Phi(\boldsymbol{b})$ and the components of the vector $\boldsymbol{E}(\boldsymbol{b})$ are defined by (12) and (13), respectively:

$$\Phi_{\alpha\beta}(\boldsymbol{b})=\sum_l\Phi_{\alpha\beta}(l)\exp[2\pi i(\boldsymbol{b}\cdot\boldsymbol{r}^l)], \qquad (12')$$

$$E_\alpha(b) = -\sum_l \Psi(l)\exp[2\pi i(b\cdot r^l)]\,. \tag{13′}$$

For simplicity, we assume here that each atom interacts only with its six nearest neighbors through Hooke's law of force. Let h be the Hooke's constant and $h\varepsilon a$ the magnitude of the force acting between nearest neighbors when the crystal is expanded from its natural state with a change in linear dimension by a factor $1+\varepsilon$ $\left(\varepsilon = \frac{a-a_0}{a}\right.$, a and a_0 being the lattice constant for the expanded and natural state, respectively$\left.\right)$. For this expanded state, the quantities $\Phi_{\alpha\beta}(l)$ and $\Psi_\alpha(l)$ can easily be determined. From definition it is evident that $\Phi_{\alpha\beta}(l)$ is equal to the α-component of the force acting on the l-th atom when the atom at the origin is displaced by a unit length along the β-direction, keeping the positions of other atoms unchanged. Similarly, $-\Psi_\alpha(l)$ is equal to the α-component of the force acting on the l-th atom when a vacant lattice point is produced at the origin. By displacing only one atom the unbalance in forces is evidently produced only between the displaced atom and its nearest neighbors, as shown in Fig 1, so that $\Phi_{\alpha\beta}(l)$'s are such matrices that have non-zero elments only for $l=0$, $l=(\pm1,0,0)$, $l=(0,\pm1,0)$, $l=(0,0,\pm1)$.

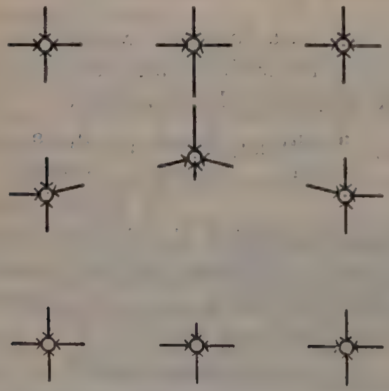

Fig. 1. The figure showing the unbalance in forces produced by displacing one atom.

We therefore have

$$\Phi(0,0,0) = 2h(1+\varepsilon)\begin{pmatrix}1&0&0\\0&1&0\\0&0&1\end{pmatrix},\quad \Phi(\pm1,0,) = 0-h\begin{pmatrix}1&0&0\\0&\varepsilon&0\\0&0&\varepsilon\end{pmatrix},$$

$$\Phi(0,\pm1,0) = -h\begin{pmatrix}\varepsilon&0&0\\0&1&0\\0&0&\varepsilon\end{pmatrix},\quad \Phi(0,0,\pm1) = -h\begin{pmatrix}\varepsilon&0&0\\0&\varepsilon&0\\0&0&1\end{pmatrix}. \tag{22}$$

On the other hand, if we take off an atom from the lattice point $l=0$, the atoms next to the produced vacancy will be subjected to unbalanced forces (see Fig. 2*a*), so that $\Psi(l)$'s are the vectors having non-zero components only for $l=(\pm1,0,0)$, $l=(0,\pm1,0)$, $l=(0,0,\pm1)$. Their components are therfore given by

$$\Psi(\pm1,0,0) = \mp h\begin{pmatrix}\varepsilon a\\0\\0\end{pmatrix},\quad \Psi(0,\pm1,0) = \mp h\begin{pmatrix}0\\\varepsilon a\\0\end{pmatrix}, \tag{22}$$

$$\Psi(0,0,+1) = \mp h\begin{pmatrix}0\\0\\\varepsilon a\end{pmatrix}.$$

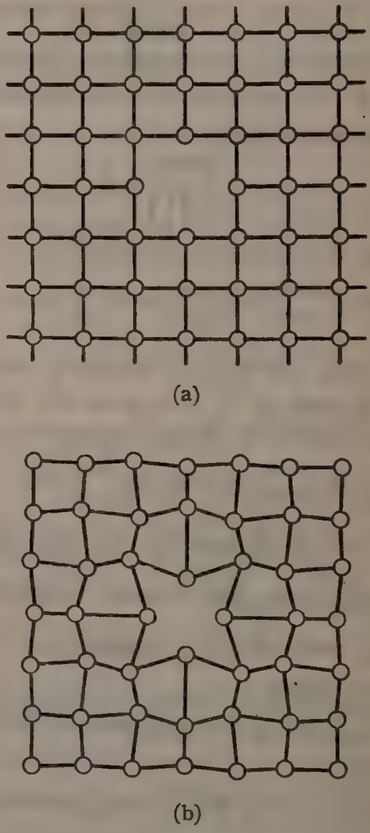

(a)

(b)

Fig. 2. The lattice distortion produced by removing one atom from a lattice point.
(a) non-equilibrium state.
(b) equilibrium state.

In equilibrium state, the whole lattice will be distorted in the manner shown in Fig. 2b. The Fourier transforms of (22) and (23) are readily constructed:

$$\boldsymbol{\Phi}(\boldsymbol{b})=$$
$$2h\begin{pmatrix}(1-\cos x_1)+\varepsilon(2-\cos x_2-\cos x_3) & 0 & 0\\ 0 & (1-\cos x_2)+\varepsilon(2-\cos x_3-\cos x_1) & 0\\ 0 & 0 & (1-\cos x_3)+\varepsilon\, 2-\cos x_1-\cos x_2)\end{pmatrix}$$

$$\boldsymbol{E}(\boldsymbol{b})=2ih\varepsilon a\begin{pmatrix}\sin x_1\\ \sin x_2\\ \sin x_3\end{pmatrix}, \tag{25}$$

with $x_i=2\pi(\boldsymbol{b}\cdot\boldsymbol{a}_i)i=1,2,3$. After some calculations, using (20), (21), (24) and (25), we finally obtain

$$\frac{J_{strain}}{I_e|f(\boldsymbol{b})|^2}=\Bigg[1+\varepsilon\Bigg\{\frac{x_1\sin x_1}{(1-\cos x_1)+\varepsilon(2-\cos x_2-\cos x_3)}+\frac{x_2\sin x_2}{(1-\cos x_2)+\varepsilon(2-\cos x_3-\cos x_1)}+\frac{x_3\sin x_3}{(1-\cos x_3)+\varepsilon(2-\cos x_1-\cos x_2)}\Bigg\}\Bigg]^2. \tag{26}$$

In Fig. 3 are drawn the iso-diffusion curves calculated from the formula (26) for the case $\varepsilon=0.1$. It should be noted that $J_{strain}\,(\boldsymbol{b})$ has remarkable dependence on the direction of scattering.

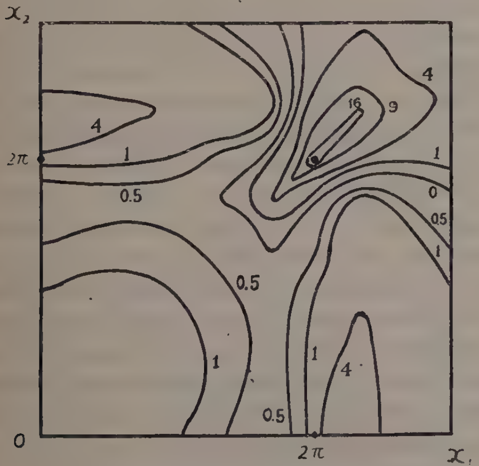

Fig. 3. The iso-diffusion curves calculated from the formula (26) for the case $\varepsilon=0.1$.

§3. Discussions

1) In order that the diffuse scattering in question can actually be observed, the number of the lattice defect n must exceed a certain value. We can obtain a rough idea of this value in the following way. We may namely compare (15) with the intensity of diffuse scattering due to thermal vibrations. The latter is given by Begbie and Born[2)] as

$$J_{vibration}(\boldsymbol{b})=I_e\frac{NkT}{4\pi^2}\sum_{k\alpha}\sum_{k'\beta}\Phi^{-1}_{\alpha\beta}\binom{\boldsymbol{b}}{kk'}W_\alpha(k)W_\beta{}^*(k'). \tag{27}$$

Confining ourselves to the simplest case of $s=1$, where we may take $\boldsymbol{w}(1)=2\pi\boldsymbol{b}f_1(\boldsymbol{b})$, we have

$$\frac{J_{strain}}{J_{vibration}}\doteq\frac{n}{N}\,\frac{4\pi^2|(\boldsymbol{E}\cdot\boldsymbol{\Phi}^{-1}(\boldsymbol{b}))|^2}{kT(\boldsymbol{b}\cdot\boldsymbol{\Phi}^{-1}\cdot\boldsymbol{b})}$$
$$\sim\frac{n}{N}\,\frac{4\pi^2|\boldsymbol{E}|\,|\boldsymbol{\Phi}^{-1}\boldsymbol{E}|}{kT}. \tag{28}$$

The quantity $\boldsymbol{E}$ has the dimension of force and its order of magnitude is

$\boldsymbol{E}\sim$(force constant) × (max. displacement of the atoms).

Therefore, denoting by u_0 the magnitude of the maximum displacement of the atoms in the crystal, we have

$$|\boldsymbol{\Phi}^{-1}\boldsymbol{E}|\approx u_0,$$
$$|\boldsymbol{E}|\cdot|\boldsymbol{\Phi}^{-1}\boldsymbol{E}|\sim(\text{force constant})\times u_0{}^2.$$

On the other hand, since kT is the thermal energy per atom, we have

$kT\sim$(force constant) × (mean square amplitude of an atom).

Denoting the mean square amplitude of an atom by $\bar{u}^2$, we therefore have

$$\frac{J_{strain}}{J_{vibration}}\sim\frac{n}{N}4\pi^2\left(\frac{u_0{}^2}{\bar{u}^2}\right). \tag{29}$$

In actual case, u_0 may amount to a value several times greater than $(\bar{u}^2)^{1/2}$, so that n must be $\gtrsim 10^{-3}\,N$ in order that the right-hand side of (29) is $\gtrsim 1$. This value for n may be somewhat too large for ordinary purified perfect crystals, but there may be cases where this condition can be fulfilled, for instance, the case of silicon or germanium containing boron or phosphorus to the maximum amount. There is, however, another factor which makes the observation of our diffuse scattering more favourable. The variation in the intensity of scattering with the direction of observation must in general be more enhanced in the case of lattice defects than in the case of thermal vibrations, because in the former case, only particular distorted arrangement is realized, whereas, in the latter case, every kind of distorted arrangedments appears one after another, so that the diffuse pattern will be smoothed out. An example of the preceding section shows clearly this circumstance.

2) In this connection, it may be interesting to suggest, with T. Nagamiya[5], that the temperature-independent "extraordinary diffuse scattering" in diamond of the "type I" observed by K. Lonsdale[4] possibly has its origin in some kind of impurity centers, probably with a concentration of $10^{-4}\sim10^{-5}$. In the case of diamond, the amplitude of lattice vibrations is small owing to a high value of the Debye temperature, while the displacements of the atoms in the lattice produced by the introduction of impurity atoms can extend over a wide range around the latter owing to the stiffness of the vanlence bond. These facts provide a favourable condition for the observation. A preliminary calculation made by S. Yomosa[5], using the method here presented, shows indeed a remarkable dependency of the scattered intensity on observed directions.

3) When the lattice distortion are produced in a macroscopic scale, they will be dealt with by the elasticity theory of continuum in the way shown by Ekstein. Even in this case our theory provides a convenient starting point. Indeed, the quantity $\Phi(b)$, which is essentially the same as the "dynamical matrix" introduced by M. Born[3] in his theory of thermal diffuse scattering, is expressible in terms of the elastic constants of the crystal, as actually shown by Begbie and Born[2]. In the limiting case of macroscopic lattice distortions, the equation (10), which determines the atomic displacements, can be shown to reduce to the fundamental partial differential equation of the elasticity theory. Our theory is thus equivalent to Ekstein's theory in this limiting case

In conclusion, the writer wishes to express his sincere thanks to Prof. T. Nagamiya for his continual interest in this investigation.

References

1) H. Ekstein: Phys. Rev. **68** (1945) 120.
2) G. H. Begbie and M. Born; Proc. Roy. Soc. **188** (1947) 179.
3) G. H. Begbie: Proc. Roy. Soc. **188** (1947) 189.
4) K. Lonsdale and H. Smith: Nature **148** (1941) 112, 257.
5) S. Yomosa and T. Nagamiya: to appear.

JOURNAL OF THE PHYSICAL SOCIETY OF JAPAN Vol. 7, No. 3, MAY—JUN., 1952

A Magnetic Ion Source of Capillary Arc Type

Akira ISOYA

Department of Physics, Faculty of Science, University of Tokyo

(Read April 3, 1950; Received Oct. 27, 1951)

In the quartz capillary part (8mm ϕ, 10cm in length) of this ion source with a coaxial magnetic field of about 800 gauss, an intense ionization is established by a collimated primary electron beam sent from one end of the capillary. No metal part being contained in the capillary, a high relative concentration of atomic hydrogen is obtained, so that the proton percentage of the ion beam extracted from the other end of the capillary is very large (60∼70%). A proton output up to 1mA is obtained from a 1.3mm hole with a small consumption of power (<200 watts) and hydrogen gas (∼3cc per hour N.T.P.). The ratio of protons to consumed gas molecules is 10∼20%.

§1. Introduction

A promising method of producing an intense proton beam will be a low voltage arc in a capillary tube of insulator. The clean insulator surfaces are generally less effective as a catalyst for the recombination of atomic hydrogen than the metal surfaces, so that neutral hydrogen atoms produced by the electron impact in the glass or quartz capillary spend the long time there before being recombined on the capillary wall or diffusing out of this part. Thus the relative concentration of atomic hydrogen gas in the capillary becomes very high and hence the abundant atomic ions are produced. The proton percentage attained in the pyrex capillary source by Larmar[1] et al. was about 60% (the proton percentage in the metal wall source is usually only about 10%). The obtainable largest output of protons, however, was limited to a rather low value by the rise of the temperature of the capillary wall due to the large energy dissipation in this part.

In an unpublished study the author found that the use of magnetic field improved remarkably the performance of the ion source of low voltage arc type with respect to the efficiency of gas and power consumption and also the life of the oxide cathode. And the feature of constriction of the arc plasma in the magnetic field seemed to be fitted for establishment of the intense ionization in the insulator capillary tube. These recognitions led to the investigation of the magnetic ion source of capillary arc type.

§2. Preliminary Experiments

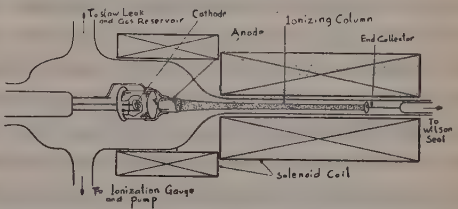

Fig. 1. Discharge tube used in preliminary experiments. Inner diameter of the capillary=7.5mm. Anode diameter =7.0mm.

The behavior of capillary arc in the strong longitudinal magnetic field was studied with pyrex discharge tubes as that shown in Fig. 1. A cylindrical anode and an oxide cathode are placed against one end of the capillary and a movable ion collector, which is charged negative to the cathode, is placed in it. Electrons from the cathode are collimated effectively into the capillary with the magnetic field of more than several hundred gauss produced by solenoid coils. The converging field at the cathode and anode region is preferable because it allows to use a cathode of large emission area. This arrangement of electrodes is fitted for maintainance of the intense arc discharge in the low gas pressure, because, primary electrons consume a large fraction of their energy for ionization before being collected at the anode or the tube wall. Moreover it is essential to operate in the low pressure, since the mean free path of primary electrons must be long enough to obtain a large density at the end part of the capillary. In the suitable pressure ($\sim 5\times10^{-3}$ mm Hg) the ionizing region forms an uniformly glowing column, the diameter of which is determined by the anode and is very sharply defined along the magnetic lines of force. In the capillary part the width of the column is 3~5mm. The distinctness of the column boundary increases at lower pressure and stronger field. Such formation of the ionizing column can be seen definitely even at the distance of 20~30 cm from the cathode.

In the magnetic field used (several hundred ~ one thousand gauss), the radius of curvature of the electron orbit in the plasma is usually less than 0.1 mm, but that of ions will be the order of 1 mm. This value will not be small enough to prevent the diffusion of ions to the capillary wall, because the distance between the column boundary and the capillary wall is of the same order. Nevertheless a drift of ions predominant in the axial direction is expected, since the ions will be retarded by the electric field between the plasma and the wall, which is probably charged somewhat positive to the plasma so as to allow the diffusion of the same number of ions and electrons. In fact it was shown by the measurement of the wall potential with cylindrical wall collectors, that a broad maximum, several volts higher than the anode potential, existed at the middle part of the capillary. This potential distribution on the capillary wall may be considered to be nearly equal to that along the ionizing column, because the potential difference between them is not expected to be much larger than the mean energy of ions. The positive ions produced nearly uniformly throughout the long column will drift down along these potential gradients to both ends. Thus if a sufficiently strong field is applied, about a half of ions produced in the capillary will be collected at the end collector and the other half drift to the cathode region, a large fraction of which will be effectively used to extract electrons from the cathode. This expectation was proved to be the case at least in the arc of small intensity, as shown in the following section. By the analogy to the general theory of arc plasma, the concentration of ions and electrons is considered to be nearly uniform along the direction of the length of the column on account of the long mean free path of ions. The ion current density drifting axially in the column is considered to have a strong maximum on the central axis.

Action of the Magnetic Field

In this discharge tube the most critical and troublesome part is the cathode and anode region. The dimensions of the cathode and anode, and the stength and convergency of the magnetic field influence sensitively on the intensity of the ionizing column and the stability of the arc. The bad arrangements increase the number of those electrons which are directly collected at the anode before consuming their energy in ionization. This results in an unduely high value of the arc voltage, or in a large anode loss inducing red heating of the anode cylinder. The increase of magnetic field applied to the cathode acts to reduce the effective emission area, which also results in the increase of cathode drop. This results from the fact that the stronger the field is, the more tightly the pathes of ions and electrons are bound to lines of force, so that the portions of the cathode surface, that does not receive the lines or force directly are not effective in supplying electrons. Regarding the capillary part there is no difficulty. The stronger the field, the better the result. The only point to be noted is that when the diameter of the ionizing column, sent into the capillary through the anode, is as large as that of the capillary, the plasma can not grow intense owing to the absorption of ions and electrons by the side wall. The capillary diameter must, therefore, be chosen large enough to give room for the sheath region surrounding the column. On the other hand its diameter must be as small as possible to prevent the diffusion of atomic hydrogen to the cathode region. The optimum size will be given by the compromise of two requirements.

In Fig. 2 is shown an example of the arc behavior. To the cathode and anode region a constant field of 750 gauss is applied and

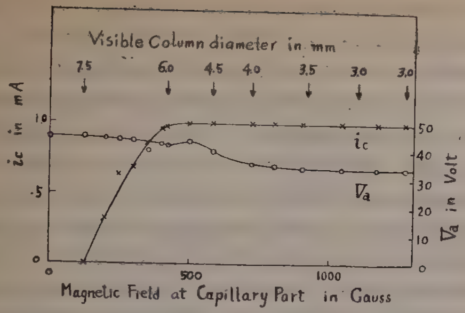

Fig. 2. A typical curve of the arc behavior showing the action of the magnetic field.
Capillary length=8cm.
Gas pressure $=5\times10^{-3}$mmHg.
Arc current=20mA.

an additional field by the solenoid coil at the capillary part is varied from zero to more than a thousand gauss. Since in this case the field condition at the cathode region does not largely be changed the emission area of the cathode is considered nearly constant. In Fig. 2 the lowest possible arc voltage V_a which is attained with the surplus emission of electrons and the corresponding collector ion current i_c at the arc current of 20mA are plotted as the function of the magnetic field. The width of the column measured with the eye at the entrance of the capillary is also indicated at the upper part of the figure. As the field increases, the plasma grows in the capillary and when the column boundary is pulled away from the capillary wall, the saturation of i_c occurs. V_a still continues to decrease gradually and becomes stationary at much stronger field (≥ 1000 gauss). In this case where the longitudinal mobilities of electrons and ions are considered to be sufficiently large, the constancy of i_c may be a matter of course, because i_c and the ion current received by the cathode will be in a definite proportion and the latter must be constant irrespectively of the magnitude of cathode drop as long as the arc current is kept constant, on account of the nature of double sheath at the cathode. On the other hand V_a is determined by the efficiency with which the cathode receives the positive ions from the ionizing region. The decrease of V_a with the increase of field means either the reduction of diffusion loss of primary electrons to the anode or the reduction of sideward diffusion of ions. At the conditions finally attained with sufficient fields, the constancy of V_a means that the distribution of flow of ions is no longer influenced by the change of field, whence the complete suppression of sideward diffusion of ions can be naturally concluded.

A more confirmative evidence for the above conclusion was obtained when the capillary length was changed by moving the end collector. For the change of capillary length from zero to 8cm with a sufficient magnetic field in the foregoing arrangement, both i_c and V_a kept their values constant except a slight increase of V_a at the shortest length. This must be a strong evidence for the fact that the plasma is completely isolated from the capillary wall, because if the ion current lost to the wall is not negligible, the increase of capillary length must induce the increase of V_a, *i.e.*, the production of more ions in order to keep the constant ion supply to the cathode. The increase of V_a at the shortest capillary length may be ascribed to the increase of density of primary electrons in the ionizing column, which results in the reduction of ionizing rate of primary electrons. This event will be treated in the next section.

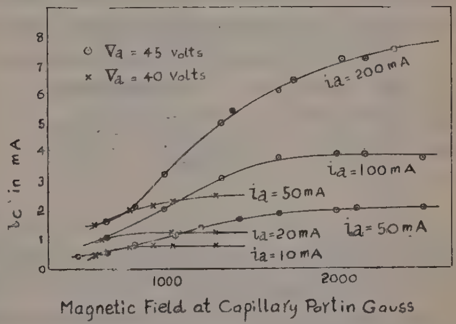

Fig. 3. End collector ion current i_c as a function of the magnetic field. Two series of measurements differing in the field conditions at the cathode and anode region are shown.

The characteristic curves in Fig. 3 are taken keeping both i_a and V_a constant in the similar conditions. In this case the collector ion current i_c is independent of the circumstances in the cathode. The strength of the magnetic field necessary to saturate

i_c increases as i_a. The easiness of saturation of i_c depends also on the configuration of the magnetic field at the cathode and anode region. Results of two series of experiments differing in this condition are shown in the figure. These facts suggest that the velocity of transverse diffusion of primary electrons increases with the intensity of the arc plasma, so that this effect promotes the diffusion loss of primary electrons to the anode and results in the reduction of ion production. To suppress this trend the increasingly larger magnetic field is needed. The cause of this swift drift of primary electrons is considered to be scattering phenomena proper to the intensely ionized gas, which will be described in the next section.

Rate of Ion Production in the Ionizing Column

The scattering effect mentioned above is also likely to induce a very strong degeneration of energy of primary electrons, which reduces considerably the rate of ion production per primary electron. An evidence is given in Fig. 4, where the ratio of the saturated value of i_c to i_a is plotted against i_a at $V_a=40$ volts. At the lowest limit of i_a (≤ 1mA), i_c/i_a assumes a constant value of 20% where the scattering effect will be negligible, so that the rate of ionization is expected to be of the maximum efficiency at the electron energy of 40 volts. With the increase of i_a, i_c/i_a falls rapidly, and at $i_a>$ 20mA it tends to a nearly stationary value of about 5%. Some part of the reduction of i_c/i_a may be ascribed to the diffusion loss of primary electrons to the anode, but the existence of the stationary condition at larger values of i_a suggests that another reason is responsible for this effect.

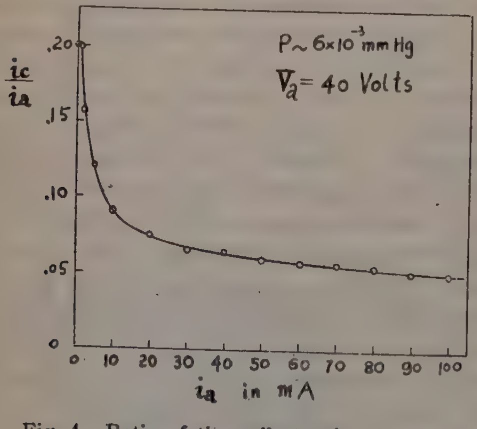

Fig, 4. Ratio of the collector ion current i_c to the arc current i_a as a function of the arc current showing the reduction of the rate of ion production at large arc current.

According to Langmuir,[2)] an electron beam traversing ionized gas suffers scattering in such a way that the resultant velocity distribution can be analysed into an uniform translation and a superposed maxwellian distribution. The lose of energy of translation is always much larger than the gain of the thermal energy. The temperature of primary electrons increases very rapidly with the current density of primary electrons (with 2nd or higher power of the current) and roughly in proportion to the traversed distance. Many experiments showed that the condensed electrons seemed not to be related with this phenomenon, and the main cause of scattering of primary electrons was some effect confined in the region traversed by the primary electron beam. Langmuir considered that this effect would be ascribed to the scattering by the joint action of radiation and excited atoms of high energy corresponding to that of primary electrons. This consideration, however, was a tentative one. Some sort of rapid fluctuation of the electric field in the plasma may be responsible for this phenomenon.

In the present case where the primary electrons are confined in a very narrow column, the current density of primary electrons is enormously large compared to the case cited above. The phenomena concerned may be much more complicated. The relaxation length, *i.e.*, the distance which the primary electrons travels before losing greater part of its original translational energy, will be very short. When the relaxation length is large enough compared to the mean free path for ionization the rate of ionization will be normal, but when the former is comparable with the latter a rapid decrease of the rate of ionization is expected with the increase of i_a owing to the large energy loss by degeneration. However in the case where the former is much shorter than the latter, the thermal equilibrium will be nearly established between the whole plasma electrons containing both primary and condensed electrons, so that the rate of ionization will be no longer influenced by the arc intensity.

The actual energy distribution of plasma electons was roughly estimated by using the end collector as a probe, or by setting a small plane probe at the same position. The usual method to interprete the volt-ampere characteristic curve can be used in this case. For arc currents of less than several mA, a break point on the characteristic curve showing the trace of primary electrons appears near the cathode potential. For larger arc currents this break point disappears and the energy distribution of whole electrons approaches to the maxwellian, the electron temperature of which is usually very high (several~ten volts). The end collector which is left in the floating condition is usually charged nearly to the cathode potential owing to incident electrons having energies larger than that corresponding to the cathode drop. In order to repel these electrons the negative potential more than 20 volts is necessary.

Effect of Gas Pressure

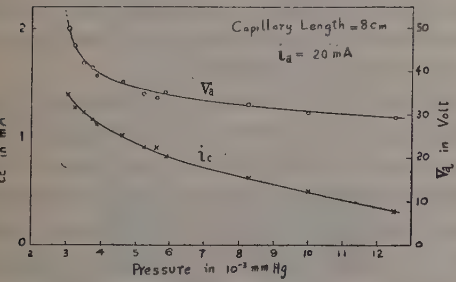

Fig. 5. A typical curve showing the pressure dependence of the anode voltage V_a and the collector ion current i_c.

In Fig. 5 the lowest anode voltage V_a which is attained with a sufficient cathode heating the ion collector current i_c are plotted as the function of the gas pressure. The experimental arrangement is the same as that in the case of Fig. 2. The magnetic field is, of course, sufficiently strong. At lower pressure i_c increases accompanying with the increase of V_a. When V_a is larger than 50 volts or so, the arc behavior shows an irregularity which is apparently due to the disintegration of the oxide cathode by ion bombardment. i_c seems to be a function of V_a which is independent of the gas pressure or the cathode condition. This is ascertained by plotting the relation of i_c to V_a obtained in various conditions on the same graph. Fig. 6 shows the relations of i_c/i_a vs. V_a at various i_a's obtained at the constant pressure together with those points in Fig. 5 at $i_a=20mA$ which are obtained changing the pressure. They show the good agreement with the corresponding curves.

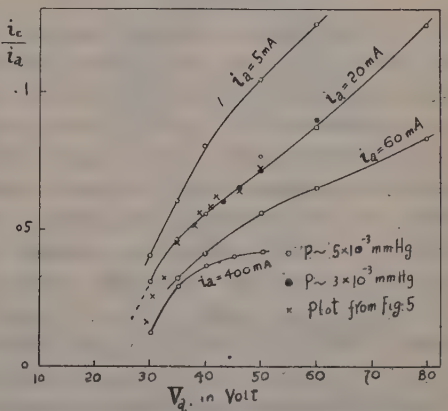

Fig. 6 Ratio of the collector ion current i_c to the arc current i_a as a function of the anode voltage V_a, which shows the reduction of the ratio at large arc currents as shown in Fig. 4.

From the similar processes in different conditions, it was found that the pressure region in which this independence of the relation of i_c *vs.* V_a held was from 8×10^{-3} mm to 3×10^{-3} mm. The deviation at higher pressure may be ascribed to the non-uniformity of ionization in the column, *i.e.*, the greater intensity near the cathode owing to the short mean free path of electrons. The deviation at lower pressure can be ascribed to the fact that the mean free path for ionization is too long to keep the rate of ionization constant.

The increase of V_a and i_c at lower pressure can be explained as due to the nature of double sheath at the cathode and the increase of electron temperature. The theory of double sheath considering initial velocities of ions and electrons[3)] shows that when their mean energies in the plasma are not negligible against the cathode drop, the largest possible number of electrons which are allowed to leave the cathode per one ion supplied from the plasma becomes smaller than that in the case where the initial energies are negligible. This relation in the case of the plane cathode is given by the following formula:

$$\frac{I_e}{I_p}=\left(\frac{m_p}{m_e}\right)^{\frac{1}{2}}\frac{1-\left(\frac{E_p}{V_{SM}}{}^{\frac{1}{2}}\right)\left(1+\frac{E_e}{2E_p}\right)+\frac{E_p}{2V_{SM}}}{1-\left(\frac{\pi E_c}{4V_{SM}}\right)^{\frac{1}{2}}-\frac{E_e-E_c}{2V_{SM}}},$$

where I_e = the largest possible electron current density, I_p = the ion current density, E_e = the potential corresponding to the electron temperature T_e ($E_e=T_e/11600$ [volt]), E_p = that corresponding to the mean velocity normal to the sheath edge, E_c = that corresponding to the cathode temperature, and V_{SM} = the potential difference between the sheath edge and the potential minimum. m_p/m_e is the mass ratio of an ion and an electron. With the decrease of gas pressure, the electron temperature increases naturally by accumulation of higher energy electrons. And the mean energy of ions at the sheath edge can be taken as about $E_e/2$ by the analogy to the general case of arc plasma. To get an idea of the order of influence of the electron temperature, one may tentatively assume the formula cited above. When $E_c=0.1$ volts, one gets, for examples,

for $V_{SM}=32$ volts and $E_e=2$ volts,
〃 $=36$ 〃 〃 〃 $=6$ 〃 ,
〃 $=40$ 〃 〃 〃 $=9$ 〃 ,
〃 $=50$ 〃 〃 〃 $=15$ 〃 ,
$I_e/I_p=0.72\ (m_p/m_e)^{\frac{1}{2}}$;
〃 $=0.53$ 〃 ;
〃 $=0.46$ 〃 ;
〃 $=0.35$ 〃 ;

where the value of E_e for each V_{SM} is assigned by trial and error so that the relation of the collector ion current i_c to V_a ($\fallingdotseq V_{SM}$) given in Fig. 5 is reproduced by the calculated value of I_e/I_p for each V_{SM}, assuming that most ions produced are molecular and that the ion current received by the cathode is equal to about 70% of i_e. Above values of the electron temperature seem to be very probable ones from the result in the last section.

Proton Percentage

Dimensions of the capillary must be chosen so as to give as large pipe friction for the axial diffusion of atomic hydrogen as possible, to raise sufficiently its concentration at the middle part of the capillary. Fortunately the limitation for the capillary length has proved to be not severe. The test of the proton percentage was carried out with the pyrex capillary of nearly the same dimensions as used in foregoing experiments (8mmϕ, 15 cm in length). Ions diffusing out of a small hole at the closed end of the capillary were accelerated to the axial direction by an auxiliary electrode. Though, in this case, there was no ion collector at the capillary end, the discharge behavior did not suffer an appreciable change, since the insulator wall of the capillary end was charged nearly to the cathode potential. After the discharge was continued for about half an hour, intense deep red colour radiation of atomic hydrogen was emitted from the end part of the capillary, though the colour was whitish at the other side. In this state the proton percentage was examined with the magnetic analyser and found to reach 80% at $i_a=400$mA.

Capillaries of various dimensions were examined by observing the intensity of the red colour radiation. In the case of the capillary of 8mmϕ, lengths longer than 10cm were necessary to get a satisfactory intensity of atomic radiation. Those of diameters smaller than 8mm seemed to be inferior to it.

Concerning the means of extracting the ion beam from the exit hole of pyrex capillary, some difficulties were experienced: the exit hole was melted by ion bombardment at the arc current more than several hundred mA, and the function of the wall surface to raise the concentration of atomic hydrogen was seriously destroyed by sputtering of the electrode which was used to extract ions. In the final arrangement these difficulties were solved by using quartz in the place of pyrex glass and by improving the electrode system for extracting ions.

The main process of proton production in this ion source is a following double process:

$$H_2 + e^- \rightarrow H + H + e^-$$
$$H + e^- \rightarrow H^+ + 2e^-.$$

The cross section of the above dissociation is theoretically known to be comparable with that of production of molecular ions:

$$H_2 + e^- \rightarrow H_2^+ + 2e^-.$$

The primary production of atomic ions from molecules will be negligible, because its cross section is of the order of 1/200 of that for molecular ions. It is therefore expected that the relative abundance of atomic ions to molecular ions increases proportionally with the electron density, since the production of atomic ions is essentially due to the double process. And the large proton percentage is also expected in lower gas pressure, since the mean energy of the condensed electrons will approach to the most effective region for the dissociation process (12~15 volts). These expectations were checked at the experiments in the following section (see Fig's. 9 and 10).

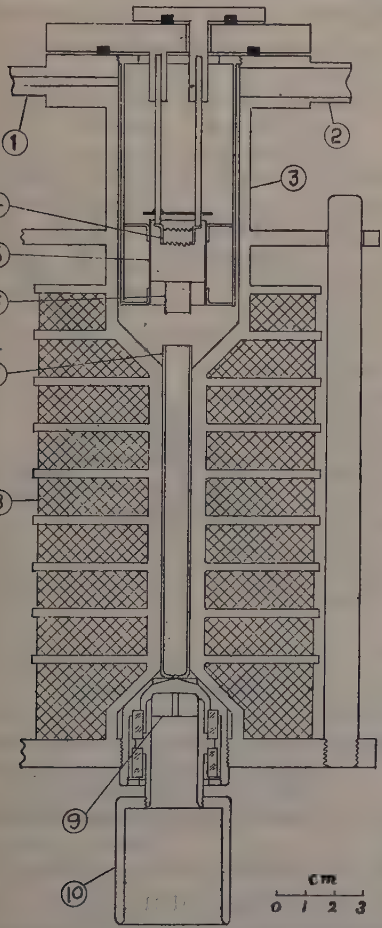

Fig. 7. Cross sectional diagram of the ion source.
(1) Gas inlet, (2) Side tube for exhaust
(3) Ion source body (copper),
(4) Cathode (5) Radiation shield,
(6) Anode (7) Quartz capillary
(8) Solenoid coil
(9) 1st. accelerating electrode (aluminium)
(10) Electrode of ion lens.

§ 3. Construction

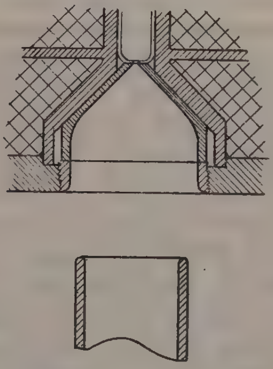

Fig. 8. An arrangement for the initial acceleration.

After the preliminary experiments, a reliable hydrogen ion source of high quality with respect to both the intensity, the proton percentage, and the gas consumpiton was constructed. As shown in Fig. 7 a quartz capillary tube (8mm in inner diameter and 11cm in length) is inserted closely into the perforation in the copper body. This construction is excellent in the mechanical ruggedness and also in the easiness for replacement of the capillary tube, but makes the cooling of the capillary wall very difficult. The several sections of solenoid coils are directly wound on the ion source body in order to produce a parallel magnetic field as strong as possible in the capillary. The largest field available with the air cooling is about 800 gauss. As the cathode, an oxide coated N_i ribbon, spirally wound or crimped, was used in this test, but with rather poor results. The life of the oxide cathode is strongly influenced by its shape. The construction of a powerful oxide cathode suitable for use in this ion source is highly desired. A side tube shown in Fig. 7 is used for the purpose of fast removal of the outgas produced at the activation of the oxide cathode or at the initial discharge. This quartz capillary source gives nearly the same result as that with the pyrex capillary, though Larmar reported that in the quartz capillary source the proton percentage was little or not better than that obtained from the metal source.[4] It is known that the surface recombination coefficient of quartz is certainly larger than that of pyrex glass, but extremely small compared to that of metals.[5] Even with quartz the gradual disintegration of the exit hole (hole diameter = 1.3mm) still occured, when the proton output is of the order of 1mA. As the method for extraction and initial acceleration of the ion beam, an arrangement shown in Fig. 8 is preferable to that in Fig. 7 on account of the absence of sputtering. In this test, however, the latter was adopted by reason of the smallness of gas consumption. The shape of electrodes was determined according to the design of an electron gun by Pierce,[6] taking the space charge effect into account, which made it possible to form the nearly parallel ion beam and actually to reduce the ion bombardment on the electrode negligibly. But it is desirable to make the electrodes from such sputteringless material as aluminium.

§4. Experimental Results

The total beam current, passing through the small hole, was converged into a fine beam of visible diameter of about 1.5mm at a distance of 20cm by the ion lens and was separated magnetically into the constituent parts. The voltages applied to the accelerating electrodes must be adjusted to the optimum values corresponding to the current intensity of the ion beam. To reduce the amount of pertinaciously residual outgas ions, a considerably long run of preliminary discharge was required.

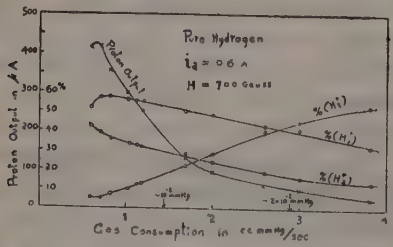

Fig. 9. Pressure dependence of the composition of hydrogen ions and the proton output.

Fig. 9 shows the pressure dependence of the composition of hydrogen ions and the proton output. At the lower pressure side the increase of the proton percentage as well as the proton output is seen. This is the fact expected in the foregoing section. We note in passing that the relative abundance of H_3^+ ions to H_2^+ ions increases roughly in proportion to the gas pressure, which suggests the following process for production of H_3^+ ion:

$$H_2^+ + H_2 \rightarrow H_3^+ + H.$$

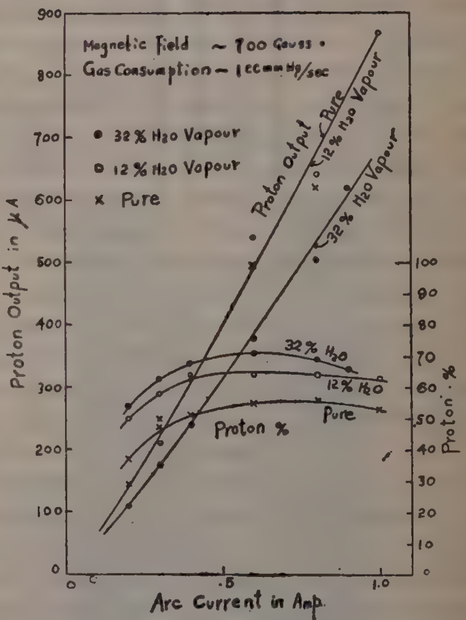

Fig. 10. Proton output and proton percentage as a function of the arc current. The effect of addition of water vapour in hydrogen gas is also shown.

Fig. 10 shows the dependence of the proton percentage and the proton output on the arc current at various concentrations of water vapour mixed in hydrogen in the gas reservoir. Since the proton production mainly depends on the double process as mentioned before, the proton percentage is first expected to increase in proportion to the arc current and then to tend to 100%. But the observed proton percentage reaches a stationary value at $i_a = 100 \sim 500$mA and shows a tendency of decrease for further increase of i_a. This fact is certainly ascribed to the change of surface condition of the capillary wall, *i.e.*, the temperature rise of the capillary wall or the stripping of the protective water film from the surface, which acts to increase the recombination of atomic hydrogen at the wall surface.5) Actually for a short interval after the increase of arc current a high value of proton percentage is obtained and then the gradual decrease to the equilibrium value follows. On the contrary, to a sudden decrease of arc current corresponds a gradual increase of proton percentage. Such features are characteristic of the temperature effect. Thus further improvement of the proton percentage is expected, if a sufficient cooling of the capillary part is employed.

The addition of water vapour is certainly effective to increase the proton percentage, but at the same time it brings about a reduction of the proton output as well as the total output. This reduction will be due to the large space charge effect of heavy impurity ions, which acts to reduce the necessary rate of ion production for maintainance of the arc discharge and so the arc voltage. This effect considerably reduces the lowest limit of the pressure region for the stable arc. The effect of addition of water vapour on the proton percentage is saturated at the partial pressure of 30% in the gas reservoir.

For the change of magnetic field, similar behaviors of the proton output and proton percentage are observed. The magnetic field available in this experiment was not strong enough to saturate the ion output.

The normal operating conditions are given in the following table.

Quartz capillary	8mmφ, 10cm in length
Ion exit hole	1.3mmφ, 0.8mm 〃
Hole in the 1st. accelerating electrode	2.5mmφ, 8mm 〃
Magnetic field at the capillary	~700 gauss
Total power consumption	<200 watts
Power consumption for coil	120 watts
〃 〃 for oxide cathode and arc	40~60 watts
Gas consumption	0.5~1 cc mm Hg per sec
Pressure in the discharge tube	~ 5×10^{-3} mm Hg

Arc current		0.4A	0.6A	0.8A
Pure hydrogen	Proton output	300μA	500μA	650μA
	Proton %	51%	56%	56%
Moist hydrogen 32%	Proton output	240μA	380μA	510μA
	Proton %	67%	71%	69%

Ratio of protons to consumed gas molecules~ 10% for 500μA Protons

1st. accelerating voltage 4~6KV

The efficiency of this ion source for producing protons is very high both in the consumption of power and in that of gas, compared to any other types of ion source hitherto reported. The output intensity of this ion source is limited by the disintegration of the exit hole. By improving this part a considerable increase of output intensity will be possible. If larger gas consumption is allowed, the diameter of the exit hole can be enlarged within the range where large reduction of gas pressure is not brought about at the end part of the capillary. moreover in this case the exit hole can stand the output of larger ion current density, so that the proton output of several or 10 mA will be possible.

The author wishes to express his sincere thanks to Prof. R. Sagane for his constant interest and kind encouragement throughout this investigation.

References

1) Larmar, Buechner, and Van de graaff: J. App. Phys. **12** (1941) 132.
2) I. Langmuir: Phys. Rev. **26** (1925) 585.
3) I. Langmuir: Phys. Rev. **33** (1929) 954.
4) E. S. Larmar: Phys. Rev. **51** (1937) 936.
5) W. V. Smith: J. Chem. Phys. **11** (1943) 110.
6) J. R. Pierce: J. App. Phys. 11 (1940) 598.

Note added in proof. Sometimes the insulation between the solenoid coil and the ion source body was destroyed by the high voltage pulse induced by the accidental discharge in the accelerating gap. To protect the insulation from this trouble, it was effective to insert a capacitance of the order of I$_\mu$F between them.

JOURNAL OF THE PHYSICAL SOCIETY OF JAPAN Vol. 7, No. 3, MAY—JUN., 1952

Quantummechanical Computations of the Lattice Energy and the Lattice Constant of LiF Crystals

Jiro YAMASHITA

Institute of Science and Technology University of Tokyo

(Received November 15, 51)

We have worked out the electronic state of F^- ion in LiF crystals by means of the variational method with the use of the analytical wave-function of 2p type with three parameters for the outermost electrons of F^- ion. We see the charge distribution of negative ion is somewhat contracted within the crystal. The lattice energy, the lattice constant and the compressibility of LiF crystals are found to become of 239 Kcal/mol, 2.00 Å and 1.96×10^{-12} cm²/dyne respectively, which results are compared with the observed values of 240 Kcal/mol, 1.99 Å and 1.4×10^{-12} cm²/dyne respectively.

§1 Introduction

The purely quantum-mechanical computations of the cohesive energies of ionic crystals have been carried out on sodium chloride[1] and on lithium hydride[2] so far. Lardshoff based his work on a Heitler-London approximation in which he used the solutions of Fock's equations for the free ions of Na^+ and Cl^- respectively. The good agreement between his results and the experiment indicates that the Heitler-London method is fairly good for the ground state of such ionic crystals. Now the cohesive energy of ionic crystals mainly consists of two parts, that is, Coulomb energy and exchange energy. The latter contains the overlapping exchange integral, which value depends quite sensibly on the behavior of the wave function of the outermost electron of the negative ion. Since the mentioned authors used the wave function of free ions, the deformation effects of the ions in the crystalline fields were completely neglected in their computations, which seems not to correspond to the real situations. In order to improve such points, we shall compute the lattice energy, the lattice constant and compressibility of LiF crystals, taking into account the deformation of electronic wave functions by the variational method.

§2. Wave Function

For the 1s-state of Li^+ ion we used the Hartree wave function[3], because the 1s electrons are bound tightly to the nucleus and the effects of the crystalline field may be neglected approximately. For the 1s and 2s state of F^- ion we adopted the Hartree wave functions[4], because their contribution to the binding energy through the exchange effect is estimated to be considerably smaller than that of 2p-electrons of F^- ion. For the trial function of 2p-electrons of F^- ion the analytical functions with three ajustable parameters α, β, B are taken as follows.

$$\left.\begin{aligned}\psi_x &= A(e^{-\alpha r}+Be^{-\beta r})r^2\sin\theta\cos\varphi\\ \psi_y &= A(e^{-\alpha r}+Be^{-\beta r})r^2\sin\theta\sin\varphi\\ \psi_z &= A(e^{-\alpha r}+Be^{-\beta r})r^2\cos\theta\end{aligned}\right\} \quad (1)$$

where A is determined from the normalization condition. According to Slater[5] the mentioned wave functions may be considered to be pretty good approximation for the 2*p*-electrons of F^- free ion. As mentioned above, in LiF crystals the wave function may be deformed by the crystalline field, which contraction may give rise to the change of the value of the above variational parameters. Although the modification of the spherical symmetric charge distribution of each of the ions within the crastal shall be generally expected to be realized, we shall tentatively neglect such modification in the following computation. For the preliminary evaluation the total energy of a free ion computed with the use of these wave functions has been minimized to determine the mentioned parameters α, β and B for a free ion. Zener[6] has already adopted the variational method with the more simple trial function $P=Ar^2$

$\exp(-\alpha r)$ for the similar problem. So in our case we have only to do the similar method of procedure, which leads to the following result.

$$\alpha=3.05, \qquad \beta=1.20, \qquad B=0.087$$

Now, for the determination of the $2p$ wave function of F^- ion within LiF crystals, we have to minimize the total energy of the crystal instead of the isolated ion. As usual, the total energy of the crystal contains not only the energy of each isolated ion, but also their mutual interaction energy, which consists of Coulomb- and exchange-energies. After the elementary but rather tedious calculations according to Landshoff's method of procedure⁷⁾, we have determined the value of parameters for certain lattice distance by the use of the variational method. (See Table I, in which we use the atomic unit.)

Table I

a	α	β	B	ΔE_c
3.5	3.05	1.25	0.090	0.0116
3.785	3.05	1.25	0.095	0.0042
4.0	3.05	1.25	0.098	0.0023

As seen in the above table, the charge distribution of the negative ion is somewhat contracted in the crystal as compared with the free state and further its contraction depends on the lattice distance. In Table I we have also tabulated the energy change of F^- ion due to contraction of its charge distribution, which contraction energy is denoted by ΔEc. Although the contraction energy becomes positive, the exchange energy is reduced due to the contraction, which situation is found to attain the minimum of the total energy at the values of parameters mentioned above. When we calculate the diamagnetic susceptibility χ of F^- ion with the use of the Hartree function⁴⁾, the variational wave functions for the free state and for the crystalline state, it follows:

$$\chi\,(\text{Hartree})=-15.6\times10^{-6}$$
$$\chi\,(\text{free}\quad)=-13.3\times10^{-6}$$
$$\chi\,(a\,;\,3.785)=-12.6\times10^{-6}$$

Unfortunately the observed values are at variance with other according to the observers as seen in Table II. Generally speaking, the consideration of the mentioned charge contraction of an ion within the crystal is seen to give a rather plaubsible result for the diamagnetic susceptibility. In view of the well-known fact that χ-value of ionic crystals is rather smaller than that calculated from Hartree-Fock wave functions, such discrepancies may be considered to be avoided through taking into account the contraction and deformation of the charge distribution of ions within the crystals since the contraction of charge distribution has reduced χ value of LiF about five percents as mentioned above.

Table II

Observer	$\chi\times10^{-6}$
Kido	−12.2
Ikenmeyer	−13.9
Pauling	−10.3

§3. Cohesive Energy, Lattice Constant and Compressibility

We have computed the cohesive energy, the lattice constant and the compressibility of LiF crystal using the following three kinds of $(2p)$ wave functions of F^- ion, i.e., (1) Hartree wave function, (2) free ion wave function determined by the variational method and (3) variational wave function which takes into account the charge contraction by crystalline field. As the computations are performed in a quite similar way as that of Landshoff, we do not repeat here the detailed process any more except for some comments regarding a few differences between his and ours.

Landshoff computed the exchange integral of NaCl at two values of a; 5.0 and 6.0, and determined the values at other points by

Summary of Results

Wave function of F ion	Cohesive energy (Kcal/mol)	Lattice constant ($\times10^{-8}$ cm)	Compressibility (10^{-13}cm²/dyne)
(1) Hartree case	208	2.09	3.96
(2) free state case	250	2.01	2.24
(3) crystalline state case	239	2.00	1.96
observed value	240 242	1.99	1.4

interpolation. In order to improve the interpolation-procedure, however, we have computed the values at three values of a; 3.5, 3.785, and 4.0. Although he considered only the Na^+-Cl^- interaction besides Madelung's energy, we have considered both Li^+-F^- and F^--F^- interaction together with the contraction energy. The obtained results for three cases have been described in the following table. (Also c.f. Table III).

By taking into account the charge-contraction of F^- ion within the crystal, a better agreement between the theory and the experiments has been obtained, as seen in the above table. As Table III shows, the contributions from the next-nearest neighboring ions are found to be quite small in our case. In conclusion, we may be right to say that the charge distribution around each ion in LiF crystal will not greatly differ from the purely ionic state.

The author wishes to express his sincere thanks to Prof. T. Muto for his continued interest and abvice during the course of this work.

Appendix

a: the distance of nearest ions,
M: Madelung energy,
$\varDelta M$: the correction of electrostatic energy between Li^+ ions and F^- ions,
$\varDelta E_P$: the exchange energy between Li^+ ions and $(2p)^6$ electrons of F^- ions,
$\varDelta E_S$: the exchange energy between Li^+ ions and $(2s)^2$ electrons of F^- ions,
B and C: the same integrals as in Landshoff's paper,
$\varDelta E_P=6\,(B+C)$,
$\varDelta M_1$: the correction of electrostatic energy between F^- ions and F^- ions,
$\varDelta E_1$: the exchange energy between F^- ions and F^- ions,
$\varDelta E_c$: the contraction energy,
E_t: the total energy.

Table III (A) Case (1)

a	M	$\varDelta M$	$\varDelta E_p$	$\varDelta E_s$	E_t
3.5	−0.4993	0.0352	0.1864	0.0111	−0.2666
3.785	−0.4617	0.0196	0.1116	0.0037	−0.3268
4.0	−0.4369	0.0125	0.0888	0.0027	−0.3329

The interpolation formula:

$$E_t(r)=-\frac{1.7476}{r}+[65.15+87.55\,(r-3.5)\,(r-4.0)]e^{-1.61r}$$

(B) Case (2)

a	M	$\varDelta M$	$6B$	$6C$	$\varDelta E_p$
3.5	−0.4993	0.0190	0.2058	−0.0717	0.1341
3.785	−0.4617	0.0104	0.1204	−0.0425	0.0779
4.0	−0.4369	0.0066	0.0894	−0.0288	0.0606

a	$\varDelta E_s$	$\varDelta M_1$	$\varDelta E_1$	$\varDelta M_1+\varDelta E_1$	E_t
3.5	0.0111	−0.0630	0.0559	−0.0071	−0.3422
3.785	0.0037	−0.0321	0.0327	0.0006	−0.3691
4.0	0.0027	−0.0178	0.0208	0.0030	−0.3640

The interpolation formula:

$$E_t(r)=-\frac{1.7476}{r}+[33.95+47.56\,(r-3.5\ (\ -4.0)]e^{-1.563r}$$

(C) Case (3)

a	M	$\varDelta M$	$6B$	$6C$	$\varDelta E_p$	F_s
3.5	−0.4993	0.0129	0.1658	−0.0579	0.1079	0.0111
3.785	−0.4617	0.0067	0.1618	−0.0370	0.0648	0.0037
4.0	−0.4369	0,0044	0.0750	−0.0260	0.0490	0.0027

a	$\varDelta M_1$	$\varDelta E_1$	$\varDelta M_1+\varDelta\varDelta E_1$	$\varDelta E_c$	E_t
3.5	−0.0528	0.0462	−0.0066	0.0116	−0.3624
3.785	−0.0270	0.0259	−0.0011	0.0042	−0.3834
4.0	−0.0162	0.0168	0.0006	0.0023	−0.3775

The interpolation formula:

$$E_t(r)=-\frac{1.7476}{r}+[46.64+60.82\,(r-3.5)\,(r-4.0)]e^{-1.666r}$$

References

1) R. Landshoff: Zeits. f. Phys. **102** (1936) 201.
2) A. Hylleraas: Zeits. f. Phys. **63** (1930) 771.
3) J. Hargreaves: Proc. Cambr. Phil. Soc. **25** (1928) 75.
4) D. R. Hartree: Proc. Roy. Soc. **151** (1935) 96.
5) J. C. Slater: Phys. Rev. **36** (1932) 33.
6) C. Zener: Phys. Rev. **42** (1930) 51.
7) R. Landshoff: loc. cit.

JOURNAL OF THE PHYSICAL SOCIETY OF JAPAN Vol. 7, No. 3, MAY—JUN., 1952

External Photoelectric Emission of Barium Oxide

Kin-ichi NOGA and Shoji KAWAMURA
Matsuda Research Laboratory, Tokyo Shibaura Electric Co.
Kawasaki-shi, Kanagawa-ken, Japan

(Received December, 4, 1951)

The spectral distribution of photoelectric yield and its temperature dependency were measured on the barium oxide, in the form of a sprayed coating on a nickel base. When sample was held at room temperature, the photoelectric emission showed an enhanced effect, that is, the photo-current from the irradiated sample increased with time. The photon energy giving the maximum enhanced effect lies at 2.3ev coincident with the peak of optical absorption by colour centers in barium oxide. This enhanced effect disappeared by warming the sample to 400°K. The results are discussed in terms of an energy level structure of barium oxide.

§1. Introduction

In 1941, Nishibori, Kawamura and Hirano1) have reported studies of the photoelectric emission from BaO which indicate an energy for the donor level lying by 1. 7ev below vacuum potential. On the other hand, a recent development in Sproull's method for preparing a single crystal has given new knowledge which informs us that an optical absorption has its maximum at $h\nu\sim$2.3ev in BaO containing colour center type lattice defects. If both the photoemission and the optical absorption were attributed to one and the same donor level, the photoelectric threshold should be located in the energy higher than the peak of optical absorption. The contradiction between these two results makes it necessary that the spectral distribution of photoelectric yield and its temperature dependency should be determined over the wide range of incident photon energy.

§2. Experimental

Figure 1 shows the form of the tubes used in this work. Barium carbonate, dispersed in a nitrocellulose binder, was sprayed on a cathode sleeve for an usual radio tube. The anode cylinder, also of pure nickel, was provided with a longitudinal slot to permit irradiation and observation of the oxide surface. The electrode assembly was sealed into an glass envelope having a fused quartz window just before the slot in anode. After exhausting and baking out, the cathode was converted from carbonate to oxide by heating slowly to about 1200’K, the heating being continued until gas evolution has substantially ceased. A small fraction of the available getter was then flashed, and the tube sealed off.

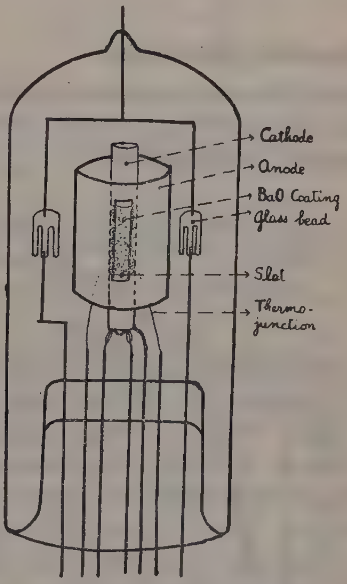

Fig. 1.

Temperatures of the oxide coating were measured by using a nickel-tungsten thermocouple welded on a sleeve.

A spectrometer with a crystal quartz prism was used as a monocrometer to illuminate the oxide. As light sources, a high pressure mercury arc and a tungsten lamp were used to cover the wide range of wave length from 3000 Å to 10,000 Å. The light was focused on the entrance slit of the monochrometer and, after passing through it, focused again on a thermopile for energy measurement and on the oxide cathode alternatively. Both are located side by side in a shielded and lighttight box.

Photo-current flowing into the anode was amplified by means of DuBridge-Brown type balancing circuit with an electrometer tube FP-54 and read by a current sensitive galvanometer. Precausion was taken so as to insure that the photoelectric currents were not limited by the electrical conductivity of the samples. The emission saturated at an applied voltage below 50V. Currents were proportional to the intensity of the incident radiation over the range used in this experiment.

§3. Spectral Distribution

Figure 2 shows the spectral distribution of external photoelectric emission from a representative BaO specimen.

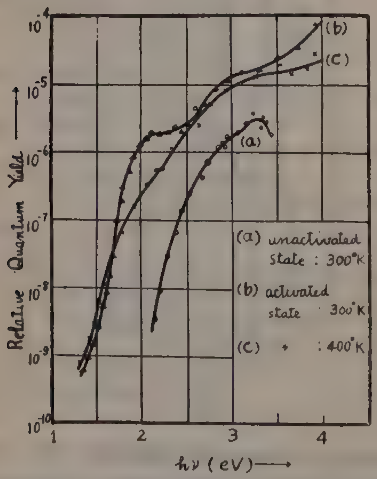

Fig. 2.

The barium oxide, after the exhausting and conversion treatment, has low thermionic activity. Photoemission measurement was made at 300°K for this unactivated state. The result is shown by curve (a). It was then activated by heating the cathode to about 1200°K and the observation repeated at 300°K and 400°K. Thus, curves (b) and (c) are obtained for the activated state, corresponding to two measurements at 300°K and 400°K respectively. To obtain a measure of the state of activation, the saturated emission from the cathode was determined as a function of temperature and Richardson plots were made before and after activation. These plots are shown in Figure 3. The change in thermionic work function determined from the slope of these curves is small during the course of the activation, but the change in thermionic emission from the unactivated to the activated state amounts to about a factor of 50.

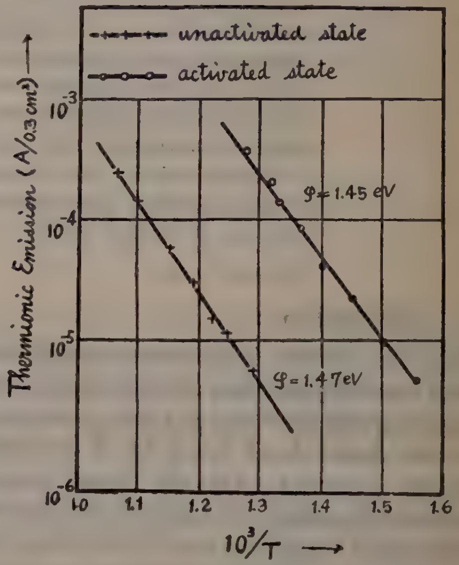

Fig. 3.

In Figure 2, a considerable increase in emission takes place during the activation treatment and the shape of all curves suggests a continuous rise in emission with increasing quantum energy and plateau at $h\nu \sim 3.1$ev. Moreover, curve (b) alone has another hump at $h\nu \sim 2.5$ev. The low energy tails of photoemission curves have often been fitted to Fowler plots. This was tried for our measurements, also, but the fit obtained was very poor. This does not seem especially significant, since present semiconductor theory does not lead one to expect such a fit.

In room temperature measurement, photocurrents increased with time (we will call such a phenomenon "enhanced effect"), but this effect disappeared completely at 400°K. In the unactivated state, we also could not find this enhanced effect. This is a reason for the above mentioned result that the curve (b) has a hump at $h\nu\sim$ 2.5ev, while the curves (a) and (c) have not. A survivor of the enhanced effect makes it difficult to obtain a temperature dependency of the spectral distribution from curves in Figure 2. However, utilizing the fact that the enhanced effect disappear by warming the sample to 400°K, we can obtain a general tendency with which the spectral distribution depends on cathode temperature. A procedure of measurements is as follows: photocurrents are measured at cathode temperatures of 300°K and 400°K respectively keeping an incident radiation at constant in the value of photon energy and this process is repeated at several photon energies between 1.5 and 3.0ev. The result obtained is shown in Figure 4.

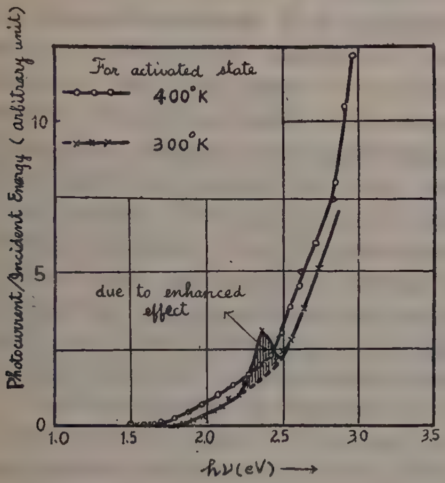

Fig. 4.

Although the enhanced effect could not be eliminated thoroughly, this figure shows that the spectral distribution curve shifted bodily towards lower energy side owing to a rise in temperature. This fact is in discord with the result of early work done by Nishibori et al., which indicates a temperatnre dependency only in the low energy tail. But, near the threshold value of photon energy, photoemission per unit incident energy rises linearly with increasing quantum energy in the same way as their result. This behavior is shown in Fig. 5 which represents the same curves as in Fig. 4 with enlarged scale.

Extrapolation of the linear part of these curves to abscissa falls on the photon energy of 1.7—1.8ev as is shown in Fig. 5. Nishibori et al. have assigned this value to a photoelectric work function and emphasized the consistency with other results of thermionic emission and electrical conductivity. In their conclusion, however, Franck-Condon principle is not taken into account. According to it rather higher energy is required for a photoelectric work function. In addition, optical absorption by colour center type lattice defect in barium oxide has its maximum at $h\nu\sim$2.3ev, which we knew from the articles kindly furnished by Dr. R.L. Sproull.[2] If both the photoemission and the optical absorption were attributed to one and the same donor level, a photoelectric work function should be larger than 2.3ev by some quantity corresponding to an electron affinity. From the basis of theoretical consideration, it seems likely that the photon energy of 1.7ev should rather be attributed to another origin.

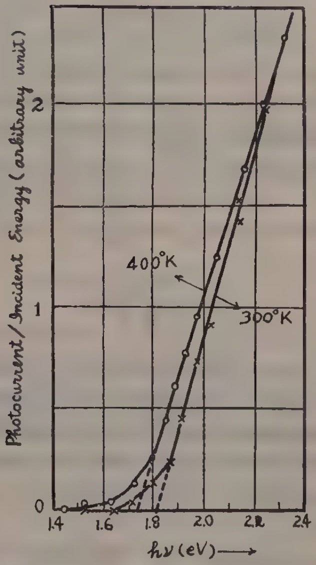

Fig. 5.

§ 4. Enhanced Effect

As is shown in Fig. 2 and Fig. 4, the photoemission from the cold oxide measured in the lower energy region shows a large increase with a peak at 2.3ev—2.5ev, in comparison with that of heated oxide. This phenomenon has its origin in enhanced effect, that is, the photocurrent increases with time and approaches to saturation after about 15 minutes duration of irradiation. When the irradiation stopped (except for the neglisible periods required to measure yield), the photocurrent decreases with time. In the case of room temperature, it decays to its original value in about two hours. This decay increases rapidly with higher temperature. At 370°K, the rise in current with time disappears. These behaviors are shown in Fig. 6.

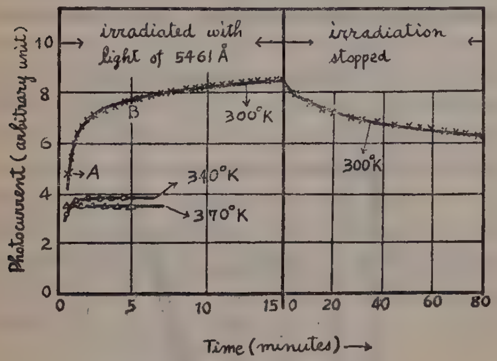

Fig. 6.

As a measure of enhanced effect, we adopted a ratio of photocurrent after a lapse of 5 minutes (point B in Fig. 6) to that after 15 seconds (point A in Fig. 6) from the beginning of irradiation. The curves similar to that in Fig. 6 are measured on the cold oxide at several values in incident photon energy. Then, a dependency of the enhanced effect upon the incident photon energy is obtained. The result is shown in Fig. 7. The curve has a shape similar with the absorption band of a colour center and maximum in both curves lie at 2.3ev coincidently. The curve of the optical absorption obtained by Kane is also shown in this figure with dotted line.

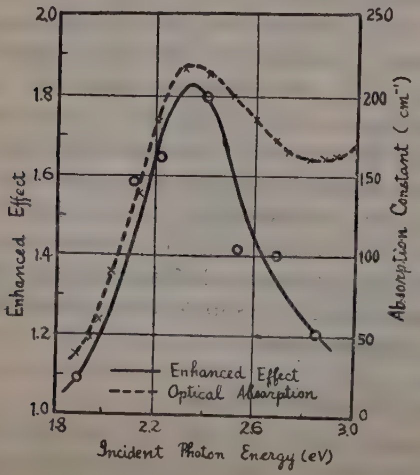

Fig. 7.

The photocurrents in this region may be increased by irradiation or decreased by annealing at will and these changes are reproducible.

§5. Discussion

Although it is perhaps too early to attempt a complete interpretation of these observation, it seems likely that the shallow trapping level lying just below the bottom of conduction band together with low lying donor level will account for the enhanced effect. Following Kane's opinion that the dotted curve in Fig. 7 may be ascribed to the optical absorption by color center and paying an attention to the coincidence of peak of the enhanced effect with that of optical absorption, the following mechanisms may be assumed for enhanced effect.

An electron in a donor site is raised to its excited level by absorbing an incident photon and then transferred by thermal agitation into the conduction band even at room temperature. This electon is captured by shallow trapping level lying just below the bottom of conduction band. Second absorption of photon energy during the periods of its stay in the trapping level causes this electron to be emitted from the surface.

From such a two-stage process, the increase of photocurrent with time and its delayed approach to saturation, the value of which is considered to correspond to an equilibrium state under the condition of measurement, will be understood. This process will also account for the coincidence of peaks of both curves in Fig. 7. A rise in temperature should increase the probability that the trapped electron would be transferred into the conduction band thermally and fall down to an vacant donor site before it absorbs a next photon, resulting in disappearance of the enhanced effect.

According to the above mentioned hypothesis, the depth of a donor level must be 2.3ev below the bottom of conduction band neglecting the small energy gap between the conduction band and the excited state. From this, the energy rather higher than 2.3ev should be required for the direct ionization of an electron in a donor site, in discord with Nishibori et al.'s consideration.

According to the rough estimation by Kubo[3], in which the lattice is replaced by the continuous medium, an optical activation energy (E_0) of electron from donor level to conduction band is related to a thermal activation energy (E_t) by following equation;

$$\frac{E_t}{E_0}=\frac{5k+11k_0}{15k+k_0}$$

where k, k_0 are static and optical dielectric constant respectively. Assuming the appropriate values for k, k_0 and E_0, E_t is able to be estimated from this equation. For the case $k=34$, $k_0=4$ and $E_0=2.3\text{eV}$, this becomes $E_t=1.0\text{eV}$. On the other hand the thermionic work function obtained on the same sample is 1.45ev as is shown in Fig. 3. The electron affinity estimated from these results is 0.95ev, not so far from the values which seemed to be currently favored. So the origin of both the thermionic and photo-electric emission may be attributed to the same donor level, as is expected from the parallelism in activity.

A further detailed interpretation of the photoemission data is rather hazardous until an observation can be made on the photoconductivity of BaO over the same range in quantum energy.

The authors wish to express their indebtedness to Professor H. Kawamura and Dr. J. Yamashita and to their other colleagues at Matsuda Research Laboratory for numerous suggestions and discussions. In addition they have been profited by the articles which Dr. R. L. Sproull sent kindly to us.

References

1) E. Nishibori, H. Kawamura and K. Hirano: Proc. Phys.-Math. Soc. Japan, **23** (1941) 37.

2) R. L. Sproull, J. A. Krumhansl, W. W. Tyler and E. O. Kane: Technical Report No. 3, Contract N 6-ORI-91 Task 11 (1950) (Office of Naval Research).

3) R. Kubo: J. Phys. Soc. Japan. **3** (1948) 254.

JOURNAL OF THE PHYSICAL SOCIETY OF JAPAN Vol. 7, No. 3, MAY—JUN., 1952

On the Energy Loss of Fast Electron

Seizaburo KAGEYAMA and Kazuaki NISHIMURA

Physical Institute, Tokyo University of Literature and Science

(Received December 21, 1951)

The energy distribution, the most probable and the average energy loss of electrons passing through matter were measured with a 180° focusing spectrometer of approximately 0.7% resolution, using K conversion lines of 606, 1414 and 1761 KeV γ-rays of RaC' as homogeneous electron source and the various thicknesses of Al, Cu, In and Pb as stopping materials.

The observed value of the most probable energy loss was in accord with Landau's theory within the limits of our experiment. That of the average energy loss, however, was not in accord with his theory but with Bloch's formula. The width of the energy distribution curve obtained was considerably greater than predicted by Landau. However, on the high energy side of the peak, the shape of the curve predicted by Landau's theory was surely better than that of White and Millington's.

§1. Introduction

The classical theory[1] failed to give a quantitative explanation of the observed straggling of β-particle[2]; so we were obliged to use the experimental straggling curve obtained by White and Millington. Recently, this problem was again treated theoretically by Landau[3] and Blunck-Leisengang[4].

According to Landau, the distribution function is expressed by a combination of a universal function $\varphi(\lambda)$ of a non-dimensional variable λ and a variable ξ, depending upon the stopping material and the velocity of electron. The distribution function, therefore, is expected to be equal for equal value of ξ, even in the case when different stopping materials and different velocities of electrons are used. Landau also obtained the following representation for the most probable value of the energy loss of the electron passing through a sheet of thickness x:

$$\varDelta_p=\xi\left(ln\frac{\xi}{\varepsilon}+0.37\right)$$

where $\xi=x\dfrac{2\pi Ne^4\rho\Sigma z}{mv^2\Sigma A}$,

$$\varepsilon=[I^2(1-\beta^2)/2mc^2\beta^2]\exp(\beta^2)$$

and m, e, v are the mass, charge and velocity of the electron respectively. N is Avogadro's number, ρ the density of the substance, ΣZ sum of the atomic numbers of the molecule in the substance, ΣA sum of the atomic weights.

Warshaw and Chen[5] compared the above formula with the K conversion line of Ba^{137} (624 KeV) and stated that the agreement between Landau's calculation and their own experimental results was excellent. However, the width of the energy loss distribution curve obtained by Birkhoff[6] with the same conversion line as Warshaw and Chen's was considerably greater than predicted by the theory, and was in accord with the resuls obtained by White and Millington.

In the previous experiment[7], we have recognized a minor discrepancy between the distribution curve calculated from White-Millington's fundamental distribution curve and our experimental results. So we have precisely examined the energy distribution curve of the electrons straggled through the various thicknesses of Al, Cu, In and Pb, using the K conversion electrons of 606, 1414 and 1761 KeV γ-rays of RaC', and have compared our results with Landau's theory and also with White-Millington's observation. The average energy loss was also measured and compared with Bloch's calculation.

§2. Experimental Arrangement and Procedure

We have used the same magnetic spectrometer as described in the previous paper[8]. But, for the convenience of the exchange of stopping materials, the β-ray source was placed immediately in front of the entrance slit outside of the vacuum chamber. This slit was about 1 mm in breadth and 10 mm in height, and was covered with a mica foil of about 1 mg/cm² in thickness. The spread of electron beams was restricted by the central slit to about 1° with respect to the normal direction at the surface of the stopping material. With Rn sealed in a small glass of about 5 mg/cm² in thickness as source, the energy distribution curves of transmitted main K conversion lines of RaC' were measured. The G-M counter used was the same one as in the previous experiment and had a mica window of 1 mg/cm² in thickness.

The strength of the magnetic field was determined only relatively through the exciting current corresponding to the conversion lines of 1240K, 1414K, L and 1761K as described in the previous paper[8)].

In order to facilitate the measurement of the distance between the peak of incident electron and that of the energy distribution curve of transmitted electron, we have used according to White and Millington the stopping materials punched with 10～8 holes of 0.2 mm in diameter at approximately equal intervals. The number of holes is adjusted to give no consequential disturbance on the energy loss distribution curve but to give only the peak of incident trace. But, in the case of much thinner foil of Al and Cu, this method could not be successful, and the measurements were made with and without the stopping materials. The stopping materials were Al, Cu, In and Pb foils of the following thicknesses:

Al:	6.0	12.0	24.0	36.0	48.0 mg/cm²
Cu:	6.4	12.8	25.6	38.3	51.1 mg/cm²
In:		14.7	25.8		48.7 mg/cm²
Pb:	10.0	18.1	29.4	35.5	45.0 mg/cm²

§3. Experimental Results and Discussion

A. The Energy Distribution Curve of Straggled Electrons

The experimental results on 1414K conversion electrons passing through Al foil are given in Fig. 1 as an example. The experimental points were corrected for the superposition of the straggled K conversion electrons of 1379 KeV γ-rays, using the relative intensity obtained in the previous experiment. The number attached to each distribution curve denotes the superficial mass of the imposed Al foil in mg/cm². The ordinate gives the intensity in arbitrary unit and the abscissae gives Hρ values in gauss-cm. The value of the dimensionless variable λ introduced by Londau is also given for the convenience of comparison with his calculation.

To compare the experimental distribution curve with the theoretical one, we must recalculate the latter, taking into consideration the condition of our experimental arrangement. This calculation was graphically done in the same way as described in the previous paper[9)] with consideration of the additional effect of glass and a mica window.

The theoretical distribution curve was adjusted to the observed one at the peak and

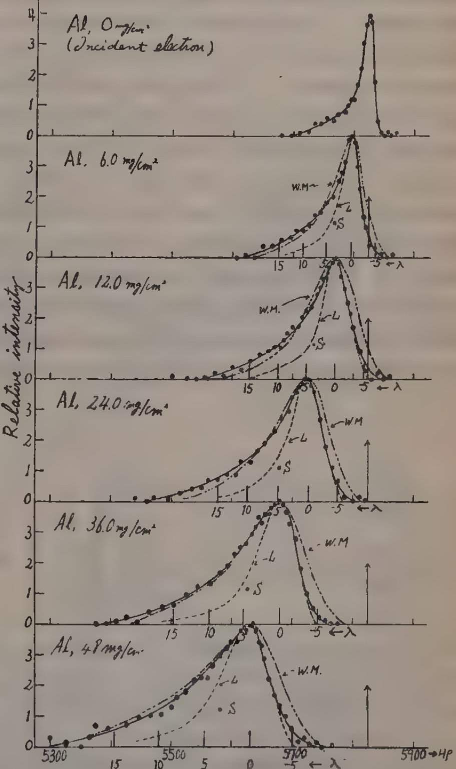

Fig. 1. Energy distribution curves of the straggled 1414K conversion electron passing through the various thickness of Al. Curve L. and W. M. are Landau's and White-Millington's distribution curve corrected for the additional effect of the glass of Rn source and the mica window respectively.

in the figure was shown with the curve L. The experimental distribution curve obtained by White-Millington was also re-calculated by the same method and shown with the curve W. M. in the same figure.

The width of the energy loss distribution curve obtained was considerably greater than predicted by theory, and was in accord approximately with White-Millington's curve. But it will be noticed that the experimental points on the high energy side of the peak are in good accord with the theoretical curve but not with White-Millington's curve; whereas the circumstance is vice versa on the low energy side of the peak.

Similar comparison was made with experimental results on the various thicknesses of Cu, In and Pb, with 606, 1414 and 1761 K conversion electrons used. The results on 18.1 mg/cm² of Pb for 1414 K and 12 mg/cm² of Al for 606 K were shown in Fig. 2 and 3. For the latter, to make easy the comparison with Birkhoff's result, the distribution curve was plotted against λ. From these measurements, we have ascertained that the conclusions described above do not change with the energies of electrons and the stopping materials. However, in the 606 K line the distribution of the continuous back-ground was largely influenced by the thickness of stopping material and in the 1761 K line the intensity was rather weak, so that the experimental results in these two lines were not so accurate as in the case of 1414 K.

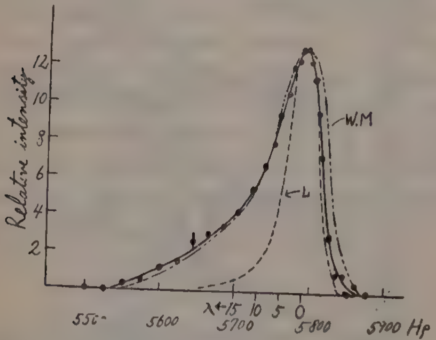

Eig. 2. The straggling curve of 1414 K conversion electron passing through 18.1 mg/cm² of Pb. The theoretical curve L is calculated from Landau's theory considering the additional effect of the glass and the mica. Curve W. M. is the experimental distribution curve calculated by White and Millington under the same condition.

Birkhoff's result was not in accord with Landau's distribution curve even on the high energy side of the peak, on the contrary to our results. But we found no exception in any measurements, so believe that the theoretical explanation on this part is rather reasonable. On the low energy side of the peak, the discrepancy between the theoretical distribution curve and the observed one is very large and could not be attributed to any experimental errors. The ratio of the half-value widths of the two curves was about 1.8±0.2.

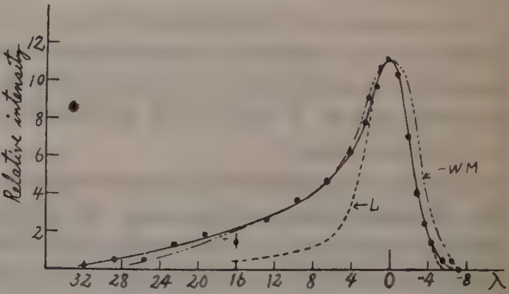

Fig. 3. The straggling curve of 606 K conversion electron passing through 12.0 mg/cm² of Al. Curves L. and W. M. gave the same meaning in Fig. 2.

B. The Most Probable Energy Loss

Since the energy degradation of electrons measured is small compared with the primary energy of electrons, the difference of the correction for the resolution of each curve is negligibly small. Moreover, since our spectrometer has a very high resolution as shown in Fig. 1, the distance between the peaks of the straggled and the incident distribution curve may be considered to correspond to the increase of the most probable energy loss by the imposed stopping material. In our case these distances were easily measured with an accuracy of 3~7 gauss-cm.

To compare with the theoretical calculation, we must correct the straggling effect by the glass of Rn source and the mica window. This correction was obtained graphically assuming the values of ξ are equal for the same superficial mass for glass, mica and Al. The comparison of the observed most probable energy loss with the theoretical value calculated from Landau's formula are given in

Fig. 4. The experimental results were in accord with the calculation with in the experimental error. The same results were also obtained with 606 K and 1761 K conversion lines.

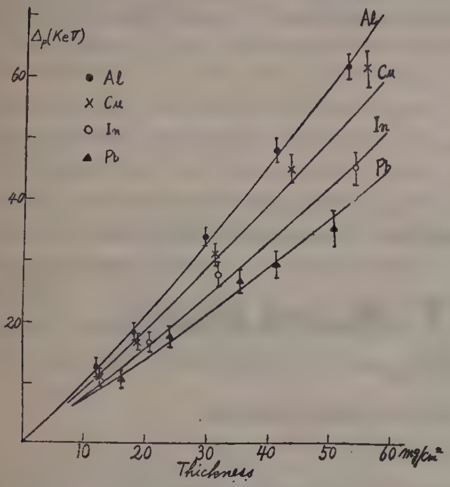

Fig. 4. The most probable energy loss. Curves are theortical (Eq. (1)).

C. The Average Energy Loss

The average energy of the straggled electrons was obtained by determining the center of gravity of the area under each distribution curve and was shown with "S" in Fig. 1. The center of gravity of the unstraggled distribution curve was found by the same method described in the case of the most probable energy loss. The experimental points plotted in Fig. 5 were measured from this extra polated point. But the accuracy of the determination of the center of gravity is not so accurate as that of the most probable energy loss, for the electrons suffering large energy losses are apt to be missing in the continuous back-ground.

To compare the observed average energy loss with the theoretical value, we must remember that the theoretical value is the average energy loss of all the straggled electrons, but the observed value is that of the straggled electrons scattered only by 1° with respect to the direction of primary beam. However, the deflection of electron is caused mostly by the elastic collision with the nucleus, while the energy degradation is generally due to the collision with the atomic electrons, by which the deflection of the β-particle would not be very large. Thus, if the length of the electron path in the stopping material were almost equal, we could expect roughly the same distribution of the straggled electron on the surface of stopping material both in theory and in experiment.

Landau suggested that the center of gravity should lie approximately by one unit of λ to lower ordinate of the most probable energy. Our findings were not in accord with his prediction. The experimental points were far more than one unit of λ away from the most probable energy ordinate to low energy side.

The effect of polarization properties of the stopping material[10)] was negligibly small for the energy of β-particle used by us. Therefore, the experimental results were compared only with Bloch's formula in Fig. 5. The experimental points were in accord with the calculated value within our experimental error.

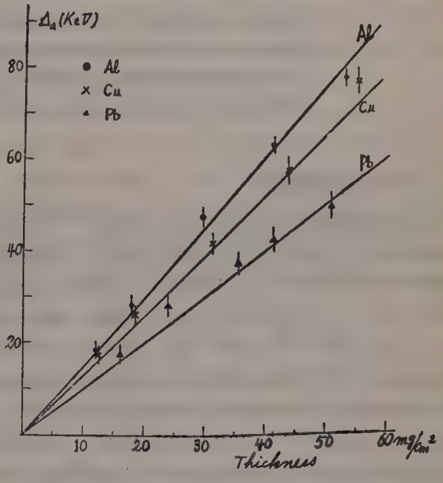

Fig. 5. The average energy loss. Curve are theoretical average energy loss according to Bloch.

In conclusion, the present authors express their thanks to Professor Yoshio Fujioka for his encouragement, and to Professor Mitsuo Miwa for his valuable discussion and helpful suggestions. The author (S. K.) wishes to express cordial gratitude to Dr. S. D. Warshaw for his kindness in sending Landau's paper, also to the Japanese Foundation for Cancer Research for the supply of Rn through Dr. Kenpo Tsukamoto and Mr. Yoshio Onai with helpful interest; also to the Ministry of Edu-

cation for financial aids.

References

1) E. J. Williams: Proc. Roy. Soc. **125** (1929) 420.
2) P. White and G. Millington: Proc. Roy. Soc. **120** (1928) 701.
3) L. Landau: J. Phys. USSR. **8** (1944) 201.
4) O. Blunck and S. Leisengang: ZS. Phys. **128** (1950) 500.
5) S. D. Warshaw and J. L. Chen: Phys. Rev. **80** (1950) 97.
6) R. D. Birkhoff: Phys. Rev. **82** (1951) 448.
7) S. Kageyama: J. Phys. Soc. Japan **6** (1951) 285.
8) M. Miwa and S. Kageyama: J. Phys. Soc. Japan. **5** (1950) 416.
9) S. Kageyama: J. Phys. Soc. Japan **7** (1952) 93.
10) O. Halpern and H. Hall: Phys. Rev. **73** (1948) 477.

JOURNAL OF THE PHYSICAL SOCIETY OF JAPAN Vol. 7, No. 3, MAY—JUN., 1952

Precise Measurement of the F^{19} Magnetic Moment

Teinosuke KANDA*

Department of Physics, Faculty of Science, Osaka University

(Received December 24, 1951)

Using a new circuit, a precise measurement of the frequency ratio of nuclear magnetic resonance of fluorine nucleus to that of proton in HF aq. was performed at the magnetic field of about 1800 gauss. The value $\nu_F/\nu_H=0.940816$ was obtained with the smallest error ± 0.000009 compared with the values by other research workers.

§1. Introduction

The magnetic moment of the F^{19} has been measured by many workers with the nuclear magnetic resonance method. After the tabulation by J. E. Mack,[1] new data was added by R. E. Sheriff and D. Williams.[2] The present author intended to measure the magnetic moment of various nuclei and the first result on the F^{19} is reported here. A brief report was already published in the Phys. Rev.[3]

§2. Experiments

(a) Magnetic Field.

The magnetic field is supplied by an electromagnet whose pole faces having each an area of 15 cm × 15 cm are finished to 0.01 mm and are kept parallel by three distant pieces of 40±0.01 mm. length. For the modulation of the magnetic field, we use the frequency of 200 cps generated by an electromagnetic tuning fork and amplified by a push pull circuit of 6L6 tubes. To vary the D. C. magnetic field near the resonance, a sweep circuit shown in Fig. 1 is used. The range of the field varied is adjusted by a suitable choice of the tube and the sweep time is adjusted by a proper selection of the time constant $(C\times R)$ of the grid circuit. To measure the current through the magnet coil, the potential difference across the standard resistance of 0.1Ω connected series to the coil is measured by a potentiometer. Without a special stabilizer of the current, the field is stable enough under good condition of the source batteries to be able to get the right resonance figure.

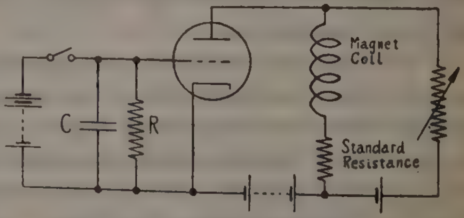

Fig. 1. The Sweep Circuit.

(b) Detector and Amplifier.

For the resonance detector, the so-called "*Inoue*'s Circuit" which had been used as a detector of small changes in capacitance was adopted. As shown in Fig. 2, a parallel resonance circuit ($L\times C$) is connected to the control grid of a pentode, and hf voltage of angular frequency ω generated by a triode oscillator is supplied to the screen grid. Varying the capacitance C, the plate current of the pentode suffers a sudden change near the position of $1/\sqrt{LC}=\omega$. For a nuclear resonance detector, the sample is put in the coil of this parallel resonance circuit, and so, the slight change of the inductance of the coil due to the resonance absorption gives the amplifier connected series fo the detector a corresponding voltage as its output. The amplifier is constituted by a R-C negative feedback circuit and has a resonance peak at 200 cps with a half width of 3cps. Following this amplifier is the phase sensitive detector composed of two 6SA7 tubes. The signal frequency voltage is put into the fourth grids in anti-phase and the reference voltage from the phase shifter is supplied to the first grids in-phase. The D. C. output voltage from this detector is amplified by one-stage D.C. amplifier which operates the recording meter of 10 mA.

---

* Now at Kobe University.

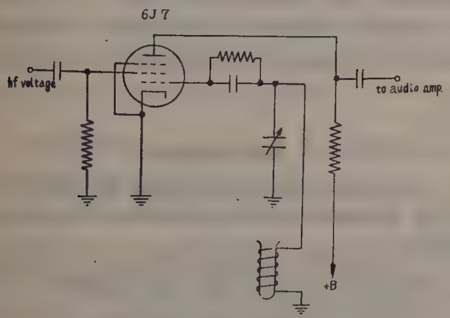

Fig. 2 The Detector Circuit.

(c) Measurement of the Frequency Ratio.

We already know, when the F^{19} resonance is operated at just 8 Mc/sec, the proton resonance appears near 8.5 Mc/sec in the same magnetic field and so these frequencies make some audio frequency basts with the harmonics of 500 kc/sec oscillator. Two similar systems each composed of oscillator, resonance detector, 200 cps amplifier, phase sensitive detector, D. C. amplifier and 10 mA recording meter are used, one for the fluorine and the other for the proton, both samples being HF aq. (20 percent solution). The hf source for the proton is a self oscillator and that for the fluorine is a crystal oscillator whose frequency is tuned to the upper 1000 cps side band of 8 Mc/sec standard wave (JJY), i.e. 8.001 Mc/sec. The difference frequencies of these two oscillators to the 500 kc/sec crystal oscillator calibrated by 8 Mc/sec standard wave are measured with the bridge type precision frequency meter. The method to decide the frequency of proton resonance f_H appearing exactly at the same field with that of 8 Mc/sec fluorine is as follows: The frequency of the proton oscillator is kept slightly higher than f_H and the magnetic field is swept slowly from a higher value to a lower, so that first the proton resonance appears and next the fluorine resonance. Then the frequency of the self oscillator for the proton is quickly lowered by a few kc/sec (Δf), so the proton resonance appears again as the field becomes lower. During this process the current through the magnet coil is measured with a potentiometer and the signs are marked on the recording meter at equal intervals of current. Assuming the linearity of the field strength to the current in the region of this small sweep, f_H is decided by measuring the frequency Δf and the distances on the recording paper between the two proton resonances and the fluorine resonance.

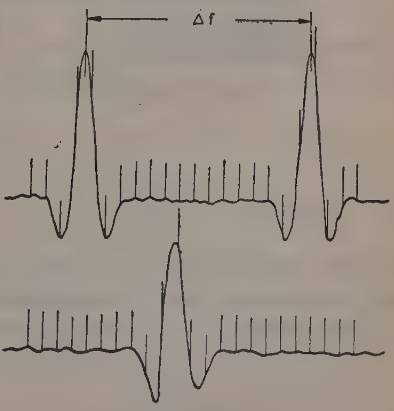

Fig. 3.

(d) Measurement of the Field Inhomogeneity.

The difference of the field strength between two samples is measured as follows: The crystal oscillator is stopped and the detector is operated by a small voltage introduced through a coupling to the self oscillator, and thus both of two detectors are operated with the same frequency to produce the proton resonance. When the field is swept, two proton resonances appear at slightly different currents. Marking on the recorder the current at the intervals equal those in the case of the proton-fluorine resonances, and measuring the distance on the recording paper between these two proton resonances, the field inhomogeneity between the two samples is decided. It measures 0.25 gauss throughout the series.

§3. Result

Because of the same spin of the proton and the F^{19}, the frequency ratio ν_F/ν_H is equal to the magnetic moment ratio μ_F/μ_H without diamagnetic correction. Table I shows the values of μ_F/μ_H of 12 independent runs obtained by the method mentioned above. Our disclosed uncertainty is taken as three times the usual probable error. As a comparison, μ_F/μ_H values in HF sample obtained by other workers are listed together showing our uncertainty minimum.

Table I. Experimental results

Run	μ_F/μ_H	
2	0.940831	
7	0.940825	
9	0.940818	
11	0.940803	
12	0.940792	
17	0.940815	
18	0.940784	
26	0.940820	
28	0.940829	
29	0.940830	
38	0.940811	
40	0.940807	
Mean	0.940814±0.000009	
	0.940816±0.000015	Reference (4)
	0.94077 ±0.00010	(5)
	0.94075 ±0.00017	(6)
	0.94086 ±0.00005	(2)

The maximum error estimated from various errors in the experiment, for example; the uncertainty of the measurement of audio frequency and so on, amounts to the same order with the uncertainty stated.

The auther wishes to express his gratitude to Professor S. Kikuchi for the encouragement and interest of the present experiment and to Professor J. Itoh under whose direction this work was made possible. Thanks are also due to Messrs. Y. Masuda, R. Kusaka, and Y. Yamagata for their kind cooperation.

References

1) J. E. Mack; Rev. Mod. Phys. **22** (1951) 64.
2) R. E. Sheriff and D, Williams: Phys. Rev. **82**, (1951) 651.
3) T. Kanda, Y. Masuda, R. Kusaka, Y. Yamagata and J. Itoh; Phys. Rev. **83**, (1951) 1066.
4) K. Siegbahn and G. Lindstrom: Arkiv Fysik **1**, **6** (1949) 193.
5) M. L. Poss: Phys. Rev. **75**, 600 (1949).
6) J. R. Zimmerman and D. Williams: Phys. Rev. **76**, (1949) 350.

JOURNAL OF THE PHYSICAL SOCIETY OF JAPAN Vol. 7, No. 3, MAY—JUN., 1952

On the Equations of the Decay of Isotropic Turbulence in Compressible Fluid

M. Z. V. KRZYWOBLOCKI
University of Illinois

(Received December 28, 1951)

Introduction

On the base of his previous works, the author derives the equations of the decay of turbulence in compressible fluid. All the random variables, like the velocity components, density, temperature, pressure, etc., fulfill the requirements of isotropy and homogeneity and are dependent. The derived equations represent the decay of velocity, temperature and density, or pressure fluctuations, respectively. The author assumes that the reader is acquainted with previous papers on the subject, and consequently, only a few items from those papers will be cited.

§1. Basic Equations and Assumptions

Four fundamental eqations are used. The equation of motion without external forces (the influence of gravitation on the compressibility phenomena also being neglected) has the form:

$$\rho(u_{i,t}+u_j u_{i,j})=\tau_{ij,j}, \tag{1.1}$$

$$\tau_{ij}=-\left(p+\frac{2}{3}\mu u_{i,i}\right)\delta_{ij}+\mu\varepsilon_{ij},\varepsilon_{ij}=u_{i,j}+u_{j,i}, \tag{1.1a}$$

where the symbol μ denotes the coefficient of viscosity (depending upon temperature and pressure or being a function of x,y), the subscripts with a comma denote partial differentiation and δ_{ij} is the Kronecker delta. Equations of continuity and state are:

$$\rho_{,t}+(\rho u_i)_{,i}=0, \quad p=R\rho T. \tag{1.2}$$

Equation of energy may be represented in the form:

$$J\rho[c_p T)_{,t}+u_i(C_p T)_{,i}]-(p_{,t}+u_i p_{,i})=J(kT_{,i})_{,i}+\Phi, \tag{1.3}$$

$$\Phi=\mu[2u_{j,i}u_{j,i}-(-\textstyle\sum_{\sigma=i,j,k}\varepsilon_{ij\sigma}u_{j,i})^2]-\frac{2}{3}\mu(u_{i,i})^2, \tag{1.3a}$$

where the symbol Φ denotes the dissipation function and the skew-symmetric quantities $\varepsilon_{ij\sigma}$ are equal to $+1$ or -1, according to whether the indices i,j,σ are even or odd permutations of the integers 1,2,3. Otherwise, they are equal to zero by definition.

§2. Fundamental Equations of Turbulence

Preserving all the symbols and notations from previous papers, multiply the equation of motion at the point P by $\rho' u'_k(\overline{\rho^2})^{-1/2}$, and that at P' by $\rho u_i(\overline{\rho^2})^{-1/2}$, where, as usually, the quantities referring to P' are denoted by primes. The procedure of obtaining the fundamental equations of turbulence was thoroughly explained in [1] and here only the final results will be given. The "generalized" fundamental equation for the propagation of the velocity correlation function for $r=0$ (equation 3.3 in [1]) in the present case takes the form:

$$\overline{(\rho u^2)}_{,t}=\frac{2}{3}[\overline{(p\rho^{-1}\rho_{,t})^2}]^{1/2}+10\overline{(\mu^2)}^{1/2}[\overline{f_{,rr}(0)}+\overline{\frac{1}{3}N(0)}], \tag{2.1}$$

where $N(0)=\overline{(\rho^2)}^{-1}\left[\overline{\eta_{,rr}(0)u^2}+\frac{1}{3}\overline{(\rho_{,t})^2}\right]$, and $\eta=\overline{\rho\rho'}$.

Since $f_{,rr}(0)=\frac{1}{2}[g_{,rr}(0)-N(0)]$, equation (2.1) can be written in the form:

$$\overline{(\rho u^2)}_{,t}=-\frac{2}{3}[\overline{(RT\rho_{,t})^2}]^{1/2}+10\overline{(\mu^2)^{1/2}}\,\overline{\left[\frac{1}{2}g_{,rr}(0)-\frac{1}{6}N(0)\right]}. \tag{2.2}$$

The "generalized" fundamental equation for the propagation of the temperature correlation function for $r=0$ (equation 5.7) in [1]) has the form:

$$\frac{1}{3}J\overline{(c_p{}^2T^2)}_{,t}-\frac{2}{3}\overline{\rho^{-1}c_p T_{p,t}}=2J\overline{kc_p\rho^{-1}\theta_{,\gamma\gamma}(0)}-\overline{10Tc_p\nu\left[f_{,rr}(0,+\frac{1}{3}N(0)\right]}, \tag{2 3}$$

or

$$\frac{1}{3}J\overline{(c^2_p T^2)}_{,t}-\frac{2}{3}\overline{c_p\rho^{-1}T_{p,t}}=2J\overline{kc_p\rho^{-1}\theta_{,rr}(0)}$$

$$\overline{-10c_pT\nu\left[\frac{1}{2}g,_{rr}0)-\frac{1}{6}N(0)\right]}, \tag{2.4}$$

where $\theta=\overline{TT'}$: the fundamental equation for the propatation of the density or pressure correlation function for $r=0$ may be derived from the equation of state:

$$\overline{p^2}=R^2\overline{\rho^2T^2}. \tag{2.5}$$

§3. Equations of the Decay of Turbulence

Preserve Taylor's definition of the length λ_u and Corrsin's λ_θ:

$$\lambda_u^2=-2\overline{u^2}/\overline{g,_{rr}(0)},\quad \lambda_\theta^2=-2\overline{T^2/\theta,_{rr}(0)}. \tag{3.1}$$

Moreover, introduce the definition of $\lambda\rho$:

$$\lambda_\rho^2=-2\overline{\rho^2/\eta,^r{}_r(0)}. \tag{3.2}$$

Then the equations (2.2) (2.4) and (2.5) can be written in the form:

$$\overline{(\rho u^2)},_t=-\frac{2}{3}\overline{[(RT\rho,_t)^2]}^{1/2}+10\overline{(\mu^2)^{1/2}A}, \tag{3.3}$$

$$\frac{1}{3}J\overline{(c_p^2T^2)},_t-\frac{2}{3}\overline{c_p\rho^{-1}T_p},_t=-4J\overline{kc_p\rho^{-1}T^2\lambda_\theta^{-2}} -10\overline{c_pT\nu A}, \tag{3.4}$$

$$A=\overline{-u^2\lambda_u}^{-2}+\frac{1}{6}\left\{\overline{2u^2\lambda_\rho^{-2}}-\frac{1}{3}\overline{[\log(\rho^2)],_t}\right\}, \tag{3.4a}$$

$$\overline{p^2}=\frac{1}{4}R^2\overline{\lambda^2{}_\rho\lambda^2{}_\theta\eta,_{r,}(0)\theta,_{rr}(0)}. \tag{3.5}$$

For an incompressible fluid, equation (3.3) transforms into that one given previously by Taylor, and (3.4) with c_p,k,ν being constant and R equal to $J(c_p-c_v)$ into:

$$Jc_v\overline{(T^2)},_t=-12Jk\rho^{-1}\overline{T^2\lambda_\theta^{-2}}+30\nu\overline{u^2\lambda_u^{-2}}, \tag{3.6}$$

which seems to be a new one due to the last term. As is seen, the magnitude A represents a link between (3.3) and (3.4). For example, for an incompressible fluid one can write:

$$Jc_v\overline{(T^2)},_t=-12Jk\rho^{-1}\overline{T^2\lambda_\theta^{-2}}-3\overline{(u^2)},_t. \tag{3.7}$$

References

1) V. KRZYWOBLOCKI, M. Z.; On the Generalized Fundamental Equations of Isotropic Turbulence in Compressible Fluids and in Hypersonics, (To be published in the Proceedings of the First U. S. National Congress of Applied Mechanics held in Chicago, June 1951.)

JOURNAL OF THE PHYSICAL SOCIETY OF JAPAN Vol. 7, No. 3, MAY—JUN., 1952

Gettering Process of Barium
—— Sorption Properties of Oxygen to Barium ——

Tetsuya ARIZUMI and Seiichi KOTANI

Kobe Kogyo Corp. Kobe

(Received August 6, 1951)

The sorption properties of Ba-O_2 system were studied. Oxygen is mainly adsorbed physically onto the active centres, below −150°C, differing from other kinds of gas. The activation energy for the physical adsorption is 0.3∼0.9 Kcal/g.mol. At temperatures between −150°C and −30°C, it is adsorbed in the activated state and its activation energy is 5.8 Kcal/g.mol. Beyond −30°C oxygen combines with barium to form oxide.

§1. Introduction

The absorption of oxygen by the barium getter at room temperature was described in the previous paper[1], but the absorption mechanism was not discussed in details except the following, because of the shortage in knowledges on the whole processes. At room temperature oxygen combines with barium and the formed oxide layer cracks to expose fresh barium surface, recovering its absorption ability when it grows to a certain thickness. As the continuation of the previous work, the sorption properties of the $Ba\text{-}O_2$ system were studied in the temperature range between −180°C and 30°C.

According to the foregoing papers[3], carbon mono-oxide is mainly captured in lattice imperfections of the getter mirror even at −180°C, but oxygen is mainly adsorbed physically on active centres. At temperatures between −150°C and −40°C, it is mainly adsorbed in the activated state similarly to carbon mono-oxide, and above about −30°C it begins to combine chemically with barium to form oxide.

§2 Experimental Procedure

The apparatus and procedure were already described in foregoing several papers[1-3]. Oxygen, the thermal decomposition product of pottasium permanganate, was dehydrated thoroughly by liquid air traps and then sent into a small glass vessel, served as a reservoir into which the end of a fine glass capillary was inserted. The gas was flowed into the experimental tube with a getter chamber and a Pirani gauge through this capillary. The getter was flashed with the wall of the getter chamber being kept at room temperature.

§3. Pressure Changes in the C. F. Method*

When oxygen was introduced into a fresh getter at below −150°C in the c. f. method, the pressure, in general, changed in a different manner from carbon mono-oxide[3]. The typical change is reproduced in Fig. 1. (a). The pressure increased rapidly at first and then begun to decrease. Such curious change is particular for oxygen, differing from other kinds of gas. After reaching to a minimum, the pressure begun to increase as encountered in all kinds of gas. This second increase is apparently caused by the remarkable reduction of the gettering ability.

The curve (b) in Fig. 1. is for the getter of the following history: After a sufficient amount of oxygen had been introduced through the capillary at −180°C until the second pressure increase took place, the capillary was sealed and then the remaining oxygen was thoroughly absorbed into the getter at room temperature. Such a "second-used" getter had no peculiarity, resembling to those of other kinds of gas. The curve (b) seems to have a slight indication of abnormality, as marked by an arrow, but it is uncertain whether this slight fall of pressure is equivalent to the above mentioned peculiarity.

Of all fresh getters there are several ones having no peculiarity, but tracing the similar change to the curve (b). Such a getter had a tendency to begin the second pressure rise in a comparatively shorter time. Perhaps the structure of such a getter resembles to the "second-used" one, as it absorbed a fairly large amount of gas at its flashing.

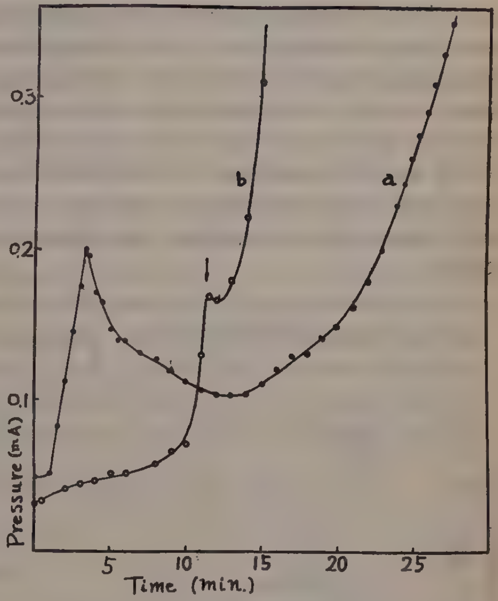

Fig. 1. Typical pressure curves at −180°C

The pressure curve at −70°C has no peculiarity, but has usually a long flat part as the case for other gases. At room temperature, however, the curve has a small hump as already mentioned in the previous paper[1]. These examples are shown in Fig. 2, together with their resistance changes. Surely the total amount of absorption is larger at −70°C and at room temperature than at −180°C, suggesting that oxygen is absorbed at −180°C in the different mechanism from at higher temperatures.

---

* The c.f. method means a procedure in which the gas is flowed into the experimental tube continuously through the fine capillary.

§4. Resistance Change

Inspite that a large amount of gas is apparently absorbed into the getter both at −180°C and at −70°C, the change in resistance of the mirror was never observed, (the curve a in Fig. 2 is the change at −39°C) except the very slow gradual change perhaps due to the rearrangement of condensed molecules or the recrystallization of the film. On the contrary, the resistance changed almost linearly as mentioned in the previous paper, keeping the getter at room temperature. Such resistance change became measurable beyond about −30°C and at the same time a small broad hump became to appear in the pressure curve (the curve b in Fig. 2). For these phenomena the full explanation was already given, leading to the conclusion that oxygen combines chemically with barium above about −30°C and the cracking in the oxide layer to expose fresh surface of barium, is the main cause for recovering the absorption ability.

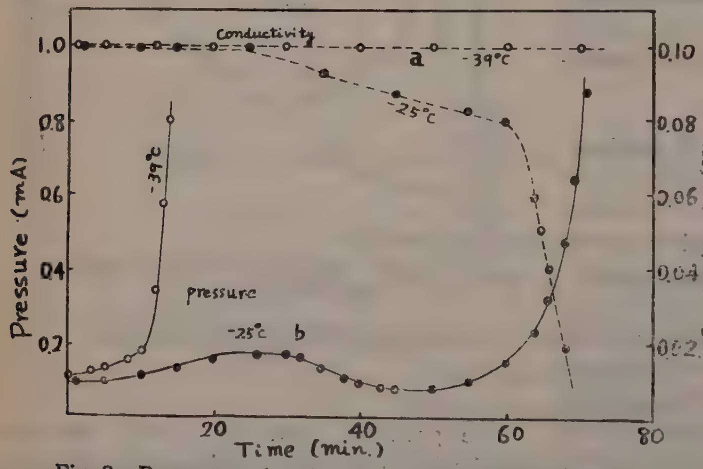

Fig. 2. Pressure and resistance curves at −39°C and −25°C.

§5. Pressure Changes in the C.V. Method*

Sealing the capillary after the pressure reached to a certain value in the c.f. method, the pressure begun to decrease even at −180°C. For instance, the curve *ab* in Fig. 4 is to be refered. The pressure change is expressed by

$$\frac{dp}{dt}=-ap(a+bp) \qquad (1)$$

similarly to the Ba−CO system. In Fig. 3 $(1/p)$ (dp/dt) is plotted against p, indicating that the eqation (1) does hold fairly well. If oxygen is adsorbed physically onto the getter surface, both constants a and b are given as followed:

$$a=\frac{L^2}{\sqrt{2\pi MRT}}\left(N'_0-\frac{NV}{RT}p_0\right)\exp\left(\frac{Q_1}{RT}\right) \qquad (2)$$

and

$$b=\frac{NV}{RT}\frac{L^2}{\sqrt{2\pi MRT}}\exp\left(\frac{Q_1}{RT}\right) \qquad (3)$$

in which all notations are the same as used in the previous report³⁾. The remaining number of unoccupied adaorption sites N_0' at the instant sealing the capillary is

$$N_0'=\frac{NV}{RT}\left(\frac{a}{b}+p_0\right) \qquad (4)$$

Table 1. Adsorption constants

tube No.	T(°C)	N_0'	$b$exp	$b$thor.	Q_1
6−1	−163	6.2×10^{18}	2.4×10^{-4}		530
6−2	−164	11.1×10^{18}	$9\,6\times10^{-5}$		330
6−3	−166	4.4×10^{18}	1.3×10^{-3}	2.1×10^{-6}	880
6−5	−164	7.1×10^{18}	5.6×10^{-4}		720

The experimental values of b and N_0' are presented in Table 1, together with theoretical ones. Besides the value of b_{exp} differing fairly from each other, both N_0' and b are much larger than those of the Ba-CO system. Perhaps the adsorption process of oxygen at −180°C is not so simple as carbon monooxide. This situation makes it difficult to evaluate the exact energy for the physical adsorption Q_1 through the comparison between theoretical and experimental values of b, but its formal calculation leads to the results in Table 1. In these calculations one barium atom was assumed, somewhat doubtful, to adsorb one oxygen molecule. Presumably the adsorption energy may be smaller than estimated above as will be discussed in §10.

§6. Stepwise Temperature Change

Raising the temperature stepwisely from about −170°C to room temperature in the

---

* The c.v. method means the procedure to pursue the pressure change without introduging the gas.

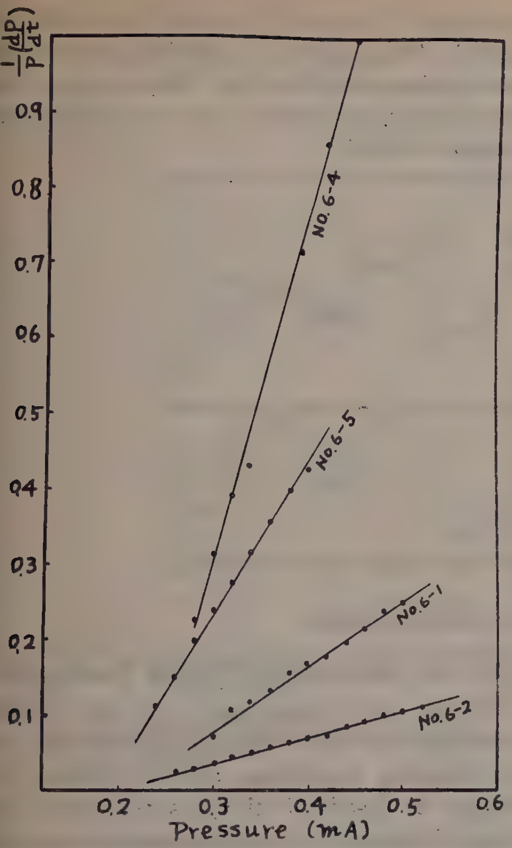

Fig. 3. $\frac{1}{p}\left(\frac{dp}{dt}\right)$ vs. pressure plots.

c.v. method, the pressure curve illustrated in Fig. 4 was obtained. Similarly to the Ba-CO system, the pressure increased stepwisely at first, but it begun to decrease after passing a maximum. The temperature at which the pressure became a maximum differs from one tube to another.

The general aspects of the pressure curve is almost similar for all getter, but precisely they differ in many respects from each other. For example, the temperature, above which the getter begins to reabsorb the gas released from itself, is not defined, depending upon the flashing conditions of the getter and its preceding history. The curve in Fig. 4 is for the "second-used" getter and the re-absorption begun at about 50°C higher temperature than usual for the "first-used".

§7. Reversible Temperature Change

If oxygen is adsorbed physically, its sorption must be reversible at the sufficient low temperature range. The experiments to ascertain this prediction were carried out and two typical results are illustrated in Fig. 5. Sealing the capillary at *a*, the pressure begun to decrease (*a*—*b*), and then raising the temperature from —164.5°C, it changed suddenly to *c*, followed by a slight continous decrease. Lowering to —164.5°C again, the pressure decreased gradually as *d*—*e*. Repeating the same process, it changed as *e*-*f*-*g*-*h*, almost reversibly. The pressure at *e* is slightly smaller than estimated from the extrapolation of the curve *a*-*b*, but in the second cycle the pressure at *h* nearly fits to the extrapolation of the curve *d*-*e*. Although in the first cycle there is a slight indication that only a small fraction of the gas is absorbed irreversibly, the reversibility of the pressure change may well be taken for holding at least below —150°C.

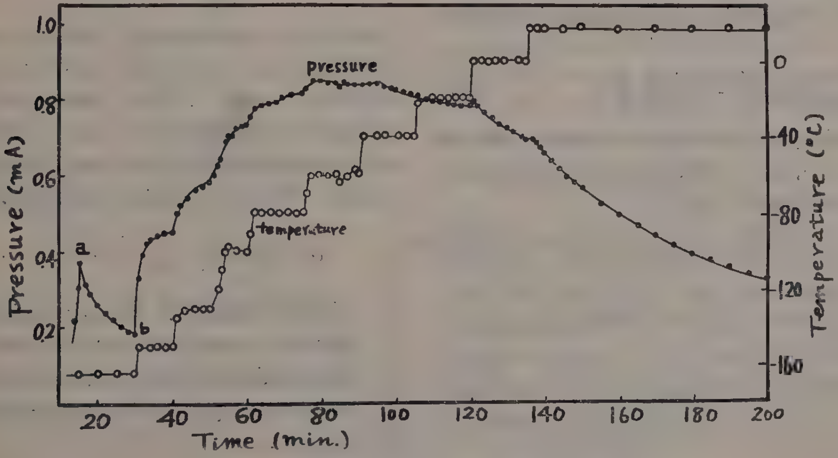

Fig. 4. The stepwise temperature change.

Raising the temperature from −164.5°C to −135°C, the pressure did not increase so much ($i-j$) and lowering to −150°C, it decreased to a smaller value ($j-k$) than the extrapolation of $f-g$, showing that a certain amount of the gas is absorbed irreversibly at 135°C. Through these experiments, the physical adsorption, not so simple as carbon mono-oxide, is known to be predominant below −150°C.

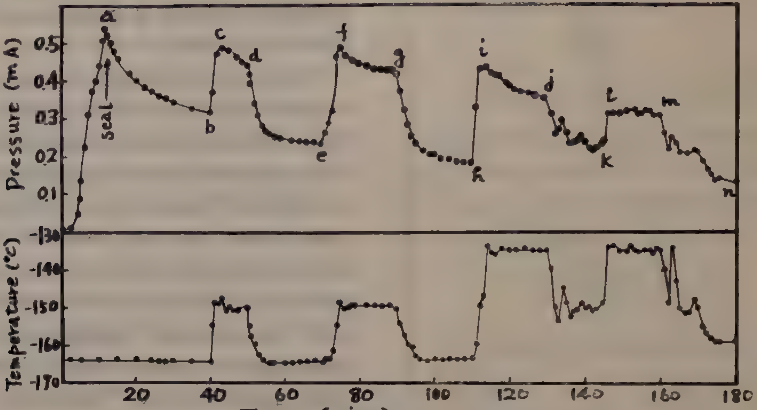

Fig. 5. The reversible temperature change.

§8. Equilibrium Pressure

In Figs. 4 and 5 there surely exists an equilibrium pressure, differing from one getter to another, corresponding to each temperature. The curves of the equilibrium pressure vs. reciprocal temperature are given in Fig. 6. The curves break sharply nearly at −150°C, above which the reversibility of pressure disappears. In the range of reversible pressure change, the equilibrium pressure is written by

$$p_{eq.}=C\exp\left(-\frac{Q_1+Q_2}{RT}\right) \quad\cdots\cdots\cdots\cdots \quad (5)$$

with Q_2 being the activation energy for desorption. Q_1+Q_2 is estimated 2.0 kcal/g.mol. from the curves in Fig. 6.

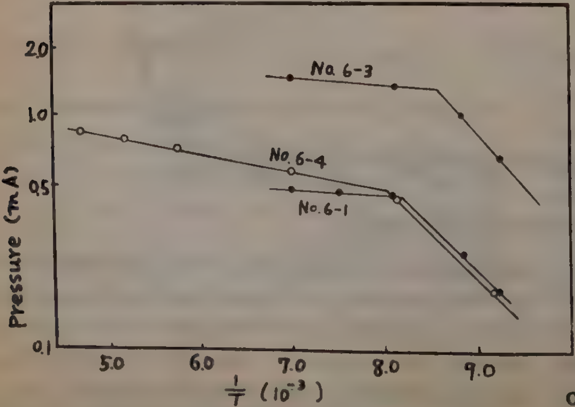

Fig. 6. Equilibrium pressure vs. reciprocal temperature.

§9. Re absorption at Higher Temperature

When the temperature of the getter surpasses a certain value, depending on the its flashing conditions and its history, it begun to re-absorb the gas released. The rate of absorption is approximately expressed by

$$\frac{dp}{dt}=-\beta p \quad\cdots\cdots\cdots\cdots\cdots\cdots \quad (6)$$

Both the experimental results and the dependency of log β upon $1/T$ are reproduced in Figs. 7 and 8. All curves in Fig. 8 are straight and parallel to each other, in spite of large difference in the available temperature range. Thus β is given as followed:

$$\beta=\beta_0\exp\left(-\frac{Q_3}{RT}\right)\cdots\cdots\cdots\cdots\cdots\cdots \quad (7)$$

with Q_3 being 5.8 Kcal/g. mol. The absorption at these higher temperatures is an irreversible process and Q_3 is considered to be the energy for activated adsorption of oxygen.

§10. Active Centre

As presumed by the initial peculiar pressure rise in the c.f. method, the getter does not almost absorb oxygen at the beginning of gas introduction, but then it becomes gradually active. These phenomena will be thoroughly explained by the following assumption

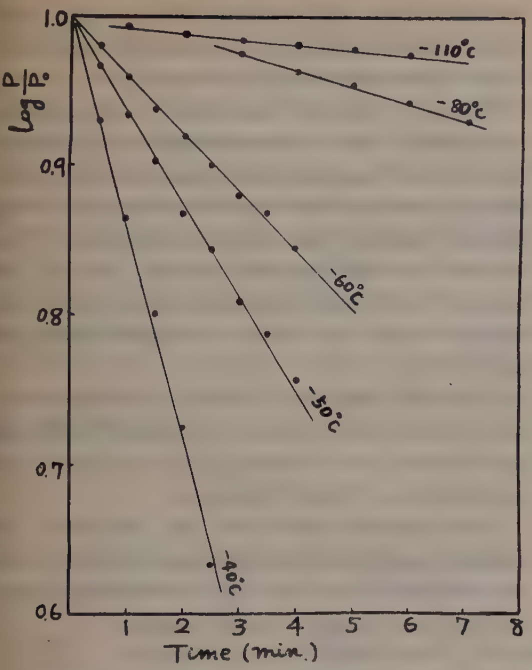

Fig. 7. Pressure changes in the activated adsorption.

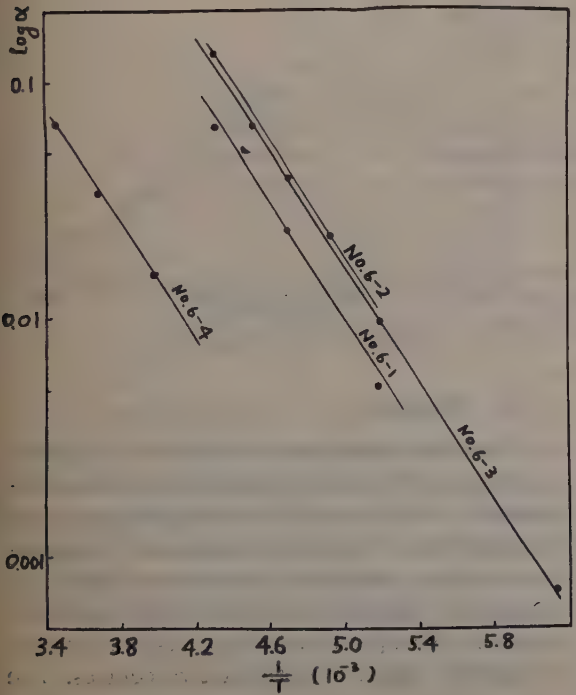

Fig. 8. Depenencies of log β upon $1/T$.

The fresh surface of getter is perhaps difficult to adsorb oxygen molecules, but an oxygen molecule happens to be adsorbed on one possible adsorption site A, (refer to Fig. 9 (*a*)), it become active centre and the neighbouring sites B adsorb oxygen molecules much more easily. If some of B sites is occupied, the sites C becomes active and so on, resulting in the gradual growth of occupied area. The initial rapid pressure increase, is supposed to be a period of forming sufficient number of nuclei for adsorption. With the getter, having many nuclei already, the abnormal pressure increase is not observed. This is usual for the "second-used" getter and sometimes encountered for the fresh ones.

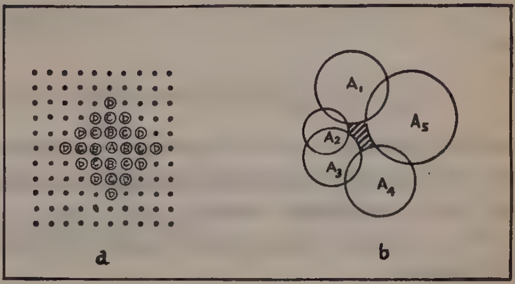

Fig. 9. Schematic model of adsorption for oxygen.

Now let us deduce the theory for the above-mentioned process. If the number of un-adsorbed oxygen molecules be N_1, the number of nuclei for adsorption (A-sites) be n_1 and that of secondary active centres (B, C and so on) be n_2, the following relation holds:

$$N_1 = st - n_1 - n_2 \quad \text{.........................} \quad (8)$$

Where s means the amount of gas flow through the capillary per unit time. As oxygen molecules are adsorbed physically inspite of taking a different model from other kinds of gas, the theory of physical adsorption will be applied without any modification: that is,

$$\frac{dn_1}{dt} = K_0 N_1 (N_0 - n_1 - n_2) \quad \text{...........} \quad (9)$$

in which N_0 is the total number of possible sites and K_0 is a constant. The increment of n_1 gives the relation;

$$\frac{dn_2}{dt} = K_1 N_1 n_1 \quad \text{.........................} \quad (10)$$

if there is sufficient number of adsorption nuclei, but their covering area does not overlap each other (refer to Fig. 10 (b)).

Both K_0 and K_1 can be represented by

$$K_n = C_n \exp\left(\frac{Q_n}{RT}\right) \qquad n=0, 1; \quad (11)$$

but Q_0 is supposed to be much larger than Q_1.

At the beginning of gas introduction, n_2 is neglisibly small and both (8) and (9) become

$$N_1 = st - n_1 \qquad \frac{dn_1}{dt} = k_0 N_1 (N_0 - n_1) \quad (12)$$

which are reduced to

$$\frac{dN_1}{dt} = s - K_0 N_1 (N_0 - n_1) \cdots\cdots\cdots\cdots \quad (13)$$

Using β defined as follows, (13) is replaced by

$$\beta = \frac{S}{N_1} - \frac{1}{N_1}\frac{dN_1}{dt} = K_0 (N_0 - st - N_1) \quad (14)$$

formally similar to the expression expression that for the normal physical adsorption, involving that β decreases linearly with time.

If n_2 is much larger than n_1, both (8) and (9) become

$$N_1 = st - n_2, \qquad \frac{dn_1}{dt} = K_0 N_1 (N_0 - n_2). \quad (15)$$

Combining (10) and (15), we obtain

$$\frac{dn_2}{dn_1} = \frac{K_1}{K_0} \frac{n_1}{N_0 - n_2}, \cdots\cdots\cdots\cdots \quad (16)$$

with the integration being,

$$N_2 n_2 - \frac{1}{2} n_2^2 = \frac{1}{2} \frac{K_1}{K_0} n_1^2 \cdots\cdots\cdots \quad (17)$$

The elimination of n_2 gives

$$n_1^2 = \frac{K_1}{K_0} (st - N_1) \{2N_0 - (st - N_1)\} \quad (18)$$

and making use of the relation,

$$\frac{dN_1}{dt} = s - \frac{dn_2}{dt} = s - K_2 N_1 n_1,$$

β is finally obtained as followed:

$$\beta = \sqrt{2K_0 K_1 N_0 \, (st - N_1)\left(1 - \frac{st - N_1}{2N_0}\right)}. \quad (19)$$

If N_1 is neglisibly small with respect to st, (19) becomes

$$\beta = \sqrt{2K_0 K_1 N_0 \, st\left(1 - \frac{st}{2N_0}\right)} \quad (20)$$

Thus, after the liner decrease at the beginning, β increases approximately in proportion to $\sqrt{t}$, but when $st/2N_0$ becomes nearly equal to 1, it begins to decrease. The estimated values of β are plotted in Fig. 10. The general behaviour of the curves is in qualitative agreement with the theory.

The above theory refers only to the surface adsorption, but experimentally the capture into lattice imperfections should not be neglected, because the amount of desorption is always smaller than that of absorption. The theory for the capture process will be, of course, much more complicated, but its main aspects shall not differ so much from the above one.

Thus the formulae (1) and (5) are applicable only approximately and it is natually difficult to estimate exact values of Q_1 and Q_2 by the application of these formulae.

The pressure curves for the activated adsorpticn and the chemical combination have no peculiarity and the gas is absorbed easily without any kind of active centre.

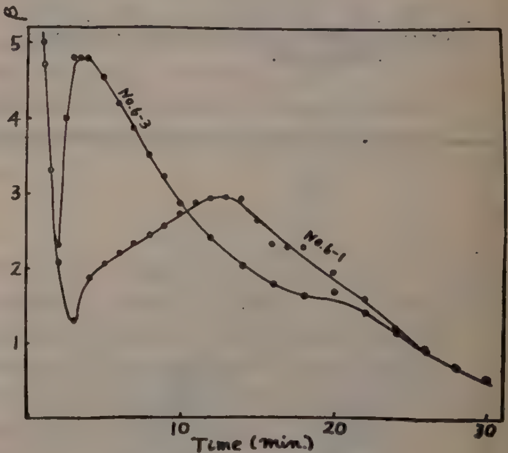

Fig. 10. The change of β.

§ 11. Summary

The sorption properties of the Ba-O_2 system were studied in the temperature range between −180°C and 30°C. At sufficiently low temperatures the pressure changes abnormally in the c.f. method; it increases at first and begins to decrease, followed by the usual increase. This peculiarity suggests that oxygen is mainly adsorbed to the active centres. The theory for such process was postulated, which agrees qualitatively with the experiments. The pressure changes in the c.v. method is similar to those of other gases at −140°C, but the exact evaluation of activation energies for physical adsorption and desorption could not be possible, because of the peculiarity in the adsorption state. However the rough estimation showed that they were about 0.3~0.9 Kcal/g. mol. and 1.1~1.7 Kcal/g. mol. respectively. The pressure curves of the activated adsorption have no peculiarity and its activation energy was 5.8 Kcal/g. mol. Above −30°C oxygen combines chemically with barium, as indicated through the small hump appeared in the pressure curve, and the change in resistance of the getter mirror.

The authors wish to acknowledge Mr. Imaeda for his co-operation and discussion.

References

1) T. Arizumi & S. Kotani; J. Phys. Soc. Japan **5** (1950) 70.
2) T. Arizumi & K. Imaeda; J. Phys. Soc. Japan **5** (1950) 163.
3) T. Arizumi & S. Kotani; J. Phys. Soc. Japan (in press).

After the presentation of this paper, Kobayashi and Furuya's article was published. Our results agree fairly well with theirs. A. Kobayashi & S. Furuya; J. Phys. Soc. Japan, **6** (1951) 238.

JOURNAL OF THE PHYSICAL SOCIETY OF JAPAN Vol. 7, No. 3, MAY—JUN., 1952

Generalized Spherical Harmonics as Representation Matrix Elements of Rotation Group

Takehito TAKAHASHI
Seizyo Gukuen High School, Setagaya, Tokyo

(Received November 17, 1951)

The aim of writing this paper is to clarify first the transformation property of spherical harmonics directly from its own definition, and the circumstance that the matrix elements of the irreducible unitary representations of three-dimensional rotation group are the eigenfunctions of the so-called symmetric rotor.

It is attempted to treat the old results more naturally and clearly from the standpoint of utilizing the generating polynomial and regarding these matrix elements as the generalization of spherical harmonics. Following this line we see some properties of Jacobi's polynomial are easily deduced.

§1. Introduction

It is well known[1] that the spherical harmonics of J-th order form the basis of irreducible unitary representations of rotation group. In calculating their coefficients we utilize the trasformation of the monomials of spinor. We must assertain the equality of these two sorts of representations above their equivalency. This method is, so to say, indirect. (Without group-theoretical consideration we can determine the transformation property of spherical harmonics only after complicated calculations.[2])

In considering the infinitesimal rotations the cirumstance is similar. We can calculate their effect on spherical harmonics directly only if we use differential operators.

The first step to the direct calculation is to express spherical harmonics as the polynomials of the spinor components. To this purpose we shall find generating polynomial, and show that spherical harmonics appear themselves as the elements of transformation matrix if we identify their auguments θ, φ with two of the Eulerian angles θ, φ, ψ which express rotation. This indicates that these matrix elements may be treated as the generalization of the spherical harmonics.

Geometrically, angles of polar coordinates θ, ψ of a point P (situated on the surface of the unit sphere) determines a straight line passing through the origin O and the point P. We can choose this straight line as the new Z-axis, and add the angle ψ to determine the position of another two axes. These three angles are the Eulerian angles of the rolation which correspond to the above mentioned movement of the coordinate axes.

The position of these coordinate axes may be indicated by the following two complex functions:

$$\xi=e^{-i(\varphi+\psi)/2}\cos\theta/2,\qquad \eta=e^{i(\varphi-\psi)/2}\sin\theta/2, \tag{1}$$

while the cartesian coordinates x, y, z of the point P are related to these ξ, η by

$$\left.\begin{aligned} x+iy&=e^{i\varphi}\sin\theta=2\eta\bar\xi,\\ x-iy&=e^{-i\varphi}\sin\theta=2\xi\bar\eta,\\ z&=\cos\theta=\xi\bar\xi-\eta\bar\eta,\\ \sqrt{x^2+y^2+z^2}&=\xi\bar\xi+\eta\bar\eta=1. \end{aligned}\right\} \tag{2}$$

The spinor (ξ, η) suffers the linear transformation which can be determined from the corresponding relations for the vector (x, y, z). If the Eulerian angles θ, φ, ψ, which express the rotation of coordinate axes from one position to another indicated respectively by the spinors (ξ_1, η_1) and (ξ_2, η_2), correspond to the spinor (ξ, η) by (1), the relation in question becomes[1)]

$$\begin{pmatrix}\xi_2\\ \eta_2\end{pmatrix}=\begin{pmatrix}\xi & -\bar\eta\\ \eta & \bar\xi\end{pmatrix}\cdot\begin{pmatrix}\xi_1\\ \eta_1\end{pmatrix}. \tag{3}$$

To determine the basis of this representation, we change the form of the expression (3) into the following:

$$(\bar\xi_2, \eta_2)=(\bar\xi_1, \bar\eta_1)\begin{pmatrix}\bar\xi & \bar\eta\\ -\eta & \xi\end{pmatrix}, \tag{4}$$

From (4) we get

$$(-\eta_2, \xi_2)=(-\eta_1, \xi_1)\begin{pmatrix}\bar\xi & \bar\eta\\ -\eta & \xi\end{pmatrix}.$$

These two together gives

$$\Gamma_2=\Gamma_1\cdot\Gamma, \tag{5}$$

where

$$\Gamma_i=\begin{pmatrix}\bar\xi_i & \bar\eta_i\\ -\eta_i & \xi_i\end{pmatrix},\ (i=\text{naught, 1 and 2}). \tag{6}$$

The representation matrix with basic vector $(\bar\xi_i, \bar\eta_i)$ or $(-\eta_i, \xi_i)$ is the inverse of Γ and is the same as given by (3).*

Even in the case of arbitrary many dimensions, any row of the inverse matrix of the representation serves as its base vector.

Then we can argue the infinitesimal rotation about fixed and rotated axes acted on the generalized spherical harmonics. The result shows that they are eigenfunctions of the symmetric rotor.

These facts, and in addition the completeness of the systems, justify the name of the generalization of spherical harmonics.

The generating polynomial used is nothing more than the well known formula determining the unitary representations, but by utilizing it many calculations are facilitated.

Finally we deduce the addition theorem for Legendre's polynomials as an application of the transformation formula.

§2. Generalized Spherical Harmonics and Their Transformation Property

As the generating polynomial of the harmonic functions of J th order we may choose the form[1)]

$$\left\{-\frac{1}{2}(x-iy)p^2+zpq+\frac{1}{2}(x-iy)q^2\right\}^J, \tag{7}$$

with parameters p and q.

Indeed we can easily prove that each term in the expression of the above formula satisfies the Laplace's equation and is homogeneous polynomial in x, y, z.

By the relations (2), (7) can be written (the point (x, y, z) being considered on the unit sphere) as

$$(\xi p+\bar\eta q)^J(-\eta p+\xi q)^J, \tag{7'}$$

Then the spherical harmonics may be expressed as the function of ξ and η.

Before going into the problem of transfor-

---

* The transformation of a function being defined as its arguments to suffer inverse transformation, the function $\bar\xi(\theta_1)$ (the other arguments φ_1, ψ_1 are understood) is transformed by the rotation $r(\theta)$: $\theta_1\to\theta_2=r\theta_1$, as

$$\bar\xi(\theta_1)\to\bar\xi'(\theta_1)=\bar\xi(r^{-1}\theta_1),$$

while by the expression (4) we mean

$$\bar\xi(\theta_1)\to\bar\xi(\theta_2)=\bar\xi(r\theta_1)$$

Then (5) becomes

$$\Gamma(\theta_2)=\Gamma(r\theta_1)=\Gamma(\theta_1)\Gamma(\theta).$$

The transformation of the function $\Gamma\to\Gamma'$ may be expressed as

$$\Gamma(\theta_2)=\Gamma'(\theta_2)\Gamma(\theta),$$

or

$$\Gamma'(\theta_2)=\Gamma(\theta_2)\Gamma^{-1}(\theta), \tag{5'}$$

where

$$\Gamma'(\theta_2)=\Gamma(r^{-1}\theta_2)=\Gamma(\theta_1).$$

mation, we generalize (7′) and define the generalized spherical harmonics $Y_J^{k,m}(|k|, |m|\leq J)$ as the coefficients in the expansion of the following generating polynomial by its parameters p, q:

$$\frac{(\bar{\xi}p+\bar{\eta})q^{J+k}(-\eta p+\xi q)^{J-k}}{\sqrt{(J+k)!(J-k)!}}$$

$$=\sum_{m=J}^{-J}Y_J^{k,m}(\xi,\eta)\frac{p^{J+m}q^{J-m}}{\sqrt{(J+m)!(J-m)!}}, \quad (8)$$

where numerical factors are chosen to make the transformation unitary. J, k and m are simultaneously integers or half integers, where we take J always positive.

The $Y_J^{k\,m}$ are the functions of Eulerian angles, as we have in (1) detormined the relations between spinor components and Eulerian angles. $Y_J^{o,m}$ become the functions of θ and φ only and are spherical harmonics.

If we put

$$\mathbf{p}=\begin{pmatrix}p\\q\end{pmatrix},\quad u_J^k(\mathbf{p})=\frac{p^{J+k}q^{J-k}}{\sqrt{(J+k)!(J-k)!}}, \quad (9)$$

(8) can be written as follows:

$$u_J^k(\Gamma\mathbf{p})=\sum_{m=J}^{-J}Y_J^{k,m}(\Gamma)u_J^m(\mathbf{p}), \quad (10)$$

or

$$\mathbf{u}_J(\Gamma\mathbf{p})=Y_J(\Gamma)\cdot\mathbf{u}_J(\mathbf{p}), \quad (10')$$

where $Y_J(\Gamma)$ (or $\mathbf{u}_J(\mathbf{p})$) means a square (or one columm) matrix whose elements are $Y_J^{k,m}(\Gamma)$ (or $u_J^m(\mathbf{p})$). $Y_J(\Gamma)$ reduces to Γ itself when $J={}^1/_2$.

The transformation property is easily determined if we put in (10) the corresponding formula for Γ, (5):

$$\mathbf{u}_J(\Gamma_2\mathbf{p})=\mathbf{u}_J(\Gamma_1\Gamma\mathbf{p})=Y_J(\Gamma_1)\mathbf{u}_J(\Gamma\mathbf{p})$$

$$=Y_J(\Gamma_1)Y_J(\Gamma)\mathbf{u}_J(\mathbf{p}),$$

from which we obtan

$$Y_J(\Gamma_2)=Y_J(\Gamma_1)Y(\Gamma), \quad (11)$$

or

$$Y_J^{k,m}(\Gamma_2)=\sum_h Y_J^{k,h}(\Gamma_1)Y_J^{h,m}(\Gamma). \quad (11')$$

(11′) gives the transformation formula for spherical harmonics for $k=0$.

The unitarity of $Y_J(\Gamma)$ follows from that of Γ. The components of the k-th row, $Y_J^{k,m}(\Gamma)$ $(|m|\leq J)$, are the basis of the representation $Y_J(\Gamma^{-1})=Y_J^{-1}(\Gamma)$.

If we write $\frac{1}{2i}S_x$, $\frac{1}{2i}S_y$, $\frac{1}{2i}S_z$ for the operators of the transformation of Γ corresponding to the infinitesimal rotations about the fixed coordinate axes x, y and z respectively,

$$\frac{1}{2i}S_z=\left\{\frac{\partial}{\partial\varphi}\begin{pmatrix}e^{-i\varphi/2} & o\\ o & e^{i\varphi/2}\end{pmatrix}\right\}_{\varphi=0}=\frac{1}{2i}\begin{pmatrix}1 & 0\\ 0 & -1\end{pmatrix}$$

In the same way, we have

$$S_x=\begin{pmatrix}0 & 1\\ 1 & 0\end{pmatrix},\ S_y=\begin{pmatrix}0 & -i\\ i & 0\end{pmatrix},\ S_z=\begin{pmatrix}1 & 0\\ 0 & -1\end{pmatrix}, \quad (12)$$

and

$$S^+=\frac{1}{2}(S_x+iS_y)=\begin{pmatrix}0 & 1\\ 0 & 0\end{pmatrix},\quad S^-=\frac{1}{2}(S_x-iS_y)$$

$$=\begin{pmatrix}0 & 0\\ 1 & 0\end{pmatrix}. \quad (13)$$

From the formal relation

$$S^+\mathbf{p}=\begin{pmatrix}q\\o\end{pmatrix}=q\frac{\partial}{\partial p}\mathbf{p},$$

we get the following formulas:

$$\left.\begin{aligned}q\frac{\partial}{\partial p}(\Gamma\ \mathbf{p},\mathbf{p}')&=(\Gamma\ S^+\mathbf{p},\mathbf{p}'),\\ p\frac{\partial}{\partial q}(\Gamma\ \mathbf{p},\mathbf{p}')&=(\Gamma\ S^-\mathbf{p},\mathbf{p}'),\\ \left(p\frac{\partial}{\partial p}-q\frac{\partial}{\partial q}\right)(\Gamma\ \mathbf{p},\mathbf{p}')&=(\Gamma\ S_z\mathbf{p},\mathbf{p}'),\end{aligned}\right\} \quad (14)$$

We write $\mathbf{S}^+$,……for the corresponding transformation operators for $Y_J^{k,m}(\Gamma)$, and operate them on the modified form of (10):

$$\frac{1}{(2J)!}(\Gamma\ \mathbf{p},\mathbf{p}')^{2J}=(Y_J(\Gamma)\mathbf{u}_J(\mathbf{p}),\mathbf{u}_J(\mathbf{p}'))$$

$$=\sum_{m,k}Y_J^{k,m}(\Gamma)u_J^m(\mathbf{p})u_J^k(\mathbf{p}'). \quad (15)$$

Thus

$$\mathbf{S}^+\frac{(\Gamma\ \mathbf{p},\mathbf{p}')^{2J}}{(2J)!}=\frac{(\Gamma\ \mathbf{p},\mathbf{p}')^{2J-1}}{(2J-1)!}(\Gamma\ S^+\mathbf{p},\mathbf{p}')$$

$$=\frac{1}{(2J)!}\,q\frac{\partial}{\partial p}(\Gamma\ \mathbf{p},\mathbf{p}')^{2J}. \quad (16)$$

On the other hand

$$q\frac{\partial}{\partial p}u_J^{m'}(\mathbf{p})=\sqrt{(J+m')(J-m'+1)}\,u_J^{m'-1}(\mathbf{p}).$$

Comparing both sides of (15) and equating the coefficients of $u_J^m(\mathbf{p})\cdot u_J^k(\mathbf{p}')$, we get

$$\mathbf{S}^+Y_J^{k,m}(\Gamma)=\sqrt{(J-m)(J+m+1)}\,Y_J^{k,m+1}(\Gamma).$$

In the same way (17)

$$\left.\begin{aligned}&\mathbf{S}^-Y_J^{k,m}(\Gamma)=\sqrt{(J-m)(J-m+1)}\,Y_J^{k,m-1}(\Gamma),\\ &\frac{1}{2}\mathbf{S}_zY_J^{k,m}(\Gamma)=mY_J^{k,m}(\Gamma),\\ &\frac{1}{4}\mathbf{S}^2Y_J^{k,m}(\Gamma)=J(J+1)Y_J^{k,m}(\Gamma),\\ &\mathbf{S}^2=\mathbf{S}_x^2+\mathbf{S}_y^2+\mathbf{S}_z^2.\end{aligned}\right\} \quad (17')$$

For the infinitesimal rotations $\mathbf{S}'$ about the axes after the rotation owing to Γ from the fixed ones, two dimensional matrices are transformed by Γ:

$$S^{1+}=\Gamma^{-1}\cdot S^{+}\cdot\Gamma,\ldots\ldots; \qquad (18)$$

As before (the exponent t means the transposing of the matrix),

$$(S^{+})^{t}\mathbf{p}'=\begin{pmatrix}o\\ p'\end{pmatrix}=p'\frac{\partial}{\partial q'}\mathbf{p}',$$

$$(\Gamma S'^{+}\mathbf{p},\mathbf{p}')=(S^{+}\Gamma\mathbf{p},\mathbf{p}')=(\Gamma\mathbf{p},(S^{+})^{t}\mathbf{p}')$$
$$=p'\frac{\partial}{\partial q'}(\Gamma\mathbf{p},\mathbf{p}').$$

Finally

$$\left.\begin{aligned}&\mathbf{S}'^{+}Y_J^{k,m}=\sqrt{(J+k)(J-k+1)}\,Y_J^{k-1,m},\\ &\mathbf{S}'^{-}Y_J^{k,m}=\sqrt{(J-k)(J+k+1)}\,Y_J^{k+1,m},\\ &\frac{1}{2}\mathbf{S}'_z\,Y_J^{k,m}=kY_J^{k,m},\quad \mathbf{S}'^2=\mathbf{S}^2.\end{aligned}\right\}\qquad(19)$$

In quantum mechanics, angular momentum $M_x,\ldots\ldots$ correspond to the operators of infinitesimal rotations multiplied by $i\hbar$.

The energy of rotation of the rigid body is expressed as

$$H=aM_x^2+bM_y^2+cM_z^2$$

where x', y', z' are the principal inertial axes fixed in the rigid body, and in the symmetric case $a=b$ becomes

$$H_s=aM'^2+(c-a)M_z^2.$$

From (19)

$$H_sY_J^{k,m}=\hbar^2\{aJ(J+1)+(c-a)k^2\}\,Y_J^{k,m}.$$

This result shows that $Y_J^{k,m}$ are the eigenfunctions of the symmetric rotor.[3)]

§3. The Function $P_J^{k,m}(\theta)$

$Y_J^{k,m}(\Gamma)$ can easily be expressed as the polynomial in ξ and η.

Comparing both sides of (15), we get after some calculations

$$Y_J^{k,m}(\Gamma)=\sum_{\nu}\frac{(-1)^{\nu}\sqrt{(J+m)!(J-m)!(J+k)!(J-k)!}}{(J+m-\nu)!(k-m)!\nu!(J-k-\nu)!}$$
$$\bar{\xi}^{J+m-\nu}\xi^{J-k-\nu}\bar{\eta}^{k-m-\nu}\eta^{\nu},\qquad(20)$$

where summations are taken so far as negative numbers do not appear in factorials.

Putting (1) in (20)

$$Y_J^{k,m}(\Gamma)=e^{ik\psi+im\varphi}P_J^{k,m}(\theta),\qquad(21)$$

where $P_J^{k,m}(\theta)$ is the polynomial in $\cos\frac{\theta}{2}$ and $\sin\frac{\theta}{2}$ and may be regarded as the generalization of Legendre's associated function.

From (11′) transformation formula for these functions are given, by

$$P_J^{k,m}(\theta_2)e^{ik\psi_2+im\varphi_2}=\sum_{h=J}^{-J}P_J^{k,h}(\theta_1)P_J^{h,m}(\theta)$$
$$\cdot e^{ik\phi1+ih(\varphi_2+\psi)+im\varphi}\qquad(22)$$

Next we shall deduce the properties of $P_J^{k,m}(\theta)$. By definition

$$P_J^{k,m}(\theta)=Y_J^{k,m}(\Theta),\qquad(23)$$

where

$$\Theta=\begin{pmatrix}\cos\theta/2 & \sin\theta/2\\ -\sin\theta/2 & \cos\theta/2\end{pmatrix}.\qquad(24)$$

For the special form of Γ, i.e.

$$\Gamma_a=\begin{pmatrix}a & o\\ o & b\end{pmatrix},\qquad \Gamma_b=\begin{pmatrix}o & c\\ d & o\end{pmatrix},\qquad(25)$$

$Y_J(\Gamma)$ have the following simple forms:

$$\left.\begin{aligned}&Y_J^{k,m}(\Gamma_a)=a^{J+k}b^{J-k}\delta_{kk,m},\\ &Y_J^{k,m}(\Gamma_b)=a^{J-k}d^{J+k}\delta_{k,-m}.\end{aligned}\right\}\qquad(26)$$

Simple properties obtained from these relations are listed below.

(i) $$P_J^{k,m}(\theta+\theta)=\sum_{h=J}^{-J}P_J^{k,h}(\theta)P_J^{h,m}(\theta');\qquad(27)$$

$$P_J^{k,m}(o)=\delta_{k,m};\qquad(28)$$

$$P_J^{k,m}(2\pi)=(-1)^{2J}\delta_{k,m};\qquad(29)$$

$$P_J^{k,m}(\pm\pi)=(-1)^{J\pm k}\delta_{k,-m};\qquad(30)$$

$$P_J^{k,m}(\theta\pm\pi)=(-1)^{J\pm k}P_J^{-k,m}(\theta)\qquad(31)$$

(ii) $$P_J^{k,m}(-\theta)=(-1)^{m-k}P_J^{k,m}(\theta)=P_J^{m,k}(\theta)$$
$$=P_J^{-k,-m}(\theta);\qquad(32)$$

$$P_J^{o,m}(\theta)=(-1)^{m}P_J^{o,-m}(\theta),$$
$$P_J^{k,o}(\theta)=(-1)^{k}P_J^{-k,o}(\theta)\qquad(33)$$

Proof: (27) is the special case of (22), if we remark

$$\Theta_\theta\cdot\Theta_{\theta'}=\Theta_{\theta+\theta'}.$$

Following three formulas are obtained if we put in (26) the values of for $\theta=o$, 2π and $\pm\pi$.

$$\Theta_0=\begin{pmatrix}1&0\\0&1\end{pmatrix},\quad \Theta_{2\pi}\begin{pmatrix}-1&0\\0&-1\end{pmatrix},\quad \Theta_{\pm\pi}=\begin{pmatrix}0&\mp1\\ \mp1&0\end{pmatrix},$$

respectively: (30) follows from (27) and (29).

To get (32), we use (27), (26) and the following relation:

$$\Theta_{-\theta}=\begin{pmatrix}1&0\\0&-1\end{pmatrix}\cdot\Theta_\theta\cdot\begin{pmatrix}1&0\\0&-1\end{pmatrix}$$

(33) and the last equation of (22) is the result of changing the forms of (31) and (32).

(iii) $$P_J^{km}(\theta)=\sum_{\nu}\frac{(-1)^{\nu}\sqrt{(J+m)!(J-m)!(J+k)!(J-k)!}}{(J+m-\nu)!(k-m+\nu)!\nu!(J-k-\nu)!}\cos^{2J+m-k-2\nu}\theta/2\,\sin^{k-m+2\nu}\theta/2;\qquad(20')$$

$$P_J^{k,m}(\theta)=(-1)^{\frac{k-m}{2}}P_J^{o,k}(\pi/2)P_J^{o,m}(\pi/2)+\sum_{h>0}^{J}P_J^{h,k}(\pi/2)P_J^{h,m}(\pi/2)\cos\{h\theta+\pi(k-m)/2\};\qquad(34)$$

$$P_J^{k,m}(\theta)=\sqrt{\frac{(J-m)!}{(J+m)!}}2^m\cos^{m+k}\theta/2\sin^{m-k}\theta/2\sum_{\nu=0}^{J-m}(-1)^\nu\sqrt{\frac{(J+m+\nu)!}{(J-m-\nu)!}}P_J^{k,m+\nu}(\pi/2)\frac{\cos^\nu\theta}{\nu!} \tag{35}$$

(iv) $$P_J^{k,m}(\theta)=\frac{(-1)^{m-k}}{2^{J-m}}\sqrt{\frac{(J-m)!}{(J+m)!(J+k)!(J-k)!}}\cos^{m+k}\theta/2\sin^{m-k}\theta/2\left(\frac{d}{d\cos\theta}\right)^{J+m}\{(\cos\theta+1)^{J-k}(\cos\theta-1)^{J+k}\} \tag{36}$$

Proof of (34):
Θ can be modified as follows:

$$\Theta=\begin{pmatrix}1 & 0\\ o & -i\end{pmatrix}\cdot\Theta_{-\pi/2}\cdot\begin{pmatrix}e^{i\theta/2} & o\\ o & e^{-i\theta/2}\end{pmatrix}\cdot\Theta_{\pi/2}\cdot\begin{pmatrix}1 & 0\\ o & i\end{pmatrix}.$$

Then we get

$$P_J^{k,m}(\theta)=\sum i^{k-m}e^{ih\theta}P_J^{h,k}(\pi/2)P_J^{h,m}(\pi/2). \tag{34'}$$

(34′) is the same as (34), if we remark that from (31) and (32).

$$P_J^{-h,k}(\pi/2)=(-1)^{J-h}P_J^{h,k}(\pi/2) \tag{37}$$

First term appears in (34) only for integral J.
Proof of (36):
The fundamental formula (8) allows us to write

$$P_J^{k,m}(\theta)=\sqrt{\frac{(J-m)!}{(J+m)!}}\left\{\left(\frac{d}{dp}\right)^{J+m}u_J^k(\Theta\mathbf{p})\right\}_{p=0,q=1} \tag{38}$$

Change the variable p to

$$t=\cos\theta-p\sin\theta,$$

then

$$u_J^k(\Theta\mathbf{p})_{q=1}=\frac{(1-t)^{J+k}(1+t)^{J-k}}{2^{2J}\sqrt{(J+k)!(J-k)!}\sin^{J+k}\theta/2\cos^{J-k}\theta/2} \tag{39}$$

(36) is the immediate result of putting (39) in (38).
To prove (35), notice that (39) becomes for the special value of $\theta=\pi/2$

$$u_J^k(\Theta_{\pi/2}\cdot\mathbf{p})=\frac{(1+p)^{J+k}(1-p)^{J-k}}{2^J\sqrt{(J+k)!(J-k)!}}=\sum P_J^{k,h}(\pi/2)\frac{P^{J+h}}{\sqrt{(J+h)!(J-k)!}},$$

and substitute this result in (36) after putting $p=-\cos\theta$.

Recurrence formulas for $P_J^{k,m}(\theta)$ may be deduced similary but are ommited here.

§ 4. Orthogonality Relation

If $\pi\geq\theta\geq0$, put $z=\cos\theta$ and write $P^{Jk,m}(z)$ for $P_J^{k,m}(\theta)$, then (36) becomes

$$P_J^{k,m}(z)=(-1)^{m-k}2^{-J}\sqrt{\frac{(J-m)!}{(J+m)!(J+k)!(J-k)!}}(1+z)^{\frac{m+k}{2}}(1-z)^{\frac{m-k}{2}}\left(\frac{d}{dz}\right)^{J+k}\{(1+z)^{J-k}(z-1)^{J+k}\}. \tag{40}$$

By (32), we can write (40) in another form;

$$P_J^{k,m}(z)=2^{-J}\sqrt{\frac{(J-k)!}{(J+m)!(J-m)!(J+k)!}}(1+z)^{\frac{k+m}{2}}(1-z)^{\frac{k-m}{3}}\left(\frac{d}{dz}\right)^{J+k}\{(z+1)^{J-m}(z-1)^{J+m}\}, \tag{41}$$

or

$$=2^{-J}\sqrt{\frac{(J+m)!}{(J-m)!(J+k)!(J-k)!}}(1+z)^{\frac{-m-k}{2}}(1-z)^{\frac{k-m}{2}}\left(\frac{d}{dz}\right)^{J-m}\{(z+1)^{J+k}(z-1)^{J-k}\}. \tag{42}$$

These formulas show that $P_J^{k,m}(z)$ coincides with Jacobi's polynomial[4) up to some factor. $P_J^{o,m}(z)$ or $P_J^{k,o}(z)$ is then Legendre's accosiated function multiplied by a constant.

Integrating these relations by parts, we have

$$\int_{-1}^{1}P_J^{k,m}(z)P_{J'}^{k,m}(z)dz=\frac{2}{2J+1}\delta_{JJ'},$$

and finally

$$\int_0^\pi\int_0^{2\pi}\int_0^{2\pi}Y_J^{k,m}\overline{Y}_{J'}^{k',m'}\sin\theta d\theta d\varphi d\psi=\frac{8\pi^2}{2J+1}\delta_{JJ'}\delta_{mm'}\delta_{kk'}. \tag{43}$$

This orthogonality relation furnishes the linear independency of $Y_J^{k,m}$, then the irreducibility of the representations. Also we can prove the completeness of the system of functions $Y_J^{k,m}$.

§5. Addition Theorem for Legendre's Polynomial

(22) gives the transformation property of spherical harmonics for $k=0$:

$$P_J^{0,m}(\theta_2)e^{im\varphi_2}=\sum_h P_J^{0,h}(\theta_1)p_J e^{h\ m(\varphi_1+\psi)+im\varphi}. \tag{44}$$

If we write $P_J(\theta)$ for $P_J^{0,0}(\theta)$ (Legendre's polynomial), (44) becomes

$$P_J(\theta_2)=\sum_{h=J}^{-J}P_J^{0,h}(\theta_1)P_J^{h,0}(\theta)e^{ih(\varphi_1+\psi)}$$

$$=P_J(\theta_1)P_J(\theta)+\sum_{h=1}^{J}\{e^{ih(\varphi_1+\psi)}P_J^{0,h}(\theta_1)P_J^{h,0}(\theta)+e^{-ih(\varphi_1+\psi)}P_J^{0,-h}(\theta_1)P_J^{-h,0}(\theta),\}$$

which can be written, on account of the relation (33),

$$P_J(\theta_2)=P_J(\theta_1)P_J(\theta)+2\sum_{h=1}^{J}P_J^{0,h}(\theta_1)P_J^{0\ h}(\theta)\cos\{h(\varphi_1+\psi+\pi)\},$$

where

$$\cos\theta_2=\cos\theta_1\cdot\cos\theta-\sin\theta_1\sin\theta\cos(\psi_1+\psi).$$

(34) is the so-called addition theorem for Legendre's polynomials.

The author wishes to acknowledge the kind interest shown by Professors T. Yamanouchi and T. Kato.

References

1) For the subjects refered, see e.g. E. Wigner: *Gruppentheorie und ihre Anwendungen auf die Quantenmechanik der Atomspektren* (1931). E. Cartan: *Leçon sur le théorie des spineurs, I* (1938).

2) Y. Sato: Bull. Earthq. Res. Inst. **28** (1951) 175. This paper implies tables for numerical calculations.

3) Infinitesimal rotations may be treated by using differential operators: A. Sommerfeld: *Atombau und Spektrallinien, II* (1939).

4) Formulas for Jacobi's polynomials are summarized in T. Inui: *Spherical, cylindrical and hypergeometric Functions* (1948) (in Japanese).

JOURNAL OF THE PHYSICAL SOCIETY OF JAPAN Vol. 7, No. 3, MAY—JUN., 1952

Note on the Velocity Distribution over an Elliptic Cylinder Submerged in a Uniform Flow of Compressible Fluid

Mitutosi KAWAGUTI

Institute of Science and Technology, University of Toyko

(Received November 24, 1951)

The exact analytical expression, correct to M^4, for the velocity distribution over an elliptic cylinder which is submerged in a uniform flow of a compressible fluid (*cf.* J. Phys Soc. Japan, **6** (1951) 168) is expanded in ascending powers of θ, the eccentric angle of the ellipse, in order to reduce the expression into a more tractable form. Numerical values of coefficients of θ and θ^3 are given for various values of thickness ratio t ranging from 0 to 1.0, and it is shown that the convergency of the M^2-expansion method is very good near the stagnation point.

§1. Introduction and Summary

In a previous paper [1] the author obtained the exact expression, correct to M^4, for the velocity distribution over an elliptic cylinder which is submerged in a uniform flow of a compressible fluid, and made numerical calculations for the cases $t=0.1$ and $t=0.5$, where t is the thickness ratio of the elliptic cylinder. However, it is very troublesome to calculate numerical values from this analytic expression; especially the calculation becomes more and more difficult for the region near the stagnation points as the thickness ratio becomes smaller.

In this paper, the exact analytic expression will be expanded in ascending powers of θ, the eccentric angle of the ellipse, in order to reduce the expression into a more tractable form. Numerical values of coefficients of θ and θ^3 are given for various values of thickness ratio from $t=0$ to $t=1.0$. It seems that the convergency of the M^2-expansion method is very good near the stagnation point.

§2. θ-expansion

In the following, we shall use, unless otherwise stated, the same notations as those given in reference [1].

As was shown in [1], the velocity potential Φ can be expanded in the form

$$\Phi(\theta,\sigma)=\Phi_0(\theta)+\Phi_1(\theta,\sigma)M^2 +\Phi_2(\theta,\sigma)M^4+O(M^6). \qquad (2.1)$$

Explicit expressions for $\Phi_0(\theta)$, $\Phi_1(\theta,\sigma)$ and $d\Phi_2(\theta,\sigma)/d\theta$ are respectively given in (3.6), (3.7) and (3.11) of [1].

Expanding the expressions $d\Phi_1/d\theta$ and $d\Phi_2/d\theta$ in ascending powers of θ, we obtain following expressions:

$$\frac{d\Phi_1}{d\theta}=F_{11}(\sigma)\theta+F_{12}(\sigma)\frac{\theta^3}{(1-\sigma^2)^2} +O\left(\frac{\theta^5}{(1-\sigma^2)^4}\right), \qquad (2.2)$$

$$\frac{d\Phi_2}{d\theta}=F_{21}(\sigma)\theta+F_{22}(\sigma)\frac{\theta^3}{(1-\sigma^2)^2} +O\left(\frac{\theta^5}{(1-\sigma^2)^4}\right), \qquad (2.3)$$

where

$$F_{11}(\sigma)=\frac{3+\sigma^2}{2\sigma^2}+\frac{1+\sigma^2}{\sigma^3}\log\frac{1-\sigma}{1+\sigma}+\frac{1+6\sigma^2+\sigma^4}{4\sigma^4}\log\frac{1+\sigma^2}{1-\sigma^2}, \qquad (2.4)$$

$$F_{12}(\sigma)=-\frac{15+131\sigma^2+13\sigma^4\ \ \sigma^6}{12\sigma^2}-\frac{(1+\sigma^2)(2+20\sigma^2+2\sigma^4)}{3\sigma^3}\log\frac{1-\sigma}{1+\sigma}-\frac{1+76\sigma^2+230\sigma^4+76\sigma^6+\sigma^8}{24\sigma^4}\log\frac{1+\sigma^2}{1-\sigma^2}, \qquad (2.5)$$

$$F_{21}(\sigma)=\frac{(3+43\sigma^2+136\sigma^4+63\sigma^6+7\sigma^8-4\sigma^{10})}{32\sigma^6(1+\sigma^2)^2}-\frac{(1+\sigma^2)(4+\sigma^2)}{4\sigma^5}\log\frac{1-\sigma}{1+\sigma}-\frac{(7+2\sigma^2+7\sigma^4)}{32\sigma^6}\left(\log\frac{1-\sigma}{1+\sigma}\right)^2$$
$$+\left\{\frac{(3-20\sigma^2-98\sigma^4-44\sigma^6-\sigma^{\ })}{64\sigma^8}-\frac{3(1+6\sigma^2+\sigma^4)}{8\sigma^4(1+\sigma^2)^2}\log 2+\frac{1}{2\sigma^3(1+\sigma^2)}\log\frac{1-\sigma^2}{\sigma^2}\right.$$
$$\left.-\frac{(3+12\sigma^2+34\sigma^4+12\sigma^6+3\sigma^8)}{16\sigma^7(1+\sigma^2)}\log\frac{1-\sigma}{1+\sigma}\right\}\log\frac{1+\sigma^2}{1-\sigma^2}-\frac{3(1+14\sigma^2+39\sigma^4\ \ 84\sigma^6+39\sigma^8+14\sigma^{10}+\sigma^{12}}{128\sigma^9(1+\sigma^2)^2}\left(\log\frac{1+\sigma^2}{1-\sigma^2}\right)^2$$

$$
\begin{aligned}
&+\left\{-\frac{3(1+6\sigma^2+\sigma^4)}{8\sigma^4(1+\sigma^2)^2}+\frac{1}{\sigma^3(1+\sigma^2)}\right\}L_1+\left\{\frac{(1+13\sigma^2+12\sigma^4+13\sigma^6+\sigma^8)}{8\sigma^4(1+\sigma^2)^2}+\frac{1}{\sigma(1+\sigma^2)}\right\}L_2\\
&-\frac{(1+14\sigma^2+\sigma^4)}{8\sigma^6}\int_0^\sigma\frac{x}{1-x^2}\log\frac{1+\sigma x}{1-\sigma x}dx+\frac{1}{\sigma(1+\sigma^2)}L_4+\frac{1}{\sigma^3(1+\sigma^2)}L_5\\
&+\gamma\left\{-\frac{(3+30\sigma^2+86\sigma^4+82\sigma^6+35\sigma^8+4\sigma^{10})}{32\sigma^6(1+\sigma^2)^2}-\frac{(3+5\sigma^2+2\sigma^4)}{4\sigma^5}\log\frac{1-\sigma}{1+\sigma}\right.\\
&\left.+\frac{(3-24\sigma^2-62\sigma^4-72\sigma^6-5\sigma^8)}{64\sigma^8}\log\frac{1+\sigma^2}{1-\sigma^2}\right\},
\end{aligned}
\tag{2.6}
$$

$$
\begin{aligned}
F_{22}(\sigma)=&\frac{(3+1277\sigma^2+8829\sigma^4+16506\sigma^6+9929\sigma^8+1925\sigma^{10}+63\sigma^{12}-4\sigma^{14})}{192\sigma^2(1+\sigma^2)^2}\\
&+\frac{(28+181\sigma^2+191\sigma^4+39\sigma^6+\sigma^8)}{6\sigma^5}\log\frac{1-\sigma}{1+\sigma}+\frac{(79+996\sigma^2+1306\sigma^4+996\sigma^6+79\sigma^8)}{192\sigma^6}\left(\log\frac{1-\sigma}{1+\sigma}\right)^2\\
&+\left\{\frac{(-3+298\sigma^2+4983\sigma^4+16380\sigma^6+5899\sigma^8+602\sigma^{10}+\sigma^{12})}{384\sigma^8}+\frac{(1+76\sigma^2+230\sigma^4+76\sigma^6+\sigma^8)}{16\sigma^4(1+\sigma^2)^2}\log 2\right.\\
&\left.-\frac{(1+10\sigma^2+\sigma^4)}{3\sigma^3(1+\sigma^2)}\log\frac{1-\sigma^2}{\sigma^2}+\frac{(3+114\sigma^2+541\sigma^4+988\sigma^6+541\sigma^8+114\sigma^{10}+3\sigma^{12})}{24\sigma^7(1+\sigma^2)}\log\frac{1-\sigma}{1+\sigma}\right\}\log\frac{1+\sigma^2}{1-\sigma^2}\\
&+\frac{(1+180\sigma^2+1884\sigma^4+6572\sigma^6+10374\sigma^8+6572\sigma^{10}+1884\sigma^{12}+180\sigma^{14}+\sigma^{16})}{256\sigma^8(1+\sigma^2)^2}\left(\log\frac{1+\sigma^2}{1-\sigma^2}\right)^2\\
&+\left\{\frac{(1+76\sigma^2+230\sigma^4+76\sigma^6+\sigma^8)}{16\sigma^4(1+\sigma^2)^2}-\frac{2(1+10\sigma^2+\sigma^4)}{3\sigma^3(1+\sigma^2)}\right\}L_1\\
&+\left\{-\frac{(1+155\sigma^2+923\sigma^4+1298\sigma^6+923\sigma^8+155\sigma^{10}+\sigma^{12})}{48\sigma^4(1+\sigma^2)^2}-\frac{2(1+10\sigma^2+\sigma^4)}{3\sigma(1+\sigma^2)}\right\}L_2\\
&+\frac{(1+156\sigma^2+838\sigma^4+156\sigma^6+\sigma^8)}{48\sigma^6}\int_0^\sigma\frac{x}{1-x^2}\log\frac{1+\sigma x}{1-\sigma x}dx-2\frac{(1+10\sigma^2+\sigma^4)}{3\sigma(1+\sigma^2)}L_4-\frac{2(1+10\sigma^2+\sigma^4)}{3\sigma^3(1+\sigma^2)}L_5\\
&+\gamma\left\{\frac{(3+1104\sigma^2+4877\sigma^4+8756\sigma^6+7077\sigma^8+2376\sigma^{10}+123\sigma^{12}+4\sigma^{14})}{192\sigma^6(1+\sigma^2)^2}\right.\\
&+\frac{(21+89\sigma^2+109\sigma^4+43\sigma^6+2\sigma^8)}{6\sigma^5}\log\frac{1-\sigma}{1+\sigma}\\
&\left.+\frac{(-3+246\sigma^2+3467\sigma^4+7028\sigma^6+5299\sigma^8+854\sigma^{10}+5\sigma^{12})}{384\sigma^8}\log\frac{1+\sigma^2}{1-\sigma^2}\right\}.
\end{aligned}
\tag{2.7}
$$

In Table I are given the numerical values of F_{11}, F_{12}, F_{21} and F_{22} for some values of t, taking $\gamma=1.4$.

Table I. Numerical value of F_{11}, F_{12}, F_{21} and F_{22},

t	F_{11}	F_{12}	F_{21}	F_{22}
0.0	.61371	−2.2430	−.0616	2.6327
0.1	.63667	−2.2433	−.0418	2.7343
0.2	.65978	−2.2427	−.0168	2.8400
0.3	.68278	−2.2398	.0130	2.9478
0.4	.70551	−2.2339	.0468	3.0604
0.5	.72788	−2.2249	.0848	3.1770
0.6	.74984	−2.2128	.1264	3.2983
0.7	.77134	−2.1979	.1718	3.4251
0.8	.79246	−2.1805	.2207	3.5567
0.9	.81312	−2.1607	.2727	3.6963
1.0	.83333	−2.1389	.3283	3.8386

For $t=0$ and $t=1.0$ we can give simple analytic expressions as follows:

$t=0$: $F_{11}=2(1-\log 2)$, $F_{12}=-40/3+16\log 2$,

$$F_{21}=\left\{\frac{\pi^2}{12}-(\log 2)^2+\frac{5}{2}\log 2-\frac{31}{16}\right\}+\gamma\left(-\frac{15}{16}+\frac{5}{2}\log 2,\right)$$

$$F_{22}=\left\{\frac{301}{6}-\frac{220}{3}\log 2+24(\log 2)^2-\pi^2\right\}+\gamma\left(\frac{95}{3}-44\log 2\right), \tag{2.8}$$

$t=1$: $F_{11}=5/6$, $F_{12}=-77/36$,

$F_{21}=19/60+\gamma/120$,

$F_{22}=677/360+1007\gamma/720$. (2.9)

§3. Discussion

It can be shown that the range of θ for which the θ-expansion of $d\Phi_t/d\theta$ is valid is given by

$$|\theta|<\mathrm{Min.}\left(\frac{1-\sigma^2}{2\sigma},\ \frac{1-\sigma}{\sqrt{\sigma}},\ \frac{1+\sigma}{\sqrt{\sigma}}\right),$$

which can also be expressed as

$$|\theta|<1-\sigma)/\sqrt{\sigma},$$

i.e.
$|\theta|<5.75°$ for $t=0.1$,
$|\theta|<31.87°$ for $t=0.5$,
$|\theta|<\infty$ for $t=1.0$.

But since this criterion is really for i finite series in powers of θ for $d\Phi_t/d\theta$, it may be expected that the range of validity of (2.2) and (2.3) will be smaller than the above.

In Figs. 1–3, the values of $d\Phi_t/d\theta$, calculated by means of (2.2) and (2.3) are given, together with some exact values calculated in [1], for the cases $t=0.1$, 0.5 and 1.0, the Mach numbers M being taken to be near

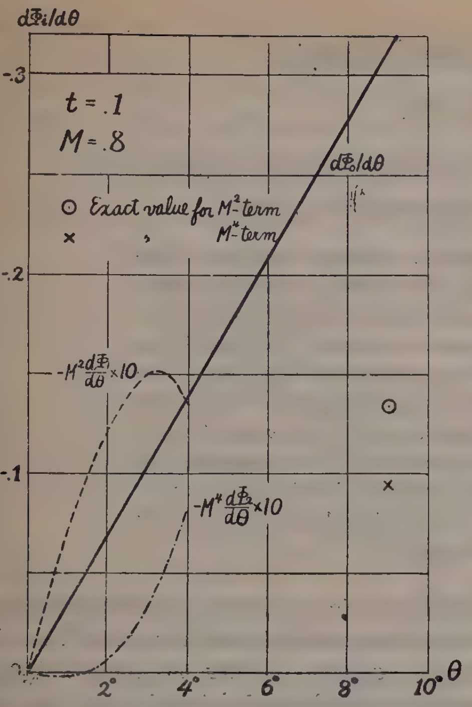

Fig. 1 $d\Phi_i/d\theta$ on the elliptic cylinder of $t=0.1$ at $M=0.8$

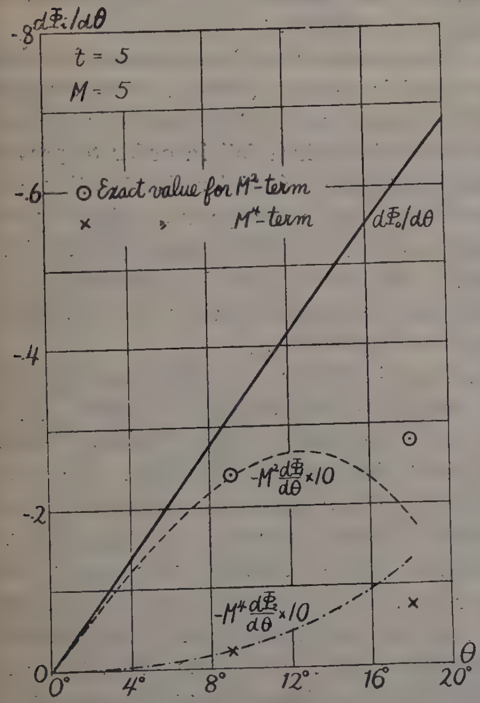

Fig. 2 $d\Phi_i/d\theta$ on the elliptic cylinder of $t=0.5$ at $M=0.5$

the critical Mach numbers for respective cases. From this we may conclude that the approximate formulae are adequate for the regions;

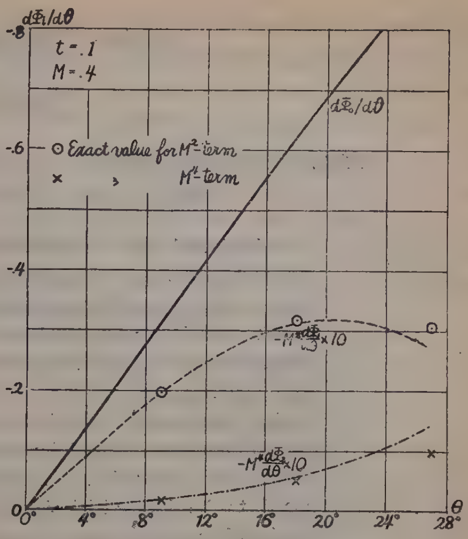

Fig. 3 $d\Phi_i/d\theta$ on the elliptic cylinder of $t=1.0$ at $M=0.4$ (Circular cylinder)

$|\theta|< 2°$ for $t=0.1$,
$|\theta|<10°$ for $t=0.5$,
$|\theta|<20°$ for $t=1.0$,

and the M^2—expansion method is very reliable near the stagnation point as far as the critical Mach number is reached, as expected from the nature of its approximation. Perhaps it may also be expected that the M^2-expansion method is convergent near the stagnation point even for the Mach number higher than the critical, although it may fail near the maximum-velocity region.

§4. Errata to [1]

		should be read
p. 168, author	Kawaguchi	Kawaguti
p. 170, in A_2	$(1+\sigma^2)^2$	$(1+\sigma^2)$
p. 171, in L_6	$\int_0^{\sigma}$	$\int_{\sigma}^{1}$
p. 171, in L_7	$\int_0^{\sigma}$	$\int_0^{\theta}$
p. 172, (3.15)	$q_2=\ldots\ldots)t^3$	$-q_2=\ldots\ldots)\}t^3$
p. 182, Table 1, fifth column	L_5	L_6

In conclusion, the author wishes to express his hearty gratitude to Prof. Imai for his kind guidance in the course of this work.

Reference

1) M. Kawaguti: Journ. Phys. Soc. Japan 6 (1951) 168.

JOURNAL OF THE PHYSICAL SOCIETY OF JAPAN Vol. 7, No. 3, MAY—JUN., 1952

Color Centers in Fused Quartz

Ryosuke YOKOTA

Matsuda Research Laboratory, Tokyo Shibaura Electric Co., Kawasaki, Kanagawa-ken

(Read October 19, 1951, Received November 28, 1951)

It is found that in fused quartz made in reducing condition three absorption bands having peaks at 2.3, 4.1 and 5.6 ev and in fused quartz made in oxidizing condition two absorption bands having peaks at 4.1 and 5.6 ev are produced by exposure to X-rays. The stability of these centers is studied by bleaching with temperature and light. The band having peak at 5.6 ev is found to be composed of two bands having peaks at 5.6 and 5.87 ev. The band at 2.3 ev is studied to be due to electrons trapped by negative-ion vacancy or by an aggregate of negative-ion vacancies. The luminescent center of fused quartz is proposed to be interstitial silicon atom. It is concluded that fused quartz has in fairly extent short range order of crystal.

§1. Introduction

The study of color centers is considered to be very powerful in developing the physics of solids. In ionic crystals, especially in the alkali halides, many valuable results have been obtained. But there is no research in the solids which contain partly the character of homopolar binding.

On the other hand, in the industry of lamps and valves, the glass is used to be the envelopes of the sources of X-rays, cathode rays or ultra-violet light and is exposed to them and consequently the change of its optical transmission occurs.

Fused quartz (SiO_2) is the simplest in the glass and is so pure that it is considered to be free from any foreign atom. Therefore the study of color conters in fused quartz is considered to be useful in physical and practical point of view.

Since 1925[1], fused quartz is known to be discolored by X-rays but a further research has not yet been performed.

§2. Color Centers Produced by X-Rays and Thermal Bleaching

There are two kinds of method to make fused quartz. In the one method quartz is put in the graphite crucible and is melted in the vacuum furnace by the heat of a very large electric current passing through a carbon resistance. In this case fused quartz is produced in a strongly reducing condition. In the other method which is called Verneiul[2] method, quartz powder is melted by the oxy-hydrogen flame in the air. In this case the flame is controlled to be oxidizing. The former is now denoted by C method and the latter by V method.

(a) The sample (30×12×4mm) produced by C method is X-rayed (100KV, 3mA, tungsten target) during which the sample is enclosed by a thin aluminium foil in order to prevent other irradiation. A violet discoloration, that is to say, an amethystine color exactly similar to that of natural amethyst, is developed. The absorption is measured by a Beckman spectrophotometer in the range from 200 to 1200 mμ.

In Fig. 1, (A) is the absorption curve of the sample X-rayed during 56 hours. (E) is that of the same sample before X-rayed corrected the loss of reflection. (A) is the difference of the measured absorption curves after and before exposure to X-rays. In the following figures through this paper, each absorption curve is always what is substracted that of no-X-rayed from the measured absorption curve. It is found that there are three absorption bands having peaks at 2.3, 4.1 and 5.6 ev. And these bands are always found in all samples measured. After the measurement of the absorption the sample was held in the dark at room temperature for two weeks and then the absorption was measured but no change was observed within the accuracy of the measurement. This stableness of these centers in the dark at room temperature enables us to carry out easily the various subsequent experiments.

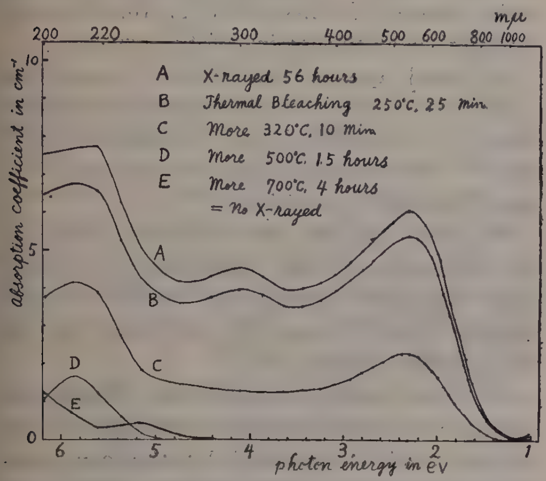

Fig. 1. The absorption bands in fused quartz made by C method, (A) after exposure to X-rays; (B) temperature bleaching, 250°C, 25 min.; (C) more treatment, 320°C, 10 min.; (D) more treatment, 500°c. 1.5 hours; (E) before exposure to X-rays.

The discolored sample in the dark emits a bluish-white luminescence when heated above 200°C, and the discoloration disappeared gradually. The expansion coefficient of fused quartz is so small (5.5×10^{-7} deg^{-1}) that we are able to manipulate very rapidly in heating and quenching. The sample is quickly inserted into the electric furnace maintained at 250°C in the dark and is taken off and quenched after 25 min. The absorption is measured and shown in Fig. 1 (B.). All bands decrease uniformly, but the band having its peak at 5.6 ev shifts its peak to 5.87 ev. After heating still (more 320° C, 10 min.), (C) curve is obtained. The band having its peak at 4.1 ev disappeared and the position of the peak at 5.87 ev remained. After heating still more (500°C, 1.5 hours), (D) curve is obtained. All bands except the band having its peak at 5.87 ev disappeared. After heating still more (700°C, 4 hours), (E) curve which is the same for the no-X-rayed is obtained. From the above experiments, it may be concluded that the left band which may correspond to the V band in the alkali halides is composed of two bands, one of which has its peak at 5.6 ev and the other at 5.87 ev. Each band having its peak at 2.3, 41., 5.6 and 5.87 ev is denoted by A, B, C, and D band respectively. It is concluded that the D band is the most stable.

(b) The sample made by V method is X-rayed during 56 hours at about 50°C and the absorption is measured. (Fig. 2)

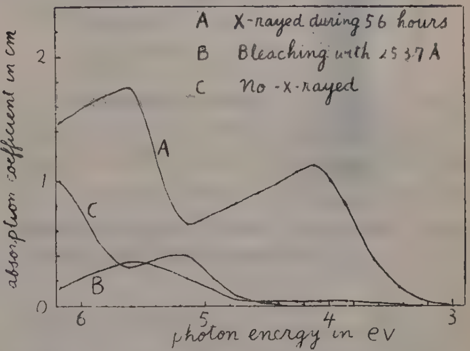

Fig. 2. The absorption bands in fused quartz made by V method. (A) after exposure to X-rays; (B) before exposure to X-rays; (c) bleaching with 2537A.

There are two absorption bands having peaks at 4.1 and 5.6 ev respectively. The absorption coefficients of the two bands are very small compared with those of the sample made by C method. There is no band at 2.3 ev which exists in the sample made by C method. This is a curious fact and this reason is discussed in §6. When this X-rayed sample is heated in the dark above 200°C, a white luminescence is observed, and the bands disappears.

§3. The Nature of the A Band

(a) The absorption of the A band is measured at room temperature and at the temperature of the liquid oxygen (90°K). In this measurement a constant deviation monochromator and the Se photo-cell and galvanometer were used. The light source is the special single filament tungsten lamp. The sample was put in the vacuum vessel shown in Fig. 3. This vessel was tightly supported by the supporting rod of the microscope of the travelling microscope in order that the sample is accurately put on the same position before the slit in the course of the measurement.

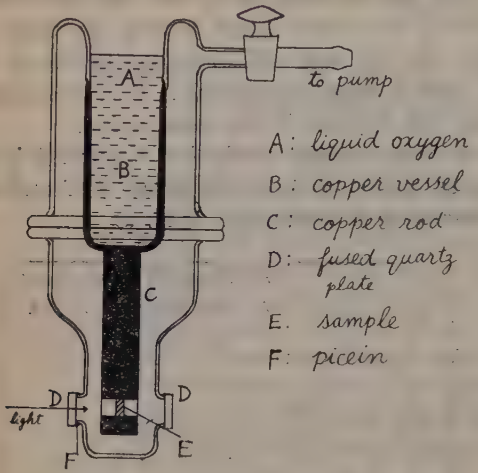

Fig. 3. Container of the sample for measuring absorption at low temperature.

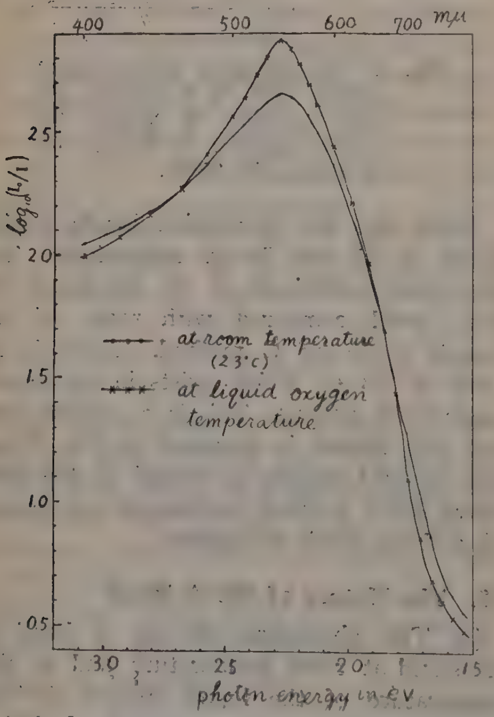

Fig. 4. Absorption curves at room temperature and liquid oxygen temperature.

Figure 4 shows two absorption curves for the same sample, one for room temperature, the other for liquid oxygen temperature. We note that the lower temperature curve is sharper than a higher and the peak remains its position within the accuracy of the measurement. In the alkali halides it is well known that the peak of the A band shifts to shorter wave-length when it is cooled to the lower temperature. According to the theory of Inui and Uemura[3], the main cause of this shift is the thermal contraction of the lattice of the crystal.

In fused quartz the thermal expansion coefficient is very small and in the range from 0°C to -190°C it is about -2×10^{-7} deg[-14]. This may be the reason why the peak remains its position.

The facts that the band becomes sharp at low temperature and disappeares with the heat treatment during 30 min. at 400°C indicate that this band is not a band due to the colloidal aggregates.

(b) The colored sample was illuminated during 6 hours by the Hg green light (about 2.3 ev) which is obtained by the condensation and filtration of the emitting light from the extra high-pressure mercury discharge lamp and is considered to be so strong as to produce any change. But no change in absorption curve was observed within the accuracy of the measurement. This fact seems to indicate that the A band is due to the transition from the ground state to the excited state which lies fairly below (about 0.5 ev or so) from the bottom of the conduction band. Therefore the configuration coordinate model of the A center is given in Fig. 5.

(c) The shape of the A band is considered

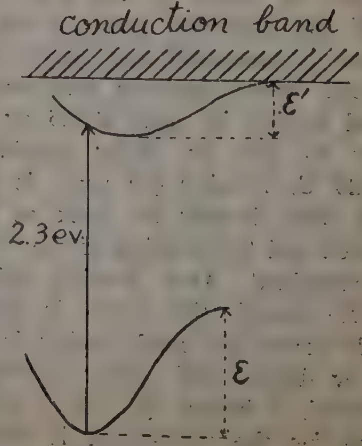

Fig. 5. Configuration coordinate model of the A center.

to be that of the resonance absorption which is characteristic of the band induced by the trapped electron or positive hole. The concentration of centers n_o is obtained by the formula given by Smakula(5).

$$n_0 f = \frac{18mc}{\pi e^2 h} \frac{n'}{(n'+2)^2} a_m W \qquad (1)$$

Here e, h, m, and c are the usual atomic constants and n' is the refractive index of medium and a_m is the absorption coefficient expressed in units of cm^{-1} at the center of the band and W is the width at half maximum of the band expressed in units of electron volts and f is the oscillator strength of the absorbing centers. Using the values of a_m and W obtained from the curves (A), (B) and (C), in Fig. 1, we have

(A) $n_0 f = 0.688 \times 10^{17}\ cm^{-3}$
(B) $n_0 f = 0.555 \times 10^{17}$ 〃
(C) $n_0 f = 0.208 \times 10^{17}$ 〃

Here n' is 1.4585. Because the oscillator strength f is assumed to be about unity, the concentration n_0 is the order of 10^{17} cm^{-13} and this value seems to be reasonable compared with the A center concentration in the alkali halides.

Because the concentration of (A) changed to (B) when heated in the dark, the change is monomolecular. Therefore the following relation holds

$$-(dn/dt) = nB_0 \exp(-\varepsilon/kT) \qquad (2)$$

where B_0 is the Reststrahlen frequency and ε is the activation energy surmounting from the ground state (see Fig. 5). From equation (2) ε is obtained to be 1.72 ev when the value of B_0 is adopted to be 5×10^{12} sec^{-1}. From the change from (B) to (C) ε is obtained to be 1.82 ev. Therefore ε is considered to be about 1.77 ev.

(d) Fused quartz made by V method is heated during 20 min. at 1350°C in the vacuum furnace in the vapour of silicon of which purity is 99.98%, and then is quenched. This sample is not discolored. But when this sample is exposed to X-rays during 56 hours, the violet coloration —A band— is obtained. The absorption curve is shown in Fig. 6.

Therefore it is concluded that the A band is due to the trapped electrons by the negative-ion vacancy.

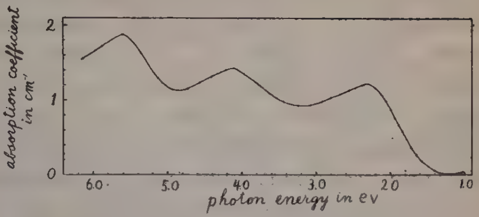

Fig. 6. Absorption curve of fused quartz which is made by V method and is heated in the silicon vapour and is exposed to X-rays.

(e) Fused quartz made by V method is inserted in the graphite crucible in the air at about 2000°C and is withdrawn after about 8 minutes. From this glass a piece of plate is cut off and polished and is exposed to X-rays during 56 hours. In this case the A band is obtained. The absorption curve is shown in Fig. 7. From this experiment it is clear that the negative-ion vacancy is produced by the strong reducing condition.

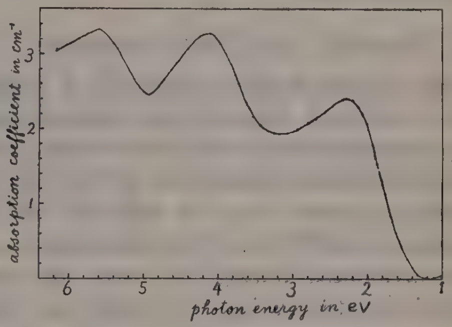

Fig. 7. Absorption curve of fused quartz which is made by V method and is heated in the strong reducing condition and is exposed to X-rays.

§4. Luminescent Center of Fused Quartz

The absorption curves of the several samples made by C and V method are always similar to that of Fig. 1 (E) and Fig. 2 (C) respectively. In all samples the small absorption band having the peak at 5.14 ev is always observed. When these samples are irradiated by the ultra-violet light, the bluish-white fluorescence which is very weak is always observed. With the use of the quartz monochromator, it is observed that the fluorescence bigins at about 2600 A and the efficiency of the fluorescence is considered to coincide with the absorption band above mentioned by a very crude experiment. Fused quartz made by V method was heated in the hydrogen furnace at 1500°C during 20 minutes and then was quenched. The efficiency of fluorescence becomes larger after this treatment than before. Therefore the absorption band having its peak at 5.14 ev may be assumed to be interstitial silicon atom with the analogy of interstitial zinc atom in zinc sulfide⁶⁾.

When the X-rayed sample made by C method was placed on the photographic plate in the dark during one week at room temperature, the image of the sample was obtained in the plate. By interposing filters, the wave-length of the emitted light was found to be in the range from 3000 to 5500 A, with the peak at about 4000 A, and this emitting radiation may be assumed to be the same as that of the glow luminescence, but this is so very weak that we cannot detect the change in the absorption curve even after two weeks.

§5. Bleaching with 2537A Radiation

The X-rayed samples made by C method were irradiated with the low pressure mercury discharge lamp made with fused quartz envelop which the large part of the emitting radiation (about 95%) is that of the Hg resonance line 2537 A. The absorption curves after irradiated during 13 hours and after more irradiated during 100 hours are given in Fig. 8 (B) and 8 (C) respectively.

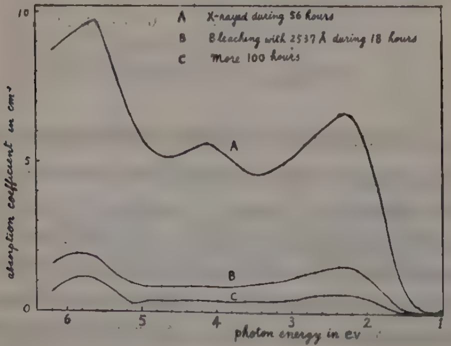

Fig. 8. Bleaching with 2537A of fuesd quartz made by C method.
(A) after exposure to X-rays; (B) bleached during 18 hours; (C) more bleached during 100 hours.

The change of the absorption curve resembles very much with the thermal bleaching shown in Fig. 1.

The absorption curve of the sample made by V method bleached during 20 hours with 2537A is given in Fig. 2 (B).

From Fig. 1, 2 and 8, it may be concluded that the A center is more stable than the B center and that the D center is more stable than the C center.

In the present stage of investigation, it is tentatively supposed that the positive holes freed from C and D centers by the stimulation of 2537A migrate in the filled band and recombine with the electrons trapped in the A and B centers.

This experiment may shows that even in the glass the positive hole is mobile in the filled band. And this fact may correspond to the study of conductivity induced by electron bombardment in fused quartz by Pensak⁷⁾.

§6. Discussions

In V method fused quartz is made in the mildly oxidizing atmosphere. Therefore the number of the negative-ion vacancy may be considered to be very small.

Fused quartz is probably the best electrical insulator known. According to the measurement of O. Gayling v. Altheim⁸⁾, specific resistivity of fused quartz at 20°C is 2.8×10^{17} ohm cm. and from the dependence of the electrical conductivity on the temperature the activation energy for diffusion of vacancy is obtained to be 1.53 ev. The measured sample in his experiment is not reported to be made whether in a reducing condition or in an oxidizing condition. But now we may consider the activation energy for difusion of vacancy to be about 1.53 ev which is about twice that of KCl. Therefore the mobility of the positive-ion vacancy or an aggregate of vacancies may be negligible small compared with the mobility in the alkali halides.

It is, therefore, considered that the number of vacancies can hardly increase during the exposure to X-rays, contrary to the case of KCl⁹⁾. This may be the reason why the A band is not produced in the sample made by V method in the oxidizing condition.

To verify the above reasoning, the measurent of density before and after exposure to X-rays is planned.

In C method fused quartz is made in the strongly reducing condition. Therefore the appreciable numbers of negativeion vacancies or aggregates of vacancies may exist and this may be the reason why the A band is produced by the exposure to X-rays. vacardes.

In the course of the exposure to X-rays and the bleaching with temperature and with the irradiation of A light or 2537A, no additional absorption band is observed. This may be partly explained by the extremely low mobility of vacancies in fused quartz.

The facts that in fused quartz made by V method when X-rayed B, C and D bands are produced and these bands disappear emitting a white luminescence when heated may indicate that the B band is a center due to a trapped electron.

It is well established that fused quartz hasn't the long range order of the crystal by the investigation of X-rays.

From the fact that the distinct absorption bands are produced in fused quartz, it may be concluded that fused quartz has in fairly extent the short range order of the crystal, in view of the absorption band being affected mainly by the situation of the neighborhood of the center. And this fact in fused quartz is well in agreement with the investigation of X-rays by Warren10) and with the consideration of thermal conductivity by Kittel11), and with some treatments of fused quartz and Na_2O-SiO_2 glasses by the author12).

In conclusion the author expresses his sincere thanks to Prof. T. Uemura for his approvement of the use of the Beckman spectrophotometer and to Mr. K. Tanaka for his assistance of the measurement of absorption, and to Prof. T. Inui and Y. Uemura and Y. Toyozawa for their kind discussions.

References

1) Hopwood and Mayneord: Nature **116** (1925) 98; A. C. Bailey and J. W. Woodraw: Phil. Mag. **6** (1928) 40; S. Ito: Matsuda Res. Rep. **7** (1932) 87.
2) Verneiul: Comptes Rendus **135** (1902) 79.
3) T. Inui and Y. Uemura: Progr. Theor. Phys. **5** (1950) 395.
4) G. W. Morey: "*Properties of Glass*" Reinhold Publishing Cooperation, New York, 1938.
5) A. Smakula: ZS. f. Phys. **59** (1930) 603,
6) F. Seitz: J. Chem. Phys. **6** (1938) 454; Trans. Faraday Soc. **35** (1939) 74.
7) L. Pensak: Phys. Rev. **75** (1949) 472.
8) O. Gayling von Altheim: Ann. d. Phys. **35** (1939) 417.
9) F. Seitz: Rev. Mod. Phys. **18** (1946) 384; I. Estermann, W. J. Leivo, and O. Stern: Phys. Rev. **75** (1949) 627.
10) B. E. Warren, H. Krutter and O. Morningstar: J. Amer. Ceram. Soc. **19** (1936) 202; B. E. Warren: J. Appl. Phys. **13** (1942) 602.
11) C. Kittel: Phys. Rev. **75** (1949) 972.
12) R. Yokota: J. Phys. Soc. Japan **5** (1950) 295; ibid. **6** (1951) 489.

JOURNAL OF THE PHYSICAL SOCIETY OF JAPAN Vol. 7, No. 3, MAY.—JUN., 1952

Application of the Thin-Wing-Expansion Method to the Compressible Flow past an Elliptic Cylinder

Hidenori HASIMOTO

Department of Physics, Faculty of Science, University of Tokyo

(Received, December 28, 1951)

Imai's thin-wing-expansion method is applied to a uniform flow past an elliptic cylinder at zero angle of attack, in order to obtain the analytic expressions correct to the third approximation for the complex velocity potential, and for the velocity distribution over the cylinder. Numerical calculation is made for the case $t=0.1$ where t is the thickness ratio of the cylinder. The convergence of the result seems to be satisfactory except near the stagnation point, where the anomalous behaviour appears.

§1. Introduction and Summary

The two-dimensional irrotational flow of a compressible fluid has been studied by various authors using various methods, e.g., the M^2-expansion method, the hodograph method, and the thin-wing-expansion method. The M^2-expansion method can be applicable only to the flow at small Mach numbers, its convergence becoming doubtful for large Mach numbers. On the other hand, the hodograph method can give successful results for several types of flow including transonic region, but it is not suited for the discussion of the flow past an arbitrarily given obstacle.

The thin-wing-expansion method seems to be most useful for studying the flow at high subsonic speeds past an arbitrarily given obstacle. Thus, Kaplan[1] has made elaborate investigations, to the order of third approximation, on the flow past a circular arc aerofoil and a kind of cusped aerofoil which is now called Kaplan's bump. Several years ago, Imai[2] developed a very elegant method and gave analytical formulae for the lift and moment of any arbitrary thin aerofoil as well as velocity distribution on its surface to the second approximation. Further, Imai and Ōyama[3] extended this method to the third approximation and applied it, with success, to the flow past a sinusoidal wall.* Now, for blunt-nosed obstacles such as an elliptic cylinder, for which the problem of the convergence of the thin-wing-expansion method occurs, have hitherto been left without detailed study.**

In this paper, Imai's procedure will be applied to a uniform flow past an elliptic cylinder at zero angle of attack, in order to obtain the analytic expressions to the third approximation for the complex velocity potential, and for the velocity distribution over the cylinder. Numerical calculations will be made for the case $t=0.1$ where t is the thickness ratio of the elliptic cylinder.

It should be mentioned here that the flow past an elliptic cylinder has already been investigated by several authors employing various methods, especially by Kawaguti[6] (the M^2-expansion method, correct to the order of M^4), Imai[7] (the transonic thin-wing-expansion method to the third approximation), and Imai and Hasimoto[8] (the simplified hodograph method based on the W.K.B. approximation). Therefore, comparison of these investigations with the present one will also be made in this paper.

§2. Thin-Wing-Expension Method of Imai

Imai's thin-wing-expansion method has been formulated to the third approximation by Imai[2], and by Imai and Ōyama[3]. But, a brief account of their results will be given here, for the sake of convenience.

---

* In this connection it may be mentioned that Görtler[4] had already treated analogous flow patterns along sinusoidal walls. However, in his investigation, the shapes of boundary walls are not fixed, but vary with the flow Mach number.

** Recently we became aware that this problem had been partly investigated by Schmieden and Kawalki.[5] But their method, depending on the stream function, is quite different from ours, and moreover they gave no numerical discussion on the velocity distribution over the cylinder because of "the prohibitive amount of calculations required."

The equations of motion of a compressible flow can be written in the form

$$u=\frac{\partial\Phi}{\partial x}=\frac{\rho_\infty}{\rho}\frac{\partial\Psi}{\partial y}, \quad v=\frac{\partial\Phi}{\partial y}=-\frac{\rho_\infty}{\rho}\frac{\partial\Psi}{\partial x}, \tag{2.1}$$

where (u, v) are the component velocities, Φ is the velocity potential, Ψ the stream function, ρ the density and ρ_∞ the density of the undisturbed fluid. For the adiabatic flow ρ is given by the formula

$$\rho/\rho_\infty=\left\{1-\frac{\gamma-1}{2}M^2\left(\frac{q^2}{U^2}-1\right)\right\}^{\frac{1}{\gamma-1}}, \tag{2.2}$$

where q is the magnitude of the velocity, U, M are the velocity and the Mach number of the undisturbed flow, and γ is the adiabatic index of the fluid. For simplicity we take $U=1$ in this paper. Then the undisturbed flow is given by $\Phi=x$, $\Psi=y$. On the assumption that the disturbance due to the presence of the aerofoil would be small, Φ and Ψ may be expressed as

$$\Phi=x+\phi_1+\phi_2+\phi_3+\dots, \quad \Psi=y+\psi_1+\psi_2+\psi_3+\dots, \tag{2.3}$$

where ϕ_1, ψ_1; ϕ_2, ψ_2; ...... are respectively $O(\varepsilon)$, $O(\varepsilon^2)$, ..., where ε is asmall parameter. We now write

$$x=\xi, \; y=\eta/\mu, \; \psi=\mu\chi, \; \mu=\sqrt{1-M^2}, \tag{2.4}$$

and introduce complex quantities

$$\zeta=\xi+i\eta, \; \bar\zeta=\xi-i\eta, \; G=\phi+i\chi. \tag{2.5}$$

Substituting (2.3), (2.4), (2.5) into (2.1) and (2.2), considering the order of magnitude of the various terms, and performing the integration after successive iterations we get

$$G_1=f(\zeta), \tag{2.6$'$}$$

$$G_2=\frac{M^2}{4}[\nu f'^2\bar\zeta+(1+\nu)\{2f'\bar f+\int(\overline{f'})^2 a\bar\zeta\}+f_2(\zeta), \tag{2.6$''$}$$

$$G_3=Af'^3\bar\zeta+B\int(\overline{j'})^3d\bar\zeta+3Bj'^2\bar f+cf'\int(\overline{f'})^2d\bar\zeta$$
$$+D\int J(f'+\overline{f'})d\bar\zeta-\frac{M^2}{2}f'\int\frac{\partial}{\partial\zeta}(G_2+\overline{G_2})d\bar\zeta$$
$$+f_3(\zeta), \tag{2.6$'''$}$$

where

$$J=2\partial\phi_2/\partial x=\partial G_2/\partial\zeta+\partial G_2/\partial\bar\zeta+\partial\bar G_2/\partial\zeta+\partial\overline{G_2}/\partial\bar\zeta, \tag{2.7}$$

$$\nu=(\gamma+1)M^2/4\mu^2, \tag{2.8}$$

$$A=M^6(\gamma+1)(2\gamma-5)/96\mu^2,$$
$$B=M^4\{6(\gamma-1)-(2\gamma-1)(3-\gamma)M^2\}/96\mu^2,$$
$$C=M^2\{8-8(3-\gamma)M^2+(13-9\gamma+2\gamma^2)M^4\}/32\mu^2, \tag{2.9}$$
$$D=M^2\{4-(3-\gamma)M^2\}/8\mu^2=M^2(1+\nu)/2.$$

These $f(\zeta)$, $f_2(\zeta)$ and $f_3(\zeta)$ are analytic functions of ζ to be determined from the following boundary conditions:

(i) $\partial G/\partial\zeta$ is one-valued and continuous in the field of flow,

(ii) $\partial G/\partial\zeta\to 0$ as $\zeta\to\infty$,

(iii) $\Psi=\text{const}$ (say $=0$) on the profile P; accordingly,

$$Im\{\mu^2G(\zeta_P, \bar\zeta_P)+\zeta_P\}=0. \tag{2.10}$$

§3. Elliptic Cylinder

We now consider a uniform flow, without circulation, past a thin elliptic cylinder at zero angle of attack. As is well known, the region outside the unit circle $Z=e^{i\theta}$ in the Z-plane ($Z=X+iY$) is mapped onto the region outside an ellipse of thickness ratio $(1-\sigma^2)/(1+\sigma^2)$ in the ζ-plane by

$$\zeta=Z+\sigma^2Z^{-1}. \tag{3.1}$$

Taking

$$\sigma^2=(1-\mu t)/(1+\mu t), \tag{3.2}$$

we obtain an ellipse of thickness ratio t in the physical plane, which is represented by (see (2.4))

$$x=(1+\sigma^2)\cos\theta, \quad y=(1+\sigma^2)t\sin\theta. \tag{3.3}$$

Substituting (3.1) into (2.10) we get, on the profile: $Z\bar Z=1$,

$$Im(\mu^2G-\varepsilon\mu^2Z^{-1})=0,$$
$$\varepsilon=(1-\sigma^2)/\mu^2=(2t/\mu)(1+\mu t)^{-1}. \tag{3.4}$$

ε is a small parameter, if the ellipse is sufficiently thin. Thus we find easily

$$G_1=f(\zeta)=\varepsilon Z^{-1}, \tag{3.5}$$

and at $Z\bar Z=1$,

$$ImG_2=ImG_3=\dots\dots=0. \tag{3.6}$$

Substituting (3.5) into (2.6$''$) we get

$$G_2=\frac{\varepsilon^2}{4}M^2\left[\frac{\nu}{(z^2-\sigma^2)^2}\left(\bar Z+\frac{\sigma^2}{\bar\sigma^2}\right)+(1+\nu)\right.$$
$$\left.\left\{-\frac{2}{Z^2-\sigma^2}\frac{1}{Z}+\frac{1}{\sigma^2}\left(\bar J_1+\frac{1}{\bar Z}\right)\right\}\right]+f_2(\zeta). \tag{3.7}$$

$f_2(\zeta)$ is obtained from the boundary conditions (2.10) and (3.6) as

$$f_2(\zeta)=-\frac{\varepsilon^2}{4}M^2\left[\frac{\nu}{(\bar Z^2-\sigma^2)^2}\left(\frac{1}{Z}+\sigma^2Z\right)\right.$$

$$-\frac{2(1+\nu)}{Z^2-\sigma^2}Z-\frac{1+\nu}{\sigma^2}\left(J_1+\frac{1}{Z}\right)\Big], \qquad (3.8)$$

where

$$J_1=\frac{1}{2\sigma}\log\frac{Z-\sigma}{Z+\sigma}.$$

These are the results already obtained by Imai in his unpublished work. We now proceed to the third approximation. For brevity, only the outline of the calculation will be given.

In general, (2.6‴) can be transformed into the form

$$\begin{aligned}G_3={}&a_1f'^3\bar{\zeta}+a_2\int(\bar{f}')^3d\bar{\zeta}+a_3f'^2\bar{f}+a_4f'\int(\bar{f}')^2d\bar{\zeta}\\&+\frac{M^4}{8}\nu f'^2f''\bar{\zeta}^2+M^2D\nu\Big(\frac{1}{6}\bar{f}'^3\zeta\\&\qquad+\frac{1}{4}f'\zeta\bar{f}'^2+\frac{1}{2}f'f''\bar{f}\bar{\zeta}\Big)\\&+\frac{M^2}{4}D(1+\nu)(f\bar{f}'^2+f''\bar{f}^2+2ff'\bar{f}')\\&+\frac{M^2}{2}\nu\bar{f}'f'_2\bar{\zeta}+D(f'\bar{f}_2+f'_2\bar{f}+\int\bar{f}'\bar{f}'_2d\bar{\zeta})\\&+f_3(\zeta),\end{aligned}$$

$$\begin{aligned}a_1&=A+M^2D(1+2\nu)/4-M^4(1+\nu)8,\\a_2&=B+M^2D(1+2\nu)/4,\\a_2&=3B+M^2D(5+6\nu)/4-M^4(1+\nu)/4,\\a_3&=C+M^2D(5+6\nu)/4-M^4\nu/8.\end{aligned} \qquad (3.9)$$

Introducing $f(\zeta)$ and $f_2(\zeta)$ as given by (3.5) and (3.8) into (3.9) and making straightforward calculations, we have the explicit expression for G_3. Here $f_3(\zeta)$ is determind from (2.10) and (3.6), remembering that it should be analytic and one-valued in the field of flow. Thus,

$$G_3=\sum_{n=1}^{23}b_nh_n+f_3(\zeta),$$

$$f_3(\zeta)=\sum_{n=1}^{23}b_ng_n(\zeta),$$

where

$b_1=\frac{B}{\sigma^4}+\frac{M^2D}{4\sigma^6}[(2+3\nu)\sigma^2-\nu]$	$h_1=\frac{1}{\bar{Z}}$	$g_1=\frac{1}{Z}$
$b_2=-\frac{1}{\sigma^2}\left\{C+\frac{M^2}{4}(6+7\nu)-\frac{M^4}{8}\nu\right\}-\frac{M^2}{2}D(1+\nu)$	$h_2=\frac{1}{V}\frac{1}{\bar{Z}}$	$g_2=-\frac{Z}{V}$
$b_3=\frac{B}{2\sigma^4}+\frac{M^2D}{32\sigma^6}\{(14\nu+22)\sigma^4+4(3+5\nu)\sigma^2+3\nu\}$	$h_3=\frac{\bar{Z}}{\bar{V}}$	$g_3=-g_2$
$b_4=\frac{M^2}{4}D(1+\nu)$	$h_4=\frac{1}{Z}\frac{1}{\bar{V}^2}$	$g_4=-g_5=g_6=\frac{Z}{V^2}$
$b_5=3B-\frac{1}{\sigma^2}\left\{C+\frac{M^2}{4}(6+7\nu)-\frac{M^4}{8}\nu\right\}-\frac{M^2}{2}D(1+\nu)$	$h_5=\frac{1}{V^2}\frac{1}{\bar{Z}}$	
$b_6=\frac{-M^2D\nu}{48\sigma^4}(13\sigma^4+17)-\frac{1}{4}M^2D$	$h_6=\frac{Z}{\bar{V}^2}$	
$b_7=\frac{M^2D\nu}{6\sigma^2}(1+\sigma^4)$	$h_7=\frac{Z}{V^3}$	$g_7=-g_8=\frac{Z}{V^3}$
$b_8=\frac{M^2D}{4}\{(3\nu-4)\sigma^4+5\nu\}$	$h_8=\frac{1}{V^3\bar{Z}}$	
$b_9=\frac{M^2D}{2}(1+\nu)$	$h_9=\frac{Z^3}{V^3}\frac{1}{\bar{Z}^2}$	$g_9=-\frac{Z^5}{V^3}$
$b_{11}=M^2D\nu\sigma^2(1+\sigma^4)$	$h_{11}=\frac{1}{V^2}\frac{1}{\bar{Z}}$	$g_{11}=-\frac{Z}{V^4}$
$b_{12}=\frac{-M^4\nu}{2}(1+\nu)$	$h_{12}=\frac{1}{V^2}\bar{\zeta}$	$g_{12}=-\frac{1}{V^2}\left(\frac{1}{Z}+\sigma^2Z\right)$
$b_{13}=-A+\frac{3M^4\nu}{8}\{\sigma^2(2+\nu)-(1+\nu)\}$	$h_{13}=\frac{1}{V^3}\bar{\zeta}$	$g_{13}=-\frac{1}{V^3}\left(\frac{1}{Z}+\sigma^2Z\right)$
$b_{14}=\frac{M^2}{4}\left(D-\frac{M^2}{2}\right)\{(4-3\nu)\sigma^4-5\nu\}$	$h_{14}=\frac{1}{V^4}\bar{\zeta}$	$g_{14}=-\frac{1}{V^4}\left(\frac{1}{Z}+\sigma^2Z\right)$

$$\begin{array}{lll}
b_{15}=-\dfrac{M^4}{2}\nu^2\sigma^2(1+\alpha^4) & h_{15}=\dfrac{1}{V^5}\bar{\zeta} & b_{15}=-\dfrac{1}{V^5}\left(\dfrac{1}{Z}+\sigma^2 Z\right) \\
b_{16}=-\dfrac{1}{2}M^2D\nu & h_{16}=\dfrac{1}{\bar{V}^3}\zeta & g_{\,6}=-g_{13} \\
b_{17}=-M^2D\nu & h_{17}=\dfrac{Z^3}{V^4}\dfrac{\bar{\zeta}}{Z} & g_{17}=-\dfrac{Z^3}{V^4}(1+\sigma^2Z^2) \\
b_{18}=\dfrac{M^4\nu^2}{2} & h_{18}=\dfrac{Z^3}{V^5}\bar{\zeta}^2 & g_{18}=-\dfrac{Z}{V^5}(1+\sigma^2Z^2)^2 \\
b_{19}=\dfrac{3B}{2\sigma^4}+\dfrac{M^2D}{32\sigma^6}\{(4+5\nu)\sigma^4 & h_{19}=\bar{J}=\dfrac{1}{2\sigma}\log\dfrac{\bar{Z}-\sigma}{\bar{Z}+\sigma} & g_{19}=J=\dfrac{1}{2\sigma}\log\dfrac{Z-\sigma}{Z+\sigma} \\
\qquad\qquad +12(2+3\nu)\sigma^2-5\nu\} & & \\
b_{21}=-\dfrac{1}{\sigma^2}\left\{C+\dfrac{M^2}{4}(6+7\nu)\quad\dfrac{M^4}{8}\nu\right\} & h_{21}=\dfrac{1}{V}\bar{J}=\dfrac{1}{2\sigma V}\log\dfrac{\bar{Z}-\sigma}{\bar{Z}+\sigma} & g_{21}=\dfrac{1}{2(1-\ {}^4\sigma)}\log\dfrac{Z-\sigma}{Z+\sigma} \\
 & & \qquad -\dfrac{1}{2\sigma}\left(\dfrac{1}{V}-\dfrac{\sigma^2}{1-\sigma^4}\right)\log\dfrac{1\quad\sigma Z}{1+\sigma Z} \\
b_{22}=\dfrac{M^2D}{2}(1+\nu) & h_{22}=\dfrac{1}{Z}\dfrac{1}{V}\dfrac{1}{\bar{V}}+\dfrac{\bar{Z}}{V\bar{V}} & g_{22}=g_{23}=0 \\
b_{23}=-\dfrac{M^2D\nu}{4} & h_{23}=\dfrac{Z}{V\bar{V}^2}\left\{\zeta-\dfrac{1+\sigma^2\bar{Z}}{Z}\right\} &
\end{array} \tag{3.10}$$

where $V=Z^2-\sigma^2$.

If we are interested only in the quantities on the ellipse $Z\bar{Z}=1$, G_1, G_2, G_3 can be reduced into simpler forms,

$$G_1/\varepsilon=\frac{1}{Z}$$

$$G_2/\varepsilon^2=\frac{M^2(1+\nu)}{4\sigma^2}\left(\frac{1}{Z}+\frac{1}{2\sigma}\log\frac{Z-\sigma}{Z+\sigma}\right)+c.c.$$

$$G_3/\varepsilon^3=\frac{A_0}{Z}+\frac{A_1}{Z^2-\sigma^2}+\frac{A_2Z}{(Z^2-\sigma^2)^2}+\frac{A_3Z}{(Z^2-\sigma^2)^3}+\frac{A_4}{(Z^2-\sigma^2)^3Z}+\frac{A_5}{2\sigma}\log\frac{Z-\sigma}{Z+\sigma}$$
$$+\frac{A_6}{2\sigma}\frac{Z^2}{1-\sigma^2Z^2}\log\frac{Z-\sigma}{Z+\sigma}+c.c. \tag{3.11}$$

where

$$A_0=\frac{1}{\sigma^4}\left[B+\frac{M^2D}{4}(2+3\nu)\right]-\frac{M^2D\nu}{4\sigma^6},\qquad A_5=\frac{3B}{2\sigma^4}+\frac{M^2D}{32\sigma^6}\{(5\nu+4)\sigma^4+12(2+3\nu)\sigma^2-5\nu\}-\frac{1}{\sigma^2}A_6,$$

$$A_1=\frac{L}{2\sigma^2}+\frac{B}{2\sigma^4}+\frac{M^9D}{32\sigma^6}\{(5\nu+4)\sigma^4+4(2+3\nu)\sigma^2+3\nu\},\quad A_6=-\frac{1}{\sigma^2}\left\{C+\frac{M^2}{4}D(5+6\nu)-\frac{M^4\nu}{8}\right\},$$

$$A_2=\frac{-M^2D\nu}{48\sigma^4}[\sigma^4+7],\qquad L=A_6\log\frac{1+\sigma^2}{1-\sigma^2},$$

$$A_3=\frac{M^2D\nu}{6\sigma^2},$$

$$A_4=-\frac{1}{6}M^2D\nu,$$

and *c.c.* denotes complex conjugate.

The velocity distribution on the surface of the elliptic cylinder ($Z=e^{i\theta}$) can be expressed in the form

$$q=\frac{d\Phi}{ds}=\frac{d\Phi}{d\theta}\frac{d\theta}{ds}, \tag{3.13}$$

where $d\theta/ds$ is obtained from (3.3) as

$$\frac{d\theta}{ds}=\frac{-1}{(1+\sigma^2)(\sin^2\theta+t^2\cos^2\theta)^{1/2}}, \tag{3.14}$$

and

$$\frac{d\Phi}{d\theta}=\frac{dx}{d\theta}+\frac{d\phi_1}{d\theta}+\frac{d\phi_2}{d\theta}+\frac{d\phi_3}{d\theta}, \tag{3.15}$$

Here,

$$\frac{d\phi_n}{d\theta}=-Im\left(Z\frac{\partial G_n}{\partial Z}-\bar{Z}\frac{\partial G_n}{\partial \bar{Z}}\right), \qquad n=1,\ 2,\ 3. \tag{3.16}$$

Hence, from (2.3) and (3.11), we have

$$\begin{aligned}
&\frac{dx}{d\theta}=-\sin\theta,\\
&\frac{1}{\varepsilon}\frac{d\phi_1}{d\theta}=-\sin\theta,\\
&\frac{1}{2\varepsilon^2}\frac{d\phi_2}{d\theta}=-\frac{M^2}{2\sigma^2}(1+\nu)\left[1-\frac{1+\sigma^2}{\Theta}\right]\sin\theta,\\
&\frac{1}{2\varepsilon^3}\frac{d\phi_3}{d\theta}=\left[-A_0+\left\{(1+\sigma^2)\left(A_0+\frac{A_6}{2\sigma^2}\log\frac{1-\sigma^2}{1+\sigma^2}\right)\right\}\frac{1}{\Theta}-B_1\sigma^2(\sigma^2+3)\frac{1}{\Theta^2}\right.\\
&\qquad\qquad\left.+\frac{\sigma^2}{12}(\sigma^6+\sigma^4-3\sigma^2-9)M^2D\nu\frac{1}{\Theta^3}\right]\sin\theta\\
&\quad-(2\sigma^2A_1+3A_2)\frac{\sin 3\theta}{\Theta^2}+\frac{1}{4}M^2D\nu(3+\sigma^4)\frac{\sin 3\theta}{\Theta^3}-\frac{M^2D\nu}{12\sigma^2}(3+5\sigma^4)\frac{\sin 5\theta}{\Theta^3}+\frac{1}{6}M^2D\nu\frac{\sin 7\theta}{\Theta^3}\\
&\quad-\frac{A_7}{\sigma}(1-\sigma^4)\frac{\sin\theta}{\Theta^2}\left[(1-\sigma^4)\cos\theta\log\frac{1-2\sigma\cos\theta+\sigma^2}{1+2\sigma\cos\theta+\sigma^2}+\{(1+\sigma^4)\cos 2\theta-2\sigma^3\}\tan^{-1}\frac{2\sigma}{1-\sigma^2}\right]
\end{aligned} \tag{3.17}$$

where

$$\Theta=1-2\sigma^2\cos 2\theta+\sigma^4.$$

Thus the velocity distribution $q(\theta)$ has been obtained correct to the order of ε^3.

For the sake of comparison, if we make $\sigma^2\to 1$ in the expression for q, and rearrange it formally into power series in t, we get

$$q_{(t)}=1+\frac{t}{\mu}+\frac{t^2}{2\mu^2}(1+\nu)(M^2-\cot^2\theta)+$$
$$t^3\left\{-E\cot^2\theta+\frac{M^2}{\mu^7}\left(F-\frac{G}{\sin^2\theta}+\frac{H}{\sin^3\theta}\right)\right\}, \tag{3.18}$$

where

$$E=\frac{1}{2\mu}\{1+M^2(1+\nu)\},$$
$$F=\frac{M^2}{12}\{6(\gamma+3)-(25-\gamma-2\gamma^2)M^2+3(2-\gamma)M^4\},$$
$$G=\frac{1}{8}\{4+7(\gamma+1)M^2+(2\gamma+5)(\gamma-3)M^4-2(\gamma-3)M^6\},$$
$$H=\frac{\pi}{128}\{32+32(\gamma-1)M^2+4(2\gamma^2-5\gamma+1)M^4-(\gamma-3)(\gamma+1)M^6\}.$$

This simple formula would give a satisfactory result so far as $\sin\theta \gg t$.

Putting $\beta=\frac{\gamma+1}{8\mu^3}t$ in $q_{(t)}$ and making $\mu\to 0$ ($M\to 1$) and $t\to 0$ so that β may be a small quantity, we have

$$q=1+\frac{8\mu^2}{\gamma+1}\beta\left[1-\beta\frac{\cos 2\theta}{\cos\theta}+\beta^3\left(\frac{32}{3}-\frac{16}{\sin^2\theta}+\frac{7}{2}\pi\frac{1}{\sin^3\theta}\right)\right],$$

which coincides with Imai's result[7)] obtained by use of his transonic thin-wing-expansion method.

On the other hand, if we expand (3.18) in powers of M^2, we arrive at a result coinciding with that of Kawaguti[6)] obtained by use of the M^2-expansion method.

§4. Numerical Discussion

As numerical examples, we shall take an elliptic cylinder of thickness ratio $t=0.1$, and calculate the velocity distribution on the surface of the cylinder for the case $M=0.7$ and $M=0.8$. Here we should take

$$\sigma^2=(1-\mu t)/(1+\mu t),\ \varepsilon=(1-\sigma^2)/(1-M^2).$$

The results of calculations are given in Table I, Fig. 1 ($M=0.7$) and Fig. 2 ($M=0.8$), where the results obtained by using various other methods are given for comparison.

Very anomalous behaviour near the stagnation point $\theta=0$ may be accounted for by the following fact. In $q_{(t)}$ we assumed $\sin\theta \gg t$, which fails near the point $\theta=0$. The anomalous behaviour of q, which appears even if we make use of the rigorous expansion in ε as given by (3.13)–(3.17), seems to be partly due to the divergence of the thin-wing-expansion method, because of the large perturbation velocity there. But if we take small values of M, this anomaly becomes small. This shows that the effect of compressibility is essential for the divergence of the thin-wing-expansion method. At any rate it will be seen that the convergence is satisfactory except near the stagnation point.

Fig. 3 shows the velocity at the point $\theta=\pi/2$ plotted against the Mach number for several values ($t=0.05$, 0.1, 0.2, 0.5) of the thickness ratio calculated by using (3.18). A curve which shows the local velocity of sound against the Mach number is also plotted there.

In conclusion the author wishes to express his hearty gratitude to Professor I. Imai for his kind guidance in the course of this work, and to Mr. M. Kawaguti for the valuable discussions.

Table I. The velocity distribution over an elliptic cylinder of $t=0.1$. $O(\varepsilon n)$ gives the values calculated neglecting $O(\varepsilon n)$.

deg.	incom-pressible	$M=0.7$				$M=0.8$			
		$O(\varepsilon)$	$O(\varepsilon^2)$	$O(\varepsilon^3)$	$O(t^3)$	$O(\varepsilon)$	$O(\varepsilon^2)$	$O(\varepsilon^3)$	$O(t^3)$
0	0.0000	0.0000	0.0000	0.0000	∞	0.0000	0.0000	0.0000	0 ∞
9	0.9302	0.9640	0.7268	0.9450	1.4282	0.9865	0.3936	1.6938	4.8151
18	1.0513	1.0896	1.0151	1.0576	1.0810	1.1151	0.9519	1.1703	1.4418
27	1.0794	1.1187	1.0939	1.1012	1.1047	1.1448	1.0859	1.1302	1.2175
36	1.0898	1.1294	1.1207	1.1229	1.1237	1.1558	1.1355	1.1502	1.1885
45	1.0945	1.1344	1.1338	1.1353	1.1349	1.1609	1.1587	1.1680	1.1867
54	1.0971	1.1370	1.1400	1.1417	1.1416	1.1636	1.1711	1.1797	1.1912
63	1.0986	1.1386	1.1439	1.1458	1.1457	1.1652	1.1782	1.1871	1.1919
72	1.0994	1.1394	1.1461	1.1483	1.1481	1.1661	1.1822	1.1919	1.1939
81	1.0998	1.1399	1.1472	1.1496	1.1494	1.1665	1.1844	1.1946	1.1951
90	1.1000	1.1400	1.1476	1.1501	1.1498	1.1667	1.1850	1.1954	1.1955

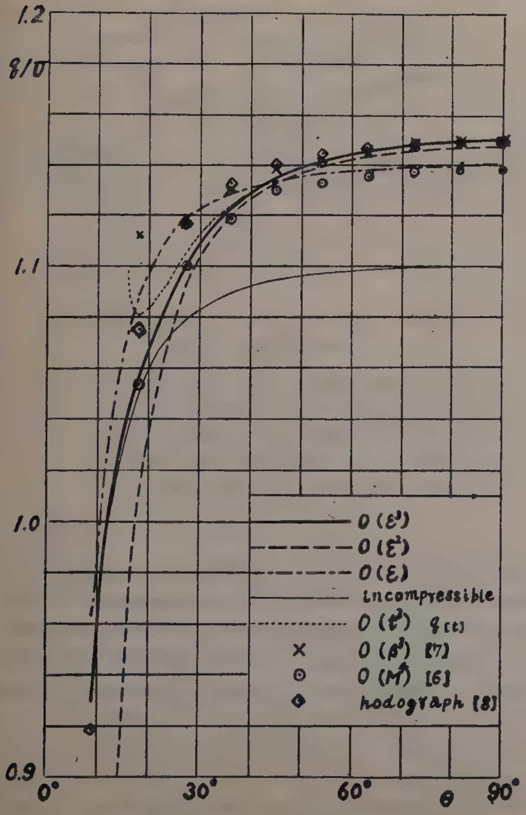

Fig. 1. The velocity distribution over an elliptic cylinder of $t=0.1$ at $M=0.7$.

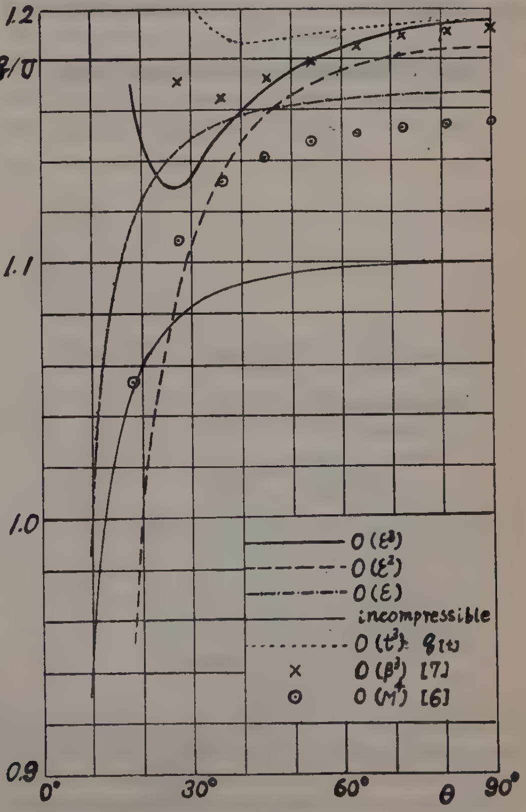

Fig. 2. The velocity distribution over an elliptic cylinder of $t=0.1$ at $M=0.8$.

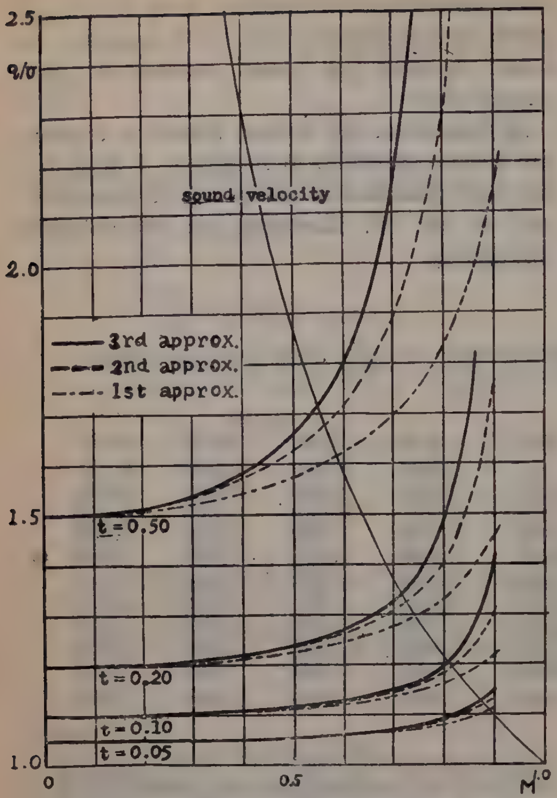

Fig. 3. The velocity at the point $\theta=\pi/2$.

References

1) C. Kaplan: N.A.C.A. Tech. Rep. No. 794 (1949); 768 (1943).

2) I. Imai: Rep. Aeron. Res. Inst. Tokyo Imp. Univ. No. 294 (1944).

3) I. Imai and S. Oyama: Rep. Inst. Sci. & Tech. Univ. Tokyo **2** (1948) 37,39.

4) H. Görtler: Z. a. M.M. **20** (1940) 254.

5) C. Schmieden and K. H. Kawalki: N.A.C.A. Tech. Mem. No. 1233 (1951).

6) M. Kawaguti: J. Phys. Soc. Japan. **6** 1951) 168.

7) I. Imai, unpublished.

8) I. Imai and H. Hasimoto: J. Math. & Phys. **28** (1950) 205.

J. PHYS. SOC. JAPAN 7 (1952) 329–330

On the Aging after Annealing of Cast Polymethylmethacrylate

By Haruzi ISIKAWA

The government Mechanical Laboratory

(Received November 22, 1951)

It has been well known that some physical properties of cast polymethylmethacrylate can be improved by appropriate heat treatments (1), though it seems that the aging effect after the treatment has been studied only insufficiently.

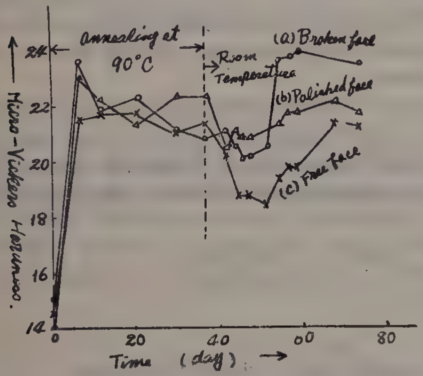

Fig. 1. Variation of the micro-Vickers hardness of cylinderical specimens during and after the annealing. The hardness was measured on (a) broken surface, (b) polished surface and (c) free surface.

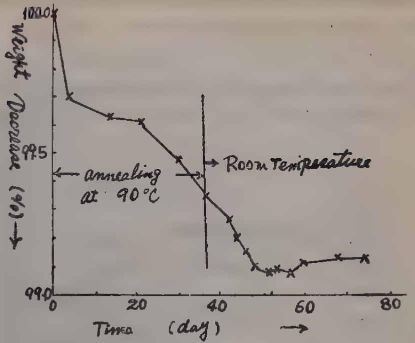

Fig. 2. Weight diminution of the same specimen as that of Fig. 1 during and after the annealing.

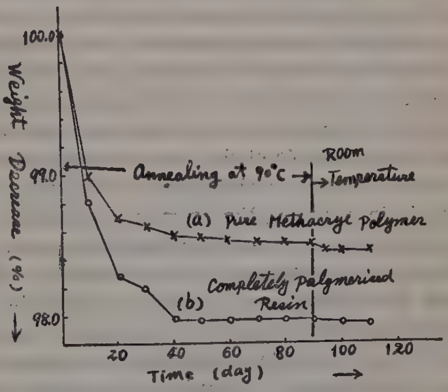

Fig. 3. Weight diminution of thin plate form specimens. Curve (a) pure polymer, curve (b) completely polymerised polymer.

The specimens were cut off crosswise out of cylindrical rods, polymerised from redistilled monomer in the temperature range 50–60°C without catalyser and annealed at about 90°C, which is just above the secondary transition point[1] of this resin and also just below the softening point[1][2]. Thereafter they were slowly cooled at a rate of 10–15°C per hour to the room temperature. The micro-Vickers hardness was measured during this treatment with respect to the cut surface of each specimen. The results are summarised in Fig. 1. For the first several days of the annealing process the hardness increased remarkably in consequence of desiccation, and reached nearly equilibrium plateau, then an aging effect was observed after the annealing terminated, namely the hardness decreased during first two weeks or so and then it returned to about the same value as that just after the annealing, durning about the next two weeks. The weight diminution of the same specimen was measured simultaneously in this experiment and the Fig. 2 was obtained. The sharp decrease in the fordmost portion of the curve corresponded to the first striking increase of the hardness already described. The rate of weight decrease gradually became nealy constant as the annealing proceeded and the weight diminution continued for nearly two weeks after the termination of the annealing. Then the weight of the specimen reached equilibrium value. This corresponded closely to the period in which the hardness attained its minimum value. Now it became clear from these experiments that this aging had close relation to the evaporation of volatile iningredients from the specimen. Another experiment was carried out on desiccation during the annealing with the thin plate form specimen which was supposed to be polymerised almost completely[2]. The results are summarised in Fig. 3. The weight diminution ceased in six weeks annealing, hence it was revealed clearly that it was not the evaporation of thermal decomposition products, but the evaporation of residual volatile ingredients contained in the specimen or the evaporation of occluded gaseous components from the desiccated surface layer of the specimen, that produced the temporary diminution of of the surface hardness after the annealing Next the surface hardness of the specimen under constant load was observed as is summarised in Fig. 4. The results were that the surface hardness decreased under tensile stress, but no variation was observed under compressive stress. These facts indicate that under the tensile stress the specimen surface is in an unstable state and hence the surface hardness diminishes from that of natural state.

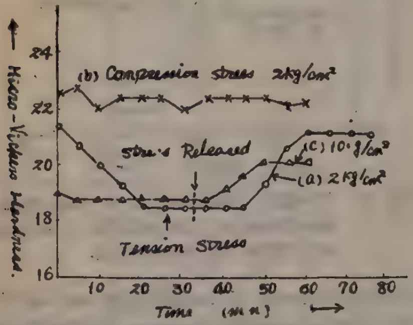

Fig. 4. Variation of the micro-Vickers hardness under constant stress. Curve (a), (c), constant tensile stresses were applied and then released. Curve (b), constant compressional stress was applied.

It may therefore be concluded from above experiments that the aging arises thoroughly from the eveporation process of the residual volatile components contained in the specimen surface, as well as the occluded gaseous ingredients such as vapour, and that the evaporation causes some structural change of the surface layer of the specimen, hence the surface structure varies from one equilibrium state, which is stable at the annealing temperature, to another, which is also stable at the room temperature, in a few weeks after the termination of the annealing. In these intermediate period the structure of the desiccated surface layer is disarranged from these two equilibrium states by the evaporating molecules, that is to say, the surface layer is in an unstable transitional state, hence there arises the temporary diminution of the surface hardness analogically to the case of tensile stress.

References

1) For example see E. W. Russel: Nature **165** (1950) 91.
2) H. A Robinson, R. Ruggy and B. Slantz: J. Appl. Phys. **15** (1944) 343.
3) Author: J. Mech. Lab. (in Japanece) **17** (1951) 101.

J. PHYS. SOC. JAPAN **7** (1952) 330-331

On the Image Formation in Phase Microscopy

By Yasuo TORIKAI

Institute of Industrial Science, University of Tokyo, Chiba-City.

(Received February 15, 1952)

The image formation in phase microscopy has been mostly treated by considering a phase grating as the object to be tested. In the following note the author will discuss the case in which the object has the most general form $f(x_0)$, where x_0 is the coordinate in the object plane.

When a monochromatic plane wave propagating parallel to the optical axis falls to the object, the image $F(x)$ is given by*

$$F(x)=K\int_{-\infty}^{\infty}a(\xi)d\xi\int_{-\infty}^{\infty}f(x_0)e^{-i\xi(x-Mx_0)}dx_0\,,$$

where x and ξ are the coordinates in the image and the diffraction plane respectively, M the magnification of the image, K a constant, and $a(\xi)$ represents the retardation and transmission given to the diffractionimage by a phase plate placed in the diffraction plane.

Now, if we assume that the plate gives the retardation δ and transmission g only to the zeroth order diffraction image, which is spread within $|\xi|\leqq\varDelta\xi$, and is transparent for the other order images, that is,

$$a(\xi)=\begin{cases}g\varepsilon^{i\delta}, & |\xi|\leqq\varDelta\xi,\\ 1\ , & |\xi|>\varDelta\xi,\end{cases}$$

then

$$\begin{aligned}F(x)=&K\int_{-\infty}^{\infty}d\xi\int_{-\infty}^{\infty}f(x_0)e^{-i\xi(x-Mx_0)}dx_0\\&+K\int_{-\varDelta\xi}^{\varDelta\xi}(g\varepsilon^{i\delta}-1)d\xi\int_{-\infty}^{\infty}f(x_0)e^{-i\xi(x-Mx_0)}dx_0\\=&C\left[f\left(\frac{x}{M}\right)-Ae^{i\varepsilon}f_0\right]\end{aligned}\qquad(1)$$

where f_0 is the zeroth order term in the Fourier expansion of $f(x_0)$, being proportional to the amplitude of the zeroth order diffraction image at $\xi=0$, and $A\varepsilon^{i\varepsilon}=1-g\varepsilon^{i\delta}$, C being a constant.

Wnen the object is perfectly transparent, that is $f(x_0)\equiv e^{i\varphi(x_0)}$, then assuming $f_0=\alpha\varepsilon^{i\beta}$, (1) becomes

$$F(x)=C\left[\varepsilon^{i\varphi(x/M)}-A\alpha e^{i(\varepsilon+\beta)}\right]$$

and

---

* e. g., A. H Bennett and others, Trans. Amer. Microsc. Soc. **65** (1946) 99.

$$|F(x)|^2=|C|^2\left[1+A^2\alpha^2-2A\alpha\cos\left\{\varphi\left(\frac{x}{M}\right)-(\varepsilon+\beta)\right\}\right].$$

This is the intensity distribution in the image plane when a perfectly transparent object is seen through the phase microscope, and shows that the phase variation $\varphi(x_0)$ in the object is transformed into an intensity variation in the image through a cosine function. As there has been made no restriction as to the form of the object, this is the most general image function when the transparent object is seen in the phase microscope.

The meanings of A and ε are seen in Fig. 1. In the figure, A is connected to the amplitude and vertical position of the transforming cosine curve and ε to the initial phase of the same cosine curve.

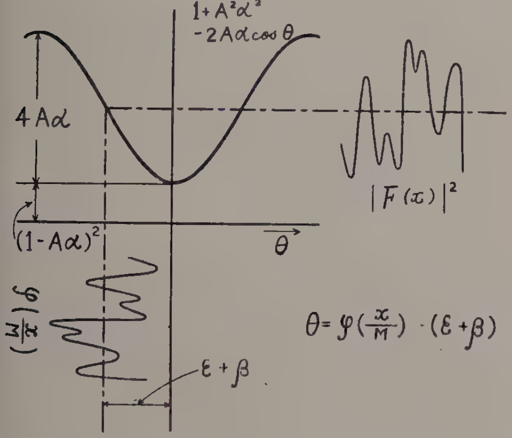

Fig. 1.

The author wishes to express his sincere thanks to Prof. H. Kubota for his kind advices.

J. PHYS. SOC. JAPAN 7 (1952) 331-332

On the Phase Transition in Tungsten Oxide

By Kinshiro HIRAKAWA

Department of Physics, Faculty of Science, Kyushu University

(Received February 25, 1952)

Optical observations on the monocrystals of ferroelectric tungsten oxide WO_3 are made.[1] As reported before,[2] monocrystals of WO_3 have the domain structures with many 45° stripes as shown in Fig. 1. According to our observations, the changes of domain patterns and the orientation of optical axis take place gradually near −50°C on cooling and −10°C on heating. Passing through these temperatures, the crystals change their colour from green to white and transparent, and they sometimes break up into pieces.

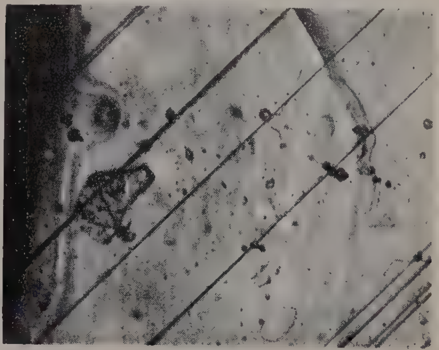

Fig. 1.

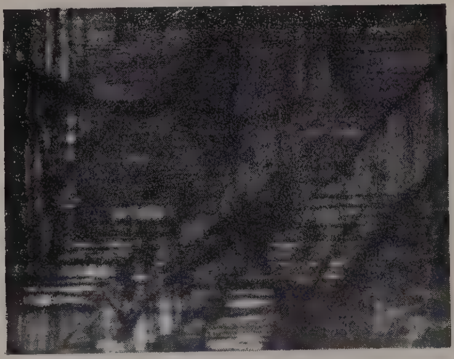

Fig. 2.

Below the transition tomperature, many small new domains with their boundaries being parallel to the cleavage surface are built up as shown in Fig. 2. The optical behaviours of WO_3 crystals at low temperatures are very close to that of $BaTiO_3$ below −70°C in many points, i. e. size of domains, direction of twin planes and orientation of optical axis. Fig. 3 shows the anomalous thermal expansion of WO_3 ceramics near the optical transition temperatures. On the other hand, the crystals of WO_3, according to the X-ray diffraction,[3] show hardly remarkable difference of crystal symmetry on either side of the transition temperature. This disagreement seems to be caused by such a reason as this

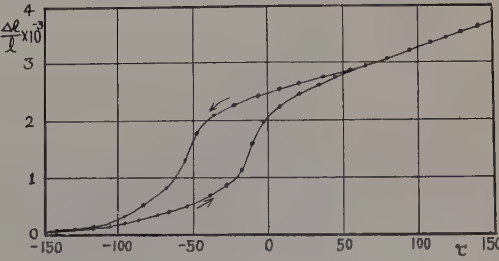

Fig. 3.

that the optical properties are due to the situations of all kinds of ions, while on the other hand the X-ray diffractions are largely due to tungsten ions only, such a disagreement being also know in $NaNbO_3$ near 640°C and 370°C.

The writer wishes to express his sincere thanks to Prof. T. Okada for his kind suggestion and encouragements.

References

1) K. Hirakawa: Busseiron Kenkyu. **38** (1951) 82.
2) R. Ueda, T. Ichinokawa and Z. Kobayashi: Ibid. **29** (1950) 75.
3) R. Ueda and T. Ichinokawa: Reported at the Annual Meeting of the Physical Soc. Japan. Oct. 1951.
4) E. A. Wood: Acta Cryst. **4** (1951) 353.

J. PHYS. SOC. JAPAN **7** (1952) 332

Ultraviolet Absorption Spectra of Glasses Containing Ti, and Heavy Metals

By Kikusaburo OSADA.

Faculty of Engineering, Nagoya University.

(Received February 25, 1952).

The characteristic ultraviolet absorption spectra of some manufactured kinds of glass were previously reported by the author⁽¹⁾, but, as their compositions were exceedingly complicated, it was difficult to understand the relation between the compositions and the spectra of them. Therefore, in order to investigate the relations, glasses containing Ti, or one of heavy metals ($3Na_2O.7SiO_2.M_2O$: M=Ti, Tl, Pb, or Bi), were prepared from pure materials, and the absorption spectra of thin films of them several microns thick were measured to λ180mμ with a small quartz spectrograph. The results obtained are shown in Fig. 1.

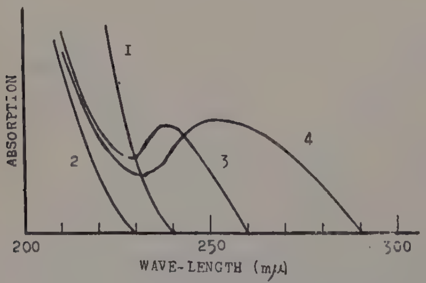

Fig. 1. (1) Ti Glass. (2) Tl Glass.
(3) Pb Glass. (4) Bi Glass.

In the Ti- and the Tl-glass, an absorption edge appears at λ240mμ and λ230mμ, respectively. In the Pb- and the Bi-glass, the edge appears at λ260mμ and λ290mμ, and a maximum of absorption bands at λ237mμ and λ250mμ, respectively. When illuminated with ultraviolet radiations, the Ti-glass fluoresces emitting a green light, and the others blue ones.

It may be supposed from the network theory of glass that the appearance of the absorption maximum at λ237mμ of the Pb glass is due to lead ions in the holes of network of SiO_4. In order to ascertain this assumption, the absorption spectra of solutions in a layer of 0.01mm thickness of acetates containing lead ions were examined and compared with that of the Pb glass.

In solutions of lead- and of sodium-acetate, the absorption edge appears at λ260mμ and λ220mμ, respectively, but in the former no appearance of the maximum of the absorption band is observed at λ237mμ. In mixed solution of lead- and sodium-acetate, the edge appears at λ260mμ and the absorption maximum at λ237mμ just as in the Pb glass. As this maximum at λ237mμ appears only in the mixed solution, the appearance of this maximum may be not due to Pb^{++}, nor to $(CH_3COO)^-$, but to lead ions bonded weakly to acetate ions.

The spectrum of the Pb glass coincides with that of the solution of sodium acetate containing lead ions. And it may be supposed that the bond system of the former is similar to that of the latter; lead ion is bonded to oxygen, and the oxygen is itself bonded to silicon in the glass and to carbon in the solution, the 2s-2p hybridization of carbon being considered the same as that of the 3s-3p system of silicon⁽²⁾. The author, therefore, considers that the appearance of the absorption maximum at λ237mμ of the Pb glass is due to lead ions bonded weakly to unsaturated oxygens in the network of SiO_4. The maximum at λ250mμ of the Bi glass may also originate from bismuth ions bonded weakly to unsaturated oxygens, since bismuth ion has the same electron configuration as lead ion.

References

(1) K. Osada: J. Phys. Soc. Japan **6** (1951) 191.
(2) L. Pauling: *The Nature of the Chemical Bond* (1940) p. 84.

J. PHYS. SOC. JAPAN 7 (1952) 333

Crystal Structure of Pb(Zr-Ti)O_3

Gen SHIRANE* and Kazuo SUZUKI

Tokyo Institute of Technology, Oh-okayama, Tokyo

(Received March 6, 1952)

Recent investigation[1] has shown that there are two kinds of crystal structure in the ferroelectric solid slutions of Pb (Zr-Ti)O_3 system. The compositions near the pure $PbTiO_3$ correspond to a tetragonal modification of perovskite structure with $c/a>1$, a similar structure as observed in ferroelectric $BaTiO_3$[2]. However, we were at that time unable to determine the true lattice type of the intermediate compositions between this phase and the antiferroelectric phase near the pure $PbZrO_3$, because they give the reflexion patterns which differ only slightly from those of a cubic lattice.

Very recently, a detailed reexamination(3) of the crystal structure of high temperature modification of Pb(Zr95-Ti5)O_3, which is surely ferroelectric, was carried out and it was found that the true lattice type of this phase is rhombohedral with $\alpha<90^0$.

In the light of this result, we have inspected again the powder photographs of ferroelectric compositions in Pb(Zr-Ti)O_3 taken at room temperature and found that the essential change in the line characteristics does occur at a certain composition between Pb(Zr60-Ti40)O_3 and Pb(Zr55-Ti45)O_3; the right hand side of which is surely tetragonal while the left hand side of which proves to be rhombohedral with $\alpha<90^0$. The lattice parameters a and α were calculated from the line splittings of the (422) and (332) groups, with the results shown in Figs. 1 and 2. Attention should be paid to the fact that this rhombohedral structure is produced from an ideal cubic cell by a slight extension along the triad axis, which is probably the direction of the spontaneous polarization. This is similar lattice type as observed in $BaTiO_3$ below −70°C[4].

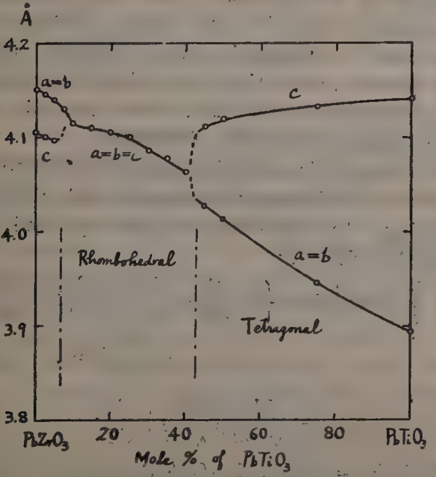

Fig. 1. Lattice spacing of Pb(Zr-TiO)$_3$ at room temperature.

Previously[1] we reported that there are some extra lines even in the ferroelectric phase near the border line to the antiferroelectric phase. The present examination with a high purity Pb(Zr95-Ti5)O_3 sample, however, has shown that no extra lines can be found in the high temperature rhombohedral phase. And it turned out that the extra lines observed previously are to be mostly attributed to impurities contained in ZrO_2 and partly to reflections from Cu Kβ radiation.

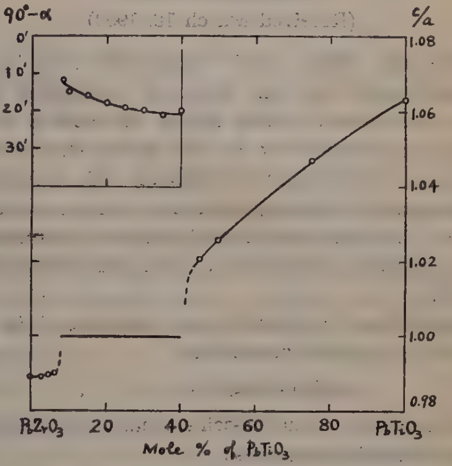

Fig. 2. Axial ratio c/a and angle of distortion α as function of composition.

The results obtained above have shown that the phase boundary of the rhombohedral and tetragonal phases lies, at room temperature, between Pb(Zr60-Ti40)O_3 and Pb(Zr55-Ti45)O_3. The precise determination of this phase boundary at higher temperatures is now in progress.

We wish to express our sincere thanks to Professors Y. Takagi and S. Miyake for their kind guidance and also to Messrs. E. Sawaguchi and S. Hoshino for their helpful discussions.

References

1) G. Shirane, K. Suzuki and A. Takeda: J. Phys. Soc. Japan 7 (1952) 12.

2) H. D. Megaw: Proc. Roy. Soc. A189 (1947) 261.

3) G. Shirane and S. Hoshino: Phys. Rev. to be published.

4) H. F. Kay and P. Vousden: Phil. Mag. **40** (1949) 1019.

---

* Now at Department of Physics, Pennsylvania State College, State College, Pa., U.S.A.

J. PHYS. SOC. JAPAN 7 (1952) 334—335

On the Conductivity of Non-Polar Crystals in Strong Electrostatic Field

By J. YAMASHITA and M. WATANABE

Institute of Science and Technology,
University of Tokyo

(Received March 18, 1952)

Recently Ryder and Shockley⁽¹⁾ have found experimentally that the electrical conduction in a pure Germanium crystal shows the marked deviation from Ohm's law in the strong electric field. Here we shall discuss theoretically this interesting phenomena by solving, to the 2nd order approximation[2)], the well-known Bloch's integral equation for the transport phenomena in non-polar semiconductors[3)].

Expanding the distribution function f in the series of Legendre polynimials

$$f=f_0(E)+k_xg(E)+\cdots\cdots,\tag{1}$$

we may easily reduce Bloch's equation to the following differential equations:

$$Ef_0''+\left(2+\frac{E}{kT}\right)f_0'+\frac{2}{kT}f_0=\frac{l}{2\sqrt{2m}\,c^2}\frac{eF}{\hbar}\frac{1}{\sqrt{E}}\left(g(E)+\frac{2}{3}E\frac{dg}{dE}\right),\tag{2}$$

$$g(E)=-(\hbar l/\sqrt{2m})(eF/\sqrt{E})df_0/dE.\tag{3}$$

Here l is the ordinary mean free path, c the velocity of sound wave and the other quantities have the usual meanings. Eliminating $g(E)$ from the equations, we obtain

$$(E+pkT)f_0''+\left(2+\frac{E}{kT}+\frac{pkT}{E}\right)f_0'+\frac{2}{kT}f_0=0,\tag{4}$$

where

$$p=(eFl)^2/6mc^2kT.\tag{5}$$

If we assume $E\gg pkT$ and neglect the latter quantity in (4), we may obtain the usual solution and the Ohmic conductivity as follows.

$$f_0=A\exp(-E/kT),\quad\text{and}\quad\sigma=4ne^2/l3\sqrt{2\pi mkT}.\tag{6}$$

On the contrary, *if* we assume $pkT\gg E$, so we obtain

$$pkT\,f_0''+\left(\frac{E}{kT}+\frac{pkT}{E}\right)f_0'+\frac{2}{kT}f_0=0,\tag{7}$$

a solution of which is

$$f_0=N\exp[-E^2/2p(kT)^2].\tag{8}$$

By the normalizing condition we find

$$N=2/[2p(kT)^2]^{\frac{3}{4}}\Gamma\left(\frac{3}{4}\right).\tag{9}$$

Using the equ. (3) the current density in strong field may be written as

$$j/n=\left[e\sqrt{2\pi}/3^{\frac{3}{4}}\Gamma\left(\frac{3}{4}\right)\right][cleF/\sqrt{mkT}]^{\frac{1}{2}}.\tag{10}$$

Thus the observed field dependency of electrical current has been found to be correctly given. From the distribution function obtained above, the energy density of the electron in the strong field is easily seen to reach its maximum at an energy value of

$$E_{\max}=(eFl/2c)(kTm)^{-\frac{1}{2}},\tag{11}$$

together with the average energy of

$$E=0.854\,E_{\max}.$$

The energy value determined from the energy balance condition,[4)] familiar in the breakdown theory,

$$(d\varepsilon/dt)_{\text{field}}+(d\varepsilon/dt)_{\text{lattice}}=0$$

has been found to coincide with our $E_{\max}$ exactly, which fact seems to justify the validity of the mentioned condition for computing the current density in the strong field.

Now in order to get the rough estimate of the critical field strength where the deviation from the Ohm's law begins to appear, we have calculated numerically the current density by using the equs. (3) and (4) for $p=1$. Then we have found the current for $p=1$ is about 80% of the Ohm's value. The field value for $p=1$ is rather indefinite, since the values of mobility and sound velocity are rather at variance with each other according to the different measurements. We, therefore, have adopted tentatively 2600 (Ge), 900 (diamond) and 300 (Si) cm²/volt sec for the mobilities at room temperature, while, for sound velocity, 0.5×10^6 (Ge), 1.75×10^6 (Diamond) and 0.9×10^6 (Si) cm/sec respectively, which leads to 300 (Ge), 3000 (Diamond) and 4700 (Si) volt/cm for the field values ($p=1$) at room temperatures respectively. The field value for Ge is about three times smaller than that observed at 80% Ohmic current.[1)] The reason for this discrepancy shall be discussed on later occasion. Our results, however, show that the critical field decreases with decreasing temperature, which fact is in qualitative agreement with the observation.

If the sample is not quite pure, we have to take account of the impurity scattering beside the lattice scattering. In this case the equs. (3) and (4) is modified as follows:

$$\left\{E+\left(\frac{l_T}{l_l}\right)pkT\right\}f_0''+\left\{2+\frac{E}{kT}+\left(\frac{l_T}{l_L}\right)\frac{pkT}{E}\left(1+\frac{2l_T}{l_{ion}}\right)\right\}f_0'+\frac{2}{kT}f_0=0,\tag{13}$$

$$g(E)=-\left(\frac{\hbar l_T}{\sqrt{2m}}\right)\left(\frac{eF}{\sqrt{E}}\right)\frac{df_0}{dE}\tag{14}$$

where l_L, $l_{ion}=(l_0E^2)$ and $l_T(=l_{ion}l/_L(l_{ion}+l_L)$ represent the mean free path due to the lattice scattering, that due to the impurity scattering[5)] and the resultant one respectively, and l_L and l_0 may be considered to be independent of the electron energy. When the field is very strong, the equs. (13) and (14) are reduced to be practically equivalent to the equs. (3) and (4) on account of $l_0E^2 \gg l_L$ and $l_T \approx l_L$, so we see the impurity effect not very appreciable in such high field region. On the contrary, when the field is not so strong or the impurity content is so large that the conditions of $l_0E^2 \ll l_L$ and $l_T \approx l_{ion}$ are valid, the critical field is diminished by the factor (l_{ion}/l_L), so we may conclude that critical field be sensitive to the impurity content.

Finally we wish to express their sincere thanks to Prof. T. Muto for his continued interest and advice during the course of this work.

References

1) E. J. Ryder and W. Shockley: Phys. Rev. **81** (1951) 139.

2) L. Landau and A. Kompanejez: Phys. Zeits. Sowj. 6 (1934) 163.

3) A. Sommerfeld and H. A. Bethe: Handb. d. Phys. **24**/2, 333.

4) F. Seitz: Phys. Rev. **76** (1949) 1376.

5) E. Conwell and W. F. Weisskopf: Phys. Rev. **77** (1950) 388.

J. PHYS. SOC. JAPAN 7 (1952) 335

On the Arc Resistance

By Morihiko KIMATA

Department of Electrical Engineering
Waseda University, Tokyo

(Received, April 7, 1952)

The experimental formula of the arc resistance for direct current has been familiar for us since H. Ayrton[1] and others. That is, the arc resistance R can be written in such formula,

$$R = C_1/i + C_2/i^2 \qquad (1)$$

where C_1, C_2 is constant, and i is current. However, physical meaning expressed in this equation is not obvious. In this paper the qualitative explanation of this constant is attempted.

For simplicity, we will imagine the parallel condenser plates separated by a distance d, and the voltage is applied between these electrodes. Primarily, n_0 photo-electrons start from cathode per sec per cm², and on the way to the anode, ionize the gas molecules. Positive ions, thus produced, return to the cathode, and raise the cathode temperature by their energy. Then the cathode becomes hot enough to emit the thermionic electrons.

If we assume the cathode temperature T is proportional to the flow of the positive ions at the cathode, $T = C(n - n_0')$, where n_0' is the total electrons emitted by the cathode, and n is the total electrons arrived at the anode per sec per cm². Then the thermionic current $n_0' - n_0$ is given by the Dushmann's formula as follows;

$$n_0' - n = A(n - n'_0)^2 \exp\,[-B/(n - n_0')] \qquad (2)$$

where, $A = emk^2C^2/2_n{}^2h^3$, $B = w/kC$,

e, m is charge and mass of electron respectively, h is Planck's constant, w is work function of cathode metal, and k is Boltzmann's constant. Using the Townsend's equation $n = n'_0, \exp\,(\alpha d)$, we have,

$$n = n_0 \exp(\alpha d) + An^2 (1 - 1/\exp(\alpha d))^2 \exp\,[(\alpha d) - B/n\,(1 - 1/\exp(\alpha d))] \qquad (3)$$

In this equation we can separate the total current into two parts. One depends on the photo electrons, and the other on the total currents. In self-sustaining state we must neglect the first term. And if we assume $\exp(\alpha d) \gg 1$, the equation reduces to simpler form,

$$An \exp(\alpha d - B/n) = 1. \qquad (4)$$

Now if we put the Townsend's first coefficient $\alpha = K''X = K'V$, where K'', K' is constant and X, V is field strength and applied voltage, which is rough approximation, we have,

$$V = (\ln\, An + B/n)/K, \qquad (5)$$

$$R = [(em\,k^2C^2 \ln\, An)/2\pi h^3K] \times i^{-1} + (we/kCK) \times i^{-2} \qquad (6)$$

where i is en.

Since ln An have weak dependency upon i, coefficient of $1/i$ and $1/i^2$ are considered as constant approximately. Thus the meaning of C_1, C_2 in eq. (1) are obtained. And we can easily find the characteristic of negative resistivity, deriving differential resistivity. On the discussion combined with the field emission at the cathode, we have already announced in the connection with the spark condition.[2]

References

1) H. Ayrton; *The Electric Arc*, The Electrician Publishing and Printing Co.

2) M. Kimata; Annual meeting of The Institute of Electrical Engineers of Japan (1951).

J, PHYS. SOC. JAPAN 7 (1952) 336—337

Antiferroelectricity and Ferroelectricity in Lead Zirconate

Etsuro SAWAGUCHI and Tomoyoshi KITTAKA

Tokyo Institute of Technology, Oh-okayama, Tokyo

(Received April 18, 1952)

According to recent theoretical investigations,[1),2)] the free energy of a crystal can be nearly equal whether its state is ferroelectric or antiferroelectric, provided some special conditions are fulfilled. And the lead zirconate,[3)4)5)] we think, is an example of this very case. In fact, if lead zirconate contains more than 3 mole-percent of lead titanate, ferroelectric phase does appear between antiferroelectric and paraelectric phases. By measuring the specific heat of this solid solution we have already determined the energy difference between the antiferroelectric phase and the ferroelectric one, it is found to be about 130 cal./mole. As regards the pure lead zirconate itself, however, the direct caloric measurement is impossible, since the intermediate ferroelectric phase disappears as the concentration of lead titanate decreases. But a reasonable estimation of the energy difference can be obtained by the following device.

Using a ceramic piece of lead zirconate immersed in an oil bath, we have observed the hysteresis loops on a cathode-ray oscilloscope with steep jumps on both ends[4)] (Fig. 1), of which the region AB corresponds to the antiferroelectric phase whereas the region CD to a ferroelectric phase. The threshold field E_c for this forced transition is shown plotted as a function of temperature in Fig. 1. E_c decreases linearly with a rate of $dE_c/dT=-1.7$ kv/cm. deg.

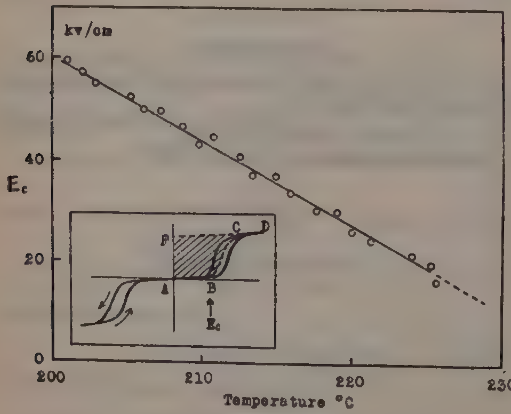

Fig. 1. Threshold field strength for the transition from the antiferroelectric phase to the ferroelectric phase.

By extrapolating the ferroelectric part CD back to the point of zero field F, and by integrating the area surrounded by the loop ABCF, we can obtain the work done per mole $(Nv/4\pi)\int EdD$ between the state A and F (Fig. 2). Where N is the Avogadro number and v is the volume of the unit cell, 71.4 A³. Since our experimental condition, a.c. field of 50 c.p.s., is rather an adiabatic, the temperatures T_a and T_f of these two states A and F should necessarily be not equal. Let the temperature difference T_a-T_f be ΔT, the arithmetical mean temperature $(T_a+T_f)/2$ be T_m and the specific heat at constant pressure be C. Then the internal energy U and the entropy S may be expanded as follows;

$$U_a(T_a)=U_a(T_m)+(C_a\Delta T/2),$$
$$U_f(T_f)=U_f(T_m)-(C_f\Delta T/2)$$
$$S_a(T_a)=S_a(T_m)+C_a\{(\Delta T/2T_m)-(1/2)(\Delta T/2T_m)^2\},\ \text{etc.},$$

where the subscripts a and f refer to the states A and F respectively. As stated above the process is adiabatic, so that $S_a(T_a)=S_f(T_f)$, and that $U_f(T_f)-U_a(T_a)$ is equal to the work done. Consequently, the difference of the free energy between the two phases at the temperature T_m is

$$F_f(T_m)-F_a(T_m)=U_f(T_f)-U_a(T_a)$$
$$-(C_f-C_a)(T_m/2)(\Delta T/2T_m)^2.$$

The first term in the right hand side estimated from Fig. 2 is the order 2 cal./mole, while the second term estimated utilizing the caloric data in Pb $(Zr_{0\cdot97}-Ti_{0\cdot03})O_3$, namely $|C_f-C_a|<3$ cal./mole.deg., $\Delta T\fallingdotseq$latent heat/specific heat$\fallingdotseq$3°C and $T_m\fallingdotseq 500$°K, is only of the negligible order 0.01 cal./mole. Therefore the curve of Fig. 2 may practically be regarded as the difference of free energy itself.

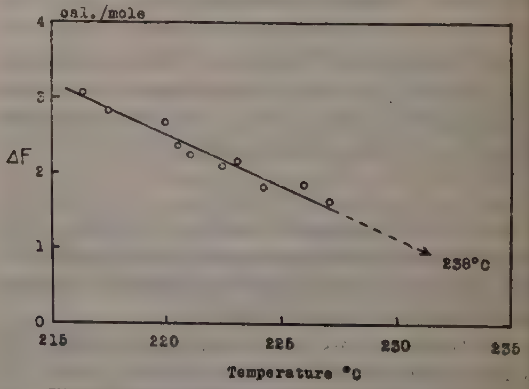

Fig. 2. Free energy difference between antiferroelectric and ferroelectric states as a function of temperature.

As was expected at the beginning, antiferroelectric phase in the pure $PbZrO_3$ is by only few calories per mole more stable than the ferroelectric one near the curie point. Similarly the fact that new ferroelectric phases appear as soon as small amount of $PbTiO_3$ or $BaZrO_3$ is added to the $PbZrO_3$ may readily be understood. The temperature where the free energy difference disappears is obtained by Figs. 1 or 2 as about 238°C. However the pure $PbZrO_3$ transforms in the paraelectric phase at 230°C, and the ferroelectric phase is not naturally realized unless forced prematurely by external field.

The internal energy difference between the two phases, that is $L=-T(\partial_{\Delta}F)/\partial T$, can also be estimated by Fig. 2, and it is about 80 cal./mole at the curie point 230°C. If compared with $L=130$ cal./mole obtained by the direct caloric measurement with $Pb(Zr_{0\cdot97}-Ti_{0\cdot03})O_3$, the present value seems to be rather small. The reason is probably because we have used a ceramic $PbZrO_3$. For, as it has long been observed in the ferroelectric $BaTiO_3$6) and the like, ceramic samples generally give the dielectric polarization less than the value expected from mere aggregation of isolated single crystals. Hence, we may suggest that the true difference of the free energy and the internal energy may respectively be about twice the value obtained above.

In conclusion, we wish to express our sincerest thanks to Professor Y. Takagi and Mr. G. Shirane for their valuable advice and discussions. This study was helped by the research grant from the Ministry of Education.

References

1) C. Kittel: Phys. Rev. **82** (1951) 729.
2) Y. Takagi: Phys. Rev. **85** (1952) 315.
3) E. Sawaguchi, G. Shirane and Y. Takagi: J. Phys. Soc. Japan **6** (1951) 333,
4) G. Shirane, E. Sawaguchi and Y. Takagi: Phys. Rev. **84** (1951) 476.
5) G. Shirane and A. Takeda: J. Phys. Soc. Japan **7** (1952) 5.
6) J. K. Hulm: Nature **160** (1947) 126.

J. PHYS. SOC. JAPAN **7** (1952) 337-338

Electrical Properties of Amorphous Carbon

By Hisao HIRABAYASHI and Hiroo TOYODA

Electrical Communication Laboratory, Telecommunication Ministry

(Read on Annual Meeting 1950)

(Received March 3, 1952)

Although a number of measurements on the electric conductivity of carbon and graphite have been reported, many of them lacked the precises pecification of specimen. To exclude the effects of ash on the properties and at the sametime to study the various steps from aromatic compound to graphite, we used the specimens carbonized from the insoluble and infusible phenol-formaldehyde resin, which contracted uniformly in the carbonization process. Carbonization was accomplished in hydrogen flow for 3 hours, its temperature ranging from 700 to 1000°C. The amorphous carbon so obtained is homogeneous without crack and its ash content lower than 0.05 per cent.

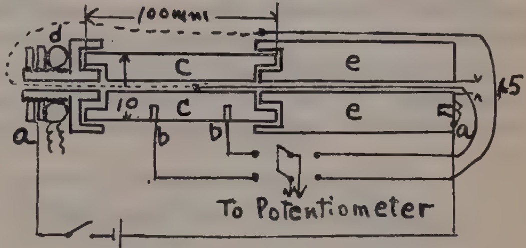

Fig. 1. Diagram of the simultaneous measurement for thermo-electric power and electric resistivity.

a. Current terminal for electric resistivity.
b. Probe for electric resistivity and terminal for thermoelectric power.
c. Carbon specimen.
d. Heater; glass tube of dough-nut type enclosing nichrome wire.
e. Heat sink; brass rod.
Attaching parts of probe and heat sink and source are lead.

Table I. Electric resistivity and activation energy

Carbonization Temperature °C	anthracite			resin		
	ρ_{300} Ωcm	ρ_{∞}Ωcm	ΔE e.v.	ρ_{300}Ωcm	ρ_{∞}Ωcm	ΔE. e.v.
1,000	0.0086	0.0066	0.013	0.0086	0.0074	0.009
900	0.013	—	—	0.016	0.0097	0.034
800	0.047	0.021	0.046	0.072	0.019	0.06
700	0.39	0.029	0.15	1.3	0.11	0.13
650	5.5	0.16	0.18			
600	1.5×10^3	1.8	0.34			
550	5×10^4	—	—			

We measured the electric resistivity potentiometrically and the thermo-electric power between 20 and 300°C. We also tried to measure the Hall coefficient at room temrerature, but its value is too small to be obtained by our method, possibly being smaller then 1 emu. in absolute value. For the measurement of thermoelectric power, we used the means as shown in Fig. 1. Over the whole temperature range, temperature difference between the terminals, b's, was 10°C.

Electric resistivity of carbon decreases as temperature rises and satisfies the semiconductive formula $\rho_T=\rho_\infty \exp\frac{\Delta E}{2kT}$. ρ_{300}, ρ_∞ and ΔE, as shown on Table I, all decrease markedly as the carbonization temperature is heightened and those lie between aromatic compound1) and graphite.2) The values of ΔE are in good agreement with the result of infrared absorption by Kmetko3). Table I also involves the values for the specimens made from the anthracite produced in Hongay, Indo-China, ash contents of which are about 2.5 per cent. These values approximately agree with those of carbonized resin. Thermo-e.m f. appeared as p-type semiconductor and thermoelectric power was inversely proportional to the absolute temperature. In Fig. 2, thermoelectric power at room temperature against ΔE is shown, and it is found that thermoelectric power of carbon is nearly proportional to $\Delta E/T$, but very small compared with the extrinsic semiconductor having the same ΔE.

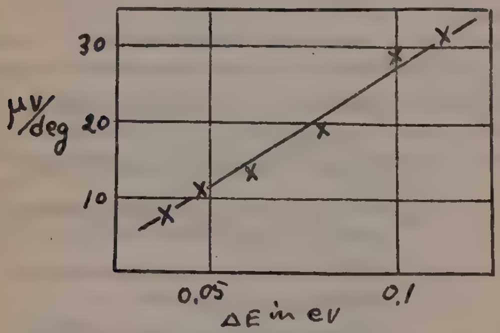

Fig. 2. Thermoelectric power at room temperature vs. ΔE.

From the results described above, we think that the amorphous carbon will be an intrinsic semiconductor, with hole's slightly higher mobility than electron's, zone structure of which is characterized by the carbonization conditions, especially temperature. It is to be considered that the electrical properties are characteristic of the microcrystallites of carbon and that the "effective size" of them plays the decisive role. Here the effective size means not only a geometrical enlargement, but also a development of internal structure, namely conjugate bond system.

In the course of thermal decomposition of aromatic compound to form the amorphous carbon, the electrons released from the chemical binding with other atoms, particularly hydrogen and oxygen, progressively form the conjugate double bond, and concurrently the effective size becomes larger, as well as the geometrical enlargement at much high temperature. As the effective size grows, the effective densities of carriers inerease in full and empty bands and the energy gap between two bands, i.e., ΔE decreases, tending to the graphite model suggested by Wallace.

However the tendency to the graphite is not monotonic. Thermoelectric effect measured by Loebner4) and Hall effect by Donogue and Eatherly5) at room temperature consistently showed consdierable negative minimum and possitive maximum respectively at about 2200°C of heat treatment temperature, and the latter, decreasing, converged to the graphite value −0.634 emu. The results suggest that only the effective size and hole's higher mobility can not picture the whole aspects of graphitization, but that the modification of the zone structure owing to lattice defects or peripheries may play other role. Mrozowski presented a periphery electron model and considered periphery level as donor. Loebner also maintained the model, but according to the various experimenis described above, involving his own, it seems to be doubtful and it is rather natural to see periphery as acceptor.

References

1) H. Akamatsu and H. Inokuchi J. Chem. Phys. **18**, (1950) 810.
2) P. R. Wallace Phys. Rev. **71** (1947) 622.
3) E. A. Kmetko Phys. Rev. **82** (1951) 456.
4) E. E. Loebner Phys. Rev. **84** (1951) 153.
5) J. J. Donogue and W. P. Eatherly Rev. Sci. Inst. **22** (1951) 513.
6) S. Mrozowski Pys. Rev, **77** (1950) 838.

JOURNAL OF THE PHYSICAL SOCIETY OF JAPAN Vol. 7, No. 4 JULY—AUG., 1952

On the Double Coil Magnetic Lens β-Ray Spectrometer

By Toshio AZUMA and Kunihiko TSUMORI

Physical Laboratory of Naniwa University

(Received November 13, 1951)

We have constructed the double magnetic lens β-ray spectrometer. Its geometry is shown in Fig. 1. We have tried the methods of Quade and Halliday[1)] to set the axis of the lens coil and the cylinder, the data of which was reported already[2)]. This paper includes the calculated values of the electron orbits and the resolving powers and the experimentally evaluated value of the energy constant of the instrument by the analysis of the Co^{60}-γ.

The magnetic field intensity $H_{0(z)}$ on the axis of the double lens coil will be calculated by the well known formula,

$$H_{0(z)}=\frac{2\pi ni}{160(a_2-a_1)}\Big\{(z+l_1)\times\log\frac{a_2+[a_2{}^2+(z+l_1)^2]^{1/2}}{a_1+[a_1{}^2+(z+l_1)^2]^{1/2}}-(z-l_1)\log\frac{a_2+[a_2{}^2+(z-l_1)^2]^{1/2}}{a_1+[a_1{}^2+(z-l_1)^2]^{1/2}}-(z+l_2)\log\frac{a_2+[a_2{}^2+(z+l_2)^2]^{1/2}}{a_1+[a_1{}^2+(z+l_2)^2]^{1/2}}+(z-l_2)\log\frac{a_2+[a_2{}^2+(z-l_2)^2]^{1/2}}{a_1+[a_1{}^2+(z-l_2)^2]^{1/2}}\Big\}$$

where a_1, a_2, l_1 and l_2 are selected as shown in fig. 2 and n is the number of turns and i the current intensity (in ampere). Our instrument has the dimensions of $a_1=9$ cm, $a_2=23$cm, $l_1=17$ cm, $l_2=9$ cm, so the magnetic field intensity $H_{0(z)}$ can be calculated numerically as shown in fig. 3. $H_0''{}_{(z)}/ni$, the second dirivative of $H_{0(z)}$ by z, is also shown in it. We have get the value of 31 gauss/amp at $z=3$ cm by means of the flux meter.

We have used the Deutsch formula(3) to calculate the value of the electron orbit,

$$\frac{r}{R}=1-\left(\frac{ni}{p_0}\right)^2\int_0^z dz\int_0^z\Big[\frac{1}{4}\left(\frac{H_0}{ni}\right)^2\frac{r}{R}-\frac{1}{8}r\left(\frac{r}{R}\right)^2\frac{H_0}{ni}\frac{H_0''}{ni}+\frac{3}{16^2}r\left(\frac{r}{R}\right)^4\left(\frac{H_0''}{ni}\right)^2-\cdots\cdots\Big]dz$$

$$\varphi=-\left(\frac{ni}{p_0}\right)\int_0^z\Big[\frac{1}{2}\left(\frac{H_0}{ni}\right)-\frac{r^2}{16}\left(\frac{H_0''}{ni}\right)+\cdots\cdots\Big]dz\,.$$

where p_0 is the initial momentum of the electron which is focussed, cylindrical coordinates $(r,\ \varphi,\ z)$ are taken as shown in Fig. 2 and R is the maximum r of electron trajec-

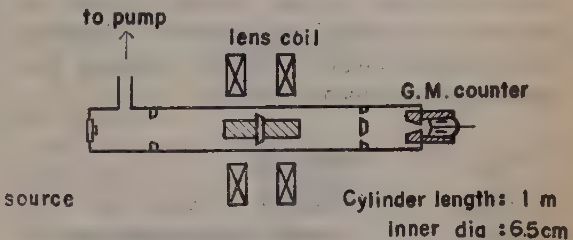

Fig. 1. Lens coil spectrometer.

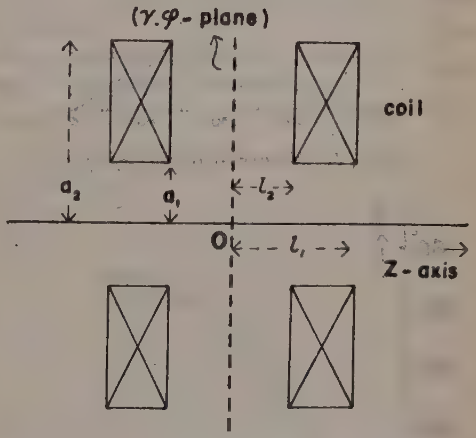

Fig. 2. Axis of double lens coil.

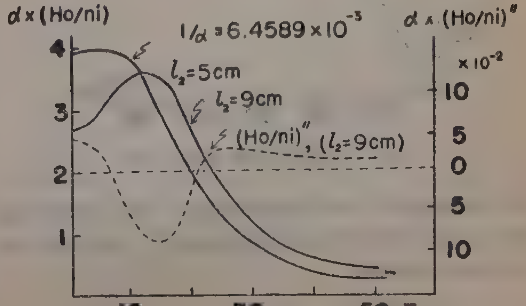

Fig. 3, Value of (Ho/ni) and (Ho/ni)″.

tory at $z=0$. Fig. 4 shows the value of $\frac{r}{R}$ and fig. 5 shows the rotation angle φ of the electron. We get the value of the virtual distance R' at the centre from Fig. 4, when we use the three different centre buffles $R=$ 5.5 cm, 4.5 cm, 3.5 cm. In Fig. 4 (b) shows the electron orbit of $R=5.5$ cm; (c), that of 4.5 cm; (d), that of 3.5 cm. From fig. 4 we can determine the magnitude of the buffle systems which we want to put in the cylinder to minimise the scattering and to fix the electron orbit. From fig. 5 we can determine the angle of the wings of the buffle wheel which we want to put in the cylinder to separate the positive and negative electrons. The rotation angle φ is 113° between the source and the focused point.

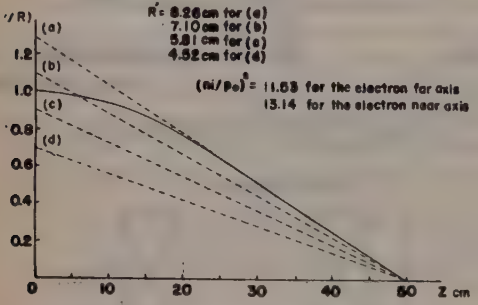

Fig. 4. Electron orbit (r/R).

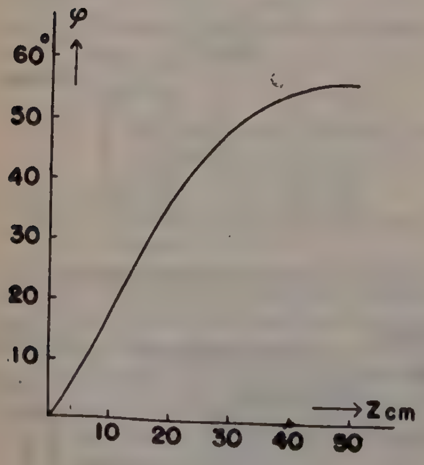

Fig. 5. Electron orbit (φ).

We estimated the magnitude of the resolving power by the Deutch formula,⁽³⁾ and get as the peak spread

$$\frac{\Delta p}{p_0}=\pm\frac{|\omega-S|}{4R'_{\max}}$$

and as the total spread

$$\frac{\Delta q}{p_0}=\pm\frac{|\omega+S|}{4R'_{\min}}$$

where ω is the radius of the source and S is the radius of the counter window, and the virtual distance $R'_{\max}$ and $R'_{\min}$ are determined by the buffle at the centre of the cylinder, Table I shows the value of the resolving power.

Table. I. Resolving power.

redius of center buffle	S cm	ω cm	$\Delta p/p_0$	
			peak %	total %
cm 5.5	0.35	0.2	0.45	1.94
		0.5	0.45	3.00
4.5	0.35	0.35		3.01
		0.5	0.45	3.66
3.5	0.35	0.35		3.88
		0.5	0.83	4.71

When the electron, whose momentum is p, is focussed by the magnetic field excited by coil current i ampere, we get the linear relation $p=ki$, where k is the energy constant of the instrument in the magnetic field having no feromagnetic substance. We determined the value of k by using the two known γ-ray of the Co^{60}-γ i.e. 1.1715 Mev and 1.3316 Mev.⁽⁴⁾ When we use the thin Pb-radiater and the Co^{60} (2 m.c.) source just behind the radiator, we can evaluate the sharp energy spectrum of the photo-electrons, which are

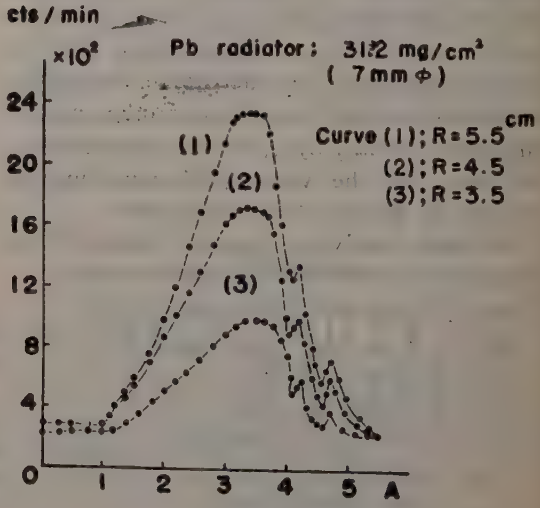

Fig. 6. Co$^{60}-\gamma$ spectrum.

radiated from the thin Pb (40 mg/cm², 14 mm ϕ), on the background of the Comptom recoil electrons. Fig. 6 shows its spectrum with three different centre anullus 1 cm, 2 cm and 3 cm. During this measurement the coil current has been stabilized within 1/1000 fluctution by means of Lawson method.(5)

The effect of the earth magnetic field and that of the thickness of the Pb-radiater on the coil current can be measured by the method of Jenzen et al(6) with 1.17 Mev γ-ray peak. The value of the former effect of this instrument is ±0.008 A. The value of the latter effect is shown in Table II. From this table we can estimate the magnitude of the resolving power to 3.4% which is almost equal to the calculated value in Table I within the experimental errors. We determined the energy constant k of this instrnment from the two know photo-peaks as 1.216 $H\rho$/amp.

Table II. The effect of the radiator thickness.

Radiator thickness	Coil current
20 (mg/cm²)	4.265 (Amp)
31	4.245
35	4.240
40.5	4.230
49.0	4.210
61	4.185
12	4.175
82	4.185

The writers wish to express their gratitude to prof. K. Kimura and his assistants of Kyoto University for their constant interest and valuable suggestions in connection with this wark and prof. Y. Mashiyama of Naniwa University for his kind guidance.

References

(1) E. A. Quade and D. Halliday: Phys. Rew. **72** (1947) 234.

(2) T. Azuma aud K. Tsumori: Kagaku **21** (1951) 417.

(3) M. Deutch and L. G. Ellsot and R. D. Evans: R. S. I. **15** (1944) 198.

(4) D. A. Linde and J. R. Brown and J. W. M. Dumond: Phys. Rew. **76** (1949) 1838.

(5) T. L. Lawson and A. W. Tyler: R. S. I. **10** (1939) 304.

(6) E. N. Jensen and L. J. Laslett and W. W. Pratt: Phys. Rew. **75** (1949) 458.

JOURNAL OF THE PHYSICAL SOCIETY OF JAPAN Vol. 7, No. 4 JULY—AUG., 1952

On the Study of the Penetrating Burst at High Altitude

By Seinosuke OZAKI, Shuji FUKUI and Takashi KITAMURA

Department of Physics, Osaka University and Osaka City University

(Received February 9, 1952)

The penetrating bursts under the thick lead plate were studied by a fast ionization chamber at 2740 m altitude. The bursts are classified with respect to the number of secondary particles which penetrate 7 cm lead under the chamber. The bursts containing one or no penetrating secondary particle are interpreted mainly as the nuclear stars produced in the wall of the ionization chamber. Most of the cases in which the bursts contain two or more penetrating particles are explained as the electronic shower accompanied with the hard shower. For these events it is plausible to take into account the gamma decay of the neutral meson.

§ 1. Introduction

It has been known that the high energy burst can be observed in an ionization chamber under such a thick lead plate that the soft component of cosmic radiation can not penetrate. It has also been pointed out[1)2)] that these phenomena at sea level may be explained as the electron shower produced by the collision, or radiation, or electromagnetic process of ordinary meson. While at high altitude it was concluded by Rossi and his co-workers[3)] from the altitude dependence of this effect that the electron shower accompaning with the nuclear event produced by the nucleon compoment of cosmic radiation played the important role. We have attempted in this work to analyze this penetrating burst through the direct and more detailed studies, viz. the measurement of the relation between the size and frequency, and the number of penetrating particles included in this event. At the same time we have also determined whether the primary particle is charged or not.

In the present paper only the observation on the top of Mt. Norikura (2740 m) during last summer is reported, The observation at sea level is now continued.

§ 2. Experimental Arrangements and Procedures

A schematic diagram of the apparatus is given in Fig. 1. A 15 cm lead plate is placed above the ionization chamber to absorb the soft component of cosmic radiation and to produce the penetrating bursts, and 7 cm lead plate placed under the ionization chamber is used to absorb the soft component of penetrating burst. The dimension of the cylindrical ionization chamber is 20 cm in

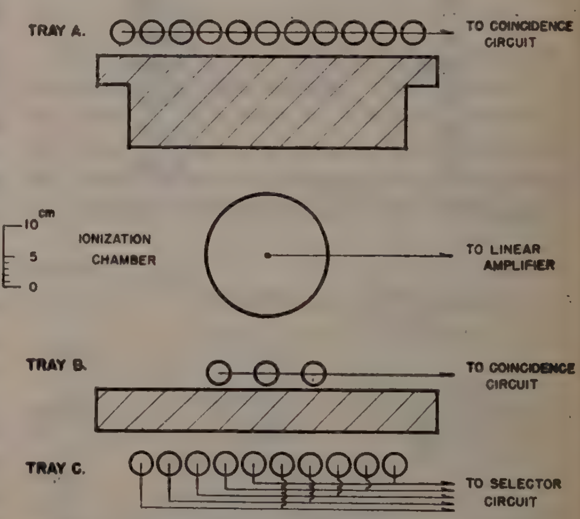

Fig. 1. Counter and ionization chamber arrangement. All counters, copper-in-glass type, were 30 cm in length and 4 cm in diameter. 11 counters of the tray A and 3 counters of the tray B were connected in parallel. 10 counters of the tray C are connected in five independent groups. The tray A indicates whether the primaries of the events have charge or not. The tray B, coincident with a pulse from the ionization chamber, makes a master pulse. The tray C indicates the number of the penetrating particles in the events. The cylindrical ionization chamber, both its diameter and effective length are 20 cm, is filled with 97% commercial argon at 7 atmospheric pressure. Po-α source is placed in the chamber for the check of the pulse height. Upper lead plate is $15 \times 50 \times 45$ cm^3 and lower one is $7 \times 55 \times 50$ cm^3.

diameter as well as in depth. This chamber is filled with 97% argon gas at 7 atmospheric pressure and is the electron collection type.

The pulses induced in the ionization chamber are amplified through the linear amplifier (almost the same as the model 100 amplifier[4]) and its heights are recorded only in the cases of the time-coincidence with the pulse from the G-M counters of the tray B. This coincident pulse was adopted as the master coincidence in this work. In the selector circuit, Fig. 2, the pulses from the counter tray C, which coincide with the master pulses, are selected by the number of counters simultaneously discharged; one of counters of the tray C discharges, two counters discharge, and more than three counters discharge, respectively.

Thus the counting system is more sensitive to the detection of the electron cascade shower than the nuclear star, because almost all of the particles included in the nuclear star can not penetrate the wall of ionization chamber. It may be expected that the counter tray C is able to determine the number of penetrating particles included in the penetrating burst, since the 7 cm lead plate upon the counter tray C is enough to absorb the soft components. These instruments are constructed to record the burst size in the case that the burst size is larger than that corresponding to the 5 Mev energy loss in the ionization chamber.

The counting of the tray C had to be corrected with respect to the following cases:

1. The penetrating particles pass through the gaps between the counters of the tray C or escape from the area of the tray C.
2. More than 2 penetrating particles pass through the same counter.
3. The electron knocked on by a penetrating particle discharges other counter.

The corrections of the first two cases were able to be calculated from the counter arrangement and these are about 7% and 3% respectively. The third correction was estimated to be 5%, from other experimental data.[5] The geometrical correction about the counting of the tray A on account of the gaps between the counters and the finiteness of the counter length is estimated to be several percent. This estimation was done experimentally by means of reducing the number of counters of the tray A from 11 to 6, since it is impossible to calculate this miscounting without the knowledge about the zenith angular dependence of the primaries of penetrating burst. All experimental data which will be shown in the next section had been corrected as mentioned above.

§ 3. Experimental Results and Conclusions

About 5000 penetrating bursts were observed on the top of Mt. Norikura (the altitude is 2740 m) during the summer 1950. Each penetrating bursts is characterized following its time-coincidence with the pulses from the counter trays A and C, and is classified to the next 6 classes A^0MC^0, $A^{>1}MC^0$, A^0MC^1, $A^{>1}MC^1$, $A^0MC^{>2}$ and $A^{>1}MC^{>2}$, M shows the master pulses corresponding to the coincidence between the pulses from the ionization chamber and the counter tray B. A and C show respectively the number of counters of trays A and C discharged simultaneously with the master pulses. The counting rate of each is given in Table I and the relation curves between the size of burst and

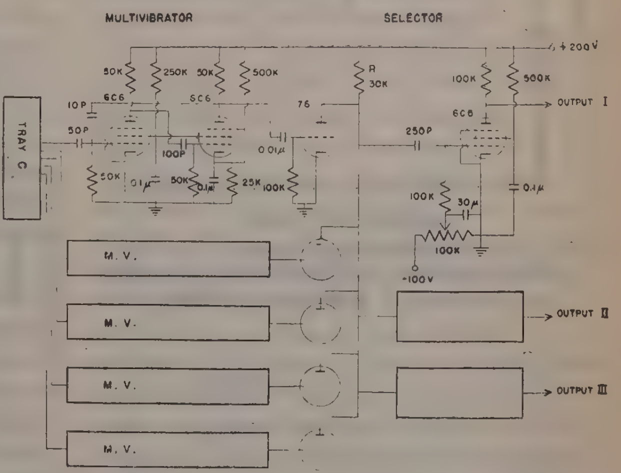

Fig. 2. Selector circuit. The value of R is determined so that the output pulse height is proportional to the number of the coincident input pulses. Thus, pulses of output I correspond to more than one coincident input pulses. Pulses of output II correspond to more than two and those of output III to more than three coincident input pulses.

its frequency are shown in Fig. 3, 4 and 5, respectively.

From Table I it may be seen that in the case where the penetrating burst contains more than two penetrating particles the frequency of these events produced by non-charged particles is equal to that is produced by charged particles within the statistical error, while in the case of the penetrating burst containing no penetrating particle the former frequency is 3 times as many as the latter. It is also clear that the slope of size-frequency curve of burst does not depend on whether the primary particle of these events is charged or not, but it depends on the number of penetrating particles included in the burst, the slope of the curve shown in Figs. 3 and 4 being more steep than that in Fig. 5.

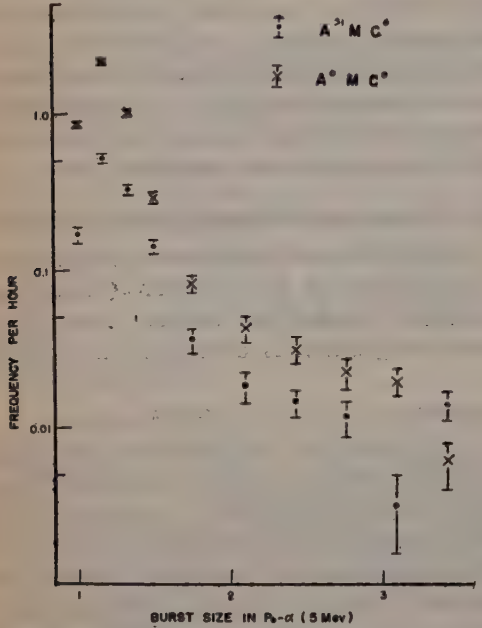

Fig. 3. Size-frequency relation of the bursts containing no penetrating particle, i.e., the cases of A^0MC^0 and $A^{>1}MC^0$.

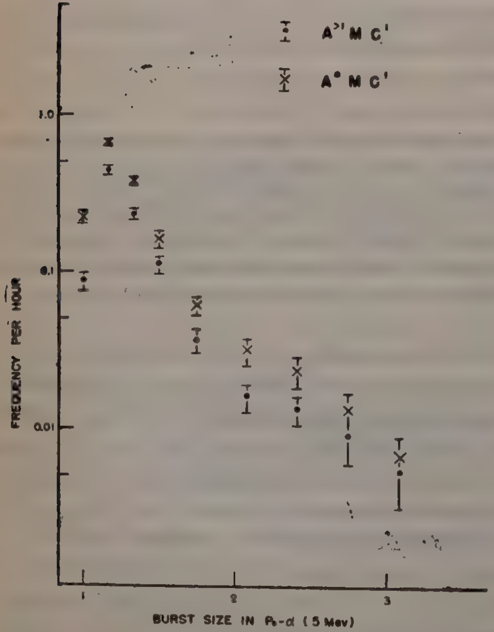

Fig. 4. Size-frequency relation of the bursts containing one penetrating particles, i.e., the case of A^0MC^1 and $A^{>1}MC^1$.

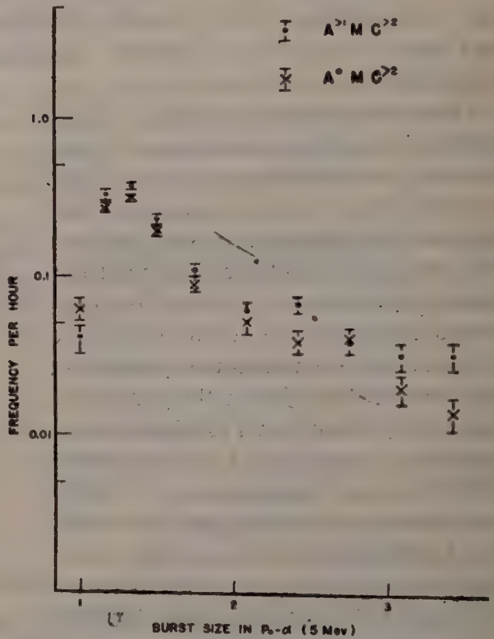

Fig. 5. Size-frequency relation of the bursts containing more than two penetrating particles, i.e., the case of $A^0MC^{>2}$ and $A^{>1}MC^{>2}$.

Firstly contribution of the electron as incident, agencies is estimated to be negligible because the electron which is able to produced showers of the observed sizes (more than 20 electrons) after penetrating 15 cm thickness of lead plate, must have energy of at least 10^{12}ev and the accepted number of such high energy electrons is too small to account for the observed coincidence rates. Then, the following cases are thought to be plausible as to explain the observed phenomena.

A) The electronic shower is iniciated from the soft components which are produced simultaneously with the hard shower in the

Table I. The total counting rate of each cases of the bursts.

Event	$A^0 MC^0$	$A^{>1} MC^0$	$A^0 MC^1$	$A^{>1} MC^1$	$A^0 MC^{>2}$	$A^{>1} MC^{>2}$
Counting rate/hour	4.7±0.1	1.3±0.05	1.6±0.06	1.0±0.04	1.3±0.06	1.6±0.06

upper lead plate by the nucleon component of the cosmic radiation.

B) The electron shower is iniciated in the upper lead plate by the electromagnetic process of an ordinary meson.

C) The penetrating particle, (nucleon component) after passing through the lead plate, produces the nuclear star at the wall of ionization chamber, which contains at least one particle of sufficient energy to penetrate the wall of ionization chamber and to discharge a counter of the tray B.

As well known, at the high altitude the rate of events produced by an ordinary meson is negligibly small compared with the events by nucleon component. Then the electronic shower produced by the electromagnetic process of an ordinary meson (case B) may be neglected in the present work. Consequently, almost all of penetrating bursts recorded as A^0MC^0, $A^{>1}MC^0$, A^0MC^1 and $A^{>1}MC^{>1}$ are thought to be interpreted as the nuclear star of case C, since the result of Bristol group's experiments⁶⁾ with the nuclear emulsion plate shows that the frequency of star decreases with the number of penetrating particles contained in it. This conclusion will be supported from the following facts: (1) The gradient of size frequency curve of A^0MC^0, $A^{>1}MC^0$ is equal to that of A^0MC^1, $A^{>1}MC^1$ and is the same as that expected from the number of star prongs and its frequency in the nuclear emulsion plate. (2) The absolute frequency of these events and the ratio between the frequency of A^0MC^0 and $A^{>1}MC^0$ shows good agreement with the Bristol group's data if a reasonable thickness is adopted as the region within which the nuclear stars are produced.

But it seems impossible to explain the phenomena $A^0MC^{>2}$ and $A^{>1}MC^{>2}$ exclusively by the star events, since the rate of events expected from the emulsion data about the star which contains at least 2 penetrating particles is less than one-tenth of the present observed rate. While the electronic shower iniciated by the nuclear interaction (case A) is taken into account, there is good agreement between the experimental results and theoretical calculation concerning with the total frequency as well as the relation curve of the size and frequency curves. Theoretically considering, only the decay gammer-rays of π^0-meson produced at the nuclear interaction is to be responsible to this electronic shower. Thus the present results give the good support to the existence of π^0-meson.

Furthermore the present results seem to be consistent with the Rossi's results.³⁾

About the Frequency ratio of the burst produced by the star to by the μ-meson or hard shower, our result is agreement with E. P. Geoge and P. T. Treut's.

However, the final conclusions must be reserved until the observation at sea level is finished, as it is of essential importance to compare the results at high altitude with those at sea level.

We wish to express my sincere gratitude to Prof. U. Watase for many helpful discussions during the course of this wook.

We wish to express our thanks to Prof. Z. Koba and Mr. K. Watanabe for their to the interpretations of our experimental results.

References

1) M. Schein and P.S. Gill: Rev. Mod. Phys. **11** (1939) 267.

2) R.F. Christy and S. Kusaka: Phys. Rev. **59** (1941) 414.

3) H.S. Bridge and B. Rossi: Phys. Rev. **75** 1949) 810.

4) W,C. Elmore and M. Sands: Electronics, McGraw-Hill Co. N. Y. 1949.

5) W.W. Brown, A.S. Mckay and E.D. Paluatier: Phys. Rev. **76** (1949) 506.

6) E. P. Geoge and P. T. Treut Proc. Phys. Soc. **64** (1951) 733.

JOURNAL OF THE PHYSICAL SOCIETY OF JAPAN Vol. 7, No. 4 JULY—AUG., 1952

Crystal Structures and Intermolecular Forces of Rare Gases

By Taro KIHARA and Saburo KOBA

Department of Physics, Faculty of Science, University of Tokyo

(Received February 15, 1952)

By means of models of intermolecular potential $U(r)$, the total energy of molecular crystals is calculated provided the additivity of intermolecular forces is valid. If the Lennard-Jones model, $U(r)=U_0(s-6)^{-1}[6(r_0/r)^s-s(r_0/r)^6]$, is used, the lattice of hexagonal closest packing has always a lower energy than that of cubic closet packing. If the model, $U(r)=U_0(\sigma-6)^{-1}[6\exp(\sigma-\sigma r/r_0)-\sigma(r_0/r)^6]$ is used, there is a critical value of σ, $\sigma_0=8.675$, above which the hexagonal is stable and below which the cubic is stable.

In general, in order that the cubic structure has a lower energy as in the case of rare gases, it is necessary (although not sufficient) that the hollow part of the intermolecular potential is wide enough, much wider than that of $U(r)=U_0[r_0/r)^{12}-2(r_0/r)^6]$ for instance.

These results are in agreement with the conclusions which Kihara has obtained by investigating the third virial coefficients of the equation of state for rare gases.

§1. Introduction and Some Results

In the statistical mechanical treatment of substances composed of inert spherical molecules, in their gaseous, liquid and solid states, it is usually assumed that the total potential energy is equal to the sum of the potential energy between two molecules, $U(r)$, r being their distance apart. This "additivity of intermolecular forces" is, in fact, regarded as valid with a considerable degree of accuracy. $U(r)$ forms, therefore, the basis of the molecular theory. As regards $U(r)$, since the exact quantummechanical calculations are very difficult, models are adopted, which should satisfy the conditions of simplicity as well as accuracy.

The Lennard-Jones potential,

$$U(r)=\frac{U_0}{s-6}\left[6\left(\frac{r_0}{r}\right)^s-s\left(\frac{r_0}{r}\right)^6\right]$$
$$=\frac{\lambda}{r^s}-\frac{\mu}{r^6}, \qquad (1.\ 1)$$

is the most generally used form of $U(r)$. In (1. 1), r_0 is the value of r corresponding to the minimum of $U(r)$, $-U_0=U(r_0)$, and s is a number larger than 6 of which the usually accepted values are 9 and 12. λ and μ are constants. With a larger value of s the hollow part of the potential becomes narrower, and vice versa.

Lennard-Jones and Ingham[1)], assuming the additivity of intermolecular forces, calculated the potential energy of molecular crystals composed of the model (1. 1) in the cases of three types of cubic lattices, — simple cubic, cubic body-centred and cubic close-packed; and they found that molecules will take up the form of a close-packed lattice in preference to a body-centred, and a body-centred in preference to a simple cubic. There are, however, two lattice-types of closest packing, i.e. cubic and hexagonal; the rare gases, except helium, crystallize at low temperatures in a lattice of cubic closest packing (henceforth denoted as c.c.p.) and not in a lattice of hexagonal closest packing (henceforth denoted as h.c.p.)[2)]. Lennard-Jones and Ingham did not refer to the h.c.p. structure, possibly because their analytical method using zeta-functions was inconvenient to the calculations of the potential energy constants of the h.c.p. lattice.

In this paper, the potential energies of c.c.p. and h.c.p. lattices are calculated by an elementary method with sufficient accuracy. The first result is: Under the assumption of the additivity of intermolecular forces, a lattice of h.c.p. has a lower energy for the Lennard-Jones model,—a contradiction with the experimental facts on rare gases. This result contrary to general expectations offers a problem how to select a model of simple analytic form making the energy of c.c.p. lower than that of h.c.p.

A natural next step may be to examine the potential model with an exponential type as its repulsive term, i.e.,

$$U(r)=\frac{U_0}{\sigma-6}\left[6\exp\left(\sigma-\frac{\sigma r}{r_0}\right)-\sigma\left(\frac{r_0}{r}\right)^6\right], \tag{1.2}$$

which is quantum-mechanically more reasonable than (1. 1). σ is a constant indicating the narrowness of the hollow part. The result is as follows: There exist a critical value of σ, $\sigma_0=8.675$, and if $\sigma>8.675$ ($\sigma<8.675$), h.c.p. (c.c.p.) has a lower energy than c.c.p. (h.c.p.)

§ 2. Lattice Point Distribution in c.c.p. Structure

First we consider the c.c.p. lattice. The distance between the molecule under consideration and one of its nearest neighbours is denoted by a. Let us represent the distance between the molecule under consideration and one of its i-th neighbours by r_{ci}, and their number by n_{ci}.

If we choose one of the lattice points as origin, the rectangular coordinates (x, y, z) of the lattice point can be represented by the following general formula,

$$x=Lb,\ y=Mb,\ z=Nb,\ 2b^2=a^2,$$
$$L,\ M,\ N=0,\ \pm1,\ \pm2,\ \pm3,\ \dots, \tag{2.1}$$

with the condition,

$$|L|+|M|+|N|=0,\ 2,\ 4,\ 6,\ \dots. \tag{2.2}$$

Counting the number of lattice points belonging to the same

$$r^2_{ci}=(L^2+M^2+N^2)b^2, \tag{2.3}$$

we can obtain n_{ci} for each $(r_{ci}/a)^2$. The results together with the values of $\sum n_{ci}$ from $i=1$ to $i=60$ are shown in Table 1. The results up to $i=13$ are found in a paper of Prins and Petersen[3].

§ 3. Calculation of the Potential Energy Constants of c.c.p. Lattice

In the case of intermolecular potential λr^{-s} the potential energy per molecule in an infinite crystal is given by

$$\frac{1}{2}\frac{\lambda}{a^s}C_s=\frac{1}{2}\frac{\lambda}{a^s}\sum_{i=1}^{\infty}n_{ci}\left(\frac{a}{r_{ci}}\right)^s, \tag{3.1}$$

C_s being called the potential energy constant. Taking a proper positive integer θ, we rewrite (3. 1) into the form

$$\frac{1}{2}\frac{\lambda}{a^s}C_s=\frac{1}{2}\frac{\lambda}{a^s}\sum_{i=1}^{\theta}n_{ci}\left(\frac{a}{r_{ci}}\right)^s+\frac{1}{2}\lambda\sum_{i=\theta+1}^{\infty}n_{ci}\left(\frac{1}{r_{ci}}\right).$$

$\tilde{C}_s$, an approximate value of C_s, may be obtained by replacing the second summation by the integral

$$\frac{1}{2}\lambda\rho_c\int_{A_\theta a}^{\infty}4\pi r^2\cdot r^{-s}dr=2\pi\lambda\rho_c\frac{(A_\theta a)^{3-s}}{s-3}, \tag{3.2}$$

ρ_c denoting the mean density of the lattice points:

$$\rho_c=\sqrt{2}\,a^{-3}. \tag{3.3}$$

Namely

$$\tilde{C}_s=\sum_{i=1}^{\theta}n_{ci}\left(\frac{a}{r_{ci}}\right)^s+\frac{4\sqrt{2}\,\pi}{(s-3)A_\theta^{s-3}}. \tag{3.4}$$

In the expression (3. 2) A_θ is defined by the relation

$$\frac{4}{3}\pi(A_\theta a)^3\rho_c=1+\sum_{i=1}^{\theta}n_{ci},$$

i.e.

$$A_\theta=\left\{\frac{3}{4\sqrt{2}\,\pi}\left(1+\sum_{i=1}^{\theta}n_{ci}\right)\right\}^{1/3}. \tag{3.5}$$

$A_\theta a$ represents the radius of the sphere of mean density corresponding to $1+n_{c1}+n_{c2}$

Table I

$(r_{ci}/a)^2$	n_{ci}	$\sum n_{ci}$	$(r_{ci}/a)^2$	n_{ci}	$\sum n_{ci}$
1	12	12	33	96	1156
2	6	18	34	48	1204
3	24	42	35	48	1252
4	12	54	36	36	1288
5	24	78	37	120	1408
6	8	86	38	24	1432
7	48	134	39	48	1480
8	6	140	40	24	1504
9	36	176	41	48	1552
10	24	200	42	48	1600
11	24	224	43	120	1720
12	24	248	44	24	1744
13	72	320	45	120	1864
15	48	368	47	96	1960
16	12	380	48	24	1984
17	48	428	49	108	2092
18	30	458	50	30	2122
19	72	530	51	48	2170
20	24	554	52	72	2242
21	48	602	53	72	2314
22	24	626	54	32	2346
23	48	674	55	144	2490
24	8	682	57	96	2586
25	84	766	58	72	2658
26	24	790	59	72	2730
27	96	886	60	48	2778
28	48	934	61	120	2898
29	24	958	63	144	3042
31	96	1054	64	12	3054
32	6	1060	65	72	3126

Table II.

$(r_{hi}/a)^2$	n_{hi}	$\sum n_{hi}$	$(r_{hi}/a)^2$	n_{hi}	$\sum n_{hi}$	$(r_{hi}/a)^2$	n_{hi}	$\sum n_{hi}$	$(r_{hi}/a)^2$	n_{hi}	$\sum n_{hi}$
1	12	12	18	18	466	35	24	1230	$50\frac{2}{3}$	12	2150
2	6	18	$18\frac{1}{3}$	12	478	$35\frac{2}{3}$	12	1242	51	36	2186
$2\frac{2}{3}$	2	20	$18\frac{2}{3}$	12	490	36	18	1260	$51\frac{2}{3}$	48	2234
3	18	38	19	24	514	$36\frac{1}{3}$	24	1284	52	36	2270
$3\frac{2}{3}$	12	50	$19\frac{2}{3}$	12	526	37	72	1356	$52\frac{1}{3}$	12	2282
4	6	56	$20\frac{1}{3}$	12	538	$37\frac{2}{3}$	12	1368	53	36	2318
5	12	68	21	36	574	38	24	1392	$53\frac{2}{3}$	24	2342
$5\frac{2}{3}$	12	80	$21\frac{2}{3}$	24	598	$38\frac{1}{3}$	12	1404	54	18	2360
6	6	89	22	12	610	$38\frac{2}{3}$	36	1440	$54\frac{1}{3}$	6	2366
$6\frac{1}{3}$	6	92	$22\frac{1}{3}$	18	628	39	36	1476	$54\frac{2}{3}$	36	2402
$6\frac{2}{3}$	12	104	$22\frac{2}{3}$	12	640	$39\frac{1}{3}$	6	1482	55	48	2450
7	24	128	23	24	664	$39\frac{2}{3}$	24	1506	$55\frac{1}{3}$	18	2468
$7\frac{1}{3}$	6	134	$23\frac{1}{3}$	12	676	40	12	1518	$55\frac{2}{3}$	24	2492
$8\frac{1}{3}$	12	146	$23\frac{2}{3}$	48	724	$40\frac{1}{3}$	12	1530	$56\frac{1}{3}$	24	2516
9	12	158	24	2	726	41	24	1554	57	48	2564
$9\frac{2}{3}$	24	182	25	36	762	$41\frac{2}{3}$	48	1602	58	36	2600
10	12	194	26	24	786	42	36	1638	$58\frac{1}{3}$	24	2624
$10\frac{1}{3}$	12	206	$26\frac{1}{3}$	12	798	$42\frac{1}{3}$	12	1650	$58\frac{2}{3}$	24	2648
$10\frac{2}{3}$	2	208	$26\frac{2}{3}$	12	810	$42\frac{2}{3}$	2	1652	59	36	2684
11	12	220	27	42	852	43	72	1724	$59\frac{1}{3}$	6	2690
$11\frac{1}{3}$	6	226	$27\frac{1}{3}$	6	858	$43\frac{1}{3}$	12	1736	$59\frac{2}{3}$	60	2750
$11\frac{2}{3}$	24	250	$27\frac{2}{3}$	12	870	$43\frac{2}{3}$	12	1748	60	12	2762
12	6	256	28	24	894	45	60	1808	$60\frac{1}{3}$	24	2786
$12\frac{1}{3}$	12	268	$28\frac{1}{3}$	12	906	$45\frac{2}{3}$	36	1844	61	72	2858
13	24	292	29	12	918	$46\frac{1}{3}$	6	1850	$61\frac{2}{3}$	24	2882
$13\frac{2}{3}$	12	304	$29\frac{2}{3}$	36	954	$46\frac{2}{3}$	24	1874			
$14\frac{1}{3}$	6	310	$30\frac{1}{3}$	12	966	47	48	1922			
$14\frac{2}{3}$	24	334	$30\frac{2}{3}$	24	990	$47\frac{1}{3}$	12	1934			
15	12	346	31	72	1062	$47\frac{2}{3}$	24	1958			
$15\frac{1}{3}$	12	358	$31\frac{1}{3}$	12	1074	48	6	1964			
$15\frac{2}{3}$	24	382	$31\frac{2}{3}$	24	1098	$48\frac{1}{3}$	12	1976			
16	6	388	$32\frac{1}{3}$	12	1110	49	60	2036			
$16\frac{1}{3}$	12	400	33	48	1158	$49\frac{2}{3}$	48	2084			
17	24	424	$33\frac{2}{3}$	24	1182	50	30	2114			
$17\frac{2}{3}$	24	448	24	24	1206	$50\frac{1}{3}$	24	2138			

$+\cdots+n_{c\theta}$ lattice points.

The A_θ's which do not satisfy the condition,

$$r_\theta < A_\theta a < r_{\theta+1}\,, \tag{3.6}$$

are omitted in the following calculations.

Taking $\theta=1, 2, 3, \cdots$ in (3.4), we obtain a sequence of $\tilde{C}_s$, which converges to a definite value as θ increases. In order to determine C_s to the fifth decimal place, it is sufficient to take

$$r_{c\theta}/a \approx 8,\ 7,\ 6,\ 5 \text{ and } 4$$

for $\quad s=6,\ 8,\ 10,\ 12$ and 14

respectively. The calculations are performed for $s=6$, 7, 8, 9, 10, 12, 14, 16 and 18, and the results are given in Table III. These results agree perfectly with those of Lennard-Jones and Ingham[1].

§ 4. Lattice Point Distribution in h.c.p. Structure

Taking the lattice point under consideration at the origin we choose the coordinate axes as shown in Fig. 1, where

$$C=2\sqrt{\frac{2}{3}}a\,. \tag{4.1}$$

Considering that the coordinates of all lattice points of h.c.p. are given by

$$\left.\begin{aligned}
&x=\frac{L}{2}a\,,\\
&y=\left[\frac{1}{3}\left\{\frac{1-(-1)^N}{2}\right\}+M\right]\frac{\sqrt{3}}{2}a\,,\\
&z=N\sqrt{\frac{2}{3}}a\,,\\
&L,\ M,\ N=0,\ \pm1,\ \pm2,\ \pm3,\ \cdots,\\
&L+M=N+2p\,,\\
&p=0,\ \pm1,\ \pm2,\ \pm3,\ \cdots,
\end{aligned}\right\} \tag{4.2}$$

we can count n_{hi}, the number of i-th neighbours for each $(r_{hi}/a)^2$, r_{hi} being the distance from the origin to the i-th neighbours. The values together with $\sum n_{hi}$ from $i=1$ to $i=130$

are shown in Table II. The results up to $i=13$ are found in the paper of Prins and Petersen[3]).

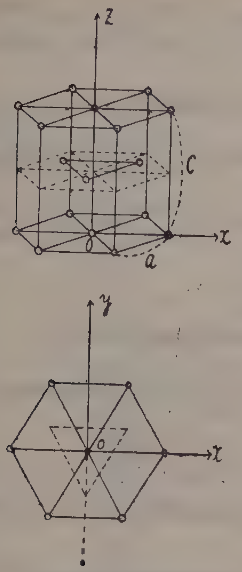

Fig. 1.

§5. Calculation of the Potential Energy Constants of h.c.p. Lattice

The average density ρ_h of h.c.p. lattice is equal to ρ_c. The potential energy constant H_s of h.c.p. lattice can be calculated by the method described in §3. The results obtained are shown in Table III.

Table III.

s	C_s	H_s
6	14.45392	14.45489
7	13.35939	13.36035
8	12.80194	12.80282
9	12.49255	12.49332
10	12.31125	12.31190
12	12.13188	12.13229
14	12.05899	12.05923
16	12.02736	12.02748
18	12.01300	12.01306

§6. Comparison of the Potential Energy of c.c.p. Lattice with that of h.c.p. Lattice According to the Lennard-Jones Model

The relation $C_6 < H_6$ reveals at once that, in a system of rigid molecules corresponding to $s=\infty$, h.c.p. should be more stable than c.c.p. Let us, therefore, investigate the case $s \neq \infty$ in the following.

The potential energy per one molecule, Φ, is given by

$$\Phi_c(a)=\frac{1}{2}\,\frac{U_0}{s-6}\left[6\left(\frac{r_0}{a}\right)^s C_s - s\left(\frac{r_0}{a}\right) C_6\right], \tag{6.1}$$

$$\Phi_h(a)=\frac{1}{2}\,\frac{U_0}{s-6}\left[6\left(\frac{r_0}{a}\right)^s H_s - s\left(\frac{r_0}{a}\right)^6 H_6\right], \tag{6.2}$$

in the case of the cubic and the hexagonal structure respectively. a_0, the distance between nearest neighbours corresponding to the minimum of Φ, is given by $d\Phi/da=0$, i.e.

$$a_{c0}=\left(\frac{C_s}{C_6}\right)^{\frac{1}{s-6}} r_0\,, \tag{6.3}$$

$$a_{h0}=\left(\frac{H_s}{H_6}\right)^{\frac{1}{s-6}} r_0\,, \tag{6.4}$$

and the minimum of Φ, denoted by Φ_0, is expressed by

$$\Phi_{c0}=\Phi_c(a_{c0})=-\frac{1}{2}\left(\frac{C_6{}^s}{C_s{}^6}\right)^{\frac{1}{s-6}} U_0\,, \tag{6.5}$$

$$\Phi_{h0}=\Phi_h(a_{h0})=-\frac{1}{2}\left(\frac{H_6{}^s}{H_s{}^6}\right)^{\frac{1}{s-6}} U_0\,, \tag{6.6}$$

Table IV.

s	a_{c0}/r_0	a_{h0}/r_0	$(a_{c0}-a_{h0})/a_{c0}\times 10^6$
7	0.9242745	0.9242789	−4.7
8	0.9411202	0.9411210	−0.8
9	0.9525517	0.9525498	+2.0
10	0.9606807	0.9606771	+3.7
12	0.9712338	0.9712284	+5.5
14	0.9776101	0.9776043	+5.9
16	0.9817899	0.9817843	+5.7
18	0.9847035	0.9846984	+5.2

Table V.

s	$-\Phi_{c0}/U_0$	$-\Phi_{h0}/U_0$	$(\Phi_{c0}-\Phi_{h0})/\Phi_{c0}\times 10^5$
7	11.59177	11.59221	− 3.8
8	10.40124	10.40188	− 6.2
9	9.674420	9.675169	− 7.8
10	9.193500	9.194309	− 8.8
12	8.610200	8.611063	−10.0
14	8.278691	8.279539	−10.3
16	8.069467	8.070285	−10.1
68	7.927255	7.928032	− 9.8

for the cubic and the hexagonal structure respectively. Calculated values of a_{c0}/r_0, a_{h0}/r_0, $(a_{c0}-a_{h0})/a_{c0}$, Φ_{c0}/U_0, Φ_{h0}/U_0 and $(\Phi_{c0}-\Phi_{h0})/\Phi_{c0}$ are shown in Table IV, Table V, Fig. 2 and Fig. 3. The relation $(\Phi_{c0}-\Phi_{h0})/\Phi_{c0}<0$ indicates that h.c.p. should be more stable for any value of s. This model, therefore, does tot explain the crystal structure of rare gases.

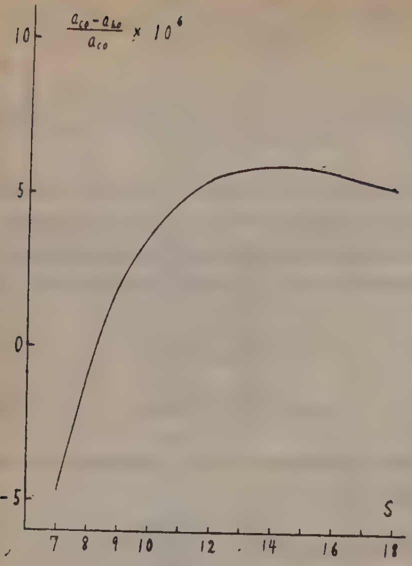

Fig. 2.

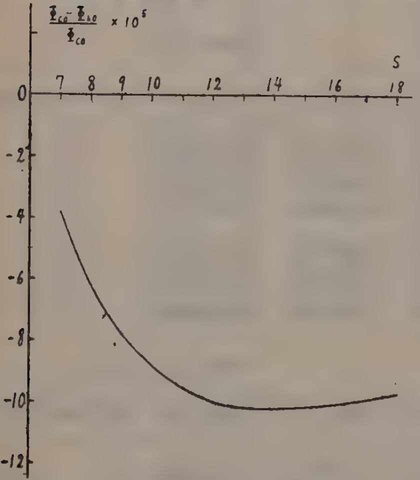

Fig. 3.

§ 7. Comparison of the Potential Energy of c.c.p. Lattice with that of h.c.p. Lattice According to the Exponential Model

For the model (1. 2), the potential energy per molecule in the c.c.p. lattice ie given by

$$\Phi_{c0}=\Phi_c(a_{c0})=\frac{1}{2}\frac{U_0}{\sigma-6}\Bigg[6e^\sigma\sum_{i=1}^{\infty}n_{ci}\times\exp\left(-\frac{\sigma a_{c0}}{r_0}\,\xi_{ci}\right)-\sigma\left(\frac{r_0}{a_{ci}}\right)^6C_6\Bigg],$$

$$\xi_{ci}=\frac{r_{ci}}{a_{c0}}\,. \tag{7. 1}$$

Here a_{c0} denotes the distance between adjacent lattice points and is obtained from the condition

$$\left(-a\frac{d\Phi_c(a)}{da}\right)_{a=a_{c0}}=\frac{3U_0}{\sigma-6}\Bigg[e^\sigma\sum_{i=1}^{\infty}n_{ci}\frac{\sigma a_{c0}}{r_0}\xi_{ci}\times\exp\left(-\frac{\sigma a_{c0}}{r_0}\xi_{ci}\right)-\sigma\left(\frac{r_0}{a_{c0}}\right)^6C_6\Bigg]=0\,. \tag{7. 2}$$

Similarly, as regards h.c.p. lattice, we get

$$\Phi_{h0}=\Phi_h(a_{h0})=\frac{1}{2}\frac{U_0}{\sigma-6}\Bigg[6e^\sigma\sum_{i=1}^{\infty}n_{hi}\times\exp\left(-\frac{\sigma a_{h0}}{r_0}\xi_{hi}\right)-\sigma\left(\frac{r_0}{a_{h0}}\right)^6H_6\Bigg],$$

$$\xi_{hi}=\frac{r_{hi}}{a_{h0}}\,,$$

which is nearly equal to

$$\Phi_h(a_{c0})=\frac{1}{2}\frac{U_0}{\sigma-6}\Bigg[6e^\sigma\sum_{i=1}^{\infty}n_{hi}\exp\left(-\frac{\sigma a_{c0}}{r_0}\xi_{hi}\right)-\sigma\left(\frac{r_0}{a_{c0}}\right)^6H_6\Bigg] \tag{7. 3}$$

(to a small quantity of the order of $(a_{c0}-a_{h0})^2/r_0^2$).

Since the summations in (7. 1), (7. 2) and (7. 3) can be achieved without any special technique, we know, taking $\sigma a_{c0}/r_0$ as a parameter, the relation between σ and $(\Phi_{c0}-\Phi_{h0})/\Phi_{c0}$. The result is shown in Fig. 4.

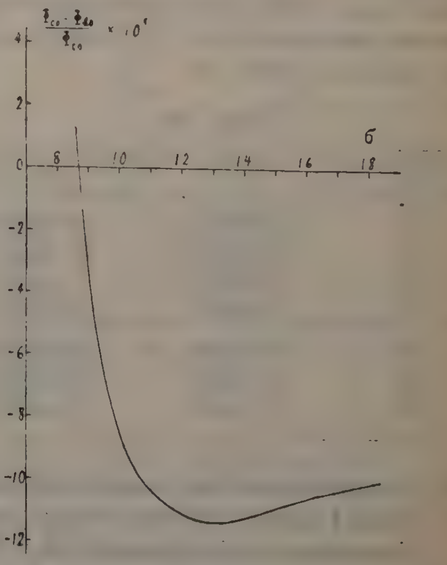

Fig. 4.

In order to explain the fact that the c.c.p. structure is more stable than the h.c.p. structure, it is necessary to choose $\sigma<8.675$. We must remember, however, that the shape of the repulsive wall of the potential (1. 2) becomes inadequate if too small values of σ (nearly $\sigma \lesssim 8.5$) are chosen.

§ 8. Discussion

In Fig. 5 four curves of intermolecular potential are shown. Curves A, B and C represent the Lennard-Jones type (1. 1) with $s=7$, 9 and 12 respectively, and curve D the exponential type (1. 2) with $\sigma=8.675$ (the critical value). From this comparison we may conclude as follows: The necessary, though not sufficient, condition of stability of the c.c.p. structure is that the hollow part of the intermolecular potential is wide enough.

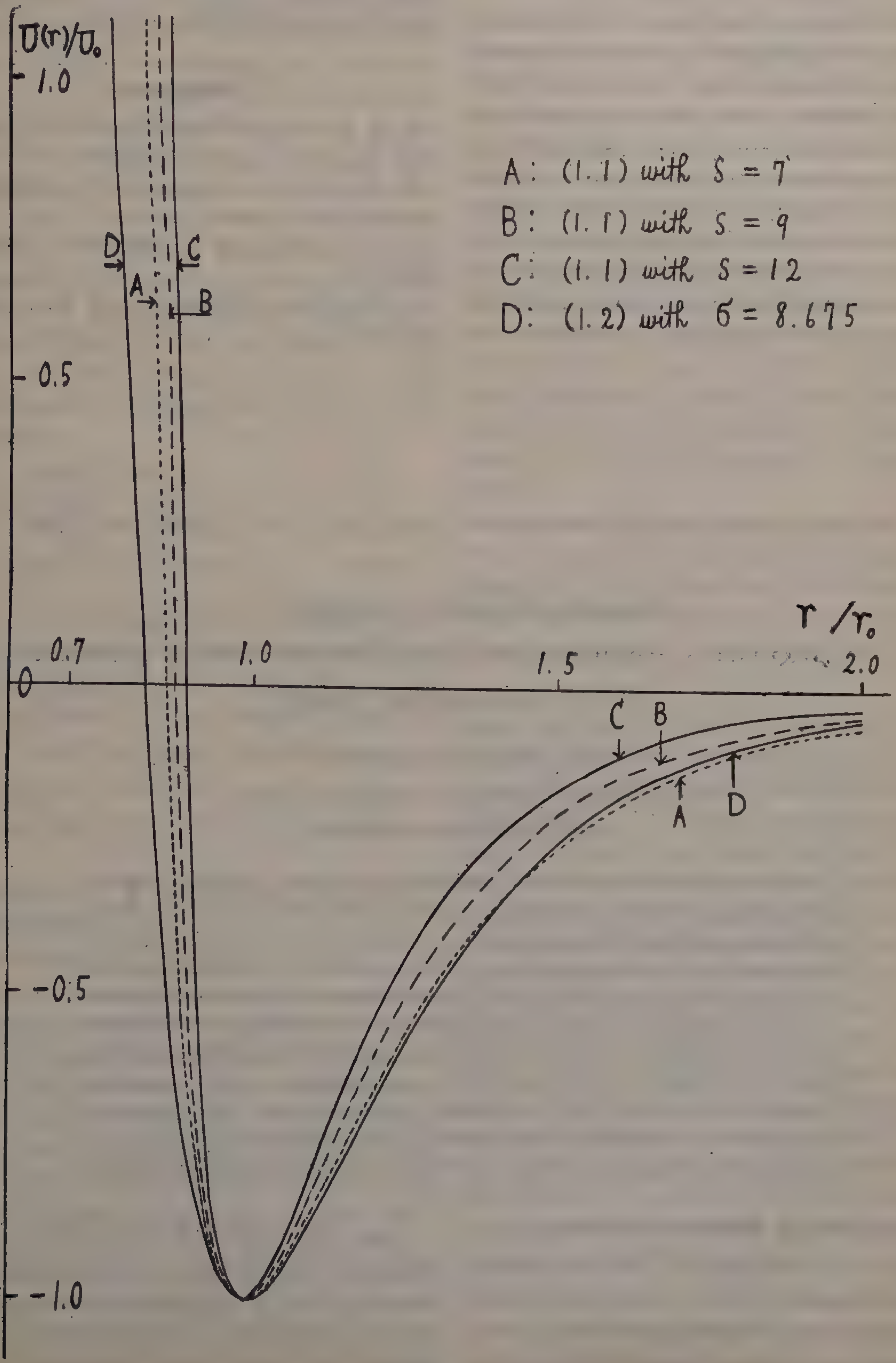

Fig. 5.

(Glancing at the third neighbour in Tables I and II, we generally understand that narrowness of the hollow part of the potential causes the stability of h.c.p.)

Since the foregoing calculations are based on the assumption of additivity of intermolecular forces, and since the energy difference above obtained is as small as 0.01%, and since we do not take into account the difference between two zero point energies for both structures, the results obtained can not be considered to have an accurate quantitative meaning. The following rather qualitative conclusion, however, seems to be reasonable: The hollow part of the intermolecular potential for rare gases must be remarkably wider than that of the most usually adopted model $U(r)=U_0[(r_0/r)^{12}-2(r_0/r)^6]$.

It should be emphasized here that one of the present authors, T. Kihara[4], obtained recently the same conclusion from a different side, namely from an investigation of the third virial coefficients of gases.

References

1) J. E. Lennard-Jonos and A. E. Ingham: Proc. Roy. Soc. **A107** (1925) 636.

2) See R. W. G. Wyckoff: The Structure of Crystals, Ed. 2 (1931).

3) J. A. Prins and H. Petersen: Physica **3** (1936) 147.

4) T. Kihara: Journ. Phys. Soc. Japan **6** (1951) 184.

JOURNAL OF THE PHYSICAL SOCIETY OF JAPAN Vol. 7, No. 4 JULY—AUG., 1952

Theory of Color Centers, I
On Mollwo's Relation and the Temperature Variation in F Absorption Band

By Takeo NAGAMIYA

Department of Physics, Osaka University

(Reseived January 18, 1952)

A very simple derivation of well-known Mollwo's relation between ionic distance and F maximum absorption frequency is given. Then, following Inui and Uemura's idea, the variation in the position and the breadth of F absorption band with temperature is correlated with the variation and the fluctuation in ionic distance by thermal motions. Finally, formula for the concentration of F centers in equilibrium with alkali vapor is given, taking into account the change in vibrational frequency of the positive ions adjacent to F vacancies. Numerical value for the parameter characterizing this change is computed by comparing with experiment the formulas for the temperature dependency of F band and for the concentration of F centers.

§1. Derivation of Mollwo's Relation

Between the frequency of the maximum absorption intensity in F band of various alkali halides and the nearest interionic distance there is a well-known relation found by Mollwo[1),2)] in 1931. If $\nu_{\max}$ denotes the maximum frequency and d the nearest ionic distance, then Mollwo's relation is

$$\nu_{\max}\, d^2 = \text{const} \doteq 0.5\,\text{sec}^{-1}.\,\text{cm}^2. \qquad (1)$$

Fröhlich[3)] derived this equation under the assumption that F absorption band corresponds to the transition of an electron from the highest full band to the next vacant conduction band, the band system being assumed as derived from free electron approximation. Although his idea cannot be justified at present, it is interesting to notice that the value for the constant in Eq. (1) derived by him comes very near to the measured one:

$$\text{const} = h/16\,m = 0.45\,\text{sec}^{-1}.\,\text{cm}^2,$$

where m is the mass of electron.

The electron in an F center may be considered as migrating over the valence states of the positive ions surrounding the halogen vacancy, in a way just as a conduction electron is migrating over the valence states of the constituent ions of the crystal. The simplest way of treating the motion of the electron in an F center would then be to assume that it is describing a circular orbit of radius d around the vacancy, passing through the centers of the surrounding alkali ions. The ground state $1s$ has no angular momentum, and the excited state $2p$ has the angular momentum determined by the quantum condition:

$$md^2\omega = h/2\pi\,, \tag{2}$$

so that its kinetic energy is

$$\frac{1}{2}md^2\omega^2 = h^2/8\pi^2md^2\,. \tag{3}$$

We may remark that there is no state other than $1s$ and $2p$ which can be constructed by a linear combination of the valence states of the ions adjacent to the halogen vacancy. Putting (3) equal to $h\nu_{\max}$ we have

$$\nu_{\max}\, d^2 = h/8\pi^2 m \tag{4}$$

This is our derivation of Mollwo's relation.

§2. Variation in F Absorption Band with Temperature

Inui and Uemura[4] have put forward an interesting idea that the observed variation in F absorption band with temperature with respect to its position and breadth would be connected with the variation in d by thermal expansion and the fluctuation in d by thermal vibrations, respectively. Now, it is a well-known fact[1, 2] that the frequency ν_0 at which the absorption intensity equals half the maximum intensity on the short wavelength side does not depend on temperature. A straightforward interpretation of this fact would be that this frequency corresponds to such an arrangement of the ions in the neighborhood of an F center that has the lowest potential energy, that is, the arrangement at absolute zero without zero-point motion. Since the potential energy between ions in an ionic lattice consists of an electrostatic interaction slowly varing with interionic distance, and a strongly varing repulsive interaction, it would rise sharply for distances smaller than d_0, the radius of the circular orbit corresponding to the arrangement mentioned above, but would rise slowly for distances larger than d_0. Therefore the vibrations of the ions adjacent to the F vacancy would be such that the mean increase in d measured from d_0 is approximately equal to the amplitude of their radial vibrations, the minimum of d being limited by d_0. Thus, through Mollwo's relation, in which the suffix "max" now is dropped, the short wave-length side of the F absorption band would be practically limited by d_0, and the shift of the maximum frequency, which at the same time equals half the half line width, would correspond to the mean increase in d measured from d_0.

Now, from Eq. (1) or (4), the suffix "max" being dropped, the change in absorption frequency, δ_ν, corresponding to a change in the radius of the circular orbit, δ_d, is given by

$$\frac{\delta_\nu}{\nu} = -2\frac{\delta_d}{d}\,. \tag{5}$$

Applying this formula to the shift of $\nu_{\max}$ with temperature and calculating the right hand side from the measured thermal expansion coefficient, Inui and Uemura obtained a value of $\delta\nu_{\max}/\nu_{\max}$ about half as large as that observed. This means that the thermal expansion of d for F center must be assumed twice as large as that for the normal lattice points, or, from the considerations above that the vibrational frequency of the ions adjacent to F vacancy is half as low as that of the ions at the normal lattice points, provided a parabolic vibrational potential can be assumed (although a strictly parabolic potential would contradict to the preceding considerations). Denoting the radial vibrational frequency of the former kind of ions as f and that of the latter kind of ions as f_0, we have

$$f_0 = sf, \quad s \doteqdot 2\,. \tag{6}$$

Inui and Uemura further computed the variation in half width of F absorption band with temperature under the assumption of harmonic vibrations of the ions adjacent to the F vacancy. The following treatment is quite an equivalent one with their somewhat lengthy calculations. The probability distribution function for a harmonic oscillator as a function of the displacement of an ion from its mean position is given by a well-known formula

$$f(x)dx=\frac{1}{\sqrt{\pi}x_0}\left[\tanh\left(\frac{\theta}{2T}\right)\right]^{\frac{1}{2}}$$
$$\times \exp\left[-\tanh\left(\frac{\theta}{2T}\right)\cdot\left(\frac{x_0}{x}\right)^2\right]dx, \quad (7)$$

where x is the displacement and

$$\theta=hf/k, \quad x_0=(h/4\pi^2Mf)^{\frac{1}{2}}, \quad (8)$$

M being the mass of the vibrating alkali ion. From this we have the mean square amplitude as

$$<x^2>=\frac{1}{2}x_0^2\coth\left(\frac{\theta}{2T}\right) \quad (9)$$

and the half width of the distribution as

$$2\sqrt{2\ln 2<x^2>}=2.36\sqrt{<x^2>}. \quad (10)$$

Since there are four positive ions on the circular orbit of the electron in an F center, the half width of the radius of the orbit is given by $1/\sqrt{4}$ times the value of (10), provided the vibrations of these ions can be treated as independent of each other. Substituting this half width of the radius for δ_d of the right hand side of (5), it follows that the half width of the F absorption band, $\Delta\nu$, is given as

$$\frac{\Delta\nu}{\nu_{\max}}=\frac{2.36\sqrt{<x^2>}}{d}=\frac{2.36\,x_0}{\sqrt{2}\,d}\left[\coth\left(\frac{\theta}{2T}\right)\right]^{\frac{1}{2}}. \quad (11)$$

In the classical limit of $T\rightarrow\infty$, this reduces to

$$\frac{\Delta\nu}{\nu_{\max}}=\frac{2.36}{d}\left(\frac{kT}{4\pi^2Mf^2}\right)^{\frac{1}{2}} \quad (12)$$

and at absolute zero, it reduces to

$$\frac{\Delta\nu}{\nu_{\max}}=1.67\frac{x_0}{d}=\frac{1,67}{d}(h/4\pi^2Mf)^{\frac{1}{2}} \quad (13)$$

The observed change in half width with temperature can be fairly well represented by these formulas as Inui and Uemura have actually shown.

Furthermore, it can be shown that the right hand side of the classical equation (12) is a function of temperature alone, but does not depend on any special choice of the substance, a remarkable fact observed also by Mollwo. Mott and Gurney[5] derived from a simple consideration the following formula

$$2\pi M^{\frac{1}{2}}f_0d=\left(\frac{\alpha e^2}{3\rho}\right)^{\frac{1}{2}}\left[\frac{\rho}{\alpha}\left(\frac{\alpha}{\rho}-2\right)\right]^{\frac{1}{2}}, \quad (14)$$

where α is the Madelung constant and ρ is the universal parameter appearing in the interionic repulsive potential of the form $Ae^{-r/\rho}$, being $\rho=0.345$ Å. The right hand side of this equation is nearly constant for all the alkali halides of the NaCl type and is

$$2\pi M^{1/2}f_0d=5.6\times10^{-6}\ \text{cgs}, \quad (14')$$

so that we have for (12), in virtue of (6),

$$\frac{\Delta\nu}{\nu_{\max}}=0.5\times10^{-2}s\sqrt{T}. \quad (15)$$

Comparison of this formula with Mollwo's observation yields the values of s in Table I.

Table I.

Substance	$\Delta\nu$(ev.) 20°C	600°C	$\nu_{\max}$(ev.) 20°C	600°C	$\Delta\nu/\nu_{\max}$ 20°C	600°C	s 20°C	600°C
NaCl	0.47	0.87	2.66	2.36	0.177	0.369	2.06	2.48
KCl	0.35	0.69	2.20	1.97	0.159	0.350	1.86	2.35
KBr	0.345	0.69	1.97	1.76	0.175	0.380	2.04	2.55
KI	0.345	0.63	1.81	1.62	0.192	0.388	2.24	2.61
SbCl	0.31	0.65	1.99	1.78	0.156	0.365	1.82	2.45

Greater values of s at 600°C would be due to a little inappropriate temperature factor $\sqrt{T}$ in our theoretical formula.

There is another way of computing the value of s. From the measurement of the infrared absorption frequency, f_r, we can compute the quantity $2\pi\mu^{1/2}f_r$, where μ is the reduced mass of positive and negative ions, and this quantity can be put equal to $2\pi M^{1/2}f_0$, for both are the force constant between them. Values of s deduced from this quantity are somewhat higher.

Table II refers to extremely low temperatures, and the values of s have been deduced by use of (13). Some greater values of s might be interpreted as indicating a broadening of the absorption band caused by other sources than the zero-point vibration, e. g. the internal strains.

Table II.

Substance	T(°K)	$\Delta\nu/\nu_{\max}$	d(Å)	$f_0\times10^{-12}$ sec	s
NaCl	20	0.127	2.81	4.94	2.44
KCl	28	0.086	3.14	3.46	1.73
KBr	28	0.099	3.29	3.31	2.40
KI	28	0.107	3.53	3.11	3.00
RbCl	—	—	3.27	2.25	—

§ 3. Number of F Centers in Equilibrium with Alkali Vapor

There is another way of estimating the quantity s. The concentration of F centers in the crystal in equilibrim with the vapor of its constituent alkali metal depends on the free energy of F centers and so on s. Now, according to Pohl, the number of F centers in the crystal of unit volume is given by the formula

$$n/n_g=\text{const.}\exp(W/kT), \qquad (16)$$

where n_g is the number of alkali metal atoms in the unit volume of the vapor. The theoretical deduction of (16) can be done in the following way. Let the number of alkali atoms in the unit volume of the crystal be $N+n$. The total free energy of the system consisting of this crystal and the alkali vapor, both being assumed to have unit volume, can be written as

$$\begin{aligned}F=&-n_g kT[1+\ln(h^{-3}n_g{}^{-1}(2\pi MkT)^{3/2})]\\ &-nW-kT[N\cdot\ln N-n\cdot\ln n\\ &\quad-(N-n)\ln(N-n)]\\ &-3nkT\cdot\ln(kT/hf_0)-6nkT[\ln(kT/hf)\\ &\quad-\ln(kT/hf_0)] \qquad (17)\end{aligned}$$

The first line represents the free energy of the vapor, considered as a perfect gas, the second line the free energy of the F centers, considered as being distributed at random in the crystal, and the third line the free energy of the vibrating n excess metal atoms and the correction term which allows for the change in the vibrational frequency of the metal ions adjacent to the F vacancies as compared with that of the metal ions at normal lattice points.

Minimizing this free energy expression with respect to n under the condition $n+n_g$ = const, we have

$$\frac{n}{n_g}=\frac{N(2\pi kT)^{3/2}(2\pi f_0)^3}{M^{3/2}(2\pi f)^6}e^{W/kT} \qquad (18)$$

This is different from (16) through a factor $T^{3/2}$ on the right hand side, which has a considerable effect on the measured value of W, because this is of the order of only a fraction of one ev. Pohl's results for KCl and KBr are

$$W=0.10\text{ ev. (KCl)},\quad 0.25\text{ ev. (KBr)}.$$

When (18) is used instead of (16), the values for W becomes approximately increased by $3kT/2$, and we have

$$W=0.21\text{ ev. (KCl)},\quad 0.36\text{ ev. (KBr)}$$

taking $T=600°\text{C}=873°\text{K}$. With these values and (18), the observed points can be better represented than by (16); indeed, the plot of the logarithm of n/n_g against $1/T$ is curved in Pohl's measurement with KCl, while the plot of $n/n_gT^{3/2}$ against $1/T$ lies perfectly on a straight line.

From the measured values of n/n_g and the values of f given in Table II, we have

$$s^6=41,\quad s=1.85\quad\text{(KCl)},$$
$$s^6=11.4\quad s=1.5\quad\text{(KBr)}.$$

Although these values are not in perfect agreement with the results obtained in the preceding section, the agreement must be considered as satisfactory in view of the approximate nature of the theory presented in this paper.

References

1) E. Mollwo: Gött. Nachr. Math.-Phys. Kl., 1931, 97 and 236; R. W. Pohl: Proc. Phys. Soc. **49** (1937) 49.

2) E. Mollwo: Z. Phys. **85** (1933) 56.

3) H. Fröhlich: Z. Phys. **80** (1933) 819.

4) T. Inui and Y. Uemura: Prog. Theor. Phys. **5** (1950) 395.

5) N. F. Mott and H. W. Gurney: *Electronic Processes in Ionic Crystals*, Oxford (1940), p. 21. The factor 2 before the Madelung constant is dimetto in our equation, for we assume the positive ions alone are vibrating, negative ions being at rest. Inui and Uemura did not drop this factor. They put (10) equal to δd, instead of half the value of (10) as in the present paper. Thus the values of s obtained by these authors should differ from our results through a factor $\sqrt{2}/2=0.7$.

the F vacancy. The following treatment is quite an equivalent one with their somewhat lengthy calculations. The probability distribution function for a harmonic oscillator as a function of the displacement of an ion from its mean position is given by a well-known formula

$$f(x)dx=\frac{1}{\sqrt{\pi}x_0}\left[\tanh\left(\frac{\Theta}{2T}\right)\right]^{\frac{1}{2}}$$
$$\times\exp\left[-\tanh\left(\frac{\Theta}{2T}\right)\cdot\left(\frac{x_0}{x}\right)^2\right]dx, \quad (7)$$

where x is the displacement and

$$\Theta=hf/k, \quad x_0=(h/4\pi^2Mf)^{\frac{1}{2}}, \quad (8)$$

M being the mass of the vibrating alkali ion. From this we have the mean square amplitude as

$$<x^2>=\frac{1}{2}x_0^2\coth\left(\frac{\Theta}{2T}\right) \quad (9)$$

and the half width of the distribution as

$$2\sqrt{2\ln 2<x^2>}=2.36\sqrt{<x^2>}. \quad (10)$$

Since there are four positive ions on the circular orbit of the electron in an F center, the half width of the radius of the orbit is given by $1/\sqrt{4}$ times the value of (10), provided the vibrations of these ions can be treated as independent of each other. Substituting this half width of the radius for δ_d of the right hand side of (5), it follows that the half width of the F absorption band, $\Delta\nu$, is given as

$$\frac{\Delta\nu}{\nu_{\max}}=\frac{2.36\sqrt{<x^2>}}{d}=\frac{2.36\,x_0}{\sqrt{2}\,d}\left[\coth\left(\frac{\Theta}{2T}\right)\right]^{\frac{1}{2}}. \quad (11)$$

In the classical limit of $T\rightarrow\infty$, this reduces to

$$\frac{\Delta\nu}{\nu_{\max}}=\frac{2.36}{d}\left(\frac{kT}{4\pi^2Mf^2}\right)^{\frac{1}{2}} \quad (12)$$

and at absolute zero, it reduces to

$$\frac{\Delta\nu}{\nu_{\max}}=1.67\frac{x_0}{d}=\frac{1{,}67}{d}(h/4\pi^2Mf)^{\frac{1}{2}} \quad (13)$$

The observed change in half width with temperature can be fairly well represented by these formulas as Inui and Uemura have actually shown.

Furthermore, it can be shown that the right hand side of the classical equation (12) is a function of temperature alone, but does not depend on any special choice of the substance, a remarkable fact observed also by Mollwo. Mott and Gurney(5) derived from a simple consideration the following formula

$$2\pi M^{\frac{1}{2}}f_0d=\left(\frac{\alpha e^2}{3\rho}\right)^{\frac{1}{2}}\left[\frac{\rho}{\alpha}\left(\frac{\alpha}{\rho}-2\right)\right]^{\frac{1}{2}}, \quad (14)$$

where α is the Madelung constant and ρ is the universal parameter appearing in the interionic repulsive potential of the form $Ae^{-r/\rho}$, being $\rho=0.345$ Å. The right hand side of this equation is nearly constant for all the alkali halides of the NaCl type and is

$$2\pi M^{1/2}f_0d=5.6\times10^{-6}\ \text{cgs}, \quad (14')$$

so that we have for (12), in virtue of (6),

$$\frac{\Delta\nu}{\nu_{\max}}=0.5\times10^{-2}s\sqrt{T}. \quad (15)$$

Comparison of this formula with Mollwo's observation yields the values of s in Table I.

Table I.

Substance	$\Delta\nu$(ev.) 20°C	$\Delta\nu$(ev.) 600°C	$\nu_{\max}$(ev.) 20°C	$\nu_{\max}$(ev.) 600°C	$\Delta\nu/\nu_{\max}$ 20°C	$\Delta\nu/\nu_{\max}$ 600°C	s 20°C	s 600°C
NaCl	0.47	0.87	2.66	2.36	0.177	0.369	2.06	2.48
KCl	0.35	0.69	2.20	1.97	0.159	0.350	1.86	2.35
KBr	0.345	0.69	1.97	1.76	0.175	0.380	2.04	2.55
KI	0.345	0.63	1.81	1.62	0.192	0.388	2.24	2.61
SbCl	0.31	0.65	1.99	1.78	0.156	0.365	1.82	2.45

Greater values of s at 600°C would be due to a little inappropriate temperature factor $\sqrt{T}$ in our theoretical formula.

There is another way of computing the value of s. From the measurement of the infrared absorption frequency, f_r, we can compute the quantity $2\pi\mu^{1/2}f_r$, where μ is the reduced mass of positive and negative ions, and this quantity can be put equal to $2\pi M^{1/2}f_0$, for both are the force constant between them. Values of s deduced from this quantity are somewhat higher.

Table II refers to extremely low temperatures, and the values of s have been deduced by use of (13). Some greater values of s might be interpreted as indicating a broadening of the absorption band caused by other sources than the zero-point vibration, e. g. the internal strains.

Table II.

Substance	T(°K)	$\Delta\nu/\nu_{\max}$	d(Å)	$f_0\times10^{-12}$ sec	s
NaCl	20	0.127	2.81	4.94	2.44
KCl	28	0.086	3.14	3.46	1.73
KBr	28	0.099	3.29	3.31	2.40
KI	28	0.107	3.53	3.11	3.00
RbCl	—	—	3.27	2.25	—

§ 3. Number of F Centers in Equilibrium with Alkali Vapor

There is another way of estimating the quantity s. The concentration of F centers in the crystal in equilibrim with the vapor of its constituent alkali metal depends on the free energy of F centers and so on s. Now, according to Pohl, the number of F centers in the crystal of unit volume is given by the formula

$$n/n_g=\text{const.}\exp(W/kT),\qquad(16)$$

where n_g is the number of alkali metal atoms in the unit volume of the vapor. The theoretical deduction of (16) can be done in the following way. Let the number of alkali atoms in the unit volume of the crystal be $N+n$. The total free energy of the system consisting of this crystal and the alkali vapor, both being assumed to have unit volume, can be written as

$$\begin{aligned}F=&-n_gkT[1+\ln(h^{-3}n_g^{-1}(2\pi MkT)^{3/2})]\\&-nW-kT[N\cdot\ln N-n\cdot\ln n\\&\quad-(N-n)\ln(N-n)]\\&-3nkT\cdot\ln(kT/hf_0)-6nkT[\ln(kT/hf)\\&\quad-\ln(kT/hf_0)]\end{aligned}\qquad(17)$$

The first line represents the free energy of the vapor, considered as a perfect gas, the second line the free energy of the F centers, considered as being distributed at random in the crystal, and the third line the free energy of the vibrating n excess metal atoms and the correction term which allows for the change in the vibrational frequency of the metal ions adjacent to the F vacancies as compared with that of the metal ions at normal lattice points.

Minimizing this free energy expression with respect to n under the condition $n+n_g$ = const, we have

$$\frac{n}{n_g}=\frac{N(2\pi kT)^{3/2}(2\pi f_0)^3}{M^{3/2}(2\pi f)^6}e^{W/kT}\qquad(18)$$

This is different from (16) through a factor $T^{3/2}$ on the right hand side, which has a considerable effect on the measured value of W, because this is of the order of only a fraction of one ev. Pohl's results for KCl and KBr are

$$W=0.10\text{ ev. (KCl)},\quad 0.25\text{ ev. (KBr)}.$$

When (18) is used instead of (16), the values for W becomes approximately increased by $3kT/2$, and we have

$$W=0.21\text{ ev. (KCl)},\quad 0.36\text{ ev. (KBr)}$$

taking $T=600°\text{C}=873°\text{K}$. With these values and (18), the observed points can be better represented than by (16); indeed, the plot of the logarithm of n/n_g against $1/T$ is curved in Pohl's measurement with KCl, while the plot of $n/n_gT^{3/2}$ against $1/T$ lies perfectly on a straight line.

From the measured values of n/n_g and the values of f given in Table II, we have

$$s^6=41,\quad s=1.85\quad\text{(KCl)},$$
$$s^6=11.4\quad s=1.5\quad\text{(KBr)}.$$

Although these values are not in perfect agreement with the results obtained in the preceding section, the agreement must be considered as satisfactory in view of the approximate nature of the theory presented in this paper.

References

1) E. Mollwo: Gött. Nachr. Math.-Phys. Kl., 1931, 97 and 236; R. W. Pohl: Proc. Phys. Soc. **49** (1937) 49.

2) E. Mollwo: Z. Phys. **85** (1933) 56.

3) H. Fröhlich: Z. Phys. **80** (1933) 819.

4) T. Inui and Y. Uemura: Prog. Theor. Phys. **5** (1950) 395.

5) N. F. Mott and H. W. Gurney: *Electronic Processes in Ionic Crystals*, Oxford (1940), p. 21. The factor 2 before the Madelung constant is dimetto in our equation, for we assume the positive ions alone are vibrating, negative ions being at rest. Inui and Uemura did not drop this factor. They put (10) equal to δd, instead of half the value of (10) as in the present paper. Thus the values of s obtained by these authors should differ from our results through a factor $\sqrt{2}/2=0.7$.

JOURNAL OF THE PHYSICAL SOCIETY OF JAPAN Vol. 7, No. 4 JULY—AUG., 1952

Theory of Color Centers, II
On the Nature of V_3 Center in Alkali Halides

By Takeo NAGAMIYA
Departmen of Physics, Osaka University

(Received January 18, 1952)

The same interpretation of V_3 center as that of Seitz is given. The energy of formation of a V_3 center in the crystal from a molecule of a halogen gas is computed and compared with Pohl's observation. The computed value in the case of KBr is 1.4 ev. as compared with the observed value 1.2 ev. Further, the mobility of V_3 centers at high temperature is discussed and a theoretical formula is derived for it. The computed value of the activation energy for the mobility in KBr is 1.2 ev., while the corresponding observed value is 0.7 ev.

§ 1. Introduction

When a crystal of an alkali halide is heated in the gas of its constituent halogen gas, an absorption band appears in ultraviolet region after Pohl.[1] The same band was observed by Alexander and Scheneider[2] when the crystal was irradiated with X-ray. Casler, Pringsheim, and Yuster[3] found also with X-ray irradiation three characteristic absorption bands in ultraviolet region and named them as V_1, V_2, and V_3 bands, the origin of the name of V being due to Molnar, and V_3 corresponding to that observed by Pohl and Alexander and Schneider. Subsequent works by Dorendorf[4] and by Delbecq, Pringsheim, and Yuster[5] revealed interesting features of these and related bands.

The V_3 center was identified by Seitz[6] as being a complex center consisting of two positive vacancies and a neutral halogen molecule, the V_2 center as a pair of positive vacancies trapping a positive electron hole, and the V_1 center as a positive vacancy trapping a positive electron hole. Before that, Pohl identified V_3 as a complex such as KI_3. The present writer put forward the same interpretation of the V_3 center as that of Seitz about at the same time and almost from the same ground, but his paper was written in Japanese in a periodical panphlet Busseiron Kenkyu, March issue of 1950, and could be known only to Japanese workers. However, since this paper deals with the nature of the V_3 center more in detail than Seitz did, the writer feels it worth while to reproduce its essential features, with slight modifications in its numerical computations.

§ 2. The Formation of V_3 Centers by X-ray Irradiation

The strongest reasons for the interpretation of the nature of the V_3 center as a complex center described above may be described as follows.

1. The concentration of the V_3 centers produced at equilibrium with the halogen gas is given according to Pohl as

$$n = \text{const.}\, p \exp(-W/kT), \qquad (1)$$

where p is the pressure of the gas. By mass action law, this means that a V_3 center contains two atoms of the halogen. The neutrality of the center requires that it further contains two vacancies of the positive ions. The electrostatically most stable arrangement of these constituents would be such that they form a square on lattice sites, each kind of the constituents lying diagonally. Then it is highly conceivable that the two halogen atoms combine to a molecule, the square becoming distorted.

2. The jamping frequency of the positive vacancy in the crystal of KCl is of the order of 1 sec^{-1} at room temperature. A positive vacancy trapping a positive electron hole produced by X-ray irradiation will thus diffuse through the crystal and combine with another positive vacancy trapping a positive electron hole to form a V_3 center within a relatively short time. This time can be estimated as follows, and is of the order of the time of X-ray irradiation.

The time t required for a vacancy to traverse a distance r is connected with its diffusion constant D by $t=r^2/4D$. Taking r as the nearest interionic distance d, the time $\tau=d^2/4D$ is the jamping period of the vacancy. If n is the number of the vacancies in unit volume, the mean distance between them is $r=n^{-1/3}$, and the time required to traverse this distance is $t=1/4Dn^{2/3}$, or $t=\tau/d^2n^{2/3}$. Assuming $n=10^{18}$ per cc and $\tau=1$ sec, we have $t=10^3$ sec, or a fraction of an hour. Now there are $4\pi r^2/2d^2=6\times10^3$ positive ions and about 6 positive vacancies on the surface of the sphere of radius $r=n^{-1/3}=10^{-6}$ cm, so that the fraction of the positive vacancies on this surface is 10^{-3}. Around each positive vacancy there are 12 sites available for another positive vacancy to form together a V_3 center. The time required for the formation of a V_3 center from two V_1 centers is therefore $10^3\times10^2=10^5$ sec $=3$ hours, from a purely geometrical consideration. However, if we take into consideration the interaction between V_1 centers, which resemble something like rotating dipoles, this time would be shortened, and we might expect the V_3 centers to be formed during exposure to X-ray.

The reaction $V_1\rightarrow V_2\rightarrow V_3$ can also be conceivable.

Alexander and Schneider observed a gradual increase in number of the V_3 centers after the X-ray irradiation was stopped. Since this increase took place for a few days, it is probable that some metastable centers different from V_3 were formed along with the latter during the exposure and converted to V_3 within a few days. As to these centers, an alternate arrangement of positive vacancies and neutral halogen atoms, each two in number, on a straight line might be suggested. Alternatively, we might expect some of the positive electron holes to have digged their own holes owing to their low mobility and to have become self-trapped for a few days.

The some explanation would be applicable to the bleaching of the V_3 centers by irradiation in V_3 band. In this case it was observed that the V_3 centers recovered after a few days.

§ 3. Energy of the Formation of a V_3 Center

This may be calculated by means of the following four stops:

1. Form two positive vacancies and two negative vacancies separately in the crystal. The work necessary for this is, according to Mott and Littleton⁷⁾, $0.96\times4=3.84$ ev. for KBr and $1.04\times4=4.16$ ev. for KCl

2. Dissociate a halogen molecule in the gas and put the resulting two halogen atoms into the negative vacancies in the crystal. The work nescessary may be assumed as equal to the dissociation energy alone (1.96 ev. for Br_2, 1.53 ev. for I_2, and 2.47 ev. for Cl_2).

3. Form in the crystal a square-formed quadrupole from two positive vacancies and two halogen stoms, which are effectively negative and positive charges, respectively. Approximating the crystal as a continuous dielectric medium, the energy liberated is

$$\frac{1}{\varepsilon}\left(\frac{4e^2}{d}-\frac{2e^2}{\sqrt{2}\,d}\right)=\frac{2.6e^2}{\varepsilon d},$$

where ε is the dielectric constant. For KBr, $\varepsilon=4.8$ and $d=3.3$ Å, and the energy is 2.4 ev., for KCl, $\varepsilon=4.7$ and $d=3.1$ Å, and the energy is 2.5 ev., and for KI, $\varepsilon=4.9$ and $d=3.5$ Å, and the energy is 2.1 ev.

4. Combine two halogen atoms of the quadrupole into a molecule. The energy liberated may be assumed as equal to the dissociation energy of a free molecule. Then it cancels the work done in 2.

The total work necessary to form a V_3 center from a molecule in the gas is therefore

$3.84-2.4=1.4$ ev. for KBr,
$4.16-2.5=1.7$ ev. for KCl.

The corresponding value for KI is expected as about 1.2 ev. These values correspond to the quantity W in Eq. (1) and are not much different from the measured values 1.2 ev. for KBr and 0.8 ev. for KI, according to Pohl.

§ 4. The Migration of V_3 Centers

At high temperatures the V_3 centers are observed to move under the influence of an electric field. This is due to the release of the positive electron holes from the V_3 centers by thermal agitation and the subsequent formation of other V_3 centers at other places. The mobility of the V_3 centers is therefore equal to the mobility of the positive holes multiplied by the degree of dissociation of the V_3 centers. According to Pohl, the mobility of the V_3 centers, μ, is related with their concentration, n, through the equation

$$\mu = \text{const. } n^{-1/2} \exp(-w/kT). \qquad (2)$$

Observed value for w is 0.7 ev. for KBr and 0.8 ev. for KI.

We can derive (2) as follows. Let the concentrations of the liberated positive electron holes, the separately existing positive vacancies, and the V_3 centers be n_h, n_v, and n, respectively. By mass action law, these are related with each other by the equation of the form

$$n_h^2 n_v^2 = \text{const. } n \exp(-E/kT), \qquad (3)$$

where E is the energy required to decompose a V_3 center into two positive electron holes and two separate positive vacancies. It is equal to the sum of the energies considered in points 3 and 4 of the preceding section. Thus, according to our calculation,

$$E = 1.96 + 2.4 = 4.4 \text{ ev. for KBr,}$$
$$E = 1.53 + 2.1 = 3.6 \text{ ev. for KI.}$$

Since the number of positive vacancies at high temperatures is practically the same as the number of Schottky defects, it is given as

$$n_v = \text{const. } \exp(-W_0/2kT), \qquad (4)$$

where W_0 is the work necessary to produce a pair of positive and negative vacancies separately. As cited before, Mott and Littleton obtained for it a value of $0.96 \times 2 = 1.92$ ev. for KBr. The value for KI may probably be a little lower. Form (3) and (4), we obtain

$$n_h = \text{const. } n^{1/2} \exp(-(E - W_0)/2kT). \qquad (5)$$

To obtain the degree of dissociation of the V_3 centers, we must divide (5) by n. In this way we arrive at (2), neglecting the dependency of the mobility of the positive holes on temperature.

Thus we have

$$w = \frac{1}{2}\left(E - W_0\right) \qquad (6)$$

In the case of KBr, we calculated to $E = 4.4$ ev. and $W_0 = 1.92$ ev., so that $w = 1.2$ ev. Nearly the same value can be expected for KI. The observed values, 0.7 and 0.8 ev., repectively, are a little lower. The discrepancy may partly be due to the neglection of a temperature dependent factor before the exponential in (2). It can be shown at the same time that complete agreement between computed and observed values for W and w cannot be attained by merely modifying the numerical values of the energies given in the four points of the preceding section.

References

1) R. W. Pohl: Proc. Phys. Soc. **49** (1937) 3.

2) J. Alexander and E. E. Schneider: Nature **164** (1949) 653.

3) R. Casler, P. Pringsheim, and P. Yuster: J. Chem. Phys. **18** (1950) 887.

4) H. Dorendorf: Z. Phys. **129** (1951) 317.

5) C. J. Delbecq, P. Pringsheim, and P. Yuster: J. Chem. Phys. **19** (1951) 574.

6) F. Seitz: Phys. Rev. **79** (1950) 529.

7) N. F. Mott and R. W. Gurney, *Electronic Processes in Ionic Crystals*, Oxford, 1940, p. 61.

JOURNAL OF THE PHYSICAL SOCIETY OF JAPAN Vol. 7, No. 4 JULY—AUG., 1952

On the Dielectric Constant of Rochelle Salt at 3000 mc/sec

By Humio AKAO, *Tatsuo TAKAKURA and Taizô SASAKI

*Osaka University and *Osaka City University*

(Received December 21, 1951)

The dielectric constant of Rochelle Salt was measured at 3000 mc/s. using a new method in which the dielectric constant is obtained by measuring Q of a rectangular H_{101} mode cavity, one E-plane of which is closed by Rochelle Salt surface.

The dielectric constant at this frequency is smaller than that at lower frequencies, though it shows two peaks at the Curie points.

§ 1. Introduction

The variation of the dielectric constant of rochelle salt near the Curie-points was measured at 3000mc/s by a new method using a cavity, and this was compared with the dielectric constant at other lower frequencies.

The dielectric constant at microwave frequency is usually measured by the methods, which are being published elsewhere*1. But if the dielectric constant and the absorption factor are large, the reflection coefficient at the surface of dielectric material should be almost −1 and small error in the measurement causes large error in the result.

In this method, large dielectric constant is determined by Q measurement of a cavity. It has been ascertained that the dielectric constant at this frequency is small compared with it at other lower frequencies, though it shows two peaks at the Curie-points.

§ 2. The Method of Measurement

The complex dielectric constant ε of the material in a wave-guide is given by the well known equation,

$$\varepsilon=\varepsilon_0\frac{(1/\lambda_c)^2-(\gamma/2\pi)^2}{(1/\lambda_c)^2-(\gamma_g/2\pi)^2}\equiv\varepsilon'-j\varepsilon'' \qquad (1)$$

$$\tan\delta=\varepsilon''/\varepsilon'$$

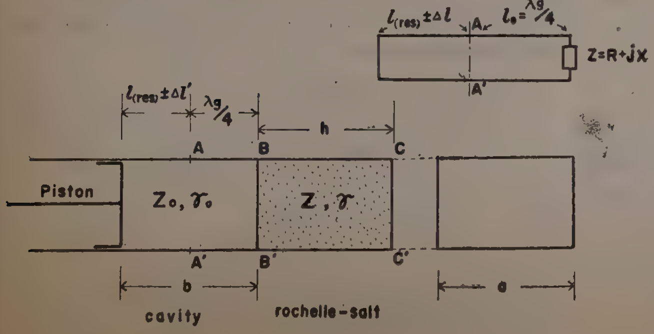

Fig. 1.

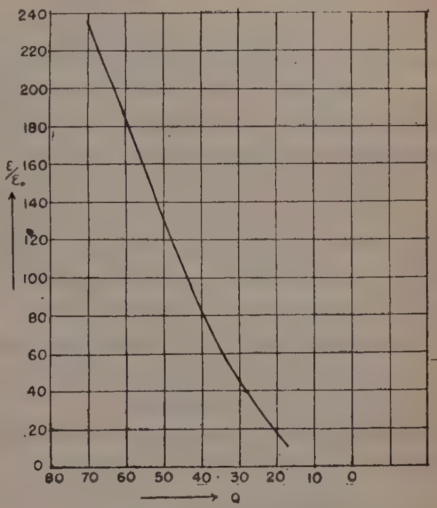

f_0=3000mc/s., a=7.0cm.
Fig. 2.

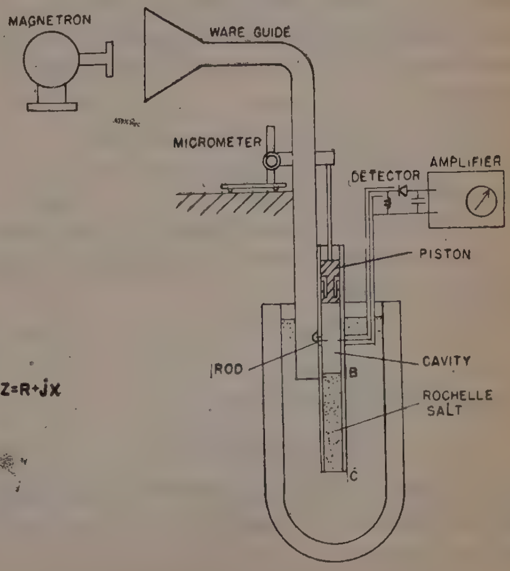

Fig. 3.

---

*1 (e. g.) S. Robert, von Hippel: J.A.P. July 1946.

where λ_c is the cut-off wave length of the H_{01} wave in the wave-guide, γ_g, γ are the propagation constants of the H_{01} wave in the air and in the dielectric material, respectively, and

$$\left.\begin{aligned}\gamma_g&=j\beta_g+\alpha_g\\ \gamma&=j\beta+\alpha\end{aligned}\right\} \qquad (2)$$

The propagation constant and the characteristic impedance in the wave guide have the following well known relationship each other.

$$\gamma/\gamma_g=Z_g/Z \qquad (3)$$

where Z_g and Z are the characteristic impedance of the wave guide in the air and in the dielectric material, respectively. As shown in Fig. 1 and Fig. 3, the wall opposite to the piston of a cavity is closed by the dielectric material filled in a wave guide, and its length h is so long that the wave which once comes into this dielectric material, will be absorbed perfectly in this medium. The cavity is excited by a probe at A and the voltage in this cavity is measured by a probe at A′.

The resonance curve is plotted by moving the piston of the cavity and the half power points $l=l_{(res)}\pm\Delta l$ is measured.

The admittance at the plane A—A′ may be given by

$$\dot{Y}\doteq\frac{1}{Z_g}\,\frac{jZ\tan\beta l_0+Z_g}{Z+jZ_g\tan\beta l_0}-j\frac{1}{Z_g\tan\beta l} \qquad (4)$$

where l_0, l indicate the distances from A—A′ plane to the dielectric material and the piston, respectively. When l_0 is $\lambda_g/4$*[2], equation (4) becomes

$$\begin{aligned}\dot{Y}&\doteq\frac{Z}{Z_g^2}-j\frac{1}{Z_g\tan\beta_g l}\quad(Z=R+jX)\\ &\doteq\frac{R}{Z_g^2}+j\left(\frac{X}{Z_g^2}-\frac{1}{Z_g\tan\beta_g l}\right).\end{aligned} \qquad (5)$$

The admittance should be minimum at the resonance. Hence,

$$Y_{(res)}\doteq R/Z_g^2 \qquad (6)$$

when $\quad \tan\beta_g l_{(res)}\doteq Z_g/X$.

At the half power points,

$$|\dot{Y}_{(l)}|=\sqrt{2}\,|\dot{Y}_{(res)}| \qquad (7)$$

This equation may be obtained when the length l satisfies in equation (5) the following condition

$$\left.\begin{aligned}R/Z_g^2&=\left|X/Z_g^2-\frac{1}{Z_g\tan\beta_g l}\right|\\ l&=l_{(res)}\pm\Delta l\end{aligned}\right\} \qquad (8)$$

which reduces to

$$\tan 2\pi\frac{l}{\lambda_g}=\frac{Z_g}{(X\mp R)} \qquad (9)$$

The imaginary component X of Z can be determined from equation (6), when the length $l_{(res)}$ will be measured. Therefore, the real component R can be determined from equation (9) when the half power points $l=l_{(res)}\pm\Delta l$ is measured, and the dielectric constant ε can be calculated from equations (3) and (1).

If we assume, however, the real part α in equation (2) is negligible compared with β (i.e. $\varepsilon'\gg\varepsilon''$), we may use the following approximation,

$$\begin{aligned}\gamma_g&\simeq j\beta_g=j\frac{2\pi}{\lambda_g}\\ \gamma&\simeq j\beta\,.\end{aligned} \qquad (2')$$

Hence the impedance Z is represented by pure real. In this case, equations (4) to (9) become

$$Y=Z/Z_g^2-j\frac{1}{Z_g\tan\beta_g l}\,. \qquad (5')$$

At the resonance,

$$Y_{(res)}=Z/Z_g^2 \qquad (6')$$

when $\quad l_{(res)}=\lambda_g/4\,.$

At the half power points,

$$\left.\begin{aligned}Z/Z_g^2&=\left|\frac{1}{Z_g\tan\beta l}\right|\\ l&=\lambda_g/4\pm\Delta l\end{aligned}\right\} \qquad (8')$$

which reduces to

$$\tan\frac{\pi}{2}\left(1\pm\frac{4\Delta l}{\lambda_g}\right)=\mp Z_g/Z\,. \qquad (9')$$

When the half power points are expressed by Q of the cavity, the following expression is convenient.

The resonance frequency of the rectangular cavity shown in Fig. 1 and Fig. 3 is given by

$$f=\frac{\sqrt{(1/a)^2+(1/b)^2}}{2}\cdot c \qquad (10)$$

where c is the light velocity in free space. At the resonance, $b=\lambda_g/2\equiv b_0$ $f=f_0$, so at the half power points

$$\begin{aligned}f&=\frac{\sqrt{(1/a)^2+(1/b_0\pm\Delta l)^2}}{2}\cdot c\\ &\simeq\frac{\sqrt{(1/a)^2+(1/b_0)^2(1\mp2\Delta l/b_0)}}{2}\cdot c\\ &=f_0\left\{1\mp\frac{\Delta l/b_0^3}{(1/a)^2+(1/b_0)^2}\right\}\end{aligned} \qquad (11)$$

---

*[2] $l_0=\lambda_g/4$ has been chosen for simplicity, but numerical calculations show that the half power points $\pm\Delta l$ and resonance length $l_0+l_{(res)}$ are identical even if A and A' are arbitrary points.

Hence,

$$Q=\frac{(1/a)^2+(1/b_0)^2}{2\Delta l/b_0^3}=\frac{1+(b_0/a)^2}{4\Delta l/\lambda_g} \qquad (12)$$

Substituting this in equation (9′) we have

$$\tan\frac{\pi}{2}\left(1\pm\frac{1+(b_0/a)^2}{Q}\right)=Z_g/Z\ . \qquad (13)$$

Therefore, when Δl or Q is measured, the dielectric constant ε' may be calculated from equations (1), (3) and (9′) or (13).

For example, when $\lambda_g=\lambda_c=14$cm and $\varepsilon/\varepsilon_0=50$, Q becomes 32 and when $\varepsilon/\varepsilon_0=100$, Q becomes 43. (refer to Fig. 2).

§ 3. Apparatus

The experimental arrangement is shown in Fig. 3. A cavity was excited by a probe projecting from a wave guide, and Q of the cavity, one E-plane of which is closed by the Rochelle Salt, was measured by moving a piston.

The part of this cavity, in which the Rochelle Salt was filled, was inserted in a thermos and its temperature was varied gradually from 40°C to −30°C.

Attention was paid to the close contact of surfaces of the Rochelle Salt to the inside walls of the cavity, especially to H-planes. The length h of this medium was 5-8cm., and this was sufficient to make the reflection from the end surface C negligible.

§ 4. Experimental Results and Discussions

Fig. 4 shows the results of the experiment at 3000cm/s. on Rochelle Salt, obtained using the apparatus in Fig. 3.

As shown in this figure, the character of temperature dependency of ε_a at 3000mc/s. somewhat differs from that at a few mc/s, but the position of the peaks at two Curie points coincide.

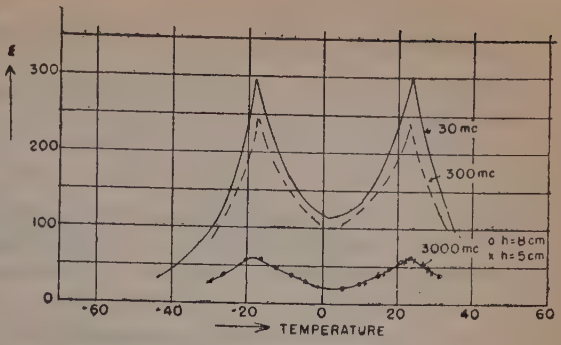

Fig. 4. ε : T.

When we compare the data at 3000mc/s. with those at a few mc/s, the dispersion of ε_a is found except at high or very low temperature.

These results show that the relaxation phenomenon in the ferroelectric region is observed at decimeter wave region (Fig. 4). However, in order to discuss the relaxation phenomenon we must study further.

By the way, ε of the water measured using this method was about 65. (at 10°C) This value is somewhat smaller than the recognized value. (ε=80).

To explain this difference, the following reason is suggested. As the surface of the water in the wave guide has a curvature by surface tension, the electro-magnetic wave may get more easily into the water.

Writers wish to express their thanks to prof. K. Okabe for his encouragement.

The expense of this research has been defrayed from the Scientific Research Expenditure of the Educational Ministry.

JOURNAL OF THE PHYSICAL SOCIETY OF JAPAN Vol. 7, No. 4 JULY—AUG., 1952

Internal Friction of Field-Cooled Ferromagnetic Substance*

By Tokutaro HIRONE and Nobuhiko KUNITOMI

Research Institute for Iron, Steel and Other Metals, Tohoku University, Sendai, Japan

(Read November 3, 1950. Received August 1, 1950)

Internal friction of ferromagnetic substance cooled in longitudinal magnetic field is studied both theoretically and experimentally. Two theories are developed on the basis of two different ideas on the elementary magnetizing process. The first theory which assumes that the substance is magnetized by the displacement of 180°-domain boundary leads to the conclusion that internal friction at the demagnetized state must vanish by field-cooling. The second theory assuming that the substance is magnetized by the reversible and irrevarsible rotation of spontaneous magnetization concludes that internal friction at the demangnetized state must increase appreciably by field-cooling in contrast to the former case. On the other hand, experimental investigation of both field-cooled and commonly annealed substances is carried out for Ni_3Fe. Comparing the experimental and two different theoretical results, the latter theory is known to be more convenient to explain the measured data than the former theory. The magnetic domain structure of field-cooled substance is so concluded from this investigation that the spontaneous magnetization in the substance is fixed to the direction closer to the applied magnetic field than in usually treated substance, and that the magnetizing process is still rotation of spontaneous magnetization from the newly fixed direction.

§1. Introduction

It is known that some of the ferromagnetic substances change their magnetic properties remarkably by the proper heat-treatment in magnetic field, that is, so-called magnetic "field-cooling". The increase of maximum permeability and the almost rectangular hysteresis loop are observed in substances thus treated¹⁾. This effect can be explained by the fact that the spontaneous magnetization in the substance is fixed to the direction of the applied magnetic field by the field-cooling. The magnetization in this case has been supposed to be carried out by the displacements of 180° magnetic domain boundaries. In the case of Ni_3Fe, however, magnetic anisotropy energy is so small²⁾ that the existence of domain boundary can be hardly realized except in the special case when the internal stresses are carefully removed. Therefore, the elementary magnetizing process is considered to be the reversible and the irreversible rotation of the spontaneous magnetization. In this research, the behavior of internal friction is studied theoretically at first for both mechanisms and then the internal friction of Ni_3Fe is measured for both field-cooled and commonly annealed specimens. It is also investigated whether the mechanism of the boundary displacement or that of the rotation of the spontaneous magnetization is more favorable for the explanation of the experimentally obtained data. The magnetizing mechanism of the field-cooled substance can supposedly be concluded from this result.

§2. Internal Friction due to the Displacement of 180° Magnetic Domain Boundary

The internal friction of ferromagnetics is extremely larger than that of the other substances. Such a high value is attributable to the characteristic energy loss by ferromagnetic origin in addition to the plastic or thermoelastic energy losses. The characteristic loss is classified into three ones according to their origins, namely, the losses due to macro- and micro-scopic eddy current and to magnetomechanical hystereis. Among these, the loss due to magnetomechanical hysteresis is proportional to the applied stress amplitude and is negligible if the above amplitude is sufficiently small. Macroscopic eddy current loss does not directly depend on the magnetizing mechanism and has been quantitatively studied by Brown[3]. Hence, we do not concern in these two losses any further. In this section, therefore, the loss due to microscopic eddy current originating from the displacement of domain boundary will be calculated theoretically. According to the idea of Becker and Döring[4], the 180° domain boundary does not displace by the applied external stress. Taking the surface energy of domain boundary into account, however, one of the present writers previously proposed[5] that the boundary moves by applying external stress. Based on this idea, the behavior of the domain boundary will be discussed below.

---

* The report of the Research Institute for Iron, Steel and Other Metals, Tohoku University. This research was supported in part by Grant in Aid for Fundamental Scientific Research by the Ministry of Education. Main part of numerical calculation in this research was performed by Miss T. Ogura.

Let the surface energy of 180° boundary per unit area be denoted by Γ, then the boundary must exist on the position where Γ is minimum, if no external field is applied. For simplicity, we confine our consideration only to the one dimensional mobel. Any essential discrepancy of the theoretical results from the practical case is not introduced by this simplification. Then, the surface energy in the specimen can be represented only by a single variable x. It is also assumed that the external magnetic field and alternating stress are applied along this direction. If the external field is not applied, the position of the boundary is given by the solution x_1 of the equation[6]

$$d\Gamma/dx=0\,. \tag{1}$$

But if a small field is applied, the position of the boundary is given by the solution x_2 of

$$d\gamma/dx=2HJ_s\,, \tag{2}$$

where H is the strength of the applied field and J_s the spontaneous magnetization. If H is sufficiently small, the displacement of the boundary $s=x_2-x_1$ by the applied field can be regarded as small, and therefore the equation $d\Gamma/dx=(d^2\Gamma/dx^2)_{x_1}\cdot(x_2-x_1)$ is valid. Hence s is given by

$$s=2J_sH/(d^2\Gamma/dx^2)_{x_1} \tag{3}$$

According to Bloch's theory[7], on the other hand, surface energy is expressed by

$$\Gamma=2a\sqrt{IC} \tag{4}$$

where a is lattice constant of the substance, I the exchange integral due to the transposition of electrons in the metallic lattice and C the stress energy given by three-seconds of the product of magnetostriction constant λ and the strength of the stress σ. In one dimensional model, stress σ may be considered as the simple sum of the internal stress σ_i and external stress Z. Therefore, Γ is represented by

$$\Gamma=\beta\sqrt{\sigma_i+Z}\,,\ \text{where}\ \beta=\sqrt{ba^2IC}\,. \tag{5}$$

By differentiating Eq. (5) with respect to x and assuming Z is very small compared with σ_i the following formulae is obtained.

$$(d^2\Gamma/dx^2)^{-1}=(d^2\Gamma/dx^2)^{-1}_{Z=0}+X'(Z/\sigma_i) \tag{6}$$

where

$$X'=X/(d^2\Gamma/dx^2)^2_{Z=0}\,. \tag{7}$$

By using Eqs. (3) and (7), the displacement s', when magnetic field and stress are simultaneously applied, is given by

$$s'=2\{(d^2\Gamma/dx^2)^{-1}_{Z=0}+X'(Z/\sigma_i)\}J_sH\,. \tag{8}$$

In this equation, the contribution of the applied stress to the boundary displacement s_z' is known to be

$$s_z'=2X'(Z/\sigma_i)J_sH\,. \tag{9}$$

In our case of mechanical vibration, the external stress is expressed by $Z\cos\omega t$. Hence the displacement velocity of the boundary is given by

$$v=-2X'J_sH\omega\sin\omega t(Z/\sigma_i)\,. \tag{10}$$

The amount of the dissipated energy by the eddy current caused by the displacement of the 180° domain boundary, δW, is given by integrating $4kJ_sv^2$ over the total area of the boundary, namely

$$\delta W=4kJ_s\int v^2df\,, \tag{11}$$

where k is a frictional constant and df is the surface element of the boundary. Since the coefficient of internal friction Δ is the ratio of δW and twice vibrational energy, it is given by

$$\Delta=8kJ_s^2H^2\omega E\int(X'/\sigma_i)df\,, \tag{12}$$

where E is Young's modulus of the substance. It is known from the Eq. (12) that internal friction Δ vanishes at $H=0$, and increases proportionally to H^2. The loss due to macroscopic eddy current, on the other hand, vanishes when $H=0$, so the total loss also vanishes for the substance magnetized by 180° boundary displacement only.

In order to determine the numerical coefficient, we assume that the internal stress in the integral sign of Eq. (12) is expressed by a sinusoidal stress modulating on a constant one, and assign the appropriate numerical values for the constants appearing in Eq. (12). But the accurate numerical values representing internal stress assumed above cannot be determined experimentally, so the value for the coefficient of internal friction thus obtained can be only ambiguously given by

$$\Delta=10^{-4}H^2\sim10^{-6}H^2\ . \qquad (13)$$

It is concluded from this equation that Δ does not increase so rapidly with the magnetic field.

§ 3. Internal Friction Due to the Rotation of the Spontaneous Magnetization

Next, the influence of the rotation of the spontaneous magnetization is to be considered as pointed out in the section 1. In the field-cooled substance, however, the directional distribution of spontaneous magnetization is assumed to be non-uniform in contrast to the case of commonly annealed substance. The complete calculation of the internal friction which is exclusively due to the rotation of the spontaneous magnetization was carried out in the previous report[8] for the case where distribution of the spontaneous magnetization is isotropic. In the present case of anisotropic distribution, the method of calculation is similar to the previous case, so the detailed description will be omitted here.

As reported in the previous paper, the dissipated energy during the mechanical vibration δW is given by the average of the eddy current loss. In order to compute the directional average, it must be remembered that the direction of the spontaneous magnetization is constrained in a small angular spread in the field-cooled substance. Let the angle between the direction of the external field and that of the spontaneous magnetization be γ, the directional average must be taken over constrained range of γ. For simplicity, it is assumed that γ changes from ϕ to $-\phi$ and from $2\pi-\phi$ to $2\pi+\phi$ with equal density. In order to decide the value of ϕ, the experimental data of magnetostriction were used. Since the experimentally obtained values of saturation magnetostriction is 0.71×10^{-6} for field-cooled specimen and 2.06×10^{-6} for the commonly annealed one, the value $\phi=30°$ is chosen for the numerical calculation.

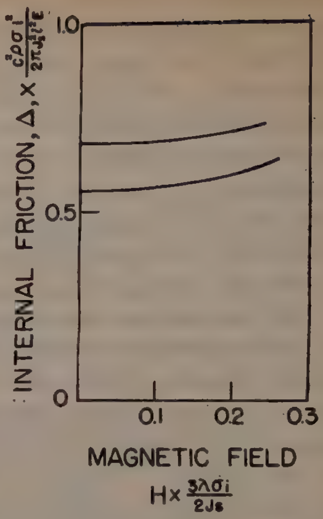

Fig. 1. The theoretical relations of internal friction versus Magnetic field: Curve (1) upper curve shows the case of field cooled substance while (2) lower curve usual one. The unit of abscissa is the ratio of energy of magnetic field and that of internal stress.

The calculated data for the weak magnetization is shown in Fig. 1. This figure indicates that internal friction at $H=0$ increases by the field-cooling.

§ 4. Results and Discussion

Next, the experimental results of internal friction for the field-cooled and usually treated Ni_3Fe will be described and compared with above theoretical results. The measuring method is similar to that developed by Förster and Köster[9] using transversal vibration. The specimen material used is Ni_3Fe. The specimen is the same as that in the previous paper[10], where the dependences of internal friction upon the magnetization and upon the degree of super-lattice formation were investigated.

After the annealing at 600°C for 2 hours, the specimen was cooled by the rate of 2°C per minute down to room temperature. The internal friction and magnetostriction were measured after this heat-treatment, and the results are shown by the curve (1) in Figs. 2 and 3. Thereafter, the specimen was annealed again at 600°C for 2 hrs and cooled to room temperature with the same cooling rate as before in the longitudinal magnetic field of about 100 Oersted. The results are shown by the curve (2) in Figs. 2 and 3. Comparing the curves (1) and (2) in Fig. 2, it is found that internal friction of field cooled substance is larger at $J=0$ than that annealed without field and that internal friction of the field cooled one shows a maximum in the earlier stage of magnetization. On the other hand, the theoretical internal friction at $J=0$ vanishes when only the displacement of the 180° domain boundary are considered, while it increases about 22% by field cooling if the rotation of the spontaneous magnetization is taking into account as described in section 2. The experimental data which increase about 41% at $J=0$ indicate that the latter theory agrees with experiment semiquantitatively while the former does not even qualitatively. Then we may conclude that the elementary magnetizing process of field-cooled substance is the rotation of the spontaneous magnetization. By using this theory, the experimental fact that curves (1) and (2) in Fig. 2 coincide beyond a critical magnetic field can be explained as follows: Below the critical magnetic field, the distributing direction of the spontaneous magnetization is strikingly different for field-cooled and usually treated substances. But in the stronger magnetic field the spontaneous magnetization in the usually treated substance, appreciably rotates to the closer direction of applied field, so the difference of both cases vanishes. It results the coincidence of two experimental curves at higher magnetic field. However, it cannot be explained that two maximums are appeared in the field-cooled specimen, Then in order to prove the reproducibility of the experiment, internal friction was measured by the specimen cooled at the rate of 1°C per minutes from 600°C to room temperature in the longitudinal field. As is seen in the curve (3) in Fig. 2, the behavior of this curve does not deviate so much from curve (2).

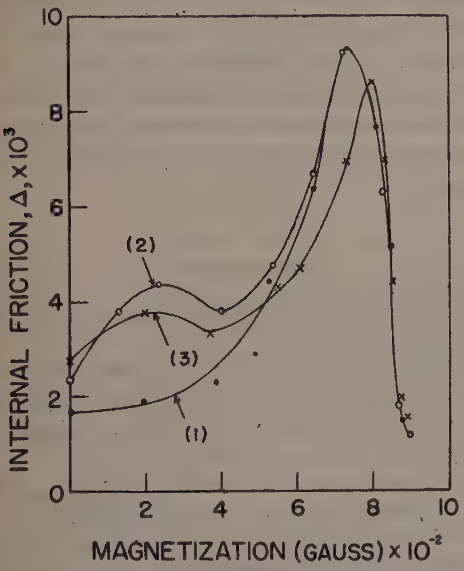

Fig. 2. The experimental relations of internal friction versus magnetization: Curve (2) shows the case cooled in the magnetic field at the rate of 2°C per minute while (3) 1°C per minute, and Curve (1) shows the usually treated case.

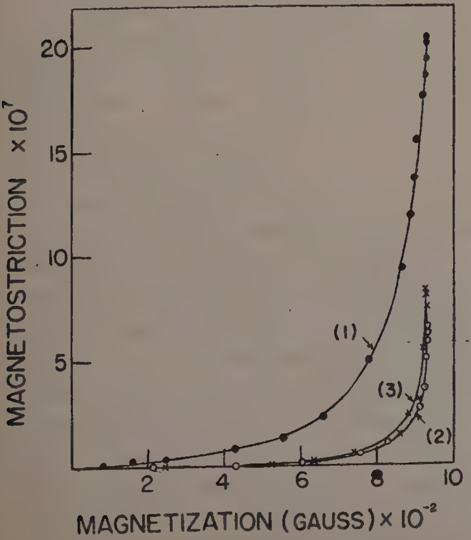

Fig. 3. Experimental relations between magnetostriction versus magnetization. The numbers characterizing the curves correspond to the same annealing procedures as in Fig. 2.

The results of magnetostriction are shown in Fig. 3. The values of saturation magnetostriction for these three annealing methods are 2.06×10^{-6}, 0.71×10^{-6}, 0.82×10^{-6} respectively.

From the experimental and theoretical investigations on the internal friction, the magnetizing mechanism of field-cooled Ni_3Fe

is concluded to be rotation of spontaneous magnetization.

Lastly the theoretical magnetization curve of field-cooled substance is studied according to the mechanism that the spontaneous magnetization rotates reversibly and irreversibly. It is to be remarked here that the experimentally obtained behavior of magnetization curve can be derived from the theoretical calculation. The magnetization J is given by

$$J=J_s\int_{-\phi}^{\phi}\cos\theta\sin\gamma d\gamma\Big/\int_{-\phi}^{+\phi}\sin\gamma d\gamma\,. \qquad (14)$$

The integration is performed over the region from −30° to +30° and from +150° to −150°, The result of calculation is shown in Fig. 4 by curve (1).

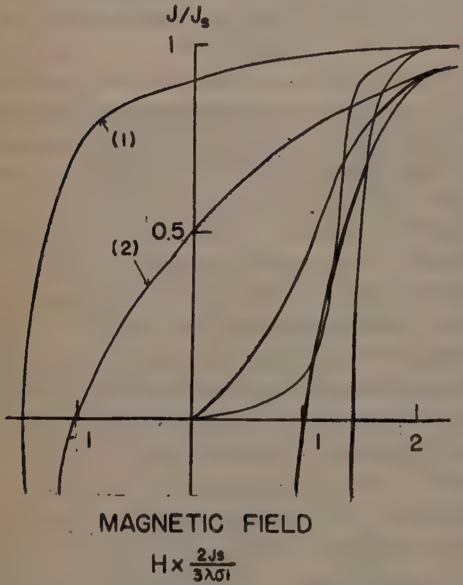

Fig. 4. The theoretical magnetizing curve: Curve (1) shows the case of field cooled substance while (2) that of usually annealed one.

For convenience of comparison, the theoretical curve for the isotropic specimen is shown by the curve (2) in the figure. In the case of field-cooled substance the initial susceptibility rather decreases but hysteresis loop takes a rectangular form and coercive force which is influenced by the internal stress is almost constant for both cases. Since the direction of the magnetostrictive internal stress concentrates to the direction of axis in the field-cooled substance, Therefore, the coercive force becomes smaller and initial permeability becomes larger than the curve shown in the figure.

References

1) J. F. Dillinger and R. M. Bozorth: Physics **6** (1935) 275.

2) E. M. Grabbe: Phys. Rev. **57** (1940) 728.

3) W. F. Brown Jr: Phys. Rev. **50** (1936) 1165.

4) R. Becker and W. Döring: Ferromagnetismus (1939) Berlin, p. 209.

5) R. Becker and W. Doring: loc. cit., p. 357.

6) F., Bloch: Z. Phys. **74** (1932) 295.

7) N. Kunitomi: J. Phys. Soc. Jap. will be published in near future.

8) F. Föster and W. Köster: Z. Metallkde. **29** (1937) 109.

9) N. Kunitomi: J. Phys. Soc. Jap. will be published in near future.

JOURNAL OF THE PHYSICAL SOCIETY OF JAPAN Vol. 7, No. 4 JULY—AUG., 1952

On the Magnetic After Effect due to the Irreversible Displacement of the Domain Boundary (IV)*

By Seiziro MAEDA

The Research Institute for Iron, Steel and Other Metals Tohoku University

(Read, April 1951. Received September 8, 1951)

The magnetic after effect in 65-permalloy under various tensions was observed. In this case the reversal of magnetization occurs in several or a single Barkhausen jumps according to the amount of the applied tension. The value of dB/dH along the descending branch of the hysteresis curve has a very sharp maximum with comparatively narrow breadth. In the cases for small tension, magnetization in the course of after effect shows almost no change until the time t reaches a critical value t_c, and after t_c changes in the usual manner of the after effect. The value of t_0 decreases with decreasing final field. When the total reversal of magnetization occurs in a single Barkhausen jump, even a slight change in the magnetization can not be observed until t_c, and the whole reversal takes place in a very short time interval after t_0. These can be interpreted on the assumption that the after effect is closely related to the irreversible displacement of domain boundaries.

§ 1. Introduction

In the previous papers, the author reported the results of his measurement on the magnetic after effect for Cr-permalloy[1)] and C-Steel[2)]. In these papers he concluded that the observed characteristic properties of the after effect were well explained by assuming magnetic retardation due to the irreversible displacement of domain boundaries under an external magnetic field. It was assumed there, that the displacement velocity V of a domain boundary under a final magnetic field H_f is given by

$$V=a(H_f-H_0) \qquad (1)$$

where a is a constant, and H_0 is a critical field strength for the domain boundary under consideration. In an usual ferromagnetic substance, H_0 changes its value from place to place. However, if a tension is applied to a 65-permalloy wire, its reversal of magnetization occurs by a few or a single Barkhausen jumps, and the value of H_0 may be restricted to a very narrow range. In the case of a single Barkhausen jump, H_0 converges to a single value throughout the substance. In such a case special characteristic feature in magnetic after effect is expected from the cited theory. In the following pages the results of an observation on a stretched permalloy wire are described.

§ 2. Experimental Results and Discussion

The methods and arrangement used for the observation of the after effect were essentially the same as described in the author's previous paper.[1)] Specimens used were wires of 65-permalloy with the diameter of 0.2 mm and 0.5 mm, having the length of 100 cm. In order to eliminate mechanical strains the specimens were annealed at 800°C by flowing an alternating current through the specimen for 15 minutes. Their magnetic hysteresis curves are shown in Figs. 1 and 5. Fig. 1 shows the hysteresis curves of the specimen of 0.5 mm diameter under various values of applied tensions and the dB/dH curves calculated from the observed hysteresis curves. The discontinuous change of magnetization was not observed in the case of no tension and a tension of 10 kg/mm², while by further increase of applied tension a part of magnetic reversal becomes discontinuous. For example, under the tension of

---

* Report from the Research Institute for Iron Steel and Other Metals, Tōhoku Univ. This investigation was supported in part by the Grant-in-Aid of Fundamental Scientific Research of Ministry of Education for 1950. Item #D 43064 "On the Magnetic After Effect of the Iron Alloys." This investigation was carried out under the supervision of Dr. T. Hirone, Professor of Tōhoku University.

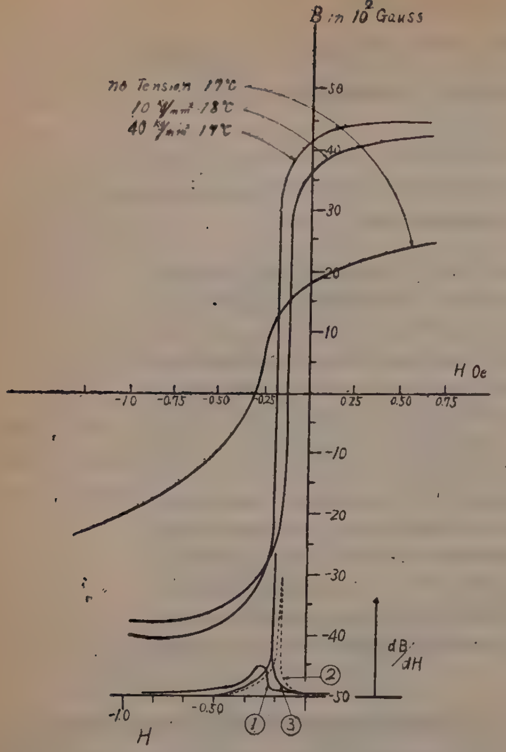

Fig. 1. The hysteresis curves and the curves of dB/dH under various tensions applied.

40 kg/mm² the magnetization changed discontinuously by 59% of the total strength of the saturation value. However, by further increasing of the tension, the magnetic reversal by a single Barkhausen jump can not be observed in this specimen, namely, a perfectly rectangular hysteresis loop was not obtained.

The magnetic after effect was measured along the descending branch of the hysteresis curve. The quantity to be measured is the total change of induction, $B_n(t)$, during the lapse of time from t second after the sudden change of magnetic field to ∞, due to the change of magnetic field from the saturation field H_s to various final field H_f.

Fig. 2 shows $B_n(t)$ *vs.* t curves in the case of the specimen of 0.5 mm diameter with no tension. As seen from it, for the comparatively large value of H_f, $B_n(t)$ shows a more slow change with t than that expected from the 1/t law described in the previous paper¹⁾, whereas rapid change was observed for the small values of H_f. These characters of $B_n(t)$ are quite analogous to that of C-Steel.²⁾

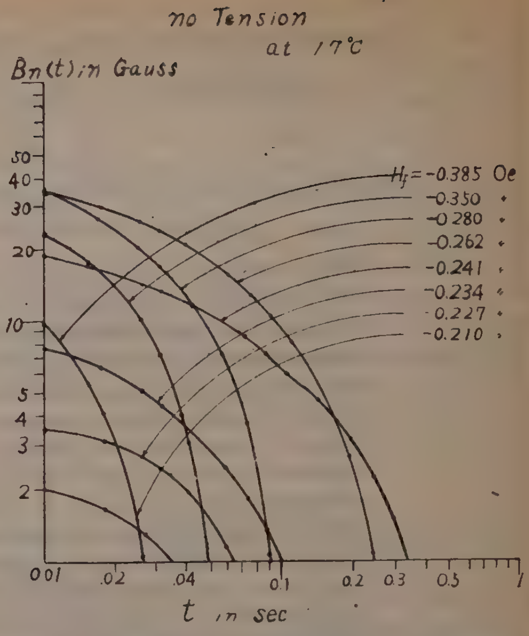

Fig. 2. Curves of $B_n(t)$ *vs.* t under no tension.

According to the formula for the after effect given there, $B_n(t)$ is

$$B_n(t)=kD/a\int_t^\infty \beta(H_{0m})1/t^2dt \qquad (2)$$

In this experession k and D are constants and $\beta(H_{0m})$ is defined as follows: If the total change of ΔB is due to the irreversible displacement of domain boundaries caused by the change of the external field $H_{0m} \rightarrow H_{0m}+\Delta H_f$, ΔB is given by $\Delta B=\beta(H_{0m})\Delta H_f$. Therefore, $B_n(t)$ takes various form according to the form $\beta(H_{0m})$. It was shown in the previous paper²⁾ that when the form of $\beta(H_{0m})$ is similar to that of curve 1 in Fig. 1, the characteristic curves of $B_n(t)$ shown in Fig. 2 were usually obtained.** In the case of the final field H_f(max) for which the after effect occurs most conspicuously, about one twelbth of the saturation induction, B_s, changes as the after effect during the lapse of time from 1/100 seconds after the instant of the field change to infinity.

Fig. 3 shows the curves of $(B_n t)$ of the same specimen under a tension of 10 kg/mm², the amount of after effect in this case exce-

---

** The actual form of $\beta(H_{0m})$ are considered to be sharper than that obtained by differentiating the observed hysteresis loop because the calculated form of dB/dH includes reversible process of magnetization in both sides of maximum value of $\beta(H_{0m})$.

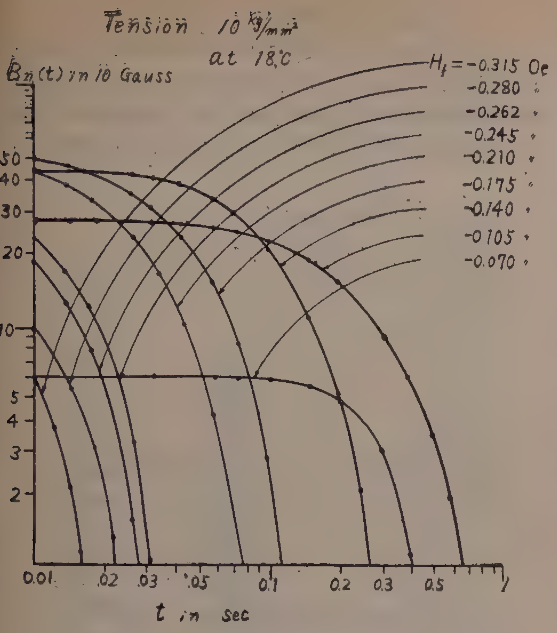

Fig. 3. Curves of $B_n(t)$ *vs.* t under tension of 10 kg/mm².

edingly increased, reaching about 12 times that in the case without tension, that is, about the same amount as B_s changes during the same period as that in the case without tension. For a specimen which has a negative magnetostriction constant the value of $\beta(H_{0m})$ decreases with increase of applied tension. Therefore, the influence of applied tension upon the amount of after effect is contrary to the present case, as mentioned in the previous papers[1)2)]. So far as the value of H_f is stronger than -0.175 *Oe*, almost no change in $B_n(t)$ was found until the time t reaches a critical value t_c, and then the induction changes rapidly to a final state. The value of t_c decreases and the amount of after effect increases with decreasing H_f. For the value of H_f smaller than -0.175 *Oe*, the value of t_c becomes less than 0.01 second and a knick of $B_n(t)$ at t_c becomes unobservable in our measurement and the characteristic curve of $B_n(t)$ shows only a smoothly decreasing one. These characters of $B_n(t)$ are expected from equation (2). It can be assumed from the curve of dB/dH in Fig. 1 that the form of $\beta(H_{0m})$ becomes more sharp with increasing tension, so the change of character of $B_n(t)$ in this case qualitatively can be explained satisfactorily in the same manner as described in the previous paper[2)].

Let $\beta(H_{0m})$ be a form as given below,

$$\beta(H_{0m})=0 \qquad \text{for } H_{0m}>H_{f0}(2)$$
$$= \text{finite value for } H_{0m}<H_{f0}(2)$$

where $H_{f0}(2)$ is a field strength at which the value of $\beta(H_{0m})$ increases discontinuously. Then according to the theory previously proposed, the critical time t_c is given by the equation

$$t_c=D/v=D/a[H_f-H_{f0}(2)] \qquad (3)$$

where D is a distance on which the domain boundary displaces with a velocity $V=a[H_f-H_{f0}(2)]$. The value of t_c in equation (3) decreases with increase of $[H_f-H_{f0}(2)]$ in a similar manner as that observed experimentally.

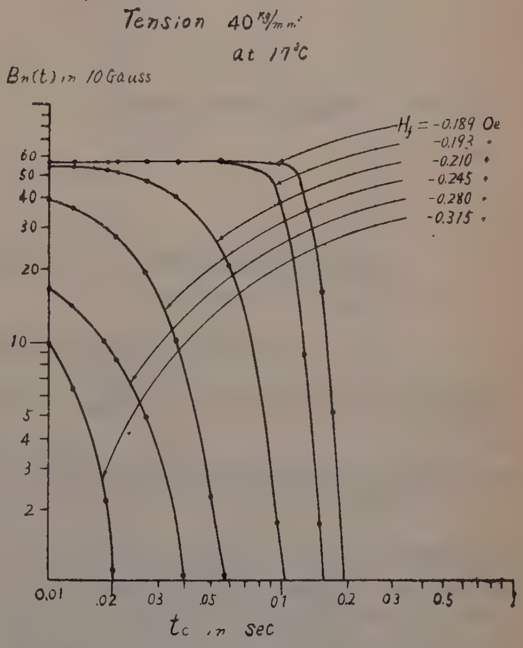

Fig. 4. Curves of $B_n(t)$ *vs.* t under tension of 40 kg/mm².

Fig. 4 shows the curves of $B_n(t)$ of the specimen under a tension of 40 kg/mm². In this case the amount of after effect further increases and t_c can be observed more clearly than in the case of tension of 10 kg/mm². This change of character of the after effect can be attributed to the sharp maximum in $\beta(H_{0m})$ according to the above Eqs. (2) and (3), since the peak in the curve of dB/dH becomes sharper than that of the former case (see Fig. 1 curve 3).

Now in order to obtain a perfectly rectangular form of the hysteresis curve, the specimen of 0.2 mm diameter was used. As shown in Fig. 5, its hysteresis curve under the tension of 25 kg/mm² takes a perfectly rectangular form, the reversal of magnetization occurring by a single Barkhausen jump. In Fig. 6 the characteristic properties of $B_n(t)$

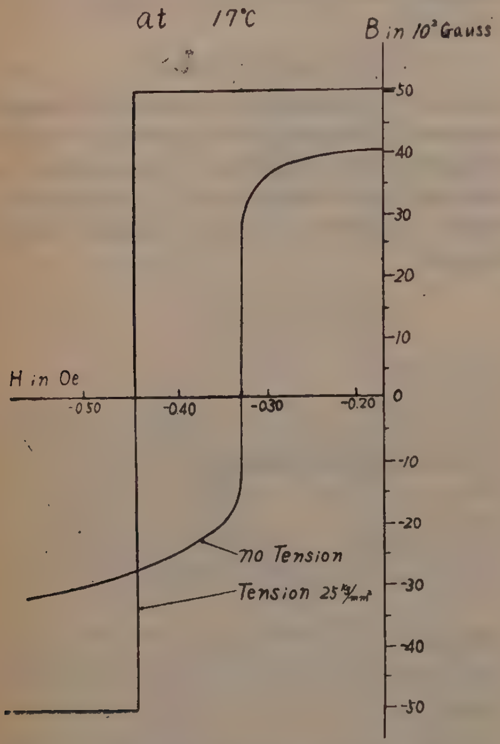

Fig. 5. The hysteresis curves under tensions applied.

in this case is shown. For the values of final field less than −0.4584 *Oe* the retarded reversal of total magnetization occurs discontinuously at an instant t_0. The time interval for changing the magnetization is negligibly small and is beyond our observation. The value of t_0 decreases with decreasing H_f and finally reaches a value less than 1/100 seconds. Since the time interval 1/100 seconds is the shortest limit of time lag which can be measured in our experiment, the lag time can not be observed for the value of H_f less than −0.4659 *Oe*. For the value of H_f larger than −0.4584 *Oe*, the after effect was not observed and hence this value of H_f is considered as the starting field strength in the large Barkhausen effect. Now in the case of a single Barkhausen jump, $\beta(H_{cm})$ is represented by

$$\beta(H_{0m}) = \sum \delta(H_{0m} - H_{0mB})$$

where δ denotes Dirac's δ-function and H_{0mB} is a field strength to which the values of H_{0m} of all domain boundaries are concentrated. By putting this form of $\beta(H_{cm})$ in Eq. (2),

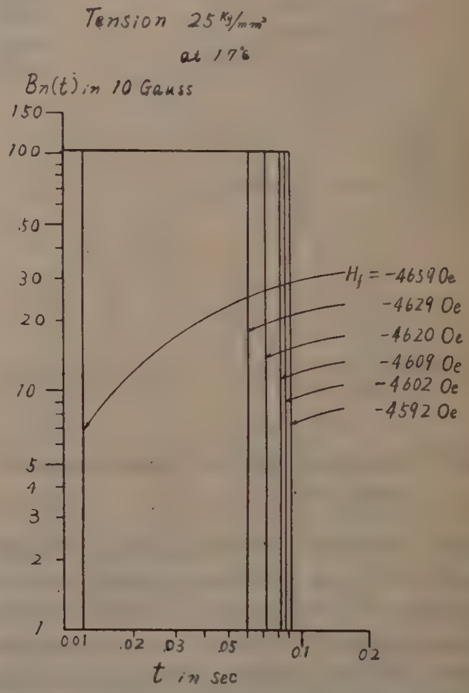

Fig. 6. Curves of $B_n(t)$ *vs.* t in a case of perfect rectangular hysteresis loop.

the value of $B_n(t)$ is obtained, namely

$$B_n(t) = \text{const} \quad \text{for } t < t_0 = D/a(H_f - H_{0mB})$$
$$= 0 \quad \text{for } t > t_0$$

The reason why t_0 has an exclusively definite value in this case is clearly explained from the above consideration. According to the Eq. (3) the relation between H_f and t_0 is given by

$$H_f = a/(Dt_0) + H_{cmB}$$

The observed values of H_f and $1/t_0$ are shown in Fig. 7. As seen from the figure, the linear relation between H_f and $1/t_0$ holds surely. The value of H_{0mB} is obtained by an extrapolation of the linear parts of H_f *vs.* $1/t_0$ curve; its value is found to be −0.4520 *Oe*.

As stated above the magnetic after effect observed in the stretched permalloy show peculiar behaviors. In the case of the application of strong tension to a thin wire, the total reversal of magnetization occurs in a single Barkhausen jump. These manifold features in magnetic after effect can be interpreted in connection with the irreversible displacement of domain boundaries. The phenomenon reported by Preisach[3] is considered as due to the same mechanism as that discussed here and his results may be explained by the present theory.

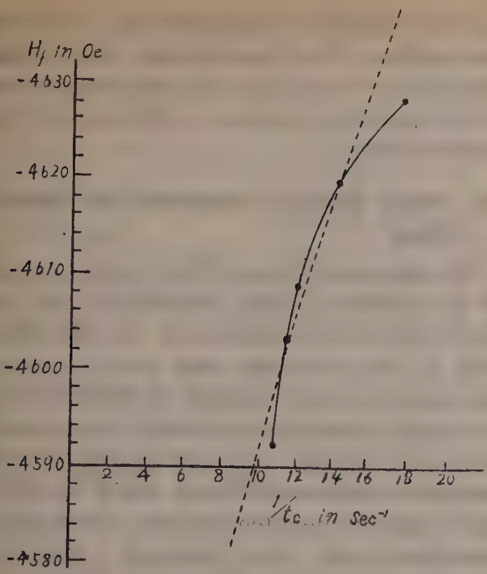

Fig. 7. Curve of H_f *vs.* $1/t_c$.

References

1) S. Maeda: Jour. Phys. Soc. Jap. **5** (1950) 358; **6** (1951) 60; Sci. Rep. RITU. A **2** (1951) 878.
2) S. Maeda: Jour. Phys. Soc. Jap. **6** (1951).
3) F. Preisach: Zeits. Phys. **94** (1935) 277.

JOURNAL OF THE PHYSICAL SOCIETY OF JAPAN Vol. 7, No. 4 JULY—AUG., 1952

Formation Energy of Superlattice for Ni_3Fe, I
Co-Operative Formation of Superlattice at the Critical Temperature*

By Shūichi IIDA

Department of Physics, Faculty of Science, University of Tokyo

(Received December 10, 1952)

Variation of inner energy for Ni_3Fe with time of the annealing at critical ordering temperature 490°C are observed first by measuring the excess specific heat of the specimen annealed with various duration, and secondly by measuring the rate of decrease of inner energy at 490°C using a new experimental method in which the necessary difference of temperature between the specimen and the surrounding wall for keeping the specimen at constant temperature 490°C is measured. Then, the variation of inner energy shows a tendency of two steps character which had been observed until now for many other physical quantities of this alloy. Next, this phenomenon has been analysed as a simple superposition of two kinds of formation processes, i.e., a formation of short range order, which starts abruptly from the beginning and ends at about 15 hours of annealing, and a formation of long range order, which begins with a sufficiently small rate, increases gradually to its maximum at 20∼30 hours and then decreases to zero at about 60 hours of annealing.

§ 1. Introduction

Since the well known discovery of permalloy by Elmen, Nickel-Iron alloys have been widely investigated not only as typical ferromagnetic metallic solid solution but also as basic high permeability materials. Then the existence of superlattice Ni_3Fe was suggested by O. Dahl1), and its confirmations were given by S. Kaya2), P. Leech & C. Sykes3) and F. E. Haworth4) by means of electric resistivity, specific heat and X-ray reflection.

---

* The experiments in this paper were made from 1948 to 1949.

An detailed study of the behaviour in the formation and in the extinction of this superlattice was first carried out by S. Kaya2) using the time change of electric resistivity. Thus it became clear that the completely ordered state of Ni_3Fe was attained by two weeks annealing from 490°C to 450°C, especially one week annealing at 490°C. At the same time, it was also found that the variation of resistivity with time of annealing at 490°C showed some characteristic tendency. Namely, the total change in resistivity at 490°C of about $9\mu\Omega$ cm was attained not by a single process, but by two processes apparently.

After that, seeking after the transitional behaviour of ferromagnetic alloy Ni_3Fe in its ordering transformation, a number of experiments were carried out in our laboratory directed by Prof. S. Kaya5)6)7)8)9). All these data concerning variations of various physical properties for Ni_3Fe with time of annealing at 490°C had indicated without an exception that the two-step process was an essential character of this annealing at 490°C. But in spite of the accumulation of experimental data, a reasonable explanation of this phenomenon has not yet been given.

In this circumstance, it became necessary to investigate the precise transitional behaviour of Ni_3Fe superlattice by measurement of its inner energy. And the first experiment of this kind was already performed by S. Kaya, M. Nakayama, H. Sato and K. Kumasaka9)5), but Sykes' apparatus they used was not so powerful to obtain the necessary structural knowledge about the problem. Fortunately, we have now a very suitable apparatus for this purpose known as Takagi-Nagasaki's adiabatic calorimeter10). The principal difference of this method from that of Sykes is; the specimen is heated by constant rate of energy, while the temperature of its surrounding wall is so regulated that the difference of the temperature between specimen and surrounding wall is zero. Using this technique and improving it to fit for our purpose, this investigation was started especially for seeking after the mechanism of the two-step process at the critical temperature 490°C.

§ 2. Inner Energy Estimated by Specific Heat

The specimen alloy of 202.1 gr was prepared by melting 24.2% electrolytic iron and 75.8% electrolytic nickel with 1% Mn added. (Fig. 4) The procedure used was as follows; the specimen was annealed at 1000°C for 1 hr in vacuum, cooled slowly to 600°C and quenched into the water. Then its specific heat was measured continuosly from 100°C to 750°C, and a specific heat-temperature curve of the disordered alloy was obtained. Next the above treatment from annealing at 1000°C to quenching at 600°C was again repeated, and thereafter it was put in a vacuum furnace kept at 490°C. After annealed for a desired time, it was again quenched into the water. Then the measurements of specific heat were carried out and a C_p-T curve of the partly ordered alloy was obtained. This procedure was repeated with various times of annealing at 490°C to obtain the complete variation character of the inner energy U with time of annealing at 490°C. In these measurements we used the power of about 25 cal/mol.min (for convenience we use a notation per mol instead of per mean gram atom.) to heat the specimen, and its temperature was recorded every 2 minutes from 50°C to 750°C by using a *Pt-PtRh* thermo-junction.

Following the mentioned procedure, 14 C_p-T curves were obtained for the different time of annealing at 490°C. All these curves had the same normal charcter of ferromagnetic metal in temperature ranges except 400°C~600°C. In this range, especially in 480°C~580°C, they showed anomalous peaks which corresponded to the transformation into disorder. They are shown in Fig. 1, where the said anomalous range alone is illustrated. The development of order will be computed in this figare by integrating the excess specific heat which increases with time of annealing.

Now for understanding the mechanism of the change of inner energy U in these measurements, these procedures are illustrated in

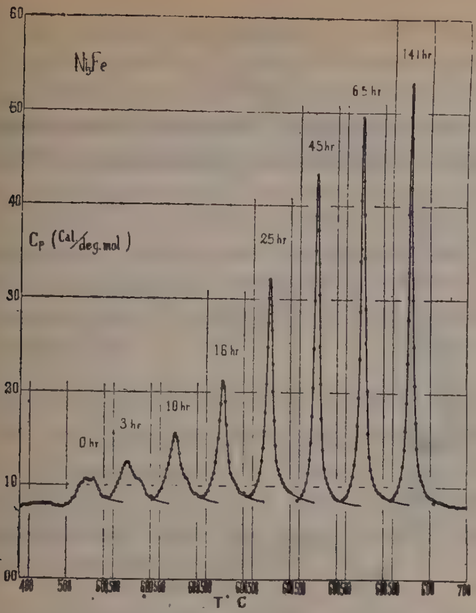

Fig. 1. Variation of specific heat-temperature curve for Ni_3Fe affected by the formation of superlattice. Letters above the curves indicate the time of annealing at 490°C.

Fig. 2 schematically. The course of energy change during the heat treatment and measurement for the disordered alloy is *ABCEA* in the figure, and these of annealed alloy are *ABCDB′C′E′A*, *ABCDB″C″E″A* etc. The decreased amounts of inner energy effectuated by annealing at 490°C are equal to the difference of inner energy $U(B')-U(B)$, $U(B'')-U(B), \cdots$. These were calculated by integrating the power given to the specimen during the measurements of specific heat between 400°C and 600°C, and comparing the same energy of 600°C quenched alloy*. The results are plotted in Fig. 3. As can be seen in the figure, it has been confirmed that the variation of inner energy with time of annealing at 490°C shows also the two-step character.

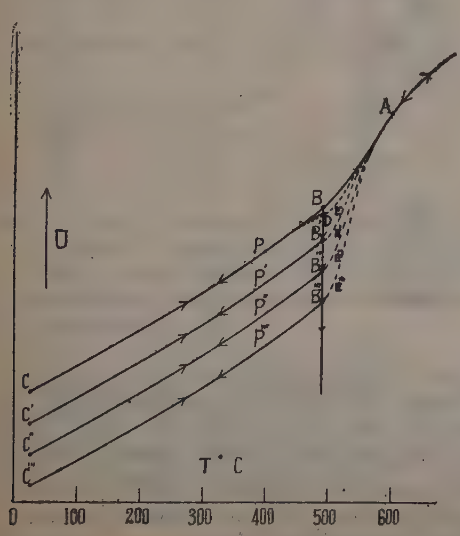

Fig. 2. Schematical diagram of energy change during the heat treatment and measurement of specific heat.

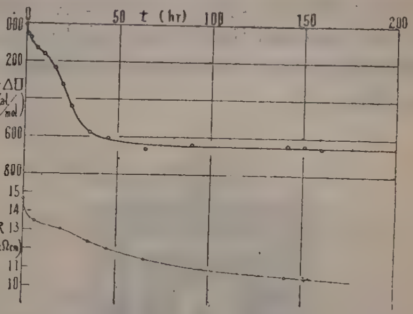

Fig. 3. Variation of inner energy for Ni_3Fe with the time of annealing at 490°C and the corresponding variation of electric resistivity measured at 0°C.

The lower curve shows the variation of electric resistivity at 0°C of a spiral wire specimen of 0.5% Mn, which has the identical treatment with the specific heat specimen. Taking account of the fact that a slight increase of Mn content has large promotive influence on the formation of order, the correspondence between these two curves can be seen as satisfactory.

§ 3. The Direct Detection of the Two-step Formation of Superlattice by the Measurements of Heats Evolved

In order to analyse more precisely the developing course of ordered state, it would be desirable to get further knowledge about the rate of formation in each stage of order. The rate of decrease of inner energy can be measured successively during the course of ordering, if the temperature of the wall surrounding the specimen is so regulated that the temperature of the specimen is kept strictly at 490°C. It will be proportional to the difference of temperature between the specimen and the surrounding wall1)2).

The curve thus obtained must show more detailed character of the process as it illustrates the differential coefficient of the $U-t$ curve in Fig. 3. And as the measurements are performed continuously and directly at 490°C, there will be no ambiguity*.

---

* Anomalous specific heat due to magnetic transformation (575°C) has no effect on these calculations.

The apparatus and the specimen used in the experiment were almost the same as these used in the previous measurements. The specimen was carefully isolated from the Cu container and the space containing the specimen was confined by the surrounding Cu container except only two holes for thermo-junctions. (Fig. 4)

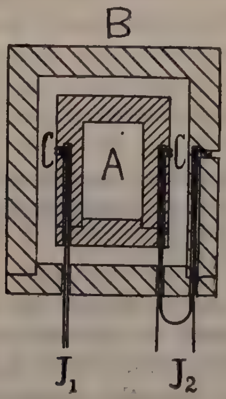

Fig. 4. The principal part of the apparatus. A, specimen. B, Cu container. C, tiny screws. J_1, Pt-PtRh thermo-junction for measuring temperature of specimen. J_2, Chromel-Alumel differential thermo-junction for indicating difference of temperature between A and B.

Now the specimen was heated to 850°C in vacuum, cooled to 600°C, kept 1 hr at this temperature and then cooled to 490°C as rapid as possible. It took 20 minutes to cool from 600$_\circ$C to 490°C, and after 1 hr at 490°C it was ready for the measurement. The deflection of a galvanometer which was connected to the chromel-alumel differential thermo-junction indicated the difference of temperature ΔT (the order of 0.05°C in the experiment) between the specimen and the Cu container, which was to be proportional to the rate of decrease of inner energy. The recording of the deflection was continued until the deflection had become zero within experimental error.

Then,

$$-\frac{dU}{dt}=k\Delta T, \quad -(U_t-U_0)=k\int_0^t \Delta T dt,$$

$$k=\frac{-(U_t-U_0)}{\int_0^t \Delta T dt}.$$

So, the proportional constant k was determined by dividing the total change of inner

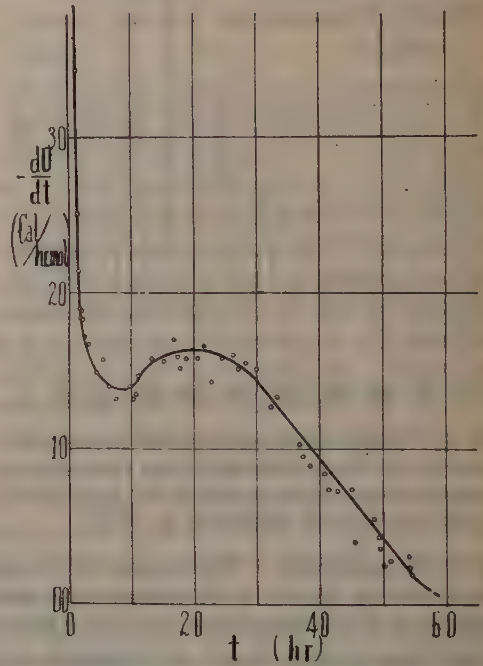

Fig. 5. Variation of the rate of decrease of inner energy with time of annealing at 490°C.

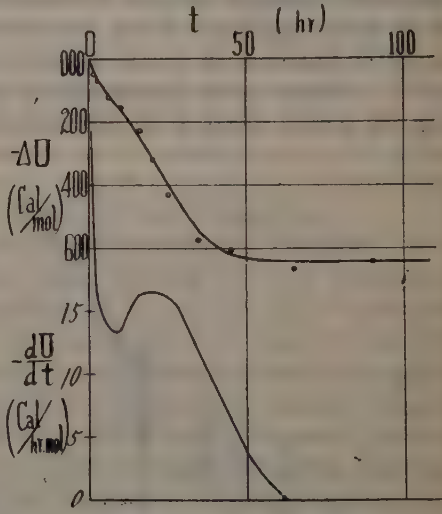

Fig. 6. Correspondence of the two experiments. The lower curve illustrates the result of Fig. 5 and the upper curve illustrates variation of inner energy obtained from the lower curve by integration with the same time ordinate. The circles show values obtained by the previous measurements of specific heat.

---

* Borelium and others kept the surrounding wall at constant temperature, so the interpretationof their results is rather complex.

energy, which was estimated at 630 cal/mol in 55 hr annealing from the previous measurements, by the corresponding area of the $\Delta T-t$ curve. The rate of decrease of inner energy thus obtained as a function of time of annealing at 490°C is shown in Fig. 5.

In Fig. 6 the correspondence between the behaviour of the inner energy obtained by the two foregoing methods is shown. The agreement is satisfactory within experimental error.

§ 4. Analysis of the Experimental Results

For the interpretation of the physical meaning of the results thus obtained, it is more adequate to connect the rate of decrease of inner energy with the inner energy itself. This is shown in Fig. 7.

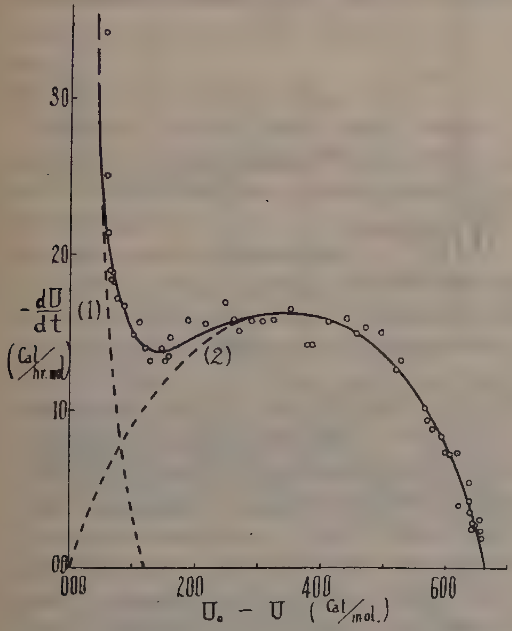

Fig. 7. Rate of decrease of inner energy as a function of inner energy. U_0 is a initial value of inner energy. Two dotted lines mean formal illustration of the two-separated reactions.

If the reaction proceeds in the form of a rate process of simple type, it must be expressed by

$$-\frac{dU}{dt}=\frac{U-U_f}{\tau} \qquad (1)$$

Where U_f is a final value of U, and τ is time of relaxation. As is shown in Fig. 7, the main part of the curve has no linear character, which shows that the process is essentially different from the simple type reaction (1) in any time interval.

In Fig. 8 the reciprocal of the instantaneous time of relaxation $-dU/dt/U-U_f$ is plotted against U. Now a straight line containing origin appears as a main part of the curve in this figure which has become a key to solve the puzzle. In a range of this straight line, the equation of the reaction will be approximated as follows,

$$-\frac{dU}{dt}=A(U_i-U)(U-U_f), \qquad (2)$$

where A=0,00017 cal.$^{-1}$ hr.$^{-1}$ mol, and U_i is a constant which is almost equal to the initial value of U. Thus by considering this part, the curve of Fig. 7 and Fig. 8 are separated into two parts which are shown by dotted lines with index (1) and (2) in the figures.

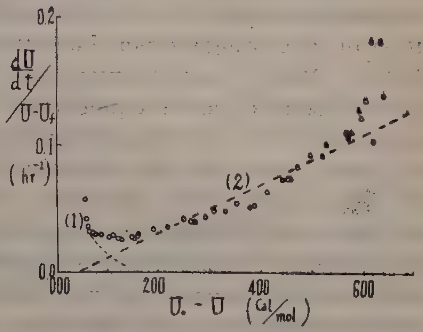

Fig. 8. Reciprocal of instantanious time of relaxiation as a function of inner energy.

This separation can be interpreted by using the formation theory of A_3B type super-

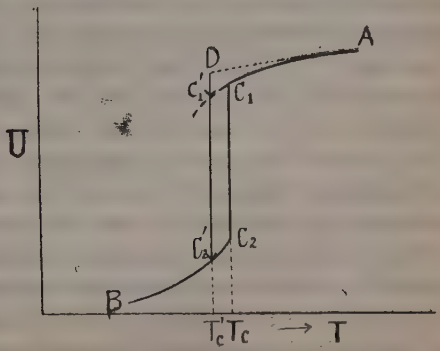

Fig. 9. Variations of inner energy with temperature for A_3B type superlattice. AC_1C_2B is a equilibrium curve on cooling and $ADC_1'C_2'$ represents a actual course by the measurements.

lattice as follows. In Fig. 9, the variation of inner energy of A_3B type superlattice against the temperature is shown. When the alloy of disordered state at high temperature A is cooled slowly, it reaches a state C_1 at critical ordering temperature Tc. Then a transformation to a state C_2 must begin at that temperature, that is the characteristic formation of long range order in A_3B type superlattice. Now it must be reminded that although the state C_1 is in equilibrium, the transformation to C_2 can proceed because it is not a stable state. So, the reaction from C_1 to C_2 must proceed in accordance with the characteristics of co-operative phenomena, with a sufficiently small rate at its beginning, and as the reaction proceed the rate of reaction will be accelerated to its maximum, and then it decreases to its final value of zero at C_2 This process can be expressed mathematically by equation (2)*.[13]

Therefore, the second part (2) of Fig. 8 can be concluded as the formation of long range order. In our experiments, the alloy has been cooled as rapid as possible from the high tempelature to Tc which is a little under Tc, so the starting point is not C_1 but D in the figure. Namely, a reaction process from D to C_1' must be added to a reaction from C_1' to C_2' which corresponds to the reaction from C_1 to C_2. This process which foregoes the development of long range order and consequently is considered as a development of short range order will compose the first part (1) of Fig. 7. And this reaction will proceed as a simple type reaction, starting with a definite reaction rate, decreasing monotonously according as the reaction proceeds and then becoming zero sufficiently before the end of the long range order reaction.

The results of this analysis into two parts are shown on a $U-t$ and $dU/dt-t$ plane in Fig. 10. As can be seen in the figure, two steps formation shown by curve (3), was superposition of the curve (1) and the curve (2). The former is the formation of short range order, which is a simple rate process, and the latter is the formation of long range order, which is the co-operative rate process expressed mathematically by the equation (2).

Fig. 11 shows the effect of the addition of Mn to the variation of electric resistivity with time while annealing at their respective critical temperatures measured by K. Takahashi. In this case, as well as the case of Kaya[2], the specimen alloys are cooled in 10°C steps, each time annealed to reach their equilibrium at that temperature. But the rapid cooling of 10°C yet effectuate a small reaction of short range ordering as is seen in the curve (a), which starts with a definite inclination to the time axis. But, as is seen in the figure, the reaction part of short range ordering disappears with addition of Mn, showing that this has large catalytic influence

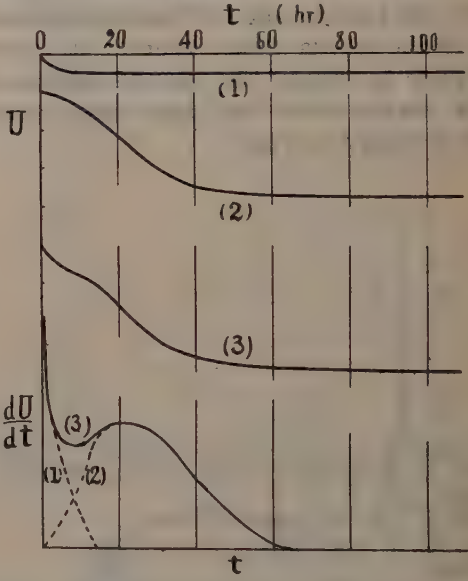

Fig. 10. Inner energy and the rate of its decrease as functions of time of annealing at 490°C. (1), a part of short range ordering, (2), a part of long range ordering, (3), actual variation which is obtained by adding (1) and (2).

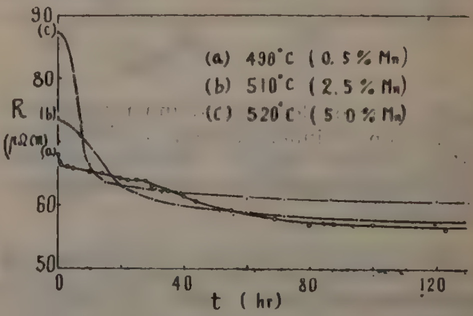

Fig. 11. Variation behaviour of electric resistivity with time of annealing at critical ordering temperature, for Ni_3Fe with various Mn content.

---

* Y. Takagi and others predicted theoretically the same characteristic of the co-operative rate process for superlattice.

upon the formation of short range order.

The effect of addition of Mo has been also investigated by K. Yasukoji[14]. Contrary to the case of Mn the addition of Mo suppresses the reaction considerably and the electric resistivity increases instead of decrease. But the curve form of the variation is a typical one of the co-operative rate process.

§ 5. Conclusion

The two-step formation of superlattice for Ni_3Fe was thus analysed in two parts, i. e. the formation of short range order and the formation of long range order. Using this result, the formation stages of Ni_3Fe when annealed at 490°C after was quenched from 600°C is analysed into 4 parts as follows,

(1) 0–20 minutes of annealing.

Although there is not so abrupt change in inner energy, most of the structure sensitive quantities are strongly influenced in this stage.

(2) 0–10 hours of annealing.

Building up the short range order. It starts with a fairly great reaction rate, and then the rate decreases monotonously to its final value zero.

(3) 5–60 hours of annealing.

Buildingu p the long range order. It proceeds with a small rate at first, is gradually accelarated until it attain to its maximum at about 20 hours, and then disappears slowly at 60 hours.

(4) 60–150 hours of annealing.

Our experiments have confirmed that the inner energy has no appreciable change after 60 hours of annealing. But it has been reported already that most of the structure sensitive quantities[2)5)6)9)] (magnetization curve, electric resistivity, hardness etc.) showed great changes in this stage of annealing. So, we have some reason to consider the existence of the forth process of different mechanism, after the co-operative rate process has ended.

Experimental proofs of the existence of short range ordering above the curie point which has a relaxation time of hours, and a theoretical treatment concerning the co-operative rate process of superlattice will be given in the later paper.

The writer should like to express his sincere thanks to Prof. S. Kaya for his constant guidance and encouragement throughout the work, and to M. Nakayama for his kind instruction of the specific heat measurement. The writer expresses his thanks also to K. Takahasi and K. Yasukoji who kindly allowed him to refer their unpublished data.

References

1) O. Dahl: Zeits. f. Metallkunde **28** (1936) 133.
2) S. Kaya: J. Hokkaido Univ. **2** (1938) 29.
3) P. Leech and C. Sykes: Phil. Mag. **27** (1939) 742.
4) F. E. Haworth: Phys. Rev. **56** (1939) 289.
5) S. Kaya, M. Nakayama and H. Sato: Proc. Phys. Math. Soc. Japan (1943) 179.
6) T. Nagasima: J. Appl. Phys. Japan **19** (1950) 53.
7) S. Chikazumi: J. Phys. Soc. Japan **5** (1950) 332.
8) S. Kaya, and etc.: Unpublished.
9) S. Kaya, H. Sato and K. Kumasaka: J. Metal. Soc. Japan **6** (1942) 188.
10) S. Nagasaki and Y. Takagi: J. Appl. Phys. Japan **17** (1948) 104.
11) G. Borelius, K. E. Larrson and H. Selberg: Ark. Fys. **2** (1950) 161.
12) N. Nyström: Ark. Fys. **2** (1950) 151.
13) Y. Takagi, T. Oguchi and G. Shirane: Bull. Tokyo Inst. Tech. B. 3 (1950) 225.
14) K. Yasukoji: Unpublished.

JOURNAL OF THE PHYSICAL SOCIETY OF JAPAN Vol. 7, No. 4 JULY—AUG., 1952

Proton Magnetic Resonance Absorption in Hydrogen Perchlorate Monohydrate and the Structure of the Oxonium Ion II

By Yoshinobu KAKIUCHI and Hachiro KOMATSU

Institute of Science and Technology, University of Tokyo, Meguro-ku, Tokyo

(Received February 23, 1952)

From the more detailed analysis of the proton magnetic resonance absorption in hydrogen perchlorate monohydrate described in the preceding paper, the pyramidal structure of the oxonium ion is again confirmed.

§ 1. Introduction

In the preceding paper[1], we have concluded that the crystal of hydrogen perchlorate monohydrate has an ionic structure $H_3O^+ClO_4^-$, rather than the structure $HClO_4 \cdot H_2O$, as the result of the proton magnetic resonance absorption measurement. We have found that the estimated second moment of the absorption line assuming the pyramidal structure of the ion agrees well with the observation. As Prof. H. S. Gutowsky* and Dr. S. Suwa* have pointed out, there may be an another interpretation of the observed type of the absorption curve. Namely, if two of the protons exsist in a form of the water of crystallization and another proton is in a position fairly distant from them, the observed absorption may be the superposition of the camel-hump-shaped absorption curve corresponding to the two proton system, and a single bell shaped one due to a single proton thus producing a shouldered peak resembling to a three proton absorption curve.

One clue for the solution of the problem is to calculate the *second moment* of the absorption curve from the supposed structure of the ion and to compare it with the observation. A part of this program was already accomplished in the perevious paper, and it was found that three protons located at each top of a regular triangle, whose sides are 1.70 Å give the result in good agreement with the observation. In the following, however, we shall treat the problem in somewhat a more general way.

§ 2. Second Moment Argument

First we shall *assume* that two protons H_1 and H_2 are 1.70 Å apart from each other as in the case of the water molecule. The condition that the second moment must be equal to the observed value restrict the freedom of the third proton H_3, which can only move along the locus given by the condition:

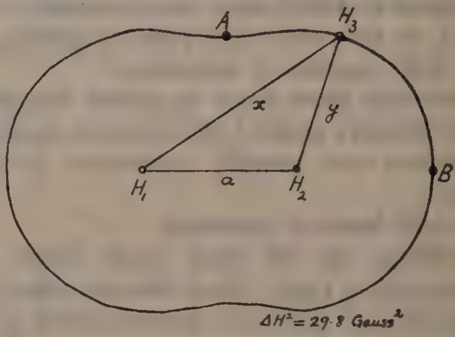

Fig. 1. Contour line for equal second moment.

$$\frac{1}{x^6}+\frac{1}{y^6}=\frac{2}{a^6}, \quad a=1.70\ \text{Å}$$

where x and y are the distances of H_3 from H_1 and H_2 respectively a being the distance between H_1 and H_2 (See appendix I). The above locus is shown in Fig. 1. From the knowledge of the second moment alone, the third proton can take any position on this cocoon-shaped curve. It shows, however, that the third proton can neither be nearer than 1.46 Å nor farther than 2.37 Å from the centre of the first and the second protons. This conclusion eliminates the possibility that the third proton exists far distant from the other two protons. Therefore, it may safely be concluded that the protons form a *three proton system* rather than a *two proton system and one proton*. In order to fix the position of the third proton more precisely, we must resort to the detailed discussion of the line shape to which we shall concern in the following.

---

* Private Communications.

§ 3. The Shape of the Absorption Line

The comparison of the calculated line shape for the regular triangle structure with the observation was already reported in a previous paper. The result, however, was based upon the formula of Andrew[2)], which contains a minute misprint. (Appendix II). Therefore, the calculation was renewed, and the result is shown in Fig. 2. The correction is found to be unimportant and the agreement with experiment is equally good as in the case reported previously.

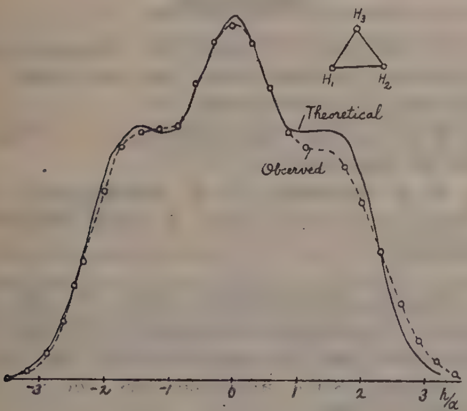

Fig. 2. Line shape for regular triangular configuration (H_3 at A).

Because it is quite troublesome to calculate the shape for every possible configuration, we have tried another possibility that the third proton is located at point B in Fig. 1, which configuration has the next higher symmetry to the case A. The result is shown in Fig. 3, and it is clear that the agreement is poorer than in the former case. Therefore, it may safely be concluded that *three protons are on the top of the regular triangle.*

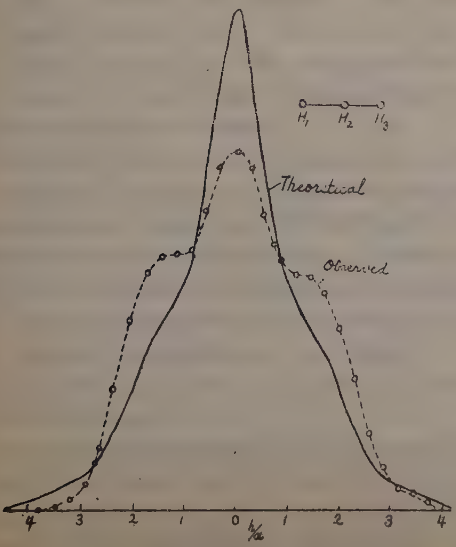

Fig. 3. Line shape for linear configuration (H_3 at B).

§ 4. The Structure of the Oxonium Ion

From above discussions, it is concluded that the oxonium ion has a structure with pyramidal symmetry similar to ammonia molecule as was suggested in the previous paper. A lone pair of the electron existing in the oxygen atom is opened by the addition of another proton, and three equivalent *sσ electron pair bonds* are thus formed. According to this opinion, the positive charge of the oxonium ion must concentrate at the oxygen nucleus, but more generally it is to be considered to distribute among the bond due to the polarisation of the electron. Besides the above mentioned pure electron pair bond, several *ionic structures* including the possibility of the resonance between three states

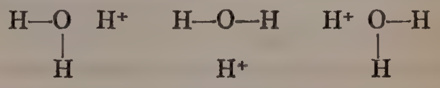

$$\begin{array}{c}\mathrm{H{-}O}\quad \mathrm{H^+}\\ \;\;|\qquad\quad\\ \;\;\mathrm{H}\qquad\quad\end{array}\qquad \begin{array}{c}\mathrm{H{-}O{-}H}\\ \mathrm{H^+}\end{array}\qquad \begin{array}{c}\mathrm{H^+}\quad\mathrm{O{-}H}\\ \qquad|\\ \qquad\mathrm{H}\end{array}$$

cannot probably be neglected.

A more detailed consideration about the type and the energy of O–H bonding in oxonium ion is highly desirable, and the quantum mechanical treatment of the problem is in the course of its developement.

Authors wish to express their hearty thanks to Prof. H. S. Gutowsky in University of Illinois and to Dr. S. Suwa in University of Tokyo for their valuable discussions and criticisms.

Appendix I

The second moment of the three proton system is from eq. (8) reference 3,

$$\Delta H^2=\frac{3}{10}g^2\beta^2\left(\frac{1}{x^6}+\frac{1}{y^6}+\frac{1}{a^6}\right)$$

where the symbol x, y and a are as described in this present paper, others being in common usage. In the case of the regular triangle, the factor in the bracket becomes $3/a^6$, which coinsides with experiment for $a=1.70$ Å. Therefore, the condition that the system has the observed second moment is

$$\frac{1}{x^6}+\frac{1}{y^6}=\frac{2}{a^6}.$$

Appendix II

There is a misprint in Andrew's formula of the powder line shape $F(h)$ for the case (ii), namely for the line component $h=y/\mu$. The formula (4) in page 160 of the text (reference 2):

$$F(h)=\frac{h}{72\alpha^2\gamma_1}\left[1-\frac{\alpha^2}{4h^2}\left(\frac{4}{3}\pm3\gamma_1\right)\right]\left(\frac{7}{9}\pm\gamma_1\right)^{-1/2}$$

should be read as

$$F(h)=\frac{h}{72\alpha^2\gamma_1}\left[1-\frac{\alpha^2}{4h^2}\left(\frac{4}{3}\pm3\gamma_1\right)^2\right]\left(\frac{7}{9}\pm\gamma_1\right)^{-1/2}$$

which reduces to the formula used in the present calculation:

$$F(h)=\frac{h}{108\alpha^2\gamma_1}\left[1-\frac{\alpha^2}{4h^2}\left(\frac{4}{3}\pm12\gamma_1\right)\right]\left(\frac{7}{9}\pm\gamma_1\right)^{-1/2}$$

considering the relation

$$\gamma_1^2=\frac{4}{81}\left(\frac{3h^2}{\alpha^2}-2\right).^{*}$$

Note added in proof:

The paper by Dr. R. E. Richards appeared in December issue of the Transaction of the Faraday Society (Vol. 47 (1951) 1261).

The result for the oxonium ion in oxonium perchlorate coinsides almost perfectly with ours. The result of the experiments for hexachloroplatinic acid and other hydrates see also his forthcoming paper to appear shortly in Transaction.

References

1) Y. Kakiuchi, S. Shono, H. Komatsu and K. Kigoshi: J. Chem. Phys. **19** (1951) 1069, J. Phys. Soc. Jap. **7** (1952) 108.

2) E. R. Andrew and R. Bersohn: J. Chem. Phys. **18** (1950) 159.

3) H. S. Gutowsky, G. B. Kistiakowsky, G. E. Pake and E. M. Purcell: J. Chem. Phys. **17** (1949) 972.

---

* Private Communication from Dr. E. R. Andrew. According to him also, Dr. Richard in Oxford have made the similar studies with ours, but his paper is not available here yet at the date Feb. 22, 1952.

JOURNAL OF THE PHYSICAL SOCIETY OF JAPAN Vol. 7, No. 4 JULY—AUG., 1952

Some Exact Solutions in Nonlinear Oscillations

By Ken-iti MUNAKATA

Physical Institute, Faculty of Science, University of Kyoto

(Received January 25, 1952)

Forced oscillations of systems with nonlinear restoring forces are treated rigorously in certain special cases which are specified by the condition that the harmonic oscillation has a similar wave form to that of the external force. From this condition we are led to the introduction of the external force represented by the function cn for a hard system and by the function sn in the case of a soft system, and consequently the solution is given by either of these functions. Response curves obtained are similar to the corresponding response curves which have been given by approximate solutions. To examine the stability of the forced oscillation one must solve Hill's equations, which can be carried out exactly in the present cases. Thus, the stable or unstable regions in the response diagrams are determined definitely and a few questions are clarified.

Introduction

In the present paper, forced oscillations of mechanical or electrical systems with nonlinear restoring forces are investigated in certain special cases in which they are dealt with in an exact manner by use of known functions only. The differential equations considered are of the form:

$$\ddot{x}+\alpha x+\beta x^3=f(t) \qquad (1)$$

which is often called Duffing's equation. Here, the function $f(t)$, which represents the external force applied to the system concerned, is a periodic function with frequency ω, and an appropriate form will be specified to it in the course of subsequent analysis. The system is usually called 'hard' if $\alpha>0$, $\beta>0$, and 'soft' if $\alpha>0$, $\beta<0$. We treat also the case of $\alpha<0$, $\beta>0$ and call it provisionally 'repulsive-attractive' system.

It is well known that the problem of free oscillation (i.e., case of $f(t)\equiv 0$) of the system can be solved rigorously by making use of elliptic integrals and functions. So far as the writer is aware of, however, it does not seem to have been noticed that the solutions can be classified according to the signs of α and β in such a manner as shown in the subsequent chapter I.

The forced oscillations of nonlinear systems under the action of an external force $f(t)=F\cos(2\pi\omega t)$ have so far been the subjects of numerous investigations. Since explicit solutions in terms of the elementary functions are not to be expected, recourse has been had to various analytic approximation methods. Most of them are either perturbation methods or iteration methods which require for convergence that the constant β be small. The results obtained are therefore subject to the limitation that the nonlinearity in the restoring force is small.

It will be shown in chapter II that under a certain condition exact solutions are obtained for the harmonic oscillations, i.e. periodic solutions $x(t)$ of (1) in which the frequency is the same as the frequency ω of the excitation $f(t)$. The said condition is that the harmonic oscillation has a similar wave form as the external force, namely: $x(t)/f(t)=\text{const.}$ It is to be noted that for such solutions there are neither question of convergence nor limitation as to the magnitudes of β or others.

If we apply the usual definition of stability of oscillations (infinitesimal stability) to our present problem, necessary analysis can be carried out rigorously, and stable and unstable regions in the response diagrams are determined definitely (see chapter III). We have thus been able to clarify a few questions concerning the stability of harmonic oscillations suggested recently by J. J. Stoker in his book [1].

I. Free Oscillations

§ 1. Differential Equations for Jacobi's Elliptic Functions

It is well known that the following relations hold for Jacobi's elliptic functions $\mathrm{sn}\,u$, $\mathrm{cn}\,u$ and $\mathrm{dn}\,u$ with modulus k

$$\left.\begin{aligned} &\mathrm{sn}^2 u+\mathrm{cn}^2 u=1\,,\\ &k^2\mathrm{sn}^2 u+\mathrm{dn}^2 u=1\,,\end{aligned}\right\} \qquad (2)$$

$$\left.\begin{aligned} &\mathrm{sn}' u=\mathrm{cn}\,u\,\mathrm{dn}\,u\,,\\ &\mathrm{cn}' u=-\mathrm{sn}\,u\,\mathrm{dn}\,u\,,\\ &\mathrm{dn}' u=-k^2\mathrm{sn}\,u\,\mathrm{cn}\,u\,,\end{aligned}\right\} \qquad (3)$$

where prime denotes differentiation with respect to u.

It can be shown without difficulty that these three functions satisfy the following differential equations of the second order respectively:

$$\left.\begin{aligned} &\mathrm{sn}'' u+(1+k^2)\,\mathrm{sn}\,u-2k^2\mathrm{sn}^3 u=0\,,\\ &\mathrm{cn}'' u+(1-2k^2)\,\mathrm{cn}\,u+2k^2\mathrm{cn}^3 u=0\,,\\ &\mathrm{dn}'' u-(2-k^2)\,\mathrm{dn}\,u+2\,\mathrm{dn}^3 u=0\,.\end{aligned}\right\} \qquad (4)$$

As will be seen readily, these equations have the same nonlinear character as in the left-hand side of equation (1) for positive or negative α and β. Thus, we see that the free oscillation of a hard system is represented by the function cn, while that of a soft system by the function sn and lastly that of a repulsive-attractive system by either of the functions cn or dn.

As is well known, the functions $\mathrm{sn}\,u$ and $\mathrm{cn}\,u$ have a (real) period $4K$, while $\mathrm{dn}\,u$ has a period $2K$, where K is the complete elliptic integral of the first kind with modulus k. The numerical value of $4K$ increases from 2π to infinity as the value of k varies from 0 to 1. The curves of the three functions are illustrated in Fig. 1 for a few values of k^2. As one sees, the curves of $\mathrm{sn}\,u$ and $\mathrm{cn}\,u$ differ only slightly from the corresponding curves of $\sin u$ and $\cos u$ (i.e. cases of $k=0$) even for comparatively large values of k.

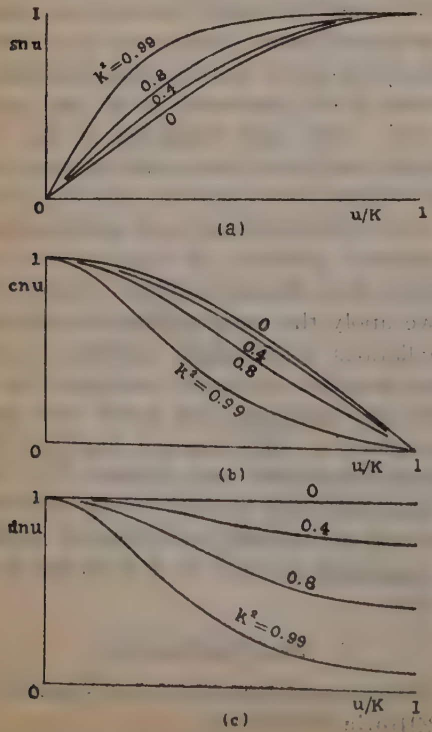

Fig. 1. Jacobi's elliptic functions.

§ 2. Free Oscillation of a Hard System

Now, we assume the solution of the equation:

$$\ddot{x}+\alpha x+\beta x^3=0 \qquad (5)$$

for the free oscillation of a hard system ($\alpha>0$, $\beta>0$) in the form:

$$x=A\,\mathrm{cn}\,(4K\omega t) \qquad (6)$$

in which A and ω are amplitude and frequency of the oscillation respectively. Bearing the relations (4) in mind, it can easily be seen that the function in (6) satisfies the differential equation

$$\frac{1}{(4K\omega)^2 A}\frac{d^2x}{dt^2}+\frac{1-2k^2}{A}x+\frac{2k^2}{A^3}x^3=0\,. \qquad (7)$$

Comparison of (7) with (5) yields

$$\alpha=(1-2k^2)(4K\omega)^2, \qquad \beta=\frac{2k^2(4K\omega)^2}{A^2}, \qquad (8)$$

from which we obtain

$$(4K\omega)^2=\alpha+\beta A^2, \qquad (9)$$

and

$$k^2=\frac{\beta A^2}{2(\alpha+\beta A^2)}\,. \qquad (10)$$

For some prescribed values of amplitude A we calculate the values of k^2 by (10), and then the values of K are found by computation or from appropriate table of elliptic integrals. Lastly, the values of the frequency ω are determined by (9). Thus, the frequency is conveniently considered as a function of amplitude. To the values of amplitude in the range $0\le|A|<\infty$ there correspond

$$\frac{1}{2\pi}\sqrt{\alpha}\le\omega<\infty \ \text{ and } \ 0\le k^2<\frac{1}{2}\,.$$

This relation is illustrated by a curve denoted by $F=0$ in Fig. 4, the magnitudes of the constants α and β being taken here as well as in what follows as $|\alpha|=1$, $|\beta|=0.1$.

From (6) we have

$$v=\dot{x}=-4K\omega A\,\mathrm{sn}\,(4K\omega t)\,\mathrm{dn}\,(4K\omega t),$$

and this gives, in conjunction with (6) itself, an equation of trajectory in the phase plane (i.e. displacement-velocity plane) as follows:

$$\left(\frac{v}{4K\omega A}\right)^2=\left\{1-\left(\frac{x}{A}\right)^2\right\}\left\{1-k^2+k^2\left(\frac{x}{A}\right)^2\right\}. \tag{11}$$

Examples of the phase trajectories are shown in Fig. 2a.

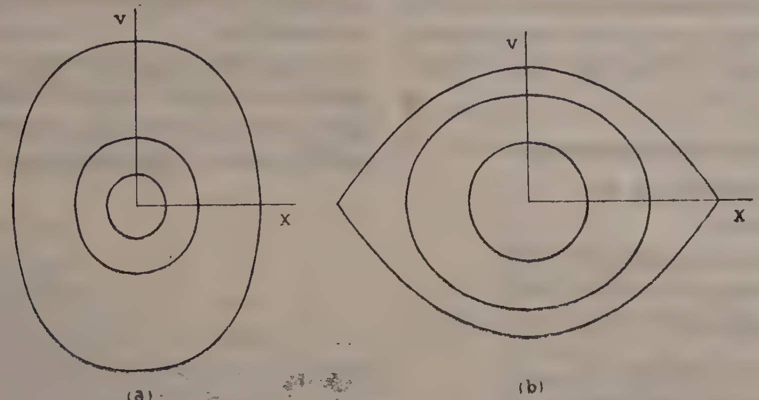

Fig. 2. Phase trajectories for hard and soft systems.

§ 3. Free Oscillation of a Soft System

Similarly, free oscillation of a soft system ($\alpha>0$, $\beta<0$) is represented by

$$x=A\,\mathrm{sn}\,(4K\omega t)\,, \tag{12}$$

with

$$\alpha=(1+k^2)(4K\omega)^2\,,\ \beta=-\frac{2k^2(4K\omega)^2}{A^2}\,, \tag{13}$$

which yield

$$(4K\omega)^2=\alpha+\frac{1}{2}\beta A^2,\ k^2=\frac{-\beta A^2}{2\alpha+\beta A^2}. \tag{14}$$

This time, ω is a decreasing function of $|A|$ (cf. Fig. 5). For $|A|=\sqrt{-\alpha/\beta}$, k^2 becomes unity, K infinite, and hence $\omega=0$. This represents the fact that the time required to attain just one of the unstable equilibrium points $x=\pm\sqrt{-\alpha/\beta}$ is infinite. Phase trajectories for the soft system are given by the equation:

$$\left(\frac{v}{4K\omega A}\right)^2=\left\{1-\left(\frac{x}{A}\right)^2\right\}\left\{1-k^2\left(\frac{x}{A}\right)^2\right\}, \tag{15}$$

and are illustrated in Fig. 2b.

§ 4. Free Oscillation of a Repulsive-Attractive System

If $\alpha<0$ and $\beta>0$, the force is repulsive for small $|x|$ and is attractive for sufficiently large $|x|$. The origin is an unstable equilibrium point and the points $x=\pm\sqrt{-\alpha/\beta}$ are stable equilibrium points. The periodic motion in this case is represented in two different forms in accordance with the distinction whether a small oscillation takes place about one of the stable equilibrium points and is confined to one side of the origin, or it occurs symmetrical about the origin passing over the two stable points.

a) *Asymmetrical oscillation*

The oscillation about the point $x=\sqrt{-\alpha/\beta}$ is given by

$$x=A\,\mathrm{dn}\,(2K\omega t) \tag{16}$$

with

$$\alpha=(k^2-2)(2K\omega)^2,\ \beta=\frac{2(2K\omega)^2}{A^2}. \tag{17}$$

In this case, equation of phase trajectory is given by

$$\left(\frac{v}{2K\omega A}\right)^2=\left\{1-\left(\frac{x}{A}\right)^2\right\}\left\{k^2-1+\left(\frac{x}{A}\right)^2\right\}. \tag{18}$$

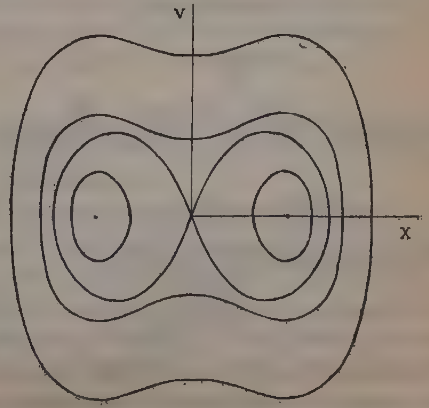

Fig. 3. Phase trajectories for a repulsive-attractive system.

b) *Symmetrical oscillation*

The function $x=A\,\mathrm{cn}\,(4K\omega t)$ discussed in § 2 represents the oscillation concerned, with the only difference that α is negative and consequently $\frac{1}{2}<k^2\leq 1$ in this case.

The phase trajectories are shown in Fig. 3, where the inner part of the curve passing through the origin corresponds to a), while the outer part to b).

II. Froced Oscillations

§ 5. Response Curves of the Hard System

When the external force $f(t)$ in (1) has a form:

$$f(t)=F\,\mathrm{cn}\,(4K\omega t,\ k), \qquad (19)$$

we can solve the problem of forced vibration of the hard system in an exact manner. Here the frequency ω and the amplitude F of the external force can be chosen arbitrarily, but the modulus k which specifies the wave form of the excitation is to be determined by the solution itself as will be seen presently.

If we assume the solution of (1) with (19) in the form:

$$x=A\,\mathrm{cn}\,(4K\omega t,\ k)\,, \qquad (20)$$

the equation can be rewritten as:

$$\ddot{x}+\left(\alpha-\frac{F}{A}\right)x+\beta x^3=0\,. \qquad (21)$$

Comparison of this equation with (7) reveals

$$\left.\begin{aligned} \alpha-\frac{F}{A}&=(1-2k^2)(4K\omega)^2\,,\\ \beta&=\frac{2k^2(4K\omega)^2}{A^2}\,. \end{aligned}\right\} \qquad (22)$$

Eliminating k^2 between these expressions we obtain

$$(4K\omega)^2=\alpha+\beta A^2-\frac{F}{A}\,, \qquad (23)$$

while the modulus k is given by

$$k^2=\frac{\beta A^2}{2(\alpha+\beta A^2-F/A)}\,. \qquad (24)$$

The response curves (though not in its strict sense of terminology) are now constructed as follows. For a certain amplitude $F(\geq 0)$ of the external force the amplitude A of the response is considered to be prescribed. From the value of k^2 as given by (24) K is determined as mentioned before. Then, the frequency ω is given by (23). This procedure which seems to be somewhat unnatural is in accord with Duffing's method as emphasized by Stoker [1].

A response diagram thus obtained are shown in Fig. 4. As is indicated in the figure, the quantity A is negative on the response curves in the right-hand side of the curve of $F=0$ and positive in its left-hand side, which means that the motion is out of phase with the excitation or in phase with it respectively. It is to be noted that as will be seen from (22) the parameter k is constant along any straight line passing through the origin of this diagram. Such lines are shown for several values of k^2. Considering Fig. 1b it will be seen that the wave forms are very close to the cosine curve in the greater part of the response diagram.

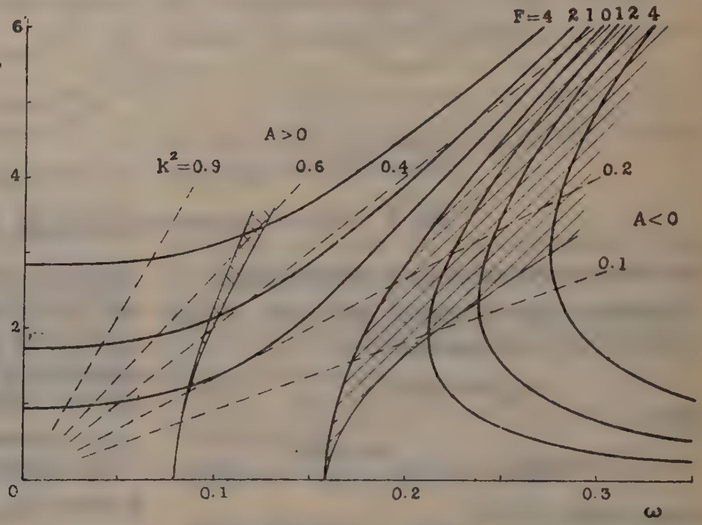

Fig. 4. Response curves and unstable regions for a hard system.

§ 6. Response Curves of the Soft System

A similar analysis applies to the soft system. In this case we consider the external force of the form:

$$f(t)=F\,\mathrm{sn}\,(4K\omega t,\ k)\,. \qquad (25)$$

Then the exact solution for the harmonic oscillation of the soft system is given by

$$x=A\,\mathrm{sn}\,(4K\omega t,\ k)\,, \qquad (26)$$

with

$$\left.\begin{aligned} \alpha-\frac{F}{A}&=(1+k^2)(4K\omega)^2\,, \\ \beta&\doteq-\frac{2k^2(4K\omega)^2}{A^2}\,. \end{aligned}\right\} \tag{27}$$

From these equations we find the response relations as follows:

$$(4K\omega)^2=\alpha+\frac{1}{2}\beta A^2-\frac{F}{A}\,, \tag{28}$$

$$k^2=\frac{-\beta A^2}{2\alpha+\beta A^2-2F/A}\,. \tag{29}$$

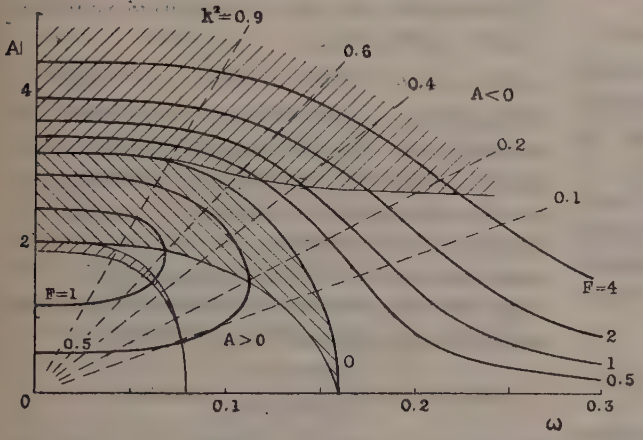

Fig. 5. Response curves and unstable regions for a soft system.

Fig. 5 shows a response diagram of a soft system. It may be worth noticing that the response curves of in-phase branch ($A>0$) shrinks to a point $A=\sqrt{-\alpha/3\beta}$, $\omega=0$ when the amplitude of the external force approaches the value $F=(2\alpha/3)\sqrt{-\alpha/3\beta}$. Consequently, for larger values of F there exist out-of-phase oscillations only.

§ 7. Comparison with the Approximate Theory

As is well known, the approximate solution of the differential equation:

$$\ddot{x}+\alpha x+\beta x^3=F\cos(2\pi\omega t) \tag{30}$$

can be put as:

$$x=A\cos(2\pi\omega t)\,, \tag{31}$$

which renders a response relation:

$$(2\pi\omega)^2=\alpha+\frac{3}{4}\beta A^2-\frac{F}{A}\,. \tag{32}$$

We now show how this equation is compatible with equation (23) of our results for the hard system. For small values of the modulus k we have, correct to the order of k^2,

$$4K\doteq2\pi\left(1+\frac{1}{4}k^2\right).$$

Substituting this expression in (23) we obtain

$$(2\pi\omega)^2\left(1+\frac{1}{2}k^2\right)\doteq\alpha+\beta A^2-\frac{F}{A}\,. \tag{33}$$

At the same time, correct to the order of k^2, the second equation of (22) becomes

$$\beta\doteq\frac{2k^2(2\pi\omega)^2}{A^2}\,,$$

and this reduces (33) into (32). The same reduction applies to the equations (28) and (32) for the soft system.

We have drawn the response diagram corresponding to Figs. 4 and 5 by the use of the relation (32) and ascertained that the corresponding curves coincide very closely with each other in the greater portion of the figure except near the $|A|$-axis. These circumstances might have been expected from the fact that the functions cn and sn are very close to cosine and sine respectively even for comparatively large values of k.

Strictly speaking, the results of the approximate theory ought not to coincide with the results of our theory even if the approximation would be improved, since the wave forms of the applied forces are different in the two cases. However, they must agree with each other at least near the curve of free vibration for all values of amplitude $|A|$, as well as near the ω-axis where the modulus k is very small in our theory.

III. Stability Problem

§ 8. Stability Problem for the Harmonic Oscillation

The problem of stability of harmonic solution (31) of Duffing's equation (30) has been dealt with in detail by Stoker [1] by making use of the perturbation method, under the assumption of small β. However, a few questions of interest concerning the instability of harmonic oscillation have been left to further investigations, since it is difficult to decide such a delicate problem by the approximate theory.

We have been able to solve exactly the stability problem of forced vibration treated in the preceding chapter by carrying out similar analysis as that of Stoker.

We take the usual definition of infinitesimal stability as follows: Let $x(t)$ and $x(t)+\delta x(t)$ be two solutions of the differential equation of motion (1), for which the initial conditions at $t=0$, say, differ slightly. If we insert $x+\delta x$ in (1) and neglect powers of δx above the first, we obtain the 'variational' differential equation for δx:

$$\delta\ddot{x}+(\alpha+3\beta x^2)\delta x=0\,, \qquad (34)$$

in which $x(t)$ is the solution of (1) whose stability is to be investigated. If all solutions δx of this equation are bounded, the $x(t)$ is said to be stable, and otherwise unstable.

For a soft system treated in § 6 we have $x=A\,\mathrm{sn}\,(4K\omega t,\,k)$. In substitution of this expression in (34), it is convenient to introduce a new independent variable $\tau=4K\omega t$. Then, (34) can be transformed in the form:

$$\frac{d^2\delta x}{d\tau^2}+\{d-e\,\mathrm{sn}^2(\tau,\,k)\}\delta x=0\,, \qquad (35)$$

where use has been made of new parameters d and e defined, in consideration of (27), as:

$$\left.\begin{aligned} d&=\frac{\alpha}{(4K\omega)^2}=1+k^2+\frac{F}{A(4K\omega)^2}\,,\\ e&=\frac{-3\beta A^2}{(4K\omega)^2}=6k^2\,. \end{aligned}\right\} \qquad (36)$$

In the case of a hard system where $x=A\,\mathrm{cn}\,(4K\omega t,\,k)$, we are led to the same equation as (35), but with different values of the constants d and e. As will easily be seen from (22) and (2), we have in this case

$$\left.\begin{aligned} d&=\frac{\alpha+3\beta A^2}{(4K\omega)^2}=1+4k^2+\frac{F}{A(4K\omega)^2}\,,\\ e&=\frac{3\beta A^2}{(4K\omega)^2}=6k^2\,. \end{aligned}\right\} \qquad (37)$$

For the purpose of determining the stability of the response of the hard as well as the soft systems it becomes necessary and sufficient to find the stable and unstable regions for Hill's equation (35) in a plane with d and e as its coordinates. The parameter values at which a transition from stability to instability occurs are then of particular interest. The following property is known: The transition values of d and e are characterized by the fact that equation (35) has one periodic solution with the period $2K$ or the period $4K$ for these values of parameters, where $2K$ is the period of the coefficient of δx in (35).

§ 9. Stable and Unstable Regions for Hill's Equation (35)

If we differentiate equation (5) of the free oscillation with respect to t, we observe that $\dot{x}$ is the solution of variational equation (34). Thus, from (12) we find a solution of Hill's equation (35) to be

$$\delta x=\mathrm{cn}\,\tau\,\mathrm{dn}\,\tau \qquad (38)$$

It corresponds to a set of transition values of d and e given by

$$\text{(II)} \qquad d=1+k^2,\quad e=6k^2, \qquad (39)$$

which have been obtained from (36) by putting $F=0$. It is to be noted that δx in (38) has the period $4K$, and that as k varies from 0 to 1, equations (39) represent a segment of a straight line extending in the d, e-plane from the point (1, 0) to the point (2, 6).

By the way, another fundamental solution can easily be obtained from (38) as:

$$\delta x=\mathrm{cn}\,\tau\,\mathrm{dn}\,\tau\left\{\int\frac{d\tau}{\mathrm{cn}^2\tau\,\mathrm{dn}^2\tau}+\text{const.}\right\}.$$

It is not a periodic function but has the form:

$$\delta x=C\tau\,\mathrm{cn}\,\tau\,dn\,\tau+\psi(\tau)$$

in which $\psi(\tau)$ is a function with the period $4K$ and C is a certain constant.

Similarly, from (6) we obtain a solution

$$\delta x=\mathrm{sn}\,\tau\,\mathrm{dn}\,\tau \qquad (40)$$

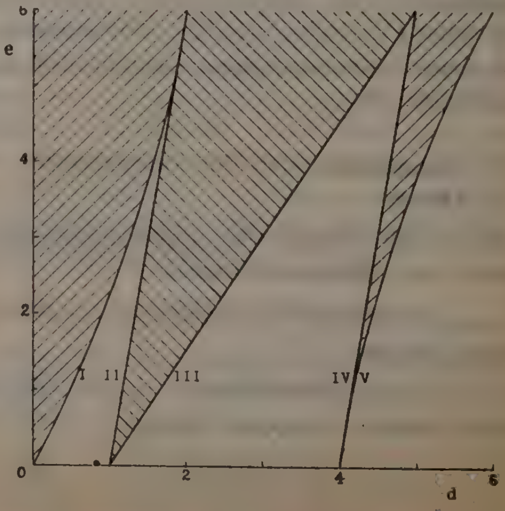

Fig. 6. Stable and unstable regions for Hill's equation (35).

with other set of transition values given by (cf. (37))

(III) $$d=1+4k^2, \quad e=6k^2. \tag{41}$$

This time, δx has also the period $4K$ and equations (41) represent a straight line-segment between the points (1, 0) and (5, 6) in the d, e-plane.

In the same way, the solution (16) for the repulsive-attractive system gives us a solution of (35) as:

$$\delta x=\mathrm{sn}\,\tau\,\mathrm{cn}\,\tau\,, \tag{42}$$

which corresponds to a set of transition values:

(IV) $$d=4+k^2\,, \quad e=6k^2\,. \tag{43}$$

As we see, δx in (42) has now the period $2K$ and equations (43) represent a line-segment connecting the two points (4, 0) and (5, 6).

In this way we have obtained three transition lines. We know from the theory of Hill's equation that one transition line starts from (0, 0) and also that one more line from (4, 0). Moreover, we know that the solutions δx corresponding to these two sets of transition values must have period $2K$.

Hence, we assume tentatively the solution with period $2K$ in the form

$$\delta x=D(k)+\mathrm{sn}^2(\tau, k) \tag{44}$$

where $D(k)$ is a constant with respect to τ but is a function of k. Substitution of (44) into (35) and comparison of the same power of $\mathrm{sn}\,\tau$ results in

$$\left.\begin{aligned} &6k^2-e=0\,,\\ &-4-4k^2+d-eD=0\,,\\ &2+dD=0\,, \end{aligned}\right\}$$

Solving these equations we obtain two sets of transition values

(I) $$\left.\begin{aligned} &d=2+2k^2-2\sqrt{1-k^2+k^4}\,,\\ &e=6k^2\,, \end{aligned}\right\} \tag{45}$$

and

(V) $$\left.\begin{aligned} &d=2+2k^2+2\sqrt{1-k^2+k^4}\,,\\ &e=6k^2\,. \end{aligned}\right\} \tag{46}$$

As one sees, (45) and (46) represent curves between the two points (0, 0) and (2, 6) and the two points (4, 0) and (6, 6) respectively. It should be noted that the e's in (39), (41), (43), (45) and (46) are the same to each other.

Thus, we have obtained the stability diagram as shown in Fig. 6 in which the unstable regions are shown shaded, and each of the transition lines is assigned numbers (I)—(V) for convenience of later use. Of course, stable and unstable regions continue alternately to the right of the figure. Here it may be useful to point out explicitly that this diagram does not provide the whole transition lines of equation (35) for any certain value of modulus k, but only gives the transition points on a horizontal line with ordinate $e=6k^2$. Hence, it is convenient to think of k^2 as a parameter in this diagram.

§ 10. Stability of the Harmonic Oscillation of the Hard System

Consider the mapping of the response diagram (ω, $|A|$-plane) into the plane of stability diagram (d, e-plane) by means of the relation (37). (cf. Fig. 7). If the image of a point in the response diagram falls in the stable (or unstable) regions of the d, e-plane the corresponding forced oscillation is stable (or unstable).

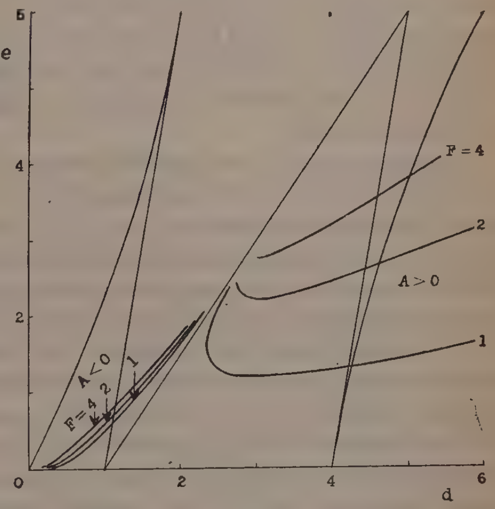

Fig. 7. Map of response curves for the hard system on the stability diagram.

We now determine the unstable regions in the response diagram by examining the (inverse) image of the transition lines of the stability diagram. To begin with, (the lower half of) the line (III) corresponds to free oscillation ($F=0$). The intersection of the out-of-phase branches with the image of (II) is given by equating d and e in (37) with d and e in (39) respectively. The second equations are compatible with each other, while the first equations lead to

$$3\beta A^3+2F=0\,. \tag{47}$$

A point on a response curve $F=\text{const.}$ which has ordinate $|A|$ determined by this equation is a boundary point between stable and unstable regions. The image of (IV) is given by (37) and (43), or

$$3\beta A^3+6\alpha A-8F=0\,. \tag{48}$$

Similarly, the image of (V) is obtained from (37) and (46):

$$3\beta^2A^5+6\alpha\beta A^3-6\beta FA^2+3\alpha^2A-4\alpha F=0\,. \tag{49}$$

In this manner the unstable regions of the response diagram has been determined and they are shown shaded in Fig. 4.

It is familiar to us from the approximate theory that the out-of-phase branches of the response curves with positive tangency ($d|A|/d\omega>0$) are unstable. This corresponds to the 'jump' phenomenon which is characteristic of the theory of nonlinear oscillations. In the present theory, however, the transition points do not coincide with the points of infinite tangency* ($d|A|/d\omega=\infty$). In fact, the relation (47) characterizes the infinite tangency of the response curve (32) of the approximate theory.

The appearance of an unstable region in the in-phase branch which corresponds to a region between the transition lines (IV) and (V) has already been pointed out by Stoker. He has attributed it to possible inaccuracy of the approximate theory for these values of ω. It seems plausible, however, to the present writer that the instability of harmonic solution indicates the occurrence of some other oscillation than the harmonic one. It should be noted that the unstable region begins at a point $\omega=\sqrt{\alpha}/4\pi$ on the ω-axis which is half the value $\omega=\sqrt{\alpha}/2\pi$ for the free oscillation with very small amplitude. Furthermore, there is a sequence of unstable regions which begin at points $\omega=\sqrt{\alpha}/2n\pi$ ($n=3, 4, \cdots$) on the ω-axis.

§ 11. Stability of the Harmonic Oscillation of the Soft System

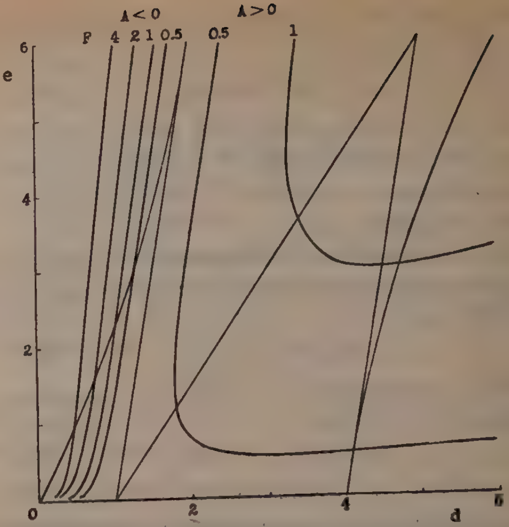

Fig. 8. Map of response curves for the soft system on the stability diagram.

Similar analysis has been applied to determine the stability question of the forced oscillation of the soft system. The results are shown in Fig. 8 and the unstable regions of the response diagram are shaded in Fig. 5. The images of transition lines are given by the following expressions respectively.

(I) and (V) $3\beta^2A^5+6\alpha\beta A^3-6\beta FA^2+3\alpha^2A-4\alpha F=0\,,$ (50)

(III) $3\beta A^3+2F=0\,,$ (51)

(IV) $3\beta A^3+6\alpha A-8F=0\,.$ (52)

The unstable regions which appear in the in-phase branches are of the same character as discussed in the preceding section for the hard system. Hence, they will not require further explanations.

The intersection of the response curve for the free oscillation with the $|A|$-axis is given by $|A_m|=\sqrt{-\alpha/\beta}$. As was mentioned in § 3, this corresponds to the condition that the point of unstable equilibrium is attained asymptotically. For the values of x such that $|x|>|A_m|$ the spring force acts in the repulsive sense. Hence, it may be natural to expect that the forced oscillation becomes unstable if the amplitude $|A|$ exceeds this value $|A_m|$. According to our results it is seen however that the out-of-phase oscillation is unstable** even for the amplitude which is somewhat smaller than $|A_m|$. This interesting feature does not seem to have been pointed out clearly up to the present, although

---

* The result seems to be contradictory to the results of F. John [2] which correlate stability or instability with negative or positive tangency of the response curves for the out-of-phase oscillation.

** See the preceding footnote.

Stoker had expressed in his book a conjecture that the response curves might show peculiarities of one kind or another in the vicinity of these points if they were calculated with greater accuracy than in the approximate theory.

In conclusion, it may be worthwhile to summarize our results. Thus, for a soft system, harmonic oscillations in-phase with the external forces exist, if and only if the amplitude F of the excitation is less than a certain magnitude. When, for such a value of F the jump phenomenon occurs at certain value of ω, the corresponding oscillation of out-of-phase branch is in most cases unstable unless F is sufficiently small. Actually, the motion might diverge at all.

Summary

It has been shown that exact solutions can be obtained for the harmonic oscillations of systems with nonlinear restoring forces under the condition that the harmonic oscillation has a similar wave form to that of the external force. From this condition we have been led to the introduction of the external force represented by the function cn for a hard system and by the function sn in the case of a soft system. Applying the usual definition of infinitesimal stability to the present problem, we have been able to determine the stable or unstable regions in the response diagrams definitely, and thus we have succeeded to clarify a few questions concerning the stability of harmonic oscillations suggested by J. J. Stoker.

Acknowledgements

The writer wishes to express his cordial thanks to Professor S. Tomotika for his kind inspection of the present paper. The writer's thanks are also due to the Ministry of Education for a grant in aid for fundamental scientific research.

References

1) J. J. Stoker, Nonlinear vibrations in mechanical and electrical systems. (1950).

2) F. John, On harmonic vibrations out of phase with the exciting force. Comm. on App. Math., **1** (1948) 341.

JOURNAL OF THE PHYSICAL SOCIETY OF JAPAN Vol. 7, No. 4 JULY—AUG., 1952

Experimental Study of the Spectrum of Isotropic Turbulence, II

By Hiroshi SATO

Institute of Industrial Science, University of Tokyo

(Received December 18, 1951)

In the isotropic turbulent field, energy spectrum was observed by an improved equipment. The measurements were made in a closed channel which was added to the exit cone of an open-type wind-tunnel. A voltage integrator was used to read the fluctuating output of low-frequency components. Low-cut filter attached to the input terminal increased the accuracy at high-frequency region.

Measured spetrum curves are nearly the same as previously reported. The decay of spectral components is severer at high wave-number throughout decay process. The energy transition is estimated from the measurements above mentioned. The wave-number of zero transition decreases as the turbulence decays. Finally, the gradient of spectrum curve is determined by differentiating the spectrum with respect to wind-speed. At medium wave-number region the power index is about -5/3. Three dimensional spectrum is also obtained by this method.

§ 1. Introduction

During recent years, many experiments have been made on the so-called isotropic turbulence in wind-tunnel. There exists, however, no quantitative observation on the energy transfer between different wave-numbers, the transfer being one of the most important problems in the statistical theory of turbulence. As the extension and improvement of previous work[1], this investigation was undertaken in order to clarify the energy flow by determining one-dimensional spectrum and decay law of spectral components at various wave-numbers. Additional measurements were made to know the power index of spectrum against wave-number which was discussed by several authors theoretically. An alternative method was adopted to check it directly.

§ 2. Equipment

Some improvements were made to the equipment previously reported[1]. An open-jet type wind-tunnel was used, but the measurements were made in a closed channel which was added down-stream of the original exit cone to prevent the free jet mixing. The added channel is about 2.5 m long having the same rectangular cross-section as the exit and diverging slightly to make the wind-speed uniform along its axis. After the divergence was adjusted, the difference in wind-speed was made within one percent.

It is a well-known phenomenon that the spectral components of low-frequency fluctuate with a very long period. The narrower the filter band-breadth is, the severer the fluctuation becomes. The method adopted by several experimenters to overcome this difficulty is to use a Galvanometer of a very long period (for instance, Fluxmeter[2]). The author constructed a new instrument as suggested by reference (3) (Fig. 1). The D. C. voltage across the vacuo-junction is converted to 50 cps. A.C. and amplified to rotate an integrating watt-hour meter. By this means, it is possible not only to take averages for a

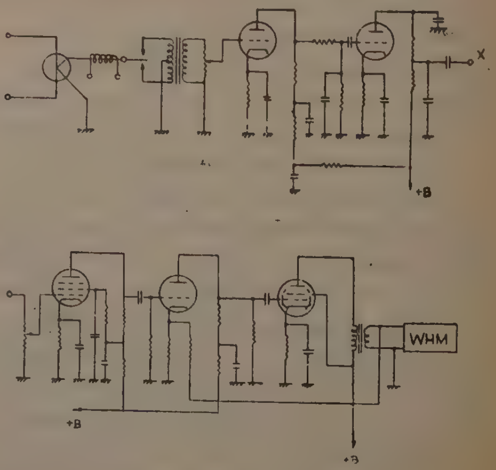

Fig. 1. Circuit diagram of voltage integrator.

very long time interval, but also to observe the statistical characteristics of spectral components, about which detailed description will be given later. Input and revolution characteristics of the integrator are shown in Fig. 2. Grid, hot-wire anemometer, amplifier, filter and other accessories are the same as those of the previous experiments¹⁾.

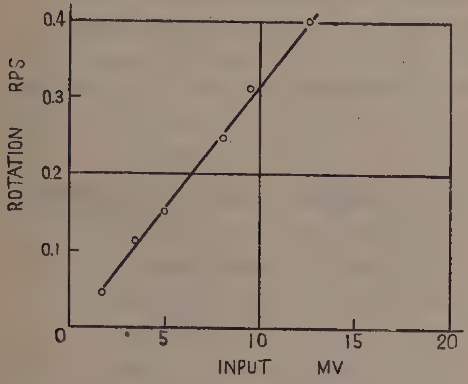

Fig. 2. Characteristics of integrator.

§ 3. One-Dimensional Spectrum of $\overline{u}^2$

One-dimensional spectrum of $\overline{u}^2$ was observed with some improvements.

(1) The low-frequency components were measured by the voltage integrator as described above. A typical result is shown in Fig. 3. It is obvious that in this case more than ten revolutions are necessary to take means of output. The scatter of measured points seems to express one of the statistical characteristics of turbulence and a more detailed investigation is now in progress.

(2) In the high-frequency range, turbulent energy is very small and the sensitivity of hot-wire falls down. So, the non-cut-off characteristics of filter and small distortion of amplifier make the results erroneous. To eliminate the influence of low-frequency components, a simple capacitance-resistance low-cut filter was placed at the input terminal of amplifier. C and R were adjusted according to the tuning frequency of the filter.

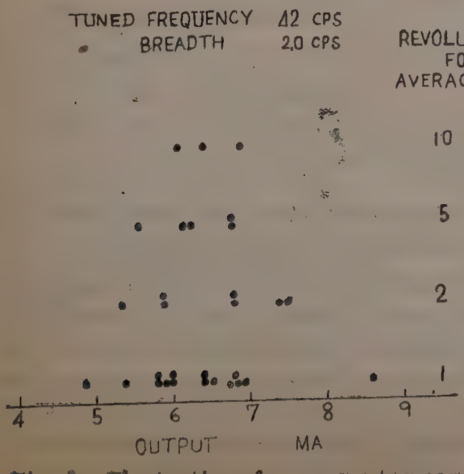

Fig. 3. Fluctuation of components measured by integrator.

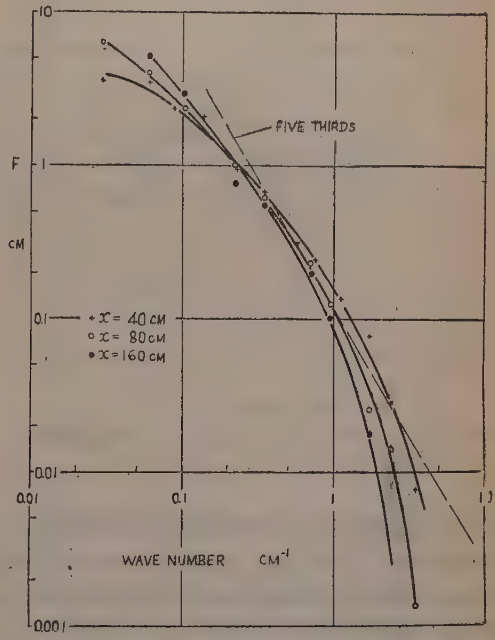

Fig. 4. One-dimensional spectrum of u^2, $U=10$ m·s^{-1}.

The results obtained are shown in Fig. 4. It is nearly the same as those reported by many authors. We observe that the decay of high-frequency component is severer than that in low-frequency region. This information is verified by direct measurement.

§ 4. Decay of Spectral Components

An alternative method for measuring directly the decay of spectral components was proposed in the previous report¹⁾. The same method was adopted. We moved the hot-wire longitudinally with tuning frequency fixed. In the low- and high-frequency region the same attentions were paid as for spectrum measurements. In the high-frequency region decay is severer and the power index of decay against the distance from grid reaches −2.5 in contrast to −1 for total energy (Fig. 5). This result shows discrepancy with that previously obtained[1]. The reason may be explained as the effect of jet mixing. The previous experiment was performed in an open jet, whereas the present measurement was made in the closed channel. The turbulent energy of mixing may be small but it seems to contain rather high wave-number components. It is a problem which needs more detailed experiments.

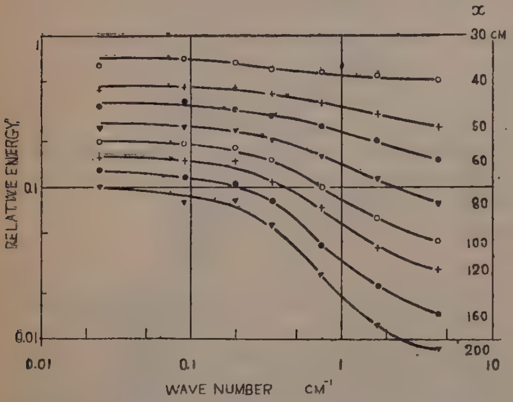

Fig. 5. Decay of spectral components, U=10 m·s^{-1}.

§ 5. Estimation of Transition Function

From the measured spectrum and the data of components decay, we can estimate the energy transference between different wave-numbers. The propagation of correlation in isotropic turbulence is[4]

$$\frac{\partial \overline{u}^2 f}{\partial t} = -2\nu\overline{u}^2\left(\frac{\partial}{\partial r}+\frac{4}{r}\right)\left(\frac{\partial f}{\partial r}-\frac{h}{r}\sqrt{\overline{u}^2}\right),$$

where f and h are double and triple correlations respectively and ν is kinematic viscosity.

By Fourier transformation it becomes

$$\frac{\partial \overline{u}^2 F}{\partial t}+2(\overline{u}^2)^{3/2} W$$
$$= -2\nu\overline{u}^2\left(fk^2+4\int_k^\infty Fkdk\right),$$

where W is the energy transfer between wave-numbers.

Putting $k=2\pi k$, $x=Ut$ we get

$$4\pi\sqrt{\overline{u}^2}\,W = -FU\frac{\partial \log \overline{u}^2 F}{\partial x}$$
$$-8\pi^2\nu F k^3 - 32\pi^2\nu\int_k^\infty Fkdk.$$

Three terms on the right side can be calculated from measurements (Fig. 6). Results obtained from faired curves show that the zero transition and maximum flow-in both move to the lower wave-number as the distance from grid increases.

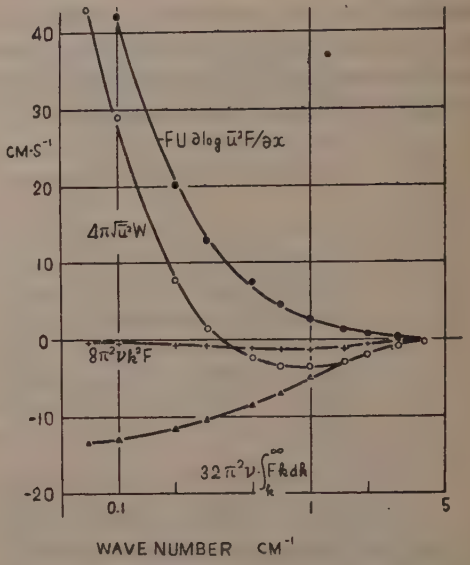

Fig. 6. Estimation of transition function, U=10 m.s^{-1}, x=80 cm.

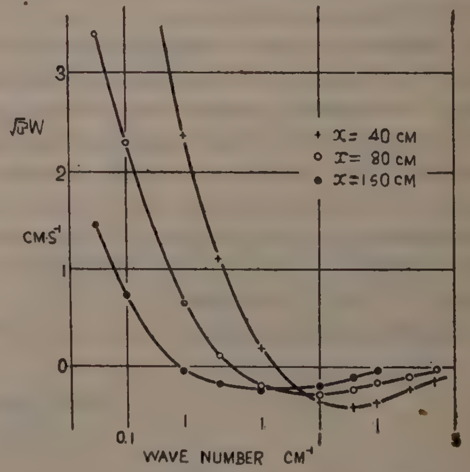

Fig. 7. Transition function at various positions, U=10 m.s^{-1}.

§ 6. Differentiation of Spectrum Curve with Respect to Wind-Speed

The gradient or power index of spectrum against wave-number is often discussed by many authors. The spectrum dealt with in theoretical considerations is usually the three-dimentional one which must be deduced by differentiating twice the one-dimentional spectrum with respect to wave-number. The accuracy of measured spectrum is not sufficient to be differentiated. We therefore tried to seek the spectrum dependency on wave-number by changing wind-speed instead of frequency, using the relation $k=\omega/U$ (where k is wave-number, ω frequency and U wind-speed). In spite of the complexity of turbulence producing mechanism, the general wind stream may be considered as the carrier of turbulence. This assumption may be invalid at high wave-number but in medium range it is approximately verified by experiments.

The output of filter at tuning frequency ω can be expressed as

$$E_\omega=\overline{u}^2\cdot s^2\cdot m^2\cdot G^2\cdot b\cdot F\,,$$

where s: sensitivity of hot-wire

m: relative sensitivity at frequency ω, taking the value at $\omega=0$ as unity

G: over-all gain of amplifier and filter

b: effective band-breadth of filter

As b is proportional to $1/U$,

$$D=\frac{\partial\log F}{\partial U}=\frac{\partial\log E_\omega}{\partial U}-\frac{\partial\log E}{\partial U}-2\frac{\partial\log m}{\partial U}+\frac{1}{U}\,,$$

where $E=G^2\cdot\overline{u}^2\cdot s^2$.

Terms on the right side can be obtained from measurements with sufficient accuracy. Then,

$$\frac{\partial F}{\partial U}=F\cdot D$$

$$\frac{\partial\log m}{\partial U}=\frac{\partial}{\partial U}\log\frac{1}{\sqrt{1+M^2\omega^2}}=-\frac{M^2\omega^2}{1+M^2\omega^2}\,\frac{\partial}{\partial U}\log M\,,$$

where M is the time constant of hot-wire introduced by Dryden[5].

Putting $F=F_0(k/k_0)^{-n}$, we get

$$\partial\log F/\partial U=n/U$$

where $n=UD$.

Further, in the isotropic field three-dimensional spectrum F_* is given by

$$F_*=\frac{1}{3}k^3\frac{d}{dk}\left(\frac{1}{k}\,\frac{dF}{dk}\right)$$

Substituting $k=\omega/U$,

$$F_*=U\left(\frac{\partial F}{\partial U}+\frac{U}{3}\,\frac{\partial^2F}{\partial U^2}\right)=\frac{1}{3}CF,$$

where

$$C=3UD+(UD)^2+U^2\left(\frac{\partial D}{\partial U}\right).$$

Output of amplifier changes with varying wind-speed as shown in Fig. 8. The scatter of measured points is rather small compared with that of spectrum curve. D is calculated

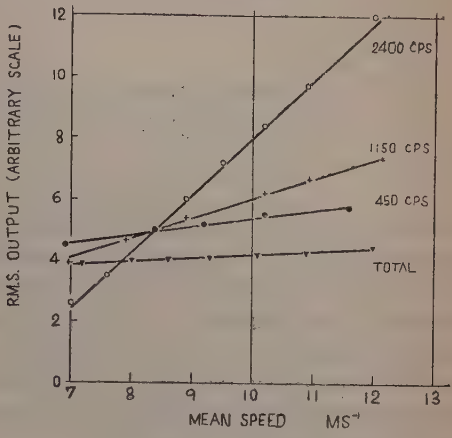

Fig. 8. Output with various wind-speed.

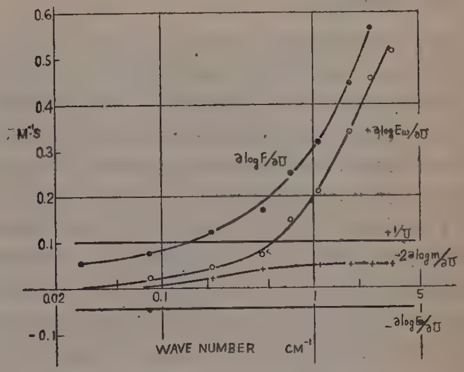

Fig. 9. Calculation of power index of one-dimensional spectrum, $U=10\,\mathrm{m\cdot s^{-1}}$ $x=80$ cm.

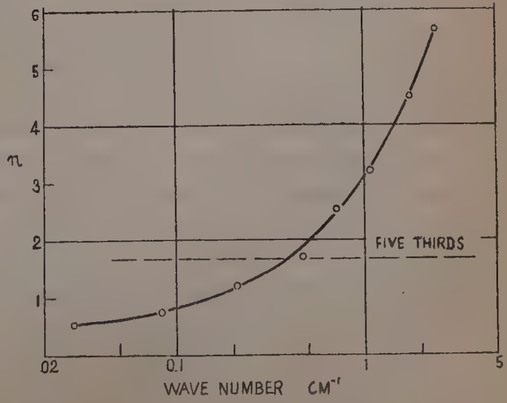

Fig. 10. Power index of spectrum, $U=10\,\mathrm{m\cdot s^{-1}}$ $x=80$ cm.

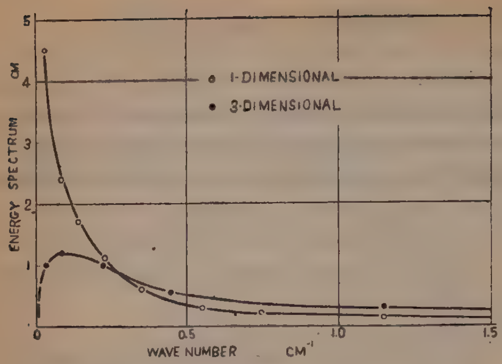

Fig. 11. Three-dimensional spectrum of $\bar{u}^2$.

as shown in Fig. 9, and n for $U=10$ m/s is given in Fig. 10. In spite of the restricted validity of this method $-5/3$ law is verified at medium wave-number. Although the accuracy of calculated C may not be enough to make quantitative discussion, three-dimensional spectrum (Fig. 11) seems to have zero value at vanishing wave-number.

§ 7. Conclusion

From the measurements of isotropic turbulent field, following results were obtained.

(1) One-dimensional spectra of $\overline{u}^2$ measured by the improved equipment are nearly the same as those previously reported, but the accuracy is slightly higher.

(2) The decay law of spectral components is different from that measured in a free jet. The power index of energy decay changes from -1 to -2.5 as the wave-number increases. The decay of total energy represented by the medium wave-number components is inversely proportional to the distance behind grid.

(3) Energy transition between different wave-numbers is estimated from spectrum and decay of components. It is seen that the wave-numbers for zero transition and maximum flow-in decrease in the process of decaying.

(4) The $-5/3$ law of spectrum is verified in the medium range by a new technique, that is, by differentiating the spectrum with respect to wind-speed.

(5) Three-dimensional spectrum was deduced by the same method.

This investigation was made possible by the financial aid from the Ministry of Education.

The author would like to express his appreciation to Prof. I. Tani and Prof. H. Kumagai for their valuable encouragements and advices. His hearty thanks are also due to Mr. H. Shono for the helpful criticism and to Mr. K. Seimiya for the assistance in measurements.

References

1) H. Sato: J. Phys. Soc. Japan **6** (1951) 388-393.

2) S. Corrsin and M. S. Uberoi: NACA Tech. Note **2124** (1950).

3) E. A. Hamacher: Rev. Sci. Instr. **17** (1946) 364-367.

4) Th. v. Kármán and L. Howarth: Proc. Roy. Soc. A **164** (1938) 192-215.

5) H. L. Dryden and A. M. Kuethe: NACA Tech. Rep. **342** (1930).

JOURNAL OF THE PHYSICAL SOCIETY OF JAPAN Vol. 7, No. 4 JULY—AUG., 1952

Dynamical Theory of Electron Diffraction for a Finite Polyhedral Crystal* **

I. Extension of Bethe's Theory

By Norio KATO***

Physical Institute, Nagoya University, Nagoya, Japan

(Received February 22, 1952)

Bethe's dynamical theory of electron diffraction has been extended by an approximate treatment first to the case of a wedge-shaped crystal, next to the case of a wedge-shaped crystal covered by opaque screens with an aperture and finally to the most general case of a polyhedral crystal of finite extension. If the incident wave, $\Phi_{\mathrm{I}}=\Psi_{\mathrm{I}}\exp j(\boldsymbol{K}_{\mathrm{I}}\cdot\boldsymbol{r})$, impinges on the entrance surface, S_e, and the transmitted and diffracted (interfracted) wave leave the crystal from the exit surface, S_a, their wave functions are given as a superposition of plane waves;

$$\text{the transimtted wave}:\quad \Phi_0(\boldsymbol{r})=\sum_{i=1,2}\int\Psi_0^{(i)}(\boldsymbol{K}_0)\exp j(\boldsymbol{K}_0\cdot\boldsymbol{r})d\boldsymbol{K}_0$$

$$\text{the diffracted wave}\quad:\quad \Phi_g(\boldsymbol{r})=\sum_{i=1,2}\int\Psi_g^{(i)}(\boldsymbol{K}_g)\exp j(\boldsymbol{K}_g\cdot\boldsymbol{r})d\boldsymbol{K}_g$$

Here, the amplitude functions, $\Psi_0^{(i)}(\boldsymbol{K}_0)$ and $\Psi_g^{(i)}(\boldsymbol{K}_g)$, are as follows;

$$\Psi_0^{(i)}(\boldsymbol{K}_0)=\Psi_{\mathrm{I}}\int\frac{c^{(1)}c^{(2)}}{c^{(1)}-c^{(2)}}\cdot\frac{(-1)^i}{c^{(i)}}\cdot\mathrm{L}(\boldsymbol{K}_{\mathrm{I}}-\boldsymbol{k}_0^{(i)}\,;\ S_e)\mathrm{L}(\boldsymbol{k}_0^{(i)}-\boldsymbol{K}_0\,;\ S_a)d\boldsymbol{k}_0^{(i)}$$

$$\Psi_g^{(i)}(\boldsymbol{K}_g)=\Psi_{\mathrm{I}}\int\frac{c^{(1)}c^{(2)}}{c^{(1)}-c^{(2)}}(-1)^i\mathrm{L}(\boldsymbol{K}_{\mathrm{I}}-\boldsymbol{k}_0^{(i)}\,;\ S_e)\mathrm{L}(\boldsymbol{k}_g^{(i)}-\boldsymbol{K}_g\,;\ S_a)d\boldsymbol{k}_g^{(i)}$$

where $c^{(i)}$ is the amplitude ratio of the primary and secondary (interfracted) waves in crystal which are related to the i-branch of the dispersion surface, and $\boldsymbol{k}_0^{(i)}$ and $\boldsymbol{k}_g^{(i)}=\boldsymbol{k}_0^{(i)}+2\pi\boldsymbol{g}$ are their wave vectors. The function L means the diffraction function due to an aperture S and expressed as

$$\mathrm{L}(\boldsymbol{K}-\boldsymbol{k}\,;\mathrm{S})=\int_s\exp j(\boldsymbol{K}-\boldsymbol{k}\cdot\boldsymbol{r}_s)d\boldsymbol{r}_s\,.$$

The most general expressions of the transmitted and diffracted waves for a finite polyhedral crystal are given as the sum of the waves mentioned above for every pair of the entrance and exit surface.

§ 1. Introduction

The resolving power of electron diffraction cameras has been recently much enhanced by the application of the technique developed in electron microscopy[1], leading to the discovery of the fine structures of diffraction patterns[2]. Sturkey & Frevel and Hillier & Baker found some of Debye-Scherrer rings due to MgO to be not single but multiple. They found that (222) and (220) rings, for example, are split respectively into doublet and quintet. Other authors[3][4], thereafter, observed the multiple structures not only in Debye-Scherrer rings, but also in Laue spots that make part of them. They attributed these phenomena to refraction effect of electrons by crystallite of regular geometrical shape, and explained it quantitatively by Snell's law in geometrical optics. This effect is called simple refraction in this paper.

Cowley & Rees[4] and Sturkey[5], however, observed in MgO that Laue spots, which are split by the effect mentioned above, are further split into doublet. Sturkey pointed out that this phenomenon can be explained by the dynamical theory of diffraction and gave

---

* The expence of this study was defrayed from the Grant in Aid for Fundamental Scientific Research of the Educational Ministry.

** A short summary of this paper has appeared in *Acta Cryst.* (1950) **4**, 227.

*** Now at Kobayasi Institnte of Physical Research, Kokubunji, Tokyo, Japan.

a formula for the angular distance between the double spots. We now call this effect, following Sturkey, double refraction, though it has nothing to do with the same term used in crystal optics.

Independently of Sturkey's investigation, the author[6] developed the dynamical theory of electron diffraction for wedge-shaped crystal, applied it on our experiment carried out earlier concerning lattice constant[7], and obtained a more rigorous formula than that of Sturkey by taking the boundary condition into account. According to our result the double refraction should be observed in most of low-order reflections. Actually, however, it was not observed as often as expected by the theory although the effect due to simple refraction has been observed consistently. This shows that we are in need of a new theory of electron diffraction applicable generally to a finite polyhedral crystal, in which splitting of Laue spot is fully taken into account.

Bethe[8] was the first to have developed a complete dynamical theory of electron diffraction for a crystal slab bounded by the parallel planes. He treated, however, only the Bragg case of reflection. Several other workers[9] extended his theory also to the Laue case, but their treatments were limited to the case of parallel planes as by Bethe. A more general mathematical formulation for a finite crystal was first given by Ekstein[10] (in the case of X-ray). His approach in its original form, however, is not capable of direct application for interpreting experimental result.

In the present paper, we intended to develope Bethe's theory by posturating certain approximations and to make it applicable to the case of a finite polyhedral crystal. After a short outline of Bethe's theory is given, we proceed to the necessary formulation by extending the boundary conditions step by step. The comparison of theory and experiment will be given in the next paper.

§ 2. The Case of Parallel Plate Crystal (Bethe's Theory)

(a) Wave function in periodic potential.

The wave function in the crystal, $\phi(\boldsymbol{r})$, should satisfy Schrödinger's equation

$$\Delta\phi(\boldsymbol{r})+\frac{8\pi^2 me}{h^2}[E+V(\boldsymbol{r})]\phi(\boldsymbol{r})=0\,, \qquad (1)$$

where all the notations bear their usual nomenclature. The potential $V(\boldsymbol{r})$ can be expanded in a Fourier series as follows

$$\frac{2me}{h^2}V(\boldsymbol{r})\equiv U(\boldsymbol{r})=\sum_{h}U_h \exp \mathrm{j}(\boldsymbol{h}\cdot\boldsymbol{r})\,, \qquad (2)$$

where $j=2\pi i$ (i: imaginary unit) and $\boldsymbol{h}$ is a vector representing a reciprocal lattice point

$$\boldsymbol{h}=h_1\boldsymbol{b}_1+h_2\boldsymbol{b}_2+h_3\boldsymbol{b}_3\,. \qquad (3)$$

The wave function $\phi(\boldsymbol{r})$ can be expanded in a form

$$\phi(\boldsymbol{r})=\sum_{\boldsymbol{g}}\psi_{\boldsymbol{g}} \exp j(\boldsymbol{k}_{\boldsymbol{g}}\cdot\boldsymbol{r})\,, \qquad (4)$$

where

$$\boldsymbol{k}_{\boldsymbol{g}}=\boldsymbol{k}_0+\boldsymbol{g}\,, \qquad (5)$$

ψ_0 means the amplitude of the primary wave and ψ_g that of reflected wave by a net plane $\boldsymbol{g}$*.

By substituting eqs. (2) and (4) into eq. (1), the latter is turned into a set of linear homogeneous equations

$$(\kappa^2-k_g{}^2)\psi_g+\Sigma\psi_{g-h}U_h=0\,, \qquad (6)^{**}$$

where $k_g=|\boldsymbol{k}_g|$ and

$$\kappa^2=\frac{2me}{h^2}(E+V_0)=K^2+U_0\,. \qquad (7)$$

Since the amplitude of interfracted wave ψ_g become appreciable only when the resonance facter $(\kappa^2-k_g{}^2)$ is small, eqs. (6) are reduced to a finite set of equations in practical application. In the present paper, the simplest case is treated where only two waves, the primary and an interfracted, are predominating over the others. Then, according to the Bethe's procedures, eqs. (6) are reduced to

$$\begin{bmatrix} \kappa_0{}^2-k_0{}^2 & U_{0g} \\ U_{g0} & \kappa_g{}^2-k_g{}^2 \end{bmatrix}\begin{bmatrix} \psi_0 \\ \psi_g \end{bmatrix}=0 \qquad (8)$$

where***

$$\kappa_0{}^2=K^2+U_{00}\,,\quad \kappa_g{}^2=K^2+U_{gg} \qquad (8\,\mathrm{a})$$

$$U_{00}\doteq U_0-\sum_{h}{}''U_hU_{-h}/(\kappa^2-k_h{}^2)\,,$$

$$U_{gg}=U_0-\sum_{h}{}''U_{h-g}U_{g-h}/(\kappa^2-k_h{}^2) \qquad (8\,\mathrm{b})$$

---

* In the following descriptions, the term diffraction is used for *diffraction by an external form of crystal or by an aperture in an infinite plane screen. Diffraction by crystal lattice* is called *reflection* (by a net plane) or *interfraction. cf.* Thomson and Cochrane; *Theory and Practice of Electron Diffraction*, 1939, p. vii.

** In the following descriptions suffices $\boldsymbol{g}$ or $\boldsymbol{h}$ are replaced by g or h for brevity.

*** Summary of notations, with references to Bethe's is given in the appendix.

$$U_{0g}=U_{-g}-\sum_h{}'' U_{-h}U_{h-g}/(\kappa^2-\boldsymbol{k}_h^2)\,,$$
$$U_{g0}=U_g-\sum_h{}'' U_hU_{g-h}/(\kappa^2-\boldsymbol{k}_h^2)\,. \qquad (8\,\mathrm{c})$$

In the following descriptions, the terms U_i and U_{ij} are called kinematical and dynamical structure factor respectively and U_{00} and U_{gg} are called apparent inner potential for primary and interfracted beam respectively.

On eliminating ψ_g/ψ_0 in eq. (8), we get

$$\begin{vmatrix} \kappa_0^2-k_0^2 & U_{0g} \\ U_{g0} & \kappa_g^2-k_g^2 \end{vmatrix}=0\,. \qquad (9)$$

This gives the dispersion surface (equi-energy surface) for an energy E. Since the resonance factor is small, eq. (9) is reduced to

$$\begin{vmatrix} 2\kappa_0(\kappa_0-k_0) & U_{0g} \\ U_{g0} & 2\kappa_g(\kappa_g-k_g) \end{vmatrix}=0\,. \qquad (9')$$

This gives hyperbolic surfaces as shown in Fig. 1. The meaning of the notations in the figure is given in the legend. If a wave point is given on the dispersion surface, the ratio of the amplitude of primary and interfracted waves is determined by eq. (8) as follows

$$c=\psi_g/\psi_0=2\kappa_0(\kappa_0-k_0)/(-U_{0g})$$
$$=(-U_{g0})/2\kappa_g(\kappa_g-k_g)\,. \qquad (10)$$

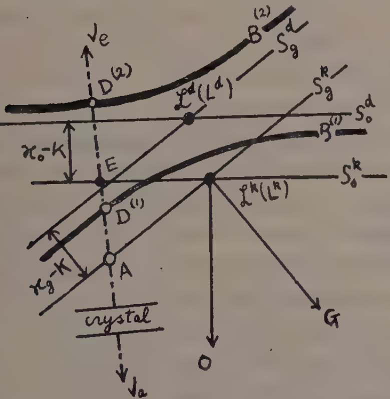

Fig. 1. Dispersion surface and wave points for parallel plate crystal. The surface is guided by a straight line vertical to the plane of this figure.

O and G: The origin and an lattice point of reciprocal lattice respectively; $\overrightarrow{\mathrm{OG}}=\boldsymbol{g}$.

Plane of this figure is determined by the vectors $\boldsymbol{g}$ and $\boldsymbol{K}_\mathrm{I}=\overrightarrow{\mathrm{EO}}$.

S_0^k and S_g^k: Spheres of radius K, drawn O and G as center respectively.

S_0^d and S_g^d: Spheres of radius κ_0 and κ_g, drawn O and G as center respectively.

These spheres can be expressed by planes under the present approximation, as shown in the figure.

L^k: Kinematical Laue circle, *i.e.*, intersection of S_0^k and S_g^k.

L^d: Dynaimcal Laue circle, *i. e.*, intersection of S_0^d and S_g^d.

$\mathcal{L}^k$: Kinematical Laue point. $\mathcal{L}^d$: Dynamical Laue point.

They are intersection of the plane of this figure with L^k and L^d respectively.

$\angle \mathrm{O}\mathcal{L}^k\mathrm{G}=2\theta_\mathrm{B}$ where θ_B is Bragg angle.

$\mathrm{B}^{(1)}$ and $\mathrm{B}^{(2)}$: Two branches of dispersion surface, approximately hyperbolic surfaces whose asymptotic surfaces are S_0^d and S_g^d.

ν_e and ν_a: Normal of the entrance and exit surface. Since they don't lie on the plane of this figure in general, their projection is shown by dotted lines in this figure.

E and A: Wave points of the transmitted primary and reflected wave respectively. E is also that of the incident wave simultaneously.

$\mathrm{D}^{(1)}$ and $\mathrm{D}^{(2)}$: Wave points of the crystal waves.

A, $\mathrm{D}^{(1)}$ and $\mathrm{D}^{(2)}$ are denoted by open circle since they are projection to the plane of the figure.

Notations of wave vectors are as follows:

Vacuum wave

Incident : $\boldsymbol{K}_\mathrm{I}=\overrightarrow{\mathrm{EO}}$
Transimitted primary : $\boldsymbol{K}_0=\overrightarrow{\mathrm{EO}}$
,, reflected : $\boldsymbol{K}_g=\overrightarrow{\mathrm{AG}}$

Crystal wave

Primary : $\boldsymbol{k}_0^{(1)}=\overrightarrow{\mathrm{D}^{(1)}\mathrm{O}}$, $\boldsymbol{k}_0^{(2)}=\overrightarrow{\mathrm{D}^{(2)}\mathrm{O}}$
Reflected : $\boldsymbol{k}_g^{(1)}=\overrightarrow{\mathrm{D}^{(1)}\mathrm{G}}$, $\boldsymbol{k}_g^{(2)}=\overrightarrow{\mathrm{D}^{(2)}\mathrm{G}}$

(b) Determination of wave vectors.

We now write the incident wave in the vacuum as

$$\Phi_\mathrm{I}(\boldsymbol{r})=\Psi_\mathrm{I}\exp j(\boldsymbol{K}_\mathrm{I}\cdot\boldsymbol{r})\,, \qquad (11)$$

where $|\boldsymbol{K}_\mathrm{I}|=K$. The wave points of crystal waves for a given $\boldsymbol{K}_\mathrm{I}$ are determined by the requirement of tangential continuity of wave vectors on the crystal surface. The procedures to determine them is as follows. In Fig. 1, E is the wave point of the incident wave, *i. e.* $\overrightarrow{\mathrm{EO}}=\boldsymbol{K}_\mathrm{I}$. Let $\nu_e(E)$* be the normal of the entrance surface passing through the point E, then the wave points of the crystal waves are given as the intersection of ν_e(E) and the dispersion surface. These points are always real in Laue case and become imaginary in the region of total reflection of Bragg case. In the present paper only the Laue case is treated by the reasons which will be explained in § 5. In Laue case, two wave points $D^{(1)}$ and $D^{(2)}$*, lie on the different branches of the hyperbolic surface. It is seen, then, that a pair of wave appears in the crystal for primary and reflected wave respectively.

---

* In the following descriptions, a normal ν through a point, say P, is denoted by ν(P), and the unit vector in the direction of ν by $\boldsymbol{\nu}$ in general.

The wave points of the primary and interfracted waves** in vacuum of the exit side are also determined by the similar procedures. Since the entrance and the exit surface are parallel in the present case, the wave points of transmitted waves derived from $D^{(1)}$ and $D^{(2)}$ coincide to each other. Thus double refraction is never observed explicitly in the case of parallel slab.

(c) Determination of amplitudes.

If the wave vectors are determined by the above procedure as illustrated in Fig. 1, the ratio of amplitude can be obtained by eq. (10). Then, the wave function in the crystal is expressed as follows

$$\left.\begin{aligned} \phi(\boldsymbol{r}) &= \phi_0(\boldsymbol{r})+\phi_g(\boldsymbol{r})=\sum_i\{\phi_0^{(i)}(\boldsymbol{r})+\phi_g^{(i)}(\boldsymbol{r})\} \\ \phi_0^{(i)}(\boldsymbol{r}) &= \psi_0^{(i)}\exp j(\boldsymbol{k}_0^{(i)}\cdot\boldsymbol{r}) \\ \phi_g^{(i)}(\boldsymbol{r}) &= c^{(i)}\psi_0^{(i)}\exp j(\boldsymbol{k}_g^{(i)}\cdot\boldsymbol{r}) \end{aligned}\right\}, \quad (12)$$

where (i) means (1) or (2). Similarly, the wave function of the transmitted waves can be expressed by

$$\left.\begin{aligned} \Phi(\boldsymbol{r}) &= \Phi_0(\boldsymbol{r})+\Phi_g(\boldsymbol{r}) \\ \Phi_0(\boldsymbol{r}) &= \Psi_0\exp j(\boldsymbol{K}_0\cdot\boldsymbol{r}) \\ \Phi_g(\boldsymbol{r}) &= \Psi_g\exp j(\boldsymbol{K}_g\cdot\boldsymbol{r}) \end{aligned}\right\}. \quad (13)$$

To determine the amplitude $\psi_0^{(i)}$, Ψ_0 and Ψ_g in term of Ψ_{I}, the boundary conditions must be taken into account. They are expressed by

$$\Phi(\boldsymbol{r}_s)=\phi(\boldsymbol{r}_s)\,, \quad (14\,\mathrm{a})$$

$$\frac{\partial}{\partial\nu}\Phi(\boldsymbol{r}_s)=\frac{\partial}{\partial\nu}\phi(\boldsymbol{r}_s)\,, \quad (14\,\mathrm{b})$$

where $\Phi(\boldsymbol{r}_s)$ and $\phi(\boldsymbol{r}_s)$ are wave functions on both sides of the boundary surface, $\boldsymbol{r}_s$ the current vector indicating a point on the surface and $\frac{\partial}{\partial\nu}$ the differentiation along its normal. In the present case, however, the tangential continuity of wave vectors is already taken into account. Therefore, eq. (14 a), when applied to the entrance and exit surfaces, is rewritten as

$$\left.\begin{aligned} \sum_i\phi_0^{(i)}(\boldsymbol{r}_e) &= \Phi_{\mathrm{I}}(\boldsymbol{r}_e) \\ \sum_i\phi_g^{(i)}(\boldsymbol{r}_e) &= 0 \end{aligned}\right\} \text{ on } F_e \quad (15)$$

$$\left.\begin{aligned} \Phi_0(\boldsymbol{r}_a) &= \sum_i\phi_0^{(i)}(\boldsymbol{r}_a) \\ \Phi_g(\boldsymbol{r}_a) &= \sum_i\phi_g^{(i)}(\boldsymbol{r}_a) \end{aligned}\right\} \text{ on } F_a\,, \quad (16)$$

where F_e and F_a denote the entrance and exit surface respectively, and $\boldsymbol{r}_e$ or $\boldsymbol{r}_a$ is current vecter indicating a point on F_e or F_a. These equations give four conditions to determine four unknown quantities, $\psi_0^{(1)}$, $\psi_0^{(2)}$, Ψ_0 and Ψ_g. Therefore, if (14 b) is taken into account moreover, the number of equations becomes twice the number of the unknown amplitudes. This apparent paradox is caused by the approximate treatment now adopted: *i. e.* eq. (9′) is used instead of eq. (9). In Laue case, however, it is usual that the normal components of all wave vectors are large compared with differences among themselves, *i. e.*

$$\left.\begin{aligned} |(\boldsymbol{K}_{\mathrm{I}}\cdot\boldsymbol{\nu}_e)| &\gg |(\boldsymbol{K}_{\mathrm{I}}-\boldsymbol{k}_0^{(i)}\cdot\boldsymbol{\nu}_e)| \\ |(\boldsymbol{K}_g\cdot\boldsymbol{\nu}_a)| &\gg |(\boldsymbol{k}_g^{(i)}-\boldsymbol{K}_g\cdot\boldsymbol{\nu}_a)| \end{aligned}\right\}. \quad (17)$$

Under these condition (14 a) and (14 b) are approximately equivalent and the apparent paradox is elucidated. The following calculation hold only under these conditions***.

By substituting (11) and (12) in (15), the amplitudes of crystal waves, turn out to be

$$\begin{aligned} \psi_0^{(i)} &= \frac{c^{(1)}c^{(2)}}{c^{(1)}-c^{(2)}}\,\frac{(-1)^i}{c^{(i)}}\Psi_{\mathrm{I}}\exp j(\boldsymbol{K}_{\mathrm{I}}-\boldsymbol{k}_0^{(i)}\cdot\boldsymbol{R}_e) \\ \psi_g^{(i)} &= c^{(i)}\psi_0^{(i)} \end{aligned} \quad (18)$$

where $(-1)^i$ means -1 or $+1$ respectively for (1) and (2), and $\boldsymbol{R}_e$ means the special case of $\boldsymbol{r}_e$ when it is normal to the entrance surface.

Similarly, upon inserting (12), (13) and (18) into (16), the amplitudes of transmitted waves turn out to be

$$\Psi_0=\frac{c^{(1)}c^{(2)}}{c^{(1)}-c^{(2)}}\Psi_{\mathrm{I}}\sum_i\frac{(-1)^i}{c^{(i)}}\exp j(\boldsymbol{K}_{\mathrm{I}}-\boldsymbol{k}_0^{(i)}\cdot\boldsymbol{R}_e)\exp j(\boldsymbol{k}_0^{(i)}-\boldsymbol{K}_0\cdot\boldsymbol{R}_a)\,, \quad (19\,\mathrm{a})$$

$$\Psi_g=\frac{c^{(1)}c^{(2)}}{c^{(1)}-c^{(2)}}\Psi_{\mathrm{I}}\sum_i(-1)^i\exp j(\boldsymbol{K}_{\mathrm{I}}-\boldsymbol{k}_0^{(i)}\cdot\boldsymbol{R}_e)\exp j(\boldsymbol{k}_g^{(i)}-\boldsymbol{K}_g\cdot\boldsymbol{R}_a)\,, \quad (19\,\mathrm{b})$$

---

* In the following descriptions, a quantity, say X, pertaining to $B^{(1)}$ or $B^{(2)}$ branch of the dispersion surface is denoted respectively by $X^{(1)}$ or $X^{(2)}$.

** In the followings, the waves in vacuum of exit side are called the transmitted waves. They consist of primary and interfracted waves.

*** The reduction of eq. (9) to (9′) implies that the reflected waves on the boundary surfaces are neglected. When the conditions (17) fail, the reflected waves should be taken into account.

where $\boldsymbol{R}_a$ has the similar meaning as $\boldsymbol{R}_e$ corresponding to the exit surface.

It must be noted here, that the crystal waves are determined by the conditions on the entrance surface independently of those on the exit surface. Although this fact holds approximately only under the conditions (17), it is very important for the extension of the theory.

§ 3. The Case of Wedge-Shaped Crystal

As the first step of extension of the theory, the case of a wedge-shaped crystal[6] is briefly treated in this section. Here, a wedge-shaped crystal means to have two surfaces not parallel to each other and their area is considered to be large enough so that the tangential continuity of wave vectors holds approximately.

Let us assume here, for simplicity, that the incident beam irradiate only one of the surfaces, the entrance surface, and both the primary and interfracted beam excited in the crystal leave the crystal from the other surface, the exit surface. Let us further assume that the wave vectors of beams do not make small angle with the boundary surfaces so that the conditions corresponding to (17) in the preceding section do not fail.

Under these assumptions, the crystal waves are determined by the entrance surface independently of the exit surface as shown in the previous paper[6]. Therefore, it is sufficient only to obtain transmitted waves which are connected with the crystal waves on the exit surface.

(a) Determination of transmitted waves.

The procedure to determine the wave points of transmitted waves is illustrated in Fig. 2. Since the normals ν_e and ν_a are not parallel in the present case, the two wave points, $E^{(i)}$, of transmitted primary waves do not coincide with that of the incident, E, and they are separated from each other. Similarly, those of the interfracted, $A^{(i)}$, are also separated. Thus the effect of double refraction should be observed in the transmitted waves. It must be noted here, however, that the double refraction described above is related with the assumption that eq. (6) is reduced to eq. (8). In general, N-ple refraction is expected if the secular equation is reduced to that of order N.

The wave functions of the transmitted wave, by adopting wave vectors given in Fig. 2, are expressed as follows,

$$\Phi(\boldsymbol{r})=\Phi_0(\boldsymbol{r})+\Phi_g(\boldsymbol{r})=\sum_i\{\Phi_0^{(i)}(\boldsymbol{r})+\Phi_g^{(i)}(\boldsymbol{r})\} \quad (20)$$

$$\Phi_0^{(i)}(\boldsymbol{r})=\Psi_0^{(i)}\exp j(\boldsymbol{K}_0^{(i)}\cdot\boldsymbol{r}) \quad (20\text{ a})$$

$$\Phi_g^{(i)}(\boldsymbol{r})=\Psi_g^{(i)}\exp j(\boldsymbol{K}_g^{(i)}\cdot\boldsymbol{r})\,. \quad (20\text{ b})$$

In the present case the boundary condition, eq. (16) of the preceding section, must be replaced by

$$\left.\begin{array}{ll}\Phi_0^{(i)}(\boldsymbol{r}_a)=\phi_0^{(i)}(\boldsymbol{r}_a) & (i=1,2)\\ \Phi_g^{(i)}(\boldsymbol{r}_a)=\phi_g^{(i)}(\boldsymbol{r}_a) & (i=1,2)\end{array}\right\}\text{ on } F_a\,. \quad (21)$$

The amplitudes of the transmitted waves, by substituting (12), (18) and (20) in (21), turn out to be

$$\Psi_0^{(i)}=\frac{c^{(1)}c^{(2)}}{c^{(1)}-c^{(2)}}\frac{(-1)^i}{c^{(i)}}\Psi_{\mathrm{I}}\exp j(\boldsymbol{K}_{\mathrm{I}}-\boldsymbol{k}_0^{(i)}\cdot\boldsymbol{R}_e)\exp j(\boldsymbol{k}_0^{(i)}-\boldsymbol{K}_0^{(i)}\cdot\boldsymbol{R}_a) \quad (22\text{ a})$$

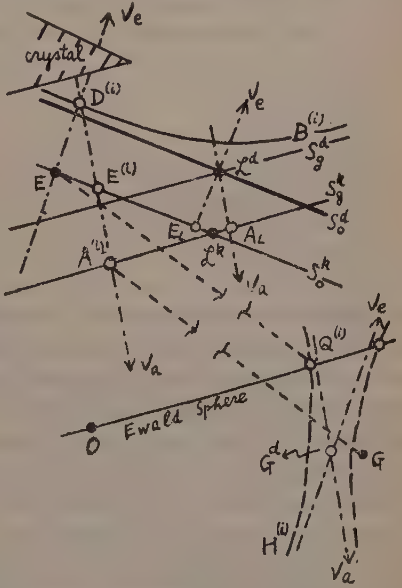

Fig. 2. Dispersion surface, wave points and Ewald construction for wedge-shaped crystal.

Only one of the branches is shown to avoid confusion.

Meaning of most of the notations is already given in Fig. 1.

Definition of E_L and A_L in eq. (24) is as follows,

E_L: Intersection point of $\nu_e(L^d)$ and S_0^k.
A_L: Intersection point of $\nu_a(L_d)$ and S_g^k.

The notations introduced in eq. (23) have the following meaning,

$$\boldsymbol{d}_e^{(i)}=\overrightarrow{\mathrm{E}\mathrm{D}^{(i)}},\ \boldsymbol{d}_a^{(i)}=\overrightarrow{\mathrm{D}^{(i)}\mathrm{A}^{(i)}},\ \boldsymbol{D}^{(i)}=\overrightarrow{\mathrm{E}\mathrm{A}^{(i)}}\,.$$

Notations of the wave vectors of the transmitted vacuum wave are as follows:

Primary : $\boldsymbol{K}_0^{(i)}=\overrightarrow{\mathrm{E}^{(i)}\mathrm{O}}$.
Reflected: $\boldsymbol{K}_g^{(i)}=\overrightarrow{\mathrm{A}^{(i)}\mathrm{G}}$.

$$\Psi_g^{(i)}=\frac{c^{(1)}c^{(2)}}{c^{(1)}-c^{(2)}}(-1)^i\Psi_{\mathrm{I}}\exp j(\boldsymbol{K}_{\mathrm{I}}-\boldsymbol{k}_0^{(i)}\cdot\boldsymbol{R}_e)\exp j(\boldsymbol{k}_g^{(i)}-\boldsymbol{K}_g^{(i)}\cdot\boldsymbol{R}_a). \quad (22\,\mathrm{b})$$

(b) Interpretation of refraction effect by Ewald construction of wave vector.

In the present section, the above results for the interfracted wave are interpreted by means of Ewald construction of wave vector*. Its derivation from the wave vector relations expressed by using the dispersion surface is accomplished if the vector $\boldsymbol{K}_g$ is transferred in parallel so that its initial point $\mathrm{A}^{(i)}$ coincides with E (*cf.* Fig. 2). If the terminal point of the displaced vector is denoted by $\mathrm{Q}^{(i)}$, the displacement can be expressed by the following vectors

$$\left.\begin{aligned}\overrightarrow{\mathrm{GQ}^{(i)}}&=\overrightarrow{\mathrm{A}^{(i)}\mathrm{E}}\\&=\boldsymbol{K}_g^{(i)}-\boldsymbol{g}-\boldsymbol{K}_{\mathrm{I}}=-\boldsymbol{D}^{(i)}\\&=\overrightarrow{\mathrm{A}^{(i)}\mathrm{D}^{(i)}}+\overrightarrow{\mathrm{D}^{(i)}\mathrm{E}}\\&=-(\boldsymbol{d}_a^{(i)}+\boldsymbol{d}_e^{(i)})\end{aligned}\right\}\quad(23)$$

When the point E moves along S_0^k in Fig. 2, *i.e.* the deviation from Bragg angle is changed at fixed azimuthal angle around the direction of $\boldsymbol{g}$, the point $\mathrm{Q}^{(i)}$ moves on a certain curve. It is easily seen, from the analytical expression of $D^{(i)}$**, that the curves are hyperbola whose asymptotes are $\nu_e(\mathrm{G}^d)$ and $\nu_a(\mathrm{G}^d)$. The point G^d is given by

$$\overrightarrow{\mathrm{GG}^d}=\overrightarrow{\mathrm{A_L E_L}} \quad (24)$$

where the points $\mathrm{A_L}$ and $\mathrm{E_L}$ are defined in Fig. 2.

If the hyperbola is constructed, the wave vectors of reflected wave are obtained by conventional Ewald's procedure. The fact that the reflected beam does not appear at the lattice point G shows refraction effect in a wide meaning. The displacement of point G to G^d implies the simple refraction*** and the further deviation from this point the double refraction mentioned in the introduction.

§ 4. The Case of Wedge Provided with an Aperture

As the second step of the extension, let us cover the surfaces of the wedge, treated in the preceding section, by two opaque screens each of which has an aperture of arbitrary shape and position.

(a) Determination of wave function.

Since the spertures are finite in size, waves are diffracted by them; mathematically speaking, the tangential continuity of wave vectors fails here. Then we must start from the wave field of the most general form of the crystal wave, which is a superposition of waves having the type of eq. (12), as follows;

$$\left.\begin{aligned}\phi(\boldsymbol{r})&=\phi_0(\boldsymbol{r})+\phi_g(\boldsymbol{r})=\sum_i\{\phi_0^{(i)}(\boldsymbol{r})+\phi_g^{(i)}(\boldsymbol{r})\}\\\phi_0^{(i)}(\boldsymbol{r})&=\int_\infty\psi_0^{(i)}(\boldsymbol{t}_e)\exp j(\boldsymbol{k}_0^{(i)}\cdot\boldsymbol{r})d\boldsymbol{t}_e\\\phi_g^{(i)}(\boldsymbol{r})&=\int_\infty c^{(i)}\psi_0^{(i)}(\boldsymbol{t}_e)\exp j(\boldsymbol{k}_g^{(i)}\cdot\boldsymbol{r})d\boldsymbol{t}_e\end{aligned}\right\},\quad(25)$$

where $\boldsymbol{t}_e$ is the tangential component of $\boldsymbol{k}_0^{(i)}$ to the plane of the entrance surface. Since the wave points, $\mathrm{D}^{(i)}$, must lie on the dispersion surface, the wave vector $\boldsymbol{k}_0^{(i)}$ and the corresponding amplitude $\psi_0^{(i)}$ are function of $\boldsymbol{t}_e$.

Although the integration in eq. (25) extends infinitely, the amplitude may vanish except in the neighbourhood of $\bar{\mathrm{D}}^{(i)}$, which is the wave point determined by the tangential continuity****. It may be assumed therefore that the boundary condition (14 a) separated into two as follows;

$$\left.\begin{aligned}\phi_0(\boldsymbol{r}_e)&=\Phi_{\mathrm{I}}(\boldsymbol{r}_e) &&\text{on } S_e\\&=0 &&\text{on } F_e-S_e\\\phi_g(\boldsymbol{r}_e)&=0 &&\text{on } F_e\end{aligned}\right\},\quad(26)$$

where S_e is the entrance aperture and F_e the whole surface of the screen.

By putting (11) and (25) in (26), it is rewritten as

---

* It is possible to deal with the primary wave along the same line.

** This expression was given in the previous paper(6) using the Bethe's notations and more general one will be given in the appendix of the next paper.

*** The index of simple refraction is not the same for incident and interfracted wave in Bethe's approximation, because U_{00} and U_{gg} deviate from U_0. This deviation is actually observed in low-order reflection11).

**** In the following descriptions, wave points, wave vectors, amplitudes and etc. determined by the tangential continuity as in the case of wedge-shaped crystal, are denoted by putting bar on their notation given in the preceding section.

$$\left.\begin{aligned}&\sum_i\int_\infty \psi_0^{(i)}\exp j(\boldsymbol{k}_0^{(i)}\cdot\boldsymbol{r}_e)d\boldsymbol{t}_e\\ &\quad=\Psi_{\mathrm{I}}\exp j(\boldsymbol{K}_{\mathrm{I}}\cdot\boldsymbol{r}_e)\quad \text{on } S_e\\ &\quad=0\qquad\qquad\qquad\qquad \text{on } F_e-S_e\\ &\sum_i\int_\infty c^{(i)}\psi_0^{(i)}\exp j(\boldsymbol{k}_g^{(i)}\cdot\boldsymbol{r}_e)d\boldsymbol{t}_e=0\\ &\qquad\qquad\qquad\qquad\qquad \text{on } F_e\end{aligned}\right\}. \tag{26'}$$

To obtain the amplitude function $\psi_0^{(i)}(\boldsymbol{t}_e)$, we multiply $\exp -j(\boldsymbol{t}^*\boldsymbol{r}_e)$ on the both sides of eq. (26′) and carry out integration of $d\boldsymbol{r}_e$ over the surface F_e. Then the δ-type function $\delta(\boldsymbol{t}_e-\boldsymbol{t}_e^*)$ appears on their left hand side. If $\boldsymbol{t}_e^*$ is rewritten again by $\boldsymbol{t}_e$ after the integration of $d\boldsymbol{t}_e$, we obtain the following expressions

$$\left.\begin{aligned}&\sum_i\psi_0^{(i)}(\boldsymbol{t}_e)\exp j(\boldsymbol{k}_0^{(i)}\cdot\boldsymbol{R}_e)\\ &\quad=\Psi_{\mathrm{I}}\exp j(\boldsymbol{K}_{\mathrm{I}}\cdot\boldsymbol{R}_e)\mathrm{L}(\boldsymbol{T}_e-\boldsymbol{t}_e\,;\,\mathrm{S}_e)\\ &\sum c^{(i)}\psi_0^{(i)}(\boldsymbol{t}_e)\exp j(\boldsymbol{k}_g^{(i)}\cdot\boldsymbol{R}_e)=0\end{aligned}\right\}, \tag{27}$$

where $\boldsymbol{T}_e$ is the tangential component of $\boldsymbol{K}_{\mathrm{I}}$ to the plane of entrance surface and L the diffraction function of an aperture. The latter is expressed in general by

$$\left.\begin{aligned}\mathrm{L}(\boldsymbol{K}-\boldsymbol{k}\,;\,\mathrm{S})&=\int_s\exp j(\boldsymbol{K}-\boldsymbol{k}\cdot\boldsymbol{r})d\boldsymbol{r}\\ &=\exp j(\boldsymbol{K}-\boldsymbol{k}\cdot\boldsymbol{R})\mathrm{L}(\boldsymbol{T}-\boldsymbol{t}\,;\,\mathrm{S})\,,\end{aligned}\right\} \tag{28}$$

where $d\boldsymbol{r}$ means surface element of the aperture $\boldsymbol{r}$ and $\boldsymbol{R}$ is the vector indicating the normal to S from the origin. Solving (27), the amplitudes of the crystal waves become as follows;

$$\left.\begin{aligned}&\psi_0^{(i)}(\boldsymbol{t}_e)=\frac{c^{(1)}c^{(2)}}{c^{(1)}-{}^{(2)}}\frac{(-1)^i}{c^{(i)}}\Psi_{\mathrm{I}}\mathrm{L}(\boldsymbol{K}_{\mathrm{I}}-\boldsymbol{k}_0^{(i)}\,;\,\mathrm{S}_e)\\ &\psi_g^{(i)}(\boldsymbol{t}_e)=c^{(i)}\psi_0^{(i)}(\boldsymbol{t}_e)\,.\end{aligned}\right\} \tag{29}$$

These equations correspond to those of eq. (18) in § 2. The correspondence becomes clearer if $\mathrm{L}(\boldsymbol{K}_{\mathrm{I}}-\boldsymbol{k}^{(i)}\,;\,\mathrm{S}_e)$ is rewritten in the second form of eq. (28). When the surface is extended infinitely, the diffraction function becomes $\delta(\boldsymbol{T}_e-\boldsymbol{t}_e)$ multiplied by a phase factor, indicating that the amplitude (29) can be reduced to eq. (18).

The wave function of the transmitted waves, similar as in the case of crystal waves, can be expressed as follows;

$$\left.\begin{aligned}&\Phi(\boldsymbol{r})=\Phi_0(\boldsymbol{r})+\Phi_g(\boldsymbol{r})=\sum_i\{\Phi_0^{(i)}(\boldsymbol{r})+\Phi_g^{(i)}(\boldsymbol{r})\}\\ &\Phi_0^{(i)}(\boldsymbol{r})=\int_\infty\Psi_0^{(i)}(\boldsymbol{T}_a)\exp j(\boldsymbol{K}_0\cdot\boldsymbol{r})d\boldsymbol{T}_a\\ &\Phi_g^{(i)}(\boldsymbol{r})=\int_\infty\Psi_g^{(i)}(\boldsymbol{T}_a)\exp j(\boldsymbol{K}_g\cdot\boldsymbol{r})d\boldsymbol{T}_a\end{aligned}\right\}, \tag{30}$$

where $\boldsymbol{T}_a$ is the tangential component of $\boldsymbol{K}_0$ or $\boldsymbol{K}_g$ to the plane of the exit surface. The boundary condition on the exit surface, similarly as in the case of the entrance surface, is stated by

$$\left.\begin{aligned}&\int\Psi_0^{(i)}\exp j(\boldsymbol{K}_0\cdot\boldsymbol{r}_a)d\boldsymbol{T}_a\\ &\quad=\int\psi_0^{(i)}\exp j(\boldsymbol{k}_0^{(i)}\cdot\boldsymbol{r}_a)d\boldsymbol{t}_e\quad\text{on } S_a\\ &\quad=0\qquad\qquad\qquad\qquad\text{on } F_a-S_a\\ &\int\Psi_g^{(i)}\exp j(\boldsymbol{K}_g\cdot\boldsymbol{r}_a)d\boldsymbol{T}_a\\ &\quad=\int\psi_g^{(i)}\exp j(\boldsymbol{k}_g^{(i)}\cdot\boldsymbol{r}_a)d\boldsymbol{t}_e\quad\text{on } S_a\\ &\quad=0\qquad\qquad\qquad\qquad\text{on } F_a-S_a\end{aligned}\right\}. \tag{31}$$

By applying the same procedure as mentioned above, the amplitudes of transmitted waves turn out

$$\Psi_0^{(i)}(\boldsymbol{T}_a)=\Psi_{\mathrm{I}}\frac{c^{(1)}c^{(2)}}{c^{(1)}-c^{(2)}}\frac{(-1)^i}{c^{(i)}}\mathrm{L}(\boldsymbol{K}_{\mathrm{I}}-\boldsymbol{k}_0^{(i)}\,;\,\mathrm{S}_e)\mathrm{L}(\boldsymbol{k}_0^{(i)}-\boldsymbol{K}_0\,;\,\mathrm{S}_a)d\boldsymbol{t}_e \tag{31 a}$$

$$\Psi_g^{(i)}(\boldsymbol{T}_a)=\Psi_{\mathrm{I}}\frac{c^{(1)}c^{(2)}}{c^{(1)}-c^{(2)}}(-1)^i\mathrm{L}(\boldsymbol{K}_{\mathrm{I}}-\boldsymbol{k}_0^{(i)}\,;\,\mathrm{S}_e)\mathrm{L}(\boldsymbol{k}_g^{(i)}-\boldsymbol{K}_g\,;\,\mathrm{S}_a)d\boldsymbol{t}_e\,. \tag{31 b}$$

These equations correspond to (22a) and (22b); the correspondence and their reduction to the case of infinite wedge crystal are easily seen as in the case of eq. (29).

(b) The behavior of wave field in the crystal.

The wave field in the crystal can be expressed from eqs. (25) and (29) by the sum of the four terms of the following form;

$$\phi(\boldsymbol{r})=\int_\infty\int_{S^e}C\exp j(\boldsymbol{K}_{\mathrm{I}}\cdot\boldsymbol{r}_e)\times\exp j(\boldsymbol{k}^{(i)}\cdot\boldsymbol{r}-\boldsymbol{r}_e)d\boldsymbol{r}_e d\boldsymbol{t}_e\,. \tag{33}$$

Since the wave length of electrons is very small (∼0.05 A) compared with the linear dimension of crystal (⩾ 10 A), the above equation can be transformed into a form convenient to study the behavior of wave field in the crystal.

Let us write

$$\boldsymbol{k}^{(i)}=\overline{\boldsymbol{k}}^{(i)}+\tau^{(i)}+\boldsymbol{n}^{(i)} \tag{34}$$

where $\overline{\boldsymbol{k}}^{(i)}$ stand for $\overline{\boldsymbol{k}}_0^{(i)}=\overrightarrow{\overline{\mathrm{D}}^{(i)}\mathrm{O}}$ or $\overline{\boldsymbol{k}}_g^{(i)}$

$=\overline{\overline{\mathrm{D}}^{(i)}\mathrm{G}}$, $\tau^{(i)}$ and $\boldsymbol{n}^{(i)}$ are respectively the tangential and normal component of $\boldsymbol{k}^{(i)}-\overline{\boldsymbol{k}}^{(i)}$ to the dispersion surface at $\overline{\mathrm{D}}^{(i)}$, The term, $\exp j(\boldsymbol{n}^{(i)}\cdot\boldsymbol{r}-\boldsymbol{r}_e)$, which appears in eq, (33) can be put almost unity* throughout the integration of dt_e. Since the factor C in (33) can be assumed to be constant during the integration, eq, (33) can be reduced** to the form,

$$\phi(\boldsymbol{r})\simeq 0 \qquad (35\,\mathrm{a})$$

for the case where $\boldsymbol{r}$ lies in the shadow of the screen (F_e-S_e) projected to the direction of $\boldsymbol{n}^{(i)}$, and

$$\phi(\boldsymbol{r})\simeq\overline{C}\exp j(\boldsymbol{K}_{\mathrm{I}}\cdot\boldsymbol{r}_e)\exp j(\overline{\boldsymbol{k}}\cdot\boldsymbol{r}_e-\boldsymbol{r}) \qquad (35\,\mathrm{b})$$

for the case that $\boldsymbol{r}$ lies out of the above shadow, and in this formula $(\boldsymbol{r}_e-\boldsymbol{r}\cdot\tau)=0$ must be satisfied.

This shows that the effect of diffraction is not remarkable even for a very small aperture (~10 A) and the direction of the wave is not the direction of wave vector $\boldsymbol{k}_0^{(i)}$ or $\boldsymbol{k}_g^{(i)}$, but that of $\boldsymbol{n}^{(i)}$. Since the direction, $\boldsymbol{n}^{(i)}$ $(i=1,2)$ are found between $\overrightarrow{\mathrm{L}^a\mathrm{O}}$ and $\overrightarrow{\mathrm{L}^a\mathrm{G}}$ in Fig, 1, the angles between $\boldsymbol{n}^{(i)}$ and $\boldsymbol{K}_{\mathrm{I}}$ are an order of Bragg angle which is very small ($\sim 10^{-2}$ rad.) in electron interfraction.

It must be noted here that the wave function $\phi(\boldsymbol{r})$ is not correct strictly in the region very near the peripheri of the aperture, because the above calculation is based on the boundary condition of Kirchhoff. A more rigorous treatment of this phenomena without any assumption concerning to the boundary conditions, as did Sommerfeld[12] in the case of diffraction by the half-infinite plane of metals, is here not feasible. However, a rough estimation showed that such a region is very limited compared with the dimentions of the crystal (~20 A) and the effect due to it may be disregarded.

§ 5. The Case of Polyhedral (Concave) Crystal

Finally, the extension to the case of polyhedral crystal may be achieved easily by using the results of previous sections.

When a parallel beam of electrons impinges on a polyhedral crystal, some of the faces are irradiated and the others are not irradiated by it. We call the former the entrance and the latter the exit surface. In some cases, the interfracted wave leaves the crystal from the entrance surface. This is called entrance surface of Bragg case. Such a surface, however, makes small angle with the incident beam. There may be further a possibility, in the case of polyhedral, that an entrance surface is exposed in the irradiation of the crystal beam propagating from the other entrance surface. We call it entrance surface of Bragg case also. According to the result (b) of the preceding section, such a surface also makes small angle with the direction of propagation of the crystal beam. Therefore, the cross section of the surface to the direction of the incident or crystal beam is very small in the above two cases; then the effects of beams which are transmitted of reflected on the entrance surface of Bragg case may be small. Therefore, it is sufficient to consider only the other entrance surface, which we call the entrance surface of Laue case.

Let us consider next an arbitrary pair of entrance and exit surface*** which are denoted respectively by $S_e^{(m)}$ and $S_x^{(n)}$; and cover these faces by opaque screens as shown in Fig. 3. Although the space between the two screens is not filled with the crystalline substance in the present case, crystal and transmitted wave functions, $\phi^{(m)}(\boldsymbol{r})$ and $\Phi^{(m,n)}(\boldsymbol{r})$, obtained in the preceding section satisfy the boundary conditions on the faces $S_e^{(m)}$ and $S_a^{(n)}$. It can be shown, moreover, by the results (b) there, that the wave function in the crystal $\phi^{(m)}(\boldsymbol{r})$ vanishes on the other entrance surface if we consider only the entrance surfaces of Laue case. Therefore, the superposition $\sum_m \phi^{(m)}(\boldsymbol{r})$ satisfies the boundary conditions approximately on the whole entrance surfaces. Similarly, the superposition of the transmitted wave for all pairs of entrance and exit surface, $\sum_{mn} \Phi^{(m,n)}(\boldsymbol{r})$ satisfies the boundary conditions on all the exit surfaces. It is worth while, here, to note that $\Phi^{(m,n)}(\boldsymbol{r})$ is the transmitted wave due to the part of crystal which lies between the entrance surface $S_e^{(m)}$ and the exit surface $S_a^{(n)}$ as shown by quadrilateral *aa′bb′* in Fig. 3.

---

* If the linear dimention of the crystal is A, the order of $|\boldsymbol{r}-\boldsymbol{r}_e|$ is A, and that of effective region of the dispersion surface can be estimated to be $1/A$. Since the radius of curveture of dispersion surface is about K, the $\boldsymbol{n}^{(i)}$ may be less than $1/KA^2$. Then $|(\boldsymbol{n}^{(i)}\cdot\boldsymbol{r}-\boldsymbol{r}_e)|$ is $1/KA\sim 1/200$ for $K=20\ \mathrm{A}^{-1}$ and $\mathrm{A}=10$ A..

** The treatment of reduction is analogous to that which will be presented in § 1 of the next paper.

*** The conditions corresponding to eq. (17) must be satisfied for every surfaces.

§ 6. Acknowledgement

The author wishes to express his sincer thanks to Professor R. Uyeda for his suggestion and helpful advices during the course of this work.

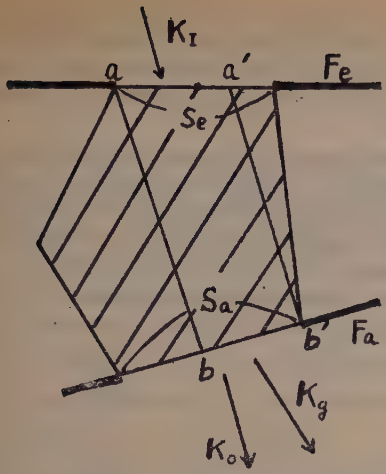

Fig. 3. Schematic diagram to illustrate the virtual diaphragms.
Thick lines: vitual diaphragms.
Hatched part; polyhedral crystal.
quadrilateral *aa′bb′*: the crystal body contributing to the wave function $\Phi^{(m,n)}(\boldsymbol{r})$ (*cf.* eqs. (30) and (32 a, b) in the text).

Appendix. *Summary of notations*

(A) Comparisons of our notations with those of Bethe.

this paper	K, k, κ	$U(\boldsymbol{r})$ U_g	U_{00} U_{gg}	U_{0g}	U_{g0}
Bethe	$K/2\pi, k/2\pi, \kappa/2\pi$	$U(\boldsymbol{r})/4\pi^2$, $v_g/4\pi^2$	$(v_0-V_{11})/4\pi^2$, $(v_0-V_{22})/4\pi^2$	$-V_{12}/4\pi^2$,	$-V_{21}/4\pi^2$

(B) Amplitudes and wave vectors.

	wave function	amplitude	wave vector	tangential component to entrance surface	 to exit surface
incident (vacuum)	$\Phi_I(\boldsymbol{r})$	Ψ_I	$\boldsymbol{K}_I$	$\boldsymbol{T}_e$	
primary (crystal)	$\phi(\boldsymbol{r})$: $\phi_0(\boldsymbol{r})$	$\psi_0^{(i)}$	$\boldsymbol{k}_0^{(i)}$	$\boldsymbol{t}_e$	$\boldsymbol{t}_a$
reflected (crystal)	$\phi_g(\boldsymbol{r})$	$\psi_g^{(i)}$	$\boldsymbol{k}_g^{(i)}$	—	—
trans. primary (vacuum)	$\Phi(\boldsymbol{r})$: $\Phi_0(\boldsymbol{r})$	$\Psi_0^{(i)}$	$\boldsymbol{K}_0$		$\boldsymbol{T}$
trans. reflected (vacuum)	$\Phi_g(\boldsymbol{r})$	$\Psi_g^{(i)}$	$\boldsymbol{K}_g$		

Remarks: Capital and small letters pertain to the quantities in vacuum and in crystal respectively. The suffix I indicates the incident wave, *o* the primary wave, *g* the reflected wave, and (*i*) the branch of the dispersion surface.

(C) Notations related to the surfaces.

	suffix	aperture	normal	current vector	normal vector
entrance	e	S_e	ν_e	$\boldsymbol{r}_e$	$\boldsymbol{R}_e$
exit	a	S_a	ν_a	$\boldsymbol{r}_a$	$\boldsymbol{R}_a$

References

1) J. Hillier and R. F. Baker: J. App. Phys. **17** (1946) 12.

2) L. Sturkey and L. K. Frevel: Phys. Rev. **68** (1945) 56. J. Hillier and R. F. Baker: Phys. Rev. **68** (1945) 98.

3) G. Honjo: J. Phys. Soc. Jap. **2** (1947) 133.

4) J. M. Cowley and A. L. G. Ress: Nature **158** (1946) 550; Proc. Phys. Soc. Lond. **59** (1947) 283.

5) L. Sturkey: Phys. Rev. **73** (1948) 183.

6) N. Kato: Proc. Jap. Academy **25** (1949) 41.

7) N. Kato: Proc. Phys. Soc. Jap. (in print).

8) H. A. Bethe: Ann. d. Phys. Lpz. **87** (1928) 55.

9) McGillavery: Physica **7** (1940) 329. R. D. Heidenreich: J. App. Phys. **20** (1947) 993.

10) H. Ekstein: Phys. Rev. **62** (1942) 255.

11) S. Miyake and G. Honjo: Nature **165** (1950) 644.

12) cf. Born: Optik, 1933, 209 p.

JOURNAL OF THE PHYSICAL SOCIETY OF JAPAN Vol. 7, No. 4 JULY—AUG., 1952

Dynamical Theory of Electron Diffraction for a Finite Polyhedral Crystal* **

II. Fraunhofer Formula

By Norio KATO***

Physical Institute, Nagoya University, Nagoya, Japan

(Received February 22, 1952)

The general formula derived in the previous paper[1] has been simplified by introducing an assumption that the wave-length of electrons compared with crystal size is very short. The simplified formula is more practical and directly applicable to the interpretation of the simple- and double-refraction as well as the Fraunhofer diffraction effects of Laue spot. A comparison of the dynamical and corresponding Kinematical formulae shows that the concept of "*Intensitätsbereich*" as advocated by von Laue[2] in his kinematical theory may be used in dynamical theory. Finally some numerical examples and comparison with theory and experiment are given.

§1. Dynamical Formula

(a) Approximate formula of amplitude

In the previous paper of the same title[1]**** it was shown that the amplitude of interfracted wave due to a domain of crystal (indicated by quadrilateral *aa'bb'* in Fig. I-3) is given as a function of the wave vector $\boldsymbol{K}_g$,

$$\Psi_g^{(i)}(\boldsymbol{K}_g)=\Psi_{\mathrm{I}}\int(-1)^i C\mathrm{L}(\boldsymbol{K}_{\mathrm{I}}-\boldsymbol{k}_0^{(i)};\ S_e)\times\mathrm{L}(\boldsymbol{k}_g^{(i)}-\boldsymbol{K}_g;\ S_a)d\boldsymbol{t}_e \quad (1)$$

where $C=c^{(1)}c^{(2)}/c^{(1)}-c^{(2)}$ and the meaning of $c^{(i)}$ and L are given in eq. (I. 10) and eq. (I.28) respectively. Since the diffraction function L vanishes except in the neighbourhood of $\overline{\mathrm{D}}^{(i)}$, especially in the case of electron interfraction, the term C which varies more slowly than the exponential term, can be taken as constant and substituted by $\overline{C}$, the value of C at $\overline{\mathrm{D}}^{(i)}$. Then (1) can be rewritten as

---

* The expence of this study was defrayed from the Grant in Aid for Fundamental Scientific Research of the Educational Ministry.

** A short summary of this paper has appeared in *Acta Cryst.* (1951) **4**, 229.

*** Now at Kobayasi Institute of Physical Research, Kokubunji, Tokyo, Japan.

****In the following descriptions, it is referred to as "part I" and the equations and figures in it are cited by adding I, such as eq. (I, 21) and Fig. I-2.

$$\Psi_g^{(i)}(K_g)=(-1)^i\bar{C}\Psi_{\mathrm{I}}\int_{S_e}\int_{S_a}d\boldsymbol{r}_e d\boldsymbol{r}_a$$
$$\times\int \exp j\{(\boldsymbol{K}_{\mathrm{I}}-\boldsymbol{k}_0^{(i)}\cdot\boldsymbol{r}_e)+(\boldsymbol{k}_g^{(i)}-\boldsymbol{K}_g\cdot\boldsymbol{r}_a)\}d\boldsymbol{t}_e \tag{2}$$

In the case of electron interfraction, moreover, the curveture of dispersion surface is very small since the Bragg angle is an order of 10^{-2} radian. Therefore, the dispersion surface effective to the integral of eq. (2) can be approximated by its tangential plane at $\bar{\mathrm{D}}^{(i)}$. We call it $\tau^{(i)}$-plane. Introducing the following notations as given in Fig. 1,

$$\boldsymbol{\tau}^{(i)}=\overrightarrow{\bar{\mathrm{D}}^{(i)}\mathrm{T}^{(i)}}, \qquad \Delta^{(i)}=\overrightarrow{\mathrm{A}^{\bar{(i)}}\mathrm{A}}, \tag{3}$$
$$\boldsymbol{d}_e^{(i)}=\overrightarrow{\mathrm{E}\bar{\mathrm{D}}^{(i)}}, \qquad \boldsymbol{d}_a^{(i)}=\overrightarrow{\bar{\mathrm{D}}^{(i)}\bar{\mathrm{A}}^{(i)}}, \tag{4}$$

we can obtain the relations readily,

$$\boldsymbol{K}_{\mathrm{I}}-\boldsymbol{k}_0^{(i)}=\overrightarrow{\mathrm{ED}^{(i)}}\simeq\overrightarrow{\mathrm{ET}^{(i)}}=\boldsymbol{d}_e^{(i)}+\boldsymbol{\tau}^{(i)} \tag{5a}$$
$$\boldsymbol{k}_g^{(i)}-\boldsymbol{K}_g=\overrightarrow{\mathrm{D}^{(i)}\mathrm{A}}\simeq\overrightarrow{\mathrm{T}^{(i)}\mathrm{A}}=-\boldsymbol{\tau}^{(i)}+\boldsymbol{d}_a^{(i)}+\Delta^{(i)}\,. \tag{5b}$$

From these relations, the argument of exponential term of (2) can be rewritten as

$$(\boldsymbol{d}_e^{(i)}\cdot\boldsymbol{r}_e)+(\boldsymbol{d}_a^{(i)}\cdot\boldsymbol{r}_a)+(\Delta^{(i)}\cdot\boldsymbol{r}_a)$$
$$+(\boldsymbol{\tau}^{(i)}\cdot\boldsymbol{r}_e-\boldsymbol{r}_a)=(\boldsymbol{d}_e^{(i)}\cdot\boldsymbol{R}_e)+(\boldsymbol{d}_a^{(i)}\cdot\boldsymbol{R}_a)$$
$$+(\Delta^{(i)}\cdot\boldsymbol{r}_a)+(\boldsymbol{\tau}^{(i)}\cdot\boldsymbol{\sigma}_e^{(i)}-\boldsymbol{\sigma}_a^{(i)}) \tag{6}$$

where $\boldsymbol{\sigma}_e^{(i)}$ and $\boldsymbol{\sigma}_a^{(i)}$ are the projection of $\boldsymbol{r}_e$ and $\boldsymbol{r}_a$ respectively on the plane which is parallel to the $\tau^{(i)}$-plane and passing through the origin of the coordinate (Fig. 2). We call this plane $\sigma^{(i)}$-plane. It is easily seen from Fig. 1a and Fig. 2a that

$$d\boldsymbol{t}_e=(\boldsymbol{z}^{(i)}\cdot\boldsymbol{\nu}_e)d\boldsymbol{\tau}^{(i)} \tag{7}$$
$$\left.\begin{aligned} d\boldsymbol{r}_e&=d\boldsymbol{\sigma}_e^{(i)}/(\boldsymbol{z}^{(i)}\cdot\boldsymbol{\nu}_e)\\ d\boldsymbol{r}_a&=d\boldsymbol{\sigma}_a^{(i)}/(\boldsymbol{z}^{(i)}\cdot\boldsymbol{\nu}_a)\end{aligned}\right\} \tag{8}$$

where $\boldsymbol{z}^{(i)}$ is the unit vector normal to $\tau^{(i)}$-plane (or $\sigma^{(i)}$-plane).*

Substituting (6), (7) and (8) into (2) and integrating over $d\boldsymbol{\tau}^{(i)}$, two-dimentional δ-function, $\delta(\boldsymbol{\sigma}_e^{(i)}-\boldsymbol{\sigma}_a^{(i)})$ appears. This implies that the i-th primary and reflected wave propagate in the direction of $\boldsymbol{z}^{(i)}$ (*cf.* § 4 (b) in the part I). After the integration of $d\boldsymbol{\sigma}_e^{(i)}$,

$$\Psi_g^{(i)}(K_g)=(-1)^{i}\bar{C}\Psi_{\mathrm{I}}\frac{1}{(\boldsymbol{z}^{(i)}\cdot\boldsymbol{\nu}_e)}$$
$$\times\exp j\{\boldsymbol{d}_e^{(i)}\cdot\boldsymbol{R}_e)+(\boldsymbol{d}_a^{(i)}\cdot\boldsymbol{R}_a)\}$$
$$\times\int_{\Sigma^{(i)*}}\exp j(\Delta^{(i)}\cdot\boldsymbol{r}_a)d\boldsymbol{\sigma}_a^{(i)} \tag{9}$$

where $\sum^{(i)*}$ is the common region of the projections of S_e and S_a on the $\sigma^{(i)}$-plane. Here, we consider a plane parallel to the S_g^k-plane and passing through the origin of the coordinate, and call it σ-plane. If the vector $\boldsymbol{r}_a$ is again decomposed into the tangential and normal component to σ-plane, such as $\boldsymbol{r}_a=\boldsymbol{\sigma}_a+\zeta_a\boldsymbol{z}$, where $\boldsymbol{z}$ is the unit vector normal to σ-plane, it follows

$$d\boldsymbol{r}_a=d\boldsymbol{\sigma}_a/(\boldsymbol{z}\cdot\boldsymbol{\nu}_a)=d\boldsymbol{\sigma}_a^{(i)}/(\boldsymbol{z}^{(i)}\cdot\boldsymbol{\nu}_a)\,. \tag{10}$$

Upon using this relation, (9) is rewritten as

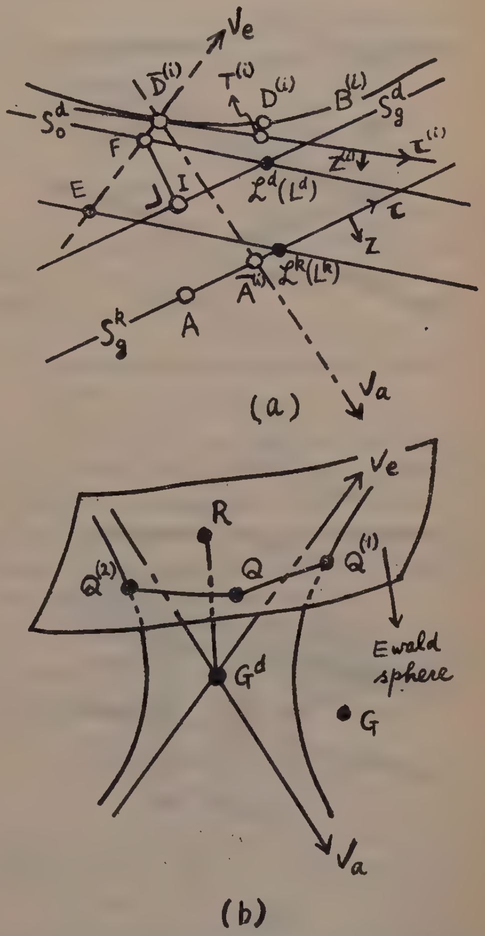

Fig. 1. Wave vector relations for the dynamical theory. Most of notations is already given in Fig. I-1 and 2 and in the text. (a) Representation by means of the dispersion surface, and (b) by means of the Ewald sphere. They are connected with each other by the relations illustrated in Fig. I-2, *i.e.*, $\overrightarrow{\mathrm{AE}}=\overrightarrow{\mathrm{GQ}}$. $\overrightarrow{\mathrm{G}^d\mathrm{R}}$ is the length of a perpendicular to the Ewald sphere. $\overline{\mathrm{FI}}=u=\overline{\mathrm{G}^d\mathrm{R}}$, since the Ewald sphere is parallel to the S_g^d-plane.

---

* $\boldsymbol{z}^{(i)}$ is the unit vector parallel to the vector $\boldsymbol{n}^{(i)}$ in § 4 (b) of the part I.

$$\Psi_g^{(i)}(\boldsymbol{K}_g)=(-1)^i\overline{C}\Psi_{\mathrm{I}}\frac{1}{(\boldsymbol{z}\cdot\boldsymbol{\nu}_a)}$$
$$\times\exp j\{(\boldsymbol{d}_e^{(i)}\cdot\boldsymbol{R}_e)+(\boldsymbol{d}_a^{(i)}\cdot\boldsymbol{R}_a)\}$$
$$\times\int_{\Sigma^{(i)}}\exp j(\boldsymbol{\Delta}^{(i)}\cdot\boldsymbol{\sigma})d\boldsymbol{\sigma}\,, \qquad (11)$$

where $\Sigma^{(i)}$ is the projection to the σ-plane of the part of S_a whose projection to the $\sigma^{(i)}$-plane is $\Sigma^{(i)*}$ (*cf.* Fig. 2). In this equation the suffix a is omitted since σ_a can be considered as a current vector on the σ-plane.

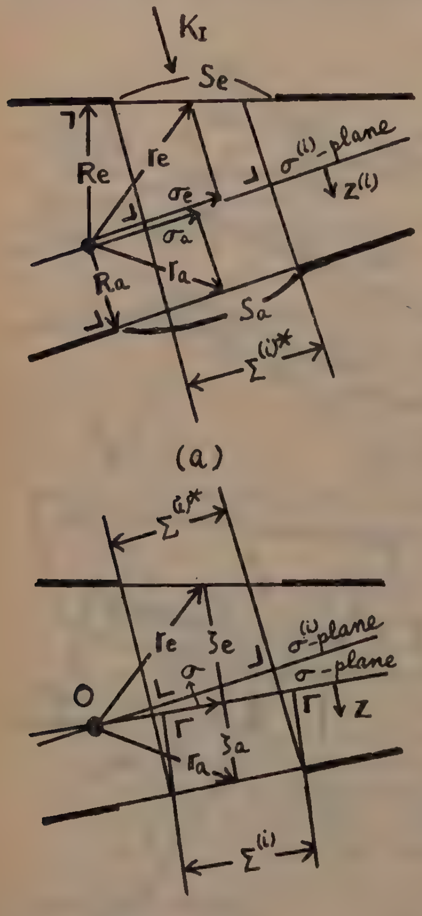

(a)

(b)

Fig. 2. Diagrams illustrating the integral regions (*cf.* the text) and the position vectors.

In some cases, the following form of $\Psi_g^{(i)}$ is also used

$$\Psi_g^{(i)}(\boldsymbol{K}_g)=(-1)^i\overline{C}\Psi_{\mathrm{I}}\frac{1}{(\boldsymbol{z}\cdot\boldsymbol{\nu}_a)}\int_{\Sigma^{(i)}}\exp j$$
$$\times\{(\boldsymbol{D}\cdot\boldsymbol{\sigma})+(\boldsymbol{d}_e^{(i)}\cdot\boldsymbol{z})\zeta_e+(\boldsymbol{d}_a^{(i)}\cdot\boldsymbol{z})\zeta_a\}d\boldsymbol{\sigma}\,, \qquad (11')$$

where $\boldsymbol{D}=\boldsymbol{d}_e^{(i)}+\boldsymbol{d}_a^{(i)}+\boldsymbol{\Delta}^{(i)}=\overrightarrow{\mathrm{EA}}$ and $\zeta_e\boldsymbol{z}$ and $\zeta_a\boldsymbol{z}$ are the normal component of $\boldsymbol{r}_e$ and $\boldsymbol{r}_a$ to the σ-plane respectively. This is easily derived from eq. (11) by the relation

$$(\boldsymbol{d}_e^{(i)}\cdot\boldsymbol{R}_e)+(\boldsymbol{d}_a^{(i)}\cdot\boldsymbol{R}_a)$$
$$=(\boldsymbol{d}_e^{(i)}\cdot\boldsymbol{r}_e)+(\boldsymbol{d}_a^{(i)}\cdot\boldsymbol{r}_a)$$
$$=(\boldsymbol{d}_e^{(i)}\cdot\boldsymbol{\sigma}+\zeta_e\boldsymbol{z})+(\boldsymbol{d}_a^{(i)}\cdot\boldsymbol{\sigma}+\zeta_a\boldsymbol{z})\,.$$

(b) The derivation of Fraunhofer formula

The wave function of the transmitted wave can be obtained by substitution of (11) or (11′) into the last equation of (I. 30), which is expressed as the sum of integrals of the following type,

$$\Phi(\boldsymbol{r})=\int_\infty\Psi(\boldsymbol{K})\exp j(\boldsymbol{K}\cdot\boldsymbol{r})d\boldsymbol{T} \qquad (12)$$

Although this expression gives the wave function at any point in whole space, it is desirable in the following discussions to obtain Fraunhofer formula, *i.e.* the expression of the wave function at large distance $\boldsymbol{r}=\boldsymbol{R}$. This transformation is easily carried out by the following mathematical procedure.

Taking the direction of $\boldsymbol{R}$ as the polar axis, it is found that

$$d\boldsymbol{T}=(\boldsymbol{K}\cdot\boldsymbol{\nu}_a)K\sin\theta d\theta d\varphi \qquad (13)$$

and $\Psi(\boldsymbol{K})$ can be considered as a function of θ and φ, which are the polar and azimuthal angle of $\boldsymbol{K}$ respectively. Then, (12) can be rewritten in the form

$$\Phi(\boldsymbol{R})=K\int_0^{2\pi}d\varphi\int_0^{\pi}\Psi(\theta,\varphi)(K\nu_a)$$
$$\times\exp jKR\cos\theta\cdot\sin\theta d\theta\,. \qquad (12')$$

Integrating by $d\theta$ by parts and taking into account of the facts that $\Psi(\pi,\varphi)=0$, $\Psi(0,\varphi)$ is independent of φ and $d/d\theta\{\Psi\cdot(\boldsymbol{K}\cdot\boldsymbol{\nu}_a)\}$ is finite, this is turned into

$$\Phi(\boldsymbol{R})\simeq(\boldsymbol{K}\cdot\boldsymbol{\nu}_a)\frac{\exp jKR}{iR}\Psi(\boldsymbol{K}) \qquad (14)$$

where $\boldsymbol{K}$ is the wave vector in the direction of $\boldsymbol{R}$.

On applying this relation to eq. (11) and using the expression for $\overline{C}$ given in the appendix, we obtain the wave function of interfracted wave as follows,

$$\Phi_g^d\simeq\frac{\exp jKR}{iR}\cdot\Psi_{\mathrm{I}}\cdot\frac{(-U_{g0})}{2\sqrt{u^2+w^2}}$$
$$\times\Big[\exp j\{(\boldsymbol{d}_e^{(1)}\cdot\boldsymbol{R}_e)+(\boldsymbol{d}_a^{(1)}\cdot\boldsymbol{R}_a)\}$$
$$\times\int_\Sigma\exp j(\boldsymbol{\Delta}^{(1)}\cdot\boldsymbol{\sigma})d\boldsymbol{\sigma}-\exp j\{(\boldsymbol{d}_e^{(2)}\cdot\boldsymbol{R}_e)$$
$$+(\boldsymbol{d}_a^{(2)}\cdot\boldsymbol{R}_a)\}\int_\Sigma\exp j(\boldsymbol{\Delta}^{(2)}\cdot\boldsymbol{\sigma})d\boldsymbol{\sigma}\Big] \qquad (15)$$

where u is $\overline{\mathrm{FI}}$ in Fig. 1a, a parameter to indicate the position of wave point E, and w is given by eq. (A. 4) in the appendix, which is equal approximately to the distance between the vertices of the hyperbolic dispersion surface. The superscript d of $\Psi_g{}^d$ indicates that it is a dynamical formula.

The another expression of (15) is obtained, using ex. (11′) instead of eq. (11) as follows:

$$\Phi_g{}^d(R) \simeq \frac{\exp jKR}{iR} \cdot \Psi_{\mathrm{I}} \cdot (-U_{g0})/2\sqrt{u^2+w^2}$$
$$\times \int_\Sigma \exp j(\boldsymbol{D}\cdot\boldsymbol{\sigma})[\exp j\{(\boldsymbol{d}_e{}^{(1)}\cdot\boldsymbol{z})\zeta_e+(\boldsymbol{d}_a{}^{(1)}\cdot\boldsymbol{z})\zeta_a\}$$
$$-\exp j\{(\boldsymbol{d}_e{}^{(2)}\cdot\boldsymbol{z})\zeta_e+(\boldsymbol{d}_a{}^{(2)}\cdot\boldsymbol{z})\zeta_a\}]d\sigma\,. \qquad (15')$$

In (15) and (15′), $\Sigma^{(1)}$ and $\Sigma^{(2)}$ are assumed to be equal approximately to the common region, Σ, of the projection of S_e and S_a to the σ-plane. The analytical expressions of $\boldsymbol{d}_e{}^{(i)}$ and $\boldsymbol{d}_a{}^{(i)}$ in terms of u and w are given in the appendix. (cf. eq. (A 7))

§ 2. Kinematical Formula

The kinematical formula for the reflected wave by a net plane g is written in general*

$$\Phi_g{}^k(R) \simeq \frac{\pi}{R}\exp jKR\cdot\Psi_{\mathrm{I}}\cdot U_g \int_V \exp j(\boldsymbol{D}\cdot\boldsymbol{r})dr\,, \qquad (16)$$

where $\boldsymbol{D}=\boldsymbol{K}_{\mathrm{I}}+\boldsymbol{g}-\boldsymbol{K}_g$, and the integral is taken over the whole crystal. Although several authors[2),3)] have transformed this formula into more practical forms, these cannot be compared directly with the dynamical formulae (15) or (15′). Then it is necessary to derive kinematical formulae which correspond to (15) and (15′). For this purpose, it is convenient to limit the integral region V to a domain of crystal as shown in Fig. I-3 by quadrilateral *aa'bb'*.

We write the current vector $\boldsymbol{r}$ in a form $\boldsymbol{\sigma}+\zeta\boldsymbol{z}$, where $\boldsymbol{\sigma}$ and $\zeta\boldsymbol{z}$ are the tangential and the normal component to the σ-plane (*cf.* Fig. 2b). Carrying out the integral of $d\zeta$ in eq. (16), it turns out to be

$$\Phi_g{}^k(R) \simeq \frac{\exp jKR}{R}\Psi_{\mathrm{I}}\cdot(-U_g)/2\,iu_0$$
$$\times\int_\Sigma \exp j(\boldsymbol{D}\cdot\boldsymbol{\sigma})\{\exp j(\boldsymbol{D}\cdot\boldsymbol{z})\zeta_e$$
$$-\exp j(\boldsymbol{D}\cdot\boldsymbol{z})\zeta_a\}d\sigma\,,$$

where $u_0=(\boldsymbol{D}\cdot\boldsymbol{z})=\overline{\mathrm{EJ}}$ in Fig. 4; ζ_e and ζ_a are the value of ζ for $\boldsymbol{r}_e$ and $\boldsymbol{r}_a$ respectively and are considered as a function of σ. Introducing the following notations as given in Fig. 3a,

$$\left.\begin{array}{ll} \boldsymbol{d}_e=\overrightarrow{\mathrm{EA}_e}\,, & \boldsymbol{d}_a=\overrightarrow{\mathrm{EA}_a} \\ \boldsymbol{\Delta}_e=\overrightarrow{\mathrm{A}_e\mathrm{A}}\,, & \boldsymbol{\Delta}_a=\overrightarrow{\mathrm{A}_a\mathrm{A}} \end{array}\right\} \qquad (17)$$

the following two formulae are obtained

$$\Phi_g{}^k(R) \simeq \frac{\exp jKR}{R}\cdot\Psi_{\mathrm{I}}\cdot(-U_g)/2iu_0$$
$$\times\int_\Sigma \exp j(\boldsymbol{D}\cdot\boldsymbol{\sigma})[\exp j(\boldsymbol{d}_e\cdot\boldsymbol{z})\zeta_e$$
$$-\exp j(\boldsymbol{d}_a\cdot\boldsymbol{z})\zeta_a]d\sigma \qquad (18')$$

$$\Phi_g{}^k(R) \simeq \frac{\exp jKR}{R}\cdot\Psi_{\mathrm{I}}\cdot(-U_g)/2iu_0$$
$$\times[\exp j(\boldsymbol{d}_e\cdot\boldsymbol{R}_e)\int_\Sigma \exp j(\boldsymbol{\Delta}_e\cdot\boldsymbol{\sigma})d\sigma$$
$$-\exp j(\boldsymbol{d}_a\cdot\boldsymbol{R}_a)\int_\Sigma \exp j(\boldsymbol{\Delta}_a\cdot\boldsymbol{\sigma})d\sigma] \qquad (18)$$

These equations correspond respectively to eqs. (15) and (15′) in the case of dynamical theory.

§ 3. Interpretation by Ewald's Construction of Wave Vector

In § 3 (b) of the part I, the refraction effect for the wedge-shaped crystal was interpreted by Ewald's construction of wave vector. The similar procedures are helpful for understanding the results obtained in the preceding two sections.

(a) Kinematical *Intensitätsbereich*

Let us transfer the vector $\boldsymbol{K}_g$ from $\overrightarrow{\mathrm{AG}}$ in Fig. 3a, to $\overrightarrow{\mathrm{EQ}}$ in Fig. 3b. Then

$$\overrightarrow{\mathrm{GQ}}=\overrightarrow{\mathrm{GQ}_e}+\overrightarrow{\mathrm{Q}_e\mathrm{Q}}=-(\boldsymbol{d}_e+\boldsymbol{\Delta}_e)$$
$$=\overrightarrow{\mathrm{GQ}_a}+\overrightarrow{\mathrm{Q}_a\mathrm{Q}}=-(\boldsymbol{d}_a+\boldsymbol{\Delta}_a) \qquad (19)$$

where Q_e and Q_a are the intersections of Ewald sphere with $\boldsymbol{\nu}_e(\mathrm{G})$ and $\boldsymbol{\nu}_a(\mathrm{G})$ respectively. The amplitude of the wave corresponding to the point Q is given by eq. (18). This shows that the amplitude is appreciable in a certain region near the reciprocal lattice point G. Such region was called '*Intensitätsbereich*' by v. Laue⁽²⁾. When the crystal surfaces S_e and S_a are large enough, the '*Intensisätsbereich*' contracts to the lines $\boldsymbol{\nu}_e(\mathrm{G})$ and $\boldsymbol{\nu}_a(\mathrm{G})$ since the diffraction function, $\int_\Sigma \exp j(\boldsymbol{\Delta}\cdot\boldsymbol{\sigma})d\sigma$, becomes a δ-type function. This implies that the two interfracted spots appear corresponding to the points Q_e and Q_a. These protrusions of '*Intensitätsbereich*' normal to the crystal surfaces were called *Stächeln* by v. Laue[2]. Of course, Q_e and Q_a coincide with the lattice point G when Bragg condition is satisfied precisely. On the other hand, when the surfaces S_e and S_a are not so large, the interfracted spots become diffuse around the points Q_e and Q_a. The behaviors of each spot are determined by the diffraction function, $\int_\Sigma \exp j(\Delta\cdot\sigma)d\sigma$, *i.e.* the diffraction function due to a single aperture Σ. If each spot overlaps to each other, there occures interference between them and the two spots become undistinguishable in extreme case.

---

* This is easily deduced from the descriptions in pp 73 and 89 of Thomson and Cochrane's *Theory and Practice of Electron Diffraction.*

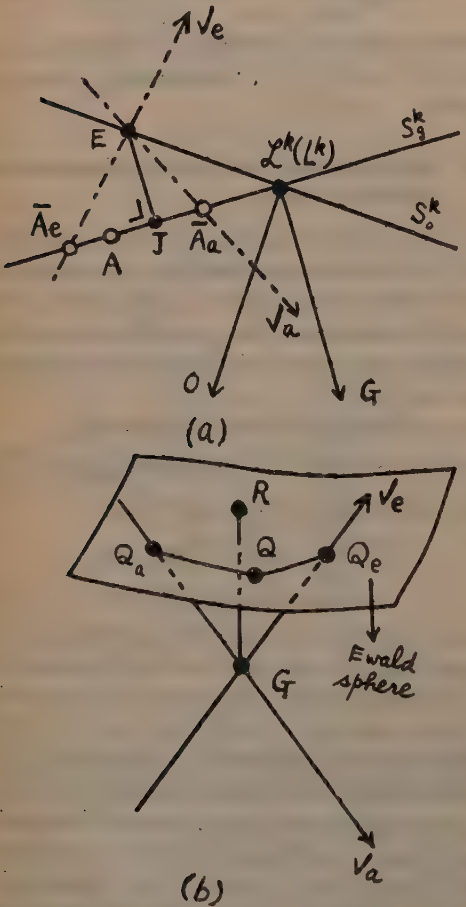

Fig. 3. The wave vector relations for the kinematical theory corresponding to Fig. 1. (a) and (b) are connected by the relation $\overrightarrow{AE}=\overrightarrow{GQ}$. $\overline{EJ}=u_0=\overline{GR}$.

(b) Dynamical *Intensitätsbereich*

In the case of dynamical theory, the interpretation of eq. (15) can be given along the same line. For this case, it is obvious that in Fig. 1b,

$$\overrightarrow{GQ}=\overrightarrow{GQ^{(1)}}+\overrightarrow{Q^{(1)}Q}=-(\boldsymbol{d}_e^{(1)}+\boldsymbol{d}_a^{(1)})-\Delta^{(1)}$$
$$=\overrightarrow{GQ^{(2)}}+\overrightarrow{Q^{(2)}Q}=-(\boldsymbol{d}_e^{(2)}+\boldsymbol{d}_a^{(2)})-\Delta^{(2)} \tag{20}$$

where $Q^{(1)}$ and $Q^{(2)}$ are the intersections of the Ewald sphere and the hyperbola as described in § 3 (b) of the part I. When the crystal surfaces are large (wege-shaped crystal), the *Intensitätsbereich* contracts to this hyperbola. Therefore the interfracted wave suffers the both effect of simple and double refraction and two spots must be observed even when the Bragg condition is satisfied precisely. When the cyrstal surfaces are small, the interfracted spots become diffuse around $Q^{(1)}$ and $Q^{(2)}$ and interfere to each other. The behaviors of each spot are the same as in the case of kinematical theory under the present approximation. The behavior of interference, however, is not the same, because the center of diffraction function and the phase factor multiplied to it are different in each case. It must be mentioned here that the *Intensitätsbereich* in the case of kinematical theory is fixed in the reciprocal lattice, and independent of the direction of the incident beam and wave length, but in the case of dynamical theory it is deformed according to the azimuthal angle of the incident beam around $\boldsymbol{g}$.

§ 4. Relations Between the Results of Kinematical and Dynamical Theory

From the results of the preceding section, it is found that the *Intensitätsbereich* in the dynamical theory around the hyperbola whose asymptotes are $\boldsymbol{\nu}_e(G^d)$ and $\boldsymbol{\nu}_a(G^d)$ corresponds to *Stächeln* around $\boldsymbol{\nu}_e(G)$ and $\boldsymbol{\nu}_a(G)$ in the kinematical theory. Then we can say that the effect of simple refraction does not appear in the kinematical theory. If this effect is taken out of consideration, the displacement $\overrightarrow{GG^d}$ can be neglected. In the present theory, the splitting of spots to $Q^{(1)}$ and $Q^{(2)}$ is called effect of double refraction and the diffuseness around $Q^{(1)}$ and $Q^{(2)}$ is called diffraction effect though the appearance of two diffuse spots around Q_e and Q_a has been interpreted hitherto as the effect of external form in the kinematical theory. It is to note that, in the present theory, the external form effect of the kinematical theory is interpreted as the refraction effect on S_e and S_a and the diffraction effect due to the aperture Σ. The term refraction does not apply in the kinematical theory, since the wave vector in crystal is not taken into account.

From the above consideration it is expected that the kinematical theory is an extreme case of the dynamical theory and the latter is approximately identical with the former if the distances between Q_e or Q_a and $Q^{(1)}$ or $Q^{(2)}$ are negligible compared with the dimension of region where the diffraction function has appreciable value. To investigate these relations quantitatively, it is convenient to compare eq. (15′) with eq. (18′), after inserting the analytical expressions of $\boldsymbol{d}_e$, $\boldsymbol{d}_a$, $\boldsymbol{d}_e^{(i)}$ and $\boldsymbol{d}_a^{(i)}$ given in the appendix. It is to be noted that the parameter u_0 in the kinematical theory corresponds to u in the dynamical theory, since the simple refraction can not be deduced in the former theory. Then it can be shown that the formulea of the both theories coincide to each other in the following two cases where the primary extinction is small.

Case I. $u \gg w$, that is, the deviation from the Bragg condition is very predominant. It is evident eq. (18′) becomes equal to eq. (15′) asymptotically.

Case II. $2\pi w|\zeta_a-\zeta_e| \ll 1$, that is, the product of the thickness of crystal and the reflection power of the net plane is very small. Since the case $u \gg w$ is already described above, it is sufficient to give the discussions only in the cases $u \simeq w$ and $u<w$. If the terms in the square bracket of eqs. (15′) and (18′) are expanded in power series of ζ_e and ζ_a, they become as follows.

The dynamical formula;

$$\Phi_g{}^d(\boldsymbol{R}) \simeq \frac{\exp jKR}{2iR}\cdot U_{0g}\cdot \Psi_{\mathrm{I}}\cdot\int_\Sigma \exp j(\boldsymbol{D}\cdot\boldsymbol{\sigma})$$
$$\times(\zeta_a-\zeta_e)[(2\pi i)-\frac{1}{2}(2\pi)^2u(\zeta_e+\zeta_a)-\frac{1}{6}(2\pi)^3 i$$
$$\times\{u^2(\zeta_e{}^2+\zeta_e\zeta_a+\zeta_a{}^2)+\frac{1}{4}w^2(\zeta_a-\zeta_e)^2\}+\cdots]d\sigma \tag{21}$$

The kinematical formula;

$$\Phi_g{}^k(\boldsymbol{R}) \simeq \frac{\exp jKR}{2iR}\cdot U_g\cdot \Psi_{\mathrm{I}}\cdot\int_\Sigma \exp j(\boldsymbol{D}\cdot\boldsymbol{\sigma})$$
$$\times(\zeta_a-\zeta_e)[(2\pi i)-\frac{1}{2}(2\pi)^2u(\zeta_e+\zeta_a)-\frac{1}{6}(2\pi)^3 i$$
$$\times\{u^2(\zeta_e{}^2+\zeta_e\zeta_a+\zeta_a{}^2)\}+\cdots]d\sigma. \tag{22}$$

It is evident that these formulae coincide to each other if $2\pi w|\zeta_a-\zeta_e| \ll 1$.

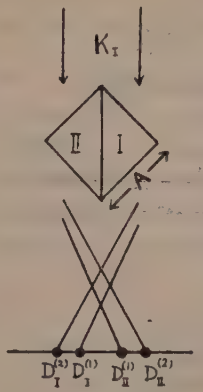

Fig. 4. Illustrating the superposition of interfracted waves by two equal halves of a cube. $D_{\mathrm{I}}^{(i)}$ or $D_{\mathrm{II}}^{(i)}$ corresponds to $Q^{(i)}$ of the interfracted wave due to the domain I or II respectively.

§ 5. Numerical Example. Comparison with Experimental Results

It was shown that our theory explains the effect of refraction and diffraction simultaneously. To illustrate the results, a numerical calculation was carried out for an ideal cube crystal. We assumed the incident beam to be parallel to [110] and satisfy the dynamical Bragg condition strictly ($u=0$) for the net plane (002). We divided the crystal into two domains, I and II, as shown in Fig. 4 and superposed the interfracted waves due to both. A set of numerical values nearly equal to those obtained by Sturkey(4) for MgO was used; $U_{00}=U_{gg}\sim 14\,ev.$ and the energy of incident electrons is assumed to be 40 *Kev.* Fig. 5 illustrates the intensity distribution along the intersection line of Ewald sphere and the plane involving $\nu_e(G)$ and $\nu_a(G)$ for various crystal size, A. Meanwhile, in Fig. 6, crystal size was taken to be constant and the value of $|U_{g0}|$ was varied. In both cases, the solid line is the intensity distribution calculated by assuming phase correlation between the waves due to the domain I and II, while the dotted line is that obtained by assuming no phase correlation.

From these figures, we find that when the crystal is very small, *ca.* 30 A, no difference appears between the kinematical theory and the dynamical theory; when the crystal is larger than *ca.* 50 A, the both theories become discernible and the simple refraction effect appears when the crystal is larger than *ca.* 100 A. But the doubly refracted spots are not distinguishable as long as the crystal is

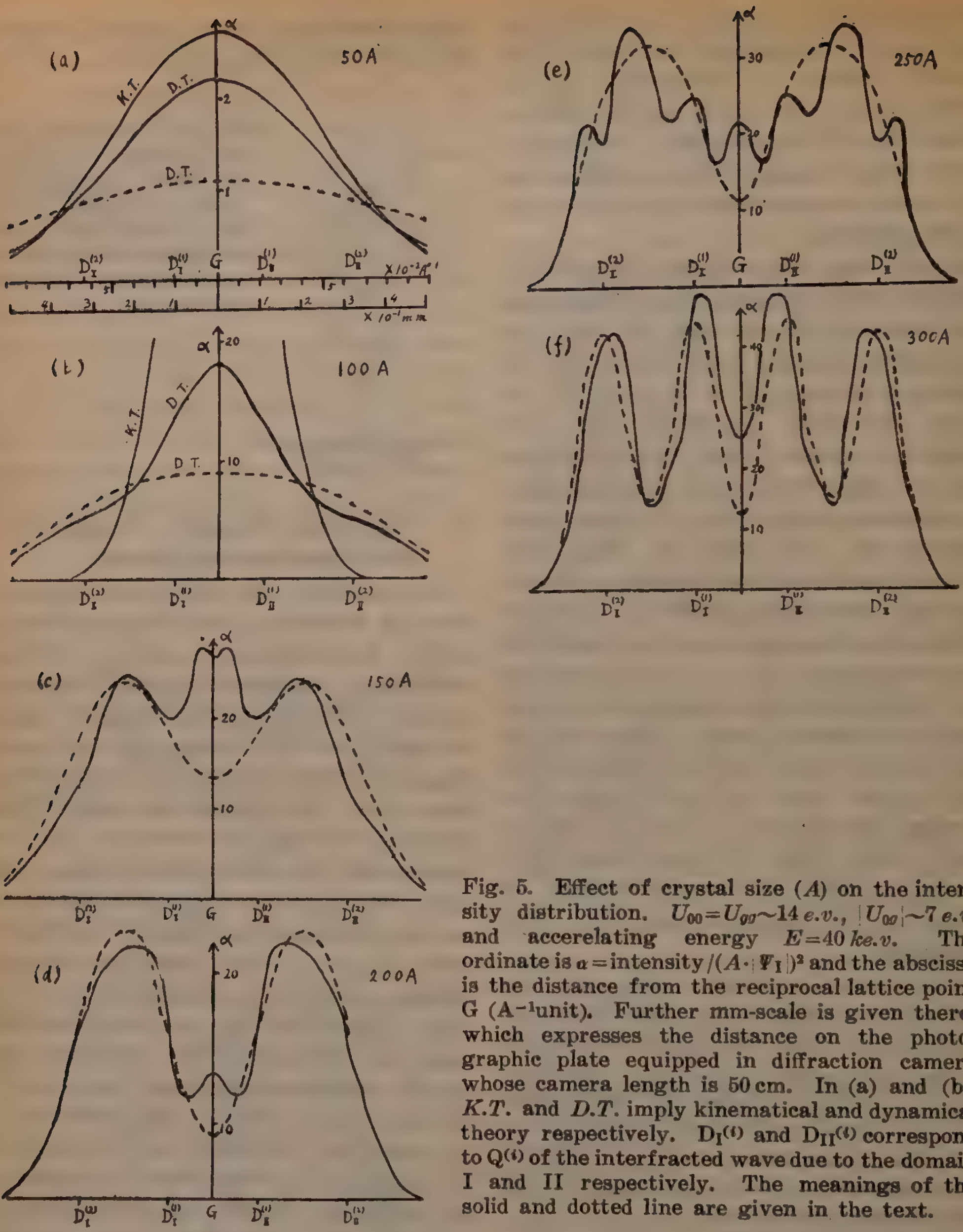

Fig. 5. Effect of crystal size (A) on the intensity distribution. $U_{00}=U_{gg}\sim 14$ *e.v.*, $|U_{0g}|\sim 7$ *e.v.* and accerelating energy $E=40$ *ke.v.* The ordinate is $\alpha=\text{intensity}/(A\cdot|\Psi_{\text{I}}|)^2$ and the abscissa is the distance from the reciprocal lattice point G (A^{-1}unit). Further mm-scale is given there, which expresses the distance on the photographic plate equipped in diffraction camera whose camera length is 50 cm. In (a) and (b), *K.T.* and *D.T.* imply kinematical and dynamical theory respectively. $\text{D}_{\text{I}}^{(i)}$ and $\text{D}_{\text{II}}^{(i)}$ correspond to $\text{Q}^{(i)}$ of the interfracted wave due to the domain I and II respectively. The meanings of the solid and dotted line are given in the text.

smaller than *ca.* 270 A. The fact that several maxima appear in the solid line of Fig. 5 for 250 A is caused by the interference of waves due to the domain I and II. From the above example it is clear that the simple and double refraction appear according to the crystal size. The existence of double refraction was found and confirmed by several authors[4)5)6)]. Some experimental features inexplicable by the present theory[6)] may be elucidated by taking into account the effect of absorption and simultaneous refraction both of which have been neglected here.* The effect of

---

* *Note added in proof:*

It was shown experimentally by Honjo & Mihama that the intensity of the wave $\Phi_g^{(1)}$ is always more intensive than that of $\Phi_g^{(2)}$, whereas the present theory predicts that they have equal intensity. When the crystal size is large enough, it is possible to take into account the absorption effect along the same way as the above treatment for the case of wedge-shaped crystal (Part I § 3). Then the crystal waves are equal to those in the case of infinitely extended crystal, which were previously given by M. v. Laue in X-rays (*Acta. Cryst.* 2 (1949) 106). In the case of electron it is evident that the same expressions can be used, if gitter function χ in his paper is replaced

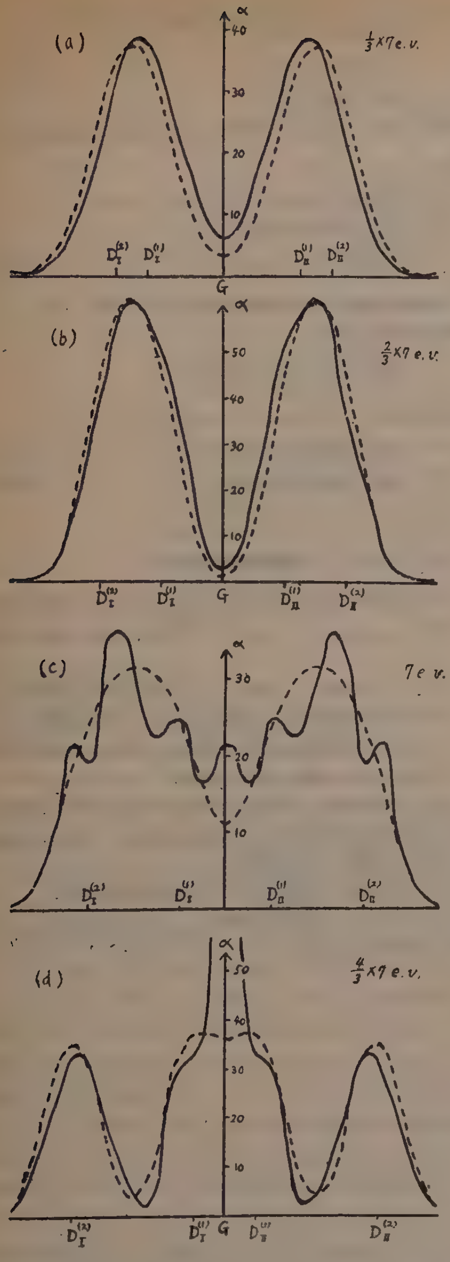

Fig. 6. Intensity distribution for various values $|U_{0g}|$, when $A=250$ A and $U_{00}=U_{gg}\sim 14$ e.v. The abscissa and the ordinate are the same as those of Fig. 5.

diffraction around interfracted spots was beautifully demonstrated by Rees and Spinks[7]. It seems now, however, experimental results are too few to confirm our theory by them.

§ 6. Acknowledgements

The author wishes to express his sincer thanks to Professor R. Uyeda for his suggestions. He has shown continued interest and has given many valuable advices during the course of this work.

Appendix

I. Dispersion surface

In fig. 1a, we take two rectangular coordinate systems, $\boldsymbol{x}_0-\boldsymbol{y}-\boldsymbol{z}_0$ system and $\boldsymbol{x}_g-\boldsymbol{y}-\boldsymbol{z}_g$ system, having their origin at L^d. Here, $\boldsymbol{z}_0$ and $\boldsymbol{z}_g$ are the unit vector parallel to the direction of $\overrightarrow{L^dO}$ and $\overrightarrow{L^dG}$ respectively and $\boldsymbol{y}$ is perpendicular to the plane of the figure. Then, the unit vectors $\boldsymbol{x}_0$ and $\boldsymbol{x}_g$ have the direction of the intersection of the plane of the figure with the S_0^d- and S_g^d-plane respectively.

Let $z_0^{(i)}$ and $z_g^{(i)}$ be the z_0- and z_g-coordinate of a point on the branch (i) of the dispersion surface.

Then it is shown that

$$\kappa_0^2-k_0^{(i)2}\simeq 2(\overrightarrow{L^dO}\cdot\overrightarrow{L^dD^{(i)}})\simeq 2Kz_0^{(i)}$$

$$\kappa_g^2-k_g^{(i)2}\simeq 2(\overrightarrow{L^dG}\cdot\overrightarrow{L^dD^{(i)}})\simeq 2Kz_g^{(i)}\ .$$

Inserting this into eq. (I. 9), the dispersion surface can be expressed as

$$z_0^{(i)}z_g^{(i)}=U_{0g}U_{g0}/4K^2\ . \qquad \text{(A 1)}$$

From eq. (I. 10), the amplitude ratio is expressed as

$$c^{(i)}=2Kz_0^{(i)}/(-U_{0g})=(-U_{g0})/2Kz_g^{(i)}\ . \qquad \text{(A 2)}$$

We write $\overrightarrow{FD^{(i)}}=l^{(i)}\nu_e$ and $\overline{FI}=u$ in Fig. I-a, where u has the following relation with the notations w and W in Bethe's original paper,

$$wW=-u \qquad \text{(A 3)}$$

and $$w=(|U_{0g}|/K)\sqrt{(\boldsymbol{z}_g\cdot\nu_e)/(\boldsymbol{z}_0\cdot\nu_e)}\ . \qquad \text{(A 4)}$$

---

by crystal potential $V(\boldsymbol{r})$ and polarization factor C is put to be 1. Then the imaginary term of the wave vector is given as, using the notations of his paper

$$\delta_i=\frac{1}{2\gamma_0}\left\{-\chi_{0i}\pm\frac{\phi_h}{[\beta_r^2+4\phi_h]^{1/2}}\right\}$$

from eq. (27) in his paper, where γ_h is assumed to be nearly equal to γ_0. The signs ± correspond to the $\Phi_g^{(1)}$-wave and $\Phi_g^{(2)}$-wave respectively. Therefore, if the sign of ϕ_h is negative the $\Phi_g^{(1)}$-wave will be more intensive than that of $\Phi_g^{(2)}$-wave in accordance with experiment. Unfortunately, however, it seems to the author now that its sign can not be determined from the other quantities such as inelastic scattering power of component atom or the degree of simultaneous Bragg reflection.

Then it is found that,

$$z_0^{(i)}=l^{(i)}(\boldsymbol{\nu}_e\cdot\boldsymbol{z}_0)$$
$$z_g^{(i)}=l^{(i)}(\boldsymbol{\nu}_e\cdot\boldsymbol{z}_g)-u .$$

From eq. (A 1), the dispersion surface can be rewritten by the terms of u as follows.

$$l^{(i)}(\boldsymbol{\nu}_e\cdot\boldsymbol{z}_0)\{(l^{(i)}(\boldsymbol{\nu}_e\cdot\boldsymbol{z}_g)-u\}=|U_{0g}|^2/4K^2 .$$

Therefore

$$\begin{aligned} l^{(i)}&=1/2(\boldsymbol{\nu}_e\cdot\boldsymbol{z})\cdot\{u\pm\sqrt{u^2+w^2}\} ,\\ z_0^{(i)}&=(\boldsymbol{\nu}_e\cdot z_0)/2(\boldsymbol{\nu}_e\cdot\boldsymbol{z}_g)\cdot\{u\pm\sqrt{u^2+w^2}\} ,\\ z_g^{(i)}&=1/2\cdot\{-u+\sqrt{u^2+w^2}\} . \end{aligned} \tag{A 5}$$

where the upper sign and the lower sign correspond to one and two primes.

2. Expression of the S_0^k- and the S_g^k-plane

If the $\boldsymbol{z}_0$-coordinate of a point on the S_0^k-plane be Z_0 and the $\boldsymbol{z}_g$-coordinate of a point on the S_g^k-plane be Z_g respectively, it is found that

$$\begin{aligned} U_{00}&=\kappa_0^2-K_{\mathrm{I}}^2=2(\overrightarrow{\mathrm{L}^d\mathrm{O}}\cdot\overrightarrow{\mathrm{L}^d\mathrm{E}})=2KZ_0 ,\\ U_{gg}&=\kappa_g^2-K_g^2=2(\overrightarrow{\mathrm{L}^d\mathrm{G}}\cdot\overrightarrow{\mathrm{L}^d\mathrm{A}})=2KZ_g . \end{aligned} \tag{A 6}$$

These are the equations of the S_0^k- and S_g^k-plane.

3. Analytical expression of $\boldsymbol{d}_e^{(i)}$ and $\boldsymbol{d}_a^{(i)}$

From (A 5), (A 6) and Fig. 1 a,

$$(\boldsymbol{d}_e^{(i)}\cdot\boldsymbol{z}_0)=(\overrightarrow{\mathrm{E}\bar{\mathrm{D}}^{(i)}}\cdot\boldsymbol{z}_0)=(\bar{z}_0^{(i)}-Z_0) ,$$

$$(\boldsymbol{d}_a^{(i)}\cdot\boldsymbol{z}_g)=(\overrightarrow{\bar{\mathrm{D}}^{(i)}\mathrm{A}}\cdot\boldsymbol{z}_g)=(Z_g-\bar{z}_g^{(i)}) ,$$

$$\boldsymbol{d}_e^{(i)}=\frac{\boldsymbol{\nu}_e}{(\boldsymbol{\nu}_e\cdot\boldsymbol{z}_0)}\left[-\frac{U_{00}}{2K}+\frac{1}{2}\frac{(\boldsymbol{\nu}_e\cdot\boldsymbol{z}_0)}{(\boldsymbol{\nu}_e\cdot\boldsymbol{z}_g)}+\{u\pm\sqrt{u^2+w^2}\}\right],$$

$$\boldsymbol{d}_a^{(i)}=\frac{\boldsymbol{\nu}_a}{(\boldsymbol{\nu}_a\cdot\boldsymbol{z}_g)}\left[\frac{U_{gg}}{2K}+\frac{1}{2}\{u\mp\sqrt{u^2+w^2}\}\right]. \tag{A 7}$$

4. $C=c^{(1)}c^{(2)}/c^{(1)}-c^{(2)}$

From eq. (A 2) and the last equation of (A 5),

$$\begin{aligned} C&=-(2K/U_{0g})z_0^{(1)}z_0^{(2)}/(z_0^{(1)}-z_0^{(2)})\\ &=-(U_{g0}/2K)1/(z_g^{(2)}-z_g^{(1)})\\ &=(U_{g0}/2K)1/\sqrt{u^2+w^2} . \end{aligned} \tag{A 8}$$

5. Analytical expression of $\boldsymbol{d}_e$ and $\boldsymbol{d}_a$

From Fig. 3a,

$$(\boldsymbol{d}_e\cdot\boldsymbol{z}_g)=(\boldsymbol{d}_a\cdot\boldsymbol{z}_g)=u_0 .$$

Therefore,

$$\begin{aligned} \boldsymbol{d}_e&=u_0\boldsymbol{\nu}_e/(\boldsymbol{\nu}_e\cdot\boldsymbol{z}_g)\\ \boldsymbol{d}_a&=u_0\boldsymbol{\nu}_a/(\boldsymbol{\nu}_a\cdot\boldsymbol{z}_g) . \end{aligned} \tag{A 9}$$

References

1) N. Kato : Journ. Phys. Soc. Jap. **7** (1952) 397.

2) M. v. Laue : Ann. d. Phys. Lpz. **26** (1936) 55.

3) M. v. Laue : Zeits. f. Krist. **64** (1926) 115.
C. C. Murdock : Phys. Rev. **35** (1930) 8.
A. L. Patterson : Phys. Rev. **49** (1936) 884 ; Phys. Rev. **56** (1939) 972.

4) L. Sturkey : Phys. Rev. **73** (1948) 183.

5) J. M. Cowley and L. G. Rees : Proc. Phys. Soc. Lond. **59** (1947) 283.

6) G. Honjo, Private Communications.

7) A. L. G. Rees and J. A. Spink : Acta Cryst. **3** (1950) 316.

JOURNAL OF THE PHYSICAL SOCIETY OF JAPAN Vol. 7, No. 4 JULY—AUG., 1952

Absorption of Carbon Mono-oxide by the Barium Getter Part IV. Absorption Experiments in the Temperature Range between 0°C and 250°C

By Tetsuya ARIZUMI and Seiichi KOTANI

Kobe Kogyo Corporation, Kobe

(Received March 5, 1951)

The absorption properties of the flashed barium getter beyond 0°C were studied. At low temperatures, carbon mono-oxide was apparently absorbed by the getter, while its resistance remained almost unvaried. At higher temperature than about 150°C, however, the resistance changed remarkably as the getter absorbed the gas. The ionization of the introduced gas made the absorption of the getter slightly vigorous. In the c.f. method the pressure decreased at first to a minimum value and then it began to increase, suggesting that another kind of gas was formed by the catalytic action on the getter surface. The phenomena were studied in details. The alternative introduction of carbon mono-oxide and oxygen gave a clue to the absorption state of carbon mono-oxide.

§1. Introduction

In Parts I-III[1)] of this paper the experiments on the sorption properties of the barium getter in the temperature range between −180°C and room temperature and their theoretical analysis were described, with the conclusion that carbon mono-oxide is mainly absorbed into lattice imperfections, existing in the getter mirror. In Part IV the sorption properties of the barium getter to the same gas in the temperature range between 0°C and 250°C shall be described, which is essentially important for the practical application of the getter. The experimental results shall indicate that lattice imperfections are also effective for the absorption of carbon mono-oxide, until the diffusion becomes predominant beyond 150°C, and that in the temperature from 0°C to about 70°C the getter surface acts as a kind of catalyser to form carbon dioxide.

§2. Experimental Procedure

The experimental apparatus and procedure are almost similar to described in foregoing several papers.[1),2),3)] The getter chamber G was placed in a small electric furnace, instead of the low temperature Duwar vessel.[1)] A small mica piece[2)] was mounted for the measurement of resistance of the getter mirror in most cases.

§3. Change of Pressure and Resistance in the C. F. Method

When the gas was introduced through the cappillary into the getter chamber kept at room temperature, the pressure and the resistance of the mirror changed as shown in Fig. 1. The pressure increased almost linearly with time, but its inclination differs from one getter to another. Although the pressure curve means that almost all amount of introduced gas was absorbed into the getter, the resistance did not change so much except first several minutes. Such behaviour in resistance was not encountered in the Ba-O_2 system[2)], but rather resembles to the Ba-N_2 system[4)]. When the gas was continuously introduced for a long time, the pressure began to increase rapidly after a while, but the resistance remained almost unvaried. The resistance change became remarkable long time after the pressure changed rapidly. The curve b in Fig. 1, the same as the curve a, is represented with the prolonged time scale. In general the resistance change is slower than this example and their brief description are summerized in Table I.

If carbon mono-oxide is absorbed by the chemical combination, the remarkable change in resistance will be occured almost at the same time as the pressure begins to increase suddenly, as in the Ba-O_2 system[2)]. The experimental results stand against this prediction, suggesting that carbon mono-oxide is mainly absorbed into lattice imperfections even at room temperature.

Extrapolating ab and cd in the pressure curve with their intersection point e, the length oe may well be considered as the measure of amount of absorbed gas. The

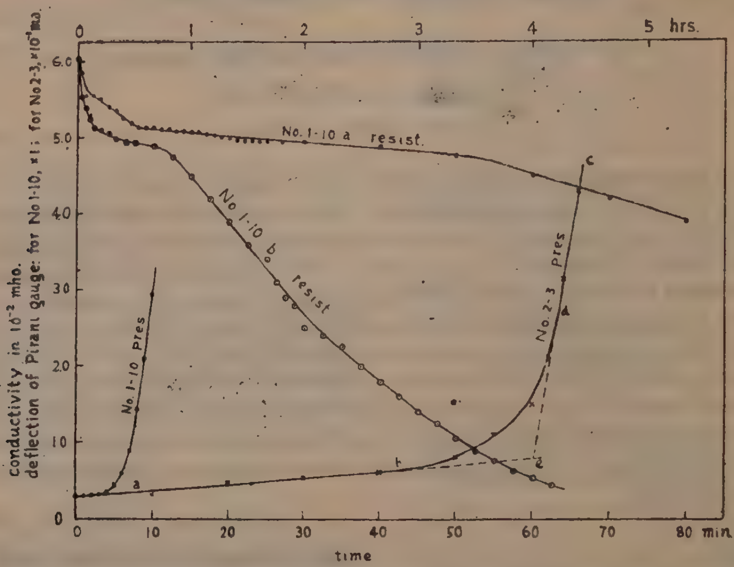

Fig. 1. The pressure and resistance curves in the c. f. method. The deflection of 0.1ma. corresponds to 3.6×10^{-4}mmHg. in all figures in the present paper.

Table I

Amount of absorption for carbon mono-oxide

tube No.	temperature	T (min.)	Q (mol/g.mol)	resistance change
1-2	14°C	4	1.46×10^{-4}	—
1-3	14	2.5	8.98×10^{-5}	—
1-4	14	10	5.94×10^{-4}	—
1-5	14	6	1.5×10^{-4}	—
1-6	13	14	4.31×10^{-4}	—
1-7	13	10.5	1.78×10^{-4}	—
1-8	14	4.5	3.6×10^{-4}	sudden change for first 30 secs. followed by very slow one.
1-9	12	14	4.1×10^{-4}	always slow change.
1-10	13	6	1.07×10^{-3}	sudden change for first one min. followed by the very slow one.
1-11	14	4	3.76×10^{-4}	similar as No. 1-10.
1-12	38	8	1.07×10^{-3}	always very slow change.
1-13	35	4	9.2×10^{-4}	always very slow change.
1-14	75	8.5	9.07×10^{-4}	always very slow change.
1-15	160	9.5	8.45×10^{-4}	rather rapid change.
1-16	165	45	2.65×10^{-3}	slow change for first 6 mins., followed by the sudden one.
1-17	95	21	$5,7\times10^{-4}$	sudden change for first 2 mins. followed by the rapid one.
1-18	125	17	4.1×10^{-4}	comparatively large change for first 20 mins. followed by the rapid one.
1-19	270	115	9.4×10^{-3}	rather slow, but continuous change.
1-20	270	40	6.6×10^{-4}	slow change for first 12 mins. followed by the rapid linear change.
1-21	210	30	5.02×10^{-4}	always rapid linear change.
2-1	30	67	6.27×10^{-5}	—
2-3	30	61	1.02×10^{-4}	—
2-4	30	113.5	—	—
2-5	30	35	—	—
2-6	30	39.6	—	—

length oe and thus the amount of absorption per unit weight of barium differ largely from one getter to another. In Fig. 1 two extreme examples are presented and many results are summerized in Table I, where T represents the length of oe in min. and $Q=sT/M$ the amount of absorbed gas per unit weight of barium (s: the amount of gas flow per unit time, and M: total weight of barium). The large difference in Q indicates that the absorption ability depends mainly upon the flashing conditions of the getter mirror.

§4. Pressure Change in the C. V. Method

After the pressure increased to a proper value in the c. f. method, the capillary was sealed and the pressure was measured in the c. v. method. Two typical curves and their logarithmic plots are illustrated in Figs. 2 and 3 respectively. At first the pressure decreased as usual, but curiously it began to increase after a while, gradually reaching to a final value. Sometimes the pressure change is found to be represented by

$$\frac{dp}{dt}=-\alpha p \qquad (1)$$

for a rather long time as seen in No. 2-5, while in several cases (1) does not hold except the very early state (No. 2-6). The pressure change in the Ba-CO system in the temperature range between −100°C and 0°C, in which the gas is mainly absorbed in the activated state, can be represented by (1). The fact that the formula (1) holds for many of present pressure changes suggests that carbon mono-oxide is absorbed mainly in the activated state even at room temperature.

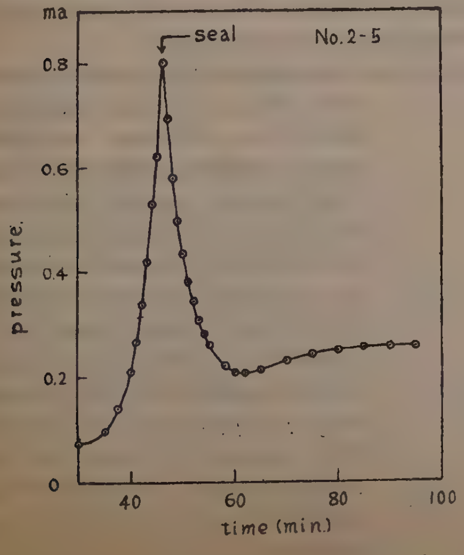

Fig. 2. The time change of pressure in the C. V. method.

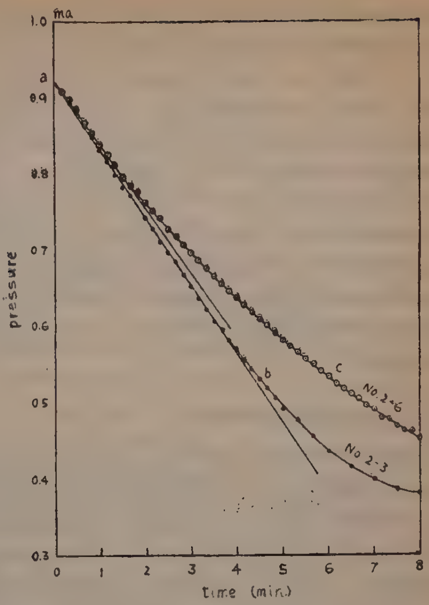

Fig. 3. The logarithmic plots of pressure changes.

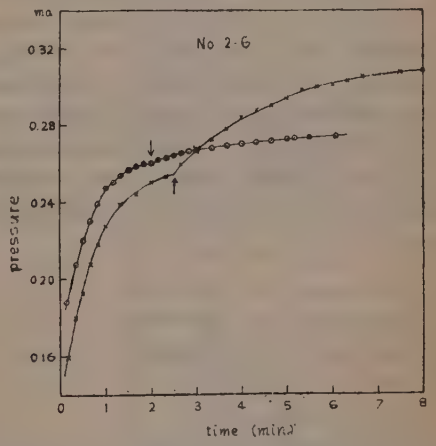

Fig. 4 The pressure change observed when the getter chamber was brought out from liquid air to room temperature suddenly.

It is apparently impossible that the same gatter absorbes the gas in a moment, while desorbes in other moment. Thus the gradual increase in pressure, illustrated in Fig. 2, is thought to be due to the desorption of other kind of gas, for which the following result will present an experimental proof. After immersing the getter chamber, already desorbed sufficient amount of unknown gas, into liquid air, the tube was suddenly brought out in the room temperature. The pressure change obtained in this procedure has a discontinuity, existing in the temperature range from −70°C to −40°C (Fig. 4). Perhaps the desorbed gas is carbon dioxide which is formed by a kind of catalytic action of the getter surface. The similar catalytic action has been frequently observed in the field of chemistry.

§ 5. Ionization of Gas

If the introduced gas was ionized by a H. F. bombarder or a tesla coil, the gettering action became slightly active. This was proved by following experiment. The gas was introduced with or without ionization alternatively each for 30 secs. The cross mark in Fig. 5 means the pressure in the period during which the gas was introduced without ionization and the small circle the pressure in the period with ionization. When the gas was ionized the pressure is always smaller than when the gas is introduced without ionization. Even after the capillary was sealed at b, the pressure remained unvaried (bc), but it began to decrease as soon as the gas was ionized (cd). Stopping the ionization, the pressure increased slightly (de), but it began to decrease again together with beginning the ionization (ef). These results support strongly that carbon mono-oxide is mainly absorbed in the activated state at room temperature.

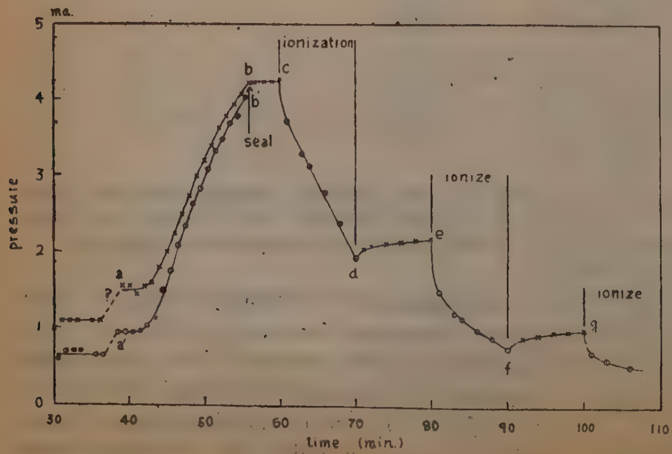

Fig. 5. The effect of the ionization of the introduced gas.

§ 6. Effect of Temperature (C. F. Method)

Placing the getter chamber in a small electric furnace of a fixed temperature, both the pressure and resistance changes in the c. f. method were measured. The time interval during which the pressure remains almost unvaried became slightly longer and the resistance had a tendency to change slightly more steeply than at room temperature, but below 150°C the general aspects in both curves of pressure and resistance did not differ from those at room temperature. Beyond 150°C, however, the co-relation between the pressure and the resistance curves became different apparently (Fig. 6). The resistance increased almost infinitely before the rapid increase in the pressure, showing that the gas combines chemically with barium to increase the thickness of the compound layer, and also that the structure of the getter mirror is not uniform, but granular[3].

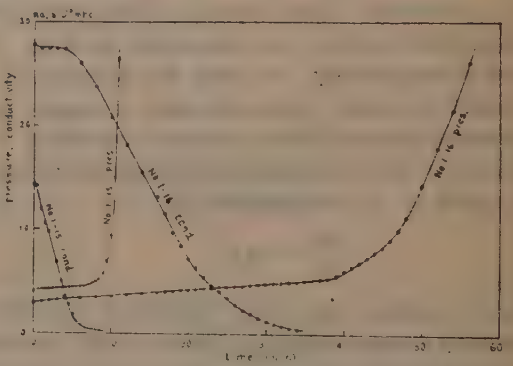

Fig. 6. The typical pressure and resistance curves at high temperature.

Sometimes, preceding to the linear increase, there existed a short period in which the resistance remained almost unvaried after the initial slight change, as well as at room temperature. Perhaps in these cases the lattice imperfections are still effective for the absorption of the gas. Beyond about 150°C, however, the lattice imperfections change gradually to the normal lattice arrangement and thus the time interval in which the resistance is almost unvaried become very shorter than at room temperature.

Most cases in Table I show that

in general T is longer in the getter whose resistance changes slightly at the initial stage, perhaps because the absorption in the lattice imperfections is still important even in the experimental temperature range.

§7. Effect of Temperature (C. V. Method)

Such curious phenomena as shown in Fig. 2 were not observed both at −180°C and at −10°C and the abnormality in the pressure curve was not also obtained. In other words carbon dioxide was formed only in a comparatively narrow temperature range from 0°C to about 70°C.

When the getter chamber, already released a sufficient amount of carbon dioxide, was immersed suddenly into ice water, the pressure began to decrease very gradually to a final value b in Fig. 7, while raising the temperature to 30°C, the pressure began to increase as bc with a slightly steeper slope than ab. Such a gradual pressure change is not caused by the desorption of surface-adsorbed molecules, but by the gradual change in the equilibrium state between carbon mono-oxide and carbon dioxide (refer to Fig. 7b). The final pressure at c is larger than that at a, while the pressure at e is smaller than that at a. Probably carbon dioxide is slowly absorbed by the barium getter even at 30°C.

When the temperature of the getter chamber was raised stepwisely from room temperature to about 150°C, the pressure increased stepwisely up to about 60°C, but beyond this temperature it began to decrease after a slight momentary increase. Fig. 8 presents a typical example. Sometimes such temporary rise in pressure was not observed. The pressure increase below 60°C is considerd to be caused by the shift in the equilibrium state between carbon mono-oxide and carbon dioxide and the decrease of pressure beyond 60°C is perhaps due to the diffusion of the surface atoms into the interior.

§8. Comparism between Oxygen and Carbon Mono-oxide

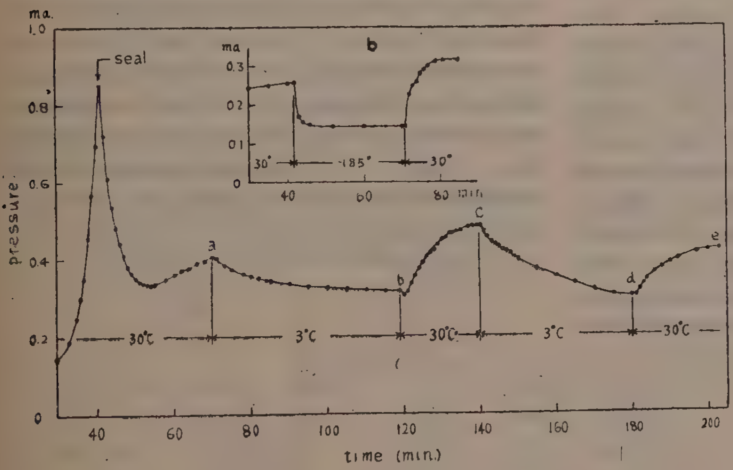

Fig. 7. The pressure change in the sudden temperature change.

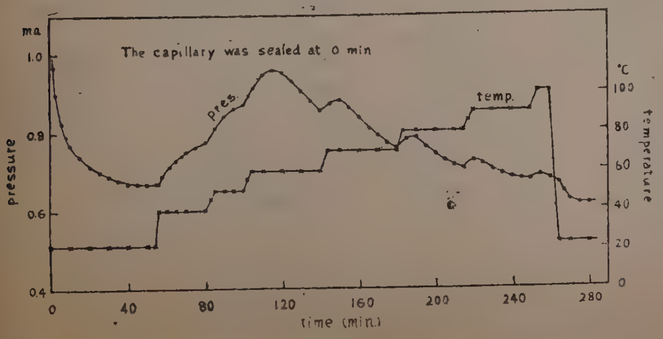

Fig. 8. The pressure chaege in the stepwise temperature change.

Introducing oxygen and carbon mono-oxide respectively into one of two getters which were flashed at as possible as similar conditions, results shown in Fig. 9 were obtained. Although the gettering ability depends largely upon the flashing conditions, the getter apparently absorbes much more amount of oxygen than carbon mono-oxide. In the case of oxygen several abnormalities were observed both in its resistrnce and pressure curve, as described previously²⁾, but in the case of carbon mono-oxide no abnormality was encountered.

Several interesting phenomena were observed if two kinds of gas were introduced alternatively. Fig. 10 is one of results obtained in such process. Oxygen was introduced at first, and then it was replaced by carbon mono-oxide at b suddenly. Judging from the curve ab, the pressure

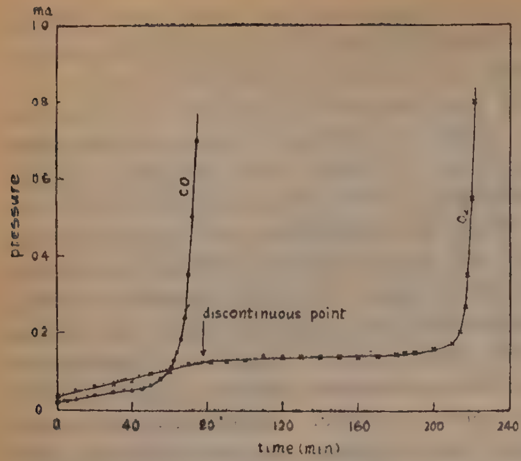

Fig. 9. Comparism between oxygen and carbon mono- oxide in the c. f. method.

should remain unvaried if oxygen is continued to be introduced, but replacing the introduced gas by carbon mono-oxide, the pressure began to increase only about 10 mins. after the replacing. Inter changing from carbon mono-oxide to oxygen, the pressure decreased rapidly as if the gettering ability recovers very much (cd). Repeating several times, similar phenomena were obtained. The cross and circle marks mean the periods in which oxygen and carbon mono-oxide were introduced respectively. This curious results suggest that the absorption of oxygen did not disturb the absorption of carbon mono-oxide, in other words, that the absorption mechanism of carbon mono-oxide differs from that of oxygen. As oxygen form oxide with barium above room temperature, the whole surface of the getter mirror is effective for its absorption, but carbon mono-oxide is mainly absorbed into lattice imperfections. Thus carbon mono-oxide and oxygen can be absorbed independently by the barium getter.

Precisely, however, oxygen and carbon mono-oxide seem to corporate to promote the absorption ability each other. Especially oxygen has the ability to promote the absorption of carbon mono-oxide. Two examples are reproduced in Fig. 11. When the capillary is sealed at a (No. 2—8a), the pressure changed as ab. Beginning to introduce carbon mono-oxide, the pressure increased as bc, but interchanging from carbon mono-oxide to oxygen, the pressure decreased suddenly as cd. If only carbon mono-oxide is introduced instead of oxygen, the rate of pressure decrease in cd must situate between rates of the pressue changes ab and ef, in quite disagreement with the experimental results.

In No. 2-8b the pressure decreased as ab when the capillary is sealed, but beginning to introduce oxygen at b, the pressure began to decrease suddenly (bc). After a complex pressure change cde, it began to increase at last. These two examples present direct foundations for oxygen having the promot-

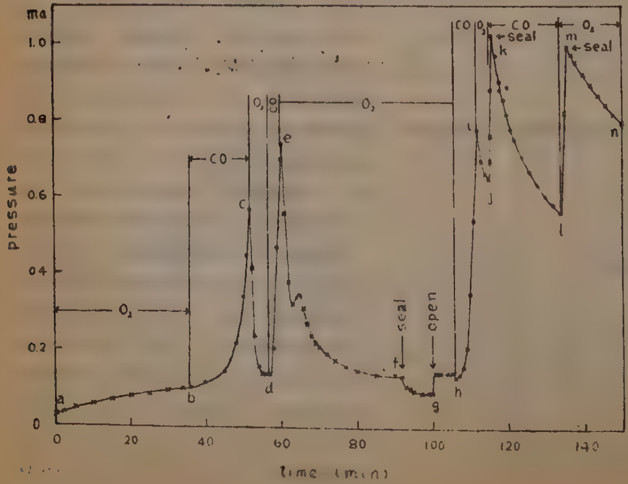

Fig. 10. Alternative introduction of oxygen and carbon mono-oxide.

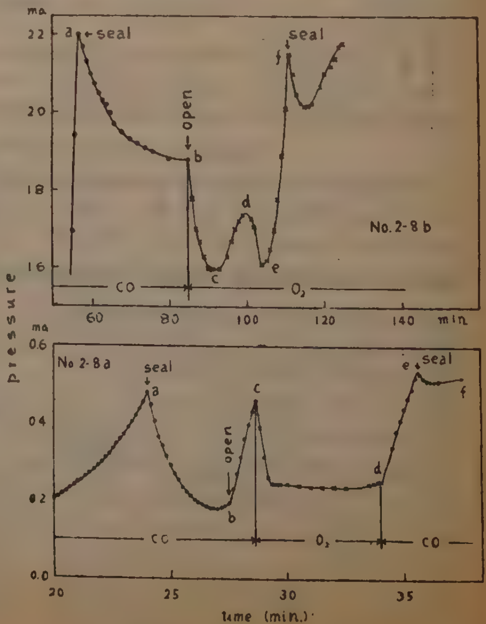

Fig. 11 Promoting action of oxygen for the absorption of carbon mono-oxide.

ing action for the absorption of carbon mono-oxide. The getter becomes active as soon as oxygen began to be introduced, suggesting that the suface absorption of oxygen is the cause for the promoting action. Similar action has been known in the case of catalytic process, but only from the present data the detailed discussion seems still difficult.

§ 9. Summary

In this paper the sorption processes for carbon mono-oxide beyond room temperature were mainly described. Important experimental results are summerzid as follow: (1) In the c. f. method the pressure increases linearly with the very slow rate, showing that almost all introduced gas is absorbed by the getter, but no remarkable resistance change is observed except the very early stage.

(2) In the c. v. method the pressure decreases at first, but it begins to increase after a while. Such pressure increase is observed only in the temperature range between −10°C and 70°C. In this temperature range carbon dioxide is formed by the catalytic action of barium. Only the surface-adsorbed atoms are effective for the formation of carbon dioxide, but atoms absorbed in lattice imperfections are not effective.

(3) Ionizing the introduced gas the absorption ability becomes slightly vigorous, because carbon mono-oxide is mainly absorbed in the activated state at room temperature.

(4) In the c. f. method the resistance change becomes remarkable beyond about 150°C. When the resistance increases to almost infinite, the gas is continuously absorbed, because of the granular structure of the getter mirror.

(5) Raising the temperature of the getter mirror, the pressure increases at first, but above 70°C it decreases gradually. The first increase is caused by the formation of carbon dioxide, while the later decrease is due to the diffusion of the surface-adsorbed atoms into the interior.

(6) Oxygen is, in general, absorbed by the getter much more easily than carbon mono-oxide. Introducing carbon mono-oxide and oxygen alternatively, oxygen promote the absorption of carbon mono- oxide.

The authors wish to acknowledge Mr. Imaeda for his cooperation in this work.

References

1) T. Arizumi & S. Kotani: J. Phys. Soc. Japan **7** (1952) 152

2) T. Arizumi & S. Kotani: J. Phys. Soc. Japan **5** (1950) 70.

3) T. Arizumi & K. Imaeda: J. Phys. Soc. Japan **5** (1950) 169.

4) K. Imaeda; unpublished.

JOURNAL OF THE PHYSICAL SOCIETY OF JAPAN Vol. 7, No. 4 JULY—AUG., 1952

Absorption of Carbon Mono-oxide by the Barium Getter
Part V. Theory of Absorption

By Tetsuya ARIZUMI and Seiichi KOTANI

Kobe Kogyo Corporation, Kobe

(Received March 5, 1951)

The theory presented in Part II was also applicable to the gettering process at room temperature. The activation energies for the activated adsorption of carbon mono-oxide and for the desorption of carbon dioxide, having been formed by the catalytic action, were estimated to be 7.5 and 8.8 Kcal/g.mol respectively. At higher temperatures than 150°C, some kind of compound was formed and the conductivity of the getter mirror changed remarkably. In addition, the probable state of activated adsorption of carbon mono-oxide on the getter surface will be postulated.

§ 1. Introduction

The sorption properties of the Ba–CO system were studied experimentally in Parts I[1] and IV[2] and the theoretical analysis of the experimental results below 0°C were described in Parts II and III[3] of this paper. The results in Part IV indicated that carbon mono-oxide is mainly absorbed into lattice imperfections even at room temperature as below 0°C. Thus the theory will be developed in the same line as described in Parts II and III, but at higher temperature both the formation of carbon dioxide and the diffusion of surface-adsorbed atoms into the interior complicate the theoretical analysis, making the quantitative treatment difficult.

§ 2. Absorption in Lattice Imperfections and Activated Adsorption

The discussions in Parts II and III indicated that at room temperature carbon mono-oxide is adsorbed in the activated state in the first stage of absorption. Glastone and others[4] presented the theory of activated adsorption of the symmetric diatomic molecules, in which they gave the following expression if a diatomic molecule is adsorbed in the dissociated state.

$$v = c_g^{1/2} c_s \frac{RT}{h} \times \left\{ \frac{(2\pi MRT)^{3/2}}{h^3} \cdot \frac{8\pi^2 IRT}{2h^2} \right\}^{1/2} \cdot \exp\left(-\frac{Q_3}{RT}\right). \tag{1}$$

In the case of carbon mono-oxide the molecule seems to adsorb without complete dissociation into carbon and oxygen atoms, as will be discussed in the later section. Thus, instead of $c_g^{1/2}$ in (1), c_g is to be used for the present case. The coefficient to $\exp(-Q_3/RT)$ may well be considered almost constant, giving the approximate formula,

$$v = cp(N_0 - n)\exp\left(-\frac{Q_3}{RT}\right)^{*}. \tag{2}$$

This has the similar form as that of physical adsorption, so the theory described in Part II will be applied formally to the activated adsorption without any modification. Thus the general equation for the absorption into the lattice imperfections,

$$\frac{d\beta}{dt} = -\beta\left(K_S + K_A\frac{NV}{RT}p\right) + K_A K_S N_0 \tag{3}$$

is valid for the present case. Assuming that p is constant, we obtain the solution,

$$\beta = a + (\beta_0 - a)\exp(-k_S a t), \tag{4}$$

where

$$a = \frac{k_A N_0}{1 + \frac{k_A}{k_S}\frac{NV}{RT}p}, \tag{5}$$

predicting that if the condition $1 \gg (k_A/k_S)(NV/RT)p$ is satisfied β decreases exponentially. The estimated values of β and the logarithmic plots of β-a are shown in Figs. 1 and 2 respectively, which indicate that (4) expresses almost correctly the experimental results. The later rapid change of β is probably due to the decrease of a, resulting from the increase of p and the gradual decrease of k_S. If $(k_A/k_S)(NV/RT)p$ is much larger than 1, (5) becomes a hyperbolic function of p, in good agreement with the later rapid change of β in the experimental curve (d and d' in Fig. 1). In the c. v. method β is replaced by α together with k_S being put zero, giving the following equation,

---

* All notations are similar as in the preceding several Parts and Q_3 is the activation energy for the activated adsorption.

$$\frac{d\alpha}{dt} = -\alpha k_A \frac{NV}{RT} p . \qquad (6)$$

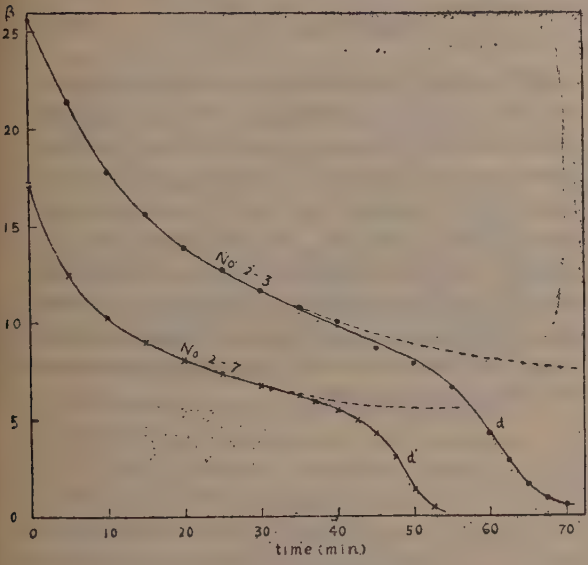

Fig. 1. Time changes of β.

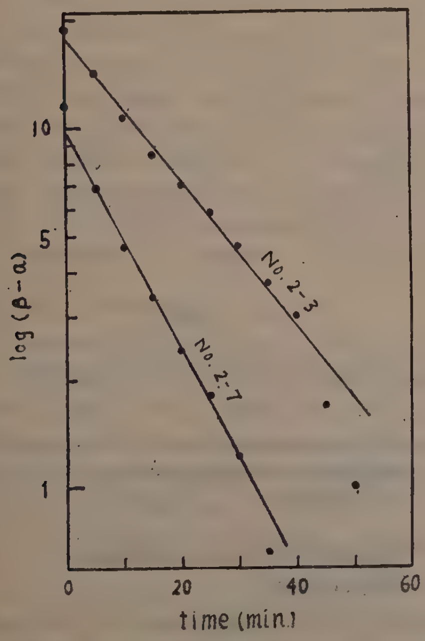

Fig. 2. Time changes of β-α.

Substituting $\alpha = -(1/p)(dp/dt)$ in this formula and integrating, we obtain

$$\frac{dp}{dt} = -ap(b-cp) , \quad a,b,c\text{: constants,} \qquad (7)$$

which is approximately identical to the empirical expression.

§ 3. Formation of Carbon Dioxide

In the c. v. method the pressure decreases at first but it begins to increase gradually as shown in Fig. IV-2. This curious pressure change is due to the formation of carbon dioxide, for which the getter surface acts as a kind of catalyser. The amount of formed carbon dioxide is then proportional to the number of surface-adsorbed molecules or the area covered by carbon mono-oxide molecules. The pressure change in the c. v. method for carbon mono-oxide is, as usually, expressed by

$$\frac{dp}{dt} = -\alpha p , \qquad (8)$$

with the solution

$$p = p_0 \exp(-\alpha t) . \qquad (9)$$

Thus the total number of surface-adsorbed carbon mono-oxide is proportional to $p_0\{1-\exp(-\alpha t)\}$, if the number of surface-adsorbed molecules which have been adsorbed in the c. f. method is neglected and on the other hand newly formed carbon dioxide desorbs to increase the pressure. Accordingly the pressure change is expressed by

$$\frac{dp}{dt} = \gamma\{p_0 - p_0 \exp(-\alpha t)\} - \delta p . \qquad (10)$$

So long as p is still sufficiently small, the second term in the right hand side may well be neglected and we obtain,

$$\frac{dp}{dt} = \gamma\alpha p_0 t . \qquad (11)$$

The solution becomes

$$p = \frac{1}{2}\alpha\gamma p_0 t^2 , \qquad (12)$$

suggesting that the partial pressure of carbon dioxide is proportional to square value of time. When t is sufficiently long, the approximate expression

$$\frac{dp}{dt} \doteq \gamma p_0 - \delta p \qquad (13)$$

is obtained whose solution is given by

$$p = \frac{\gamma}{\delta} p_0 \{1-\exp(-\delta t)\} , \qquad (14)$$

showing that p tends to gradually to $(\gamma/\delta)p$ if t tends to infinity.

To compare the theory with the experiments, the initial part of the pressure change, expressed by (9), is extrapolated (see Fig. IV-3) and the differences between the observed pressures and these extrapolated values are plotted against log. t (Fig. 3). There exists the linear relation with their slopes being almost 1/2, in satisfactory agreement with the theory. The result suggests that no molecules absorbed into lattice imperfections but only surface-adsorbed molecules are effective for the formation of carbon dioxide.

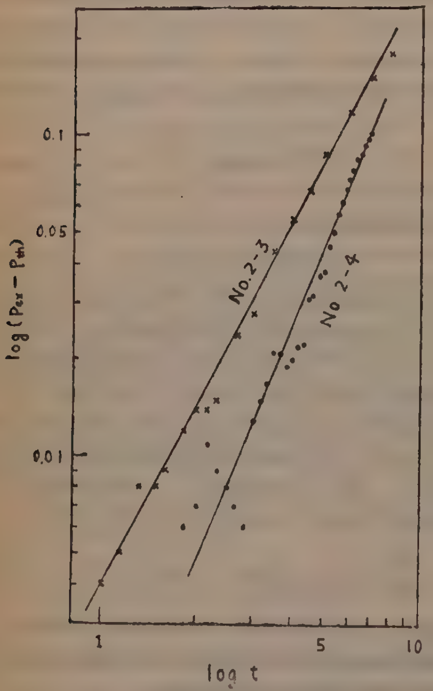

Fig. 3. Partial pressure of CO_2.

When t tends to infinity, p is expressed by

$$p=\frac{\gamma}{\delta}p_0\ , \qquad (15)$$

where both γ and δ are coefficients for the catalytic action and for the activated adsorption of carbon dioxide, which are represented by

$$\gamma=\gamma_0\exp\left(-\frac{Q_4}{RT}\right) \qquad (16)$$

and

$$\delta=\delta_0\exp\left(-\frac{Q_5}{RT}\right) \qquad (17)$$

respectively. Then (15) becomes

$$p=c_1\exp\left(-\frac{Q_4-Q_5}{RT}\right). \qquad (18)$$

Plotting the logarithmic value of equilibrium pressure against $1/T$, the energy difference Q_4-Q_5 can be estimated and substituting (16) and (17) in (11) we obtain

$$\frac{dp}{dt}=c_2t\exp\left(-\frac{Q_4+Q_5}{RT}\right), \qquad (19)$$

which makes the evaluation of Q_4+Q_5 possible. In Fig. 4 these logarithmic values are plotted. Although only two points are plotted for each case, several number of curves are parallel each other, suggesting that the expressions are correctly applied. In the figure Q_4+Q_5 and Q_4-Q_5 are estimated to be 16.33 and 1.88 Kcal/g. mol. respectively, giving $Q_4=8.79$ and $Q_5=7.53$ Kcal/g. mol. They are slightly larger than the energy for the activated adsorption of carbon mono-oxide.

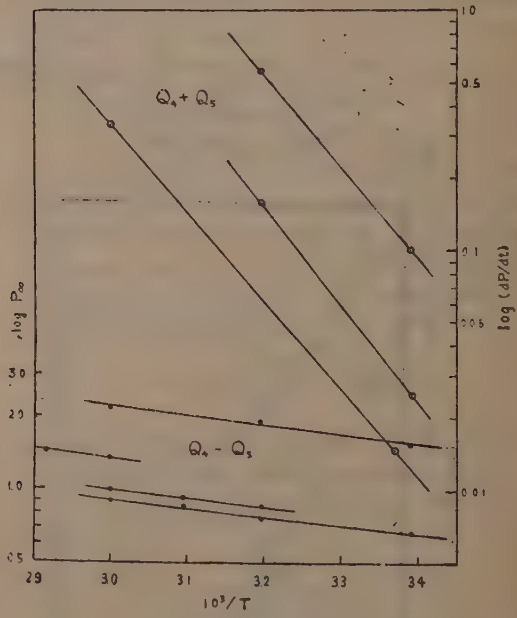

Fig. 4. Logarithmic plots of equilibrium pressure of carbon dioxide and its rate of formation.

§ 4. Pressure Decrease at Higher Temperature

Raising the temperature of the getter mirror gradually, the pressure increases at first, but begins to decrease beyond about 65°C. Assuming that the pressure increases by the formation of carbon dioxide, the maximum pressure must not exceed one-half of the initial value in the c. v. method, because one carbon dioxide molecule is formed from two molecules of carbon mono-oxide. In many cases the maximum pressure is less than one-half of the initial pressure, but sometimes it exceeds the predicted value. Especially the getter whose initial pressure change is small, has the tendency to exceed this limit, probably because in the later rapid pressure change in the c.f. method carbon mono-oxide does not absorb into lattice imperfections but is mainly adsorbed on the getter surface, as described in Part II.

If the temperature of the getter chamber is raised further, the pressure, in general, decreases gradually after the initial slight increase, as shown in Fig. IV-8. Such complex pressure change is probably caused by the successive or simultaneous realization of following four phenomena;

(1) The formation of carbon dioxide increases at higher temperature.

(2) The ability for the activated adsorption of carbon dioxide becomes larger.

(3) Surface-adsorbed carbon mono-oxide molecules are gradually consumed.

(4) The diffusion of surface atoms becomes larger at higher temperature.

At temperatures from 70° to 150°C surface atoms diffuse mainly through lattice imperfections and the normal body diffusion is considered to be fairly small. It is perhaps determined by the surface state of the getter mirror and remaining number of lattice imperfections, whether is the most important factor of these four phenomena.

§ 5. Change of Resistance

At higher temperature than 150°C, the change in resistance becomes remarkable, but in many cases the resistance curve has the similar flat part in its initial stage as observed at room temperature, suggesting that lattice imperfections are not completely destroyed and still effective for the absorption of the gas. The rapid linear resistance change is due to the chemical combination of the gas with the getter itself as pointed out in the case of Ba–O_2 system[5)]. In these cases the diffusion of the gas atoms is the rate-determining factor. The theory applicable for such cases was developped by Imaeda[6)], but only the simple treatment will be mentioned. Neglecting the surface-adsorbed atoms, the change in the conductivity of the getter mirror proportions to the number of absorbed atoms, giving the following expression.

$$\frac{RT}{V}s-\frac{dp}{dt}=k\left(-\frac{d\sigma}{dt}\right). \qquad (20)$$

So long as dp/dt is neglisibly small, (20) becomes

$$\frac{d\sigma}{dt}=-k\frac{RT}{V}s \qquad (21)$$

meaning that the change of conductivity proportions to the amount of the gas flow. Fig. IV-6 presented a good example. But all curves deviate from the expected linearity, until the pressure begins to increase rapidly, because of the granular structure of the getter mirror.

§ 6. Probable State of Surface Adsorption

In Fig. IV-11 the rate of absorption of the getter was found to decrease suddenly as soon as the introduced gas is interchanged from oxygen to carbon mono-oxide, showing that the phenomenon refers to the surface problem and also that new adsorption centres are formed by the adsorption of oxygen. That is to say, oxygen is able to be adsorbed without desorption of already adsorbed carbon mono-oxide and moreover as soon as oxygen is adsorbed the gettering ability recovers suddenly.

On the other hand carbon dioxide is formed catalytically when the absorption of carbon mono-oxide becomes larger. This phenomenon also refers to the surface problem. There are two possibilities to explain for the formation of carbon dioxide:

(1) One carbon mono-oxide molecule collides with an already adsorbed one to release one carbon dioxide molecule remaining one carbon atom.

(2) Carbon dioxide is formed by the interaction of two already adsorbed carbon mono-oxide molecules.

Of these two possibilities the latter one seems to be reasonable, because it takes rather long time for the formation of carbon dioxide. Assuming that carbon mono-oxide molecule dissociate completely into carbon and oxygen atoms, oxygen atoms are to be combined with barium to form barium oxide and they are probably not effective for the formation of carbon dioxide. Thus the formation of carbon dioxide shows that carbon mono-oxide molecules are adsorbed in the activated state without dissociation.

One possibility to explain the promoting action of oxygen for the absorption of carbon mono-oxide will be given by the mechanism described schematically in the following.

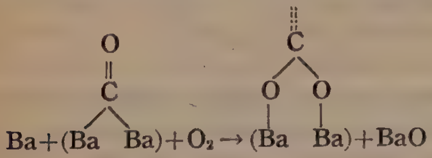

or

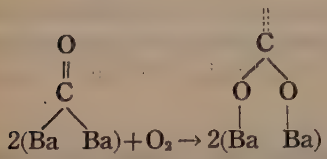

Oxygen atoms breaks the Ba–C bond to enter the intermediate position and at the same time oxygen atom of carbon mono-oxide rotate to make bond with barium atom, making the new adsorption of carbon mono-oxide to the position marked by the dotted line possible. The result that the pressure change is rather small in the case of interchanging of the introduced gas suggests that the first reaction which requires the remaining absorption sites of barium is rather probable.

§ 7. Summary

(1) At temperatures from room temperature to about 150°C, lattice imperfections are effective for the absorption of the gas.

(2) At temperatures from −10°C to about 70°C carbon dioxide is formed and the amount of formed carbon dioxide is in proportion to the number of surface-adsorbed carbon mono-oxide molecules.

(3) The activation energy for the formation of carbon dioxide is estimated 8.8 Kcal/g. mol. and that for the activated absorption of carbon dioxide 7.5 Kcal/g. mol.

(4) The pressure decrease at higher temperature is not a simple process. The decrease of the conductivity at higher temperatures than 150°C is caused by the combination of carbon mono-oxide with barium itself.

(5) Carbon mono-oxide is adsorbed in the undissociated state giving its electrons to the metal.

The authors wish to express their grateful thanks to Mr. Imaeda for his discussions.

Refrences

1) T. Arizumi & S. Kotani: J.Phys. Soc. Japan **7** (1952) 152

2) T. Arizumi & S. Kotani: J. Phys. Soc. Japan **7** (1952) 415

3) T. Arizumi & S. Kotani: J. Phys. Soc. Japan **7** (1952) 158, 163

4) S. Classtone, K. J. Laidler & H. Eyring: The Theory of Rate Process, (1941) New York.

5) T. Arizumi & S. Kotani: J. Phys. Soc. Japan **5** (1950) 70.

6) K. Imaeda: Kobe Kogyo Technical Papers, (in Japanese) 3, No. 8 (1950) 41.

JOURNAL OF THE PHYSICAL SOCIETY OF JAPAN Vol. 7, No. 4 JULY—AUG., 1952

Electromicroscopie de la Surface d'une Cassure de Verre*

Par
Nobuzo TÉRAO et Shigéfumi OKADA
Institut de Science industrielle, Université de Tokyo, Chiba,
Faculté de Médecine, Université de Tokyo

(Received December 12, 1951)

La surface du foyer d'éclatement du verre a été observée avec le microscope électronique. Nous avons observé surtout les petits corps ronds qui se trouvent dans l'endroit lisse du foyer d'éclatement. Nous concluons que ces petits corps sont peut-être des cassures en forme de lentilles qui se produisent parallèlement à la surface de la cassure principale au cours de la rupture soudaine du verre.

Lorsqu'un corps fragile, comme le verre ou le bitume, se rompt brusquement, on trouve au point de départ de la cassure une petite surface sensiblement plane d'un aspect tout particulier que nous appelons "foyer d'éclatement" ou "miroir."[1)-5)] Cette petite surface donne une indication très importante sur l'origine de l'éclatement et M. M. Hirata a montré qu'il y a des rapports intimes entre la résistance à la rupture et le miroir[6)]. Dans le but d'éclaircir le mécanisme de la rupture soudaine du verre, nous avons observé la surface de ce foyer d'éclatement avec le microscope électronique.

D'abord, nous avons cassé une baguette de verre ayant un diamètre de 7 *mm* par la flexion statique pour obtenir une cassure où se trouve un foyer d'éclatement convenable. Aussitôt après cela, nous avons fait une réplique en aluminium de 300–500 Å d'épaisseur suivant la méthode de méthylméthacrylate-aluminium[7)] et de plus nous l'avons ombrée avec le chrome. On fait l'observation de cette réplique avec le microscope électronique de Hitachi HU Type 4 dont le voltage accélérateur est de 50 kV. Les clichés, de la figure 0 à la figure 12, montrent un des résultats obtenus. La figure 0 est une microphotographie optique du foyer d'éclatement et les figures 1 à 12 sont des microphotographies électroniques qui représentent respectivement les points marqués par les chiffres correspondants dans la figure 0. Nous avons aussi arrangé ces 12 figures de sorte qu'elles indiquent la même direction que la figure 0. La surface ronde de ce foyer d'éclatement, qui se produit en partant du centre de cercle, est très lisse au début, mais à mesure que la surface de sectionnement s'approche de la circonférence, elle devient peu à peu inégale. (La surface du foyer d'éclatement n'est pas composée d'un seul plan mais de deux plans qui se coupent avec un angle léger. Ce qui apparaît comme deux plumes noires dans la figure 0 montre le plan oblique qui se trouve à l'endroit où ces deux plans se croisent[8)].) Près de la circonférence, les photographies montrent la cassure en forme de rayon qui chemine du centre vers la circonférence comme l'on s'y attend d'après l'observation avec le microscope optique. Mais, ici, ce qui est surtout digne de remarque, ce sont de petits corps ronds que l'on voit, par exemple, dans les figures 3,4,7,10 etc.. Les résultats principaux que nous avons obtenus à ce sujet sont les suivants :

1° C'est exclusivement dans la partie lisse du foyer d'éclatement que ces petits corps ronds se présentent.

2° Ils commencent dans un endroit un peu éloigné du point de départ du foyer d'éclatement et ils ont une tendance à devenir plus grands à mesure qu'ils s'approchent de la circonférence. Spécialement, ils sont assez grands près de la circonférence et leur diamètre atteint de temps en temps plus de 1 μ.

3° On peut juger par la direction de l'ombre du chrome s'il est concave ou convexe par rapport au plan environnant. En fait, tous les deux, le plan concave et le plan convexe, se mélangent à la surface de la cassure du verre ; mais d'après les photographies que nous avons obtenues jusqu'à présent, le plan convexe est beaucoup moins fréquent que l'autre. Cette caractéristique est à peu près la même sur les deux surfaces complément-

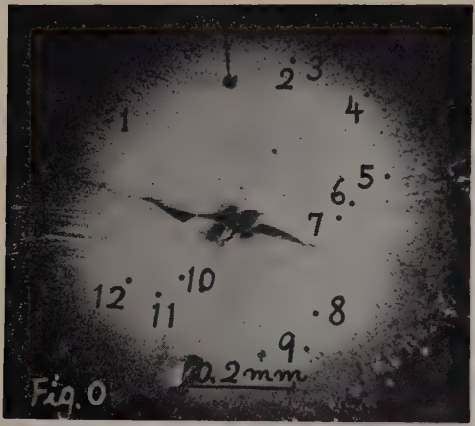

Fig. 0

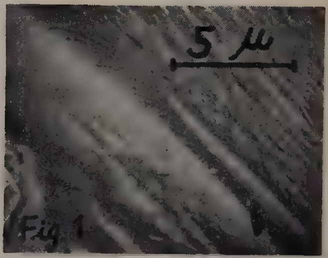

Fig. 1

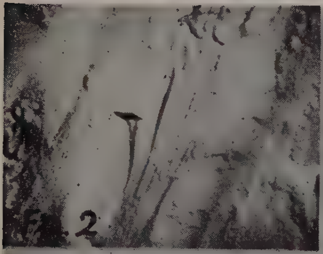

Fig. 2

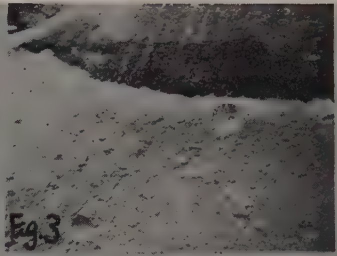

Fig. 3

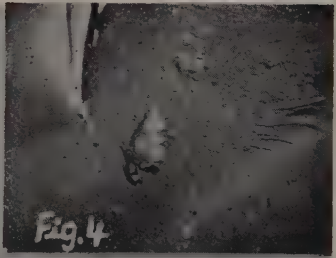

Fig. 4

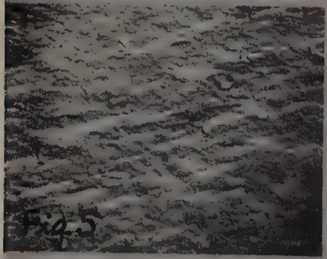

Fig. 5

Fig. 6

Fig. 7

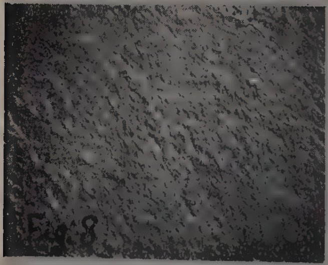

Fig. 8

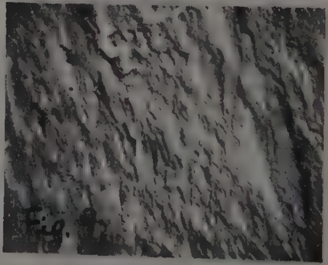

Fig. 9

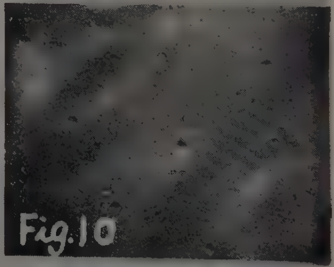

Fig. 10

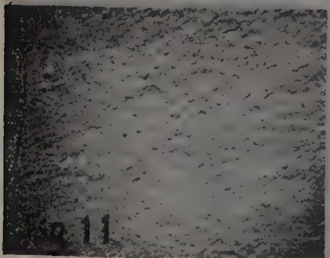

Fig. 11

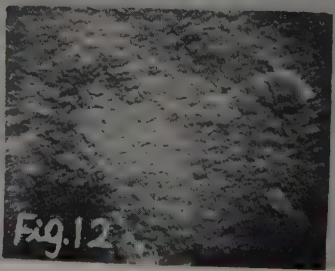

Fig. 12

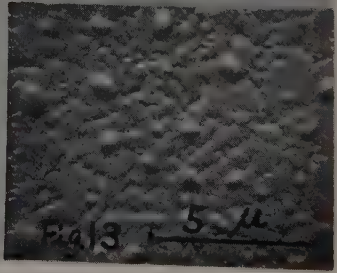

Fig. 13

Électromicrophotographies du foyer d'éclatement du verre.

aires du même foyer d'éclatement.

4° Ce petit corps n'est pas d'une forme parfaitement sphérique mais il est un peu aplati avec une surface assez lisse.

D'après cela, nous supposons que ce petit corps rond est peut-être une cassure en forme de lentille qui se produit parallèlement au plan du foyer d'éclatement, pendant que la cassure se développe. Il nous semble, comme M. M. Hirata l'a dit, que cette petite cassure est de la même espèce que celle en forme de lentille qui se produit abondamment au milieu de la masse quand on durcit la phénolate ou l'ambre dont la recuisson n'est pas parfaite. On l'explique par le fait qu'au moment où le verre arrive à un état d'effort particulier par l'application de la force extérieure, beaucoup de petites cassures en forme de lentilles naissent premièrement. Ensuite la surface principale du foyer d'éclatement se propage le long de la surface dans laquelle les cassures antérieures sont rangées. La figure 13 qui est obtenue à la surface en disposition linéaire de la cassure d'une vitre montre aussi des corps ronds. Nous supposons que si le plan concave à la surface de cassure se présente plus fréquemment que le plan convexe, c'est dû au fait que cette petite cassure en forme de lentille est arrachée du verre et s'attache à la réplique. On peut faire l'hypothèse que cette petite cassure particulière, qui se trouve dans l'endroit plane de la surface de cassure du verre, s'est produite au cours de la formation de la réplique; mais il est plus probable que ce petit corps rond existe réellement à la surface de la cassure parce que l'on ne peut jamais en trouver si l'on fait la réplique de la même façon à la surface d'un verre poli ou d'un autre objet. Mais, d'un autre côté, il y a encore une possibilité qu'il soit un phénomène produit par l'effet secondaire dû à la réaction particulière entre la réplique et la surface de la cassure, parce qu'il est possible que la surface sensiblement lisse de la cassure ait un caractère très différent chimiquement de la surface ordinaire. Cette question fera l'objet d'une étude ultérieure avec une autre méthode de réplique.

Ce travail a été effectué au Laboratoire du microscope électronique à l'Université de Tokyo. Nous tenons à exprimer ici nos vifs remerciements à M. M. Hirata, Professeur de la Faculté des Sciences, pour l'intérêt qu'il a porté à ce travail et pour les encouragements qu'il n'a cessé de nous prodiguer. Nos remerciements aussi à M. H. Eto, Sous-directeur de la Faculté de Médecine, pour son accueil bienveillant.

Bibliographie

1) W. Winkelmann, u. O. Schott: Ann. Phys. u. Chem. **51** (1894) 718.

2) Ch. de Fréminville: Revue de Métallurgie. **11** (1914) 971.

3) M. Hirata: J. Appl. Phys. Japan. **5** (1936) 386.

4) H. Wallner: Zeits. f. Phys. **114** (1939) 368.

5) A. Smekal: Phys. Zeits: **41** (1940), 475.

6) M. Hirata: *Kikai no Kenkyû*. **1** (1949) 186.

7) B. Tadano: J. Appl. Phys. Japan. **16** (1947) 113.

8) M. Hirata: Sci. Pap. I. P. C. R. **16** (1931) 172.

---

* Séance de la Société d'électromicroscopie, le 23 mars 1950.

J. Phys. Soc. Japan 7 (1952) 430–431

Dissociation of Oxide-Coated Cathode by Primary Electron Bombardment

By Shigetomo Yoshida, Ikuo Takeda and Hikaru Arata

Electrical Communication Laboratory, Ministry of Telecommunication, Tokyo, Japan

(Received January 18, 1952)

The temperature dependence of the secondary electron yield of the oxide-coated cathode has been studied in considerable detail[1)2)3)4)] in view of the importance in technical fields. The effect of primary electron impact on the oxide-coated cathode has, however, not yet been well known. We attempted, therefore, the measurement on this subject.

Using a D.C. standard electron gun measuring technique, the values of δ for barium strontium oxide, ranging between 3.0 and 10 at room temperature, are obtained at $E_T=100$ volts. In Fig. 1 are shown δ values scattered in wide range due to various conditions of heat treatment and electron bombardment.

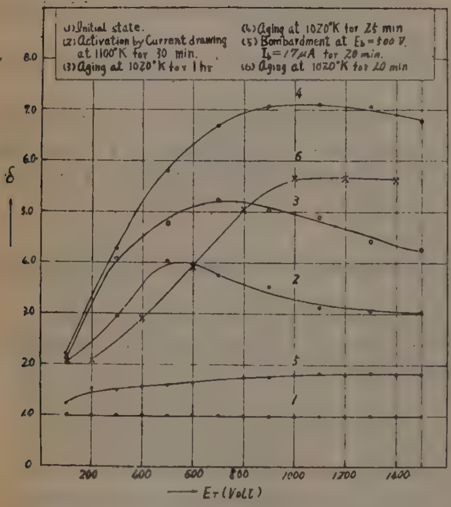

Fig. 1. Yield curves for barium strontium oxide.

The difference of the thermionic emission current from the oxide-coated cathode was measured before and after the primary electron impact. Three types are found in the thermionic emission characteristics after cutting off the primary current as in Fig. 2 (A), (B) and (C). The stationary value of the thermionic emission current before the primary electron bombardment is denoted by the symbol ⊕ in Fig. 2.

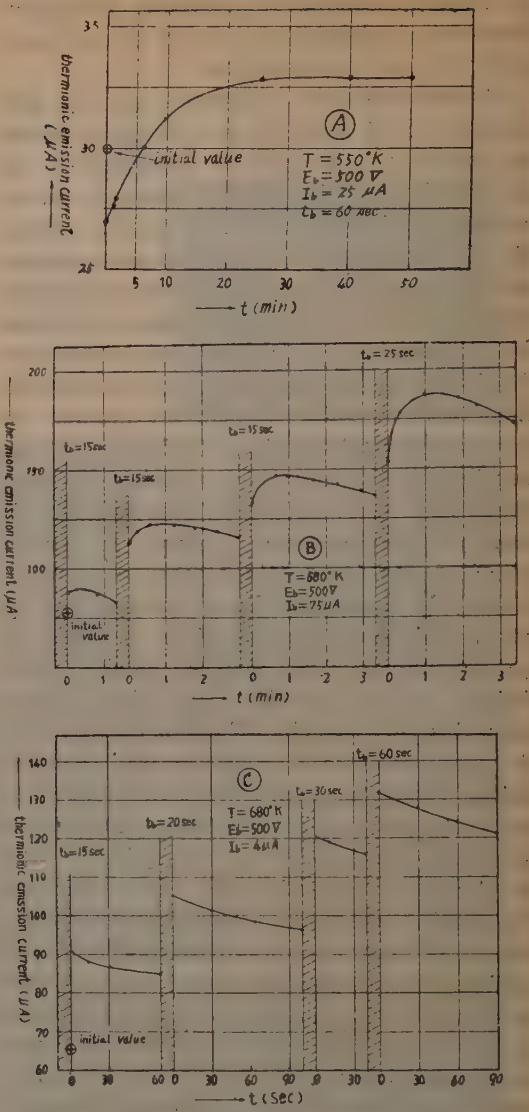

Fig. 2. Three typical variation of the thermionic emission after the primary electron impact.

At low temperature the thermionic emission current measured immediately after the bombarding by primary electron starts from a lower point than the initial stationary value and gradually increases. After a long time, the thermionic emission current exceeds the initial value (Fig. 2 (A)).

At somewhat higher temperature, after the bombardment by primary electron the thermionic emission current of the oxide-coated cathode starts from a higher value than initial one and arrives at a maximum value. Then it decreases but does not fall to values lower than that of initial emission current (Fig. 2 (B)).

The decreasing in the primary bombardment current I_b at the same temperature as in the case (B) has the same effect on the emission characteristics after the impact, as that caused by the increasing in the temperature at the same bombarding current. In both cases the thermionic emission current also starts from the higher point than the initial one and falls, but does not decrease to the initial value. (Fig. 2 (C)).

It is the general characteristics common to three types (A), (B) and (C) that the oxide-coated cathode is activated after the electron impact. It will be possible to suppose that barium oxide dissociates into barium atom and oxygen molecule by electron impact, and thus layers of excess barium atoms are formed on the oxide-coated cathode, whereas the oxygen molecules formed may be liberated from the surface.

Barium atoms thus produced on the oxide-coated cathode surface, at a comparatively lower temperature, do not diffuse easily into barium oxide cathode and are consequently accumulated on the surface. Excess accumulation of barium atoms on the surface causes decrease in the thermionic emission of the cathode, so that it must remains at some lower value than that of initial stationary state immediately after the electron impact. When the primary current is cut off, however, accumulated barium atoms diffuse into the barium oxide cathode and compose the impurity centers gradually. This process corresponds to the activation of oxide-coated cathode, (Fig. 2 (A)).

At the higher temperature than that of case (A), barium atoms which is formed during the bombardment can diffuse easily than in case (A) and excess accumulation of barium atoms on the surface does not take place.

After cutting off the primary current, because of above mentioned reason, the thermionic emission starts from a higher value than the initial one. A small amount of excess barium atoms which depress the thermionic emission, diffuses with time and the thermionic emission reaches at a maximum value. Then the decay of the thermionic emission appeares owing to the decreasing in the concentration of barium impurity centers in the layer immediately under the oxide-coated cathode surface. (Fig. 2 (B)).

When the temperature is higher or the bombarding current density is smaller than in the case (B), no excess accumulation of barium atoms on the surface takes place, so the thermionic emission characteristics are similar to that of case (B) after the maximum point. (Fig. 2 (C)).

The critical energy of the bombarding electron causing the dissociation of barium oxide is obtained by varying primary electron voltage E_b. The value obtained lies between 6 and 7 eV. Estimating the contact potential difference between the oxide-coated cathode and tungsten primary filament as rougly 4 eV, the threshold value becomes 10.5 (=4+6.5) eV. This is found to be identical with the energy of 10.3 eV⁵⁾ which corresponds to the energy of dissociation of solid state barium oxide into barium atoms and oxygen molecules.

References

1) N. Morgulis and A. Nagorsky: Tech. Phys. USSR **5** (1938) 848.

2) M. A. Pomerantz: Phys. Rev. **70** (1946) 33.

3) J. B. Johnson: Phys. Rev. **73** (1948) 1058.

4) T. J. Jones: Nature **161** (1948) 846.

5) J. P. Blewett: J. App. Physics **10** (1939) 668, 831.

J. PHYS. SOC. JAPAN **7** (1952) 431-432

Study of Supersonic Gas Flow through Nozzle by Plastic Deformation

By Nobuo INOUE

Faculty of Engineering, Doshisha University, Kyoto

(Received April 15, 1952)

Recently the author has pointed out¹⁾ an analogy between a steady irrotational flow of a non-viscous compressible fluid and a statically determinate state of stress in a plastic material. In effect, in a plane problem, the two equations of equilibrium of the plastic state of stress are equivalent to the equations of continuity and irrotationality, if the plastic state of stress is made correspond to the gas flow by the following relations:

$$dq/q=-[(1-\tau')/(2\tau)]d\sigma,\ d\rho/\rho=d\sigma/\tau,\ \theta=a_1,\quad \text{for}\ \ \tau'<1, \tag{1}$$

or

$$dq/q=[(1+\tau')/(2\tau)]d\sigma,\ d\rho/\rho=-d\sigma/\tau,\ \theta=\alpha_2,\quad \text{for}\ \ \tau'>-1, \tag{2}$$

where q, θ are the magnitude and direction of the gas velocity, ρ the gas density, and σ the mean normal stress $(\sigma_1+\sigma_2)/2$ with algebraically greater and smaller principal stresses σ_1 and σ_2, $\tau=(\sigma_1-\sigma_2)/2$, α_1 and α_2 the directions of σ_1 and σ_2, and finally $\tau'=d\tau/d\sigma$. In accordance with various yield conditions $\tau=\tau(\sigma)$ of the plastic material, we can determine, by use of (1) or (2), the pressure-density relations $p=p(\rho)$ of hypothetical gases to be introduced and the velocity-stress correspondence. Several hypothetical gases, all of which have had the same local sound velocity O at their stagnation points, have been introduced in the previous paper[2)].

It is to be noted here that the stream-lines and equipotential lines of the gas flows correspond to the isostatics of the plastic states of stress, and the Mach lines to the slip-lines. And besides, the slip-lines of the plastic material can be observed directly or by etching, sometimes as failure lines when the material fails by shear, and the isostatics, on the other hand, are failure lines when the material fails by cleavage. Therefore, the steady irrotational flow of the non-viscous compressible fluid without any stagnation point can be studied visually by observing the plastic deformation of the material.

As an example, there are shown supersonic gas flows through nozzles by the three photographs (Figs. 1, 2, 3), which have been taken when a punch was forced into iron pieces. Figs. 1′, 2′, 3′ show the corresponding Mach lines (by broken lines) of the gas flows, having their pressure-density relation $p/\rho^{\gamma}=$const.($\gamma=-\sin\phi$ for $\theta=\alpha_1$, or $\gamma=\sin\phi$ for $\theta=\alpha_2$), or $p/\log\rho=$const., and forms of the nozzles (by full lines), through which the gas flows. The iron is assumed here to obey either the theory of internal friction or the theory of maximum shear, and the Mach number M is calculated from the angle $(\pi/2)-\phi$ between the two families of the Mach lines, by making use of the relation $M=2^{1/2}(1-\gamma)^{-1/2}$. In each figure, the latter analogy (2) is used, and the gas flows from left to right or from right to left.

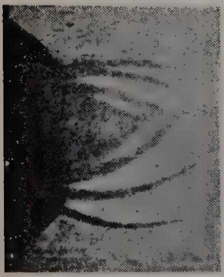
Fig. 1.
$\phi=20°$.

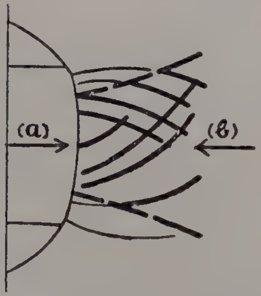

Fig. 1′.
$p/\rho^{0.342}=$const., $M=1.74$.

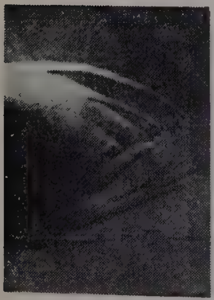
Fig. 2.
$\phi=10°$.

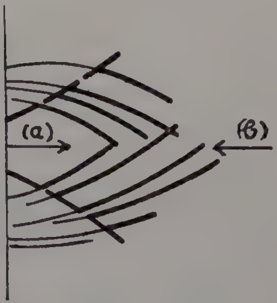

Fig. 2′.
$p/\rho^{0.174}=$const., $M=1.56$.

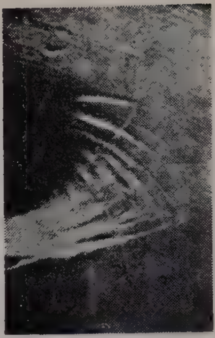
Fig. 3.
$\phi=0°$.

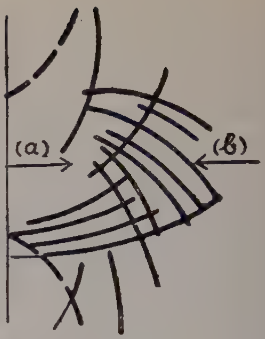

Fig. 3′.
$p/\log\rho=$const., $M=1.41$.

All the photographs have been taken from A. Nádai's famous monograph: Der bildsame Zustand der Werkstoffe (1927). The author wishes to express his sincere thanks and honour to Dr. Nádai for his valuable work.

References

1) N. Inoue: Proc. Phys. Soc. Japan 7 (1952) 45 (in Japanese).
2) N. Inoue: J. Phys. Soc. Japan 7 (1952) 119.

J. Phys. Soc. Japan 7 (1952) 432-434

Rhombohedral Crystals of Ba-Ca and Sr-Ca Double Carbonates

By Jitsuo Terada
Matsuda Research Laboratory, Tokyo
Shibaura Electric Co.
Kawasaki, Kanagawa-ken

(Received April 30, 1952)

As is well known the alkaline earth carbonates have usually two crystal structures; the calcite type (rhombohedral) and the aragonite type (orthorhombic). $CaCO_3$ has both structures but the carbonates of those elements which have larger ion radii than Ca appear as aragonite type structures, whereas the carbonates of those which are smaller than Ca form calcite type structures in minerals[1)].

These alkaline earth carbonates can be artificially precipitated from their nitrates solution by adding sodium carbonate or ammonium carbonate. As to $CaCO_3$, the temperature of precipitation affects its crystal structure and the deposits become aragonite when precipitated at boiling state while, on the contrary, the deposits become calcite when precipitated at room temperature.

The authors have co-precipitated double carbonates by adding sodium carbonate to a mixed solution of barium and calcium nitrates or to a mixed solution of strontium and calcium nitrates in the desired proportions, and examined these crystalline powders by a Geiger counter x-ray spectrometer employing copper K_α radiation.

The barium and calcium double carbonates which have been co-precipitated at room temperature show uniform crystal structure over the range from 20 to 55 mol percents of barium carbonate, and each diffraction line shifts monotonously in accordance with the composition showing that these crystals are solid solutions of barium and calcium carbonates. Moreover the diffraction patterns of these double carbonates are very similar to that of calcite as shown in Fig. 1 except that the $(BaCa)CO_3$ patterns always lack (210) diffraction line. (Presumably $(2\bar{1}0)$ line also disappears.)

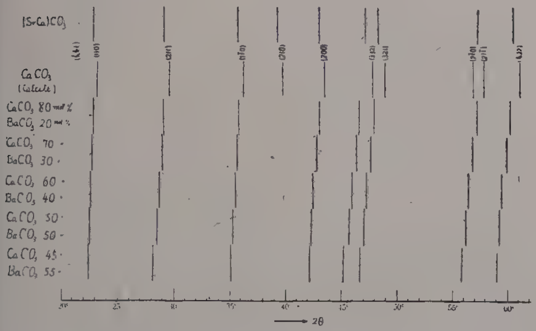

Fig. 1. Rhombohedral patterns of the double carbonates.

The lattice constants of these rhombohedral crystals of barium and calcium double carbonates, which contain two molecules of carbonates, are determined and the values are listed in Table I. The constants of calcite which are calculated from our observations are also shown in this table.

Table I.

	a	α
$CaCO_3$ (calcite)	6.35 A	46° 3′
$CaCO_3$ 80 mol% $BaCO_3$ 20 ″	6.48	45°27′
$CaCO_3$ 70 ″ $BaCO_3$ 30 ″	6.54	45°10′
$CaCO_3$ 60 ″ $BaCO_3$ 40 ″	6.58	45°13′
$CaCO_3$ 50 ″ $BaCO_3$ 50 ″	6.63	44°56′
$CaCO_3$ 45 ″ $BaCO_3$ 55 ″	6.67	44°55′

Fig. 2 shows the relation between the volume of unit cell and the mol fractions of barium carbonate. The volume of unit cell increases linearly with increasing barium carbonate mol fraction within the experimental errors. Rhombohedral crystals of barium and calcium double carbonates with the unit cells larger than the listen will exist, but they are always accompanied with the aragonite type solid solutions of barium and calcium carbonates and in most cases only the strongest (211) line is detected.

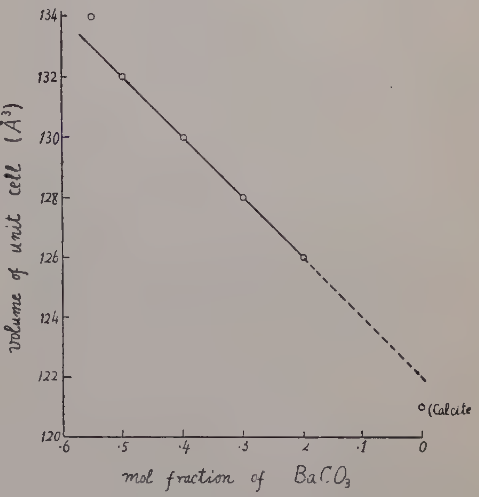

Fig. 2. Relation between the volume of unit cell and the mol fraction of $BaCO_3$.

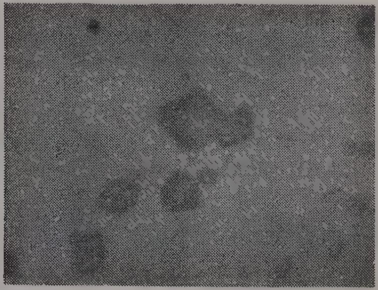

Fig. 3. Microscopic photograph of the rhombohedral crystals of $(BaCa)CO_3$ which is about 10 microns large.

The rhombohedral crystals of strontium and calcium double carbonates have usually appeared accompanied with the aragonite type solid solutions of Sr and Ca carbonates in the co-precipitated specimens which contain below 40 mol percents of strontium carbonate. One of these rhombohedral patterns is also shown in Fig. 1 which is obtained from the specimen containing totally 30 mol percents of strontium carbonate.

In the rhombohedral crystals of $(SrCa)CO_3$ the (210) line does not disappear and the lattice constants of them are slightly larger than the calcite. For instance from the pattern indicated in Fig. 1 we obtain $a=6.46$, $\alpha=45°41'$.

The disappearance of (210) diffraction line in the case of $(BaCa)CO_3$ will be attributed to the extraordinary shrinkage of oxygen atoms in the carbonate radicals.

Reference

1) L. Pauling: *The Nature of the Chemical Bond* (1940).

J. Phys. Soc. Japan 7 (1952) 434–435

On the Effect of the Counter Window for Beta-Ray Spectrum

By Yasukazu Yoshizawa

Department of Physics, Faculty of Science, Osaka University

(Received May 9, 1952)

As recently beta-ray spectra have been precisely measured down to the low energy part, for the discussion of the true shapes of spectra we must consider the effects of scattering and absorption of beta-rays in spectrometer. As regards the effects due to the counter, the absorption and the scattering by the window film,[1][2] by the gas in the counter,[3] and by the lattice of the counter window, and also the efficiency of the counter must be considered. In this note the effect of the window lattice of the counter is discussed.

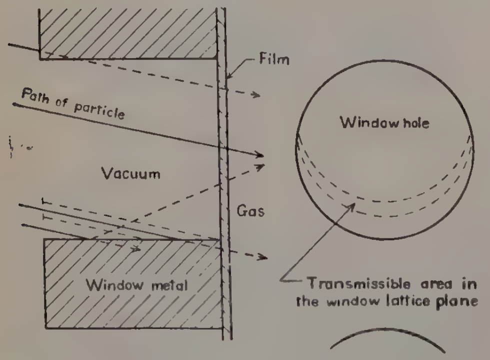

Fig. 1. Diagram of the hole of the counter window.

The measurement of low energy beta-particles demands thin window counter. In order to support the thin window film, the lattice type window is often used, and the effect of the scattering and the absorption by itself cannot be entirely neglected. Since all of the path of the beta-ray at the window is not vertical to the plane of the window, the effective thickness of the metal of the lattice against the incident particle changes with the position and the angle of the path as shown in Fig. 1, i.e., the effective thickness for the oblique incident particle is so thin near the edge of the lattice hole that some of particles can pass through the lattice material. In this note the area near the edge of the hole in the window surface plane will be called the transmissible area, where the effective thickness is thinner than the maximum range of the particles arrived at the window. This transmissible area becomes larger with increase of the incident angle and energy of particles. Though in fixed experimental condition the total transmission of the window depends on the energy of the particles, it depends not only on the energy of the beta-particles, but also on the density of the metal, the dimension of the lattice, and on the incident angle of the beta-particles. Besides some of the scattered particles at the side wall of lattice may enter into the counter and their number also depends on the incident angle and the energy, but the energy dependence of this effect may be far less than that of the absorption. The number of these countable scattered particles propably amounts to the order of, or less than one percent of total particles reached the window. The absorption by such a complicated shape material as the edge of the window hole is not well known. Therefore referring the

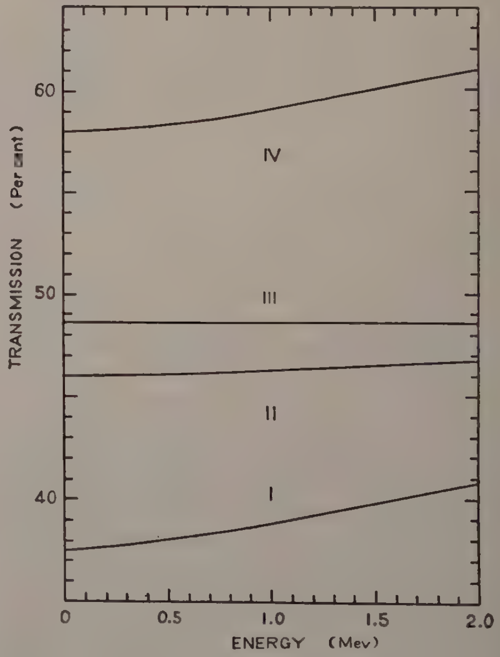

Fig. 2. Transmission of the counter window.

results of Bothe4) and Varder,5) we assume that the number of the transmitted particles is about 30 percent of the number of particles reached the transmissible area. In Fig. 2 typical examples of the transmission *vs.* the energy are shown, where the lattice has holes 1.0 mm diameter, 1.5 mm distance between the center of holes, and 1.0 mm thickness, and is made of the metal of density 8.5. Curve I is the transmission of a semicircular spectrometer with the radius of 10 cm, Curve II is that of a lens type spectrometer having maximum radius 10 cm and the distance of 100 cm between the source and the detector, and Curve III shows that of the vertical beam which has no energy dependency in less than about 2 Mev. Curve IV is the case of Witcher's helix type spectrometer and the counter window,6) which has holes 3.2 mm in diameter and 1.6 mm thick. As fhe higher the energy of particles the larger is the transmission of the window, the relative deviation of the spectrum from true distribution in low energy part is larger for the spectrum with high maximum energy than for that with low maximum energy, because the transmission is larger for large energy beta-particles. Therefore, the Kurie plot of the observed spectrum which has the high maximum energy is distorted slightly concave to the energy axis, but for the spectrum having the low maximum energy the distortion is not so predominant.

Because of the lack of the knowledge in the absorption and the diffusion, the energy dependency of the window transmission shown in Fig. 2 must be checked by experiments. In order to decrease this effect, one should choose the thickness of the window metal as thin as the maximum range corresponding to the maximum energy of beta-ray spectrum and the window metal having the density as large as possible.

Though this effect has not generally been taken into consideration, the distortion of the beta-ray spectrum due to this effect was small enough in most cases, for in spectra with low maximum energies, for example. S^{35}, Co^{60}, Cu^{64}, etc., this effect is too small to be observed.7) But since the experimental accuracy became increased in recent years, the experimental arrangement to avoid this effect should be taken when spectra with high maximum energies, for example, P^{32}, Cl^{38}, K^{42}, ete., are measured.8)

The author would like to thank Professor J. Itoh for the kind discussion.

References

1) D. Saxon: Phys. Rev. **81** (1951) 639.
2) Heller, Sturcken, and Weber: Rev. Sci. Inst. **21** (1950) 898.
3) Langer, Motz, and Price: Phys. Rew. **77** (1950) 798.
4) W. Bothe: Hundbuch der Physik XXII/2 Kap. 1.
5) Varder: Phil. Mag. **29** (1915) 726.
6) C. M. Witcher: Phys. Rev. **60** (1941) 32.
7) J. Backus: Phys. Rev. **68** (1945) 59. He used the counter having the hole of 0.013 inch diameter spaced 0.020 inch apart to measure Cu^{64} spectra. As he investigated only low energy part the effect of the lattice did not appear, but the effect may be predominant if we use such a small hole counter to measure a spectrum of much higher maximum energy.
8) The dimensions of counter windows were not clearly shown in most cases. Therefore, in this note we cannot discuss the effect for the observed spectra having high maximum energies.

J. Phys. Soc. Japan **7** (1952) 435-436

On the Transistor Action of Silicon Crystals

By Yasuo Kanai

The Electrical Communication Laboratory, Ministry of Telecommunications, Tokyo, Japan

(Read. October 8. 1951, received May 20, 1952)

The existence of the transistor action in silicon crystals was reported in the first paper of Bardeen and Brattain1) in which they announced the invention of the transistor. The data of the silicon transistor, however, have not yet been published so far, so it seems to be worthwhile to describe briefly about the transistor action of silicon crystals.

The samples were prepared by the method of vacuum melting of pure silicon powders with about 0.5 weight percent of aluminium. The heat treatment, which was carried out in air of about 1200°C for approximately 3.5 hours, improved the backward characteristics of our samples and the peak back voltages became to about −35 volts.

The experiments were carried out in the A-type arrangement; i.e. two metal probes were placed on the surface of silicon crystals as the emitter and the collector, and spacing of which was approximately 0.2-0.05 mm. The voltages were supplied potentiometrically and no load resistance was inserted in the collector circuit. As in the case of p-type germanium transistor2), the emitter-forming improved the transistor characteristics of silion crystals (which were p-type).

Characteristics of silicon transistors were shown in Fig. 1. Since the current amplification characteristic was the main purpose of our experiments, the collector resistance was lowered to produce such behaviors. Our characteristics differed from that of the germanium transistor reported by Bardeen and Brattain[3] in the following respects; our collector voltage (V_c) was not a double-valued function of the collector current (I_c) when the emitter current (I_e) was taken as the paramater.

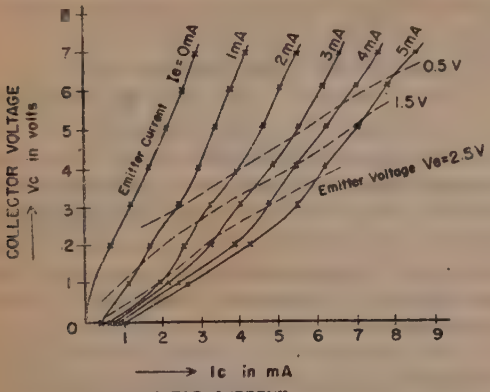

Fig. 1.

Analysing our result by the Hunter's method[4]. Fig. 2 was obtained. Following the Shockley's discussion[5], and considering the fact that the collector resistance was low in our experiment, a few modification of the Hunter's procedure was taken into account in our analysis.

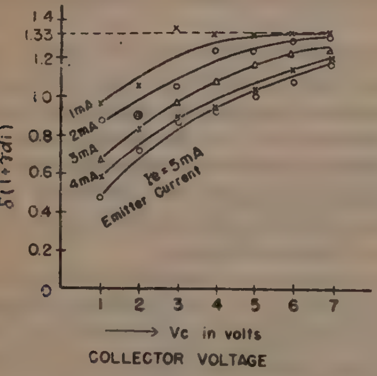

Fig. 2.

γ=fraction of the emitter current carried by electrons,

δ=fraction of the emitter current leaving emitter which arrive at the collector,

α_i=“intrinsic α”=increase in collector current per unit increase of electron current to the collector point at constant collector voltages.

If the complicated multiplication processes such as the “p-n Hook”[6] were absent at the collector, then α_i should equal to b which is the ratio of hole mobility to electron mobility in silicon (i.e.$=1/3$)[7]. Assuming $\alpha_i=b=0.33$ and $\delta=1$, Fig. 2 showed that $\gamma=1$; namely the emitter current were all carried by electrons.

References

1) J. Bardeen and W. H. Brattain: Phys. Rev. **74** (1948) 230.

2) J. Bardeen and W. G. Pfann: Phys. Rev. **77** (1950) 401.

3) J. Bardeen and W. H. Brattain: Phys. Rev. **75** (1949) 1208.

4) L. P. Hunter: Phys. Rev. **77** (1950) 558.

5) W. Shockley: “*Electrons and Holes in Semiconductors*”. Van Nostrand Company, Inc. New York, 1950, p. 101.

6) W. Shockley: Phys. Rev. **78** (1950) 865.

7) G. L. Pearson aud J. Bardeen: Phys. Rev. **75** (1949) 865.

J. PHYS. SOC. JAPAN **7** (1952) 433-437

A Preliminary Study on the Anomalous Scattering of Cosmic-Rays at 50 m.w.e. Underground

By I. HIGASHINO, M. ODA, T. OSHIO,
H. SHIBATA and Y. WATASE

Osaka City University, Osaka University

(Received May 22, 1952)

The anomalous scattering of the penetrating component of cosmic-rays in 15 cm Pb at 50 m.w.e. underground (in Isohama Tunnel) was investigated with a counter hodoscope, and the angular distribution (from 20° to 90° of projected angle) and the cross section for anomalous scattering were obtained.

The experimental arrangement is shown in Fig. 1. A record was obtained whenever the 6-fold coincidence ($A_{\geq 1}B_{\geq 1}C_{\geq 1}D_{\geq 1}E_{\geq 1}F_{\geq 1}$.) was completed. When an event seemed to concern with a single particle and the trajectory of the latter could not be situated on a straight line, we regarded it as a “scattered event”, the trays L, M, and H being set up to confirm this. The tray S was used when numbers of the incident particles and knock-on events were measured.

During 990 hrs. of the observation, 19 scattered events were obtained, of which spurious events were estimated as follows; 9 knock-on events, at most 1 chance coincidence and 2 multiple Coulomb scattering events. Taking into consideration of

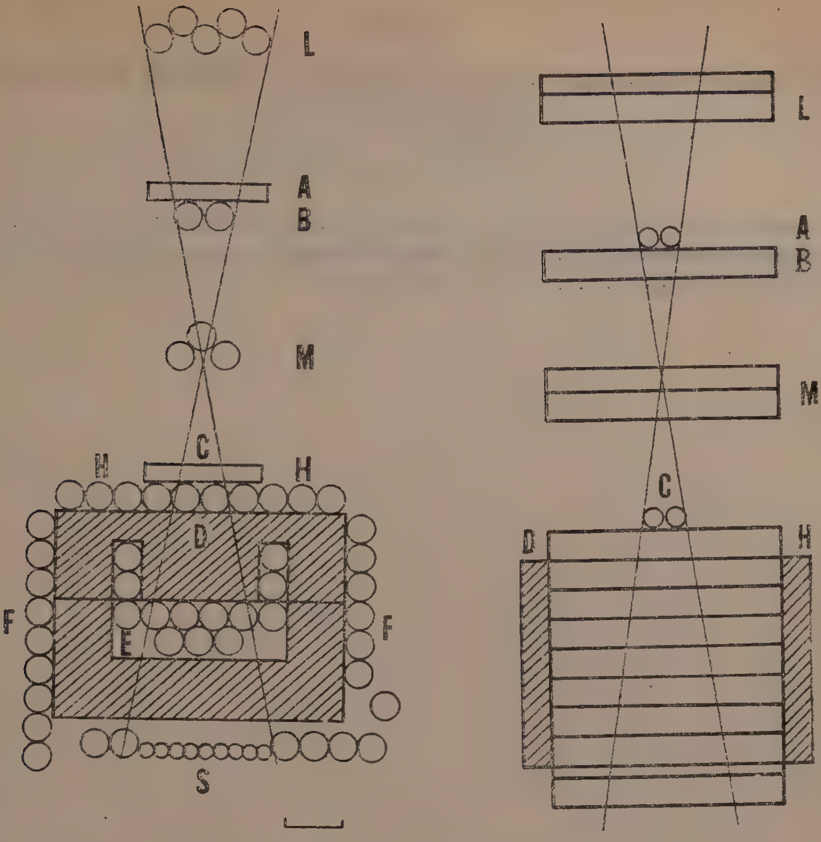

a b

Fig. 1.

the geometrical efficiency of the apparatus. the corrected anomalous scattering events seemed to be 11 during the period of the observation.

The angular distribution of the scattered events is shown in Fig. 2. From our preceding experiment, the total number of incident particles was expected as 2373±89 during the same time interval. Consequently an upper limit of the cross section for the anomalous scattering of the penetrating component of cosmic-rays underground is

$$\sigma_{\geq 200} \simeq 55\pm 19 \quad \mu \text{ barns/nucleon}$$

This value is much larger than that of Amaldi and Fidecaro[1], and of George and Evans[2], and compares well with the results obtained by George and Trent[3] and by Braddick, Nash and Wolfendale[4].

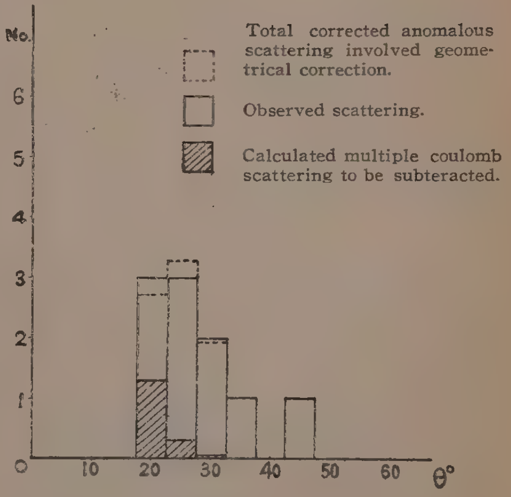

Fig. 2. The knock-on events have been subtracted.

References

1) Amaldi, E., and Fidecaro, G.: Phys. Rev. **81** (1951) 339.

2) George. E. P., and Evans, J.: Proc. Phys. **63** (1950) 1248.

3) George. E. P., and Trent. P. T., 1951, Private communication to Dr. Hayakawa.

4) Braddick, H. J. J., Nash, W. F., and Wolfendale, A. W.: Phil. Mag. **42** (1951) 1277.

Errata

Proton Magnetic Resonance Absorption in Hydrogen Perchlorate and the Structure of the Oxonium Ion I

By Y. KAKIUCHI, H. SHONO, H. KOMATSU and K. KIGOSHI

J. Phys. Soc. Jap. **7** (1952) 102

The scale of the abcissa in Fig. 5 (a) to (f) was in error, and all the numbers must be multiplied by a factor of 1.67. Namely, the tails of the curve (b), for instance, correspond not to ±10 Gauss, but to ±16.7 Gauss.

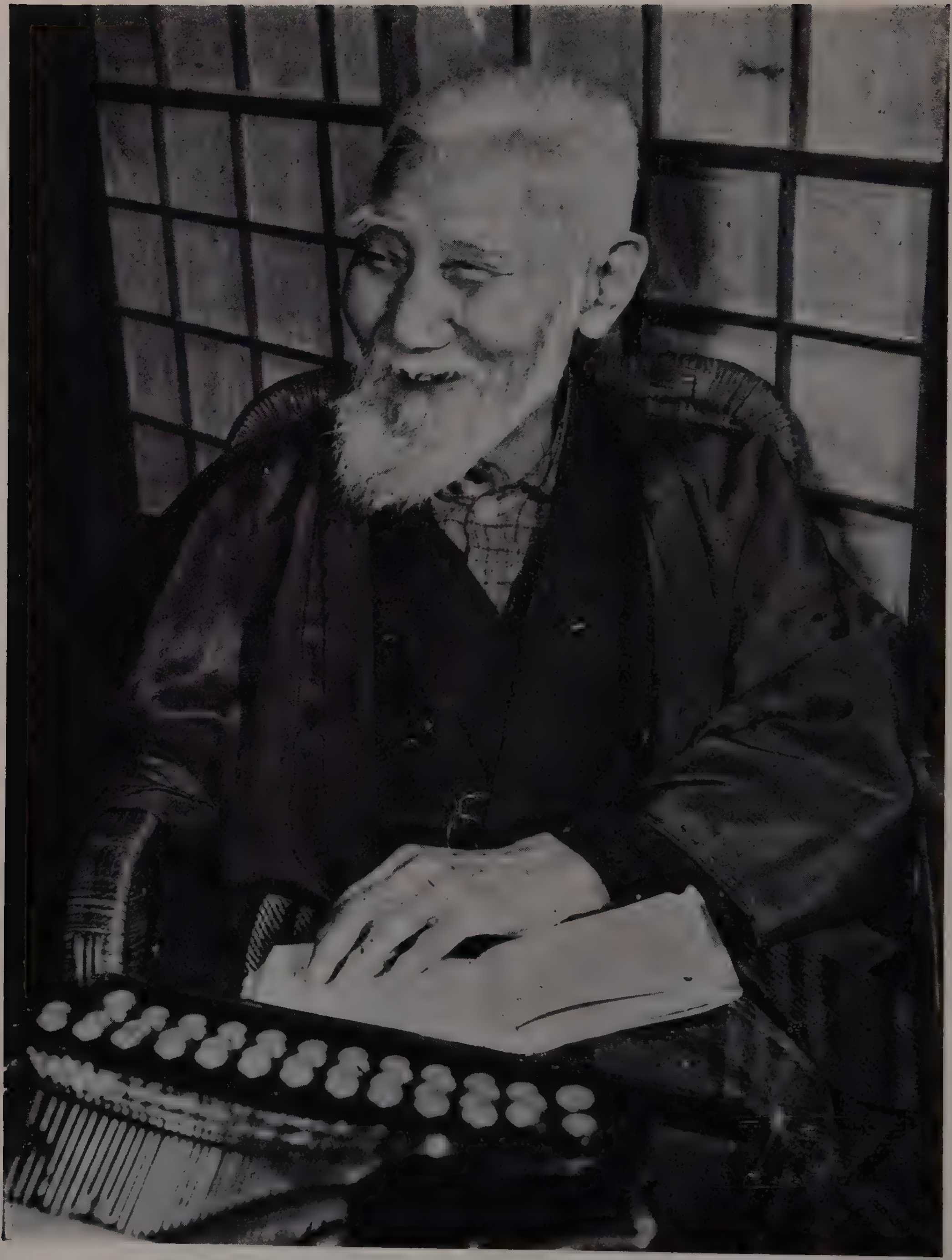

Tanakadate-A

(1856—1952)

Obituary Notice of Professor Aikitu TANAKADATE

Professor Aikitu Tanakadate, an honorary member of the Society, emeritus professor of the University of Tokyo and member of the Academy of Japan, passed away peacefully, after a short illness, on May 21st, 1952, in his ninety-sixth year. By his death Japan has lost one of the most distinguished pioneers in physics in general and geophysics and aeronautics in particular.

Born on September 18th, 1856, at Hukuoka-town, Iwate Prefecture, Prof. Tanakadate graduated the course of physics in the College of Science of the Tokyo Imperial University in 1882. After three years' study at Glasgow, England under the guidance of Sir William Thomson (Lord Kelvin), he returned home in July, 1891, and immediately he was appointed a professor of physics in his Alma Mater, the Tokyo Imperial University, which position he held until 1917, up to the time of his retirement. In August, 1891, he took the degree of Rigakuhakusi (D. Sc.) at the Tokyo Imperial University and in 1906 he was elected a member of the Imperial Academy of Japan.

The scope of his research works was wide and extensive. In its earlier stage, a great deal of work was done on geophysics with the late Professor H. Nagaoka, Professor S. Nakamura and others. Thus, detailed measurements were carried out, with considerable achievement, on the force of gravity and terrestrial magnetic field at various places in Japan, especially after the great Mino-Owari earthquake in October, 1891.

Immediately after the Mino-Owari earthquake just mentioned, the necessity of studying various problems relating to earthquakes was widely recognized and the Earthquake Investigation Committee was established in the Ministry of Education. Prof. Tanakadate was one of its active members and made distinguished contributions to the progress in seismology in Japan. It is not too much to say that the remarkable progress in later years in geophysics and particularly in seismology in Japan owes much to Prof. Tanakadate.

Prof. Tanakadate was also the foremost scholar in Japan in the science of aviation and contributed more than anyone else to the progress of aeronautics in this country. As early as 1908 he constructed a small wind-tunnel in his laboratory and investigated the flow of air around various bodies, such as models of airships and aeroplane wings. In 1910 he succeeded in contriving to take instantaneous photographs of the whirlwinds generated by airscrews, and when he made a short trip to Europe in the same year, he brought with him those interesting photographs which were much appreciated by his French *confrères*.

When one speaks about Prof. Tanakadate, one cannot but refer to his famous Romazi movement. He was very enthusiastic in the furtherance of the movement to adopt the Roman letters in writing out the Japanese language. Whenever he was asked to make an address on scientific subjects, he invariably consented to do so on the condition that he might digress to the Romazi question; and the peroration of his speeches was always to the effect that unless the Japanese nation adopted the Romazi in writing they could never expect to make a satisfactory progress in science.

Prof. Tanakadate's activity in scientific world became rather animated more and more after his retirement from his post in the Tokyo Imperial University; he went abroad 22 times in all to attend, as a Japanese delegate, various international conferences, such as those of the International Research Council, those of the International Union for Terrestrial Magnetism and Atmospheric Electricity, and those of the Comité international des Poids et Mesures, the total number of which amounts to 68.

In recognition of his outstanding contributions to science, a Bunkakunsyo (Order of Cultural Merits) was conferred on him in 1944.

He is survived by one daughter.

(The Chief Editor)

JOURNAL OF THE PHYSICAL SOCIETY OF JAPAN Vol. 7, No. 5, SEPT.—OCT., 1952

Generalized Theory of Thermal Fluctuations

By Hidetosi TAKAHASI

Department of Physics, University of Tokyo

(Received May 10, 1952)

A general theory of thermal fluctuations, or Brownian motions, in a system in thermal equilibrium is developed on the basis of Gibbs's classical statistical mechanics. Taking advantage of the deterministic character of classical systems and applying fluctuation formula for a canonical ensemble, a formula for the cross-correlation function for two quantities u and X is given as

$$\overline{u(t+\tau)X(t)}=kT(\Psi(\infty)-\Psi(\tau)),$$

where $\Psi(\tau)$ is the after-effect function for u responding to a unit-function change of x, while X is the force associated with the generalized coordinate x. Thus the formula indicates the identity of the statistical after-effect to the dynamical after-effect. It may be shown to comprise virtually all the known results pertaining to thermal fluctuation derivable from classical statistical mechanics. A generalization of Onsager's reciprocity relation to a system with after-effect is also obtained.

§ 1. Introduction

There exist a number of fluctuation phenomena which, in spite of its different outer appearances, are closely related to each other in its nature. Here we mean: the Brownian motions of particles and sensitive measuring instruments, critical opalescence and the blue colour of the sky, noise of radio receivers, etc., which are different forms of the fluctuation phenomena in thermal equilibrium. Since the pioneering work of A. Einstein[1] on Brownian motion, numerous theoretical works[2-5] have been done to reveal the quantitative aspects of each of these phenomena. Special mention may be made to some quite recent works[6,7] which attempt a unified treatment of all of them and also to found them on the basic principles of (quantum) statistical mechanics.

Previous works may now be divided into two classes, one static and the other dynamic. The former, mostly due to W. Gibbs,[3] rests on the direct application of the fundamental relations of statistical mechanics, i.e. Boltzmann's distribution law and the equipartition law, and has proved successful in dealing with relations regarding momentary quantities—its mean square variations as well as cross-products.

The representative of the latter class, Nyquist's theory[4] of thermal noises in electrical circuits, is unique in that it successfully introduced *time* into thermodynamic considerations. His formula gives the frequency spectrum of thermal noise voltage but it may be transformed so as to give the auto-correlation function $\overline{E(t)E(t+\tau)}$. The formula is shown to be adaptable to any other fluctuation phenomena.[8]

Onsager's[9,10] proof of the reciprocity theorem for irreversible processes, although not properly intended to deal with fluctuations, may be regarded as one of the most important contributions.

A careful inspection of all these existing theories will now reveal a rather remarkable fact, that fluctuation is always accompanied by an *irreversible* process. Incidentally, a convincing intuitive explanation for this may be that an irreversible process is a transfer of energy from a macroscopic degree of freedom to microscopic degrees of freedom (that is, random motion), while fluctuation is the transfer of energy in the reverse direction. It turns out also that these theories all state the relation of the *statistical* behaviour of a system to its *dynamical* behaviour, that is, its response to an external forcing, and it is this fact that led Onsager to prove the reciprocity theorem.

The present paper, which is intimately related to Onsager's, is intended to generalize the latter by connecting it more directly to Gibbs's formalism of statistical mechanics and so to develop a theory that includes the both classes mentioned above, and to obtain a formula for the cross-correlation function $\overline{X_1(t)X_2(t+\tau)}$ for a pair of quantities. X_1 and X_2. We hope thus to unify the ideas of Gibbs, Nyquist and Onsager.

§2. Fluctuation Formula for a Canonical Ensemble

We shall first evaluate certain average values in Gibbs's canonical ensemble. Consider a dynamical system consisting of a very large number of degrees of freedom, whose canonical coordinates shall be denoted $q_1, q_2, \cdots, q_N$ and momenta $p_1, p_2, \cdots, p_N$. Let u be any function of these coordinates and momenta. The average value of u in this ensemble will then be given by

$$\bar{\bar{u}}=\frac{\int\cdots\int u e^{-\frac{H(p,q)}{kT}}dp_1\cdots dq_N}{\int\cdots\int e^{-\frac{H(p,q)}{kT}}dp_1\cdots dq_N}, \qquad (1)$$

where $H(p,q)$ is the Hamiltonian or energy of the system, the double bar denoting always the averaging over the canonical ensemble.

Now let us consider that H as well as u depends also on some "external coordinates" $x_1, x_2, \cdots, x_n$, which are in a sense subject to our control. The "generalized force" associated with these coordinates will then be defined by

$$X_i=-\frac{\partial H}{\partial x_i}. \qquad (2)$$

The negative sign denotes that we have to do with the reaction of the system against the external system. Table I gives some pairs of x's and X's, to which our subsequent discussion will apply.

Now, it should be noted that the relation between x's and X's are in a certain sense reciprocal. Consider a system, in which the pressure X (instead of the volume x) is the given quantity. Such a system by itself cannot be regarded as a closed system, but it becomes so if a term xX representing the work done to the external system is included in the Hamiltonian. Thus, if H is the original Hamiltonian of the system, and if we put

$$H'=H+xX, \qquad (3)$$

Table 1.
External coordinates and its conjugate forces

Coordinates (extensive) x	Forces (intensive) X
angular displacement	moment
displacement	force
volume	pressure
electric charge	voltage
electric polarization	electric field
concentration	chemical potential
X Forces	$-x$ Coordinates

(External momenta and its conjugate velocities)

Momenta (intensive) y	Velocities (extensive) Y
angular momentum	angular velocity
magnetization	magnetic field
Y Velocities	$-y$ Momenta

we have

$$\frac{\partial H'}{\partial X}=x, \qquad (4)$$

meaning that $-x$ is the generalized force associated with the coordinate X. Generally, *if X_i is the generalized force associated with the external coordinate x_i, then $-x_i$ is the generalized force associated with the external coordinate X_i.*

Now, differentiating $\bar{\bar{u}}$ with respect to x_i, we have

$$\frac{\partial\bar{\bar{u}}}{\partial x_i}=\frac{\int\cdots\int\left(\frac{\partial u}{\partial x_i}-\frac{u}{kT}\frac{\partial H}{\partial x_i}\right)e^{-H/kT}dp_1\cdots dq_N}{\int\cdots\int e^{-H/kT}dp_1\cdots dq_N}+\frac{\bar{\bar{u}}}{kT}\frac{\int\cdots\int\frac{\partial H}{\partial x_i}e^{-H/kT}dp_1\cdots dq_N}{\int\cdots\int e^{-H/kT}dp_1\cdots dq_N}$$

$$=\overline{\overline{\frac{\partial u}{\partial x_i}}}+\frac{1}{kT}\overline{\overline{uX_i}}-\frac{1}{kT}\bar{\bar{u}}\bar{\bar{X}}_i$$

or

$$\overline{\overline{uX_i}}-\overline{\overline{u}}\,\overline{\overline{X_i}}=kT\left(\frac{\partial\overline{\overline{u}}}{\partial x_i}-\overline{\overline{\frac{\partial u}{\partial x_i}}}\right). \tag{5}$$

Rewriting the left hand side,

$$\overline{\overline{(u-\overline{\overline{u}})(X_i-\overline{\overline{X_i}})}}=kT\left(\frac{\partial\overline{\overline{u}}}{\partial x_i}-\overline{\overline{\frac{\partial u}{\partial x_i}}}\right). \tag{6}$$

This result, which is originally due to Gibbs[8)], has been interpreted as a formula giving the *fluctuation quantities* in the left hand side in terms of the experimentally observable *average quantities* in the right hand side, in case u represents a *macroscopic function* of p's and q's, the validity of the formula (6) itself, meanwhile, has nothing to do with the macroscopic character of u.

Taking advantage of this arbitrary choice for u, we will now replace it with a function

$$u^\tau(q(t),p(t);x)=u(q(t+\tau),p(t+\tau);x)$$

that is, the value that u would take at a moment τ seconds after the moment to which the p's and q's are referred. Since in classical mechanics $q_i(t+\tau)$ and $p_i(t+\tau)$ are well-defined (although very complex) functions of the initial values $q(t)$ and $p(t)$, it is certain that we can express, in principle, $u(q(t+\tau),p(t+\tau);x)$ directly in terms of p's and q's referred to the time t, although this might not be a "macroscopic" function. Thus we have

$$\overline{\overline{(u^\tau-\overline{\overline{u^\tau}})(X_i-\overline{\overline{X_i}})}}=kT\left(\frac{\partial\overline{\overline{u^\tau}}}{\partial x_i}-\overline{\overline{\frac{\partial u^\tau}{\partial x_i}}}\right). \tag{7}$$

Here we have to make some remarks concerning the significance of the right side of (7). By tracing back the way we have derived this formula, we find that the dependence of this expression upon x is threefold. The first dependence comes from the factor $e^{-H/kT}$ and therefore come into play only in the process of averaging, and therefore be called the "statistical" part.

The second dependence comes from the dynamical behaviour of the whole system during the time interval t to $t+\tau$, and it is the whole history of x in this interval that influences $p(t+\tau)$ and $q(t+\tau)$, and consequently u^τ, whence this will be called the "dynamical" part.

The last comes from the direct dependence of u on x, already contained in the very definition of u. This will be called the "static" part.

In principle, all these three parts of the dependence on x are independent of each other, and different values of x may be inserted for each case. Incidentally, the only part that has anything to do with the left hand side of (7), is the statistical part, and the remaining parts must cancel out, for the first term $\partial\overline{\overline{u^\tau}}/\partial x$ represent the sums of all the three parts mentioned, whereas in the last term $\overline{\overline{\partial u^\tau/\partial x}}$ the statistical part does no more play a part in differentiation, but the static and dynamic parts are still present and cancel out the first term.

However, in order to make our result include (6) as a special case $\tau=0$, we prefer to use the same value of x in all three parts. With this assumption, the situation to be considered in evaluating $\partial\overline{\overline{u^\tau}}/\partial x$ will be as follows:

We consider an ensemble canonically distributed with respect to a certain x. At the instant t_0 we have the set of values $p_1,\cdots,p_N;q_1,\cdots q_N$, which we take as the reference coordinate of the ensemble. The system is left alone with x unchanged until $t_0+\tau$, when the value of u is observed. What is the dependence of $u(t_0+\tau)$ on x?

Since the system suffers no change at all at t_0, it remains canonically distributed until $t_0+\tau$, and so $\overline{\overline{u^\tau}}=\overline{\overline{u}}$ for all x. Therefore we have

$$\frac{\partial\overline{\overline{u^\tau}}}{\partial x}=\frac{\partial\overline{\overline{u}}}{\partial x} \tag{8}$$

The situation for obtaining $\overline{\overline{\partial u^\tau/\partial x}}$ will next be considered. Since no differentiation is made after averaging, the ensemble over which to average should be fixed. Let it be the canonical ensemble for $x=x_0$. Since our differentiation is with respect to the change in the value of x after t_0, the situation to be considered is the behaviour of the ensemble which has been canonically distributed with $x=x_0$ at $t=t_0$ and obeying thereafter the equation of motion in which $x=x_0+\Delta x$. This corresponds, however, to what we expect when the external coordinate x of the system is suddenly increased at $t=t_0$ from its initial value x_0 by an amount Δx and thenceforth left alone (Fig. 1). Since the average over a canonical ensemble should duplicate approx-

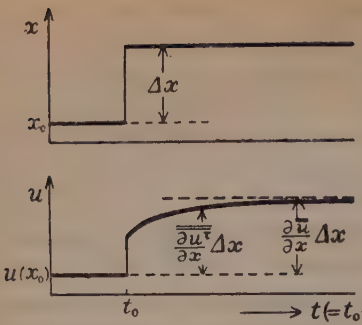
x
Δx
x_0
u
$\overline{\overline{\frac{\partial u^\tau}{\partial x}}}\Delta x$
$\frac{\partial \bar{\bar{u}}}{\partial x}\Delta x$
$u(x_0)$
t_0
$t(=t_0+\tau)$

Fig. 1.

imately what we would observe in the real system, $\overline{\overline{\frac{\partial u^\tau}{\partial x}}}\Delta x$ is the change produced in u at the time $t_0+\tau$ in response to a sudden increase of x at the time t_0 by an amount Δx. We therefore call

$$\overline{\overline{\frac{\partial u^\tau}{\partial x}}}=\Psi(\tau) \qquad (9)$$

the after-effect function for u.

Since $\frac{\partial \bar{\bar{u}}}{\partial x}\Delta x$ is the change of u after the thermal equilibrium at the temperature T is established, we may expect

$$\frac{\partial \bar{\bar{u}}}{\partial x}=\Psi(\infty) \qquad (10)$$

provided the change of x does not produce temperature change. This is certainly the case when $H(p, q; x)$ is an *even* function of x and the initial value $x_0=0$, as in the cases that x is the electric field, the bending or torsion of a uniform straight rod, etc. Then we may write (7) as

$$\overline{\overline{(u^\tau-\bar{\bar{u}})(X-\bar{\bar{X}})}}=kT(\Psi(\infty)-\Psi(\tau)) \qquad (11)$$

whereas in the contrary case, $\partial\bar{\bar{u}}/\partial x$ is always larger than $\Psi(\infty)$, the former denoting the value that would be reached when the system is allowed to restore the original temperature by coming into contact with a heat reservoir.

By differentiating $\Psi(\tau)$ we obtain the after-effect function with respect to impulse excitation. This may also be written

$$\Psi'(\tau)=\overline{\overline{\frac{\delta u(t+\tau)}{\delta x(t)}}} \qquad (12)$$

when $\delta/\delta x$ denotes the functional or Eulerian derivative. With this notation,

$$-\frac{d}{d\tau}\overline{\overline{(u^\tau-\bar{\bar{u}})(X-\bar{\bar{X}})}}=kT\overline{\overline{\frac{\delta u(t+\tau)}{\delta x(t)}}} \qquad (13)$$

We may call the left hand side of (11) or (13) as the statistical after-effect in the thermal fluctuation of the quantity u, while the right hand side is the dynamical after-effect of the average or "causal" dependence of u on x, which may be observed by a macroscopic experiment.

Our formula may thus be regarded as a general link between the laws governing the statistical and the causal behaviour of a system in thermal equilibrium, the proportionality factor being kT.

It is of some interest to observe that each side of (11) corresponds to two major types of physical measurement. The left hand side represents a quantity, which can be obtained by a purely passive observation, without the deliberate participation on our part in the system observed, while the right hand side is obtained by an active measurement by introducing a special exitation into the system. Or it may be said, in a certain sense, that fluctuation is "nature's own experiment".

§ 3. The Fluctuation Formula for a Closed System

The average over a canonical ensemble, discussed in the foregoing section, is something that does not occur in the real system, for which we make observations. The real closed system for which alone a deterministic point of view as we have adopted really apply, must have a definite energy. The proper formula should accordingly be related to the ensemble of all systems having definite energy, the so called microcanonical ensemble.

Suppose now the averaging over a canonical ensemble is made in two steps, first averaging over the ensemble of systems with constant energy H, and secondly averaging over different values of H with proper weighting. Obviously we are interested in the first step.

Now the second step in the averaging will be dispensed with altogether in the following manner by taking the difference of (11) for two values of τ. Thus

$$\overline{\overline{(u^\tau-u^{\tau'})(X-\bar{\bar{X}})}}=kT\left(\overline{\overline{\frac{\partial u^{\tau'}}{\partial x}}}-\overline{\overline{\frac{\partial u^\tau}{\partial x}}}\right). \qquad (14)$$

Denoting by a single bar the average over a microcanonical ensemble, we split the left hand side:

$$\overline{\overline{(u^{\tau}-u^{\tau'})(X-\bar{X})}}+\overline{\overline{(u^{\tau}-u^{\tau'})(\bar{X}-\bar{\bar{X}})}}\ .$$

By taking the average in two steps, the second term is seen to vanish since it vanishes already in the first step, namely

$$\overline{u^{\tau}-u^{\tau'}}=\bar{u}-\bar{u}=0\ .$$

We see further, that the result of the first averaging in the first term, as well as in the right hand side, does not depend significantly (that is, to the order $1/N$) on the energy, so that the double bar may be replaced by a single one. Thus

$$\overline{(u^{\tau}-u^{\tau'})(X-\bar{\bar{X}})}=kT\frac{\overline{\partial(u^{\tau'}-u^{\tau})}}{\partial x}$$

$$=kT(\Psi(\tau')-\Psi(\tau))\ . \qquad (15)$$

Letting τ' tend to infinity, we obtain the desired formula valid for a closed system:

$$\overline{(u^{\tau}-\bar{u})(X-\bar{\bar{X}})}=kT\left(\left.\frac{\overline{\partial u}}{\partial x}\right|_{\mathrm{ad}}-\frac{\overline{\partial u^{\tau}}}{\partial x}\right) \qquad (16)$$

$$=kT(\Psi(\infty)-\Psi(\tau))\ . \qquad (17)$$

Here we have denoted $\left.\frac{\overline{\partial u}}{\partial x}\right|_{\mathrm{ad}}$ instead of $\frac{\overline{\partial u^{\infty}}}{\partial x}$, since this represents the derivative of u with respect to the adiabatic change of x. Putting $\tau=0$ in (16), we have

$$\overline{(u-\bar{u})(X-\bar{\bar{X}})}=kT\left(\left.\frac{\overline{\partial u}}{\partial x}\right|_{\mathrm{ad}}-\frac{\overline{\partial u}}{\partial x}\right)\ . \qquad (18)$$

§ 4. Reversibility of a Dynamical System and the Reciprocity Theorem

Owing to the invariance of the ensemble against the transformation $t\to t-\tau$ we obtain from (16)

$$\overline{(u-\bar{u})(X^{-\tau}-\bar{\bar{X}})}=kT\left(\left.\frac{\overline{\partial u}}{\partial x}\right|_{\mathrm{ad}}-\frac{\overline{\partial u^{\tau}}}{\partial x}\right)\ .$$

By a formal substitution $\tau\to-\tau$ we have

$$\overline{(u-\bar{u})(X^{\tau}-\bar{\bar{X}})}=kT\left(\left.\frac{\overline{\partial u}}{\partial x}\right|_{\mathrm{ad}}-\frac{\overline{\partial u^{-\tau}}}{\partial x}\right)\ . \qquad (19)$$

However, the interpretation of this formal result is not obvious on account of the unusual expression $\overline{\partial u^{-\tau}/\partial x}$. $u^{-\tau}$ may be defined as an obvious extension of u for $\tau<0$, but the derivative $\partial u^{-\tau}/\partial x$ is related to the change in $p(t-\tau)$ and $q(t-\tau)$ that is to be made in order that the *final* value $p(t)$ and $q(t)$ should not change in spite of the change in x during the interval $t-\tau$ to t. This, however, cannot be associated to any experimentally realizable situation.

We shall give (19) another interpretation. In most cases of real interest, where the Hamiltonian is an even function of p's, the dynamics of the system is reversible, in the sense that for every possible motion corresponding to the initial values $(p_1, \cdots, p_N, q_1, \cdots, q_N)$ there exists an inverse motion corresponding to the "final" values $(-p_1, \cdots, -p_N, q_1, \cdots, q_N)$ whose energy is the same as the original motion, and for any τ the values of $p(t+\tau)$ and $q(t+\tau)$ for the original motion are identical to $-p(t-\tau)$ and $q(t-\tau)$ for the inverse motion. In these cases, to any value of $u^{-\tau}$ corresponds the same value of $u^{*\tau}$ in the inverse motion with the same statistical weight, so that we have

$$\frac{\overline{\partial u^{-\tau}}}{\partial x}=\frac{\overline{\partial u^{*\tau}}}{\partial x} \qquad (20)$$

where u^* is the conjugate function defined by $u^*(p, q)=u(-p, q)$. If u is an even function of p's, $u^*=u$.

The Hamiltonian contains odd terms in p's if the system is in a magnetic field, or if the coordinate axis are rotating. Then we can no longer imagine the inverse motion in the same system, but we can do so in the inverse system, for which the Hamiltonian is equal to $H(-p, q)$ of the original system.

Confining ourselves to the reversible system, we have

$$\overline{(u-\bar{u})(X^{\tau}-\bar{\bar{X}})}=k\,T\left(\left.\frac{\overline{\partial u}}{\partial x}\right|_{\mathrm{ad}}-\frac{\overline{\partial u^{*\tau}}}{\partial x}\right)\ . \qquad (21)$$

Subtracting (18) from (21), we obtain

$$\overline{(u-\bar{u})(X^{\tau}-X)}=k\,T\frac{\overline{\partial(u-u^{*\tau})}}{\partial x}\ . \qquad (22)$$

(18) will also be written as

$$\overline{(u^{\tau}-\bar{u})(X^{\tau}-\bar{\bar{X}})}=k\,T\left(\left.\frac{\overline{\partial u}}{\partial x}\right|_{\mathrm{ad}}-\frac{\overline{\partial u}}{\partial x}\right)\ . \qquad (23)$$

Subtracting (16) from (23) we obtain

$$\overline{(u^{\tau}-\bar{u})(X^{\tau}-X)}=k\,T\frac{\overline{\partial(u^{\tau}-u)}}{\partial x}\ . \qquad (24)$$

Subtracting (22) from (24), we obtain finally

$$\overline{(u^{\tau}-u)(X^{\tau}-X)}=k\,T\frac{\overline{\partial(2u-u^{\tau}-u^{*\tau})}}{\partial x}\ . \qquad (25)$$

This result is useful since it contains neither $\bar{u}$ nor $\bar{X}$, and so is applicable to astatic cases, that is, systems for which $\bar{X}$ is indeterminate and $\Psi(\infty)$ is infinite, as it is for a free particle.

Putting $u=X$, we obtain

$$\overline{(X^\tau-X)^2}=-2kT\overline{\frac{\partial}{\partial x}(X^\tau-X)}\,, \qquad (26)$$

a formula directly applicable to the Brownian motion of a free particle, if X is the coordinate and $-x$ the force acting on the particle. It states that the mean square displacement of a particle within a time interval τ along one coordinate direction is $2kT$ times the mean displacement, which the particle would undergo within the same time interval if acted upon by a unit force in that direction.

Formula (26) is equivalent to Einstein's formula when the inertia of the particle is negligible and motion is determined solely by the viscosity of the medium, while the former is more general in that it is valid even when the inertia of the particle as well as the visco-elastic behaviour of the medium is taken into account.

If u is odd in p's, $u^*=-u$, Also, from the even properties of $H(p, q)$ and x, it is easily shown that $\overline{\partial u/\partial x}=0$, so that

$$\overline{(X^\tau-X)(u^\tau-u)}=0 \quad (\text{for odd } u)\,. \qquad (27)$$

Some of the external coordinates, of which the magnetic field and magnetic flux are typical, belongs to a different class in that their signs must be changed with the reversal of time axis. They would therefore more preperly be called "external momenta" and their conjugate forces the "conjugate velocities", and will be denoted by y and Y respectively. Most of our previous results have counterparts in y's and Y's, of which we give here only those corresponding to (26) and (27):

$$\overline{(Y^\tau-Y)(u^\tau-u)}=kT\overline{\frac{\partial}{\partial y}(2u-(u^\tau-u^{*\tau}))}\,, \qquad (28)$$

$$\overline{(Y^\tau-Y)(u^\tau-u)}=0 \qquad (\text{for even } u)\,. \qquad (29)$$

Generalized Reciprocity Theorem

If we substitute for u in (16) a generalized force X_k associated with another external coordinate x_k, and write x_i for x, we obtain

$$\overline{(X_i-\bar{X}_i)(X_k^\tau-\bar{X}_k)}=kT\left(\overline{\frac{\partial X_k}{\partial x_i}}\bigg|_{\text{ad}}-\overline{\frac{\partial X_k^\tau}{\partial x_i}}\right). \qquad (30)$$

Also,

$$\overline{(X_k-\bar{X}_k)(X_i^\tau-\bar{X}_i)}=kT\left(\overline{\frac{\partial X_i}{\partial x_k}}\bigg|_{\text{ad}}-\overline{\frac{\partial X_i^\tau}{\partial x_k}}\right). \qquad (31)$$

For reversible system, the left hand sides of these equations are identical, as stated above. So we have

$$\overline{\frac{\partial X_k}{\partial x_i}}\bigg|_{\text{ad}}-\overline{\frac{\partial X_k^\tau}{\partial x_i}}=\overline{\frac{\partial X_i}{\partial x_k}}\bigg|_{\text{ad}}-\overline{\frac{\partial X_i^\tau}{\partial x_k}}\,. \qquad (32)$$

Since we know that

$$\overline{\frac{\partial X_k}{\partial x_i}}\bigg|_{\text{ad}}=-\overline{\frac{\partial^2 H}{\partial x_i\partial x_k}}\bigg|_{\text{ad}}=\overline{\frac{\partial X_i}{\partial x_k}}\bigg|_{\text{ad}}\,. \qquad (33)$$

we have

$$\overline{\frac{\partial X_k^\tau}{\partial x_i}}=\overline{\frac{\partial X_i^\tau}{\partial x_k}}\,. \qquad (34)$$

Differentiating (34) with respect to τ, as in (13), we obtain the formula in Eulerian derivatives

$$\overline{\frac{\delta X_i(t+\tau)}{\delta x_k(t)}}=\overline{\frac{\delta X_k(t+\tau)}{\delta x_i(t)}}\,. \qquad (35)$$

Verbally, *the influence of the change of one external coordinate x_i at the time t upon the force associated to another coordinate x_k at the time $t+\tau$ is identical to the influence of the change of the latter coordinate x_k at the time t on the force associated to the former coordinate x_i at the time $t+\tau$.*

As already mentioned, the words force and coordinate in the above theorem may be interchanged. That is

$$\overline{\frac{\delta x_i(t+\tau)}{\delta X_k(t)}}=\overline{\frac{\delta x_k(t+\tau)}{\delta X_i(t)}}\,. \qquad (36)$$

(35) or (36) is evidently a generalization of the reciprocity theorem of Onsager[9)], which states that

$$\overline{\frac{\partial \dot{x}_i}{\partial X_k}}=\overline{\frac{\partial \dot{x}_k}{\partial X_i}}\,. \qquad (37)$$

This will be obtained from (36) by differentiation and taking the limit $\tau\to+0$.

Discussion of the Generalized Reciprocity Theorem

Our theorem, as it appears, is certainly a generalization of Onsager's theorem, since it also applies to systems with after-effects, such as lossy dielectrics, viscoelastic solids, etc., with the obvious restriction that they obey linear laws. There is, however, one case of considerable importance for which our theorem appears to be inferior to Onsager's, namely the process involving the heat flow. Our theory is not capable of proving the Kelvin relation concering the thermoelectric effects, one of the most remarkable consequences of Onsager's theory, since there is no "force" that is capable of sustaining a finite temperature gradient in equilibrium state. This seems rather perplexing, since the likeness of the underlying thought of Onsager's theory and ours is so close, and since Onsager's proof seems to be quite free of objection. Moreover, it seems almost certain that (35) and (36) is really valid if we regard energy and the reciprocal temperature as a coordinate and its associated force. It might perhaps be possible to show this by introducing some virtual "force" that would counteract the temperature gradient, but no positive result has yet been obtained.

§ 5. Fourier Transforms

In order to compare our results with Nyquist's theory, we shall transform them into the frequency domain using Fourier transformation. Let $u(\nu)$ anda$X(\nu)$ be the Fourier transforms for $u(t)$ and $X(t)$ defined by

$$u(\nu)=\frac{\sqrt{2}}{\mathrm{T}}\int_t^{t+\mathrm{T}} u(t)e^{-2\pi i\nu t}dt\ , \tag{38}$$

$$X_i(\nu)=\frac{\sqrt{2}}{\mathrm{T}}\int_t^{t+\mathrm{T}} X_i(t)e^{-2\pi i\nu t}dt\ , \tag{39}$$

where T should be sufficiently large so that $\Psi(\mathrm{T})\doteqdot\Psi(\infty)$, and $\nu=m/\mathrm{T}$, $m=1, 2, \cdots$. $\sqrt{2}$ is necessary in order to make the absolute values equal to the r.m.s. values. We then have

$$\begin{aligned}\overline{X_i{}^*u}&=\frac{2}{\mathrm{T}^2}\int_{t_0}^{t_0+\mathrm{T}}\int_{t_0}^{t_0+\mathrm{T}}\overline{X_i(t)\,u(t')}\,e^{2\pi i\nu(t-t')}dtdt'\\&=\frac{2}{\mathrm{T}^2}\int_{-\mathrm{T}}^{\mathrm{T}}\overline{X_i(t)u(t+\tau)}\,e^{-2\pi i\nu\tau}(\mathrm{T}-|\tau|)d\tau\\&\doteqdot\frac{2}{\mathrm{T}}\int_{-\infty}^{\infty}\overline{X_i(t)u(t+\tau)}\,e^{-2\pi i\nu\tau}d\tau\ .\end{aligned} \tag{40}$$

If u is even in p's and the system is reversible, $\overline{u(t-\tau)X(t)=u(t+\tau)X(t)}$, so

$$\begin{aligned}\overline{X_i{}^*u}&=\frac{4}{\mathrm{T}}\int_0^{\infty}\overline{X_i(t)u(t+\tau)}\cos 2\pi\nu\tau d\tau\\&=\frac{4kT}{\mathrm{T}}\int_0^{\infty}\frac{\overline{\partial(u^{\infty}-u^{\tau})}}{\partial x_i}\cos 2\pi\nu\tau d\tau\\&=\frac{4kT\varDelta\nu}{2\pi\nu}\int_0^{\infty}\frac{\overline{\delta u(t+\tau)}}{\delta x_i(t)}\sin 2\pi\nu\tau d\tau\ .\end{aligned} \tag{41}$$

Where we write $\varDelta\nu$ for 1/T, since this is the distance between the neighbouring frequencies.

Now if x's undergo sinusoidal variation: $x_i=\sqrt{2}\,\Re({}_i x e^{2\pi i\nu t})$, u will also vary sinusoidally as $u=\sqrt{2}\,\Re(ue^{2\pi i\nu t})$. They will be related according to

$$u=\Sigma f_i x_i \tag{42}$$

where

$$f_i=f_i'-if_i''=\int_0^{\infty}\frac{\overline{\delta u(\ +\tau)}}{\delta x_i(t)}e^{-2\pi i\nu\tau}d\tau\ . \tag{43}$$

From (41) and (43) we have

$$\overline{X_i{}^*u}=\frac{4kT\varDelta\nu f_i''}{2\pi\nu} \tag{44}$$

If we put specifically $u=X_k$ and write (42) as

$$X_k=-2\pi i\nu\sum_i Z_{ki}x_i \tag{45}$$

where

$$Z_{ki}=\frac{1}{2\pi i\nu}\int_0^{\infty}\frac{\overline{\delta X_k(t+\tau)}}{\delta x_i(t)}e^{-2\pi i\nu\tau}d\tau\ , \tag{46}$$

Z_{ki} may be called the impedances of the system, for they represent the elements of the impedance matrix of a $2n$-terminal network if $2\pi i\nu x_i$ and $-X_i$ denote the currents through and the voltages across the terminals of the network respectively. Then we have

$$\begin{aligned}\overline{X^*{}_iX_k}&=2\varDelta\nu\int_{-\infty}^{\infty}\overline{X_i(t)X_k(t+\tau)}e^{-2\pi i\nu\tau}d\tau\\&=2\varDelta\nu\int_0^{\infty}\{\overline{X_i(t)X_k(t+\tau)}e^{-2\pi i\nu\tau}\\&\qquad+\overline{X_i(t+\tau)X_k(t)}e^{2\pi i\nu\tau}\}d\tau\\&=\frac{2\varDelta\nu kT}{2\pi i\nu}\int_0^{\infty}\left\{\frac{\overline{\delta X_k(t+\tau)}}{\delta x_i(t)}e^{-2\pi i\nu\tau}\right.\\&\qquad\left.+\frac{\overline{\delta X_i(t+\tau)}}{\delta x_k(t)}e^{2\pi i\nu\tau}\right\}d\tau\\&=2\varDelta\nu kT(Z_{ki}+Z^*{}_{ik})\ .\end{aligned} \tag{47}$$

Thus we have the extension of Nyquist's noise theorem to $2n$-terminal systems. This coincides, meanwhile, with the one obtained by the author in a more phenomenological way.[12] Nevertheless, to the author's feeling, the present derivation is regarded as more enlighting.

For ordinary networks satisfying the reciprocity relations $Z_{ki}=Z_{ik}$, we have

$$\overline{X_i{}^*X_k}=4\varDelta\nu kT\Re(Z_{ik})\ . \tag{48}$$

It is however to be noted that our formula (47) is valid even for the systems that do not satisfy $Z_{ki}=Z_{ik}$, that is, for systems containing "gyrators".[13]

§ 6. General Remarks

The result of the present argument may be summarized in a single statement, that the after-effect of the statistical fluctuation duplicates the after-effect in the causal dynamical behaviour of the same quantity under a certain external excitation. In order to obtain the correlation with a quantity X, it was necessary to consider an ensemble in which occur states with positive values of x more frequently and states with negative x less frequently than in the original ensemble. Such an ensemble was realized by introducing an external coordinate x to which X is the conjugate force. It will, however, be not a priori obvious that such a coordinate x always exists. If not, the generality of our theory will be greatly restricted. Our argument as to this point goes as follows: Since we are speaking of fluctuations of a quantity X, this quantity must be precisely defined. This definition must be operational, that is, it must be based on some method of measurement. For example, the pressure of a gas in an enclosure should be defined as the force acting on the wall of the enclosure or any other surface per unit area. Similarly, by the volume of the gas should be meant the inner volume of the enclosure, which may be deformable. The concentration of one component in a mixture may be measured by its dielectric constant. Here we would emphasize that thermodynamic equation of state cannot be applied in these matters, say, for replacing pressure measurement by volume measurement, for it is just the deviation from the thermodynamical relations that we call fluctuation.

The process of measurement, now, will always involve some form of coupling with an external system, which is in general reciprocal. So we can use it in the reverse direction to change a parameter of the system being observed. We now find that the external parameter thus introduced is the required coordinate. Thus, the wall used for the measurement of pressure may be used to change the volume. A local electric field used for concentration measurement will tend to attract the component with higher dielectric constant to that region, creating a gradient of chemical potential. In this way, we see that, whenever we can measure X, we can find the corresponding x.

Our argument has been based throughout on classical statistical mechanics. This, by no means, is a satisfactory way, since we know no system, that can with confidence be stated as obeying strictly to classical mechanics. Our theory therefore would have to be translated into the language of quantum statistical mechanics before any conclusion regarding the real physical system could be drawn. This, however, introduces a rather profound difficulty, which originates in the very nature of quantum mechanical observation, that every observation disturbs the system that is observed. As the result, the ensemble after the observation can no more be regarded as canonical nor microcanonical. We could indeed proceed analogously as we have done and obtain formally a quantum-mechanical version of our formula, which, however, would not be as simple as that already obtained. Meanwhile, we have good reason to believe, that our result remains substantially valid as long as the frequency involved is small compared to kT/h. It is also interesting to see that the quantum-mechanical proof of the reciprocity theorem itself is much simpler, nay, almost trivial. These questions, however, will be dealt with in a later paper.

References

1) A. Einstein: Ann. d. Phys. **17** (1905) 549.

2) General survey on these subjects will be found in: R.B. Barnes and S. Silverman: Rev. Mod. Phys. **6** (1934) 162. "Brownian motion as a natural limit to all measuring processes."

Chandrasekhar: Rev. Mod. Phys. **15** (1943) 1. "Stochastic problems in physics and astronomy." M. Ch. Wang and G.E. Uhlenbeck: Rev. Mod. Phys. **17** (1945) 323. "On the theory of Brownian motion."

3) J.W. Gibbs: Elementary Principles in Statistical Mechanics. Chapter 7. (Yale Univ. Press 1914).

4) H. Nyquist: Phys. Rev. **32** (1928) 110.

5) G.E. Uhlenbeck and S. Goudsmit: Phys. Rev. **34** (1929) 145.

6) H.B. Callen and T.A. Welton: Phys. Rev. **83** (1951) 34.

7) R.F. Green and H.B. Callen: Phys. Rev. **83** (1951) 1231.

8) J.W. Gibbs: p. 83 of the reference (3).

9) L. Onsager: Phys. Rev. **37** (1931) 405; **38** (1931) 2265.

10) H.B.G. Casimir: Rev. Mod. Phys. **17** (1945) 323.

11) H.M. James, N.B. Nicols and R.S. Philips: Theory of Servomechanisms (MIT Rad. Lab. Series), pp. 278-288.

12) H. Takahasi: Proc. Phys.-Math. Soc. Japan, **23** (1941) 548.

13) A word coined by Tellegen. See B. D. H. Tellegen: Philips Res. Rep. **3** (1948) 81.

JOURNAL OF THE PHYSICAL SOCIETY OF JAPAN Vol. 7, No. 5, SEPT.—OCT., 1952

A Remark on the Hydrodynamical Theory of the Viscosity of Solutions of Macromolecules

By Nobuhiko SAITÔ

Kobayasi Institute of Physical Research, Kokubunzi, Tokyo

(Received March 22, 1952)

The hydrodynamical problem of many particles interacting in a laminar flow is discussed on the basis of Stokes approximation. Two methods of approximation are introduced in order to derive the concentration dependence of the viscosity of solutions of rigid spheres. In any case an improper integral is involved which can be evaluated to be of different values according to different ways of integration. This physically absurd result comes from Stokes approximation. A new fundamental equation is proposed for the problems in a laminar flow from an analogous reasoning given by Oseen for the case of uniform flow.

§ 1. Introduction

The theories of the viscosities of macromolecular solutions, especially for intrinsic viscosities, have made a great progress in the past several years.

Almost all these theories are the natural extensions of the theory of Einstein for rigid spheres and are revised according to the models adopted or are supplemented by physical considerations such as the influence of the Brownian motion. Up to now, however, when one treats the viscosity of solutions of long chain molecules along the macroscopic theory of hydrodynamics, a doubt has been thrown on the validity of the hydrodynamical considerations in which one regards the solvent as continuous medium in contrast to the segments of polymers not so large compared with solvent molecules, and in particular, on the validity of the Stokes resistance formula. A reply of this doubt may be the theory of Kirkwood1), which concludes the validity of Stokes formula under certain conditions, although it will not necessarily certify it for segments of polymers. It is not on this point that the present author wishes to raise a question. Even when we admit the hydrodynamical treatments, we want to point out a defect in the current theories based on Stokes approximation, and to derive a new fundamental equation. This defect will not lead to a serious error in the theory of the intrinsic viscosity, but it turns out to be fatal in the theory of the concentration dependence of the viscosity. In the latter theory, in particular in flexible macromolecules, we must take into account besides hydrodynamical interaction the thermodynamical and mechanical ones5), 9) such as temporary association and entanglement of two or more molecules or the change of sizes of molecules with concentration etc. These factors play an essential rôle in the study of the effect of solvents and temperature, but we do not engage in it here.

§ 2. Hydrodynamical Interaction of Particles in Stokes Approximation

The Stokes approximation consists in neglecting a part of inertia terms in the fundamental equation of Navier-Stokes. This is a useful approximation, and indeed almost all theories of the viscosity of macromolecules are based on this approximation as is mentioned in § 1.

Let the coordinate system be x_i, and the velocity of the fluid be $u_i (i=1,2,3)$. The original flow is assumed to be

$$u_i^0=\sum_{k=1}^{3} g_{ik}x_k\,, \qquad (1)$$

where we have

$$\sum_{i=1}^{3} g_{ii}=0\,, \qquad (2)$$

in accordance with the incompressibility. A sphere of radius a is introduced in the generalized laminar flow expressed by Eq. (1). We want to solve this problem in Stokes approximation. The equations of Stokes in steady state are written as follows,

$$\left.\begin{aligned}&\partial p/\partial x_i=\kappa\nabla^2 u_i\,,\\&\Sigma\partial u_i/\partial x_i=0\,,\\&\kappa=\eta/\rho\,,\end{aligned}\right\}\qquad(3)$$

where η and ρ are respectively the viscosity and density of solvent. The flow (1) is divided into dilatational and rotational parts,

$$u_i^0=\frac{1}{2}\sum_k(g_{ik}+g_{ki})x_k+\sum_k\omega_j x_k\,,\qquad(4)$$

$$\omega_j=\frac{1}{2}(g_{ik}-g_{ki}),\quad(i,\ k,\ j=1,\ 2,\ 3)\,.\ (5)$$

The sphere rotates with the angular velocity ω_j, and therefore we concern ourselves only in the first term of Eq. (4) and solve the problem with the boundary condition for the velocity of fluid to cancel the first term of Eq. (4). In this way the perturbation of the velocity u_i' is obtained as follows,

$$\left.\begin{aligned}&u_i'=-\frac{x_i}{r^5}\Big(\sum_{j,k}A_{jk}x_jx_k\Big)\\&\qquad+\frac{\partial}{\partial x_i}\Big\{\sum_{j,k}B_{jk}\frac{\partial^2}{\partial x_j\partial x_k}\Big(\frac{1}{r}\Big)\Big\}\,,\\&p=p_0-\frac{2\kappa}{r^5}(\Sigma A_{jk}x_jx_k)\,,\\&r^2=x_1^2+x_2^2+x_3^2\,,\end{aligned}\right\}\qquad(6)$$

where A_{jk} and B_{jk} are determined by the boundary condition as follows,

$$\left.\begin{aligned}&A_{jk}=(5/2)a^3g_{jk}\,,\\&B_{jk}=-(1/6)a^5g_{jk}\,.\end{aligned}\right\}\qquad(7)$$

In the next step, we consider a dilute solution of N rigid spheres in volume V. The original flow is assumed to be

$$u_1=g_{12}^0x_2,\quad u_2=0,\quad u_3=0.\qquad(8)$$

If we put $g_{ik}^{(p)}$ the velocity gradient acting on pth particle, $g_{ik}^{(p)}$ is determined by the interactions of the other particles, and is obtained as the solution of a set of the simultaneous equation,

$$g_{ik}^{(p)}=g_{ik}^0+\sum_{\substack{s=1\\ \neq p}}^{N}\frac{\partial u_i'^{(s)}}{\partial(x_k^{(p)}-x_k^{(s)}}\,,\qquad(9)$$

where $u_i'^{(s)}$ is the perturbation of the velocity by sth particle at the place of pth particle and is a function of $x_k^{(p)}-x_k^{(s)}$, $(k=1,$ $2,\ 3)$, and $g_{ik}^{(s)}$, just as Eq. (6). When N is large it is formidably difficult to solve exactly these equations. Consequently two methods of approximation may be adopted. First, in our problem to derive the coefficient of c^2 in series expansion of the specific viscosity, it is permitted to put g_{ik} contained in $u_i'^{(s)}$ to be equal to g_{ik}^0.. This approximation is due to Guth-Simha[2], and Simha[3]. The second is to put all g_{ik} in Eq. (9) to be equal to $<g_{ik}>$ common to all p and s, and is used by Saitô[4],[5]* and Riseman-Ullman[6]**. The hydrodynamical interaction is effective at a long range as it is $0(r^{-3})$ and the velocity field around a particle will be considerably averaged out. This approximation will correspond to Debye-Hückel approximation in the theory of strong electrolyte.

Both methods must give the same value for the coefficient of c^2. The first method gives in averaging

$$<g_{12}+g_{21}>=g_{12}^0+n\int_V\rho\Delta dxdydx\,,\qquad(10)$$

where $n=N/V$ is the number of particles in unit volume,

$$\Delta=\frac{\partial u_2'}{\partial x_1}+\frac{\partial u_1'}{\partial x_2}\,,\qquad(11)$$

and ρ is the distribution function of the particles arround a particle under consideration which is normalized as

$$(1/V)\int\rho dxdydz=1\,,$$

and is assumed to be uniform in whole space except the region where the two particles cannot penetrate one another. If we put g_{ik} equal to g_{ik}^0 we have

---

* We had recourse of the basis of this approximation to the translational Brownian motion. However this is not permitted as is shown below. The relaxation time τ_1 of the rotation of spheres is given by $\tau_1\simeq I/\eta a^3$, I being the moment of inertia of the sphere. The time τ_2 necessary for a particle to move a distance a on account of the Brownian motion is $\tau_2\simeq a/v$, where $v=\sqrt{kT/m}$ and m is the mass of the particle. Therefore if we assume the density of the particle to be unity, we obtain $\tau_1/\tau_2\simeq\sqrt{kT/a\eta^2}$. Therefore the smaller the particle, the more contented the condition $\tau_1\gg\tau_2$ is. But in room temperature and for $\eta\sim 10^{-2}$ poise a must be smaller than Å in order to be $\tau_1\simeq\tau_2$.

** Riseman-Ullman do not use g_{ik} explicitely, but their method is essentially same as this approximation.

$$\left.\begin{aligned}&\int \rho \Delta dxdydz/g^0_{12}\\&=-\frac{5}{2}\int\left(\frac{a}{r}\right)^3\left(\frac{x^2+y^2}{r^2}-10\frac{x^2y^2}{r^4}\right)dxdydz\\&\quad-\int\left(\frac{a}{r}\right)^5\left(1-5\frac{x^2+y^2}{r^2}+35\frac{x^2y^2}{r^4}\right)dxdydz.\end{aligned}\right\} \quad (12)$$

The region of integration in Eq. (12) is the exterior of the sphere of radius $2a$. In this respect an attention must be paid, that is, the first term of Eq. (12) is an improper integral which is evaluated to be of different values according to different ways of integration. Considering the structure of Couette viscometer, and carrying out the integration in a region between two parallel planes perpendicular to x_2-axis, we have[4)]

$$-\frac{5}{2}\int\left(\frac{a}{r}\right)^3\left(\frac{x^2+y^2}{r^2}-10\frac{x^2y^2}{r^4}\right)dxdydz = -2\pi a^3. \quad (13)$$

If we carry out the integration using polar coordinates first over a spherical surface and then to radial direction, we have*

$$-\frac{5}{2}\int\left(\frac{a}{r}\right)^3\left(\frac{x^2+y^2}{r^2}-10\frac{x^2y^2}{r^4}\right)dxdydz=0. \quad (14)$$

The second term of Eq. (12) has not such a complexity as above and we have

$$\int\left(\frac{a}{r}\right)^5\left(1-5\frac{x^2+y^2}{r^2}+35\frac{x^2y^2}{r^4}\right)dxdydz=0. \quad (15)$$

Finally in this way we have for Eq. (10) using Eq. (13),

$$\langle g_{12}+g_{21}\rangle = g^0_{12}(1-2\pi a^3 n)+0(n^2), \quad (16)$$

or using Eq. (14)

$$\langle g_{12}+g_{21}\rangle = g^0_{12} \qquad +0(n^2). \quad (17)$$

§ 3. Specific Viscosity

The method of Burgers[7)] gives for specific viscosity η_{sp}

$$\left.\begin{aligned}&\eta_{sp}=(g^0_{12}-\kappa_{eff})/\kappa_{eff},\\&\kappa_{eff}=g^0_{12}-(10\pi/3)\langle g_{12}+g_{21}\rangle na^3.\end{aligned}\right\} \quad (18)$$

Defining the volume concentration $c=(4\pi/3)a^3n$, we have using Eq. (16)

$$\eta_{sp}=2.5c(1+c+\dots)=2.5c+2.5c^2+\dots, \quad (19)^{**}$$

using Eq. (17)

$$\eta_{sp}=2.5c(1+2.5c+\dots)=2.5c+6.3c^2+\dots, \quad (20)^{**}$$

and by another method (see Appendix)

$$\eta_{sp}=2.5c(1+1.5c+\dots)=2.5c+3.8c^2+\dots, \quad (21)^{**}$$

It is physically absurd to obtain different values according to different ways of integration. This comes from Stokes approximation and all the attempts[2)-6)] in Stokes approximation are meaningless in their quantitative nature in order to obtain the coefficient of c^2 of specific viscosity.

§ 4. A New Fundamental Equation

Already in previous days Stokes, Whitehead and others discussed that Stokes approximation leads to several paradoxes, and it is well-known that Oseen[8)] proposed a new fundamental equation now called after his name. In our present problem in order to avoid the defect in Stokes approximation we have to treat the problem analogously as Oseen did in the case of uniform flow.

Navier-Stokes equation is written, in the absence of body force,

$$\frac{\partial u_i}{\partial t}+\sum_j u_j\frac{\partial u_i}{\partial x_j}=-\frac{1}{\rho}\frac{\partial p}{\partial x_i}+\kappa\nabla^2 u_i. \quad (22)$$

In Stokes approximation the second term in the left-hand side of Eq. (22) is neglected, but if we substitute the solution Eq. (6) in Stokes approximation into Eq. (22) we will find that the second term is not always smaller than the viscosity term $\kappa\Delta u_i$ over all space. In this point lies the failure of Stokes approximation.

The original flow is assumed to be

$$\left.\begin{aligned}&u_i^0=A_i x_i, \quad (i=1,2,3)\\&A_1+A_2+A_3=0,\end{aligned}\right\} \quad (23)$$

transformed in diagonal form. Let the disturbance by particle in this flow be u_i';

$$u_i=u_i^0+u_i'. \quad (24)$$

Substituting Eq. (24) into Eq. (22) we have for the left-hand side

$$\frac{\partial u_i'}{\partial t}+(u_i^0+u_i')A_i+\sum_{j=1}^{3}(u_j^0+u_j')\frac{\partial u_i'}{\partial x_j}. \quad (25)$$

In this equation $u_j'\partial u_i'/\partial x_j$ may be neglected, and in steady state we have

---

* Another method is discussed in Appendix.

** k which is defined by $\eta_{sp}=\alpha c+k\alpha^2c^2+\dots$ is given respectively by 0.4, 1 and 0.6 in the cases (19), (20) and (21).

$$(u_i^0+u_i')A_i+\sum_j u_j^0\frac{\partial u_i'}{\partial x_j}=-\frac{1}{\rho}\frac{\partial p}{\partial x_i}+\kappa\nabla^2 u_i'. \tag{26}$$

The equation of continuity is given by

$$\frac{\partial u_1'}{\partial x_1}+\frac{\partial u_2'}{\partial x_2}+\frac{\partial u_3'}{\partial x_3}=0. \tag{27}$$

Eq. (26) is transformed into

$$\kappa\nabla^2 u_i'-\frac{1}{\rho}\frac{\partial p'}{\partial x_i}-\sum_{j=1}^{3}A_j x_j\frac{\partial u_i'}{\partial x_j}-A_i u_i'=0, \tag{28}$$

where

$$p'=p+p_0, \qquad p_0=\frac{\rho}{2}\sum_{i=1}^{3}A_i^2 x_i^2. \tag{29}$$

This is the fundamental equation in Oseen approximation. It is hoped to solve the individual problem using this equation and then the treatment of Oseen[8] will be useful for this purpose, however we will be content here only to give a new equation.

Strictly speaking the intrinsic viscosity must be treated using Eq. (28). However considering the fact that Stokes' resistance formula gives a good approximation to Oseen's formula and has not a serious defect, the intrinsic viscosity based on Stokes approximation will not lead to an important difference.

Appendix. Another Approach to the Integration of Eq. (10)

Guth-Simha[2], and Riseman-Ullman[6] carried out the integration of the type of Eq. (10) in the following manner. From Eq. (11) we have

$$\int \rho\Delta\, dxdydz=\int\left(\frac{\partial u_1'}{\partial x_2}+\frac{\partial u_2'}{\partial x_1}\right)dxdydz \tag{A1}$$

which is transformed into surface integral as follows,

$$=\int\left(u_1'\frac{x_2}{r}+u_2'\frac{x_1}{r}\right)dS. \tag{A2}$$

They neglected the surface integral over a small sphere enclosing the particle. Although this is not correct (if one takes into account this contribution, one obtains the same result as Eq. (14)), if we follow their argument, we have

$$=-g_{12}^0(4\pi a^3/3).$$

Consequently Eq. (18) gives

$$\eta_{sp}=2.5c(1+1.5c+\dots)$$
$$=2.5c+0.6(2.5)^2c^2+\dots. \tag{A4}$$

The factor 0.6 in the coefficient of c^2 is same as is obtained by Riseman-Ullman for the case of symmetric flexible molecules.

References

1) J.G. Kirkwood: J. Chem. Phys. **14** (1946) 180.

2) E. Guth, R. Simha: Koll. Zeits. **74** (1936) 266.

3) R. Simha: J. Research Natl. Bur. Standards **42** (1949) 409.

4) N. Saitô: J. Phys. Soc. Japan **5** (1950) 4.

5) N. Saitô: Busseiron Kenkyû No. **24** (1950) 6. (in Japanese).

6) J. Riseman, R. Ullman: J. Chem. Phys. **19** (1951) 578.

7) J.M. Burgers: *Second Report on Viscosity and Plasticity*, Amsterdam, 1938. Chap. III.

8) C.W. Oseen: *Hydrodynamik*, Leipzig, 1927.

9) S. G. Weissberg, R. Simha, S. Rothman: J. Research Natl. Bur. Standards **47** (1951) 298.

JOURNAL OF THE PHYSICAL SOCIETY OF JAPAN Vol. 7, No. 5, SEPT.—OCT., 1952

Numerical Tables of Overlap Integrals for 3s, 3p Hybrid A.-O.

By Yoshimasa AOKI

The Institute of Polytechnics Osaka City University

(Received April 3, 1952)

The numerical calculations for the overlap integrals between 3s, 3p hybrid A.-O. (atomic orbitals) and 1s, 2s, 3s 3p hybrid A.-O. are tabulated in this paper by the use of Slater's A.-O.

The calculation about polyatomic molecules and activated states of molecules during the chemical reactions is so complicated that various rough approximations have been required to make the calculations possible. The calculations of the interatomic distances at equilibrium and the molecular dissociation energies by the overlap integrals, which have been tried by Pitzer[1] and Mulliken[2,3] are such examples of these approximated calculations. The following numerical tables are primarily performed for the benefit of the calculation of the various states of the molecules which contain the s, p hybrid *A.-O.* (atomic orbitals) in the 2nd row.

The calculations of the overlap integrals are explained in Mulliken's papers[3,4)] and the present auther wishes to make a brief introduction of the formulas applied in the calculation about the hybrid *A.-O.* which was used in the calculations of the numerical tables. Now, s, p hybrid *A.-O.* of the principal quantum number $n=3$ is represented by

$$3h_\beta=\alpha 3s+\beta 3p\sigma \qquad (1)$$

$$\alpha^2+\beta^2=1 \qquad (2)$$

where α and β are constants. Then, if $S(a,b)$ is an overlap integral of a and b *A.-O.*,

$$S(3h_\beta,\ 3h_\beta)=\alpha^2S(3s,\ 3s)+2\alpha\beta S(3s,\ 3p)+\beta^2S(3p\sigma,\ 3p\sigma) \qquad (3)$$

$$S(a,\ 3h_\beta)=\alpha S(a,\ 3s)+\beta S(a,\ 3p\sigma) \qquad (4)$$

The letters in the tables represent the following quantites, in which the suffixes a and b are the same meaning as in $S(a, b)$

$$t=(\mu_a-\mu_b)/(\mu_a+\mu_b) \qquad (5)$$

where, $\mu_a=Z_{a,n}/n$ whose values for various atoms are given in reference 4.

$$\rho=1/2(\mu_a+\mu_b)R/a_H \qquad (6)$$

where R is interatomic distance, and a_H is the lowest Bohr radius.

at $3\,te$, $\alpha=(1/4)^{1/2}$, $\beta=(3/4)^{1/2}$;
$3\,tr$, $\alpha=(1/3)^{1/2}$, $\beta=(2/3)^{1/2}$;
$3\,di$, $\alpha=(1/2)^{1/2}$, $\beta=(1/2)^{1/2}$.

The Slater *A.-O.* is used in calculating these numerical tables.

From these numerical tables, we can explain the many interesting facts. For example: the difficulty of forming the double bond in 2nd row atoms is not due to the repulsion of the closed shells, (while Pitzer[1] claims that it is due to the repulsion, Mulliken[2] denies his view) but the present auther has an opinion from the result of the numerical calculation that it is due to the relations of $3tr$ and $3p\pi$ instead of due to the repulsion of the closed shells. However, since these have been so many arguments about applying these numerical tables, the present auther wishes to introduce the discussions of the above point in further detail in future paper.

Tables from 1 to 9 are overlap integrals between 1s, 2s, $2p\sigma$, and $3te$, $3tr$, $3di$, for different values of t; table 10 is for the overlap integrals between $3te$ and $3te$, $3tr$ and $3tr$, $3di$ and $3di$ ($t=0$), and tables 11 and 12 are overlap integrals of $3h_\beta$, for different values of β($\beta>0$ positive; $\beta>0$ negative).

References

1) Pitzer: J. Am. Chem. Soc. **70** (1948) 2140.

2) R. S. Mulliken: J. Am. Chm. Soc. **72** (1950) 4493.

3) R.S. Mulliken: J. Chem. Phys. **19** (1951) 900.

4) R. S. Mulliken. C. A. Rike, D. Orloff and H. Orloff: J. Chem. Phys. **17** (1949) 1248.

Table 1. $S(1s,\ 3te)$

$\rho \backslash t$	−0.4	−0.3	−0.2	−0.1	0.0	0.1	0.2	0.3
0.0	0.477	0.464	0.429	0.377	0.316	0.253	0.191	0.135
0.5	613	619	594	542	471	390	305	223
1.0	719	744	730	683	609	517	414	311
1.5	782	823	820	782	711	616	505	388
2.0	799	848	857	830	768	678	569	449
2.5	774	827	844	827	777	701	602	488
3.0	719	769	789	782	748	688	605	503
3.2	690	738	760	756	727	674	598	503
3.4	660	704	727	726	702	657	588	501
3.6	628	669	691	692	675	635	574	496
3.8	594	633	654	657	644	612	558	487
4.0	560	595	615	620	611	585	541	477
4.2	526	557	576	583	578	558	521	465
4.4	492	520	537	546	543	529	499	451
4.6	459	482	499	508	509	499	476	436
4.8	426	446	462	471	475	469	452	418
5.0	396	413	425	436	441	440	428	402
5.5	324	334	342	352	360	368	369	357
6.0	261	265	270	279	289	302	310	311
6.5	209	207	210	217	228	243	257	267
7.0	164	161	161	167	177	192	210	225
7.5	129	123	121	126	136	150	169	188
8.0	100	093	091	094	103	117	135	155
9.0	059	052	049	050	057	067	083	103
10.0	035	029	026	027	031	038	049	066

Table 2. $S(2s,\ 3te)$

$\rho \backslash t$	−0.6	−0.5	−0.4	−0.3	−0.2	−0.1	0.0	0.1	0.2	0.3
0.0	0.240	0.334	0.413	0.469	0.495	0.490	0.457	0.401	0.330	0.253
0.5	239	349	452	535	587	606	588	537	458	365
1.0	240	362	484	589	666	705	702	657	576	470
1.5	244	375	509	631	725	780	790	754	674	562
2.0	252	388	528	658	761	826	848	821	747	635
2.5	261	397	538	667	774	845	872	855	791	685
3.0	267	401	537	660	762	832	866	856	804	711
3.5	271	398	522	635	727	494	829	829	790	712
4.0	271	388	498	596	676	735	770	778	753	692
4.5	267	370	465	546	612	663	696	709	697	655
5.0	258	348	425	490	542	583	612	632	631	607
5.5	246	321	381	430	469	501	529	549	559	550
6.0	232	292	337	371	398	423	446	468	485	489
6.5	217	263	294	317	334	351	371	393	416	430
7.0	198	232	252	264	273	285	302	323	348	369
7.5	181	204	214	218	222	229	243	262	288	314
8.0	164	177	180	178	177	181	192	210	235	264
9.0	131	131	123	115	110	109	116	130	152	181
10.0	103	094	084	072	065	064	067	077	094	120

Table 3. $S(2p\sigma,\ 3te)$

$\rho \backslash t$	−0.6	−0.5	−0.4	−0.3	−0.2	−0.1	0.0	0.1	0.2	0.3
0.0	−0.415	−0.578	−0.715	−0.812	−0.857	−0.848	−0.791	−0.694	−0.571	−0.437
0.5	−0.345	−0.487	−0.613	−0.707	−0.759	−0.766	−0.728	−0.653	−0.550	−0.431
1.0	−0.252	−0.358	−0.456	−0.535	−0.589	−0.611	−0.599	−0.555	−0.485	−0.395
1.5	−0.144	−0.205	−0.266	−0.322	−0.369	−0.402	−0.417	−0.409	−0.381	−0.329
2.0	−0.034	−0.048	−0.068	−0.097	−0.133	−0.173	−0.210	−0.238	−0.250	−0.241
2.5	+0.069	+0.099	+0.116	+0.114	+0.090	+0.048	−0.005	−0.062	−0.111	−0.142
3.0	159	222	286	287	275	235	+0.171	+0.096	+0.020	−0.043
3.5	230	316	381	414	411	374	309	224	133	+0.047
4.0	281	381	455	494	496	463	400	315	217	121
4.5	315	417	491	530	535	505	448	369	274	175
5.0	333	430	497	532	535	509	460	390	304	211
5.5	338	425	481	507	508	486	444	386	313	230
6.0	333	406	449	466	463	444	410	364	304	233
6.5	321	380	410	417	409	392	366	330	284	227
7.0	303	345	362	361	351	334	314	289	256	213
7.5	282	310	316	309	294	281	265	247	224	194
8.0	259	274	271	258	243	230	218	207	193	173
9.0	212	209	192	173	157	147	140	138	135	130
10.0	168	152	131	111	097	089	086	086	089	092

Table 4. $S(1s, 3tr)$

ρ \ t	−0.4	−0.3	−0.2	−0.1	0.0	0.1	0.2	0.3
0.0	0.551	0.536	0.495	0.435	0.365	0.292	0.220	0.155
0.5	678	681	650	590	511	422	328	239
1.0	775	796	777	722	640	541	432	323
1.5	829	865	857	813	736	635	519	397
2.0	837	882	886	853	786	692	579	456
2.5	806	854	866	844	790	711	608	493
3.0	744	789	806	795	757	695	610	506
3.2	713	757	775	767	735	680	602	506
3.4	681	721	740	736	710	662	591	503
3.6	647	685	703	701	681	639	577	497
3.8	611	646	664	665	650	615	560	489
4.0	576	607	624	627	616	588	543	478
4.2	540	568	584	589	581	560	522	465
4.4	505	529	544	550	546	531	501	451
4.6	470	491	505	512	512	501	477	436
4.8	436	454	467	474	477	470	452	419
5.0	405	420	430	439	443	441	429	402
5.5	331	339	345	354	361	369	369	356
6.0	267	269	273	280	290	302	310	310
6.5	213	210	212	218	228	243	257	266
7.0	168	163	162	167	177	192	209	224
7.5	132	125	122	127	136	150	169	188
8.0	101	094	092	094	103	117	134	155
9.0	060	053	049	051	057	067	083	103
10.0	035	029	026	027	030	038	049	066

Table 5. $S(2s, 3tr)$

ρ \ t	−0.6	−0.5	−0.4	−0.3	−0.2	−0.1	0.0	0.1	0.2	0.3
0.0	0.277	0.385	0.477	0.541	0.571	0.565	0.527	0.463	0.381	0.292
0.5	276	399	513	603	658	674	650	590	496	398
1.0	276	410	541	651	728	764	755	702	612	497
1.5	280	421	562	686	780	831	835	791	703	583
2.0	286	430	576	707	808	869	884	851	770	651
2.5	293	436	580	709	813	879	902	878	808	697
3.0	297	436	574	696	794	860	889	874	817	720
3.5	299	430	554	665	753	816	847	842	799	718
4.0	297	415	525	621	697	752	783	788	760	697
4.5	291	395	488	566	629	676	706	716	702	659
5.0	279	369	444	506	554	593	618	637	635	609
5.5	265	339	397	442	479	508	534	552	561	551
6.0	249	308	350	381	405	428	450	471	486	490
6.5	232	276	305	324	339	355	374	395	416	430
7.0	212	243	260	270	277	288	303	324	348	369
7.5	192	213	221	223	225	231	244	263	288	314
8.0	174	185	185	181	179	183	192	210	235	264
9.0	139	136	127	117	111	109	117	130	152	181
10.0	108	097	086	073	065	064	067	077	094	120

Table 6. $S(2p\sigma, 3tr)$

ρ \ t	−0.6	−0.5	−4.0	−0.3	−0.2	−0.1	0.0	0.1	0.2	0.3
0.0	−0.391	−0.545	−0.674	−0.765	−0.808	−0.799	−0.746	−0.654	−0.538	−0.412
0.5	−0.314	−0.445	−0.563	−0.652	−0.703	−0.714	−0.681	−0.613	−0.518	−0.408
1.0	−0.214	−0.310	−0.400	−0.477	−0.531	−0.557	−0.552	−0.517	−0.455	−0.374
1.5	−0.103	−0.154	−0.208	−0.263	−0.312	−0.351	−0.374	−0.375	−0.356	−0.311
2.0	+0.009	+0.005	−0.011	−0.041	−0.080	−0.127	−0.172	−0.208	−0.228	−0.226
2.5	112	150	+0.169	+0.165	+0.137	+0.089	+0.027	−0.038	−0.093	−0.130
3.0	210	271	317	333	316	269	198	+0.117	+0.035	−0.033
3.5	271	361	425	454	446	402	330	240	144	+0.054
4.0	319	421	493	528	525	486	417	327	226	127
4.5	351	453	524	559	558	523	461	378	280	179
5.0	365	462	526	555	553	523	470	396	309	214
5.5	368	453	505	526	522	496	451	391	316	232
6.0	360	431	469	481	474	452	415	367	306	235
6.5	346	401	426	429	418	398	370	332	286	228
7.0	324	363	375	371	357	339	317	291	257	214
7.5	301	325	327	316	299	284	266	248	225	194
8.0	275	287	280	263	246	232	219	208	193	173
9.0	225	217	198	177	159	148	141	138	135	130
10.0	178	158	144	113	098	089	086	086	088	091

Table 7. $S(1s,\ 3di)$

ρ \ t	−0.4	−0.3	−0.2	−0.1	0.0	0.1	0.2	0.3
0.0	0.675	0.656	0.606	0.533	0.447	0.357	0.269	0.190
0.5	783	780	739	667	574	470	363	264
1.0	861	874	845	779	685	574	455	339
1.5	897	925	907	851	764	655	532	405
2.0	890	926	920	878	803	701	584	458
2.5	845	885	887	858	798	713	607	490
3.0	773	810	819	801	758	692	605	500
3.2	739	774	785	771	734	675	596	499
3.4	704	736	747	738	707	656	583	496
3.6	667	697	709	701	677	633	569	489
3.8	629	657	668	664	645	608	551	480
4.0	591	616	627	625	610	581	534	470
4.2	554	576	585	586	576	552	513	456
4.4	517	535	545	547	540	523	492	442
4.6	481	496	505	508	506	493	468	427
4.8	446	458	467	470	471	463	443	409
5.0	413	423	429	435	436	434	420	393
5.5	337	340	344	350	356	361	361	348
6.0	271	269	271	277	285	296	303	303
6.5	216	210	210	215	224	238	251	260
7.0	170	163	161	165	174	188	204	219
7.5	133	125	121	124	133	146	165	183
8.0	103	094	091	093	100	114	131	151
9.0	061	052	049	050	055	065	081	100
10.0	035	029	025	026	030	037	047	064

Table 8. $S(2s,\ 3di)$

ρ \ t	−0.6	−0.5	−0.4	−0.3	−0.2	−0.1	0.0	0.1	0.2	0.3
0.0	0.339	0.472	0.584	0.663	0.699	0.692	0.616	0.566	0.466	0.357
0.5	338	483	614	714	772	785	750	676	571	449
1.0	337	490	634	751	828	857	837	770	665	535
1.5	339	496	646	774	863	907	899	842	741	610
2.0	342	499	651	781	876	928	932	887	796	668
2.5	346	498	645	771	868	924	936	902	823	705
3.0	347	491	629	746	836	892	912	888	824	721
3.5	344	478	600	705	784	838	861	849	800	715
4.0	338	458	564	652	720	767	791	789	756	690
4.5	327	431	519	590	645	685	709	714	696	650
5.0	312	400	469	524	566	598	617	632	627	599
5.5	294	365	417	456	487	511	532	547	552	541
6.0	274	330	366	391	410	429	446	465	478	480
6.5	255	294	318	332	342	354	371	389	409	421
7.0	231	258	270	275	279	286	300	319	341	361
7,5	209	226	228	226	226	229	240	258	382	307
8.0	189	195	191	184	180	181	190	206	230	257
9.0	150	143	130	118	111	108	115	127	149	176
10.0	117	102	088	074	065	063	066	076	092	117

Table 9. $S(2p\sigma,\ 3di)$

ρ \ t	−0.6	−0.5	−0.4	−0.3	−0.2	−0.1	0.0	0.1	0.2	0.3
0.0	−0.339	−0.472	−0.584	−0.663	−0.699	−0.692	−0.646	−0.566	−0.466	−0.357
0.5	−0.249	−0.358	−0.458	−0.537	−0.586	−0.600	−0.578	−0.525	−0.448	−0.356
1.0	−0.141	−0.214	−0.289	−0.358	−0.413	−0.447	−0.455	−0.436	−0.392	−0.327
1.5	−0.025	−0.056	−0.098	−0.149	−0.202	−0.250	−0.287	−0.303	−0.301	−0.272
2.0	+0.088	+0.100	+0.093	+0.064	+0.018	−0.040	−0.098	−0.149	−0.183	−0.194
2.5	190	240	264	257	221	+0.161	+0.086	+0.009	−0.057	−0.105
3.0	275	354	401	411	384	325	243	151	+0.061	−0.014
3.5	340	436	497	518	499	445	363	264	162	+0.067
4.0	383	487	554	579	565	516	439	343	237	134
4.5	409	511	574	599	588	544	475	387	286	183
5.0	418	511	566	586	574	537	477	400	310	215
5.5	415	495	537	549	537	504	455	391	315	231
6.0	402	466	495	499	484	456	416	366	303	232
6.5	383	431	447	442	424	400	368	330	282	225
7.0	356	388	392	380	361	339	315	287	253	210
7.5	329	346	339	323	301	283	264	245	221	190
8.0	300	304	290	268	248	231	216	204	190	169
9.0	243	229	204	179	159	146	139	135	132	127
10.0	192	166	138	114	098	088	084	084	086	089

Table 10

S ρ	S (3te, 3te)	S (3tr, 3tr)	S (3di, 3di)
0.0	−0.500	−0.333	0.000
0.5	−0.393	−0.222	110
1.0	−0.244	−0.076	240
1.5	−0.064	+0.094	385
2.0	+0.130	275	531
2.5	321	450	669
3.0	493	605	784
3.5	632	727	869
4.0	731	809	917
4.5	784	848	927
5.0	801	851	906
5.2	796	841	888
5.4	788	829	869
5.6	773	811	844
5.8	757	791	818
6.0	735	765	787
6.2	711	738	756
6.4	686	710	724
6.6	657	679	689
6.8	628	648	655
7.0	597	615	619
7.2	567	582	584
7.4	536	550	550
7.6	505	517	516
7.8	473	484	482
8.0	444	453	450
8.5	370	377	372
9.0	306	310	306
9.5	248	251	246
10.0	198	201	196

Table 11

$S(3h_\beta,\ 3h_\beta)$, positive hybrid. $(t=o)$

$2\alpha\beta$	0.0	0.19900	0.39192	0.57236	0.73322	0.78460	0.86603	0.96	0.99980	0.99980	0.96	0.86603	0.78460	0.73322	0.57236	0.39192	0.19900	0.0
α	1.0	0.99499	0.97980	0.95394	0.91652	0.9	0.86603	0.8	0.71414	0.7	0.6	0.5	0.43589	0.4	0.3	0.2	0.1	0.0
ρ \ β	0.0	0.1	0.2	0.3	0.4	0.43589	0.5	0.6	0.7	0.71414	0.8	0.86603	0.9	0.91652	0.95394	0.97980	0.99499	1.0
3.0	0.772	0.856	0.919	0.958	0.969	0.966	0.949	0.893	0.793	0.775	0.638	0.493	0.401	0.349	0.210	0.080	−0.038	−0.140
3.5	708	801	877	933	966	971	971	943	875	862	754	632	551	505	378	254	+0.137	+0.031
4.0	641	738	823	891	941	953	966	962	922	912	831	731	661	621	506	390	277	171
4.5	572	669	758	834	894	911	934	948	929	923	864	784	725	690	588	483	376	273
5.0	504	599	687	766	832	852	882	909	908	904	864	801	752	722	633	538	440	342
5.2	477	569	657	735	803	823	855	886	889	887	853	796	750	723	639	548	454	359
5.4	451	541	627	706	773	795	827	861	869	868	839	788	746	720	641	554	464	372
5.6	425	512	596	674	741	763	796	832	844	843	820	773	735	711	637	555	468	380
5.8	400	485	566	642	709	731	764	803	818	817	798	757	721	699	630	552	470	385
6.0	375	456	535	609	675	696	730	769	787	787	772	735	703	682	617	544	466	385
6.2	351	429	505	576	641	662	696	736	755	756	744	711	681	662	602	533	459	382
6.4	328	402	475	545	608	628	662	702	723	724	716	686	659	641	585	520	450	377
6.6	306	377	447	513	574	594	626	666	688	690	684	657	632	616	564	504	437	368
6.8	285	352	418	482	541	560	592	631	654	655	651	628	606	591	542	486	424	358
7.0	264	327	390	451	507	526	556	595	618	620	618	597	577	563	518	466	408	346
7.2	245	305	364	422	475	493	523	560	583	585	585	567	548	535	494	445	391	333
7.4	227	283	339	394	445	462	490	526	549	551	552	536	519	507	469	424	373	319
7.6	209	261	314	366	414	430	457	492	515	516	518	505	489	479	444	402	355	304
7.8	193	242	291	339	385	400	426	459	481	483	485	473	459	450	417	379	335	288
8.0	177	223	269	315	357	372	396	428	449	451	454	444	431	423	393	357	317	273
8.5	141	179	217	255	291	304	324	352	371	373	378	370	361	354	331	302	269	233
9.0	114	145	176	208	238	248	265	288	305	306	311	306	298	293	274	251	224	195
9.5	089	114	139	165	189	198	212	231	245	247	251	248	242	238	224	206	184	161
10.0	070	090	110	130	150	157	168	184	195	197	201	198	194	191	180	165	149	130

Table 12

$S\ (3h_\beta,\ 3h_\beta)$, negative hybrid. $(t=o)$

$-2\alpha\beta$	0.0	0.19900	0.39192	0.57236	0.73322	0.78460	0.86603	0.96	0.99980	0.99980	0.96	0.86603	0.78460	0.73322	0.57236	0.39192	0.19900	0.0
α	0.0	0.1	0.2	0.3	0.4	0.43589	0.5	0.6	0.7	0.71414	0.8	0.86603	0.9	0.91652	0.95394	0.97980	0.99499	1.0
ρ \ $-\beta$	1.0	0.99499	0.97980	0.95394	0.91652	0.9	0.86603	0.8	0.71414	0.7	0.6	0.5	0.43589	0.4	0.3	0.2	0.1	0.0
3.0	−0.140	−0.224	−0.287	−0.326	−0.337	−0.334	−0.317	−0.261	−0.161	−0.143	−0.006	0.139	0.232	0.283	0.422	0.552	0.670	0.772
3.5	+0.031	−0.062	−0.138	−0.194	−0.227	−0.232	−0.232	−0.204	−0.136	−0.123	−0.015	107	188	234	362	485	602	708
4.0	171	+0.074	−0.011	−0.079	−0.129	−0.141	−0.154	−0.150	−0.110	−0.100	−0.019	081	151	191	306	422	535	641
4.5	273	176	+0.088	+0.011	−0.049	−0.066	−0.089	−0.103	−0.084	−0.078	−0.019	061	120	155	257	363	469	572
5.0	342	248	159	080	+0.014	−0.006	−0.036	−0.063	−0.062	−0.058	−0.018	045	094	124	213	308	406	504
5.2	359	267	180	101	033	+0.013	−0.018	−0.050	−0.053	−0.051	−0.017	041	086	114	197	288	382	477
5.4	372	282	196	118	050	028	−0.004	−0.038	−0.046	−0.045	−0.016	036	077	103	182	269	359	451
5.6	380	293	209	132	064	043	+0.009	−0.027	−0.039	−0.038	−0.015	032	071	094	169	250	337	425
5.8	385	301	219	143	076	054	021	−0.018	−0.033	−0.032	−0.013	028	064	086	155	233	315	400
6.0	385	304	225	151	085	064	030	−0.009	−0.027	−0.027	−0.012	025	058	078	143	216	294	375
6.2	382	304	228	157	092	071	037	−0.003	−0.022	−0.023	−0.011	022	052	071	131	200	274	351
6.4	377	303	230	160	097	077	044	+0.003	−0.018	−0.019	−0.011	019	046	064	120	185	255	328
6.6	368	297	228	161	100	080	048	008	−0.014	−0.016	−0.010	017	042	058	110	171	237	306
6.8	358	291	225	161	102	083	051	012	−0.011	−0.012	−0.008	015	038	053	101	157	220	285
7.0	346	283	220	159	103	084	054	015	−0.008	−0.010	−0.008	013	033	047	092	144	202	264
7.2	333	274	214	156	103	085	056	018	−0.005	−0.007	−0.007	012	030	043	084	133	187	245
7.4	319	263	207	152	101	084	056	020	−0.003	−0.005	−0.006	010	027	039	077	122	173	227
7.6	304	252	199	147	099	083	056	021	−0.002	−0.003	−0.005	009	024	034	069	111	158	209
7.8	288	239	190	142	096	081	056	022	+0.001	−0.002	−0.004	008	022	032	064	102	146	193
8.0	273	227	181	136	093	078	054	022	001	−0.001	−0.004	006	019	027	057	093	133	177
8.5	233	195	157	119	083	070	050	022	003	+0.001	−0.004	004	013	020	043	072	105	141
9.0	195	164	133	101	071	061	044	021	004	003	−0.002	004	011	016	035	058	085	114
9.5	161	136	111	085	061	052	038	019	005	003	−0.001	002	008	012	026	044	066	089
10.0	130	110	090	070	050	043	032	016	005	003	−0.001	002	006	009	021	035	052	070

JOURNAL OF THE PHYSICAL SOCIETY OF JAPAN Vol. 7, No. 5, SEPT.—OCT., 1952

On the Group Velocity, Wave Path and their Relations to the Poynting Vector of the Electromagnetic Field in an Absorbing Medium

By Koichi FURUTSU

Central Radio Wave Observatory, Kokubunji, Tokyo

(Received April 5, 1952)

The physical meanings of concepts such as group velocity and wave path, are first carefuly examined and mathematically founded, and it is then investigated whether the significant concepts of group velocity and wave path do exist or not, when the Maxwell field energy is lost in a medium. It is concluded that, in a rigorous sense, they generally do not exist in absorbing non-uniform medium, and that, when the energy loss in a medium is sufficiently small that only the first order changes in group velocity and wave path due to the energy loss are required to be taken into account, they approximately exist and are concordant with the ones obtained when the field energy is not lost in that medium, so that it is anyhow meaningless to discuss their changes due to the energy loss in a medium.

§ 1. Introduction

It sometimes happens that the group velocity at some frequency calculated by the usual method is larger than the light velocity in the vacuum, or that the wave path calculated by the theory of wave packet is not concordant with the one obtained by the Poynting vector method, when the field energy is lost in a medium. Though the wave packet theory in an absorbing medium was discussed by a few authors*, it seems that the definite answer for this problem has not been obtained.

In this paper, the mathematical preparations for these problems are first made and then, the problems are discussed from two different points of view from each of which the same conclusion is obtained.

§ 2. Kemmer Formulation of Vector Field

In this paper, we employ the following notation: Latin subscripts assume values ranging from 1 to 3, and a repeated index is to be so summed. The coordinate vector in space is denoted by $x_i=(x)$.

Using the usual notations, Maxwell's equations are

$$\begin{aligned} &\mathrm{rot}\, H - j\frac{\omega}{c}\varepsilon E = \frac{4\pi}{c} I_e \\ &\mathrm{rot}\, E + j\frac{\omega}{c}\mu H = 0\,, \end{aligned} \tag{2. 1}$$

where ε is generally a three-rowed matrix operating on the vector E, and I_e is the external current. We now introduce S_i and ∂_i defined by

$$S_1=\begin{pmatrix} 0 & 0 & 0 \\ 0 & 0 & j \\ 0 & -j & 0 \end{pmatrix}, \qquad S_2=\begin{pmatrix} 0 & 0 & -j \\ 0 & 0 & 0 \\ j & 0 & 0 \end{pmatrix},$$
$$S_3=\begin{pmatrix} 0 & j & 0 \\ -j & 0 & 0 \\ 0 & 0 & 0 \end{pmatrix} \tag{2. 2}$$

and

$$\partial_1 = j\frac{\partial}{\partial x_1}\,, \quad \partial_2 = j\frac{\partial}{\partial x_2}\,, \quad \partial_3 = j\frac{\partial}{\partial x_3}\,, \tag{2. 3}$$

then, "rot" as a three-rowed matrix is expressed by

$$\mathrm{rot} = S_i\partial_i = (S\partial)\,. \tag{2. 4}$$

Similarly, we can generally express ε as a function of S_i's. For example, an ionized gas under the effect of the static magnetic field H_0 gives for ε

$$\varepsilon = 1 - \frac{\omega_0^2}{\omega[\omega - j\nu + (\omega_H S)]}\,, \tag{2. 5}$$

with

$$\omega_0^2 = 4\pi N e^2/m\,, \quad \omega_H = eH_0/mc\,,$$

---

* H.G. Booker, Phil. Trans. R. Soc. A, **237** (1938) 411-451; C.O. Hines, J. Geophys. Res. **56**, (1951) 63-72, 197-206, 207-220; J.A. Stratton, Electromagnetic Theory, Mc Graw-Hill Book Co. Inc. New York (1941).

where m, e, N, ν and c are the mass, charge, density, collision frequency of the electron and the light velocity in the vacuum, respectively (Appendix 1).

Thus, the equations (2. 1) are replaced by

$$(S\partial)H-\frac{\omega}{c}\varepsilon jE=\frac{4\pi}{c}I_e$$

$$(S\partial)jE-\frac{\omega}{c}\mu H=0 \quad ,$$

or

$$(S\partial)\begin{pmatrix}0&1\\1&0\end{pmatrix}\begin{pmatrix}jE\\H\end{pmatrix}-\frac{\omega}{c}\begin{pmatrix}\varepsilon&0\\0&\mu\end{pmatrix}\begin{pmatrix}jE\\H\end{pmatrix}=\frac{4\pi}{c}\begin{pmatrix}I_e\\0\end{pmatrix},$$

which gives

$$\left.\begin{array}{l}[\rho_1(S\partial)-U/c]\psi=\dfrac{4\pi}{c}F\,,\\ \text{where}\\ \rho_1=\begin{pmatrix}0&1\\1&0\end{pmatrix},\ \rho_2=\begin{pmatrix}0&-j\\j&0\end{pmatrix},\ \rho_3=\begin{pmatrix}1&0\\0&-1\end{pmatrix},\\ \psi=\begin{pmatrix}jE\\H\end{pmatrix},\quad F=\begin{pmatrix}I_e\\0\end{pmatrix},\\ \text{and}\\ U=\dfrac{\omega}{2}[(1+\rho_3)\varepsilon+(1-\rho_3)\mu]\,,\end{array}\right\}\quad(2.\ 6)$$

or gives

$$[\gamma_i\partial_i-U/c]\psi=4\pi F/c\,, \qquad (2.\ 7)$$

where

$$\gamma_i=\rho_1 S_i\,. \qquad (2.\ 8)$$

Between S_i's and ρ_i's, there are the following relations:

$$S_iS_jS_k+S_kS_jS_i=S_i\delta_{jk}+S_k\delta_{ji}\,,$$
$$S_1S_2-S_2S_1=-jS_3\,,\quad \rho_1{}^2=1\,,\quad \rho_1\rho_2=j\rho_3\,,\quad \text{etc.} \qquad (2.\ 9)$$

The equation (2. 7) is the generalized Kemmer formulation of the electromagnetic field for an arbitray medium, and will be exclusively used in the following discussions as the fundamental equation of the field.

The Poynting vector P_i is represented by

$$P_i=\frac{c}{8\pi}\psi^*\gamma_i\psi\,. \qquad (2.\ 10)$$

The complex conjugate equation of (2. 7) is

$$-\partial_i\psi^*\gamma_i-\psi^*(U^*/c)=4\pi F^*/c\,, \qquad (2.\ 11)$$

where ψ^*, F^* and U^* are respectively the complex conjugates of ψ, F, and the Hermitian conjugate of U.

Thus,

$$\begin{aligned}\partial_iP_i&=(c/8\pi)[(\partial_i\psi^*\gamma_i)\psi+\psi^*(\gamma_i\partial_i\psi)]\\&=(c/8\pi)[\psi^*(U-U^*)\psi+4\pi(\psi^*F-F^*\psi)].\end{aligned}$$

On the other hand, by taking suitable Hermitian Matrices for υ and σ, we can express U in the following form:

$$U=\upsilon+\frac{4\pi\sigma}{j}\,. \qquad (2.\ 12)$$

Hence,

$$U-U^*=-j8\pi\sigma\,,$$

and thus,

$$\partial_iP_i+j\psi^*\sigma\psi-\frac{1}{2}(\psi^*F-F^*\psi)=0\,, \qquad (2.\ 13)$$

or, by (2. 3),

$$\operatorname{div}P+\psi^*\sigma\psi+j(\psi^*F-F^*\psi)/2=0\,,$$

of which the second and the third terms represent the energy lost in a medium and that given to the external system per unit volume, respectively.

In a case in which $F=0$, the adjoint vector $\bar\psi$ of ψ satisfies

$$\partial_i\bar\psi\gamma_i+\bar\psi(U/c)=0\,. \qquad (2.\ 14)$$

Hence, by comparison of the above equation with (2. 11), we find from (2. 12)

$$\bar\psi=(\psi^*)_{\sigma\to-\sigma}\,. \qquad (2.\ 15)$$

If we introduce $\bar P_i$ defined by

$$\bar P_i=(c/8\pi)\bar\psi\gamma_i\psi\,, \qquad (2.\ 16)$$

in the same way as P_i in (2. 10), then, we have as the equation corresponding to (2. 13)

$$\partial_i\bar P_i=0\,, \qquad (2.\ 17)$$

thus $\bar P_i$ is the continuous vector in all space. However, it is generally a complex vector in an absorbing medium and hence its physical meaning is not so evident as that of P_i.

§ 3. Approximate Solution in a Slowly Varying Medium

Putting

$$\psi=\eta e^{-j\phi}\,,\quad \bar\psi=\bar\eta e^{j\bar\phi}\,, \qquad (3.\ 1)$$

and inserting these into (2. 7) and (2. 14) respectively, we find ($F=0$)

$$\left.\begin{array}{l}\left(\gamma_i\dfrac{\partial\phi}{\partial x_i}-U/c\right)\eta+\gamma_i\partial_i\eta=0\\ \bar\eta\left(\gamma_i\dfrac{\partial\bar\phi}{\partial x_i}-U/c\right)-\partial_i\bar\eta\gamma_i=0\,.\end{array}\right\}\quad(3.\ 2)$$

If we mean by δ the order of magnitude of $|\partial\eta|/|\partial\phi/\partial x\eta|$ in the following, δ is very small compared to 1 when the spatial change of a medium can be neglected over the distance of a wave length. Taking into account that the second term of (3. 2) are thus δ-order, we define ϕ and $\bar\phi$ by

$$\left.\begin{aligned}\left(\gamma_i\frac{\partial\phi}{\partial x_i}-U/c\right)\eta_0=0\\ \bar{\eta}_0\left(\gamma_i\frac{\partial\bar{\phi}}{\partial x_i}-U/c\right)=0\ ,\end{aligned}\right\}\qquad(3.\,3)$$

where η_0 and $\bar{\eta}_0$ are the vectors proportional to the solutions right in the 0-th order of δ. Then, $\bar{\phi}=\phi$ and they satisfy

$$\mathrm{Det}\left(\gamma_i\frac{\partial\phi}{\partial x_i}-U/c\right)=0\ .\qquad(3.\,4)$$

The complete solution of (3. 4) contains three arbitrary constants.

Now when ϕ satisfying (3. 4) is known, we can introduce η_ν and $\bar{\eta}_\nu$ ($\nu=0, 1, \cdots, 5$) defined by

$$\left.\begin{aligned}\left(\gamma_i\frac{\partial\phi}{\partial x_i}-U/c\right)\eta_\nu=\lambda_\nu\eta_\nu\\ \bar{\eta}_\nu\left(\gamma_i\frac{\partial\phi}{\partial x_i}-U/c\right)=\bar{\eta}_\nu\lambda_\nu\end{aligned}\right\}\qquad(3.\,5)$$

i.e. η_ν's are the eigen vectors of matrix $\gamma_i\partial\phi/\partial x_i-U/c$ having the eigen values λ_ν's and $\bar{\eta}_\nu$'s are the adjoint vectors of η_ν's. Thus, we can normalize them in the following way:

$$\bar{\eta}_\mu\eta_\nu=\delta_{\mu\nu}\ ,\qquad(3.\,6)$$

where the left hand side denotes the scalar product of vectors $\bar{\eta}_\mu$ and η_ν having six components. One of λ_μ, say λ_0, is at least zero on account of (3. 3). In the following, we shall consider a case in which λ_0 only is zero, for brevity. General cases will be discussed in Appendix 4 and the same results will be obtained.

Now, any η and $\bar{\eta}$ can be expressed in the forms

$$\eta=\Sigma_{\nu=0}^{5}a_\nu\eta_\nu\ ,\quad \bar{\eta}=\Sigma_{\nu=0}^{5}\bar{a}_\nu\bar{\eta}_\nu\ .\qquad(3.\,7)$$

Hence, inserting these into (3. 2), we get

$$\Sigma_{\nu=1}^{5}a_\nu\lambda_\nu\eta_\nu+\gamma_i\partial_i\eta=0\ ,$$

or, by multiplication with $\bar{\eta}_\mu$ and use of (3.6),

$$\left.\begin{aligned}a_\nu+\lambda_\nu^{-1}(\bar{\eta}_\nu\gamma_i\partial_i\eta)=0\quad(\nu\neq0)\\ (\bar{\eta}_0\gamma_i\partial_i\eta)=0\ .\end{aligned}\right\}\qquad(3.\,8)$$

Eq. (3. 7) and (3. 8) give the differential equations for a_ν. It is easily deduced from the above formulae that a_ν/a_0 ($\nu\neq0$) are of the order of δ; putting $\eta\simeq a_0\eta_0$, then

$$a_\nu\simeq-\lambda_\nu^{-1}(\bar{\eta}_\nu\gamma_i\partial_i(a_0\eta_0))\quad(\nu\neq0)\ ,\qquad(3.\,9)$$

and

$$(\bar{\eta}_0\gamma_i\partial_i(a_0\eta_0))=0\ .\qquad(3.\,10)$$

The solution for a_0 obtained from (3. 10) is right in the 0-th order of δ.

§ 4. Really Observed Waves

The wave discussed in the previous section is the one corresponding to the complete solution of (2. 7) for $F=0$ or (2. 14) and have only mathematical meaning, but not physical meaning in general. The really observed waves are the ones induced by an external or forced electric current and not special modes such as plane waves. To discuss the group velocity and wave path of the real wave, it is further necessary to limit the external current into so small a region, both in space and time, that we can consider it as a point source, as will be shown later. These conditions are satisfied by the Green's function of the electromagnetic field in space and time, i.e., ψ satisfying

$$[\gamma_i\partial_i-U/c]\psi(x\cdot t)=4\pi\delta(x-x_0)\delta(t-t_0),\quad(4.\,1)$$

together with the boundary condition of outward propagating wave to the infinity, where x_0 and t_0 are the coordinates of a current source in space and time.

Now, when the spatial change of a medium is sufficiently small and only the 0-th order approximation with respect to δ in the sense of section 3 is required*, then, by use of solution obtained in section 3, we can generally express the solution $\psi(x, t)$ of (4. 1) in the following form:

$$\begin{aligned}\psi(x, t)=\iiint d\omega dk_1dk_2a_0(x, \omega, k_1, k_2)\\ \times\eta_0(x, \omega, k_1, k_2)f(\omega, k_1, k_2)\exp(-j[\omega(t-t_0)\\ -\{\phi(x, \omega, k_1, k_2)-\phi(x_0, \omega, k_1, k_2)\}])\ ,\quad(4.\,2)\end{aligned}$$

where $\phi(x, \omega, k_1, k_2)$ is any solution of (3. 4) which is reduced to $(\omega/c)|x|$ at $|x|\sim\infty$, k_1 and k_2 being integration constants, and $\eta_0(x, \omega, k_1, k_2)$ and $a_0(x, \omega, k_1, k_2)$ are the ones determined from this ϕ by (3. 5), (3. 6) and (3. 10) respectively, and the paths of the integrations are to be suitably chosen: Especially for that of ω, it is generally convenient to take a line parallel to the real axis, having an infinitesimal negative imaginary part.

---

* Of course, this assumption does not hold for ω smaller than some value. However, such a range of frequency is out of the scope of this paper and will not be considered in the following.

In (4.2), $\phi(x, \omega, k_1, k_2) - \phi(x_0, \omega, k_1, k_2)$ is generally of the order of $(\omega/c)|x-x_0|$ and thus, if $(\omega/c)|x-x_0| \gg 1$, the integrand rapidly changes along the integration paths of k_1, k_2 and ω due to the phase part, whereas the change due to $f(\omega, k_1, k_2)$, as well as due to $\eta_0(x, \omega, k_1, k_2)$, is sufficiently small, since the external current is limited within an infinitely small region in space and time.

Using the conditions

$$\lim_{\omega\to\infty} \varepsilon = 1\,, \quad \lim_{\omega\to\infty} f(\omega, k_1, k_2) = 0\,,$$

which are generally considered to be satisfied, it can generally be shown that $\psi(x, t) = 0$ for $|x-x_0| > c[t-t_0]$. For $c(t-t_0) - |x-x_0| \gg c/\omega$, we can apply the approximation by the method of steepest descent or "Sattelpunkt" method to the integration for the reasons stated above: denoting ω by k_0, (4.2) approximately gives*

$$\psi(x, t) \simeq (2\pi)^{2/3} \frac{a_0(x, k')\eta_0(x, k')}{[\operatorname{Det} \phi_{ij}(k')]^{1/2}} f(k') \times e^{j[k_0'(t-t_0) - \phi(x, x_0, k') + \theta]}\,. \qquad (4.3)$$

Here,

$$\phi(x, x_0, k') \doteq \phi(x, k') - \phi(x_0, k')\,, \quad |\theta| \leqq \frac{3}{4}\pi\,, \qquad (4.4)$$

and $k' = (k_0', k_1', k_2')$ are the roots of

$$\frac{\partial}{\partial k_1}\phi(x, x_0, k) = \frac{\partial}{\partial k_2}\phi(x, x_0, k) \doteq t - t_0 - \frac{\partial}{\partial k_0}\phi(x, x_0, k) = 0\,, \qquad (4.5)$$

and

$$\phi_{ij}(k') \doteq \frac{\partial^2}{\partial k_i' \partial k_j'}\phi(x, x_0, k') \quad \text{(Appendix 2).}$$

It is to be remembered that higher approximation than (4.3) is meaningless, since (4.2) is right in the 0-th order of δ and (4.3) is also right in this approximation.

§ 5. Physical Meaning of Group Velocity and Wave Path

The expression (4.5) mathematically means that the value of $\psi(x, t)$ is almost contributed by the integration about k', or, in other words, $\psi(x, t)$ is decisively contributed by the mode of wave $\eta_0(x, k')e^{j[k_0't - \phi(x, x_0, k')]}$. On the other hand, one usually defines the wave path in space and time by such a trace of points on which the field strength ψ is decisively contributed by some same mode of the wave. For example, when group velocity in one-dimensional space is considered, then, if $\psi(x_2, t_2)$ is decisively contributed by the same frequency component of the wave as that which decisively contribute to $\psi(x_1, t_1)$ in a same degree, one would define the group velocity of that frequency at a point x_1 by $\lim_{t_2\to t_1} x_2 - x_1 / t_2 - t_1$. Similarly, as to the wave path in space for a given frequency, one would define it by such a group of traces on each of which the field sfrength is decisively determined by the same wave component radiated into a given direction at the transmitting point. Comparing, in this way, the physical meaning of the wave path in space and time with the mathematical meaning of the approximation by the method of steepest descent used in (4.3), close connection between them is naturally expected, i.e., since the mode which decisively contributes to the field strength at (x, t) is specified by the values of k's satisfying (4.5), we may formally be able to define the equation of line of the wave path passing through a point (x_1, t_1) by

$$k_i' = k_i(x_1, t_1) = k_i(x, t) \quad (i = 0, 1, 2)\,, \qquad (5.1)$$

here k's are considered as functions of position where the field is observed. It will next be shown that, when the field energy is not lost in a medium, the line determined by (5.1) does exist in real space and time, and further the direction of the wave path thus defined is concordant with that of the Poynting vector of the field in the 0-th order of δ at any point of space and time.

Now, if a receiving point x is infinitely near from a transmitting point x_0, its coordinate differences being $\delta x_1'$, $\delta x_2'$, $\delta x_3'$ and $\delta t'$, then, taking into account of $\phi(x_0, x_0, k') = 0$, (4.5) gives

$$\frac{\partial^2}{\partial k_a' \partial x_i}\phi(x, x_0, k')\delta x_i - \delta_{k_\alpha' k_0'}\delta t = 0\,, \qquad (5.2)$$
$$(\alpha = 0, 1, 2)$$

where $\delta x_i = \delta x_i'$, $\delta t = \delta t'$ and $x = x_0$ in this case. We firstly determine the values of k''s by (5.2) for a given value of $\delta x_i'$'s and $\delta t'$, and secondly examine whether the line in space and time defined by (5.1) for those values of k''s does really exist or not. Generally, we get from (3.3)

---

* We shall not consider such a case when ε does not depend on frequency.

$$\frac{\partial}{\partial k_\alpha'}\left[\bar{\eta}_0\left(\gamma_i\frac{\partial\phi}{\partial x_i}-\frac{U}{c}\right)\eta_0\right]_{k=k'}$$
$$=\bar{\eta}_0\left(\gamma_i\frac{\partial^2}{\partial k_\alpha'\partial x_i}\phi-\frac{1}{c}\frac{\partial}{\partial k_\alpha'}U\right)\eta_0$$
$$+\left(\frac{\partial}{\partial k_\alpha'}\bar{u}_0\right)\left(\gamma_i\frac{\partial\phi}{\partial x_i}-\frac{1}{c}U\right)\eta_0$$
$$+\bar{\eta}_0\left(\gamma_i\frac{\partial}{\partial x_i}\phi-\frac{1}{c}U\right)\left(\frac{\partial}{\partial k_\alpha'}\eta_0\right)$$
$$=\bar{\eta}_0\left(\gamma_i\frac{\partial^2}{\partial k_\alpha'\partial x_i}\phi-\frac{1}{c}\frac{\partial}{\partial k_\alpha'}U\right)\eta_0,$$

which must definitely be zero, and thus find

$$\frac{\partial^2}{\partial k_\alpha'\partial x_i}\phi(x, x_0, k')(\bar{\eta}\gamma_i\eta_0)_{k=k'} -\delta_{k_\alpha' k_0'}\frac{1}{c}\left(\bar{\eta}_0\frac{\partial U}{\partial k_0}\eta_0\right)_{k=k'}=0 \tag{5. 3}$$

since U does not depend on k_1' and k_2'. Hence, comparing (5. 2) and (5. 3), we get

$$\frac{\delta x_1}{(\bar{\eta}_0\gamma_1\eta_0)_{k=k'}}=\frac{\delta x_2}{(\bar{\eta}_0\gamma_2\eta_0)_{k=k'}} =\frac{\delta x_3}{({}_0\bar{\eta}\gamma_3\eta_0)_{k=k'}}=\frac{c\delta t}{\left(\bar{\eta}_0\frac{\partial U}{\partial k_0'}\eta_0\right)_{k=k'}}. \tag{5. 4}$$

When $U(x, k_0)$ is Hermitian for any real values of k_0, we first suppose, in order to know the values of k''s, that k_0' is a real and the values of k_1' and k_2' are the ones so that real values of $\partial\phi/\partial x_i$'s at $x=x_0$ are secured, then $\gamma_i\partial\phi/\partial x_i-U/c$ is Hermitian matrix and thus all denominators in (5. 4) at $x=x_0$ are always real on account of $\bar{\eta}=\eta^*$. Hence, under the above presuppositions, we can take the suitable values for k_1', k_2' and k_0' so that (5. 4) for $\delta x_i=\delta x_i'$ and $\delta t=\delta t'$ is satisfied, which are also values satisfying (5. 2). For such constant values for k_1', k_2' and k_0', ϕ and $\partial\phi/\partial x_i$'s are always real, and Hermitian condition of $\gamma_i\partial\phi/\partial x_i-U/c$ and thus the condition of $\bar{\eta}=\eta^*$ are secured in all space, since $\phi=0$ and $\partial\phi/\partial x_i$'s are real at $x=x_0$, and $U(x, k_0')$ is Hermitian in all space.

It is now evident from (5. 2) and (5. 4) that the line defined by (4. 5) or (5. 1) for the above values of k''s is really existing in space and time, since, denoting line elements of this line at x and t by δx and δt, then, from (4. 5), they satisfy the same equations as (5. 2) and thus also (5. 4), for all values of x and t on this line, and also all denominators in (5. 4) take real values. Further it is easily deduced that all space and time satisfying $c(t-t_0)>|x-x_0|$ can be covered with such lines by taking suitable values for k''s.

We can now conclude that, when $U(x, k_0)$ is Hermitian for any real value of k_0, i.e., when the field energy is not lost in a medium, the wave path defined by (5. 1) really exists and its direction is concordant with that of the Poynting vector of the field in the 0-th order of δ at any point of space and time, as it is evident from (5. 4), (4. 3) and the expression of the Poynting vector (2. 10), and the velocity components of the wave v_i's at any point in space are expressed by

$$v_i=\frac{\partial x_i}{\partial t}=c\frac{(\bar{\eta}_0\gamma_i\eta_0)_{k=k'}}{\left(\bar{\eta}_0\frac{\partial U}{\partial\omega}\eta_0\right)_{k=k'}}, \tag{5. 5}$$

which are evident from (5. 4), and this velocity is usually called by the name 'group velocity' of the wave at the frequency $\omega=k_0'$.

Mathematically, the condition that the lines defined by (5. 1) really exist in space and time is reduced to that of whether, in the complex plane of k_0, such a path of integration connecting $-\infty$ and ∞ on which $U(x, k_0)$ is always Hermitian in all space does exist or not, though it is actually restricted to the real axis, if it exists.

We now consider the case when such an integration path does not exist. All terms in the denominator of (5. 4) are now complex numbers on account of $\bar{\eta}\neq\eta^*$ and change along the line of (5. 1) and their arguments are generally not concordant with each other, though they are so at x_0 and t_0, except when the medium is uniform, and thus the direction of the line is generally complex number, so that such a line does not exist in real space and time.

Conversely, this means that the values of k''s satisfying (4. 5) or k''s as functions of position in space do not distribute on the lines in k'-complex planes as in a case of nonabsorbing or uniform medium, but on planes to any point of which one point of space and time correspond. In other words, one mode of the wave which decisively contributes to the field strength at some point in space and time never contributes, in a same degree as it does at that point, to the field strength at any other point of space and time, there the other mode of the wave dicisively contributing to the field strength.

To understand the physical meanings of

k''s more clearly, we consider k''s as functions of $\delta x'/\delta t'$ defined by (5. 2) or (5. 4) for $\delta x=\delta x'$, $\delta t=\delta t'$ and $x=x_0$, $t=t_0$ and use $\delta x'/\delta t'$ as variables instead of k'. $\delta x_i'/\delta t'$'s are of course real at $x=x_0$ and, from the results discussed above, the line of (5. 1) for given real values of $\delta x_i'/\delta t'$'s ($|\delta x'/\delta t'|<c$) really exist in a non-absorbing medium or in uniform medium, and all space and time in the range $c(t-t_0)>|x-x_0|$ can be covered with such lines by giving suitable real values for $\delta x_i'/\delta t'$'s. In an absorbing non-uniform medium, $\delta x_i'/\delta t'$'s considered as functions of position in space and time, are generally complex numbers and distribute not on lines, but on planes in $\delta x_i'/\delta t'$'s complex planes.

Now, physical meaning of $\delta x'/\delta t'$ is that the field strength at any point is decisively contributed by the wave radiated at $x=x_0$ whose velocity components are given by the values taken by $\delta x_i'/\delta t'$'s at the receiving point, so that, if their imaginary parts are sufficiently small compared to their "real" parts, i.e., the energy loss in a non-uniform medium is sufficiently small, we shall be able to under stand the real parts of $\delta x_i'/\delta t'$'s as the velocity of the wave at $x=x_0$ which decisiverly contribute to the field strength at the position giving those values for $\delta x_i'/\delta t'$'s.

On the other hand, k''s and thus also $\delta x'/\delta t'$'s are analytic functions of the measure producing the energy loss, e.g. conductivity. Hence, $\delta x'/\delta t'$'s must be real for any purely imaginary value of that measure, as it is evident from (2. 12), so that the real parts of $\delta x'/\delta t'$'s do not change in the first order of that measure for its real value by the theory of conformal respresentation.

From the point of view of this section, it is concluded that the concept of wave path generally does not exist in an absorbing non-uniform medium, and that, when the energy loss in a medium is sufficiently small that the first order changes of wave path due to the energy loss in a medium are only required to be taken into account, it approximately exists and is concordant with the one obtained when the field energy is not lost in that medium.

In the next section, the wave path will be discussed in the more rigorous way from the other point of view and mathematically founded and it will be found that all conclusions obtained there are the same as those obtained in this section.

§ 6. Mathematical Foundation of Wave Path

The formula (4. 3) for the field strength $\psi(x, t)$ is of the form of

$$\psi(x, t)=\xi(x, t)e^{j[k_0'(t-t_0)-\phi(x,x_0,k')]}\,, \qquad (6.\ 1)$$

where k''s are functions of x and t defined by (4. 5) and k_0' is assumed to be sufficiently large in the sense of the foot note of (4. 2). It is to be emphasized that the phase part of (6. 1) does not depend on the special choice of k' introduced as integration constants of (3. 4), since it is the only solution of (3. 4), in which ω is replaced by $-j\cdot\partial/\partial t$, satisfying the conditions that it is zero at $x=x_0$ and $t=t_0$ and take the minimum or stationary value of all the possible solutions for any given set of values of x and t. (6. 1) is the same form as that of (3. 1) and thus $\xi(x, t)$ is expected to be calculated by the same method as that by which $\eta(x)$ is calculated. Since

$$\partial_i[\, j\{k_0'(t-t_0)-\phi(x, x_0, k')\}]$$
$$=\begin{cases} \dfrac{\partial\phi}{\partial x_i}+j\Sigma_{\nu=0}^{2}\dfrac{\partial}{\partial k_\nu'}\Big[\quad\Big]\dfrac{\partial k_\nu'}{\partial x_i}=\dfrac{\partial\phi}{\partial x_i} & (i=1, 2, 3) \\ k_0'-j\,\Sigma_{\nu=0}^{2}\dfrac{\partial}{\partial k_\nu'}\Big[\quad\Big]\dfrac{\partial k_\nu'}{\partial x_0}=k_0' & (i=0)\,, \end{cases} \qquad (6.\ 2)$$

with

$$\partial_0=-j\cdot\partial/\partial t\,,\quad [\ ]=j\{k_0'(t-t_0)-\phi(x, x_0, k')\,,$$

are satisfied on account of (4.5), we get, by inserting (6. 1) into (2. 7) with $F=0$,

$$\Big[\gamma_i\Big\{\frac{\partial}{\partial x_i}\phi(x, x_0, k_1', k_2', k_0')+\partial_i\Big\}$$
$$-\frac{1}{c}U(x, k_0'+\partial_0)\Big]\xi(x, t)=0\,, \qquad (6.\ 3)$$

in which $\omega=k_0$ is replaced by $k_0'+\partial_0$ (Appendix 3). Using the condition $|\partial_0\xi|\ll|k_0'\xi|$, or $|\partial_0|\ll|k_0'|$, we have

$$U(x, k_0'+\partial_0)\simeq U(x, k_0')$$
$$+\frac{1}{2}\Big[\partial_0\frac{\partial}{\partial k_0'}U(x, k_0')+\frac{\partial}{\partial k_0'}U(x, k_0')\partial_0\Big], \qquad (6.\ 4)$$

which is right to the first order of ∂_0*. Using the above formula, (6. 3) is reduced to

---

* The second term of (6.4) is due to Hermitian condition of U in a case in which U is Hermitian matrix, and also holds for general cases.

$$\left[\gamma_i\frac{\partial}{\partial x_i}\phi(x, x_0, k')-\frac{1}{c}U(x, k_0')\right]\xi(x, t)$$
$$+\left[\gamma_i\partial_i-\frac{1}{2c}\left\{\partial_0\frac{\partial}{\partial k_0'}U(x, k_0')\right.\right.$$
$$\left.\left.+\frac{\partial}{\partial k_0'}U(x, k_0')\partial_0\right\}\right]\xi(x, t)=0 \qquad (6.5)$$

which corresponds to (3. 2), so that, by putting

$$\xi(x, t)=\Sigma_{\mu=0}^{5}A_\mu(x, t)\eta_\mu(x, k')$$

as (3. 7), we have

$$\xi=A_0\eta_0-\Sigma_{\nu=1}^{5}\lambda_\nu^{-1}\eta_\nu\left[\bar{\eta}_\nu\left\{\gamma_i\partial_i-\frac{1}{2c}\left(\partial_0\frac{\partial U}{\partial k_0'}\right.\right.\right.$$
$$\left.\left.\left.+\frac{\partial U}{\partial k_0'}\partial_0\right)\right\}A_0^0\,\eta_0\right], \qquad (6.6)$$

where A_0 and A_0^0 are right to the first order and 0-th order of δ, respectively, and the latter satisfy

$$\bar{\eta}_0(x, k')\left[\gamma_i\partial_i-\frac{1}{2c}\left\{\partial_0\frac{\partial}{\partial k_0'}U(x, k_0')\right.\right.$$
$$\left.\left.+\frac{\partial}{\partial k_0'}U(x, k_0')\partial_0\right\}\right](A_0^0\eta_0(x, k'))=0\,, \quad (6.7)$$

or

$$(\bar{\eta}_0\gamma_i\eta_0)_{k=k'}\partial_iA_0^0-\frac{1}{c}\left(\bar{\eta}_0\frac{\partial U}{\partial k_0}\eta_0\right)_{k=k'}$$
$$\times\partial_0A_0^0+jWA_0^0=0\,, \qquad (6.8)$$

where

$$jW=\bar{\eta}_0\left(\gamma_i\partial_i-\frac{1}{2c}\left\{\partial_0\frac{\partial U}{\partial k_0'}+\frac{\partial U}{\partial k_0'}\partial_0\right\}\right)\eta_0\,.$$

(6. 8) is the differential equation for A_0^0 and its general solution in given by

$$A_0^0L(x, t)=f(n_1(x, t), n_2(x, t), n_3(x, t))\,, \quad (6.9)$$

where f is the arbitrary function of $n_i(x, t)$'s which, together with $L(x, t)$, are defined so that, for any constant values of n_i''s and L',

$$n_1(x, t)=n_1'\,, \quad n_2(x, t)=n_2'\,, \quad n_3(x, t)=n_3'$$

and

$$A_0^0L(x, t)=L' \qquad (6.10)$$

constitute the four independent solutions of

$$\frac{dx_1}{(\bar{\eta}_0\gamma_1\eta_0)_{k=k'}}=\frac{dx_2}{(\bar{\eta}\gamma_2\eta_0)_{k=k'}}=\frac{dx_3}{(\bar{\eta}_0\gamma_3\eta_0)_{k=k'}}$$
$$=\frac{cdt}{\left(\bar{\eta}_0\frac{\partial U}{\partial k_0}\eta_0\right)_{k=k'}}=\frac{-dA_0^0}{A_0^0W(x, t)}\,. \qquad (6.11)$$

On the other hand, we know from (4.3)

$$\xi(x, t)=(2\pi)^{3/2}\frac{a_0(x, k')\eta_0(x, k')}{(\mathrm{Det}\,\phi_{ij}(k'))^{1/2}}f(k')e^{j\theta}$$
$$=A_0^0\eta_0(x, k')\,,$$

and thus find

$$A_0^0\frac{[\mathrm{Det}\,\phi_{ij}(k')]^{1/2}}{(2\pi)^{3/2}a_0}e^{-j\theta}=f(k')\,. \qquad (6.12)$$

Comparing (6. 9) and (6. 12), also (5. 1) and (6. 10), it is evident that k''s have the same meanings as n''s, and $f(n)$ is the function determined by the angle dependence of radiation intensity at (x_0, t_0); assuming that $f(n)$ is not zero only in the range $n'<n<n'+\Delta n'$, then A_0^0 is not zero only on the lines in space and time determined by (6. 10) for the values of n''s between n' and $n'+\Delta n'$, provided that such lines really exist. This means that A_0^0 on those lines is uniquely determined by the wave radiated in this range of direction, so that the wave path must be that line to which such lines are reduced at the limit of $\Delta n'\to 0$ and which is just the one given by (6. 10) for those values of n''s, in so far as it exists in real space and time.

Conversely if such a line does not exist in real space and time for any suitable values of n''s, or, in other words, if $n_i(x, t)$'s do change for any suitable line in real space and time, we must conclude that concept of wave path does not exist, or, in a certain sense, A_0^0 is not uniquely determined by the wave radiated in one direction, but depends on all the waves radiated in various directions. Hence it is evident from the discussion in section 5, that the condition of existance of wave path depends on whether the direction cosines determined by the first four terms of (6.21) which are just the same as those of (5. 4) take real values or not in all space and time, and this is generally satisfied only if $U(x, k_0')$ is Hermitian in all space and time, except in an uniform medium, and further that, when the energy loss of the field is sufficiently small, the deductions are also same as those of section 5 and so are the results.

§ 7 Summary of Results

In an absorbing non-uniform medium, the concepts of the wave path and group velocity or, more generally, wave packet do not exist in a rigorous sense, and when the energy loss of the field in a medium is sufficiently small that only the first order change of the wave path and group velocity due to the energy loss is required to be taken into account, they approximately exist and are concordant with the ones obtained when the field energy is not lost in that medium, so that it is anyhow meaningless to discuss their changes due to energy loss of the field in an absorbing non-uniform medium. In a non-absorbing medium, the direction of wave path is concordant with that of the Poynting vector of the field, as it is expected, and more briefly given by (5. 4), and also the group velocity by (5. 5). In an absorbing but uniform medium, the wave path exists and is a group of straight lines radiating from (x_0, t_0), while the paths obtained by tracing the direction of the Poynting vector of the field may be the curved lines radiating from (x_0, t_0) if $(\overline{\eta}_0 \gamma_i \eta_0)_{k=k'}$'s are not proportional to $(\eta_0{}^* \gamma_i \eta_0)_{k=k'}$'s respectively, though they are straight lines in non-absorbing medium, and thus not concordant with the wave path. This is due to the fact that the wave path is directly connected with the determination of the amplitude of the field strength, while the path obtained from the Poynting vector has no direct connection with that determination.

Appendix

(1) Using $(\omega_H s)^3 = \omega_H{}^2 (\omega_H s)$, we find

$$\{\omega - j\nu + (\omega_H s)\}[(\omega - j\nu)^2 - (\omega - j\nu)(\omega_H s) + \{(\omega_H s)^2 - \omega_H{}^2\}] = (\omega - j\nu)\{(\omega - j\nu)^2 - \omega_H{}^2\},$$

which gives

$$\{\omega - j\nu + (\omega_H s)\}^{-1} = \frac{(\omega - j\nu)^2 - \omega_H{}^2 + (\omega_H s)^2 - (\omega - j\nu)(\omega_H s)}{(\omega - j\nu)\{(\omega - j\nu)^2 - \omega_H{}^2\}} .$$

On the other hand, by the definitions of s_i's

$$(\omega_H s)^2 = \omega_H{}^2 - \omega_H \cdot \omega_H ,$$

where the second term of the right hand side denotes the direct product, so that

$$\{\omega - j\nu + (\omega_H s)\}^{-1} = \frac{(\omega - j\nu)}{\{(\omega - j\nu)^2 - \omega_H{}^2\}} \times \left[1 - \frac{\omega_H \cdot \omega_H}{(\omega - j\nu)^2} - \frac{(\omega_H s)}{(\omega - j\nu)} \right] .$$

Hence, we have from (5)

$$\varepsilon = 1 - j \frac{\omega_0{}^2 (\nu + j\omega)}{\omega\{(\nu + j\omega)^2 + \omega_H{}^2\}} \times \left[1 + \frac{\omega_H \cdot \omega_H}{(\nu + j\omega)^2} - j \frac{(\omega_H s)}{\nu + j\omega} \right],$$

which is the formula generally used.

(2) Set

$$\Phi(k_0, k_1, k_2) = k_0(t - t_0) - \phi(x, x_0, k_0, k_1, k_2) ,$$

then, (4. 5) is reduced to

$$\partial \Phi / \partial k_i = 0 \quad (i = 0, 1, 2) ,$$

hence, expanding $\Phi(k)$ in powers of $(k - k')$,

$$\Phi(k) = \Phi(k') + \frac{1}{2} \Sigma_{ij} \left(\frac{\partial^2}{\partial k_i \partial k_j} \Phi(k) \right)_{k=k'} \times (k_i - k_i')(k_j - k_j') + 0[(k - k')^3] ,$$

and thus by the suitable linear transformation of $(k_i - k_i')$'s to X_1, X_2 and X_3, we have

$$\Phi(k) = \Phi(k') + 1/2(\lambda_1 X_1{}^2 + \lambda_2 X_2{}^2 + \lambda_3 X_3{}^2) + 0[X^3],$$

and $$dk_0 dk_1 dk_3 = dX_1 dX_2 dX_3 ,$$

where λ_i's are the eigen values of Matrix $(\partial^2/\partial k_i \partial k_j \cdot \Phi(k))_{k=k'}$ and thus

$$\lambda_1 \lambda_2 \lambda_3 = \mathrm{Det}\,(\phi_{ij}(k'))$$

on account of $(\partial^2/\partial k_i \partial k_j \cdot \Phi(k))_{k=k'} = \phi_{ij}(k')$. Now, any integral of the form

$$\iiint dk_0 dk_1 dk_2 C(k_0, k_1, k_2) e^{j\Phi(k)}$$

can be approximatly reduced to

$$C(k') e^{j\Phi(k')} \iiint dX_1 dX_2 dX_3 e^{j/2(\lambda_1 X_1{}^2 + \lambda_2 X_2{}^2 + \lambda_3 X_3{}^3)},$$

under the assumptions stated in Section 4. Hence, after the change of variables $(-j \cdot \lambda_i/2)^{1/2} X_i = t_i$, we get

$$(2j)^{3/2} (\lambda_1 \lambda_2 \lambda_3)^{-1/2} C(k') e^{j\Phi(k')} \times \iiint_{\mp\infty}^{\pm\infty} e^{-(t_1{}^2 + t_2{}^2 + t_3{}^2)} dt_1 dt_2 dt_3 ,$$

where the paths of integration for t_i's are the ones from $-\infty$ to $+\infty$ or from $+\infty$ to $-\infty$. Hence, the above integral is reduced to $(2\pi)^{3/2} (\mathrm{Det}\,(\phi_{ij}(k')))^{-1/2} C(k') e^{j\Phi(k') + j\theta}, (\theta \leqq 3/4 \cdot \pi)$.

(3)

$$\partial_0 (\xi e^{jk_0 t}) = e^{jk_0 t} (k_0 + \partial_0) \xi ,$$

generally

$$\partial_0{}^n (\xi e^{jk_0 t}) = e^{jk_0 t} (k_0 + \partial_0)^n \xi ,$$

hence

$$U(x, \partial_0) \xi e^{jk_0 t} = e^{jk_0 t} U(x, k_0 + \partial_0) \xi ,$$

(4) If one of the eigen value of η_ν's other than η_0, say η_1, does vanish, ξ is represented in the 0-th order of δ by the form of $A_0{}^0 \eta_0 + A_1{}^0 \eta_1$ and (6. 7) is replaced by

$$\begin{aligned} &\overline{\eta}_0(x, k') \left[\gamma_i \partial_i - \frac{1}{2c} \left\{ \partial_0 \frac{\partial}{\partial k_0'} U(x, k_0') + \frac{\partial}{\partial k_0'} U(x, k_0') \partial_0 \right\} \right] (A_0{}^0 \eta_0 + A_1{}^0 \eta_1) = 0 \\ &\overline{\eta}_1(x, k') \left[\gamma_i \partial_i - \frac{1}{2c} \left\{ \partial_0 \frac{\partial}{\partial k'_0} U(x, k_0') + \frac{\partial}{\partial k_0'} U(x, k_0') \partial_0 \right\} \right] (A_0{}^0 \eta_0 + A_1{}^0 \eta_1) = 0. \end{aligned} \tag{A. 1}$$

On the other hand, differentiate the both sides of

$$\bar{\eta}_\nu(x, k')\left[\gamma_i\frac{\partial}{\partial x_i}\phi(x, k')-U(x, k_0')/c\right]\eta_\mu(x, k')=0 \quad (\mu, \nu=0, 1) \qquad \text{(A. 2)}$$

by k_α', we have, as the equations corresponding to (5. 3),

$$(\bar{\eta}_\nu\gamma_i\eta_\mu)\frac{\partial^2}{\partial k_\alpha'\,\partial t_i}\phi(x, k') -\delta_{k_\alpha' k_0'}\frac{1}{c}\left(\bar{\eta}_\nu\frac{\partial U}{\partial k_0'}\eta_\mu\right)=0 \quad (\mu, \nu=0, 1) \qquad \text{(A. 3)}$$

Denoting the line elements of the line defined by (5. 1) by δx_i and δt, then, they satisfy

$$\frac{\partial^2}{\partial k_\alpha'\partial x_i}\phi(x, x_0, k')\delta x_i-\delta_{k_\alpha' k_0'}\delta t=0\,, \qquad \text{(A. 4)}$$

on account of (4. 5). Hence, comparing with (A. 3), we get the following formula

$$\frac{\delta x_1}{(\bar{\eta}_\nu\gamma_1\eta_\mu)_{k=k'}}=\frac{\delta x_2}{(\bar{\eta}_\nu\gamma_2\eta_\mu)_{k=k'}}=\frac{\delta x_3}{(\bar{\eta}_\nu\gamma_3\eta_\mu)_{k=k'}} =\frac{c\delta t}{\left(\bar{\eta}_\nu\frac{\partial U}{\partial k_0}\eta_\mu\right)_{k=k'}} \quad (\mu, \nu=0, 1). \qquad \text{(A. 5)}$$

The above means that $(\bar{\eta}_\nu\gamma_i\eta_\mu)_{k=k'}$'s are proportional to δx_i's for any values of μ, $\nu=0, 1$. Hence, (A. 1) is expressed in the form

$$\Sigma'^{3}_{i=0} P_i^0(C_{00}\partial_i A_0^0+C_{01}\partial_i A_1^0) +j(W_{00}A_0^0+W_{01}A_1^0)=0$$

$$\Sigma'^{3}_{i=0} P_i^0(C_{10}\partial_i A_0^0+C_{11}\partial_i A_1^0) +j(W_{10}A_0^0+W_{11}A_1^0)=0\,, \qquad \text{(A. 6)}$$

where

$$P_i^0=(\bar{\eta}_0\gamma_i\eta_0)_{k=k'}\,, \quad P_0^0=-\frac{1}{c}\left(\bar{\eta}_0\frac{\partial U}{\partial k_0}\eta_0\right)_{h=k'}.$$

Eliminating $P_i^0\partial_i A_0^0$ or $P_i^0\partial_i A_1^0$ from (A. 6), we get

$$(C_{11}C_{00}-C_{10}C_{01})P_i^0\partial_i A_1^0+j[\{C_{00}W_{10} -C_{10}W_{00}\}A_0^0+\{C_{00}W_{11}-C_{10}W_{01}\}A_1^0]=0 \qquad \text{(A. 7 a)}$$

$$(C_{11}C_{00}-C_{10}C_{01})P_i^0\partial_i A_0^0+j[\{C_{11}W_{00} -C_{01}W_{10}\}A_0^0+\{C_{11}W_{01}-C_{01}W_{11}\}A_1^0]=0. \qquad \text{(A. 7 b)}$$

Now, set

$$A_1^0=f A_0^0\,, \qquad \text{(A. 8)}$$

then, (A. 7 a)$-$(A. 7 b)$\times f$ gives the equation of the form

$$\Sigma^3_{=0}P_i^0\partial_i f+j(V_0+V_1 f+V_2 f^2)=0\,. \qquad \text{(A. 9)}$$

After f is obtained from (A. 9), we can get A_0^0 from (A. 7 b) which can be reduced to the same equation as (6.8), except the functional formula for W. Hence, the discussions in section 6 can be applied to A_0^0 and thus also to A_1^0 by (A. 8), as they are.

JOURNAL OF THE PHYSICAL SOCIETY OF JAPAN Vol. 7, No. 5, SEPT.—OCT., 1952

Structure of the Line λ4686 of He II

By Kiyoshi MURAKAWA and Shigeki SUWA

Institute of Science and Technology, Komaba-machi, Meguro-ku, Tokyo.

(Received May 27, 1952)

The fine structure of the line He II λ4686 was measured, and it was found that the shift of the 3S term relative to the $3^2P_{1/2}$ term is 0.135±0.005 cm^{-1}. This is to be compared with the calculated value 0.138±0.001 cm^{-1}. That of the 4S term was found to be 0.056±0.009 cm^{-1}, the calculated value being 0.0584±0.0005 cm^{-1}.

§ 1. Introduction

The fine structure of the line He II λ4686 was studied by many authors, notably by Paschen[1] for the first time. Further detailed investigation was afterwards recognized important as a test of the theory of level shift in hydrogen-like atoms[2].

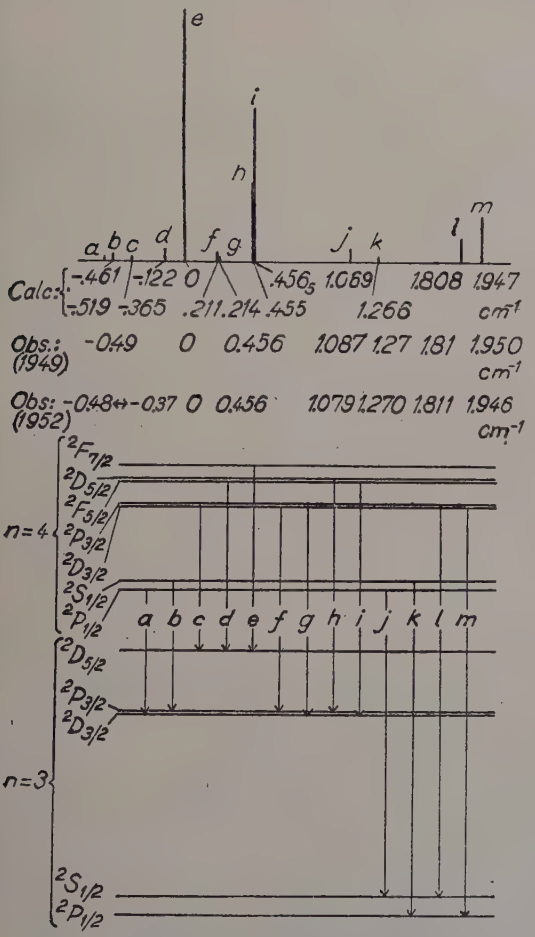
e
i
h
m
l
a b c d f g j k
Calc.: -.461 -.122 0 .456$_5$ 1.069 1.808 1.947
-.519 -.365 .211 .214 .455 1.266 cm^{-1}
Obs.: (1949) -0.49 0 0.456 1.087 1.27 1.81 1.950 cm^{-1}
Obs.: (1952) -0.48↔-0.37 0 0.456 1.079 1.270 1.811 1.946 cm^{-1}
n=4
$^2F_{7/2}$
$^2D_{5/2}$
$^2F_{5/2}$
$^2P_{3/2}$
$^2D_{3/2}$
$^2S_{1/2}$
$^2P_{1/2}$
a b c d e f g h i j k l m
n=3
$^2D_{5/2}$
$^2P_{3/2}$
$^2D_{3/2}$
$^2S_{1/2}$
$^2P_{1/2}$

Fig. 1. Calculated and observed structure and transition scheme of He II λ4686.

The structure of the line λ4686 calculated according to the theory is shown in Fig. 1. Mack and Austern[3] resolved for the first time the components j and k. Kamei and the present writers[4] resolved the components l and m, and Hirschberg and Mack[5] resolved independently the same components. Kopfermann et al[6] measured the shift of the 3S term in an indirect way.

§ 2 Experimental Arrangement

A liquid-air cooled hollow cathode discharge tube was used as the light source. It was found that in order to get maximun sharpness of the components the discharge current should be as small as possible. The light from the source passed through a lens and a slit and then a silvered Fabry-Pérot etalon. The interference fringes were projected on to the slit of the collimator of a prism-spectrograph. With a discharge current of about 40 milliamperes the line He II λ4686 could be photographed in four or five hours.

The structure was measured with the aid of a microphotometer and a comparator.

In addition to our own plates we had at our disposal the plates which Dr. Austern had taken with the large concave grating (second order with a dispersion of 3.6282 mm/A) of the University of Chicago using a liquid-air cooled hollow cathode source of his own design and kindly gave to one of us (K. M.) during the stay in Madison.

§ 3 Result of Measurements

Fig. 2 shows two enlarged pictures taken by an etalon with 1.5 mm and 2 mm spacers respectively, and Fig. 3 shows an example of a microphotometric resolution of the components l and m where both the wave-number and the intensity are represented with linear scales.

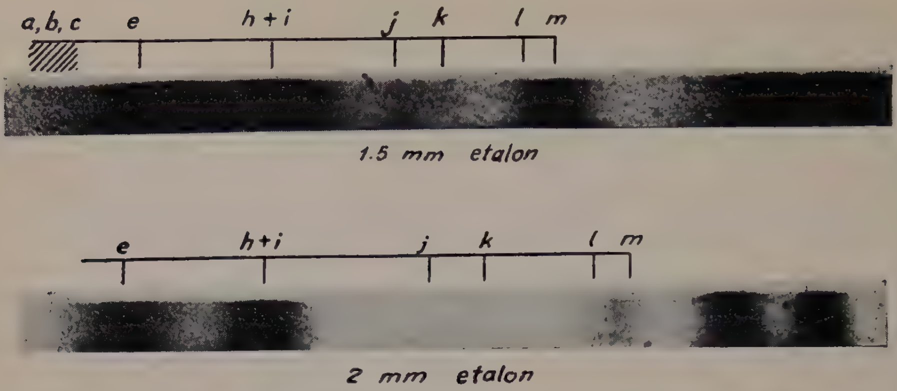

Fig. 2. Enlargement of interference patterns of He II λ4686 taken with a Fabry-Pérot etalon.

In Fig. 1 the result of our measurment is given together with the calculated relative positions of the components. If the shifts of terms other than the S-terms are neglected, the distance between the components l and m gives directly the shift of the $3S$ term relative to $3^2P_{1/2}$. The calculated value and the values measured by various authors are summarized in Table I. The calculated value is based on the observed value7) of the shift of the $2S$ term of He II (14020 ± 100 mc/sec$=0.4673 \pm 0.0033$ cm^{-1}) and the n^{-3}-law2).

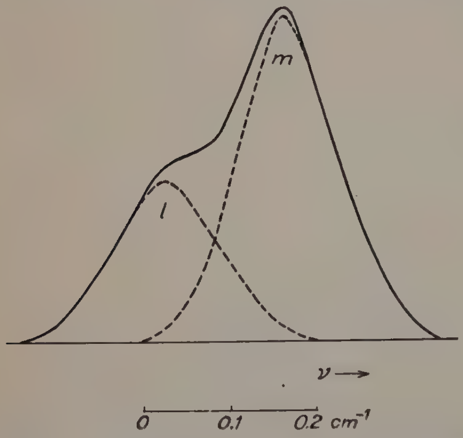

Fig. 3. Microphotometric resolution of the components l and m.

Hirschberg and Mack5), who measured the shift with a 20 mm etalon crossed by the second order of a large concave-grating, concluded that the measured shift is smaller than the value predicted by the n^{-3}-law. Our value is in fairly good agreement with their value, but th eaccuracy of our measurement is not large enough to state the same conclusion as theirs. Somewhat similar case occurred in the measurement of the shift of the $3S$ term of hydrogen by Series8). The shift measured by Kopfermann et al.6) seems to be too small. In view of the rather large discharge current employed by them, we consider that the range of the limits of error given by them is too small.

Table I Shift of the 3^2S term relative to the $3^2P_{1/2}$ term (cm^{-1}).

Calculated	$0.138_5 \pm 0.001$*
Observed	Murakawa, Suwa and Kamei (1949): 0.14 ± 0.01
	Kopfermann, Kruger u. Ohlmann: 0.118 ± 0.003
	Hirschberg and Mack: $0.1314\ (+0.003, -0.006)$
	Murakawa and Suwa** (1952) 0.135 ± 0.005
	Murakawa and Suwa*** (1952): $0{\cdot}133 \pm 0.015$

* The limit of error given here only comes from the limit of uncertainty of the observed value of the shift of the $2S$ term (ref. 7). It does not include the limit of accuracy of the n^{-3}-law.

** Measured interferometrically.

*** Measured on concave-grating spectrograms taken by Dr. Austern.

The shift of the $4S$ term relative to the $4^2P_{1/2}$ term cannot be measured directly, but since the distance between the components j and k ($=0.191 \pm 0.004$ cm^{-1}) is the sum of the shift of the $4S$ and $3S$ term, we find:

Shift of the $4S$ term$=0.191-0.135=0.056 \pm 0.009$ cm^{-1}.

This is to be compared with the calculated value 0.0584±0.0005 cm^{-1}*, but the accuracy of our measurement is insufficient to make a detailed comparison.

The positions of the components relative to the component *e* are generally in agreement with the calculation to within ±0.004 cm^{-1}, except *a*, *b*, *c*, and *j* and *k*. The position of the component *k* is rather difficult to determine, and we have tentatively adopted the value (1.270 cm^{-1}) that was determined in 1949, and the position of the component *j* was determined relative to *k*. The group of the components *a*, *b* and *c* was found to constitute a broadened patch (see the picture taken by a 1.5mm etalon in Fig. 1), so that this is expressed by a two-headed horizontal arrow in Fig. 1.

The helium gas that we used in the earlier part of our experiment was kindly lent to us by Professor Kiuchi whom our thanks are due. It was a great pleasure to one of us (K. M.) to be able to talk with Professor Mack and Dr. Austern and Dr. Hirschberg about many interesting aspects of the He II fine structure problem during the stay in Madison.

Literature

1) F. Paschen: Ann. d. Phys. **50** (1916) 901; **82** (1927) 689.

2) H. A. Bethe: Phys. Rev. **72** (1947) 33. N. M. Kroll and W. E. Lamb: Phys. Rev. **75** (1949) 388. J. B. French and V. F. Weisskopf: Phys. Rev. **75** (1949) 1240. H. A. Bethe, L. M. Brown and J. R. Stehn: Phys. Rev. **77** (1950) 370.

3) J. E. Mack and N. Austern: Phys. Rev. **72** (1947) 219.

4) K. Murakawa, S. Suwa and T. Kamei: Phys. Rev. **76** (1949) 1721.

5) J. G. Hirschberg and J. E. Mack: Phys. Rev. **77** (1950) 745.

6) H. Kopfermann, H. Krüger u. H. Öhlmann: ZS. f. Phys. **126** (1949) 760.

7) W.E. Lamb and M. Skinner: Phys. Rev. **78** (1950) 539.

8) G.W. Series: Proc. Roy. Soc. London **208** (1951) 277.

---

* The limit of error given here is based on the same assumption as that given in the footnote of Table I.

JOURNAL OF THE PHYSICAL SOCIETY OF JAPAN Vol. 7, No. 5, SEPT.—OCT., 1952

On the Effect of Dispersion and Multiple Reflection upon the Interference Color

Hiroshi KUBOTA and Teruji OSE
Institute of Industrial Science, Tokyo University, Chiba-City

(Received April 10, 1952)

Interference color of thin film was calculated taking multiple reflection within the layer and/or dispersion of the layer into account, both having not been taken into account in our previous papers. The result shows that the effect of the former changes the purity of color without altering its hue, whereas the latter changes its hue and purity.

§ 1. Introduction

Although the beautiful colors which appear when white light is reflected from a thin layer have been studied thoroughly, neither the multiple reflection within the film nor the variation of refractive index of the layer with wave length (i.e., dispersion) has been taken into account in our previous papers[1)2)]. In this paper, their effects upon the interference color are demonstrated.

§ 2. Effect of Multiple Reflection

(*a*) *Method of calculation*

If we denote the coefficient of reflection of the upper and lower boundaries of the layer, whose thickness is d and refractive index n_0 by B and C, then the reflectivity of the layer becomes as follows[1)]:

$$R^2=\frac{B^2+C^2+2BC\cos\delta}{1+B^2C^2+2BC\cos\delta}\,,\qquad \delta=4\pi(n_0d)/\lambda. \tag{1}$$

In the former papers, the denominator was put equal to 1, assuming that B and C are small and this corresponds, approximately, to the neglect of the multiple reflection within the layer. But, for the layer of higher refractive indices, as B and C become large, this is not permissible and we have to use Eq. (1) as it is. From (1), we have,

$$R^2=\frac{(B^2+C^2)/2BC+\cos\delta}{(1+B^2C^2)/2BC+\cos\delta}$$
$$=1+\frac{F-G}{G+\cos\delta}\,,$$

where

$$F=\frac{B^2+C^2}{2BC}\,,\qquad G=\frac{1+B^2C^2}{2BC}\,.$$

So the tristimulous values of the interference color can be obtained by putting the energy distribution of the light source as $E(\lambda)$,

$$X=\int E\bar{x}d\lambda+(F-G)\int\frac{E\bar{x}}{G+\cos\delta}d\lambda\,;$$
$$Y=\ldots.,\quad Z=\ldots.. \tag{2}$$

To give the general idea of the effect of these multiple reflection, we first calculated (2) for the case of a thin film suspended in the air, for which $B=-C$, and calculated the trichromatic coordinates,

$$x=\frac{X}{X+Y+Z}\,,\quad y=\frac{Y}{X+Y+Z}$$

therefrom. The result of calculation is shown in Fig. 1 with fine lines for various B^2 values

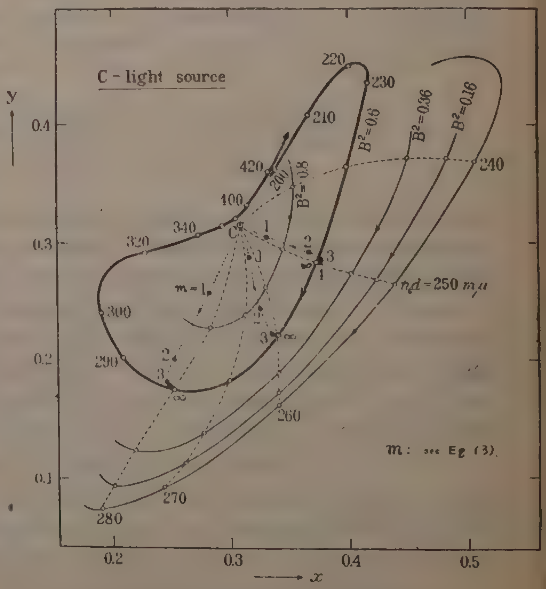

Fig. 1. Effect of Multiple reflection.
○: Effect of multiple reflection. (Eq. (2).)
●: Effect of each step of multiple reflection. (Eq. (3))

(In the figure, the colors are shown only in the neighborhood of the sensitive color, because only this part is useful for the practical purpose.) The outermost curve is the one in which the multiple reflection was neglected; accordingly independent of the value of B. As B increases larger and larger—although a thin film having such a large reflectivity does not exist—the interference color having the same (n_0d) changes as shown with broken lines in the figure. As seen from the figure, they have similar form as the loci of constant hue given by MacAdam[3], so, we can conclude that "the effect of multiple reflection is in decresing the purity of the color, almost not altering its hue." This is, though qualitatively, expected from the curves of the reflectivity shown in Fig. 2.

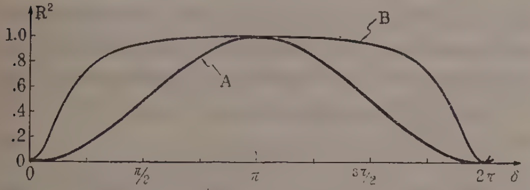

Fig. 2. Curves of the reflectivity.

A: Multiple reflection is not taken into account ($R^2=\sin^2(\delta/2)$).

B: Multiple reflection is taken into account ($B=-C=\sqrt{0.6}$; $R^2=a(1-\cos\delta)/(G+\cos\delta)$, "$a$" is a factor to make $R^2=1$ at $\delta=\pi$).

To make clear the effect of each step of infinite numbers of the multiple reflections, (1) is expanded into Fourier's series,

$$R^2=R_0+\sum_{m=1}^{\infty}R_m\cos(m\delta) \qquad (3),$$

in which,

$$R_0=\frac{B^2+C^2-2B^2C^2}{1-B^2C^2},$$

$$R_m=\frac{2(1-B^2)(1-C^2)}{B^2C^2-1}(-BC)^m;$$

then, the m-th term of this series gives the effect of the m-th reflection*. In Fig. 1, the result of calculation of (2) by taking m of (3) as 1, 2, 3……, are shown with ● marks for $(n_0d)=250$, 260 and 280 $m\mu$.

(b) TiO₂ layer

For the case of thin layer on glass, we calculated the case of TiO_2 $(n=2.6)$ upon glass surface, for which F and G become as follows.

$$F=-1.13011, \qquad G=-4.25284.$$

The result of calculation of (2), using these values, are shown with ● marks in Fig. 3,

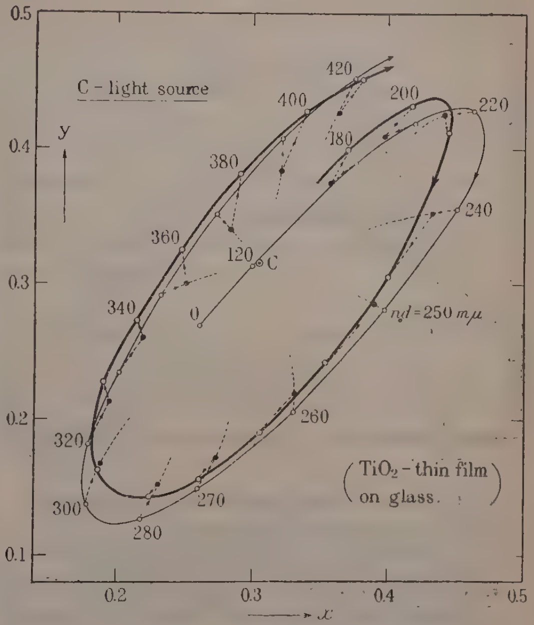

Fig. 3. Effect of multiple reflection and dispersion.

○, (thin line): no multiple reflection.

● : effect of multiple reflection.

○ (thick line): effect of multiple reflection and dispersion.

the fine line in the figure written for reference being the loci of the interference color in which multiple reflection was not taken into account.

To study the sensitive color, we transcribed them into MacAdam's U.C.S. and calculated the sensitivity $\Delta S/\Delta(n_0d)$ therefrom, as was done in the former paper[1]. The result is shown with ● marks in Fig. 4. They show that the sensitivity decrease a little, but the

---

* Complex amplitudes of the successive reflected lights from the layer are, B, $(1-B^2)Ce^{-i\delta}$, $-(1-B^2)BC^2e^{-2i\delta}$, ……, $(1-B^2)(-B)^{p-1}C^pe^{-ip\delta}$, …… So, for the intensity of the reflected light, by summing up these terms and taking square we get;

$$R_p^2=R_0+\sum_{m=1}^{p}R_m\cos(m\delta)+[R'_0+\sum_{m=1}^{p}R'_m\cos(m\delta)],$$

where,

$$R'_0=\frac{C^2(1-B^2)^2(-BC)^{2p}}{B^2C^2-1}\quad R'_m=\frac{2C^2(1-B^2)}{B^2C^2-1}(-BC)^{2p-m}.$$

So, if we make $p=\infty$, $R'_0=R'_m=0$, above equation is reduced to (3).

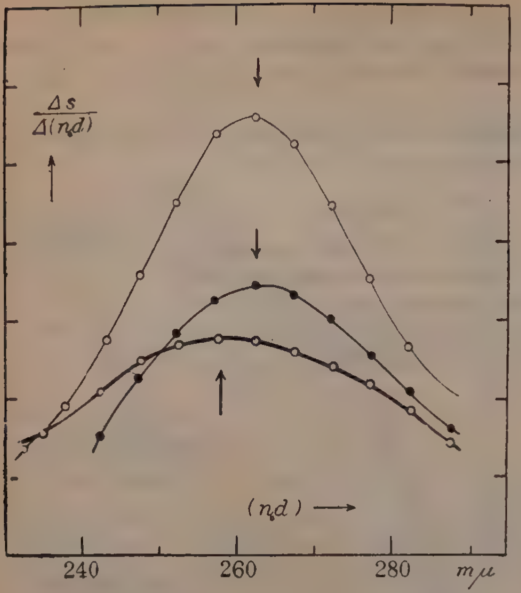

Fig. 4. Effect of dispersion and multiple reflection upon the sensitive color.
○ (thin line) : no multiple reflection.
● (thin line) : effect of multiple reflection.
○ (thick line): effect of multiple reflection and dispersion.

position of peak (indicated by arrows in the figure) does not shift from that without multiple reflection.

§ 3. Effect of Dispersion

(*a*) *Method of calculation*

Next we shall consider the effect of dispersion, that is, change of refractive index of the layer with wave length. In all the former discussions, the refractive indices were assumed to be constant irrespective of the variation of wave length. But, this may not be permissble for the layer of large dispersion such as ZnS or TiO_2. To calculate the interference color, taking the dispersion into account, following method is preferable to avoid troublesome calculations.

As the first term of (2) is independent of the refractive index of the layer and F and G of the second term can also be considered as constant, so we have only to take the variation of n in $\cos\delta$ of the denominator of the second term into account. This is given as follows.

$$\int_{\lambda_1}^{\lambda_2}\frac{E(\lambda)\bar{x}(\lambda)}{G+\cos(4\pi(nd)/\lambda)}d\lambda,$$

so, by putting the refractive index for a standard wave length λ_0 as n_0, then,

$$\int_{\lambda_1}^{\lambda_2}\frac{E(\lambda)\bar{x}(\lambda)}{G+\cos(4\pi(n_0d)/n_0\lambda/n)}d\lambda.$$

Now ,if we put $n_0\lambda/n=\lambda'$ ·········(4), then

$$\int_{\lambda_1'}^{\lambda_2'}\frac{E(n\lambda'/n_0)\bar{x}(n\lambda'/n_0)}{G+\cos(4\pi(n_0d)/\lambda')}d(n\lambda'/n_0),$$

$$\lambda_i'=n_0\lambda/n_i, \quad (5)$$

By this formula, as $\cos(4\pi(n_0d)/\lambda')$ were already calculated for various (n_0d) in the numerical calculation of the former papers, we can calculate (5) using these values. The values of $[E(n\lambda'/n_0)\cdot\bar{x}(n\lambda'/n_0)]$ for given values of λ', can be calculated from Hardy's Table[4], and once they are calculated, they can be utilized for the calculation of all values of (n_0d). But, to calculate $n\lambda'/n_0$, we have to find $n(\lambda)$ for a given λ'. This is given from (4), inserting the dispersion formula of the layer into it. As the dispersion formula of TiO_2 or ZnS is given in the form,

$$n(\lambda)=a+c/(\lambda-b),$$

by putting this in (4), and solving it, one obtains :

$$\lambda=\left(\frac{b}{2}+\frac{a}{2n_0}\lambda'\right)\pm\sqrt{\left(\frac{b}{2}+\frac{a}{2n_0}\lambda'\right)^2-\frac{(ab-c)}{n_0}\lambda'}.$$

(*b*) TiO_2 *layer*

For the case of TiO_2, from the values of refractive indices (given in the International critical Table), we get,

$$a=2.33554,\quad b=0.2818 \text{ and } c=0.0583948 \quad (\lambda \text{ in } \mu).$$

The result of numerical integration of (5) using these values and taking $\lambda_0=0.580\mu$ are shown with thick line in Fig. 3. This shows, unlike the effect of the multiple reflection, that the dispersion changes the hue of the color.

To give a measure of the change of hue, we have calculated from Fig. 3, two thicknessces $(n_0d)'$ and (n_0d) of the same dominant wave length. But, the former is the thickness of the layer in which dispersion is taken into account and the latter is the corresponding one for no dispersion. Difference of them $\Delta(n_0d)=(n_0d)'-(n_0d)$ may be considered to give a measure of the amount of the change of hue due to dispersion. It is shown in Fig. 5 graphically. To study the sensitive color, we transcribed the locus into U. C. S. and calculated the sensitivity $\Delta S/\Delta(n_0d)$ therefrom. It gives the result as shown with thick line in Fig. 4, showing that the dispersion not only decreases the sensitivity but ~~also it~~ shifts the peak slightly towards smaller (n_0d), although its amount is negligibly small for the practical purpose.

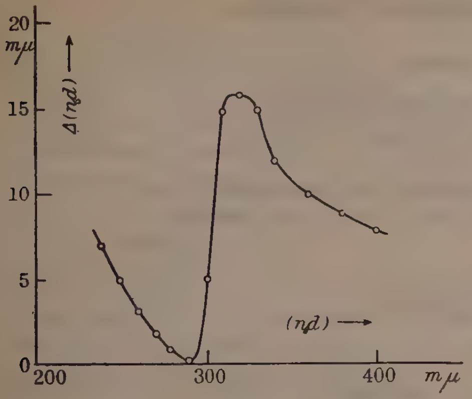

Fig. 5. Amount of the effect of dispersion.

§ 4. Summary

In this paper, we have studied the effect of dispersion and multiple reflection upon the interference color of thin layer, both of them having not been taken into account in the previous studies. The colorimetrical analysis and calculation thereof showed that multiple reflection causes the decrease of the purity of the color without changing its hue, while the effect of dispersion changes the hue and purity of the color. As an example the case of the layer of TiO_2 was given. From this example, the effect in case of the layer of lower dispersion and refractive index such as MgF_2, may be considered as negligibly small for the practical purposes.

The authors wish to express their sincere thanks to Mrs. Ose and Miss. K. Ogawa, for their valuable assistances in the numerical calculation.

References

1) H. Kubota: J. Phys. Soc. Japan, **5** (1950) 10; J. Opt. Soc. Am. **40** (1950) 146.

2) H. Kubota and T. Ara; J. Opt. Soc. Am. **41** (1951) 16.

3) D. L. MacAdam; J. Opt. Soc. Am. **40** (1950) 589.

4) A.C. Hardy: "Handbook of Colorimetry." (Cambridge (Mass.), 1936).

JOURNAL OF THE PHYSICAL SOCIETY OF JAPAN Vol. 7, No. 5, SEPT.—OCT., 1952

Some Complex Boundary Valued Problem and its Application to Kapur-Peierls' Dispersion Formula

By Tunezo SATOH

Faculty of Engineering, University of Tokyo

(Received February 12, 1952)

The method to find the dispersion-formula for the partial cross-section, due to Kapur and Peierls (Proc. Roy. Soc. A, 166 (1938), 277) may be stated as follows:

To express

$$S=\cos kr_0\phi(r_0)-k^{-1}\sin kr_0(d\phi/dr)_{r0}$$

by finding the solution of

$$\frac{h^2}{2m}\frac{d^2\phi}{dr^2}+[E-V(r)]\phi=0\,,\qquad 0\leqq r\leqq r_0\,,$$

which satisfies at ends

$$\phi(0)=0\,,\ [d\phi/dr-ik\phi(T)]_{r0}=Ie^{-ikr_0}\,,$$

By suitable variable-transformations, however, the above statement will be simplified as follows:

$$L[\Phi]+\lambda\Phi=0\,,\qquad 0\leqq x\leqq 1\,,$$

with $\Phi(0)=0\,,\quad \Phi'(1)-ik\Phi(1)=I_0e^{-i\kappa}\,;$

and $S=e^{-i\kappa}\Phi(1)-\kappa^{-1}\sin\kappa I_0e^{-i\kappa}\,.$

Here $L[\ \ ]$ means the differential operator: $[d^2/dx^2-q(x)]$.

By making use of Green's function, we can express $\Phi(x)$ and S in the forms:

$$\Phi(x)=I_0e^{-i\kappa}\Gamma(x,\ 1\,;\lambda)$$

and $S=I_0\{e^{-i2\kappa}\Gamma(1,\ 1\,;\lambda)-\kappa^{-1}\sin\kappa\cdot e^{-i\kappa}\}\,.$

These results involve the same meaning as the expansion (21) in Kapur-Peierls' paper, and furthermore have the advantage of more simple expressions.

In this paper, we treat the following boundary-value problem:

$$L[\varphi]+\lambda\varphi=0\,,\quad (0\leqq x\leqq 1) \tag{1}$$

with boundary conditions:

$$\varphi(0)=0\,,\quad \varphi'(1)-i\kappa\varphi(1)=I_0e^{-i\kappa}\,, \tag{2}$$

where κ is a parametric constant.

Notations and Symbols:

A^*: the complex conjugate of the number or function A in question,

$(A,\ B)=\int_0^1 A(x)B(x)dx\,,$

$L[X]=[d^2/dx^2-q(x)]X\,,$

$M[X]=L[X]+\lambda X\,,$

$G(x,y)$: Green's function, belonging to the differential equation $L[X]=0$ and satisfying the following boundary conditions:

$$X(0)=0,\quad X'(1)-i\kappa X(1)=0\,. \tag{3}$$

$\Gamma(x,y;\lambda)$: Green's function, belonging to the differential equation $M[X]=0$ and satisfying the boundary conditions (3),

$K(x,y)$: Green's function, belonging to $L[X]=0$, and satisfying the boundary conditions:

$$X(0)=0,\quad X'(1)=0 \tag{4}$$

$H(x,y)$: Green's function, belonging to $L[X]=0$ and satisfying the boundary conditions:

$$X(0)=0\,,\quad X(1)=0 \tag{5}$$

$\Gamma_K(x,y;\lambda)$: Green's function, belonging to $M[X]=0$ and satisfying the boundary conditions (4),

$\Gamma_H(x,y;\lambda)$: Green's function, belonging to $M[X]=0$ and satisfying the boundary conditions (5),

$D(\lambda)$, $D_K(\lambda)$, $D_H(\lambda)$: Fredholm's determinant belonging to G, K and H respectively,

λ_h, μ_h, ν_h: an eigenvalue of G, K and H respectively,

$\phi_h, \varphi_h, \psi_h$: an eigenfunction, corresponding to λ_h, μ_h, ν_h and $(\phi_h, \phi_h{}^*)=(\varphi_h, \varphi_h)=(\psi_h, \psi_h)=1$,

$N_{0h}=(\phi_h, \phi_h)$,

G.F. : abbreviation for Green's Function,

K.P.-paper : abbreviation for P. L. Kapur and R. Peierls "The dispersion formula for nuclear reactions", Proc. Roy. Soc. A, 166 (1938), pp. 277–295.

§ 1. Construction of G.F.

Following usual definition of G.F. and starting with a pair of independent solutions of the differential equation $L[u]=0$, we construct $G(x, \xi)$ in the following form :

$$G(x, \xi)=\frac{1}{\alpha+i\kappa}\{\alpha K(x, \xi)+i\kappa H(x, \xi)\}, \qquad (6)$$

since the boundary conditions (3) is linear in $i\kappa$. Here α is a real constant, independent of κ, which, from (3) and (6), is determined by the equation :

$$\alpha=H_1(\xi)/K_1(\xi), \qquad (7)$$

where

$$H_1(\xi)=(\partial H(x, \xi)/\partial x)_{x=1}, \quad K_1(\xi)=K(1, \xi) \quad (8)$$

Both $H_1(\xi)$ and $K_1(\xi)$ satisfy the differential equation $L[u]=0$ with the end-condition $u(0)=0$, and may be expressed by $u(x)$ in the following form :

$$H_1(\xi)=lu(\xi), \quad K_1(\xi)=l'u(\xi).$$

Hence (7) will be also written as follows :

$$\alpha=l/l'. \qquad (9)$$

Example 1. Let $L[X]=d^2X/dx^2$, $q=0$. Then, as is well-known, we have

$$\left.\begin{array}{l} K(x, y)=x \quad (x\leqq y); \quad =y \quad (x\geqq y) \\ H(x, y)=x(1-y) \quad (x\leqq y); \quad =y(1-x) \\ \qquad\qquad\qquad\qquad\qquad\qquad (x\geqq y) \end{array}\right\} \quad (10)$$

Hence by (8),

$$H_1(y)=-y, \ K_1(y)=y, \text{ where } u(y)=y,$$

and so from (7) or (9), it follows that $\alpha=-1$; so that from (6)

$$G(x, y)=\frac{1}{-1+i\kappa}\{-K(x, y)+i\kappa H(x, y)\}. \quad (11)$$

This result coincides with that obtained directly by the definition of G.F.

§ 2. Reciprocal Kernel of $G(x, y)$

By the same method as stated in the preceeding section, we have

$$\Gamma(x, y; \lambda)=\frac{1}{A(\lambda)+i\kappa}\{A(\lambda)\Gamma_K(x, y; \lambda) + i\kappa\Gamma_H(x, y; \lambda)\}. \qquad (12)$$

As in the case of real boundary valued conditions, it is easily shown that there exists the reciprocal relation between G and Γ, from which $-\Gamma$ can be concluded to be the reciprocal kernel of G. Of course, $-\Gamma_K$ and $-\Gamma_H$ are recipocal kernels of K, H respectively. Hence, if we use the known theorem in the theory of integral equations, we have the relations :

$$-\int_0^1\Gamma(x, x; \lambda)dx=D'(\lambda)/D(\lambda),$$

$$-\int\Gamma_K(x, x; \lambda)dx=D_K'(\lambda)/D_K(\lambda),$$

and $$-\int\Gamma_H(x, x; \lambda)dx = D_H'(\lambda)/D_H(\lambda),$$ and

then from (12) :

$$\frac{D'(\lambda)}{D(\lambda)}=\frac{1}{A(\lambda)+i\kappa}\left\{A(\lambda)\frac{D_K'(\lambda)}{D_K(\lambda)}+i\kappa\frac{D_H'(\lambda)}{D_H(\lambda)}\right\}. \qquad (13)$$

Now we shall determine the function $A(\lambda)$. Considering Γ in (12) as a function of x, and putting it into the boundary conditions (3), the following relation is obtained :

$$H_1(y, \lambda)=A(\lambda)K_1(y, \lambda), \qquad (14)$$

where

$$H_1(y, \lambda)=(\partial\Gamma_H/\partial x)_{x=1}, \quad K_1(y, \lambda)=\Gamma_K(1, y; \lambda).$$

On the other hand, we notice that both $K_1(y, \lambda)$ and $H_1(y, \lambda)$ must satisfy the differential equation $M[X]=0$ and one end-condition : $X(0)=0$. Thus, making use of the representation of the reciprocal kernel by Fredholm's determinant, we have

$$K_1(y, \lambda)=u_\lambda(y)\cdot\Delta_K(\lambda)/D_K(\lambda),$$
$$H_1(y, \lambda)=u_\lambda(y)\cdot\Delta_H(\lambda)/D_H(\lambda),$$

where $L[u_\lambda]+\lambda u=0$ and $u_\lambda(0)=0$ is independent of λ, and both of $\Delta_K(\lambda)$ and $\Delta_H(\lambda)$ are integral functions of order less than 1.

Thus if we put these results into the equation (14), we have the relation :

$$A(\lambda)=\Delta_H D_K/\Delta_K D_H. \qquad (14')$$

Comparing (6) with (12) for $\lambda=0$, it is seen that $A(0)=\alpha$. Putting (14′) in (13), we obtain :

$$\frac{D'(\lambda)}{D(\lambda)}=\frac{\Delta_H D_K'+i\kappa\Delta_K D_H'}{\Delta_H D_K+i\kappa\Delta_K D_H}. \qquad (15)$$

We proceed now to simplify (14′) and (15). Suppose that $\Delta_k(\lambda)$ (or Δ_H) has a zero, say

$\Delta_K(\lambda_0)=0$ (or $\Delta_H(\lambda_0)=0$). Then from (12), it follows that

$$\Gamma(x,y;\lambda_0)=\Gamma_K(x,y;\lambda_0)\quad(\text{or } \Gamma_H(x,y;\lambda_0)).$$

By using this result and the reciprocal relation, we can prove that all eigenvalues and eigenfunctions of G and K (or H) are coincident with each other. This is contradiction. Therefore each of $\Delta_K(\lambda)$ and $\Delta_H(\lambda)$ should have the form $ae^{b\lambda}$, so that Δ_H/Δ_K the form $\alpha e^{\beta\lambda}$, since $A(0)=\alpha$.

Now, noting that every zero of $D(\lambda)$ is simple, we can obtain from (15)

$$\alpha e^{\beta\lambda}D_K(\lambda)+i\kappa D_H(\lambda)=P(\lambda)D(\lambda)\,, \tag{15'}$$

where $P(\lambda)$ is a certain integral function of order not greater than that of D_K (or D_H). By taking the logarithmic derivatives of both sides of the last equation, and by utilizing (15), we have

$$\begin{aligned}P'(\lambda)/P(\lambda)&=\alpha\beta e^{\beta\lambda}D_H(\lambda)/\{\alpha e^{\beta\lambda}D_K(\lambda)+i\kappa D_H(\lambda)\}\\&=\alpha\beta e^{\beta\lambda}D_H(\lambda)/P(\lambda)D(\lambda)\,;\end{aligned}$$

hence $\alpha\beta e^{\beta\lambda}D_H(\lambda)=P'(\lambda)D(\lambda)$, from which it follows that all zeros of $D(\lambda)$ are involved in those of $D_H(\lambda)$. But this is contradiction. For, if we apply Green's formula to $\phi_n(x)$ and G^*, which is meant by G.F., satisfying the conjugate boundary conditions of (3), i.e. conjugate complex of $G(x,y)$, then we have

$$\phi_n(x)=\lambda_n\int_0^1 G^*(x,y)\phi_n(y)dy+2i\kappa\phi_n(1)G^*(x,1)\,. \tag{16}$$

This leads to

$$(\phi_n,\phi_n^*)=\frac{\lambda_n}{\lambda_n^*}(\phi_n,\phi_n^*)+2i\kappa\,\phi_n(1)\frac{1}{\lambda_n}\phi_n^*(1)\,,$$

that is,

$$\lambda_n^*-\lambda_n=2i\kappa\,|\phi_n(1)|^2\,,$$

or

$$-\Im(\lambda_n)=\kappa\,|\phi_n(1)|^2\,. \tag{17}$$

In the other words, all eigenvalues of G are not real, while, those of H are all real.

Consequently we must have $\beta=0$, $P(\lambda)$ =const., and $\Delta_H/\Delta_K=\alpha$, hence from (14'),

$$A(\lambda)=\alpha D_k(\lambda)/D_H(\lambda)\,, \tag{18}$$

and from (15')

$$D(\lambda)=\{\alpha D_K(\lambda)+i\kappa D_H(\lambda)\}/(\alpha+i\kappa)\,. \tag{19}$$

Example 2. Let us consider the most simple example:

$$L[\varphi]+\lambda\varphi=d^2\varphi/dx^2+\lambda\varphi\,.$$

In this case we can find easily:

$$\Gamma_K(x,y;\lambda)=\sin kx.\cos k(1-y)/k.\cos k\,,\quad \text{for } x\leqq y\,;$$

$$\Gamma_H(x,y;\lambda)=\sin ky.\sin k(1-x)/k.\sin k\,,\quad \text{for } x\leqq y\,,$$

where $\lambda=k^2$. Hence we have

$H_1(y,\lambda)=-\sin ky/\sin k$, $K_1(y,\lambda)=\sin ky/k.\cos k$;
$D_H(\lambda)=\sin k/k$, $D_K(\lambda)=\cos k$;
$u_\lambda(y)=\sin ky$, $\alpha=-1$.

From (14) it follows $A(\lambda)=-k.\cos k/\sin k$ $=-D_K(\lambda)/D_H(\lambda)$. Accordingly, from (12) it is found that

$$\Gamma(x,y;\lambda)=\frac{-k\cos k\Gamma_K(x,y;\lambda)+i\kappa\sin k\Gamma_H(x,y;\lambda)}{-k\cos k+i\kappa\sin k}\,,$$

and from (19)

$$D(\lambda)=\{-k\cos k+i\kappa\sin k\}/k(-1+i\kappa)\,.$$

Remark. The values of α and $A(\lambda)$, arising in expressions of G and Γ are also obtained as follows:

Let $\Phi(x,y)=K(x,y)-H(x,y)$. Then we find that $\Phi(x,y)$ is continuous throughout the intervals and symmetrical with respect to x and y, moreover satisfies the differential equation $L[X]=0$ and one end condition $X(0)=0$. Thus the function $\Phi(x,y)$ may be written as

$$\Phi(x,y)=p\cdot u(x)u(y)\,,$$

where p is a certain constant and $L[u]=0$, $u(0)=0$. By the boundary conditions (4) and (5), we are led to

$$p\cdot u(1)u(y)=K_1(y)\,,\quad p\cdot u'(1)u(y)=-H_1(y)\,;$$

Hence we get, by (7)

$$\alpha=-u'(1)/u(1)\,, \tag{20}$$

and in a like manner

$$A(\lambda)=-u_\lambda'(1)/u_\lambda(1)\,, \tag{21}$$

where u_λ is a solution of $L[u_\lambda]+\lambda u_\lambda=0$, which satisfies the end-condition $u_\lambda(0)=0$.

§ 3. Inhomogeneous Boundary Conditions

In the present section we shall find the solution of the differential equation (1), satisfying inhomogeneous boundary conditions (2).

Now let ϕ be such a solution. Let X be any function, satisfying the boundary conditions: (2) $X(0)=0$, $X'(1)-i\kappa X(1)=I_0e^{-i\kappa}$. Then if we put $\phi-X=f$, we have evidently

$$L[f]+\lambda f=-\{L[X]+\lambda X\}$$

and moreover f satisfies the homogeneous boundary conditions (3) at both ends.

Also, using G.F. Γ, this function f will be uniquely expressed as

$$f(x)=\int_0^1 \Gamma(x,y;\lambda)\cdot\{L[X]+\lambda X(y)\}dy\,,$$

unless λ is not an eigenvalue, Further by applying Green's formula to the right side of this equation, it can be written in the form:

$$f(x)=I_0e^{-i\kappa}\Gamma(x,1;\lambda)-X(x)\,.$$

Hence the required solution is given by

$$\phi(x)=I_0e^{-i\kappa}\Gamma(x,1;\lambda)\,. \qquad (22)$$

Conversely, it is easily verified that the function $\phi(x)$, given by (22), satisfies the differential equation (1), and at the same time also the boundary conditions (2), on account of discontinuity of $\partial\Gamma(x,1;\lambda)/\partial x$ at $x=1$.

Example 3. We shall again treat the previous example:

$$L[u]+\lambda u=[d^2/dx^2+k^2]u\,.$$

As shown before,

$$\Gamma_K(x,1;\lambda)=\sin kx/k.\cos k. \quad \Gamma_H(x,1;\lambda)=0\,;$$
$$\partial/\partial x\cdot\Gamma_K(x,1;\lambda)=\cos kx/\cos k,$$
$$\partial/\partial x\cdot\Gamma_H(x,1;\lambda)=0.$$

Hence

$$\Gamma(x,1;\lambda)|_{x\to1}=-\sin k/(-k.\cos k+i\kappa\sin k)\,;$$
$$\partial/\partial x\cdot\Gamma(x,1;\lambda)|_{x\to1}$$
$$=-k.\cos k/(-k.\cos k+i\kappa\sin k)\,.$$

We have thus proved

$$[\phi'(x)-i\kappa\phi(x)]_{x\to1}$$
$$=I_0e^{-i\kappa}[\partial/\partial x\cdot\Gamma(x,1;\lambda)-i\kappa\Gamma(x,1;\lambda)]_{x\to1}$$
$$=I_0e^{-i\kappa}\,.$$

Remark. We can prove that the value of λ, involved in (22), never take any eigenvalue of G. By means of G.F. $G(x,y)$, $f(x)$ is also expressed as follows:

$$f(x)=\lambda\int_0^1 G(x,y)f(y)dy+\left\{\lambda\int_0^1 G(x,y)X(y)dy\right.$$
$$\left.-X(x)+i\kappa G(x,1)\right\}.$$

In this equation, in order that λ might be an eigenvalue, say λ_n, it is necessary and sufficient that

$$(X,\phi_n)+i\kappa\lambda_n^{-1}\phi_n(1)-(X,\phi_n)=0 \text{ i.e. } \phi_n(1)=0.$$

Hence from (2), $\phi_n'(1)=0$, in the sequel $\phi_n(x)$ should be zero identically.

§ 4. Expansible Kernel

We call $G(x,y)$ to be expansible when it can be expanded by the uniformly convergent series of eigenfunctions as follows:

$$G(x,y)=\sum_1^\infty\frac{\phi_h(x)\phi_h(y)}{N_{0h}\lambda_h}\,. \qquad (23)$$

It is evident that if the above stated series converges uniformly and the system $\{\phi_h\}$ is closed, $G(x,y)$ becomes to be expansible. For, let

$$G(x,y)=\sum\frac{\phi_h(x)\phi_h(y)}{N_{0h}\lambda_h}+Q(x,y)\,.$$

Then we have $\int Q(x,y)\phi_h(y)dy=0$. Since $\{\phi_h\}$ is closed, it should be $Q(x,y)=0$ identically.

Here we add some remarks on the existence of eigen-values.

Remarks (i) Let $G(x,y)=A(x,y)+iB(x,y)$ where A and B have the same sign and $|A|>|B|$ or $|A|<|B|$ through the region. Then $G(x,y)$ has at least one eigenvalue.

(ii) If a certain repeated kernel of G, say $G_h(x,y)=0$ identically, then $\int G_h(x,x)dx=0$ for all $h\geqq3$. Hence in this case there exists no eigenvalue.

(iii) Let $G_h=A_h+iB_h$. Then if for some h one of A_h and B_h vanishes identically and the other does not vanish identically, G has at least one eigenvalue.

Remark. If we solve the equation (16) by using $\Gamma^*(x,y;\lambda)$, we obtain

$$\phi_n(x)=2i\kappa\phi_n(1)\Gamma^*(x,1;\lambda_h)\,,$$

since λ_n is not an eigenvalue.

§ 5. Relation Between K and H

As shown already in the remark of § 2, the difference between K and H may be written in the simple form. For dealing with G.F., this fact will be very useful; for instsnce, if one of K and H is known, the other will soon be found out. We shall investigate this difference in more detail.

Let $\delta(x,y)=K(x,y)-H(x,y)$. Then as before we have

$$\delta(x,y)=lu(x)u(y),\ \text{where } L[u]=0,\ u(0)=0.$$

While, by using $H_1(y)$, $K_1(y)$, defined by (8),

$$K_1(y)=lu(1)u(y), \quad -H_1(y)=lu'(1)u(y)\,;$$

in the sequel we have

$$l=K_1(y)/u(1)u(y)=-H_1(y)/u'(1)u(y). \qquad (25)$$

Likewisely, if we put $\delta(x,y;\lambda)=\Gamma_K(x,y;\lambda)-\Gamma_H(x,y;\lambda)$, this takes the form:

$$l(\lambda)u_\lambda(x)u_\lambda(y), \qquad \text{where } L[u_\lambda]+\lambda u_\lambda=0,$$

$u_\lambda(0)=0$. Further

$$l(\lambda)=K_1(y,\lambda)/u_\lambda(1)u_\lambda(y)=-H_1(y,\lambda)/u_\lambda'(1)u_\lambda(y). \qquad (26)$$

Example 4. Again let $L[u]=d^2u/dx^2$. In previous Example 1,2, we have obtained following G.F.'s:

$$K(x,y)=x \ (x\leqq y)\,;\ H(x,y)=x(1-y) \ (x\leqq y)\,;$$
$$\Gamma_K=\sin kx.\cos k(1-y)/k.\cos k \quad (x\leqq y)\,;$$
$$\Gamma_H=\sin kx.\sin k(1-y)/k.\sin k \quad (x\leqq y)\,.$$

On the other hand, take $u(x)=x$ and $u_\lambda(x)=\sin kx$. Then from (25) and (26), it follows:

$$l=K_1(y)/u(y)=K(1,y)/u(y)=1\,,$$
$$l(\lambda)=K_1(y,\lambda)/u_\lambda(1)u_\lambda(y)=1/(k.\cos k.\sin k)\,;$$

hence there exist

$$K(x,y)-H(x,y)=xy\,,$$
$$\Gamma_K-\Gamma_H=\sin kx.\sin ky/(k\cos k.\sin k)\,.$$

Now if we use the above stated $\delta(x,y)$, $G(x,y)$ may be expressed in the form:

$$G(x,y)=K(x,y)-\frac{i\kappa l}{\alpha+i\kappa}u(x)u(y)$$
$$=H(x,y)+\frac{\alpha l}{\alpha+i\kappa}u(x)u(y)\,.$$

Also, similarly for $\Gamma(x,y;\lambda)$.

§ 6. Application I: $L[u]=[d^2/dx^2+1/4x^2]u$

We shall consider the more complicated example than that already treated. Let

$$L[u]=\frac{d^2u}{dx^2}+\frac{1}{4x^2}u\,.$$

By substitution: $y=\sqrt{x}\cdot z$,

$$L[y]+\lambda y=\sqrt{x}\,(z''+x^{-1}z'+\lambda z)\,.$$

Since the differential equation $z''+x^{-1}z'+\lambda z=0$ is well-known Bessel's equation of the zero-th order, one system of two independent solutions of the differential equation: $L[u]+\lambda u=0$ is given by $\sqrt{x}\,J_0(kx)$, $\sqrt{x}\,R(kx)$, where $\lambda=k^2$ and $R(x)=J_0(x).\log x+$(a certain analytic function). As one end point $x=0$ is the singular point of the given differential equation, our boundary conditions should be some-what modified in this case, namely to the usual conditions (3), (4) and (5) at $x=0$, further condition: $(u/\sqrt{x}\,)_{x\to 0}=$finite must be added.

First, we have to determine G.F.'s K and H. The form of H is well known:

$$H(x,y)=-\sqrt{xy}\log y \ (x\leqq y);$$
$$=-\sqrt{xy}\log x \ (x\geqq y)\,.$$

With this result and the similar treatment in the preceding section, we shall find K. Let

$$K(x,y)=H(x,y)+l\sqrt{xy},\quad u(x)=\sqrt{x}\,.$$

Inserting $H_1(y)=(\partial H(x,y)/\partial x)_{x=1}=-\sqrt{y}$ into (25),

$$l=-H_1(y)/u'(1)u(y)=2\,,$$

so that $K(x,y)=H(x,y)+2\sqrt{xy}$, i.e. for $x\leqq y$, is equal $\sqrt{xy}(2-\log y)$. Thus if we regard $\alpha=-u'(1)/u(1)=-1/2$ by (20), it follows from (6)

$$G(x,y)=\frac{1}{-\frac{1}{2}+i\kappa}\{-\tfrac{1}{2}K(x,y)+i\kappa H(x,y)\}\,.$$

In the same manner, Γ_K can also be calculated with the aid of Γ_H in the usual form:

$$\Gamma_H(x,y;\lambda)=\sqrt{xy}\cdot J(kx)[\,J(ky)R(k)$$
$$-R(ky)\,J(k)]/\,J(k),\ \text{for } x\leqq y,$$

where, for convenience'sake, we drop the suffix 0 from J_0. In this case if we choose $u_\lambda(x)=\sqrt{x}\,J(kx)$, $u_\lambda(0)=0$, then from (26) we have

$$l(\lambda)=-(\partial\Gamma_H/\partial x)_{x=1}/\{u_\lambda'(1)u_\lambda(y)\}$$
$$=1/[\,J(k)\{\tfrac{1}{2}J(k)+kJ'(k)\}]\,,$$

since $[\partial\Gamma_H(x,y;\lambda)/\partial x]_{x=1}=-\sqrt{y}\cdot J(ky)/\,J(k)$. Thus we get

$$\Gamma_K(x,y;\lambda)=\Gamma_H(x,y;\lambda)+\frac{\sqrt{xy}\,J(kx)\,J(ky)}{J(k)\{\frac{1}{2}J(k)+kJ'(k)\}}.$$

Using the relations:

$$D_H(\lambda)=J(k),\ D_H'/D_H=J'(k)/(2k\,J(k))\,,$$

from the above equation,

$$\frac{D_K'(\lambda)}{D_K(\lambda)}=-\int_0^1\Gamma_K(x,x;\lambda)dx$$
$$=\frac{D_H'(\lambda)}{D_H(\lambda)}-\frac{1}{2}\frac{J^2(k)+J'^2(k)}{J(k)\{\frac{1}{2}J(k)+kJ'(k)\}}$$
$$=\frac{1}{2k}\frac{\frac{1}{2}J'(k)-kJ(k)}{\frac{1}{2}J(k)+kJ'(k)}\,.$$

Finally we have

$$D_K(\lambda)=J(k)+2kJ'(k)\,.$$

On the other hand, since the solution, satisfing the boundary conditions (3), is $\varphi_\lambda(x)=\sqrt{x}\,J(kx)$, eigenvalues will be given by the equation: $\varphi_\lambda'(1)-i\kappa\varphi_\lambda(1)=0$ i.e. roots of

$$\tfrac{1}{2}J(k)+kJ'(k)-i\kappa J(k)=0\,.$$

Thus by the order condition of integral functions, it must be

$$D(\lambda)=D(k^2)=\text{const.}\{\tfrac{1}{2}J(k)+kJ'(k)-i\kappa J(k)\}\,.$$

Consequently

$$D(\lambda)=\{-\tfrac{1}{2}D_K(\lambda)+i\kappa D_H(\lambda)\}/\{-\tfrac{1}{2}+i\kappa\},$$

since $D(0)=1$. This verifies the formula (19). Further

$$A(\lambda)=H_1(y,\lambda)/K_1(y,\lambda)$$
$$=\frac{-\sqrt{y}\,J(ky)}{J(k)}\times\frac{J(k)\{\frac{1}{2}J(k)+kJ'(k)\}}{\sqrt{y}\,J(k)J(ky)}$$
$$=-\tfrac{1}{2}\{J(k)+2kJ'(k)\}/J(k)\,,$$

which is equal to $-\frac{1}{2}D_K(\lambda)/D_H(\lambda)$ by using D_K and D_H. This result varifies (18).

Remark: In this example, both of K and H are expansible kernels.

$$K(x,y)=\Sigma\frac{\varphi_n(x)\varphi_n(y)}{\mu_n}\qquad H(x,y)=\Sigma\frac{\psi_n(x)\psi_n(y)}{\nu_n}$$
$$J(\mu_n)+2\mu_n J'(\mu_n)=0\qquad J(\nu_n)=0$$
$$\varphi_n(x)=\sqrt{2x}\,J(\mu_n x)/\eta_n\qquad \psi_n(x)=\sqrt{2x}\,J(\nu_n x)/\delta_n$$
$$\eta_n=\mu_n^{-1}(\tfrac{1}{2}+\mu_n^2)^{1/2}J(\mu_n)\qquad \delta_n=J'(\nu_n)$$
$$(\mu_n>0)$$

§ 7. Application II

In the present section, we shall deal with dispersion-formula, appearing in K.P.-paper ((20) or (21)). This formula seems to be based upon the following mathematical statement:

To express

$$S=\cos kr_0\cdot\phi(r_0)-k^{-1}\sin kr_0(d\phi/dr)_{r_0}\,,$$

by finding such a solution as

$$\frac{h^2}{2m}\frac{d^2\phi}{dr^2}+[E-V(r)]\phi=0\,,\quad 0\leqq r\leqq r_0\,,$$

which satisfies at ends

$$\phi(0)=0,\qquad \left[\frac{d\phi}{dr}-ik\phi(r)\right]_{r=r_0}=Ie^{-ikr_0},$$
$$k^2=2mE/h^2.$$

If we make the variable-transformations:

$$x=r/r_0,\ q(x)=V(xr_0)2mr_0^2/h^2,\ \varPhi(x)=\phi(r_0x),$$
$$\lambda=2mEr_0^2/h^2,\quad \kappa=kr_0,\quad I_0=r_0I,$$

then above statement will become:

$$L[\varPhi]+\lambda\varPhi=0\quad(0\leqq x\leqq 1)$$

with

$$\varPhi(0)=0,\quad \varPhi'(1)-i\kappa\varPhi(1)=I_0e^{-i\kappa};$$

and

$$S=e^{-i\kappa}\varPhi(1)-\frac{\sin\kappa}{\kappa}I_0e^{-i\kappa}\,.$$

This statement is none but that treated in § 3.

Hence from (22)

$$\varPhi(x)=I_0e^{-i\kappa}\Gamma(x,1;\lambda)\,,\tag{27}$$

from which it follows

$$S=I_0\left\{e^{-i2\kappa}\Gamma(1,1;\lambda)-\frac{\sin\kappa}{\kappa}e^{-i\kappa}\right\}.\tag{28}$$

Particularly, $\Gamma(x,y;\lambda)$ will be also expansible by Abel's Lemma in summation, provided $G(x,y)$ is expansible; and it is written in the form:

$$\Gamma(x,y;\lambda)=\sum_{n=1}^{\infty}\frac{\phi_n(x)\phi_n(y)}{N_{0n}(\lambda_n-\lambda)}\,.$$

Hence in this case by (27)

$$\varPhi(x)=I_0e^{-i\kappa}\sum_{n=1}^{\infty}\frac{\phi_n(1)\phi_n(x)}{N_{0n}(\lambda_n-\lambda)}\,,$$

consequently (28) takes the following form:

$$S=I_0\left\{\sum_{n=1}^{\infty}\frac{e^{-i2\kappa}\phi_n^2(1)}{N_{0n}(\lambda_n-\lambda)}-\frac{\sin\kappa}{\kappa}e^{-i\kappa}\right\}.\tag{29}$$

Since we can take N_n in the place of N_{0n}/r_0, $2mW_nr_0^2/h^2$ in the place of λ_n, the last result (29) coincides completely with the formula (21) of K.P.-paper. Here it is noted that the presense of the function $X(r)$ in (20a) of K.P-paper seems us to have little meaning and in practice the last two terms in the right side of (20a) should be null identically.

Now, from the boundary conditions (5), $\Gamma_H(x,1;\lambda)=0$, so that

$$\Gamma(x,1;\lambda)=\frac{A(\lambda)}{A(\lambda)+i\kappa}\Gamma_K(x,1;\lambda)\,.$$

Hence from (27),

$$\varPhi(x)=I_0\frac{A(\lambda)e^{-i\kappa}}{A(\lambda)+i\kappa}\Gamma_K(x,1;\lambda)\tag{27'}$$

and from (28).

$$S=I_0\left\{\frac{A(\lambda)e^{-i2\kappa}}{A(\lambda)+i\kappa}\Gamma_K(1,1;\lambda)-\frac{\sin\kappa}{\kappa}e^{-i\kappa}\right\},\tag{28'}$$

where $A(\lambda)=\alpha D_K(\lambda)/D_H(\lambda)$.

Remark I. Provided real G.F. K is expansible, it is clear from (27′) that our solution $\varPhi(x)$ is expanded by uniformly convergent series of eigenfunctions of K.

As seen in usual case, G.F. $K(x,y)$ is in general positive definite, consequently K is expansible.

Remark II. On account of (6), $G(x,1)=\alpha K(x,1)/(\alpha+i\kappa)$. Hence

$$|\phi_n(1)|=\left|\frac{\alpha\lambda_n}{\alpha+i\kappa}\int_0^1K(x,1)\phi_n(x)dx\right|,$$

is, by Schwarz′ inequality, not greater than

$$\left|\frac{\alpha\lambda_n}{\alpha+i\kappa}\right|\left[\int_0^1K^2(1,x)dx\right]^{1/2},$$

or

$$|\phi_n(1)|\leqq\left|\frac{\alpha\lambda_n}{\alpha+i\kappa}\right|\sqrt{K_2(1,1)}\,.$$

On the other hand, in viewing K.P.-paper

$$W_n=E_n-\tfrac{1}{2}i\gamma_n\ \text{i.e.}\ -\Im(\lambda_n)=\gamma_nmr_0^2/h^2\,.$$

Hence from (19),

$$\gamma_n=|u_n|^2,\ \text{where}\ u_n=\phi_n(1)\sqrt{\kappa n^2/mr_0^2}\,.$$

Thus the above obtained inequality may be written in the form:

$$|u_n| \leq \frac{\sqrt{\kappa}\,|\lambda_n|}{|\alpha+i\kappa|} C, \qquad C^2 = \frac{\pi^2}{m r_0^2} K_2(1,1)\,.$$

Here it should be noted that the constant C is independent on κ and n.

§ 8. Modified Green's function of $K(x,y)$

Let μ_0 any one of eigenvalues of K. Let us consider the following boundary valued problem:

$$L[\varphi]+\mu_0\varphi(x)=f(x), \quad 0\leq x\leq 1, \tag{30}$$

$$\varphi(0)=0, \quad \varphi'(1)=0\,. \tag{4}$$

Let $\varphi_0(x)$ be the corresponding eigenfunction to μ_0, where $(\varphi_0,\varphi_0)=1$. If we denote G.F., satisfying the differential equation:

$$L[\varphi]=\varphi_0(x)\cdot\varphi_0(y)$$

and belonging to the boundary conditions (4), by $K'(x,y)$, then there exists the relation:

$$\int_0^1 K'(x,y)\varphi_0(x)dx=0\,.$$

It should be noted that this equation does not always hold when $\mu_0=0$.

We can prove that, excepting μ_0 and φ_0, eigenvalues and eigenfunctions are all coincident with those of K'.

Let $\Gamma_K'(x,y;\mu)$ be G.F. as to satisfy the differential equation: $L[\varphi]+\mu\varphi=\varphi_0(x)\cdot\varphi_0(y)$. Then,

$$\int_0^1 \Gamma_K'(x,y;\mu)\varphi_0(x)dx=0,$$

and the reciprocal relation between K' and Γ_K' as well as the one between K and Γ_K also holds, in other words, $-\Gamma_K'$ is the reciprocal kernel of K'.

Thus with the aids of Γ_K', we obtain our solution of the boundary problem, given at the beginning of the present section, in the form:

$$\varphi(x)=(\varphi,\varphi_0)\varphi_0(x)-\int_0^1 \Gamma_K'(x,y;\mu_0)f(y)dy. \tag{31}$$

Remark: It is found that there exists a relation

$$\Gamma_K(x,y;\mu)=\Gamma_K'(x,y;\mu)+\frac{\varphi_0(x)\varphi_0(y)}{\mu_0-\mu}\,.$$

§ 9. Successive Approximations

The idea lying on the base of treatise on "Perturbation theory for small width of the level" in K.P.-paper, §3 is nothing but one of successive approximations for the small value of κ (or k).

We proceed now to deal with successive approximations of the eigenvalue and the eigenfunction in the vicinity of $\kappa=0$. Let $F(\lambda,t)=D_K(\lambda)+tD_H(\lambda)$. Then $F(\lambda,t)$ is one valued and analytic for any finite domain of each λ or t; hence, of course, λ, defined implicitly by the equation $F(\lambda,t)=0$, is contineous as to the variable t. Let $F(\mu,0)=0$. That is $D_K(\mu)=0$. But $D_K'(\mu)\neq 0$, since every eigenvalues of G.F. $K(x,y)$ is simple. Hence at $t=0$, $d\lambda/dt$ exists uniquely and its value will be given by $(d\lambda/dt)_{t=0}=-D_H(\mu)/D'(\mu)$. This result leads us to the conclusion: λ is an analytic function of t in the neighborhood of $t=0$.

Hence the eigenvalue may be expanded as follows:

$$\lambda_n=\mu_n+i\kappa\mu_{n1}+(i\kappa)^2\mu_{n2}+ \tag{32}$$

Next we shall assume

$$\phi_n=\varphi_n+i\kappa\varphi_{n1}+(i\kappa)^2\varphi_{n2}+ \tag{33}$$

Then from $(\phi_n,\phi_n^*)=1$ it follows:

$$\left.\begin{aligned}&(\varphi_{n1},\varphi_n)-(\varphi_{n1}^*,\varphi_n)=0,\\&(\varphi_{n2},\varphi_n)+(\varphi_{n2}^*,\varphi_n)-(\varphi_{n1},\varphi_{n1}^*)=0,\\&(\varphi_{n3},\varphi_n)-(\varphi_{n3}^*,\varphi_n)\\&\qquad-(\varphi_{n2},\varphi_{n1}^*)+(\varphi_{n2}^*,\varphi_{n1})=0\\&\cdots\cdots\cdots\cdots\cdots\cdots\end{aligned}\right\} \tag{34}$$

Now by inserting (32) and (33) into the differential equation and the boundary conditions, we have

$$\left.\begin{aligned}&L[\varphi_n]+\mu_n\varphi_n=0\,,\\&\varphi_n(0)=0, \quad \varphi_n'(1)=0\,,\end{aligned}\right\} \tag{35a}$$

$$\left.\begin{aligned}&L[\varphi_{n1}]+\mu_n\varphi_{n1}=-\mu_{n1}\varphi_n\,,\\&\varphi_{n1}(0)=0\,, \quad \varphi_{n1}'(1)=\varphi_n(1)\,,\end{aligned}\right\} \tag{35b}$$

$$\left.\begin{aligned}&L[\varphi_{n2}]+\mu_n\varphi_{n2}=-\mu_{n2}\varphi_n-\mu_{n1}\varphi_{n1}\,,\\&\varphi_{n2}(0)=0, \quad \varphi_{n2}'(1)=\varphi_{n1}(1)\,,\end{aligned}\right\} \tag{35c}$$

in general, for the $(h+1)$-th approximation

$$\left.\begin{aligned}&L[\varphi_{nh}]+\mu_n\varphi_{nh}=-\mu_{nh}\varphi_n\\&\qquad-\mu_{nh-1}\varphi_{n1}-\cdots-\mu_{n1}\varphi_{nh-1}\\&\varphi_{nh}(0)=0, \quad \varphi_{nh}'(1)=\varphi_{nh-1}(1)\,.\end{aligned}\right\}$$

(35a) is self-evident.

To solve (35b), if, using G.F. Γ_K', we apply the results of the preceding section, then

$$\varphi_{n1}(x)=(\varphi_{n1},\varphi_n)\varphi_n(x)+\varphi_n(1)\Gamma_K'(x,1;\mu_n)\,. \tag{36}$$

Regarding the second repeated kernel of Γ_K' to be expansible,

$$\int_0^1 \varphi_{n1}^2 dx=(\varphi_{n1},\varphi_n)^2+\varphi_n^2(1)\sum_{m=1}^{\infty}{}' \frac{\varphi_m^2(1)}{(\mu_m-\mu_n)^2}\,,$$

where the dash in summation symbol sigma means to except the to $m=n$ corresponding term.

For the particular case when K or K' is expansible,

$$\varphi_{n1}(x)=(\varphi_{n1},\varphi_n)\varphi_n(x)+\varphi_n(1)\sum_{m=1}^{\infty}{}' \frac{\varphi_m(1)\varphi_m(x)}{\mu_m-\mu_n}. \tag{37}$$

This formula corresponds to K.P.-paper, (37). But in the latter the first term of the right side of (37) is excluded, owing to the reason in order to keep ϕ_n normalized. However, as evident from (34), the reason seems us to be incorrect.

Now we regard that (36) (or (37)) does not involve μ_{n1}, in spite of being involved in (35b). Hence in order that (36) might satisfy the differential equation of (35b), it must be anticipated that $\mu_{n1}=-\varphi_n^2(1)$. This is explained as follows.

Applying Green's formula to $\phi_n L[\varphi_n]$ we have

$$(\lambda_n-\mu_n)(\phi_n,\varphi_n)=-i\kappa\varphi_n(1)\phi_n(1)\,.$$

Replacing (32) and (33) in this result, it follows:

$$\begin{aligned}&\mu_{n1}=-\varphi_n^2(1)\,,\ (<0)\\&\mu_{n2}+\mu_{n1}(\varphi_{n1},\varphi_n)=-\varphi_n(1)\cdot\varphi_{n1}(1)\,,\\&\mu_{n3}+\mu_{n2}(\varphi_{n1},\varphi_n)+\mu_{n1}(\varphi_{n2},\varphi_n)=-\varphi_n(1)\varphi_{n2}(1),\\&\cdots\cdots\ \cdots\cdots\cdots\cdots\cdots\cdots\end{aligned}$$

In the same manner as in the second approximation, we can find the third approximation from (35c) in the form:

$$\varphi_{n2}(x)=(\varphi_{n2},\varphi_n)\varphi_n(x)+\mu_{n1}\varphi_n(1)\Gamma_{K2}'(x,1;\mu_n)+\varphi_{n1}(1)\Gamma_K'(x,1;\mu_n)\,,$$

where Γ_{K2}' means the second repeated kernel of Γ_K'.

§ 10. A Contribution to Eigenfunction-Expansions

In the present section, we shall show that the required solution of our boundary valued problem is in either case expanded uniformly by certain system of orthogonal functions.

Firstly, let us choose a function $X_\lambda(x)$ that satisfies the following end conditions:

$$\begin{aligned}&X(0)=0,\ X''(0)=0\ (\text{where } Xq\to 0 \text{ as } x\to 0)\,;\\&X'(1)-i\kappa X(1)=I_0e^{-i\kappa}\,;\\&X'''(1)+i\kappa X''(1)+\{\lambda-q'(1)-q(1)\}X'(1)\\&\qquad+\{i\kappa\lambda-i\kappa q(1)-q'(1)\}X(1)=0\,.\end{aligned}$$

Let $U_\lambda(x)=L[X_\lambda]+\lambda X_\lambda=M[X_\lambda]$,
$L[U_\lambda]+\lambda U_\lambda=M[U_\lambda]$, say $M^2[X_\lambda]$.

Then we have $U_\lambda(0)=0$, $U_\lambda'(1)+i\kappa U_\lambda(1)=0$.

Now we consider the compound boundary problem as follows:

$$\begin{aligned}&L[\Phi]+\lambda\Phi=-M[X_\lambda]\\&L[U_\lambda]+\lambda U_\lambda=M^2[X_\lambda]\\&\Phi(0)=0,\quad \Phi'(1)-i\kappa\Phi(1)=0\,.\end{aligned}$$

This is equivalent to

$$\left.\begin{aligned}\Phi(x)&=\int\Gamma(x,y;\lambda)U_\lambda(y)dy\,,\\U_\lambda(x)&=-\int\Gamma^*(x,y;\lambda)M^2[X_\lambda(y)]dy\,.\end{aligned}\right\}$$

Combining these two equations, we have

$$\Phi(x)=-\int_0^1\Pi(x,y;\lambda)M^2[X_\lambda(y)]dy\,, \tag{38}$$

where Π is defined by

$$\Pi(x,y;\lambda)=\int_0^1\Gamma(x,t;\lambda)\Gamma^*(t,y;\lambda)dt\,.$$

For any real λ, $\Pi^*(y,x;\lambda)=\Pi(x,y;\lambda)$, that is, Π is the Hermitian kernel; further for any g

$$\iint_0^1\Pi(x,y;\lambda)g(x)g^*(y)dxdy$$

$$=\int_0^1 dt\left|\int_0^1\Gamma(x,t;\lambda)g(x)\,dx\right|^2\geqq 0\,.$$

In this case it never occurs that the above stated value is equal to zero for any g other than $g=0$, since G.F. Γ is closed. Hence Π is positive definite; consequently $\Phi(x)$ in (38) is always expanded uniformly by eigenfunctions of $\Pi(x,y;\lambda)$.

Now if we put $\phi=\Phi+X_\lambda$, then clearly ϕ is the solution of the inhomogeneous boundary valued problem as same as stated in § 3: $L[\phi]+\lambda\phi=0$, $\phi(0)=0$, $\phi'(1)-i\kappa\phi(1)=I_0e^{-i\kappa}$.

We have thus the required solution in another form:

$$\phi(x)=2i\kappa U_\lambda(1)\Pi(x,1;\lambda)+2i\kappa X_\lambda(1)\Gamma^*(x,1;\lambda)+I_0e^{-i\kappa}\Gamma^*(x,1;\lambda)\,,$$

provided Green's formula is twice used continuously in (38).

This work has been performed by suggestion of Prof. Takahiko Yamanouchi, and concerning many mathematical points the author is indebted to kind advices of Prof. Toshizo Matsumoto. The author expresses his hearty thanks to them. This research is carried out by the financial aids of the Ministry of Education.

Journal of the Physical Society of Japan Vol. 7, No. 5, Sept.—Oct., 1952

Reflection of a Wave at an Interface of Supersonic Flows and Wave Patterns in a Supersonic Compound Jet

By Ryuma KAWAMURA

Institute of Science and Technology, University of Tokyo

(Received March 14, 1952)

In the first half of this paper, the behavior of the reflected wave of a weak incident one at an interface of two supersonic flows is studied. The weakness of the incident wave makes it possible to use the isentropic characteristic theory with good approximation and, as a result, complication in the analysis is greatly reduced. It is found in this study that under a certain condition the reflected wave of an incident compression (or expansion) one is an expansion (or compression). The condition is given as a function of the Mach numbers of the flows and the ratios of the specific heats. In the latter half, similar treatment is applied to the analysis of wave patterns in a supersonic compound jet. The treatment of the problem in flow deflection and pressure plane simplifies the analysis greatly. It becomes clear in this study that there are two different types of wave pattern in the jet. In the one, pressure is oscillatory in the jet and in the other non-oscillatory. The conditions which discriminate the both cases are also obtained.

§ 1. Introduction

In a supersonic flow, sometimes there occurs a three-shock interaction. The phenomenon is called the Mach reflection when three shock waves meet with each other at one point. The analytical and experimental studies have been published so far by many authors[1)2)3)4)]. The treatments of this problem are very complicated mainly because of the entropy change across each shock. Therefore, a great simplification will be expected in the analysis in case of a weak incident shock where the entropy change can be neglected and, as a result, the method of isentropic characteristics becomes available.

In the first half of this paper, an approximate treatment of a three-shock interaction at an interface of two supersonic parallel flows is described when the incident shock is weak. The same treatment is applied, in the latter half, to the case of a supersonic compound jet and wave patterns in the jet are studied.

§ 2. Reflection and Refraction of a Weak Shock at an Interface of Two Supersonic Flows

Two supersonic parallel flows are separated from each other by an interface *APB* (Fig. 1). When a plane incident shock, *IP*, meets with the interface at the point *P*, there appear a transmitted wave, *I′P*, and a reflected wave, *RP*, as shown in Fig. 1. In case of a weak incident shock, the corresponding reflected and transmitted waves are also weak, and consequently, the entropy change across each wave may be neglected. These weak shocks are considered to be concentrated lines of Mach waves, and therefore, the method of characteristics can be applied with good approximation.

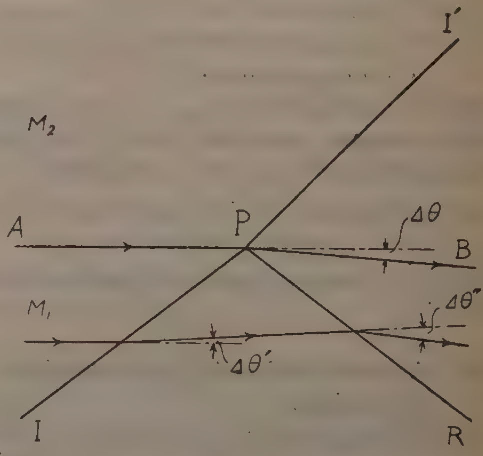

Fig. 1.

In an isentropic flow, the relation between the Mach number, *M*, and the pressure, *p*, is given in the following form.

$$(p_0/p)^{(\gamma-1)/\gamma}-1=\frac{1}{2}(\gamma-1)M^2, \qquad (1)$$

where p_0 is the adiabatic stagnation pressure of the flow and γ the ratio of the specific heats.

The deflection angle, θ, of the flow is also a function of M in a simple wave region, and its differential form is obtained from the two-dimensional characteristic theory[5] as

$$\pm(d\theta/dM)=\sqrt{M^2-1}/M[1+\frac{1}{2}(\gamma-1)M^2]. \qquad (2)$$

Eliminating M from Eqs. (1) and (2), a relation between θ and p is obtained as follows.

$$d\theta/dp=\mp\sqrt{M^2-1}/\gamma M^2 p \qquad (3)$$

$$\text{or} \quad d\theta/dp=\mp(\sin\mu\cos\mu)/\gamma p, \qquad (4)$$

where μ is the Mach angle of the flow and is equal to $\sin^{-1}(1/M)$.

Applying the above equations to each wave in Fig. 1 and neglecting higher order terms of pressure jumps, the following relations are derived.

$$\left.\begin{aligned}
\Delta\theta' &= -\frac{1}{\gamma_1}\frac{\Delta p'}{p_1}\sin\mu_1\cos\mu_1, \quad \text{(across } IP)\\
\Delta\theta'' &= \frac{1}{\gamma_1}\frac{\Delta p''}{p_1}\sin\mu_1\cos\mu_1, \quad \text{(across } RP)\\
\Delta\theta &= -\frac{1}{\gamma_2}\frac{\Delta p}{p_2}\sin\mu_2\cos\mu_2, \quad \text{(across } I'P)
\end{aligned}\right\} \qquad (5)$$

where $(\Delta\theta', \Delta p')$, $(\Delta\theta'', \Delta p'')$ and $(\Delta\theta, \Delta p)$ are the changes of the flow direction measured clockwise and the pressure jumps across the incident, reflected and transmitted waves, and subscripts 1 and 2 denote the flow variables in the upper and lower flows in Fig. 1.

The boundary conditions imposed on this three-shock configuration are non-existence of discontinuities in pressure and flow direction between the two flows on the interface. These are expressed as follows.

$$\left.\begin{aligned}
&p_1=p_2=p,\\
&\Delta p=\Delta p'+\Delta p'',\\
\text{and} \quad &\Delta\theta=\Delta\theta'+\Delta\theta''.
\end{aligned}\right\} \qquad (6)$$

Provided that the strength of the incident wave or $\Delta p'/p$ is given, all other unknown variables can be determined from Eqs. (5) and (6):

$$\left.\begin{aligned}
\Delta p &= 2\frac{\lambda_1}{\lambda_1+\lambda_2}\Delta p',\\
\Delta\theta &= -2\frac{\lambda_1\lambda_2}{\lambda_1+\lambda_2}\frac{\Delta p'}{p}=2\frac{\lambda_2}{\lambda_1+\lambda_2}\Delta\theta',\\
\Delta p'' &= \frac{\lambda_1-\lambda_2}{\lambda_1+\lambda_2}\Delta p',\\
\Delta\theta'' &= -\frac{\lambda_1-\lambda_2}{\lambda_1+\lambda_2}\frac{1}{\lambda_1}\frac{\Delta p''}{p}=-\frac{\lambda_1-\lambda_2}{\lambda_1+\lambda_2}\Delta\theta',
\end{aligned}\right\} \qquad (7)$$

where $\lambda_1=(\sin\mu_1\cos\mu_1)/\gamma_1$ and $\lambda_2=(\sin\mu_2\cos\mu_2)/\gamma_2$.

In Eq. (7), $\Delta p/\Delta p'$ and $\Delta\theta/\Delta\theta'$ are always positive, since λ_1 and λ_2 are positive. On the other hand, signs of $\Delta p''/\Delta p'$ and $\Delta\theta''/(-\Delta\theta')$ depend on the sign of $(\lambda_1-\lambda_2)$.

Therefore, it is concluded that the transmitted wave, $I'P$, is always of the same character as the incident wave, IP, while the character of the reflected wave depends on whether $(\lambda_1-\lambda_2)$ is positive or not. $I'P$ is a compression or expansion wave according to the character of IP being a compression or an expansion one. As for the reflected wave, RP, it has the opposite character as the incident one when $(\lambda_1-\lambda_2)$ is negative.

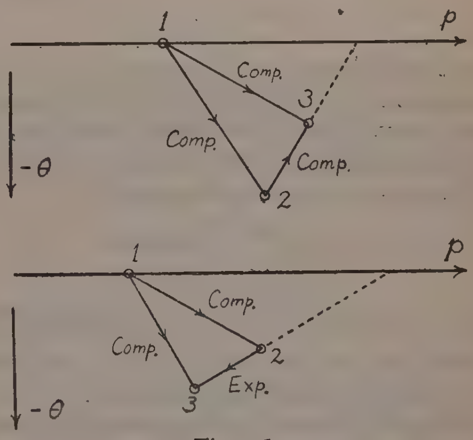

Fig. 2.

These are most clearly understood if we consider the problem in the θ, p-plane (Fig.2). In Fig. 2, points marked 1, 2 and 3 correspond to the regions in front of IPI', between IP and RP and behind RPI' in the physical plane. The slopes of the lines $\overline{12}$, $\overline{13}$ and $\overline{23}$ are given by Eq. (3). It is clear in Fig. 2 that the reflected wave has the same character as the incident one when the absolute value of the slope of $\overline{12}$ is greater than that of $\overline{13}$ and *vice versa*.

§ 3. Wave Patterns in a Supersonic Compound Jet

The considerations mentioned above are also valid for the waves in a two-dimensional supersonic compound jet. When a jet is placed in a uniform flow, it is called a compound jet. If both of the jet flow and the surrounding uniform flow are supersonic and discontiunity in pressure between the flows exists at the exit of the jet, trains of waves such as is shown in Fig. 3 will appear. In case of a small pressure difference at the exit, the analytical treatment is all the same as that mentioned already.

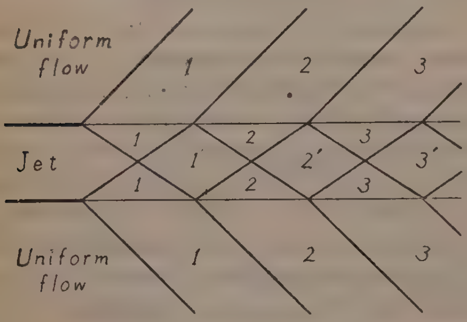

Fig. 3.

Let subscripts j and u denote the flow variables in the jet and the surrounding uniform flow. Then, deflection angle, $\Delta\theta_1$, of the flow across the first waves is expressed by Eq. (4) in the following forms.

$$\Delta\theta_1 = -\lambda_j \frac{\Delta p_j}{p_j} \quad \text{in the jet}$$

and
$$\Delta\theta_1 = \lambda_u \frac{\Delta p_u}{p_u} \quad \text{in the uniform flow,}$$

where $\Delta p_j = p_1 - p_j$, $\Delta p_u = p_1 - p_u$ and p_1 is the pressure behind the first wave.

Neglecting higher order terms in the above equations, we get

$$\Delta p_u = \frac{\lambda_j}{\lambda_j + \lambda_u} \Delta p$$

and
$$\Delta\theta_1 = \frac{\lambda_j \lambda_u}{\lambda_j + \lambda_u} \frac{\Delta p}{p_u},$$

where $\Delta p = p_j - p_u$.

Across the second wave in the jet, the deflection angle is $-\Delta\theta_1$ since the flow must be deflected back and become parallel to the undisturbed flow on the center line of the jet. The corresponding pressure change can be calculated from Eq. (4).

$$p_1' - p_1 = \frac{p_j}{\lambda_j} \Delta\theta_1 = \frac{\lambda_u}{\lambda_j + \lambda_u} \Delta p,$$

where p_1' is the pressure behind the second wave in the jet. Then, the pressure, p_2, and the deflection angle, $\Delta\theta_2$, behind the second wave in the uniform flow (or behind the third wave in the jet) are obtained by using equation similar to Eq. (4).

Although all flow patterns can be determined by repeating the above procedures from one wave to the next, the treatment becomes simpler if we consider the problem in θ, p-plane (Fig. 4). In Fig. 4, points marked J and U represent the undisturbed regions in the jet and in the uniform flow, and points marked 1, 2, ... also correspond to the regions of the same number in Fig. 3. The slopes of the straight lines $\overline{\mathrm{J1}}$, $\overline{\mathrm{11'}}$, $\overline{\mathrm{12}}$, ... are equal to $\mp\lambda_j/p_j$ and that of $\overline{\mathrm{U1}}$ equal to $-\lambda_u/p_u$.

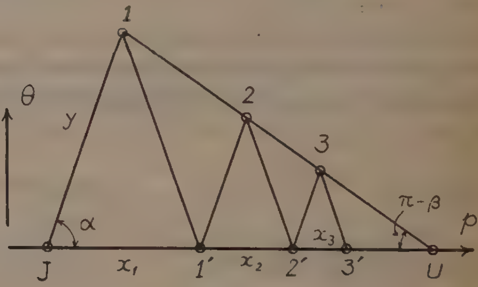

Fig. 4.

Let $\overline{\mathrm{JU}} = x$, $\overline{\mathrm{J1'}} = x_1$, $\overline{\mathrm{J2'}} = x_2$, ... , $\overline{\mathrm{J1}} = y$ and $\angle \mathrm{1JU} = \alpha$, $\angle \mathrm{1UJ} = \pi - \beta$, the following relations are derived by simple geometry.

$$y = \frac{\sin(\pi - \beta)}{\sin(\beta - \alpha)} x \quad \text{and} \quad x_1 = 2y\cos\alpha.$$

$$\left.\begin{aligned}
&\text{Therefore,}\\
&\quad x_1 = Ax,\\
&\text{and similarly,}\\
&\quad x_2 = A(x - x_1) = A(1 - A)x,\\
&\quad x_3 = A(x - x_1 - x_2) = A(1 - A)^2 x,\\
&\quad \cdots\cdots\cdots\cdots\cdots\cdots\cdots\cdots\\
&\quad x_n = A(x - x - \ldots\ldots - x_{n-1}) = A(1 - A)^{n-1} x,
\end{aligned}\right\} \quad (8)$$

where

$$A = \frac{2\cos\alpha\sin\beta}{\sin(\beta - \alpha)} = 1 - \frac{\tan\alpha - \tan(\pi - \beta)}{\tan\alpha + \tan(\pi - \beta)}.$$

From the definitions of α and β,

$$\tan\alpha = \lambda_j/p_j \quad \text{and} \quad \tan(\pi - \beta) = \lambda_u/p_u.$$

Therefore,

$$A=1-\frac{\lambda_j-\lambda_u}{\lambda_j+\lambda_u}$$

since p_j is nearly equal to p_u. Then,

$$\sum_1^n x_k = Ax\sum_0^{n-1}(1-A)^k.$$

It is easy to verify that

$$|1-A|<1.$$

Therefore,

$$\sum_1^n x_k=[1-(1-A)^n]x. \qquad (9)$$

From Eq. (9) we can calculate the pressure, p_n', in the n'th region in Fig. 3.

$$p_n'=p_j+\sum_1^n x_k=p_j+[1-(1-A)^n]\Delta p \qquad (10)$$

since $x=\Delta p$. The pressure in the nth region is

$$p_n=p_n'-\frac{1}{2}x_n=p_j+\left[1-(1+\frac{1}{2}A)(1-A)^{n-1}\right]\Delta p \qquad (11)$$

and the deflection angle, $\Delta\theta_n$, in the nth region is

$$\Delta\theta_n=-\frac{1}{2}x_n\tan\alpha=-\frac{1}{2}A(1-A)^{n-1}\Delta p\cdot\lambda_j/p_j. \qquad (12)$$

Thus, using Eqs. (10), (11) and (12), it is possible to determine all flow variables in the jet and in the surrounding uniform flow.

It is of most importance in the results obtained above that there are two different types of wave pattern in a supersonic compound jet.

In Eq. (8),

$x_n>0$ for $1>1-A>0$ or $\lambda_j>\lambda_u$

and

$x_{2n}<0$, $x_{2n+1}>0$ for $-1<1-A<0$ or $\lambda_j<\lambda_u$.

Therefore, in the first case, all waves in the jet are of the same character (compressive or expansive). The wave patterns of this type are shown schematically in Fig. 5, where black and dotted lines in the physical planes represent compression and expansion waves, respectively. In this case, the pressure on the center line of the jet gradually falls down or rises to the value in the undisturbed uniform flow.

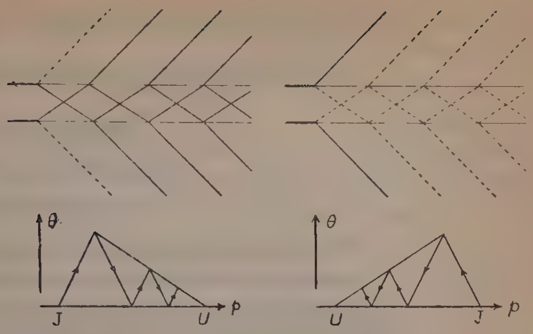

Fig. 5.

In the second case two waves of the same character are succeeded by two waves of the opposite character in the jet. Fig. 6 shows the wave patterns of the second type. In this case, the pressure in the jet is oscillatory and ultimately approaches p_u.

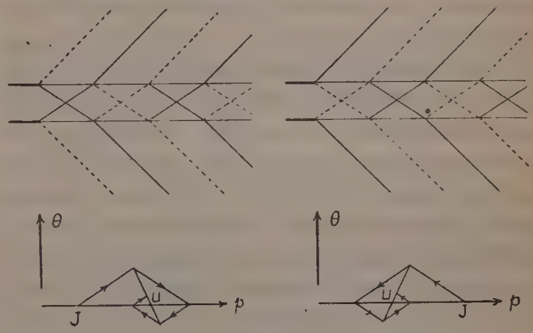

Fig. 6.

References

1) R. Kawamura: Rep. Aeron. Res. Inst. **23** (1945).

2) A.H. Taub: Phys. Rev. **72** (1947).

3) R. Courant and K. O. Friedrichs: Supersonic Flow and Shock Waves. Inters. Pub., Inc. New York (1948).

4) W. Bleakney and A.H. Taub: Rev. Mod. Phys. **21** (1949).

5) A. Ferri: *Elements of Aerodynamics of Supersonic Flows.* The Macmillan Co., New York (1949).

JOURNAL OF THE PHYSICAL SOCIETY OF JAPAN Vol. 7, No. 5, SEPT.—OCT., 1952

On the Detached Shock Wave in front of a Body of Revolution moving with Supersonic Speeds

By Tōru KAWAMURA

Shiga Prefectural Junior College

(Received March 28, 1952)

The uniform supersonic flow past a body of revolution with a finite radius of curvature at its nose is studied. Various hydrodynamical quantities are expanded in power series of the coordinates in the neighbourhood of the stagnation point of the body. The coefficients of the series are determined by the boundary conditions at the surface of the body as well as by the shock wave conditions at the shock wave. Numerical results are compared with the existing experiments as well as with the theoretical results obtained previously by the writer.

§ 1. Introduction

It is well known that when a uniform supersonic flow of air impinges upon a body of revolution parallel to its axis of symmetry, a sheet of symmetric detached shock wave is formed in front of it, provided that certain conditions are satisfied. In a previous paper (**1**) the writer has approximated the flow behind the detached shock wave by an incompressible potential flow with suitable boundary conditions, but in the present paper, various hydrodynamical quantities in that region are expanded in power series of the coordinates as in a work by Dugundji (**2**). Accordingly, compressibility effects of the air as well as the contributions of the existence of vorticity are taken into account. At the stage of the first approximation, however, only first few terms of the series are retained. The aim of the present work is partly to check, from another standpoint, the results of the conventional method used in the previous paper and partly to discuss the accuracy of the method of power-series expansion. The further approximate solution along the lines of the present method has been obtained, but details of the result will be reported at a future opportunity.

§ 2. Condition at the Shock Wave

We now propose to study a steady supersonic flow of air about a body of revolution at zero angle of attack. Since the air stream is necessarily compressed in the vicinity of the body, a shock wave is formed in front of it. We shall assume that the body has a blunt nose and a sheet of co-axial detached shock wave is formed in front of it. The entire flow is then symmetric about the axis of the body, and therefore we may confine ourselves to a meridian section with cylindrical coordinates x, y and ω as shown in Fig. 1.

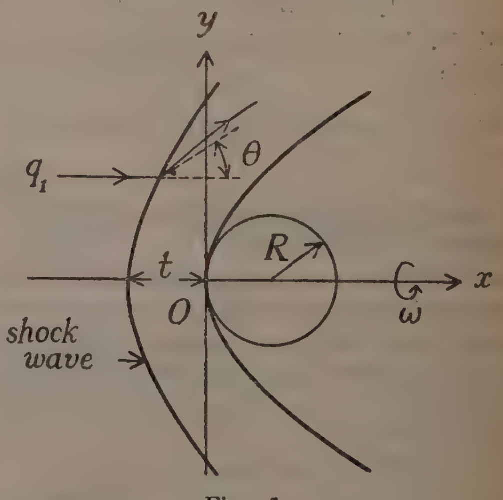

Fig. 1.

The equation for the section of the detached shock wave in the meridian plane is given by $x=f(y^2)$. Change of the state of the air as it passes through the shock wave is determined by the physical conditions; namely, the conservation of mass, momentum and energy. Except for that portion, change of the state takes place adiabatically. Let the Mach number, the density, the pressure, the magnitude of velocity and the angle of deflection of the streamline be denoted by M, ρ, p, q and θ respectively, and suffices 1, 2 and 0 indicate the corresponding quantities in front of and immediately behind the shock wave, and at the stagnation point of the body respectively. The relations between various hydrodynamical quantities in front of and immediately behind the shock wave are determined if the analytical expression for the detached shock wave is given. At the normal portion of the shock wave, these relations are reduced to the well-known shock wave conditions. The inclination of the stream-line at any point immediately behind the shock wave is given by

$$\tan\theta_2=(u_y/u_x)_2\,, \tag{1}$$

where u_x and u_y are the components of velocity so that $q^2=u_x{}^2+u_y{}^2$.

§ 3. Flow in the Vicinity of the Body

If the Mach number of the undisturbed stream is sufficiently great, the location of the normal portion of the detached shock wave is considerably close to the nose of the body. Then we may approximate various hydrodynamical quantities behind the shock wave by polynomials of the coordinates. This idea was used by Dugundji (**2**).

Now we shall introduce non-dimensional coefficients :

$$u_x=u\sqrt{\frac{p_0}{\rho_0}}\,,\quad u_y=v\sqrt{\frac{p_0}{\rho_0}}\,,\quad \tau=\frac{\rho_0}{\rho}\,,\quad P=\frac{p}{p_0}\,.$$

Then the hydrodynamical equations in the region behind the shock wave are reduced to

$$\left.\begin{aligned} u\frac{\partial u}{\partial x}+v\frac{\partial u}{\partial y}&=-\tau\frac{\partial P}{\partial x}\,,\\ u\frac{\partial v}{\partial x}+v\frac{\partial v}{\partial y}&=-\tau\frac{\partial P}{\partial y}\,,\end{aligned}\right\} \tag{2}$$

and

$$\tau\left(\frac{\partial u}{\partial x}+\frac{\partial v}{\partial y}+\frac{v}{y}\right)=u\frac{\partial \tau}{\partial x}+v\frac{\partial \tau}{\partial y} \tag{3}$$

Since the air obeys the adiabatic law, we have

$$P\tau+\frac{\gamma-1}{2\gamma}(u^2+v^2)=1\,. \tag{4}$$

These relations are employed by Lin and Rubinov (**3**).

§ 4. The First Approximation

As the first approximation we shall consider a case when the velocity components and the meridan section of the detached shock wave are given by

$$\left.\begin{aligned} u&=u_1x+u_{11}x^2\,,\\ v&=v_2y+v_{12}xy\,.\end{aligned}\right\} \tag{5}$$

and

$$x+t=b_2y^2\,, \tag{6}$$

where t is the distance of the normal portion of the shock wave from the stagnation point of the body. The boundary condition at the surface of the body is

$$v/u=(R-x)/y\,, \tag{7}$$

where R is the radius of curvature of the nose of the body. The coefficients in the above equations (5) and (6) are determined in such a way that the relations (2), (3), (4) and (7) are satisfied. After some calculations we obtain

$$\left.\begin{aligned} u&=ax+abx^2-\frac{a}{R}y^2\,,\\ v&=-\frac{a}{2}y-abxy\,,\end{aligned}\right\} \tag{8}$$

and

$$P=1-\frac{1}{2}a^2x^2-\frac{a^2}{4}y^2-a^2bx+\ldots\ldots \tag{9}$$

The inclination, θ, of the streamline at any point is deduced from (8). Thus,

$$\tan\theta=\frac{v}{u}=\frac{y}{2}\,\frac{1-2bt}{t(1-bt)}\left[1+\frac{2bb_2}{1-2bt}y^2\right.$$
$$\left.-\frac{1}{Rt(1-bt)}y^2+\frac{b_2(1-2bt)}{t(1-bt)}y^2+0(y^4)\right]. \tag{10}$$

Since the two expressions (7) and (10) for the inclination of the streamline must be equal to each other at an arbitrary point immediately behind the detached shock wave, we have, after some reductions,

$$\frac{8(M_1{}^2-1)B_2}{2+(\gamma-1)M_1{}^2}=\frac{1-2BT}{T(1-BT)}\,, \tag{11}$$

and

$$-\frac{2B_2\{(\gamma+3)M_1{}^4-4M_1{}^2+2\}}{(M_1{}^2-1)\{2+(\gamma-1)M_1{}^2\}}(1-2BT)$$
$$=B-\frac{4(M_1{}^2-1)}{2+(\gamma-1)M_1{}^2}\,, \tag{12}$$

where for convenience's sake we have put $B_2=Rb_2$, $B=Rb$, $T=t/R$ and $A=Ra$.

Computing the pressure and velocity at the normal portion of the shock wave, we get

$$\sqrt{2\gamma\{2+(\gamma-1)M_1{}^2\}}$$
$$=-AT(1-BT)(\gamma+1)M_1{}^2\,, \tag{13}$$

and

$$2-2\left(1+\frac{\gamma-1}{2}M_2{}^2\right)^{-\frac{\gamma}{\gamma-1}}=A^2T^2(1-2BT)\,. \tag{14}$$

Eliminating A between these two equations and combining the resulting equation with (11) and (12), we obtain, after some calculations,

$$B_2T=\frac{1}{8(M_1^2-1)}\Big[2+(\gamma-1)M_1^2$$

$$-\{2+(\gamma-1)M_1^2\}^{1/2}[2+(\gamma-1)M_1^2$$

$$-\frac{(\gamma+1)^2}{\gamma}M_1^2\{1-(1+\frac{\gamma-1}{2}M_2^2)^{-\gamma/(\gamma-1)}\}]^{1/2}\Big], \tag{15}$$

and

$$T=\frac{2+(\gamma-1)M_1^2}{4(M_1^2-1)}$$

$$\times\Big[\frac{8\gamma(M_1^2-1)B_2T}{(\gamma+1)^2M_1^2\{1-(1+\frac{\gamma-1}{2}M_2^2)^{-\gamma/(\gamma-1)}\}}$$

$$\times\Big\{\frac{16(B_2T)^2\{\gamma+3)M_1^4-4M_1^2+2\}}{\{2+(\gamma-1)M_1^2\}^2}-1\Big\}+1\Big]. \tag{16}$$

We can calculate the values of B_2 and T (and therefore those of b_2 and t.) from these two equations, and if these values of b_2 and t are substituted in (6), the complete form of the detached shock wave is determined.

§ 5. Numerical Discussions

Using the numerical value $\gamma=1.405$ for the air, the relative distance $T(=t/R)$ of the normal portion of the detached shock wave has been calculated for various Mach numbers and is shown in Fig. 2, where circles and a cross indicate respectively the experimental values obtained by Sugimoto (4), and Ladenburg and his co-workers (5). A thin-line curve in the figure shows the result for the sphere obtained in the previous work (1) by the present writer. It will be seen that the present analysis justifies the conventional method in the writer's previous work. The power-series expansion seems to be correct especially when the undisturbed Mach number is sufficiently large.

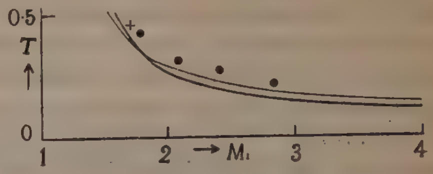

Fig. 2.

§ 6. Summary

The location of the detached shock wave in front of a body of revolution is discussed. To do this, power-series expansion of the hydrodynamical quantities in the vicinity of the body is applied as in a work by Dugundji. Numerical values of the distance of the normal portion of the detached shock wave are calculated for the case of air, and the results are compared with the existing experiments as well as with the results of our previous paper.

The writer expresses his best thanks to Prof. S. Tomotika for his continued interest and encouragement throughout the work.

References

1) T. Kawamura: Mem. Kyoto Univ. **26** (1950) 207.

2) J. Dugundji: Journ. Aeron. Sci. **15** (1948) 699.

3) C.C. Lin and S.I. Rubinov: Journ. Math. and Phys. **27** (1948) 105.

4) M. Sugimoto, Unpublished. (A part of the work is shown in (1)).

5) R. Ladenburg, J. Winkler and C.C. van Voohris: Phys. Rev. **73** (1948) 1359.

JOURNAL OF THE PHYSICAL SOCIETY OF JAPAN Vol. 7, No. 5, SEPT.—OCT., 1952

Stability of the Laminar Inlet-flow prior to the Formation of Poiseuille Régime, I

By Tomomasa TATSUMI

Department of Physics, Faculty of Science, University of Kyoto

(Received April 26, 1952)

Velocity distribution in the axisymmetric laminar inlet-flow through a circular tube is obtained, under the assumption of "almost similarity" of velocity profiles. Theoretical velocity distribution curves obtained agree fairly well with the experimental one in a rather limited region near the entrance where the approximation is valid.

Introduction

The theory of hydrodynamical stability furnishes us with one of the theoretical aspects of the study on the origin of turbulence. It concerns with the questions: Whether or not is a given laminar flow ultimately unstable for sufficiently high Reynolds numbers, and how the instability oscillation, if any, begins to appear? A large part of the numerous existing contributions to the subject is based on the linear theory, using the method of small perturbation.

Up to the present time, following typical cases have been discussed by various authors, namely: (a) *Couette flow* (between two concentric cylinders), (b) *Plane Couette flow*, (c) *Poiseuille flow* (in a circular tube), (d) *Plane Poiseuille flow*, and (e) *Blasius flow*. Although the linear theory of stability has given us useful informations to the transition phenomena in these special problems, it contains yet at least two points of criticism (cf. v. Neumann (**1**)).

In the cases (a), (d) and (e), the theory has predicted instability of the laminar flow for sufficiently high Reynolds numbers. However, the stability criteria given by the theory are not always in agreement with the "critical Reynolds numbers" found experimentally, and the predicted unstable oscillations are too regular to be identified with the proper "turbulent" fluctuations. This contradiction is essentially due to the assumption of "small perturbation", i.e. to the linearity of the theory, which is inevitably limiting the potentiality of the theory to describe the development of transition where nonlinear effects are essential. Concerning this, it seems plausible to conclude that the laminar instability given by the linear theory is not to be taken as the transition itself but as its initial state when external disturbances are very small.

In the cases (b) and (c), the theory has given indications of stability which are obviously inconsistent with the general impression (case (b)) or the experimental evidences (case (c)) of the existence of transition. This contradiction seems, however, in contrast with the first one, and to be attributed to the incomplete applications of the theory to the specified problems. For instance, for the case (b), a possibility of instability may be expected in the transitional flow from rest to the formation of linear velocity profile. From this point of view, Schlichting (**2**) investigated this unsteady flow, and found as the critical Reynolds number for the Couette flow the lowest stability limit during the transitional period.

The same kind of idea can be applied to the case (c) which is mathematically more similar to the case (b) than to the case (d), by ascribing the instability to the "laminar inlet-flow" where the velocity profiles are not yet parabolic. The main object of the present work is indeed to carry out this idea in the case (c). If the theory could find any decisive result in this case, the second contradiction would be settled down so far as the above typical cases are concerned, and the theory would establish its self-consistency at least in the limitation of linearity; or otherwise, its conclusions might be seen doubtful even for other successful cases.

In Part I of this paper, the velocity distribution in the inlet-flow will be obtained under the assumption of "almost similarity" of velocity profiles, and Part II deals with the stability calculation for these velocity profiles.

The author wishes to express his cordial thanks to Professor S. Tomotika for suggesting the problem of hydrodynamical stability. The author is indebted to Professor I. Imai for many kind suggestions, and to Dr. K. Tamada for several helpful discussions. The author's thanks are also due to the Ministry of Education for a grant in aid for fundamental scientific research.

Part I. The Velocity Distributions in the Inlet-flow.

§1. Existing Theories

It was Boussinesq (3) who first made a theoretical investigation on the velocity distribution in the inlet-flow. Assuming that the deviation of the velocity profile of the inlet-flow from that of the parabolic flow is small he obtained a velocity distribution, which is in good agreement with the measurement by Nikuradse (4) at some distance away from the entrance of a tube, but is not so satisfactory near the entrance. Since the circumstances in the neighbourhood of the entry are most important in our problem, we cannot use his result as the main flow to be examined.

In order to obtain the velocity distribution in the entrance flow, Prandtl suggested that the velocity profile may be assumed to consist of a constant-velocity core bounded by two parabolic arcs. Then the equation of continuity and the momentum equation lead to a relation between the velocity in the core and the distance from the entrance, resulting in the determination of the velocity distribution. The calculation carried out by Schiller (5) gave a velocity distribution in excellent agreement with the measurement, at least for the first one-third of the inlet-length from the entrance. Although Schiller's result offers an useful explanation for the general characters of the flow, it cannot represent the accurate variation of the curvature of velocity profile over the inlet length, owing to its approximation of the profile by parabolic arcs. As will be seen in Part II, the curvature of the profile has a serious effect upon the stability characters of the flow, so that Schiller's velocity distribution cannot be taken as the fundamental flow to which the stability calculation is applied.

An attempt to obtain a more accurate solution near the entrance was made by Atkinson and Goldstein (6), using a method similar to that of Schlichting (7) for the two-dimensional problem. Their calculation is, however, divergent except in the immediate vicinity of the entry, and this also is inadequate to our problem.

Thus, failing to obtain the velocity profile appropriate to our problem in the existing theories, we must proceed to seek for it under some approximation.

§2. Assumption of Almost Similarity

The equations of motion for a steady axisymmetric flow in the cylindrical polar coordinates (r, z), where the z-axis is taken along the axis of symmetry, are given by

$$\left.\begin{aligned} u\frac{\partial u}{\partial z}+v\frac{\partial u}{\partial r}&=-\frac{1}{\rho}\frac{\partial p}{\partial z}\\ &\quad+\nu\left(\frac{\partial^2 u}{\partial r^2}+\frac{1}{r}\frac{\partial u}{\partial r}+\frac{\partial^2 u}{\partial z^2}\right),\\ u\frac{\partial v}{\partial z}+v\frac{\partial v}{\partial r}&=-\frac{1}{\rho}\frac{\partial p}{\partial r}\\ &\quad+\nu\left(\frac{\partial^2 v}{\partial r^2}+\frac{1}{r}\frac{\partial v}{\partial r}-\frac{v}{r^2}+\frac{\partial^2 v}{\partial z^2}\right),\end{aligned}\right\}\quad(2.1)$$

where u and v denote the axial and radial components of the velocity respectively, p the pressure, and ν the kinematic viscosity.

The equation of continuity leads to the existence of a stream function such that

$$u=-\frac{1}{r}\frac{\partial\psi}{\partial r},\qquad v=\frac{1}{r}\frac{\partial\psi}{\partial z}.\qquad(2.2)$$

Since we are concerned only with high Reynolds numbers, the approximations made customarily in the boundary layer theory can also be made. We define here the Reynolds number $R=a\bar{u}/\nu$, where a is the radius of the tube and $\bar{u}$ the mean velocity of flow over the cross section of tube. Introducing new variables

$$x=\frac{z}{aR},\qquad y=\frac{1}{2}\left[1-\left(\frac{r}{a}\right)^2\right],\qquad(2.3)$$

and replacing all quantities by the corresponding non-dimensional quantities:

$$u^*=\frac{u}{\bar{u}},\quad v^*=\frac{v}{\bar{u}},\quad \psi^*=\frac{a^2\psi}{\bar{u}},\quad p^*=\frac{p}{\rho\bar{u}^2},$$

the equations of motion (2.1) and (2.2) reduce, for large values of R, to

$$\left.\begin{aligned}&\frac{\partial\psi^*}{\partial y}\frac{\partial^2\psi^*}{\partial x\partial y}-\frac{\partial\psi^*}{\partial x}\frac{\partial^2\psi^*}{\partial y^2}\\&\quad=-\frac{\partial p^*}{\partial x}+(1-2y)\frac{\partial^3\psi^*}{\partial y^3}-2\frac{\partial^2\psi^*}{\partial y^2},\\&\frac{\partial p^*}{\partial y}=0,\end{aligned}\right\}\quad(2,4)$$

and

$$u^*=\frac{\partial\psi^*}{\partial y},\quad v^*=R^{-1}(1-2y)^{-1/2}.\frac{\partial\psi^*}{\partial x},\quad(2,5)$$

where terms of the order of R^{-1} have been neglected.

From the second equation of (2.4) p^* may be taken to be a function of x only, and so long as there is a core uninfluenced by viscosity,

$$-\frac{\partial p^*}{\partial x}=u_1^*\frac{du_1^*}{dx},$$

where $u_1^*=u_1/\bar{u}$, and u_1 is the velocity in the core. Substituting this into the first equation of (2.4), we have the fundamental equation for our problem as follows:

$$\begin{aligned}&\frac{\partial\psi^*}{\partial y}\frac{\partial^2\psi^*}{\partial x\partial y}-\frac{\partial\psi^*}{\partial x}\frac{\partial^2\psi^*}{\partial y^2}\\&=u_1^*\frac{du_1^*}{dx}+(1-2y)\frac{\partial^3\psi^*}{\partial y^3}-2\frac{\partial^2\psi^*}{\partial y^2}.\quad(2.6)\end{aligned}$$

Now we put ψ^* formally in the form:

$$\psi^*=u_1^*(x)\delta(x)f(\eta,x),\quad(2.7)$$

where δ is the displacement-thickness of the boundary layer as defined by

$$\delta\equiv\int_0^{1/2}(1-u^*/u_1^*)\,dy=\int_0^{1/2}(1-u/u_1)dy,\quad(2.8)$$

and

$$\eta=y/\delta.\quad(2.9)$$

Here we make an assumption that the curve of velocity profile is almost similar throughout the inlet-length. Then substituting (2.7) into (2.6), and neglecting the terms involving $\partial f/\partial x$ under this assumption, equation (2.6) reduces to

$$\begin{aligned}&\delta\frac{du_1^*}{dx}(f'^2-1)-\frac{d}{dx}(\delta u_1^*)ff''\\&\qquad-\frac{1}{\delta}f'''+2(\eta f'')'=0,\quad(2.10)\end{aligned}$$

where dashes denote differentiation with respect to η.

The condition of constant flux requires that

$$\pi a^2\bar{u}=\pi\int_0^a urdr=\pi a^2\int_0^{1/2}udy$$

which, in conjunction with (2.8), gives

$$u_1=\frac{\bar{u}}{1-2\delta},\quad\text{i.e.}\quad u_1^*=\frac{1}{1-2\delta}\quad(2.11)$$

Substituting (2.11) into (2.10), we obtain

$$\begin{aligned}&\frac{2\delta^2}{(1-2\delta)^2}\frac{d\delta}{dx}(f'^2-1)-\frac{\delta}{(1-2\delta)^2}\frac{d\delta}{dx}ff''\\&\qquad-f'''+2\delta(\eta f'')'=0,\quad(2.12)\end{aligned}$$

which is similar to the generalized Falkner-Skan's equation.

If we now introduce the transformations:

$$Y=A\eta,\quad F=Af,\quad(2.13)$$

with

$$A(\delta)=\left[\frac{\delta}{(1-2\delta)^2}\frac{d\delta}{dx}\right]^{1/2},\quad(2.14)$$

equation (2.12) becomes

$$2\delta(F'^2-1)-FF''-F'''+2\delta A(YF'')'=0.\quad(2.15)$$

Throughout this section as well as in a subsequent section dashes denote differentiation with respect to Y.

From (2.13), (2.7) and (2.5) we have

$$F'=\frac{df}{d\eta}=\frac{u^*}{u_1^*}=\frac{u}{u_1}.\quad(2.16)$$

Hence, the solution F of (2.15) must satisfy the boundary conditions:

$$F'(0)=0,\quad F'(B)=1,$$

where $Y=B$ denotes an arbitrary point in the core.

Let δ_Y denote the value of Y corresponding to $y=\delta$. Then from (2.13) and (2.16) we get

$$\begin{aligned}A=\delta_Y=\int_0^B\left(1-\frac{u^*}{u_1^*}\right)dY&=\int_0^B(1-F')dY\\&=B-F(B),\quad(2.17)\end{aligned}$$

and this is another condition for equation (2.15).

§ 3. Solution by Iteration Method

Solutions of equation (2.15) for given values of δ can be obtained by an iteration method which is essentially due to Hartree (8). The most suitable method of iteration for finding a solution of (2.15) is to construct a sequence of functions F_n satisfying

$$F'''_{n+1}-2\delta A_n(YF''_{n+1})'+F_nF''_{n+1}=2\delta(F_n'^2-1),\quad(3.1)$$

with

$$A_n=B-F_n(B),\quad(3.2)$$

or

Table 1.

δ	0	0.05	0.1	0.15
$F''(0)$	0.4696	0.557	0.632	0.700
A	1	1.058	0.948	0.865
Y	F'			
0	0	0	0	0
0.1	0.0470	0.056	0.063	0.069
0.2	0.0939	0.111	0.125	0.138
0.3	0.1408	0.165	0.186	0.204
0.4	0.1876	0.219	0.246	0.270
0.5	0.2342	0.272	0.305	0.333
0.6	0.2806	0.325	0.363	0.396
0.7	0.3266	0.377	0.419	0.455
0.8	0.3720	0.427	0.473	0.513
0.9	0.4167	0.477	0.526	0.569
1.0	0.4606	0.524	0.577	0.621
1.2	0.5453	0.615	0.671	0.718
1.4	0.6244	0·697	0.754	0.800
1.6	0.6967	0.769	0.824	0.867
1.8	0.7610	0.831	0.881	0.919
2.0	0.8167	0.881	0.924	0.955
2.2	0.8633	0.920	0.955	0.978
2.4	0.9011	0.949	0.976	0.991
2.6	0.9306	0.969	0.988	0.997
2.8	0.9529	0.982	0.995	0.999
3.0	0.9691	0.991	0.998	1.000
3.2	0.9804	0.995	0.999	
3.4	0.9880	0.998	1.000	
3.6	0.9929	0.999		
3.8	0.9959	1.000		
4.0	0.9978			
4.2	0.9988			
4.4	0.9994			
4.6	0.9997			
4.8	0.9999			
5.0	1.0000			

$$[(1-2\delta A_nY)F''_{n+1}]'+G_n(1-2\delta A_nY)F''_{n+1}=2\delta(F_n'^2-1)\,, \qquad (3.3)$$

where

$$G_n=F_n/(1-2\delta A_nY)\,. \qquad (3.4)$$

Multiplying (3. 5) by $\exp[\int_0 G_n dY]$ and integrating we have

$$F''_{n+1}=F''_{n+1}(0)\cdot H_n+2\delta H_nK_n\,, \qquad (3.5)$$

where

$$\left.\begin{aligned} H_n&=\exp\left[-\int_0 G_n dY\right]\Big/(1-2\delta A_nY),\\ K_n&=\int_0 (F_n'^2-1)\exp\left[\int_0 G_n dY\right]dY. \end{aligned}\right\}\qquad (3.6)$$

Integrating (3. 5) again

$$F'_{n+1}=F''_{n+1}(0)\int_0 H_n dY+2\delta\int_0 H_nK_n dY\,. \qquad (3.7)$$

$F''_{n+1}(0)$ should be determined so as to satisfy the condition $F'_{n+1}(B)=1$, so that from (3. 7) we have

$$F''_{n+1}(0)=\left(1-2\delta\int_0^B H_nK_n dY\right)\Big/\int_0^B H_n dY. \qquad (3.8)$$

If functional values of F_n are given from the previous stage of iteration for a given δ, A_n and G_n are found from (3. 2) and (3. 4) respectively, so that H_n and K_n are obtained from (3. 6) by numerical integration. Then substituting the value of $F''_{n+1}(0)$ obtained from (3. 8) into (3. 7), the formal solution F'_{n+1} are evaluated numerically, and the next stage of iteration goes quite similarly and so on.

As the zero approximation F_0', we may use Hartree's solution of the equation

$$y'''+yy''-\beta(y'^2-1)=0\,, \qquad (3.9)$$

corresponding to $\beta=2\delta$. The convergence of this iteration process is satisfactory for small values of δ, as can be seen also by comparing (2. 15) with (3. 9).

Actual calculations have been made for $\delta=0.05$, 0.1 and 0.15, results of which are given in Table 1 and illustrated in Fig. 1. In these table and figure, the column or the curve corresponding to $\delta=0$ are reproduced from Hartree's result, since in this case (2. 15) is identical with (3.9).

Since the fundamental equation (2. 6) has been obtained on the basis of the assumption that there is always a constant-velocity core around the axis, this method of approximation becomes invalid when the core vanishes with increasing δ. As for $\delta=0.15$ the condition $F''(B)=0$ is just satisfied at $B=2.9$ ($r=0$) as can be seen from Table 1, and so there is undoubtedly no core for $\delta>0.15$ and the method breaks down in this region.

Having thus obtained the non-dimensional velocity profiles for some values of δ, we now proceed to find the development of the profile in the inlet-length. From (2. 14) we have

$$x=\int_0^\delta \delta(1-2\delta)^{-2}A(\delta)^{-2}d\delta\,. \qquad (3.10)$$

Since $A(\delta)$ can be obtained for any value of δ (practically for some specified values by iteration method), it is possible to calculate $x(\delta)$ for values of δ lying between 0 and 0.15 from (3. 10), Then, using the relation (2. 11), $x(u_1^*)$ is obtained and thus the velocity distribution $u^*(\eta, x)$ is fully determined.

In practice, A^{-2} is an almost linear function of δ for values of δ lying between 0 and 0.15,

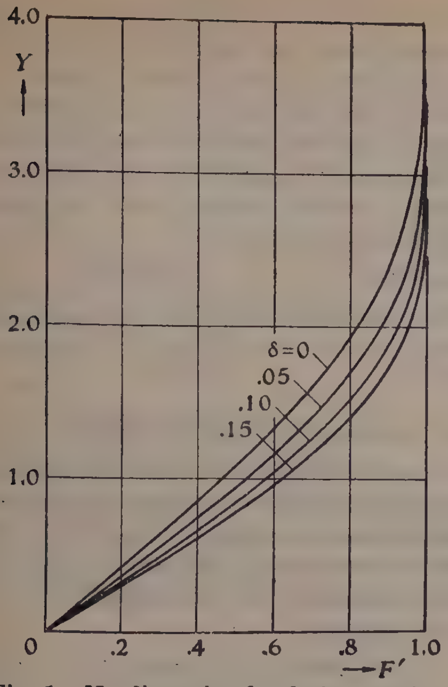

Fig. 1. Nondimensional velocity profiles in the inlet-flow.

Table 2.

δ	0.05		0.1		0.15	
	δA^{-1}	u_1	δA^{-1}	u_1	δA^{-1}	u_1
	0.047	1.111	0.105	1.250	0.173	1.429
Y	r	u	r	u	r	u
0	1	0	1	0	1	0
0.1	0.995	0.062	0.989	0.079	0.983	0.099
0.2	0.991	0.123	0.979	0.156	0.965	0.196
0.3	0.986	0.183	0.968	0.232	0.947	0.292
0.4	0.981	0.243	0.957	0.307	0.928	0.385
0.5	0.976	0.303	0.946	0.381	0.909	0.476
0.6	0.971	0.361	0.935	0.453	0.890	0.565
0.7	0.966	0.418	0.923	0.523	0.870	0.651
0.8	0.962	0.475	0.912	0.592	0.850	0.733
0.9	0.957	0.529	0.900	0.657	0.830	0.812
1.0	0.952	0.583	0.888	0.721	0.808	0.887
1.2	0.942	0.683	0.864	0.838	0.764	1.025
1.4	0.932	0.774	0.840	0.942	0.718	1.143
1.6	0.921	0.855	0.814	1.030	0.667	1.239
1.8	0.911	0.923	0.788	1.101	0.613	1.313
2.0	0.901	0.979	0.761	1.155	0.554	1.365
2.2	0.890	1.022	0.732	1.194	0.487	1.398
2.4	0.879	1.054	0.703	1.220	0.410	1.416
2.6	0.868	1.077	0.672	1.235	0.314	1.425
2.8	0.858	1.091	0.640	1.244	0.172	1.428
3.0	0.846	1.101	0.606	1.248	...	...
3.2	0.835	1.106	0.570	1.249		
3.4	0.824	1.109	0.532	1.250		
3.6	0.812	1.110	0.491	1.250		
3.8	0.801	1.111	0.446	1.250		
4.0	0.789	1.111	...	...		
4.2	0.777	1.111				
	...	...				

so that we may put

$$A^{-2}=4.396\,\delta+0.674\,, \qquad (3.11)$$

which is a least square approximation of A^{-2} determined by data for $\delta=0$, 0.05, 0.1 and 0.15. Errors introduced by this approximation are only 0.001∼0.002. Substituting (3.11) into (3.10) we obtain

$$\begin{aligned} x=&-0.169+0.718(1-2\delta)^{-1} \\ &+1.268\cdot\log(1-2\delta)-0.550(1-2\delta), \end{aligned} \qquad (3.12)$$

or

$$\begin{aligned} x=&-0.169+0.718\,u_1^* \\ &-1.268\cdot\log u_1^*-0.550\,u_1^{*-1}. \end{aligned} \qquad (3.13)$$

Results thus obtained are shown in Table 2 and Fig. 2.

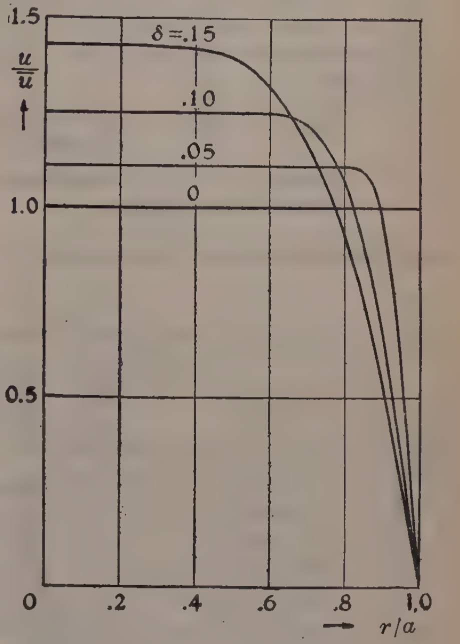

Fig. 2. Velocity distribution near the entrance.

Fig. 3 shows a number of curves for the non-dimensional velocity $u^*(=u/\bar{u})$ plotted against $x(=z/aR)$, for various distances r/a from the axis. It is seen that the theoretical curves are, so long as they exist, in fairly good agreement with Nikuradse's measurements; however, their region of existence $(0\leqq\delta\leqq0.15)$ is rather limited in comparison with the whole inlet-length. As will be found in Part II, instability is due to a very limited region near the entrance $(0\leqq\delta\leqq0.1)$, and it may therefore be said that these results are useful enough for our problem, but are not satisfactory for practical purpose.

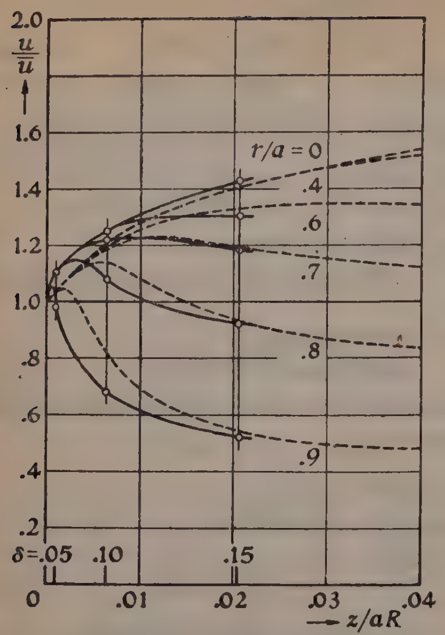

Fig. 3. Variation of velocity distribution along the inlet-length.

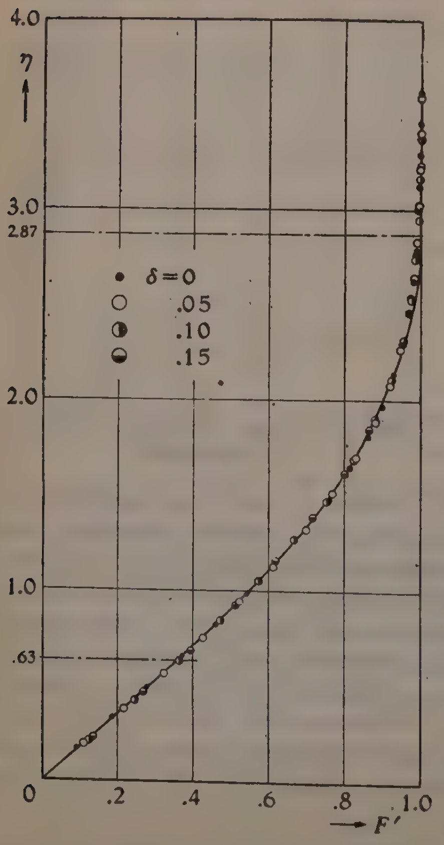

Fig. 4. Similarity of nondimensional velocity profile. Full line represents approximated profile.

Fig. 4 shows non-dimensional velocity profiles plotted against η, from which it may be seen that our assumption of almost similarity of the profile is completely satisfied. Finally, it should be noted that these similar profiles can be approximated by a curve which consist of two straight and a parabolic segments as follows:

$$\left.\begin{aligned}&u/u_1=0.571\,\eta, && 0\leqq\eta\leqq0.63,\\ &u/u_1=1-(1.025-0.357\,\eta)^2, && 0.63\leqq\eta\leqq2.87,\\ &u/u_1=1, && 2.87\leqq\eta.\end{aligned}\right\}\quad(3.\ 14)$$

§ 4. Solution by Series Expansion

In order to obtain an accurate expression for the curvature of the velocity profile, which will be found to play an important role in Part II, we study a solution of (2. 15) by series expansion. If we develop F in powers of Y, we have

$$F=Y^2(a_0+a_1Y+a_2Y^2+\cdots)\,,\qquad(4.\ 1)$$

and substituting this into (2. 15), equations for the a's are found by equating the coefficients of the several powers of Y to zero. Thus,

$$\left.\begin{aligned}a_1&=\frac{\delta}{3}(1-2Aa_0)\,,\\ a_2&=-\frac{\delta^2}{3}A(1-2Aa_0)\,,\\ a_3&=\left(-\frac{1}{30}+\frac{2}{15}\delta\right)a_0^2\\ &\quad-\frac{2}{5}\delta^3A^2(1-2Aa_0)\,,\end{aligned}\right\}\quad(4.\ 2)$$

where a_0 is to be determined in such a way that F satisfies the condition $F'(B)=1$. If, for such values of $a_0(=F'(0))$, we use those obtained by iteration method, the a's are given by (4. 2), and the profile $U=u/\bar{u}$, its gradient and curvature are represented respectively by

$$U=F'=(2a_0A)\eta+(3a_1A^2)\eta^2+(4a_2A^3)\eta^3+(5a_3A^4)\eta^4+\cdots,\qquad(4.\ 3)$$

$$\frac{dU}{d\eta}=F''A=(2a_0A)+(6a_1A^2)\eta+(12a_2A^3)\eta^2+(20a_3A^4)\eta^3+\cdots,\qquad(4.\ 4)$$

$$\frac{d^2U}{d\eta^2}=F'''A=(6a_1A^2)+(24a_2A^3)\eta+(60a_3A^4)\eta^2+\cdots,\qquad(4.\ 5)$$

Table 3 gives the coefficients of these series for $\delta=0$, 0.05, 0.1 and 0.15.

Table 3.

δ	0	0.05	0.1	0.15
$2a_0A$	0.5714	0.5892	0.5996	0.6057
$6a_1A^2$	0	−0.0461	−0.0719	−0.0886
$12a_2A^3$	0	−0.0052	−0.0128	−0.0199
$20a_3A^4$	−0.0806	−0.0524	−0.0346	−0.0228
$6a_1A^2$	0	−0.0461	−0.0719	−0.0886
$24a_2A^3$	0	−0.0103	−0.0257	−0.0398
$60a_3A^4$	−0.2417	−0.1573	−0.1039	−0.0684

In the limiting case when $\delta=0$, our profile is identical with Blasius' one, and our series expansion:

$$U(\eta)=0.5714\,\eta-0.0201\,\eta^4\cdots$$

should be equal to Lin's expression:

$$W(y)=2y-3y^4=0.5734\,\eta-0.0203\,\eta^4,$$

(since $y=0.2867\,\eta$ in his notation). Agreement between these two is quite satisfactory.

References

1) J. v. Neumann: 'Recent theories of turbulence,' (unpublished).

2) H. Schlichting: Ann. d. Phys. **14** (1932) 905.

3) J. Boussinesq: Compt. Rend. **113** (1991) 9, 49.

4) J. Nikuradse: (unpublished). Cf. Prandtl and Tietjens: Hydro-und Aeromechanik, Bd. 2 (Berlin, 1931) 28.

5) L. Schiller: ZS. angew. Math. Mech. **2** (1922) 96.

6) Atkinson and Goldstein: (unpublished). Cf. Goldstein: Modern developments in fluid dynamics, vol. 1 (Oxford, 1938) 304.

7) H. Schlichting: ZS. angew. Math. Mech. **14** (1934) 368.

8) D.R. Hartree: Proc. Camb. Phil. Soc. **33** (1937).

JOURNAL OF THE PHYSICAL SOCIETY OF JAPAN Vol. 7, No. 5, SEPT.—OCT., 1952

Stability of the Laminar Inlet-flow prior to the Formation of Poiseuille Régime, II

By Tomomasa TATSUMI

Department of Physics, Faculty of Science, University of Kyoto

(Received June 4, 1952)

As a continuation of Part I, the stability of the inlet-flow is now discussed, obtaining the result that there exists a stability limit whose minimum critical Reynolds number is 9700 at the point 17 times of the radius of tube downstream from its entrance.

Part II. Stability of the Inlet-flow

§ 5. The Equation for First Order Disturbance

Using the same symbols as in Part I, the equation of motion for the flow symmetrical about an axis is given by

$$\left.\begin{aligned}&\frac{\partial}{\partial t}(\nabla^2\psi)+\frac{1}{r}\frac{\partial(\psi,\nabla^2\psi)}{\partial(r,z)}+\frac{2}{r^2}\frac{\partial\psi}{\partial z}\nabla^2\psi=\nu\Delta^4\psi,\\ &\text{with}\qquad \nabla^2\equiv\frac{\partial^2}{\partial r^2}-\frac{1}{r}\frac{\partial}{\partial r}+\frac{\partial^2}{\partial z^2}.\end{aligned}\right\}\tag{5.1}$$

Now, we divide all velocities into two parts, by putting

$$\psi=\Psi(r,z)+\psi_*(r,z,t),\tag{5.2}$$

or

$$\left.\begin{aligned}&u=U+u_*,\quad v=V+v_*,\\ &U=-\frac{1}{r}\frac{\partial\Psi}{\partial r},\quad V=\frac{1}{r}\frac{\partial\Psi}{\partial z};\\ &u_*=-\frac{1}{r}\frac{\partial\psi_*}{\partial r},\quad v_*=\frac{1}{r}\frac{\partial\psi_*}{\partial z},\end{aligned}\right\}\tag{5.3}$$

where capital letters refer to the steady main flow and letters with asterisk the disturbance.

In our problem, we find *a posteriori* that the main flow is essentially parallel to the z-axis for high Reynolds numbers. It may be allowed, therefore, instead of studying the stability of the inlet-flow itself, to deal with the stability of pure parallel flows which have the same velocity profiles $U=U(r)$, $V=0$, as those at each point of the inlet-length.

If we substitute (5.2) into (5.1) the terms corresponding to the main flow cancel out. Then, using the boundary-layer approximation and dropping, by the assumption of small disturbancc, the terms quadratic in ψ_* and its derivatives, we have the linear differential equation for ψ_* as:

$$\left(\frac{\partial}{\partial t}+U\frac{\partial}{\partial z}\right)\nabla^2\psi_* -\left(\frac{d^2U}{dr^2}-\frac{1}{r}\frac{dU}{dr}\right)\frac{\partial\psi_*}{\partial z}=\nu\nabla^4\psi_* . \qquad (5.4)$$

Since this equation is linear, we may regard ψ_* as a linear combination of spatially periodic components, and we may consider the behaviour of any one of them, instead of the resultant ψ_*. Such a Fourier component may be represented by the stream function $\psi_*=\phi(r)\exp[i\alpha(z-ct)]$, and the differential equation for ϕ is readily found to be

$$\left.\begin{aligned}&(U-c)D^2\phi-\left(\frac{d^2U}{dr^2}-\frac{1}{r}\frac{dU}{dr}\right)\phi=\frac{\nu}{i\alpha}D^4\phi\,,\\ &\text{with}\qquad D^2\equiv\frac{d^2}{dr^2}-\frac{1}{r}\frac{d}{dr}-\alpha^2 .\end{aligned}\right\} \qquad (5.5)$$

We take α to be always real and positive, while c may be complex so that $c=c_r+ic_i$. If all velocities are referred to $U_{\max}$ $(=u_1$ in Part I), and all lengths to a, and moreover, if the variable y defined in (2.3) is introduced, equation (5.5) can be written in the form:

$$(U-c)\left[(1-2y)\frac{d^2}{dy^2}-\alpha^2\right]\phi-(1-2y)\frac{d^2U}{dy^2}\phi =\frac{1}{i\alpha R_1}\left[(1-2y)\frac{d^2}{dy^2}-\alpha^2\right]^2\phi\,, \qquad (5.6)$$

where $R_1=aU_{\max}/\nu$ is defined as the local Reynolds number of the flow. Further, replacing the variable y by η as defined in (2.9), equation (5.6) becomes

$$(U-c)\left[(1-2\delta\eta)\frac{d^2}{d\eta^2}-\alpha_*^2\right]\phi-(1-2\delta\eta)U''\phi =\frac{1}{i\alpha_*R_*}\left[(1-2\delta\eta)\frac{d^2}{d\eta^2}-\alpha_*^2\right]^2\phi\,, \qquad (5.7)$$

where $\alpha_*=\alpha\delta$ and $R_*=\delta R_1$. Here and in what follows, dashes denote differentiation with respect to η.

Disturbance velocities u_* and v_* given by (5.3) to gether with $\psi_*=\phi(r)\exp[i\alpha(z-ct)]$ as:

$$u_*=\delta^{-1}\phi'(\eta)\exp[i\alpha(z-ct)]\,,$$

$$v_*=i\alpha(1-2\delta\eta)^{-1/2}\phi(\eta)\exp[i\alpha(z-ct)]\,,$$

should vanish on the solid boundary and should be finite over the whole region of flow. Equation (5.7) is, therefore, to be solved under the boundary conditions

$$\left.\begin{aligned}&\phi=0,\ \phi'=\text{finite at }\eta=1/2\delta,\ (r=0)\\ &\phi=\phi'=0\qquad\ \text{at }\eta=0.\qquad (r=1)\end{aligned}\right\} \qquad (5.8)$$

Since (5.7) has four independent solutions, these four boundary conditions lead to a secular equation for determining a relationship between parameters α, c and R_1. If c_i is turned to be positive the disturbence is unstable, while if c_i is negative disturbance is stable.

The Reynolds number for transition phenomena is usually very large, and αR_1 is also large even when α is small. Hence, for finding solutions of (5.7) for high values of αR_1, the so-called 'inviscid equation' corresponding to $\alpha R_1\to\infty$:

$$(U-c)[(1-2\delta\eta)\phi''-\alpha_*^2\phi]-(1-2\delta\eta)U''\phi=0 \qquad (5.9)$$

plays an important role under some necessary cares.

§ 6. Asymptotic Solution

A method for obtaining solutions of equation (5.7) for high values of αR_1 or α_*R_* has been developed by Heisenberg (**9**), Tietjens (**10**), Tollmien (**11**) and Schlichting (**12**) during the period 1924–35. Recently, Lin (**13**) has made a revision of the mathematical method, clarifying some points that had been adversely criticized. The method appears now to have been almost settled, and therefore, we shall here make use of the method for obtaining appropriate solutions necessary for our present problem.

For high values of α_*R_* the problem can be attacked by the use of asymptotic series. Asymptotic solutions are divided into two groups, i.e. into 'inviscid solution' and 'boundary-layer solution', according to different kinds of asymptotic series.

(*a*) *Inviscid solution.* If we develop ϕ in powers of $(\alpha_*R_*)^{-1}$ as:

$$\phi=\phi^{(0)}+(\alpha_*R_*)^{-1}\phi^{(1)}+\ldots\ldots ,$$

and substitute it in (5.7), we get the inviscid equation (5.9) to be satisfied by $\phi^{(0)}$, namely:

$$\phi^{(0)\prime\prime}-\left(\frac{U''}{U-c}+\frac{\alpha_*^2}{1-2\delta\eta}\right)\phi^{(0)}=0. \qquad (6.1)$$

As a first approximation we may use $\phi^{(0)}$ which can be obtained from (6.1) in the form of power series of α_*^2. Two particular solutions of (6.1) are given by

$$\left.\begin{aligned}\phi_1&=\phi_1^{(0)}=(U-c)[k_0+\alpha_*^2k_2(\eta)+\ldots],\\ \phi_2&=\phi_2^{(0)}=(U-c)[k_1(\eta)+\alpha_*^2k_3(\eta)+\ldots],\end{aligned}\right\} \qquad (6.2)$$

where $k_0=1,\quad k_1(\eta)=\int\frac{d\eta}{(U-c)^2}$,

$$k_n(\eta)=\int\frac{d\eta}{(U-c)^2}\int\frac{(U-c)^2}{1-2\delta\eta}k_{n-2}(\eta)d\eta \quad (n\geqq 2).$$

As will be seen immediately, equation (6.1) has a singularity at the point $\eta=\eta_c$ where $U-c=0$, and therefore, we shall now discuss the behaviour of the above formal solutions at this singular point.

Near the singular point $\eta=\eta_c$,

$$U-c\approx U_c'\eta_1+\frac{U_c''}{2\,!}\eta_1^2, \quad (\text{with } \eta_1=\eta-\eta_c)$$

and ϕ_1, ϕ_2 can be expanded in power series of η_1 as:

$$\left.\begin{aligned}\phi_1&\approx U_c'\left(\eta_1+\frac{U_c''}{2U_c'}\eta_1^2+\ldots\right),\\ \phi_2&\approx-\frac{1}{U_c'}\left(1+\frac{U_c''}{U_c'}\eta_1\log\eta_1+\ldots\right)\end{aligned}\right\} \qquad (6.3)$$

Thus, it will be seen that ϕ_1 is regular for all values of η_1, while ϕ_2 is a many-valued function, having the differential coefficient logarithmically infinite at $\eta_1=0$. This point $\eta_1=0$ is, however, merely an ordinary point in the exact equation (5.7), and an exact solution, if any, should be a single-valued function. So far as ϕ_2 is concerned, therefore, the inviscid solution does not seem to be taken as a good approximation in the neighbourhood of the critical point and should be replaced by an exact solution.

(b) *Boundary-layer solution.* In order to find other two asymptotic solutions of (5.7), we first make the transformation:

$$\phi=\exp\left[\int g\,dn\right]. \qquad (6.4)$$

Then, the equation for g becomes

$$\begin{aligned}&(U-c)[(1-2\delta\eta)(g^2+g')-\alpha_*^2]-(1-2\delta\eta)U''\\ &=\frac{1}{i\alpha_*R_*}[(1-2\delta\eta)^2(g^4+6g^2g'+3g'^2+4gg''+g''')\\ &\qquad-4\delta(1-2\delta\eta)(g^3+3gg'+g'')\\ &\qquad-2\alpha_*^2(1-2\delta\eta)(g^2+g')+\alpha_*^4]. \qquad (6.5)\end{aligned}$$

We now try to find a solution g of this equation in the form of power series of $(\alpha_*R_*)^{-1/2}$:

$$g=(\alpha_*R_*)^{1/2}g_0+g_1+(\alpha_*R_*)^{-1/2}g_2+\ldots. \qquad (6.6)$$

Substituting this series into equation (6.5) and equating the coefficients of various powers of $(\alpha_*R_*)^{1/2}$ on both sides, we obtain a set of equations for $g_0, g_1, \ldots$ as:

$$\left.\begin{aligned}&(U-c)g_0^2=-i(1-2\delta\eta)g_0^4,\\ &(U-c)(2g_0g_1+g_0')\\ &\quad=-i[(1-2\delta\eta)(4g_0^3g_1+6g_0^2g_0')-4\delta g_0^3],\\ &\quad\cdots\qquad\cdots\qquad\cdots\end{aligned}\right\} \qquad (6.7)$$

from which it follows immediately

$$g_0=\pm\sqrt{\frac{i(U-c)}{1-2\delta\eta}},\quad g_1=-\frac{5}{2}\frac{g_0'}{g_0}+\frac{2\delta}{1-2\delta\eta}. \qquad (6.8)$$

Hence, we obtain the two asymptotic solutions

$$\left.\begin{aligned}\phi_3\\ \phi_4\end{aligned}\right\}=(1-2\delta\eta)^{1/4}(U-c)^{-5/4}$$

$$\times\exp\left[\mp\int_{\eta_c}\sqrt{\frac{i\alpha_*R_*(U-c)}{1-2\delta\eta}}d\eta\right], \qquad (6.9)$$

where quantities of the order of $(\alpha_*R_*)^{-1/2}$ have been neglected. Due to large values of α_*R_*, ϕ_3,ϕ_4 are always of rapid variation, so that in order to secure their finiteness in the fluid region they must have a non-vanishing value only in the immediate vicinity of the solid boundary.

The critical point η_c; which is a logarithmic branch-point in the preceding case (a), is here an algebraic branch-point. Infinity and multivaluedness occur at η_c as before, and these questions also will be discussed in the next section.

§7. Inner Friction-layer Solution

As mentioned above, the inviscid and the boundary-layer solutions have a logarithmic singularity and an algebraic one respectively at the critical point η_c which is however merely an ordinary point of equation (5.7). Near the point η_c, therefore, these solutions must be replaced by exact solutions, and a proper path around their singularity should be determined uniquely as corresponding to that of the regular solution. For this purpose we attempt to see the behaviour of exact solutions of (5.7) in the neighbourhood of the critical point which is called usually the 'inner friction-layer', by introducing a new variable:

$$\zeta=\varepsilon^{-1}\eta_1=\left(\frac{\alpha_* R_* U_c'}{1-2\delta\eta_c}\right)^{1/3}(\eta-\eta_c). \qquad (7.1)$$

Near the point η_c, we may use the expansion:

$$U-c=U_c'(\varepsilon\zeta)+\frac{U_c''}{2\,!}(\varepsilon\zeta)^2+\dots, \qquad (7.2)$$

and develop ϕ in powers of ε as:

$$\phi(\eta_1)=\chi(\zeta)=x^{(0)}+\varepsilon\chi^{(1)}+\varepsilon^2\chi^{(2)}+\dots. \qquad (7.3)$$

Substituting (7.2) and (7.3) into (5.7), and equating the coefficients of several powers of ε to zero, we obtain equations for χ's in the forms:

$$\left.\begin{aligned} &i\frac{d^4\chi^{(0)}}{d\zeta^4}+\zeta\frac{d^2\chi^{(0)}}{d\zeta^2}=0, \\ &i\frac{d^4\chi^{(n)}}{d\zeta^4}+\zeta\frac{d^2\chi^{(n)}}{d\zeta^2}=L_n(\chi^{(n-1)}), \ (n\geqq 1) \end{aligned}\right\} \qquad (7.4)$$

where for instance

$$L_1(\chi^{(0)})=\frac{U_c''}{U_c'}\left(\chi^{(0)}-\frac{\zeta^2}{2}\frac{d^2x^{(0)}}{d\zeta^2}\right) +2\delta i(1-2\delta\eta_c)\left(\zeta\frac{d^4\chi^{(0)}}{d\zeta^4}+2\frac{d^3\chi^{(0)}}{d\zeta^3}\right).$$

Four particular solutions of (7.4) are composed of

$$\left.\begin{aligned} &\chi_1^{(0)}=\zeta, \quad \chi_3^{(0)}=\int d\zeta\int h_1(\zeta)d\zeta, \\ &\chi_2^{(0)}=1, \quad \chi_4^{(0)}=\int d\zeta\int h_2(\zeta)d\zeta, \\ &x_i^{(n)}=\frac{\pi}{6}\int d\zeta\int\Big[h_2\int h_1L_n(\chi_i^{(n-1)})d\zeta \\ &\qquad -h_1\int h_2L_n(\chi_i^{(n-1)})d\zeta\Big]d\zeta, \\ &\qquad\qquad (i=1\sim 4), \end{aligned}\right\} (7.5).$$

where h's are functions related to Hankel functions as:

$$h_{1,2}(\zeta)=\zeta^{1/2}H_{1/3}^{(1),(2)}\left[\frac{2}{3}(i\zeta)^{3/2}\right]. \qquad (7.6)$$

Having thus obtained four regular solutions in the friction-layer, we can proceed to correlating them with the asymptotic solutions (6.2) and (6.9), and to the correct determination of a path around the singularity. The regular and the asymptotic solutions should be connected in a region where both of them are valid with sufficient accuracy.

Making use of the asymptotic expansion formulae of $H_{1/3}^{(1)}$ and $H_{1/3}^{(2)}$:

$$\left.\begin{aligned} &H_{1/3}^{(1)}\left[\frac{2}{3}(i\zeta)^{3/2}\right]\sim\left(\frac{3}{\pi}\right)^{1/2}(i\zeta)^{-3/4} \\ &\qquad\times\exp\left[\frac{2}{3}\zeta^{3/2}e^{5/4\pi i}-\frac{5}{12}\pi i\right], \\ &\qquad\left(-\frac{7}{6}\pi<\arg\zeta<\frac{5}{6}\pi\right), \\ &H_{1/3}^{(2)}\left[\frac{2}{3}(i\zeta)^{3/2}\right]\sim\left(\frac{3}{\pi}\right)^{1/2}(i\zeta)^{-3/4} \\ &\qquad\times\exp\left[\frac{2}{3}\zeta^{3/2}e^{1/4\pi i}+\frac{5}{12}\pi i\right], \\ &\qquad\left(-\frac{11}{6}\pi<\arg\zeta<\frac{\pi}{6}\right). \end{aligned}\right\} \qquad (7.7)$$

the χ's reduce to, for large values of ζ,

$$\left.\begin{aligned} &\chi_1\sim\zeta+\frac{\varepsilon}{2}\frac{U_c''}{U_c'}\zeta^2, \\ &\chi_2\sim 1+\varepsilon\frac{U_c''}{U_c'}\zeta\log\zeta. \\ &\chi_3\sim\zeta^{-5/4}\exp\left[\frac{2}{3}\zeta^{3/2}e^{5/4\pi i}\right], \\ &\chi_4\sim\zeta^{-5/4}\exp\left[\frac{2}{3}\zeta^{3/2}e^{1/4\pi i}\right]. \end{aligned}\right\} \qquad (7.8)$$

Bearing the relation (7.1) in mind it can be seen that in the region under consideration the functions χ_1, χ_2 are respectvely the same as ϕ_1, ϕ_2 as given in (6.3) except for constant multipliers.

In evaluating the asymptotic expression (7.8) the argument of ζ must satisfy both the conditions specified in (7.7) which, when combined together, may be written as:

$$-\pi<\arg\zeta<\frac{\pi}{6}. \qquad (7.9)$$

Hence, the argument of the real negative ζ or η_1 must be $-\pi$, so that the branch of ϕ_2 is determined to be

$$\phi_2\sim-\frac{1}{U_c'}\left[1+\frac{U_c''}{U_c'}\eta_1(\log|\eta_1|-\pi i)\right], \qquad \eta_1<0. \qquad (7.10)$$

For the boundary-layer solutions, we obtain the following forms near the inner layer:

$$\left.\begin{aligned} &\phi_3\approx\text{const. }\eta_1^{-5/4}\exp\left[-\frac{2}{3}i^{1/2}\varepsilon^{-3/2}\eta_1^{2/3}\right], \\ &\phi_4\approx\text{const. }\eta_1^{-5/4}\exp\left[\frac{2}{3}i^{1/2}\varepsilon^{-3/2}\eta_1^{3/2}\right], \end{aligned}\right\}$$

from which it will be seen that these are the same functions as χ_3 and χ_4 respectively in the region under consideration. Multivaluedness and infinity of ϕ_3, ϕ_4 are also secured by the condition (7.9) and replacing χ_3, χ_4 for them respectively in the inner layer. The correct branches of ϕ_3, ϕ_4 for real η_1 are then found to be

$$\left.\begin{aligned}
&\phi_3\sim\text{const. }\eta_1^{-5/4}\exp\left[\frac{2}{3}\left(\frac{\eta_1}{\varepsilon}\right)^{3/2}e^{5/4\pi i}\right], \\
&\qquad\qquad\qquad\qquad\qquad \eta_1>0, \\
&\phi_3\sim\text{const. }|\eta_1|^{-5/4} \\
&\quad\times\exp\left[\frac{2}{3}\left|\frac{\eta_1}{\varepsilon}\right|^{3/2}e^{-1/4\pi i}+\frac{5}{4}\pi i\right];\ \eta_1<0; \\
&\phi_4\sim\text{const. }\eta_1^{-5/4}\exp\left[\frac{2}{3}\left(\frac{\eta_1}{\varepsilon}\right)^{3/2}e^{1/4\pi i}\right], \\
&\qquad\qquad\qquad\qquad\qquad \eta_1<0, \\
&\phi_4\sim\text{const. }|\eta_1|^{-5/4} \\
&\quad\times\exp\left[\frac{2}{3}\left|\frac{\eta_1}{\varepsilon}\right|^{3/2}e^{-5/4\pi i}+\frac{5}{4}\pi i\right],\ \eta_1<0,
\end{aligned}\right\} \tag{7.12}$$

§ 8. Solution in the Central Region

As far as the velocity profile has the constant-velocity core $U=1$, we have $U''=0$ there. In this region equation (5.7) reduces to

$$\left[(1-2\delta\eta)\frac{d^2}{d\eta^2}-\alpha_*^2\right]\left[(1-2\delta\eta)\frac{d^2}{d\eta^2}-\alpha_*^2-i\alpha_*R_*(1-c)\right]\phi=0, \tag{8.1}$$

which is separated into two second order differential equations as:

$$\left[(1-2\delta\eta)\frac{d^2}{d\eta^2}-\alpha_*^2\right]\phi=0, \tag{8.2}$$

and

$$\left[(1-2\delta\eta)\frac{d^2}{d\eta^2}-\delta^2\beta^2\right]\phi=0, \tag{8.3}$$

where $\beta^2=\alpha^2+i\alpha R_1(1-c)$.

Four particular solutions $\phi=\omega_i$ $(i=1\sim4)$ of these two equations are easily found to be given respectively by

$$\begin{pmatrix}\omega_1\\ \omega_2\end{pmatrix}=(i\alpha)^{-1}(1-2\delta\eta)^{1/2}\begin{pmatrix}J_1\\ N_1\end{pmatrix}[i\alpha(1-2\delta\eta)^{1/2}], \tag{8.4}$$

and

$$\begin{pmatrix}\omega_3\\ \omega_4\end{pmatrix}=(i\beta)^{-1}(1-2\delta\eta)^{1/2}\begin{pmatrix}J_1\\ N_1\end{pmatrix}[i\beta(1-2\delta\eta)^{1/2}], \tag{8.5}$$

where J and N denote Bessel and Neumann functions respectively.

It is to be noted that in the central region, equation (8.2) is equal to the inviscid equation (5.9), so that ω_1, ω_2 are nothing but the inviscid solutions in this region.

§ 9. Eigenvalue Problem

Having thus obtained four asymptotic solution ϕ's as the first approximation for four particular solutions of (5.7) for large αR_1, we shall next proceed to the formulation of eigenvalue problem.

In the first place, we seek for such solutions that satisfy the first condition in (5.8). In the central region the functions ϕ's become equal to the ω's, of which only ω_1 and ω_3 satisfy the said condition. Hence, appropriate eigenfunctions must be such two linear combinations of ϕ's:

$$\left.\begin{aligned}\Phi_1&=c_1\phi_1+c_2\phi_2,\\ \Phi_2&=c_3\phi_3+c_4\phi_4,\end{aligned}\right\} \tag{9.1}$$

that satisfy the conditions

$$\left.\begin{aligned}\Phi_{1b}&=\omega_{1b}, \quad \Phi'_{1b}=\omega'_{1b};\\ \Phi_{2b}&=\omega_{3b}, \quad \Phi'_{2b}=\omega'_{3b},\end{aligned}\right\} \tag{9.2}$$

where suffix b refers to the values of function at a certain point $\eta=b$ in the central region.

For Φ_{1b}, we have from (8.4)

$$\left.\begin{aligned}&c_1\phi_{1b}+c_2\phi_{2b}\\ &\qquad=(i\alpha)^{-1}(1-2\delta b)^{1/2}J_1[i\alpha(1-2\delta b)^{1/2}],\\ &c_1\phi'_{1b}+c_2\phi'_{2b}=-\delta J_0[i\alpha(1-2\delta b)^{1/2}],\end{aligned}\right\} \tag{9.3}$$

so that

$$\left.\begin{aligned}c_1&=(\alpha\Delta)^{-1}J_0[i\alpha(1-2\delta b)^{1/2}](\alpha_*\phi_{2b}+p\phi'_{2b}),\\ c_2&=-(\alpha\Delta)^{-1}J_0[i\alpha(1-2\delta b)^{1/2}](\alpha_*\phi_{1b}+p\phi'_{1b}),\end{aligned}\right\} \tag{9.4}$$

where

$$\left.\begin{aligned}\Delta&=\begin{vmatrix}\phi_{1b} & \phi_{2b}\\ \phi'_{1b} & \phi'_{2b}\end{vmatrix};\\ p&=(1-2\delta b)^{1/2}\times\frac{J_1[i\alpha(1-2\delta b)^{1/2}]}{iJ_0[i\alpha(1-2\delta b]^{1/2}]}\end{aligned}\right\} \tag{9.5}$$

For Φ_{2b}, we have from (6.9)

$$\begin{aligned}&c_3\phi_{3b}+c_4\phi_{4b}\\ &\approx c_3'(1-2\delta b)^{1/4}\exp[\sqrt{i\alpha R_1(1-c)}(1-2\delta b)^{1/2}]\\ &+c_4'(1-2\delta b)^{1/4}\exp[-\sqrt{i\alpha R_1(1-c)}(1-2\delta b)^{1/2}],\end{aligned} \tag{9.6}$$

where c_3' and c_4' are constants related to c_3 and c_4 respectively.

On the other hand, we have from (8.5)

$$\begin{aligned}\omega_{3b}&=\text{const. }(1-2\delta b)^{1/2}J_1[i\alpha(1-2\delta b)^{1/2}]\\ &\sim c_3''(1-2\delta b)^{1/4}\\ &\quad\times\exp[\sqrt{\alpha^2+i\alpha R_1(1-c)}(1-2\delta b)^{1/2}]\\ &\quad+c_4''(1-2\delta b)^{1/4}\\ &\quad\times\exp[-\sqrt{\alpha^2+i\alpha R_1(1-c)}\,(1-2\delta b)^{1/2}],\end{aligned} \tag{9.7}$$

where c_3'' and c_4'' are constants that can be easily obtained from the asymptotic expansion of J. Comparing (9.6) with (9.7) and remembering that $\alpha^2 \ll \alpha R_1$, we can formally construct Φ_2 as a linear combination corresponding to $c_3'=c_3''$, $c_4'=c_4''$.

In the second place, the functions Φ_1 and Φ_2 must satisfy another boundary condition in (5.8), so that we have

$$\Phi_{10}+\Phi_{20}=0, \quad \Phi_{10}'+\Phi_{20}'=0,$$

or

$$\frac{\Phi_{10}}{\Phi_{10}'}=\frac{\Phi_{20}}{\Phi_{20}'}. \tag{9.8}$$

Now it is readily verified that the real part of

$$\int_0^{\eta_c}\sqrt{\frac{i\alpha_* R_*(U-c)}{1-2\delta\eta}}\,d\eta$$

is always positive when $c_i>0$ (cf. Lin (**13**) p. 136). Hence, ϕ_{40} may be neglected in comparison with ϕ_{30} for large αR_1, and

$$\Phi_{20} \approx \text{const. } \phi_{30}$$

Hence, equation (9.8) reduces to

$$\begin{aligned}\frac{\phi_{30}}{\phi_{30}'}&=\frac{c_1\phi_{10}+c_2\phi_{20}}{c_1\phi_{10}'+c_2\phi_{20}'}\\ &=\frac{(\alpha_*\phi_{2b}+p\phi_{2b}')\phi_{10}-(\alpha_*\phi_{1b}+p\phi_{1b}')\phi_{20}}{(\alpha_*\phi_{2b}+p\phi_{2b}')\phi_{10}'-(\alpha_*\phi_{1b}+p\phi_{1b}')\phi_{20}'}\\ &\equiv E(\alpha,\ c\,;\ \delta).\end{aligned} \tag{9.9}$$

Since, in the limiting case of $\alpha R_1 \to \infty$, it is verified that the neutral solution is only possible when $c_r=0$, it would be natural to expect c_r to be small for large αR_1, as will be confirmed *a posteriori*. In such a case the inner friction-layer is in the immediate vicinity of the solid boundary, and it is more accurate to replace ϕ_3 by $\chi_3(\zeta)$ as given by (7.5). Thus we have arrived at a secular equation:

$$F(\zeta_0)=-\frac{1}{\eta_c}E(\alpha,\ c\,;\ \delta), \tag{9.10}$$

where

$$F(\zeta_0)\equiv\frac{\chi_{30}}{\zeta_0(d\chi_3/d\zeta)_0},$$

and

$$\zeta_0=-\left(\frac{\alpha_* R_* U_0'}{1-2\delta\eta_c}\right)^{1/3}\eta_c.$$

The value of the function $F(\zeta_0)$ has been calculated numerically by Tietjens (**10**) and recently by Lin (**13**).

Putting

$$\mathbf{F}(\zeta_0)\equiv[1-F(\zeta_0)]^{-1},$$

the secular equation (9.10) can also be written as:

$$\begin{aligned}\mathbf{F}(\zeta_0)&=\frac{(\alpha_*\phi_{2b}+p\phi_{2b}')\eta_c\phi_{10}'-(\alpha_*\phi_{1b}+p\phi_{1b}')\eta_c\phi_{20}'}{(\alpha_*\phi_{2b}+p\phi_{2b}')(\phi_{10}+\eta_c\phi_{19}')-(\alpha_*\phi_{1b}+p\phi_{1b}')(\phi_{20}+\eta_c\phi_{20}')}\\ &\equiv\mathbf{E}(\alpha,\ c\,;\ \delta).\end{aligned} \tag{9.11}$$

The value of $\mathbf{F}(\zeta_0)$ has also been calculated by Lin.

§ 10 Numerical Results and Summary

Numerical work has been carried out for several cases in which $\delta=0$, 0.03, 0.05, 0.07, 0.08, 0.09 and 0.1 respectively, the velocity profiles of main flow corresponding to $\delta=0.03$, 0.07, 0.08 and 0.09 having been obtained by numerical interpolation from those corresponding to $\delta=0$, 0.05, 0.1 and 0.15.

Calculation of $\mathbf{E}(\alpha,\ c\,;\ \delta)$ has been made following essentially Lin's procedure (cf. Appendix of (**13**)). Corresponding to real c, $\mathbf{E}(\alpha,\ c\,;\ \delta)$ represents a group of curves in the complex plane. On the other hand, the known function $\mathbf{F}(\zeta_0)$ gives a curve in the same plane. Then, it is obvious from (9.11) that the points of intersection of these two sets of curves are sufficient enough to determine the neutral curve $\alpha(R_1)$ for each δ.

In the limit $\alpha^2 \to 0$, $\mathbf{E}(\alpha,\ c\,;\ \delta)$ reduces to

$$\mathbf{E}(0,\ c\,;\ \delta)=\left[K_1(c)+\frac{1-2\delta b}{2\delta}\,\frac{1}{(1-c)^2}\right]U_0'c+1, \tag{10.1}$$

where $K_1(c)=k_1((2\delta)^{-1})$.

Asymptotic behaviours of the $\alpha(R_1)$ curve as $\alpha^2 \to 0$ are then found from the equation:

$$\mathbf{F}(\zeta_0)=\mathbf{E}(0,\ \alpha\,;\ \delta),$$

and tabulated in Table 4.

Table 4

δ	R_*	
0.03	$1.01\times10^3 \cdot \alpha_*^{-1}$	……
0.05	$2.18\times10^2 \cdot \alpha_*^{-1}$	$1.03\times10^4 \cdot \alpha_*^{-1}$
0.07	$1.85\times10^2 \cdot \alpha_*^{-1}$	$2.86\times10^3 \cdot \alpha_*^{-1}$
0.08	$1.69\times10^2 \cdot \alpha_*^{-1}$	$1.72\times10^3 \cdot \alpha_*^{-1}$
0.09	$1.78\times10^2 \cdot \alpha_*^{-1}$	$1.01\times10^3 \cdot \alpha_*^{-1}$
0.1	$2.39\times10^2 \cdot \alpha_*^{-1}$	$4.34\times10^2 \cdot \alpha_*^{-1}$

Table 5

δ											
0		0.03		0.05		0.07		0.08		0.09	
α_*	R_*	α_*	R_*	α_*	R_*	α_*	R_*	α_*	R_*	α_*	R_*
0.155	1.08×10^3	0.13	1.30×10^3	0.165	8.72×10^2	0.16	9.13×10^2	0.12	1.25×10^3	0.105	1.63×10^3
0.205	7.17×10^2	0.195	6.97×10^2	0.213	6.76×10^2	0.205	7.95×10^2	0.17	1.01×10^3	0.135	1.59×10^3
0.24	6.42×10^2	0.235	6.06×10^2	0.25	6.61×10^4	0.23	8.91×10^2	0.193	1.08×10^3	0.14	2.06×10^3
0.27	6.67×10^2	0.275	6.05×10^2	0.27	7.47×10^2	0.23	1.19×10^3	0.195	1.48×10^3	0.12	3.54×10^3
0.29	7.48×10^2	0.295	7.04×10^2	0.275	9.81×10^2	0.215	1.86×10^3	0.18	2.29×10^3	0.075	9.33×10^3
0.29	9.55×10^2	0.30	8.88×10^2	0.26	1.51×10^3	0.18	3.44×10^3	0.15	4.36×10^3		
0.28	1.37×10^3	0.285	1.30×10^3	0.235	2.55×10^3	0.14	$7.75\times.0^3$	0.085	1.38×10^4		
0.265	2.00×10^3	0.255	2.20×10^3	0.2	4.97×10^3						
0.24	3.38×10^3	0.225	3.86×10^3								
0.21	6.03×10^3	0.19	8.10×10^3								
0.18	1.20×10^4	0.145	2.01×10^4								
0.155	2.19×10^4	0.11	5.08×10^4								
R_{*c}											
640		590		650		790		1000		1490	
R_c											
∞		1.85×10^4		1.17×10^4		9.72×10^3		1.05×10^4		1.36×10^4	

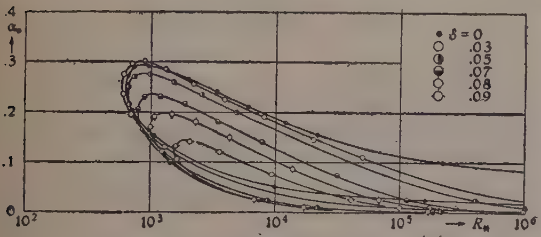

Fig. 5. Curves of neutral stability for the inlet-flow.

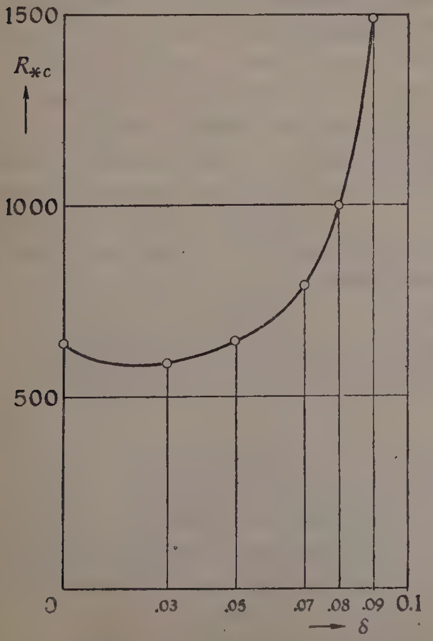

Fig. 6. Critical values of the local Reynolds number R_* for each δ.

The numerical results for constructing the neutral curve are tabulated in Table 5 and are shown graphically in Fig. 5. The critical values, R_{*c} say, of the Reynolds number R_* are given in Fig. 6 for each δ, which shows that R_{*c} increases generally with increasing δ and tends to infinity at $\delta=0.1$, indicating that there is no region of instability above it.

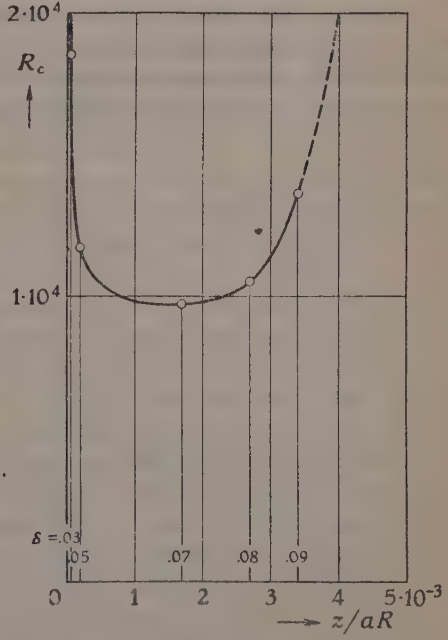

Fig. 7. Variation of the critical Reynolds number R_c along the inlet-length.

Variation along the inlet-length of the critical value, R_c say, of the original Reynolds number R is easily obtained from the above results together with (2.11) and (3.12), and is illustrated in Fig. 7. It will be seen that the curve has a minimum critical Reynolds number:

$$R_c=9.7\times10^3 \text{ at } z/aR=1.5\times10^{-3}, \quad (10.2)$$

and there is an upper limit of the inlet-length for occurence of instability at about $z/aR=6.6\times10^{-3}$. For instance, in a critical case when $R=10^4$, the flow is definitely stable at the entrance, but becomes unstable rather rapidly at $z/a=8\sim23$, and again becomes stable in the further downstream region.

Although a large number of experiments have been made on the transition phenomena from laminar to turbulent motion, no direct experimental evidence for these results is yet available, owing mainly to the lack of specification of the magnitude of initial disturbances in these measurements. Indeed, the value of the critical Reynolds number R_c varies from 10^3 to $2\sim2.5\times10^4$ with decreasing magnitude of disturbance. As will be seen from the fact that the experimental verification of Tollmien-Schlichting wave in the laminar boundary-layer has been first made quite recently by Schubauer and Skramstad (**14**) in a "laminar wind tunnel" whose inherent turbulence was artificially reduced with the damping screen, the theoretical limit of instability predicted by small perturbation theory does not seem to be checked by conventional measurement where outer disturbance is not small enough.

However, we find some favourable evidence for the theory even in ealier experiments such as Reynolds' measurements (**15**). Using a circular pipe with a well-rounded entrance, he found that the critical values of R were $6\sim7\times10^3$ and that the transition occured at about $z/a=60$. Remembering the fact that it needs some time for the growth of unstable oscillation up to the so-called "transition", Reynolds' data seem to render a fairly good evidence for our theoretical predictions:

References

9) W. Heisenberg: Ann. d. Phys. **74** (1924) 577.

10) O. Tietjens: ZS. angew. Math. Mech. **5** (1925) 200.

11) W. Tollmien: Nachr. Ges. Wiss. Göttingen (1929) 21.

12) H. Schlichting: Nachr. Ges. Wiss. Göttingen **1** (1935) 47.

13) C.C. Lin: Quart. Appl. Math. **3** (1945-46) 117, 218, 277.

14) G.B. Schubauer and H. K. Skramstad: J. Aero. Sci. **14** (1947) 69.

15) O. Reynolds: Phil. Trans. Roy. Soc. London **174** (1881) 935.

JOURNAL OF THE PHYSICAL SOCIETY OF JAPAN Vol. 7, No. 5, SEPT.—OCT., 1952

Some Remarks on the Lagrangian Correlation Coefficient of Turbulent Diffusion in a Wind Tunnel Flow

By Eiichi INOUE

Division of Meteorology, National Institute of Agricultural Sciences, Nishigahara, Kita-ku, Tokyo

(Read April 3, 1952. Received April 24, 1952)

Many influences of physical, chemical and geometrical properties of the diffused substances on the Lagrangian correlation coefficient for the turbulent diffusion in a wind tunnel flow are considered theoretically. Influences of the decaying phenomena of a wind tunnel turbulence are also taken into consideration. Influences of these factors on the Lagrangian smallest eddy λ_η introduced by Sir Geoffrey Taylor are discussed in detail making use of the concept of the smallest turbulon $\Lambda_\infty \sim \nu^{3/4}\varepsilon^{-1/4}$ due to the similarity theory of turbulence, where ν and ε mean the kinematic viscosity of a fluid material and the dissipation rate of turbulon energy respectively.

§ 1. Introduction

Since a work by Sir Geoffrey Taylor[1] there have appeared a number of considerations on the so-called Lagrangian correlation coefficient for turbulent diffusion of the fixed-source type.

In particular J. Kampé de Fériet[2] has pointed out theoretically that this coefficient is the Fourier transform of the so-called Lagrangian spectrum of turbulent velocity and has shown many forms of the coefficient as well as those of the spectrum, On the other hand, from the empirical points of view several functional forms of the coefficient have been proposed and some experimental results have become available.

Recently the author[3],[4],[5] has obtained the functional form $R(\xi)$ of the coefficient making use of the functional form $F(n)$ of the so-called Lagrangian spectrum of turbulent velocity and has shown that the most familiar form of

$$R(\xi)=\exp(-\xi/\tau_0)$$

which has been anticipated empirically for a long time is the sufficiently appropriate form of the Lagrangian correlation coefficient and that near the origin of $R(\xi)$ another form of $R(\xi)=1-\text{const.}\xi^2$ is theoretically obtained provided the fine structure of turbulence is taken into account. In other words, the existence of the smallest turbulon puts a limit of application on the former $R(\xi)$ and make the latter $R(\xi)$ necessary.

In this paper the author intends to make clear the relations between these functional forms of $R(\xi)$'s and the wind velocity in a wind tunnel and also between the former and the physical, chemical and geometrical properties of the diffused substances.

§ 2. $R(\xi)$ for Turbulent Diffusion of Non-Dynamical Substances in a Wind Tunnel Flow

Taking the x-axis from the source of diffused substance in a wind tunnel to the downwind direction, the turbulent diffusion of substance in a direction perpendicular to the x-axis, y-direction, say, is considered.

When the diffused substance can be regarded to have no influence upon the turbulent characteristics of the wind tunnel flow at all and are supposed to be able to follow exactly even the finest movements of the smallest turbulons in the flow, the turbulent diffusion of such substances can be dealt with exactly, by taking account of the relative movements of the smallest turbulons themselves to the source of diffusion. Sometimes substances such as momentum and smoke particles are called the non-dynamical substances, and, on the contrary, sand or fluid particles of large scale which do not follow exactly the movements of the smallest turbulons in flow are called the dynamical particles. Since the author has recently discussed on another occasion the criteria distinguishing any particles between being non-dynamical and being dynamical, the author does not want to enter into this problem further.

Following Sir Geoffrey Taylor[1], J. Kampé de Fériet[2], F. N. Frenkiel[6] and G. K. Batchelor[7], the Lagrangian correlation coefficient $R_V(\xi)$ for the turbulent diffusion of non-dynamical substances in the y-direction is both defined and given by

$$R_V(\xi)=<V(\xi_0)V(\xi_0+\xi)>/<V^2> \\ =\int_0^\infty F_V(n)\cos 2\pi n\xi dn\,, \qquad (2.1)$$

where

$V(\xi_0)$ = velocity in the y-direction of a particle which leaves the source at the process time ξ_0,

$V(\xi_0+\xi)$ = velocity of the same particle at the process time $\xi_0+\xi$, *i.e.*, at the time ξ after its departure from the source,

$< >$ = Lagrangian average over the Lagrangian averaging-time sufficiently longer than the life-time of the largest turbulon in the flow,

n = Lagrangian turbulon frequency,

$F_V(n)$ = Lagrangian turbulon spectrum for fluctuations in velocity V of the same particle,

and by means of this function the diffusion width $<Y^2>^{1/2}$ and the diffusion coefficient K_y are given by

$$<Y^2>=2<V^2>\int_0^\xi\int_0^{\xi'} R_V(\xi'')\,d\xi''d\xi' \qquad (2.2)$$

and

$$K_y=\frac{1}{2}\frac{d<Y^2>}{d\xi}=<V^2>\int_0^\xi R_V(\xi')\,d\xi' \qquad (2.3)$$

respectively with regard to the Lagrangian process-time ξ.

On the other hand, C. F. von Weizsäcker[8] has set out the similarity theory of turbulence and has first shown that the Lagrangian turbulon spectrum is given by

$$F_V(n)\sim n^2 \qquad (2.4)$$

in the intermediate range of n. Thus from (2.1) and (2.4) the tentative form of $R_V(\xi)$ has been given by[3]

$$R_V(\xi)=1-(\xi/\tau_0), \quad \tau_\infty<\xi\ll\tau_0, \qquad (2.5)$$

assuming that the spectral function (2.4) is cut off respectively at both ends by n_0 and n_∞, which mean the Lagrangian turbulon frequencies of the largest and the smallest turbulon corresponding to the reciprocal of their respective life-time τ_0 and τ_∞. The above result (2.5) has been ascertained also by Y. Ogura[9] from somewhat different point of view and seems to be in good agreement with experimental results by D. C. Collis[10].

Introducing other assumptions on the smallest and the largest turbulon ranges the author[5] has also obtained the modified form of $R_V(\xi)$ as

$$R_V(\xi)=\begin{cases} 1-\dfrac{(\nu\varepsilon)^{1/2}}{<V^2>}\dfrac{\xi^2}{\tau_\infty^2}\,, & \xi<\tau_\infty, \qquad (2.6) \\ \exp(-\xi/\tau_0)\,, & \xi>\tau_\infty, \qquad (2.7) \end{cases}$$

which obviously includes the relation (2.5) as a particular case, where ν and ε are respectively the molecular kinematic viscosity of fluid material and the dissipation rate of turbulon energy by mutual interaction, and the term $(\nu\varepsilon)^{1/2}$ can be regarded as the square of velocity of the smallest turbulon in the flow. Making use of the transformations such as

$$\zeta=U\xi \qquad (2.8)$$

and

$$\eta=<V^2>^{1/2}\xi\,, \qquad (2.9)$$

we can get spatial descriptions of the Lagrangian correlation coefficient as follows:

(a)

$$R_V(\xi)=\begin{cases} 1-\dfrac{(\nu\varepsilon)^{1/2}}{<V^2>^2}\dfrac{\zeta^2}{U^2\tau_\infty^2}\,, \\ \qquad\qquad \zeta<\tau_\infty U\,, \qquad (2.10) \\ \exp(-\xi/U\tau_0)\,, \quad \zeta>\tau_\infty U\,; \qquad (2.11) \end{cases}$$

(b)

$$R_V(\eta)=\begin{cases} 1-\dfrac{(\nu\varepsilon)^{1/2}}{<V^2>^2}\dfrac{\eta^2}{\tau_\infty^2} \\ \qquad\qquad \eta<\tau_\infty<V^2>^{1/2}\,, \qquad (2.12) \\ \exp(-\eta/\tau_0<V^2>^{1/2})=\exp(-\eta/\Lambda_0), \\ \qquad\qquad \eta>\tau_\infty<V^2>^{1/2}\,. \qquad (2.13) \end{cases}$$

From the phenomenological viewpoints, the author should like to propose new terms for ζ and η as the process-length for fixed-source type diffusion and the process-length for floating-source type diffusion respectively in order to avoid any probable confusions with another process-length such as used in the Kolmogoroffian or Eulerian descriptions of the turbulent flow. The result (2.11) is quite in agreement with the experimental one obtained by A. A. Kalinske and C. L. Pien[11] for water flowing in open channels. On the other hand, the length λ_η of the Lagrangian smallest eddy, first introduced by Sir Geoffrey Taylor[12)] from the geometrical form of $R(\eta)$ extremely near the origin $\eta=0$, is obtained from (2. 12) as[5)]

$$\lambda_\eta = \frac{<V^2>\tau_\infty}{(\nu\varepsilon)^{1/4}} \approx \left(\frac{K_0}{\nu}\right)^{1/2} \Lambda_\infty\,, \qquad (2.\,14)$$

where K_0 is the turbulent diffusion coefficient of the flow. In some of earlier papers on turbulence, $R_V(\zeta)$ and $R_V(\eta)$ were apt to be confused with another spatial correlation coefficient $R_V(r)$, *i.e.* the so-called Kolmogoroffian correlation coefficient, and, moreover, λ_η was apt to be confused with another length λ of the smallest eddy, *i.e.* the Eulerian or Kolmogoroffian smallest eddy, also introduced by Taylor[12)].

In order to remove such misunderstandings, the author will show here the corresponding theoretical relations (*cf.* Batchelor[13)], Inoue[14)]):

$$R_V(r) = \begin{cases} 1-(r/\lambda)^2\,, & r<\Lambda_\infty\,, \qquad (2.\,15) \\ 1-(r/\Lambda_0)^{2/3}\,, & \Lambda_\infty<r\ll\Lambda_0\,, \qquad (2.\,16) \end{cases}$$

where

$$\lambda \approx \frac{<V^2>^{1/2}}{(\varepsilon/\nu)^{1/2}} \approx \left(\frac{K_0}{\nu}\right)^{1/4} \Lambda_\infty\,. \qquad (2.\,17)$$

The term $(\varepsilon/\nu)^{1/2}$ in (2. 17) corresponds to the Lagrangian frequency of the smallest turbulon n_∞ in the flow. The obvious discrepancies both between $R_V(\xi)$, $R_V(\eta)$ and $R_V(r)$ and between λ_η and λ will be readily found.

In a wind tunnel flow field several characteristic quantities such as ε, τ_∞, τ_0, and K_0 are considered to depend upon both the mean wind velocity U and the distance X from the turbulence-producing grid, and thus the relations (2. 5), (2. 6), (2. 7) and (2. 8) are naturally supposed to be dependent also on both U and X. Fixing the distance X at a certain constant value in the region of initial decay of turbulence, several characteristic quantities are considered to be given by

$$\left.\begin{array}{lll} \varepsilon & \backsim & U^3 \\ K_0 & \backsim & U \\ \Lambda_0 & \sim & \text{const.} \\ V_0 & \backsim & U \\ \tau_0 & \sim & \Lambda_0/V_0 \;\backsim\; U^{-1} \\ \Lambda_\infty & \backsim & U^{-3/4} \\ V_\infty & \backsim & U^{3/4} \\ \tau_\infty & \backsim & U^{-3/2} \\ \lambda_\eta & \backsim & U^{-1/4} \\ \lambda & \backsim & U^{-1/2} \end{array}\right\} \qquad (2.\,18)$$

some of which have been experimentally verified[5)].

In particular, from the relatians (2. 7) and (2. 18) we can get

$$\begin{aligned} R_V(\xi) &= \exp\left(-\text{const.}\;\xi<V^2>^{1/2}/\Lambda_0\right) \\ &= \exp\left(-\text{const.}\;\xi U/\Lambda_0\right)\,, \qquad (2.\,19) \end{aligned}$$

that is to say, $R_V(\xi)$ at a fixed point in a wind tunnel flow is anticipated to change regularly with respect to the mean speed of flow. This result has been anticipated also by J. M. Burgers[15)].

In general, the turbulence in a wind tunnel flow decays with respect to the distance X measured downwind direction from the turbulence-producing grid, and in the initial stage of decay the intensity and the length of the largest turbulon (or the scale of turbulence) are shown to be (*cf*. Heisenberg[16)])

$$\left.\begin{array}{lll} <V^2>^{1/2}/U & \backsim & 1/\sqrt{X} \\ V_0 & \backsim & 1/\sqrt{X} \\ \Lambda_0 & \backsim & \sqrt{X} \\ \multicolumn{3}{l}{K_0 \sim \Lambda_0<V^2>^{1/2} \sim \text{const.}} \\ \multicolumn{3}{l}{\tau_0 \sim \Lambda_0/<V^2>^{1/2} \backsim X\,,} \end{array}\right\} \qquad (2.\,20)$$

provided the mean wind velocity U is fixed. Thus the dependency of $R_V(\xi)$ on X will be readily obtained. In fact, some characteristic quantities are obtained as follows:

$$\left.\begin{array}{lll} \tau_\infty & \backsim & X \\ \Lambda_\infty & \backsim & \sqrt{X} \\ V_\infty & \backsim & 1/\sqrt{X} \\ \lambda_\eta & \backsim & \sqrt{X} \\ \lambda & \backsim & \sqrt{X}\,. \end{array}\right\} \qquad (2.\,21)$$

§ 3. Physical and Chemical Influences of Diffused Substance on $R(\xi)$

Strictly speaking, the above considerations must be applicable only to the diffusion phenomena of momentum and non-dynamical particles which are capable of following exactly the movements even of the smallest turbulons in the flow, In other words, the life-time τ_∞ and τ_0 are considered to correspond to the dynamical life-times of the smallest- and the largest turbulon respectively.

For diffusions of other substances such as heat, humidity, and gases of different kinds, the life-time of turbulon of different kinds must be taken into account. For example, let us consider the instantaneous diffusion of both momentum and heat, such as a problem of turbulent wake behind a heated wire, provided the wire is of so small diameter and the heat supplied is of so small amount that the existence of the heated wire does not affect the dynamical properties of turbulons in the flow. Naturally, both substances of momentum and heat are conceived to be diffused by the same turbulons passing the heated wire. As to the interrelation between the dynamical life-time τ_M and the thermal one τ_H, the author[17] has already pointed out that they are connected with each other as

$$\frac{\tau_H}{\tau_M}=\frac{\nu}{\kappa}\,, \tag{3. 1}$$

where κ denotes the molecular heat diffusion coefficient. In the case of air, κ is slightly larger than ν, *i.e.* the Prandtl number $\sigma=\nu/\kappa$ is of the magnitude of 0.7, so that τ_H is conceived to be slightly smaller than τ_M.

Thus the Lagrangian correlation coefficient for turbulent diffusions of heat is supposed to be given on replacing τ by τ_H or $\sigma\tau$ as follows:

$$R_V(\xi)=\begin{cases} 1-\dfrac{(\nu\varepsilon)^{1/2}}{<V^2>}\dfrac{\xi^2}{\sigma^2\tau_\infty{}^2}\,, & \xi<\sigma\tau_\infty, \quad (3.\,2)\\ \exp(-\xi/\sigma\tau_0)\,, & \xi>\sigma\tau_\infty. \quad (3.\,3)\end{cases}$$

The Lagrangian smallest eddy for heat diffusion is also obtained as

$$\lambda_{\eta H}=\sigma\,\lambda_{\eta M}\,. \tag{3. 4}$$

These results will explain rather easily the experimental fact that in the turbulent air flow the heat wake is slightly wider than the velocity wake. On the contrary, since the value of σ for water is much larger than unity, *i.e.*, of the magnitude of about 10, the heat wake in the case of turbulent water flow is supposed to be remarkably narrower than the velocity wake.

For turbulent diffusions of other substances of different kinds in the air or water, the quite similar considerations might be applicable provided that relevant physical or chemical life-time of turbulon is appropriately taken into account.

§ 4. Geometrical Influences of Diffused Substance on $R(\xi)$

When the turbulent diffusion of some particular substances such as soap bubbles of zero-lift in a wind tunnel flow is concerned (*cf.* Kampé de Fériet[18]), the geometrical scale of diffused substances must be taken into account. In brief, the effect of definite scale Λ_0 of diffused substance is seen in the cut-off of the contribution of turbulons smaller than Λ_0, that is to say, the turbulon of length Λ_0 is regarded as the effective smallest turbulon and is designated by $\Lambda_\infty{}^*$. In other words, the length $\Lambda_\infty{}^*$ might be regarded as the averaging-length for measurement.

This effect is conceived to reveal in two rôles. One is the diminishing of $<V^2>$, and the other is the change in the functional form of $R(\xi)$ extremely near the origin. The former problem has been already discussed by the author[14] and Y. Ogura[9], and the diminishing ratio of new $<V^2>$, $<V^2(\Lambda^*_\infty\sim\Lambda_0)>$, say, without partial contributions to the whole $<V^2>$, $<V^2(\Lambda_\infty\sim\Lambda_0)>$, say, is readily given by

$$<V^2(\Lambda_\infty{}^*\sim\Lambda_0)>\approx\{1-(\Lambda_\infty{}^*/\Lambda_0)^{2/3}\}$$
$$<V^2(\Lambda_\infty\sim\Lambda_0)>\,, \tag{4. 1}$$

provided $\Lambda_\infty{}^*$ is much smaller than Λ_0. This rôle does not seem to be so important when $\Lambda_\infty{}^*/\Lambda_0\ll1$. The latter is supposed to appear when the practical computation of $R_V(\xi)$ is carried out tracing the fluctuating movements of soap bubbles. In this case the movement of soap bubble corresponds exactly to that of effective smallest turbulon surrounding bubble itself, and then the terms of $\nu(=K_\infty)$, τ_∞ and $<V^2>$ should be replaced by those of $K_\infty{}^*$, $\tau_\infty{}^*$ and $<V^2(\Lambda_\infty{}^*\sim\Lambda_0)>$ respectively, being interpreted that the smallest turbulon is substituted by the effective smallest turbulon of length $\Lambda_\infty{}^*$. Consequently, neglecting the difference betweeh $<V^2(\Lambda_\infty{}^*\sim\Lambda_0)>$ and $<V^2>$ as mentioned above, the relevant $R_V(\xi)$ is given by

$$R_V(\xi)=\begin{cases} 1-\dfrac{(K_\infty{}^*\varepsilon)^{1/2}}{<V^2>}\dfrac{\xi^2}{\tau_\infty{}^{*2}}\,, & \xi<\tau_\infty{}^*, \quad (4.\,2)\\ \exp(-\xi/\tau_0)\,, & \xi>\tau_\infty{}^*, \quad (4.\,3)\end{cases}$$

and the corresponding effective Lagrangian smallest eddy $\lambda_\eta{}^*$ is shown to be

$$\begin{aligned}\lambda_\eta{}^*&=\lambda_\eta(K_\infty/K_\infty{}^*)^{1/2}(\Lambda_\infty{}^*/\Lambda_\infty)\\ &=\lambda_\eta(\Lambda_\infty{}^*/\Lambda_\infty)^{1/3}\,,\end{aligned} \tag{4. 4}$$

which shows obviously that, unless the ratio $(\Lambda_\infty{}^*/\Lambda_\infty)$ is very great, the increase in the scale of bubble affects only slightly the curvature of $R_V(\xi)$ at the origin.

§ 5. Conclusion

Though the Lagrangian correlation coefficient in a wind tunnel flow is chiefly dealt with in this paper, this consideration may be applicable to any other turbulent flows, such as the atmosphere and oceans. Since the life-time τ_0 of the largest turbulon in a wind tunnel flow is usually conceived not so great, namely, at most 1 sec, we can regard any turbulent diffusion phenomena in a wind tunnel flow as belonging to the ultimate state of diffusion, in which the change in the averaging-time or the duration of observation does not affect the observed results. In the case of atmosphere and oceans, on the contrary, the change in the averaging-time usually influences the observed diffusion phenomena remarkably,[4),5),9)] that is to say, they are in the transient state of turbulent diffusion, and characteristic quantities such as $<V^2>$, $R(\xi)$ and λ_η are dependent upon not only the diffused substances but also the Lagrangian averaging-time for analysis.

It may be worth mentioning here that the consideration on $R(\xi)$ of this paper is only applicable to the turbulent diffusion phenomena corresponding to both turbulent wakes and jets, in which turbulons in the outside turbulent flow play principal rôles, but not to those corresponding to both turbulent wakes and jets, in which newly created turbulons at the source play principal rôles for diffusion independently of turbulons in the outside flow. As to the latter phenomena, say, of the inside turbulence type, the author will discuss in a near future.

References

1) G.I. Taylor : Proc. London Math. Soc. **20** (1921), 196.

2) J. Kampé de Fériet: Ann. Soc. Sci. Bruxelles, **59** (1939) 145.

3) E. Inoue: J. Meteor. Soc. Japan **28** (1950) 441.

4) E. Inoue: Ibid. **29** (1951) 246.

5) E. Inoue: to be published in Geophys. Res. Pap. Air Force Camb. Res. Centr. 1951.

6) F.N. Frenkiel: J. Aeron. Sci. **15** (1948) 57.

7) G.K. Batchelor: Aust. J. Sci. Res. A **2** (1949) 437.

8) C.F. von Weizsäcker: Z. Phys. **124** (1948) 614.

9) Y. Ogura: J. Meteor. Soc. Japan **30** (1952) 23 and 53.

10) D.C. Collis: Coun. Sci. Industr. Res. Aust. Div. Aeron. Rep. A. **53** (1948).

11) A. A. Kalinske and C. L. Pien: Indstr. Engng. Chem. **36** (1944) 220.

12) G.I. Taylor: Proc. Roy. Soc. A **151** (1935) 421.

13) G.K. Batchelor: Proc. Camb. Phil. Soc. **43** (1947) 533.

14) E. Inoue: J. Meteor, Soc. Japan **28** (1950) 367.

15) J.M. Burgers: Turbulent Fluid Motion, Lecture Notes C.I.T. 1951.

16) H. Heisenberg: Proc. Roy. Soc. A **195** (1948) 402.

17) E. Inoue: Geophys. Notes, Tokyo Univ. **3** (1950) no. 30.

18) J. Kampé de Fériet: Proc. fifth Intern. Congr. Appl. Mech. Camb., (1938) 352.

JOURNAL OF THE PHYSICAL SOCIETY OF JAPAN Vol. 7, No. 5, SEPT.—OCT., 1952

Influences of the Length of Hot-Wire Anemometer on the Measurement of Turbulent Flow

By Eiichi INOUE

Division of Meteorology, National Institute of Agricultural Sciences, Nishigahara, Kita-ku, Tokyo

(Received May 10, 1952)

Making use of informations on the fine structure of turbulence due to the modern similarity theory, influences of hot-wire length or instrumental sensitivity on measurement of G.I. Taylor's smallest eddy in a turbulent fluid are dealt with theoretically in this paper. It is assumed that the hot-wire anemometer of length L cuts off the contribution of turbulons (turbulence elements) smaller than L, and the result is obtained that the practically measured diameter of the effective smallest eddy is in proportion to $L^{2/3}$, provided L is slightly greater than the smallest turbulon length given by $\nu^{3/4}\varepsilon^{-1/4}$, where ν and ε denote the kinematic viscosity of the fluid and the mass rate of turbulent dissipation respectively.

Concerning the problem of influences of the length of hot-wire anemometer on mesurements of turbulent flow there have appeared several considerations from aerodynamical viewpoints (*e.g.*, Dryden *et al.*¹⁾, Dryden²⁾, Frenkiel³⁾), and recently the present author⁴⁾ and Y. Ogura⁵⁾ have dealt with problems of the same nature, *i.e.*, the influences of instrumental sensitivity on measurement of atmospheric turbulence, taking into consideration the modern similarity theory of turbulence. That is to say, in treatments of Dryden and Frenkiel the correlation functions of turbulent velocities of either timely or spatially characteristic nature are *a priori* assumed, *e.g.*, either

$$R(r)=\exp(-r/\Lambda_0) \text{ or } R(r)=\exp(-r^2/\Lambda_0^2)$$

for the spatial correlation, say, the Kolmogoroffian, and, on the other hand, in latter ones the correlation coefficients are theoretically introduced from the spectral function making use of the similarity theory of turbulence.

Since these considerations mentioned above seem to have made clear fairly well the influences of the hot-wire length or the instrumental sensitivity on the observed intensity and correlation coefficient of turbulent velocities those on measurements of the smallest eddy introduced by Sir Geoffrey Taylor⁶⁾ will be chiefly considered in this paper.

As is well known, the length λ of Taylor's smallest eddy is defined by

$$\lambda^2=15\,\nu\langle u^2\rangle/\varepsilon \qquad (1)$$

and is practically measured by determining the osculating parabola at the vertex of the observed $R(r)$ curve. Here ν and ε denote the kinematic molecular (or laminar) viscosity coefficient of the fluid material and the mas rate of turbulent energy dissipation respectively. On the other hand, in the modern similarity theory of turbulence the length Λ_∞ of the smallest turbulon, which is given by

$$\Lambda_\infty \doteqdot \nu^{3/4}\varepsilon^{-1/4}\,, \qquad (2)$$

is considered to be one of the most essential characteristic representatives, and several relations between Λ_∞ and λ have been obtained eliminating ε from (1) and (2) as follows⁴⁾,⁷⁾:

$$\frac{\lambda^2}{\Lambda_\infty^2}=15\frac{\Lambda_\infty^2\langle u^2\rangle}{\nu^2}\,. \qquad (3)$$

Moreover, since ν and ε, and hence also Λ_∞, are naturally regarded to be independent of the instrumental sensitivity, the length λ is simply connected with the turbulence intensity $\langle u^2\rangle$ as

$$\lambda^2 \backsim \langle u^2\rangle\,. \qquad (4)$$

Hitherto the term $\langle u^2\rangle$ is naturally considered to be the mean square value of all turbulent velocity components *i.e.*, the turbulon energy per unit mass of all rank in the fluid, and to be approximately equivalent to the energy per unit mass of the largest turbulon V_0^2. As far as the atmospheric turbulence is concerned, however, the term $<u^2> \approx V_0^2$ must be considered to be related to the averaging procedure for analysis, *i.e.*, the Eulerian averaging-time for analysis T_* or the averaging-length for analysis L_*, and hence the practically obtained length of the smallest eddy by means of either $<u^2>$ or $R(r)$ both of which are observed without contribution of smaller turbulon energy cut off relatively to the averaging procedure must be regarded to depend upon the averaging procedure itself. For example, the length λ^* of the effective smallest eddy in the atmosphere is theoretically anticipated to increase with the time duration of observation, *i.e.*, T_* or L_*, as

$$\lambda^* \backsim T_*^{1/3} \qquad (5)$$

or

$$\lambda^* \backsim L_*^{1/3}, \qquad (6)$$

provided these observations are carried out under analytically transient conditions of phenomena[4].

Many years ago, Sir Geoffrey Taylor[8] stressed that his concept of the smallest eddy gives the absolute length within which laminar (molecular) diffusion predominates, even in the turbulent atmosphere, contrary to meteorological views of L. F. Richardson[9] and J. Kampé de Fériet[10] such that there is a certain smallest scale of atmospheric turbulence beyond which the turbulent viscosity coefficient increases with the four-thirds power of the scale of atmospheric diffusion, and which is clearly corresponding to the present concept of the smallest turbulon. That is to say, in Taylor's view λ seems to be confused with Λ_∞. Now, it is clear that λ obtained under the analytically transient condition of observation is neither absolutely constant nor equivalent to Λ_∞, which is independent of the observational procedure[4].

On the other hand, the observed value of $<u^2>$ also cannot be independent of the instrumental sensitivity, when the contribution to $<u^2>$ of turbulons smaller than the effective smallest turbulon of length Λ_∞^*, which is cut off by the limitation of instrumental sensitivity, cannot be ignored[4],[5]. Therefore, when the relation (1) is concerned, the computed λ is readily anticipated to be influenced by the instrumental sensitivity.

Concerning the geometrical form of the $R(r)$ curve near the origin $r=0$, it will be also readily expected that the lower the instrumental sensitivity the more rounded is $R(r)$'s configuration at its top, *i.e.*, the radius of cuavature at the vertex of $R(r)$ increases and consequently also does the virtual smallest eddy's length λ^*, which is the primary problem of this note.

First, it seems natural to suppose that a hot-wire anemometer of length $_*L$ cannot detect velocity fluctuations due to turbulons of scale smaller than $_*L$, even if it is well compensated. In other words, the hot-wire anemometer of length $_*L$ cuts off the contribution of turbulons smaller than $_*L$ to the observed quanties of $<u^2>$ and $R(r)$. In such meanings, the length $_*L$ may be called the instrumental averaging-length, and the length Λ_∞^* of the smallest detectable turbulon may be considered equivalent to $_*L$, which is called here the effective smallest turbulon.

As has been pointed out by G. K. Batchelor[7] the form of $R(r)$ near the origin $r=0$ is given by

$$\begin{aligned} R(r) &= 1-C_1\{(\varepsilon/\nu)/<u^2>\}r^2 \\ &= 1-C_2\{(V_\infty/\Lambda_\infty)^2/<u^2>\}r^2\,; \end{aligned} \qquad (7)$$

where C_1 and C_2, and other C's referred to hereunder, denote numerical constants of the order of unity respectively and V_∞ denotes the smallest turbulon velocity corresponding to $(\nu/\Lambda_\infty)=\nu^{1/4}\varepsilon^{1/4}$.

On the other hand, the length λ of Taylor's smallest eddy is defined by

$$R(r)=1-C_3(1/\lambda^2)r^2\,. \qquad (8)$$

Thus, comparing the above two relations with each other, it is readily obtaind that

$$\lambda=C_4(<u^2>^{1/2}/V_\infty)\Lambda_\infty\,, \qquad (9)$$

which is quite correspondent to another form of $(\lambda/\Lambda_\infty)=C_5(K_0/\nu)^{1/4}$ pointed out by the present author, where K_0 is the kinematic turbulent viscosity[4].

Clearly the above considerations have been carried out under the circumstance that even the contribution of the smallest turbulon can be referred to, and it will be reasonably considered that when the hot-wire length $_*L$ is greater than the smallest turbulon length Λ_∞ some alterations in quantities in the above relations are required. Since, when the length

$_*L$ is sufficiently smaller than the largest turbulon length Λ_0 or the analytical averaging-length L_*, the influence of cutting-off of smaller turbulons than $_*L$ scarecely affects the observed value of $<u^2>$, the alteration of $<u^2>$ may not be necessarily required. And the relevant $R(r)$, say $R^*(r)$, is anticipated to be given by

$$R^*(r)=1-C_1\{(\varepsilon/K_\infty{}^*)/<u^2>\}r^2$$
$$=1-C_2\{(V_\infty{}^*/\Lambda_\infty{}^*)^2/<u^2>\}r^2\,, \quad (10)$$

where $V_\infty{}^*$ and $K_\infty{}^*(=V_\infty{}^*\Lambda_\infty{}^*)$ mean the turbulon velocity and the kinematic turbulent viscosity of the relevant effective smallest turbulon of length $\Lambda_\infty{}^*$ respectively. Consequently the effective smallest eddy length λ^* is readily obtained as

$$\lambda^*=C_4(<u^2>^{1/2}/V_\infty{}^*)\Lambda_\infty{}^*\,, \quad (11)$$

and from relations (9) and (11) it is shown to be

$$\lambda^*/\lambda=(V_\infty/V_\infty{}^*)\cdot(\Lambda_\infty{}^*/\Lambda_\infty)\,. \quad (12)$$

And making use of the well-known turbulon relation in the similarity theory such that

$$V_\infty{}^{*3}/\Lambda_\infty{}^*=V_\infty{}^3/\Lambda_\infty=\varepsilon\,, \quad (13)$$

we can get eventually

$$\lambda^*/\lambda=(\Lambda_\infty/\Lambda_\infty)^{2/3}\,, \quad (14)$$

which indicates that the length of the effective smallest eddy increases in proportion to the 2/3 power of the hot-wire length or the instrumental averaging-lenth $_*L=\Lambda_\infty{}^*$, provided $_*L$ is greater than Λ_∞ but sufficiently smaller than Λ_0 or L_* *i.e.*, provided the observation is carried out under the instrumentally transient condition. This is the final result that the author has intended to point out in this paper. He also expects to examine it by practical observation in the turbulent atmosphere.

References

1) H.L. Dryden et al.: NACA Tech. Rep. No. 581 (1937).

2) H.L. Dryden: Quart. Appl. Math. **1** (1943) 7.

3) F.N. Frenkiel: Phys. Rev. **75** (1949), 1263; **76** (1949), 999.

4) E. Inoue: J. Meteor. Soc. Japan **28** (1950) 219, 339, 367.

5) Y. Ogura: J. Meteor. Soc. Japan **30** (1952) 103.

6) G.I. Taylor: Proc. Roy. Soc. A **151** (1935) 421.

7) G.K. Batchelor: Proc. Camb. Phil. Soc. **43** (1947) 533.

8) G.I. Taylor: Proc. fifth Intern. Congr. Appl. Mech., Cambridge. (1938) 294.

9) L.F. Richardson: Proc. Roy. Soc. A **110** (1926) 709.

10) J. Kampé de Fériet: J. Tech. Intern. Aeron (1936) 431.

Journal of the Physical Society of Japan Vol. 7, No. 5, Sept.—Oct., 1952

On the Equations of the Decay of Isotropic Turbulence in Magneto-Hydrodynamics

By M. Z. E. Krzywoblocki

University of Illinois

(Received June 19, 1952)

On the basis of his previous works, the author derives the equations of the decay of isotropic turbulence in magneto-turbulence in compressible media. All the random variables fulfill the requirements of isotropy and homogeneity and are dependent. The author assumes that the reader is acquainted with previous papers on the subject, and consequently, only a few items from those papers will be cited.

§ 1. Additional Tensor Forms

In addition to the known tensor forms derived in the works of Kármán-Howarth, Robertson, and others, in a turbulent vector field in magneto-hydrodynamics there appear a few additional tensor forms. These will be given below. Let the symbol σ denote the electric conductivity, $\mu^{(1)}$ the magnetic permeability, $\mu_0^{(1)}$ a constant mean value of the magnetic permeability and ρ_0 a constant mean density. Let the symbol H (or H_i) denote the magnetic field intensity which is a solenoidal vector. The following vector and tensor forms will be introduced:

$$h_i^{(m)}=[\mu_0^{(1)}(4\pi\rho_0)^{-1}]H_i\,;\qquad \overline{h_i^{(m)2}}=\overline{h_j^{(m)2}}=\overline{h^{(m)2}(t)}\,, \tag{1. 1}$$

$$\overline{h_ih'_j}=r^{-1}H_{,r}\xi_i\xi_j-(rH_{,r}+2H)\delta_{ij}\,, \tag{1. 2}$$

or

$$\overline{h_ih'_j}=r^{-2}(f^{(m)}-g^{(m)})\xi_i\xi_j+g^{(m)}\delta_{ij}\,, \tag{1. 2a}$$

$$H=H_0+H_2r^2+O(r^4),\quad f^{(m)}=-2H,\qquad f_{,rr}^{(m)}(0)=-4H_2\,, \tag{1. 2b}$$

$$\overline{\rho\rho' h_ih_ju'_k}=S^{(1)}{}_{ijk}=S_1^{(1)}\xi_i\xi_j\xi_k+S_2^{(1)}(\xi_i\delta_{jk}+\xi_j\delta_{ik})+S_4^{(1)}\xi_k\delta_{ij},$$

$$S_4^{(1)}=S_{40}^{(1)}+S_{42}^{(1)}r^2+O(r^4),\ \text{for}\ r\to 0, \tag{1. 3}$$

$$\overline{(h_iu_k-h_ku_i)h'_j}=P(\xi_i\delta_{jk}-\xi_k\delta_{ij})\,, \tag{1. 4}$$

$$P=P_0+P_2r^2+O(r^4)\,,\ \text{for}\ r\to 0\,,\ \text{(i.e., small)}, \tag{1. 4a}$$

$$\overline{u_ih'_j}=R^{(0)}(r,t)\varepsilon_{ijl}\xi_l,\qquad R^{(0)}=R_0^{(0)}+R_2^{(0)}r^2+\cdots, \tag{1. 5}$$

$$\overline{\rho\rho' u_iu_kh'_j}=U(\xi_i\varepsilon_{kjl}\xi_l+\xi_k\varepsilon_{ijl}\xi_l)\,, \tag{1. 6}$$

with U being an even function of r, i.e.,

$$U=U_0+U_2r^2+O(r^4),\ \text{for}\ r\to 0,\ \text{(i.e., small)}, \tag{1. 6a}$$

$$\overline{h_ih_kh'_j}=V(\xi_i\varepsilon_{kjl}\xi_l+\xi_k\varepsilon_{ijl}\xi_l)\,, \tag{1. 7}$$

$$V=V_0+V_2r^2+O(r^4),\ \text{for}\ r\to 0,\ \text{(i.e., small)}, \tag{1. 7a}$$

$$\overline{\rho\rho' u_i(h'_ju'_k-h'_ku'_j)}=r^{-1}W_{,r}^{(1)}(\xi_j\varepsilon_{kil}\xi_l+\xi_k\varepsilon_{ijl}\xi_l)+(2W^{(1)}+\tfrac{1}{2}\textstyle\int rW^{(0)}dr)\varepsilon_{ijk}\,, \tag{1. 8}$$

$$\overline{\rho_{,t}\rho'(h'_ju'_k-h'_ku'_j)+\rho\rho'_{,t}(h_ju_k-h_ku_j)}=W^{(0)}\varepsilon_{jkl}\xi_l\,, \tag{1. 8a}$$

with $W^{(1)}$ again being an even function of r:

$$W^{(1)}=W_0^{(1)}+W_2^{(1)}r^2+O(r^4),\qquad \text{for}\ r\to 0,\ \text{(i.e., small)}, \tag{1. 8b}$$

$$\overline{\eta u_i}=w_1\xi_i\,;\ \overline{\eta u'_k}=w_2\xi_k\,;\qquad \overline{\eta u'_k}=-\overline{\eta u_k}\,;\ \eta=\overline{\rho\rho'}\,, \tag{1. 9}$$

with w_i's, $i=1,2$, being even functions of r of the form:

$$w_1=w_{10}+w_{12}r^2+O(r^4),\ w_{10}=\overline{\rho^2(u^2)^{1/2}}\,, \tag{1. 9a}$$

under the assumption that there exists a correlation between ρ^2 and $(u^2)^{1/2}$ at $r=0$.

§ 2. Equations of the Decay of Turbulence

In [2] the author derived six fundamental equations for the propagation of (velocity, temperature, etc.) correlation functions in magneto-hydrodynamics of a compressible medium with the interaction between the electro-magnetic field and the turbulent motion when there is no externally imposed electric or magnetic field. For $r=0$, with the symbols used in [1, eqs. (3. 1), (3. 2)] and with the symbol

$$\lambda_m{}^2=-2\,\overline{h^{(m)2}/f_{,rr}^{(m)}(0)}\,, \tag{2. 1}$$

those equations reduce to the following forms:

$$\overline{(\rho u^2)}_{,t}=-\frac{2}{3}[\overline{(RT\rho_{,t})^2}]^{1/2}+10\mu\bar{A}$$
$$\overline{+\rho_0(\mu^{(1)}/\mu_0^{(1)})(10S_{40}^{(1)}+\frac{11}{3}\rho_{,t}\rho^{-1}h^{(m)2})}\,, \tag{2. 2}$$

$$A=-\overline{u^2\lambda_u^{-2}}+\frac{1}{6}\{2\overline{u^2\lambda_\rho^{-2}}-\frac{1}{3}\overline{[\log(\rho^2)],_t}\}\,, \tag{2, 2a}$$

$$(\overline{\rho^2}),_t=6\,\rho^2(u^2)^{1/2}\,, \tag{2. 3}$$

$$\overline{p^2}=R^2\,\overline{\rho^2T^2}\,, \tag{2. 4}$$

$$\frac{1}{3}\overline{J(c_p{}^2T^2),_t}-\frac{2}{3}\overline{[(\rho^{-1}c_pTp,_t)^2]}^{1/2}$$
$$=-4J\overline{\rho^{-1}kc_pT^2\lambda_\theta^{-2}}-10\overline{c_p\nu TA}$$
$$+(\rho_0/\mu_0{}^{(1)})\overline{\mu^{(1)}\rho^{-1}c_pT[20h^{(m)2}\lambda_m^{-2}}$$
$$\overline{-(2/3)\rho,_t\rho^{-1}h^{(m)2}]}\,, \tag{2. 5}$$

$$H_{0},_t=2P_0+10\,\overline{\lambda^{(1)}h^{(m)2}\lambda_m^{-2}}\,, \tag{2. 6}$$

$$\overline{\rho^2R_{0,t}^{(0)}}+\overline{\rho\rho,_tR_0{}^{(0)}}=5U_0-5(\rho_0/\mu_0{}^{(1)})\overline{\rho\mu^{(1)}V_0}$$
$$-10W_{2,rr}^{(1)}(0)-8\,\overline{\lambda_\rho^{-2}W_0{}^{(1)}}-\tfrac{1}{2}W^{(0)}(0)$$
$$+10\overline{(\lambda^{(1)}\rho^2+\mu\rho)R_{,rr}^{(0)}(0)}\,. \tag{2. 7}$$

It seems reasonable to expect that in a turbulent vector field of flow all the equations governing the scalar functions should be mutually inter-related and -connected. In fact, the equations of the above system are inter-connected by means of defining scalar functions or such random functions as $\overline{\rho^2}$, $\overline{\mu^{(1)2}}$, etc. The simplest equation is that one originated from the continuity equation (2. 3) which can be associated with the form:

$$\rho^2=\text{Const.}\exp[6\textstyle\int(\overline{u^2})^{1/2}dt]\,. \tag{2. 8}$$

Bibliography

1) v. Krzywoblocki, M. Z.: On the equations of the decay of isotropic turbulence in compressible fluid. J. Physi. Soc. Japan **7** (1952) 299.

2) Krzywoblocki, M. Z. E.: On the equations of isotropic turbulence in magneto-hydrodynamics of compressible media. Acta Physica Austriaca. To be published.

JOURNAL OF THE PHYSICAL SOCIETY OF JAPAN Vol. 7, No. 5, SEPT.—OCT., 1952

Some Cases of the Axially Symmetrical Flow of Perfectly Plastic Materials

By Nobuo INOUE

Faculty of Engineering, Doshisha University, Kyoto

(Received January 25, 1952)

This paper deals theoretically with one of the three-dimensional isostatical problems in the theory of plasticity.

Fundamental equations for plastic states of stress in a solid of revolution are established under the assumptions that the circumferential principal stress is equal to one of the other two lying in the meridian section and that materials obey the theory of constant elastic strain energy of distortion.

The author discusses the method of solving these equations for the case when the equations for slip-lines are known and two plastic states of stress having slip-lines of logarithmic spirals and straight lines are considered in details as practical examples of applying his method of solution.

§ 1. Introduction

When we want to determine the stress distribution in purely elastic materials under certain boundary conditions, we must prepare the equations of equilibrium of stresses and some definite relations existing between stress and strain such as Hooke's law. However, for the flow of perfectly plastic materials, we can determine the state of stress without any knowledge of stress-strain relations; namely, we can solve the three components of stress from the two equations of equilibrium of them and the yield condition of perfectly plastic materials, when we restrict ourselves to two-dimensional problems assuming that the materials flow in planes parallel to the x, y-plane. The equations governing this phenomenon are nonlinear partial differential equations of the hyperbolic type and their characteristics are the traces of the slip-surfaces in the x, y-plane, in which the maximum shearing stress occurs. They intersect at 45° the isostatics which follow the direction of the principal stress, and are visible on the surface of the body subjected to plastic flow without any artifice or may be brought out by etching.

Thus, the two-dimensional isostatical problem in the theory of plasticity is readily accessible to analytical treatment and several authors have studied the geometrical properties of the characteristics and the integration of the fundamental differential equations by means of Riemann's method. However, if we try to extend the theory to the three-dimensional case, the difficulty arises that the yield condition of the perfectly plastic materials involves only two principal stresses leaving the third principal stress undetermined and the solutions in this case have never been obtained for aught we know.

In this paper we consider the axially symmetrical flow of the perfectly plastic materials and establish the fundamental equations under our assumption proposed here firstly concerning the circumferential normal stress and the condition of yielding in the plane of symmetry, and simplify them by making use of the stress plane similar to the so-called hodograph plane, effectively used in the other branch of mechanics. Several cases of the axially symmetrical plastic flow are shown as the results of applying our method of solution.

§ 2. Fundamental Equations and their Characteristics

Since the flow is axially symmetrical we introduce the cylindrical coordinates z, ρ and φ, taking the z-axis as the axis of symmetry, and designate by σ_z, σ_ρ and σ_φ the normal stresses in the z-, ρ- and φ-directions and by $\tau_{z\rho}$ the shearing stress in the ρ-direction acting on the section normal to the z-direction. The equations of equilibrium take the simplified forms in consequence of the axial symmetry:

$$\left.\begin{aligned} &\frac{\partial\sigma_z}{\partial z}+\frac{\partial\tau_{z\rho}}{\partial\rho}+\frac{\tau_{z\rho}}{\rho}=0\,,\\ &\frac{\partial\tau_{z\rho}}{\partial z}+\frac{\partial\sigma_\rho}{\partial\rho}+\frac{\sigma_\rho-\sigma_\varphi}{\rho}=0\,. \end{aligned}\right\}\qquad(1)$$

Here, we postulate that the normal stress σ_φ becomes one of the three principal stresses intersecting orthogonally to each other and is equal to one of the other principal stresses lying in the z, ρ-plane, and consequently the yielding in this plane occurs by the difference of them. Therefore, the value of σ_φ and the condition of yielding in the z, ρ-plane are

$$\sigma_\varphi=(\sigma_z+\sigma_\rho)/2\pm k\,,\qquad(2)$$

and

$$(\sigma_z-\sigma_\rho)^2+4\tau_{z\rho}^2=4k^2\qquad(3)$$

respectively, where k has the constant values for either of the theory of constant energy of distortion and the maximum shear theory. The fundamental assumption (2) in this paper means that the axially symmetrical flow of the perfectly plastic materials has two families of the slip-surfaces, one of which is perpendicular to the z, ρ-plane and the other is perpendicular to the surface determined by the direction of σ_φ and one of the two principal stresses in the z, ρ-plane, having a different value from σ_φ. We consider here only the former one and look for its traces in the z, ρ-plane.

If, instead of the cylindrical coordinates, we use the polar coordinates r, θ and φ, the four equations (1)~(3) of the axially symmetrical plastic flow assume the forms:

$$\left.\begin{aligned} &\frac{\partial\sigma_r}{\partial r}+\frac{1}{r}\frac{\partial\tau_{r\theta}}{\partial\theta}+\frac{1}{r}(2\sigma_r-\sigma_\theta-\sigma_\varphi\\ &\qquad\qquad+\tau_{r\theta}\cot\theta)=0\,,\\ &\frac{\partial\sigma_\theta}{\partial\theta}+r\frac{\partial\tau_{r\theta}}{\partial r}+(\sigma_\theta-\sigma_\varphi)\cot\theta+3\tau_{r\theta}=0\,, \end{aligned}\right\}\qquad(1')$$

$$\sigma_\varphi=(\sigma_r+\sigma_\theta)/2\pm k\,,\qquad(2')$$

$$(\sigma_r-\sigma_\theta)^2+4\tau_{r\theta}^2=4k^2\,,\qquad(3')$$

where we designate by σ_r, σ_θ and σ_φ the normal stresses in the r-, θ- and φ-directions and by $\tau_{r\theta}$ the shearing stress in the θ-direction acting on the section normal to the r-direction.

Now let us introduce the mean value of the normal stresses σ and the four angles α, β, α' and β' (Fig. 1), in order to discuss the above two cases represented by different coordinates at the same time:

$$\sigma=(\sigma_z+\sigma_\rho)/2=(\sigma_r+\sigma_\theta)/2\,, \tag{4}$$

$\alpha=$ the angle which the algebraically greater principal stress makes with the z-axis,

$\beta=$ the angle which the first principal shearing stress makes with the z-axis,

$\alpha'=$ the angle which the algebraically greater principal stress makes with the radius vector,

$\beta'=$ the angle which the first principal shearing stress makes with the radius vector.

Then, it is obvious that the following relations hold between the variables:

$$\beta=\alpha+\pi/4,\ \beta'=\alpha'+\pi/4,\ \alpha=\alpha'+\theta,\ \beta=\beta'+\theta, \tag{5}$$

$$\left.\begin{aligned}\sigma_z&=\sigma+k\cos 2\alpha,\\ \sigma_\rho&=\sigma-k\cos 2\alpha,\\ \tau_{z\rho}&=\quad k\sin 2\alpha,\end{aligned}\right\} \tag{6}$$

$$\left.\begin{aligned}\sigma_z&=\sigma+k\sin 2\beta,\\ \sigma_\rho&=\sigma-k\sin 2\beta,\\ \tau_{z\rho}&=\ -k\cos 2\beta,\end{aligned}\right\} \tag{7}$$

$$\left.\begin{aligned}\sigma_r&=\sigma+k\cos 2\alpha',\\ \sigma_\theta&=\sigma-k\cos 2\alpha',\\ \tau_{r\theta}&=\quad k\sin 2\alpha',\end{aligned}\right\} \tag{6'}$$

$$\left.\begin{aligned}\sigma_r&=\sigma+k\sin 2\beta',\\ \sigma_\theta&=\sigma-k\sin 2\beta',\\ \tau_{r\theta}&=\ -k\cos 2\beta'.\end{aligned}\right\} \tag{7'}$$

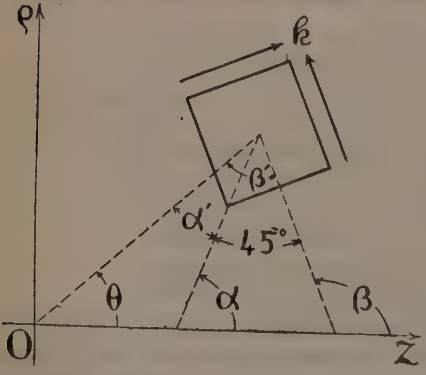

Fig. 1. Directions of the principal stress and the principal shear.

Substituting Eqs. (6) or (7) and (2) into Eqs. (1) in cylindrical coordinates, or Eqs. (6′) or (7′) and (2′) into Eqs. (1′) in polar coordinates, we obtain the fundamental equations for the axially symmetrical plastic flow, Eqs. (3) or (3′) being satisfied automatically. But it is sufficient for us now only to deal with one case, e.g. for the equations for σ and β, because there exist the relations (5) between the four variables α, β, α' and β', by which we are able to know all the four when an arbitrary one of them has been determined. Thus the fundamental equations for σ and β may be given as follows:

$$\left.\begin{aligned}&\frac{\partial\sigma}{\partial z}+2k\cos 2\beta\frac{\partial\beta}{\partial z}+2k\sin 2\beta\frac{\partial\beta}{\partial\rho}\\ &\qquad-\frac{k}{\rho}\cos 2\beta=0\,,\\ &\frac{\partial\sigma}{\partial\rho}+2k\sin 2\beta\frac{\partial\beta}{\partial z}-2k\cos 2\beta\frac{\partial\beta}{\partial\rho}\\ &\qquad-\frac{k}{\rho}(\pm1+\sin 2\beta)=0\,,\end{aligned}\right\} \tag{8}$$

where the double signs have the same meanings as in Eq. (2).

The theory of partial differential equations shows that the characteristic equations of the simultaneous partial differential equations (8) are given by

$$\mathrm{C}_+:\quad \frac{\partial\rho}{\partial\mu}=\tan\beta\frac{\partial z}{\partial\mu} \tag{9}$$

and

$$\mathrm{C}_-:\quad \frac{\partial\rho}{\partial\nu}=-\cot\beta\frac{\partial z}{\partial\nu} \tag{10}$$

on the physical z, ρ-plane, and are

$$\Gamma_+:\quad \frac{\partial\sigma}{\partial\mu}+2k\frac{\partial\beta}{\partial\mu}-\frac{k}{\rho}\left(\pm\frac{\partial\rho}{\partial\mu}+\frac{\partial z}{\partial\mu}\right)=0 \tag{11}$$

and

$$\Gamma_-:\quad \frac{\partial\sigma}{\partial\nu}-2k\frac{\partial\beta}{\partial\nu}-\frac{k}{\rho}\left(\pm\frac{\partial\rho}{\partial\nu}-\frac{\partial z}{\partial\nu}\right)=0 \tag{12}$$

on the σ, β- or stress plane, where μ and ν are the parameters of the characteristics and the double signs must be taken in the same order.

If we use the polar coordinates, these equations are replaced by

$$\mathrm{C}_+:\quad \frac{\partial\theta}{\partial\mu}=\tan\beta'\frac{1}{r}\frac{\partial r}{\partial\mu}\,, \tag{9'}$$

$$\mathrm{C}_-:\quad \frac{\partial\theta}{\partial\nu}=-\cot\beta'\frac{1}{r}\frac{\partial r}{\partial\nu} \tag{10'}$$

and

$$\begin{aligned}\Gamma_+:\quad &\frac{\partial\sigma}{\partial\mu}+2k\frac{\partial\beta}{\partial\mu}+k(1\mp\cot\theta)\frac{\partial\theta}{\partial\mu}\\ &\qquad-k(\pm1+\cot\theta)\frac{1}{r}\frac{\partial r}{\partial\mu}=0\,,\end{aligned} \tag{11'}$$

$$\Gamma_-:\quad \frac{\partial\sigma}{\partial\nu}-2k\frac{\partial\beta}{\partial\nu}-k(1\pm\cot\theta)\frac{\partial\theta}{\partial\nu}$$
$$-k(\pm1-\cot\theta)\frac{1}{r}\frac{\partial r}{\partial\nu}=0. \quad (12').$$

We can discuss the state of stress by solving the linear equations (9)~(12) or (9′)~(12′) instead of grappling with nonlinear equations (1)~(3) or (1′)~(3′).

§ 3. General Solution of the Axially Symmetrical Plastic Flow

The fundamental equations and their characteristics having been established so far, let us now solve these equations. First, we assume the equation of one of the two families of the slip-lines as follows:

$$f(z,\ \rho)=\nu \qquad (13)$$

in cylindrical coordinates, and

$$f(r,\ \theta)=\nu \qquad (13')$$

in polar coordinates. Then, that of the other is obtained as its orthogonal trajectories to be

$$g(z,\ \rho)=\mu, \qquad (14)$$

or

$$g(r,\ \theta)=\mu, \qquad (14')$$

and β is determined by Eq. (13) or (13′) as a function of z and ρ or r and θ as follows:

$$\beta=-\tan^{-1}\frac{f_z}{f_\rho}=\tan^{-1}\frac{g_\rho}{g_z}, \qquad (15)$$

or

$$\beta=\theta-\tan^{-1}r\frac{f_r}{f_\theta}=\theta+\tan^{-1}\frac{1}{r}\frac{g_\theta}{g_r}. \qquad (15')$$

Substituting the derivatives of z, obtained by differentiating Eqs. (13) and (14) or (13′) and (14′) with respect to μ and ν, into Eqs. (11) and (12) or (11′) and (12′) respectively, and integrating the results, we have the following relations which hold along the slip-lines:

$$\Gamma_+:\quad \sigma+2k\beta\mp k\log\rho-k\int\frac{1}{\rho}\frac{f_\rho}{f_z}d\rho$$
$$=4kn(\nu), \qquad (16)$$

$$\Gamma_-:\quad \sigma-2k\beta\mp k\log\rho+k\int\frac{1}{\rho}\frac{g_\rho}{g_z}d\rho$$
$$=-4km(\mu), \qquad (17)$$

or

$$\Gamma_+:\quad \sigma+2k\beta\mp k(\log r+\log\sin\theta)$$
$$-k\left(\int\frac{\cot\theta}{r}\frac{f_\theta}{f_r}d\theta-\theta\right)=4kn(\nu), \qquad (16')$$

$$\Gamma_-:\quad \sigma-2k\beta\mp k(\log r+\log\sin\theta)$$
$$+k\left(\int\frac{\cot\theta}{r}\frac{g_\theta}{g_r}d\theta-\theta\right)=-4km(\nu), \qquad (17')$$

where $m(\mu)$ and $n(\nu)$ are arbitrary functions of the parameters μ and ν respectively, and the double signs must be taken in the same order. The last two terms in the left sides of these equations (16), (17), (16′) and (17′) show the difference between the axially symmetrical flow and the plane flow. It will be seen, therefore, that on the curve C_+

$$\frac{d\rho}{dz}=\tan\beta \text{ and } \sigma+2k\beta\mp k\log\rho$$
$$-k\int\frac{1}{\rho}\frac{f_\rho}{f_z}d\rho=\text{const.}, \qquad (18)$$

or

$$r\bigg/\frac{dr}{d\theta}=\tan\beta' \text{ and } \sigma+2k\beta\mp k(\log r+\log\sin\theta)$$
$$-k\left(\int\frac{\cot\theta}{r}\frac{f_\theta}{f_r}d\theta-\theta\right)=\text{const.}, \qquad (18')$$

and on the curve C_-

$$\frac{d\rho}{dz}=-\cot\beta \text{ and } \sigma-2k\beta\mp k\log\rho$$
$$+k\int\frac{1}{\rho}\frac{g_\rho}{g_z}d\rho=\text{const.}, \qquad (19)$$

or

$$r\bigg/\frac{dr}{d\theta}=-\cot\beta' \text{ and } \sigma-2k\beta\mp k(\log r+\log\sin\theta)$$
$$+k\left(\int\frac{\cot\theta}{r}\frac{g_\theta}{g_r}d\theta-\theta\right)=\text{const.} \qquad (19')$$

These are the relations which hold along two sets of curves called the traces of the slip-surfaces of the plastic state of stress, crossing each other everywhere at right angles.

From Eqs. (16) and (17) or (16′) and (17′) we obtain

$$\sigma\mp k\log\rho-\frac{k}{2}\int\frac{1}{\rho}\left(\frac{f_\rho}{f_z}-\frac{g_\rho}{g_z}\right)d\rho=2k(n-m) \qquad (20)$$

and

$$\beta-\frac{1}{4}\int\frac{1}{\rho}\left(\frac{f_\rho}{f_z}+\frac{g_\rho}{g_z}\right)d\rho=m+n, \qquad (21)$$

or

$$\sigma\mp k(\log r+\log\sin\theta)$$
$$-\frac{k}{2}\int\frac{\cot\theta}{r}\left(\frac{f_\theta}{f_r}-\frac{g_\theta}{g_r}\right)d\theta=2k(n-m) \qquad (20')$$

and

$$\beta-\frac{1}{4}\int\frac{\cot\theta}{r}\left(\frac{f_\theta}{f_r}+\frac{g_\theta}{g_r}\right)d\theta+\frac{\theta}{2}=m+n. \qquad (21')$$

Determining the forms of the arbitrary functions $m(\mu)$ and $n(\nu)$ by Eq. (21) or (21′), we can obtain σ as a function of z and ρ or r

and θ by Eq. (20) or (20′). Since β is already known as a function of z and ρ or r and θ by Eq. (15) or (15′), the distribution of stress in the z, ρ- or r, θ-plane may be wholly settled and computing σ_φ from Eq. (2) or (2′), the axially symmetrical flow of the plastic materials may be analysed completely. If the equation of one of the two families of the isostatics is given, we can obtain the slip-lines as two sets of curves intersecting at 45° with it and proceed in all the same way as mentioned above.

§ 4. Simple Waves

General method to attack the axially symmetrical flow having been established so far, we want to consider here the more accessible case that at least one family of slip-lines is that of straight lines. If a certain region D in the z, ρ-plane represents the straight line $m=$ const, in the m, n-plane, the characteristics C_+ on which the parameter n is constant becomes a family of straight lines in this region D and is called a simple wave. We give to these straight lines C_+ the following expression:

$$z=a(\lambda)+s\cos\beta(\lambda),\quad \rho=b(\lambda)+s\sin\beta(\lambda), \tag{22}$$

where λ is a parameter and s is the abscissa on these straight lines $\lambda=$ const. Since σ is obtained from Eqs. (17) and (22) to be

$$\sigma=2k\beta+(k\tan\beta\pm k)\log\rho+\text{const.}, \tag{23}$$

the state of stress in this case is solved as follows:

$$\left.\begin{aligned}\sigma_z&=2k\beta+(k\tan\beta\pm k)\log\rho+k\sin2\beta+c\,,\\ \sigma_\rho&=2k\beta+(k\tan\beta\pm k)\log\rho-k\sin2\beta+c\,,\\ \sigma_\varphi&=2k\beta+(k\tan\beta\pm k)\log\rho\pm k+c\,,\\ \tau_{z\rho}&=-k\cos2\beta\,,\end{aligned}\right\} \tag{24}$$

where c is constant throughout the region D and the double signs have the same meanings as before. Therefore, if the state of stress along an arbitrary curve in the z, ρ-plane is given so as to satisfy the conditions (23), at least one of the two families of the slip-lines in the z, ρ-plane determined by this boundary condition becomes that of straight lines. When we express this boundary condition for the straight slip-lines in three components of stress, Eq. (23) becomes

$$\frac{\sigma_z+\sigma_\rho}{2k}=\sin^{-1}\frac{\sigma_z-\sigma_\rho}{2k}+\left\{\frac{\sigma_z-\sigma_\rho}{2(k-\tau_{z\rho})}\pm1\right\}\log\rho+\text{const.}\,,$$

or

$$\frac{\sigma_z+\sigma_\rho}{2k}+\cos^{-1}\frac{\tau_{z\rho}}{k}=\left\{\frac{\sigma_z-\sigma_\rho}{2(k-\tau_{z\rho})}\pm1\right\}\log\rho+\text{const.}$$

in cylindrical coordinates, and

$$\frac{\sigma_r+\sigma_\theta}{2k}=\sin^{-1}\frac{\sigma_r-\sigma_\theta}{2k}+2\theta+\left\{\frac{\sigma_r-\sigma_\theta+2(k-\tau_{r\theta})\tan\theta}{2(k-\tau_{r\theta})-(\sigma_r-\sigma_\theta)\tan\theta}\pm1\right\}\log\rho+\text{const.}\,,$$

or

$$\frac{\sigma_r+\sigma_\theta}{2k}+\cos^{-1}\frac{\tau_{r\theta}}{k}=2\theta+\left\{\frac{\sigma_r-\sigma_\theta+2(k-\tau_{r\theta})\tan\theta}{2(k-\tau_{r\theta})-(\sigma_r-\sigma_\theta)\tan\theta}\pm1\right\}\log\rho+\text{const.}$$

in polar coordinates.

Proceeding further we consider the problem to search for the isostatics generally when an arbitrary one of them is given by the equations:

$$z=a(\lambda)\,,\quad \rho=b(\lambda)\,. \tag{25}$$

Since the slopes of the isostatics are given by $\tan\alpha$ (Fig. 1), the following relations hold for the boundary isostatics expressed by Eq. (25) and for arbitrary isostatics of the same family:

$$\frac{db}{d\lambda}\bigg/\frac{da}{d\lambda}=\frac{\partial\rho}{\partial\lambda}\bigg/\frac{\partial z}{\partial\lambda}=\tan\alpha\,.$$

Making use of $\partial z/\partial\lambda$ and $\partial\rho/\partial\lambda$ obtained by differentiating Eq. (22) assumed here for the equations for the isostatics, we can transform the above equations for the slopes of the isostatics into

$$\frac{ds}{d\lambda}+s\frac{d\beta}{d\lambda}=0\,,$$

which is easily integrated to give

$$s=Se^{-\beta(\lambda)}\,,$$

where S is a constant of integration. Substituting this equation into Eq. (22), the equations for the isostatics of the same family as that of the boundary one are obtained as follows:

$$\left.\begin{aligned} z&=a(\lambda)+Se^{-\beta(\lambda)}\cos\beta(\lambda)\,, \\ \rho&=b(\lambda)+Se^{-\beta(\lambda)}\sin\beta(\lambda)\,. \end{aligned}\right\} \qquad (26)$$

On the other hand, the other family of the isostatics is solved by the orthogonality condition as follows:

$$\left.\begin{aligned} z=a(\lambda)-\Bigg[\int\Bigg\{&\frac{da(\lambda)}{d\lambda}\cos\beta(\lambda) \\ &+\frac{db(\lambda)}{d\lambda}\sin\beta(\lambda)\Bigg\}d\lambda+\text{const.}\Bigg]\cos\beta(\lambda)\,, \\ \rho=b(\lambda)-\Bigg[\int\Bigg\{&\frac{da(\lambda)}{d\lambda}\cos\beta(\lambda) \\ &+\frac{db(\lambda)}{d\lambda}\sin\beta(\lambda)\Bigg\}d\lambda+\text{const.}\Bigg]\sin\beta(\lambda)\,. \end{aligned}\right\} \qquad (27)$$

Similarly, when an arbitrary curve (25) is given for the envelope of a family of straight slip-lines, it is trivial to show that the other family of them is also given by Eq. (27) as the involute of the curve (25), and if an arbitrary curve is given for one of the other family, the envelope of the family of straight slip-lines becomes the evolute of the given curve.

§ 5. Practical Examples

(*a*) Radial yielding.

When we consider the distribution of stress having the slip-lines of logarithmic spirals (Fig. 2), we assume the equation of one of the two families of the slip-lines as follows:

$$f(r,\theta)\equiv re^{-\theta}=\nu\,, \qquad (13'')$$

then that of the other becomes

$$g(r,\theta)\equiv re^{\theta}=\mu\,, \qquad (14'')$$

and β is calculated to be

$$\beta=\theta+\pi/4\,. \qquad (15'')$$

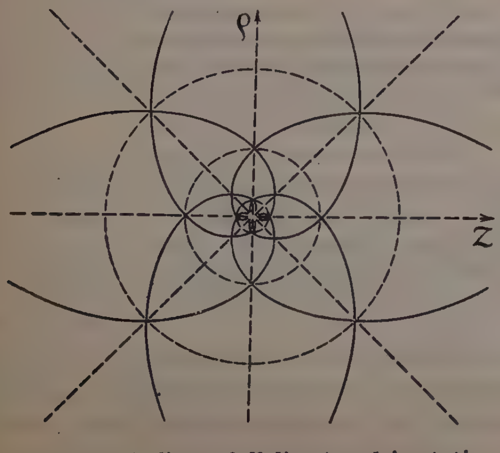

Fig. 2. Slip-lines (full lines) and isostatics (dotted lines) on the plane of symmetry in the case of radial yielding.

The equations of the characteristics in the stress plane are readily obtained to be

$$\Gamma_+:\quad \sigma+\frac{k\pi}{2}+3k\theta\mp k\log r=2kn(\nu)\,, \qquad (16'')$$

and

$$\Gamma_-:\quad \sigma-\frac{k\pi}{2}-3k\theta\mp k\log r=-2km(\mu)\,. \qquad (17'')$$

From these equations (16′′) and (17′′) we obtain the equations which determine σ and the form of the arbitrary functions $m(\mu)$ and $n(\nu)$ as follows:

$$\sigma=\pm 2k\log r+2k(n-m)\,, \qquad (20'')$$

$$k\pi+6k\theta=2k(m+n)\,, \qquad (21'')$$

from which $m(\mu)$ and $n(\nu)$ are determined to be

$$m(\mu)=\frac{3}{2}\log\mu+\frac{\pi}{4}\,,\quad n(\nu)=-\frac{3}{2}\log\nu+\frac{\pi}{4}\,.$$

Substituting these values of m and n into Eq. (20′′), we obtain

$$\sigma=\pm 4k\log r\,.$$

Therefore the state of stress having the slip-lines of logarithmic spirals may be expressed as follows:

$$\left.\begin{aligned} \sigma_r&=\pm 4k\log r\mp k\,, \\ \sigma_\theta&=\pm 4k\log r\pm k\,, \\ \sigma_\varphi&=\pm 4k\log r\pm k\,, \\ \tau_{r\theta}&=0\,, \end{aligned}\right\}$$

where the double signs must be taken in the same order.

(*b*) Radial distribution of stress in a conical plastic mass.

Here, we consider one example of the simple wave. When the family of straight lines passing through the origin in the r, θ-plane is given for one of the two families of the slip-lines, it is obvious that $\beta'=0$ or π and consequently $\beta=\pm\theta$. Therefore, the stress distribution in this case is readily obtained as follows:

$$\left.\begin{aligned} \sigma_r=\sigma_\theta=\pm\{&2k\theta+\tan\theta\,(\log r+\log\cos\theta)\} \\ &\pm k(\log r+\log\cos\theta)+\text{const.}\,, \\ \sigma_\varphi=\pm\{&2k\theta+\tan\theta\,(\log r+\log\cos\theta)\} \\ &\pm k(\log r+\log\cos\theta+1)+\text{const.}\,, \\ \tau_{r\theta}=\mp k\,&, \end{aligned}\right\}$$

and it is trivial to show that the other family of the slip-lines is that of the concentric circles $r=$ const. and the trajectories of the principal stress in the r, θ-plane are logarithmic spirals (Fig. 3).

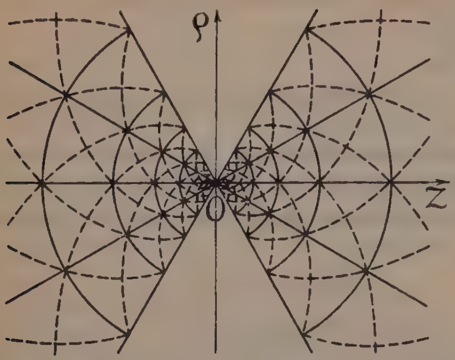

Fig. 3. Slip-lines (full lines) and isostatics (dotted lines) on the plane of symmetry in a conical plastic mass.

§ 6. Conclusions

The axially symmetrical flow of the perfectly plastic materials is discussed in a general manner, making use of the stress plane which has been useful for the plane plastic flow, under the assumption that the circumferential normal stress is one of the three principal stresses and is equal to either of the other two lying in the plane of symmetry. When we are given one of the two families of the slip-surfaces which are possible to occur in our case, the general method of solving the stress distribution is shown, and moreover the family of straight slip-lines is discussed in detail. Lastly two cases of the axially symmetrical flow are considered as examples of applying our method of solution.

In conclusion, the author wishes to express his cordial thanks to Professor S. Tomotika for his kind inspection of the present paper.

JOURNAL OF THE PHYSICAL SOCIETY OF JAPAN Vol. 7, No. 5, SEPT.—OCT., 1952

A New Method of Solution of the Two-Dimensional Isostatical Problem in the Mathematical Theory of Plasticity

By Nobuo INOUE

Faculty of Engineering, Doshisha University, Kyoto

(Received April 26, 1952)

The author discusses an analogy between the statically determinate state of stress in the perfectly plastic material and the steady irrotational flow of a hypothetical non-viscous fluid introduced by him, the pressure in which is proportional to the logarithm of its density and which has the same local Mach number $\sqrt{2}$ throughout the whole field of flow.

The hodograph method for this fluid flow is developed in detail, and besides an application of the W.K.B. method is considered.

Several exact solutions of the fundamental differential equations illustrate the present new method of solving the isostatical problem in the theory of plasticity.

§ 1. Introduction

In a previous paper[1] we have pointed out an analogy between the theory of supersonic flow of non-viscous compressible fluid and the theory of plastic flow of perfectly plastic material. As stated there, we are able to consider the two-dimensional isostatical problem as one of the problems of aerodynamics of our hypothetical fluid, the characteristic equation of which is given by

$$p/\log \rho = \text{const.}, \tag{1. 1}$$

where p and ρ are the pressure and density of the fluid respectively. This fluid has a special property that its local Mach number is $\sqrt{2}$ throughout the whole field of flow if we choose the local velocity of sound in the fluid at rest to be zero, and it is just this very flow with its Mach number $\sqrt{2}$ that makes the said similarity to hold. If we establish the mechanics of such a fluid, it will be nothing but that of the plastic material, the velocity of the former corresponding to the stress of the latter, stream lines and equipotential lines to isostatics, and Mach lines to slip lines. Since the mechanics of compressible fluid and the theory of supersonic flow in particular have been the subjects of quite a large number of ingenious investigations, it will be very interesting to apply its well-established methods to the isostatical problem in the theory of plasticity and to interpret the latter in a hydrodynamical manner.

The method of characteristics, which has been very useful in solving supersonic flow of fluid, having been successfully applied to the isostatical problem in the previous paper¹⁾, we want here to deal with this by the hodograph method in the aerodynamics, due originally to Molenbroek²⁾ and Chaplygin³⁾, and later on developed by Ringleb⁴⁾.

Further, the fundamental equations of the hodograph method, applied to the plastic flow, will be expressed in terms of new variables suggested by the W. K. B. method, which is well known in the quantum mechanics and has been recently applied to the flow of compressible fluid by Imai⁵⁾.

Several practical examples will be sufficient to illustrate the usefulness of our hodograph method, or, may be better to call, the stress method, in the field of plastic deformation.

§ 2. Correspondence of Stress in Plastic Material to Velocity in Hypothetical Fluid

It will easily be seen from the considerations given in the previous paper¹⁾ that the following relations hold between the variables of plastic material and those of our hypothetical fluid:

$$\sigma_*-\sigma=2k\log(q/q_*),\quad \alpha=\theta\,, \qquad (2.1)$$

$$\left.\begin{aligned} u&=q_*\exp[(\sigma_*-\sigma)/(2k)]\cos\alpha\,,\\ v&=q_*\exp[(\sigma_*-\sigma)/(2k)]\sin\alpha,\end{aligned}\right\} \qquad (2.2)$$

where u and v are the rectangular coordinates of the fluid-velocity vector, q and θ the polar coordinates in the hodograph plane, σ is the mean principal stress of the plastic material, α the angle which the algebraically greater principal stress makes with the x-axis, $2k$ the yield stress in tension, and the subscript $*$ refers to an arbitrary but fixed point in the material (Figs. 1, 2).

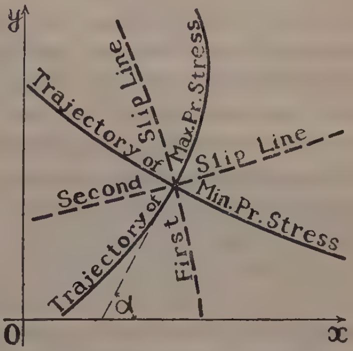

Fig. 1. State of stress in perfectly plastic material.

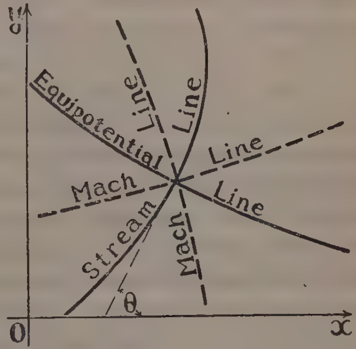

Fig. 2. Supersonic flow of hypothetical fluid.

Since three components of stress σ_x, σ_y, and τ_{xy} in rectangular coordinates, or σ_r, σ_t, and τ_{rt} in polar coordinates can be expressed by σ and α, or σ and $\alpha'=\alpha-\varphi$ by the relations

$$\left.\begin{aligned} &\sigma_x=\sigma+k\cos2\alpha,\quad \sigma_y=\sigma-k\cos2\alpha,\\ &\qquad\tau_{xy}=k\sin2\alpha,\\ &\sigma_r=\sigma+k\cos2\alpha',\quad \sigma_t=\sigma-k\cos2\alpha',\\ &\qquad\tau_{rt}=k\sin2\alpha',\end{aligned}\right\} \qquad (2.3)$$

Eq. (2.1) yields them in terms of velocity components of our hypothetical fluid. By substituting these stress components expressed by velocity components into the fundamental equations of plasticity, i.e., the equations of stress equilibrium, it will readily be seen that the fundamental equations of compressible fluid, i.e., the equation of irrotationality and that of continuity, which will be shown in the next section, are satisfied.

Besides, the analogy can be extended to a plastic mass of revolution, if it is assumed that a principal stress, directed perpendicularly to a meridian plane, is equal to the smaller one of the two principal stresses lying in the meridian plane. Indeed, when we take the x-axis as the axis of symmetry and the x, y plane as the meridian plane, a steady axially symmetrical irrotational flow of our hypothetical fluid also represents a plastic state of stress in the perfectly plastic material, equations of correspondence of velocity to stress being given by Eqs. (2. 1) and (2. 2). On the other hand, if the principal stress, directed perpendicularly to the meridian plane, is equal to the greater one of the two others, it must be needed in Eqs. (2.1) and (2. 2) to change the sign of k and to interpret α as the angle which the algebraically smaller principal stress makes with the x-axis. Thus, plastic states of stress in a plastic mass of revolution can be wholly replaced by an axially symmetrical flow of our hypothetical fluid.

Lastly, we must refer to discontinuous solutions in the theory of plasticity. As has been mentioned, the flow of our hypothetical fluid is everywhere supersonic having the same local Mach number $\sqrt{2}$, and so it may be inferred that a shock occurs when a large disturbance happens to appear. Jump conditions at the shock front can be obtained by the condition of continuity of tangential velocity component and that of conservation of mass, momentum, and energy, which have been assumed to hold for our fluid, in the fluid passing across it. The first and second conditions become equivalent to each other and give the continuity of the shearing stress at the surface of discontinuity when translated into the terminology of the plasticity. The third condition, on the other hand, requires the continuity of the normal stress and the fourth one is trivial. Thus we see that the shock considered in the dynamics of compressible fluid is wholly equivalent to the stress discontinuity in the plastic material, which has been first introduced by Prager[6] into the theory of plasticity.

§ 3 Differential Equations of Hypothetical Fluid Flow

Since we have designated by u and v the rectangular coordinates and by q and θ the polar coordinates of the fluid-velocity vector in the hodograph plane, we have

$$u=q\cos\theta, \quad v=q\sin\theta\,. \qquad (3.\ 1)$$

On the other hand, Bernoulli's theorem, together with the characteristic equation (1. 1) of our fluid, yields the relation

$$c^2-q^2/2=\text{const.}\,, \qquad (3.\ 2)$$

where c is the local speed of sound. By taking the integration constant in Eq. (3. 2) to be zero, we obtain

$$q/c=q_*/c_*=\sqrt{2}\,. \qquad (3.\ 3)$$

The two-dimensional irrotational flow of our hypothetical fluid in the x, y plane is governed by the equations

$$u=\Phi_x, \quad v=\Phi_y\,, \qquad (3.\ 4)$$

$$-(\rho/\rho_*)v=\Psi_x\,, \quad (\rho/\rho_*)u=\Psi_y\,, \qquad (3.\ 5)$$

where Φ is the velocity potential and Ψ the stream function.

When we go over to the hodograph plane, taking q and θ as independent variables, we have

$$\left.\begin{aligned} dx&=\frac{\cos\theta}{q}d\Phi-\frac{q\sin\theta}{q_*^2}d\Psi\,,\\ dy&=\frac{\sin\theta}{q}d\Phi+\frac{q\cos\theta}{q_*^2}d\Psi\,, \end{aligned}\right\} \qquad (3.\ 6)$$

and

$$\Phi_q=(q/q_*^2)\Psi_\theta\,, \quad \Phi_\theta=(q^3/q_*^2)\Psi_q\,. \qquad (3.\ 7)$$

Eliminating Ψ or Φ from Eq. (3. 7), we have the fundamental linear differential equation for Ψ or Φ as follows:

$$q^2\Phi_{qq}-q\Phi_q-\Phi_{\theta\theta}=0\,, \qquad (3.\ 8)$$

or

$$q^2\Psi_{qq}+3q\Psi_q-\Psi_{\theta\theta}=0\,. \qquad (3.\ 9)$$

Starting with this equation, the usual procedure of the hodograph method yields solutions of our hypothetical fluid flow, and, by making use of Eq. (2. 1) or (2. 2), we can determine plastic states of stress in the perfectly plastic material.

Our method of solving plastic state of stress in the above mentioned way will be exemplified by several particular examples.

§ 4. Application of the W. K. B. Method to the Flow of Perfectly Plastic Material

Before proceeding further to illustrate several exact solutions obtained by applying the hodograph method to our hypothetical fluid, let us now pay attention to the W. K. B. method well-known in the quantum mechanics and rewrite the fundamental equations after Imai[6], by making use of new variables suggested by this method.

When we introduce a new variable t defined as

$$t=-\int_{\infty}^{q}(\rho/\rho_*)(dq/q)=(1/2)(q_*/q)^2\,, \qquad (4.\ 1)$$

Eq. (3. 7) becomes

$$\Phi_t=-K\Psi_\theta\,,\quad \Phi_\theta=-\Psi_t\,, \qquad (4.\ 2)$$

with

$$K=(q/q_*)^4=(\rho_*/\rho)^2=1/(4t^2)\,. \qquad (4.\ 3)$$

Elimination of Φ from Eq. (4. 2) gives at once

$$4t^2\Psi_{tt}-\Psi_{\theta\theta}=0\,. \qquad (4.\ 4)$$

Now we introduce new variables ω, ϕ, and ψ such that

$$\omega=\int_{1/2}^{t}K^{1/2}\,dt=\int_{q}^{q_*}(dq/q)=\log\,(q_*/q)\,, \qquad (4.\ 5)$$

$$\Phi=K^{1/4}\phi\,,\quad \Psi=K^{-1/4}\psi\,. \qquad (4.\ 6)$$

Substituting Eqs. (4. 3), (4. 5), and (4. 6) into Eq. (4. 2), we get

$$\phi_\omega+\psi_\theta=-\phi\,,\quad \phi_\theta+\psi_\omega=\psi\,, \qquad (4.\ 7)$$

from which we obtain, by eliminating ψ or ϕ,

$$\phi_{\omega\omega}-\phi_{\theta\theta}=\phi\,,\quad \psi_{\omega\omega}-\psi_{\theta\theta}=\psi\,. \qquad (4.\ 8)$$

The theory of partial differential equation shows that the characteristics of the simultaneous equations (4. 7) are the same as those of

$$\phi_\omega+\psi_\theta=0\,,\quad \phi_\theta+\psi_\omega=0\,,$$

and are given by

$$\omega\pm\theta=\text{const.}\,,$$

or, if we make use of Eq. (4. 5)

$$\log\,(q_*/q)\pm\theta=\text{const.} \qquad (4.\ 9)$$

Rewriting Eq. (4. 2) as

$$\Phi_\omega=-K^{1/2}\Psi_\theta\,,\quad \Phi_\theta=-K^{1/2}\Psi_\omega\,, \qquad (4.\ 10)$$

and putting

$$\xi=\omega+\theta\,,\quad \eta=\omega-\theta\,;$$

we have, from Eq. (4. 10),

$$\Phi_\xi=-K^{1/2}\Psi_\xi\,,\quad \Phi_\eta=K^{1/2}\Psi_\eta\,. \qquad (4.\ 11)$$

If we take $z=x+iy$, then

$$dz=dx+idy=q^{-1}e^{i\theta}[d\Phi+i(\rho_*/\rho)d\Psi]$$
$$=(q/q_*{}^2)e^{i\theta}[-(1-i)\Psi_\xi d\xi+(1+i)\Psi_\eta d\eta].$$

Since we have

$$1\pm i=\sqrt{2}\,\exp\,[\pm(\pi/4)i]\,,$$

where $\pi/4$ becomes the Mach angle, it follows that

$$dz=\sqrt{2}(q/q_*{}^2)e^{i\theta}[e^{(\pi/4)i}\Psi_\eta d\eta-e^{-(\pi/4)i}\Psi_\xi d\xi]. \qquad (4.\ 12)$$

Therefore, two families of characteristics $\xi=$const. and $\eta=$const. are respectively given by

$$dz=\sqrt{2}(q/q_*{}^2)e^{i[\theta+\pi/4]}\Psi_\eta d\eta\,,$$
$$dz=-\sqrt{2}(q/q_*{}^2)e^{i[\theta-\pi/4]}\Psi_\xi d\xi\,,$$

so that the angle between the velocity vector and each one of the characteristics is equal to the Mach angle $\pi/4$, as should be expected.

§ 5. Some Exact Solutions of Plastic State of Stress

The fundamental equations for our hypothetical fluid flow or, in other words, those for the perfectly plastic state of stress having been established, we shall now discuss some particular solutions of them.

Although we may take any one of Eqs. (3. 8), (3. 9), and (4. 4) as the basic equation for our discussion, we shall here choose the last one and try to obtain its particular solutions in the following. The fundamental equation (4. 4) can be solved exactly by assuming $\Psi(t,\theta)$ in the following forms:

(a) $\Psi=\Theta(\theta)$, (b) $\Psi=T(t)$, (c) $\Psi=T(t)+\Theta(\theta)$, (d) $\Psi=T(t)\Theta(\theta)$,

where $T(t)$ and $\Theta(\theta)$ are functions of t and θ alone respectively.

(a) $\Psi=\Theta(\theta)$. First, we consider a plastic state of stress, isostatics of which are a pencil of rays radiating from the origin. Since this condition can be expressed by the relation $\Psi=\Theta(\theta)$, we start with this Ψ, and then the hodograph method yields the state of stress for this case as follows:

$$\sigma_r=2k\log\,(a/r)+k\,,\quad \sigma_t=2k\log\,(a/r)-k,$$
$$\tau_{rt}=0\,. \qquad (5.\ 1)$$

This solution has been well known as the radial flow[7].

(b) $\Psi=T(t)$. Second case of fluid flow, which we can solve exactly, will be obtained by assuming that Ψ is a function of t only, and the plastic state of stress for this case can be determined as

$$\sigma_r=2k\log(r/a)-k\,,\quad \sigma_t=2k\log(r/a)+k\,,\quad \tau_{rt}=0\,,\tag{5.2}$$

which is substantially equivalent to the preceding case.

(b′) Linear combination of the two cases (a) and (b). Since the fundamental equation (4.4) is linear, we can obtain a new solution as a linear combination of the preceding two particular solutions; assuming

$$\Psi=q_*(C_1\theta+C_2t)\,,$$

with arbitrary constants C_1 and C_2, the plastic state of stress for this case can be written as follows:

$$\left.\begin{aligned}&\sigma_r=\pm k[\log\{(C_1/C_2)\tan\alpha'\}+\cos 2\alpha'],\\&\sigma_t=\pm k[\log\{(C_1/C_2)\tan\alpha'\}-\cos 2\alpha'],\\&\tau_{rt}=k\sin 2\alpha'\,,\quad \sin 2\alpha'=-2C_1C_2/r^2\,,\end{aligned}\right\}\tag{5.3}$$

which has been well known as the vortical flow in the plastic mass[7)].

(c) $\Psi=T(t)+\Theta(\theta)$. When we substitute this Ψ into Eq. (4.4), the equations to determine $T(t)$ and $\Theta(\theta)$ are able to be readily integrated to give

$$\Psi=C_1(\log q+\theta^2)+C_2\theta+C_3/q^2+C_4\,,$$

where C_1, C_2, C_3, and C_4 are arbitrary constants. Since the case where $C_1=0$ and C_2, C_3, $C_4\neq 0$ has been already studied in (b′), it is sufficient for us here to consider $C_2=C_3=C_4=0$ and $C_1\neq 0$, and we obtain, by choosing $\sigma_*=0$,

$$\left.\begin{aligned}&\sigma_r=-k\log(r^2\sin^2\alpha')+k\cos 2\alpha',\\&\sigma_t=-k\log(r^2\sin^2\alpha')-k\cos 2\alpha',\\&\tau_{rt}=k\sin 2\alpha'\,,\quad 4\alpha^2\tan^2\alpha'=1\,,\end{aligned}\right\}\tag{5.4}$$

which is the state of stress in the plastic mass pressed between two rigid plates inclined at $\pi/2-1\fallingdotseq 32°42'$.

(d) $\Psi=T(t)\Theta(\theta)$. Lastly, we shall consider a solution of the form $\Psi=T(t)\Theta(\theta)$. Substituting this value of Ψ into Eq. (4.4), we obtain

$$4t^2T''/T-\Theta''/\Theta=0\,.$$

Since the first term is a function of t alone, while the second term that of θ alone, the following relation must hold:

$$4t^2T''/T=\Theta''/\Theta=\lambda\,,\tag{5.5}$$

where λ is a constant. The sign of λ has a considerable influence on the nature of the solution, and so we want to discuss the two cases of positive and negative λ separately as follows:

(d. 1) First, we consider a case where λ is negative and assume $\lambda=-n^2$, with a real constant n, and divide the solutions of Eq. (5.5) into three classes according as $n\gtreqless 1$.

(d. 11) $n=1$. One of the most distinguished solutions obtained in this case is

$$\left.\begin{aligned}&\sigma_x=(k/a)x\pm 2k\sqrt{1-(y/a)^2}+\text{const.}\,,\\&\sigma_y=(k/a)x+\text{const.}\,,\\&\tau_{xy}=-(k/a)y\,,\end{aligned}\right\}.\tag{5.6}$$

which appears when the plastic mass is pressed between two rough parallel plates[7)], and has the slip lines of cycloidal form.

(d. 12) $n<1$. In this case it will be seen after some calculations that the following states of stress can be obtained:

the active plastic state of stress in the plastic mass pressed between two rigid plates inclined at an angle of

$$2\left[\tan^{-1}\sqrt{(1+\sqrt{1-n^2})/(1-\sqrt{1-n^2})}\right]/n-\pi/2,$$

$$\left.\begin{aligned}&\sigma_r=-\frac{k}{\sqrt{1-n^2}}\log\frac{r^2(1-\sqrt{1-n^2}\cos 2\alpha')}{Cn^2(1-\sqrt{1-n^2})}\\&\qquad\qquad+k\cos 2\alpha'\,,\\&\sigma_t=-\frac{k}{\sqrt{1-n^2}}\log\frac{r^2(1-\sqrt{1-n^2}\cos 2\alpha')}{Cn^2(1-\sqrt{1-n^2})}\\&\qquad\qquad-k\cos 2\alpha'\,,\\&\tau_{rt}=k\sin 2\alpha'\,,\\&\tan n\alpha=[n/(1-\sqrt{1-n^2})]\tan\alpha'\,,\end{aligned}\right\}\tag{5.7}$$

the passive plastic state of stress in the plastic mass pressed between two rigid plates inclined at an angle of

$$\pi/2-2\left[\tan^{-1}\sqrt{(1-\sqrt{1-n^2})/(1+\sqrt{1-n^2})}\right]/n\,,$$

$$\left.\begin{aligned}&\sigma_r=\frac{k}{\sqrt{1-n^2}}\log\frac{r^2(1+\sqrt{1-n^2}\cos 2\alpha')}{Cn^2(1+\sqrt{1-n^2})}\\&\qquad\qquad+k\cos 2\alpha'\,,\\&\sigma_t=\frac{k}{\sqrt{1-n^2}}\log\frac{r^2(1+\sqrt{1-n^2}\cos 2\alpha')}{Cn^2(1+\sqrt{1-n^2})}\\&\qquad\qquad-k\cos 2\alpha'\,,\\&\tau_{rt}=k\sin 2\alpha'\,,\\&\tan n\alpha=[n/(1+\sqrt{1-n^2})]\tan\alpha'\,,\end{aligned}\right\}\tag{5.8}$$

where C is an arbitrary constant, and finaly the plastic state of stress expressed by Eq. (5.4).

(d. 13) $n>1$. In this case, the following plastic state of stress can be obtained:

$$\left.\begin{aligned}x=&C_1[\cos\{\sqrt{n^2-1}\sigma/(2k)\}(n\cos\alpha\cos n\alpha+\sin\alpha\sin n\alpha)+\sqrt{n^2-1}\sin\{\sqrt{n^2-1}\sigma/(2k)\}\\&\times\sin\alpha\sin n\alpha]+C_2[\sin\{\sqrt{n^2-1}\sigma/(2k)\}(n\cos\alpha\cos n\alpha+\sin\alpha\sin n\alpha)\\&+\sqrt{n^2-1}\cos\{\sqrt{n^2-1}\sigma/(2k)\}\sin\alpha\sin n\alpha]+\text{const.}\,,\\y=&C_1[\cos\{\sqrt{n^2-1}\sigma/(2k)\}(n\sin\alpha\cos n\alpha-\cos\alpha\sin n\alpha)+\sqrt{n^2-1}\sin\{\sqrt{n^2-1}\sigma/(2k)\}\\&\times\cos\alpha\sin n\alpha]+C_2[\sin\{\sqrt{n^2-1}\sigma/(2k)\}(n\sin\alpha\cos n\alpha+\cos\alpha\sin n\alpha)\\&-\sqrt{n^2-1}\cos\{\sqrt{n^2-1}\sigma/(2k)\}\cos\alpha\sin n\alpha]+\text{const.}\,,\end{aligned}\right\}\quad(5.9)$$

where C_1 and C_2 are arbitrary constants.

(d. 2) $\lambda=n^2$. In this case the following plastic state of stress can be obtained:

$$\left.\begin{aligned}\sigma_r&=\mp\frac{k}{\sqrt{1+n^2}}\left[\log\frac{r^2}{C\sqrt{1+n^2}(\sqrt{1+n^2}\mp1)}-2n\alpha\right]+k\cos2\alpha'\,,\\\sigma_t&=\mp\frac{k}{\sqrt{1+n^2}}\left[\log\frac{r^2}{C\sqrt{1+n^2}(\sqrt{1+n^2}\mp1)}-2n\alpha\right]-k\cos2\alpha'\,,\\\tau_{rt}&=k\sin2\alpha'\,,\quad\tan(\alpha+\varphi)=n/(-1\pm\sqrt{1+n^2})\,,\end{aligned}\right\}\quad(5.10)$$

where the double signs must be taken in the same order and C is an arbitrary constant. The slip lines and isostatics of the state of stress are logarithmic spirals.

§ 6. Conclusion

The analogy as pointed out in a previous paper¹⁾ between plastic state of stress and supersonic flow of our hypothetical fluid is now extended, and the hodograph method applied to the plastic flow is developed in detail. The fundamental equations of the hodograph method are rewritten, by making use of new variables suggested by the W. K. B. method in the quantum mechanics.

This method seems to be more convenient to obtain exact solutions than the method of characteristics, which has been developed in the previous paper¹⁾, and yields several exact solutions of the isostatical problem in the theory of plasticity.

Although our discussions have been limited exclusively to the plastic material obeying the theory of constant strain energy of distortion or the maximum shear theory both in "plane strain", the same method can be applied also to those plastic materials which obey the other yield conditions as will be seen elsewhere in future.

In conclusion, the author wishes to express his cordial thanks to Professor S. Tomotika for his kind inspection of the present paper.

References

1) N. Inoue: J. Phys. Soc. Japan **6** (1951) 460.

2) P. Molenbroek: Arch. Math. Phys. **9** (1890) 157.

3) S.A. Chaplygin: Scientific Memoirs, Moscow Univ. Math. Phys. Sec. **21** (1904) 1.

4) F. Ringleb: Z. a. M. M. **20** (1940) 185.

5) I. Imai: J. Math. Phys. **28** (1949) 173.

6) W. Prager: "Discontinuous Solutions in the Theory of Plasticity", Courant Anniversary Volume, Interscience Publishers, New York (1948) pp. 289-300.

7) A. Nádai: "Theory of Flow and Fracture of Solids", McGraw-Hill Book Company, New York (1950) pp. 533-543.

JOURNAL OF THE PHYSICAL SOCIETY OF JAPAN Vol. 7, No. 5, SEPT.—OCT., 1952

Electron Multiplication in Hard Flows of Selenium Rectifiers

By Masao TOMURA and Yukiaki ABIKO

Institute of Polytechnics of Osaka City University

(Read April 3, 1951: Received September 27, 1951)

Noises generated in a selenium rectifier were measured at 600 kc for various reverse voltages and temperatures. They were analyzed by the method of F.E. Haworth and R.M. Bozorth, and attributed to electron multiplication in the barrier layer owing to very high fields in the layer. Because the barrier layer is composed of selenide of about 10^{-5} cm thickness, the internal field will be as high as 10^6 volt/cm at reverse voltages of the order of ten volts, thus creating impact ionization. The observed negative temperature coefficient of the avalanche noises will account for the abnormal temperature dependency of hard flows at high reverse voltages, since the latter may also be attributed to the electron multiplication.

At higher temperatures and lower voltages, however, the noises seemed to be of the flicker type.

§1. Introduction

The present paper is the details and the continuation of the preceding survey[1)] which has been reported under the same title.

Internal fields in a barrier layer of a selenium rectifier are in the order of 10^6 volt/cm at reverse voltage of about 10 volts, for the thickness of the barrier layer is about 10^{-5}cm[2)]. Field of this order lie in the region of the breakdown strengths of normal ionic crystals. It is known that currents at very high fields are due to electron multiplication, and have noisy characters[3)]. Thus in the present works, hard flows of the rectifier are studied from the standpoint of electron multiplication by observing noises generated in the rectifier.

At the same time the survey is intended to explain the abnormal temperature dependencies of the hard flows of the selenium rectifier at high reverse voltages.[4)] Knowledges on the hard flows at high voltages will be important in manufacturing the rectifier of high inverse voltage type.

§2. Measurements of Noises in the Hard Flows

In the previous paper it was reported that selenium rectifier elements as small as 1 mm² in area showed very high maximum back voltages.[5)] The capacities of these small elements are about 10pF and then measurements at high frequencies become possible. The elements tested were made just in the same way as that reported before.

The method presented by F. E. Haworth and R. M. Bozorth[6)] was adopted in measuring noises generated in the rectifiers. If noises are due to electron multiplication, the mean size of some kind of electron avalanches can be determined by this method. Fig. 1 shows the circuit for the measurement.

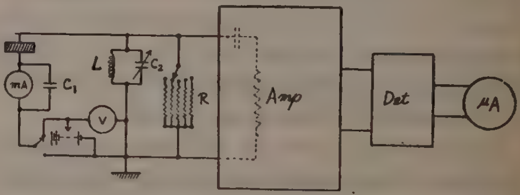

Fig. 1. The apparatus for measuring noises.

The noises generated in the rectifier were amplified through a high gain amplifier of about 120 DB which was tuned at three stages to 600 kc, and then detected by a microammeter after passing through a vacuum tube rectifier which had quadratic character. A tuned circuit was inserted in parallel with the input circuit to eliminate the shunting effect of the capacity of the input circuit including the sample.

According to F. E. Haworth and R. M. Bozorth, the relation between the noise power i_s^2 due to electron avalanche in the sample and the power i_r^2 of the thermal noise of the input impedance R is shown as

$$\frac{\overline{n^2}}{\overline{n}}=\frac{2kT\,i_s^2}{eiR\,i_r^2} \tag{1}$$

Here $\overline{n^2}/\overline{n}$ is a kind of average value of the number n of unit charge in a single avalanche group, and i is the mean current through the rectifier owing to electron avalanche. e is the electronic charge, k Boltzmann constant, and T the absolute temperature of R. If we take ν as the number of avalanche groups in unit time, then

$$i=\nu ne\,. \tag{2}$$

The reliability of our apparatus was tested by observing the shot noise generated in a diode vacuum tube which was operated at the space charge-free condition. As the shot noise is due to fluctuation in the flow of single electronic charges, the value of $\overline{n^2}/\overline{n}$ must be unity. In our case the value was 0.86 and it was sufficient for our purposes.

Observations were carried out at various reverse voltages for a few temperatures. The results are shown in Fig. 2 and Fig. 3.

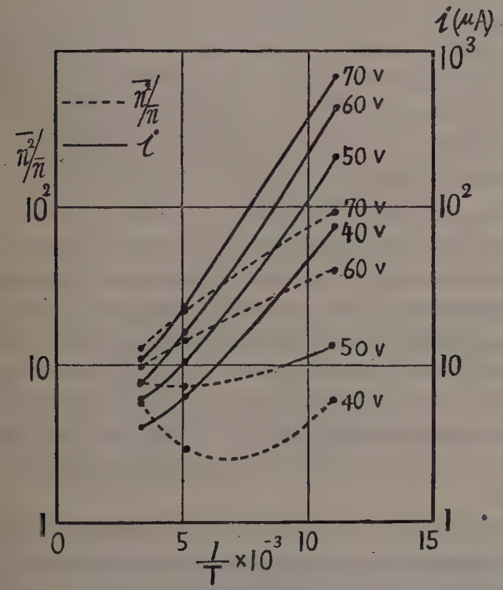

Fig. 2. Temperature dependencies of hard flow and noises at various reverse voltages.

Fig. 2 indicates conspicuous abnormal temperature dependencies of hard flows, because higher voltages could be applied in this case than in the previous works[4].

In the forward direction, only small noises were detected though the easy flows were very large.

From Fig. 3 it is known that $\overline{n^2}/\overline{n}$ increases with voltage and decreases with temperature. But at lower voltage other characteristics are found.

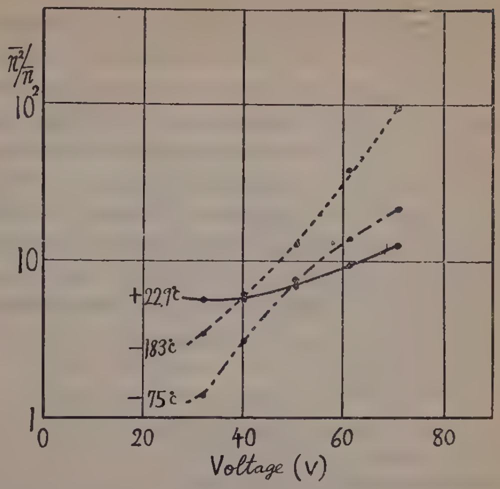

Fig. 3. Relations between $\overline{n^2}/\overline{n}$ and reverse voltages at some temperatures.

§ 3. Discussions of the Results

Some studies on noises of rectifiers or detectors have been reported, but all of them were treated on the standpoint of flicker noises and the measurements were carried out only at small bias voltages. In the present works, however, the results were analyzed on the viewpoint of electron multiplication at high reverse voltages.

Generally the flicker noise decreases with frequency and lowering of temperature; but the frequency characteristics of the electron avalanche noise is flat up to high frequency* and the variation of the electron avalanche noise with temperature is negative as will be mentioned afterwards.

The barrier layer of the selenium rectifier is made of selenide[7], so it is natural to take up the electron multiplication theory of F. Seitz[8] concerning with ionic crystals. According to him, the average distance Λ the electron travels before receiving sufficient energy to produce a secondary by impact ionization is shown as

$$\Lambda=\frac{Eh\nu_0}{eE_H^2}\exp\left(3.8\,E_H/E\right)^{**}. \tag{3}$$

---

* Estimating the thickness of the barrier layer as 10^{-5} cm and the mobility of charge carrier in the layer as 10 cm^2/volt·sec, the transit time of the carrier through the layer is in the order of 10^{-13} sec at 10^6 volt/cm. Thus the frequency characteristic of electron avalanche noise will be flat up to 10^{13} cycles.

Here E is the field in the barrier layer and E_H the field at which a conduction electron would receive on the average more energy from the applied field than it expends in exchange with lattice vibration of the selenide for all values of its kinetic energy at temperature T. ν_0 is the lattice vibration frequency of the polar mode of longest wave length in the reduced zone scheme and related to Debye temperature Θ as $h\nu_0=k\Theta$. Here h and k are Planck and Boltzmann constants respectively.

The temperature dependence of E_H is derived easily as

$$E_H=E_{H0}(1+\frac{2}{e^{\Theta/T}-1}), \qquad (4)$$

where E_{H0} is E_H at $T=0$.

If the thickness of the barrier layar is d, the number m of collisons at which impact ionization occur is d/Λ. At each impact collision one secondary electron is made, so an electron avalanche consists of 2^m electrons for a given field. Supposing that the distribution of avalanche size is narrow, $\overline{n^2}/\overline{n}$ is nearly equal to 2^m. Then $\overline{n^2}/\overline{n}$ increases according to Eq. (3) with field intensity. These characteristics are shown in Fig. (3) excepting the region of lower voltages. At small field intensities the avalanche noise may be masked by the flicker noise. Thus the above explanation will be correct only at high fields and low temperatures where the avalanche noises are dominant over the flicker ones.

With lowering of temperature, the interaction between electrons and lattice vibrations become small, resulting in large values of $\overline{n^2}/\overline{n}$ as known from Eq. (3) and Eq. (4). The metal electrode is composed of Bi, Sn and Cd; and then the selenide of the barrier layer may consist of selenides of these metals. From the melting points of these selenides, we can estimate their mean Debye temperature as about 200°K.*** The low value of Debye temperature like this makes E_H in Eq. (4) so sensitive to temperature in the temperature range of the present measurements. The results shown in Fig. 3 are good evidence that the noises observed are not of flicker type, but are attributed to electron multiplication. But as mentioned above, we must notice that the flicker noises are rather dominant at lower voltages in the room temperature even at 600kc.

The smaller inclinations of $\overline{n^2}/\overline{n}$ *versus* voltage curves than that which are expected from Eq. (3), make us suppose that impact ionization of impurity centers takes place or rather that the nonuniform natures of the barrier layer play important rôles.

§ 4. Characteristics of Rectification

Usually the rectification of the selenium rectifier has been explained with the diffusion theory, for the thickness of the barrier layer is larger than the mean free path of the charge carrier. In other words, electrons collide with lattice vibrations in the barrier layer. In the present case this assumption was confirmed by the fact that impact collisions occured in the barrier layer.

The conventional diffusion theory has been discussed on the standpoint that a single electronic charge migrates through the barrier layer. This consideration is correct in the forward direction, but not at high voltages in the backward direction, because of electron multiplication. The hard flow consists not of a single electronic charge, but groups of electrons which are related with $\overline{n^2}/\overline{n}$ in some way. Suppose that $\overline{n^2}/\overline{n}$ is nearly equal to $\overline{n}$; from Eq.(2), $i/(\overline{n^2}/\overline{n})$ is incident current into the barrier, being the source of electron avalanches. This current is one which should be treated with the diffusion theory. As mentioned above, however, non-uniform natures of the barrier layer make it impossible to discuss quantitatively. Thus further analyses of Eq. (3) and (4) could not be taken up.

But the result that $\overline{n^2}/\overline{n}$ increases with lowering of temperature made clear why the abnormal temperature dependence were observed.

§ 5. Further Considerations

The breakdown of the selenium rectifier in the blocking direction will be mentioned. F. Seitz[8)] has estimated the electron avalanche size which leads to electronic impact breakdown. Estimating its size for the thickness of the barrier layer, that is, about 10^{-5}cm, $\overline{n^2}/\overline{n}$ must be 10^5. Our samples, however,

---

** F. Seitz has calculated Λ at the zero absolute temperature.

*** The formula $\Theta=123\sqrt{T_e/Av^{2/3}}$ was used. Here T_e is the melting point, A atomic weight and v molecular volume. See Hand. Exp. Phys., VIII-1, p. 250.

gave 150～200 volts at the room temperature as the breakdown voltages for which the observed values of $\overline{n^2}/\overline{n}$ were about 10^2～10^3. Thus the breakdown is not attributed to the electronic multiplication, but to other types of breakdowon mechanism, such as the thermal breakdown or high temperature breakdown presented by H. Fröhlich⁹⁾.

Next the creep phenomena of the selenium rectifier will be discussed from the standpoint of the noise measurements. T. Numata, Y. Matukura and A. Okazaki have tried to explain these phenomena with impact ionization of impurity centers in the barrier layer.¹⁰⁾ But the relaxation time of the effect did not agree in order with the observed value. In the present measurement the impact ionization can been seen as the noise patterns on the oscilloscope, so we can see whether its relaxation time is in the order of minutes or less. Secondary electrons produced by impact ionization will make the thermal noise larger immediately after the voltage is removed, because the number of electrons in the conduction band becomes larger than in the normal state. The results were as follows. When the voltage was removed, the size of the noise patterns on the oscilloscope decreased instantaneously to the normal one of the thermal noise. Thus the life of the ionized electrons due to impact collision was much smaller than the order of minutes. Considering these results, the creep phenomena were not attributed to the impact ionization of impurity centers.

§ 6. Summary

From measurements of noises generated in the selenium rectifier in the blocking direction, several interesting results were obtained. In the present work all measurements were made with the frequency of 600 kc instead of 60 kc in the preceding paper¹⁾. The results were as follows.

(1) The noises consist from the flicker and electron avalanche types. The latter is dominant at high voltages and low temperatures.

(2) The existence of electron multiplication made us to explain the abnormal temperature dependencies of hard flows.

(3) The mechanism of breakdown in the backward direction was presented.

Lastly some relations of avalanche noise with the creep phenomena were mentioned.

The authors thank Dr. H. Kawamura for his interest in this work and Mr. M. Ōnuki for his useful discussions in the measurements of noises.

References

1) M. Tomura and Y. Abiko: J. Phys. Soc. Japan **7** (1952) 220

2) M. Tomura: Tsūshinkōgyō (in Japanese) **2** (1946) 20.

3) e.g. A. von Hippel: J. App. Phys. **8** (1937) 815.

4) M. Tomura: J. Phys. Soc. Japan **5** (1950) 349.

5) M. Tomura and Y. Abiko: J. Phys. Soc. Japan **7** (1952) 167

6) F.E. Haworth and R.M. Bozorth: Physics **5** (1934) 15.

7) M. Tomura: Bull. Chem. Soc. Japan **22** (1949) 82.

8) F. Seitz: Phys. Rev. **76** (1949) 1376.

9) H. Fröhlich: Proc. Roy. Soc. **188** (1947) 521.

10) T. Numata, Y. Matukura and A. Okazaki: Mem. Fac. Sci. Kyusyu Univ. B **1** (1949) 1.

JOURNAL OF THE PHYSICAL SOCIETY OF JAPAN Vol. 7, No. 5, SEPT.—OCT., 1952

Statistical Time Lag and Electron Avalanche in Dielectric-Breakdown of Mica

Hazimu KAWAMURA, Masami ONUKI and Hirosi OKURA
Department of Science and Engineering, Osaka City University

(Received January 30, 1951)

According to the "avalanche theory" of dielectric breakdown, the breakdown occurs by the energy dissipation of electron avalanche composed of sufficient number of secondary electrons. Therefore, the breakdown probability is equal to the average frequency with which the avalanches of such a sufficient sizes occur. On the other hand, the breakdown probability can be obtained by the measurement of the statistical time lag of the breakdown. In this paper, we measured the statistical time lag of breakdown of mica and the pulse size distribution of avalanche noise in the pre-breakdown region. Correlating the both results from the view point of avalanche mechanism, we obtained 10^8 as the avalanche size which is just sufficient to produce disruption for our specimens which were $3\sim5\times10^{-4}$ cm in thickness.

§ 1. Avalanche Theory

The electron avalanche mechanism of the dielectric breakdown at low temperature was first proposed by A. von Hippel[1], and formulated quantum mechanically by H. Fröhlich[2], F. Seitz[3] and H. B. Callen[4]. The conduction electron in solid under the electric field E gains the energy at the following rate,

$$(d\varepsilon/dt)_E=(e^2/m)E^2\tau_m, \qquad (1)$$

where $1/\tau_m$ is transport collision frequency due to the interaction between conduction electron and lattice vibration. On the other hand, the electron transfers its energy to the lattice vibration at the rate

$$-(d\varepsilon/dt)_\angle=\hbar\omega/\tau_t\ , \qquad (2)$$

where $1/\tau_t$ is the true collision frequency, and ω is the angular frequency of the vibration of the longitudinal optical mode. Rate of loss of energy due to the non-polar interaction is given by

$$-(d\varepsilon/dt)_\angle=\hbar ck/\tau_t\ , \qquad (3)$$

were c is the propagation velocity of the logitudinal accoustical mode, and k is the magnitude of wave number vector of electron. If the relation

$$(d\varepsilon/dt)_E+(d\varepsilon/dt)_\angle=0 \qquad (4)$$

holds for the whole range of electron energy from zero to ionization potential V, all electrons are accelerated to the energy V, which is sufficient to produce secondary electrons by exciting the electron from valence band to conduction band, If E is smaller than this critical value, the electrons whose energies are in a certain range lose their energies on the average as the result of the collision with the lattice. But this is only an average behavior of electron and there is a certain chance that electron passes through this energy range without collision, so that it can produce secondary electron while drifting a certain distance, due to this chance. According to Seitz[3] the mean range λ with which the electron produces one secondary electron is given by

$$\lambda=E(e/m)\tau_m\tau_t\cdot\exp(\alpha E_H/E)\ , \qquad (5)$$

where E_H is the critical field determined by equation (4). If the probability of producing one secondary is $1/\lambda$ per unit length, the probability that an electron is multiplied to n electrons after path L is given by[5]

$$P(n)=1/\bar{n}\cdot\exp(-n/\bar{n})\ , \qquad (6)$$

where $\bar{n}$ is the expectation value of n given by $\exp(L/\lambda)$. When starting electrons are supplied at the rate ν_0 sec^{-1}, the number of avalanches per second, whose sizes are larger than n is given by

$$\nu(n)=\nu_0\int_n^\infty P(n)dn=\nu_0\exp(-n/\bar{n}). \qquad (7)$$

If the lower limit of the avalanche size which can just produce disruption is assumed to be n_0, the breakdown probability is equal to $\nu(n_0)$, and the average statistical time lag of breakdown τ is given by

$$\tau=1/\nu(n_0)=1/\nu_0\cdot\exp(n_0/\bar{n}) . \qquad (8)$$

The distribution of number of electrons of the avalanches which are produced under the pre-breakdown field and the statistical time lag of the breakdown under the slight over voltage can be correlated by the above equation.

§ 2. Statistical Time Lag of Breakdown

The statistical time lags were measured with circuit shown in fig. 1. A single pulse of 3×10^{-3} sec and 0~10kV was applied on the specimen through resistance R (100 kΩ). Corresponding to the transients of the pulse application and the consequently occurring disruption, a negative and positive shock were sent to the flip-flop circuit. Observing by oscilloscope the maximum height of the linearly rising pulse which continues during the time interval between two shocks, we can measure the time lag between the instant of pulse application and disruption. The measurement of time interval of 5×10^{-6} sec to 3×10^{-3} sec was possible by this apparatus.

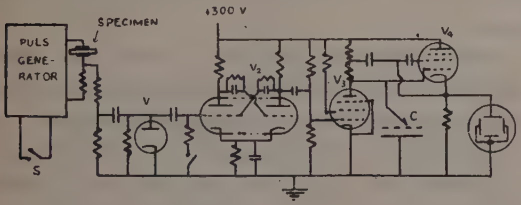

Fig. 1.

The specimens were Indian muscovite (colorless mica) about $3\sim5\times10^{-4}$ cm thick, on whose surfaces aluminium films of 1.5 mm dia. were deposited by evaporation in vacuum, after the cleaning treatment by exposing in glow discharge. The specimen was inserted between steel balls 3 mm dia. and the whole was coated with silicone oil. The thickness of the specimen was determined from the measurement of electric capacity, assuming that the dielectric constant is 6.7.

If n disruption out of n_0 lag beyond t second, we get

$$n=n_0\exp(-t/\tau) , \text{ or } \log(n/n_0)=-t/\tau , \qquad (9)$$

where τ is the average statistical time lag. We measured the time lags for about ten different specimens, applying a constant field strength and obtained fig. 2. The average time lags can be obtained as the gradients of these lines. In fig. 3 we plotted τ vs. field strength E. The measurements were made at room temperature (290°K) and 370°K.

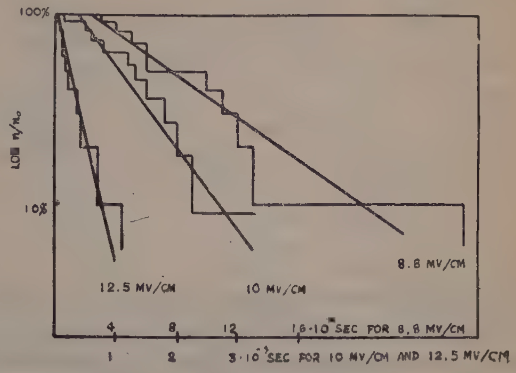

Fig. 2.

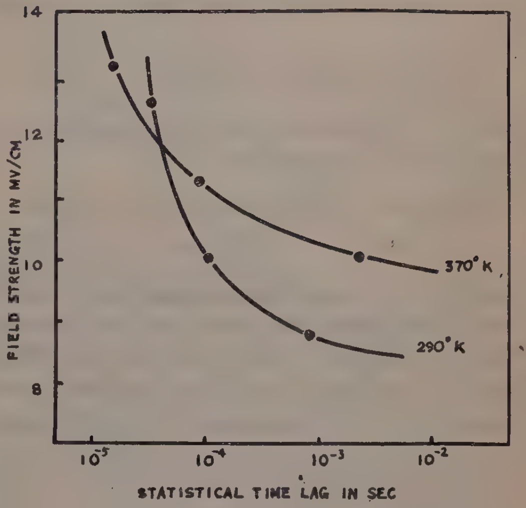

Fig. 3.

§ 3 Distribution of Avalanche Size

The circuit for the measurement of the pules size distribution was similar to the counting circuit employed for nuclear research, as shown in fig. 4. The pulse voltage appearing at resistance R (1 kΩ and 100 Ω), which was inserted in a high voltage circuit in series with the specimen, by four stages pre-amplifier and seven stages main amplifier. The amplified pulse which is larger than some desired value was picked up by a discriminator and counted by a counting rate meter or scale of sixteen counter. The amplifier was negative feed back linear amplifier whose total gain was 110 db for 20kc~3Mc, which could be decreasd by an

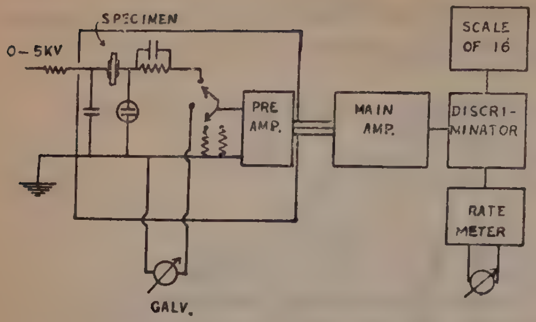

Fig. 4.

amount of 50 db by steps of 6 db. In order to check our apparatus, we measured the shot noise of saturated current of thermionic emission. If T is the response time of amplifier, the number of noise pulses per unit time whose sizes are larger than V is given by[6)]

$$P(V)=1/T\cdot\exp\left(-V^2/2\bar{V}^2\right)\ , \qquad (10)$$

were $\bar{V}^2$ is the meam square voltage of noise pulses which is given by

$$\bar{V}^2=2iRe^2\int_0^\infty G^2(\nu)/[1+(2\pi\nu RC)^2]d\nu=2iRe^2\Gamma\ , \qquad (11)$$

were i is the saturated emisson current, R and C are input resistance and stray capacitance, and $G(\nu)$ is the gain of amplifier. The plots of log P *vs.* V^2 for various i are shown in fig. 5. Calculating $\bar{V}^2$ and Γ from the gradients of these lines, we obtain following table. We can see that Γ_{cal} calculated from measured $G(\nu)$ and Γ_{obs} obtained from the measurement of shot noise coincide within the limit of experimental error.

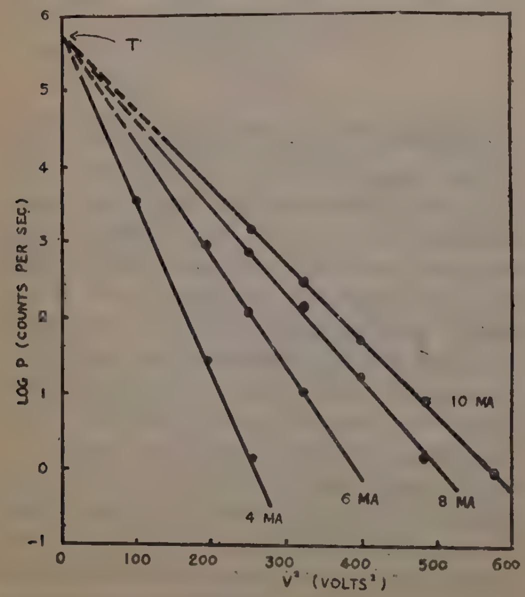

Fig. 5.

Table 1

i (ma)	$\bar{V}^2$ (volts²)	Γ_{obs} (sec⁻¹)	Γ_{cal} (sec⁻¹)
10	21.7	6.8×10^{13}	
8	19.1	7.5×10^{13}	
6	15.0	7.8×10^{13}	
4	10.0	7.5×10^{13}	5.7×10^{13}

When charge en flows through resistance R in a sufficiently short time as compared with the response time of the amplifier, the amplified pulse voltage is given by

$$V=2enR\int_0^\infty G(\nu)d\nu,^{*)}$$

if an assumption that the phase delay of the amplifier is proportional to ν is allowed. Thus we can calculate the effective avalanche size n which is smaller than true size by factor l/L, where l is the average range of avalanches.

Specimens which were similar to those employed for the study of the time lag, were inserted between hemisherical electrodes and were coated with paraffine. Noise pulses appearing at high voltage near the breakdown strength, were selected by varying the gain of amplifier and the bias voltage of the discriminator. Thus the counts of the pulses per second whose sizes are larger than n were plotted as a function of n in semi-log scale as shown in fig. 6. These curves seem to be almost straight lines except the parts for extremely small and large n. The distribution for large n differs for different specimen and predominates during the change of the applied voltge. Therefore, this part may be ascribed to the noise of Schönfeld[7)] type due to the sudden discharge of local space charge trapped between the specimen and the electrode or in some defects in the

---

* If the input stray capacitance is so large that the width of current pulse through R can not be neglected, we must replace this formula by

$$V=2enR\int_0^\infty G(\nu)/[1+(2\pi\nu RC)^2]d\nu\,.$$

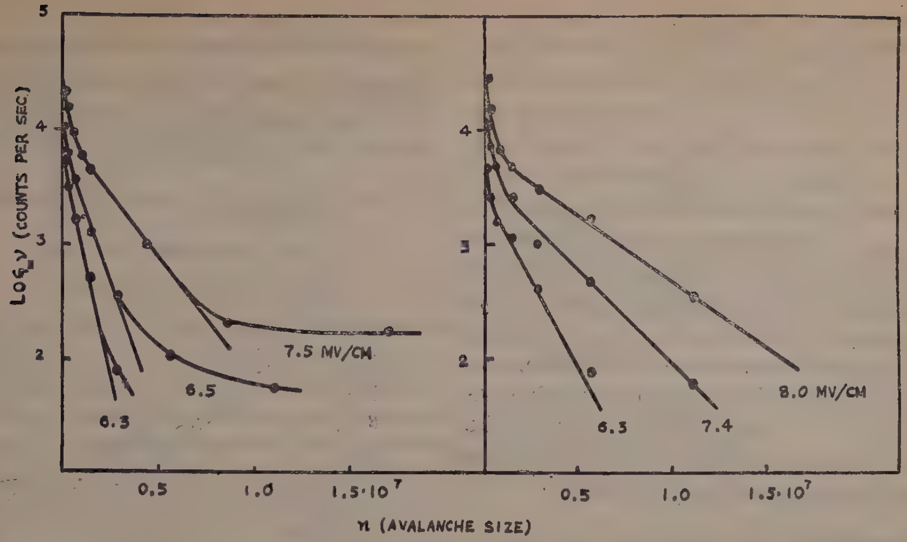

Fig. 6.

interior of the specimen. The part for small n may be due to the avalanches which do not range from cathode to anode. From these linse we can determine the average size $\bar{n}$ and the total number ν_0 per second as seem from the equation (7), which were plotted as a function of field strength in fig. 7. The measurements were made for various specimens at room temperature. In fig. 8 d.c. currents were plotted *vs.* field strength. The current due to avalanches $e\nu\bar{n}$ calculated from fig. 7 were shown in dotted line, which is only few hundredths of the measured current. This may shows that there are enormously great number of small avalanches which does not range from cathode to anode, and that the occurrence of main avalanche is limited to an extreme locality.

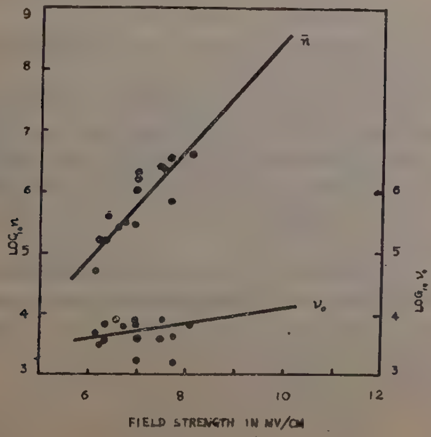

Fig. 7.

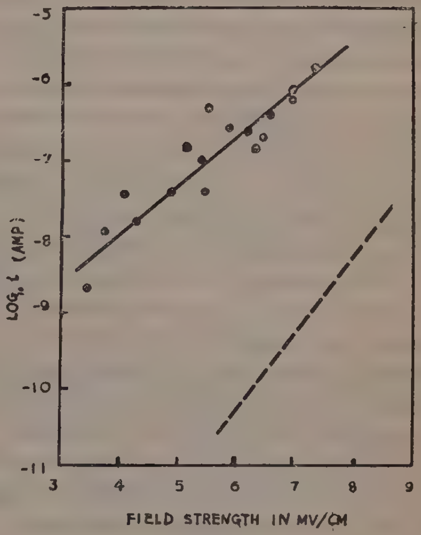

Fig. 8.

§ 4. Statistical Time Lag and Avalanche Size

The measurements of statistical time lag were made under the field above breakdown strength, but the studies of avalanche size were limited in the pre-breakdown region. There-fore, in order to correlate these results, we must extrapolate either results beyond their limits of experiments. If we combine the value of $\bar{n}$ and ν_0 at 8.8MV/cm and 10 MV/cm, obtained by extrapolation of lines in fig. 7, with the experimental value of average statistical time lag, according to the equation (8), we can find that the threshold avalanche size n_0, which is just sufficient to produce disruption, is 6×10^7 for 8.8 MV/cm and 1.3×10^8 for 10MV/cm. According to the estimation of Seitz³⁾, n_0 is about 10^{12} for the speciam of diamond 1 cm thick. But if his method of estimation is applied to the specimen of 3×10^{-4}cm thick, we can obtain $10^8\sim10^9$ for n_0. If the time lags at 8.2MV/cm and 7.6MV/cm, which can not be obtained experimentally, were calculated from $\bar{n}$ and ν_0 employing 10^8 for n_0, we get 10 seconds and 10^8 years respectively. Therefore, we can determine the breakdown strength relatively sharply to be 8 MV/cm even if the statistical fluctuation due to the avalanche mechanism were taken into account.

§ 5. Discussion

We have discussed the relation between the statistical time lag of breakdown and the distribution of avalanche size from the viewpoint of avalanche mechanism of breakdown and found that the result of the both measurements are consistent. But the studies of avalanche size which were made under the static field below the breakdown strength could not be correlated with the study of the time lag of breakdown made under the transient over voltage, without careful precaution. The distribution of the avalanche size may have an abrupt or discontinuous variation at the breakdown field. Or, even if this variation is continuous as we have assumed in the above discussion, the avalanche size may have a time variation. In fact at 60°C we have observed such a cases that the avalanche sizes decrease after the application of the field, or avalanche sizes do not increase even if the applied voltage is increased as shown in fig. 9. These facts seem to show that the growth of the avalanche is prevented owing to the interaction with a large number of electrons and holes due to the preceding avalanches, which is not completely swept to electrodes and accumulated very locally. These phenomena may have some relation with the breakdown mechanism proposed by Fröhlich⁸⁾ who have taken into account the rise of electron temperature. In fact, at 100°C the breakdown strength by transient field was 10 *MV*/cm as shown in fig. 3, but by the static field the strength was only 8 MV/cm. Thus the breakdown mechanism seems to be different in both cases.

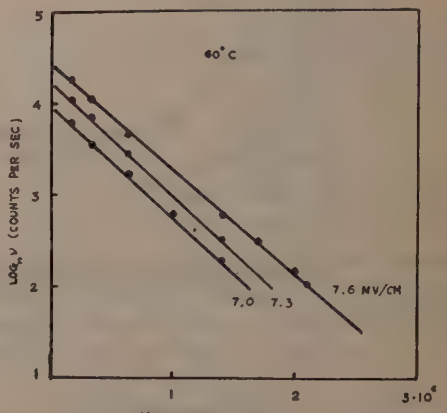

Fig. 9.

In order to make such a study unambiguously, it is necessary to measure the time lag of the breakdown and the distribution of avalanche during this time lag simultaneously applying the transient over-voltage.

In conclusion we wish to express our thanks to Prof. F. Seitz and Prof. T. Muto for their encouragements and interests to our works. We are also indebted to Mr. Y. Inuishi and Mr. M. Tomura for their helpful discussion.

References

1) Av. Hippel: Z.S. f. Phys. **75** (1932) 145 Jour. Appl. Phys. **8** (1937) 815.
2) H. Fröhich: Proc. Roy. Soc. **160** (1937) 230, **172** (1939) 172.
3) F. Seitz: Phys. Rev. **76** (1949) 1376.
4) H.B. Callen: Phys. Rev. **76** (1949) 1394.
5) W.H. Furry: Phys. Rev. **52** (1937) 569 R., A. Wijsmann: Phys. Rev. **75** (1949) 833.
6) B.R. Gossick: Jour. Appl. Phys. **21** (1950) 847.
7) H. Schönfeld: Ann. d. Phys. **19** (1934). 733.
8) H. Fröhlich: Proc. Roy. Soc. **188** (1947) 521

Short Notes

J. PHYS. SOC. JAPAN **7** (1952) 533

A Variational Method for Determination of the Propagation Parameter

Mikio NAMIKI

Department of Applied Physics, Faculty of Science and Engineering
Waseda University, Tokyo

(Received May 26, 1952)

In treating wave motions which are reducible to one-dimensional problem, we must take the reflection coefficient as an important quantity. The reflection coefficient can be computed from the given propagation function or potential. There are several methods for this problem, including the variational method proposed by G.T. di Francia[1]. Conversely, it is interesting to consider problem of infering the features of the propagation function or potential from given values of the reflection coefficient. But, since we can consider various functions giving the same values of the reflection coefficient, they cannot be uniquely determined from a few number of values of reflection coefficient. In practical problems, however, we sometimes encounter with the simple case in which the propagation function is known except for an unknown parameter. In the present note we shall treat such a case and give a variational method to determine the unknown parameter from a given reflection coefficient.

The wave function $u(x)$ must satisfy the following equation under appropriate boundary conditions:

$$u''(x)+k^2(x)u(x)=0\,. \qquad (1)$$

Suppose that the propagation function $k^2(x)$ varies in a certain interval $(0<x<a)$, that is,

$$\begin{aligned} k^2&=k_0^2\,, && (x<0)\\ &=k_1^2+Av\,, && (0<x<a)\\ &=k_2^2\,, && (x>a)\end{aligned}$$

where k_0 and k_2 are given constants, k_1^2 and v are given functions, and A is an unknown parameter. If we denote the reflection and transmission coefficients by R and T, respectively, the wave function $u(x)$ outside the anomalous domain will take the following forms

$$\begin{aligned} u&=\exp(ik_0x)+R\exp(-ik_0x) && (x<0)\\ &=T\exp(ik_2x) && (x>a)\,,\end{aligned}$$

provided that the amplitude of incident wave is normalized to unity. Thus the wave function inside the anomalous domain must satisfy the following expressions as the boundary conditions:

$$\left(\frac{u'}{u}\right)_{x=0}=ik_0\frac{1-R}{1+R}\,,\qquad \left(\frac{u'}{u}\right)_{x=a}=ik_2\,. \qquad (2)$$

Now we consider the following functional of u:

$$J=-\frac{J_1}{J_2}=-\frac{\int_0^a u(u''+k_1^2u)dx}{\int_0^a vu^2dx}\,, \qquad (3)$$

$$J_1=\int_0^a u(u''+k_1^2u)dx\,,\quad J_2=\int_0^a vu^2dx\,.$$

Then J is equal to A for exact solution u of eq. (1). Taking the first variation of J_1 due to the variation of u, we get

$$\delta J_1=2\int_0^a(u''+k_1^2u)\delta u dx-\left[u^2\delta\left(\frac{u'}{u}\right)\right]_0^a\,.$$

The last term vanishes by the boundary condition (2) with given R. Then

$$\delta J=-\frac{2}{J_2}\int_0^a[u''+(k_1^2+J)u]\delta u dx\,.$$

Thus, since the variational expression J has eq. (1) as its Euler's equation, the functional J gives the parameter A at the stationary point. The form of J resembles to the energy expression $E=(\psi, H\psi)/(\psi,\psi)$ in the quantum mechanics.

Let us try the above variational method for the simple and illustrative case, $v=1$ and $k_0=k_1=k_2$. We use a simplest trial function $(1+R)\exp[ik_0x(1-R)/(1+R)]$ which satisfies the boundary condition (2) and gives an approximation of the true function for $k_0^2\gg|Av|$ and $k_0a\lesssim 1$. Hence, it is expected that the expression J gives a good approximation for $|R|\ll 1$. Then we get

$$|R|\simeq 0.5\frac{|A|}{2k_0^2}$$

and, on the other hand, from the exact calculation

$$\begin{aligned}|R|&=\left[1+\frac{4k_0^2(k_0^2+A)}{A^2\sin^2(\sqrt{k_0^2+A}\,a)}\right]^{-1/2}\,,\\ &\simeq|\sin k_0a|\cdot\frac{|A|}{2k_0^2}\,.\end{aligned}$$

The approximation is satisfactory in spite of the fact that a simplest trial function was used.

References

1) G.T. di Francia: Phys. Rev. **78** (1950) 298.

J. PHYS. SOC. JAPAN 7 (1952) 534

Effect of Magnetic Field on Precipitation of Ferromagnetic Phase

By Syôhei MIYAHARA and Tadayasu MITUI

Department of Physics, Faculty of Science, Hokkaidô University

(Received June 9, 1952)

Effect of magnetic field on precipitation of Co-rich phase from Cu-2%Co alloy was studied. The alloy ingot was forged and cut into discs of 13.3 mm in diameters and 6.4 mm in thicknesses. Then, they were annealed in an electric furnace at 1000°C for an hour and cooled down by 5°C in each minute without or within the magnetic field of ca. 10000 Oersteds between pole pieces of an electromagnet, taking care that the field direction lie on the disc plane.

The magnetic anisotropy of the specimens was measured by a torque meter made of phosphor-bronze helical spring. The specimen cooled without field showed no measurable magnetic anisotropy, but the one cooled within field showed remarkable anisotropy.

Next, in order to find the temperature region effective to the magnetic field cooling, the field was applied to the specimen for each region of consecutive 50°-intervals under the same cooling rate above mentioned. Besides, we studied the effect of quenching from the temperature, where the field was got off. When the field has been applied between 765°C and 715°C, the greatest anisotropy is observed. Little difference is found between the specimen cooled in the furnace and the one quenched soon after the field is removed. In fig. 1 the torque curves of the specimen treated in the field in different temperature regions are shown, where the azimuth is measured from the direction of the field during cooling.

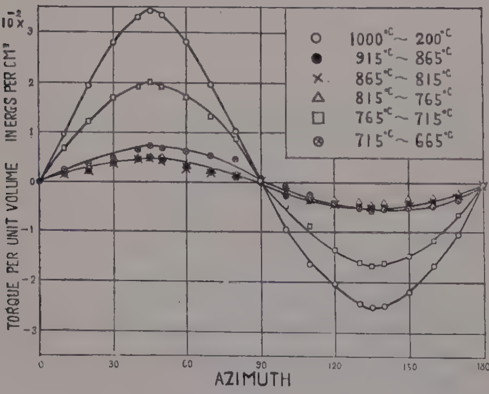

Fig. 1.

Further we are studying the tempering in the magnetic field of the quenched alloy. Full report will be published soon in another paper.

J. PHYS. SOC. JAPAN 7 (1952) 534-535

Artificial Preparation of Silicon Single Crystals

By Yasuo KANAI

The Electrical Communication Laboratory, Ministry of Telecommunications, Tokyo, Japan

(Received June 17, 1952)

It is very important to prepare artificially silicon single crystals, and to work experimentally their physical properties in comparison with the theory of semiconductors, as in the case of germanium.

Silicon single crystals were prepared by the following techniques: After the complete melting of silicon, the input power of the molybdenum-furnace was decreased rapidly. When the quartz crucible was placed in a suitable position of the furnace, the cooling process took place firstly at the surface of the melt. In this cooling process the single crystals began to grow up along the surface. Before the solidifying process progressed deeply into the interior of the melt, the single crystals were pulled out from the melt.

Silicon single crystals which grew up by the above procedures were very thin slabs of the following apprarance: (1) Regular Triangle, (2) Rhombic form (See Fig. 1, (a)), (3) Hexagonal one, and (4) Needle-like one. (See Fig. 1, (b)).

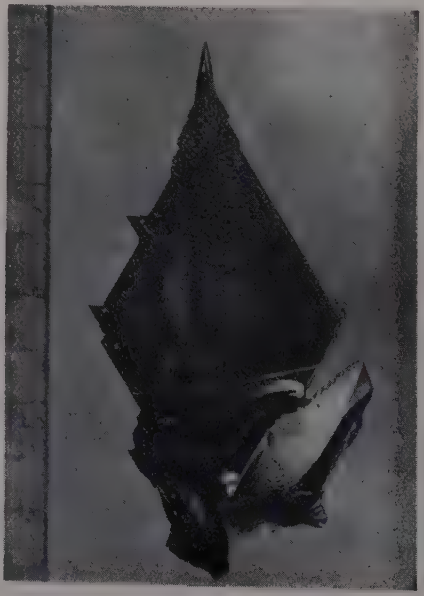

(a)

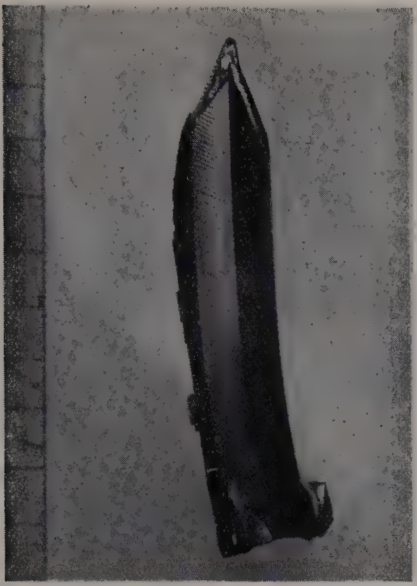

(b)

Fig. 1. The photographs of silicon single crystals. (the unit of the scale is 1mm) (a): Rhomb, (b): Needle-like crystals.

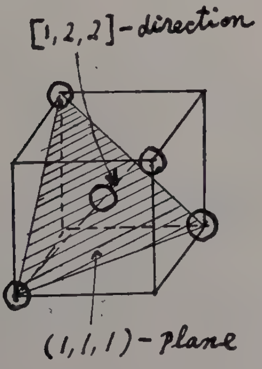

Fig. 2. The unit cell of silicon crystals. (Diamond-type lattice).

X-ray tests have shown that the all single crystals have grown up along the (1, 1, 1) plane. (See Fig. 2). Moreover, the direction of the longitudinal axis of the needle-like crystals was the same as that of the diagonal of the rhombic crystals, being along the direction of [1, 2, 2], or [2, 1, 2], or [2, 2, 1].

The author is indebted to Mr. K. Ono in our Laboratory for his X-ray tests and valuable discussions.

J. Phys. Soc. Japan **7** (1952) 535-536

On the Frequency Dependence of Widths in Paramagnetic Resonance of $CuK_2Cl_4 \cdot 2H_2O$

H. Kumagai, H. Abe, J. Shimada, I. Hayashi, K. Ôno and H. Ibamoto*

Institute of Science & Technology, University of Tokyo, Tokyo, Japan

(Received July 12, 1952)

The results of measurements of microwave paramagnetic resonance of $CuK_2Cl_4 \cdot 2H_2O$ and other salts at 3000 Mc have been reported by J. Itoh et al.[1] We recently observed the resonance of the salt at 9970 Mc and 20,000 Mc and found a remarkable frequency dependence of widths.

The symmetry of this crystal is tetragonal and each unit cell contains two Cu^{++} ions as shown in Fig. 1.[2] One is located at the origin and the other at the body centre. Both ions are surrounded by four chlorine atoms and two water molecules. Chlorine atoms are on a rhomb in the aa-plane, two rhombs in unit cell being rotated each other by 90° about the c-axis. Thus the electric field acting on copper ion has rhombic symmetry. We can expect two different g-values at some orientations, but we observed only one g-value in every case, which may be caused by the exchange coupling.

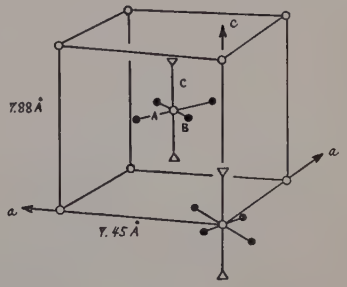

○ = Cu A = 2.95 Å
● = Cl B = 2.26 Å
▽ = O C = 2.52 Å

Fig. 1.

The observed half-value widths and g-values are shown in Figs. 3 and 4. The angles θ and φ indicate the orientation of the static magnetic field H_s, as shown in Fig. 2. The magnetic field of the microwave is always perpendicular to H_s.

Widths at 3000 Mc in these figures are those measured by J. Itoh et al. by the static method[3]. They are a little different from their published data which were obtained from differentiated

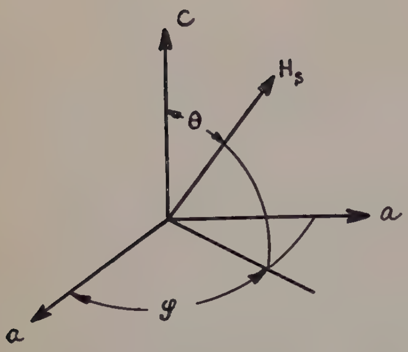

Fig. 2.

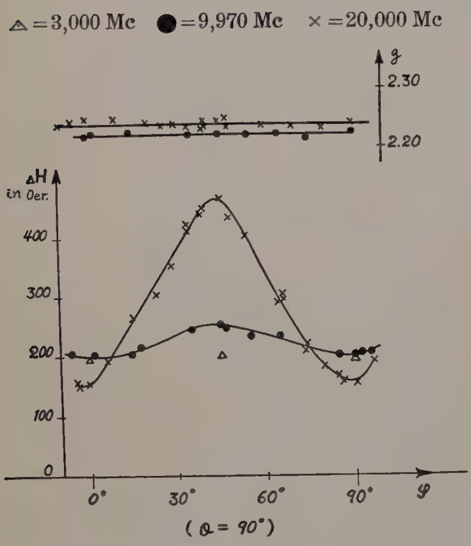

Fig. 3.

curves assuming that the shapes of absorption curves are electric resonance type. In the aa-plane, the widths are almost constant at 3000 Mc, but at 9970 Mc and 20,000 Mc they have maxima at $\varphi=45°$, 135° in which different g-values are expected and minima at $\varphi=0°$, 90° in which the g-values of two kinds of ions coincide. The maximum widths at 20,000 Mc are about twice as large as those at 9970 Mc. The minimum widths decrease a little when the frequency is increased, this fact being checked by repeated measurements. The widths at $\theta=0°$ (c-direction) are small and also decrease with increasing frequency.

The results of ammonium salt $Cu(NH_4)_2Cl_4 \cdot 2H_2O$ have the same nature, except that widths are generally slightly smaller than those of potassium salt. The crystals used are optically checked and are not twins.

The broadening of line widths in higher frequencies at $\varphi=45°$ and 135° may be explained by the nature of exchange coupling, but small and definite sharpening at $\varphi=0°$ and 90° and c-direction can not be easily explained. It must be remembered that the electric field acting on copper ions is of rhombic symmetry.

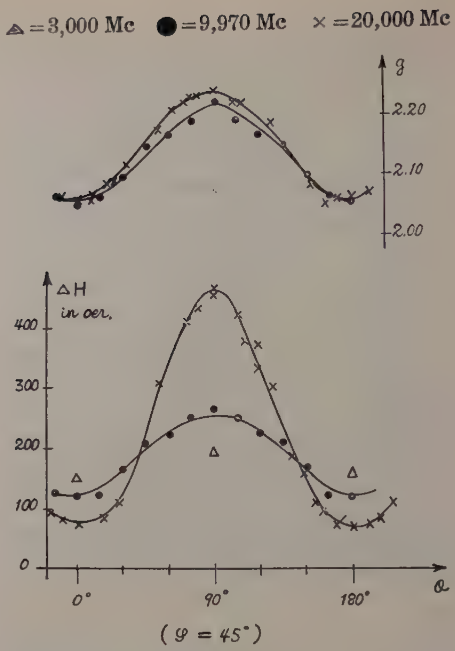

Fig. 4.

It must be taken into account that the fine and hyperfine structure affect the widths in our case. But, in copper ions ($S=1/2$), the fine structure vanishes[4),5)]. As to the hyperfine structure, the second order effect has frequency dependence[4)] in general, but it has little effect in our case of copper ions. Thus the fine and hyperfine structure may be insufficient to explain the sharpening at some directions.

References

1) J. Itoh, M. Fujimoto & H. Ibamoto: Phys. Rev. **83** (1951) 852.
2) L. Chrobak, Z. Krist: **88** (1934) 35.
3) J. Itoh et al: Private communication.
4) B. Bleaney: Phil. Mag. **42** (1951) 441.
5) B. Bleaney & D. J. E. Ingram: Proc. Roy. Soc. **205** (1951) 336.

---

* Department of Chemistry, Faculty of Science, Ôsaka University.

J. PHYS. SOC. JAPAN 7 (1952) 537-538

Ultrasonic Absorption in Carbon Disulphide

Tadashi KISHIMOTO and Otohiko NOMOTO
Kobayashi Institute of Physical Research, Kokubunji, Tokyo

(Received July 12, 1952)

The absorption of ultrasonic waves in carbon disulphide (CS_2) has been investigated by many authors and the results interpreted as the molecular absorption by Kneser[1], Bauer[2], Sette[3], and Lamb and Andreae[4][5]. The existing absorption data, however, are rather scattered, so that the theoretical interpretations proposed by these authors are also widely different one another.

So we performd the absorption measurement in this substance by the pulse technique at three frequencies 1.43 Mc/sec, 2.86 Mc and 7.7 Mc, and at temperatures between 0° and 35°C in order to add some reliable absorption data and to select among various interpretations proposed.

Fig. 1 shows the absorption curves α/f^2 *vs.* temperature at the three frequencies employed, where α means the amplitude absorption coefficient and f the frequency. As is to be seen in the figure, α/f^2 is almost independent of frequency above the room temperature, but it decreases at higher frequency and lower temperature. The value of α/f^2 at room temperature was found to be 5700×10^{-17} sec^2/cm and no appreciable change was to be noticed between the absorption coefficients of distilled sample of CS_2 and non-distilled one.

The existing absorption data are summarized in Fig. 2. The present result is in agreement with that of Huddart[6], and does not contradict with the absorption data of Sette[3], Lamb and Andreae[4] and Rapuano[7][8] obtained at higher frequencies, while the absorption coefficients obtained by Claeys, Errera and Sack[9] are much higher than the present result and those of Parthasarathy[10] and Ouang[11] are much lower.

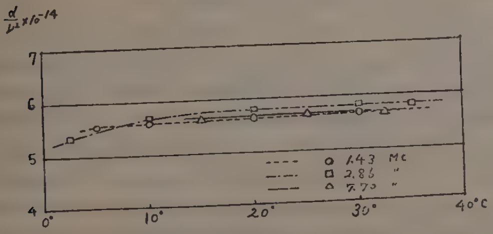

Fig. 1. α/f^2 *vs.* temperature at three frequencies 1.43 Mc/sec, 2.86 Mc, and 7.7 Mc in carbon disulphide.

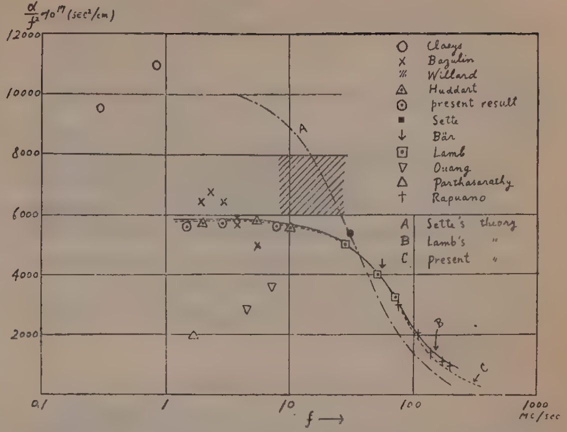

Fig. 2. α/f^2 *vs.* frequency in carbon disulphide; existing result by various authors and the interpretation by molecular absorption theory.

The data by Willard[12] and Bazulin[13] are approximately in agreement with the present result, though somewhat scattered.

Following Lamb and Andreae[4] we have interpreted the absorption data by assuming the thermal relaxation between the vibrational modes of the molecule and other degrees of freedom (translation and rotation). But we have postulated a single and common relaxation time for all the vibrational modes of the molecule while Lamb and Andreae have assumed that only the deformation vibrations relax between the observed limits of frequency and that the other modes of vibration with higher frequency of vibration relax at higher frequency. This, however, does not seem reasonable on the basis of the Arrhenius' equation

$$P=A\exp(-E/RT),\quad (A=\text{const.}) \qquad (1)$$

where P means the transition probability for extinction of the molecular vibration and E the activation energy, because E may be supposed to be increasing monotonously with increase in frequency of molecular vibration. So we have to expect a smaller transition probability P, and accordingly a larger relaxation time, i.e., a lower frequency of relaxation for higher vibrational mode. We have assumed, however, a common relaxation time considering that the experimental data seems to indicate a constant value of α/f^2 at lower frequency. In this respect our interpretation is analogous to that of Sette, first proposed by Kneser, though the value of the relaxation time is much shorter.

We have calculated the absorption curve and illustrated it in Fig. 2 employing Herzfeld's formula[14]

$$\frac{\alpha}{f^2}=\frac{2\pi^2}{V_0}\frac{C_i(C_{p0}-C_{v0})}{C_{v0}(C_{p0}-C_i)}\frac{\beta(C_{p0}-C_i)/C_{p0}}{1+\omega^2\{\beta(C_{p0}-C_i)/C_{p0}\}^2} \qquad (2)$$

and employing the values of the constants (at 25°C):

molar vibrational specific heat $C_i=3.934$ cal/mole/deg, low frequency molar specific heat at constant volume $C_{v0}=11.13$, low frequency molar specific heat at constant pressure $C_{p0}=18.37$, ultrasonic velocity $V_0=1.14\times10^5$ cm/sec, and

relaxation time (period of adjustment of vibrational energy)

$$\beta=2.38\times10^{-9}\ \text{sec}.$$

Here the value of β was computed from the experimental value of absorption at low frequency by means of the equation

$$\frac{\alpha}{f^2}=\frac{2\pi^2}{V_0}\frac{C_i(C_{p0}-C_{v0})}{C_{v0}C_{p0}}\beta. \qquad (3)$$

The frequency of relaxation corresponding to β is given by

$$f_m=\frac{1}{2\pi\beta}\frac{C_{p0}}{C_{p0}-C_i} \qquad (4)$$

and becomes $f_m=85.6$ Mc/sec (at 25°C).

We obtained further the temperature dependence of β and found that the expression

$$\beta=B\exp(E/RT),\quad (B=\text{const.}) \qquad (5)$$

holds true approximately. The activation energy was found to be $E=1.3$ kcal/mole. This value is smaller than the known value of activation energy for CS_2 vapour, $E'=5.4$ kcal/mole obtained by Richards and Reid[15]. More experiments will be needed before any reliable theoretical conclusion concerning this difference between gaseous and liquid CS_2 may be obtained.

We express our hearty thanks to Prof. S. Okui of the Institute of Pharmaceutics, Faculty of Medicine, Tokyo University, for his aid in purification of the sample liquid.

The financial aid for this research has been furnished by the Ministry of Education in a Grant in Aid of Scientific Research.

Detailed account of this research will be published in Bulletin of the Kobayasi Institute of Physical Research.

References

1) H. O. Kneser: Erg. exakt. Naturwiss. **22** (1949) 169.

2) E. Bauer: Proc. Phys. Soc. (London) **A62** (1949) 141.

3) D. Sette: J. Chem. Phys. **19** (1951) 1942.

4) J. Lamb and J. H. Andreae: Nature **167** (1951) 898.

5) J. H. Andreae and J. Lamb: Proc. Phys. Soc. **B64** (1951) 1021.

6) D. H. Huddart, Thesis London (1950) (cited in (4)).

7) R. A. Rapuano: Res. Lab. Electronics, Mass. Inst. Techn. Rep. No. 151 (April 15, 1950), (cited in (4)).

8) R. A. Rapuano: Phys. Rev. **72** (1947) 78.

9) J. Claeys, J. Errera and H. Sack: Trans. Faraday Soc. **33** (1937) 136.

10) S. Parthasarathy: Current Science, **6** (1937) 55.

11) J. Ouang: C. R. **222** (1946) 1215 (cited in (3)).

12) G. W. Willard: J. Acous. Soc. Amer. **12** (1941) 438.

13) P. Bazulin: J. exper. theor. Phys. URSS. **8** (1938) 457 (cited in (4)).

14) K. F. Herzfeld: J. Acous. Soc. Amer. **12** (1941) 33.

15) W. T. Richards and J. A. Reid: Nature **130** (1932) 739 J. Chem. Phys. **2** (1934) 193.

J. Phys. Soc. Japan **7** (1952) 538-540

Electronic Conductivities of Amorphous Solids at High Electric Fields

By Masao TOMURA and Takeo KIKUCHI

Institute of Polytechnics of Osaka City University

(Received June 26, 1952)

H. Fröhlich[1] has proposed a new theory of electric breakdown of amorphous solids in which the collision between electrons themselves is dominant than that between electrons and lattice vibrations. C. H. M. Turner and W. E. Lewis[2] measured electronic conductivity of soda lime glass and explained the results on the standpoint of the above theory, considering the observed conductivity as stationary one. On the other hand, J. H. Simpson[3] explained the same results as transient phenomena.

The measurement of Turner and Lewis was carried out by using the electric field of linearly rising pulse, so the obtained data was too ambiguous to select the either of the above two explanations. Hence in the present work, top flatted pulses were used and the current-time curves of samples were shown on a oscilloscope. Thus from the figures of the curves, the real currents could be read avoiding charging currents into the specimens and polarization currents. The pulse durations were 30 and 110 μ sec. Samples were soda lime glass plates of about 10^{-3} cm thickness which had about 0.1 cm² evapolated Al electrodes.

The observed current densities at various voltages and temperatures are shown in Fig. 1. The breakdown strengths were also measured. (See Fig. 2)

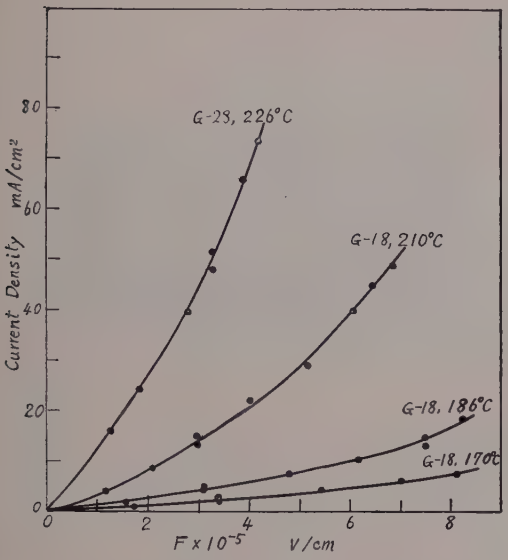

Fig. 1.

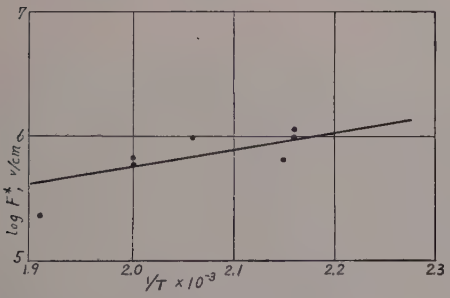

Fig. 2.

According to Fröhlich1),

$$\log(\sigma/\sigma_0)=\frac{F^2}{F^{*2}}\cdot\frac{V}{\Delta V}\quad (F\ll F^*)\,, \tag{1}$$

$$F^*=C\exp(\Delta V/2kT)\,, \tag{2}$$

$$\sigma_0=D\exp(-V/kT)\,. \tag{3}$$

Here σ is conductivity at a given temperature and field, and σ_0 the conductivity at that temperature and zero field. C and D are constants. F is an applied field strength and F^* breakdown strength. V is the depth of the deep trapping level and ΔV that of the shallow level. k is Boltzmann's constant and T the absolute temperature.

The plots of $\log\sigma$ *versus* F^2 curves are shown in Fig. 3 in which the square law relationship between F and σ of Eq. (1) is well verified. As $V/\Delta V$ is constant for a given kind of sample, temperature dependence of $\log\sigma$ in Eq. (1) comes from temperature dependence of F^*. Fig. 4 shows this relation and ΔV is obtained as 0.65V by using Eq. (2). On the other hand, from the direct measurements of F^* at various temperatures ΔV was given as 0.57V which agreed fairly with the above value. σ_0 was obtained from Fig. 3. while V was obtained as 0.67V from its variation with temperature and by using Eq. (3). (See Fig. 5)

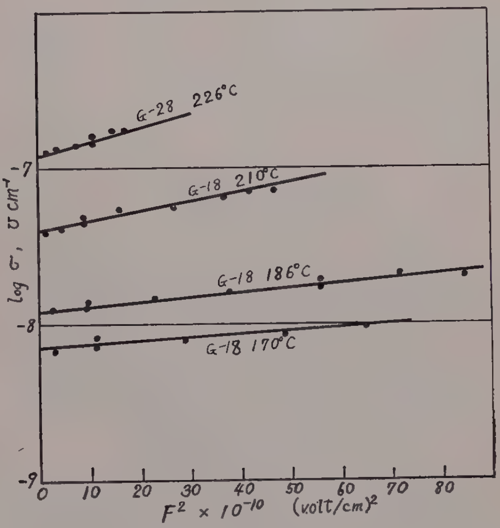

Fig. 3.

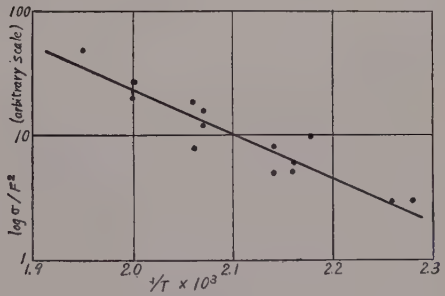

Fig. 4.

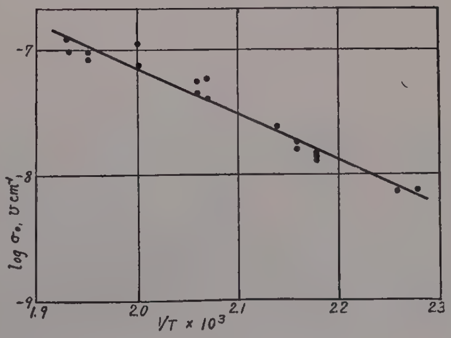

Fig. 5.

The relaxation of conduction which was derived by Simpson could not be observed in our case. His analysis, attributing the conductivity dependence on field to relaxation of conduction, is doubtful. The relaxation time will be less than 10^{-6} sec. In other words, the observed conductivity is stationary.

References

1) e.g. H. Fröhlich: Proc. Roy. Soc. **188** (1947) 521.
2) C. H. M. Turner and W. E. Lewis: Nature **159** (1947) 334.
3) J. H. Simpson: Proc. Roy. Soc. **A63** (1950) 86.

J. Phys. Soc. Japan **7** (1952) 540-541

The Formative Time Lag of Dielectric Breakdown

Hazime Kawamura & Hirosi Okura
Department of Science and Engineering, Osaka City University, Osaka

(Received June 26, 1952)

The formative time lag of dielectric breakdown was investigated by Striegel[1] and by Inuishi and Suita[2]. They have measured the time lag of breakdown, applying transient overvoltage of steep rise, and eliminated the statistical time lag by testing many specimens.

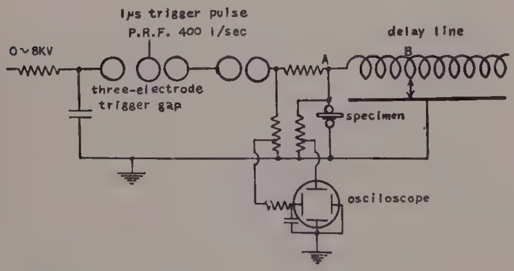

Fig. 1.

Our present method is as shown in fig. 1. Applying trigger pulse of 1μs to the center electrode of three-electrode trigger gap, with P.R.F. of 400 1/sec, we obtained transient voltages of extremely short rise time (less than 1×10^{-8} sec), which was fed on delay line through the resistance equivalent to its characteristic impedance. The characteristic impedance and delay time were 750Ω and 4×10^{-10} sec/cm respectively. When one point B on the delay line is connected to the earth potential, very short pulse having a duration of twice as long as the delay time from A to B is generated at A. The pulse duration can be varied from 1×10^{-8} sec to 6×10^{-8} sec. The pulse form was fairly sharp as shown in fig. 2. Sliding the point B from left to right, the pulse duration is increased continuously. The breakdown occurs on the specimen inserted between A and earth, when the pulse duration reaches the time lag of the breakdown. We can determine the formative time lag by measuring the length from A to B. The statistical time lag has been removed, since the pulses are repeated by the frequency of 400.1/sec.

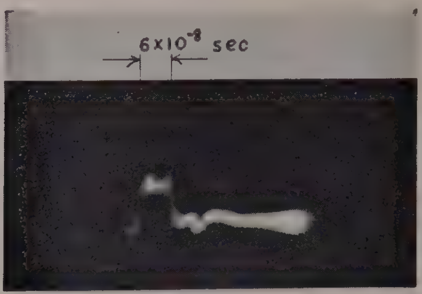

Fig. 2.

If the formative time lag is the time interval required for electron to drift from cathode to anode, producing electron avalanche, the drift mobility of such a high energy electron is given by $\mu=d/\tau E$, where d is the thickness of the specimen and E is the field strength. The measurement were made for green mica (biotite) 3~6×10^{-4} cm thick, both at room temperature and 100°C. The results are as follows:

	μ(cm²/V.sec)	E_B(V/cm)
290°K	$4.9\pm1.5\times10^{-3}$	$4.3\pm0.12\times10^{6}$
370°K	$3.3\pm1.0\times10^{-3}$	$4.9\pm0.05\times10^{6}$

E_B is the breakdown strength measured under the application of 30μs pulses with P.R.F. of 60 1/sec. μ is only about 1/1000 of the value theoretically expected from von Hippel's criterion $E_B=(1/\mu)\sqrt{(\varepsilon/m)}$, where $\varepsilon\simeq0.05$ eV. The actual breakdown field may be reduced to 1/10 of the above field E_B, if the fluctuation of the behaviours of electrons is taken into account as shown by Seitz. In spite of such a consideration, μ is only about 1/100 of the expected value.

As the avalanche size increases exponentially while drifting toward anode, electrons and holes are generated densely at the neighbourhood of the anode. Therefore, the energy dissipated by holes drifting to cathode is greater than the energy due to electrons. If we assume that the breakdown occurs due to the energy of these holes, the formative time lag must be the time required for the holes to drift from anode to cathode. Assuming that the effective mass of a hole is about ten times of the electronic mass, we can understand the anomalously small mobility, since the mobility is proportional to $m^{*3/2}$ or m^{*3} for the case of polar or nonpolar interaction respectively.

The fact that the breakdown path splits toward cathode is also favourable to the above assumption that the drifts of holes produce the breakdown. Although the mobility of the hole should be isotropic because of the low velocity, the holes may drift through the path of electron avalanche whose motion is anisotropic, and split near the cathode.

References

1) R. Striegel: Wiss. Veröff. Siem. Werk. **18** (1939) 101.

2) Y. Inuishi, C. Yamanaka, T. Suita: Tech. Rept. Osaka Univ. **2** (1952) 71.

3) F. Seitz: Phys. Rev. **76** (1949) 1376.

4) A. von Hippel: Z.S. f. Phys. **67** (1931) 707, **68** (1931) 309.

ERRATA

A Study on Corrosion-Process of Iron by Means of Electron Diffraction

By Ryuji Abe

J. Phys. Soc. Jap. **6** (1951) 345～350

P. 345 synopsis line 6	so very low......	should be read......	is very low
P. 345 left colomn			
line 16	$Fe_1O_3\cdot H_2O$	〃	$Fe_2O_3\cdot H_2O$
P. 346 left colomn			
line 8	vey	〃	very
P. 349 left colomn			
line 14	H_2O_2	〃	H_2O
P. 347 Table I			
1st colomn	0.224	〃	0.244
last colomn	$Fe_2(OH)_3$	〃	$Fe(OH)_3$
last colomn	0.154 (101), 0.249 (111), 0.309 (212) (112), 0.528 (321), 0.618 (404), 0.710 (602)	〃	0.154 $(10\bar{1})$, 0.249 $(11\bar{1})$, 0.309 $(20\bar{2})$ $(11\bar{2})$, 0.528 $(32\bar{1})$, 0.618 $(40\bar{4})$, 0.710 $(60\bar{2})$
P. 349 Table IV			
last colomn line 6	Wyckoff(6)	〃	Wyckoff(9)
6th colomn ($\alpha-Fe_2O_3\cdot H_2O$)	$c=5.03$	〃	$c=3.03$

JOURNAL OF THE PHYSICAL SOCIETY OF JAPAN Vol. 7, No. 6 NOV.—DEC., 1952

Notes on the Crystallite Theory of Liquid

By Akiya OOKAWA

Department of Physics and Chemistry, Gakushuin University, Mejiro, Tokyo

(Read April 1 and received May 21, 1952)

In specifying the interfaces by the crystallite theory of liquid, here is proposed to replace the excess boundary energy by the excess free energy. A correction is also made as to the previous procedure in determining the value of the orientational order parameter. With these modifications the theoretical results can be formulated in considerable agreement with the experimental rules, such as the Lindemann's formula as to the melting point, the melting entropy, and the Andrade's formula as to the coefficient of viscosity. Just above the melting point, more-over, we have expectation of some abnomalities of the specific heat and of the viscosity coefficient, due to the structural change more or less sharp there.

§ 1. Preface

The crystallite theory of liquid[1][2][3] has been formulated with special interest on subjects such as the specific heat, the solid-liquid transformation, and the viscous flow. It is noted, however, that the theoretical predictions are in some respects not in accord with the experimental data. The contradictory points are enumerated as follows:

(a) While the latent heat Q of melting is nearly equal to the thermal energy kT_m at the melting point, the ratio Q/kT_m estimated according to Eq. (II, 36) is much smaller than unity.

(b) The anomalous specific heat is observed just above the melting point but not just below it. The specific heat versus temperature curve shown in Fig. 5 of Ref. II is, contradictory to the observation, abnormal in the solid range rather than in the liquid range.

(c) The frequency factor of the viscosity coefficient given by Eq. (III, 17) is too larger than that required by experiment.

It is shown in the present note that most of these discrepancies can be avoided by the process of replacing the 'excess energy' at the crystallite boundary by the 'excess free energy', introducing the 'excess entropy' in effect.

In connection with the modification, some misunderstandings in the previous representation of the orientational correlation are corrected.

§ 2. On the Nature of Cooperation

The partition function of a system constituted of crystallites of linear size αa is, according to Ref. II, § 3, written as

$$\Xi=[kT/h\nu]^{3N}\sum_{\alpha}[\xi_t(\alpha)]^N\ , \tag{1}$$

where

$$\xi_t(\alpha)=\left[\left(\frac{h\nu}{kT}\right)^3\frac{(2\pi m_0kT)^{3/2}a^3}{h^3}\alpha^{19/2}\{g_{t1}(\alpha)\}^3\right]^{\alpha^{-3}} \tag{2}$$

with

$$g_{t1}(\alpha)\doteq\frac{\pi}{16}\exp\left(-\frac{p\alpha^2k_1}{8kT}\right)\times\left[I_0\left(\frac{pt\alpha^2k_1}{8kT}\right)-I_1\left(\frac{pt\alpha^2k_1}{8kT}\right)\right]. \tag{3}$$

The parameter t was introduced to represent the orientational order of the constituent crystallites, such that the state with $t=1$ corresponds to the perfectly ordered state and the state with $t=0$ to the perfectly disordered state.

A numerical constant p is introduced in modifying Eq. (II, 5) to

$$\varepsilon_p=pn\alpha^2\varepsilon_0\ . \tag{4}$$

Its value depends on the geometry of packing the crystallites, varying from 6/2 for the cubes of edge length αa to approximately $(1/2)4\pi/(4\pi/3)^{2/3}\simeq 2.4$ for the spheres of diameter length αa. On account of the average roughness of the treatment, we must be satisfied at present by assigning a tentative value for p. In this treatment, p is put equal to 2.5.

The functional relation of Eq. (II, 23) determining the thermodynamical value of the parameter t has been introduced in error. It is because the thermodynamical probability $g_t(\alpha)$, obtained by integrating over the whole range of the orientational coordinate, does not represent the probability of the crystallite in a specified orientation. To be consistent, indeed, the value of the parameter t must be adjusted to the effect that, for any specified value of t, the weighted orientational distribution of the crystallites should result, in return, for each orientation just the mean boundary energy predicted by the same value of t.

The problem under consideration have a nature somewhat alike that of an order-disorder transformation. The exact formulation in the present case is yet prohibitively difficult, because the statistical elements, the crystallites, take orientational 'sites' much numerous than a few.

By the way, it seems that the continuous variation of the orientational order parameter with varying temperature has but a secondary significance in the solid-liquid transformation. One of the sustaining evidences is the fact that the observed specific heat is abnormal in the higher temperature range than the transformation point; the usual order-disorder transformation is characterized by the specific heat curve of the λ-type.

In these circumstances, it may be sufficient to estimate the probable value of the orientational order parameter in a qualitative manner. If we approximate the orientational sites of the constituent crystallites by the two sites, the site of good fit and the site of bad fit with the neighbouring crystallites, then the order parameter should satisfy the relation

$$t=\tanh\,(c\,pt\alpha^2k_1/2kT)\,. \qquad (5)$$

Here, $c\,pt\alpha^2k_1$ is the excess boundary energy of a crystallite in the most unfavourable condition over that in the most favourable condition. The numerical factor c is estimated of order of unity.

According to Eq. (5), a state of perfect orientational disorder ($t=0$) is always allowed and a state of imperfect order ($t\neq0$) is possible when the parameter $c\,p\alpha^2k_1/2kT$ is larger than unity. The degree of order of the latter state is almost perfect for sufficiently large value of $c\,p\alpha^2k_1/2kT$. It is expected that these situations concerning the degree of order remains true also with the real system, at least qualitatively.

If the parameter α were kept constant, the system satisfying Eq. (5) should undergo a transformation of the second order. It was shown in Ref. II, however, that the parameter α specifying the linear size of the most probable crystallites varies with temperature, specifically for systems characterized by different degrees of order.

§ 3. The Solid-Liquid Transformation

The partition function Ξ, given by Eq. (1), can be represented substantially by the largest term among $\xi_t(\alpha)$. Owing to the factor (I_0-I_1) in Eq. (3), the function $\xi_t(\alpha)$ for specified α and T has a largest value for $t=0$ in the range $p\alpha^2k_1/8kT<3.2$ and a largest value for $t=1$ in the range $p\alpha^2k_1/8kT>3.2$.

Accordingly, so long as the condition

$$Z_0\equiv p\alpha^2k_1/8kT<3.2 \qquad (6)$$

is provided, we have a candidate for the representative term among the states of perfect orientational disorder. With $t=0$, we have

$$\log\xi_0(\alpha)=\alpha^{-3}\Big[\frac{3}{2}\log\frac{\theta_0}{T} -3\frac{p\alpha^2k_1}{8kT}+\frac{19}{2}\log\alpha\Big], \qquad (7)$$

where

$$\theta_0=\Big(\frac{\pi}{16}\Big)^2\Big(\frac{h\nu}{k}\Big)^3\frac{(2\pi m_0k)a^2}{h^3} \qquad (8)$$

The function $\xi_0(\alpha)$ has a maximum value

$$\log\xi_0(\alpha_0)=2\alpha_0^{-3}\Big[\frac{19}{12}-\frac{p\alpha_0^2k_1}{8kT}\Big] \qquad (9)$$

at $\alpha=\alpha_0$; the linear size α_0a of the most probable crystallites in the disordered state is determined according to

$$\log\alpha_0^2=\frac{2}{3}+\frac{6}{19}\log\frac{T}{\theta_0}+\frac{4}{19}\frac{p\alpha_0^2k_1}{8kT}\,. \qquad (10)$$

On the other hand, if provided

$$Z_1\equiv p\alpha^2k_1/8kT>3.2\,, \qquad (11)$$

we have a candidate for the representative term among the states of perfect orientational order. With $t=1$, we have

$$\log\xi_1(\alpha)=\alpha^{-3}\Big[-\log\{2^3(2\pi)^{3/2}\}+\frac{3}{2}\log\frac{\theta_0}{T} -\frac{9}{2}\log\frac{pk_1}{8kT}+\frac{1}{2}\log\alpha\Big]; \qquad (12)$$

the modified Bessel functions I_0 and I_1 in Eq. (3) are, under expectation of large argument Z_1, approximated by the first two terms of their asymptotic expansions. The function $\xi_1(\alpha)$ has a maximum value

$$\log \xi_1(\alpha_1)=\frac{1}{6}\alpha_1^{-3} \tag{13}$$

at $\alpha=\alpha_1$; the linear size $\alpha_1 a$ of the most probable crystallite in the ordered state is determined by

$$\alpha_1 \doteq 2^9\pi^3 e^{1/3}\left(\frac{T}{\theta_0}\right)^3\left(\frac{pk_1}{8kT}\right)^9 . \tag{14}$$

With the values of θ_0 and k_1, estimated below to fit the experimental data at the melting point, the linear size α_1 of the representative crystallites in the ordered state is of order of a few hundreds at the melting point and it increases sharply below it. The solid state can therefore be characterized by large constituent crystallites in perfect orientational order to each other. The linear size α_0 of the representative crystallites in the disordered state is shown to be of order of two or three. The liquid state is therefore characterized by small constituent crystallites in perfect orientational disorder to each other.

The representative term $\xi_t(\alpha)$ in the partition function Ξ is the larger one between the maximum term $\xi_0(\alpha_0)$ among the disordered states and the maximum term $\xi_1(\alpha_1)$ among the ordered states. The transformation temperature T_m is determined by the condition

$$\log \xi_0(\alpha_0)=\log \xi_1(\alpha_1) \quad \text{at} \quad T=T_m . \tag{15}$$

The maximum $\log \xi_0(\alpha_0)$, according to Eq. (9), increases with increasing temperature, while the maximum $\log \xi_1(\alpha_1)$, according to Eq. (13), remains but negligibly larger than zero throughout. We can then replace the condition (15) by the approximate condition

$$Z_0 \equiv p\alpha_0^2 k_1/8kT=19/12 \quad \text{at} \quad T=T_m . \tag{16}$$

This is equivalent to requiring that the partition function $\xi_0(\alpha_0)$ per molecule in disordered state should be equal to unity at the melting point. Thus we can estimate the melting point T_m according to Eq. (16) combined with the general relation (10) between α_0 and T.

In order to proceed in a somewhat quantitative manner, we must decide upon the probable values of the quantities k_1 and p. As to the boundary quantity k_1, which is reinterpreted in § 4 as the boundary free energy, we tentatively assume

$$(f/kT)_{T_m} \equiv 3k_{1m}/8kT_m=0.3 \tag{17}$$

at the melting point. Inserting Eq. (17) and $p=2.5$ into Eq. (16), we have

$$\alpha_{0m}^2 \simeq 6.30 , \quad \alpha_{0m}^3 \simeq 15.9 . \tag{18}$$

Eq. (10) is transformed at the melting point, referring Eq. (16), to

$$T_m/\theta_0=C_1 , \tag{19}$$

where

$$C_1=\exp\left[\frac{19}{6}(\log \alpha_{0m}^2-1)\right]. \tag{20}$$

Corresponding to Eq. (18),

$$C_1 \simeq 14.5 . \tag{21}$$

Substitution of Eq. (8) for θ_0 into (19) gives

$$\nu=\frac{16}{\pi}\left(\frac{k}{2\pi C_1}\right)^{1/2}\left(\frac{T_m}{m_0 a^2}\right)^{1/2} . \tag{22}$$

According to Eq. (21), the frequency ν is estimated in order of magnitude to $\nu \sim 10^{12}\,\mathrm{sec}^{-1}$. This value of frequency is rather small in comparison with the atomic frequency ν_0 or the characteristic Debye frequency ν_D. The frequency ν in expression $\xi_t(\alpha)$ corresponds, as was discussed in Ref. II, § 5, to the vibrational modes in the solid state which are to be replaced by the translational modes of the constituent crystallites in the liquid state. It is consequently natural that the frequency ν is smaller than the frequency ν_0 of the atomic vibration.

Eq. (22) can also be written in the form

$$\nu=C_2(T_m/M_0 V^{2/3})^{1/2} \tag{23}$$

by use of the molecular weight $M_0=Nm_0$ and the molar volume $V=Na^3$, N being the Avogadro's number. This is the same form as the Lindemann's formula⁴⁾, satisfied empirically for many substances at the melting point. The present constant C_2 is given by

$$C_2=\frac{16}{\pi}\left(\frac{k}{2\pi C_1}\right)^{1/2} N^{5/6} . \tag{24}$$

According to Eq. (21),

$$C_2 \simeq 4.12\times 10^{11} . \tag{25}$$

The value of α_1 at the melting point is estimated by Eq. (14), referring to Eqs. (17), (19), and (21), to obtain

$$\alpha_{1m} \simeq 128 . \tag{26}$$

Thus the representative crystallites in the ordered state is sufficiently large, even at the melting point, satisfying the presumptions introduced above.

§ 4. The Heat of Melting and the Specific Heat

Taking a perfectly crystalline solid as the standard state, the mean excess free energy Δf per molecule is expressed, according to Eq. (1), by

$$\Delta f=-kT\log[\xi_{\iota}(\alpha^{*})]\,. \tag{27}$$

The representative term $\xi_{\iota}(\alpha^{*})$ is given by $\xi_1(\alpha_1)$ of Eq. (13) or by $\xi_0(\alpha_0)$ of Eq. (9), respectively below and above the transformation point.

Heretofore the quantity k_1 characterizing the interface between crystallites has been interpreted as the excess boundary energy. From the view point of an atomistic structure of the interface, however, it seems more legitimate to introduce the excess boundary entropy characterizing the interface. It is because the molecules at an interface are expected in the potential, different from that in the bulk of the crystallite not merely in its absolute value but also in its shape. We propose accordingly to reinterprete the quantity k_1 as the excess boundary free energy. In this concern, it may deserve noting that Mott[5] has introduced a similar modification of the theoretical activation energy as to the process of viscous flow at the grain boundary.

We set the mean boundary free energy $3/8\cdot k_1$ in the disordered state in the form

$$\frac{3}{8}k_1=f=e-Ts, \tag{28}$$

where e and s are the mean boundary energy and the mean boundary entropy per unit lattice area, respectively. In order to obtain the excess energy Δe and the excess specific heat Δc of the system, it is required definite relations between the mean quantities e and s and the temperature. As we have at present but scant knowledge of these relations, we propose in this paper the approximate constancy of the quantities, at least near the melting point.

For the solid state, substituting Eq. (13) into Eq. (27), we have

$$\Delta f_1=-\frac{1}{6}kT\alpha_1^{-3}\,. \tag{29}$$

The size α_1 of the representative crystallites is determined by Eq. (14), according to which it follows

$$\frac{d\alpha_1}{dT}=-3\,\frac{\alpha_1}{T}\,\frac{2e+Ts}{f}\,. \tag{30}$$

The excess energy Δe_1 is calculated to obtain

$$\Delta e_1=\frac{3}{2}kT\alpha_1^{-3}\frac{2e+Ts}{f} \tag{31}$$

and the excess specific heat Δc_1 is given by

$$\Delta c_1=\frac{3}{2}k\alpha_1^{-3}\left[\frac{2e+Ts}{f}+\frac{3eTs}{f^2}+\frac{9(2e+Ts)^2}{f^3}\right]. \tag{32}$$

It can be seen that, in the temperature range where the ordered state is stable, the crystallite size α_1 decreases and the quantities Δe_1 and Δc_1 increases with increasing temperature. But the order of magnitude of the ratios $\Delta e_1/kT$ and $\Delta c_1/k$ is, as will be shown later, estimated negligibly small even at the melting point.

For the liquid state, substituting Eq. (9) into Eq. (27), we have

$$\Delta f_0=-\frac{2}{3}kT\alpha_0^{-3}\left(\frac{19}{4}-\frac{p\alpha_0^2 f}{kT}\right). \tag{33}$$

The size α_0 of the representative crystallites is given by Eq. (10), according to which we have

$$\frac{d\alpha_0}{dT}=-\frac{\alpha_0}{2T}\left(\frac{p\alpha_0^2 e}{kT}-\frac{9}{2}\right)\Big/\left(\frac{57}{4}-\frac{p\alpha_0^2 f}{kT}\right). \tag{34}$$

In the temperature range where the disordered state is stable, the denominator in the right-hand side of Eq. (34) is, according to Eq. (16), always positive. The constituent crystallite is expected to decrease in its size with increasing temperature just above the melting point, tending to a minimum at temperature corresponding to $p\alpha_0^2 e/kT=9/2$.

The excess energy Δe_0 and the excess specific heat Δc_0 in the disordered state are given by

$$\Delta e_0=kT\alpha_0^{-3}\left(\frac{p\alpha_0^2 e}{kT}-\frac{3}{2}\right), \tag{35}$$

and

$$\Delta c_0=-\frac{3}{2}k\alpha_0^{-3}\left[1-\frac{1}{3}\left(\frac{p\alpha_0^2 e}{kT}-\frac{9}{2}\right)^2\Big/\left(\frac{57}{4}-\frac{p\alpha_0^2 f}{kT}\right)\right]. \tag{36}$$

The value for the mean boundary energy e is not yet given experimentally. Here we have recourse to an empirical relation

$$Q/kT_m\simeq 1.0 \tag{37}$$

between the heat of melting Q and the melting temperature T_m, satisfied for most metallic elements. Anticipating a negligible contribution of Δe_1 compared to that of Δe_0, we require

$$\frac{Q}{kT_m}\simeq\frac{\Delta e_0}{kT_m}=\alpha_{0m}^{-\frac{1}{3}}\left(\frac{p\alpha_{0m}{}^2e}{kT_m}-\frac{3}{2}\right)=1.0\,. \quad (38)$$

Then it follows, referring to Eq. (18),

$$e/kT_m\simeq 1.10\,. \quad (39)$$

Substitution of the relations (17) and (39) into Eq. (28) gives

$$s/k\simeq 0.798(\simeq\log 2.2)\,. \quad (40)$$

This value for the mean boundary entropy is not unreasonable from the atomistic view of the interface.

The excess quantities corresponding to the solid state, estimated with the values of α_{1m}, e, and s, are as follows:

$$\left.\begin{aligned}-\Delta f_1/kT&\sim 8.0\times 10^{-8}\\ \Delta e_1/kT&\sim 7.2\times 10^{-4}\\ \Delta c_1/k&\sim 7.0\times 10^{-2}\end{aligned}\right\}\ \text{at}\ T=T_m\,. \quad (41)$$

The variation of size α_1 with decreasing temperature is estimated by

$$\frac{\alpha_1}{\alpha_{1m}}\simeq\left(\frac{T_m}{T}\right)^6\left(3.66-2.66\frac{T}{T_m}\right)^9, \quad (42)$$

obtaining the result shown in Tab. I.

Table I.

T/T_m	1.0	0.9	0.8	0.7	0.6	0.5
α_1/α_{1m}	1	1.61×10	1.75×10^2	1.68×10^3	8.32×10^3	1.29×10^5
α_1	1.28×10^2	2.06×10^3	2.24×10^4	2.15×10^5	1.06×10^6	1.65×10^7
$\alpha_1 a$(cm)	2.91×10^{-6}	4.69×10^{-5}	5.10×10^{-4}	4.90×10^{-3}	2.41×10^{-2}	3.76×10^{-1}

$\alpha_{1m}\simeq 128$; $a\simeq 2.72$ Å.

The size α_0 of the representative crystallites in the liquid state is determined by Eq. (10) and the corresponding excess specific heat Δc_0 by Eq. (36). With the numerical values estimated above, that is, $p=2.5$, $C_1=14.5$, and $3/8\cdot k_1\equiv f=1.10kT_m-0.798kT$, the calculated results are shown in Fig. 1. It can be seen that the representative crystallite increases its size with decreasing temperature near the melting point. The excess specific heat is positive near the melting point, where the partial specific heat due to structural change makes predominant contribution. In the temperature range, however, where the size of the crystallite is almost stationary, the excess specific heat is negative; this is due to the translational thermal mode in the liquid replacing the transversal thermal wave in the solid. These affairs are in their quality the same as the predictions made in Ref. I.

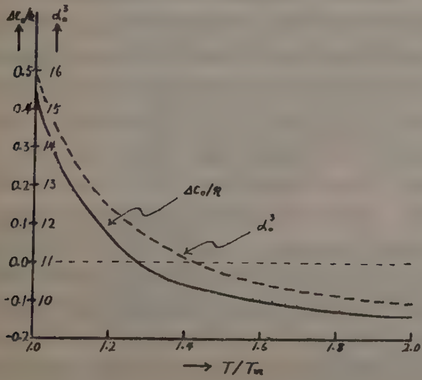

Fig. 1. Variation with temperature of the excess specific heat Δc_0 and the volume $\alpha_0{}^3$ of the representative crystallites in the liquid state, estimated according to Eqs. (10) and (36).

§ 5. The Viscous Flow

The viscous flow of the normal liquid under sufficiently weak external force can be shown to follow the Newtonian law with the coefficient of viscosity given by Eq. (III, 17):

$$\eta=\frac{kT}{\beta_0{}^{2/3}(\alpha_0 a)^3\nu}\exp\left[\frac{\varepsilon_c{}^*+\varepsilon_e{}^*}{kT}\right]. \quad (43)$$

The configurational activation energy $\varepsilon_c{}^*$ is, according to Eq. (III, 1) with the modifications introduced above, written as

$$\varepsilon_c{}^*=(\gamma+\gamma')p\alpha_0{}^2f\,. \quad (44)$$

With the numerical value for the coefficient $(\gamma+\gamma')$ estimated below, the strain activation energy $\varepsilon_e{}^*$ is of minor magnitude compared with the configurational activation energy $\varepsilon_c{}^*$. Then, substituting Eq. (44) for $\varepsilon_c{}^*$ into Eq. (43), we have

$$\eta=\frac{kT}{\nu\bar{\beta}_0^{2/3}(\alpha_0 a)^3}\exp\left\{-(\gamma+\gamma')p\alpha_0^2\frac{s}{k}\right\}$$
$$\times\exp\left\{(\gamma+\gamma')p\alpha_0^2\frac{e}{kT}\right\}. \quad (45)$$

This can also be written in the form

$$\eta=AT\exp(E/kT)\,, \quad (46)$$

where the frequency factor A as well as the activation energy E is not constant but varies with temperature through the size α_0 of the representative crystallites.

We have estimated in the preceding paragraphs the probable values of the constants in Eq. (45) except that of the coefficient $(\gamma+\gamma')$, which we want to estimate to fit the experimental data on the relation between the viscosity coefficient and the temperature.

The relation (46) with constant A and E is approximately in accord with the experimental data on many molten metals⁶⁾, with E/kT_m nearly equal to 3.0. We have, according to Eq. (46) with constant A and E,

$$\{d(\log\eta)/d(1/T)\}_{T_m}=E/kT_m-1\,. \quad (47)$$

Then, in order to satisfy the empirical relation

$$\{d(\log\eta)/d(1/T)\}_{T_m}=2.0\,, \quad (48)$$

the coefficient $(\gamma+\gamma')$ in our expression (45) is required to be

$$\gamma+\gamma'\simeq 0.3\,. \quad (49)$$

The $\log(\eta/\eta_m)$ to T_m/T curve, calculated numerically with the estimated values for the constants, is shown in Fig. 2. It can be seen that $\log\eta$ varies in nearly linear relation to $1/T$ in the higher temperature range, where the variation of size α_0 of the constituent crystallites is small. Near the melting point, however, the viscosity increases with decreasing temperature much larger deviating from the linear relation. This is the effect of the increasing activation energy E due to the increase in size α_0 of the constituent crystallite, covering the effect of the decreasing frequency factor A thereby.

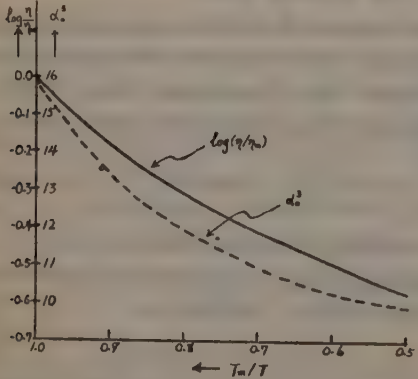

Fig. 2. Variation of the coefficient η of viscosity with the temperature, estimated according to Eq. (45). The variation of the volume α_0^3 of the representative crystallites is the same as in Fig. 1.

As to the absolute value of the viscosity coefficient η_m, Eq. (45) can be written at the melting point, referring to Eq. (23) for ν, as

$$\eta=C_3[T_m^{1/2}M_0^{1/2}/V^{2/3}] \quad (50)$$

with

$$C_3=\frac{Nk}{C_2\bar{\beta}_0^{2/3}}\left[\alpha_0^{-3}\exp\left\{(\gamma+\gamma')\frac{p\alpha_0^2 f}{kT}\right\}\right]_{T_m}. \quad (51)$$

Eq. (50) is of the same form as the Andrade's formula⁷⁾ satisfied by many molten metals with the empirical constant $C_3=5.1\times10^{-4}$. For the value of the present constant we have

$$C_3\simeq 13.7\times10^{-4}\,. \quad (52)$$

In the present poor state of the theory, such as in the vagueness of representing the geometry of packing the constituent crystallites, more quantitative agreement can not be expected.

§ 6. Discussion

The boundary excess energy and the boundary excess entropy introduced to characterize the interface between crystallites are treated phenomenologically in the present theory. To match with our understanding on the atomic structure of matter, it seems the most urgent request to interrelate these boundary quantities with the atomic quantities.

The recent enrichment of knowledge about the static as well as the dynamic properties of the grain boundary in the field of crystal plasticity is believed of much interest concerning the foundation of the crystallite theory. As to the theoretical researches on the grain boundary, we have the dislocation model theory suggested by Burgers⁸⁾ and by Bragg⁹⁾ and developed recently by Read and Shockley¹⁰⁾ and by van der Merwe¹¹⁾, and the island model theory proposed by Mott⁵⁾, the relative merit between them being not yet decided. When the neighbouring crystallites are in such a simple relation as the interface between them has lower crystallographic indices, it is promising to depicture the grain boundary by the dislocation model theory with considerable preciseness. With the grain boundary in general, however, it remains doubtful whether the picture of dislocations in an array is a good representation. Further study on the alternatives is hoped in near future.

References

1) A. Ookawa: J. Phys. Soc. Japan **2** (1947) 108.

2) A. Ookawa: J. Phys. Soc. Japan **3** (1948) 295.

3) A. Ookawa: J. Phys. Soc. Japan **4** (1949) 14.

4) F. A. Lindemann: Phys. Zeits. **11** (1911) 609.

5) N. F. Mott: Proc. Phys. Soc. London **60** (1948) 391.

6) R. Fürth: Proc. Camb. Phil. Soc. **37** (1941) 281.

7) E. N. Da C. Andrade: Phil. Mag. (vii) **17** (1934) 497.

8) J. M. Burgers: Proc. Phys. Soc. London **52** (1940) 23.

9. W. L. Bragg: Proc. Phys. Soc. London **52** (1940) 54.

10) W. T. Read, W. Shockley: Phys. Rev. **78** (1950) 275.

11) J. H. van der Merwe: Proc. Phys. Soc. London **A63** (1950) 616.

JOURNAL OF THE PHYSICAL SOCIETY OF JAPAN Vol. 7, No. 6, NOV.—DEC., 1952

Atomic Distribution in Binary Solid Solutions
I. General Theory

By Terutosi MURAKAMI

Institute of Applied Science, Faculty of Engineering, Kyushu University

(Received June 2, 1952)

Mayer's cluster method is developed in the crystal statistics analogously with the one in imperfect gases. The discussion is confined to the problem for the two cases, one for the two phase separation and another for the order-disorder transition. These problems are treated just as the one for one-component imperfect gases, and the order parameters in binary crystal are calculated in the same way as is used to obtain the radial distribution functions in imperfect gases by Montroll and Mayer. By means of the chain approximation, the expression for the pair distribution function is obtained in the closed form which is somewhat like Zernike's formula. And the transition temperatures are identified with the temperatures at which singular points of the distribution function begin to appear. It seems, however, that the results are not better than those obtained from Bethe's approximation.

§ 1. Introduction

We have two typical problems in the field of statistical theory of cooperative phenomena, one for imperfect gases and another for binary solid solutions. One of these problems seems to have been treated differently from another; a two dimensional problem in the latter has been exactly solved, whereas the solutions obtained for the former are of approximative nature without exception. So it seems to be of importance to investigate the relation between these two types of problems.

Previously, Muto[1] pointed out that regular solution may be treated just as one-component imperfect gas, and applied Mayer's[2] *cluster-integral* method for imperfect gases to regular solutions. And a similar cluster theory was developed by Fuchs[3] in crystal statistics independently of Muto, though the thauor has not yet been aware of it in detail. Recently, Ono and the present author[4] attempted to apply the integral equation method, which has been used to calculate the molecular distribution function in gases, to crystal statistics and obtained the same expression for the degree of short range order as that given by Bethe's approximation, imposing the several restrictions on the *assumption of superposition*. On the other hand, Kikuchi[5] has attempted to extend his method for crystal statistics to the general cases of continuous aggregates.

The problem of propagation of order in crystal lattices, which is closely related to the diffuse scattering of X-rays and originally treated by Zernike[6], seems to be entirely analogous to the one for obtaining the radial distribution functions in imperfect gases. In this paper, following Montroll and Mayer[7], the general method will be developed to obtain the probability of finding a pair of atoms on the two given lattice points at the same time. As a result, we obtained the formula for the distribution function of two atoms which is like Zernike's one. Furthermore, the present method is effective even when the interactions between atoms are not restricted to the nearest neighbor, as far as the contributions of the cluster sums other than chain sums are not important.

§ 2. Atomic Distribution Functions

Let us consider a binary system composed of n_a A atoms and n_b B atoms distributed over N lattice points without vacant sites, and denote the concentration of A and B atoms by x_a and x_b, respectively. Then we have the following relations:

$$x_a=\lim_{N\to\infty} n_a/N, \quad x_b=\lim_{N\to\infty} n_b/N,$$
$$x_a+x_b=1, \qquad n_a+n_b=N.$$

In such a binary system, the configuration of the entire system is determined only if the distribution of atoms of either kind is given. Here we shall denote the positional coordinates of the i-th A atom by $\boldsymbol{r}_{ia}$ and the set of the coordinates of n_a A atoms, $\boldsymbol{r}_{1a}, \boldsymbol{r}_{2a}, \dots, \boldsymbol{r}_{na}$, by $\{\boldsymbol{r}_{na}\}$, which specifies the configurational state of the total system, the arrangement produced by any interchange between only B atoms being regarded as the same configuration. As in Mayer's theory, let us define the distribution function $F_{ma}\{\boldsymbol{r}_{ma}\}$, which is proportional to the probability that there be a set of m_a A atoms at the set of lattice points $\{\boldsymbol{r}_{ma}\}$; the normalization constant is so defined that

$$\lim_{N\to\infty} N^{-m_a} S'_N\{\boldsymbol{r}_{ma}\} F_{ma}\{\boldsymbol{r}_{ma}\}=1. \tag{1}$$

Then the probability that each of the set $\{\boldsymbol{r}_{ma}\}$ is occupied by any of A atoms is equal to $x_a^{ma} F_{ma}\{\boldsymbol{r}_{ma}\}$. $S'_N\{\boldsymbol{r}_{ma}\}$ in Eq. (1) implies the summation over all possible arrangements of m_a A atoms, the arrangement for which some A atoms overlap each other being excluded. This manipulation corresponds to the integration over the continuous space in the theory of gases. We shall refer to it as *lattice summation*, and use the above symbol in order to distinguish it from the usual summation Σ. By definition, the different distribution functions are related by the equation:

$$F_{ma'}\{\boldsymbol{r}_{ma'}\}=N_{ma'-ma} S'_N\{\boldsymbol{r}_{ma-ma'}\} F_{ma}\{\boldsymbol{r}_{ma}\}, \qquad (m_a'<m_a) \tag{2}$$

where $S'_N\{\boldsymbol{r}_{ma-ma'}\}$ denotes the lattice summation refered to the remaining m_a-m_a' atoms with $\{\boldsymbol{r}_{ma'}\}$ fixed.

The configurational partition function of the system $Q_\tau/n_a\,!$ is given by

$$(Q_\tau/n_a\,!)=(1/n_a\,!) \times S'_N\{\boldsymbol{r}_{na}\} \exp[-U\{\boldsymbol{r}_{na}\}/kT], \tag{3}$$

where $U\{\boldsymbol{r}_{na}\}$ is the total potential energy of the system at the given configuration $\{\boldsymbol{r}_{na}\}$. Let us now suppose that $U\{\boldsymbol{r}_{na}\}$ is expressible by the sum of the mutual potential energy of the pairs of atoms, which depends only on the distances between the atoms. Let the interaction energy between two atoms, one at $\boldsymbol{r}_i$ and another at $\boldsymbol{r}_j$ be $\varepsilon_{aa}(\boldsymbol{r}_i-\boldsymbol{r}_j)$, $\varepsilon_{bb}(\boldsymbol{r}_i-\boldsymbol{r}_j)$ or $\varepsilon_{ab}(\boldsymbol{r}_i-\boldsymbol{r}_j)$, according as these two atoms are A and B, B and B or A and B. For the case where one of the atoms is the p-th neighbor to another, the above interactions will be denoted by $\varepsilon_{aa}^{(p)}$, $\varepsilon_{bb}^{(p)}$ and $\varepsilon_{ab}^{(p)}$, respectively. Then $U\{\boldsymbol{r}_{na}\}$ may be written in the form:

$$U\{\boldsymbol{r}_{na}\}=u+\sum_p z_p X_p\{\boldsymbol{r}_{na}\} 2\Delta\varepsilon^{(p)} \tag{4}$$

where

$$2\Delta\varepsilon^{(p)}=\varepsilon_{aa}^{(p)}+\varepsilon_{bb}^{(p)}-2\varepsilon_{ab}^{(p)}, \tag{5}$$

and

$$u=\sum_p z_p\left[\frac{1}{2}(n_b-n_a)\varepsilon_{bb}^{(p)}-n_a\varepsilon_{ab}^{(p)}\right], \qquad (6)$$

in which $z_pX_p\{\boldsymbol{r}_{n_a}\}$ is the total number of such $A-A$ pairs that one is the p-th neighbor to another in the specified configuration $\{\boldsymbol{r}_{n_a}\}$, z_p being the number of p-th neighbors of each atom. u defined by Eq. (6) may be determined from the numbers of A and B atoms and the lattice structure, and accordingly is independent of the atomic configuration $\{\boldsymbol{r}_{n_a}\}$.

The distribution function of the n_a A atoms is given by the equation

$$F_{n_a}\{\boldsymbol{r}_{n_a}\}=(N^{n_a}/Q_\tau)\exp[-U\{\boldsymbol{r}_{n_a}\}/kT], \qquad (7)$$

n_a being the total number of A atoms. Using Eqs. (2) and (4), one obtains the following equation

$$F_{m_a}\{\boldsymbol{r}_{m_a}\}=\frac{N^{m_a}}{Q_\tau}S'_N\{\boldsymbol{r}_{n_a-m_a}\}$$
$$\times\exp[-\{u+\sum_p z_pX_p\{\boldsymbol{r}_{n_a}\}2\Delta\varepsilon^{(p)}\}/kT], \qquad (8)$$

in which the factor $\exp\{-u/kT\}$ cancels the one in Q_τ. Then $F_{m_a}\{\boldsymbol{r}_{m_a}\}$ is determined by $\Delta\varepsilon^{(p)}$ alone, irrespective of the individual values of $\varepsilon_{aa}^{(p)}$, $\varepsilon_{bb}^{(p)}$ and $\varepsilon_{ab}^{(p)}$. Hence, we have only to carry out the calculation for the case where $\varepsilon_{ab}^{(p)}=\varepsilon_{bb}^{(p)}=0$, to obtain the distribution function of atoms. Thus we have

$$F_{m_a}\{\boldsymbol{r}_{m_a}\}=\frac{N^{m_a}}{Q'_\tau}S'_N\{\boldsymbol{r}_{n_a-m_a}\}$$
$$\times\exp[-\sum_p z_pX_p\{\boldsymbol{r}_{n_a}\}\varepsilon_{aa}^{(p)}/kT], \qquad (9)$$

where

$$Q'_\tau=S'_N\{\boldsymbol{r}_{n_a}\}\exp[-\sum_p z_pX_p\{\boldsymbol{r}_{n_a}\}\varepsilon_{aa}^{(p)}/kT]. \qquad (10)$$

And the lattice summation $S'_N\{\boldsymbol{r}_{n_a}\}$ which hitherto has excluded overlapping of A atoms may be replaced by the summation $S_N\{\boldsymbol{r}_{n_a}\}$ which permit overlapping, provided the mutual potential energy is taken to be infinity whenever two or more atoms simultaneously occupy the same lattice point. Consequently, we may rewrite Eq. (9) as follows

$$F_{m_a}\{\boldsymbol{r}_{m_a}\}=\frac{N^{m_a}}{Q'_\tau}S_N\{\boldsymbol{r}_{n_a-m_a}\}$$
$$\times\exp[-\sum_{i>j}\varepsilon_{aa}(\boldsymbol{r}_{i,j})/kT], \qquad (11)$$

where $\boldsymbol{r}_{i,j}=\boldsymbol{r}_j-\boldsymbol{r}_i$.

Eq. (11) has the entirely same form as Eq. (34) in Mayer and Montroll's paper[8)], if one replaces the total volume V by the total number of lattice points N and the integration by the *lattice summation* $S_N\{\boldsymbol{r}_n\}$. Thus the problem for two-component regular solutions may be reduced to the problem for the corresponding one-component imperfect gases, and then the sufficies to indicate the species of atoms may be dropped hereafter.

Now we introduce the function $\xi(\boldsymbol{r})$ defined by

$$\xi(\boldsymbol{r})=\exp[-\varepsilon(\boldsymbol{r})/kT]-1, \qquad (12)$$

and employ the Ursell expansion as in the theory of imperfect gases. If the mutual interaction $\varepsilon_{aa}(\boldsymbol{r})$ vanishes at great distances (in the usual treatments for crystal statistics, only the nearest neighbor interactions are taken into account), one may introduce the conception of *cluster sum*, corresponding to the *cluster integral* appeared in the theory of gases. Then we may proceed in the exactly analogous way to that in Mayer and Montroll's paper on molecular distribution. Thus the distribution function of two A atoms is written as

$$F_2(\boldsymbol{r}_{1,2})=\exp\{-\varepsilon(\boldsymbol{r}_{1,2})/kT\}[G_1(1)G_1(1)$$
$$+G_2(\boldsymbol{r}_{1,2})]$$
$$=\exp\{-\varepsilon(\boldsymbol{r}_{1,2})/kT\}[1+G_2(\boldsymbol{r}_{1,2})], \qquad (13)$$

where $F_1(1)=G_1(1)=1$. G is defined by

$$G_2(\boldsymbol{r}_{1,2})=\sum_{l\geq 1}(Z/x)^2Z^lB_{2,l}(\boldsymbol{r}_{1,2}), \qquad (14)$$

and

$$B_{2,l}(\boldsymbol{r}_{1,2})=\frac{1}{l!}S_N\{\boldsymbol{r}_l\}\sum\Pi\xi_{ij}\xi_{\kappa k}, \qquad (15)$$
$$l\geq i>j\geq 1$$
$$l\geq k\geq 1$$
$$2\geq\kappa\geq 1$$

(sum over all connected products)

Z being the fugacity. And an alternative expression for $G_2(\boldsymbol{r}_{1,2})$ is

$$G_2(\boldsymbol{r}_{1,2})=\sum_{m\geq 1}x^mH_{2,m}(\boldsymbol{r}_{1,2}), \qquad (16)$$

where

$$H_{2,m}(\boldsymbol{r}_{1,2})=\frac{1}{m!}S_N\{\boldsymbol{r}_m\}\sum\Pi\xi_{ij}\xi_{\kappa k}. \qquad (17)$$
$$m\geq i>j\geq 1$$
$$m\geq k\geq 1$$
$$2\geq\kappa\geq 1$$

(sum over all connected products for which each atom of the set $\{\boldsymbol{r}_m\}$ is connected by an independent path to two atoms of the $\{\boldsymbol{r}_2\}$.)

To calculate atomic distribution function, we shall order the components of $H_{2,m}$ in Eq. (16), the sets $H_{2,m}^{(0)}$, $H_{2,m}^{(1)}$, ..., such that the $H_{2,m}^{(0)}$ correspond to sum over chains without internal connections, $H^{(1)}_{2,m}$ to those with one internal connection, etc.. We shall define the chain sum, corresponding to Montroll and Mayer's chain integral by

$$P_m(\boldsymbol{r}_{i,j})=S_N\{\boldsymbol{r}_m\}\xi(\boldsymbol{r}_{i,1})\xi(\boldsymbol{r}_{1,2})\ldots\xi(\boldsymbol{r}_{m,j})\,. \tag{18}$$

Since $m\,!$ terms which are produced by simple permutations of identical atoms leads to the same value, one immediately has the relation $H^{(0)}_{2,m}=P_m$. If $H^{(\mu)}_{2,m}$ for $\mu\geq 1$ is neglected, the pair distribution function of A atoms may be given by

$$\begin{aligned}F_{aa}(\boldsymbol{r}_{1,2})= &\exp\{-\varepsilon_{aa}(\boldsymbol{r}_{1,2})/kT\}\\ &\times[1+\sum_{m_a\geq 1}x_a^{m_a}P_{m_a}(\boldsymbol{r}_{1,2})]\,,\end{aligned} \tag{19}$$

As pointed out by Rodriguez[9)], Mayer and Montroll's expression for pair distribution function is equivalent to the Born-Greens'[10)] expression. It is, however, not clear for the present that the treatment neglecting the more complicated connections can at all serve as good approximation in crystal statistics. This procedure may be good, if the tightly connected configurations do not appear so frequently.

§ 3. The Fourier Transform of $\xi(\boldsymbol{r})$

If a crystal has the primitive translational vectors $\boldsymbol{a}_1, \boldsymbol{a}_2$, and $\boldsymbol{a}_3$, the lattice point may be specified by the vector $\boldsymbol{r}=l\boldsymbol{a}_1+m\boldsymbol{a}_2+n\boldsymbol{a}_3$, where l, m, and n are integers. And similarly, let us consider the vector $\boldsymbol{b}$ expressed in the form $\boldsymbol{b}=h_1\boldsymbol{b}_1+h_2\boldsymbol{b}_2+h_3\boldsymbol{b}_3$, where $\boldsymbol{b}_1$, $\boldsymbol{b}_2$ and $\boldsymbol{b}_3$ are the primitive translational vectors of the reciplocal lattice, and where h_1, h_2 and h_3 assume positive real values less than unity.

Now we shall introduce the auxiliary function

$$g(\boldsymbol{b})=\lim_{N\to\infty}S_N(\boldsymbol{r})\xi(\boldsymbol{r})\exp\{-2\pi i\boldsymbol{b}\cdot\boldsymbol{r}\}\,, \tag{20}$$

of which the reciplocal relation is

$$\xi(\boldsymbol{r})=\int g(\boldsymbol{b})\exp\{2\pi i\boldsymbol{b}\cdot\boldsymbol{r}\}d\boldsymbol{b}\,, \tag{21}$$

where $d\boldsymbol{b}$ represents the volume element of the reciplocal space. The integration is extended over a unit cell of the reciplocal space. From the above relations we see that the values of $\xi(\boldsymbol{r})$ are the Fourier coefficients of the function $g(\boldsymbol{r})$ defined in a unit cell of the reciprocal lattice. Then we have from Eqs. (19) and (21),

$$P_1(\boldsymbol{r}_{1,3})=\int g(\boldsymbol{b})I(\boldsymbol{b})\exp\{-2\pi i\boldsymbol{b}\cdot\boldsymbol{r}_1\}d\boldsymbol{b}\,, \tag{22}$$

where

$$I(\boldsymbol{b})=\int g(\boldsymbol{b}+\boldsymbol{b}')\exp\{2\pi i(\boldsymbol{b}+\boldsymbol{b}')\cdot\boldsymbol{r}_3\}D_N(\boldsymbol{b}')d\boldsymbol{b}' \tag{23}$$

and

$$D_N(\boldsymbol{b})=\prod_{i=1}^{3}\frac{\sin 2\pi h_i(N_i+\frac{1}{2})}{\sin(2\pi h_i/2)}\,, \tag{24}$$

in which N_i is the number of lattice points in the $\boldsymbol{a}_i$ direction. According to the Dirichlet integral, we have, in the limit $N\to\infty$,

$$\begin{aligned}\lim_{N\to\infty}&\int g(\boldsymbol{b}'+\boldsymbol{b})\exp\{2\pi i(\boldsymbol{b}+\boldsymbol{b}')\cdot\boldsymbol{r}_3\}D_N(\boldsymbol{b})d\boldsymbol{b}\\ &=g(\boldsymbol{b})\exp\{2\pi i\boldsymbol{b}\cdot\boldsymbol{r}_3\}\,,\end{aligned} \tag{25}$$

and consequently Eq. (22) may be written as

$$P_1(\boldsymbol{r}_{1,3})=\int\{g(\boldsymbol{b})\}^2\exp\{2\pi i\boldsymbol{b}\cdot(\boldsymbol{r}_3-\boldsymbol{r}_1)\}d\boldsymbol{b}\,. \tag{26}$$

Repeating the above series of manipulations, we have

$$P_m(\boldsymbol{r}_{1,m+2})=\int\{g(\boldsymbol{b})\}^{m+1}\exp\{2\pi i\boldsymbol{b}\cdot\boldsymbol{r}_{1,m+2}\}d\boldsymbol{b}\,. \tag{27}$$

Substituting Eq. (27) into (19), one finds

$$\begin{aligned}F_{aa}(\boldsymbol{r})= &\exp\{-\varepsilon_{aa}(\boldsymbol{r})/kT\}\\ &\times\left[1-\xi(\boldsymbol{r})+\frac{1}{x_a}\int\frac{\exp\{2\pi i\boldsymbol{b}\cdot\boldsymbol{r}\}}{1-x_a g(\boldsymbol{b})}d\boldsymbol{b}\right].\end{aligned} \tag{28}$$

§ 4. Nearest Neighbor Systems

In this section, we shall confine ourselves to the case of the nearest neighbor systems, for which we have $\varepsilon^{(0)}_{aa}=\infty$, $\varepsilon^{(1)}_{aa}=2\varDelta\varepsilon$ and $\varepsilon^{(p)}_{aa}=0$ $p\geq 2$, and we shall denote $\xi(\boldsymbol{r})$ for the nearest neighbor by $\xi=\exp\{-2\varDelta\varepsilon/kT\}-1$. Then $g(\boldsymbol{b})$ defined by Eq. (20) is expressed by

$$g(\boldsymbol{b})=2\xi\cdot G(\boldsymbol{b})-1\,, \tag{29}$$

where $G(\boldsymbol{b})$ represents one of the following functions:

$$G_1(\boldsymbol{b})=\cos 2\pi h_1 \quad \text{for linear chain;} \tag{30.1}$$

$$G_{2S}(\boldsymbol{b})=\sum_{i=1}^{2}\cos 2\pi h_i \quad \text{for square lattice;} \tag{30.2}$$

$$G_{2T}(\boldsymbol{b})=\cos 2\pi h_1+2\cos\pi h_1\cos\sqrt{3}\,\pi h_2 \quad \text{for triangular lattice;} \tag{30.3}$$

$$G_{3S}(\boldsymbol{b})=\sum_{i=1}^{3}\cos 2\pi h_i \quad \text{for simple cubic;} \tag{30.4}$$

$$G_{3D}(\boldsymbol{b})=4\prod_{i=1}^{3}\cos 2\pi h_i$$
for body centered cubic; (30.5)

and $$G_{3F}(\boldsymbol{b})=2\sum_{i>j}^{3}\cos 2\pi h_i\cdot\cos 2\pi h_j$$
for face-centered cubic. (30.6)

Since, $F_{aa}(\boldsymbol{r})$ approaches unity at extremely high temperature as seen from (28) and (29), it may be convenient that one may express the pair distribution function in the following forms:

$$\begin{aligned}F_{aa}(\boldsymbol{r})&=1+\alpha(\boldsymbol{r}),\\ F_{ab}(\boldsymbol{r})&=1-(x_a/x_b)\alpha(\boldsymbol{r}),\end{aligned}\qquad(31)$$

using the normalization condition and considering $F_a(\boldsymbol{r}_1)=F_b(\boldsymbol{r}_1)=1$. According to Eq. (28), $\alpha(\boldsymbol{r})$ is given by

$$\alpha(\boldsymbol{r})=-\xi^2(\boldsymbol{r})+\frac{1+\xi(\boldsymbol{r})}{2x_a\xi}\int\frac{\exp\{2\pi i\boldsymbol{b}\cdot\boldsymbol{r}\}}{(C/\xi)-G(\boldsymbol{b})}d\boldsymbol{b}\,,\qquad(32)$$

where $C=(1+x_a)/2x_a$, Eqs. (29) and (30) being used.

In general two cases are possible for nearest neighbor system, one corresponds to $\Delta\varepsilon=\frac{1}{2}(\varepsilon_{aa}+\varepsilon_{bb})-\varepsilon_{ab}>0$, another to $\Delta\varepsilon<0$, and we shall denote the corresponding ξ's by ξ^- and ξ^-, respectively. As the temperature increases, ξ^+ increases from -1 to 0, while ξ^- decreases from ∞ to 0. On the other hand, we always have, according to the set of equations (30.1)∼(30.6),

$$\left.\begin{aligned}&-1\leqq G_1\leqq 1,\quad -\tfrac{3}{2}\leqq G_{2T}\leqq 3,\quad -4\leqq G_{3B}\leqq 4,\\ &-2\leqq G_{2S}\leqq 2,\quad -3\leqq G_{3S}\leqq 3,\quad -2\leqq G_{3F}\leqq 6.\end{aligned}\right\}\qquad(33)$$

Therefore, $\alpha(\boldsymbol{r})$ given by Eq. (32) can never have the singular point at the temperatures above the critical value, at which the maximum value of $G(\boldsymbol{b})$ is equal to C/ξ, whereas it may have a singular point at the temperatures below this critical value. This critical temperature, at which the singular point of Eq. (32) begins to appear, may be identical with the transition temperature, at which the homogeneous solution separates into two phases or the order-disorder transition occurs according as $\Delta\varepsilon$ is positive or negative.

Let the value of ξ^+ and ξ^- at this critical temperature be ξ_c^+ and ξ_c^-, respectively. Their values are given in Table I for the different types of lattices. For the case of equal concentration, $x_a=x_b=\frac{1}{2}$, $\exp\{-\Delta\varepsilon/kT_c\}$ and $\exp\{\Delta\varepsilon/kT_c\}$ obtained from these values of ξ are shown in Table II, being compared with those from Bethe's approximations. From Table II it seems that the approximation employed in the present treatment, in which only chain configurations are taken

Table I.

	Linear chain	Square lattice	Triangular lattice	Simple cubic	Body-centered cubic	Face-centered cubic
ξ_c^+	$-C$	$-\frac{1}{2}C$	$-\frac{2}{3}C$	$-\frac{1}{3}C$	$-\frac{1}{4}C$	$-\frac{1}{2}C$
ξ_c^-	C	$\frac{1}{2}C$	$\frac{1}{3}C$	$\frac{1}{3}C$	$\frac{1}{4}C$	$\frac{1}{6}C$

Table II.

Types of Lattices	Linear chain	Square lattice	Triangular lattice	Simple cubic	Body-centered cubic	Face-centered cubic
Two-Phase separation: $\exp\{-\Delta\varepsilon/kT_c\}$	1.58	1.32	1.22	1.22	1.17	1.12
Order-Disorder transition: $\exp\{\Delta\varepsilon/kT_c\}$	—	2.00	∞	1.41	1.26	2.00
Bethe: $\exp\{\lvert\Delta\varepsilon\rvert/kT_c\}=z/z-2$	∞	2.00	1.50	1.50	1.33	1.20

where z is the coordination number, T_c is critical temperature and $\Delta\varepsilon=\frac{1}{2}(\varepsilon_{aa}+\varepsilon_{bb})-\varepsilon_{ab}$ is the potential-difference.

into account, becomes poor especially in the case of two phase separation, and also is poorer than Bethe's one even in the case of the order-disorder transition. Such a situation is presumably due to the neglection of the contributions of tightly connection which may become more prominent in the concentrated solutions.

References

1) Y. Muto: Journal of Physico-Mathematical Society of Japan (in Japanese) **17** (1943) 86; J. Chem. Phys. **16** (1948) 519.

2) J. E. Mayer & M. G. Mayer: *Statistical Mechanics* (New York 1940) p. 277.

3) H. Fuchs: Proc. Roy. Soc. **A 179** (1942) 340.

4) S. Ono & T. Murakami: Memoirs of Faculty of Engineering, Kyushu University **12** (1951) 309, 319.

5) R. Kikuchi: J. Chem. Phys. **9** (1951) 1230.

6) F. Zernike: Physica **7** (1940) 565.

7) E. W. Montroll & J. E. Mayer: J. Chem. Phys. **9** (1941) 626.

8) J. M. Mayer & E. W. Montroll: J. Chem. Phys. **9** (1941) 2.

9) A. E. Rodriguez: Proc. Roy. Soc. **A 193** (1948) 73.

10) M. Born & H. S. Green: Proc. Roy. Soc. **A 188** (1946) 10; H. S. Green: Proc. Roy. Soc. **A 189** (1947) 103.

JOURNAL OF THE PHYSICAL SOCIETY OF JAPAN Vol. 7, No. 6 NOV.—DEC., 1952

Energy Dissipation and Entropy Production in Irreversible Processes of Dilute Systems

By Nobuhiko SAITÔ*

Kobayasi Institute of Physical Research, Kokubunzi, Tokyo

and Motoyosi SUGITA

Department of Physics, Hitotubasi University, Kunitati, Tokyo

(Received June 7, 1952)

Thermodynamical considerations are given on the diffusion of ideal gases, sedimentation of dilute colloidal solution, dielectric anomalies of polar solution and intrinsic viscosity of macromolecule of non-spherical shape. In all these phenomena an important rôle is played by differential equations of diffusion type which determine the distribution functions of molecules and the currents of the probability density. It is shown that the energy dissipation and the entropy increasing multiplied by absolute temperature are given by the works done by the external force and by the diffusion force respectively against the current of the probability density, and in particular the irreversible production of entropy multiplied by absolute temperature is given by the heat produced by the friction of the particles with the velocity equal to the current of the probability density. Finally, the theories by W. Kuhn and H. Kuhn and by one of the authors for the non-Newtonian viscosity of macromolecules are discussed and the equivalence of the final results of the two theories is demonstrated.

§1. Introduction

We consider here only the systems which do not deviate so largely from equilibrium. In these cases it is possible to extend the thermodynamical considerations to non-equilibrium irreversible systems, using such notions as temperature, entropy or free energy etc., which are firstly introduced in equilibrium state or quasi-static processes. Small parts of these systems may be regarded as in equilibrium and there temperature, mole fraction, chemical potential and other thermodynamical quantities can be easily defined. In the limit of the parts to be vanishingly small in macroscopic scale but still large from microscopic view point, these quantities are considered as point functions. From statistical mechanical point of view the phase integrals cannot be extended over whole system, but are limited to the small parts considered as in equilibrium. In a system not in equilibrium, the extensive quantities of the whole system are sums of those of small parts considered as in equilibrium.

---

* Now at Department of Applied Physics, Waseda University, Tokyo.

Following Tolman and Fine[1] the first and the second laws of thermodynamics are written as

$$dU=-\delta Q+\delta W\,, \qquad (1.\,1)$$

$$dS=-\delta Q/T+(dS)_{irr}\,, \qquad (1.\,2)$$

where U and S are respectively the internal energy and the entropy, δQ the heat flowing out of the vessel into heat reservoir, δW the work done by external force and $(dS)_{irr}$ the irreversible production of entropy.

We consider the cases where it is possible to give differential equations of generalized diffusion type, and we want to clarify the connection between the current of the probability density and the energy dissipation (δQ) or the irreversible production of entropy in these systems.

In the following sections we will take up as tractable examples diffusion of two ideal gases, sedimentation of dilute colloidal solution, dielectic loss of polar solution, and the intrinsic viscosity of macromolecules, all in constant temperature.

§ 2. Diffusion and Mixing Entropy[2]

Let us consider the ideal mixture of two gases. The temperature and the pressure are held constant and equal in the whole system. As mentioned in § 1, chemical potentials, and numbers of molecules per unit volume of two species etc. are determined as point functions, and they are denoted by μ_1, μ_2 and n_1, n_2 respectively. The Gibbs' free energy of the whole system is given by

$$G=\int(n_1\mu_1+n_2\mu_2)dxdydz\,, \qquad (2.\,1)$$

$$\mu_i=kT\log\{n_i/(n_1+n_2)\}+\mu_i^0(T)\,. \qquad (2.\,2)$$

If we can determine the numbers of molecules n_i in Eqs. (2. 1) and (2. 2) as functions of position and time, it is possible to pursue the thermodynamical behavior of the whole system.

From the phenomenological theory we have

$$\partial n_i/\partial t=-\operatorname{div}\boldsymbol{j}_i n_i\,, \qquad (2.\,3)$$

$$\boldsymbol{j}_i=-D_i\operatorname{grad}\log n_i\,, \qquad (2.\,4)$$

where $\boldsymbol{j}_i$ is regarded as the mean velocity of diffusion of i species. If a set of initial and boundary conditions is given, we can solve Eq. (2. 3) and determine, for example, the entropy production during diffusion.

In our system of an ideal mixture of two gases, the time derivative of the entropy is given by

$$\frac{\partial S}{\partial t}=-\frac{1}{T}\frac{\partial G}{\partial t} \qquad (2.\,5)$$

which is rewritten from Eqs. (2. 1) and (2. 2), making use of $n_1+n_2=$const. (pressure=const.) as

$$\frac{\partial S}{\partial t}=-\frac{1}{T}\int\left(\frac{\partial n_1}{\partial t}\mu_1+\frac{\partial n_2}{\partial t}\mu_2\right)dxdydz\,. \qquad (2.\,6)$$

Substitution of Eq. (2. 3) into Eq. (2. 6) and partial integration lead

$$T\frac{\partial S}{\partial t}=\int\sum_{i=1,\,2}(\operatorname{div}\boldsymbol{j}_i n_i)\mu_i dxdydz$$

$$=-\int\sum_{i=1,\,2}(n_i\boldsymbol{j}_i,\operatorname{grad}\mu_i)dxdydz\,, \qquad (2.\,7)$$

as $\boldsymbol{j}$ vanishes at the boundaries.

Eq. (2. 7) is interpreted as follows ;—grad μ_i is a kind of force which may be called diffusion force, and $T(\partial S/\partial t)$, rate of the entropy increasing multiplied by T, is equal to the work done in unit time by the diffusion force against the diffusion current. Alternatively, as we have

$$n_i\boldsymbol{j}_i=-D_i\operatorname{grad}n_i=-n_iD_i/kT\operatorname{grad}\mu_i\,, \qquad (2.\,8)$$

Eq. (2. 7) is written as

$$T\frac{\partial S}{\partial t}=\int\sum\frac{kT}{D_i}n_i\boldsymbol{j}_i^2dxdydz \qquad (2.\,9)$$

which is interpreted as the heat produced by the current $n_i\boldsymbol{j}_i$, because kT/D_i is a kind of frictional constant as is seen from Eq.(2.8).

In our present case $dU=0$ and $\delta W=0$. Eq. (1. 1) gives $\delta Q=0$, and $\partial S/\partial t$ given by Eq. (2. 9) is equal to $(\partial S/\partial t)_{irr}$, which is nothing but the mixing entropy when integrated from

$t=0$ to $t=\infty$.

§ 3. Sedimentation of Dilute Colloidal Solution in Gravitational Field

The gravitational potential energy U is here considered as an internal energy and therefore there is no external force acting on this system*. Eqs. (1.1) and (1.2) are written respectively as

$$dU=-\delta Q\,, \tag{3.1}$$

$$dS=-\delta Q/T+(dS)_{irr} \tag{3.2}$$

From (3.1) the rate of energy dissipation is given by $-\partial U/\partial t$, and the rate of increasing of free energy F defined by $U-TS$ is given by

$$\frac{\partial F}{\partial t}=\frac{\partial U}{\partial t}-T\frac{\partial S}{\partial t}=-T\left(\frac{\partial S}{\partial t}\right)_{irr} \tag{3.3}$$

Now taking the x-axis of the coordinate downwards, the density ρ of a colloidal solution is determined by

$$\frac{\partial \rho}{\partial t}=-\frac{\partial}{\partial x}\left(v\rho-D\frac{\partial \rho}{\partial x}\right), \tag{3.4}$$

where v is the terminal velocity of a colloidal particle of mass m and D is the diffusion constant. Defining j by

$$j=v-(D/\rho)(\partial\rho/\partial x)\,, \tag{3.5}$$

we have

$$\partial\rho/\partial t=-\partial(j\rho)/\partial x\,. \tag{3.6}$$

The potential energy and the entropy of the system are given by

$$U=-\int_0^h mgx\rho(x)dx\,, \tag{3.7}$$

$$S=-k\int_0^h \rho\log\rho dx\,, \tag{3.8}$$

where h is the height of the vessel, and g is the constant of gravity. Denoting the frictional constant by ζ, we have $v=mg/\zeta$ and $D=kT/\zeta$. From Eqs. (3.7) and (3.6) we have

$$\frac{\delta Q}{\partial t}=-\frac{\partial U}{\partial t}=\int_0^h mgx\frac{\partial\rho}{\partial t}dx=\int_0^h mg\,j\rho dx \tag{3.9}$$

and

$$\begin{aligned} T\frac{\partial S}{\partial t}&=-kT\int_0^h\frac{\partial\rho}{\partial t}\log\rho dx\\ &=\int_0^h\left(-\frac{kT}{\rho}\frac{\partial\rho}{\partial x}\right)j\rho dx\,, \end{aligned} \tag{3.10}$$

where $-kT/\rho\cdot\partial\rho/\partial x$ is considered as diffusion force. Eqs. (3.9) and (3.10) are interpreted as follows: the energy dissipation, $\delta Q/\partial t$, and the entropy increasing multiplied by T, $T\partial S/\partial t$, are given by the works done by external force mg and by diffusion force $(-kT/\rho)\partial\rho/\partial x$ respectively against the current of the probability density. Eq. (3.10) is divided into two terms by use of Eq. (3.5):

$$T\frac{\partial S}{\partial t}=-\int_0^h mg\,j\rho dx+\zeta\int_0^h j^2\rho dx\,, \tag{3.11}$$

where the first term is equal to $-\delta Q/\partial t$. Referring to Eq. (3.2) we have

$$T\left(\frac{\partial S}{\partial t}\right)_{irr}=\zeta\int_0^h j^2\rho dx\,, \tag{3.12}$$

which shows that the rate of irreversible production of entropy multiplied by T, is equal to the frictional heat produced by the particles with the velocity j which is regarded as the macroscopically observable average velocity of the particles.

It would be of some theoretical interest to consider a hypothetical case of gravity changing with time. In this case U and S are given as before by Eqs. (3.7) and (3.8) respectively. However the work done to this system is not zero and is given by

$$\frac{\delta W}{\partial t}=-m\frac{\partial g}{\partial t}\int_0^h \rho x dx\,. \tag{3.13}$$

From Eqs. (1.1) and (3.7) we obtain

$$\frac{\delta Q}{\partial t}=\int_0^h mg\,j\rho dx\,. \tag{3.14}$$

This formulation is same as Eq. (3.9) and the irreversible production of entropy is given by Eq. (3.10), although the behavior of $j\rho$ is different from the case of constant gravity. If we stand on the viewpoint to regard the gravity as external force and take $dU=0$, δW is given by $\int_0^h mg\,j\rho dx$, and we always reach

---

* Alternatively the gravitational force may be considered as an external force. Then Eq. (3.1) is replaced by

$$dU=-\delta Q+\delta W \tag{3.1'}$$

where δW is the work done by gravity, and $dU=0$ because of the infinitely dilute solution. However in this equation there is an ambiguous point about the formulation of δW owing to the presence of the Brownian motion. This kind of ambiguity also arises in the problem of the viscosity of macromolecules discussed in § 5. However compared with Eq. (3.1), (3.1′) and (3.9), δW is easily formulated and the extensition to the case of viscosity becomes obvious. In this point consists the reason why we use Eq. (3.1) in place of Eq. (3.1′)

to Eqs. (3. 14) and (3. 12) irrespective of the nature of the gravity, whether constant or not.

§ 4. Dielectric Properties of Dilute Solutions of Polar Molecules

Let E be the applied electric field and D the dielectric displacement. Denoting ρ the orientation probability of dipoles with the normalization $\int \rho d\Omega = 1$, we have

$$D = n^2 E + 4\pi N \int \mu_e \cos\theta \rho d\Omega \ , \qquad (4.1)$$

where n is the optical refractive index, N the number of dipoles in unit volume, μ_e the external dipole moment defined by Fröhlich[4] and θ the angle between the electric field and the axis of dipole. The internal energy U and entropy S per unit volume are given respectively by

$$U = n^2 E / 8\pi \qquad (4.2)$$

and

$$S = -kN \int \rho \log \rho d\Omega \ , \qquad (4.3)$$

while ρ is determined by

$$\frac{\partial\rho}{\partial t} = -\frac{1}{\sin\theta}\frac{\partial}{\partial\theta}(\sin\theta\, j\rho) \ ,$$
$$j = -\frac{E\mu_e \sin\theta}{\zeta} - \frac{kT}{\zeta\rho}\frac{\partial\rho}{\partial\theta} \ , \qquad (4.4)$$

where ζ is the rotatory frictional constant. On the other hand the work done by external field is given by

$$\frac{\delta W}{\partial t} = \frac{E}{4\pi}\frac{\partial D}{\partial t}$$
$$= \frac{n^2 E}{4\pi}\frac{\partial E}{\partial t} + EN \int \mu_e \cos\theta \frac{\partial\rho}{\rho t} d\Omega \ . \qquad (4.5)$$

Eqs. (1. 1) and (1. 2) of general validity lead

$$\frac{\delta Q}{\partial t} = NE \int \mu_e \cos\theta \frac{\partial\rho}{\partial t} d\Omega \qquad (4.6)$$

and

$$T\frac{\partial S}{\partial t} = -NkT \int \log\rho \frac{\partial\rho}{\partial t} d\Omega \qquad (4.7)$$

Introducing Eq. (4. 3) into Eqs. (4. 6) and (4. 7) we obtain after partial integration

$$\frac{\delta Q}{\partial t} = -N \int E\mu_e \sin\theta\, j\rho d\Omega \ , \qquad (4.8)$$

and

$$T\frac{\partial S}{\partial t} = N \int j\rho\left(-\frac{kT}{\zeta\rho}\frac{\partial\rho}{\partial\theta}\right) d\Omega \qquad (4.9)$$

$$T\left(\frac{\partial S}{\partial t}\right)_{irr} = T\left(\frac{\partial S}{\partial t}\right) + \frac{\delta Q}{\partial t}$$
$$= N\zeta \int j^2 \rho d\Omega \ . \qquad (4.10)$$

Eqs. (4. 8) and (4. 10) are analogous to those in the case of sedimentation. Eq. (4. 8) means that the work done by the moment of external force $-E\mu_e \sin\theta$ against the angular current $j\rho$ is equal to the energy dissipation, and this was the fundamental idea of the previous work[3], where it was shown that the imaginary part of the complex dielectric constant is derived from Eq. (4. 8), but if use is made of the complex quantities from the outset we can derive both real and imaginary parts of the dielectric constant. Equations derived here are general and are applied to the charging or discharging processes as well.

§ 5. Intrinsic Viscosity of Solutions of Macromolecules

For non-spherical macromolecules the effect of the rotatory Brownian motion is very important for the problem of the intrinsic viscosity. For the sake of simplicity we take free draining pearl-necklace model for linear polymers which was previously treated by one[5],[6] of the authors. Same notations are used as in the previous paper[5].

The orientation probability or the distribution function for the orientation, ρ, is determined by[4]

$$\partial\rho/\partial t = -\mathrm{div}\, \boldsymbol{j}\rho \qquad (5.1)$$
$$\boldsymbol{j} = \omega^0 - (kT/\rho)\ \mathrm{grad}\ \rho \qquad (5.2)$$

where ω^0 is the angular velocity determined hydrodynamically due to the velocity gradient G and the operations div and gard must be taken in a certain Riemannian space (R). The frictional force acting on the fluid by the i th segment of radius a_i is given by

$$F_i(\omega) = f\eta_0 a_i([\boldsymbol{\omega} \boldsymbol{R}_i] - \mathrm{G}\boldsymbol{R}_i) \qquad (5.3)$$

ω being the angular velocity given to the molecule. Hereupon opinion is divided on the question of calculating the increase of energy dissipation due to the presence of macromolecules. We will enumerate the diverse methods:

(I) by Kuhn (1932), Eisenschitz (1933), Burgers (1938), and Peterlin (1938) et al[7].

$$E^{(1)} = \int \sum_i f\eta_0 a_i([\omega^0 \boldsymbol{R}_i] - \mathrm{G}\boldsymbol{R}_i)^2 \rho d\Omega \ , \qquad (5.4)$$

(II) by Simha[8] (1940) for complete Brownian motion

$$E^{(2)}=\int \sum_i f\eta_0 a_i(-\mathrm{G}\boldsymbol{R}_i)^2 \frac{1}{4\pi} d\Omega\,, \qquad (5.5)$$

(III) by W. Kuhn and H. Kuhn[9] (1945)

$$E^{(3)}=\int \sum f\eta_0 a_i([\boldsymbol{j}\boldsymbol{R}_i]-\mathrm{G}\boldsymbol{R}_i)^2 \rho d\Omega\,, \qquad (5.6)^*$$

(IV) by Saitô[6] (1951) and by Kirkwood[10] (1949, 1951)

$$E^{(4)}=\int \sum f\eta_0 a_i([\boldsymbol{j}\boldsymbol{R}_i]-\mathrm{G}\boldsymbol{R}_i)(-\mathrm{G}\boldsymbol{R}_i)\rho d\Omega\,. \qquad (5.7)$$

In these equations the integrations with ρ over $d\Omega$ mean the averages over all the orientations of molecules.

$\boldsymbol{F}_i(\omega)([\omega\boldsymbol{R}_i]-\mathrm{G}\boldsymbol{R}_i)$ is the work done by frictional force, and is divided into $\boldsymbol{F}_i(\omega)[\omega\boldsymbol{R}_i]$ and $-\boldsymbol{F}_i(\omega)\mathrm{G}\boldsymbol{R}_i$. The former is equal to the work done by the external force acting on the molecule in order to make it rotate with angular velocity ω and the latter to the work done by the fluid upon the molecule rotating with the angular velocity ω.

In method (I) one uses ω^0 for ω in Eq. (5.3) and in consequence the work done by the external force $\sum \boldsymbol{F}_i(\omega^0)[\omega^0\boldsymbol{R}_i]$ vanishes because ω^0 is determined by the condition of vanishing of the total moment of force, therefore $E^{(1)}$ is equal to the work done by the fluid in the absence of the Brownian motion. $E^{(1)}$, $E^{(3)}$ and $E^{(4)}$ lead to the same result in the absence of the Brownian motion. The inadequacies of the treatments of (I) and (II) are discussed elswhere[5], we will give some discussions on the other two methods (III) and (IV).

In the methods (III) and (IV) one uses $\boldsymbol{j}$ for ω in Eq. (5.3). From what has been mentioed in the above sections, it will be easily surmised that $E^{(3)}$ corresponds to irreversible production of entropy and $E^{(4)}$ to external work by the fluid. In fact

$$-f\eta_0 a_i([\boldsymbol{j}\boldsymbol{R}_i]-\mathrm{G}\boldsymbol{R}_i)=-\boldsymbol{F}_i(\boldsymbol{j})$$

is the frictional force of the fluid acting on the i-th segment of a molecule with angular velocity $\boldsymbol{j}$ which is regarded as the macroscopically observable average one, and $\mathrm{G}\boldsymbol{R}_i$ is the rate of the displacement of fluid at the i-th segment. Therefore $E^{(4)}$ is the external work done by the fluid upon the molecule (see foot-note of § 3). $E^{(3)}$ contains $E^{(4)}$ as well as the contribution due to the work done by the current of the probability density which is written as

$$E'=\int \sum f\eta_0 a_i([\boldsymbol{j}\boldsymbol{R}_i]-\mathrm{G}\boldsymbol{R}_i)[\boldsymbol{j}\boldsymbol{R}_i]\rho d\Omega\,, \qquad (5.8)$$

where $\boldsymbol{j}$ is divided into ω^0 and $\boldsymbol{j}_D$ (diffusion current) and it is easy to show

$$E'=\int \sum f\eta_0 a_i([\boldsymbol{j}\boldsymbol{R}_i][\boldsymbol{j}_D\boldsymbol{R}_i])\rho d\Omega$$
$$=\int (w_\xi j_\xi j_{D\xi}+w_\eta j_\eta j_{D\eta}+w_\zeta j_\zeta j_{D\zeta})\rho d\Omega\,, \qquad (5.9)$$

$$w_\xi=f\eta_0 \sum a_i(\eta_i^2+\zeta_i^2), \text{ etc.},$$

where ξ_i, η_i and ζ_i are the components of $\boldsymbol{R}_i$ in $\xi\eta\zeta$-system whose axes coincide with the principal axes of moment of inertia ($\sum a_i\xi_i\eta_i=0$, etc.), a_i being regarded as if it were mass of i-th segment. Eq. (5.9) is rewritten by use of vectors in Riemannian space (R), as follows

$$E'=-\int \frac{kT}{\rho} \operatorname{grad} \rho\, j\rho d\Omega\,, \quad d\Omega=\sqrt{g}\, \Pi dx^k$$
$$=-kT\int \frac{\partial \log \rho}{\partial x^i} j_i \rho\sqrt{g}\, \Pi dx^k$$
$$=-kT\frac{\partial}{\partial t}\int \rho \log \rho \sqrt{g}\, \Pi dx^k\,. \qquad (5.10)^{**}$$

In consequence the term E' is yielded from the increasing of entropy.

In this system under consideration we have the thermodynamical relations similar to Eqs. (3.1′) and (3.2) with $dU=0$,

$$0=-\delta Q+\delta W \qquad (5.11)$$
$$dS=-\delta Q/T+(dS)_{irr} \qquad (5.12)$$

From what has been mentioned above, we have

$$\left.\begin{aligned} E^{(3)}&=E^{(4)}+E' \\ E^{(4)}&=\delta W/\partial t=\delta Q/\partial t \\ E'&=T\partial S/\partial t \end{aligned}\right\} \qquad (5.13)$$

Consequently

$$E^{(3)}\doteqdot \frac{\delta Q}{\partial t}+T\frac{\partial S}{\partial t}=T\left(\frac{\partial S}{\partial t}\right)_{irr} \qquad (5.14)$$

---

* It is easy to show that

$$E^{(3)}=\int \sum f\eta_0 a_i([\omega^0\boldsymbol{R}_i]-\mathrm{G}\boldsymbol{R}_i)^2\rho d\Omega$$
$$+\int \sum f\eta_0 a_i[\boldsymbol{j}_D\boldsymbol{R}_i]^2\rho d\Omega \qquad (5.6')$$

where $\boldsymbol{j}_D=\boldsymbol{j}-\omega^0$ is the diffusion current, and this is the formula adopted by W. Kuhn and H. Kuhn.

** In the space (R) ρ is normalized as

$\int \rho\sqrt{g}\, \Pi dx^i=1$, where $\sqrt{g}=w_\xi\sqrt{w_\zeta}\sin\theta$[5].

In usual spherical coordinate $\sqrt{g}=\sin\theta$ and ρ is normalized by $\int \rho \sin\theta d\theta d\varphi=1$. Therefore Eq. (5.10) does not differ from usual expression $\int \rho \log \rho \sin\theta d\theta d\varphi$.

which shows that Kuhn-Kuhn's calculation corresponds to irreversible production of entropy. However, in periodic or steady state such as encountered in viscosity problem $\partial S/\partial t$ or its time average is zero. This proves the equivalence of the two results of the methods (III) and (IV).

§ 6. Conclusions

We have shown through several examples in the above sections the relations between the energy dissipation or entropy increasing and the current of the probability density of molecules of dilute systems. The latter is the current of density which is macroscopically observable. Therefore it will be self-evident that in the cases where the work given to the particles of the system under consideration by external force is transformed directly to heat, the energy dissipation is to be calculated by the work done by external force against this current (Eqs. (3. 9), (4. 8) and (5. 7)). In fact Eyring's theory[11] of the viscosity of liquids is based on this principle. It is further shown that the rate of entropy increasing multiplied by absolute temperature is equal to the work done by diffusion force against the current of the probability density (Eqs. (2. 7), (3. 10), (4. 9) and (5. 10)) and especially the irreversible production of entropy multiplied by temperature is equal to the heat which would be produced by the friction of molecules with the velocity equal to the current of the probability density (Eqs. (2. 9), (3. 12), (4. 10) and (5. 6)).

Generalization of the above considerations to the stochastic processes governed by generalized Fokker-Planck equations will be straight forward.

We should like to thank Professor H. Takahasi of Tokyo University for his useful discussions. This work was supported by the research grant from the Ministry of Education.

References

1) R. C. Tolman, P. C. Fine: Rev. Mod. Phys. **20** (1948) 51.

2) M. Sugita: Proc. Phys. Soc. Japan **4** (1949) 134 (in Japanese).

M. Sugita: *Thermodynamics of Transient Phenomena*, Iwanami Syoten, 1950. (in Japanese)

3) N. Saitô: J. Phys. Soc. Japan **6** (1951) 201.

4) H. Fröhlich: *Theory of Dielectrics*, Oxford, 1949.

5) N. Saitô: J. Phys. Soc. Japan **4** (1949) 85.

6) N. Saitô: J. Phys. Soc. Japan **6** (1951) 297, 302.

7) W. Kuhn: Z. phys. Chem. **A161** (1932) 1.

R. Eisenschitz: Z. phys. Chem. **A163** (1933) 133.

J. M. Burgers: *Second Report on Viscosity and Plasticity*, Amsterdam, 1938.

A. Peterlin: Zeits. f. Phys. **111** (1938) 232.

8) R. Simha: J. Phys. Chem. **44** (1940) 25.

9) W. Kuhn, H. Kuhn: Helv. Chim. Acta **28** (1945) 97.

10) J. G. Kirkwood: Rec. trav. chim. **68** (1949) 649.

J. G. Kirkwood, P. L. Auer: J. Chem. Phys. **19** (1951) 281.

11) S. Glasstone, K. J. Laidler, H. Eyring: *The Theory of Rate Processes*, McGraw-Hill, 1941, Chap. 9.

JOURNAL OF THE PHYSICAL SOCIETY OF JAPAN Vol. 7, No. 6 NOV.—DEC., 1952

Crystal Structure and Phase Transition of Some Metallic Halides (II)*

On the Phase Transition and the Crystal Structures of Cuprous Bromide

By Sadao HOSHINO

Tokyo Institute of Technology, Oh-okayama, Tokyo, Japan

(Read April 1 and Received June 25, 1952)

The phase transition and the crystal structures of the three modifications in cuprous bromide (CuBr) were studied by the X-ray powder method and the calorimetric measurement. The crystal structures in γ, β and α phases were determined to be face centered cubic, hexagonal and body centered cubic respectively. In the γ-phase, the structure belongs to the zincblende type, but it shows an anomalous change with temperature. This anomalous change of the structure was investigated by the same method as applied to the recent study of γ-CuI, and it was found that this anomaly is analogous to that of γ-CuI. The structures of β and α-CuBr were ascertained to be both the average structures closely resembling to those of β and α-AgI respectively.

§1. Introduction

It has been known that some crystals of silver and cuprous halide show phase transitions and have large ionic conductivity at high temperatures. Recently we have studied on the phase transition in cuprous iodide (CuI) and reported¹⁾ in Part I of the present paper. On silver iodide (AgI), investigations on the change of crystal structure have been previously published by Strock²⁾ and by Helmholz³⁾. It was shown, in these investigations, that the crystal structures of high temperature modifications in these substances may be the "average structure".

There is no detailed study on the crystal structures of high temperature forms and the nature of the phase transition in cuprous bromide (CuBr), though it may be expected that this substance might possess close resemblances to AgI or CuI.

The present study is to obtain the detailed informations about this substance, especially to ascertain the existence of average structure, by X-ray and calorimetric methods.

§2. Sample

The sample was prepared by the following chemical processes.

$$2CuSO_4+4KBr \longrightarrow 2CuBr_2+2K_2SO_4$$

$$2CuBr_2 \xrightarrow{(SO_2)} 2CuBr+Br_2$$

The precipitate was washed with water repeatedly to eliminate cupric bromide $CuBr_2$ as perfectly as possible.

§3. Specific Heat Measurement

We measured, at first, the temperature change of the specific heat in order to determine the transition temperatures and to know the energy and entropy changes at the phase transitions by use of an adiabatic calorimeter⁴⁾. The specimen (13.5 g) was

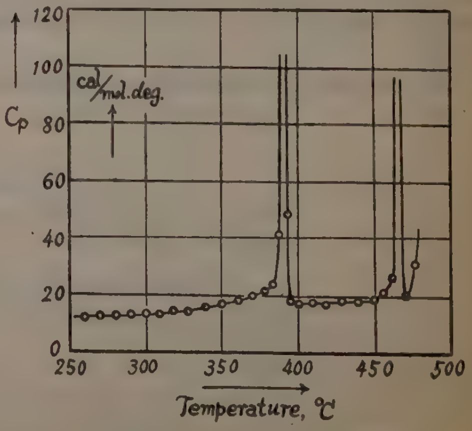

Fig. 1. Specific heat vs. temperature curve of CuBr.

---

* Our previous study "On the Phase Transition in Cuprous Iodide" will be referred to as Part I.

sealed in a hard glass vessel (3 g). The heat input given to the specimen was about 0.008 cal/g. sec. The obtained specific heat vs. temperature curve is shown in Fig. 1. There are two main anomalies at 385°C and 470°C, and these correspond to the transition from γ to β and from β to α respectively. After the latter peak the curve rises again, owing to fusion.

From the curve we estimated transition energies ΔE and corresponding entropy changes ΔS as follows:

$\Delta E_{\gamma\to\beta}=1.4$ Kcal/mol. $\Delta S_{\gamma\to\beta}=2.1$ cal/mol.deg.

$\Delta E_{\beta\to\alpha}=0.7$ Kcal/mol. $\Delta S_{\beta\to\alpha}=0.9$ cal/mol.deg.

§ 4. Crystal Structure of each Phase

The X-ray analysis of the crystal structures of the above phases was performed by Debye method. Powdered sample was sealed in a thin hard glass capillary (diameter about 0.3 mm), and placed in a high temperature X-ray camera with the radius of about 55.5 mm, and the photographs were taken at various temperatures with CuKα radiation.

a) Structure in γ-phase

The photograph at room temperature shows that the crystal lattice of γ-CuBr is face centered cubic with the lattice constant $a=5.679_4$ kX at 20°C and the structure belongs to the zincblende type as was reported formerly. However, the relative intensities of reflexion lines at high temperatures of this phase are somewhat different from those at room temperature, i.e., the intensities of some reflexion lines, for instance (200), (222), (420) etc., increase with temperature whereas those of the other lines decrease by the general temperature effect. Since just the similar kind of intensity anomaly has been found also for γ-CuI in our recent work¹⁾, the procedure of experiment and analysis the same as used for the study of CuI was applied here. We measured, at first, the intensity change for each reflexion line as a function of temperature by the method using a standard specimen. The result for several important lines is shown in Fig. 2, where the ordinate shows the observed intensity in a scale which makes the intensity of (111) at 8°C equal to 100. This figure shows entirely the same tendency as found for γ-CuI, expect for a fact that the intensity anomaly for γ-CuBr already begins at room temperature, while that for CuI begins at about 150°C. Concerning the nature of the structure change of γ-CuBr with temperature, therefore, the analogous reasoning used for CuI may be applied to this case also, as follows.

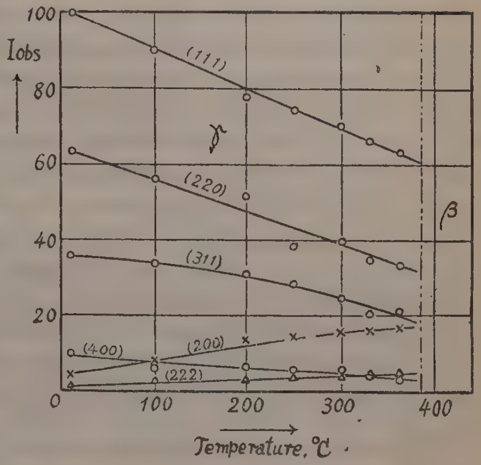

Fig. 2. The intensities of the several reflexions in the γ-phase region as functions of temperature.

The square of structure factors $|F(hkl)|^2$ for zincblende structure may be expressed by the following formulae:

$(f_{\mathrm{Br}}e^{-M_{\mathrm{Br}}}+f_{\mathrm{Cu}}e^{-M_{\mathrm{Cu}}})^2$ for (220), (400), (422) etc.

$(f_{\mathrm{Br}}e^{-M_{\mathrm{Br}}})^2+(f_{\mathrm{Cu}}e^{-M_{\mathrm{Cu}}})^2$ for (111), (311), (331) etc.

$(f_{\mathrm{Br}}e^{-M_{\mathrm{Br}}}-f_{\mathrm{Cu}}e^{-M_{\mathrm{Cu}}})^2$ for (200), (222), (420) etc.,

wherein f_{Br} and f_{Cu} are the atomic scattering factor and $e^{-M_{\mathrm{Br}}}$ and $e^{-M_{\mathrm{Cu}}}$ correspond to the Debye temperature factor for bromine and copper atoms respectively. The reflexion lines showing the anomalous intensity increase with rising temperature are known to be corresponding to the structure factor belonging to the last category.

As explained in the previous paper, such tendency of the temperature change of line intensities can be understood at least qualitatively when we assume that the temperature dependency of the Debye factor for metallic atoms is much drastic than for halogen atoms. By this assumption, the anomalous intensity increase of the line group (200), (222) etc. can be well explained, because the sqaure of the structure factor for this line group, $(f_{Br}e^{-M_{Br}}-f_{Cu}e^{-M_{Cu}})^2$, increases with temperature when $e^{-M_{Cu}}$ decreases more drastically compared with $e^{-M_{Br}}$. Inversely, these temperature dependencies of Debye factor for every atoms can be formally deduced from the observed intensity change. The quantities proportional to $f_{Br}e^{-M_{Br}}$ and $f_{Cu}\ e^{-M_{Cu}}$ for every temperatures may be estimated from the intensities of several reflexions by use of the mathematical relation between the structure factors of the three different forms as mentioned above. The logarithms of the ratios of these quantities $ln(fe^{-M_{T_1}}/fe^{-M_{T_2}})$ for the different temperatures T_1 and T_2 give the values of $(M_{T_2}-M_{T_1})$ for bromine or copper atoms. In Fig. 3 values of $(M_{T_2}-M_{T_1})\cdot(\lambda/\sin\theta)^2$, which are the mean values for the several reflexions, are indicated for both atoms as functions of temperature T_2 when T_1 is fixed at 281°K. In it the similar quantities for CuI is also plotted. As seen in this figure, the higher the temperature the curve for copper shows the larger deviation from that for bromine which is quite linear, and it will be seen the fact that, as mentioned before, the anomaly in the case of CuBr already begins at low temperature, presumably below the room temperature, while that for CuI begins at about 150°C.

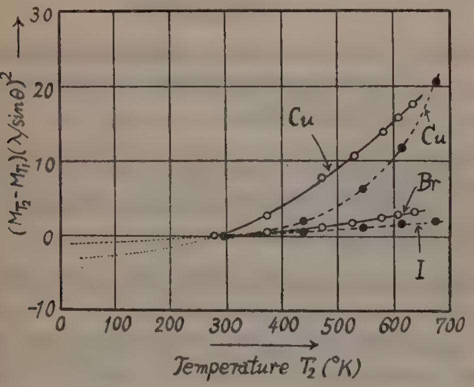

Fig. 3. $(M_{T_2}-M_{T_1})\cdot(\lambda/\sin\theta)^2$ as functions of temperature T_2.
——○—— plots for γ-CuBr, $T_1=281$°K.
····●···· plots for γ-CuI, $T_1=293$°K.

In Part I the similar anomalous intensity change in the γ and α phases of CuI have been interpreted in the following way, whereby the α-phase is regarded to be the continuation of the γ-phase. At sufficiently low temperatures, the Cu-atoms in CuI will be probably in the positions for zincblende structure (4(c) of T_d^2), but there may be four metastable positions for Cu-atom deviated in the [[111]] directions around every 4(c) position, and the probability of finding a Cu-atom in these metastable positions gradually increases with temperature, and finally, at sufficiently high temperature corresponding to that of the α-phase, the atoms is distributed over these positions with equal probability. This assumption was supported by the agreement of the calculated and observed values of the entropy change from γ to α-phase. Though, for our present case of CuBr, however, the similar thermodynamical informations can not be obtained by reason that the structure of α-CuBr is different from that of α-CuI as it will be described in later section, it may be conceivable that the proposed model for γ-CuI assuming the existence of the four metastable positions for Cu-atom will be also applied to the structure of γ-CuBr. This assumption is highly plausible since, as will be shown in the next section, also the structure of β-CuBr is known to be the same kind of the average structure as for α-CuI.

b) Structure in β-phase

The crystal structure of β-CuBr was determined by the photograph at 430°C of the β-phase region. The positions of reflexion lines indicate that the lattice belongs to hexagonal system with the lattice constants $a=4.0_4$ kX and $c=6.5_8$ kX and $c/a=1.63$ and the corresponding space group may be C_{6v}^4. The axial ratio and the space group seem to show that the lattice of β-CuBr may be of the wurtzite type. The observed intensities of main lines, however, are somewhat different from those expected for the wurtzite type structure. From this fact we may suppose that the structure of the β-phase is also an average one.

In the wurtzite type structure, the one kind of atoms, say Br, should be in the positions (0, 0, 3/8 ; 1/3, 2/3, 7/8) and the other, say Cu, in (0, 0, 0 : 1/3, 2/3, 1/2), and therefore, the each atom is surrounded by the four another kind of atoms tetrahedrally. This relation of the neighbourring atoms, as is generally known, is analogous to that in the zincblende structure. It seems to be very presumable, therefore, that if the structure of β-CuBr is also an average one, it may possess a similar atomic arrangement to that in the cubic α-CuI. In fact, such average structure for hexagonal lattice has been formerly proposed by Helmholz (1935)[3] for the structure of the hexagonal β-AgI. According to this model, then, there are new four positions for Cu-atom added to every $2(b)$ position of the wultzite type structure, and all of these five positions or only the new four positions are equally and statistically occupied by one copper atom, as shown in Fig. 4. The configurations of these new positions in a unit cell are $2(b)$: $(0, 0, u)$; $(1/3, 2/3, 1/2+u)$ and $6(c)$: $(x, \bar{x}, z)$; $(x, 2x, z)$, $(2\bar{x}, \bar{x}, z)$; $(\bar{x}, x, 1/2+z)$; $(2x, x, 1/2+z)$; $(\bar{x}, 2\bar{x}, 1/2+z)$.

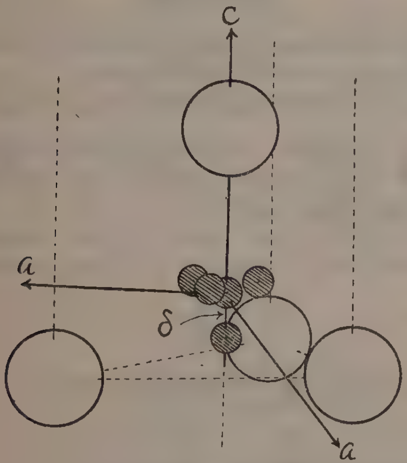

Fig. 4. Proposed average structure of β-CuBr, showing a part of the hexagonal unit cell. White circles: bromine atoms, Hatched circles: positions for copper atom.

Table I. The observed and calculated intensities for the several reflexions of β-CuBr.

hkil	$I_{obs.}$ (430°C)	$I_{cal.}$ (wultz. type)	$I_{cal.}$ (1)	$I_{cal.}$ (2)
$10\bar{1}0$	8	147	78	77
0002	4	87	42	43
$10\bar{1}1$	10	100	100	100
$10\bar{1}2$	3	54	27	31
$11\bar{2}0$	5	115	54	55
$10\bar{1}3$	5	116	44	50
$20\bar{2}0$	1	16	5	10
$11\bar{2}2$	3	65	34	38

The parameters u, x, and z are determined by δ, the deviation from the position of the wurtzite type structure (see Fig. 4), so that the reflexion intensities can be calculated as functions of δ. The calculated intensities, corresponding to the new models, showing the best accordance with the observed values are shown in the third and fourth columns in Table I. The first and the second columns show respectively the observed intensities and the calculated ones corresponding to the wurtzite type structure. The third column ($I_{cal}(1)$) shows the calculated values of $\delta=0.5$ kX for the average structure with the five positions for one copper atom, and the fourth column ($I_{cal}(2)$) indicates the values of $\delta=0.3$ kX for another average structure with four positions. The calculated values for these two types of average structure are both in good agreement with the observed intensities within the accuracy of the photometric measurement. In our present study, however, there is no decisive evidence to determine whether the positions for copper atom are five or four, but it would be sure that β-CuBr has the same type of average structure as that of β-AgI as reported by Helmholz.

c) Structure in α-phase

It was difficult to determine the crystal structure of α-CuBr by reason of that the Debye lines of the photographs taken in this phase range always showed not smooth but fibrous characteristic, so we could only give the qualitative considerations.

The positions of the diffraction lines indicate that the lattice of α-CuBr belongs to the body centered cubic one with $a=4.5_3$ kX at 480°C, but the intensities of lines with fibrous character are not always in agreement among the several photographs taken at same temperature. This may be explained as follows; the fibrous character of the diffraction lines is caused by the recrystallization and the orientation of the powdered sample in the capillary, the extent of which are liable to change by only slight differences in the experimental conditions. In order to avoid such crystal growth and its orientation, the specimen of coarse powder was used. Of course, then, the diffraction pattern consists of the spotty lines, but it is without fibrous characteristic so that the intensity measurement could be done at least qualitatively.

Since the structure of α-AgI is also the body centered cubic one, it may be supposed that the structure of α-CuBr will be analogous to that of α-AgI. This is actually justified by the comparison of the photographs taken for both the substances, paying regard to that the ratio of the scattering factor for Cu and Br is, on the whole, almost similar to that for Ag and I. Namely, the relative values of reflexion intensities for α-CuBr is nearly accordance with that of α-AgI except a difference due to the contribution of the temperature factor.

The crystal structure of α-AgI has been studied by Strock (1934)[2], and it was shown that this structure may be an average one in which two Ag atoms in a unit cell are equally distributed to the thirteen positions in the space within the body centered cubic lattice composed of the iodine atoms. There are some questions in this structure model, especially with respect to the distribution of Ag atoms, but that α-CuBr has the same type of average structure as α-AgI is regarded to be sure.

This investigation was done throughout the kind guidance of Prof. S. Miyake, to whom the author wishes to express his best thanks. Thanks are also due to Mr. H. Maniwa and Mr. M. Hirabayashi for the facilities of specific heat measurement.

This work was supported by the grant for the promotion of science from the Ministry of Education.

References

1) S. Miyake, S. Hoshino and T. Takenaka: J. Phys. Soc. Japan **7** (1952) 19.

2) L. W. Strock: Z. Phys. Chem., **B 25** (1934) 441.

3) L. Helmholz: J. Chem. Phys., **3** (1935) 740.

4) S. Nagasaki and Y. Takagi: J. App. Phys. Japan **17** (1948) 104.

JOURNAL OF THE PHYSICAL SOCIETY OF JAPAN Vol. 7, No. 6 NOV.—DEC., 1952

Statistical Study of the Barkhausen Effect Part I, Distribution of Domain Size

By Harunobu SAWADA

Taihei Mining & Metallurgical Laboratory, Omiya

(Read May 2, 1950. Received March 11, 1952)

The size distributions of Barkhausen impulses were obtained, at twelve different portions on the hysteresis loop of a silicon steel wire, with seven searchcoils, which had the same turn-density but different coil-lengths from each other. An experimental regularity was found in the relation between the distribution of impulse size and the coil-length. The distribution of domain size was calculated from this regularity, by making some assumptions on the mechanism of Barkhausen effect. The main numerical results obtained are as follows; average length of domain: 0.345-5.20 mm; average volume; $0.298\text{-}6.40 \times 10^{-5}$ mm^3; average diameter: $3.32\text{-}3.96 \times 10^{-3}$ mm; minimum average propagating velocity of the magnetic reversal: 3-50 m/sec.

§ 1. Experimental Procedure

The specimen used was an annealed steel wire containing 3% Si, 100 mm long, 2 mm thick. Silicon was added in order to reduce eddy-current. For picking up Barkhausen impulse, seven search-coils of enameled copper wire, 0.05 mm thick, were wound directly on the specimen wire, to reduce leakage flux. The details of the search-coils are given in Table I.

In a preliminary experiment with two search coils, one long and one short, having the same

Table I. Search-Coils

Coil-length in mm.	1.2	2.0	3.4	4.3	4.8	6.2	8.2
Total turns	500	1000	1500	2000	2500	3000	4000
Turn-density per mm.	420	500	440	470	520	480	490
Resistance in ohms	58	125	180	240	340	370	510

turn-density, it was found that the long search-coil catched more numerous impulses, containing larger impulses, than the short coil.

On the basis of this fact, the author attempted to determine more extensively the relation between the distribution of impulse size and the search-coil length with these seven coils.

The amplifier of the impulse voltage was of a resistance-capacity coupling type, consisting of carefully selected parts, and had a voltage amplification factor of 134 db in the frequency range 40 to 3000 cycles per second.

The magnetizing coil consisted of two windings, each 210 mm long. The first winding was used to produce a main external magnetic field, whose maximum effective intensity was 15.5 oersteds. This main field could specify the magnetic state of the specimen at an arbitrary definite point on the hysteresis loop. The second winding was used to produce an additional field, and to shift the magnetic state of the specimen from the above-mentioned point, with a properly controlled speed, which was in most cases very slow, along the hysteresis loop. Controlling these two magnetic fields, successive magnetic reversals with time intervals, suitable for measurement, could be produced in the specimen at arbitrary portions of its hysteresis loop. Then, they were picked up as the Barkhausen impulses by one of the seven search-coils.

The electrical connection diagram of the measuring system is shown in Fig. 1.

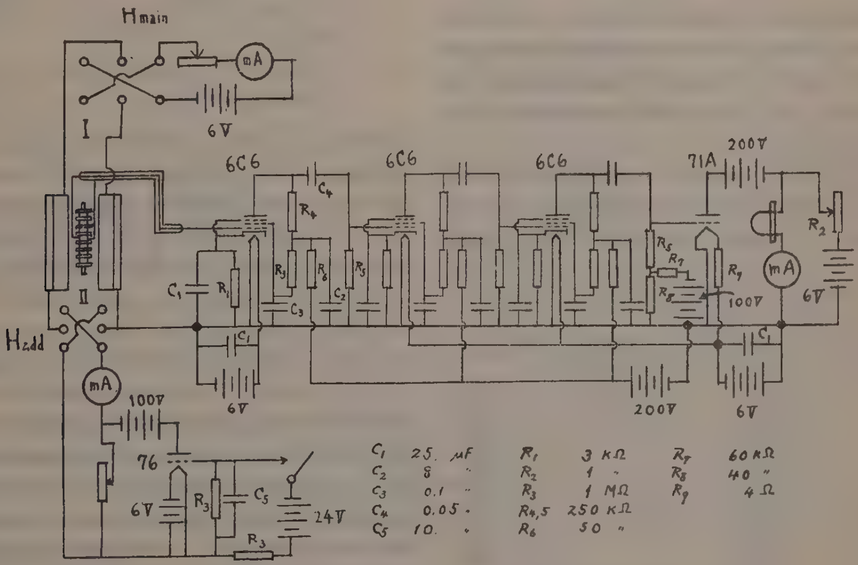

Fig. 1. Electrical Connection Diagram of Measuring System.

In this experiment, the Barkhausen impulses were recorded on the high sensitive bromide papers by a Yokogawa type electromagnetic oscillograph. The object of this experiment was not to record the real wave form of individual impulse, but to record many successive impulses as a group, for the purpose of determining their size distribution, during a certain small change of additional field. To indicate the impulse size, the height of each impulse figure, obtained on the oscillogram, was utilized as a measure, assuming that the vibrator of electromagnetic oscillograph acted ballistically for every individual impulse. In the preliminary experiment, the real wave form of the impulse was observed by a cathoderay oscillograph with a suitable sweeping speed. On the other hand, a regular sinusoidal wave was also projected on the same screen with the same sweeping speed. And the half wave breadth of the sinusoidal wave was equalized with the impulse breadth on the screen, by controlling the frequency of the sinusoidal wave. From thus determined frequency of the sinusoidal wave, it was found that the duration time of the individual impulse was usually shorter than 10^{-4} seconds.

The motion of the vibrator, immersed in liquid paraffin, may safely be assumed to be ballistic for such short impulses, as are encountered in this experiment. On the other hand, if the successive impulses occur at a time interval which is too short, then the vibrator can not resolve them. Such disadvantage could be avoided, by using the sufficiently slow rate of changing the additional field. The fact that almost all the impulses occur successively at much longer time intervals, will be confirmed by the study of the time interval distribution, described in later paper.

The Barkhausen impulses were recorded directly, on each of twelve sheets of bromide paper, by each of seven search-coils, at twelve points on the half cycle of the hysteresis loop.

In Table II are given intensities of the magnetic fields and of the magnetization of the specimen, at these twelve observed points.

Table II. Observed Points

Obs. points	H_{eff} in Oe	H_{add} in Oe/sec	I in gauss
A	−15,5	0.0113	−1,045
B	− 3,20	〃	− 968
C	+ 716	〃	− 402
D	+ 778	〃	− 197
E	793	〃	− 116
F	805	〃	− 60
G	815	〃	0
H	832	〃	+ 80
I	860	〃	195
J	880	〃	283
K	920	〃	482
L	3,50	〃	958
A'	+15,5	〃	+1,045

§ 2. Experimental Results

The height of every individual impulse figure was measured in mm from the zero line, on the oscillogram obtained, as a measure of its size. However, the usual method calculating the magnetization change, or the magnetic domain volume, from the measured impulse size, taking account of the ballistic constant and the amplification factor of the measuring system, was not used, because of the difficulties in the determination of these factors, with a sufficient accuracy for such small irregular waves.

As an example of experimental distribution curve of the impulse size, the result obtained at the observed point F in Fig. 5 or 6, under the conditions, $H_{eff}=0.805$ Oe, $I=60$ gauss, $H_{add}=0.0113$ Oe/sec, is given in Fig. 2. The typical feature of these distribution curves were not so clear as a proper conclusion could be drawn out from them. However, the following two features were suggested;

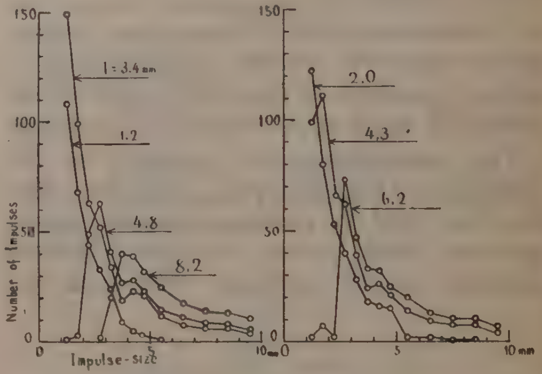

Fig. 2. Experimental Distribution of Barkhausen Impulse Size.

(1) The distribution curve of the impulse size has a maximum point in many cases.

(2) This maximum point has a tendency to shift to the side of larger impulse size, as the search-coil length becomes longer.

Furthermore, these experimental data were rearranged in the following different manner. Instead of the number of the impulses contained in a certain size range, the number of impulses, whose sizes were larger than a certain lower limit, was plotted against the search-coil length. This new method for plotting the impulse size distribution, disclosed a remarkable regularity, as is shown in Fig. 3.

The features of these straight line groups are as follows;

(1) The inclinations of these straight lines, to the axis of the coil-length, decrease, as the lower limit of impulse size increases.

(2) The intersection points of the extensions of these straight lines with the axis of

the coil-length, shift to the right hand side with increasing lower limit of the impulse size.

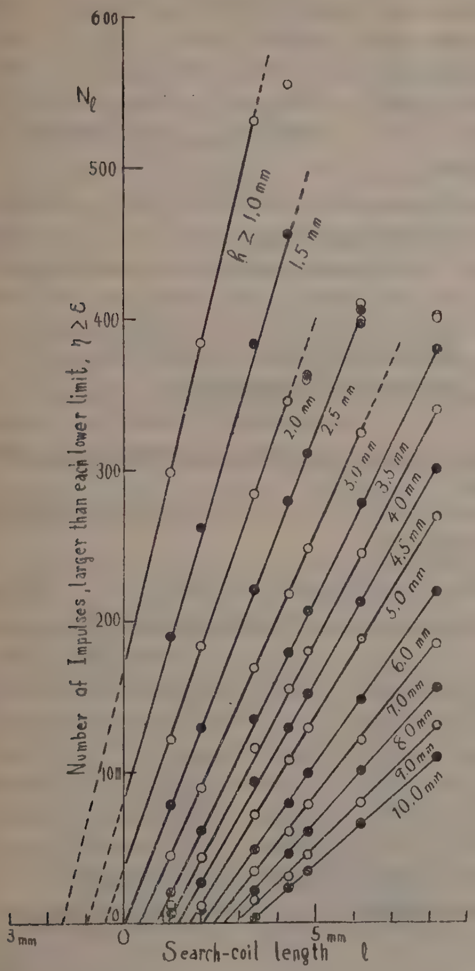

Fig. 3. Rearranged Distribution of Impulse Size.

Obviously, there are some points, which do not follow this rule, as are shown in Fig. 3. However, the fact that almost all the observed points follow this regularity, seems to be a significant phenomenon.

If the domain length along the wire is very small, as compared with the search-coil length, then the longer search-coil would pick up the more numerous impulses, without increasing their sizes. Inversely, if the domain is so large to cover the whole length of the specimen, then the search-coils, whether long or short, would pick up the same number of impulses.

However, both were not the case. Therefore, the other type of the distribution must be considered for the domain length along the wire, or for the domain size.

The author could derive mathematical formulae for the distribution of domain size, consistent with the experimental fact, and could estimate the average domain size, using the relations derived from this size distribution.

Many distribution curves of the impulse size, obtained at the other observed points, do not need to be represented, as they are essentially similar to Fig. 2.

§ 3. Theory of the Domain size Distribution

According to the above consideration for the experimental results, a normalized distribution function $\varphi(\xi)$ must be assumed for the domain length ξ.

The shape of domain may be assumed simply as a circular cylinder, with the axis parallel to that of the specimen wire, of equal cross-section, but of different lengths. Some additional assumptions on the magnetic domsins, such as those about the distribution of the cross-sections or about the distribution of the orientations, would have to be made.

The uniform domain density ρ denotes the number of the domain centers per unit length of the specimen wire in mm^{-1}, whose magnetization reverses by the change of the magnetic field, $H_{\text{eff}}=1$ Oe.

Then, the number of reversing domains, having the length between ξ and $\xi+d\xi$, is $\rho\varphi(\xi)d\xi$.

To determine the size h of Barkhausen impulse, picked up by a search-coil of length l, accompanied with the reversal of the domain ξ, it is necessary to make more assumptions on the mechanism of impulse formation. The following simple assumptions were made;

(1) The impulse size h is proportial to the length η of the part of domain, covered by the search-coil. It is not affected by the position of the reversing domain in the wire, whether it is located near surface or at center. $h \propto \eta \leq l$ or ξ.

(2) When the impulse passes through the amplifier, the smaller impulses would be masked by the amplifier noise, and only larger impulses, corresponding $\eta > \varepsilon$, may be recorded distinctly.

The straight line group in Fig. 4a is expressed by the following formula.

$$N_l=m(l-l_0)\ ,$$

where N_l is the number of the impulses, picked up by a search-coil of length l, corresponding to $\eta>\varepsilon$.

According to the experimental result,

$$\frac{\partial m}{\partial\varepsilon}<0,\quad (2)\qquad \frac{\partial l_0}{\partial\varepsilon}>0\ .\quad (2')$$

The indefinite integral of $\varphi(\xi)$, i.e. $\Phi(z)$, is a monotonously increasing, positive bounded function.

$$\int_0^z\varphi(\xi)d\xi=\Phi(z)\ ,\quad 0\leq\Phi(z)\leq 1$$

Then N_l is expressed with this $\Phi(z)$ as follows.

$$N_l=\rho[1-\Phi(\varepsilon)](l-\varepsilon)+\rho\int_\varepsilon^\infty[1-\Phi(z)]dz \qquad (3)$$

Comparing the equations (1) and (3), we get

$$m=\rho[1-\Phi(\varepsilon)]\ , \qquad (4)$$

$$l_0=\varepsilon-\int_\varepsilon^\infty[1-\Phi(z)]dz\Big/(1-\Phi(\varepsilon))\ . \qquad (5)$$

As is easily seen, the condition (2) is satisfied by the equation (4). Namely this feature of the impulse size distribution, is not caused from the domain size distribution itself, but affected only by the mechanism of the impulse formation.

The condition (2′) is not always satisfied by the equation (5) with an arbitrary function $\varphi(\xi)$. Resolving these as functional equations, the following conditions can be made for $\varphi(\xi)$, satisfying the condition (2′).

Putting,

$$\bar{\xi}=\int_0^\infty\xi\varphi(\xi)d\xi\ ,\quad F(\varepsilon)=\int_\varepsilon^\infty[1-\Phi(z)]dz\ ,$$

then

$$\left.\begin{array}{l}F(\varepsilon)>0,\ F'(\varepsilon)<0,\ F''(\varepsilon)=\varphi(\varepsilon)>0,\\ F(0)=1,\ F'(0)=-1,\end{array}\right\}\qquad (6)$$

$$F(\varepsilon)<1/1+\varepsilon\ . \qquad (7)$$

Unfortunately, the unique solution for (6) and (7) does not exist. Therefore, some proper function $\varphi(\xi)$, which satify (6) and (7), must be selected, considering at the same time other physical conditions which have not yet been incorporated. For this purpose, the following two functions $\varphi_1(\xi)$ and $\varphi_2(\xi)$ were selected for the distribution of the domain length ξ.

$$\varphi_1(\xi)=1/\lambda_1\exp(-\xi/\lambda_1)d\xi,\ \bar{\xi}_1=\lambda_1 \qquad (8)$$

$$\varphi_2(\xi)d\xi=\xi/\lambda_2^2\exp(-\xi/\lambda_2)d\xi,\ \bar{\xi}=2\lambda_2 \qquad (9)$$

These are shown schematically in Fig. 4b. Taking account of the masking effect of noise for the small impulses, it can not be determined, which of $\varphi_1(\xi)$ and $\varphi_2(\xi)$ is more exactly fitted for the experimental fact. Using $\varphi_1(\xi)$ or $\varphi_2(\xi)$, equation (1) is expressed as follows.

$$N_l=\rho_1\exp(-\varepsilon/\lambda_1)\{l-(\varepsilon-\lambda_1)\}\ , \qquad (10)$$

$$N_l=\rho_2(1+\varepsilon/\lambda_2)\exp(-\varepsilon/\lambda_2)\times[l-\{\varepsilon-\lambda_2(2\lambda_2+\varepsilon)/(\lambda_2+\varepsilon)\}]\ , \qquad (11)$$

or

$$m_1=\rho_1\exp(-\varepsilon/\lambda_1)\ ,\quad l_{01}=\varepsilon-\lambda_1\ , \qquad (12)$$

$$m_2=\rho_2(1+\varepsilon/\lambda_2)\exp(-\varepsilon/\lambda_2)\ ,\quad l_{02}=\varepsilon-\lambda_1(2\lambda_2+\varepsilon)/(\lambda_2+\varepsilon)\ . \qquad (13)$$

These $(m_1,\ l_{01})$ or $(m_2,\ l_{02})$ are plotted in Figs. 4c, d.

For $\varepsilon=\lambda_1$ or $\varepsilon=\sqrt{2}\lambda_2$, (12) or (13) becomes as follows.

$$l_{01}=0,\quad m_1=\rho_1/e,\quad \varepsilon=\lambda_1, \qquad (14)$$

$$l_{02}=0,\quad m_2=\rho_2(1+\sqrt{2})\exp(-\sqrt{2}),\quad \varepsilon=\sqrt{2}\lambda_2\ . \qquad (15)$$

Although the numerical value of ε is unknown,

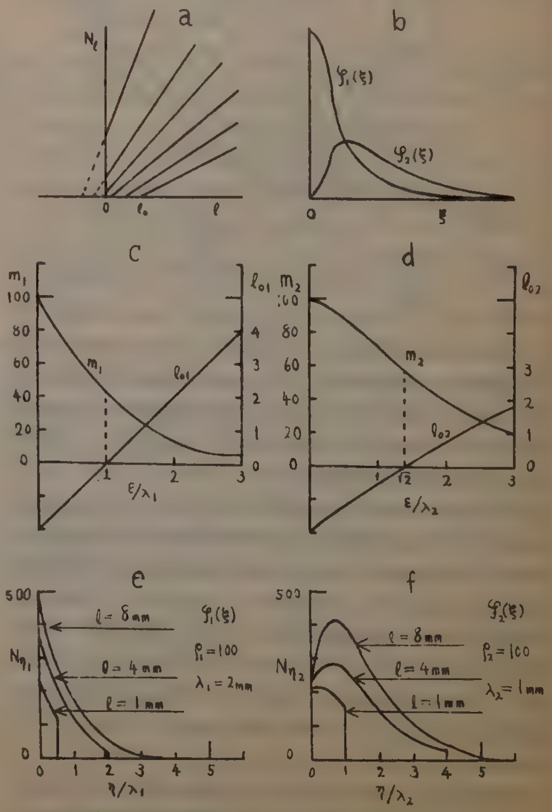

Fig. 4a-f Theoretical Distributions.

the other similar curves to Figs. 4c, d can be obtained from the experimental results, using the impulse height h itself intested of ε. Thus at first, the value of the domain density ρ_1 or ρ_2 was evaluated. Then, using this ρ_1 or ρ_2, the value of λ_1 or λ_2 was calculated, from the same curves and the equation (12) or (13) for another value of h.

The typical distribution of the impulse size, calculated from $\varphi_1(\xi)$ and $\varphi_2(\xi)$ are shown in Figs. 4e, f. In these theoretical curves, some thresholds of the impulse size, which were found in no experiment, appeared for the shorter searchcoil. This situation would be due to the neglection of the distribution of the domain cross-section, in the present theory.

The average domain length $\bar{\xi}_1$ or $\bar{\xi}_2$ was obtained from λ_1 or λ_2, according to the equation (8) or (9).

The product $\rho\bar{\xi}$ has a physical meaning similar to irreversible susceptibility, since the constant domain cross-section has been assumed. The ratio of $\int_C^D d(\rho\bar{\xi})$ to magnetization change observed $\Delta I(CD)$, calculated for the interval CD along the hysteresis loop, would have the maximum value when $\Delta I(CD)$ was perfectly irreversible. Therefore, these ratios were calculated for all intervals, $A\rightarrow B$, $B\rightarrow C$, $\cdots$, $K\rightarrow L$, $L\rightarrow A'$, and the following equation was assumed to calculate the domain crossection A for such interval of the maximum ratio.

$\int d(\rho\bar{\xi})\times A\times 2J_s=\Delta I\times$ cross-section of the specimen wire, where J_s is the saturation value of the magnetization. Then, the ratio of the irreversible part to the total change, for the other intervals, were calculated with the value of A determined above.

$$\frac{\int d(\rho\bar{\xi})\times A\times 2J_s}{\Delta I\times \pi/4\times (2\,\mathrm{mm})^2}\times 100\%\ .$$

On the other hand, the domain diameter $D=\sqrt{4A/\pi}$ and the dimension ratio $\bar{\xi}/D$ were obtained for each observed point. The mean values of the average domain length $\bar{\xi}$ through each interval were obtained as $\bar{\bar{\xi}}=\int d(\rho\bar{\xi})/\int d\rho$, and also the mean volume of the domain $\bar{\bar{v}}=A\bar{\bar{\xi}}$.

All calculated values are listed in Table III and IV, and are shown in Figs. 5 and 6 schematically, together with the measured[7] hysteresis loop.

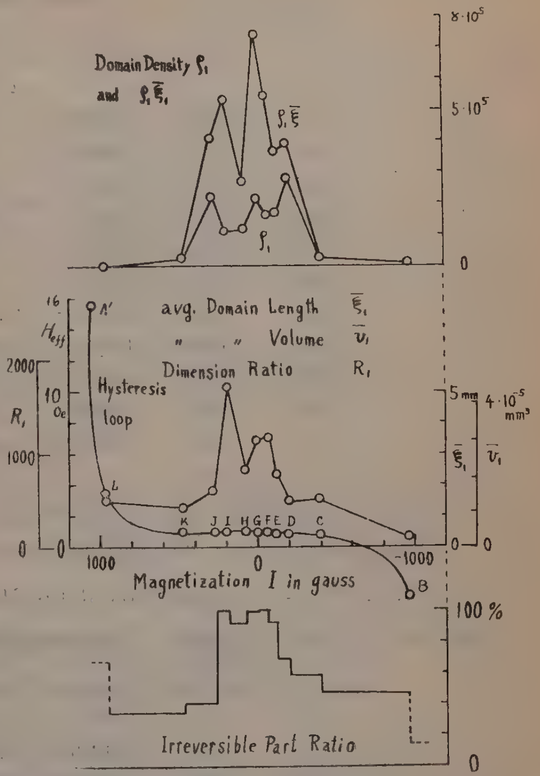

Fig. 5. Domain Data Calculated from $\varphi_1(\xi)$.

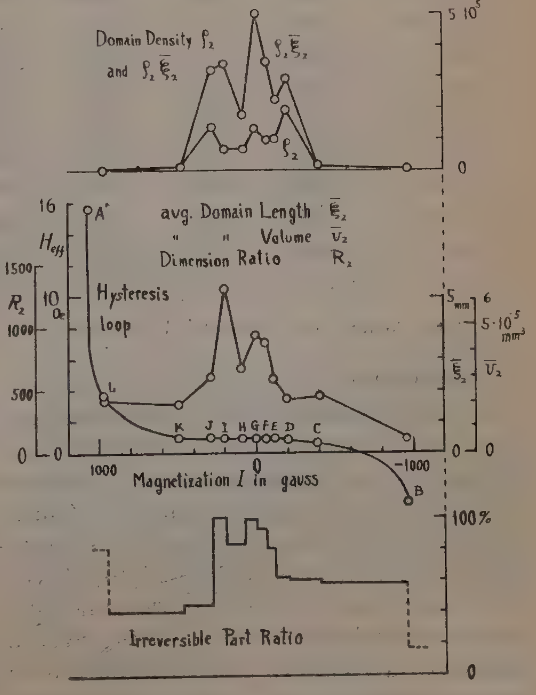

Fig. 6. Domain Data Calculated from $\varphi_2(\xi)$.

Table III. Domain Length, Density, Volume and Dimension Ratio
(Subscript 1 or 2 corresponds to $\varphi_1(\xi)$ or $\varphi_2(\xi)$ respectively)

Obs. pt.	Average Length in mm		Density per mm per Oe $\times 10^{-5}$		Average Volume in 10^{-5} mm^{-3}		Dimension Ratio	
	$\bar{\xi}_1$	$\bar{\xi}_2$	ρ_1	ρ_2	$\bar{v}_1$	$\bar{v}_2$	$\bar{\xi}_1/D_1$	$\bar{\xi}_2/D_2$
A	0	0	0	0	0	0		
B	.345	.405	.00532	.00398	.298	.498	104	102
C	1.59	1.78	.0904	.0700	1.38	2.19	479	449
D	1.45	1.70	2.74	1.73	1.25	2.09	439	429
E	2.33	2.24	1.58	.982	2.02	2.76	702	566
F	3.51	3.56	1.55	.965	3.04	4.38	1058	899
G	3.43	3.72	2.14	1.345	2.97	4.58	1032	939
H	2.46	2.62	1.07	.673	2.12	3.22	704	661
I	5.11	5.20	1.04	.655	4.43	6.40	1540	1312
J	1.82	2.30	2.22	1.39	1.57	2.83	548	581
K	1.29	1.54	.0895	.0681	1.12	1.89	388	389
L	1.52	1.65	.00979	.00531	1.32	2.03	458	416
A′	0	0	0	0	0	0		

Domain Cross-section: $A_1=8.65\times10^{-6}$ mm^2, $A_2=12.3\times10^{-6}$ mm^2
Domain Diameter : $D_1=3.32\times10^{-3}$ mm, $D_2=3.96\times10^{-3}$ mm

Table IV. Irreversible Part Ratio, Mean Domain Volume and Domain Length

Interval	ΔH in Oe	ΔI in Gauss	Irr. part ratio in %		Mean volume in 10^{-5} mm^3		Mean length in mm	
			φ_1	φ_2	$\bar{\bar{v}}_1$	$\bar{\bar{v}}_2$	$\bar{\bar{\xi}}_1$	$\bar{\bar{\xi}}_2$
A→*B*	12.2	77	(13.6)	(17.0)	(.295)	(.498)	(.345)	(.405)
B→*C*	4.016	566	46.7	59.2	1.32	2.09	1.53	1.70
C→*D*	.062	205	58.1	61.3	1.22	2.09	1.41	1.70
D→*E*	.015	81	66.6	63.3	1.53	2.34	1.77	1.90
E→*F*	.012	56	91.6	80.2	2.52	3.57	2·92	2.90
F→*G*	.010	60	100.	93.5	3.00	4.50	3.47	3.66
G→*H*	.017	80	99.5	95.5	2.70	4.14	3.12	3.36
H→*I*	.028	115	90.3	83.6	3.26	4.68	3.76	3.80
I→*J*	.020	88	99.5	100.	2.48	3.98	2.86	3.23
J→*K*	.040	199	39.2	44.1	1.56	2.67	1.80	2.17
K→*L*	2.58	476	32.1	41.0	1.12	1.91	1.30	1.55
L→*A′*	12.0	87	(66.5)	(80.5)	(1.31)	(2.03)	(1.52)	(1.65)

The values for intervals *A*→*B* and *L*→*A′* are not reliable.

§ 4. Discussion

The size ditributions of Barkhausen impulses were studied at first in 1924 by E. P. T. Tyndall[1] for several materials, and it was concluded that they had no regularity. Thereafter, his result was utilized by Bozorth-Dillinger[2] and by Förster-Wetzel[3], to calculate the average domain volume from the measurements of Barkhausen impulses. However, as described above, the size distribution of domain and that of impulse have clear regularities. Some considerations for the origin of these regularities, will be discussed in next paper.

Above obtained values 0.345–5.20 mm, for the average domain length, coincide in order with the results of K. Murakawa[4], 0.9–2.0 mm. The average domain diameters, 3.32–3.96$\times10^{-3}$ mm, are very close to the width of the magnetic powder pattern on Fe–Si single crystal, 4×10^{-3}mm, obtained by L. W. McKeehan and W. C. Elmore[5]. In the recent study[6] of the magnetic powder patterns are described several figures, whose widths are in order of 10^{-2}mm. It seems to the author to be probable that the reversal of such broad domain is not completed at once, but it is composed of several independent subdivisions.

Combining the maximum duration time of the individual impulse, 10^{-4} sec., and the average value of the domain length, 0.345–5.20 mm, the numerical value, 3–50 m/sec, was obtained as the minimum average value of the propagating velocity of the magnetization reversal in the small Barkhausen effect.

In conclusion, the author wishes to express his sincere thanks to Professor T. Shimizu, Professor T. Kobayashi, Professor S. Kaya, and Professor K. Murakawa for their hearty guidances and also to Doctor M. Takagi of Matsuda laboratory for his useful discussions.

References

1) E. P. T. Tyndall: Phys. Rev. **24** (1924) 439.

2) R. M. Bozorth and J. F. Dillinger: Phys. Rev. **35** (1930) 733.

3) F. Förster und H. Wetzel: Zeits. f. Metalkde, **33** (1941) 115.

4) K. Murakawa: Proc. Phys.-Math. Soc. Jap. **18** (1936) 380, **19** (1937) 715.

5) L. W. McKeehan and W. C. Elmore: Phys. Rev. **46** (1934) 229.

6) H. J. Williams, R. M. Bozorth and W. Schockley: Phys. Rev. 75 (1949) 155.

JOURNAL OF THE PHYSICAL SOCIETY OF JAPAN Vol. 7, No. 6 NOV.—DEC., 1952

Statistical Study of the Barkhausen Effect Part II, Relation between Domain Size and Internal Stress

By Harunobu SAWADA

Taihei Mining & Metallurgical Laboratory, Omiya

(Read May 2, 1950. Received March 11, 1952)

The numerical values for domain size, obtained in Part I, were discussed, in comparison with the results by Bloch's theory of ellipsoidal domain. It was concluded that the distribution of internal stress plays a leading role in the determination of the remaining position of domain boundary. The distribution of internal stress were determined from the standpoint of the probability theory. Domain size distribution formulae, showing the experimental regularties between the impulse size and the search-coil length, as described in Part I, were deduced from consideration on the relations between the distribution of internal stress and that of domain boundary.

§1. On the Shape of Magnetic Domain

In part I of this study, the following numerical values were obtained for the magnetic domains in the polycrystalline wire of silicon steel, from the measurements of its Barkhausen impulses.

Average length	0.345—5.20 mm
Average volume	$0.298-6.40\times10^{-5}$ mm³
Average diameter	$3.32-3.96\times10^{-3}$ mm
Average dimension ratio (length/diameter)	102—1540

On the other hand, Bloch[1] calculated the length and the width of magnetic domain as a prolate rotational ellipsoid. According to his theory, this ellipsoidal domain corresponds to minimum for the sum of the boundary wall energy and the demagnetizing energy, when the lengths of its two principal axes, a and b, have respectively the following values:

$$a\simeq(v^3/\delta^2)^{1/7},\quad b\simeq(v^2\delta)^{1/7}, \tag{1}$$

where δ denotes the thickness of Bloch-wall, approximately 30—100 times the lattice constant, and v the volume of domain.

Substituting the values $b=1/2\ (3.32\text{–}3.96)\times 10^{-3}$ mm and $\delta=10^{-5}$ mm to the relation $v\simeq(b^7/\delta)^{1/2}$, the values, $v\simeq(6\text{–}11)\times 10^{-8}\,\text{mm}^3$ and $a/b\simeq(12\text{–}14)$, are obtained for the Bloch-model domain whose width is equal to that of our circular cylinder model. In our experiment, a wire-formed specimen was employed, and the values obtained for the dimension ratios, 102–1540, thus turned out to be 10–100 times greater than that of the Bloch-model.

This discrepancy may be attributed mainly to the situation that the shape of magnetic domain is considerably affected by the external shape of the specimens. Suppose the magnetization of a specimen of the form of a circular cylinder, 200 a long and $2b$ thick, to satisfy the Bloch relation (1). According to the Bloch's theory, this specimen will be magnetized in 100 equally separated parts, each $2a$ long and $2b$ thick. However, it can be expected more naturally that this will be magnetized in parts less than above, on account of the tendency to reduce the effect of demagnetizing field. In this case, the shape of magnetic domain, or the position of boundary wall, may be determined by the other factors not considered in Bloch's theory. Namely the lattice distortion, caused by the internal stress, will play the principal part in the determination of the detailed position of the Bloch-wall.

§ 2. The Position of Domain Boundary

The wall energy γ per cm² of magnetic domain is given as follows[2]:

$$\gamma=2a\sqrt{IC} \qquad (2)$$

where a denotes the lattice constant, I the exchange energy and C the stress energy. There are following relations.

$$\delta=aI/C\,,$$
$$C=3/2\lambda\sigma\,,$$

where λ denotes the magnetostriction constant and σ the internal stress. Substituting these relations into the equation (2), we have

$$\gamma=3\lambda\sigma\delta\,. \qquad (3)$$

In this equation, the quantities λ and σ can be positive or negative, according to the characteristic of material, but the wall thickness δ must be always positive. Accordingly, there are conditions for the minima of γ as follows;

If $\lambda\sigma>0$, then minima of $|\sigma|$, or if $\lambda\sigma<0$, then maxima of $|\sigma|$ correspond to the minima of γ, respectively.

Thus the boundary wall remains at the maxima or at the minima of the internal stress in accordance with the above conditions. Hereafter, only these positions which are actually occupid by the boundary wall will be considered simply as the extrema of internal stress, neglecting other small extrema where the wall can not be stable. In other words, the wall can not always be stable at every one of these extrema of internal stress, since there is generally a tendency to minimize the total boundary wall energy, consequently a tendency to reduce the number of individual boundaries.

§ 3. The Distribution of Internal Stress Extrema

The exact information, on the distribution of these extrema of internal stress, has not yet been obtained. Therefore, this distribution may be treated only as a problem of the probability, under some physically acceptable assumptions.

Suppose a one-dimensional ferromagnetic substance, for simplicity. D denotes the distance between the adjoining extrema of internal stress. To determine the distribution of D, from the standpoint of the probability theory, the following two cases may be suggested.

Case I. The probability of non-existence of the other extremum in a distance D is independent of the probability of existence of a subsequent extremum in a small extension dD of D.

This is the case analoguous to that of the mean free path of gas molocules, in the kinetic theory. Then, the distribution of the distance D is given as follows.

$$G_1(D)dD=1/\nu_1\exp(-D/\nu_1)dD,\ \ \bar{D}=\nu_1 \qquad (4)$$

Case II. The extremum of internal stress has the physical meaning as a concentrated position of neighbouring stresses, under some unknown mechanism. Accordingly, there is such a tendency that another extremum scarcely exists in the vicinity of a extremum. This circumstance may be simplified as follows.

This probability of existence of the second extremum, at the distance D from the first, increases proportionally to D.

$$C_2(D) = \text{const.} \times D\,.$$

This is a relative probability, and divergent in such an expression. However, if the total number n of the extrema, in the ferromagnetics of length L, is given, then the following equation holds.

$$\sum_{i=1}^{n} D_i = L\,.$$

With this limiting condition, the variable range of D is limited in some scale. Consequently, the probability $G_2(D)$ can be normalized in the following way.

$$G_2(D)dD = \frac{D\,dD\cdot \overbrace{G_2{*}G_2{*}\,..\;\,{*}G_2}^{n-1}(L-D)}{\underbrace{G_2{*}G_2{*}\,\ldots\ldots{*}G_2}_{n}(L)}\,, \tag{5}$$

where * is the symbol for "Faltung" of probability. The denominator of the right hand side means the probability of such condition that the sum of n independent distances D_i equals to the specimen length L. For example, the probability of such condition that the sum of two distances D_1 and D_2 equals to D, is given as follows.

$$G_2{*}G_2(D) = \text{const} \times \int_0^D (D-D')D'dD' = \text{const} \times D^3$$

$$\therefore \quad G_2{*}G_2{*}\ldots{*}G_2(D) = \text{const} \times D^{2n-1}$$

Also, the following conditions can be set.

$$L \gg D_i, \quad n \gg 1, \quad n\bar{D} = L\,.$$

Then, the equation (5) becomes

$$G_2(D)dD \rightarrow D\,dD \times (L-D)^{2n-3} = D\,dD(n\bar{D}-D)^{2n-3} \rightarrow D\,dD\left(1-\frac{D}{n\bar{D}}\right)^{2n-3},$$

$$n\rightarrow\infty\,;\; G_2(D)dD \rightarrow D\exp(-2D/\bar{D})dD\,.$$

Putting

$$\bar{D} = 2\nu_2, \quad \int_0^\infty G_2(D)dD = 1,$$

we get

$$G_2(D)dD = D/\nu_2^2 \exp(-D/\nu_2)dD\,. \tag{6}$$

Assuming the distribution of internal stress, as $G_1(D)$ in the equation (4) or $G_2(D)$ in (6), the relation, concerning these distributions and the length distribution of the magnetic domains, will be further discussed.

§ 4. The Relations between the Internal Stress Distributions and the Domain Length Distributions

If the change of magnetization in all magnetizing process, except the rotation process, is to occur as the result of wall displacement, reversible or irreversible, then the length of the magnetic domain ξ would coincide with the above considered distance D. Then the distribution of distance D, G_1 in equation (4) or G_2 in (6), can be considered as the distribution of domain length ξ, in Part I of this report.

Usually, the elementary process of magnetization, in a ferromagnetic substance, is assumed to consist of translation process for weak field and rotation process for intense field. Consider the magnetic state of a ferromagnetic body, the magnetization of which is just beginning to shift from a saturation along the descending branch of hysteresis loop. Then, the rotation process, to the inverse sense, will have to occur at first. In this case, the maximum change of the direction of spontaneous magnetization, in the individual domain, would not exceed $\pi/2$. Therefore, the formation of a domain, in which the direction of spontaneous magnetization makes an angle greater than $\pi/2$ with the direction of the previous magnetic saturation, can not be expected. Consequently, it can not easily be explained, why the first translation process actually occurs in the descending branch of hysteresis loop.

On the other hand, K. J. Sixtus[3] found, in his excellent experiment, the formation of reversal nucleus in large Barkhausen effect. The circumstances for both, Sixtus' large Barkhausen effect and our small one, are not exactly same in scale. However, the formation of such reversal nuclei in small scale, in interior of our small domain, can be expected at the magnetic state above mentioned. Or else the occurrence of translation process, in the descending branch of hysteresis loop, can not be explained. So far as the formation of reversal nuclei being assumed, $\xi = D$ can not hold directly, without considering more precisely the relations, concerning the domain length, the growth of the nucleus and the extrema distance of the internal stress.

There has not yet been obtained any definite information on the mechanism of the formation of reversal nuclei. Therefore, the most probable four cases will be chosen for it. The relation between the domain length and the distance D between two extrema will be discussed for each cases.

Case I. The boundary wall displacement begins always from the one-side end of D to the other.

Namely the reversal nucleus is formed in the boundary wall. And the wall shifts from this point to the other end of domain which is not yet reversed. Consequently, $\xi=D$ holds, and if D has the distribution $G_1(D)$ or $G_2(D)$, then ξ has $\varphi_1(\xi)$ or $\varphi_2(\xi)$, respectively, as the distribution, and vice versa.

Case II. The reversal nucleus is formed in the interior of D, and the wall shifts from it to the one end of D (one directional displacement).

In this case, the residual part of D at this reversal will reverse in several times independently, new reversal nuclei being formed in it. Therefore, the initial domain will be divided in many small subdomains, and will reverse independently of each other. The ξ has the unique distribution $\varphi_1(\xi)$ in spite of D, which has either $G_1(D)$ or $G_2(D)$ as its distribution.

Case III. The reversal nucleus is formed in the interior of D, and the walls shift from it to both ends of D (two directional displacement).

In this case, $\xi=D$ holds always, and the same conclusion is obtained as in the case I.

Case IV. The internal stress is so small that it does not affect the stable position of boundary wall.

This is such a case, as if a large ball rolls on a road, on which may pebbles are scattered. Therefore, the wall displacement must be considered independent of the distribution of internal stress. There are two cases, where the wall displacement is either one-directional or two-directional.

If the wall shifts one-directionally, then the domain length ξ will have the distribution $\varphi_1(\xi)$, as in the motion of gas molecule in the kinetic theory.

If the wall shift two-directionally and the two travelling distances x and x' are independent of each other, then the domain length $\xi=x+x'$ becomes as follows.

$$\int_0^{\xi} 1/\lambda \exp(-x/\lambda) 1/\lambda \exp(-x'/\lambda)dx' = \xi/\lambda^2 \exp(-\xi/\lambda)$$

Namely ξ follows $\varphi_2(\xi)$.

As the conclusion, it can be expected that the domain length ξ follows $\varphi_1(\xi)$ or $\varphi_2(\xi)$, according to the conditions described above.

$$\varphi_1(\xi)=1/\lambda_1 \exp(-\xi/\lambda_1), \quad \bar{\xi}=\lambda_1$$

$$\varphi_2(\xi)=\xi/\lambda_2^2 \exp(-\xi/\lambda_2), \quad \bar{\xi}=2\lambda_2.$$

The formation of reversal nucleus in the boundary wall would be affected mainly by the magnetizations of adjoining domains. However, the formation in the interior of the domain would arise from some other causes, such at temporary concentration of energy in a small part, for example, due to thermal agitation.

§ 5. Summary

1. The shapes of magnetic domains, which have been obtained in Part I, are 10—100 times longer than the Bloch model, though having nearly the same width as the latter.

2. This discrepancy would arise from the fact that the shape of magnetic domain was affected by the external shape of specimen.

3. The stable position of the boundary wall was discussed in detail.

4. The distribution of internal stress was determined from the standpoint of probability theory.

5. The relations between the internal stress distributions and the domain length distributions were discussed in detail.

6. It was shown that the distribution functions of domain length $\varphi_1(\xi)$ and $\varphi_2(\xi)$, assumed in Part I, were obtained from the conclusion of above considerations.

7. It was pointed out that the formation of reversal nuclei are necessary to interpret the hysteresis loop.

The author takes great pleasure in thanking Professor K. Fushimi and Professor T. Nagamiya of the University of Osaka for their kind encouragements during various stages of the work.

References

1) F. Bloch: Zeits. f. Phys. 74 (1932) 295.

2) R. Becker u. W. Döring: Ferromagnetismus 1939. Julius Springer.

3) K. J. Sixtus: Phys. Rev. 48 (1935) 425.

JOURNAL OF THE PHYSICAL SOCIETY OF JAPAN Vol. 7, No. 6 Nov.—Dec., 1952

Statistical Study of the Barkhausen Effect Part III, Distribution of Time Interval

By Harunobu SAWADA

Taihei Mining & Metallurgical Laboratory, Omiya

(Read May 2, 1950. Received March 11, 1952)

The time interval distributions of the Barkhausen impulses were investigated. The experimental results show beautiful regularities, in contrast with Tyndall's conclusion. An explanation for the experimental result was given, by assuming a simple mechanism for the reversal of domain magnetization. It was concluded that the magnetic reversal is not perfectly accidental, as is the case in the disintegration of radioactive substance. The reversal of domain magnetization needs always some accumulation of energy by some effects, either magnetic or of origins of other kinds.

Introduction

About a quarter century ago Tyndall[1] reported on the distribution of the time intervals, in the Barkhausen impulses of a silicon steel specimen. He concluded that this distribution showed no regularity.

On the other hand, the distribution of time intervals, in the disintegration impulses of radio-active substances, follows a simple exponential formula. These disintegration impulses are perfectly accidental, and independent of each other. Inversely, if the time intervals of the Barkhausen impulses have a simple exponential behavior, and if there are no particular reason to consider otherwise, it may be concluded that they occurs accidentally and spontaneously and are independent of each other.

Several reports have been published on the mechanism of growth or extinction of the individual magnetic domain, or on the magnetic powder patterns. However, no report has yet been published on the dynamical relations, in the successive reversals of magnetic domains, during a certain change of magnetic field.

Considering these facts, the author repeated a study of the distribution of time intervals in the Barkhausen impulses, and found a regularity in it. A simple interpretation will be given for the origin of this distribution.

§ 1. Experimental Procedure and Results

The specimen and the experimental apparatus are the same as those described in Part I. As a measure of the individual time interval of Barkhausen impulse, the distance between adjacent impulses on each oscillogram record was measured directly by a scale, neglecting the very small breadth of impulse itself.

Some examples of the experimental results, obtained by the seven search-coils, at the observed point F in Fig. 5 or 6 of Part I, are shown in Figs. 1a-g, together with their theoretical curves. The experimental results, obtained at the other observed points, were not so essentially different from each other.

§ 2. Theoretical Consideration

Each of the experimental distribution curves has one maximum point. These maxima shift to the side of origin, according as more numerous impulses occur, during a definite change of magnetic field.

This fact shows us that the reversals of magnetic domains are not perfectly accidental. It is also generally known that the successive occurrences of Barkhausen impulses, are not exactly similar, for each iteration of the magnetic change, even at the same point of the same hysteresis loop. Namely the hyperfine structure, in successive occurrence of Barkhausen impulses, could not remain unchanged, for each cycle of the hysteresis, under the same maximum field. Whether this fact, is due to the change of domain size for each hysteresis cycle, or it is due to the change in the reversing order of individual domain is not yet clear. However, the ma-

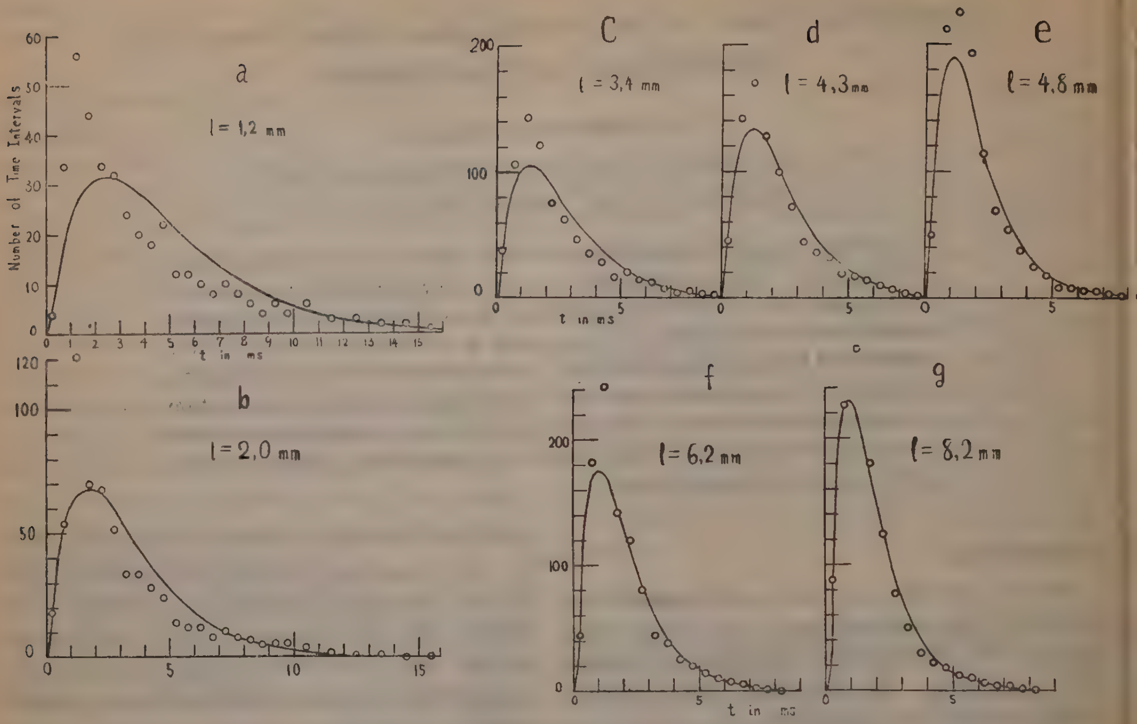

Fig. 1. Time Interval Distribution of Barkhausen Impulse

croscopic hysteresis loop of a specimen, is quite similar, for the same change of magnetic field.

Considering all these facts, an explanation is proposed, for the experimental curves of time interval distribution of Barkhausen impulses as follows.

Suppose the magnetic state of a specimen as a set consisting of magnetic domains which are not yet reversed and the domains already reversed. The domains, reversed or not yet reversed, have some energies, caused by the external field as well as the internal stress in them.

If the external magnetic field changes by a very small part of its strength, and if some one of the domains reverses its mangetization, than the energies of the other domains change in individual ways. However, it can be supposed from the statistical standpoint of view that the individual magnitudes of these energies are of the same order with those of the previous state. A numbering is made for these domains, according to the order of their reversals. Suppose the $(i-1)th$ reversal is now finished, and the $(i)th$ domain is going to reverse in the next moment. In this state of the domain set, this $(i)th$ domain has an energy, say $(E_i)_0$, at the instant $t=0$, just after the reversal of the $(i-1)th$ domain.

From this instant, $t=0$, the external magnetic field increases in strength, very slowly in proportion to the time t. Thus the energies of all the domains are accumulated, in proportion to the time, and the energy of the $(i)th$ domain E_i can be expressed as follows:

$$E_i=(E_i)_0+m_i\delta H=(E_i)_0+m_i(dH/dt)\delta t$$
$$=(E_i)_0+\beta_i\delta t,$$

where m_i represents the magnetization of the $(i)th$ domain.

When this E_i reaches a certain limiting value, then the $(i)th$ domain will reverse suddenly its magnetization. Therefore, the probability of reversal in the $(i)th$ domain is affected mostly by the energy increase $\beta_i t$, and it increases in proportion to the time elapsed after the instant of the preceeding $(i-1)th$ reversal.

From such considerations, the relative probability of the time interval, $f(t)$, from a reversal to the next, can be put quite naturally as follows:

$$f(t)=\text{cost.}\times t \qquad (1)$$

This relative probability, $f(t)$, in above described form, is, of course, of a divergent type. However, there are an additional limiting condition for t, *i. e.*, the total observing time T will be expressed as the sum of such time intervals t_i, neglecting the duration of individual reversal in comparison with the time interval itself. (In Part I of this study, it has reported that the duration of individual reversal is usually shorter than 10^{-4} sec., and that the time interval of reversal, in this experiment, is in the order of several milliseconds.) Denoting the total number of domains with n,

$$T=\sum_{i=1}^{n} t_i \,. \qquad (2)$$

From this condition, and assuming that the probability of reversing individual domain is independent of each other, the following normalized probability for $f(t)$ can be formulated :

$$f(t)dt\frac{\overbrace{f*f*\dots*f}^{n-1}(T-t)}{\underbrace{f*f*\dots*f}_{n}(T)}\,, \qquad (3)$$

where * denotes the "Faltung" procedure of probability.

This formula is exactly the same with the second distribution function of internal stress $G_2(D)$, previously given in the Part II. Therefore, when the total time of measurement, T, is very long in comparison with the individual time interval t_i, *i. e.*, $T\gg t_i$, that is, the number of domains considered, n, is very numerous, $n\gg 1$, and the average values of the time interval, $\bar{t}$, remains finite, then above formula becomes

$$f(t)dt=t/\alpha^2 \exp(-t/\alpha)dt\,,\ \bar{t}=2\alpha\,. \qquad (4)$$

This is the time interval distribution of Barkhausen impulses. Denoting the total number of the Barkhausen impulses observed by N, in the time of measurement, T, we get

$$\bar{t}=N/T=2\alpha\,, \qquad (5)$$

Then,

$$N f(t)=4N^3/T^2 t \exp(-2Nt/T) \qquad (6)$$

gives the actual distribution of the time intervals, in the case of N Barkhausen impulses measured in the time duration T.

These theoretical curves are shown in Figs. 1*a*–*g* together with the experimental results.

§ 3. Discussion

Agreement of the theoretical curves with the experimental results, is sufficiently good, in the case of longer time intervals, or of the results obtained by the longer search-coil. However, for every search-coil, the maximum value of the theoretical curve is always a little lower than the experimental one. Further, there is such a tendency that the theoretical curve agrees more closely with the experimental results, if a larger value than the experimental one were postulated for the total number of the impulses N. This tendency is more remarkable in the case of the relatively shorter search-coil. This fact indicates that there would be miscounting of smaller impulses. If the counted impulses are the signals of reverse occurring independently, the effects of those miscounted small impulses are negligible. The agreement of the theoretical curves, with the experimental results, is more closer, in the case of relatively longer search-coil. This fact indicates that there is no definite relation between the size of the impulses and the time intervals, or between the size of the magnetic domain and the probability of their reversals, since the miscounting of the impulses is expected to increase with the longer search-coils, as described in Part I.

Summarizing above considerations, the following conclusion can be obtained. The time interval distribution of Barkhausen impulses is not simply exponential. The reversal of magnetic domain is not perfectly accidental, as in the disintegration of radioactive substance. The reversal of spontaneous magnetization, in the individual domain, needs always some accumulation of the energy by some external effects, magnetic or of other kinds.

……………………

The experiments of this study were carried out, during about three years since October 1940, under guidance of Professor T. Kobayashi, at the Aeronautical Research Institute (now the Institute of Science and Technology), University of Tokyo. A primary report on the distribution of domain size and time interval, at two observed points of hysteresis loop, was read at the annual meeting of Physico-mathematical Society of Japan on July 17, 1943 and published thereafter2). After the War, the author analysed the results more extensively, covering all the observed points along the hysteresis loop, and obtained several new conclusions, such as, the variations of domain volume, domain density, dimension ratio, irreversible part ratio along the hysteresis loop, or the average values of domain cross-section, domain diameter and the propagating velocity of reversal. Accordingly, the author rearranged the total study in these forms, Part I, II, III of this report.

References

1) E. P. T. Tyndall: Phys. Rev. 24 (1924) 439.
2) H. Sawada: Proc. Phys. Cos. Japan 1 (1946) 3.

JOURNAL OF THE PHYSICAL SOCIETY OF JAPAN Vol. 7, No. 6 NOV.—DEC., 1952

Internal Friction of Ferromagnetic Substance Due to Rotation of Spontaneous Magnetization

By Nobuhiko KUNITOMI

The Research Institute for Iron, Steel and Other Metals, Tohoku University, Sendai, Japan

(Read May 3, 1950. Received October 30, 1950)

In ferromagnetic substance, the origin of internal friction under low stress amplitude has been considered to be due to two kinds of eddy current. The first named macroscopic eddy current was studied by Brown and its theoretically predicted contribution to internal friction was known to be consistent with the experimental data. But the second named microscopic eddy current has not yet been investigated except in demagnetized state. In this paper, this loss is calculated as a function of magnetization assuming that magnetic anisotropy energy is negligibly small compared with the internal stress energy. The result shows that internal friction increases initially with increase of magnetization but decreases rapidly near the magnetic saturation. The experimental behavior of internal friction obtained previously can be qualitatively explained by this theoretical result.

§ 1. Introduction

In ferromagnetic substances, the values of internal friction known by experiments are considerably larger than those of non-ferromagnetic substances, and the reasons for high internal friction were qualitatively interpreted by Kersten1), Brown2), and Becker and Döring3). However, any complete and quantitative description has not been given because the internal friction is one of the structure sensitive properties. Moreover, though it is known by experiments that the internal friction varies remarkably with the change of magnetization, this behavior has never been explained even qualitatively. The main purpose of this paper consists in theoretical representation of internal friction as a function of magnetization, and also in elucidation of the mechanism of internal friction by comparing experimental data with these theoretical results.

Becker and Döring have proposed three kinds of losses as origings of internal friction characteristic of ferromagnetic substances, namely, the loss due to magnetomechanical hysteresis and the losses due to macroscopic eddy currents. The internal friction due to magnetomechanical hysteresis loss originates from the irreversibility in macroscopic stress-strain curve and is proportional to the amplitude of the external stress. Hence this part of internal friction may be neglected if we

---

* This research was carried out under Professor Hirone's guidance in his research laboratory, and was supported in part by the Research Fund for Natural Science by the Ministry of Education in 1949. Numerical calculations of this research was performed by Miss T. Ogura.

assume very small stress amplitude. The internal friction due to macroscopic eddy current loss depends solely on the total change of the magnetization under alternating stress, and the quantitative theory developed by Brown is applicable to all ferromagnetic substances, so it can be eliminated from our observed values. Therefore, this loss will not be discussed further. If the frequency of the applied stress is very high and its amplitude is very small only the third part, of the loss namely the one due to microscopic eddy current has remarkable effect on the value of internal friction. But this loss is affected by the microscopic change of the magnetization and is therefore very difficult to calculate because the entire knowledge of the mechanism of magnetization is indispensable.

In this paper, the magnetization curve is introduced by investigating the mechanism of magnetization for various strengths of applied magnetic field under the assumption that the magnetic anisotropy energy is negligibly small as compared with the internal stress energy. Based on the obtained results, the loss due to microscopic eddy current has been obtained as a function of magnetic field or magnetization.

§ 2. The Mechanism of Magnetization

In the ferromagnetic substances, the rotation of the spontaneous magnetization plays an important role in the change of magnetization, if the energy due to magnetic anisotropy is negligible as compared with the energy due to internal stress existing in it. In this case, we can hardly realize the existence of the magnetic domain boundary from the simple consideration of the energy equilibrium of spontaneous magnetization, so that it is to be desired that the magnetic properties of such substances can be explained without regard to the displacement of the magnetic domain boundary. But since the spontaneous magnetization has been in general, supposed to rotate only reversibly, the displacement of the magnetic domain boundary must be introduced only when the discontinuous process in magnetization is concerned and the attempt to calculate the magnetic properties by considering only the rotation is restricted to the reversible properties, for example, the initial susceptibility4), the reversible susceptibility at remanence5), approach to saturation6), etc. However, Katayama and the writer7) previously pointed out the occurence of the irreversible rotation besides the reversible one. Then it seems to be possible that even the irreversible magnetic properties are explained by considering the irreversible rotation proposed in the previous paper. Along this idea, the circumstantial discussion of the direction of the spontaneous magnetization under various magnetic fields is carried out taking into account both reversible and irreversible rotation of the spontaneous magnetization.

The free energy F of a ferromagnetic substance is given by the sum of the anisotropy energy, the stress energy and the magnetic energy. Here the anisotropy energy is neglected and the external magnetic field H and the external stress Z are assumed to be applied along x-axis. Let us designate the angle between x-axis and the spontaneous magnetization by ϑ and that between x-axis and the internal stress by γ. Then the free energy per unit volume is given by

$$F=-\frac{3}{2}\lambda\{\sigma_i\cos^2(\gamma-\vartheta)+Z\cos^2\vartheta\}-HJ_s\cos\vartheta\,,\quad(1)$$

where λ is the magnetostriction constant, σ_i and Z are the magnitudes of internal and applied stress respectively, and H is the external magnetic field. In acquiring Eq. (1), the magnetostriction in this substance is supposed to be isotropic, and the internal stress and the applied stress are assumed to be simple tensions. Moreover, the directions of internal stresses are assumed to be distributed with equal probability over all directions. The magnitude of the internal stress is assumed to be constant. The equilibrium orientation ϑ of the spontaneous magnetization under the applied magnetic field and the applied stress can be obtained by solving

$$\frac{\partial F}{\partial\vartheta}=-\frac{3}{2}\lambda\{\sigma_i\sin 2(\gamma-\vartheta)-Z\sin 2\vartheta\}+HJ_s\sin\vartheta=0\,.\quad(2)$$

If the magnitude of the applied stress is very small compared with that of the internal stress, the second term in Eq. (2) vanishes and we find

$$\sin 2(\gamma-\vartheta)-A\sin\vartheta=0\,,\quad(3)$$

where $A=2HJ_s/3\lambda\sigma_i$.

The ϑ *vs.* γ relations for different values of A are derivable from this equation; the results are shown in Fig. 1.

In case of $A=0$, the solution obtained from Eq. (2) is readily found to be

$$\vartheta=\gamma+\frac{n}{2}\pi \quad (n \text{ is an arbitrary integer}), \quad (4)$$

conseqently the ϑ *vs.* γ relations are represented by many straight lines as shown in Fig. 1 (a). If we choose γ from 0 to π and ϑ from $-\pi$ to π, whole relations between ϑ and γ can be reprented by using Eq. (4) when $A=0$ and generally by Eq. (3). Though some solutions corresponding to even n in Eq. (4) are associated with the minimum free energy and give the stable equilibrium directions of the spontaneous magnetization yet the others corresponding to odd n are associated with the maximum free evergy, giving unstable directions. In order to make these facts obvious the curves corresponding to the minium free energy are drawn by full lines and the curves corresponding to maximum free energy by dotted lines in Fig. 1. Considering the above statement, it is easy to see from Fig. 1 (a) that the direction of the spontaneous magnetization is either parallel or antiparallel to that of internal stress.

If the magnetic field has been applied to this substance, the spontaneous magnetization rotates towards the direction of magnetic field so that the absolute values of ϑ become smaller than those of γ. In Fig. 2 (b), the ϑ *vs.* γ relation when A is equal to 0.5 is given as a typical example of such a case.

If A takes the value unity the decrease of the absolute value of ϑ becomes more appreciable than that in the former case. In this latter case the solutions of Eq. (3) are given by

$$\left.\begin{array}{ll} & \vartheta=2/3\cdot\gamma+2/3\cdot n\pi \\ \text{or} & \vartheta=2\gamma-(2m+1)\pi \\ & (n \text{ and } m \text{ are arbitrary integers}), \end{array}\right\} \quad (5)$$

and the ϑ *vs.* γ curves are shown in Fig. 1 (c). The most remarkable fact in this figure is that the curves corresponding to the minimum and maximum free energies contact each other at the points indicated by $\gamma=1/4\cdot\pi$ and $3/4\cdot\pi$. These points are proved to be the inflection points of the free energy F, namely, they satisfy the condition $\partial^2F/\partial\vartheta^2=0$. The spontaneous magnetization having the directions represented by these points must irreversibly rotate to the more stable orientations along the dotted arrows shown in this figure. This process is different from what hitherto usually considered, because the spontaneous magnetization, once rotated, cannot turn back reversibly to the original direction. Such irreversible process takes place more remarkably if the value of A becomes larger than unity. Figure (d) for the case $A=1.5$ shows an example of such case. The spontaneous magnetization which has larger $|\vartheta|$ than $\pi/2$ rotates irreversibly to the more stable orientations with $|\vartheta|$ smaller than $\pi/2$, if γ of which lies between γ_1 and γ_2 or γ_1' and γ_2' as shown in this figure. Consequently, the distribution density of spontaneous magnetization on the thick curve is twice that of the other parts. The irreversible rotation finishes itself completely when the value of A reaches 2.0, then the equilibrium orientation which has larger $|\vartheta|$ than $\pi/2$ vanishes as is shown in figure (e). If the value of A increases beyond 2.0, only reversible

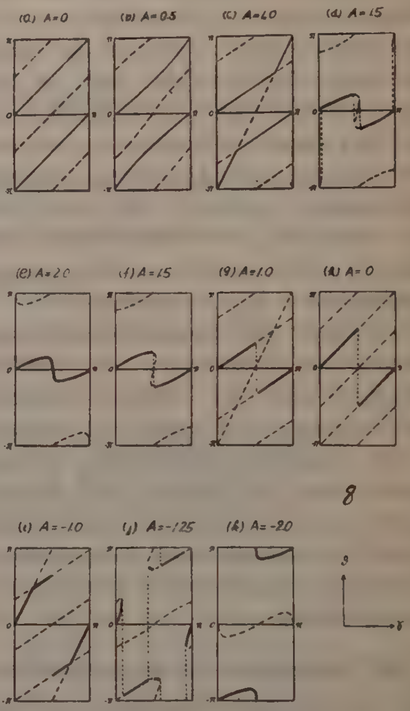

Fig. 1. ϑ *vs.* γ curves: Full lines show stable equilibrium orientations of spontaneous magnetization and dotted lines show unstable ones. Thick lines show the equilibrium orientation having twice as much as the spontaneous magnetization.

rotation can take place. It has been already stated that the experimental results near magnetic saturation discussed previously by the same method as that considered in this paper, so that we shall not concern it any further than merely to note that the ϑ *vs.* γ curves become flatter if the value of A becomes larger than 2.

If inversely the magnetic field decreases from saturation the ϑ *vs.* γ relation reversibly follows the virgin curve at first, but if A becomes smaller than 2.0, the equilibrium ϑ *vs.* γ curves become different from that in the virgin magnetization curve. The spontaneous magnetization rotates reversibly until $A=-1.0$, and parts from the direction of the field initially applied. These states are represented successively by the four figures (f) $A=1.5$, (g) $A=1.0$ (h) $A=0$ and (i) $A=-1.0$.

After the magnetic field decreases below -1.0, the irreversible rotation of spontaneous magnetization begins. For an example of such states, the curves corresponding to $A=-1.25$ are shown in figure (j). At last the curves for $A=-2.0$ are given in (k), which is the same figure as (e) except that ϑ differs by the amount $\pm\pi$. Along the hysteresis loop, the density of spontaneous magnetization is always twice that of the demagnetizing state.

Based on these figures, various properties of the ferromagnetic substances can be obtained, for example the magnetization curve is given by the method which will be mentioned below. According to Fig. 1, the distribution density and orientation of spontaneous magnetization for an arbitrary magnetic field are definned for every value of γ. Hence the value of J/Js is obtained as a function of A by integrating the equation

$$J/J_s=\frac{1}{2}\int_0^\pi \cos\vartheta\sin\gamma d\gamma \qquad (6)$$

using the relations shown in Fig. 1. The result of this calculation is shown in Fig. 2. The alphabetical signs marked in this figure correspond to those used in Fig. 1.

As given above, the magnetization mechanism by rotation of spontaneous magnetization is calculated by the ϑ *vs.* γ diagram. The most interesting behavior of this mechanism is the existence of irreversible rotation. The remarkable difference between the rotation and the displacement of magnetic domain boundary is as follows. In the irreversible displacement of magnetic domain boundary, a finite region in the ferromagnetic substance is swept by a boundary and hence a finite change of magnetization takes place, even if the velocity of increasing magnetic field is infinitely small. In irreversible rotation, however if the applied field changes its value sufficiently slowly, it is possible to make the volume infinitely small, where the spotaneous magnetization irreversibly changed its direction. In such specimens as Permalloy the Barkhausen effect can be observed although the magnetizing mechanism is considered to be the rotation of spontaneous magnetization. It is caused by the heterogeneity in the specimens and is not essentially related to the domain structure.

§ 3. Internal Friction Due to Microscopic Eddy Current

Based on the same idea described in the preceeding section, the behavior of internal friction of the ferromagnetic substances due to microscopic eddy current caused by mechanical vibration can be calculated. Let us suppose three Cartesian coordinates in the substance and the direction of the external magnetic field is assumed to agree with x-axis. The orientational distribution of the internal stress is assumed to obey the rule $\gamma=\pi/l\cdot z$ where z shows a distance along z-axis. This assumption shows that the internal stress changes its direction periodically along z-axis with a wave length $2l$. It seems to be quite different from the assumption proposed in section 2, but any essential contradiction does not exist between these, because the directional distribution of the internal stress is uniform for both cases. In a ferromagnetic body vibrating freely, the amplitude of alternating stress generated in it diminishes gradually, owing to the internal friction. Let the frequency and amplitude of this induced stress be given by $\omega/2\pi$ and Z_1, respectively, then the stress Z is expressed by $Z=Z_1\cos\omega t$. If Z is small, the value of $(d\vartheta/dt)$ is given by

$$\left(\frac{d\vartheta}{dt}\right)_{z=0}=\left(\frac{d\vartheta}{dZ}\right)_0\frac{dZ}{dt}=-\left(\frac{d\vartheta}{dZ}\right)_0\omega Z_1\sin\omega t \qquad (7)$$

The formula including $d\vartheta/dZ$ is obtained by differentiating Eq. (2) by Z. By considering the limit when the ratio Z/σ_i approaches zero, the value of $(d\vartheta/dZ)_{z=0}$ is given by

$$\left(\frac{d\vartheta}{dZ}\right)_{z=0}=-\frac{1}{\sigma_t}\frac{2\sin\vartheta\cos\vartheta}{2\cos 2(\gamma-\vartheta)+A\cos\vartheta}\,, \tag{8}$$

then we can eliminate $(d\vartheta/dZ)_{z=0}$ in Eq. (7) by using (8). Since the x and y components of magnetization are denoted by $J_x=J_s\cos\vartheta$ ane $J_y=J_s\sin\vartheta$, respectively, $\partial J_x/\partial t$ and $\partial J_y/\partial t$ are obtained from (7):

$$\left.\begin{aligned}\partial J_x/\partial t&=J_s(d\vartheta/dz)_0\omega Z_1\sin\vartheta\sin\omega t\,,\\ \partial J_y/\partial t&=-J_s(d\vartheta/dz)_0\,\omega Z_1\cos\vartheta\sin\omega t\,.\end{aligned}\right\} \tag{9}$$

Founded on Maxwell equations

$$\partial E_y/\partial z=\frac{4\pi}{c}(\partial J_x/\partial t)\,,\quad \partial E_x/\partial z=\frac{4\pi}{c}(\partial J_y/\partial t)$$

and the assumption $\gamma=\pi/l\cdot z$, the values of $\partial E_y/\partial\vartheta$ and $\partial E_x/\partial\vartheta$ are given by

$$\left.\begin{aligned}\frac{\partial E_y}{\partial\vartheta}&=\frac{4lJ_s\omega Z_1}{c\sigma_t}\frac{\sin^2\vartheta\cos\vartheta}{\sqrt{1-A^2\sin^2\vartheta}}\sin\omega t\,,\\ \frac{\partial E_x}{\partial\vartheta}&=\frac{4lJ_s\omega Z_1}{c\sigma_t}\frac{\sin\vartheta\cos^2\vartheta}{\sqrt{1-A^2\sin^2\vartheta}}\sin\omega t\,.\end{aligned}\right\} \tag{10}$$

where c is the light velocity. Substituting in this equation the value of ϑ obtained from Eq. (2) and integrating it with respect to γ, we get

$$\begin{aligned}E_x=&\frac{4lJ_s\omega Z_1}{c\sigma_t}\frac{1}{2A^3}[\cos^2 2(\gamma-\vartheta)A\cos\vartheta\\ &+(A^2-1)\log\{\cos^2 2(\gamma-\vartheta)\\ &+A\cos\vartheta\}]\sin\omega t+\alpha\,,\\ E_y=&\frac{4lJ_s\omega Z_1}{c\sigma_t}\frac{1}{A^3}\left[(\gamma-\vartheta)-\frac{1}{4}\sin 4(\gamma-\vartheta)\right]\\ &\times\sin\omega t+\beta\,.\end{aligned} \tag{11}$$

The integration constants α and β are determined by the symmetry of the electric field and also by the condition that volume integral of electric field must vanish for both x and y components. The energy dissipated per unit volume in unit time can be obtained by averaging $E_x^2+E_y^2$ over time and space and dividing it by the specific electric resistance ρ. The ratio of the dissipated energy and the twice of the vibrational energy gives the logarithmic decrement Δ. As the relation between Δ and A is not convenient for the comparison with experiment, it is transformed to the relation between Δ *vs.* J/J_s which is given in Fig. 3.

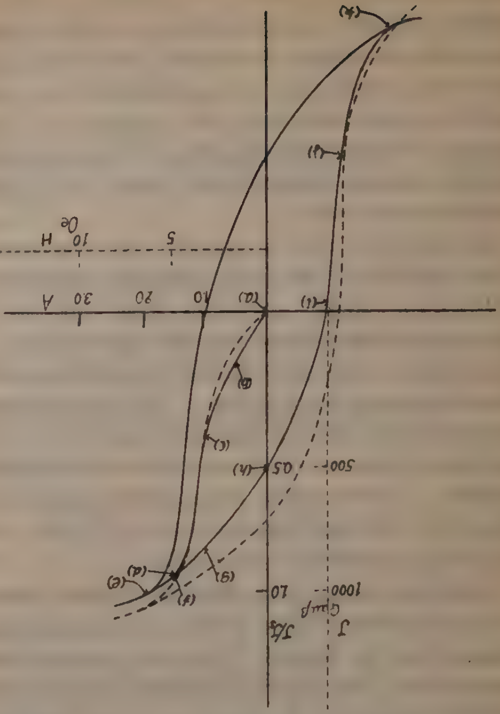

Fig. 2. The theoretical and the experimental magnetization curve: Full curve denotes theoretical dotted one experimental.

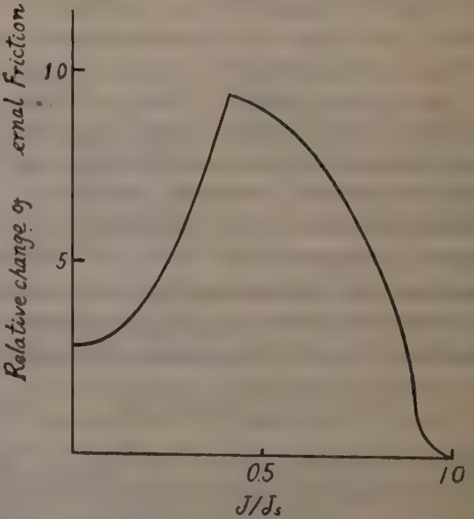

Fig. 3. Theoretical $\Delta-J/J_s$ curve: For convenience, the unit of the ordinate is chosen as $\Delta\times(c^2\rho\sigma_t^2/J_s^2l^2E\omega)$, where E is Young's modulus.

§ 4. Discussion of the Results

At first, the relation between magnetization and magnetic field is considered. It is obvious from Fig. 1 that the theoretical magnetization curve is very similar to the experimental one. Therefore, it is evident that the hysteresis behavior of the substance of small anisotropy energy can be well explained by this theory.

The first remarkable character of this curve is that the shape of the curve is specified only by the ratio of $2J_s/3\lambda\sigma_i$, that is, the only change is elongation or contradiction of the curve along H axis. Consequently, the intersecting point of J axis and the curve, namely the value of remanent magnetization, is always constant and is equal to $(1/2)J_s$. Such a theoretical conclusion is attributed to the assumption that the internal stress has a constant magnitude and uniform directional distribution. But even if we assume that the magnitude of internal stress is not strictly constant but diffuses in some extent as it is in the actual substance, the shape of theoretical magnetization curve is unchanged, because it is determined by superposing many magnetization curves obtained under the assumption of constant internal stress. But, on the other hand, if the assumption of uniform directional distribution of the internal stress were not applicable to the actual substance, then the shape of the curve should become appreciably different even if the external stress were not applied. For example, it is supposed that the value of remanent magnetization becomes different from $(1/2)J_s$, if the calculation had been carried out successfully without any assumption of uniform directional distribution. Therefore, the measurement for the substance with uniform directional distribution of internal stress is very desirable, but such a specimen must be necessarily of a small dimension ratio, so that we have not been able to obtain the accurate experimental data by the effect of the demagnetizing field.

Also the theoretical $\Delta-J$ curve has the same character as the theoretical $J-H$ curve. According to the change of $2J_s/3\lambda\sigma_i$, the shape of the curve elongates or contradicts only along the J axis. However, if the assumption of uniform angular distribution of the internal stress is not applicable, the shape of the curve differs appreciably. In contrast to the $J-H$ relation, the shape of the curve becomes different if the assumption of constant magnitude does not exist. As shown in Fig. 3 it has a breaking point at $A=1.0$ but this point will vanish if, instead of being constant, the magnitude of internal stress varies to some extent.

Next, the experimental facts found hitherto are compared with our theoretical results. For comparison, the experimental facts on the substance with negligibly small anisotropy energy must carefully be chosen, and so let us use the magnetization curve of Perminvar wire obtained by Katayama and the present author shown in Fig. 2. If the value of $3\lambda\sigma_i/2J_s$ is so chosen that the theoretical curve agrees with the experimental one, best fit is obtained for the value of 3.3 Oe. Substituting the experimental values of $J_s=1090$ Gauss and $\lambda=1.1\times10^{-5}$ into the relation $3\lambda\sigma_i/2J_s=3.3$ Oe, the value of σ_i turns out to be about 22 Kg/mm². This value is twice as large as the value given previously by Katayama and the writer from the relation between external tension and reversible susceptibility at the remanence point, and also from the relation between remanent magnetization and the latter. This discrepancy is caused by the fact that the assumptions on the distribution of internal stress made in these papers do not fully represent the details in the actual cases.

Some of the experimental results obtained hitherto by other workers using the substances which satisfy the assumption made in this paper can be well explained by the present theory, for example, some curves on 68 permalloy given by Williams, Bozorth and Christiansen[8] can be will explained. The present author is now carrying out the experimental research on the internal friction of these substances and the circumstantial criterion on the theory will be published in near future in this *Journal*.

References

1) M. Kersten: Z. techn. Phys. **15** (1934) 463.

2) W. F. Brown: Phys. Rev. **50** (1936) 1165.

3) R. Becker and W. Döring: Ferromagnetismus, (1939) p. 362.

4) M. Kersten: Z. Phys. **71** (1931) 553.

5) R. Becker and W. Döring: loc. cit. p. 165.

6) R. Becker and W. Döring: loc. cit. p. 168.

7) T. Katayama and N. Kunitomi: Sci. Rep. Res. Institutes, Tohoku Univ. **2** (1950) 22.

8) H. J. Williams, R. M. Bozorth and H. Christiansen: Phys. Rev. **59** (1941) 1005.

Journal of the Physical Society of Japan Vol. 7, No. 6 Nov.—Dec., 1952

Internal Friction of Ferromagnetic Superlattice Alloy Ni_3Fe

By Nobuhiko KUNITOMI

The Research Institute for Iron, Steel and Other Metals,
Tohoku University, Sendai, Japan

(Read May 3, 1950. Received March 7, 1951)

Internal friction of Ni_3Fe is measured as a function of magnetization for different stages of superlattice formation by using transversal vibration of about 500 c. p. s. For every stage of superlattice formation, the relation of internal friction vs. magnetization shows one or two maximums. This behavior can be explained by considering that one maximum is due to macroscopic and the other due to microscopic eddy current. By using the theoretical conclusion, on the microscopic eddy current which is given in the previous paper, the detailed behaviors of experimental relations can be explained by considering internal stress which is closely related to the superlattice formation.

§ 1. Introduction

Becker and Döring[1] have attempted to explain theoretically the reason of high internal friction of ferromagnetic substance. But as internal friction is affected by the internal structure of the substance and as inevitable background internal friction originating from many causes prevents accurate measurement, their theory has not yet been supported by experimental results. However, if we find relations between internal friction and other physical quantities by both experimental and theoretical methods, the comparison of these two relations will ascertain the theory without comparing the absolute values. In the previous paper[2], internal friction of ferromagnetic substance was calculated by the present writer as a function of magnetization. This theoretical relation is much easier to examine experimentally than the other relations, for example, the frequency and the amplitude dependences of internal friction. In this paper the results of the measurement are compared with the theory.

According to Becker and Döring's theory, the internal stress accumulated in the ferromagnetic substance plays an important role in magnetizing process, if the magnetic anisotropy energy is negligibly small as compared with the internal stress energy. The theoretical value of internal friction also contains parameters concerning internal stress. Therefore, it is desired that internal friction is measured by a substance which can easily change the magnitude and distribution of internal stress. Ferromagnetic alloy Ni_3Fe is known to have very small anisotropy energy[3] and to change its internal stress considerably according to the degree of order of the superlattice[4], so it seem that this subtance is suitable for our purpose. For this reason, Ni_3Fe was used for the present investigation as specimen material.

§ 2. Experimental Method

The experimental method adopted here was essentially that developed by Förster and Köster[5] using transverse vibration. A cylindrical specimen was hung with two pieces of fine thread of silk. The mechanical vibration generated by the vibrater drived the specimen through a thread. Through another thread, the free damping curve of mechanical vibration of the specimen at resonance was picked up by a reciver and was observed by an electromagnetic oscilograph. The coefficient of internal friction Δ, which is defined by the formula $\Delta = \textit{dissipated energy}/2 \times (\textit{vibrational energy})$, can be given from this observation. This Förster and Köster's method was chosen for the present experiment, because it is much simpler that other methods to determine whether the internal friction depends upon the applied strain amplitude or not. The magnetizing coil, which magnetized the specimen suspended with two pieces of thread, was composed of three parts with the same diameter and coil constant. One of these was the principal solenoid and was 117 mm long. The specimen was suspended freely in its central axis. Two other solenoids, both 152 mm long, were used to induce the uniform magnetic field at both ends of the specimen. The slits between three solenoids were narrowed so long as the thread did not touch the solenoids, hence these were about 2 mm. In this way magnetic field of the same strength could be applied to every part of the specimen. The specimen must be tied with the threads near the nodes of its vibration in order to measure internal friction accurately by decreasing background internal friction. But if the distances between the tied positions and nodes are smaller, the sensitivity of the measuring set becomes lower, so it is necessary to choose proper positions which satisfy these two conditions. In the present case the position of each thread is 2 mm apart from each node of the ground vibration.

---

* From the report of the Research Institute for Iron, Steel and Other Metals. This research was carried out under the guidance of Prof. Dr. T. Hirone in his research laboratory, and was supported in part by the Grant-in-Aid for Fundamental Scientific Research of Ministry of Education.

The specimen material is Ni_3Fe containing 0.3% manganese. After being melted in vacuume, it was forged and shaped, then circular cylindrical specimens 5.5 mm in diameter and 196 mm long were prepared after such treatment. As the distorsion of the specimen and the roughness of its surface was considered to affect the accuracy of the measurement, the specimens were so made that these formed the perfectly right circular cylinders.

§ 3. Internal Friction of Disordered Ni_3Fe

In order to remove internal stress accumulated during the preparation of the specimen, these were annealed at 900°C for 2 hours in vacuum. Thereafter, these were annealed again at 600°C for 1 hour and cooled rapidly. The atomic arrangement in such specimens is considered to be at random and is called disordered state. Since the rapid cooling was carried out by throwing each specimen into water together with the vacuum vessel containing the specimen in it, the specimen was not oxidized and not distorted. However, if the cooling velocity is not infinitely fast, a slight occurence of superlattice is to be found. And in the present case, the cooling velocity remained slower than that in usual water cooling. Hence the effect of superlattice formation during cooling is more appreciable in this experiment. The detailed discussions of this effect will be described in the following section.

As remarked by Förster and his coworker, if there is an inhomogeneity in the specimen, such as a slip or a crack, internal friction depends on the suspended direction, that is, the direction of the vibrating plane of the specimen. As the specimen showing such an inhomogeneity is inappropriate to the accurate measurement, internal friction of each specimen was measured for several vibrating planes. From the results of this preliminary experiment, the specimen showing the smallest directional dependency was selected for the following experiment. The maximum Δ of this selected specimen was 5.6×10^{-3} and the minimum Δ was 4.8×10^{-3}. It is noted, however, that these observed values were approximately 7 times larger than that given by Sato⁶⁾ who measured by using the specimen having the same composition as that of the specimen used here. It means that specimens which have different past histories show different internal frictions, even if these have the same composition.

Subsequently, the relation between internal friction and magnetization was measured by thus selected specimen. Though the internal friction in a demagnetized state was nearly the same for different vibrating planes, those in a magnetized state were not always the same. But the amount of this discrepancy was not so considerable and, as it will be described later, it hardly appeared in the measurement for ordered specimen. Then we conclude that it is attributed to the experimental errors. Consequently, the averaged internal friction for several vibrating planes is shown in Fig. 1.

Now we consider the reason why internal friction shows such a behavior in disordered state. The causes of internal friction in ferromagnetic substances can be classified into two groups, namely the pure plastic and ferromagnetic causes. The contribution of the former, which does not relate to ferromagnetism, is supposed to depend on the magnetization not so appreciably as appeared in Fig. 1. Then the obtained result is thoroughly explained by considering only ferromagnetic origins which consisted of three kinds of losses. The first loss, that is, the loss due to magnetomechanical hysteresis is considered to contribute nothing to our experimental data, because amplitude used here is very small. This conclusion is also supported by the fact that the observed damping curve is perfectly exponential and therefore that the internal friction is independent of the strain amplitude. Then the experimental result can be explained by considering the other two sources, namely the losses due to macroscopic and microscopic eddy currents. The theoretical relation between the former and the magnetization was previously given by Brown.[7] But he neglected the influence of demagnetizing field and calculated only in the case of longitudinal vibration, so we can not calculate the quantitative contribution from the former according to his theory. However, it is known qualitatively that this loss must vanish when the specimen is perfectly demagnetized or magnetized to saturation, and that it has a maximum between these two extreme cases. Therefore, the experimental result is explained by only considering the loss due to microscopic eddy current. Recently, the auther of the present paper has elucidated the loss due to microscopic eddy current as a function of magnetization on the substances which have negligibly smaller magnetic anisotripy energy as compared with the energy of internal stress.[2] Since the anisotropy energy of Ni_3Fe is very small,[3] the experimental curve in Fig. 1 must be consistent with the theoretical result of the pervious paper. Comparing these two results, we can find qualitative agreement between those. A discrepancy is that a breaking point appears in the theoretical curve but does not apper in the experimental one. It is due to the assumption in the theory that the strength of the internal stress is constant.

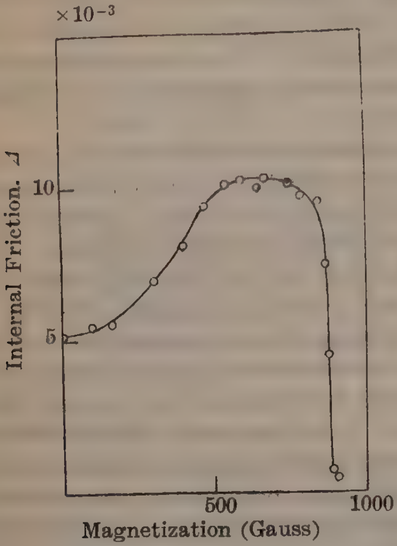

Fig. 1. Internal friction vs. magnetization in disordered state.

§ 4. Cange of Internal Friction by Annealing

In this section, we discuss the relations between internal friction and magnetization which were measured after the superlattice had developed in the specimen. As pointed out by Kaya,[8] the degree of order in Ni_3Fe is given by the annealing time at 490°C which is the temperature just below the Curie point of superlattice. In our experiment, however, considerable durations were necessary for heating and cooling because the specimen was heattreated in vacuum by the reason mentioned above. Actually, the time for heating was 2.4 minutes and for cooling 0.5 minutes. Therefore, the formation of superlattice during heating and cooling can not be neglected especially in the case of short time annealing. Hence, it is a question to represent the degree of order only by the annealing time at 490°C. To avoid such a difficulty, the specimen was annealed for long time at the temperature having slower velocity of superlattice formation, instead of the short time annealing at 490°C. By using this method, the effect of heating and cooling times could be negected. In order to determine the proper annealing time, the relaxation time of superlattice formation at several temperatures were decided from experimental results of electric resistance measured by Kaya.[8] Then the relaxation times were plotted as a function of $1/T$. This curve was nealy straight as expected theoretically. From the curve, the temperature, at which the relaxation time is ten-fold larger than that at 490°C, was determined to be 444°C. Then, in place of annealing at 490°C for n minutes, the specimen was annealed for $10n$ minutes at 444°C. According to this method, the annealing time becomes longer and the effect of heating and cooling become negligibly small. But since Ni_3Fe has relaxation times of several origines,⁹⁾ it might be not so simply concluded that the annealing at 490°C has precisely ten-fold influence as compared with that at 444°C. But the reproducibility of the measurement is improved by annealing at the temperature having such a long relaxation time.

The curve maked (1) in Fig. 2 shows the relation of Δ vs. magnetization obtained after being annealed at 444°C for 30 minutes. Compared with the curve shown in Fig. 1 remarkable differences of this figure are that the internal friction is very small in the demagnetized state and that it has a very sharp peak. These two facts are explained as follows: in the beginning of superlattice formation many nuclei are supposed to be formed throughout the specimen. Since the volume of Ni_3Fe contracts by superlattice formation, these nuclei of superlattice induce sticking internal stress around them. Consequently internal friction must be smaller than that in disordered state, because the spontaneous magnetization is fixed more strongly in the direction of internal stress. The appearance of a sharp peak is explained by considering microscopic eddy current. As already described, the previously obtained theoretical curve has a breaking point because the theory assumes the existence of internal stress having a constant magnitude. But this breaking point will vanish by taking the proper distribution of its magnitude into account. The sharpness of the curve decreases by such a correction. Therefore if, on the contrary, the internal stress is constant throughout the specimen, the curve of internal friction must have a sharp maximum. It is possible to suppose that these conditions are satisfied in the earlier stage of superlattice formation. It causes the appearance of a very sharp peak in the curve (1). Other three curves in Fig. 2 show the curves of internal friction versus magnetization obtained after annealing at 444°C for 50 min., 100 min., and 200 min. It is obvious from these figures that internal friction in demagnetized state is nearly invariable and that the behaviors of the curves are similar to each other. Each curve has two maxima and these maxima are not so sharp as compared with those obtained by 30 minutes annealing. The flat maximum is attributed to the fact that the magnitude of internal stress has an irregular distribution by the development of superlattice formation. The appearance of two maxima is explained by regarding that one maximum is due to macroscopic eddy current and other to microscopic eddy current. These two maxima have been previously found by Cooke.¹⁰⁾ He observed internal friction of

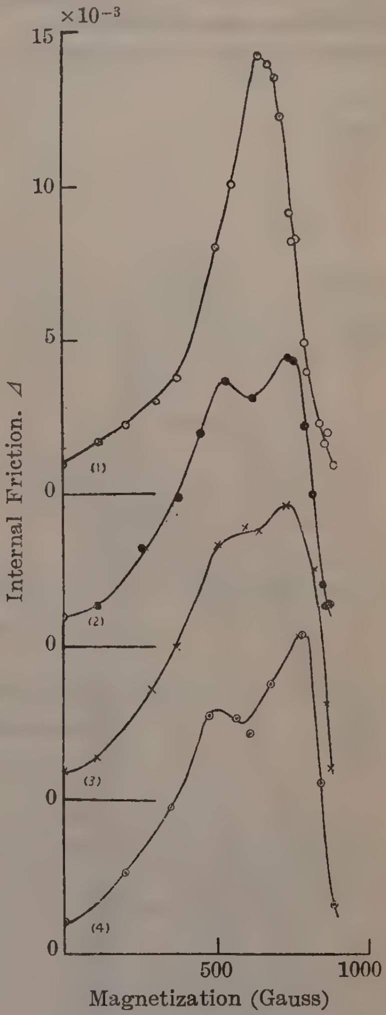

Fig. 2. The experimental relations between internal friction and magnetization after being annealed at 444°C for various durations. Curve (1) shows the result obtained by 30 minutes annealing and (2), (3), (4) show respectively the results obtained by 50, 100 and 200 minutes annealings.

iron as a function of magnetization and found the existence of two maxima. He also pointed out that one maximum is caused by the loss due to macroscopic eddy current. Then the remained maximum is considered to be caused by microscopic eddy current.

The curves in Fig. 3 were given by the specimen which were annealed at 490°C after being annealed at 444°C for 200 minutes. The curve (1) shows the behavior of internal friction when the specimen was annealed at 490°C for 40 minutes. If the relaxation time at 444°C is ten times larger than that at 490°C, this annealing is equivalent to the annealing at 490°C for 1 hour. Similarly, the effect of annealing corresponding to the other four curves marked with (2), (3), (4) and (5) is equivalent to the annealing at 490°C for 3 hours, 10 hours, 30 hours and 100 hours respectively. The reason why the specimen was annealed at 490°C in this figure is that the annealing time is sufficiently large in this stage of superlattice formation as compared with heating and cooling durations and that the annealing at 490°C required shorter times than that at 444°C in order to obtain the same ordering. It can be seen by comparing Fig. 1, 2 and 3 that internal friction in demagnetized state is nearly invariant by annealing excepting the abrupt decreasing in the begining of superlattice formation. This fact is a remarkable character of internal friction as compared with the other magnetic properties such as initial permeability which varies gradually by heat treatment. At present, we can not give a definite interpretation of this fact, but the experimental results obtained by Sato show the same behavior as reported here, except that a small maximum appeared in his experiment by the annealing at 490°C for 10 or 20 minutes. This discrepancy is supposed to be attributed to the difference of annealing methods. Very short time annealing at 490°C was superposed in his experiment in order to form succesive ordering. But by the reason explained above, the temperature of the specimen is supposed to be unable to reach 490°C in such a short time, hence heating and cooling give larger effect than the annealing at 490°C in his case. It is also found from Fig. 3 that with the increase of annealing time the maximum values of internal friction become smaller and shapes of curves become flatter. This can not be explained quantitatively because the experimental results originate from both micro and macroscopic eddy currents. Qualitatively, however, it can be explained by considering that directional distribution of internal stress becomes uniform and its inten-

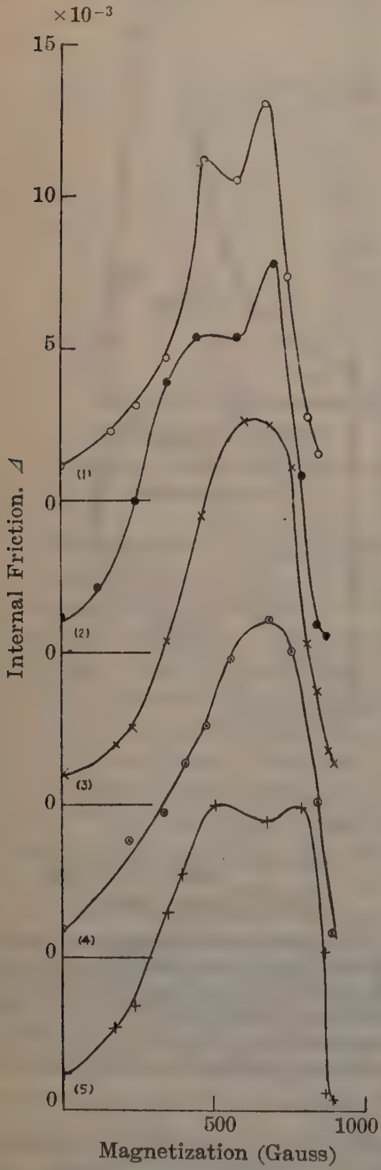

Fig. 3. The experimental relations of internal friction vs. magnetization obtaind by the annealing at 490°C for various durations after being annealed for 200 minutes at 444°C. Curves (1), (2), (3), (4) and (5) show the results obtained by the annealing at 490°C for 40 mins., 2 hrs. 40 mins., 9hrs. 40 mins., 2^9 hrs. 40 mins. and 9^9 hrs. 40 mins., respectively.

sity distribution diverges with the disappearance of nuclei of superlattice. The next remarkable experimental result is that the maximum values of internal friction in Fig. 3 are rather larger than the values in Fig. 2. It is supposed to originate from the fact that several sorts of relaxation times exist in Ni_3Fe as mentioned above and that the annealing at 490°C does not give the tenfold influence as compared with the annealing at 444°C.

It is noted, in conclusion, that the experimental results of internal friction for Ni_3Fe are explained qualitatively by the theories obtained by Becker, Brown and the present author.

The author expresses his sincere thanks to Dr. H. Sato for his kind advices.

References

1) R. Becker & W. Döring: Ferromagnetismus, Berlin (1939) p. 357-382.

2) N. Kunitomi: J. Phys. Soc. Jap. to be pubulished.

3) E. N. Grabbe: Phys. Rev. **57** (1940) 728.

4) S. Chekaxumi: J. Soc. Jap. **5** (1950) 327.

5) F. Förster & W. Köster: Z. Metallkde. **29** (1937) 109.

6) H. Sato: Sci. Rep. RITU **1** (1949) 65.

7) W. F. Brown Jr.: Phys. Rev. **50** (1936) 1165.

8) S. Kaya: J. Fac. Sci. Hok. Imp. Univ. **2** (1938) 29.

9) S. Kaya, M. Nakayama and H. Sato: Proc. Phys.-Math. Soc. Jap. III **25** (1943) 179.

10) F. T. Cooke: Phys. Rev. **50** (1936) 1158.

JOURNAL OF THE PHYSICAL SOCIETY OF JAPAN Vol. 7, No. 6 NOV.—DEC., 1952

On the Magneto-thermoelectric Power of Iron Crystal at low Temperatures

By Yasuo GONDÔ and Zenya FUNATOGAWA

Yokohama National University

(Received October 23, 1951)

The magneto-thermoelectric power of iron single crystal was measured in a temperature region between room temperature and -195°C and the anisotropic constants $(E_m)_{100}$ and $(E_m)_{111}$ (which specify the effect along the direction [100] and [111], respectively) were calculated, at various temperatures. From thes results and those at high temperatures reported in the provious papers both the constants $(E_m)_{100}$ and $(E_m)_{111}$ were found to have the maximum values near room temperature and decrease gradually with decreasing temperature and may tend to zero at 0°K.

§1. Introduction

The thermal e.m.f. of metals is changed by magnetization. The difference of the thermal e.m.f. between a demagnetized and a magnetized state of a ferromagnetics, each of which is measured against such a non-ferromagnetic metal as copper, is called a magneto-thermal e.m.f. The magneto-thermal e.m.f. per degree, that is called the magneto-thermoelectric power, should be given by the next formula,

$$(E_m)_{\alpha\beta\gamma}=a_0+a_1\sum\alpha_i^2\beta_i\gamma_i+a_2\sum_{i\neq j}\alpha_i\beta_i\alpha_j\gamma_j\,,$$
$$a_0=-a_1/3\,,$$

where $(E_m)_{\alpha\beta\gamma}$ is the induced magneto-thermoelectric power measured along a direction with direction cosines β_1, β_2 and β_3 with respect to the principal axes of a cubic crystal, provided the crystal is magnetized in a direction α_1, α_2 and α_3, and a temperature gradient in the crystal exists along a direction γ_1, γ_2 and γ_3. a_1 and a_2 are constants at a given temperature and are called anisotropic constants of the magneto-thermoelectric power.

In order to determine the constants a_1 and a_2 by measurements of real crystal rods we must choose at first a standard distribution of magnetic domains and adopt the remanent point as a standard state. It will be unnecessary to repeat the reason why the remanent point rather than a demagnetized state must be adopted as a standard state, because we have already described it in the previous paper[1)][2)]. Then the magnitude of the magneto-thermoelectric power between a saturation state and a remanent point of a cubic crystal is given by

$$(E_m)_{\text{sat.-rem.}}=a_1\left[1-\frac{\beta_1{}^3+\beta_2{}^3+\beta_3{}^3}{\beta_1+\beta_2+\beta_3}\right]$$
$$+2(a_2-a_1)(\beta_2{}^2\beta_3{}^2+\beta_3{}^2\beta_1{}^2+\beta_1{}^2\beta_2{}^2).$$

We have already determined the constants a_1 and a_2 at room temperature[1)] and moreover, the temperature dependence of a_1 and a_2 at high temperatures[2)]. The results obtained are again shown in Fig. 5. It is desired to extend the measurements to a region of low temperatures in order to obtain more detailed information on this effect.

§ 2. Experimental Methods and Samples

A Fe-Cu thermocouple was constructed, by connecting copper wires with each end of a specimen. The temperatures at the junctions were measured, separately, by inserting a copper-constantan thermocouple to each junction. The temperature of the hot junction was kept always 10°C∼20°C higher than the cold one.

The experimental arrangement is shown in Fig. 1. A is a magnetizing coil placed vartically, B is a compensating coil wound on the outside of A to avoid the effect of terrestrial magnetism. A slender Dewar flask, filled with a freezing mixture, is placed inside the magnetizing coil A. The specimen S is surrounded by two coaxial glass tubes D in the flask, and the lead wires of the thermocouples are wound together extending to the bottom of D, and drawn out through lumps of lead and then connected with a potentiometer, in order to avoid disturbances including those caused by heat conduction. The surfaces of the specimen and lead wires were covered with insulating lacquer to avoid a leakage current. H_1 and H_2, both of which are electric furnaces constructed non-inductively, are used to regulate the temperatures or temperature differences of the specimen. The ordinary thermal e.m.f. arising from the Fe-Cu thermocouple was nearly balanced by a potentiometer. Then the change of the thermal e.m.f., that is the induced magneto-thermal e.m.f., set up in consequence of magnetization of the specimen by the magnetizing coil A, is detected by the deflection of a sensitive galvanometer connected in series with the potentiometer. We used ice and salt, dry ice and liquid oxygen as freezing mixtures.

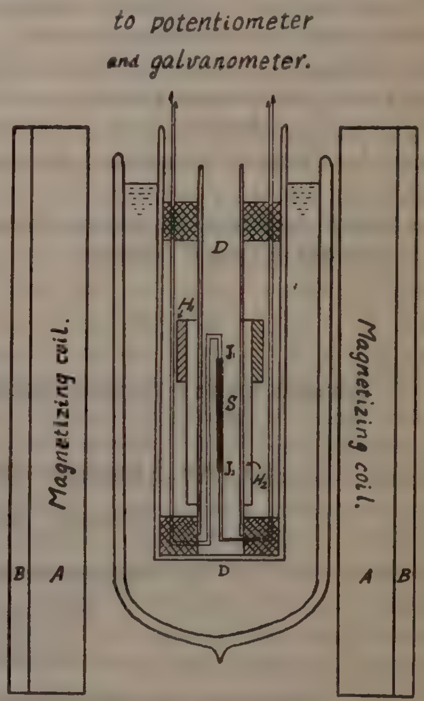

Fig. 1. Schematic representation of the experimental arrangement.

Specimens used for this experiment were

Table I.

Sample number	Diam. (mm)	Length (mm)	Direction cosines β_1	β_2	β_3	$J_{r.\,\text{calc.}}$	$J_{r.\,\text{obs.}}$
1	1.930	140.0	0.749	0.571	0.167	1116	1115
10	2.842	189.6	0.996	0.065	0.054	1533	1535
105	1.955	230.4	0.659	0.542	0.522	992	995

cylindrical rods made of electrolytic Swedish iron by Edwards' recrystalization method. The characteristic properties of the specimens at room temperature are shown in Table I.

The residual magnetization calculated by Kaya's formula, $J_{r.\text{calc.}}=J_\infty/(\beta_1+\beta_2+\beta_3)$, where J_∞ is the saturation value at given temperature, coincides satisfactorily with the observed value $J_{r.\text{obs.}}$ even at low temperatures.

§ 3. Fxperimental Results

Measurements of the magneto-thermoelectric power were carried out at several points on the descending hysteresis curve at various temperatures between 98°C and −194°C. In Fig. 2 the magneto-thermoelectric power of the specimen No. 10, a tetragonal crystal, is shown as a function of magnetization. The values of $(E_m)_{\text{sat.-rem.}}$ at several temperatures are given in Table II. As shown there, the values of $(E_m)_{\text{sat.-rem.}}$ decrease gradually as the temperature decreases below room temperature.

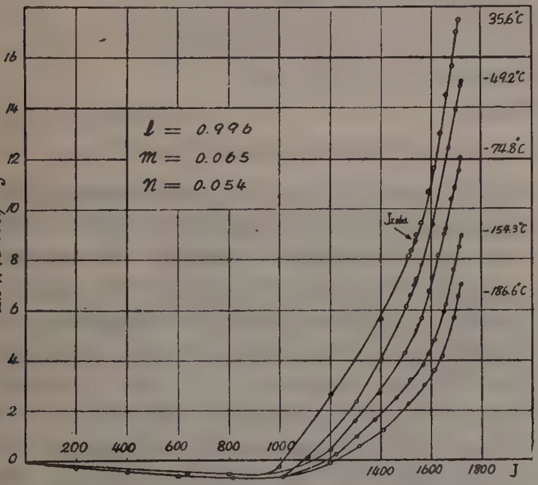

Fig. 2. Tetragonal crystal, No. 10.

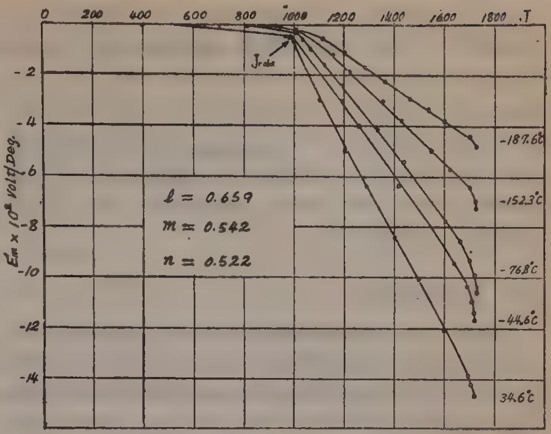

Fig. 3. Trigonal crystal, No. 105.

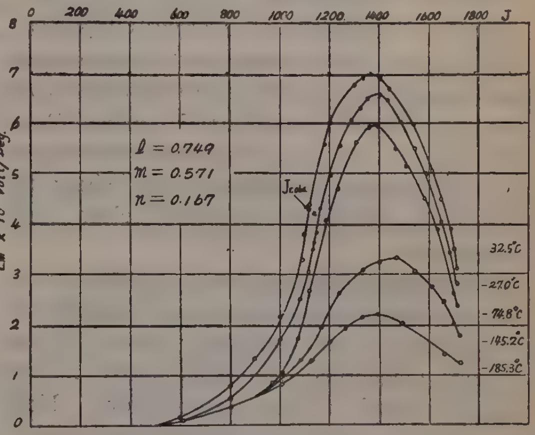

Fig. 4. Diagonal crystal, No. 1.

Fig. 3 is the result of the specimen No. 105, a trigonal crystal. In this specimen the variation of the remanence with temperature is not so remarkable, the changes concentrate between the remanent and the saturation points, and the curves become gradually flatter with decreasing temperature. Thus, the values of $(E_m)_{\text{sat.-rem.}}$ decrease rapidly

Table II.

Temperature °C	$(E_m)_{\text{sat.-rem.}}\times 10^8$Volt/deg.			$a_1\times10^8$ (Volt/deg)	$a_2\times10^8$ (Volt/deg)	$a_1/a_{1,\,30°\text{C}}$	$a_2/a_{2,\,30°\text{C}}$
	No. 10	No. 105	No. 1				
75	8.6	−13.8	−1.4	89.8	−22.1	0.91	1.01
30	9.0	−13.6	−1.1	98.4	−21.9	1.00	1.00
0	8.8	−12.8	−1.0	91.6	−20.6	0.93	0.94
− 50	7.9	−11.3	−0.6	82.2	−18.2	0.84	0.83
− 75	6.3	−10.7	−0.4	66.0	−17.1	0.67	0.78
−150	4.6	− 7.1	−0.1	46.4	−11.4	0.47	0.52
−185	3.4	− 4.6	−0.3	35.3	− 7.4	0.36	0.34

with decreasing temperature as shown in Table II. The results of specimen No. 1, a diagonal crystal, are shown in Fig. 4. As expected from the results of No. 10 and No. 105, the values of $(E_m)_{\text{sat.-rem.}}$ of this sample are too small to determine precisely. The results from the three specimens are compared in Table II.

§ 4. Discussion

From the measurements of $(E_m)_{\text{sat.-rem.}}$ we can determine the anisotropic constants a_1 and a_2 at given temperature by solving the following equations:

No. 10: $(E_m)_{\text{sat.-rem.}}=0.0993a_1+0.0142a_2$
No. 105: $(E_m)_{\text{sat.-rem.}}=0.0070a_1+0.6520a_2$
No. 1: $(E_m)_{\text{sat.-rem.}}=0.0843a_1+0.4644a_2$.

The a_1 and a_2 calculated and their temperature dependence at several temperatures are shown in Table II and Fig. 5. a_1 or $(E_m)_{100}$ and $|a_2|$ or $|(E_m)_{111}|$ decrease very rapidly with decreasing temperature and show the same temperature decreases below room temperature.

Considering together the variations of a_1 and a_2 at high¹⁾ and at low temperatures, we can recognize that maximum values of both of the anisotropic constants exist in the neighbourhood of room temperature. However, it is not clear at present why such a remarkable phenomenon appears.

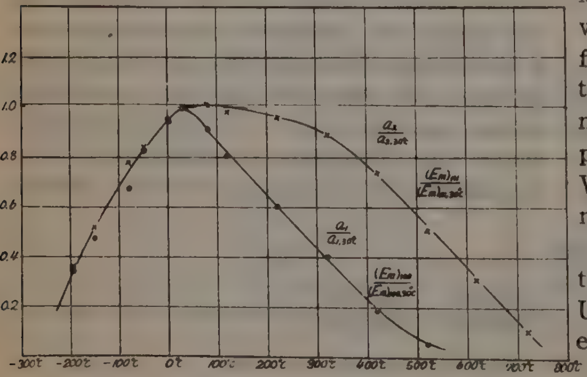

Fig. 5. Temperature dependence of the constants.

Suppose the curves obtained are extrapolated smoothly down to 0°K in Fig. 5, both a_1 and a_2 seem to tend to zero in spite of the fact that the extrapolation is not always satisfactory, particularly at very low temperature. When the absolute thermoelectric powers of the magnetized- and demagnetized states of the metal are defined by

$$S_{\text{mag.}}=\int_0^T \frac{\sigma_{\text{mag.}}}{T}\,dT \text{ and } S_{\text{dem.}}=\int_0^T \frac{\sigma_{\text{dem.}}}{T}\,dT,$$

respectively, where $\sigma_{\text{mag.}}$ is the Thomson coefficient of the magnetized state and $\sigma_{\text{dem.}}$ is that of the demagnetized state, the magneto-thermoelectric power between them is given by

$$E_m=S_{\text{mag.}}-S_{\text{dem.}}\ .$$

As the magneto-thermoelectric power defined in such a way should satisfy Nernst's heat theorem³⁾, which states that the ordinary thermal e.m.f. disappears at 0°K, so

$$\lim_{T=0} E_m=\lim_{T=0} S_{\text{mas.}}-\lim_{T=0} S_{\text{dem.}}=0.$$

Thus we have

$$\lim_{T=0} a_0+\lim_{T=0} a_1 \sum \alpha_i^2\beta_i\gamma_i$$
$$+\lim_{T=0} a_2 \sum_{i\neq j} \alpha_i\beta_i\alpha_j\gamma_j=0$$

identically in α_i, β_i and γ_i. Hence

$$\lim_{T=0} a_1=0 \quad\text{and}\quad \lim_{T=0} a_2=0\ .$$

Thus, we can see at least that the magneto-thermoelectric power should be zero at 0°K.

It is an important problem whether the magneto-thermoelectric power is directly related to ferromagnetism or related only indirectly, for instance through the magnetostrictive lattice distortion. In the previous papers¹⁾²⁾, we emphasized that there is no intimate relation between the magnetostrictive lattice distortion and this phenomena. We would rather repeat it again here. But unfortunately, we have not obtained magnetostriction data at low temperatures, Measurements of the magnetostriction at low temperature are needed to complete the study. We are now preparing to carry out these measurements.

In conclusion we wish to express our hearty thanks to Dr. S. Kaya, Professor of the University of Tokyo, for his kind interest and encouragement.

References

1) Z. Funatogawa: J. Phys. Soc. Japan **5** (1950) 311.

2) Z. Funatogawa: J. Phys. Soc. Japan **6** (1951) 256.

3) W. Nernst: Theoretische Chemie. (1913) 751.

JOURNAL OF THE PHYSICAL SOCIETY OF JAPAN Vol. 7, No. 6 Nov.—Dec., 1952

On the A. C. Magnetization Characteristics of a Perminvar Wire*

By Tokutaro HIRONE, Hiroshi WATANABE,
Takao IWATA and Kenzi IKEDA
*Research Institute for Iron, Steel and Other Metals,
Tohoku University*

(Received February 16, 1952)

A. C. magnetization characteristics of a perminvar wire under tension were observed and discussed on the basis of the pipe-domain theory, the results of the discussion being compared with those based on the classical eddy current theory. It was found that the said domain theory would give a semi-quantitative interpretation of the a. c. data, and suggest the existence of an effect other than eddy currents. These results were, in essential, in agreement with the prediction by Williams and others on the a. c. magnetization characteristics of a single crystal of silicon iron. In connection with this, an account was given of an experiment based on the usual technique of estimation of the mean volume of domains and it was found that estimated sizes of the volume had little significance for the a. c. characteristics.

§ 1. Introduction

It is a matter of no dispute that the primary factor controlling the a. c. magnetization characteristics of ferromagnetic alloys is due to the eddy currents produced in the substances owing to the change of magnetization. Now magnetization in ferromagnetic substance proceeds by the displacement of magnetic domain boundaries as well as by the rotation of spontaneous magnetization. Hence, the exact knowledge of a. c. characteristics can only be obtained from the informations concerning the behaviors of these two elementary processes due to applied alternate magnetic field. However, this point has been conventionally ignored in engineering calculations although it has often[1] been pointed out that the assumption of a homogeneous permeability throughout the specimen will lead to a quantitative disagreement with observations concerning a. c. losses. Now the magnetic reversal of a perminvar wire under proper tension proceeds in a large single discontinuous jump associated with 180°-boundary displacement alone if we assume for the domain distribution to be similar to that in static state and in this case its a. c. characteristics may also be specified mainly by 180°-wall displacements. Thus by observing the a. c. and d. c. behaviors in this case, some informations concerning influence of 180°-boundary displacement upon the a. c. characteristics were obtained in the present investigation.

§ 2. The Measurements of Voltage Pulses during Large Barkhausen Jumps

For the comprehension of a. c. characteristics the results of a preliminary experiment are first described which will give some knowledge of dynamical feature of domain structure of the ferromagnetic substance. The information on this would be furnished by the technique usually adopted for the estimation of the volume of domains[2], viz., the evaluation of the area under induced voltage pulse in a search coil wound on a ferromagnetic material due to a change of magnetic field.

The specimen here used was a perminvar wire. The descending branches of the hysteresis curves without and under tension of 12.3 kg/mm^2 are shown in Fig. 1 and 2, respectively. The expected large single discontinuous jump was still interrupted at several steps, which was an indication of incomplete annealing. Oscillograms of the voltage pulses were taken at the points marked as small circles. By such an observation, it was found that the whole magnetic reversal

---

* The experimental part of this work was carried out in 1948–49, and was financed in part by the Grant in Aid of Fundamental Scientific Research of the Ministry of Education in 1948 and 1949.

proceeds under the successive occurence of a number of small Barkhausen jumps, although the descending branch of magnetic hysteresis curve consists of a few discontinous jumps as shown in Fig. 2. By analysing the oscillograms obtained the mean volume and duration time of the small magnetic reveasals attributive to those Barkhausen jumps are resp. 10^{-8}cm^3 and 10^{-4} sec.*

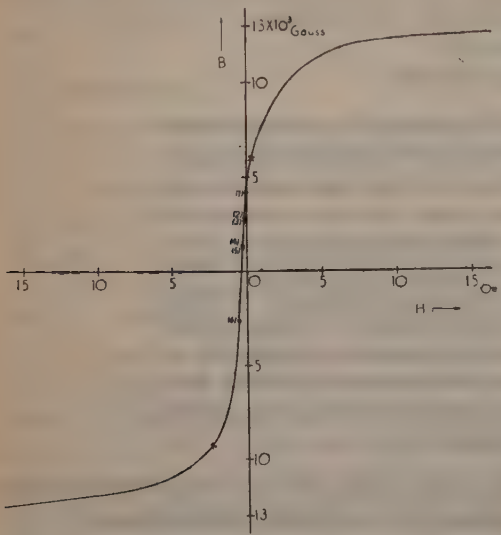

Fig. 1. Circles are those points where the Barkhausen voltage pulses were photographed. Two crosses show the limits between which the Barkhausen pulses can be observed.

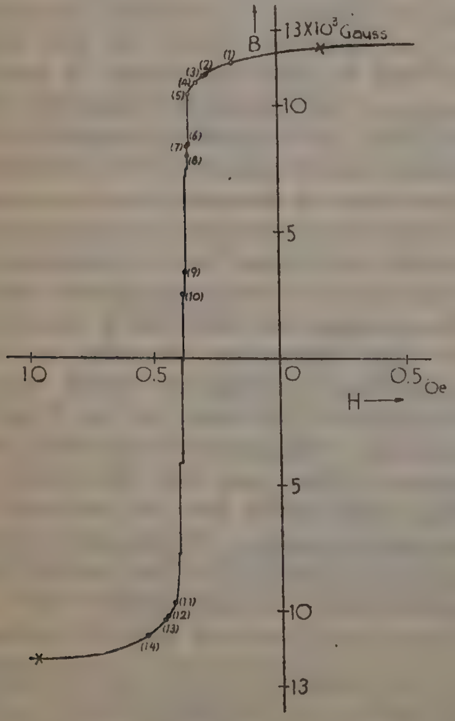

Fig. 2.

For the interpretation of the fact mentioned above Becker's[3)] theory of domain boundary displacement was found to be inadequate. According to his theory the motion of the domain boundary is hindered by the microscopic eddy currents produced by the said motion itself. Basing on an assumed prismatic form of domains, whose edge and axial lengths are l and l' respectively (Fig. 3a), he proposed a formula

$$4\pi^2 J_s l l' \sigma = H\tau_B \qquad (1)$$

where J_s is the saturation magnetization, σ the electrical conductivity in e.m.u. and H the driving field which is the difference between the applied field and the critical one required to move the domain boundary. τ_B is the time of duration of the jump under consideration. In our case, $J_s \sim 1.0\times10^3$, $H\sim 10^{-2}$Ö, $\sigma\sim10^{-4}$ and $\tau_B=7\times10^{-4}$; in this case following result was obtained:

$$ll' \sim 1.8\times10^{-6}\text{cm}^2 . \qquad (2)$$

Since the volume of the domain is l^2l' and is roughly equal to 5.10^{-8}cm^3, it follows that

$$l\sim2.8\times10^{-2}\text{cm} , \quad l'\sim6.4\times10^{-5}\text{cm} . \qquad (3)$$

This result which shows the dimension ratio of Barkhausen volume to be of the order of 1/1000, is, however, improbable, since the free charges which appear on the boundaries of the volume would make the magnetostatic energy large. In this case, we should have taken an alternative picture in which the plane of the boundary and its direction of motion were such as indicated in Fig. 3b in contrast to Becker's case (Fig. 3a). With this picture,

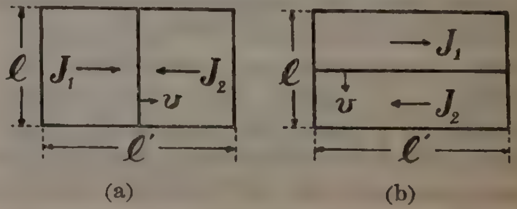

(a) (b)

Fig. 3.

the formulas (1), (2) and (3) should be replaced respectively by

---

* The detailed description of those oscillograms will be given in Sci. Rep. Res. Inst, Tohoku Univ. Series A,

$$32\pi^{-1/2}J_s\sigma l^2=H\tau_B{}^* \qquad (1)'$$

$$l^2\sim3.9\times10^{-6}\text{cm}^2 \qquad (2)'$$

and $l\sim2\times10^{-3}$cm, $l'\sim1.2\times10^{-2}$cm . (3)'

Since there are several effects for enlarging the value of the eddy current field, the value of l may be reduced considerably. This will give a probable estimate of dimension ratio of a Barkhausen domain (a few score). The reason for the preponderance of the case (b) over the case (a) in Fig. 3 is to be found in that the boundaries parallel to the magnetic field are more extensive than those perpendicular to it. Thus, with an extension of this idea a pipe domain picture in magnetic reversal process can be introduced. As the following discussions will show, this picture seems to be adaptable to the explanation of d. c. behavior mentioned above and of the following a. c. characteristics observed in a perminvar wire under tension. In this picture the magnetic reversal germ originated first at the peripheral portion of the wire specimen. The germ soon grew into pipe-formed domain, whose direction of magnetization oriented antiparallel to the inclosed inner portion of the specimen. The magnetic reversal was completed by closing the inner surface of pipe. This picture was taken from Williams and others' idea in interpreting the large Barkhausen jump in a single crystal of silicon iron.

Standing on this view point, the large Barkhausen jump as a whole was described as an inward motion of a cylindrical domain boundary coaxial with the axis of the wire**, and the total time required for the jump was calculated by integrating the following formula:

$$\frac{v_r}{H}=-\frac{1}{32\pi^2\sigma J_s r\ln(a/r)} \qquad (4)$$

viz.,

$$\frac{a^2}{4}-\frac{r^2}{2}\left(\ln\frac{a}{r}+\frac{1}{2}\right)=\frac{Ht}{32\pi^2\sigma J_s}\,, \qquad (5)$$

where a and r are the radii of the wire and the boundary surface, respetively. Putting $a=0.02$ cm, $\sigma=0.53\times10^{-4}$ and $J_s=1.0\times10^3$ and with vanishing r we obtain

$$t=1.6\times10^{-3}/H\,, \qquad (6)$$

which becomes 0.16 sec for a driving field of 10^{-2} Öe, in satisfactory agreement with experience. Then the values of l and l' given in the formula (3'), which are much smaller than the dimensions of the specimen, are considered to be the linear dimensions of a volume swept by a locally irregular motion of the boundary, and hence, they do not have primary importance on the a. c. magnetization characteristics.

From our experimental data on the superposition of high frequency field on a 50 c/s one, described later, the time which is given by the above formula is observed to be $t=2.7\times10^{-3}/H$, which is 1.7 times larger than that given in (6). In view of the simplicity of the adopted model and the inaccuracy in the measurement, this may be considered to be in agreement with experiment.

§ 3. The Domain Theory under Alternate Magnetic Field

Now the flux change in a stretched perminvar wire under the action of alternate magnetic field will be discussed in the light of the pipe domain picture. We shall tentatively assume that, under the action of the applied field, the domain boundary as considered in § 2 (pipe domain) moves radially in an infinitely long circular cylinder. The motion can be described as

$$\frac{r^2}{2}\left(\ln\frac{a}{r}+\frac{1}{2}\right)=\frac{1}{32\pi^2\sigma J_s}\int|H|dt \qquad (5)'$$

where r is the radius of the boundary. If an alternate field of the form $H_0\sin\omega t$ is applied, then the driving field H acting on the boundary in the region of the large Barkhausen jump is $H_0\sin\omega t-H_s$ where H_s is the coercive force of the specimen. Let the integration in (5)' be made within a half cycle, it is seen that

$$\int H dt=\frac{1}{\omega}\{2H_0\cos\theta-H_s(\pi-2\theta)\}$$

---

* This formula is obtained by applying Becker's method for the case considered here with some approximatons in evaluating the integral included in the ex pression of the eddy current field.

** According to Williams' paper, the value of the magnetic field below which the domain boundary is to be considered as plane, happens to lie near those used here (~10^{-2} ö). It may, however, be justified to persist in pipe-domain picture, when we are concerned with the a.c. magnetization characteristics (see following sections), since the values of the field used there are usually much larger.

where $\theta=\sin^{-1}H_s/H_0$. Hence starting from $r=a$, the radius r_1 of the pipe domain boundary after a half cycle is given by

$$\frac{a^2}{4}-\frac{r_1^2}{2}\left(\ln\frac{a}{r_1}+\frac{1}{2}\right)=\frac{2H_0\cos\theta-H_s(\pi-2\theta)}{32\pi^2\sigma J_s\omega}\,. \tag{7}$$

Below the critical circular frequency ω_c, (7) has no solution for r_1 and the boundary moves in full from the periphery to central axis of the wire, whereas, if the frequency exceeds ω_c, there exists a solution which is smaller than a, the boundary sweeping only a part of its path. Such a frequency ω_c is given by

$$\omega_c=\frac{2H_0\cos\theta-H_s(\pi-\cos\theta)}{8\pi^2\sigma J_s a^2}\,. \tag{8}$$

Using ω_c or $f_c=\omega_c/2\pi$, the flux change Φ, which can be defined as $\Phi=4\pi^2 J_s(2a^2-2r^2)$ and which is easily measurable, can be given by the following formula ($\Phi_0=(\Phi)_{r=0}$),

$$1-(1-\Phi/\Phi_0)(1-\ln(1-\Phi/\Phi_0))=f_c/f \tag{9}$$

which represents the decay of Φ with frequency.

On the basis of the above theoretical results, the amplitude of flux in a stretched perminvar wire with and without biassing d. c. field was studied with the usual technique of observing the a. c. hysteresis curve. The amplitude of the mean flux was measured and was plotted against frequency for the specimen described above ($H_{\text{ext}}=2.25$ Öe, r.m.s.) (Fig. 4). It fell monotonously with frequency. The classical theory cannot be applied to the case with tension, though it well reproduces the experimental curve of the case without tension, since in the former case the whole magnetic reversal occurs in a single large Barkhausen jump and the differential permeability becomes infinite. The results are compared with that obtained by pipe domain picture. In the sample here used H_s and H_0 are equal to 0.33 and 3.18 respectively; hence, the critical circular frequency ω_c is calculated from eq. (8) as follows:

$$f_c=\omega_c/2\pi=538\ c/s\ .$$

The flux amplitude remains constant till this frequency is reached and then decays continuously with the increase of frequency. The result of calculation based on eq. (9) is given in Fig. 4 in full line. The observed points lie a little lower than the theoretical

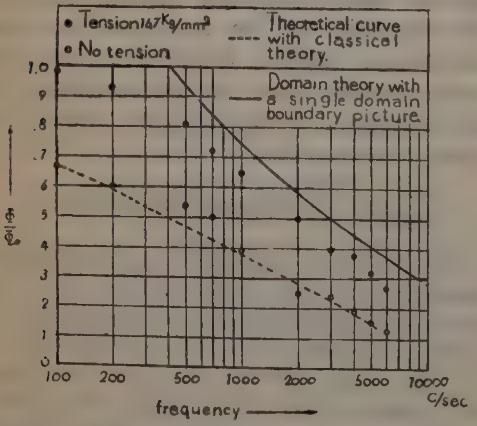

Fig. 4. Theoretical curve with classical eddy current theory was derived after referring to Wvedensky's paper: Ann. d. Phys. (4) **64** (1921) 609.

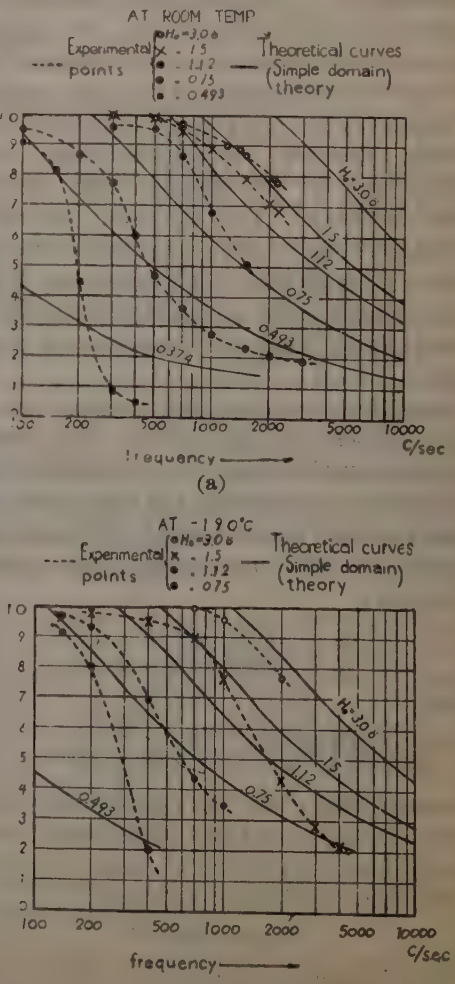

(a)

(b)

Fig. 5.

curve, but the general decay character seems to be reproduced theoretically.

Similar experiments were performed on a thinner perminvar wire, whose diameter was 0.19 mm. Applying a tension of 16.6 kg/mm^2 and various exciting a. c. fields, observations were made at room temperature as well as at liquid air temperatures. The results are shown in Figs. 5a and 5b and are compared with theoretical curves based on eq. (9) of pipe-domain picture. It may be seen from the figures that the domain theory describes again the behavior of the experimental curves fairly well, but there remains some discrepancies: (1) the observed frequency is smaller than the expected one and (2) the decaying of the mean flux with frequency is faster than that in the theory for low fields.

The former fact suggests us that the process of the flux change is controlled not solely by eddy currents but also by some other effects. Any effect that forces on v and H the linear relation $v=GH$ will reduce the high frequency characteristics roughly by an amount $1:(1+1/8\pi^2\sigma J_s aG)$ and hence, shift all the theoretical curves of the above figures towards low frequency side. Such effects, for example, include that mentioned in Katayama's paper[3)4)] or the relaxation effect considered by Landau and Lifshitz.*

The second fact may perhaps be caused by the inhomogeneity in the critical field H_s. At low fields, the fluctuation of the H_s value becomes important, since the driving field is not so large compared with this fluctuation. When the boundary moves near the peak of H_s, its propagation velocity is much diminished or in some cases it is almost stopped. If such peaks are statistically distributed in the specimen, the Barkhausen jumps must be interrupted somewhere. The time required for a boundary exposed to a given external field to cover a given volume is, of course, larger in an uneven path than in a smooth one, because it can be shown quite easily that $\int dx/(H-H_s)$ is the smallest for constant H_s.[5)]

§ 4. Superposition of High Frequency Fields

A more direct indication of the pipe-domain picture was furnished by an experiment, in which a high frequency a. c. field was superimposed on a 50 cycle field excitation.

In our experiment the amplitude of the superposed high frequency field H_h was kept constant at 4.25 Ö and was larger than that of the 50 cycle field (3.43 Ö), hence the movement of the boundary was stopped and reversed its moving direction at the end of every half cycle of the high frequency field. If we denote the successive three stationary values of the radius by r_1, r_2 and r_3 respectively, it is seen from (5) that

$$\frac{r_1^2}{2}\left(\ln\frac{a}{r_1}+\frac{1}{2}\right)-\frac{r_2^2}{2}\left(\ln\frac{a}{r_2}+\frac{1}{2}\right)=\frac{1}{32\pi^2 J_s\sigma}\int_{t_1}^{t_2}(\bar{H}_l+H_h\sin\omega t-H_s)dt \quad (10)$$

$$\frac{r_3^3}{2}\left(\ln\frac{a}{r_3}+\frac{1}{2}\right)-\frac{r_2^2}{2}\left(\ln\frac{a}{r_2}+\frac{1}{2}\right)=\frac{1}{32\pi^2 J_s\sigma}\int_{t_3}^{t_4}(-\bar{H}_l+H_h\sin\omega t-H_s)dt \quad (11)$$

where $\bar{H}_l$ is the mean 50 cycle field during the time under consideration. There, $t_1, \cdots, t_4$ should be determined from the condition that the driving fields in (10) and (11) are positive. By taking origin of the time as the beginning of the large Barkhausen jump, following relations are obtained:

$$\sin\omega t_{1,2}=-\frac{\bar{H}_l-H_s}{H_h},$$

$$\sin\omega t_{3,4}=-\frac{\bar{H}_l+H_s}{H_h}.$$

After integrating and summing (10) and (11) and dividing by a^2 we obtain

$$\left(\frac{r_1}{a}\right)^2\left[\ln\left(\frac{a}{r_1}\right)^2+1\right]+\left(\frac{r_3}{a}\right)^2\left[\ln\left(\frac{a}{r_3}\right)^2+1\right]-2\left(\frac{r_2}{a}\right)^2\left[\ln\left(\frac{a}{r_2}\right)^2+1\right]$$
$$=\frac{1}{4\pi^2a^2J_s\sigma\omega}[\bar{H}_l(\theta_1+\theta_2)-H_s(\pi+\theta_1+\theta_2)+H_h(\cos\theta_1+\cos\theta_2)] \quad (12)$$

where

$$\sin\theta_{1,2}=\frac{\bar{H}_l\mp H_s}{H_h}. \quad (13)$$

An apparent permeability μ_a was derived from

---

* Snoek gives an interpretation of this relaxation effect with an idea of spin-spin relaxation. J. L. Snoek, *New Developments in ferromagnetic materials*, Elsevier, New York (1947) 63. J. K. Galt has performed a similar experiment to Williams' on a synthetic single crystal of magnetite.

(12). Calculated and observed results for 4000 c/s are compared in Fig. 6. They agree in that the values of μ_a decrease as the mean radius of the boundary becomes smaller. The full curve in Fig. 6 shows the quantity corresponding to the apparent permeability which was calculated multiplying the right hand side of (12) by $(2\pi J_s/H_h)/(\ln(a/r)^2+1)$ where r is the mean value of r_1, r_2 and r_3.

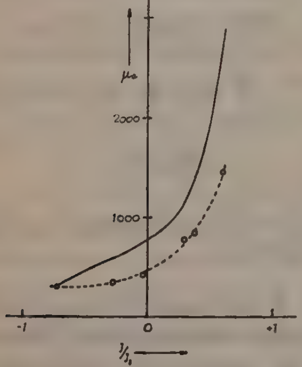

Fig. 6.

The dotted curve is the corresponding quantity derived from the left-hand side of (12). The observed values are also, on the whole, smaller than those calculated, which may be attributed to the effect other than that of eddy currents.

The authors wish to express their sincere thanks to Messrs. T. Kadoya and T. Takahashi for their cooperation and to Mr. N. Tsuya for his helpful discussions. The authors are also indebted to Dr. K. Honda for his supervision and encouragements throughout this work.

References

1) H. J. Williams, W. Shockley and C. Kittel: Phys. Rev. **80** (1950) 1090: R. Becker and W. Döring: *Ferromagnetismus*, Berlin, Julius Springer (1939) 360: L. W. McKeechan and R. M. Bozorth: Phys. Rev. **46** (1924) 527 (L).

2) K. Murakawa: Proc. Phys.-Math. Soc. Jap. **18** (1936), 380; **19** (1937), 715.

3) R. Becker: Zeits. f. tech. Phys. **19** (1938) 542; Ann Phys. (5) **36** (1939) 340.

4) T. Fujimura and T. Katayama: J. Phys. Soc. Jap. **5** (1950) 56: Ditto **4** (1949) 164.

5) Arguments analogous to this have been given for the after effect of some ferromagnetics: T. Fujimura J. Phys. Soc. Jap. **5** (1950) 293; S. Maeda. J. Phys. Soc. Jap. **5** (1950) 358.

JOURNAL OF THE PHYSICAL SOCIETY OF JAPAN Vol. 7, No. 6 Nov.—Dec., 1952

Hydrogen-Like Absorption Spectrum of Cuprous Oxide

By Masakazu HAYASHI

Department of Physics, Faculty of Science,
Hokkaidô University, Sapporo

and Kiichirô KATSUKI

Department of Physics, Muroran College of Technology, Muroran

(Received July 9, 1952)

In cuprous oxide we discovered a new hydrogen-like absorption spectrum besides that found in the previous work. Thus we have two groups of hydrogen-like energy levels, of which the one previously found seems to be due to a self-trapped electron and the other newly found, on the other hand, seems to be due to an exciton and leads to the estimation of the static dielectric constant of cuprous oxide, being 9·5.

§1. Introduction

In our previous work[1] on the absorption spectrum of cuprous oxide a series of *sharp* and *discrete* absorption lines, the so-called hydrogen-like absorption spectrum as expected from the theory of the optical absorption of crystals, was discovered at liquid air temperature. Their energies at −184°C were found to be expressed by the equation:

$$E(\mathrm{eV})=2.161-0.090/n^2, \qquad (1)$$

where $n=2, 3, 4, \cdots$ and 2.161eV is the energy of their series limit measured from the ground state. The absorption line corresponding to $n=1$ was not observed, just in accordance with the theory of Mott and Gurney.[2]

Now, by using a thinner crystal sheet of cuprous oxide than that used in the previous work, we have discovered another hydrogen-like absorption spectrum located at shorter wave-lengths. According to the interpretation here developed, the hydrogen-like energy levels previously found are due to an electron trapped in the crystal, i.e. to the so-called self-trapped electron, while the newly found levels are due to an exciton and lead to the estimation of the static dielectric constant of cuprous oxide, which approximately coincides with the value measured.

§2. Experiment

The sample used in the previous work was prepared by oxidizing a thin copper sheet (0.02 mm thick) at 950°C in the atmosphere of oxygen gas at 20 mm Hg pressure. In the course of experiment this underwent repeated change of temperature between room and liquid air temperature, until it happened to cleave of itself to form an extremely thin sheet of cuprous oxide, which served as the sample used in the present investigation.

The absorption tube used at low temperatures was one of the three tubes constructed in the previous work, which was there denoted as the "absorption tube (**B**)." The principal part of the absorption tube consists of a double-walled glass tube. The sample was mounted at the bottom of the inner tube, which was first highly evacuated and then filled with dry air at suitable pressure. Liquid air was introduced into the space between the inner and the outer tube by means of a water-jet pump, and cooled the sample as well as the inner tube. The liquid air layer around the sample was sufficiently thin, so that the investigation of the absorption spectrum was not interfered with by the absorption due to liquid air in the visible region.

An incandescent lamp served as light source. The spectrograph used was of the Hilger's E_1 type, of which the dispersion in the region in question was 29Å/mm.

At low temperatures we discovered a series of new absorption lines on the shorter wave-length side of those found in the previous work. The newly discovered lines will be denoted hereafter as the "absorption lines *Q*" or briefly "*Q*," while those found in the previous work as the "absorption lines *P*" or "*P*." An absorption line* appearing at the long wave-length end of Q was already described in the previous work as an absorption band, which then appeared broader in breadth than each of the absorption lines P and led to the presumption in favor of the existence of two separate empty bands, as proposed by Bruining and de Boer[3] in their study of the secondary electron emission of some crystals, e.g. Cu_2O.

---

* It has come out reasonable to regard this as having line- rather than band-character.

At −180°C four absorption lines of Q could distinctly be observed but less at higher temperatures. Two lines, the first and the second counted from the longer wave-length side, are broader in breadth than the others. Table I shows the wave-lengths and energies of the absorption lines Q at −130°C and −180°C respectively.

Table I. Absorption lines Q

−130°C		−180°C		
552.3 mμ	2.245 eV	550.3 mμ	2.253 eV	diffuse
	(0.022)		(0.020)	
546.9	2.267	545.5	2.273	〃
	(0.008)		(0.007)	
545.1	2.275	543.7	2.280	sharp
			(0.003)	
		543.0	2.283	〃

As for the temperature dependency of the absorption lines Q, we had only to investigate the dependency relative to P, since the temperature dependency of P was already fully studied in the region between −184°C and +60°C. The two lines each appearing at the long wave-length end of P and Q were compared and the result is shown in Fig. 1. It is seen that the energy difference between them is roughly constant at lower temperatures below −70°C. Hence, the temperature dependency of the absorption line at the long wave-length end of Q can be expressed by the equation:

$$E(\mathrm{eV})=2.25_4-0.04_0\exp(-\Theta/T)^* \quad (T<200°\mathrm{K}), \qquad (2)$$

where Θ is the characteristic temperature of cuprous oxide and takes the value 250°K.

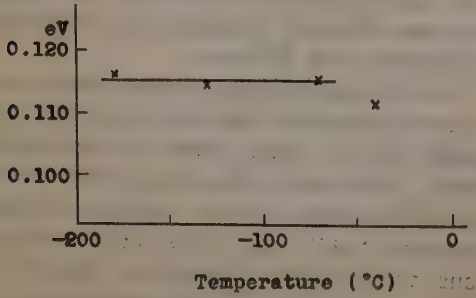

Fig. 1. Temperature dependency of the absorption lines Q relative to P. *Ordinate*: Energy difference between the two absorption lines (cf. the text).

§ 3. Interpretation for the Absorption Lines P and Q

As shown in Table I, the mutual spacing among the absorption lines Q remains constant with temperature. Just as in the case of P, the energies given in Table I can approximately be expressed by the equations:

$$E=2.284-0.150/n^2 \quad (\text{at } -130°\mathrm{C})\,; \qquad (3)$$

and

$$E=2.290-0.150/n^2 \quad (\text{at } -180°\mathrm{C})\,. \qquad (4)$$

Table II gives the observed values (see Table I) and the values calculated from Eqs. (3) and (4) for comparison. They show satisfactory coincidence with each other.

Table II. Comparison between the observed and the calculated values (energies in eV).

n	−130°C		−180°C	
	From (3)	Observed	From (4)	Observed
1	2.134		2.140	
2	2.246	2.245	2.252	2.253
3	2.267	2.267	2.273	2.273
4	2.275	2.275	2.281	2.280
5	2.278		2.284	2,283
⋮				
∞	2.284		2.290	

We have thus obtained two groups of hydrogen-like energy levels each adjoining an empty band, one of which corresponds to the absorption lines P and the other to Q. For the sake of simplicity, the former group including the empty band will be denoted as "group P," and the empty band alone as "band P"; similarly, "group Q" and "band Q" for the latter group. The energy difference between the level corresponding to $n=1$ and the series limit corresponding to the lowest level of the empty band in the group P is found to be 0.090 eV (see § 1) and in the group Q 0.150 eV (see Eqs. (3) and (4)). As shown in Table II, we have been unable, similarly to the case of the group P, to observe the absorption line corresponding to $n=1$, which if existed should have appeared at the wave-length 580.9 mμ (2.134 eV) at -130°C and 579.4 mμ (2.140 eV) at -180°C. Hence it may be inferred that the absorption lines P and Q are due to the electronic transitions from a *common* level. According to this interpretation, we obtain a diagram of energy levels for groups P and Q as shown in Fig. 2. The energy values indicated in the figure are those measured from the common level at -180°C. Apart from these values, the diagram itself is independent of temperature (see Table I and Fig. 1).

---

* See Eq. (2) of the previous work for "the edge (*b*)."

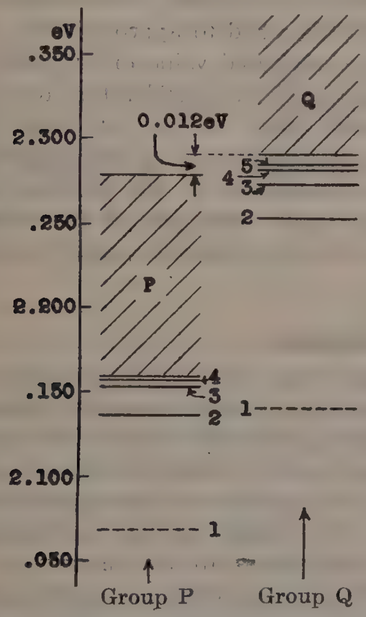

Fig. 2. Configuration of electronic levels of the groups P and Q at -180°C.

Now, as was stated in § 2, the two absorption lines corresponding to $n=2$ and 3 of the group Q appear broader than the others. This fact might be explained by the so-called *Auger process*, i.e. by the circumstances that the electrons in the two levels of Q under consideration have a finite probability of transition to the continuous empty band P. If this explanation be permitted, we arrive at the conclusion that the top level of the band P falls somewhere between the levels corresponding to $n=3$ and 4 of Q, that is, that the band P is *finite in width*, being ca. 0.120 eV, and the gap between the top level of the band P and the bottom level of the band Q isto be estimated ca. 0.012 eV (cf. Fig. 2).

On the ground of their study on the secondary electron emission of semi-conductors, of which some crystals including Cu_2O were much smaller in yield of secondary electrons than others including, for instance, alkali-halides, Bruining and de Boer(4) suggested that the empty band of the sort of crystals including Cu_2O consists of two parts separated from each other. The lower band is assumed to gain more electrons excited from a ground state by the incident primary electrons, which situation is due to the greater probability of direct transition from the ground state to the lower band and, in addition, due to the transition of some excited electrons in the upper band down to the lower. The energy gap between the two empty bands obtained in the present work is 0.012 eV, that is, only half the energy of kT at room temperature. The question if such a situation would still be in harmony with the expectation of Bruining and de Boer must be left to further studies.

It is natural to suppose that the hydrogen-like energy levels are due to the existence of an electron which behaves in a sort of Coulomb field. In fact, the theoretical investigations for the electronic processes in a crystal have led to the existence of such Coulomb field both for an exciton(5) and for a self-trapped electron.(6) The exciton, because of the mobility of both the electron and the positive hole, is freely mobile throughout the crystal; the electron trapped in a polar crystal, on the other hand, can move only by virtue of the rearrangement of the surrounding ions, which can hardly take place even at room temperature, so that it can safely be considered as immobile at low temperatures.(7) The band theory of electrons in polar crystals as well as in metals shows that the band-width should be inversely proportional to the effective mass of an electron and hence the band, in which the immobile electron participates, must be very small in width. We, therefore, arrive at the conclusion that the group P[*] is due to the self-trapped electron.

---

[*] The group P was interpreted in the previous work as the conducting state in Mott and Gurney's sense,(8) because then only the group P was observed and the missing line corresponding to $n=1$ of P was in accordance with the selection rule for the electronic transition from the filled band to the conducting state by absorbing light quanta.

In the previous work two sharp absorption edges besides the bands P and Q were observed and they were interpreted as an electron affinity spectrum of oxygen atom, that is, the electronic transition from the doublet (${}^2P_{1/2}$ and ${}^2P_{3/2}$) of oxygen ion O^- to a continuous energy band, which is now to be attributed to the band Q but not to the band P. Hence the energy differences between the ground state and the doublet (${}^2P_{1/2}$, ${}^2P_{3/2}$) come out to be 0.287 eV for ${}^2P_{1/2}$ and 0.259 eV for ${}^2P_{3/2}$ at −180°C.

It cannot immediately be determined whether the group Q is the hydrogen-like energy levels due to the conducting state or to the exciton, on the ground of the selection rule that the line corresponding to $n=1$ should be missing in the optical absorption spectrum of a crystal. Because, according to Mott and Gurney's explanation,[9] the above selection rule can be applied both to the case of the conducting state and of the exciton, of which the former is considered to be due to a positive hole trapped in the field around a positive ion vacancy and the latter to an electron trapped in the field around another positive hole. Both the positive hole and the electron which are trapped as stated above behave with the Coulomb energy $-e^2/(\kappa_{\rm eff}\, r)$, where $\kappa_{\rm eff}$ is the "effective" dielectric constant of cuprous oxide, whose value is some one between the dielectric constant for static fields (κ) and for high-frequencies (κ_0), and hence the stationary states of the positive hole and of the electron both will be expressed by the same formula**

$$E=-\frac{R}{\kappa_{\rm eff}^2 n^2}\cdot\frac{m^*}{m}, \qquad (5)$$

in which m^* is the effective mass of the positive hole *in the case of the conducting state* and of the electron *in the case of the exciton* respectively, and also R is the Rydberg constant (13.60 eV).

Now, the energy levels of the group Q, as Eqs. (3) and (4) indicate, are in accordance with those expressed by the formula (5). Comparing Eqs. (3) or (4) with (5), we can easily estimate the value of $\kappa_{\rm eff}$ in the two cases:

i) *In the case of the conducting state* the value of m^* of the positive hole was estimated by Fröhlich and Mott,[11] being $0.25m$ (m represents the mass of free electron), and hence

$$R/(4\kappa_{\rm eff}^2)=0.150. \text{ Therefore } \kappa_{\rm eff}=4.8\,; \qquad (6)$$

ii) *In the case of the exciton* it could be assumed that $m^*=m$, and therefore

$$\kappa_{\rm eff}=9.5\,. \qquad (7)$$

The value of κ_0 is 6.3, which comes from the value of refractive index (2.5) for B-line.[12] The values of κ measured with radio-frequencies, on the other hand, are distributed over a wide range, being 7.0,[13] 10.5,[14] and 12.0.[15] The value of $\kappa_{\rm eff}$ *in the case of the conducting state* is too small to coincide with any of the values measured, while that *in the case of the exciton*, at the present status, might be assumed to approximately coincide with the measured value of κ instead of κ_0. Taking the above consideration for granted, we could arrive at the conclusion that the group Q corresponds to the hydrogen-like energy levels due to the exciton, and the electron which takes part in the exciton behaves with the Coulomb energy *screened* by κ.

§ 4. Summary

Using a very thin crystal of cuprous oxide, we discovered a new hydrogen-like absorption spectrum (Q) besides the one (P) found in the previous work. Hence, in cuprous oxide we have two groups of hydrogen-like energy levels. The results of the investigation for these two groups are as follows:

1) The energy difference between the two groups is roughly constant with temperature;

2) The empty band belonging to the group P is 0.120 eV in band-width;

3) The group P seems to be attributed to the energy levels due to a self-trapped electron;

4) The group Q seems to be due to an exciton;

5) The two empty bands belonging to P

** This formula, having resulted from the discussion[10] for the case of electrons moving throughout a crystal lattice including their singly charged attractive centers, is now assumed to be extended to the case of positive holes round the same kind of centers, of which the former in cuprous oxide are to be ascribed to positive holes instead of negative ion vacancies and the latter to positive ion vacancies.

and Q are separated from each other by a gap of 0.012 eV;

6) The static dielectric constant of cuprous oxide is estimated to be 9.5.

In conclusion, we wish to express our hearty gratitudes to Professor T. Hori, Hokkaidô University, for his continued interest in our work and for his kindness in reading the original manuscript. Further, we should like to sincerely thank Professor T. Muto, Tokyo University, for his interest in our present work.

This work is indebted to the Educational Ministry for its financial aid.

References

1) M. Hayashi: J. Facul. Sci. Hokkaido Univ. (II), **4** (1952) 107.

2) N. F. Mott and R. W. Gurney: *Electronic Processes in Ionic Crystals*, Clarendon Press, Oxford, (1940) p. 93.

3) H. Bruining and J. H. de Boer: Physica, **6** (1939) 834.

4) H. Bruining and J. H. de Boer: loc. cit.

5) J. Frenkel: Phys. Rev. **37** (1931) 17; Phys. Z. Sowjet. **8** (1935) 185; ibid., **9** (1936) 158; G. H. Wannier: Phys. Rev. **52** (1937) 191.

6) L. Landau: Phys. Z. Sowjet. **3** (1933) 664; R. W. Gurney and N. F. Mott: Proc. Phys. Soc. **49** (1937) 32; F. Seitz: Phys. Rev. **76** (1949) 1376.

7) R. W. Gurney and N. F. Mott: loc. cit.

8) N. F. Mott and R. W. Gurney: loc. cit.

9) N. F. Mott and R. W. Gurney: loc. cit.

10) N. F. Mott and R. W. Gurney: loc. cit., p. 83.

11) H. Fröhlich and N. F. Mott: Proc. Roy. Soc. (A), **171** (1939) 496.

12) Landolt-Börnstein: *Physikalisch-Chemische Tabellen* (II), Julius Springer, Berlin, (1923) p. 924.

13) A. Völkl: Ann. d. Physik, **14** (1932) 210.

14) K. Højendahl: Z. phys. Chem. (B), **20** (1933) 54.

15) A. Guntherschulz and F. Keller: Z. f. Physik **75** (1932) 78.

JOURNAL OF THE PHYSICAL SOCIETY OF JAPAN Vol. 7, No. 6 NOV.—DEC., 1952

Application of Gasdynamical Method to Soil Mechanics and Theory of Plasticity (I)

By Nobuo INOUE

Faculty of Engineering, Doshisha University, Kyoto

(Read April 3, 1952; Received May 29, 1952)

The author discusses the two-dimensional isostatical problem in the mechanics of either perfectly plastic or pulverulent body, obeying the maximum shear theory in "plane strain" or Coulomb's plasticity condition in "plane stress" respectively, as a kind of gasdynamics of the hypothetical gas here introduced. This gas is non-viscous compressible and obeys the following pressure-density relation: $p/\rho^\gamma=$ const., $-1<\gamma<1$, or $p/\log\rho=$const. The velocity of sound of the gas at rest is chosen to be zero in either case.

By applying the hodograph method, well-known in gasdynamics, to the gas flow, a general solution of the problem is obtained.

After considering simple waves and shocks of the gas flow, an extension of the analogy to plastic bodies of revolution is briefly mentioned.

§ 1. Introduction and Summary

As is well known, the fundamental equation of a non-viscous compressible fluid is a nonlinear partial differential equation of mixed type, and its essential difficulty has let some investigators introduce hypothetical gases, which have transformed the equation into as simple types as have yielded exact solutions but not so deformed one as has lost its characteristics. It will be inferred, therefore, new fields may be developed before us if we try some hypothetical gases, which are as much different from a real gas as to change the essential property of its fundamental equation, as has been recently reported on this journal[1]. In this paper, we shall discuss a theory of hypothetical gases of this kind.

Hypothetical gases, which we introduce here, are non-viscous compressible, having the following two specific properties; first, their pressure-density relations are given by

$$p/\rho^\gamma=\text{const.},\quad -1<\gamma<1, \tag{1.1}$$

$$p/\log\rho=\text{const.}, \tag{1.1'}$$

where p, ρ denote the pressure and density of the gases, and second, the velocity of sound of the gas at rest is zero in either case. We will call our hypothetical gas a gas of the first kind and one of the second kind according as it obeys the characteristic equation (1.1) or (1.1′) respectively. When we let the gas velocity correspond to the state of stress in a mass of sand or in a perfectly plastic material in each proper way, assuming "plane stress" or "plane strain", we shall find that a two-dimensional steady irrotational gas flow of the first kind represents a stress distribution in the mass of sand, which is in a limiting state of equilibrium, that is, just about to collapse, under so large an external load that the influence of its own weight can be neglected*, and similarly, a two-dimensional steady irrotational gas flow of the second kind represents a statically determinate state of stress in the perfectly plastic material, obeying the maximum shear theory in "plane strain". Although the latter analogy has been discussed in our previous papers[2][3][4], it will be considered anew in this paper from a somewhat different point of view.

Once the analogy has been established between these three branches of nonlinear mechanics, useful methods of one of the three can be applied to the others, and it is most interesting to apply the well-established methods of gasdynamics to the other two. Since a general solution of the two-dimensional irrotational flow of the compressible fluid has been obtained by the hodograph method of Chaplygin[5], an application of this method to our hypothetical gas flow will be considered here in detail.

---

* When the gravity has to be taken into account, we are to deal with a rotational gas flow.

Solving fundamental equations of the plane plastic flow of the mass of sand and the perfectly plastic material by the hodograph method, or the stress method, we can obtain general solutions of these stress distribution. Besides, we will discuss a representation of the equations with the variables, which have been introduced into the mechanics of the compressible fluid by Imai[6], after the W.K.B. method in the quantum mechanics. After considering simple waves and an occurrence of shocks, an extension of the analogy to bodies of revolution will be proposed.

The method of solution, which is developed in this paper, seems to be particularly suitble to obtain exact solutions of states of stress, slip lines, and isostatics in the soil mechanics and the theory of plasticity, as will be seen in the following articles.

§ 2. Thermodynamic Relations of Hypothetical Gases

If q, c denote magnitudes of the gas velocity and the local sound velocity respectively, Bernoulli's theorem

$$qdq+dp/\rho=0$$

yields, for the gas of the first kind,

$$q^2/c^2=2/(1-\gamma), \qquad (2.1)$$

and, for the gas of the second kind,

$$q^2/c^2=2 \qquad (2.1')$$

From (1.1) and (2.1), or (1.1′) and (2.1′), the following relations are easily obtained:

$$\left.\begin{aligned} &q^2/c^2=q_*^2/c_*^2=2/(1-\gamma),\\ &\rho/\rho_*=(q_*/q)^{2/(1-\gamma)}=(c_*/c)^{2/(1-\gamma)},\\ &p/p_*=(\rho/\rho_*)^{\gamma}=(q_*/q)^{2\gamma/(1-\gamma)}=(c_*/c)^{2\gamma/(1-\gamma)}, \end{aligned}\right\} \qquad (2.2)$$

or

$$\left.\begin{aligned} &q^2/c^2=q_*^2/c_*^2=2,\\ &\rho/\rho_*=(q_*/q)^2=(c_*/c)^2,\\ &p/p_*=\log\rho/\log\rho_*, \end{aligned}\right\} \qquad (2.2')$$

where the suffix $*$ means that the values with it are to be taken at an arbitrary but fixed point P. Therefore, our gases are everywhere supersonic, having the same local Mach number $[2/(1-\gamma)]^{1/2}$ or $2^{1/2}$ throughout them.

§ 3. Fundamental Equations

If σ_x, σ_y and σ_r, σ_t denote the normal stresses in the x-, y- and r-, φ-directions, τ_{xy} and τ_{rt} the shearing stresses, σ_1 and σ_2 the algebraically greater and smaller principal stresses, $\sigma=(\sigma_1+\sigma_2)/2$, $\tau=(\sigma_1-\sigma_2)/2$, α_1 and α_2 the angles which the algebraically greater and smaller principal stresses σ_1 and σ_2 make with the x-axis respectively (Fig. 1), we have

$$\left.\begin{aligned} \sigma_x=\sigma+\tau\cos 2\alpha_1,\ \ \sigma_y=\sigma-\tau\cos 2\alpha_1,\\ \tau_{xy}=\tau\sin 2\alpha_1, \end{aligned}\right\} \qquad (3.1)$$

or

$$\left.\begin{aligned} \sigma_x=\sigma-\tau\cos 2\alpha_2,\ \sigma_y=\sigma+\tau\cos 2\alpha_2,\\ \tau_{xy}=-\tau\sin 2\alpha_2, \end{aligned}\right\} \qquad (3.2)$$

in rectangular coordinates, and

$$\left.\begin{aligned} \sigma_r=\sigma+\tau\cos 2\alpha_1',\ \ \sigma_t=\sigma-\tau\cos 2\alpha_1',\\ \tau_{rt}=\tau\sin 2\alpha_1', \end{aligned}\right\} \qquad (3,3)$$

or

$$\left.\begin{aligned} \sigma_r=\sigma-\tau\cos 2\alpha_2',\ \ \sigma_t=\sigma+\tau\cos 2\alpha_2',\\ \tau_{rt}=-\tau\sin 2\alpha_2', \end{aligned}\right\} \qquad (3.4)$$

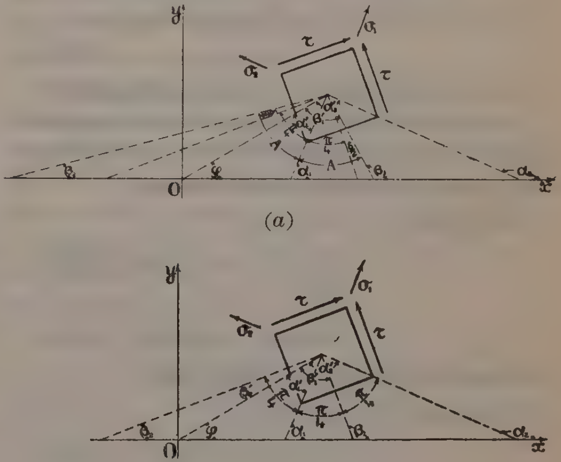

(a)

(b)

Fig. 1. α_1, α_2 are angles which algebraically greater and smaller principal stresses make with the x-axis, and β_1, β_2 are angles which first and second principal shear directions make with the x-axis, (a) in the mass of sand, and (b) in the perfectly plastic material.

in polar coordinates.

The plasticity condition, due to Coulomb for the mass of sand in "plane stress", or to Saint Venant for the perfectly plastic material in "plane strain", yields τ in terms of σ as follows:

$$\tau=(\sigma_0-\sigma)\sin\delta, \qquad (3.5)$$

or

$$\tau=k, \qquad (3.5')$$

respectively, where δ is the angle of internal

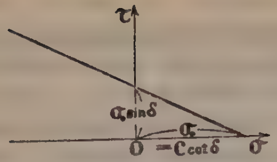

Fig. 2. Plasticity condition of internal friction for the mass of sand, due to Coulomb. δ is angle of internal friction of sand and C is its cohesion.

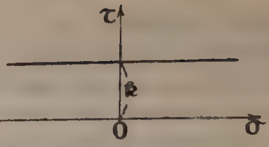

Fig. 3. Plasticity condition of maximum shearing stress for the perfectly plastic material, due to Saint Venant. k is yield stress in pure shear.

friction of the sand, $\sigma_0 = C\cot\delta$ with its cohesion C (Fig. 2), and k is the resistance of plastic flow of the perfectly plastic material, being equal to the yield stress in pure shear when the Saint Venant condition of maximum shearing stress is adopted (Fig. 3). These equations form the fundamental equations of the plane plastic flow in each case, together with the equation of equilibrium

$$\partial\sigma_x/\partial x + \partial\tau_{xy}/\partial y = 0, \quad \partial\tau_{xy}/\partial x + \partial\sigma_y/\partial y = 0, \tag{3.6}$$

where the weight of the sand is neglected.

Now we let the velocity of our hypothetical gas flow correspond to the plastic state of stress by the following relations:

$$q/q_* = [(\sigma_0 - \sigma_*)/(\sigma_0 - \sigma)]^{(1-\gamma)/(2\gamma)},$$

$$\left\{\begin{array}{ll} \theta = \alpha_1, \ \gamma = -\sin\delta, & (3.7) \\ \text{or} & \\ \theta = \alpha_2, \ \gamma = \sin\delta, & (3.8) \end{array}\right.$$

for the gas of the first kind, and

$$q/q_* = \exp[(\sigma - \sigma_*)/(2\kappa)],$$

$$\left\{\begin{array}{ll} \theta = \alpha_1, \ \kappa = -k, & (3.7') \\ \text{or} & \\ \theta = \alpha_2, \ \kappa = k, & (3.8') \end{array}\right.$$

for the gas of the second kind, where θ is the angle which the gas velocity makes with the x-axis. Then, it will be seen after some calculations that the fundamental equations of the plastic flow become the equation of continuity and irrotationality of our gas flows

$$\frac{\partial}{\partial x}\left(\frac{\rho}{\rho_*}u\right) + \frac{\partial}{\partial y}\left(\frac{\rho}{\rho_*}u\right) = 0, \quad \frac{\partial v}{\partial x} = \frac{\partial u}{\partial y}, \tag{3.9}$$

u and v being the rectangular components of the gas velocity in the hodograph plane

$$u = q\cos\theta, \quad v = q\sin\theta. \tag{3.10}$$

The fundamental equations of the gas flow (3.9) show the existence of the velocity potential Φ and the stream function Ψ, which are defined by the following equations:

$$\left.\begin{array}{l} u = \partial\Phi/\partial x, \ v = \partial\Phi/\partial y, \ u = (\rho_*/\rho)(\partial\Psi/\partial y), \\ v = -(\rho_*/\rho)(\partial\Psi/\partial x). \end{array}\right\} \tag{3.11}$$

§ 4. Application of the Hodograph Method

When we go over to the hodograph plane, taking q and θ as independent variables, we have the fundamental equations of the hodograph method as follows:

$$dx + i\,dy \equiv dz = q^{-1}e^{i\theta}[d\Phi + i(\rho_*/\rho)d\Psi], \tag{4.1}$$

$$\frac{\partial\Phi}{\partial q} = q\frac{d}{dq}\left(\frac{\rho_*}{q\rho}\right)\frac{\partial\Psi}{d\theta}, \quad \frac{\partial\Phi}{\partial\theta} = q\frac{\rho_*}{\rho}\frac{\partial\Psi}{\partial q}, \tag{4.2}$$

which can be simplified by taking a dimensionless variable $t \equiv \rho/\rho_*$ as an independent variable in place of q:

$$t = 2(1-\gamma)^{-1}\int_q^\infty (\rho/\rho_*)dq/q = (q_*/q)^{2/(1-\gamma)}, \tag{4.3}$$

$$= [(\sigma_0 - \sigma)/(\sigma_0 - \sigma_*)]^{1/\gamma},$$

for the gas of the first kind, (4.4)

$$= \exp[(\sigma_* - \sigma)/\kappa],$$

for the gas of the second kind, (4.4′)

and become

$$dz = q_*^{-1}t^{(1-\gamma)/2}e^{i\theta}[d\Phi + it^{-1}d\Psi]$$

$$= q_*^{-1}t^{(1-\gamma)/2}[\cos\theta\, d\Phi - t^{-1}\sin\theta\, d\Psi$$

$$+ i(\sin\theta\, d\Phi + t^{-1}\cos\theta\, d\Psi)], \tag{4.5}$$

$$\left.\begin{array}{l} \partial\Phi/\partial\theta = -2(1-\gamma)^{-1}\partial\Psi/\partial t, \\ \partial\Phi/\partial t = -2^{-1}(1-\gamma)K\partial\Psi/\partial\theta, \end{array}\right\} \tag{4.6}$$

with

$$\left.\begin{array}{l} K = [(q/c)^2 - 1](\rho_*/\rho)^2 = \mu^2 t^{-2}, \\ \mu = (1+\gamma)^{1/2}(1-\gamma)^{-1/2}, \end{array}\right\} \tag{4.7}$$

for the gas of the first kind. Equations for the gas of the second kind will be omitted to avoid unnecessary complexity, because they can readily be obtained by putting $\gamma = 0$ formally in the equations for the gas of the first kind. By eliminating Φ from (4.6) we obtain the hodograph equation as follows;

$$4t^2\partial^2\Psi/\partial t^2-(1-\gamma^2)\partial^2\Psi/\partial\theta^2=0\,. \qquad (4.8)$$

A general solution of this equation can be obtained by separation of the variables to give

$$\Psi=\sum_n T_n(t)\left(A_n\cos\frac{n\theta}{\sqrt{1-\gamma^2}}+B_n\sin\frac{n\theta}{\sqrt{1-\gamma^2}}\right), \qquad (4.9)$$

where n, A_n, B_n are arbitrary constants and $T_n(t)$ is the solution of the ordinary differential equation

$$4t^2d^2T_n/dt^2+n^2T=0\,, \qquad (4.10)$$

and is given by

$$\left.\begin{aligned}&T_1=t^{1/2}(a_1+b_1\log t)\,,\\&T_n=t^{1/2}(a_nt^{\sqrt{1-n^2}/2}+b_nt^{-\sqrt{1-n^2}/2})\,,\\&\quad\text{for } n<1\,,\\&T_n=t^{1/2}[a_n\cos\{(\sqrt{n^2-1}/2)\log t\}\\&\quad+b_n\sin\{(\sqrt{n^2-1}/2)\log t\}]\,,\\&\quad\text{for } n>1\,,\end{aligned}\right\} \qquad (4.11)$$

with arbitrary constants a_n and b_n. Therefore, the general solution of the hodograph equation can be written as follows:

$$\begin{aligned}\Psi=\,&t^{1/2}(a_1+b_1\log t)\\&\times\left(A_1\cos\frac{\theta}{\sqrt{1-\gamma^2}}+B_1\sin\frac{\theta}{\sqrt{1-\gamma^2}}\right)\\&+t^{1/2}\sum_{n<1}(a_nt^{\sqrt{1-n^2}/2}+b_nt^{-\sqrt{1-n^2}/2})\\&\times\left(A_n\cos\frac{n\theta}{\sqrt{1-\gamma^2}}+B_n\sin\frac{n\theta}{\sqrt{1-\gamma^2}}\right)\\&+t^{1/2}\sum_{n>1}[a_n\cos\{(\sqrt{n^2-1}/2)\log t\}\\&+b_n\sin\{(\sqrt{n^2-1/2}\log t\}]\\&\times\left(A_n\cos\frac{n\theta}{\sqrt{1-\gamma^2}}+B_n\sin\frac{n\theta}{\sqrt{1-\gamma^2}}\right),\end{aligned} \qquad (4.12)$$

for the gas of the first kind, and

$$\begin{aligned}\Psi=\,&t^{1/2}(a_1+b_1\log t)(A_1\cos\theta+B_1\sin\theta)\\&+t^{1/2}\sum_{n<1}(a_nt^{\sqrt{1-n^2}/2}+b_nt^{-\sqrt{1-n^2}/2})\\&\times(A_n\cos n\theta+B_n\sin n\theta)\\&+t^{1/2}\sum_{n>1}[a_n\cos\{(\sqrt{n^2-1}/2)\log t\}\\&+b_n\sin\{(\sqrt{n^2-1}/2)\log t\}]\\&\times(A_n\cos n\theta+B_n\sin n\theta)\,,\end{aligned} \qquad (4.12')$$

for the gas of the second kind.

The remaining procedure of the hodograph method is to get $\partial\Psi/\partial t$ and $\partial\Psi/\partial\theta$ by differentiating (4.12), to find $\partial\Phi/\partial t$ and $\partial\Phi/\partial\theta$ by making use of (4.6), to substitute these values into (4.5), and finally to obtain x and y as functions of t and θ by integration as follows:

$$x=x(t,\theta)\,,\quad y=y(t,\theta)\,.$$

After obtaining equations for the gas of the second kind by putting $\gamma=0$ formally in those for the gas of the first kind, we can write the plastic state of stress in the mass of sand and in the perfectly plastic material by making use of (3.7) or (3.8), and (3.7′) or (3.8′) respectively in the following form:

$$x=x(\sigma,\alpha),\quad y=y(\sigma,\alpha)\,,$$

where α represents either α_1 or α_2. Besides, lines of maximum and minimum principal stresses are given by $\Psi[\sigma(x,y),\ \alpha(x,y)]=\text{const.}$ and $\Phi[\sigma(x,y),\ \alpha(x,y)]=\text{const.}$ respectively, when the velocity-stress correspondence (3.7) or (3.7′) are adopted, and inversely, when (3.8) or (3.8′) are done.

For example, a stream function Ψ, which includes only t or θ, gives a circulatory or a radial flow, respectively. When we put all the constants in (4.12) and (4.12′) zero, except a_1 and A_1 or a_1 and B_1, we get a state of stress in a plastic mass pressed between two rough parallel plates, as will be seen in the following part (II) of this paper.

To conclude this section, we must remark that the one-to-one correspondence between points in the physical and hodograph planes fails when the following Jacobian J of the hodograph transformation becomes zero or infinity:

$$\begin{aligned}J=\,&\frac{\partial(x,y)}{\partial(u,v)}\\=\,&-\frac{1}{\rho_*{}^2q_*{}^4}\left(\frac{q}{q_*}\right)^{2(\mu^2-1)}\left[\left(q\frac{\partial\Psi}{\partial q}\right)^2-\left(\mu\frac{\partial\Psi}{\partial\theta}\right)^2\right],\end{aligned} \qquad (4.13)$$

for the gas of the first kind, and

$$J=-\frac{1}{\rho_*{}^2q_*{}^4}\left[\left(q\frac{\partial\Psi}{\partial q}\right)^2-\left(\frac{\partial\Psi}{\partial\theta}\right)^2\right] \qquad (4.13')$$

for the gas of the second kind.

§ 5. Slip Lines

In this section we want to introduce new variables, suggested by the W. K. B. method, and rewrite the fundamental equations of the hodograph method.

When we introduce a new variable ω defined as

$$\omega=2^{-1}(1-\gamma)\int_1^t K^{1/2}dt=2^{-1}(1-\gamma^2)^{1/2}\log t$$

$$=\mu\log(q_*/q) \qquad (5.1)$$

$$=[(1-\gamma^2)^{1/2}/(2\gamma)]\log[(\sigma_0-\sigma)/(\sigma_0-\sigma_*)],$$

for the gas of the first kind, (5.2)

$$=(\sigma_*-\sigma)/(2\kappa),$$

for the gas of the second kind, (5.2′)

(4.6) becomes

$$\partial\Phi/\partial\omega=-K^{1/2}\partial\Psi/\partial\theta,\quad \partial\Phi/\partial\theta=-K^{1/2}\partial\Psi/\partial\omega, \qquad (5.3)$$

which can be further transformed by making use of

$$\phi=K^{-1/4}\Phi,\quad \psi=-K^{1/4}\Psi, \qquad (5.4)$$

into

$$\left.\begin{aligned}\partial\phi/\partial\omega-\partial\psi/\partial\theta&=(1-\gamma^2)^{-1/2}\phi,\\ \partial\phi/\partial\theta-\partial\psi/\partial\omega&=(1-\gamma^2)^{-1/2}\psi.\end{aligned}\right\} \qquad (5.5)$$

The characteristics of these simultaneous equations are given by

$$\omega\pm\theta=\text{const.}, \qquad (5.6)$$

which can be written by making use of (3.7), (3.8), (5.2) or (3.7′), (3.8′), (5.2′) as follows:

$$\left.\begin{aligned}&(\sigma_0-\sigma)e^{\pm2(\tan\delta)\alpha_1}=\text{const.},\\ \text{or}\quad &(\sigma_0-\sigma)e^{\mp2(\tan\delta)\alpha_2}=\text{const.},\end{aligned}\right\} \qquad (5.7)$$

for the mass of sand, or

$\sigma\pm2k\alpha_1=\text{const.}$, or $\sigma\mp2k\alpha_2=\text{const.}$, (5.7′)
for the perfectly plastic material**.

When we take $\xi=\omega+\theta$ and $\eta=\omega-\theta$ as independent variables in (5.3), we have

$$\partial\Phi/\partial\xi=-K^{1/2}\partial\Psi/\partial\xi,\ \partial\Phi/\partial\eta=K^{1/2}\partial\Psi/\partial\eta. \qquad (5.8)$$

Hence (4.1) can be written as follows:

$$dz=\frac{\rho_*}{\rho q}e^{i\theta}\left[-(\mu-i)\frac{\partial\Psi}{\partial\xi}d\xi+(\mu+i)\frac{\partial\Psi}{\partial\eta}d\eta\right]$$

$$=\frac{\rho_*}{\rho c}e^{i\theta}\left(e^{iA}\frac{\partial\Psi}{\partial\eta}d\eta-e^{-iA}\frac{\partial\Psi}{\partial\xi}d\eta\right), \qquad (5.9)$$

where $A=\cot^{-1}\mu$ is the Mach angle, which becomes $\pi/4+\delta/2$, when the correspondence (3.7) is adopted, or $\pi/4-\delta/2$, when (3.8) is done, for the mass of sand, and $\pi/4$ for the perfectly plastic material. Therefore, the two families of slip lines in the physical plane, $C_+:\ \xi=\text{const.}$ and $C_-:\ \eta=\text{const.}$, are respectively given by

$$C_+:\ dz=c_*^{-1}e^{i[\alpha_1+(\pi/4)+\delta/2]}\left(\frac{\sigma}{\sigma_*}\right)^{\frac{1-\sin\delta}{2\sin\delta}}\frac{\partial\Psi}{\partial\eta}d\eta,$$

$$C_-:$$

$$dz=-c_*^{-1}e^{i[\alpha_1-(\pi/4)-\delta/2]}\left(\frac{\sigma}{\sigma_*}\right)^{\frac{1-\sin\delta}{2\sin\delta}}\frac{\partial\Psi}{\partial\xi}d\xi,$$

or

$$C_+:\ dz=c_*^{-1}e^{i[\alpha_2+(\pi/4)-\delta/2]}\left(\frac{\sigma_*}{\sigma}\right)^{\frac{1+\sin\delta}{2\sin\delta}}\frac{\partial\Psi}{\partial\eta}d\eta,$$

$$C_-:$$

$$dz=-c_*^{-1}e^{i[\alpha_2-(\pi/4)+\delta/2]}\left(\frac{\sigma_*}{\sigma}\right)^{\frac{1+\sin\delta}{2\sin\delta}}\frac{\partial\Psi}{\partial\xi}d\xi, \qquad (5.10)$$

for the mass of sand, and

$$C_+:\ dz=c_*^{-1}e^{(\sigma_*-\sigma)/(2k)+i[\alpha_1+(\pi/4)]}\frac{\partial\Psi}{\partial\eta}d\eta,$$

$$C_-:\ dz=-c_*^{-1}e^{(\sigma_*-\sigma)/(2k)+i[\alpha_1-(\pi/4)]}\frac{\partial\Psi}{\partial\xi}d\xi,$$

or

$$C_+:\ dz=c_*^{-1}e^{(\sigma-\sigma_*)/(2k)+i[\alpha_2+(\pi/4)]}\frac{\partial\Psi}{\partial\eta}d\eta,$$

$$C_-:\ dz=-c_*^{-1}e^{(\sigma-\sigma_*)/(2k)+i[\alpha_2-(\pi/4)]}\frac{\partial\Psi}{\partial\xi}d\xi, \qquad (5.10')$$

for the perfectly plastic material.

§ 6. Simple Waves

If a certain region D in the physical x, y plane represents a straight line $\eta=$ const. in the ξ, η plane, a family of slip lines $\xi=$const. becomes one of straight lines in this region D, and is called simple waves. Let an equation of these simple waves be

$$\left.\begin{aligned}x&=a(\lambda)+s\cos\beta_1(\lambda),\\ y&=b(\lambda)+s\sin\beta_1(\lambda),\end{aligned}\right\} \qquad (6.1)$$

where λ is a parameter, and s is an abscissa on a simple wave $\lambda=$ const. (Fig. 4). The mean normal stress σ becomes in the region D, from (5.7),

$$\sigma=(\text{const.})e^{2(\tan\delta)\alpha_1}+\text{const.}, \qquad (6.2)$$

for the mass of sand, or, from (5.7′),

$$\sigma=2k\alpha_1+\text{const.}, \qquad (6.2')$$

for the perfectly plastic material.

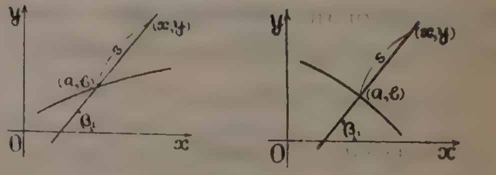

(a) (b)

Fig. 4. Simple waves, (a) in the mass of sand, and (b) in the perfectly plastic material.

** According as we adopt whether the upper or lower sign, we obtain the equation of so-called first (Γ_+) or second (Γ_-) slip lines in the stress plane, when (3.7) or (3.7′) is used, and inversely, when (3.8) or (3.8′) is done.

When an arbitrary one of the isostatics in the region D is given by

$$x=a(\lambda), \quad y=b(\lambda), \tag{6.3}$$

with a parameter λ, it will readily be seen that the other ones of the same family are

$$\left.\begin{aligned} x&=a(\lambda)+S\exp[(\tan\delta-\sec\delta)\beta_1(\lambda)]\cos\beta_1(\lambda),\\ y&=b(\lambda)+S\exp[(\tan\delta-\sec\delta)\beta_1(\lambda)]\sin\beta_1(\lambda),\end{aligned}\right\} \tag{6.4}$$

for the mass of sand, and

$$\left.\begin{aligned} x&=a(\lambda)+S\exp[-\beta_1(\lambda)]\cos\beta_1(\lambda),\\ y&=b(\lambda)+S\exp[-\beta_1(\lambda)]\sin\beta_1(\lambda),\end{aligned}\right\} \tag{6.4'}$$

for the perfectly plastic material, where S is an arbitrary constant.

Moreover, the following two properties of the simple waves will easily be verified:

1) in the region D, mean normal stress is expressed by

$$\sigma=(\text{const.})s^{-2}, \tag{6.5}$$

along cross slip lines in the mass of sand, and distances between two arbitrary cross slip lines measured along simple waves, which cut them orthogonally, are constant in the perfectly plastic material,

2) the stream function Ψ is given by, with a constant initial value Ψ_0,

$$\Psi=\Psi_0+(\text{const.})\,\sigma^{\pm 1/(2\sin\delta)}, \tag{6.6}$$

in the mass of sand, or

$$\Psi=\Psi_0+(\text{const.})\,e^{\pm\sigma/(2k)}, \tag{6.6'}$$

in the perfectly plastic material, along cross slip lines in the interior of the centered simple waves, and, on the contrary, if Ψ can be expressed by this equation, the simple waves are centered. These relations are particularly useful when problems of reflection and interference of the simple waves are considered.

§ 7. Shocks

Since the flow of our hypothetical gases are everywhere supersonic, it may be inferred that a shock occurs when a large disturbance happens to appear. Therefore, we may safely conclude that a plastic state of stress with shocks is more natural than the one without shocks, and still further we can determine a shock condition, which has been obtained for a real gas, obeying the adiabatic law, by conditions of conservation of mass, momentum, and energy in the gas passing across a shock, because it is justifiable to maintain these conditions must be kept for our hypothetical gases. Detailed discussions of plastic states of stress with shocks will be reported in our forthcoming paper.

§ 8. Extension of the Analogy to a Body of Revolution

It will be justifiable to state that in a plastic mass of revolution a principal stress, directed perpendicularly to a meridian plane, is equal to the smaller or greater one of the two principal stresses, lying in the meridian plane, according as the mass is in a compressed state or in an expanded one, that is, the inner pressure is smaller or greater than the outer one. When we take the x-axis as the axis of symmetry and the x, y plane as the meridian plane, a steady, axially symmetrical, irrotational flow of our hypothetical gases also represents a plastic state of stress in the mass of sand or in the perfectly plastic material, equations of correspondence of velocity to stress being (3.7) or (3.7′) in the compressed mass and (3.8) or (3.8′) in the expanded mass. Therefore, a plastic state of stress in a body of revolution can be replaced by an axially symmetrical flow of our hypothetical gases.

The fundamental equations of the axially symmetrical gas flow are

$$\left.\begin{aligned} u&=\partial\Phi/\partial x, & v&=\partial\Phi/\partial y,\\ u&=y(\rho_*/\rho)\partial\Psi/\partial y, & v&=-y(\rho_*/\rho)\partial\Psi/\partial x,\end{aligned}\right\} \tag{8.1}$$

but exact solutions of these nonlinear equations have never been obtained except those of centered simple waves and of centered straight isostatics⁷⁾.

§ 9. Acknowledgement

In conclusion, the author wishes to express his deep gratitude to Prof. S. Tomotika of Kyoto University, for his kind guidance and encouragement.

References

1) N. Inoue: J. Phys. Soc. Japan **7** (1952) 119.
2) N. Inoue: J. Phys. Soc. Japan **6** (1951) 460.
3) N. Inoue: Doshisha Engineering Review **2** (1951) 1, (in Japanese).
4) N. Inoue: J. Phys. Soc. Japan **7** (1952) 518.
5) S. A. Chaplygin: Scientific Memoirs, Moscow Univ. Math. Phys. Sec., **21** (1904) 1.
6) I. Imai: J. Math. Phys. **28** (1949) 173.
7) N. Inoue: J. Phys. Soc. Japan **7** (1952) 512.

JOURNAL OF THE PHYSICAL SOCIETY OF JAPAN Vol. 7, No. 6 NOV.—DEC., 1952

Application of Gasdynamical Method to Soil Mechanics and Theory of Plasticity (II)

By Nobuo INOUE

Faculty of Engineering, Doshisha University, Kyoto

(Read April 3, 1952; Received May 29, 1952)

The new method of solving the isostatical problem in the soil mechanics and theory of plasticity, which has been developed in the part (I) of this paper, is applied to practical problems, resulting in a demonstration of several plastic states of stress, slip lines, and isostatics.

There are illustrated, with mathematical expressions, figures, and photographs, slip lines on surface of a metal or soil produced by forcing a cylindrical punch into it, those in a plastic mass pressed between two rough parallel or inclined plates, regular markings on face of compressed prism of paraffin, and spiral cracks in safety glass disks broken under a concentrated load, etc.

§1. Introduction and Summary

Since the hodograph equation for our hypothetical gas has been established and its general solution has been obtained in the part (I) of this paper, we are now in a position to be able to get every plastic state of stress in the mass of sand or in the perfectly plastic material, by superposing some of the particular solution so far sobtained. In this paper, however, we want to show several plastic states of stress, which can be obtained by solving the hodograph equation (4. 8) in the part (I) exactly.

It is well known that slip lines are sometimes visible, without any artifice, on the surface of a body subjected to plastic flow, or in other cases they can be brought out by etching, and so several photographs of slip lines are used, in this paper, for the purpose of illustrating gas flows or plastic states of stress here obtained.

On the other hand, the photograph of spiral cracks in safety glass disks is used here to show a figure of a family of stream lines and equipotential lines or isostatics, because its fracture in this case is a cleavage and it is believed that the orientation of the cleavage surface is perpendicular to the largest tensile principal stress.

§2. Exact Solutions

The fundamental equation (4. 8) in the part (I) of this paper can be solved exactly by assuming $\Psi(t, \theta)$ in the following forms:

(a) $\Psi=T(t)$, (b) $\Psi=\Theta(\theta)$,
(c) $\Psi=T(t)+\Theta(\theta)$, (d) $\Psi=T(t)\Theta(\theta)$,

where $T(t)$ and $\Theta(\theta)$ are functions of t and θ only respectively.

(a) $\Psi=T(t)$. in this case Eq. (4. 8) becomes

$$d^2T/dt^2=0\,,$$

which can be integrated immediately to give

$$\Psi=C_1t+C_2\,,$$

where C_1 and C_2 are arbitrary constants. Starting with this Ψ, making use of (4. 5)* and (4. 6), and integrating, we obtain finally

$$\left.\begin{aligned} x&=-[2C_1/\{q_*(1-\gamma)\}]t^{(1-\gamma)/2}\sin\theta+D_1\,,\\ y&=[2C_1/\{q_*(1-\gamma)\}]t^{(1-\gamma)/2}\cos\theta+D_2\,,\end{aligned}\right\}\tag{2. 1}$$

where D_1 and D_2 are arbitrary constants. Choosing $C_1=q_*(1-\gamma)/2$, $D_1=D_2=0$, and making use of (4. 3), a circulating flow with the following speed around a cylinder having an arbitrary radius and its centre at the origin can be obtained:

$$q=q_*r^{-1}\tag{2. 2}$$

(Fig. 1). If the gas flows are translated into the plastic states of stress, we obtain, by making use of (3. 7) and (4. 4) or (3. 7′) and (4. 4′),

$$\left.\begin{aligned} \sigma_r&=\sigma_0-(\sigma_0-\sigma_*)(1+\sin\delta)r^{-2\sin\delta/(1+\sin\delta)}\,,\\ \sigma_t&=\sigma_0-(\sigma_0-\sigma_*)(1-\sin\delta)r^{-2\sin\delta/(1+\sin\delta)}\,,\\ \tau_{rt}&=0\,,\end{aligned}\right\}\tag{2. 3}$$

---

* When equation numbers with their head number greater than 2 are referred to, it is to be understood, in the following, that they indicate those equations which have been shown in the part (I) of this paper.

in the mass of sand, or

$$\left.\begin{aligned} \sigma_r &= \sigma_* - k + 2k\log r, \\ \sigma_t &= \sigma_* + k + 2k\log r, \\ \tau_{rt} &= 0\ , \end{aligned}\right\} \quad (2.\,3')$$

in the perfectly plastic material. It need scarcely be mentioned that lines of maximum principal stress are concentric circles with their common centre at the origin 0, and those of minimum one are a pencil of rays radiating from the origin. Further, (5. 7) yields immediately

$$\left.\begin{aligned} &C_+(\text{first slip lines}): \\ &\quad r\exp[-\{(1+\sin\delta)/\cos\delta\}\varphi] = \text{const.}, \\ &C_-(\text{second slip lines}): \\ &\quad r\exp[\{(1+\sin\delta)/\cos\delta\}\varphi] = \text{const.}, \end{aligned}\right\} \quad (2.\,4)$$

in the mass of sand, and (5. 7′) does

$$\left.\begin{aligned} &C_+: \quad r\exp(-\varphi) = \text{const.}, \\ &C_-: \quad r\exp(\varphi) = \text{const.}, \end{aligned}\right\} \quad (2.\,4')$$

in the perfectly plastic material.

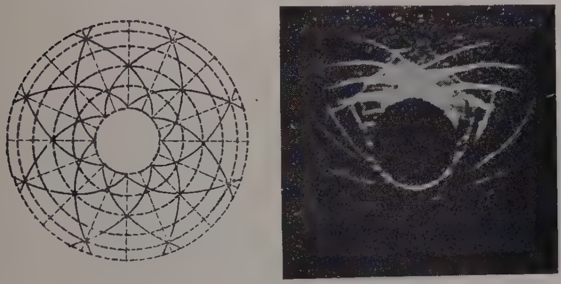
a) b)

Fig. 1. Circulating flow.

a) Supersonic flow with $M=\sqrt{2}$ of the gas obeying $p/\log\rho=$const., full lines showing Mach lines, thick broken lines stream lines, and fine broken lines equipotential lines.

b) Slip lines on surface of an iron piece produced by forcing a cylindrical punch into it.

On the contrary, if we make use of (3. 8) or (3. 8′) as the equation of velocity-stress correspondence, the plastic state of stress becomes, in the mass of sand, as follows:

$$\left.\begin{aligned} \sigma_r &= \sigma_0 - (\sigma_0 - \sigma_*)(1+\sin\delta)r^{2\sin\delta/(1-\sin\delta)}\ , \\ \sigma_t &= \sigma_0 - (\sigma_0 - \sigma_*)(1-\sin\delta)r^{2\sin\delta/(1-\sin\delta)}\ , \\ \tau_{rt} &= 0\ , \end{aligned}\right\} \quad (2.\,5)$$

while in the perfectly plastic material, as follows:

$$\left.\begin{aligned} \sigma_r &= \sigma_* + k - 2k\log r, \\ \sigma_t &= \sigma_* - k - 2k\log r, \\ \tau_{rt} &= 0\,. \end{aligned}\right\} \quad (2.\,5')$$

In this case, lines of maximum principal stress become a pencil of rays radiating from the origin, those of minimum being concentric circles with their common centre at the origin. And besides, first and second slip lines in this case are replaced by the second and first slip lines in (2. 3) and (2. 3′) respectively.

(**b**) $\Psi=\Theta(\theta)$. Eq. (4. 8) now becomes

$$d^2\Theta/d\theta^2 = 0\ ,$$

which can readily be integrated to give

$$\Psi = C_1\theta + C_2\ ,$$

where C_1 and C_2 are arbitrary constants. Starting with this Ψ, we obtain, after the same procedure as has been used in (a),

$$\left.\begin{aligned} x &= (C_1/q_*)t^{-(1+\gamma)/2}\cos\theta + D_1\ , \\ y &= (C_1/q_*)t^{-(1+\gamma)/2}\sin\theta + D_2\ , \end{aligned}\right\} \quad (2.\,6)$$

where D_1 and D_2 are arbitrary constants. When we choose $C_1=q_*$, $D_1=D_2=0$, and make use of (4. 3), we obtain the radial flow with the following speed from a source (or to a sink) at the origin:

$$q = q_* r^{(1-\gamma)/(1+\gamma)}\ , \qquad (2.7)$$

for the gas of the first kind, or

$$q = q_* r\ , \qquad (2.\,7')$$

for the gas of the second kind (Fig. 2).

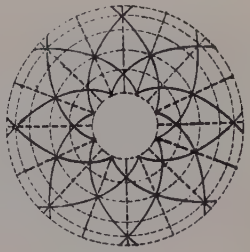

Fig. 2. Radial flow with $M=\sqrt{2}$ of the gas obeying $p/\log\rho=$const., full lines showing Mach lines, thick broken lines stream lines, and fine broken lines equipotential lines.

It will easily be seen that the plastic states of stress, obtained in this case by making use of the velocity-stress correspondences (3. 7) or (3. 7′) and (3. 8) or (3. 8′), are equivalent to those in the preceding case (a), which have been calculated by making use of (3. 8) or (3. 8′) and (3. 7) or (3. 7′) respectively.

(**ab**) Linear combination of the preceding two particular solutions. Since the fundamental equation (4. 8) is linear, we can get a new solution by forming a linear combination of the preceding two particular exact solutions. Thus,

$$\Psi=C_1t+C_2\theta+C_3\ ,$$

where C_1, C_2, and C_3 are arbitrary constants. The solution in this case can be obtained from (2.1) and (2.6) as follows:

$$\left.\begin{aligned}x&=at^{(1-\gamma)/2}\sin\theta+bt^{-(1+\gamma)/2}\cos\theta\ ,\\ y&=-at^{(1-\gamma)/2}\cos\theta+bt^{-(1+\gamma)/2}\sin\theta\ ,\end{aligned}\right\}\quad(2.8)$$

where a and b are arbitrary constants. The flow is vortical, having the speed determined by the following equation:

$$r^2=a^2(q_*/q)^2+b^2(q/q_*)^{2(1+\gamma)/(1-\gamma)}\ ,\qquad(2.9)$$

for the gas of the first kind, and

$$q^2=(r^2\pm\sqrt{r^4-4a^2b^2})/(2b^2)\ ,\qquad(2.9')$$

for the gas of the second kind.

When we use the velocity-stress correspondence (3.7), we obtain the following plastic state of stress in the mass of sand:

$$\left.\begin{aligned}\sigma_r&=\sigma_0\sin\delta\cos2\alpha_1'+(1-\sin\delta\cos2\alpha_1')\\&\qquad\times[\sigma_0-(\sigma_0-\sigma_*)\{(b/a)\tan\alpha_1'\}^{-\sin\delta}]\ ,\\ \sigma_t&=-\sigma_0\sin\delta\cos2\alpha_1'+(1+\sin\delta\cos2\alpha_1')\\&\qquad\times[\sigma_0-(\sigma_0-\sigma_*)\{(b/a)\tan\alpha_1'\}^{-\sin\delta}]\ ,\\ \tau_{rt}&=(\sigma_0-\sigma_*)\sin\delta[(b/a)\tan\alpha_1']^{-\sin\delta}\sin2\alpha_1',\\ \sin2\alpha_1'&=2abt^{\sin\delta}/r^2\ ,\\ r^2&=t^{\sin\delta}(a^2t+b^2t^{-1})\ ,\end{aligned}\right\}\quad(2.10)$$

and, if (3.7′) is employed, we obtain that in the perfectly plastic material as follows:

$$\left.\begin{aligned}\sigma_r&=\sigma_*-k[\log\{(b/a)\tan\alpha_1'\}-\cos2\alpha_1']\ ,\\ \sigma_t&=\sigma_*-k[\log\{(b/a)\tan\alpha_1'\}+\cos2\alpha_1']\ ,\\ \tau_{rt}&=k\sin2\alpha_1'\ ,\quad \sin2\alpha_1'=2ab/r^2\ .\end{aligned}\right\}\quad(2.10')$$

Slip lines of these vortical flows of the plastic masses can be given in parametric forms, as follows:

$$\left.\begin{aligned}C_+:&\left\{\begin{aligned}x&=ad^{1+\sin\delta}\exp[-\{(1+\sin\delta)/\cos\delta\}\alpha_1]\sin\alpha_1+bd^{-(1-\sin\delta)}\\&\qquad\times\exp[\{(1-\sin\delta)/\cos\delta\}\alpha_1]\cos\alpha_1\ ,\\ y&=-ad^{1+\sin\delta}\exp[-\{(1+\sin\delta)/\cos\delta\}\alpha_1]\cos\alpha_1+bd^{-(1-\sin\delta)}\\&\qquad\times\exp[\{(1-\sin\delta)/\cos\delta\}\alpha_1]\sin\alpha_1\ ,\end{aligned}\right.\\ C_-:&\left\{\begin{aligned}x&=ad^{1+\sin\delta}\exp[\{(1+\sin\delta)/\cos\delta\}\alpha_1]\sin\alpha_1+bd^{-(1-\sin\delta)}\\&\qquad\times\exp[-\{(1-\sin\delta)/\cos\delta\}\alpha_1]\cos\alpha_1\ ,\\ y&=-ad^{1+\sin\delta}\exp[\{(1+\sin\delta)/\cos\delta\}\alpha_1]\cos\alpha_1+bd^{-(1-\sin\delta)}\\&\qquad\times\exp[-\{(1-\sin\delta)/\cos\delta\}\alpha_1]\sin\alpha_1\ ,\end{aligned}\right.\end{aligned}\right\}\quad(2.11)$$

in the mass of sand, where d is constant along each one of the slip lines, and those in the perfectly plastic material can be obtained by putting $\delta=0$ in (2.11). It will readily be seen that the slip lines have, as their envelope, a circle with its radius $\sqrt{ab}$ and its centre at the origin (Fig. 3).

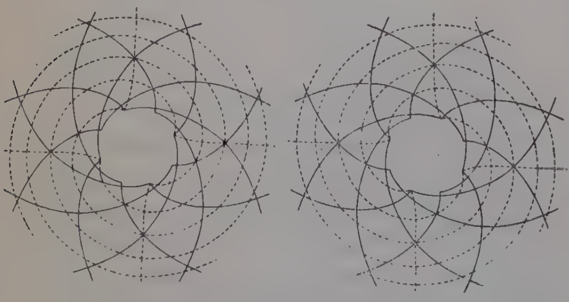

Fig. 3. Mach lines or slip lines (full lines) and a family of stream lines and equipotential lines or isostatics (broken lines) of the vortical flow in the gas obeying $p/\log\rho=$const., or in the perfectly plastic material obeying $\tau=k$, turning left (the left figure) and right (the right figure) respectively.

On the contrary, if we use (3.8) as the velocity-stress correspondence, plastic states of stress and their slip lines for this case can be obtained by changing the sign of δ and replacing α_1 or α_1' by α_2 or α_2' in (2.10), (2.10′), and (2.11).

(**c**) $\Psi=T(t)+\Theta(\theta)$. Inserting this Ψ into (4.8), we obtain the following integral:

$$\Psi=-(C_1/4)\log t+[C_1/\{2(1-\gamma^2)\}]\theta^2\\ +C_2t+C_3\theta+C_4\ .$$

When we choose $C_2=C_3=C_4=0$, the hodograph method yields the solution as follows:

$$\left.\begin{aligned}x&=\frac{C_1}{q_*}t^{-(1+\gamma)/2}\left[\frac{\sin\theta}{2(1-\gamma)}-\frac{\sin\theta-\theta\cos\theta}{1-\gamma^2}\right]+D_1\ ,\\ y&=\frac{C_1}{q_*}t^{-(1+\gamma)/2}\left[-\frac{\cos\theta}{2(1-\gamma)}+\frac{\cos\theta+\theta\sin\theta}{1-\gamma^2}\right]+D_2\ ,\end{aligned}\right|\quad(2.12)$$

from which the following plastic states of stress can be obtained, by making use of (3.7) and taking $C_1=2q_*$, $D_1=D_2=0$:

$$\left.\begin{aligned} \sigma_r&=\sigma_0-(\sigma_0-\sigma_*)[(1-\sin\delta)\,r\sin\alpha_1']^{2\sin\delta/(1-\sin\delta)}(1-\sin\delta\cos 2\alpha_1')\,,\\ \sigma_t&=\sigma_0-(\sigma_0-\sigma_*)[(1-\sin\delta)\,r\sin\alpha_1']^{2\sin\delta/(1-\sin\delta)}(1+\sin\delta\cos 2\alpha_1')\,,\\ \tau_{rt}&=(\sigma_0-\sigma_*)\sin\delta[(1-\sin\delta)\,r\sin\alpha_1']^{2\sin\delta/(1-\sin\delta)}\sin 2\alpha_1'\,,\\ \tan\alpha_1'&=-(1+\sin\delta)/(2\alpha_1)\,, \end{aligned}\right\} \qquad (2.13)$$

in the mass of sand, and, by making use of (3.7′),

$$\left.\begin{aligned} \sigma_r&=\sigma_*-k\log r^2\sin^2\alpha_1'+k\cos 2\alpha_1'\,, &\quad \sigma_t&=\sigma_*-k\log r^2\sin^2\alpha_1'-k\cos 2\alpha_1'\,,\\ \tau_{rt}&=k\sin 2\alpha_1'\,, & \tan\alpha_1'&=-1/(2\alpha_1)\,, \end{aligned}\right\} \qquad (2.13')$$

in the perfectly plastic material.

Slip lines of this state of stress in the wedge-shaped plastic mass of sand are

$$\left.\begin{aligned} C_+:&\ \begin{cases} x=de^{\alpha_1/\cos\delta}\left[\dfrac{\sin\alpha_1}{2(1+\sin\delta)}-\dfrac{\sin\alpha_1-\alpha_1\cos\alpha_1}{\cos^2\delta}\right],\\ y=de^{\alpha_1/\cos\delta}\left[\dfrac{-\cos\alpha_1}{2(1+\sin\delta)}+\dfrac{\cos\alpha_1+\alpha_1\sin\alpha_1}{\cos^2\delta}\right], \end{cases}\\ C_-:&\ \begin{cases} x=de^{-\alpha_1/\cos\delta}\left[\dfrac{\sin\alpha_1}{2(1+\sin\delta)}-\dfrac{\sin\alpha_1-\alpha_1\cos\alpha_1}{\cos^2\delta}\right],\\ y=de^{-\alpha_1/\cos\delta}\left[\dfrac{-\cos\alpha_1}{2(1+\sin\delta)}+\dfrac{\cos\alpha_1+\alpha_1\sin\alpha_1}{\cos^2\delta}\right], \end{cases} \end{aligned}\right\} \qquad (2.14)$$

where d is a constant along each one of the slip lines, and those in the perfectly plastic material can be obtained by putting $\delta=0$ in (2.14). Two inclined straight lines, which the two families of slip lines have as their envelope, and at an angle of $\{\pi/2-\delta-1\}$ in the mass of sand, and at an angle of $\{\pi/2-1\}$ in the perfectly plastic material (Fig. 4).

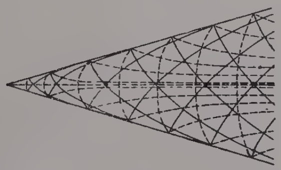

Fig. 4. Mach lines or slip lines (full lines) and a family of stream lines and equipotential lines or isostatics (broken lines) in the gas flow obeying $p/\log\rho=$const., through channels, or in the perfectly plastic material obeying $\tau=k$, pressed between two rigid plates inclined at an angle of about 32°42′ (passive plastic state).

There is no doubt that we can discuss the case where the velocity-stress correspondence (3.8) is used in the same way as before.

(**d**) $\Psi=T(t)\Theta(\theta)$. Substituting this Ψ into (4.8), we obtain

$$(4t^2/T)d^2T/dt^2-[(1-\gamma^2)/\Theta]d^2\Theta/d\theta^2=0\,.$$

The first term on the left-hand side depends on t along, while the second on θ alone, and therefore the following relation must hold:

$$(4t^2/T)d^2T/dt^2=[(1-\gamma^2)/\Theta]d^2\Theta/d\theta^2=\lambda\,, \qquad (2.15)$$

with a constant λ. The solutions of this equation can be classified into the following two cases.

(**d. 1**) Let us now consider a case where λ is negative and assume that $\lambda=-n^2$, with a real constant n, and discuss the solution of (4.8) separately according as n is greater or smaller than, or equal to, unity.

(**d. 1–1**) When $n=1$, the solution of (4.8) is given by

$$\Psi=t^{1/2}(a_1+b_1\log t)[A_1\cos(\theta/\sqrt{1-\gamma^2})+B_1\sin(\theta/\sqrt{1-\gamma^2})]\,, \qquad (2.16)$$

as has been seen in (4.12).

If we put

$$b_1=A_1=0\,,\quad a_1B_1=C_1\,,$$

we have

$$\Psi=C_1t^{1/2}\sin(\theta/\sqrt{1-\gamma^2})\,, \qquad (2.17)$$

for the gas of the first kind, or

$$\Psi=C_1t^{1/2}\sin\theta\,, \qquad (2.17')$$

for the gas of the second kind, where C_1 is an arbitrary constant. The hodograph method yields for this Ψ the following solution, with arbitrary constants D_1 and D_2:

$$\left.\begin{aligned} x&=[C_1/(\gamma q_*)]^{-\gamma/2}[\{(1+\gamma)/(1-\gamma)\}^{1/2}\cos\theta\\ &\quad\times\cos(\theta/\sqrt{1-\gamma^2})+\sin\theta\sin(\theta/\sqrt{1-\gamma^2})]\\ &\quad+D_1\,,\\ y&=[C_1/(\gamma q_*)]t^{-\gamma/2}[\{(1+\gamma)/(1-\gamma)\}^{1/2}\sin\theta\\ &\quad\times\cos(\theta/\sqrt{1-\gamma^2})-\cos\theta\sin(\theta/\sqrt{1-\gamma^2})]\\ &\quad+D_2\,, \end{aligned}\right| \qquad (2.18)$$

in the mass of sand, or

$$\left.\begin{aligned} x&=[C_1/(2q_*)](-\log t+\cos 2\theta)+D_1\,, \\ y&=[C_1/(2q_*)]\sin 2\theta+D_2\,, \end{aligned}\right\} \quad (2.\,18')$$

in the perfectly plastic material. If we take $C_1=-2q_*a$, $D_1=D_2=0$, with an arbitrary constant a, and make use of (4. 3), we obtain the flow of the gas of the second kind through channel with the following speed:

$$q/q_*=\exp[-x/(2a)\mp\{1-(y/a)^2\}/2\,, \quad (2.\,19)$$

where the upper sign of the double signs is to be taken when $0\leqq\theta\leqq\pi/4$ and $3\pi/4\leqq\theta\leqq\pi$, while the lower one when $\pi/4\leqq\theta\leqq3\pi/4$. If we translate the gas flow into plastic states of stress, we obtain those in the plastic mass pressed between two rough parallel plates, by making use of (3. 7′), as follows:

$$\left.\begin{aligned} x&=\frac{2a}{\sin\delta}\left(\frac{\sigma_0-\sigma}{\sigma_0-\sigma_*}\right)^{-1/2}\left(\sqrt{\frac{1-\sin\delta}{1+\sin\delta}}\cos\alpha_1\cos\frac{\alpha_1}{\cos\delta}+\sin\alpha_1\sin\frac{\alpha_1}{\cos\delta}\right), \\ y&=\frac{2a}{\sin\delta}\left(\frac{\sigma_0-\sigma}{\sigma_0-\sigma_*}\right)^{-1/2}\left(\sqrt{\frac{1-\sin\delta}{1+\sin\delta}}\sin\alpha_1\cos\frac{\alpha_1}{\cos\delta}-\cos\alpha_1\sin\frac{\alpha_1}{\cos\delta}\right), \end{aligned}\right\} \quad (2.\,20)$$

in the mass of sand, or

$$\sigma_x=\sigma_*+(k/a)x\pm2k\sqrt{1-(y/a)^2}\,, \quad \sigma_y=\sigma_*+(k/a)x\,, \quad \tau_{xy}=-(k/a)y\,, \qquad (2.\,20')$$

in the perfectly plastic material. Also, the slip lines of this state of stress can be given in parametric forms as follows:

$$\left.\begin{aligned} C_+:&\left\{\begin{aligned} x&=de^{(\tan\delta)\alpha_1}\left(\sqrt{\frac{1-\sin\delta}{1+\sin\delta}}\cos\alpha_1\cos\frac{\alpha_1}{\cos\delta}+\sin\alpha_1\sin\frac{\alpha_1}{\cos\delta}\right), \\ y&=de^{(\tan\delta)\alpha_1}\left(\sqrt{\frac{1-\sin\delta}{1+\sin\delta}}\sin\alpha_1\cos\frac{\alpha_1}{\cos\delta}-\cos\alpha_1\sin\frac{\alpha_1}{\cos\delta}\right), \end{aligned}\right. \\ C_-:&\left\{\begin{aligned} x&=de^{-(\tan\delta)\alpha_1}\left(\sqrt{\frac{1-\sin\delta}{1+\sin\delta}}\cos\alpha_1\cos\frac{\alpha_1}{\cos\delta}+\sin\alpha_1\sin\frac{\alpha_1}{\cos\delta}\right), \\ y&=de^{-(\tan\delta)\alpha_1}\left(\sqrt{\frac{1-\sin\delta}{1+\sin\delta}}\sin\alpha_1\cos\frac{\alpha_1}{\cos\delta}-\cos\alpha_1\sin\frac{\alpha_1}{\cos\delta}\right), \end{aligned}\right. \end{aligned}\right\} \quad (2.\,21)$$

in the mass of sand, or

$$\left.\begin{aligned} C_+:&\quad x=a(2\alpha_1+\cos 2\alpha_1)+\text{const.}\,, \quad y=a\sin 2\alpha_1\,, \\ C_-:&\quad x=-a(2\alpha_1-\cos 2\alpha_1)+\text{const.}\,, \quad y=a\sin 2\alpha_1\,, \end{aligned}\right\} \quad (2.\,21')$$

in the perfectly plastic material (Fig. 5).

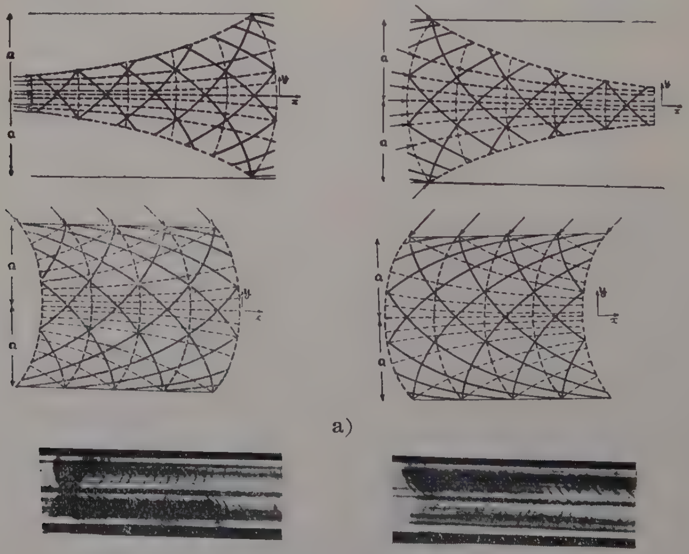

a)

b)

Fig. 5. a) Supersonic flow with $M=\sqrt{2}$ of the gas obeying $p/\log\rho=$const., through channel, full lines showing Mach lines, thick broken lines stream lines, and fine broken lines equipotential lines.

b) Slip lines on surface of an iron piece produced by pressing between two rough parallel plates, the left photograph showing active and the right one passive state.

On the contrary, the case, where the velocity-stress correspondence (3. 8) or (3. 8′) is used, can be discussed in the same way as before, resulting in a demonstration of the essentially equivalent gas flows or plastic states of stress.

(d. 1–2) $n<1$. When $n\neq 0$, we obtain

$$\Psi=t^{1/2}(a_n t^{\sqrt{1-n^2}/2}+b_n t^{-\sqrt{1-n^2}/2})[A_n\cos(n\theta/\sqrt{1-\gamma^2})+B_n\sin(n\theta/\sqrt{1-\gamma^2})]\,, \tag{2. 22}$$

which becomes, by putting $A_n=0$, $b_nB_n=C_1'$, $a_nB_n=C_2'$ with arbitrary constants C_1', C_2',

$$\Psi=(C_1' t^{(1-\sqrt{1-n^2})/2}+C_2' t^{(1+\sqrt{1-n^2})/2})\sin(n\theta/\sqrt{1-\gamma^2})\,. \tag{2. 23}$$

Making use of (4. 5), (4. 6), and integrating the results, we obtain finally

$$\left.\begin{aligned}
x=&\frac{C_1' t^{-(\sqrt{1-n^2}+\gamma)/2}}{q_*(\sqrt{1-n^2}+\gamma)}\left[n\sqrt{\frac{1+\gamma}{1-\gamma}}\cos\theta\cos\frac{n\theta}{\sqrt{1-\gamma^2}}+(1-\sqrt{1-n^2})\sin\theta\sin\frac{n\theta}{\sqrt{1-\gamma^2}}\right]\\
&-\frac{C_2' t^{(\sqrt{1-n^2}-\gamma)/2}}{q_*(\sqrt{1-n^2}-\gamma)}\left[n\sqrt{\frac{1+\gamma}{1-\gamma}}\cos\theta\cos\frac{n\theta}{\sqrt{1-\gamma^2}}+(1+\sqrt{1-n^2})\sin\theta\sin\frac{n\theta}{\sqrt{1-\gamma^2}}\right]+D_1\,,\\
y=&\frac{C_1' t^{-(\sqrt{1-n^2}+\gamma)/2}}{q_*(\sqrt{1-n^2}+\gamma)}\left[n\sqrt{\frac{1+\gamma}{1-\gamma}}\sin\theta\cos\frac{n\theta}{\sqrt{1-\gamma^2}}-(1-\sqrt{1-n^2})\cos\theta\sin\frac{n\theta}{\sqrt{1-\gamma^2}}\right]\\
&-\frac{C_2' t^{(\sqrt{1-n^2}-\gamma)/2}}{q_*(\sqrt{1-n^2}-\gamma)}\left[n\sqrt{\frac{1+\gamma}{1-\gamma}}\sin\theta\cos\frac{n\theta}{\sqrt{1-\gamma^2}}-(1+\sqrt{1-n^2})\cos\theta\sin\frac{n\theta}{\sqrt{1-\gamma^2}}\right]+D_2\,,
\end{aligned}\right\} \tag{2. 24}$$

for the gas of the first kind, and

$$\left.\begin{aligned}
x=&[C_1'/(q_*\sqrt{1-n^2})]t^{-\sqrt{1-n^2}/2}[n\cos\theta\cos n\theta+(1-\sqrt{1-n^2})\sin\theta\sin n\theta]\\
&-[C_2'/(q_*\sqrt{1-n^2})]t^{\sqrt{1-n^2}/2}[n\cos\theta\cos n\theta+(1+\sqrt{1-n^2})\sin\theta\sin n\theta]+D_1\,,\\
y=&[C_1'/(q_*\sqrt{1-n^2})]t^{-\sqrt{1-n^2}/2}[n\sin\theta\cos n\theta-(1-\sqrt{1-n^2})\cos\theta\sin n\theta]\\
&-[C_2'/(q_*\sqrt{1-n^2})]t^{\sqrt{1-n^2}/2}[n\sin\theta\cos n\theta-(1+\sqrt{1-n^2})\cos\theta\sin n\theta]+D_2\,,
\end{aligned}\right\} \tag{2. 24′}$$

for the gas of the second kind, where D_1 and D_2 are arbitrary constants. In order to avoid unnecessary complexity, we shall confine ourselves to discuss plastic states of stress in the perfectly plastic material. When we choose

$$C_1'\exp[\sqrt{1-n^2}\sigma_*/(2k)]/(q_*\sqrt{1-n^2})=C\,,\quad C_2'=D_1=D_2=0$$

with an arbitrary constant C, we obtain the following active state of stress in the plastic mass pressed between two rigid plates inclined at an angle of $2[\tan^{-1}\sqrt{(1+\sqrt{1-n^2})/(1-\sqrt{1-n^2})}]/n-\pi/2$:

$$\left.\begin{aligned}
\sigma_r&=-(k/\sqrt{1-n^2})\log[r^2(1-\sqrt{1-n^2}\cos 2\alpha_1')/\{C^2n^2(1-\sqrt{1-n^2})\}]+k\cos 2\alpha_1'\,,\\
\sigma_t&=-(k/\sqrt{1-n^2})\log[r^2(1-\sqrt{1-n^2}\cos 2\alpha_1')/\{C^2n^2(1-\sqrt{1-n^2})\}]-k\cos 2\alpha_1'\,,\\
\tau_{rt}&=k\sin 2\alpha_1'\,,\qquad \tan n\alpha_1=[n/(1-\sqrt{1-n^2})]\tan\alpha_1'\,,
\end{aligned}\right\} \tag{2. 25′}$$

slip lines of which can be given by

$$\left.\begin{aligned}
&\mathrm{C}_+:\ \begin{cases} x=de^{\sqrt{1-n^2}\alpha_1}[n\cos\alpha_1\cos n\alpha_1+(1-\sqrt{1-n^2})\sin\alpha_1\sin n\alpha_1]\,,\\ y=de^{\sqrt{1-n^2}\alpha_1}[n\sin\alpha_1\cos n\alpha_1-(1-\sqrt{1-n^2})\cos\alpha_1\sin n\alpha_1]\,,\end{cases}\\
&\mathrm{C}_-:\ \begin{cases} x=de^{-\sqrt{1-n^2}\alpha_1}[n\cos\alpha_1\cos n\alpha_1+(1-\sqrt{1-n^2})\sin\alpha_1\sin n\alpha_1]\,,\\ y=de^{-\sqrt{1-n^2}\alpha_1}[n\sin\alpha_1\cos n\alpha_1-(1-\sqrt{1-n^2})\cos\alpha_1\sin n\alpha_1]\,,\end{cases}
\end{aligned}\right\} \tag{2. 26′}$$

where d is a constant along each one of the slip lines. On the other hand, if we choose $C_1'=D_1=D_2=0$, $-C_2'\exp[-\sqrt{1-n^2}\sigma_*/(2k)]/(q_*\sqrt{1-n^2})=C$ with an arbitrary constant C, the passive state of stress in the plastic mass pressed between two rigid plates inclined at an angle of $\pi/2-2[\tan^{-1}\sqrt{(1-\sqrt{1-n^2})/(1+\sqrt{1-n^2})}]/n$ as follows:

$$\left.\begin{aligned}
\sigma_r&=(k/\sqrt{1-n^2})\log[r^2(1+\sqrt{1-n^2}\cos 2\alpha_1')/\{C^2n^2(1+\sqrt{1-n^2})\}]+k\cos 2\alpha_1'\,,\\
\sigma_t&=(k/\sqrt{1-n^2})\log[r^2(1+\sqrt{1-n^2}\cos 2\alpha_1')/\{C^2n^2(1+\sqrt{1-n^2})\}]-k\cos 2\alpha_1'\,,\\
\tau_{rt}&=k\sin 2\alpha_1'\,,\qquad \tan n\alpha_1=[n/(1-\sqrt{1-n^2})]\tan\alpha_1'\,,
\end{aligned}\right\} \tag{2. 27′}$$

slip lines of which can be given by

$$\begin{aligned} \mathrm{C}_+ &: \begin{cases} x=de^{-\sqrt{1-n^2}\alpha_1}[n\cos\alpha_1\cos n\alpha_1+(1+\sqrt{1-n^2})\sin\alpha_1\sin n\alpha_1]\,, \\ y=de^{-\sqrt{1-n^2}\alpha_1}[n\sin\alpha_1\cos n\alpha_1-(1+\sqrt{1-n^2})\cos\alpha_1\sin n\alpha_1]\,, \end{cases} \\ \mathrm{C}_- &: \begin{cases} x=de^{\sqrt{1-n^2}\alpha_1}[n\cos\alpha_1\cos n\alpha_1+(1+\sqrt{1-n^2})\sin\alpha_1\sin n\alpha_1]\,, \\ y=de^{\sqrt{1-n^2}\alpha_1}[n\sin\alpha_1\cos n\alpha_1-(1+\sqrt{1-n^2})\cos\alpha_1\sin n\alpha_1]\,, \end{cases} \end{aligned} \qquad (2.\,28')$$

where d is a constant along each one of the slip lines (Fig. 6).

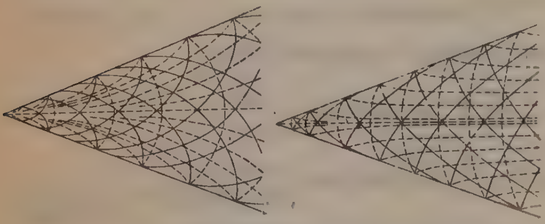

Fig. 6. Slip lines (full lines) and isostatics (broken lines) in the plastic mass pressed between two rigid plates inclined at angle of about 40°, the left figure showing active plastic state, while the right one passive plastic state.

When $n=0$, Eqs. (2. 15) become

$$T''=\Theta''=0\,,$$

which can readily be integrated to give

$$\Psi=(C_1t+C_2)(C_3\theta+C_4)\,. \qquad (2.\,29)$$

If we choose $C_1C_3=-2q_*$, $C_2=C_4=0$, the following solution can be obtained:

$$\left.\begin{aligned} x&=t^{1/2}(\cos\theta+2\theta\sin\theta), \\ y&=t^{1/2}(\sin\theta-2\theta\cos\theta)\,, \end{aligned}\right\} \qquad (2.\,30')$$

from which the state of stress in the plastic material pressed between two rigid plates inclined at an angle of $\pi/2-1\doteqdot 32°42'$ can be written as follows, by taking $\sigma_*=0$, :

$$\left.\begin{aligned} \sigma_r&=k\log[r^2\cos^2(\pi/4-\beta_1')]+k\sin 2\beta_1'\,, \\ \sigma_t&=k\log[r^2\cos^2(\pi/4-\beta_1')]-k\sin 2\beta_1'\,, \\ \tau_{rt}&=-k\cos 2\beta_1'\,, \quad \tan\alpha_1'=2\alpha_1\,, \end{aligned}\right\} \qquad (2.\,31')$$

and the slip lines as follows:

$$\left.\begin{aligned} \mathrm{C}_+:&\quad x=de^{-\alpha_1}(\cos\alpha_1+2\alpha_1\sin\alpha_1)\,, \quad y=de^{-\alpha_1}(\sin\alpha_1-2\alpha_1\cos\alpha_1)\,, \\ \mathrm{C}_-:&\quad x=de^{\alpha_1}(\cos\alpha_1+2\alpha_1\sin\alpha_1)\,, \quad y=de^{\alpha_1}(\sin\alpha_1-2\alpha_1\cos\alpha_1)\,. \end{aligned}\right\} \qquad (2.\,32')$$

It is obvious that this case is wholly equivalent to the case which has been discussed in (c).

(**d. 1-3**) $n>1$. Eqs. (2. 15) can readily be integrated to give

$$T=\sqrt{t}\,[C_1\sin(\sqrt{n^2-1}\log\sqrt{t})+C_2\cos(\sqrt{n^2-1}\log\sqrt{t})]\,, \quad \Theta=C_3\sin n\theta+C_4\cos n\theta\,. \qquad (2.\,33')$$

When we choose $C_4=0$, we obtain

$$\Psi=[C_1'\sin(\sqrt{n^2-1}\log q)+C_2'\cos(\sqrt{n^2-1}\log q)][(\sin n\theta)/q]\,, \qquad (2.\,34')$$

from which the following solution can be obtained:

$$\left.\begin{aligned} x=\;&C_1''[\cos(\sqrt{n^2-1}\log q)(n\cos\theta\cos n\theta+\sin\theta\sin n\theta)-\sqrt{n^2-1}\sin(\sqrt{n^2-1}\log q)\sin\theta\sin n\theta] \\ &+C_2''[\sin(\sqrt{n^2-1}\log q)(n\cos\theta\cos n\theta+\sin\theta\sin n\theta)-\sqrt{n^2-1}\cos(\sqrt{n^2-1}\log q)\sin\theta\sin n\theta], \\ y=\;&C_1''[\cos(\sqrt{n^2-1}\log q)(n\sin\theta\cos n\theta-\cos\theta\sin n\theta)-\sqrt{n^2-1}\sin(\sqrt{n^2-1}\log q)\cos\theta\sin n\theta] \\ &+C_2''[\sin(\sqrt{n^2-1}\log q)(n\sin\theta\cos n\theta+\cos\theta\sin n\theta)+\sqrt{n^2-1}\cos(\sqrt{n^2-1}\log q)\cos\theta\sin n\theta]. \end{aligned}\right\} \qquad (2.\,35')$$

If we choose $q_*\exp[\sigma_*/(2k)]=1$, the plastic state of stress

$$\left.\begin{aligned} x=\;&C_1''[\cos\{\sqrt{n^2-1}\,\sigma/(2k)\}(n\cos\alpha_1\cos n\alpha_1+\sin\alpha_1\sin n\alpha_1) \\ &\qquad+\sqrt{n^2-1}\sin\{\sqrt{n^2-1}\,\sigma/(2k)\}\sin\alpha_1\sin n\alpha_1] \\ &-C_2''[\sin\{\sqrt{n^2-1}\,\sigma/(2k)\}(n\cos\alpha_1\cos \mathrm{n}\alpha_1+\sin\alpha_1\sin n\alpha_1) \\ &\qquad+\sqrt{n^2-1}\cos\{\sqrt{n^2-1}\,\sigma/(2k)\}\sin\alpha_1\sin n\alpha_1]\,, \\ y=\;&C_1''[\cos\{\sqrt{n^2-1}\,\sigma/(2k)\}(n\sin\alpha_1\cos n\alpha_1-\cos\alpha_1\sin n\alpha_1) \\ &\qquad+\sqrt{n^2-1}\sin\{\sqrt{n^2-1}\,\sigma/(2k)\}\cos\alpha_1\sin n\alpha_1] \\ &-C_2''[\sin\{\sqrt{n^2-1}\,\sigma/(2k)\}(n\sin\alpha_1\cos n\alpha_1+\cos\alpha_1\sin n\alpha_1) \\ &\qquad-\sqrt{n^2-1}\cos\{\sqrt{n^2-1}\,\sigma/(2k)\}\cos\alpha_1\sin n\alpha_1]\,, \end{aligned}\right\} \qquad (2.\,36')$$

and the slip lines

$$\left.\begin{aligned}
\mathrm{C}_+ :\ &\left\{\begin{aligned}
x=&C_1''[\cos\{\sqrt{n^2-1}(d-\alpha_1)\}(n\cos\alpha_1\cos n\alpha_1+\sin\alpha_1\sin n\alpha_1)\\
&\qquad+\sqrt{n^2-1}\sin\{\sqrt{n^2-1}(d-\alpha_1)\}\sin\alpha_1\sin n\alpha_1]\\
&-C_2''[\sin\{\sqrt{n^2-1}(d-\alpha_1)\}(n\cos\alpha_1\cos n\alpha_1+\sin\alpha_1\sin n\alpha_1)\\
&\qquad+\sqrt{n^2-1}\cos\{\sqrt{n^2-1}(d-\alpha_1)\}\sin\alpha_1\sin n\alpha_1]\,,\\
y=&C_1''[\cos\{\sqrt{n^2-1}(d-\alpha_1)\}(n\sin\alpha_1\cos n\alpha_1-\cos\alpha_1\sin n\alpha_1)\\
&\qquad+\sqrt{n^2-1}\sin\{\sqrt{n^2-1}(d-\alpha_1)\}\cos\alpha_1\sin n\alpha_1]\\
&-C_2''[\sin\{\sqrt{n^2-1}(d-\alpha_1)\}(n\sin\alpha_1\cos n\alpha_1+\cos\alpha_1\sin n\alpha_1)\\
&\qquad-\sqrt{n^2-1}\cos\{\sqrt{n^2-1}(d-\alpha_1)\}\cos\alpha_1\sin n\alpha_1]\,,
\end{aligned}\right.\\
\mathrm{C}_- :\ &\left\{\begin{aligned}
x=&C_1''[\cos\{\sqrt{n^2-1}(d+\alpha_1)\}(n\cos\alpha_1\cos n\alpha_1+\sin\alpha_1\sin n\alpha_1)\\
&\qquad+\sqrt{n^2-1}\sin\{\sqrt{n^2-1}(d+\alpha_1)\}\sin\alpha_1\sin n\alpha_1]\\
&-C_2''[\sin\{\sqrt{n^2-1}(d+\alpha_1)\}(n\cos\alpha_1\cos n\alpha_1+\sin\alpha_1\sin n\alpha_1)\\
&\qquad+\sqrt{n^2-1}\cos\{\sqrt{n^2-1}(d+\alpha_1)\}\sin\alpha_1\sin n\alpha_1]\,,\\
y=&C_1''[\cos\{\sqrt{n^2-1}(d+\alpha_1)\}(n\sin\alpha_1\cos n\alpha_1-\cos\alpha_1\sin n\alpha_1)\\
&\qquad+\sqrt{n^2-1}\sin\{\sqrt{n^2-1}(d+\alpha_1)\}\cos\alpha_1\sin n\alpha_1]\\
&-C_2''[\sin\{\sqrt{n^2-1}(d+\alpha_1)\}(n\sin\alpha_1\cos n\alpha_1+\cos\alpha_1\sin n\alpha_1)\\
&\qquad-\sqrt{n^2-1}\cos\{\sqrt{n^2-1}(d+\alpha_1)\}\cos\alpha_1\sin n\alpha_1]
\end{aligned}\right.
\end{aligned}\right\}\quad (2.37')$$

can be obtained in the same way as before.

(**d. 2**) $\lambda=n^2$. Lastly we consider the case where λ is posotive and put $\lambda=n^2$, with a real constant n. The fundamental equations (2. 15) become in this case

$$4t^2d^2T/dt^2-n^2T=0\,,\quad d^2\Theta/d\theta^2-n^2\Theta=0\,, \qquad (2.38')$$

which can readily be integrated to give

$$T=\sqrt{t}\,[C_1t^{\sqrt{1+n^2}/2}+C_2t^{-\sqrt{1+n^2}/2}]\,,\quad \Theta=C_3e^{n\theta}+C_4e^{-n\theta}\,. \qquad (2.39')$$

When we choose $C_4=0$, the expression for Ψ becomes

$$\Psi=(C_1'q_-^{1+\sqrt{1+n^2}}+C_2'q^{-1-\sqrt{1+n^2}}e^{n\theta}\,. \qquad (2.40')$$

Starting with this Ψ, the hodograph method gives the solution as follows:

$$\left.\begin{aligned}
x&=C_1''q^{\sqrt{1+n^2}}e^{n\theta}[n\cos\theta+(1-\sqrt{1+n^2})\sin\theta]+C_2''q^{-\sqrt{1+n^2}}e^{n\theta}[n\cos\theta+(1+\sqrt{1+n^2})\sin\theta]\,,\\
y&=C_2''q^{\sqrt{1+n^2}}e^{n\theta}[n\sin\theta-(1-\sqrt{1+n^2})\cos\theta]+C_2''q^{-\sqrt{1+n^2}}e^{n\theta}[n\sin\theta-(1+\sqrt{1+n^2})\cos\theta]\,,
\end{aligned}\right\} \qquad (2.41')$$

from which the following plastic state of stress can be obtained, by taking $C_1''q_*^{\sqrt{1+n^2}}=C_1'''$, $C_2''=0$, :

$$\left.\begin{aligned}
\sigma_r&=-(k/\sqrt{1+n^2})[[\log[r^2/\{2C_1'''^2\sqrt{1+n^2}(\sqrt{1+n^2}-1)\}]-2n\alpha_1]]+k\cos 2\alpha_1'\,,\\
\sigma_t&=-(k/\sqrt{1+n^2})[[\log[r^2/\{2C_1'''^2\sqrt{1+n^2}(\sqrt{1+n^2}-1)\}]-2n\alpha_1]]-k\cos 2\alpha_1'\,,\\
\tau_{rt}&=k\sin 2\alpha_1'\,,\quad \tan(\alpha_1+\varphi)=-n/(1-\sqrt{1+n^2})\,.
\end{aligned}\right\} \qquad (2.42')$$

Slip lines and isostatics of this state of stress are the following logarithmic spirals (Fig. 7):

$$\left.\begin{aligned}
&\mathrm{C}_+:\ r=C\exp(m\varphi)\,,\qquad \mathrm{C}_-:\ r=C\exp(-\varphi/m)\,,\\
&\text{lines of maximum principal stress}:\ r=C'\exp[\{(m-1)/(m+1)\}\varphi]\,,\\
&\text{lines of minimum principal stress}:\ r=C'\exp[-\{(m+1)/(m-1)\}\varphi]\,,
\end{aligned}\right\} \qquad (2.43')$$

where $m=-(n+\sqrt{1+n^2})$ and C is an arbitrary constant.

If we take $C_1''=0$, $C_2''q_*^{-\sqrt{1+n^2}}=C_2'''$ in (2. 41′), we obtain the plastic state of stress and its slip lines as follows:

$$\left.\begin{aligned}
\sigma_r&=(k/\sqrt{1+n^2})[[\log[r^2/\{2C_2'''^2\sqrt{1+n^2}(\sqrt{1+n^2}+1)\}]-2n\alpha_1]]+k\cos 2\alpha_1'\,,\\
\sigma_t&=(k/\sqrt{1+n^2})[[\log[r^2/\{2C_2'''^2\sqrt{1+n^2}(\sqrt{1+n^2}+1)\}]-2n\alpha_1]]-k\cos 2\alpha_1'\,,\\
\tau_{rt}&=k\sin 2\alpha_1'\,,\quad \tan(\alpha_1+\varphi)=-n/(1+\sqrt{1+n^2})\,,
\end{aligned}\right\} \qquad (2.44')$$

$$\left.\begin{array}{ll} C_+: \ r=C\exp(-\varphi/m)\,, & C_-: \ r=C\exp(m\varphi)\,, \\ \text{lines of maximum principal stress}: & r=C'\exp[-\{(m-1)/(m+1)\}\varphi]\,, \\ \text{lines of minimum principal stress}: & r=C'\exp[\{(m+1)/(m-1)\}\varphi]\,, \end{array}\right\} \quad (2.45')$$

which are essentially equivalent to those which have been obtained in the preceding case.

Since it is well known that a cleavage fracture of a glass occurs along isostatics, the photograph in Fig. 7 of a spiral crack in a safety glass disk clamped at its periphery and subjected to a concentrated load at its centre illustrates the equations of the isostatics obtained above.

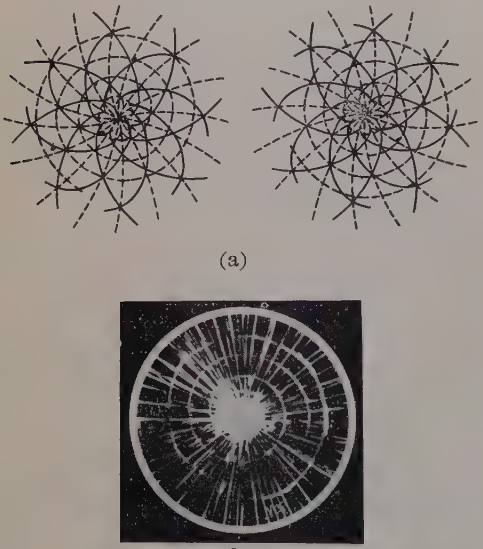

(a)

b)

Fig. 7. Spiral flow.

a) Supersonic flow with $M=\sqrt{2}$ of the gas obeying $p/\log\rho=$const., or plastic state of stress in a circular glass disk acted by a concentrated load at its centre, turning left (the left figure) and right (the right one) respectively, full lines showing Mach lines or slip lines, and broken lines a family of stream lines and equipotential lines or isostatics.

b) Spiral cracks in a safety glass disk clamped at its periphery and subjected to a concentrated load at its centre.

§ 3. Simple Waves

Lastly, as another example of studying the gas flow by the plastic deformation, we consider the simplest case of simple waves, that is, the case where they are two families of parallel straight lines are illustrated with figures and photographs in Figs. 8 and 9.

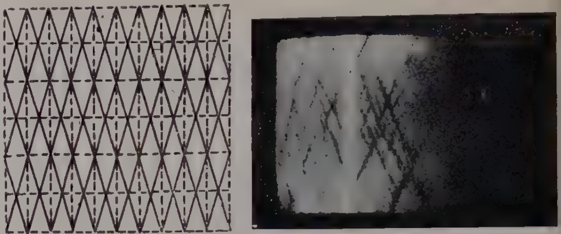

a) b)

Fig. 8. Simple waves in the gas flow obeying $p/\rho^{\gamma}=$const. or in the plastic material obeying $\tau=(\sigma_0-\sigma)\sin\delta$.

a) Mach lines or slip lines (full lines) and a family of stream lines and equipotential lines or isostatics (broken lines).

b) Slip lines on surface of compressed cylinder of Carraramarmor.

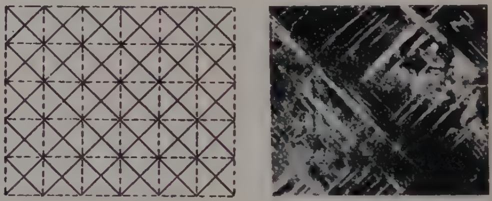

a) b)

Fig. 9. Simple waves in the gas flow obeying $p/\log\rho=$const. or in the plastic material obeying $\tau=k$.

a) Mach lines or slip lines (full lines) and a family of stream lines and equipotential lines or isostatics (broken lines).

b) Lüder's line pattern on a steel sheet. After the thin steel plate was stretched by a small strain (in the direction parallel to the short side of the photograph) the scale fell off, disclosing the flow lines.

§ 4. Acknowledgment

All the photographs used in this paper, for the purpose of comparing the theory with observations, have been taken from the famous monographs of Dr. A. Nádai: Der bildsame Zustand der Werkstoffe (1927) and Theory of flow and fracture of solids (1950). The author wishes to express his sincere thanks and honor to him for his valuable works.

JOURNAL OF THE PHYSICAL SOCIETY OF JAPAN Vol. 7, No. 6 NOV.—DEC., 1952

Note on Discrepancies between Two Theories on the Stability of Plane Poiseuille Flow

By Tomomasa TATSUMI

Department of Physics, Faculty of Science, University of Kyoto

(Received July 1, 1952)

Existing theories of the hydrodynamical stability of plane Poiseuille flow are divided into two groups by their quite different conclusions. Results attained by Lin and other earlier authors are that this flow is unstable for sufficiently large Reynolds numbers. On the other hand, Pekeris has obtained different results that the flow is stable for any value of the Reynolds number and that, in addition to the ordinary disturbances discussed by earlier authors, there exists another class of perturbation which is characterized by $c_r \to 1$ as $\alpha R \to \infty$.

In this paper, a critical survey for these conflicting results is presented. It is shown that Pekeris's first result arises essentially from the poor convergency of his series expansion of c, namely $c = c_0 + \alpha^2 c_1 + \dots$, and that if this procedure is avoided, the existence of Lin's stability limit is asymptotically confirmed. It is also found that Pekeris's second prediction is erroneous.

§ 1. Introduction

One of the most interesting results in the theory of hydrodynamical stability is the prediction of the so-called "Tollmien-Schlichting waves" in the laminar boundary-layer flow. The stability of this flow was investigated respectively by Tollmien[1], Schlichting[2], and recently by Lin[3], obtaining the result that unstable waves can exist when the Reynolds number becomes greater than a certain critical value. Experimental evidence for this theoretical result has been made first available in 1940 by Schubauer and Skramstad[4]. After some subsequent experiments the theoretical prediction has been completely confirmed, and thus the theory of hydrodynamical stability has established its validity so far as this example of flow is concerned.

The theory had already been applied by Heisenberg[5] to another typical case of flow, namely, the plane Poiseuille flow, and Lin[3] has undertaken a revision of the mathematical theory as well as a refinement of numerical works. Lin's work gives a neutral curve in the $\alpha - R$ plane as shown in Fig. 1, where α is the wave number of disturbance and R the Reynolds number of the flow. For values of α and R in the inside of this neutral curve,

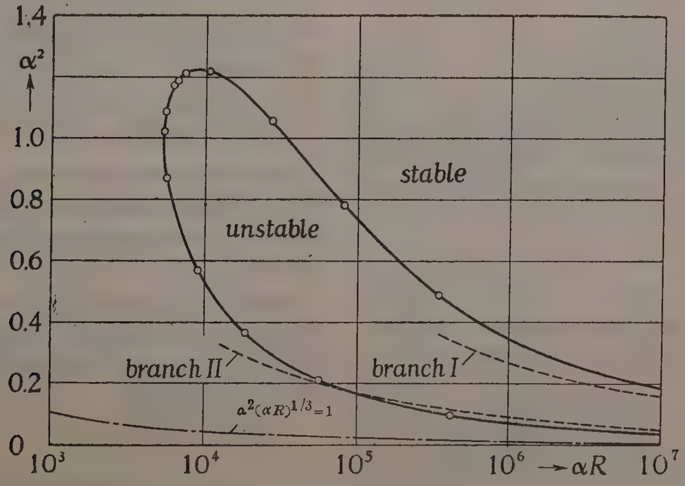

Fig. 1. Lin's neutral curve.

the disturbance is unstable. The critical Reynolds number R_c as a minimum value of R corresponding to the neutral curve is found to be about 5300.

Recently, Pekeris[6] has treated the same problem theoretically by employing a slightly different method from the conventional one used by previous authors. To our surprise, however, his result is not consistent with that of Lin, indicating the stability of disturbance over the whole $\alpha-R$ plane. Moreover, he predicts the existence of disturbance of the "second class" which has not been involved in earlier calculations. Apart from many other trivial differences, these two discrepancies cast a serious doubt on the existence of the stability limit as well as on the validity of the conventional method of analysis (cf. v. Neumann[7]).

In the present paper an attempt is made to clarify the cause of these discrepancies between two theories on the stability of plane Poiseuille flow.

§2. Two Conflicting Results

The plane Poiseuille flow between two parallel walls $y=\pm h$ is represented non-dimensionally by

$$U(y)=1-y^2, \tag{1}$$

where h, U_0 (the maximum velocity at $y=0$) and h/U_0 are taken as units of length, velocity and time respectively.

If we superpose on the main flow U a small disturbance (u, v) corresponding to the stream function ψ:

$$\left.\begin{aligned} &u=\frac{\partial\psi}{\partial y}, \quad v=-\frac{\partial\psi}{\partial x}, \\ &\psi=f(y)\exp[i\alpha(ct-x)], \end{aligned}\right\} \tag{2}$$

we obtain, from the Navier-Stokes equations of motion, the following linear differential equation for f, neglecting the second terms in f:

$$\begin{aligned} &f^{\mathrm{iv}}-2\alpha^2 f''+\alpha^4 f \\ &\quad +i\alpha R[(U-c)(f''-\alpha^2 f)-U''f]=0, \end{aligned} \tag{3}$$

where $R=U_0h/\nu$ and dashes denote differentiation with respect to y. In general c is a complex number: $c=c_r+ic_i$ where c_r means the phase velocity and αc_i the logarithmic decrement of disturbance. Hence, if equation (3), together with appropriate boundary conditions, gives eigenvalues c with negative c_i the flow is unstable, while if there exist only such eigenvalues that have positive c_i, the flow is stable.

Since, in Lin's and Pekeris's work, the discussion is confined to odd disturbance corresponding to the even stream function f, we are here solely concerned with boundary conditions for such an even stream function:

$$f(1)=f'(1)=0, \quad f'(0)=f'''(0)=0. \tag{4}$$

Before proceeding to detailed calculations of the boundary-value problem, we shall now make the point at issue clearer by summarizing the conflicting features of the two authors' arguments.

(a) *Lin's method* (Reference 3): In this method f is developed into a power series of α^2 as:

$$f=f_0+\alpha^2 f_1+\dots,$$

and f_0, f_1, ... are determined successively. The four boundary conditions (4) for four particular solutions of (3) lead to a secular equation of the form: $F(\alpha, R, c)=0$. Then, an $\alpha(R, c)$ curve for real values of c, if any, represents the neutral curve.

Results: (i) The neutral curve really exists, and (ii) asymptotic behaviour of this curve when $\alpha\to0$ is represented by the two branches:

$$\left.\begin{aligned} &R^{1/3}=8.44(\alpha^2)^{-11/6}, \quad c=(4/15)\alpha^2, \\ &R^{1/3}=5.96(\alpha^2)^{-7/6}, \quad c=0.611\alpha^2. \end{aligned}\right\} \quad \text{L (13. 2)*}$$

(b) *Pekeris's method* (Reference 6): In this method, both f and c are expanded into power series of α^2 as:

$$f=f_0+\alpha^2 f_1+\dots, \qquad \text{P (8)*}$$

$$c=c_0+\alpha^2 c_1+\dots, \qquad \text{P (5)}$$

and equation (3) then gives

$$f_0^{\mathrm{iv}}+i\alpha R[(1-y^2-c_0)f_0''+2f_0]=0, \qquad \text{P (9)}$$

$$\begin{aligned} &f_1^{\mathrm{iv}}+i\alpha R[(1-y^2-c_0)f_1''+2f_1] \\ &\quad =2f_0''+i\alpha R[(1-y^2-c_0)f_0+c_1f_0'']. \end{aligned} \qquad \text{P (10)}$$

After some integration by part c_0 and c_1 can be determined from a knowledge of f_0 only, obviating the logarithmic complications arising in f_1.

Results: (i) Lin's "neutral curve" is not essentially neutral and there is no region of instability for the parabolic flow. (ii) In fact, for the first mode

$$c_0=1.617e^{i\pi/6}(\alpha R)^{-1/3}, \qquad \text{P (6)}$$

---

* L( ) or P( ) shows the corresponding equation in Lin's or Pekeris's paper.

$$c_1=0.395-0.546c_0+i(\alpha R)^{-1}\,, \qquad \mathrm{P}(7)$$

which indicate that the flow is stable. (iii) Whereas in the above-mentioned class of modes, $c\to 0$ as $\alpha R\to\infty$ when $\alpha^2=0$, there exists another class of modes corresponding to the solution

$$f_0=\int dx\int e^{-x/2}{}_1F_1(a,5/2,x)dx, \qquad \mathrm{P}(55)$$

where

$$x=(i\alpha R)^{1/2}y^2\,,\ a=[5-(1-c_0)(i\alpha R)^{-1/2}]/4, \qquad \mathrm{P}(53)$$

and ${}_1F_1$ denotes the confluent hypergeometric function. This class of modes is characterized by the result that $c\to 1$ as $\alpha R\to\infty$, and in effect we have

$$c_{(m)}=1-(1+4m)(i\alpha R)^{-1/2}\,,\quad m=1,2,\ldots. \qquad \mathrm{P}(60)$$

§ 3. Solution by Successive Approximation

The main difference between the above two methods lies in that the expansion P(5) for c is used in Pekeris's work but not in Lin's work. To avoid this procedure we shall now use the method of successive substitution, confining ourselves to the case of small α^2. Then, equation (3) can be written as:

$$\begin{aligned}&f^{\mathrm{iv}}+i\alpha R[(1-y^2-c)f''+2f]\\&\quad=\alpha^2[2f''+i\alpha R(1-y^2-c)f]+O(\alpha^4)\,.\end{aligned} \qquad (3\,\mathrm{a})$$

As zeroth approximation, we have, neglecting the right-hand side of this equation,

$$f_0^{\mathrm{iv}}+i\alpha R[(1-y^2-c_0)f_0''+2f_0]=0. \qquad (5)$$

Then, the first approximation f_{I} is obtained by solving the equation:

$$\begin{aligned}&f_{\mathrm{I}}^{\mathrm{iv}}+i\alpha R[(1-y^2-c_{\mathrm{I}})f_{\mathrm{I}}''+2f_{\mathrm{I}}]\\&\quad=\alpha^2[2f_0''+i\alpha R(1-y^2-c_0)f_0]\,.\end{aligned} \qquad (6)$$

One exact even solution of (5) is given by

$$f_0^{(1)}=1-y^2-c_0\,. \qquad (7)$$

In order to obtain another even solution of (5), we put

$$\left.\begin{aligned}&y-y_c=\varepsilon\eta\,,\\ &\text{with}\\ &y_c=(1-c_0)^{1/2}\,,\quad \varepsilon=(2y_c\alpha R)^{-1/3}e^{-i\pi/2}\,,\end{aligned}\right\} \qquad (8)$$

and expand $f_0(y)$ in a power series of ε as:

$$f_0(y)=\varphi(\eta)=\varphi_0(\eta)+\varepsilon\varphi_1(\eta)+\ldots. \qquad (9)$$

Substituting (8) and (9) into (5) and equating the coefficients of ε^0 and ε to zero we get

$$\varphi_0^{\mathrm{IV}}+\eta\ddot{\varphi}_0=0\,, \qquad (10)$$

$$\varphi_1^{\mathrm{IV}}+\eta\ddot{\varphi}_1=y_c^{-1}\left(\varphi_0-\frac{\eta^2}{2}\ddot{\varphi}_0\right), \qquad (11)$$

where dots denote differentiation with respect to η.

Bearing in mind the second condition in (4) we find that the appropriate solution of (10) for large αR is given by

$$\ddot{\varphi}_0=h(\eta)\equiv\eta^{1/2}H_{1/3}^{(2)}\left[\frac{2}{3}\eta^{3/2}\right]. \qquad (12)$$

Thus, neglecting terms of order of ε the general even solution of (5) becomes

$$f_0=(1-y^2-c_0)+B_0\varphi_0(\eta)\,, \qquad (13)$$

where B_0 is an arbitrary constant.

Taking the second condition in (4) into account, equations (5) and (10) integrate respectively into

$$f_0'''+i\alpha R[(1-y^2-c_0)f_0'+2yf_0]=0\,, \qquad (14)$$

$$\dddot{\varphi}_0+\eta\dot{\varphi}_0-\varphi_0=0\,, \qquad (15)$$

and the first condition in (4) yields

$$f_0'''(1)==0\,. \qquad (16)$$

Hence, we have, from (13),

$$\dddot{\varphi}_0(\eta_1)=\dot{h}(\eta_1)=\eta_1H_{-2/3}^{(2)}\left[\frac{2}{3}\eta_1^{3/2}\right]=0\,, \qquad (17)$$

where $\eta_1=(1-y_c)/\varepsilon$. The roots of this equation are found to be given by*

$$\eta_{10}=\tau_m e^{i2\pi/3}\,,\quad (m=1,2,\ldots);$$
$$\tau_1=1.091,\quad \tau_2=3.248,\ \ldots$$

Corresponding to the first root, we have from (8)

$$\begin{aligned}c_0&=2\tau_1e^{i\pi/6}(2\alpha R)^{-1/3}+O(\varepsilon^2)\\&=1.617e^{i\pi/6}(\alpha R)^{-1/3}+O(\varepsilon^2)\,,\end{aligned} \qquad (18)$$

which is identical with P (6). Thus, Pekeris's result is confirmed up to its initial stage of approximation.

Turning next to equation (6), it is readily known that the particular solutions of this equation fall into two groups: the inviscid and viscous solutions. In the first place, neglecting terms of the order of $(\alpha R)^{-1}$, equation (6) becomes

$$(1-y^2-c_{\mathrm{I}})f_{\mathrm{I}}''+2f_{\mathrm{I}}=\alpha^2(1-y^2-c_0)f_0\,. \qquad (19)$$

Inhomogeneous solutions of this equation are expressed by

$$\begin{aligned}&\alpha^2(1-y^2-c_{\mathrm{I}})k(y)\equiv\alpha^2(1-y^2-c_{\mathrm{I}})\\&\quad\times\int^y(1-y^2-c_{\mathrm{I}})^{-2}dy\int^y(1-y^2-c_0)f_0dy\,,\end{aligned} \qquad (20)$$

and if we take the solution (7) as f_0, the even inviscid solution of (6) is given by

---

* See 'Table of the modified Hankel functions of order one-third and of their derivatives', (Harvard University Press, 1945), p. xxxvi.

$$
\begin{aligned}
f_{\mathrm{I}}^{(1)} &= (1-y^2-c_{\mathrm{I}})[1+\alpha^2 k(y)] \\
&= (1-y^2-c_{\mathrm{I}}) \\
&\quad \times\left[1+\alpha^2\int_0^y (1-y^2-c_{\mathrm{I}})^{-2}dy\int_0^y (1-y^2-c_0)^2 dy\right].
\end{aligned} \tag{21}
$$

In the second place, in order to obtain the viscous solution of (6) we introduce again the transformations (8) and (9) into (6). Then, we have

$$
\left.
\begin{aligned}
&\varphi_{\mathrm{I}}^{\mathrm{IV}}+\eta\ddot{\varphi}_{\mathrm{I}}+\varepsilon\left[\frac{\eta^2}{2y_c}\ddot{\varphi}_{\mathrm{I}}-\varphi_{\mathrm{I}}\right] \\
&\quad =\alpha^2\varepsilon^2\left[2\ddot{\varphi}_0+\left(\eta+\frac{\eta^2}{2y_c}\right)\varphi_0\right]+O(\varepsilon^3) \\
&\quad =O(\varepsilon^2).
\end{aligned}
\right| \tag{22}
$$

Hence, as far as terms of the highest order are concerned, φ_{I} is identical with φ_0 and under the same boundary conditions (4) we have

$$
\text{and}\quad
\left.
\begin{aligned}
\ddot{\varphi}_{\mathrm{I}} &= h(\eta)+O(\varepsilon), \\
\varphi_{\mathrm{I}} &= \varphi_0+O(\varepsilon).
\end{aligned}
\right\} \tag{23}
$$

Thus, neglecting terms of the order of ε the general even solution of (6) is given by

$$
f_{\mathrm{I}}=(1-y^2-c_{\mathrm{I}})[1+\alpha^2 k(y)]+B_{\mathrm{I}}\varphi_0(\eta), \tag{24}
$$

where B_{I} denotes an arbitrary constant. Proceeding similarly to the case of obtaining (16) from (5) we have

$$
f_{\mathrm{I}}'''(1)=i\alpha R\cdot\alpha^2\int_0^1 (1-y^2-c_0)f_0 dy. \tag{25}
$$

Substituting (13) and (24) into (25) and making use of the relations:

$$
\int_0^1 (1-y^2-c_0)B_0\varphi_0(\eta)dy=O(\varepsilon^3), \qquad \mathrm{P}\,(40)
$$

$$
\int_0^1 (1-y^2-c_0)^2 dy=\frac{8}{15}-\frac{4}{3}c_0+c_0^2,
$$

$$
\Big[(1-y^2-c_{\mathrm{I}})k(y)\Big]'''_{y=1}=-\frac{2}{c_{\mathrm{I}}^2}\left(\frac{8}{15}-\frac{4}{3}c_0+2c_0c_{\mathrm{I}}\right),
$$

we obtain, neglecting terms of the order of $(\alpha R)^{-1}$,

$$
\dddot{\varphi}(\eta_1)=-\frac{\alpha^2}{2y_cB_{\mathrm{I}}}\left(\frac{8}{15}-\frac{4}{3}c_0+c_0^2\right). \tag{26}
$$

On the other hand, from the first condition in (4) we have

$$
f_{\mathrm{I}}'(1)=-2+\alpha^2k'(1)+B_{\mathrm{I}}\varepsilon^{-1}\dot{\varphi}_0(\eta_1)=0, \tag{27}
$$

$$
\left.
\begin{aligned}
k'(1) &= -2\int_0^1 (1-y^2-c_{\mathrm{I}})^{-2}dy\int_0^y (1-y^2-c_0)^2 dy \\
&\qquad -\frac{1}{c_{\mathrm{I}}}\int_0^1 (1-y^2-c_0)^2 dy \\
&= -\frac{2}{5}+\frac{(1-c_0)^2}{1-c_{\mathrm{I}}} \\
&\quad +\left(\frac{4}{15}-\frac{2}{3}c_0+\frac{2}{5}c_{\mathrm{I}}\right)\left(\log\frac{c_{\mathrm{I}}}{1-c_{\mathrm{I}}}-i\pi\right).
\end{aligned}
\right\} \tag{28}
$$

Eliminating B_{I} from (26) and (27) we finally arrive at a secular equation of the form:

$$
\frac{\dddot{\varphi}(\eta_1)}{\dot{\varphi}(\eta_1)}=\frac{\alpha^2}{2y_c\varepsilon}\,\frac{\dfrac{8}{15}-\dfrac{4}{3}c_0+c_0^2}{-2+\alpha^2k'(1)}. \tag{29}
$$

§ 4. Concerning the First Discrepancy

We now introduce two new functions:

$$
F(\eta_1)=\frac{\varphi_0(\eta_1)}{\eta_1\dot{\varphi}_0(\eta_1)}, \tag{30}
$$

$$
\mathbf{F}(\eta_1)=[1-F(\eta_1)]^{-1}. \tag{31}
$$

Then, by the use of the relations (15) and (8), equation (29) becomes

$$
\mathbf{F}(\eta_1)=\frac{c_{\mathrm{I}}}{\alpha^2}\,\frac{2-\alpha^2k'(1)}{\dfrac{8}{15}-\dfrac{4}{3}c_0+c_0^2}. \tag{32}
$$

For real values of c_{I} this equation is essentially identical with Lin's secular equation (the second equation on p. 283, Part III of reference 3).

Indeed, asymptotic behaviours of $\mathbf{F}(\eta_1)$ for $\alpha R\to\infty$ are known from Lin's calculation as

$$
\begin{aligned}
&\text{I.}\quad \eta_1\to i\infty,\quad \mathbf{F}\approx 1+i(2i\eta_1^3)^{-1/2} \\
&\qquad\qquad\qquad = 1+i2^{1/2}(\alpha Rc^3)^{-1/2}.
\end{aligned} \tag{33}
$$

$$
\text{II.}\quad \eta_1=2.294\,i,\quad \mathbf{F}=2.292. \tag{34}
$$

In case I, we have, from (28) and (32),

$$
1=\frac{15}{4}\frac{c_{\mathrm{I}}}{\alpha^2},\qquad \sqrt{2}\,(\alpha Rc_{\mathrm{I}}^3)^{-1/2}=\frac{\pi}{2}c_{\mathrm{I}},
$$

so that

$$
R=601\,\alpha^{-11},\quad c_{\mathrm{I}}=(4/15)\alpha^2, \quad \text{(the first branch)}. \tag{35}
$$

In case II, we have similarly

$$
2.292=\frac{15}{4}\frac{c_{\mathrm{I}}}{\alpha^2},\qquad 2.294=\left(\frac{\alpha R}{4}\right)^{-1/3}c_{\mathrm{I}},
$$

so that

$$
R=212\,\alpha^{-7},\quad c_{\mathrm{I}}=0.611\,\alpha^2, \quad \text{(the second branch)}. \tag{36}
$$

Since these two branches (35) and (36) are in agreement with L(13.2), *Lin's results* (i) *and*

(ii) *have been completely confirmed.*

On the other hand, if we expand the left-hand side of (29) near the point $\eta_1=\eta_{10}$, we have

$$\frac{\dddot{\varphi}(\eta_1)}{\dot{\varphi}(\eta_1)}=(\eta_1-\eta_{10})\frac{\varphi^{\mathrm{IV}}(\eta_{10})}{\dot{\varphi}(\eta_{10})}$$

$$=-(\eta_1-\eta_{10})\frac{\eta_{10}\ddot{\varphi}(\eta_{10})}{\dot{\varphi}(\eta_{10})}\quad\text{(from (10))}$$

$$=-(\eta_1-\eta_{10})\frac{1}{N},\qquad(37)$$

where $N=1.483$ the computation of which is given by Pekeris (see Appendix of reference 6). Further, if we introduce the expansion P(5) for c into our argument, we obtain, on remembering (8),

$$\eta_1-\eta_{10}=\frac{1}{2y_c\varepsilon}(c-c_0)=\frac{\alpha^2c_1}{2y_c\varepsilon}+O(\alpha^4).\qquad(38)$$

Hence, inserting (37) and (38) into (29) and neglecting terms of the order of α^4 on both sides, we have

$$c_1=\left(\frac{4}{15}-\frac{2}{3}c_0+\frac{1}{2}c_0{}^2\right)N,\qquad(39)$$

which is equal to P(7) so far as the principal term is concerned. Thus, disregarding trivial disagreement of the order of ε due to the difference between Pekeris's method of argument and our own, *Pekeris's second result* (ii) *has been deduced by dealing with only the first terms in the α^2-development of* (29).

Now, the cause of the first discrepancy becomes clear. Thus, in Pekeris's method, an assumption is made that 'for small values of α^2, P(5) would be expected to be adequate', and indeed he contents himself with retaining only the second term in the α^2-development. Unfortunately, as seen from the above discussions, the second approximation $c_0+\alpha^2c_1$ is quite inadequate for evaluating the real eigenvalue c. In effect, this approximation gives rise to the missing out of the rapid variation of φ_0 on the left-hand side of (29), and to the neglecting, on the right-hand side, of the imaginary part in k' which plays usually an important role for stability. In other word, it may be said that in such a method of approximation eigenvalue cannot always be approximated enough by the same stage of approximation as that of eigenfunction.

From another point of view, P(5) may also be expressed as:

$$c=c_0(1+0.244e^{i\pi/6}\alpha^2(\alpha R)^{1/3}+O(\alpha^2)),$$

so that its domain of effective convergence must be in a rather limited region in the $\alpha-R$ plane where the condition:

$\alpha^2(\alpha R)^{1/3}=$ a small quantity of the order of unity

holds. (see Fig. 1) Therefore, his comparative discussion of his own and Lin's result near the point $\alpha^2(\alpha R)^{1/3}=20$ seems to be nonsence.

Thus, it may be concluded that *if we want to make use successfully of Pekeris's method,* i.e. the standard procedure in the perturbation theory in which both eigenvalue and eigenfunction are developed in powers of a certain small parameter, *we should go up to the third or further stage of approximation in which, however, elegance of the calculation in the first two stages would be inevitably destroyed.*

§ 5. Concerning the Second Discrepancy

The second class of modes P(60) has been given by Pekeris by proceeding as follows: Inserting the transformations P(53) to (14) and differentiating once with respect to x, we obtain

$$x\frac{d^4f_0}{dx^4}+\frac{5}{2}\frac{d^3f_0}{dx^3}+\left(\frac{5}{4}-a-\frac{x}{4}\right)\frac{d^2f_0}{dx^2}=0,\qquad\text{P (54)}$$

the even solution of which is given by

$$\frac{d^2f_0}{dx^2}=e^{-x/2}{}_1F_1(a,5/2,x).\qquad\text{P (55)}$$

From the condition (16), we obtain after some transformations

$$b(a,x_1)={}_1F_1(a,3/2,x_1)+{}_1F_1(a-1,3/2,x_1)=0,\qquad\text{P (56)}$$

with $x_1=(i\alpha R)^{1/2}$.

This relation determins a, and with it c_0, as a function of αR.

Now for large αR it follows from

$${}_1F_1(\alpha,\gamma,x)\sim\frac{\Gamma(\gamma)}{\Gamma(\alpha)}e^xx^{\alpha-\gamma}(1+O(x^{-1})),\qquad\text{P (57)}$$

that

$$b(a,x_1)\sim\frac{\Gamma(3/2)}{\Gamma(a)}e^xx^{a-(3/2)}(1+O(x^{-1})).\qquad\text{P (58)}$$

Hence,

$$\Gamma(a)^{-1}=0,\quad a=1-m,\ m=1,2,\ldots.\qquad\text{P (59)}$$

Thus, we have finally

$$c_{(m)}=1-(1+4\,m)(i\alpha R)^{-1/2}.\qquad\text{P (60)}$$

In the above argument Pekeris has made a careless mistake in adopting the asymptotic expansion P (57) for ${}_1F_1$, since P (57) represents the asymptotic behaviour of ${}_1F_1$ for $x \to \infty$ but for finite α and γ, while in our problem both x and a tend to ∞ as $\alpha R \to \infty$.

Mathematically speaking, P (54) is equivalent to (5) (or P (9)), so that its solutions must be the same as that of the latter when their correct asymptotic expressions for $\alpha R \to \infty$ are used. A method for obtaining such asymptotic expressions has been developed by Langer[8].

Letting

$$z=(i\alpha R)^{-1/2}x=y^2\,, \tag{40}$$

two asymptotic solutions of P (54) (valid as $\alpha R \to \infty$ uniformly in $0<z\leq 1$) are

$$\frac{d^2f_0}{dz^2}=z^{-5/4}\left(1-\frac{y_c^2}{z}\right)^{-1/4}s^{1/2} \times H_{1/3}^{(1),(2)}\left[\frac{1}{2}(-i\alpha R)^{1/2}s\right], \tag{41}$$

where $$s=\int_{y_c^2}^{z}\left(1-\frac{y_c^2}{z}\right)^{1/2}dz\,, \tag{42}$$

and two other solutions are easily shown to be $f_0=\text{const.}$ and $f_0=z$.

For large αR, the even solution P (55) must be asymptotically represented by a linear combination of the solutions (42). On the other hand, near the critical point $z=y_c^2$, we have, from (42),

$$s\sim\frac{2}{3}y_c^{-1}(z-y_c^2)^{3/2}\sim\frac{4}{3}(2y_c)^{1/2}(y-y_c)^{3/2}$$

so that (41) reduces to

$$\begin{aligned}\frac{d^2f_0}{dz^3}&\sim\frac{2}{\sqrt{3}\,y_c^2}(y-y_c)^{1/2}\\&\quad\times H_{1/3}^{(1),(2)}\left[\frac{2}{3}(-2y_c i\alpha R)^{1/2}(y-y_c)^{3/2}\right]\\&=\text{const.}\ \eta^{1/2}H_{1/3}^{(1),(2)}\left[\frac{2}{3}\eta^{3/2}\right].\end{aligned}$$

Representing once the asymptotic expression of P (55) as a linear combination of (41) and imposing the second condition in (4), it is found that for large αR we have approximately

$$\left.\begin{aligned}\frac{d^2f_0}{dz^2}&\sim\text{const.}\ \eta^{1/2}H_{1/3}^{(2)}\left[\frac{2}{3}\eta^{3/2}\right]\\&=\text{const.}\ \ddot{\varphi}_0(\eta)\,.\end{aligned}\right\} \tag{43}$$

Thus, as mentioned before, *the solution* P(55) *is nothing but alternative expression of the same solution φ_0 which leads of course only to the first class of perturbation.*

§ 6. Summary

Among many disagreements between Lin's and Pekeris's calculations on the stability of plane Poiseuille flow, two main discrepancies are examined in the present paper.

The first one, i.e. the stability-instability discrepancy, is found to be attributed to the poor convergency of Pekeris's series expansion of c, and Lin's prediction of the existence of the neutral curve seems to be completely confirmed.

The second discrepancy concerning the "second class" of disturbance arises, in contrast to the first, from a rather careless error on Pekeris's part of adopting an inadequate asymptotic expansion formula. Thus, the existence of the "second class" of mode seems to be quite excluded.

In conclusion, the author wishes to express his sincere thanks to Professor S. Tomotika for suggesting this problem. The author is indebted to Professor I. Imai for kind suggestions, and to Dr. K. Tamada for many helpful advices and discussions. Throughout this study the author has been in receipt of a grant in aid for fundamental scientific research from the Ministry of Education.

References

1) W. Tollmien: Nachr. Ges. Wiss. Göttingen (1929) 21.

2) H. Schlichting: Nachr. Ges. Wiss. Göttingen **1** (1935) 47.

3) C. C. Lin: Quart. Appl. Math. **3** (1945-46) 117 (Part I), 218 (Part II), 277 (Part III).

4) G. B. Schubauer and H. K. Skramstad: J. Aero. Sci. **14** (1947) 69.

5) W. Heisenberg: Ann. d. Phys. **74** (1924) 577.

6) C. L. Pekeris: Phys. Rev. **74** (1948) 191.

7) J. v. Neumann: 'Recent theories of turbulence', (unpublished) (1949).

8) R. E. Langer: Trans. Amer. Math. Soc. **33** (1931) 23, **34** (1932) 447. Cf. M. J. Lighthill: Quart. J. Mech. Appl. Math. **3** (1950) 303.

JOURNAL OF THE PHYSICAL SOCIETY OF JAPAN Vol. 7, No. 6 NOV.—DEC., 1952

On the Solution of Trans-sonic Flow using Laplace Transformation

By Tatudiro SASAKI

Numerical Computation Bureau

(Received July 10, 1952)

The solution of trans-sonic flow is treated by the use of Laplace transformation in the hodograph method. As an example, the trans-sonic flow past a nearly circular cylinder is calculated.

In the hodograph transformation in trans-sonic flow, the stream function is usually expressed in the form of series, which makes the solution very complicated, I propose here a new method using Laplace transformation, and obtain the solution of the stream function in the form of an integral.

The primitive solution of the fundamental equation in the hodograph plane is expressed in the form

$$\psi=\Im(f)=\Im[Q_\alpha(q)e^{-i\alpha\theta}], \qquad (1)$$

where ψ is the stream function, q is the absolute value of the velocity, θ is its inclination and α is a parameter. $Q_\alpha(q)$ is expressed by

$$\left.\begin{aligned} &Q_\alpha(q)=(q/U)^\alpha F(a_\alpha,b_\alpha,\alpha+1\,;\ q^2/q^2_{\max}),\\ &a\alpha+b\alpha=\alpha-(\gamma-1)^{-1},\\ &a\alpha b\alpha=-2^{-1}(\gamma-1)^{-1}\alpha(\alpha+1). \end{aligned}\right\} \qquad (2)$$

Let $\alpha=-t$, $p=\tau-i\theta$, and integrate (1) with respect to t from 0 to ∞, as follows

$$f(p)=\int_0^\infty A(t)F(a_{-t},\,b_{-t},-t+1\,;\ q^2/q^2_{\max})e^{-pt}dt, \qquad (3)$$

where $A(t)$ is the inverse Laplace transformation corresponding to the complex velocity potential of the incompressible fluid flow, expressed as a function of $(q/U)e^{-i\theta}$, *i.e.* e^p, U being the undisturbed flow velocity.

Example

As an example of the above method we take the case of the stream function of compressible fluid flow past a nearly circular cylinder.

The complex velocity potential of the incompressible fluid flow past a circular cylinder is exprcssed as a function of $(q/U)e^{-i\theta}$, *i.e.* e^p is

$$F_0(p)=U\left(\sqrt{1-e^p}+\frac{1}{\sqrt{1-e^p}}\right). \qquad (4)$$

It is expressed by Laplace transformation as follows

$$F_0(p)=\int_0^\infty A(t)e^{-pt}dt, \qquad (5)$$

and its invers Laplace transformation is

$$A(t)=\frac{1}{2\pi i}\int_{-i\infty}^{+i\infty}F_0(p)e^{pt}dp \qquad (6)$$

we expand the hypergeometric function in (3) in series, and as the first approximation take the first two terms:

$$F(a_{-t},\,b_{-t},\,-t+1\,;\ q^2/q^2_{\max}) \doteqdot 1+\frac{t}{2(\gamma-1)}\frac{q^2}{q^2_{\max}}. \qquad (7)$$

Puting (7) in (3) we obtain

$$\begin{aligned} f(p)=&\int_0^\infty A(t)e^{-pt}dt+\\ &\frac{1}{2(\gamma-1)}\frac{q^2}{q^2_{\max}}\int_0^\infty tA(t)e^{-pt}dt\\ =&F_0(p)-\frac{1}{2(\gamma-1)}\frac{q^2}{q^2_{\max}}\frac{dF_0}{dp} \end{aligned} \qquad (8)$$

Hence

$$\begin{aligned} \psi=\Im U\Bigg\{&\sqrt{1-e^p}+\frac{1}{\sqrt{1-e^p}}\\ &-\frac{1}{4(\gamma-1)}\frac{q^2}{q^2_{\max}}\frac{e^{2p}}{(1-e^p)^{3/2}}\Bigg\}. \end{aligned} \qquad (9)$$

To obtain $z=x+iy$ in terms of q and θ we have to make use of the relation

$$\frac{\partial z}{\partial\theta}=\frac{\rho_0}{\rho q}\left(q\frac{\partial\psi}{\partial q}+i\frac{\partial\psi}{\partial\theta}\right)e^{i\theta}. \qquad (10)$$

Let $2^{-1}(\gamma-1)q^{-2}_{\max}=B$ and $-dF_0/dp=F_1$; we get from (8)

$$f(p)=F_0(p)+Bq^2F_1(p). \qquad (11)$$

Putting this relation in (10) we get

$$\begin{aligned} \frac{\partial z}{\partial\theta}=\frac{\rho_0}{\rho q}\Bigg\{&\Im\left[\frac{dF_0}{dp}+Bq^2\frac{dF_1}{dp}+2Bq^2F_1\right]\\ &-i\Re\left[\frac{dF_0}{dp}+Bq^2\frac{dF_1}{dp}\right]\Bigg\}e^{i\theta} \end{aligned}$$

$$=\frac{\rho_0}{\rho q}[\Im F_2(e^{-i\theta})-i\Re F_3(e^{-i\theta})]e^{i\theta}$$

$$=\frac{\rho_0}{\rho q}\left[\frac{F_2(e^{-i\theta})-F_2(e^{i\theta})}{2i}\right.$$

$$\left.-i\frac{F_3(e^{-i\theta})+F_3(e^{i\theta})}{2}\right]e^{i\theta}. \qquad (12)$$

Integrating (12) with respect to θ we obtain z in terms of q and θ as follows;

$$z=\frac{\rho_0}{\rho}\left[\frac{1}{\sqrt{1-e^p}}(1-2Bq^2)\right.$$

$$\left.-\frac{B}{2}q^2\frac{e^p}{(1-e^p)^{3/2}}\right]$$

$$-\frac{\rho_0}{\rho}B\left[e^{p_1}\left\{\sqrt{1-e^{p_1}}+\frac{1}{\sqrt{1-e^{p_1}}}\right\}\right.$$

$$\left.+2\left\{\frac{(1-e^{p_1})^{3/2}}{3}+\sqrt{1-e^{p_1}}\right\}\right] \qquad (13)$$

where p_1 stands for $\tau+i\theta$.

Numerical Calculations

We perform the numerical calculations in the case of a circular cylinder when $U=0.4c_\infty$. At first calculate the stream line $\psi=0$, and then calculate the corresponding z.

The stream function is a continuous function in the two sheeted Riemann surface in the hodograph plane, and is symmetric with respect to the line $\theta=0$. The part of the stream line $\psi=0$ from ∞ to the stagnation point corresponds to the straight line from the point $q=U$, $\theta=0$ to $q=0$. The other part of the stream line $\psi=0$ is calculated as in Table I, and is shown in Fig. 1.

Table I

θ	q/U
0°	2.542
15°	2.410
21°	2.290
30°	2.058
45°	1.574
60°	1.050
75°	0.510
90°	0.000

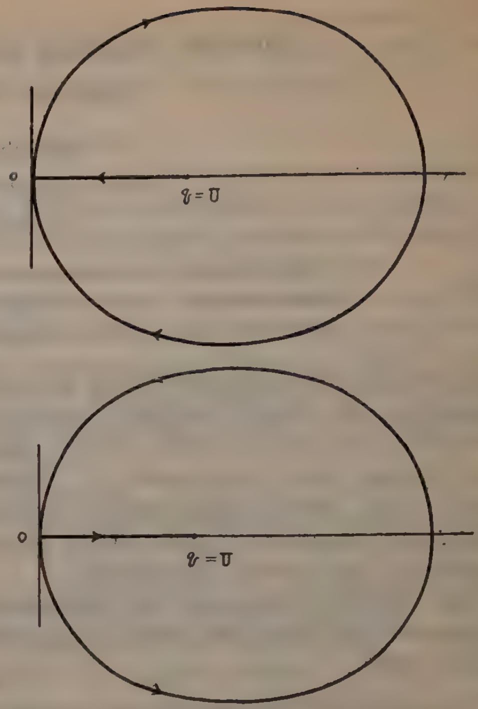

Fig. 1.

The upper sheet of the Riemann surface corresponds to the upper half of the z plane, and the lower sheet to the lower half of the z plane.

Using the values in Table I, we calculate the corresponding z by the equation (13). The results are shown in Table II. The local Mach numbers on each point on the cylinder are also calculated in Table II.

Table II.

θ	X	Y	M
0	0	1.1669	1.1436
15	0.3354	1.1030	1.0699
21	0.4543	1.0438	1.0054
30	0.6138	0.9321	0.8868
45	0.8220	0.7349	0.6586
60	0.9776	0.5076	0.4277
75	1.0698	0.2821	0.2049
90	1.1067	0	0

JOURNAL OF THE PHYSICAL SOCIETY OF JAPAN Vol. 7, No. 6 NOV.—DEC., 1952

Un Traitement Statistique de la Résistance à la Rupture du Verre — Sur l'Influence de la Température*

Par Nobuzo TERAO

Institut de Physique, Faculté des Sciences, Université de Tokyo

(Reçu le 26 juin 1952)

We have studied on the effect of temperature especially on the fluctuation of the strength of glass under uniformly increasing load with time on the center of glass plate suspended freely at the two ends. The region of temperature was between the room temperature and 300°C. $\mu(t)$, the probability of breakdown at the time t, is described as follows,

$$\mu(t)= a \exp \left[-\frac{E_0(T)-\beta f}{kT}\right]$$

Here, $E_0(T)$ is the activation energy for breakdown when there is no applied load, f the load, βf the energy applied by external load, T the absolute temperature and k is the Boltzmann's constant. According to the result of experiment, β is not constant but depends on the temperature, having a minimum at about 150°C. The magnitude of E_0 is some kcals/mol and increases with the temperature.

§ 1. Introduction

A cause de la structure corpusculaire de la matière, diverses grandeurs physiques que nous pouvons observer ont inévitablement des caractères statistiques. Surtout, dans le cas de phénomènes où un changement microscopique se développant dans une direction entraine un changement macroscopique, les valeurs obtenues par l'observation ne sont jamais constantes, mais on reconnait qu'il y a des diffréences remarquables entre elles, même si l'on règle toutes les conditions d'observation avec une grande précision. Un phénomène tel que la rupture appartient à cette catégorie. Par exemple, lorsqu'un corps fragile comme le verre ou le bitume se rompt, savoir par quel effort, à quel endroit un tel nombre de cassures se présente, c'est un problème que l'on ne peut traiter sans recourir à l'idée de probabilité, Le point où se trouve l'origine d'une cassure ne s'accorde pas toujours avec le lieu qui a subi l'effort le plus grand et en certaines circonstances plusieurs cassures partent presque en même temps des points très nombreux d'une étendue placée sous un effort à peu près uniforme[1]. Par conséquent, nous croyons que quant à la résistance à la rupture de la matière et à la distribution spatiale des cassures, il est nécessaire d'adopter un traitement statistique. D'après cette conception, M. M. Hirata a fait en 1948 des expériences pour examiner la variation des temps de retard au moment où casse un échantillon de verre auquel a été appliqué un effort constant "f"[2].

Nous prenons comme origine du temps le moment où un effort constant se met à peser sur un èchantillon de verre. A quel moment sera-t-il rompu, c'est un problème de probabitité. Nous désignerons par $\mu(t)dt$ la probabilité pour que la cassure du verre naisse entre les temps t et $t+dt$, $q(t)dt$ montre la proportion des échantillons qui se rompent entre les temps t et $t+dt$, et enfin $p(t)$ la probabilité pour que le temps de retard de rupture soit plus long que t. Voici les relations que l'on obtient entre ces quantités,

$$p(t)=\int_t^\infty q(t)dt \tag{1}$$

$$p(0)=1 \tag{2}$$

$$\mu(t)dt=-dp/p=-d(ln p) \tag{3}$$

D'après les résultats obtenus, $\mu(t)$ est constant lorsque f est d'une valeur invariable.

$$\mu(t)=m \tag{4}$$

Cela veut dire que la probabilité de transition à l'état de rupture est constante, c'est à dire, la naissance de la cassure est complètement accidentelle comme dans le cas des désintegrations de corpuscules élémentaires. De plus, en ce qui concerne la relation entre μ et f, M. M. Hirata a obtenu la relation approchée suivante

---

* Séance de la Société de Phys. le 13 avril et le 9 octobre 1951.

$$\mu = A \exp(\alpha f) \qquad (5)$$

Puis, nous avons étudié les variations de la résistance à la rupture de verre au cas où l'effort augmente proportionellement au temps et nous avons constaté que l'équation (5) est vérifiée approximativement[3]. Dans ce cas, on a successivement

$$f = rt \qquad (6)$$

$$\mu = A \exp(\alpha rt) \qquad (7)$$

$$p = \exp\left\{\frac{A}{\alpha r}(1 - e^{\alpha rt})\right\} \qquad (8)$$

$$q = A e^{\alpha rt} \exp\left\{\frac{A}{\alpha r}(1 - e^{\alpha rt})\right\} \qquad (9)$$

On pourrait montrer par l'équation suivante la probabilité de la naissance de la cassure μ, selon la théorie thermodynamique de la vitesse de réaction, telle que[4]

$$\mu = a \exp\left\{-\frac{E_0 - E}{kT}\right\} \qquad (10)$$

où E_0 représente l'énergie d'excitation au cas où il n'y a pas de force extérieure, E l'énergie donnée par la force extérieure, k la constante de Boltzmann et T la température absolue. Basé sur cette relation, on peut conclure expérimentalement d'après l'équation (5) que E est proportionel à la force extérieure f. C'est à dire

$$E = \beta f \qquad (11)$$

$$a \exp\left(-\frac{E_0}{kT}\right) = A \qquad (12)$$

$$\beta / kT = \alpha \qquad)13)$$

μ doit avoir une relation intime avec la température comme l'on voit en (10). Sur ce sujet nous avons fait les essais suivants.

§ 2. Expérience

Nous avons mis l'échantillon de verre "S" sur deux appuis cunéiformes placés par intervalle de 100 *mm* dans un four dont la température intérieure était fixée à une certaine valeur (Fig. 1). "A" est un réservoir de verre où l'on met du sable fin et sec et on le fait tomber dans une boîte B à travers un petit trou percé au fond pour donner du poids de la part de "B" sur l'échantillon "S" au point central entre deux appuis. La vitesse de l'écoulement de sable est constante[5].

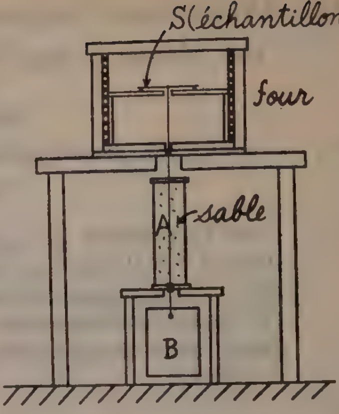

Fig. 1. Appareil

Ainsi, nous pouvons donner à l'échantillon un effort qui augmente en proportion de la longueur du temps. Et, nous avons mesuré les temps entre le commencement de la charge et la rupture soudaine. Mais, dans ce cas, le poids de la boîte "B", s'il est assez léger, est déjà donné sur "S" au moment $t = 0$. La vitesse de la charge employée ici était $r = 8.56$ *gr/sec*. La largeur des échantillons, de verre ordinaire de sodium-chaux, était de 10,0 *mm*, leur épaisseur de 2.0 *mm* en cas de (I) et de 1.65 *mm* en cas de (II). Nous avons effectué les essais successivement où la température était respéctivement 10°C, 50°C, 100°C, 150°C, 200°C, 250°C, 300°C et le nombre total N des échantillons était d'environ 50 à 100 dans chaque cas. La Fig. 2 montre la distribution du temps de retard de rupture en cas de (II), c'est à dire, la distribution de la résistance à la rupture. Les relations en deux cas entre des valeurs moyennes de la résistance à la rupture f en exprimant l'effort maximum de tension au point central de l'échantillon et la température, sont indiquée par les courbes de la Fig. 3 qui ont des minima près de 170～180°C. Ce caractère s'accorde avec les résultats obtenus jusqu'ici.[6]

§ 3. Sur μ et Discussion

Dans le traitement statistique ci-dessus de la résistance à la rupture, ce qui est le plus important est la probabilité μ de la naissance de la cassure. Nous pouvons la calculer, selon les équations (1) et (3), avec le diagramme de la distribution de la résistance à la rupture comme Fig. 2. La Fig. 4 montre la relation entre $\log \mu$ gagné comme-ci et l'effort f.

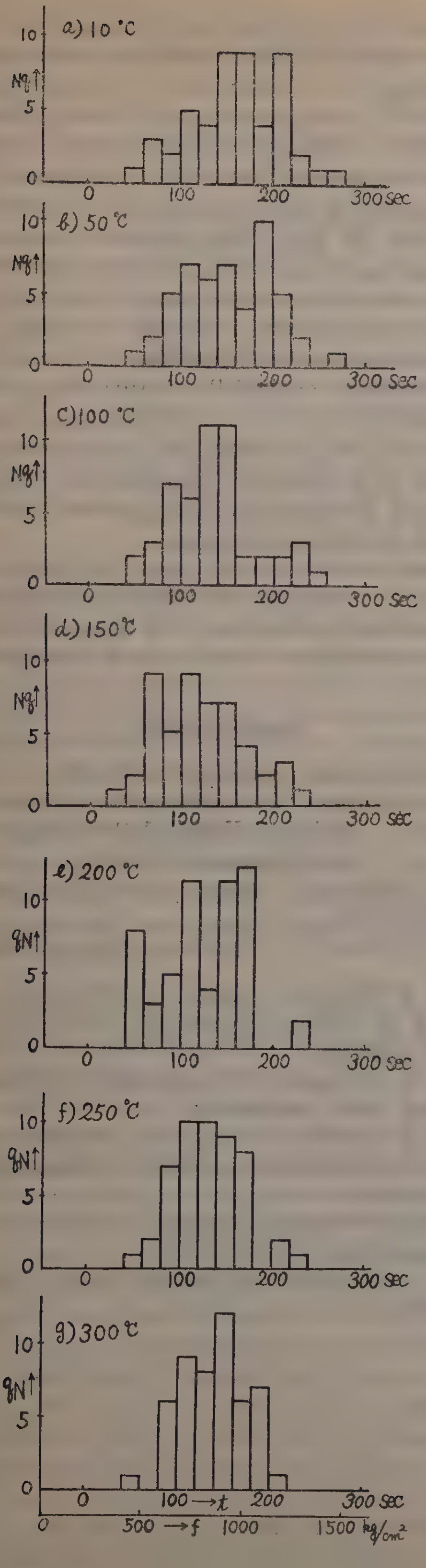

Fig. 2. Distribution de la Résistance à la Rupture.

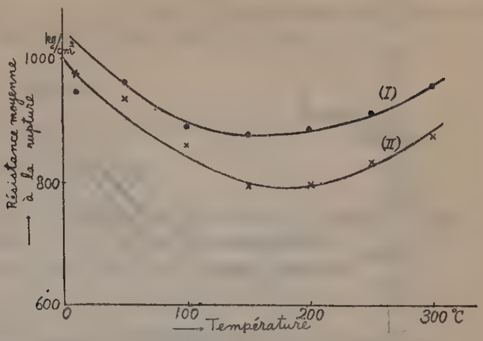

Fig. 3. Relation entre la Résistance moyenne à la Rupture et la Température.

Elle indique que l'équation (5) est assez bien satisfaite.

Si considère l'équation (10), on peut obtenir une connaissance jusqu'à un certain degré de l'énergie d'excitation E_0 et l'énergie E donnée par la force extérieure. D'abord, on a β lié à E par l'inclinaison de la ligne droite à la Fig. 4. La Fig. 5 montre les valeurs de β en exprimant f par l'effort maximum de tension calculée par la théorie ordinaire simple de l'elasticité.

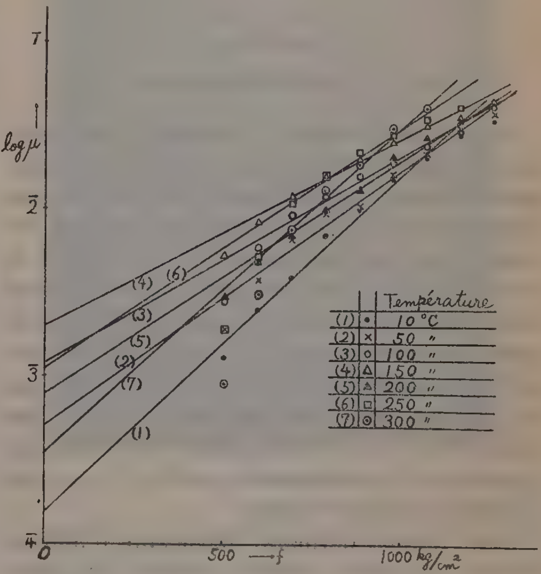

Fig. 4. Relation entre log μ et l'effort f.

On ne peut avoir définitivement l'énergie d'excitation E_0 car le coefficient "a" n'est pas encore fixé. Mais, la Fig. 6 montre des relations entre la température et E_0 dans le cas où l'on pose $a \approx kT/h \approx 10^{13}$ sec^{-1} qui est du même ordre que le nombre de fréquence de l'oscillation thermique de l'atome et dans le cas où l'on pose $a \approx 10^{10}$ sec^{-1}.

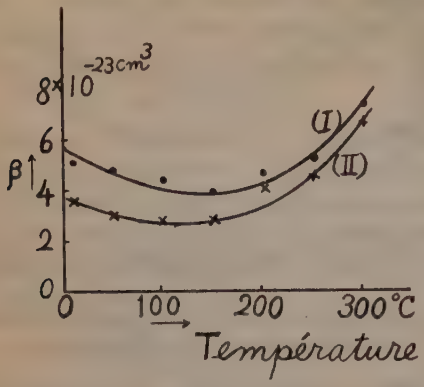

Fig. 5. $\beta(T)$

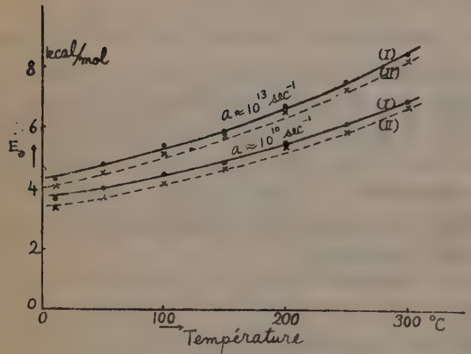

Fig. 6. Energie d'excitation E_0

Dans tous les deux, l'énergie d'excitation est au plus plusieurs *kcals/mol* et elle augmente avec la température. Ces valeurs sont sensiblement moindres que 150 *kcal/mol* supposé dans les phénomènes où il s'agit de la viscosité. Ce fait indiquerait que l'élément ayant des relation avec le mécanisme de rupture est sensiblement plus grand que l'atome ou la molécule. De plus, on peut voir que E_0 au cas de (II) est plus petit que celui au cas de (I) et en conséquence la résistance moyenne à la rupture au cas de (I) est plus grande que celle d'autre.

Ces temps derniers, beaucoup d'auteurs publient des traitements théoriques sur le phénomène de rupture selon des conceptions basées sur la theorie de la vitesse de réaction$^{7)-11)}$. Mais, dans ce cas, il faut d'abord réfléchir au mécanisme de la rupture. Donc, il est nécessaire d'éclaircir le mécanisme de la naissance et de la croissance d'une cassure. On doit, de plus, faire attention à ce que μ que nous avons introduit ne dépend pas seulement de l'effort maximum de tension mais aussi de la manière de charger un effort et de la dimension de l'échantillon. Et, la matière adsorbée, quoiqu'elle ait sans doute une relation intime avec la température, influe beaucoup sur la résistance à la rupture du verre. Par exemple, l'adsorption de l'eau la diminue notablement. Ces questions feront l'objet d'études ultérieures.

Nous exprimons enfin notre profonde gratitude au Professeur M. Hirata pour l'intérêt bienveillant qu'il a porté à ce travail et toutes les possibilité qu'il a mis à notre disposition.

Bibliographie

1) M. Hirata: *Kagaku* **7** (1937) 585.
2) M. Hirata: Bull. Math. Stat. **3** (1949) 57.
Kikai no Kenkyu **1** (1949) 182, 231.
Ôyo Tôkei-gaku (1949) 11.01.
3) M. Hirata, N. Terao: J. App. Phys. Japan **20** (1951) 234.
4) K. Ômori: J. Eng. Kyushu Univ. **16** (1942) 239.
5) K. Takahashi: *Riken-iho* **12** (1934) 984.
6) R. N. Haward: The Strength of Plastics and Glass (1949) 57.
7) J. C. Fisher, J. H. Hollomon. D. Turnbull: J. App. phys. **19** (1948) 775.
8) J. C. Fisher: J. App. Phys. **19** (1948) 1062.
9) D. Turnbull, J. C. Fisher: J. Chem. Phys. **17** (1949) 71.
10) F.B. Hodgon, D. A. Stuart, F. E. Bjorklund: J. App. Phys. **21** (1950) 1156.
11) T. Yokobori: J.Phys. Soc. Japan. **7** (1952) 44, 122.

JOURNAL OF THE PHYSICAL SOCIETY OF JAPAN Vol. 7, No. 6 NOV.—DEC., 1952

Sur la Réfraction de la Cassure par les Chocs*

Par Nobuzo TERAO

Institut de Physique, Faculté des Sciences, Université de Tokyo

(Reçu le 7 juillet 1952)

An uniform dilatational stress was produced in a thin layer of resin melted on a metallic tray by rapid cooling. This layer of resin holded on the tray was floated on the water and some mechanical shocks were given by electric discharges at two or three adjacent points near the bottom of the tray. The phenomena of the refractions of the cracks thus produced in the resin starting from each of these points were studied. At the places where $\alpha > 90°$ (α, angle between the direction of the crack starting from one of the sources A′ and that of the shock wave from the other source A), the cracks refracted towards the point A, while if $\alpha < 90°$, the cracks refracted in the direction diverging from the point A. The velocity of propagation of these cracks was estimated from the relation between the distances travelled by the crack and the shock wave.

On peut obtenir une couche de résine de pin dans un état de tension remarquable quand on fait fondre par la chaleur la résine de pin sur un plateau en métal et qu'on la fait refroidir rapidement. Dès qu'une pointe d'aiguille touche un point de la surface de cette couche, une cassure radiale part de ce point et elle s'étend sur le plateau entier en un instant. Sur ce phénomène, M. R. Taguti a déjà publié un mémoire en 1931[1)], et il a mesuré aussi la vitesse approximative de croissance de cette cassure grâce à une méthode ingénieuse.

Nous avons mis deux ou trois paires d'éclateurs dans une eau peu profonde et fait flotter un plateau susdit (l'épaisseur de la couche de résine est d'environ 0.2 à 1.0 mm) d'aluminium ou d'acier sans tache auprès des éclateurs. Une tension d'environ 30 à 50 kv permet de faire passer les étincelles au milieu de l'eau et des cassures se forment sous les chocs mécaniques de ces décharges. Les Fig. 1 et Fig. 2 montrent respectivement deux cassures qui naissent presque en même temps avec les décharges de deux paires d'éclateurs. Lorsque la tension de la couche de résine due à l'action de la chaleur est forte, des cassures partant de deux points de chocs A_1 et A_2 se développent le long des lignes courbes lisses comme les Fig. 1 et Fig. 3, tandis que si la tension est faible et le choc est fort, il se produit des cassures qui se réfractent brusquement comme on voit dans la Fig. 2.

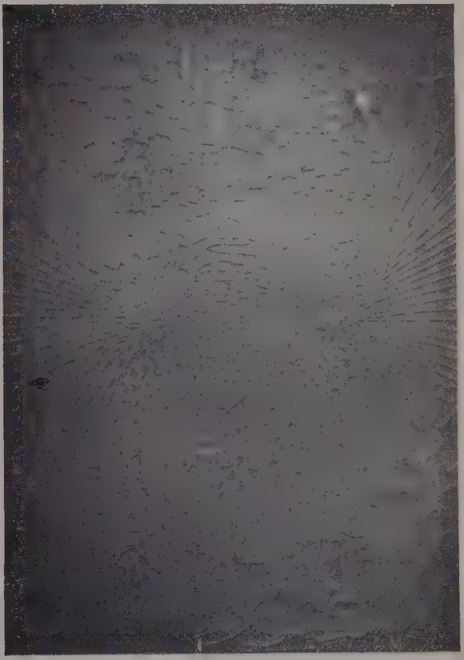

Fig. 1.

Des cassures partant des points A_1 et A_2 pour le domaine compris entre des angles $\angle P_1A_1P_2$ et $\angle P_1A_2P_2$ se développent en s'approchant l'une de l'autre, mais celles à l'extérieur de ces angles se développent en s'écartant (Fig. 3). Nous désignons les points qui limitent les zones d'attraction des zones de répulsion par B_1, B_2, B_3 et B_4. Les angles $\angle A_1B_1A_2$, $\angle A_1$

---

* Séance de la Société de Physique, le 29 avail 1949.

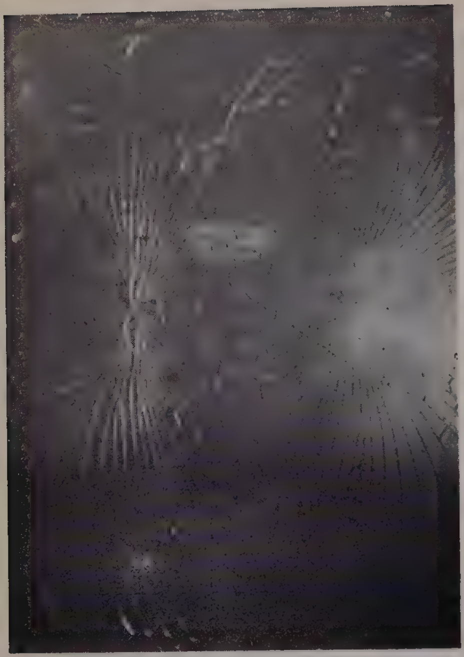

Fig. 2.

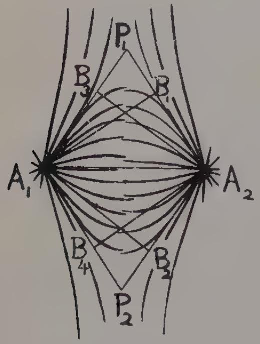

Fig. 3.

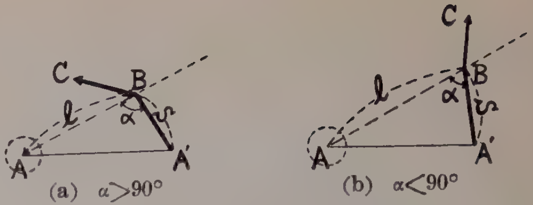

Fig. 4 Réfraction d'une cassure par un choc.
A: Point de choc.
A': Point de départ d'une cassure.
B: Point de réfraction.

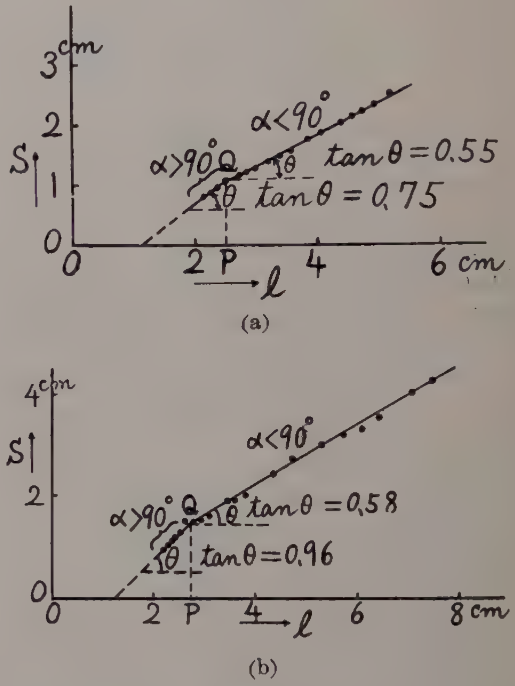

(a)

(b)

Fig. 5.

B_2A_2, $\angle A_1B_3A_2$ et $\angle A_1B_4A_2$ sont tous de 90°. Si on produit un choc au point A_1 et qu'une cassure parte spontanément par hasard sans choc du point de A_2, seule la cassure A_2 se réfracte avec le choc de A_1 et la cassure A_1 ne donne pas lieu à la réfraction. D'après ce fait, on voit que le phénomène remarquable susmentionné de la réfraction de cassure est dû au choc. Supposons, dans la Fig. 4, que l'onde de choc arrive au point de B au moment où la cassure se développe du point A' jusqu'au point B. Si l'angle $\alpha > 90°$, la cassure se réfracte vers le point A comme la Fig. 4(a), si $\alpha < 90°$, elle se réfracte en s'éloignant du point A comme la Fig. 4(b).

Les Fig. 5(a) et (b) sont des exemples qui montrent la relation entre s, distance de croissance de la cassure et l, distance de traversée du choc dans le cas où il se produit des cassures ayant des réfractions brusques comme dans la Fig. 2. Ces relations sont en général linéaires et des valeurs des pentes de ces lignes, tan θ, sont d'environ 0.5 à 0.9 même si elles sont très rarement plus grande que 1.0. Plus la déformation thermique de la couche de résine est grande et plus le choc est fort, plus tan θ a tendance à être grand. Les valeures de tan θ dans les domaines de $\alpha > 90°$ et de $\alpha < 90°$ ne sont pas les mêmes et celle-ci est moins grande que celle-là à l'exception d'exemples très rares. Si la tension de la résine est plus faible, la relation entre s et l s'écarte d'une relation linéaire, et s augmente proportionellement moins que l.

Un phénomène analogue de réfraction de cassure par des chocs avait été observé autrefois sur une dalle mince de verre par M. M. Hirata[2]. Dans ce cas, la dalle de verre avait reçu des chocs directement et il n'y avait pas eu de matière intermédiaire comme le plateau employé ici. Par conséquent, nous avons conclus que la réfraction de cassure est provoquée par l'onde de choc traversant l'intérieur du verre ou de la résine eux-mêmes. Si nous posons que l'onde de choc s'avance avec la vitesse constante d'environ 1600 m/sec de celle de l'onde longitudinale dans la résine de pin[3], on aurait la valeur de 800 m/sec à 1400 m/sec comme vitesse de propagation de la cassure produite ici et ceci s'accorde à peu près avec les résultats obtenus par M. R. Taguti. On peut supposer, selon la Fig. 5, qu'il y a le temps de retard d'environ 10^{-6} sec dans le départ de la cassure. Et, $\tan \angle B_1A_1A_2 = A_2B_1/A_1B_1$ (Fig. 3)$=PQ/OP$ (Fig. 5). Si $PQ/OP=0.7$, $\angle B_1A_1A_2 \approx 35°$. Donc $\angle A_1P_1A_2 \approx 70°$. Si $PQ/OP=0.6$, $\angle B_1A_1A_2 \approx 30°$ et $\angle A_1P_1A_2 \approx 60°$. En effet, lorsque la vitesse de propagation de la cassure de résine semble grande, des angles $\angle A_1P_1A_2$ et $\angle A_1P_2A_2$ dans la Fig. 3 sont d'environ 70° et lorsque la vitesse de propagation de la cassure semble petite, les angles sont de moins de 60°. D'après l'étude rapportée plus haut sur le verre par M. M. Hirata, les angles $\angle A_1P_1A_2$ et $\angle A_1P_2A_2$ sont d'environ 90°, si l'on donne des chocs très forts à une dalle mince de verre. Cela veut dire que la vitesse de propagation de la cassure est alors presque égale de celle de l'onde de choc et le temps de retard de la naissance de la cassure est trop court. Des essais où la cassure se réfracte deux fois par deux chocs en employant trois paires d'éclateurs nous montrent que la vitesse de la cassure diminue un peu après une réfraction.

L'auteur se permet de remercier M. M. Hirata, professeur de la Faculté des Sciences, Université de Tokyo, pour l'intérêt qu'il à porte à ce travail et les encouragements qu'il n'a cessé de lui prodiguer.

Références

1) R. Taguti: *Riken-iho* **10** (1931) 110.
2) M. Hirata: Séance de la Societe de Physique appliquée, le 29 juin 1947.
3) Eric J. Irons: J. Sci. Inst. **7** (1930) 323.

JOURNAL OF THE PHYSICAL SOCIETY OF JAPAN Vol. 7, No. 6 NOV.—DEC., 1952

The Direct Current associated with Microwave Gas Discharge between Coaxial Cylinders, I

By Kenji MITANI

Yoshida College, University of Kyoto

(Received July 5, 1952)

The author has found that when the microwave gas breakdown occurs, the direct current flows, without application of any direct voltage, in the external circuit from the outer conductor to the central wire of a cylindrical cavity containing gas.

An attempt has been made to explain this phenomenon by use of the diffusion theory of Herlin and Brown. The electron diffusion current density potential has been determined and thence the maximum electron density has been derived.

§ 1. Introduction

Recently Herlin and Brown¹⁾ have proposed the diffusion theory of microwave gas discharge, in which they consider that the generation by collision and the loss by diffusion of electrons balance themselves and therefore the gas discharge is maintained. In the d. c. gas discharge, the generation of electrons has been expressed by three Townsend cofficients, α. β, γ, and the loss of electrons ascribed to the drift motion by a d. c. field. In the microwave gas discharge, however, the generation of electrons can be ascribed only to collision which corresponds to Townsend coefficient α, and the loss of electrons can be ascribed to the diffusion instead of the drift motion by a d. c. field.²⁾

Herlin and Brown have introduced the function $\psi=Dn$ and derived the fundamental equation:

$$\nabla^2\psi-\zeta E^2\psi=0\ ,$$

where D, n and E are respectively the diffusion coefficient, the electron density and the r. m. s. value of the microwave field intensity. ψ is called the electron diffusion current density potental, and ζ the high frequency ionization coefficient. They have measured the coefficient ζ and showed that the microwave gas discharge can well be explained by their theory.

The present author has made experiment, using the coaxial cylinders as a microwave discharge tube and has found the appearance of a direct current flowing in the external circuit from the outer cylinder to the central conductor when the microwave gas discharge occurs.

The author has shown the possibility of the occurrence of this direct current on the basis of the diffusion theory of Herlin and Brown, and has been able to determine the absolute value of the function ψ from the experimental results. The experiment has been performed on air at a frequency $f=2.6\times10^3$ Mc/sec corresponding to the free space wave length $\lambda=11.5$ cm.

§ 2. Experimental Apparatus

Fig. 1. shows the block diagram of the apparatus used. For the high frequency source, M 112 N C. W. magnetron ($\lambda=11.5$ cm, and output power about 30 watts) manufactured by the Japan Radio Co. was used, and the output power varied with the variable attenuator A₁. B₁ and B₂ are the crystal detectors to detect the occurrence of the breakdown in the discharge tube. The directional coupler is of Schwinger type. The discharge tube formed by coaxial cylinders is shown in Fig. 2. The both ends of the part of the

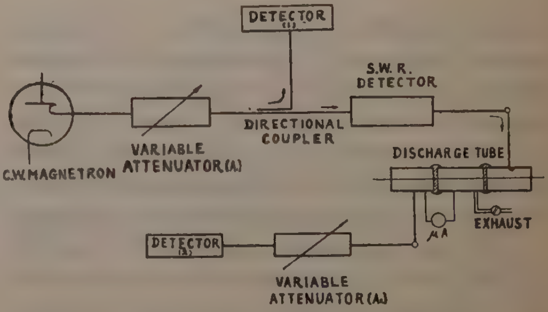

Fig. 1. Block diagram of the apparatus.

outer cylinder, cut off at the middle of the coaxial cylinders, were sealed by glass (B). The length of this part war selected to be 11.5 cm corresponding to approximately the wave length of the driving power. This vessel (A) is filled with a desired gas and the breakdown is caused.

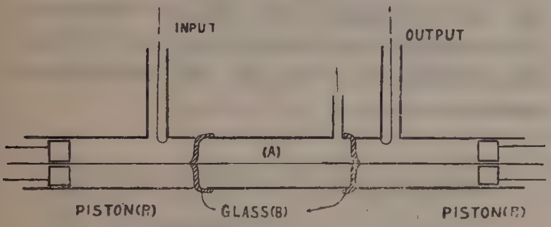

Fig. 2. Discharge tube.

As the length of the vessel (A) is about one wave length, the loops of electric field intensity occur at the sealed parts and the middle. The piston P_1 and P_2 sliding in the cylinders are used to match the cavity. The inlet and the outlet of the power to the cavity are situated at the positions corresponding to the loops of magnetic field intensity. The outer conducter of the vessel is formed by brass cylinder of radius $b=12.5$ mm, and the inner conductor by tungsten wire of radius $a=0.1$ mm, so the ratio b/a is 125. Furthermore, in order to observe the state of the discharge in the cavity, a mica window (about 7 mm long and 2 mm wide) is made on the outer cylinder along the cylinder axis.

The breakdown is attained as follows. As the input power is increased by use of the variable attenuator A_1, the crystal current of the detector B_2 increases, but when this current reaches a certain value, it suddenly drops to a lower value. This is because the breakdown has occurred in the discharge tube and its Q-value has dropped.

At the same time when the breakdown has been reached, we can find the appearance of the direct current by the meter M in Fig. 1 flowing from the outer cylinder to the central conducter, and also we can observe a glow through the mica window.

§ 3. Experimental Results

The direct current J which occurs associated with the breakdown of air has been measured at various pressures. Fig. 3 shows these results. By the magnetron used in this experiment, the breakdown has not been attained outside the pressure range shown in Fig. 3. This is because a very large power is needed for very high as well as very low pressures, as is easily expected and also can be concluded from the experimental results of Herlin and Brown.[1]

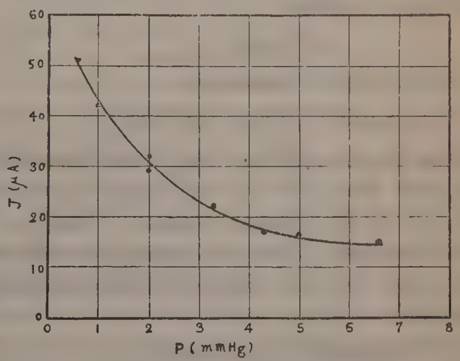

Fig. 3. Direct current J versus pressure P.

The length of the glow appearing along the central conductor of the cavity has been about 9 mm for $P=4.3$ mmHg and $J=17.0$ μA. The detailed discussion of the length of the glow is given in a subsequent report.

§ 4. Discussion on the Direct Current

Herlin and Brown have applied their diffusion theory to the discharge in the coaxial cylindrical cavity[3] and have obtained the electron diffusion current density potential ψ in the form:

$$\psi=AJ_0(\rho)+BN_0(\rho)\,, \qquad (1)$$

where J_0 is the Bessel function of the first kind and N_0 the Neumann function, and ρ is given by

$$\rho=2ka(a/r)^{(\beta-2)/2}/(\beta-2)\,, \qquad (2)$$

where a is the radius of the central conductor, r the distance from the central axis, and β and k are certain constants. Constants A and B in Eq. (1) are determined by the boundary condition that ψ becomes zero at the walls. From this condition, the ratio A/B is obtained as:

$$A/B=\frac{N_0[(b/a)^{(\beta-2)/2}x]}{J_0[(b/a)^{(\beta-2)/2}x]}\,, \qquad (3)$$

where a and b are respectively the radii of the inner and outer conductors, and x is defined as:

$$x=2ka(a/b)^{(\beta-2)/2}/(\beta-2)\ , \qquad (4)$$

We can determine the values of β, k and A/B so as to adapt our experimental conditions.

From the definition of function ψ, the electron current density (i. e the number of electrons that flow per unit time through unit area is given

$$\Gamma=-\text{grad}\,\psi\ . \qquad (5)$$

In our case Γ becomes:

$$\Gamma=-k(a/r)^{\beta/2}[AJ_1(\rho)+BN_1(\rho)]/2\ , \qquad (6)$$

where J_1 is as before the Bessel function of the first kind and N_1 the Neumann function. Since Γ is the electron current density, the total current J in the external circuit from the outer cylinder to the central conductor is given by

$$J=-\{2\pi ale(\Gamma)_{r=a}+2\pi ble(\Gamma)_{r=b}\}\ , \qquad (7)$$

where e is the charge of electron, and $(\Gamma)_{r=a}$ and $(\Gamma)_{r=b}$ are respectively the values of Γ at $r=a$ and at $r=b$.

§ 5. Conclusion

From Eq. (7) and the experimental results, we can determine the constant A and also ψ. As an example, we shall determine the constant A at $P=4.3$ mmHg or $P\lambda=50$ mmHg-cm. In our case $b/a=125$, so from the above-mentioned paper by Herlin and Brown, we obtain

$$\beta=2.13,\quad k=75.6\ \text{cm}^{-1} \text{ and } B/A=-0.1429\ .$$

Furthermore, from these values the electric field intensity at $r=a$ is obtained as:

$$E_a=1670\ \text{volts/cm}\ ,$$

and the potential difference V between the outer cylinder and the central conductor becomes

$$V=80\ \text{volts}.$$

By use of the above values, ψ is given as follows:

$$\psi=A\{J_0[11.65\times(a/r)^{0.065}] -0.1429\,N_0[11,65\times(a/r)^{0.065}]\}\ . \qquad (8)$$

In our experiment, we have $J=17.0\ \mu$A and $l=9$ mm at $P=4.3$ mmHg so the constant A in (8) is determined from Eq. (7) to be

$$A=-1,41\times10^{15}\ \text{cm}^{-1}\text{sec}^{-1}. \qquad (9)$$

In this manner, we can completely determine the function ψ. In Fig 4. this function ψ is plotted. The diffusion coefficient D is not generally uniform through the discharge tube, but if we estimate that D is about 10^5 cm² sec⁻¹, the density of electrons becomes roughly 3.5×10^9 cm⁻³ from Fig. 4.*)

§ 6. Acknowledgment

In conclusion, the author wishes to express his sincere thanks to Dr. I. Takahashi for his encouragement and helpful discussion. The author is also indebted to Mr. H. Kubo who devoted his efforts to the experimental apparatus.

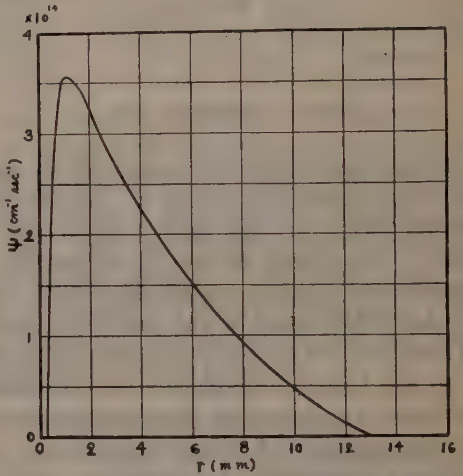

Fig. 4. ψ-function at p-4.3 mmHg and $J=4.3\ \mu$A.

References

1) M. A. Herlin and S. C. Brown: Phys. Rev. **74** (1948) 291.

2) S. C. Brown: I. R. E. **39** (1951) 1493.

3) M. A. Herlin and S. C. Brown: Phys. Rev., **74** (1948) 910.

---

*) According to Townsend's paper (J, Franklin Inst, **200** (1942), 563, the mean free path λ_e of electron is about 10^{-2} cm, and the mean velocity V_e of electron is obtained to be about 8.7×10^7 cm/sec from the relation $V_e=6.7\times10^5\sqrt{T}$ if we put T (electron temperature)$=17,000k$. Thus from the relation $D=\lambda_e V_e/3$ we obtain $D=3\times10^5$ cm² sec⁻¹.

JOURNAL OF THE PHYSICAL SOCIETY OF JAPAN Vol. 7, No. 6 Nov.—Dec., 1952

The Direct Current associated with Microwave Gas Discharge between Coaxial Cylinders, II

By Kenji MITANI
Yoshida College, University of Kyoto

(Received July 5, 1952)

If the microwave gas breakdown once occurs, the microwave gas discharge continues even at the lower power and at the same time the direct current continues to flow, without application of any direct voltage, in the external circuit. From the observation of the length of the microwave glow appearing along the axis of the cylindrical cavity, the direct current J has been shown to be proportional to E and nearly inversely proportional to P, where E is the maximum value of the microwave electric field intensity and P the gas pressure.

§1. Introduction

The microwave breakdown does not occur till the microwave power reaches a certain value. But if the breakdown once occurs, the discharge continues at the lower power. This fact has already been reported by Alpert and McCoubrey.[1] We have investigated the behavior of the discharge which starts with the breakdown and continues.

When the microwave gas discharge tube is of coaxial cylinder type, the discharge takes place at the loop of electric field intensity and the glow appears thereabout. The length l of this glow along the central conductor depends on the electric field intensity.

In this paper, it is shown, through this length l, that the direct current associated with microwave gas discharge is proportional to the electric field intensity and nearly inversely proportional to the gas pressure.

§2. Experimental results and discussion

The apparatus used is the same as that reported in our preceding paper and the experiment was performed at a wave length $\lambda = 11.5$ cm.

At an instant when the breakdown occurs, glows appear at two or three positions along the central conducter and it has been found that the distance between consecutive glows is almost of one-half wave length. Then, when the input power is reduced, the number of glow is also decreased to only one which corresponds to the maximum electric field intensity. Moreover, the less the power absorbed in the cavity becomes, the shorter becomes the length of glow and also the smaller the direct current.

Fig. 1 shows the direct current J which starts with the breakdown and decreases with l/λ when the power is reduced. The curves are plotted against l/λ for various pressures. The gas used is argon. The righthand ends of the curves all correspond to the breakdown.

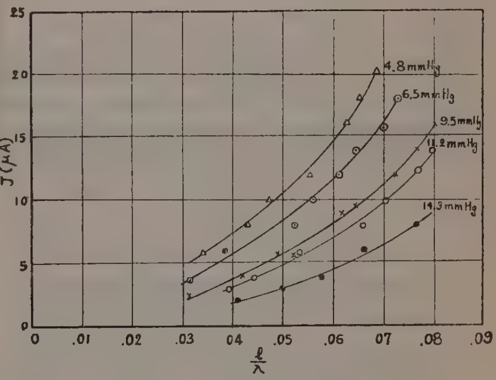

Fig. 1. J versus l/λ [illegible]

Since we had not completed the power measuring apparatus, we could not know the field intensity in the cavity. Accordingly the author tried to determine analytically the relation between the direct current J and the electric field intensity E at the loop. Now if we denote by E_0 the minimum electric field intensity necessary for maintaining the discharge in the cavity, the length l is twice the smallest x which satisfies the equation:

$$E_0 = E \cos 2\pi x/\lambda \, , \qquad (1)$$

as is seen in Fig. 2.

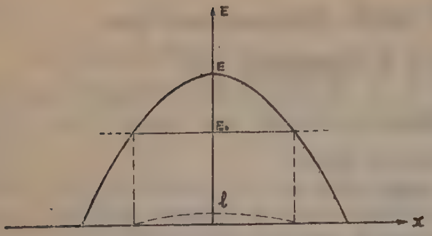

Fig. 2. The relation between E and l.

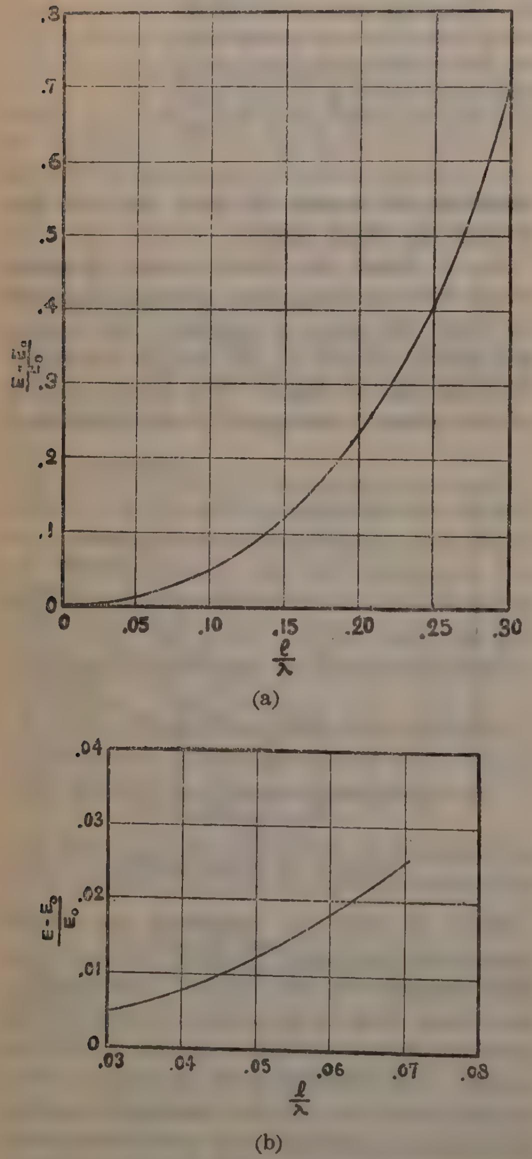

Fig. 3. $(E-E_0)/E_0$ versus l/λ.

Fig. 3 shows the curve of $(E-E_0)/E_0$ plotted against l/λ. In this figure, (b) shows a part of (a) on an enlarged scale for convenience's sake of comparison with Fig. 1. The relation between J and $(E-E_0)/E_0$ can be determined through l/λ. As is shown in Fig. 4, J is proportional to $(E-E_0)/E_0$ or E for various pressures.

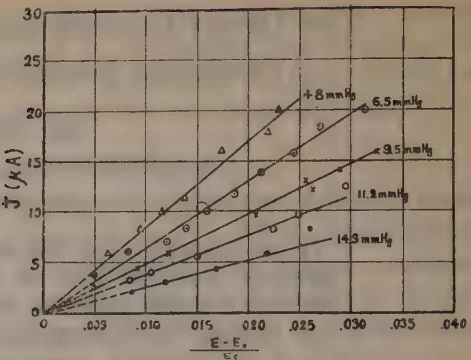

Fig. 4. J versus $(E-E_0)/E_0$ for various P.

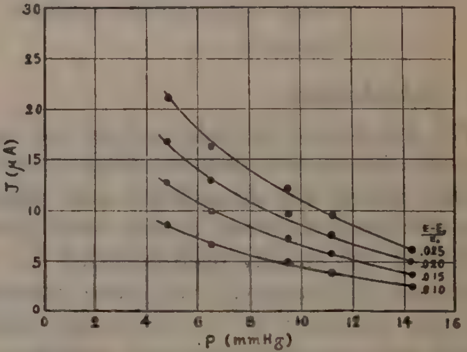

Fig. 5. J versus P for various $(E-E_0)/E_0$.

From Fig. 4, we can derive the relation between J and P for various $(E-E_0)/E_0$. Fig. 5 shows that J is nearly inversely proportional to P. Finally we can conclude that among J, E and P, there holds a relation of the form:

$$J=kE/P\ , \qquad (2)$$

where k is a constant depending upon the form of cavity and the kind of gas.

From our experiment, it can be concluded that the factor E/P governs the direct current J associated with the microwave gas discharge between coaxial cylinders, as in the direct current gas discharge, and that E/P is the important factor which determines the energy acquired by an electron between two consecutive collisions. This supports Herlin and Brown who have pointed out that E/P is also the important factor in the microwave gas discharge.[2),3)] Strictly speaking, however, in the microwave gas discharge, as Brown and McDonald have pointed out,[4] the effective electric field intensity depends on the pressure and so the dependency of J on P cannot be concluded simply to be the inverse proportionality.

The author wishes to thank Dr. I. Takahashi for his encouragement and useful discussions about this work.

References

1) S. K. D. Alpert and A. O. McCoubrey; Phys. Rev. **76** (1949) 722.
2) M. A. Herlin and S. C. Brown; Phys. Rev. **74** (1948) 291.
3) M. A. Herlin and S. C. Brown; Phys. Rev. **74** (1948) 910.
S. C. Brown and A. D. McDonald; Phys. Rev. **76** (1949) 1629.

Short Notes

J. PHYS. SOC. JAPAN **7** (1952) 639~640

Secondary Electron Emission from Oxide-Coated Cathode

By Shigetomo YOSHIDA and Ikuo TAKEDA
Electrical Communication Laboratory, Tokyo, Japan

(Received June 24, 1952)

In a previous paper[1] the authors stated the fact that barium oxide was dissociated into barium atom and oxygen molecule by the primary electron impact and consequently excess barium atom layers were formed on the oxide-coated cathode.

In this paper we will discuss the effects of excess barium atom layers on the secondary emission ratio (δ), the variation of δ due to the change of primary electron current density, and the effect of the temperature of the cathode on δ.

The yield curve for the initial state of cathode is shown in Fig. 1, (1). Curve (1) rises to curve (2) following the activation processes by current drawing and aging at about 1100°K. Bombarding this surface for 20 min. at 500 volts and 17 microamperes, the emission ratio decreased markedly as shown in Fig. 1, (3). Aging this surface at 1020°K for 20 min., this decreased ratio recovers nearly to the value of activated state (Fig. 1, (4)). Timofeew and Pjatnitzki (2) reported that, depositing the excess caesium atoms on the activated caesium oxide surfaces, its secondary electron emission ratio decreased, and raising the temperature of this surface in order to allow diffusion of caesium atoms into the layer, the emission ratio recovered. Taking account of their experimental results, we suppose that the state of our curve (3) in Fig. 1 corresponds to the state of surface on which excess barium atom layers are formed by primary electron bombardment.

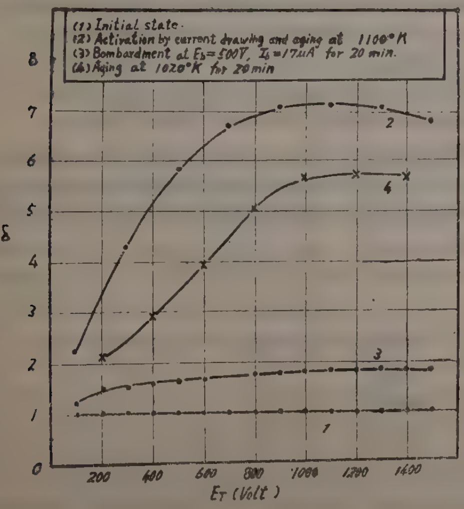

Fig. 1. Yield curves for barium-strontium oxide.

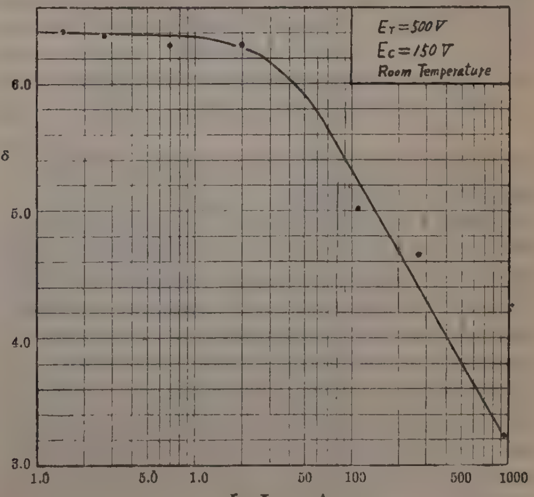

Fig. 2. Dependence of δ on Is-Ip.

The state after aging this at 1020°K for 20 min. perhaps might correspond to that of surface in which these excess barium atoms diffused into barium oxide layers.

In Fig. 2, δ of the activated barium oxide at room temperature is plotted as a function of net current flowing through the barium strontium oxide layer (secondary emission current I_s - primary electron current I_p). In the range of small current density the ratio is almost constant independently of the net current density, but beyond this range the ratio decreases to low value. In addition, we found that the range of constant δ became larger with increasing the temperature of barium strontium oxide.

The δ *vs.* the collector voltage, as shown in Fig. 3, depends on the primary current density and temperature. The smaller the primary current density and the higher the temperature, the smaller the collector voltage becomes sufficient to saturate the secondary emission current. Every curve approches to the constant value at sufficient high collector voltage.

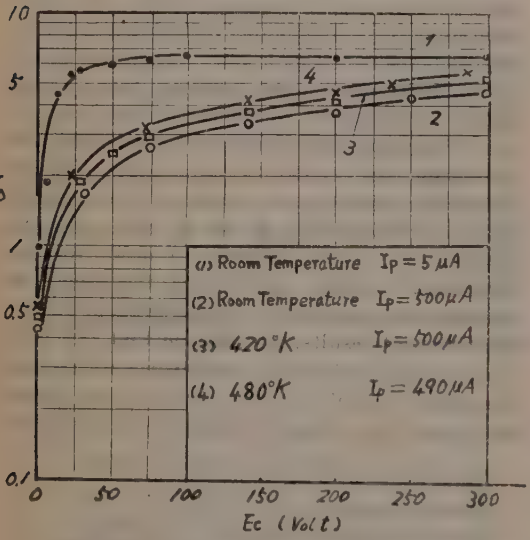

Fig. 3. Saturation curves of barium strontium oxide.

Except the increasing effect of δ due to electric field in the thin layer of high registivity[3], the effects mentioned above together with the results obtained by other authors[4],[5] may be explained by the fact that differences of resistance at various portions of the surface bring about different potential drops, and that the combined effect of these potential drops and the applied collector voltage prevents all of the secondary electrons from reaching the collector. Temperature and impurity effects contribute only to change the potential drop of the layers. Essentially the secondary electron emission ratio of barium oxide is independent of the primary current density, temperature and impurity concentration.

References

1) S. Yoshida and I. Takeda: J. Phys. Soc. Japan **7** (1952) 430.

2) P. W. Timofeew and A. I. Pjatnitzi: Phys. Zeit. Sowjet Union **10** (1936) 518.

3) H. Kawamura and K. Hirano: Phys. Math. Soc. Japan **24** (1924) 211.

4) N. Morgulis and A. Nagorsky: Tech. Phys. USSR, **5** (1938) 848.

5) M. A. Pomerantz: Phys. Rev. **70** (1946) 33.

J. PHYS. SOC. JAPAN **7** (1952) 640~641

Breakdown Probability and Time Lag of Single Crystals

By Y. INUISHI and T. SUITA

Faculty of Engineering, Osaka University

(Received July 3, 1952)

In the previous report[2],[3] we mentioned the experimental results on the time lag in dielectric breakdown of KCl & sulphur single crystals. Here we shall examine them from theoretical standpoint, and try to obtain some knowledges of the breakdown mechnism in these solids.

We confine ourselves in the case of square voltage application as that in our experiment. As is mentioned previously[3],[2] observed time lag T may be experimentally divided into two part's, statistical time lag σ and formative time lag T_F. First, let us consider σ theoretically. Seitz suggested that an electron avalanche having a certain number of electrons causes breakdown by giving their energies to the lattice atoms.

According to this idea the chance for the breakdown is that for the occurence of a avalanche larger than this critical size n_c.

Wijsmann[4] & Furry proved that the probability by which an electron from cathode grows to an avalanche of n electrons at anode is given by,

$$\left.\begin{aligned} P_n &= \frac{1}{\bar{n}} \exp(-n/\bar{n}) \\ \bar{n} &= \exp(\alpha l) \end{aligned}\right\} \qquad (1)$$

α: average number of ionization per unit length

l: electrode distance

$\bar{n}$: average number of electrons at the anode

Now let ν_0 be the average number of starting electrons emitted from the cathode per unit time, then the average frequency f_A that avalances larger than n_c occur is given

$$f_n = \nu_0 \int_{n_c}^{\infty} P_n dn = \nu_0 \exp(-n_c/\bar{n}) \, . \qquad (2)$$

As mentioned above, f_n is equal to the chance for the breakdown. Henceforth the statistical time lag σ must be given by the reciprocal of this chance or

$$\sigma = 1/f_n = 1/\nu_0 \cdot \exp(n_c/\bar{n}) \, . \qquad (3)$$

If we assume Poisson's distribution for the starting electron about time coordinate, then from (3) the empirical formula for the distribution of observed time lag

$$N = 100 \times \exp(T - T_F/\sigma) \qquad (4)$$

easily follows, where N is the % of samples which have larger time lag than T.

Here we must notice that not only α or $\bar{n}$ but ν_0 is a function of the applied field E.

The nature of the formative time lag T_F is rather complicated. It may be the transit time of the breakdown avalanche plus the formation time of plasma-like state succeeding to that avalanche. If we neglect the second term

$$T_F = l/b \cdot E \qquad (5)$$

b: electron mobility of avalanche
E: field strength

Combining (4), (5) with the experimental data in the previous report, we can estimate the starting electron frequency ν_0, and mobility of an avalanche electron b as shown in Table I.

Table I

Sample		ν_0(1/sec)		b(cm^2/sec V)	
Geometry		Needle	Hemisphere	Needle*	Hemisphere
Sulphur (10° & 60°C)		(−)10^7	5×10^5	2	0.2
KCl	10°C	2×10^7	3×10^6	(+) 7 (−) 1.5	0.7
	180°C	3×10^7	10^7	(+) 5 (−) 1.5	

* calcurated for mean field

ν_0 is the same order of that for gas breakdown which may be attributed to field emission. The polarity effect and temperature insensitivity of ν_0 in sulphur suggest that field emission from cathode is the main supply for starting electrons in sulphur.

On the contrary, the increase of ν_0 with increasing temperature, and polarity effect in KCl suggest some mechanism besides field emission from cathode, e.g. the decomposition of exciton and the release of electrons from shallow traps in the crystal etc, but these points must be examined by further experiment on pulse conduction.

The mobilities b for uniform field are rather smaller comparing with Seitz's theoretical estimation 5.6 cm^2/V. sec.

This discrepancy may be attributed to

1) Neglect of the formation time of plasma-like state,

2) Existence of co-operation of several avalanches fot breakdown through γ action of positive holes or photons.

Experiments to clarify these points are now in progress.

References

1) The content of this paper was read by the author before the annual meeting of J.P.S. Sept. 1951.

2) Y. Inishi, & T. Suita: J. Phys. Soc. of Japan "Time lag in Dielectric breakdown". **7** (1952) 641.

3) Y. Inuishi, C. Yamanaka, & T. Suita: Tech. Rep. Osaka University Vol. **21** No. 3, p. 71, 1952.

4) Wijsmann: Phys. Rev. **75** (1949) 833.

5) Seitz: Phys. Rev. **76** (1949) 1376.

J. PHYS. SOC. JAPAN **7** (1952) 641~643

Time Lag in Dielectric Breakdown of Single Crystals

By Y. INUISHI and T. SUITA

Faculty of Engineering, Osaka University

(Received July 3, 1952)

In dielectric Breakdown of solids[1], a "time lag" from the instant of voltage application is required before breakdown actually occurs. This observed time lag may be diveded into two parts; statistical and formative time lag.[3] The former gives the the knowledge of the time rate of initial electrons, and the latter the mobility of breakdown electron or hole.

Theoretical consideration on these subjects will be presented in our following report. Some experimental results on time lag in two kinds of single crystals; i.e. KCl & sulphur; are reported here.[1] (The former represents polar solids, the latter non-polar solids).

These two sorts of single crystals were shaped; 10×10×1(mm^3) plate for non-uniform field (Fig. 1), 10×10×2(mm^3) plate concaved hemispherically at it's center to 1 mm minimum thickness. The electric field were applied in the normal direction to the principal plane (100) for KCl, (110) for orthorhombic sulphur. Nearly square voltage[2] (rise time 0.03μs, time constant of tail 200μs) was generated by triggered three electrodes gap, and applied on the specimens immersed in transformer oil. Electrodes of needle to plane, and hemispherical cap to plane geometry were used, plane and concaved electrode were made by coating aquadug on samples.

Time lags were measured by high speed cathode ray[2] oscilloscope and by Strigil's Zeittransformator[3] simultaneously. Varying the temperature and impulse height, 20 samples were (Fig. 1) tested under each condition. Fig. 1. shows the statistical distribution of observed time lag, taking N or the % of samples as ordinate which do not break before the time duration T (abscissa), we can see that empirical formula

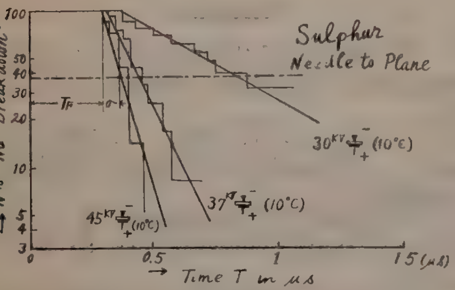

Fig. 1.

$$N=100\exp(T-T_F/\sigma) \qquad (1)$$

holds as suggested by Strigel where T_F or the formative time lag is the minimum time required for the breakdown, and σ or the statistical time lag is the measure of statistical fluctuations concerning with starting electron. (See, our following report.) T_F and σ obtained graphically from series of distribution curves like Fig. 1, are shown in Fig. 2 & 3 for needle to plane geometry and in Fig. 4 for hemisphere to plane. From our experiments some interesting facts were obtained. (Fig. 4)

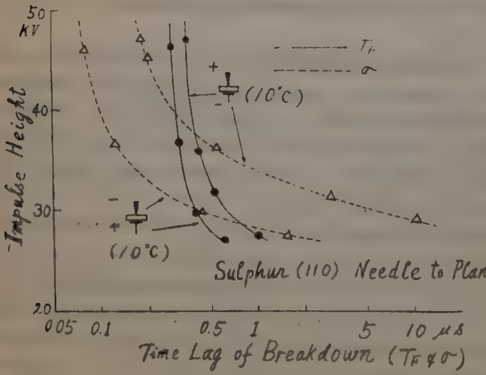

Fig. 2.

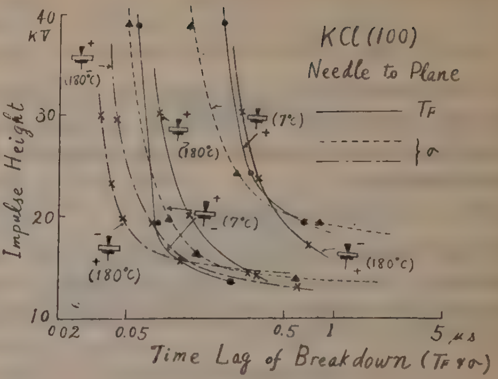

Fig. 3.

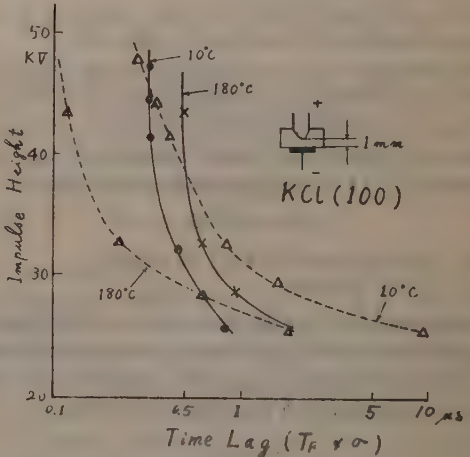

Fig. 4.

(1) In needle to plane geometry the polarity effect exists: T_F for positive needle is remarkably shorter than for negative needle in KCl. On the contrary, in sulphur, polarity effect of T_F is not remarkable, but σ for negative needle is shorter than for positive needle.

The threshold breakdown strength is higher for negative needle in KCl, and higher for positive needle in sulphur.

(2) σ decreases with increasing temperature in KCl, but such effect is not remarkable in sulphur.

(3) The time lags both σ and T_F are longer in sulphur than in KCl for the same over voltage. Especially the ratio σ/T for sulphur is remarkably larger than that for KCl at smaller over voltages.

(4) σ, T_F for non uniform field are larger than in comparatively uniform field for both type of solids.

(5) Superposition of D. C. voltage on impulse increases the threshold breakdown voltage at lower temperatures (20°C) but decreases it at higher temperatures, (170°C) for KCl.

T_F are not affected remarkably.

The last item (5) are now in more detailed experiment.

References

1) The content of this note was read by the author before the annual meeting of J. P. S. Sept. 1951.

2) Y. Inuishi, C. Yamanaka and T. Suita: Tech. Rep. Osaka University. **21** No. 3, (1952) 71.

3) Strigel: Wiss. Veröff. Siem. Werke. **18** (1939) 101.

J. Phys. Soc. Japan **7** (1952) 643～644

A Note on the Furry-Wijsmann's Distribution in Case Which Contains Electron Trapping

By Y. Inuishi and T. Suita

Faculty of Engineering, Osaka University

(Received July 22, 1952)

In our previous papers on dielectric breakdown of solids, we have pointed out the importance of probability P_n that an electron starting from cathode grows to a "n" electron avalanche at anode by impact ionization, in order to consider theoretically the time lags of breakdown and observed avalanche size distribution. Furry³⁾ and Wijsmann²⁾ independently found that the fundamental transition equation's for P_n are

$$\frac{dP_n(x)}{dx}=-n\alpha P_n(x)+(n-1)\alpha P_{n-1}(x) \qquad (1)$$

X: distance from the cathode

α: 1st Townsend coefficient or the mean number of ionizing collision for an electron in drifting unit length

$P_n(x)$: the probability that an electron from the cathode grow's to a "n" electron avalanche at x. Solving (1) under the initial condition that one electron starts at $x=0$, they got¹⁾²⁾³⁾

$$\left.\begin{aligned}&P_n(x)=1/\ (1-1/\bar{n})^{n-1}\\&\bar{n}=e^{\alpha x}\end{aligned}\right\} \qquad (2)$$

and $P_n(x)\doteqdot 1/\bar{n}\cdot\exp(-n/\bar{n})$ for $\bar{n}\gg 1$ and $n>1$. This is the distribution that should be called "Furry-Wijsmann's".

But in case of Solid breakdown, we have been confronted with many phenomena that can not be explained without considering electron trapping besides α mechanism. So we have tried to extend the Furry-Wijsmann's distribution to case of contaning electron trapping.

Let ζ be the mean number of trapping collision in drifting unit length for an electron, then the transition equation (1) is altered to

$$\frac{dP_n(x)}{dx}=-n(\alpha+\zeta)P_n+(n-1)\alpha P_{n-1}+(n+1)\zeta P_{n+1}. \qquad (3)$$

The difference between (2) and (1) is as follows:

1) the first term contains the decreasing of P_n by trapping

2) the third new term is the contribution from the increasing of P_n by decreasing of "$n+1$" avalanche to "n" due to trapping ζ.

Hereafter we assume $\alpha>\zeta$.

To solve equation (3) under initial condition that one electron starts from cathode at $x=0$, put

$$P_n(x)=a(x)\{b(x)\}^{n-\gamma} \qquad (4)$$

Substituting (4) into (3) gives for $n\geq 1$.

$$\frac{1}{a}\frac{da}{dx}+\frac{(n-\gamma)}{b}\frac{db}{dx}=-n(\alpha+\zeta)+(n-1)\frac{\alpha}{b}+(n+1)\zeta b \qquad (5)$$

Since (5) must be satisfied for all n (0 or positive integer) the terms which do not contain n must be equal in both sides of the equation,

$$\frac{1}{a}\frac{da}{dx}=\frac{\gamma}{b}\frac{db}{dx}-\alpha\frac{1}{b}+\zeta b\,. \qquad (6)$$

Equating the terms multiplied to n in both sides,

$$\frac{1}{b}\frac{db}{dx}=-(\alpha+\zeta)+\alpha\frac{1}{b}+\zeta b \qquad (7)$$

for $n=0$, we get. directly from (3)

$$\frac{dP_0}{dx}=\zeta P_1 \text{ or } P_0(x)=\int_0^x\zeta P_1(x)dx \qquad (8)$$

since $P_0(0)=0$.

Solving the differential equation (7), we get

$$\left.\begin{aligned}&b(x)=\frac{1-\alpha/\zeta\cdot Ke^{-(\alpha-\zeta)x}}{1-Ke^{-(\alpha-\zeta)x}}\\&K=\frac{1-b(0)}{\alpha/\zeta-b(0)}\end{aligned}\right\} \qquad (9)$$

next, substituting (9) into (6), we get

$$a(x)=a(0)e^{-(\alpha-\zeta)x}\frac{\left(\dfrac{1-\alpha/\zeta\cdot Ke^{-(\alpha-\zeta)x}}{1-\alpha/\zeta\cdot K}\right)^{\gamma-1}}{\left(\dfrac{1-Ke^{-(\alpha-\zeta)x}}{1-K}\right)^{\gamma+1}} \qquad (10)$$

Combining (9) and (10), we get the ultimate solution as (4) for $n\geq 1$, and as (8) for $n=0$. But we must determine arbitrary constants K and γ to satisfy initial conditions or

$$P_1(0)=1,\ P_i(0)=0 \text{ for } i\neq 1\,.$$

From the distubation for $\zeta=0$, we may put

$$\gamma=1,\quad a(0)=0,\quad b(0)\to 0\,.$$

then the initial condition is certainly statisfied, so (4)

$$\left.\begin{aligned} P_n(x) &= e^{-(\alpha-\zeta)x}\left(\frac{1-\zeta/\alpha\cdot e^{-(\alpha-\zeta)x}}{1-\zeta/\alpha}\right)^{-2} \\ &\quad\times\left(\frac{1-e^{-(\alpha-\zeta)x}}{1-\zeta/\alpha\cdot e^{-(\alpha-\zeta)x}}\right)^{n-1} \quad \text{for } n\geq 1 \\ P_0(x) &= \int_0^x \zeta P_1 dx \qquad\qquad \text{for } n=0 \end{aligned}\right\} \quad (11)$$

It is easy to see that (11) approaches to Wijsmann-Furry distribution (2), provided $\alpha \gg \zeta$.

For $e^{(\zeta-\alpha)x}=\bar{n}(x)\gg 1$ and $n>1$ (11) can be substituted approximately by

$$P_n(x)=\frac{1}{\bar{n}}\left(1-\frac{\zeta}{\alpha}\right)^2 e^{-n/\bar{n}\cdot(1-\zeta/\alpha)} \quad (22)$$

(12) doe's not differ so markably from "Furry-Wijsmann's if α is replaced by effective ionization coefficient $\alpha-\zeta$. Contrary to our expectation, trapping can not explain large deviation from Furry-Wijsmann distribution which has been observed in our avalanche experiments. So it seems to us that some spatial inhomogencities play important rôle. The solution for $\zeta>\alpha$ is easily got from (11).

References

1) Furry: Phys. Rev. **52** (1937) 569.
2) Wijsmann: Phys. Rev. **75** (1949) 833.
3) Fushimi: "Kakuritsuron Oyobi Tōkeiron (Probability & statistics" in Japanese) p. 335.

J. PHYS. SOC. JAPAN 7 (1952) 644~645

Electronic Spectroscopy for Soft X-ray Region

By Gunji SHINODA, Tatsuro SUZUKI, and Susumu KATO

Faculty of Engineering, Osaka University

(Received July 31, 1952)

Soft X-ray region may be studied either by diffraction grating or photoelectric device. Recently the former method has been improved by using electronic multipliers,[1] while the latter method has been abandoned nearly twenty years.[2] The main difficulty of the latter has been the inaccuracy due to the graphical differentiation. However this can be overcome by an electrical differentiation, by which we can observe an instantaneous state of the surfaces of materials. This is a new advantage of our photoelectric method. The method we applied is as follows.

Fig. 1 shows the circuit and Fig. 2 is the X-ray tube similar to that of Skinner.[2] If saw-tooth wave voltages are applied to the target and the photoelectric surface is irradiated by resulting soft X-ray, photoelectric currents corresponding to the saw-tooth wave will be obtained. Then if the curve showing the relation between the current and the voltages is differentiated electrically, certain break point corresponding to the energy band will appear directly on an cathode-ray oscillograph. The manner in which sawtooth voltages are applied is as shown in Fig. 3, where the main accelerating voltage V_0 is varied according to the wavelength range to be observed.

Fig. 4 is an example thus obtained and shows an energy band of Al (99.992%), photoelectric surface being pure Cu. As shown in the figure extra energy bands other than Al−L appear, but as these bands change their shape according to the condition of the experiment, this will be that due to an oxide contaminating the target surface.

Another method similar to that of colour analyser, which had been reported by us formerly[3], will also be conceivable. We used a method which is a modification of that due to Sziklai[4]. The differentiation has been done thrice instead of twice. If we assume that the distribution of photoelectrons obeys DuBridge's law, the differentiation must be done three times to obtain a curve similar to that by spectrophotometric method.

If we assume the width at half-value height of the maximum in the curve obtained by differentiating photoelectric current to be the

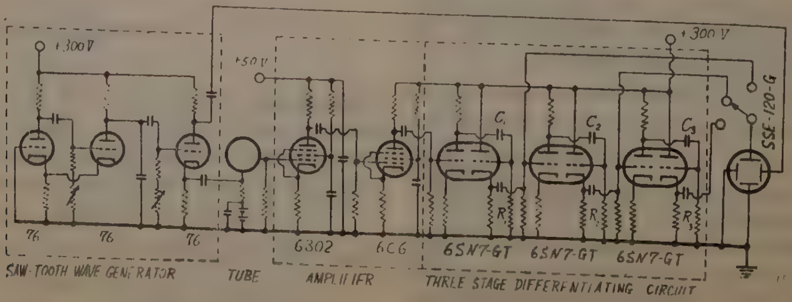

Fig. 1. Circuit diagram of the experiment.
$R_1=R_2=R_3=20\ \mathrm{K}\Omega$, $C_1=C_2=C_3=400\ \mu\mu\mathrm{F}$.

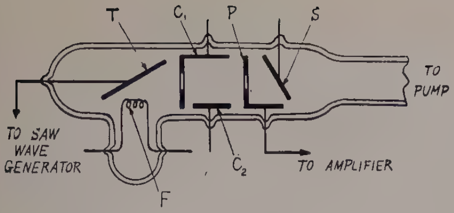

Fig. 2. Diagram of tube.
T. Target (material to be studied.)
F. Filament.
C_1, C_2. Ion filtering plate.
P. Collector for photoelectric current.
S. Copper photoelectric surface.

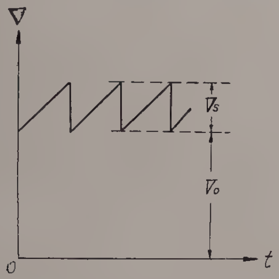

Fig. 3. Saw-tooth wave voltage to be applied.

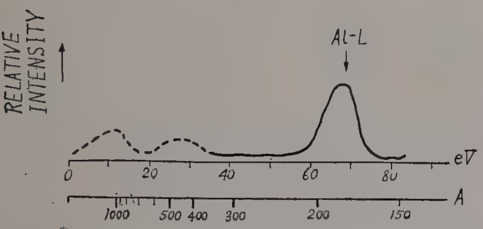

Fig. 4. Emisson band of Al

resolution $\Delta\lambda$, this becomes,

$$\Delta\lambda=3.52kT/ch\cdot\lambda^2$$

while that of the diffraction grating is,

$$\Delta\lambda=1/mn\cdot\lambda$$

where, k; Boltzmann's constant, T; absolute temperature of the photoelectric surface, c; light velocity, h; Planck's constant, λ; wave-length, m; order of the spectrum, and n; number of rulings. Fig. 5 shows the curves calculated from these eqations, and we can see that photoelectric method is not inferior to the grating method.

References

1) E. R. Piore, G. G. Harvey, E. M. Gyorgy, and R. H. Kingston: Rev. Sci. Instr. **23** (1952) 8.

2) H. W. B. Skinner: Pro. Roy. Soc. **A 135** (1932) 84.

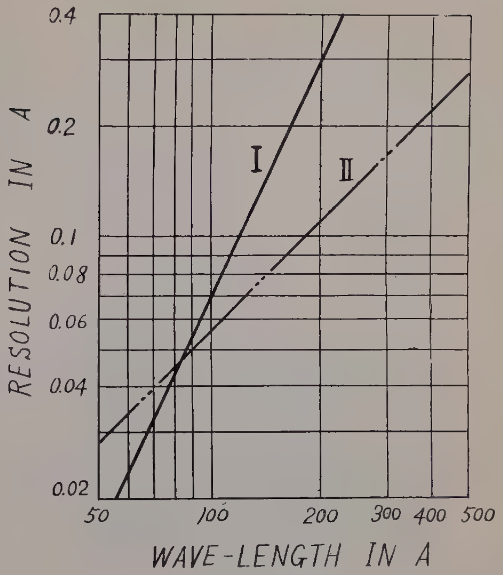

Fig. 5. Resolution of differentiating method at $T=293°K$ (I), and grating utilizing $n=1800$ lines (II).

3) Authors: J. Appl. Phys. Japan **21** (1952) 20. (*in Japanese*)

4) G. C. Sziklai and A. C. Schroeder: J. Appl. Phys. **17** (1946) 763.

J. PHYS. SOC. JAPAN **7** (1952) 645~647

Electrolytic Conduction in Cs_3Sb

By Hisao MIYAZAWA and Shun-ichi FUKUHARA
Matsuda Research Laboratory, Tokyo Shibaura Electric Co., Kawasaki-shi, Kanagawa-ken, Japan

(Received August 10, 1952)

The intermetallic compound Cs_3Sb, which shows the largest photoelectric quantum efficiency (of the order of $\sim 10^{-1}$) among all photocathodes for visible and ultraviolet light, appears to have the electronic energy structure of an intrinsic semiconductor.1)

In order to estimate the forbidden energy gap, temperature dependency of the electrical conductivity was measured in the activated thin layers on glass substrate. It was found, however, that the conduction current through the layers decreased slowly with time at a constant applied voltage. Deviation from Ohmic law can easily be observed whenever the field strength surpasses only several volts per centimeter.

More detailed studies have indicated that aftre prolonged application of dc field of several scores volts per centimeter the process is characterized by electrolysis from anode side of the active layers, and that the electrolyzed part, distinguished sharply from the remaining active part, is converted entirely into another material, of which tint is pale yellow in constrast with deep red of the rest. Such an example is shown in Fig. 1, where the result was obtained after two hours electrolysis at room temperatures, using 150 volts dc source. It will be seen that the transformation proceeds uniformly from anode towards cathode.

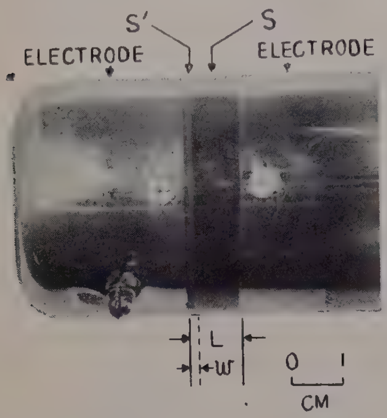

Fig. 1. Electrolytic effect in Cs_3Sb.
S: original activated layers (deep red).
S′: layers transformed by electrolysis (pale yellow).

These phenomena suggest that either caesium- or antimony ion must be readily mobile through the material with rather weak electric field. Therefore, an attempt was carried out with the experimental tube as shown in Fig. 2 in order to determine which constituent would take part in the conduction. If the caesium ion (cation) were able to be transfered, the electrolyzed layers would recover again by the heat treatment allowing the diffusion of caesium into the material. On the other hand, if the antimony ion (anion) were able to move, the recovery would not be expected by the same process.

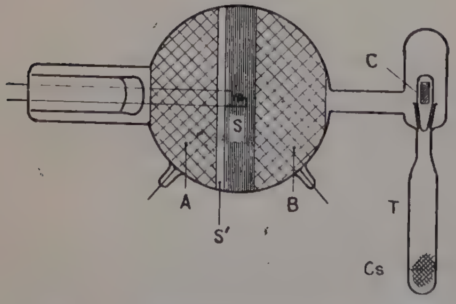

Fig. 2. Experimental tube to confirm that Cs^+ ions are mobile.
A, B: electrodes,
S: activated layers,
S′: transformed layers,
C: greaseless cock,
T: side tube containing metallic Cs.

That the former case took place was confirmed by the following procedures: In Fig. 2, (1) after Cs_3Sb layers S were prepared in the bulb as usually, (2) constant dc source of about 150 volts was applied between electrodes A and B so that A may be positive. (3) Since the layers S′ near anode A were partially converted as already shown in Fig. 1, (4) caesium was introduced from the side tube T into the bulb by opening the greaseless cock C, and (5) the bulb was heated in a controlled oven for the suitable time. The converted erea S′ was then entirely restored as expected in the former case. The recovery was so perfect that no traces of the electrolysis could be detected despite of careful observations.

It may be asserted from these facts that monovalent positive caesium ions contribute fairly to the electrical conductivity. Although the transport number has not been clarified at this moment, the proportion of the ionic conductivity to the electronic one may be roughly evaluated as follows. Since the composition of the transformed material is believed to be CsSb by experience,[2)] it is assumed that the number of caesium ions per unit volume in the electrolyzed layers will be decreased to one third of the original value. Then the real number of caesium ions removed away should equal twice that of antimony staying there, which is enumerated by the following formula provided that the normal deposition to the substrate takes place,

$$Z_{sb}=\frac{M_{sb}/m_{sb}}{4\pi R^2},$$

where Z_{sb} is the number of antimony atoms deposited on the substrate per unit area, M_{sb} is the mass of antimony measured previously before evaporation, m_{sb} is the atomic mass of antimony, and R is the distance between the substrate and the source of evaporation. If it is also assumed that these mobile ions will be transfered one after another from anode towards cathode, the total ionic charge Q_i, contributing to the electrical conduction per unit length along the electrode, is given by

$$Q_i=\frac{|e|Zw}{L}\left(L-\frac{w}{2}\right),$$

where Z equals $2Z_{sb}$, L is the distance between two electrodes, and w is the width of the electrolyzed layers. (cf. Fig. 1.)

Preliminary results have shown that the proportion of Q_i so obtained to the total charge Q expended during the electrolyzing process is of the order of several percent at room temperatures and is not so very structure-sensitive. The proportion is somewhat larger at higher temperatures.

Further details will be discussed in a later paper.

References

1) This has been speculated also by other authors. See, for example, V. K. Zworykin and E. G. Ramberg, "Photoelectricity" (John Wiley & Sons, New York, 1949) p. 58.

2) Oral presentation to the meeting of Phys. Soc. Japan (Oct. 1944). When Cs vapor effused through a pin-hole onto the evaporated Sb film, intermetallic compound CsSb was first formed which was poor conductive, not yet so photosensitive, and just pale yellow.

J. PHYS. SOC. JAPAN 7 (1952) 647~649

On the Composition of Antimony-Caesium Photocathode*

By Hisao MIYAZAWA, Kin-ichi NOGA,
Soshin CHIKAZUMI** and Akio KOBAYASHI***

Matsuda Research Laboratory, Tokyo Shibaura Electric Co., Kawasaki-shi, Kanagawa-ken, Jnpan

(Received August 16, 1952)

Since Görlich has first discovered in 1936 the highly photosensitive alloy composed of antimony and caesium,[1] it has been applied to photomultipliers, television pick-up tubes, and many other devices in wide scientific and technical fields.

Attaching importance to find out the optimum ratio of caesium to antimony which gives the maximum sensitivity, an experimental study was carried out in which were observed the changes in photoelectric emission, electrical conductivity, and caesium vapor pressure with increasing the caesium concentration in the antimony layers through effusion.

The construction of the experimental tube adopted is shown in Fig. 1. The antimony previously balanced is placed in a small evaporator A of tungsten spiral at the center of the spherical bulb B. After evacuating the bulb, uniform antimony layers were evaporated from A onto the inner surface of B, and metallic caesium was stored in the side tube T by reducing caesium-chromate with aluminum powder.

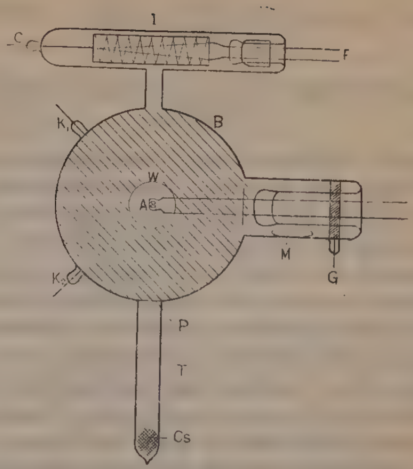

Fig. 1. Construction of the experimental tube.

A: Evaporator of tungsten spiral, serving later as anode.
B: Bulb for cathode preparation.
I: Positive ion gauge.
C: Ion collector.
F: Filament ionizing caesium.
G: Guard ring.
K_1, K_2: Cathode terminals.
W: Small window for light incidence.
M: Mica sheet used for making W.
P: Thin Pt plate with a pin-hole for effusion
T: Caesium source side tube.

Then the bulb was sealed off and was set in a thermostat, whose temperature was carefully controlled at 150°C. Since a thin platinum plate P having at the center a small opening separates T from B, the caesium vapor will effuse through the pinhole into B in accordance with the following formula,[2]

$$Z = PS/(2\pi mkT)^{1/2} = 3.537\times10^{22} PS/(mT)^{1/2}\cdot\mathrm{sec}^{-1}.$$

Here Z represents the number of caesium atoms flowing into B per unit time provided the temperature is kept at T°K, S is the area of the pin-hole, m is the atomic mass of caesium, and k is the Boltzmann's constant. P represents the vapor pressure of caesium at T°K and is given[3] by

---

* The experimental work reported here has been carried out during the World War II, but left unpublished except an oral presentation to the meeting of Phys. Soc. Japan on October 1944. Believing the results obtained are still informative, we wish to describe here the essentials of them though it seems too late to do so.

** Now at Department of Physics and Chemistry, Gakushuin University, Mejiro, Tokyo.

*** Now at Hokkaido University, Sapporo.

$$\log_{10} P(\mathrm{mmHg}) = 10.5460 - 1.00 \log_{10} T - 4150/T, \quad T < 302°\mathrm{K},$$

$$\log_{10} P(\mathrm{mmHg}) = 11.0531 - 1.35 \log_{10} T - 4041/T, \quad T > 302°\mathrm{K}.$$

In addition, effusive flow of these caesium atoms will reach the antimony layers everywhere in equal density according to the cosine law. As the number of antimony atoms deposited on B is known, the ratio R of caesium atoms to antimony atoms at the desired stage of effusion can be readily calculated. Hence the photoelectric emission, the electrical conductivity, and the caesium vapor pressure may be measured as a function of R in the alloyed layers. Procedures of these measurements were as follows: (i) After a suitable effusion, T was cooled by liquid air so that no more caesium might flow into B, and the bulb was subjected to a heat treatment at about 150°C so that the quantities to be measured might reach the steady state. (ii) For the photoelectric emission measured between K_1 and A, an incandescent tungsten lamp was used as the light source in a fixed geometry. A small window W for the light incidence was due to a mica sheet M which was later removed to the neck of B. G is a guard ring to prevent unfavorable leakage disturbing the photo-currents. (iii) The electrical conductivity was measured between K_1 and K_2 at various temperatures. (iv) The caesium vapor pressure of the alloyed layers was observed by the Langmuir's positive ion gauge I, in which all caesium atoms hitting the heated tungsten filament F were ionized and were collected by C kept at negative potential to F. Proper calibration will give the pressure of caesium in equilibrium with the layers.

A typical result obtained is shown in Fig. 2. It must be noted that the rapid decrease in the conductivity occurs as soon as a small quantity of caesium is introduced, while the metallic appearances of the original antimony are lost at once and changed into the fairly transparent layers. The first minimum in the conductivity comes without fail at $R=1.0$, where the transmitted color of the layers is pale yellow. As R increases larger than 1, the layers become more and more deep red and show the subsequent minima in the conductivity at $R=1.5$ and 3.0. Sometimes the second minimum at $R=1.5$ could not be observed. It is seen that the photoelectric emission increases gradually with R and saturates approximately as R approaches 3. The caesium vapor pressure of the layers was too small to be observed until R passes over 3. It corresponds to the pressure less than 10^{-13} mm Hg. At $R=3.33$, it amounts to 1.6×10^{-10} mm Hg at 150°C for the first time. Temperature coefficient of the electrical conductivity was always negative at $R>1.0$ as usual semiconductors. The voltage-current characteristics were, however, somewhat non-ohmic. Spectral response of the photoelectric emission measured at $R=2.01$ showed the maximum at about 4200 A, but its long wave-length tails near 6000 A could not be fitted to Fowler plots.

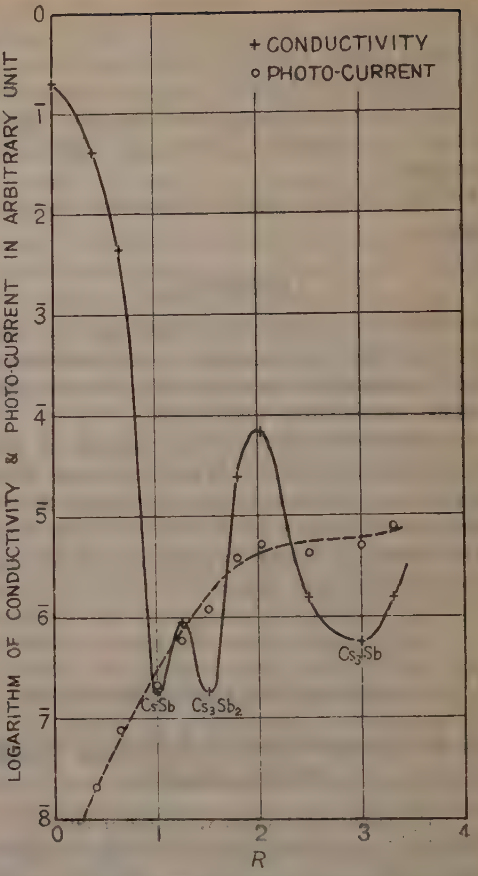

Fig. 2. Changes in electrical conductivity and photoelectric sensitivity with ratio R of caesium to antimony. Values observed at 150°C are plotted.

After getting through all of these measurements, to make sure of the rate of effusion the bulb was broken and the quantitative chemical analysis determing the composition of the layers was carried out. It was confirmed that the value R in both cases was in excellent agreement.

It comes to the conclusion from these facts that there are no alloys betwen antimony and caesium which have many free electrons and behave as usual metals, but there are at least intermetallic compounds CsSb and Cs_3Sb which show the properties of semiconductors. The active photo-surface to be aimed appears to be the latter compound Cs_3Sb. The high photoelectric sensitivity should be ascribed to the electronic structure of that semiconducting material.

References

1) P. Görlich: Zeits. f. Phys. **101** (1936) 335.
2) See, for example, Mayer and Mayer: "Statistical Mechanics", (John Wiley & Sons, New York, 1940) p. 18.
3) J. B. Taylor and I. Langmuir: Phys. Rev. **51** (1937) 753.

J. Phys. Soc. Japan **7** (1952) 649~650

Quadrupole Resonance in Solid Iodine

By Tohru Kamei

Institute of Science and Technology,
Komaba-machi, Meguro-ku, Tokyo

(Received August 22, 1952)

Using a decimeter-wave spectrograph[1], nuclear quadrupole resonance frequencies in solid iodine (I_2) were measured at various temperatures. According to Dehmelt[1] two kinds of frequencies are expected and were observed by him in the case of iodine (nuclear spin=5/2); they are due to the following transitions:

$$\nu_1: \quad m_z=\pm5/2 \longleftrightarrow m_z=\pm3/2$$
$$\nu_2: \quad m_z=\pm3/2 \longleftrightarrow m_z=\pm1/2 .$$

In the present work, Acorn tubes were used as the oscillator tubes and the quadrupole resonance was detected in pure polycrystalline iodine. The frequency ν_2 was measured in the temperature range from 85°C to the liquid air temperature. However, it was possible to measure the frequency ν_1 only at room temperature. In Fig. 1, the values of ν_1 and ν_2 that were measured by Dehmelt[1], Pound[2] as well as the present author are plotted as functions of the temperature. The frequencies obtained by extrapolating these curves to 0°K are as follows:

$$\nu_1=642.8\text{ mc}; \quad \nu_2=334.0\text{ mc} .$$

If φ_{zz} is assumed to have an axial symmetry, the frequency ratio ν_1/ν_2 should be equal to 2. Actually, this ratio is 1.925, indicating a slight deviation of φ_{zz} from axial symmetry. In order to evaluate the quadrupole coupling constant $eQ\varphi_{zz}$, therefore, it is necessary to take deformation factor ε into account, using the formulas that are due to Krüger[3].

$$\nu_1=\frac{3}{10}eQ\varphi_{zz}(1-0.20370\,\varepsilon^2+0.184\,\varepsilon^4);$$
$$\nu_2=\frac{3}{20}eQ\varphi_{zz}(1+1.0926\,\varepsilon^2-0.633\,\varepsilon^4);$$
$$\varepsilon=\left|\frac{\varphi_{xx}-\varphi_{yy}}{\varphi_{zz}}\right| .$$

Putting the actual values of ν_1 and ν_2 of iodine in the above formulas, we get

$$\varepsilon=0.173, \qquad eQ\varphi_{zz}=2156\text{ mc} .$$

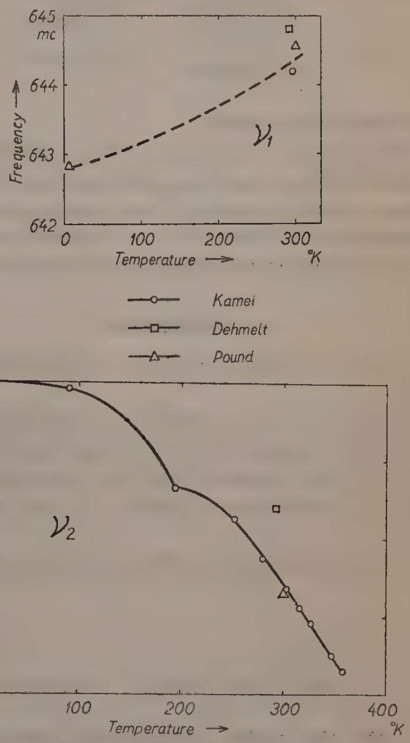

Fig. 1. Plot of ν_1 and ν_2 *versus* temperature.

To evaluate the quadrupole moment of I^{127} the value of φ_{zz} must be calculated. In the case of a simple covalent p-bonding, the value of φ_{zz} can be calculated approximately by the following formula which was given by Townes[4] and which is, in addition, given the relativity correction (H).

$$\varphi_{zz}=\frac{8}{15}\frac{e\Delta\nu}{HZ_iR\alpha^2a_0^3}$$

Putting $\Delta\nu$ (the doublet separation of the p-electron)=7603 cm^{-1}, Z_i (the effective nuclear charge for the p-electron)=53−4=49 and H=1.06, we obtain

$$\varphi_{zz}=43\times10^{15}\text{ esu} ,$$

and therefore

$$Q=-0.69\times10^{-24}\text{ cm}^2.$$

Though the sign of this quadrupole moment could not be determined by the present experiment, the negative sign had been determined by optical[5] or microwave spectra[6]. Table 1 lists the values of the quadrupole moments obtained

Table 1

$Q(10^{-24}\,cm^2)$	method	sample	reference
−0.69	quadrupole resonance	solid iodine	present work
−0.46	atomic spectra		5
−0.75	microwave spectrum	ICN (gas)	6
−0.59	microwave spectrum	CH_3I (gas)	6

by different methods.

The author wishes to thank Professor K. Murakawa for his kind guidance and encouragement. The expense of the present work was defrayed in part from the Scientific Research Expenditure of the Ministry of Education.

References

1) H. G. Dehmelt: Zeits. f. Physik **130** (1951) 356.
2) R. V. Pound: Phys. Rev. **82** (1951) 343.
3) H. Krüger: Zeits. f. Physik **130** (1951) 371.
4) C. H. Townes, Phys. Rev. **71** (1948) 909.
5) K. Murakawa: Zeits. f. Physik **114** (1939) 651.
6) W. Gordy: Rev. Mod. Phys. **20** (1938) 668.

J. PHYS. SOC. JAPAN **7** (1952) 650~651

On the Noise of Decaying Electrets

Shoji KOJIMA and Kiyoe KATO
Tokyo University of Education

(Received September 19, 1952)

In a short note¹⁾ the authors reported that the decay of homocharge accompanied some noise. There the noise was called the Barkhausen noise by the current theory²⁾. The following experiments, however, reveal that the noise is not due to the Barkhausen effect, but to the discharge in the interface between electrode and dielectric.

(**a**) Electrets which had not been lowered below about 33°C after solidification showed few noise. Electrets with aluminium electrodes generated less noise than those with copper, tin or iron electrodes. These results suggest that electrets whose electrodes are tightly bound to dielectric have little noise. (**b**) The noise was reduced by a bias potential applied to cancel the potential difference of the interface. (**c**) By the irradiation of gamma rays the number of noise pulses was increased and its size was decreased.

These results are favourable for the discharge theory, and unfavourable for the Barkhausen effect. However, it remains a question why the noise is generated at the decay of homocharge and not at the decay of heterocharge, of which equivalent surface charge density seemed to be larger than that of the homocharge as shown in Fig. 2 of the previous note.

Since the noise was observed by a short circuit, the charge had to be measured in a similar condition. This was fulfilled by the use of the generating voltmeter mentioned previously *in a conducting atmosphere*, which was produced by the irradiation of gamma rays from radium of 5 millicurie. Every time two identical samples were made simultaneously at the same condition and one was measured with gamma rays and the other without it. One of the measurements of the decaying charge is reproduced in Fig. 1, where the temperature is raised at the rate of 1°C/min. Since the heterocharge drops easily by the flow of current, it acts equivalently as a cell with high internal resistance. Thus the heterocharge is hard to flow in an external circuit, but it consumes away internally. On the contrary the homocharge acts as a cell with low internal resistance and gives relatively large currents to the external circuit. This fact has been verified by a direct measurement on the external current. The above question may be answered by these experiments.

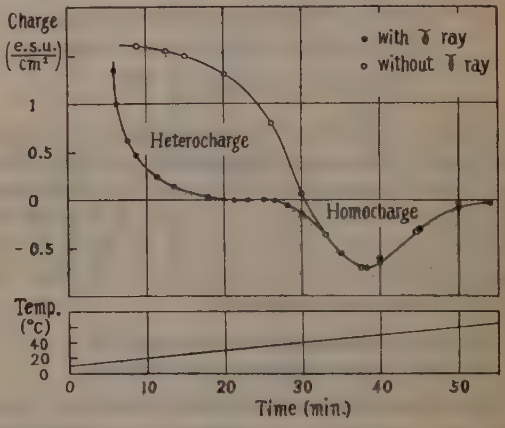

Fig. 1.

If discharges take place in air, the minimum gap length of about 7×10^{-4} cm is required by Pashen's law. The existence of such small air gaps in the interface between electrode and dielectric may be permissible. On this gap length the size of the minimum electron avalanche is theoretically estimated as 100 electrons or 1.6×10^{-17} coulombs. The observed pulses were found in the region from 10^{-17} to 3×10^{-15} coulombs. These figures are not in conflict.

It is concluded that the observed noise was due to the discharge in the interface. This agrees with the opinion by Gross[3], who had observed discharges of about 10^{-8} coulombs in the charging current of carnauba wax and not found Barkhausen effect. If the Barkhausen noise exist, it will be smaller than 10^{-17} coulombs in size.

References

1) S. Kojima and K. Kato: J. Phys. Soc. Japan **6** (1951) 207.

2) F. Gutmann: Rev. Mod. Phys. **20** (1948) 457.

3) B. Gross: J. Chem. Phys. **17** (1949) 866. (see foot note 11).

ERRATA

Crystal Structures and Intermolecular Forces of Rare Gases

By Taro Kihara and Saburo Koba

J. Phys. Soc. Japan Vol. 7 (1952) 348∼354

P. 348 Abstract line 2	is calculated provided	should be read	is calculated, provided
left column line 13	quantummechanical	〃	quantum-mechanical
line 23	than 6 of which	〃	than 6, of which
P. 349 eq. (3. 2)	$\ldots=2\pi\lambda\rho_c\dfrac{(A_\theta a)^{s-3}}{s-3}$	〃	$\ldots=2\pi\lambda\rho_c\dfrac{(A_\theta \alpha)^{s-3}}{s-3}$
P. 350 Table II 3rd column line 10	89	〃	86
eq. (4. 1)	$C=\ldots$	〃	$c=\ldots$
P. 351 right column line 4∼5	bet-ween	〃	be-tween
Table V 1st column line 9	68	〃	18
P. 352 eq. (7. 1)	$\left[\ldots -\sigma\left(\dfrac{r_0}{a_{c1}}\right)^6 C_6\right]$	〃	$\left[\ldots -\sigma\left(\dfrac{r_0}{a_{c0}}\right)^6 C_6\right]$
Fig. 4	"$\dfrac{\Phi_{c0}-\Phi_{h0}}{\Phi_{c0}}\times 10^5$" is printed ambiguously.		

On the Transient Phenomena in the Wave Guide

By M. Namiki and K. Horiuchi

J. Phys. Soc. Japan Vol. 7 (1952) 190∼193

In this paper we discovered later a mistake in the formula giving the amplitude of the disturbance at $s\sim s_p$ in the illustrative case (A).

We must adopt the following expression as correct formula:

$$|A-|=\frac{|F_0|}{2\sqrt{\pi\mu\varepsilon}\sqrt{\omega_0^2-\omega^2_{mm}}}\left\{1-\frac{1}{2}\left(\frac{\omega_0}{\omega_{mn}}\right)\left[\left(\frac{\omega_0}{\omega_{mn}}\right)^2-1\right]^{\frac{1}{2}}(s-s_p)\right\}.$$

Thus the standing-up curve in Fig. 4 is slightly modified at $s\sim s_p$ as follows.

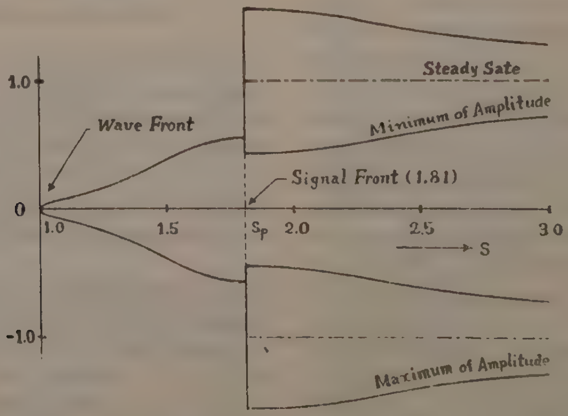

Moreover, it is necessary to discuss more deeply the deformations of pulse oscillations in § 3, which will be reported later.

CONTENTS

(Vol. 7)

No. 1

Gen SHIRANE and Akitsu TAKEDA: Transition Energy and Volume Change at Three Transitions in Barium Titanate 1

Gen SHIRANE and Akitsu TAKEDA: Phase Transitions in Solid Solutions of $PbZrO_3$ and $PbTiO_3$ (I) Small Concentrations of $PbTiO_3$........ 5

Gen SHIRANE, Kazuo SUZUKI and Akitsu TAKEDA: Phase Transitions in Solid Solutions of $PbZrO_3$ and $PbTiO_3$ (II) X-ray Study........ 12

Shizuo MIYAKE, Sadao HOSHINO and Toshio TAKENAKA: On the Phase Transition in Cuprous Iodide 19

Masakazu MARUTAKE: The Effect of Electric Field on the Domain Structures in Rochelle Salt 25

Jiro KAKINOKI and Yukitomo KOMURA: Intensity of X-ray Diffraction by an One-Dimensionally Disordered Crystal (I) General Derivation in Cases of the "Reichweite" $S=0$ and 1 30

Shiro OGAWA and Denjiro WATANABE: Electron Diffraction Study on the Ordered Alloy Au_3Cu........ 36

Yasuo GONDO and Zenya FUNATOGAWA: On the Temperature Dependency of Magnetoresistance Effect of Iron Single Crystal........ 41

Takeo YOKOBORI: Failure and Fracture of Metals as Nucleation Processes 44

Takeo YOKOBORI: Creep Fracture of Copper as Nucleation Process 48

Takahiko YAMANOUCHI and Hisashi HORIE: Intensities of Forbidden Lines of Atoms in P^n-configuration........ 52

Hisashi HORIE: Line Strengths for Transitions $d^n \to d^{n-1}p$ and $d^n \to d^{n-1}f$, and Probabilities of Photo-Ionization and Recombination $d^n \leftarrow d^{n-1}$ 58

Kazuo NIIRA and Kiyoshi OOHATA: The Electronic Energies of the CH_2 Radical... 61

Michika MIYANISHI and Kunihiko WATADANI: The Aging Phenomenon in Inert Gas Discharge Tubes 66

Michika MIYANISHI and Kunihiko WATADANI: The Effect of Hydrogen Gas on the Excitation of Auroral Green Line λ 5577 in Discharge Tubes 69

Goro KUWABARA and Kozo ISIGURO: Optical Constants of ZnS Films 72

Shigenori NAWATA: On the Lamellar Reflectivity and Phase Shift for Multiple Reflections........ 75

Hiiro NAKAMURA and Hiroshi KUBOTA: On the Effects of Errors of Micoid Disc in Polanret Microscope 79

Shoji KOJIMA and Soji KONO: A Light Effect of a Diamond Alpha Ray Counter... 84

Itaru NONAKA: Counting Losses of Long Beaded Counters for X-ray Measurements 89

Seizaburo KAGEYAMA: On the Intensities of γ-Rays of RaC 93

Jyumpei SANADA and Yasukazu YOSHIZAWA: On the Binding Energies of Light Nuclei 99

Yoshinobu KAKIUCHI, Hisao SHONO, Hachiro KOMATSU and Kunihiko KIGOSHI: Proton Magnetic Resonance Absorption in Hydrogen Perchlorate Mono-hydrate and the Structure of the Oxonium Ion (I)........ 102

No. 2

Obituary Notice of Professor Shoji NISHIKAWA

Norio RUY: Polarization of Electrons by Scattering, I........ 125

Norio RUY: Polarization of Electrons by Scattering, II 130

Shotaro YAMABE and Jyumpei SANADA: Backward Scattering of D-D Neutrons... 136

Shotaro YAMABE, Masao NOZAWA and Jumpei SANADA: Energy Dependence of the Capture Cross Sections of Ag, Cu and Al for Fast Neutrons........ 140

Naruo TAKETA and Toyoki KOGA: On States not in Thermal Equilibrium, II 143

Takehiko OGUCHI and Yutaka TAKAGI: Statistical Theory of Rotational Phase Transition I 145

Tetsuya ARIZUMI and Seiichi KOTANI: Absorption of Carbon Mono-oxide by the Barium Getter. Part I. Experiments at Low Temperatures 152

Tetsuya ARIZUMI and Seiichi KOTANI: Absorption of Carbon Mono-oxide by the Barium Getter. Part II. Theory of Physical Absorption 158

Tetsuya ARIZUMI and Seiichi KOTANI: Absorption of Carbon Mono-oxide by the Barium Getter. Part III. Lattice Imperfections 163
Masao TOMURA and Yukiaki ABIKO: The Non-Uniform Natures of the Selenium Rectifier 167
Jiro YAMAGUCHI, Takeshi MIYAUCHI and Hideo MORI: Electrical Dispersion of Selenium Rectifier at High Frequency 171
Yuzo TOMONO: Magnetic After Effect of Cold Rolled Iron, I 174
Yuzo TOMONO: Magnetic After Effect of Cold Rolled Iron, II 180
Hiroshi ICHIMURA: A Note on the Theory of the High Polymer Solution 182
Tokio SAKURAI: Microwave Circuit Theory 185
Mikio NAMIKI and Kazuo HORIUCHI: On the Transient Phenomena in the Wave Guide 190
Kazuo NIIRA: On the Abnormal Rotation of OH Radicals 193
Ken'ichi KUSUKAWA: On the Shock Wave in the Elastic Medium 200
Yûkichi NOMURA and Kôshun TAKAKU: On the Propagation of Elastic Waves in an Isotropic Homogeneous Sphere 204
Yoshimasa WADA: On the Recurrent Figure of a Jet 211
Sakae MORITA: Sonde Method of Measuring the Ultrasonic Field Intensity 214

No. 3

Hiroshi ICHIMURA: Statistical Thermodynamics of the Superconducting State 233
Tomoyosi KAWADA: On the Discontinuous Elongation of Aluminium Crystals, IV 240
Tunezo SATOH: On the Mathematical Analysis of the Problem of the Heat Conduction with the Variable Transfer Coefficient 245
Tetsuo WAKATSUKI and Kenzo SUGIMOTO: On the Excitation of Gamma-rays by Fast Neutrons 249
Ryumyo ITO: The End Effects in Geiger Mueller Counters 256
Jiro YAMASHITA and Masao KOJIMA: On the Electronic States of the Doubly-charged Negative Ions of Oxygen in Oxide Crystals 261
Tutô NAKAMURA: Statistical Theory of Hindered Rotation in Molecular Crystals 264
Takeo MATSUBARA: Theory of Diffuse Scattering of X-rays by Local Lattice Distortions 270
Akira ISOYA: A Magnetic Ion Source of Capillary Arc Type 275
Jiro YAMASHITA: Quantummechanical Computations of the Lattice Energy and the Lattice Constant of LiF Crystals 284
Kin-ichi NOGA and Shoji KAWAMURA: External Photoelectric Emission of Barium Oxide 287
Seizaburo KAGEYAMA and Kazuaki NISHIMURA: On the Energy Loss of Fast Electron 292
Teinosuke KANDA: Precise Measurement of the F^{19} Magnetic Moment 296
M. Z. V. KRZYWOBLOCKI: On the Equations of the Decay of Isotropic Turbulence in Compressible Fluid 299
Tetsuya ARIZUMI and Seiichi KOTANI: Gettering Process of Barium; Sorption Properties of Oxygen to Barium 300
Takehito TAKAHASHI: Generalized Spherical Harmonics as Representation Matrix Elements of Rotation Group 307
Mitutosi KAWAGUTI: Note on the Velocity Distribution over an Elliptic Cylinder Submerged in a Uniform Flow of Compressible Fluid 313
Ryosuke YOKOTA: Color Centers in Fused Quartz 316
Hidenori HASIMOTO: Application of the Thin-Wing-Expansion Method to the Compressible Flow past an Elliptic Cylinder 322

No. 4

Toshio AZUMA and Kunihiko TSUMORI: On the Double Coil Magnetic Lens β-ray Spectrometer 341
Seinosuke OZAKI, Shuji FUKUI and Takashi KITAMURA: On the Study of the Penetrating Burst at High Altitude 344

Taro KIHARA and Saburo KOBA: Crystal Structures and Intermolecular Forces of Rare Gases 348
Takeo NAGAMIYA: Theory of Color Centers, I. On Mollwo's Relation and the Temperature Variation in F Absorption Band 354
Takeo NAGAMIYA: Theory of Color Centers, II. On the Nature of V_3 Center in Alkali Halides 358
Humio AKAO, Tatsuo TAKAKURA and Taizô SASAKI: On the Dielectric Constant of the Rochelle Salt at 3000 mc/sec 361
Tokutaro HIRONE and Nobuhiko KUNITOMI: Internal Friction of Field-Cooled Ferromagnetic Substance 364
Seiziro MAEDA: On the Magnetic After Effect due to the Irreversible Displacement of the Domain Boundary (IV) 369
Shûichi IIDA: Formation Energy of Superlattice for Ni_3Fe (I) Co-operative formation of Superlattice at the Critical Temperature 373
Yoshinobu KAKIUCHI and Hachiro KOMATSU: Proton Magnetic Resonance Absorption in Hydrogen Perchlorate Monohydrate and the Structure of the Oxonium Ion II 380
Ken-iti MUNAKATA: Some Exact Solutions in Nonlinear Oscillations 383
Hiroshi SATO: Experimental Study of the Spectrum of Isotropic Turbulence, II... 392
Norio KATO: Dynamical Theory of Electron Diffraction for a Finite Polyhedral Crystal. I. Extension of Bethe's Theory 397
Norio KATO: Dynamical Theory of Electron Diffraction for a Finite Polyhedral Crystal. II. Fraunhofer Formula 406
Tetsuya ARIZUMI and Seiichi KOTANI: Absorption of Carbon Mono-oxide by the Barium Getter. Part IV. Absorption Experiments in the Temperature Renge between 0°C and 250°C 415
Tetsuya ARIZUMI and Seiichi KOTANI: Absorption of Carbon Mono-oxide by the Barium Getter. Part V. Theory of Absorption 422
Nobuzo TÉRAO and Shigéfumi OKADA: Electromicroscopie de la Surface d'une Cassure de Verre 427

No. 5

Obituary Notice of Professor Aikitu TANAKADATE
Hidetosi TAKAHASI: Generalized Theory of Thermal Fluctuations 439
Nobuhiko SAITÔ: A Remark on the Hydrodynamical Theory of the Viscosity of Solutions of Macromolecules 447
Yoshimasa AOKI: Numerical Tables of Overlap Integrals for 3s, 3p Hybrid A.-O... 451
Koichi FURUTSU: On the Group Velocity, Wave Path and their Relations to the Poynting Vector of the Electromagnetic Field in an Absorbing Medium 458
Kiyoshi MURAKAWA and Shigeki SUWA: Structure of the Line λ4686 of He II ... 467
Hiroshi KUBOTA and Teruji OSE: On the Effect of Dispersion and Multiple Reflection upon the Interference Color 470
Tunezo SATOH: Some Complex Boundary Valued Problem and its Application to Kapur-Peierls' Dispersion Formula 474
Ryuma KAWAMURA: Reflection of a Wave at an Interface of Supersonic Flows and Wave Patterns in a Supersonic Compound Jet 482
Tōru KAWAMURA: On the Detached Shock Wave in front of a Body of Revolution moving with Supersonic Speeds 486
Tomomasa TATSUMI: Stability of the Laminar Inlet-flow prior to the Formation of Poiseuille Régime, I 489
Tomomasa TATSUMI: Stability of the Laminar Inlet-flow prior to the Formation of Poiseuille Régime, II 495
Eiichi INOUE: Some Remarks on the Lagrangian Correlation Coefficient of Turbulent Diffusion in a Wind Tunnel Flow 503
Eiichi INOUE: Influences of the Length of Hot-Wire Anemometer on the Measurement of Turbulent Flow 508
M.Z.E. KRZYWOBLOCKI: On the Equations of the Decay of Isotropic Turbulence in Magneto-Hydrodyamics 511

Nobuo INOUE: Some Cases of the Axially Symmetrical Flow of Perfectly Plastic Materials 512
Nobuo INOUE: A Now Method of Solution of the Two-Dimensional Isostatical Problem in the Mathematical Theory of Plasticity 518
Masao TOMURA and Yukiaki ABIKO: Electron Multiplication in Hard Flows of Selenium Rectifiers 524
Hazimu KAWAMURA, Masami ONUKI and Hirosi OKURA: Statistical Time Lag and Electron Avalanche in Dielectric-Breakdown of Mica 528

No. 6

Akiya OOKAWA: Notes on the Crystallite Theory of Liquid 543
Terutosi MURAKAMI: Atomic Distribution in Binary Solid Solutions I. General Theory 549
Nobuhiko SAITÔ and Motoyosi SUGITA: Energy Dissipation and Entropy Production in Irreversible Processes of Dilute Systems 554
Sadao HOSHINO: Crystal Structure and Phase Transition of Some Metallic Halides (II) On the Phase Transition and the Crystal Structures of Cuprous Bromide... 560
Harunobu SAWADA: Statistical Study of the Barkhausen Effect. Part I. Distribution of Domain Size 564
Harunobu SAWADA: Statistical Study of the Barkhausen Effect. Part II. Relation between Domain Size and Internal Stress 571
Harunobu SAWADA: Statistical Study of the Barkhausen Effect. Part III. Distribution of Time Interval 575
Nobuhiko KUNITOMI: Internal Friction of Ferromagnetic Substance Due to Rotation of Spontaneous Magnetization 578
Nobuhiko KUNITOMI: Internal Friction of Ferromagnetic Superlattice Alloy Ni_3Fe... 584
Yasuo GONDÔ and Zenya FUNATOGAWA: On the Magneto-thermoelectric Power of Iron Crystal at low Temperatures 589
Tokutaro HIRONE, Hiroshi WATANABE, Takao IWATA and Kenzi IKEDA: On the A. C. Magnetization Characteristics of a Perminvar Wire 593
Masakazu HAYASHI and Kiichirô KATSUKI: Hydrogen-Like Absorption Spectrum of Cuprous Oxide 599
Nobuo INOUE: Application of Gasdynamical Method to Soil Mechanics and Theory of Plasticity (I) 604
Nobuo INOUE: Application of Gasdynamical Method to Soil Mechanics and Theory of Plasticity (II) 610
Tomomasa TATSUMI: Note on Discrepancies between Two Theories on the Stability of Plane poiseuille Flow 619
Tatudiro SASAKI: On the Solution of Trans-sonic Flow using Laplace Transformation 625
Nobuzo TÉRAO: Un Traitement Statistique de la Résistance à la Rupture du Verre—Sur l'Influence de la Température 627
Nobuzo TÉRAO: Sur la Réfraction de la Cassure par les Chocs 631
Kenji MITANI: The Direct Current associated with Microwave Gas Discharge between Coaxial Cylinders, I 634
Kenji MITANI: The Direct Current associated with Microwave Gas Discharge between Coaxial Cylinders, II 637

SHORT NOTES

No. 1

Wataru SASAKI: Electrical Resistivity of SiC 107
Masayasu UETA: On the Bleaching of Color Centers (M-Center) in KCl Crystal with Polarized Light 107
Yoichi UCHIDA and Hisao YAGI: Absorption of Color-centers in the Region between F-band and M-band 109
Etsuro SAWAGUCHI: Lattice Constant of $PbZrO_3$ 110

Kiichi KIMURA, Ryutaro ISHIWARI, Kazunori YUASA, Sukeaki YAMASHITA, Kozo MIYAKE and Sadao KIMURA: On the Range-Energy Relation and Ionization Energy Relation for Alpha-Particles in Air 111
Tasaburô YAMAGUTI: A Simple Method Obtainingl a Large Single Crystal of Sodium Nitrate 113
Zen'iti KIYASU and Nobuichi IKENO: On the Theory of Multi-terminal Network Synthesis and the Theory of Equivalent Networks 114
Tadashi OSHIDA, Hirohide MIWA and Toshio KATO: On the Depping Counter 114
Masao TOMURA and Yukiaki ABIKO: The Magnetoeffect in Germanium point Contacts 115
Otohiko NOMOTO, Takuro IKEDA and Tadashi KISHIMOTO: Dispersion of Ultrasonic Waves in Ethylene 117
Tasaburô YAMAGUTI and Minoru NISHINO: Micro Analysis of Solutions by Arc of Alternating Currents 118
Nobuo INOUE: On Some Hypothetical Gases 119
Hazimu KAWAMURA and Masami ONUKI: The pulse Size Distribution of the Pre-breakdown Noise 121
Takeo YOKOBORI: Failure and Fracture of Metals as Rate Processes 122

No. 2

Masao TOMURA and Yukiaki ABIKO: Electron Multiplication in hard Flows of Selenium Rectifiers 220
Shin-ichiro NARITA: On the Electrical Conductivity of Oxide-Coated Cathode the Interpretation of Nijboer Theory for BaO from the Viewpoint of Co-existence of Various Impurity Levels 221
Ryosuke YOKOTA: Color Center of Quartz and Fused Quartz 222
Hiroshi YOSHINAGA and Yashiko YAMADA: Construction of a Far Infra-red Spectrometer with Echelette Grating 223
Chiyoe YAMANAKA and Tokuo SUITA: Electron Avalanche and Dielectric Breakdown in Solids II 225
Nobuhiko SAITÔ and Yuichi IKEDA: The Light Scattering by Non-Spherical Particles in Solutions, II. Analytical Formulation 227
Masao TOMURA and Takeo KIKUCHI: Electronic Mobilities of Diamond at Very High Electrostatic Fields 227
Taiji ARAKAWA: Microwave Generation on Opening Electrical Contacts 228
Morikazu TODA: On the Relation between Fermions and Bosons 230

No. 3

Haruzi ISIKAWA: On the Aging after Annealing of Cast Polymethylmethacrylate... 329
Yasuo TORIKAI: On the Image Formation in Phase Microscopy 330
Kinshiro HIRAKAWA: On the Phase Transition in Tungsten Oxide 331
Kikusaburo OSADA: Ultraviolet Absorption Spectra of Glasses Containing Ti, and Heavy Metals 332
Gen SHIRHNE and Kazuo SUZUKI: Crystal Structure of $Pb(Zr-Ti)O_3$ 333
J. YAMASHITA and M. WATANABE: On the Conductivity of Non-polar Crystals in Strong Electrostatic Field 334
Morihiko KIMATA: On the Arc Resistance 335
Etsuro SAWAGUCHI and Tomoyoshi KITTAKA: Antiferroelectricity and Ferroelectricity in Lead Zirconate 336
Hisao HIRABAYASHI and Hiroo TOYODA: Electrical Properties of Amorphous Carbon 337

No. 4

Shigetomo YOSHIDA, Ikuo TAKEDA and Hikaru ARATA: Dissociation of Oxide-Coated Cathode by Primary Electron Bombardment 430
Nobuo INOUE: Study of Supersonic Gas Flow through Nozzle by Plastic Deformation 431
Jitsuo TERADA: Rhombohedral Crystals of Ba-Ca and Sr-Ca Double Carbonates... 432
Yasukazu YOSHIZAWA: On the Effect of the Counter Window for Beta-ray Spectrum 434

Yasuo KANAI: On the Transistor Action of Silicon Crystals 435
I. HIGASHINO, M. ODA, T. OSHIO, H. SHIBATA and Y. WATASE: A preliminary Study on the Anomalous Scattering of Cosmic-rays at 50 m.w.e. Underground 436

No. 5

Mikio NAMIKI: A Variational Method for Determination of the Propagation Parameter 533
Syōhei MIYAHARA and Tadayasu MITUI: Effect of Magnetic Field on Precipitation of Ferromagnetic Phase 534
Yasuo KANAI: Artificial Preparation of Silicon Single Crystals 534
H. KUMAGAI, H. ABE, J. SHIMADA, I. HAYASHI, K. ÔNO and H. IBAMOTO: On the Frequency Dependence of Widths in Paramagnetic Resonance of $CuK_2Cl_4 \cdot 2H_2O$ 535
Tadashi KISHIMOTO and Otohiko NOMOTO: Ultrasonic Absorption in Carbon Disulphide 537
Masao TOMURA and Takeo KIKUCHI: Electronic Conductivities of Amorphous Solids at High Electric Fields 538
Hazime KAWAMURA and Hirosi OKURA: The Formative Time Lag of Dielectric Breakdown 540

No. 6

Shigetomo YOSHIDA and Ikuo TAKEDA: Secondary Electron Emission from Oxide-Coated Cathode 639
Yoshio INUISHI and Tokuo SUITA: Breakdown Probability and Time Lag 640
Yoshio INUISHI and Tokuo SUITA: Time Lag in Dielectric Breakdown of Single Crystals 641
Yoshio INUISHI and Tokuo SUITA: A Note on the Furry-Wijsmann's Distribution in Case which Contains Electron Trapping 643
Gunji SHINODA, Tatsuro SUZUKI and Susumu KATO: Electronic Spectroscopy for Soft X-ray Region.. 644
Hisao MIYAZAWA and Shun-ichi FUKUHARA: Electrolytic Conduction in Cs_3Sb 645
Hisao MIYAZAWA, Kin-ichi NÔGA, Sôshin CHIKAZUMI and Akio KOBAYASHI: On the Composition of Antimony-Caesium Photocathode 647
Tohru KAMEI: Quadrupole Resonance in Solid Iodine.. 649
Shoji KOJIMA and Kiyoe KATO: On the Noise of Decaying Electrets...................... 650
VOLUME CONTENTS.. i
AUTHOR INDEX TO VOL. 7 vii

Errata

Hiroshi FUJITA and Akira KISHIMOTO: A Method for Determining the Concentration Dependence of Diffusion Coefficient.. 124
Tohru KAMEI: Mechanical Barkhausen Effect 124
Ken'iti HIGASI and Yasumoto OZAWA: On High Frequency Power Loss of Dielectrics 124
M. HIRABAYASHI: Existence of the Superlattice $CuAu_3$ 339
Shizuo MIYAKE, Sadao HOSHINO and Toshio TAKENAKA: On the Phase Transition in Cuprous Iodide 339
Zen'iti KIYASU and Nobuiti IKENO: On the Theory of Multi-terminal Network Synthesis and Theory of Equivalent Networks 339
Y. KAKIUCHI, H. SHONO, H. KOMATSU and K. KIGOSHI: Proton Magnetic Resonance Absorption in Hydrogen Perchlorate and the Structure of the Oxonium Ion I... 438
Ryuji ABE: A Study on Corrosion-Process of Iron by Means of Electron Diffraction 542
Taro KIHARA and Saburo KOBA: Crystal Structures and Intermolecular Forces of Rare Gases.. 652
Mikio NAMIKI and Kazuo HORIUCHI: On the Transient Phenomena in the Wave Guide.. 652

AUTHOR INDEX TO Vol. 7

ABE H.

- H. KUMAGAI, ———, J. SHIMADA, I. HAYASHI, K. ONO and H. IBAMOTO: On the Frequency Dependence of Widths in Paramagnetic Resonance of CuK$_2$Cl$_4$·2H$_2$O 535

ABE Ryuji: (Errata) A Study on Corrosion-Process of Iron by Means of Electron Diffraction 542

ABIKO Yukiaki;

- M. TOMURA and ———: The Magnetoeffect in Germanium Point Contacts 115
- M. TOMURA and ———: The Non-Uniform Natures of the Selenium Rectifier 167
- M. TOMURA and ———: Electron Multiplication in Hard Flows of Selenium Rectifiers 220
- M. TOMURA and ———: Electron Multiplication in Hard Flows of Selemium Rectifiers 524

AKAO Humio;

- ———, T. TAKAKURA and T. SASAKI: On the Dielectric Constant of the Rochelle Salt at 3000mc/sec 361

AOKI Yoshimasa: Numerical Tables of Overlap Integrals for 3s, 3p Hybrid A.-O. 451

ARAKAWA Taiji: Microwave Generation on Opening Electrical Contacts 228

ARATA Hikaru;

- S. YOSHIDA, I. TAKEDA and ———: Dissociation of Oxide-Coated Cathode by Primary Electron Bombardment 430

ARIZUMI Tetsuya;

- ——— and S. KOTANI: Absorption of Carbon Mono-oxide by the Barium Getter. Part I. Experiments at Low Temperatures 152
- ——— and S. KOTANI: Absorption of Carbon Mono-oxide by the Barium Getter. Part II. Theory of Physical Absorption 158
- ——— and S. KOTANI: Absorption of Carbon Mono-oxide by the Barium Getter. Part III. Lattice Imperfections 163
- ——— and S. KOTANI: Gettering Process of Barium; Sorption Properties of Oxygen to Barium 300
- ——— and S. KOTANI: Absorption of Carbon Mono-oxide by the Barium Getter. Part IV. Absorption Experiments in the Temperature Renge between 0°C and 250°C 415
- ——— and S. KOTANI: Absorption of Carbon Mono-oxide by the Barium Getter. Part V. Theory of Absorption 422

AZUMA Toshio;

- ——— and K. TSUMORI: On the Double Coil Magnetic Lens β-ray Spectrometer 341

CHIKAZUMI Soshin;

- H. MIYAZAWA, K. NOGA, ——— and A. KOBAYASHI: On the Composition of Antimony-Caesium Photocathode 647

FUJITA Hiroshi;

- ——— and A. KISHIMOTO: (Errata) A Method for Determining the Concentration Dependence of Diffusion Coefficient 124

FUKUHARA Shun-ichi;

- H. MIYAZAWA and ———: Electrolytic Conduction in Cs$_3$Sb 645

FUKUI Shuji;

- S. OZAKI, ——— and T. KITAMURA: On the Study of the Penetrating Burst at High Altitude 344

FUNATOGAWA Zenya;

- Y. GONDO and ———: On the Temperature Dependency of Magneto-resistance Effect of Iron Single Crystal 41
- Y. GONDO and ———: On the Magneto-thermoelectric Power of Iron Crystal at Low Temperatures 589

FURUTSU Koichi: On the Group Velocity, Wave Path and their Relations to the Poynting Vector of the Electromagnetic Field in an Absorbing Medium... 458

GONDO Yasuo;
——— and Z. FUNATOGAWA: On the Temperature Dependency of Magneto-resistance Effect of Iron Single Crystal 41
——— and Z. FUNATOGAWA: On the Magneto-thermoelectric Power of Iron Crystal at Low Temperatures 589
HASIMOTO Hidenori: Application of the Thin-Wing Expansion Method to the Compressible Flow past an Elliptic Cylinder 322
HAYASHI I.
H. KUMAGAI, H. ABE, J. SHIMADA, ———, K. ONO and H. IBAMOTO: On the Frequency Dependence of Widths in Paramagnetic Resonance of $CuK_2Cl_4 \cdot H_2O$ 535
HAYASHI Masakazu;
——— and K. KATSUKI: Hydrogen-Like Absorption Spectrum of Cuprous Oxide 599
HIGASI Ken'iti;
——— and Y. OZAWA: On High Frequency Power Loss of Dielectrics 124
HIGASHINO I.
———, M. ODA, T. OSHIO, H. SHIBATA and Y. WATASE: A Preliminary Study on the Anomalous Scattering of Cosmic-Rays at 50 m.w.e. Underground 436
HIRABAYASHI Hisao;
——— and H. TOYODA: Electrical Properties of Amorphous Carbon 337
HIRABAYASHI M.: (Errata) Existence of the Superlattice $CuAu_3$ 339
HIRAKAWA Kinshiro: On the Phase Transition in Tungsten Oxide 331
HIRONE Tokutaro;
——— and N. KUNITOMI: Internal Friction of Field-Cooled Ferromagnetic Substance 364
HIRONE Tokutaro;
———, H. WATANABE, T. IWATA and K. IKEDA: On the A.C. Magnetization Characteristics of a Perminvar Wire 593
HORIE Hisashi;
T. YAMANOUCHI and ———: Intensities of Forbidden Lines of Atoms in P^n-configuration 52
———: Line Strengths for Transitions $d^n \to d^{n-1}p$ and $d^n \to d^{n-1}f$, and Probabilities of Photo-Ionization and Recombination $d^n \leftarrow d^{n-1}$ 58
HORIUCHI Kazuo;
M. NAMIKI and ———: On the Transient Phenomena in the Wave Guide 190
M. NAMIKI and ———: (Erata) On the Transient Phenomena in the Wave Guide 652
HOSHINO Sadao;
S. MIYAKE, ——— and T. TAKENAKA: On the Phase Transition in Cuprous Iodide 19
S. MIYAKE, ——— and T. TAKENAKA: (Errata) On the Phase Transition in Cuprous Iodide 339
- - : Crystal Structure and Phase Transition of Some Metallic Halides, II. On the Phase Transition and the Crystal Structures 560
IBAMOTO H.
H. KUMAGAI, H. ABE, J. SHIMADA, I. HAYASHI, K. ÔNO and ———: On the Frequency Dependence of Widths in Paramagnetic Resonance of $CuK_2Cl_4 \cdot 2H_2O$ 535
ICHIMURA Hiroshi: A Note on the Theory of the High Polymer Solution 182
- - : Statistical Thermodynamics of the Superconducting State 233
IIDA Shuichi: Formation Energy of Superlattice for Ni_3Fe (I) Co-operative Formation of Superlattice at the Critical Temperature 373
IKEDA Kenzi;
T. HIRONE, H. WATANABE, T. IWATA and ———: On the A.C. Magnetization Characteristics of a Perminvar Wire 593

IKEDA Takuro;
O. NOMOTO, ——— and T. KISHIMOTO: Dispersion of Ultrasonic Waves in Ethylene 117
IKEDA Yuichi;
N. SAITÔ and ———: The Light Scattering by Non-Spherical Particles in Solutions, II. Analytical Formulation 227
IKENO Nobuichi;
Z. KIYASU and ———: On the Theory of Multi-terminal Network Synthesis and the Theory of Equivalent Networks........ 114
Z. KIYASU and ———: (Errata) On the Theory of Multi-terminal Network Synthesis and Theory of Equivalent Networks 339
INOUE Eiichi: Some Remarks on the Lagrangian Correlation Coefficient of Turbulent Diffusion in a wind Tunnel Flow 503
———: Influences of the Length of Hot-Wire Anemometer out the Measurement of Turbulent Flow........ 508
INOUE Nobuo: On Some Hypothetical Gases 119
———: Study of Supersonic Gas Flow through Nozzle by Plastic Deformation 431
———: Some Cases of the Axially Symmetrical Flow of Perfectly plastic Materials........ 512
———: A Now Method of Solution of the Two Dimensional Isostatical Problem in the Mathematical Theory of Plasticity 518
———: Application of Gasdynamical Method to Soil Mechanics and Theory of Plasticity (I) 604
———: Application of Gasdynamical Method to Soil Mechanics and Theory of Plasticity (II) 610
INUISHI Yoshio;
——— and T. SUITA: Breakdown Probability and Time Lag 640
——— and T. SUITA: Time Lag in Dielectric Breakdown of Single Crystals... 641
——— and T. SUITA: A Note on the Furry-Wijsmann's Distribution in Case which Contains Electron Trapping 643
ISHIWARI Ryutaro;
K. KIMURA, ———, K. YUASA, S. YAMASHITA, K. MIYAKE and S. KIMURA: On the Range-Energy Relation and Ionisation Energy Relation for Alpha-Particles in Air 111
ISIGURO Kozo;
G. KUWABARA and ———: Optical Constants of ZnS Films 72
ISIKAWA Haruzi: On the Aging after Annealing of Cast Polymethylmethacrylate 329
ISOYA Akira: A Magnetic Ion Source of Capillary Arc Type........ 275
ITO Ryumyo: The End Effects in Geiger Mueller Counters 256
IWATA Takao;
T. HIRONE, H. WATANABE, ——— and K. IKEDA: On the A. C. Magnetization Characteristics of a Perminvar Wire 593
KAGEYAMA Seizaburo: On the Intensities of γ-Rays of RaC 93
——— and K. NISHIMURA: On the Energy Loss of Fast Electron 292
KAKINOKI Jiro;
——— and Y. KOMURA: Intensity of X-ray Diffraction by an One-Dimensionally Disordered Crystal (I) General Derivation in Cases of the "Reichweite" $S=0$ and 1 30
KAKIUCHI Yoshinobu;
———, H. SHONO, H. KOMATSU and K. KIGOSHI: Proton Magnetic Resonance Absorption in Hydrogen Perchlorate Mono-hydrate and the Structure of the Oxonium Ion (I) 102
——— and H. KOMATSU: Proton Magnetic Resonance Absorption in Hydrogen Perchlorate Monohydrate and the Structure of the Oxonium Ion (II) 380

———, H. SHONO, H. KOMATSU and K. KIGOSHI: (Errata) Proton Magnetic Oxonium Resonance Absorption in Hydrogen Perchlorate and the Structure of the Ion (I) 438
KAMEI Tohru: (Errata) Mechanical Barkhausen Effect........ 124
———: Quadrupole Resonance in Solid Iodine........ 649
KANAI Yasuo: On the Transistor Action of Silicon Crystals 435
———: Artificial Preparation of Silicon Single Crystals 534
KANDA Teinosuke: Precise Measurement of the F^{19} Magnetic Moment 296
KATO Kiyoe;
S. KOJIMA and ———: On the Noise of Decaying Electrets........ 650
KATO Norio: Dynamical Theory of Electron Diffraction for a Finite Polyhedral Crystal. I. Extension of Bethe's Theory 397
———: Dynamical Theory of Electron Diffraction for a Finite Polyhedral Crystal. II. Fraunhofer Formula 406
KATO Susumu;
G. SHINODA, T. SUZUKI and ———: Electronic Spectroscopy for Soft X-ray Region 644
KATO Toshio;
T. OSHIDA, H. MIWA and ———: On the Depping Counter 114
KATSUKI Kiichiro;
M. HAYASHI and ———: Hydrogen-Like Absorption Spectrum of Cuprous Oxide........ 599
KAWADA Tomoyosi: On the Discontinuous Elongation of Aluminium Crystals, IV... 240
KAWAGUTI Mitutosi: Note on the Velocity Distribution over an Elliptic Cylinder Submerged in a Uniform Flow of Compressible Fluid 313
KAWAMURA Hazimu;
——— and M. ONUKI: The Pulse Size Distribution of the Prebreakdown Noise........ 121
———, M. ONUKI and H. OKURA: Statistical Time Lag and Electron Avalanche in Dielectric-Breakdown of Mica 528
——— and H. OKURA: The Formative Time Lag of Dielectric Breakdown... 540
KAWAMURA Ryuma: Reflection of a Wave at an Interface of Supersonic Flows and Wave Patterns in a Supersonic Compound Jet 482
KAWAMURA Shoji;
K. NOGA and ———: External Photoelectric Emission of Barium Oxide ... 287
KAWAMURA Tōru: On the Detached Shock Wave in front of a Body of Revolution moving with Supersonic Speeds 486
KIGOSHI Kunihiko;
Y. KAKIUCHI, H. SHONO, H. KOMATSU and ———: Proton Magnetic Resonanc Absorption in Hydorgen Perchlorate Mono-hydrate and the Structure of the Oxonium Ion (I) 102
Y. KAKIUCHI, H. SHONO, H. KOMATSU and ———: (Errata) Proton Magnetic Resonance Absorption in Hydrogen Perchlorate and the Structure of the Oxonium Ion I........ 438
KIHARA Taro;
——— and S. KOBA: Crystal Structures and Intermolecular Forces of Rare Gases........ 348
——— and S. KOBA: (Errata) Crystal Structures and Intermolecular Forces of Rare Gases........ 652
KIKUCHI Takeo;
M. TOMURA and ———: Electronic Mobilities of Diamond at Very High Electrostatic Fields........ 227
M. TOMURA and ———: Electronic Conductivities of Amorphous Solids at High Electric Fields 538
KIMATA Morihiko: On the Arc Resistance 335
KIMURA Kiichi;
———, R. ISHIWARI, K. YUASA, S. YAMASHITA, K. MIYAKE and S. KIMURA: On the Range-Energy Relation and Ionization Energy Relation for Alpha-Particles in Air........ 111

KIMURA Sadao;
  K. KIMURA, R. ISHIWARI, K. YUASA, S. YAMASHITA, K. MIYAKE and ———: On the Range-Energy Relation and Ionization Energy Relation for Alpha-Particles in Air 111
KISHIMOTO Akira;
  H. FUJITA and ———: (Errata) A Method for Determining the Concentration Dependence of Diffusion Coeffcient 124
KISHIMOTO Tadashi;
  O. NOMOTO, T. IKEDA and ———: Dispersion of Ultrasonic Waves in Ethylene 117
  ——— and O. NOMOTO: Ultrasonic Absorption in Carbon Disulphide 537
KITAMURA Takashi;
  S. OZAKI, S. FUKUI and ———: On the Study of the Penetrating Burst at High Altitude 344
KITTAKA Tomoyoshi;
  E. SAWAGUCHI and ———: Antiferroelectricity and Ferroelectricity in Lead Zirconate 336
KIYASU Zen'iti;
  ——— and N. IKENO: On the Theory of Multi-terminal Network Synthesis and the Theory of Equivalent Networks 114
  ——— and N. IKENO: (Errata) On the Theory of Multi-terminal Network Synihesis and Theory of Equivalent Networks 339
KOBA Saburo;
  T. KIHARA and ———: Crystal Structures and Intermolecular Forces of Rare Gases 348
  T. KIHARA and ———: (Errata) Crystal Structures and Intermolecular Forces of Rare Gases 652
KOBAYASHI Akio;
  H. MIYAZAWA, K. NOGA, S. CHIKAZUMI and ———: On the Composition of Antimony-Caesium Photocathode 647
KOGA Toyoki;
  N. TAKETA and ———: On States not in Thermal Equilibrium, II 143
KOJIMA Shoji;
  ——— and S. KONO: A Light Effect of a Diamond Alpha Ray Counter ... 84
  ——— and K. KATO: On the Noise of Decaying Electrets 650
KOJIMA Masao;
  J. YAMASHITA and ———: On the Electronic States of the Doubly-charged Negative Ions of Oxygen in Oxide Crystals 261
KOMATSU Hachiro;
  Y. KAKIUCHI, H. SHONO, ——— and K. KIGOSHI: Proton Magnetic Resonance Absorption in Hydorgen Perchlorate Mono-hydrate and the Structure of the Oxonium Ion (I) 102
  Y. KAKIUCHI and ———: Proton Magnetic Resonance Absortion in Hydrogen Perchlorate Monohydrate and the Sturcture of the Oxonium Ion II 380
  Y. KAKIUCHI, H. SHONO, ——— and K. KIGOSHI: (Errata) Proton Magnetic Resonance Absorption in Hydrogen Perchlorate and the Structure of the Oxonium Ion (I) 438
KOMURA Yukitomo;
  J. KAKINOKI and ———: Intensity of X-ray Diffraction by an One-Dimensionally Disordered Crystal. (I) General Derivation in Cases of the "Reichweite" $S=0$ and 1 30
KONO Soji;
  S. KOJIMA and ———: A Light Effect of a Diamond Alpha Ray Counter... 84
KOTANI Seiichi;
  T. ARIZUMI and ———: Absorption of Carbon Mono-oxide by the Barium Getter. Part I. Experiments at Low Temperatures 152
  T. ARIZUMI and ———: Absorption of Carbon Mono-oxide by the Barium Getter. Part II. Theory of Physical Absorption 158

T. ARIZUMI and ———: Absorption of Carbon Mono-oxide by the Barium Getter. Part III. Lattice Imperfections 163
T. ARIZUMI and ———: Gettering Process of Barium; Sorption Properties of Oxygen to Barium 300
T. ARIZUMI and ———: Absorption of Carbon Mono-oxide by the Barium Getter. Part IV. Absorption Experiments in the Temperature Renge between 0°C and 250°C 415
T. ARIZUMI and : Absorption of Carbon Mono-oxide by tne Barium Getter. Part V. Theory of Absorption 422
KRZYWOBLOCKI M.Z.V.: On the Equations of the Decay of Isotropic Turbulence in Compressible Fluid 299
: On the Equations of the Decay of Isotropic Turbulence in Magnetohydrodynamics 511
KUBOTA Hiroshi;
H. NAKAMURA and ———: On the Effects of Errors of Micoid Disc in Polanret Microscope 79
- and T. OSE: On the Effect of Dispersion and Multiple Reflection upon the Interference Color 470
KUMAGAI H.;
, H. ABE, J. SHIMADA, I. HAYASHI, K. ONO and H. IBAMOTO: On the Frequency Dependence of Widths in Paramagnetic Resonance of $CuK_2Cl_4\cdot 2H_2O$ 535
KUNITOMI Nobuhiko;
T. HIRONE and ———: Internal Friction of Field-Cooled Ferromagnetic Substance 364
———: Internal Friction of the Ferromagnetic Substances Due to Rotation of the Spontaneous Magnetization 578
———: Internal Friction of Ferromagnetic Superlatties Alloy Ni_3Fe 584
KUSUKAWA Ken'ichi: On the Shock Wave in the Elastic Medium 200
KUWABARA Goro;
——— and K. ISIGURO: Optical Constants of ZnS Films 72
MAEDA Seiziro: On the Magnetic After Effect due to the Irreversible Displacement of the Domain Boundary (IV) 369
MARUTAKE Masakazu: The Effect of Electric Field on the Domain Structures in Rochelle Salt 25
MATSUBARA Takeo: Theory of Diffuse Scattering of X-rays by Local lattice Distortions 270
MITANI Kenji: The Direct Current associated with Microwave Gas Discharge between Coaxial Cylinders, I 634
———: The Direct Current associated with Microwave Gas Discharge between Coaxial Cylinders, II 637
MITUI Tadayasu;
S. MIYAHARA and ———: Effect of Magnetic Field on Precipitation of Ferromagnetic Phase 534
MIYAHARA Ryohei;
——— and T. MITUI: Effect of Magnetic Field on Precipitation of Ferromagnetic Phase 534
MIYAKE Shizuo;
———, S. HOSHINO and T. TAKENAKA: On the Phase Transition in Cuprous Iodide 19
: S. HOSHINO and T. TAKENAKA: (Errata) On the Phase Transition in Cuperous Iodide 339
MIYAKE Kozo;
K. KIMURA, R. ISHIWARI, K. YUASA, S. YAMASHITA, ———, and S. KIMURA: On the Range-Energy Relation and Ionization Energy Relation for Alpha-Particles in Air 111
MIYANISHI Michika;
— and K. WATADANI: The Aging Phenomenon in Inert Gas Discharge Tubes 66

MIYANISHI Michika;
—— and K. WATADANI: The Effect of Hydrogen Gas on the Excitation of Auroral Green Line λ 5577 in Discharge Tubes 69
MIYAUCHI Takeshi;
J. YAMAGUCHI, —— and F. MORI: Electrical Dispersion of Selenium Rectifier at High Frequency 171
MIYAZAWA Hisao;
—— and S. FUKUHARA: Electrolytic Conduction in Cs_3Sb 645
——, K. NOGA, S. CHIKAZUMI and A. KOBAYASHI: On the Composition of Antimony-Caesium Photocathode 647
MIWA Hirohide;
T. OSHIDA, —— and T. KATO: On the Depping Counter 114
MIYAHARA Syohei;
—— and T. MITUI: Effect of Magnetic Field on Precipitation of Ferromagnetic Phase 534
MORI Hideo;
J. YAMAGUCHI, T. MIYAUCHI and ——: Electrical Dispersion of Selenium Rectifier at High Frequency 171
MORITA Sakae: Sonde Method of Measuring the Ultrasonic Field Intensity 214
MUNAKATA Ken-ichi: Some Exact Solutions in Nonlinear Oscillations 383
MURAKAMI Terutosi: Atomic Distribution in Binary Solid Solutions, I. General Theory 549
MURAKAWA Kiyoshi;
—— and S. SUWA: Structure of the Line λ 4886 of He II 467
NAGAMIYA Takeo: Theory of Color Centers, I. On Mollow's Relation and the Temperature Variation in F Absorption Band 354
——: Theory of Color Centers, II. On the Nature of V_3 Center in Alkali Halides 358
NAKAMURA Hiiro;
—— and H. KUBOTA: On the Effects of Errors of Micoid Disc in Polanret Microscope 79
NAKAMURA Tutô: Statistical Theory of Hindered Rotation in Molecular Crystals... 264
NAMIKI Mikio;
—— and K. HORIUCHI: On the Transient Phenomena in the Wave Guide... 190
—— and K. HORIUCHI: (Errata) On the Transient Phenomena in the Wave Guide 652
——: A Variational Method for Determination of the Propagation Parameter 533
NARITA Shin-ichiro: On the Electrical Conductivity of Oxide-Coated Cathode the Interpretation of Nijboer Theory for BaO from the Viewpoint of Coexistence of Various Impurity Levels 221
NAWATA Shigenori: On the Lamellar Reflectivity and Phase Shift for Multiple Reflections 75
NIIRA Kazuo;
—— and K. OOHATA: The Electronic Energies of the CH_2 Radical 61
——: On the Abnormal Rotation of OH Radicals 193
NISHIMURA Kazuaki;
S. KAGEYAMA and ——: On the Energy Loss of Fast Electron 292
NISHINO Minoru;
T. YAMAGUTI and ——: Micro Analysis of Solutions by Arc of Alternating Currents 118
NOGA Kin-ichi;
—— and S. KAWAMURA: External Photoelectric Emission of Barium Oxide 287
H. MIYAZAWA, ——, S. CHIKAZUMI and A. KOBAYASHI: On the Composition of Antimony-Caesium Photocathode 647
NOMOTO Otohiko;
——, T. IKEDA and T. KISHIMOTO: Dispersion of Ultrasonic Waves in Ethylene 117

T. KISHIMOTO and : Ultrasonic Absorption in Carbon Disulphide...... 537

NOMURA Yûkichi;
- and K. TAKAKU: On the Propagation of Elastic Waves in an Isotropic Homogeneous Sphere........ 204

NONAKA Itaru: Counting Losses of Long Beaded Counters for X-ray Measurements 89

NOZAWA Masao;
S. YAMABE, ——— and J. SANADA: Energy Dependence of the Capture Cross Sections of Ag, Cu and Al for Fast Noutrons........ 140

ODA M;
I. HIGASHINO, ———, T. OSHIO, H. SHIBATA and Y. WATASE: A Priliminary Study on the Anomalous Scattering of Cosmic-Rays at 50 m.w.e. Underground........ 436

OGAWA Shiro;
——— and D. WATANABE: Electron Diffraction Study of the Ordered Alloy Au_3Cu........ 36

OGUCHI Takehiko;
——— and Y. TAKAGI: Statistical Theory of Rotational Phase Transition I 145

OKADA Shigéfumi;
N. TÉRAO and ———: Electromicroscopie de la Surface d'une Cassure de Verre........ 427

OKURA Hirosi;
H. KAWAMURA, M. ONUKI and ———: Statistical Time Lag and Electron Avalanche in Dielectric-Breakdown of Mica........ 528
H. KAWAMURA and ———: The Formative Time Lag of Dielectric Breakdown........ 540

ÔNO K.
H. KUMAGAI, H. ABE, J. SHIMADA, I. HAYASHI, ——— and H. IBAMOTO: On the Frequency Dependence of Widths in Paramagnetic Resonance $CuK_2Cl_4 \cdot 2H_2O$........ 535

ONUKI Masami;
H. KAWAMURA and ———: The Pulse Size Distribution of the Prebreakdown Noise........ 121
H. KAWAMURA, ———, and H. OKURA: Statistical Time Lag and Elecron Avalanche in Dielectric-Breakdown of Mica........ 528

OOKAWA Akiya: Notes on the Crystallite Theory of Liquid........ 543

OOHATA Kiyoshi;
K. NIIRA and ———: The Electronic Energies of the CH_2 Radical........ 61

OSADA Kikusaburo: Ultraviolet Absorption Spectra of Glasses Containing Ti, and Heavy Metals........ 332

OSE Teruji;
H. KUBOTA and : On the Effect of Dispersion and Multiple Reflection upon the Interference Color........ 470

OSHIDA Tadashi;
———, H. MIWA and T. KATO: On the Depping Counter........ 114

OSHIO T.;
I. HIGASHINO, M. ODA, ———, H. SHIBATA and Y. WATASE: A preliminary Stady on the Anomalous Scattering of Cosmic-Rays at 50 m.w.e. Underground........ 436

OZAKI Seinosuke;
———, S. FUKUI and T. KITAMURA: On the Study of the Penetrating Burst at High Altitude........ 344

OZAWA Yasutomo;
K. HIGASI and ———: On High Frequency Power Loss of Dielectrics........ 124

RYU Norio: Polarization of Electrons by Scattering, I........ 125
———: Polarization of Electrons by Scattering, II........ 130

SAITÔ Nobuhiko;
——— and Y. IKEDA: The Light Scattering by Non-Spherical Particles in Solutions II. Analytical Formulation........ 227

———: A Remark on the Hydrodynamical Theory of the Viscosity of Solutions of Macromolecules ... 447
——— and M. SUGITA: Energy Dissipation and Entropy Production in Irreversible Processes of Dilute Systems ... 554
SAKURAI Tokio: Microwave Circuit Theory ... 185
SANADA Jumpei;
——— and Y. YOSHIZAWA: On the Binding Energies of Light Nuclei ... 99
S. YAMABE and ———: Backward Scattering of D-D Neutrons ... 136
S. YAMABE, M. NOZAWA and ———: Energy Dependence of the Capture Cross Sections of Ag, Cu and Al for Fast Noutrons ... 140
SASAKI Taizo;
H. AKAO, T. TAKAKURA and ———: On the Dielectric Constant of the Rochelle Salt at 3000 mc/sec ... 361
SASAKI Tatudiro: On the Solution of Trans-sonic Flow using Laplace Transformation ... 625
SASAKI Wataru: Electrical Resistivity of SiC ... 107
SATO Hiroshi: Experimental Study of the Spectrum of Isotropic Turbulence, II... 392
SATOH Tunezo: On the Mathematical Analysis of the Problem of the Heat Conduction with the Variable Transfer Coefficient ... 245
———: Some Complex Boundary Balued Problem and its Application to Kapur-Peierls' Dispersion Formula ... 474
SAWADA Harunobu: Statistical Study of the Barkhausen Effect. Part I. Distribution of Domain Size ... 564
———: Statistical Study of the Barkhausen Effect. Part II. Relation between Domain Size and Internal Stress ... 571
———: Statistical Study of the Barkhausen Effects. Part III. Distribution of the Interval ... 575
SAWAGUCHI Etsuro: Lattice Constant of $PbZrO_3$ ... 110
——— and T. KITTAKA: Antiferroelectricity and Ferroelectricity in Lead Zirconate ... 336
SHIBATA H.;
I. HIGASHINO, M. ODA, T. OSHIO, ———, and Y. WATASE: A preliminary Study on the Anomalous Scattering of Cosmic-Rays at 50 m.w.e. Underground ... 436
SHIMADA J.;
H. KUMAGAI, H. ABE, ———, I. HAYASHI, K. ÔNO and H. IBAMOTO: On the Frequency Dependence of Widths in Paramagnetic Resonance of $CuK_2Cl_4 \cdot 2H_2O$ ... 535
SHINODA Gunji;
———, T. SUZUKI and S. KATO: Electronic Spectroscopy for Soft X-ray Region ... 644
SHIRANE Gen;
——— and A. TAKEDA: Transition Energy and Volume Change at Three Transitions in Barium Titanate ... 1
——— and A. TAKEDA: Phase Transitions in Solid Solutions of $PbZrO_3$ and $PbTiO_3$ (I) Small Concentrations of $PbTiO_3$ ... 5
———, K. SUZUKI and A. TAKEDA: Phase Transitions in Solid Solutions of $PbZrO_3$ and $PbTiO_3$ (II) X-ray Study ... 12
——— and K. SUZUKI: Crystal Structure of Pb(Zr-Ti)O_3 ... 333
SHONO Hisao;
Y. KAKIUCHI, ———, H. KOMATSU and K. KIGOSHI: Proton Magnetic Resonance Absorption in Hydrogen Perchlorate Mono-hydrate and the Structure of the Oxonium Ion (I) ... 102
Y. KAKIUCHI, ———, H. KOMATSU and K. KIGOSHI: (Errata) Proton Magnetic Resonance Absorption in Hydrogen Perchlorate and the Structure of the Oxonium Ion (I) ... 438

SUGIMOTO Kenzo;

T. WAKATSUKI and ———: On the Excitation of Gamma-rays by Fast Neutrons 249

SUGITA Motoyosi:

N. SAITÔ and ———: Energy Dissipation and Entropy Production in Irreversible Processes of Dilute Systems 554

SUITA Tokuo;

C. YAMANAKA and ———: Electron Avalanche and Dielectric Breakdown in Solids II 225

Y. INUISHI and ———: Breakdown Probability and Time Lag 640

Y. INUISHI and ———: Time Lag in Dielectric Breakdown of Single Crystals 641

Y. INUISHI and ———: A Note on the Furry-Wijsmann's Distribution in Case which Contains Electron Trapping 643

SUWA Shigeki;

K. MURAKAWA and ———: Structure of the Line λ4686 of the He II 467

SUZUKI Kazuo;

G. SHIRANE, ——— and A. TAKEDA: Phase Transitions in Solid Solutions of PbZrO$_3$ and PbTiO$_3$ (II) X-ray Study 12

G. SHIRANE and ———: Crystal Structure of Pb(Zr-Ti)O$_3$........ 333

SUZUKI Tatsuro;

G. SHINODA, ——— and S. KATO: Electronic Spectroscopy for Soft X-ray Region. 644

TAKAGI Yutaka;

T. OGUCHI and ———: Statistical Theory of Rotational Phase Transition I 145

TAKAHASHI Takehito: Generalized Spherical Harmonics as Representation Matrix Elements of Rotation Group........ 307

TAKAHASI Hidetosi: Generalized Theory of Thermal Fluctuations 439

TAKAKU Koshun;

Y. NOMURA and ———: On the Propagation of Elastic Waves in an Isotropic Homogeneous Sphere........ 204

TAKAKURA Tatsuo;

H. AKAO, ——— and T. SASAKI: On the Dielectric Constant of the Rochelle Salt at 3000 mc/sec........ 361

TAKEDA Akitsu;

G. SHIRANE and ———: transition Energy and Volume Change at Three Transitions in Barium Titanate 1

G. SHIRANE and ———: Phase Transitions in Solid Solutions of PbZrO$_3$ and PbTiO$_3$ (I) Small Concentrations of PbTiO$_3$........ 5

G. SHIRANE, K. SUZUKI and ———: Phase Transitions in Solid Solutions of PbZrO$_3$ and PbTiO$_3$ (II) X-ray Study 12

TAKEDA Ikuo;

S. YOSHIDA, ——— and H. ARATA: Dissociation of Oxide-Coated Cathode by Promary Electron Bombardment........ 430

S. YOSHIDA and ———: Secondary Electron Emission from Oxide-Coated Cathode 639

TAKENAKA Toshio;

S. MIYAKE, S. HOSHINO and ———: On the Phase Transition in Cuprous Iodide 19

S. MIYAKE, S. HOSHINO and ———: (Errata) On the Phase Transition in Cuprous Iodide........ 339

TAKETA Naruo;

——— and T. KOGA: On States not in Thermal Equilibrium, II 143

TATSUMI Tomomasa: Stability of the Laminar Inlet-flow prior to the Formation of Poiseuille Régime, I 489

———: Stability of the Laminar Inlet-flow prior to the Formation of Régime, II........ 495

———: Note on Discrepancies between Two Theories on the Stability of Plane Poiseuille Flow 619

TERADA Jitsuo: Rhombohedral Crystals of Ba-Ca and Sr-Ca Double Carbonates ... 432
TÉRAO Nobuzo;
——— and S. OKADA: Electromicroscopie de la Surface d'une Cassure de Verre ... 427
———: Un Traitement Statistique de la Résistance à laR upture du Verre—Sur l'Influence de la Température ... 627
———: Sur la Refraction de la Cassure par les Chocs ... 631
TODA Morikazu: On the Relation between Fermions and Bosous ... 230
TOMONO Yuzo: Magnetic After Effect of Cold Rolled Iron, I ... 174
———: Magnetic After Effect of Cold Rolled Iron, II ... 180
TOMURA Masao;
——— and Y. ABIKO: The Magnetoeffect in Germanium Point Contacts ... 115
——— and Y. ABIKO: The Non-Uniform Natures of the Selenium Rectifier 167
——— and Y. ABIKO: Electron Multiplication in hard Flows of Selenium Rectifiers ... 220
——— and T. KIKUCHI: Electronic Mobilities of Diamond at Very High Electrostatic Fields ... 227
——— and Y. ABIKO: Electron Multiplication in Hard Flows of Selenium Rectifiers ... 524
——— and T. KIKUCHI: Electronic Conductivities of Amorphous Solids at High Electric Fields ... 538
TORIKAI Yasuo: On the Image Formation in Phase Microscopy ... 330
TSUMORI Kunihiko;
T. AZUMA and ———: On the Double Coil Magnetic Lens β-ray Spectrometer 341
TOYODA Hiroo;
H. HIRABAYASHI and ———: Electrical Properties of Amorphous Carbon... 337
UCHIDA Yoichi;
——— and H. YAGI: Absorption of Color-centers in the Region between F-band and M-band ... 109
UETA Masayasu: On the Bleaching of Color Centers (M-Center) in KCl Crystal with Polarized Light ... 107
WADA Yoshimasa: On the Recurrent Figure of a Jet... 211
WAKATSUKI Tetsuo;
——— and K. SUGIMOTO: On the Excitation of Gamma-rays by Fast Neutrons 249
WATADANI Kunihiko;
M. MIYANISHI and ———: The Aging Phenomenon in Inert Gas Discharge Tubes ... 66
M. MIYANISHI and ———: The Effect of Hydrogen Gas on the Excitation of Auroral Green Line λ 5577 in Discharge Tubes ... 69
WATANABE Denjiro;
S. OGAWA and ———: Electron Diffraction Study on the Ordered Alloy Au_3Cu ... 36
WATANABE M.;
J. YAMASHITA and ———: On the Conductivity of Non-polar Crystals in Strong Electrostatic Field ... 334
WATANABE Hiroshi;
T. HIRONE, ———, T. IWATA and K. IKEDA: On the A.C. Magnetization Characteristics of a Perminvar Wire... 593
WATASE Y.;
I. HIGASHINO M. ODA, T. OSHIO, H. SHIBATA and ———: A Priliminary Study on the Anomalous Scattering of Cosmic-Rays at 50 m.w.e. Underground... 436
YAGI Hisao;
Y. UCHIDA and ———: Absorption of Color-centers in the Region between F-band and M-band ... 10
YAMABE Shotaro;
——— and J. SANADA: Backward Scattering of D-D Neutrons... 136
———, M. NOZAWA and J. SANADA: Energy Dependence of the Capture Cross Sections of Ag, Cu and Al for Fast Noutrons ... 140

YAMADA Yashiko;
H. YOSHINAGA and ———: Construction of a Far Infra-red Spectrometer with Echelette Grating 223
YAMAGUCHI Jiro;
———, T. MIYAUCHI and H. MORI: Electrical Dispersion of Selenium Rectifier at High Frequency........ 171
YAMAGUTI Tasaburo: A Simple Method Obtaining a Large Single Crystal of Sodium Nitrate 113
——— and M. NISHINO: Micro Analysis of Solutions by Arc of Alternating Currents........ 118
YAMANAKA Chiyoe;
——— and T. SUITA: Electron Avalanche and Dielectric Breakdown in Solids II........ 225
YAMANOUCHI Takahiko;
——— and H. HORIE: Intensities of Forbidden Lines of Atoms in P^n-configuration 52
YAMASHITA Jiro;
——— and M. KOJIMA: On the Electronic States of the Doubly-charged Negative Ions of Oxygen in Oxide Crystals 261
———: Quantummechanical Computations of the Lattice Energy and the Lattice Constant of Lif Crystals 284
——— and M. WATANABE: On the Conductivity of Non-polar Crystals in Strong Electrostatic Field........ 334
YAMASHITA Sukeaki;
K. KIMURA, R. ISHIWARI, K. YUASA, ———, K. MIYAKE and S. KIMURA: On the Range-Energy Relation and Ionization Energy Relation for Alpha-Particles in Air 111
YOKOBORI Takeo: Failure and Fracture of Metals as Nucleation Processes........ 44
———: Creep Fracture of Copper as Nucleation Process 48
———: Failure and Fractrue of Metals as Rate Processes 122
YOKOTA Ryosuke: Color Center of Quartz and Fused Quartz 222
———: Color Centers in Fused Quartz 316
YOSHIDA Shigetomo;
———, I. TAKEDA and H. ARATA: Dissociation of Oxide-Coated Cathode by Primary Electron Bombardment 430
——— and I. TAKEDA: Secondary Electron Emission from Oxide-Coated Cathode 639
YOSHINAGA Hiroshi;
——— and Y. YAMADA: Construction of a Far Infra-red Spectrometer with Echelette Grating........ 223
YOSHIZAWA Yasukazu;
J. SANADA and ———: On the Binding Energies of Light Nuclei 99
———: On the Effect of the Counter Window for Beta-Ray Spectrum...... 434
YUASA Kazunori;
K. KIMURA, R. ISHIWARI, ———, S. YAMASHITA, K. MIYAKE and S. KIMURA: On the Range-Energy Relation and Ionization Energy Relation For Alpha-Particles in Air........ 111